

PROCEEDINGS OF THE INTERNATIONAL CONFERENCE CENTRIFUGE 94  
SINGAPORE / 31 AUGUST - 2 SEPTEMBER 1994

# CENTRIFUGE 94

*Edited by*

**C.F. LEUNG, F.H. LEE & T.S. TAN**

*Department of Civil Engineering, National University of Singapore*

Accession For	
DTIS - CRA&I	<input checked="" type="checkbox"/>
DTIS - TAB	<input type="checkbox"/>
DTIS - C&I	<input type="checkbox"/>
form 50	
A1	



19941202 039

A.A. BALKEMA / ROTTERDAM / BROOKFIELD / 1994

---

*The texts of the various papers in this volume were set individually by typists under the supervision of each of the authors concerned.*

Authorization to photocopy items for internal or personal use, or the internal or personal use of specific clients, is granted by A.A. Balkema, Rotterdam, provided that the base fee of US\$1.50 per copy, plus US\$0.10 per page is paid directly to Copyright Clearance Center, 222 Rosewood Drive, Danvers, MA 01923, USA. For those organizations that have been granted a photocopy license by CCC, a separate system of payment has been arranged. The fee code for users of the Transactional Reporting Service is: 90 5410 352 3 /94 US\$1.50 + US\$0.10.

Published by

A.A. Balkema, P.O. Box 1675, 3000 BR Rotterdam, Netherlands (Fax: +31.10.413.5947)

A.A. Balkema Publishers, Old Post Road, Brookfield, VT 05036, USA (Fax: +1.802.276.3837)

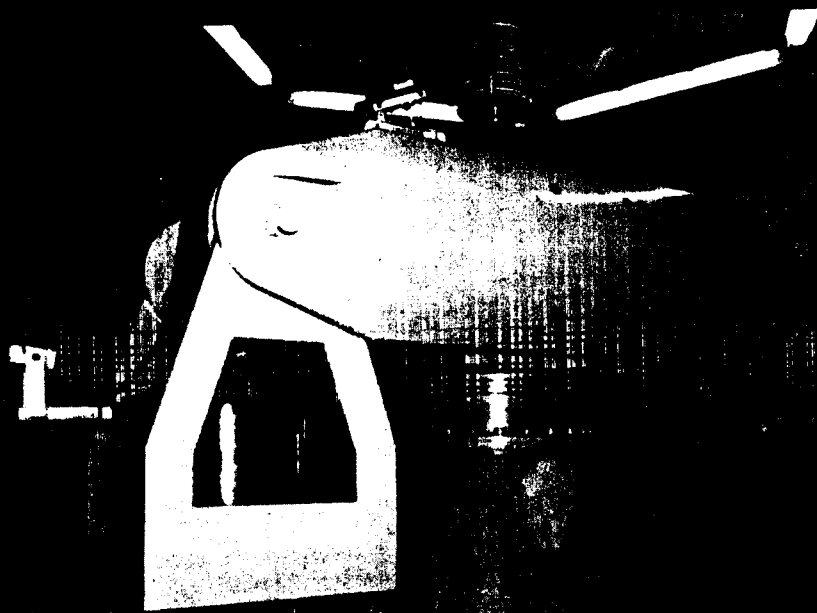
ISBN 90 5410 352 3

© 1994 A.A. Balkema, Rotterdam

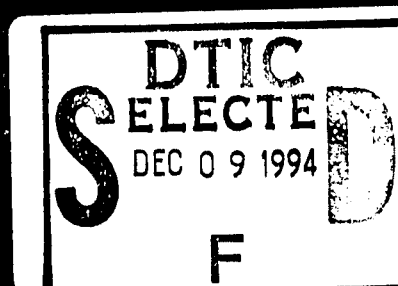
Printed in the Netherlands



# CENTREF



C.F. Leung,  
F.H. Lee  
& T.S. Tan  
Editors



This document has been approved  
for public release and sale; its  
distribution is unlimited.

CENTRIFUGE 94



## Preface

The Technical Committee TC2 on Centrifuge Testing of the International Society of Soil Mechanics and Foundation Engineering (ISSMFE) is the body coordinating the worldwide efforts to develop and promote the use of centrifuge modelling in geotechnical engineering. The last two major international conferences on geotechnical centrifuge testing were CENTRIFUGE 88 held in Paris, France in April 1988 and CENTRIFUGE 91 held in Boulder, USA in June 1991. During the TC2 meeting held right after the Boulder conference, the National University of Singapore (NUS) proposed to host the next conference in Singapore and was invited to submit a formal proposal by TC2. In February 1992, TC2 officially accepted Singapore's proposal and endorsed Singapore as the next venue for CENTRIFUGE 94 to be held from 31 August to 2 September 1994.

The call for papers in early 1993 drew overwhelming response as over 160 abstracts were received. After the review process, about 130 papers were eventually accepted. The significant increase in the number of papers over the previous conferences underscore the increase in popularity in the use of centrifuge modelling for the study of geotechnical problems in the past few years. This volume contains research studies which were carried out on centrifuges at 46 institutions and organisations all over the world. The papers were written by a total of more than 280 authors and co-authors coming from 20 countries of six continents.

When the Conference Organising Committee was formed in February 1992, the themes of the conference were established as:

1. Centrifuge modelling in the study of natural and manmade disasters, as a contribution to the International Decade of Natural Disaster Reduction;
2. Latest developments in centrifuge modelling facilities and equipment;
3. Centrifuge modelling of geotechnical problems with special attention to those which are relevant to Southeast Asia and Australasia.

It is worthy to note that Theme 1 is in fact one of the terms of reference for TC2. This theme is addressed by Professor H.-Y. Ko's keynote paper on 'Modeling seismic problems in centrifuges' and Professor K. Arulanandan's report on the VERification of Liquefaction Analysis using Centrifuge Studies (VELACS) project. In addition, more than 45 papers in this volume deal directly or indirectly with the studies of natural and manmade disasters such as earthquake effects, blast loading, wave loading, contaminant transport and flow problems. These areas see the strongest growth in terms of the number of research studies in recent years especially on the study of liquefaction effects on geotechnical structures. Another area worth mentioning is the study of contaminant transport problems which have also gained increasing popularity.

The centrifuge and associated equipment, instrumentation and testing technologies are constantly going through upgrading all the time in various parts of the world. For example, drum centrifuges are being developed to carry out specified types of studies in recent years. Professor A.N. Schofield is

invited to deliver a keynote lecture on 'Drum centrifuges' at the conference which will lead off Theme 2 of CENTRIFUGE 94. In addition, no less than 20 papers deal with topics on centrifuge modelling facilities and equipment.

One of the main objectives of organising the conference in Singapore is to publicize the applications of centrifuge modelling technique to geotechnical engineers in Singapore, Southeast Asia and Australasia. This is the main reason why Theme 3 is established. Many of the cities in this region are near to the coast. In coastal regions, the soil is often a mixture of clay and sand, termed as 'intermediate soils' by our third keynote lecture, Professor T. Kimura, who will speak on 'Mechanical behaviour of intermediate soils'. There are also 15 papers from Singapore and Australia presented at the conference. A number of the research studies reported are on joint research efforts between the universities and the industry indicating the keen interest in the latter. Besides the above papers, we believe that at least 70% of the papers in this volume are of direct relevance to geotechnical practices in Southeast Asia and Australasia. As engineers from Southeast Asia and Australasia become more familiar with the applications of centrifuge modelling techniques, we hope that more and more joint research between the institutions and industry would take place.

As every paper in this proceedings has undergone a rigorous review process and many geotechnical areas have been covered, we trust that this volume will provide readers a useful source of reference for the state of art and information on the applications of geotechnical centrifuge modelling in various geotechnical fields in the mid-nineties.

Last but not the least, we wish to thank the members of TC2, reviewers of manuscripts, institution sponsors and financial donors who have assisted and supported the organisation of CENTRIFUGE 94.

C.F. Leung  
F.H. Lee  
T.S. Tan

Editors  
Department of Civil Engineering  
National University of Singapore

## Organisation

### ORGANISATION OF THE CONFERENCE

This conference was organised by the Department of Civil Engineering, National University of Singapore in collaboration with the International Society of Soil Mechanics and Foundation Engineering Technical Committee TC2 on Centrifuge Testing. The conference was sponsored by the Australian Geomechanics Society, Institution of Engineers Singapore and the Southeast Asian Geotechnical Society.

### ORGANISING COMMITTEE

C.F. Leung, Chairman  
F.H. Lee, Co-chairman & Treasurer  
T.S. Tan, Secretary  
S.H. Chew, Co-secretary  
G.P. Karunaratne, Member  
M.F. Randolph, Member  
K.Y. Yong, Member

### STEERING & ADVISORY COMMITTEE ISSMFE Technical Committee TC2 (1991-1994)

H.Y. Ko (Chairman), USA	C.F. Leung, Southeast Asia
B.L. Kutter (Secretary), USA	M.P. Luong, France
K. Anderson, Norway	J. Malek, Czechoslovakia
R.F. Azevedo, Brazil	R.J. Mitchell, Canada
V.S. Chandrasekaran, India	H.A.M. Nelissen, Netherlands
J.F. Corté, France	M.F. Randolph, Australia
W.H. Craig, UK	A.N. Schofield, UK
S. Frydman, Israel	R.F. Scott, USA
L. Fuglsang, Denmark	F.C. Townsend, USA
H.L. Jessberger, Germany	T.G. Yakovleva, Russia
T. Kimura, Japan	

## Acknowledgements

### FINANCIAL DONORS

This conference was organised with financial support provided by the following organisations:

Singapore Totalisator Board  
European Research office of the US Army  
Kajima Corporation  
Nikken Sekkei Nakase Geotechnical Institute  
Obayashi Corporation  
Shimizu Corporation  
Taisei Corporation  
Toyo Construction Company Limited  
National Science Foundation, USA

## MANUSCRIPT REVIEWERS

The editors would like to thank the following persons who help to review the manuscripts and hence greatly assist in improving the overall technical standard and presentation of the papers in this proceedings:

H.G.B. Allersma	H.L. Jessberger	R. Phillips
K. Arulanandan	R.J. Jewell	W. Powrie
D. Bloomquist	G.P. Karunaratne	J.L. Pu
M.D. Bolton	M. Kazama	M.F. Randolph
R. Boulanger	S. Ketcham	R. Renzi
B.B. Broms	E. Khoo	R.M. Schmidt
E.S. Chan	G.J.W. King	A. Schürmann
V.S. Chandrasekaran	M. Kitazume	R.F. Scott
S.H. Chew	H.Y. Ko	H. Sekiguchi
Y.K. Chow	D. Konig	S.M. Springman
B. Cooke	O. Kusakabe	R.S. Steedman
J.F. Corté	B.L. Kutter	D.P. Stewart
W.H. Craig	H.K. Law	S. Sture
M.C.R. Davies	K.M. Lee	N. Takada
E.T.R. Dean	E.C. Leong	R.N. Taylor
E.A. Dickin	X.S. Li	T. Taylor
Y. Dou	M.P. Luong	J. Takemura
A.W. Elgamal	S.P.G. Madabhushi	M. Terashi
M. Fahey	C.M. Merrifield	J. Tohda
R.J. Fragaszy	R.J. Mitchell	F.C. Townsend
S. Frydman	C.W.W. Ng	D.M. Wood
J. Garnier	T.G. Ng	N.S. Yet
S.H. Goh	M. Okamura	K.Y. Yong
D.J. Goodings	T. Okumura	X. Zeng
A. Hiro-oka	K. Onitsuka	T.F. Zimmie
Y. Hou	R.Y.S. Pak	D. Znidarčič
R.G. James	M.J. Paulin	



## Table of contents

<b>1 Keynote lectures and VELACS report</b>	
Modeling seismic problems in centrifuges	3
<i>H.-Y. Ko</i>	
Mechanical behaviour of intermediate soils	13
<i>T. Kimura, J. Takemura, A. Hiro-oka &amp; M. Okamura</i>	
What the VELACS project has revealed	25
<i>K. Arulanandan, M. Manzari, X. Zeng, M. Fagan, R. F. Scott &amp; T. S. Tan</i>	
<b>2 Centrifuge facilities</b>	
LXJ-4-450 geotechnical centrifuge in Beijing	35
<i>Y. Du, S. Zhu, L. Han, L. Ru, P. Jia &amp; W. Wang</i>	
Takenaka centrifuge facility	41
<i>K. Suzuki, R. Babasaki &amp; Y. Suzuki</i>	
The University of Delft geotechnical centrifuge	47
<i>H. G. B. Allersma</i>	
Development of medium-size geotechnical centrifuge at Tsinghua University	53
<i>J. L. Pu, F. D. Liu, J. K. Li, S. Q. Li, K. T. Yin, Y. S. Sun &amp; P. F. Jin</i>	
Canadian national centrifuge centre with cold regions capabilities	57
<i>R. Phillips, J. I. Clark, M. J. Paulin, R. Meaney, D. E. L. Millan &amp; K. Tuff</i>	
US Army's engineering centrifuge: Design	63
<i>R. H. Ledbetter, R. S. Steedman, A. N. Schofield, J. F. Corté, J. Perdriat, J. Nicolas-Font &amp; H. M. Voss</i>	
Development of NHRI – 400g. t geotechnical centrifuge	69
<i>Y. Dou &amp; P. Jing</i>	
<b>3 Equipment and instrumentation</b>	
Cone penetration tests in the centrifuge: Experience of five laboratories	77
<i>R. Renzi, J. F. Corté, G. Rault, G. Bagge, M. Gui &amp; J. Laue</i>	

Performance of a sand hopper <i>M.A.Allard, A.G.I.Hjortnæs-Pedersen &amp; J.G.Out</i>	83
Development of a miniature piezocone <i>E.R.Esquivel &amp; H.-Y.Ko</i>	89
Earth pressure distribution on sheet pile walls <i>A.Schürmann &amp; H.L.Jessberger</i>	95
Pore pressure measurement during centrifuge model tests: Experience of five laboratories <i>D.König, H.L.Jessberger, M.Bolton, R.Phillips, G.Bagge, R.Renzi &amp; J.Garnier</i>	101
Performance of an automated centrifuge control system <i>K.L.Goh</i>	109
Side friction effects in plane strain models <i>E.Khoo, T.Okumura &amp; F.H.Lee</i>	115
Techniques for saturating sand with oil <i>Y.S.Hsu, C.H.Collison, E.T.R.Dean &amp; R.G.James</i>	121
Effect of pore fluid in dynamic centrifuge modelling <i>S.P.Gopal Madabhushi</i>	127
The Delft Geotechnics model pore fluid for centrifuge tests <i>M.A.Allard &amp; F.M.Schenkeveld</i>	133
Design and performance of an electrohydraulic shaker for the RPI centrifuge <i>P.A.Van Laak, A.-W.Elgamal &amp; R.Dobry</i>	139
Effect of model containers on dynamic soil response <i>G.L.Fiegel, M.Hudson, I.M.Idriss, B.L.Kutter &amp; X.Zeng</i>	145
Development of an earthquake simulator for the TAISEI centrifuge <i>K.Nagura, M.Tanaka, K.Kawasaki &amp; Y.Higuchi</i>	151
A new dynamic geotechnical centrifuge and performance of shaking table tests <i>M.Sato</i>	157
A device for cyclic displacement-controlled actuation of an integral bridge abutment <i>S.M.Springman, A.Norrish &amp; K.Wilkinson</i>	163
Design of a large earthquake simulator at UC Davis <i>B.L.Kutter, I.M.Idriss, T.Khonke, J.Lakeland, X.S.Li, W.Sluis, X.Zeng, R.C.Tauscher, Y.Goto &amp; I.Kubodera</i>	169
Dynamic capabilities of the Wright Laboratory geotechnical centrifuge facility <i>K.Brownell, M.Purcell, C.A.Hollopeter, R.Fragaszy, T.Taylor &amp; K.L.Olen</i>	177
Development of a dynamic loading device for model foundations <i>T.G.Ng, F.H.Lee, C.Y.Liaw &amp; E.S.Chan</i>	183
 <b>4 Earthquake effects</b>	
Seismic response of gravity type quay wall <i>X.Zeng</i>	191

Comparison of 1g and centrifuge models of a dynamic earth pressure problem <i>M. Kazama, T. Inatomi &amp; E. Iizuka</i>	197
Validation of a computer code for the analysis of dike retaining structures <i>K. K. Muraleetharan, K. Arulmoli, S. V. Jagannath, R. C. Wittkop &amp; J. E. Foxworthy</i>	203
Modeling of tilting retaining wall with saturated backfill <i>N.-H. Ting &amp; R. V. Whitman</i>	209
Liquefaction of sandy ground and settlement of embankments <i>J. Koseki, Y. Koga &amp; A. Takahashi</i>	215
Assessment of earthquake effects on soil embankments <i>S. M. F. Aftaneh, H.-Y. Ko &amp; S. Sture</i>	221
Seismic settlements and pore pressures of shallow foundations <i>L. Liu &amp; R. Dobry</i>	227
Slope stability with seepage in centrifuge model earthquakes <i>N. K. Pilgrim &amp; X. Zeng</i>	233
Permanent displacement of sloping ground due to liquefaction <i>H. Nagase, H.-Y. Ko, H. K. Law &amp; R. Y. S. Pak</i>	239
Simulation of O'Neill Forebay Dam, California, subjected to the 1989 Loma Prieta earthquake <i>H. K. Law, H.-Y. Ko &amp; R. Scavuzzo</i>	245
Liquefaction of the ground reclaimed by urban refuse ash <i>H. Akamoto, M. Miyake, M. Wada &amp; A. Maruyama</i>	251
Dynamic response of a shaft in dry sands <i>M. Honda, N. Ohno, H. Hayashi, J. Zheng &amp; R. F. Scott</i>	257
 <b>5 Dynamic problems</b>	
Behaviour of foundation systems in sand with dynamic sinusoidal loadings <i>J. Laue &amp; H. L. Jessberger</i>	265
Physical simulation of dynamic soil-foundation systems on unbounded media <i>R. Y. S. Pak &amp; B. B. Guzina</i>	271
Experimental study of dynamic soil-pile interaction in sand <i>A. T. Gobert &amp; R. Y. S. Pak</i>	277
Efficiency of a stress-wave mitigation barrier <i>M. P. Luong</i>	283
Simulation of failure of dikes by water infiltration by waves <i>H. G. B. Allersma, I. A. G. Ligtenberg &amp; B. A. N. Koehorst</i>	289
Wave-induced instability of sand beds <i>H. Sekiguchi, K. Kita &amp; O. Okamoto</i>	295
Study of geosynthetic interface friction <i>T. F. Zimmie, A. De &amp; M. B. Mahmud</i>	301

Wave propagation and active vibration control in sand <i>Th. Siemer &amp; H.L. Jessberger</i>	307
Assessing the reliability of results in a dynamic centrifuge test <i>R.J. Frigaszy, K.L. Olen, M. Purcell &amp; K.C. Brownell</i>	313
Dynamic soil structure interaction resulting from blast loading <i>M.C.R. Davies</i>	319
Simulation of cratering in a small geotechnical centrifuge <i>H.G. Ballersma, A.P. Kooijman &amp; W.J. van Niekerk</i>	325
Moisture content effects on explosion-induced craters in sand <i>K.C. Brownell, T. Taylor &amp; W.A. Charlie</i>	331
Comparison between field and centrifuge model tests of heavy tamping <i>N. Takada &amp; A. Oshima</i>	337
 <b>6 Contaminant transport and flow problems</b>	
LNAPL penetration into porous media <i>R.J. Mitchell &amp; B.C. Stratton</i>	345
A flexible, no lateral strain apparatus for clay liner-leachate testing <i>R.J. Mitchell</i>	351
A study of contaminant transport involving density driven flow and hydrodynamic clean up <i>E.E. Hellawell &amp; C. Savvidou</i>	357
Experimental aspects of modelling of migration phenomena <i>H.P. Villar, C.M. Merrifield &amp; W.H. Craig</i>	363
Studies on groundwater transport of radioactive waste <i>H.P. Villar &amp; C.M. Merrifield</i>	369
Simulation of long term performance of landfill covers <i>T.F. Zimmie, M.B. Mahmud &amp; A. De</i>	375
Contaminant migration through clay in a mini-drum centrifuge <i>D.C. Evans, C. Savvidou &amp; A.N. Schofield</i>	381
Scaling concerns for immiscible multiphase flow in porous media <i>S.E. Petersen &amp; B. Cooke</i>	387
Implications of changes in seepage flow regimes for centrifuge models <i>D.J. Goodings</i>	393
Initial stage of soft soil consolidation <i>Z. You &amp; D. Znidarčič</i>	399
Study of sedimentation and flow in thickener tanks <i>R.G. Campbell &amp; M.F. Randolph</i>	405
Determination of soil hydraulic properties <i>B. Cooke</i>	411

Moisture migration and stability of iron ore concentrate cargoes <i>J.H. Atkinson &amp; R.N. Taylor</i>	417
 <i>7 Deep foundations</i>	
Effects of repeated stress on toe resistance of cast-in-place concrete piles <i>F. Okumura, S. Mokutani, M. Okamura, J. Takemura &amp; T. Kimura</i>	425
Pullout resistance of steel pipe piles in improved ground <i>M. Miyake, M. Wada, T. Satoh &amp; Y. Katoh</i>	431
Investigation of pile group efficiencies in sand <i>T. Feld, D. Bloomquist, F.C. Townsend &amp; M.C. McVay</i>	437
Pile uplift and pile cap interaction studies in sand <i>E.A. Dickin &amp; A. Lyndon</i>	443
Settlement of piled raft foundations on clay <i>K. Horikoshi &amp; M.F. Randolph</i>	449
Modelling the behaviour of piles in sand subjected to axial load <i>V. Fioravante, M. Jamiolkowski &amp; S. Pedroni</i>	455
Behaviour of axially loaded piles in sand <i>N.S. Yet, C.F. Leung &amp; F.H. Lee</i>	461
Design and limitations of a pile driving robot <i>A. Zelikson, R.D. Raines &amp; P. Malalel</i>	467
Development of a miniature pile driving actuator <i>A. de Nicola &amp; M.F. Randolph</i>	473
Studies on laterally loaded pile groups in sand <i>M. McVay, D. Bloomquist, D. Vanderlinde &amp; J. Clausen</i>	479
Lateral resistance of a long pile in soft clay <i>M. Kitazume &amp; S. Miyajima</i>	485
Reducing lateral thrust on piles: The 'buttonhole' method <i>S. Springman, F. Bransby &amp; A. Kremer</i>	491
Single piles and pile rows subjected to static and dynamic lateral load <i>M. Kotthaus, T. Grundhoff &amp; H.L. Jessberger</i>	497
Effect of slope and soil density on <i>p-y</i> reaction curves for piles in sand <i>S. Mezazigh, J. Garnier, C. Favraud &amp; D. Levacher</i>	503
Behavior of laterally loaded pile groups in dense sand <i>T. Adachi, M. Kimura, A. Morimoto &amp; H. Kobayashi</i>	509
The interpretation of data from tests on laterally loaded piles <i>G.J.W. King</i>	515
Interaction between foundation of beam-pillar offshore platform and soil <i>C.G. Bao, M. Li, R.G. Shan &amp; H.H. Wang</i>	521

Geometric factors influencing the behaviour of side-bearing foundations in sand <i>E.A. Dickin &amp; R. Nazir</i>	527
 8 <i>Shallow foundations</i>	
Bearing response of shallow foundations in uncemented calcareous soil <i>I.M.S. Finnie &amp; M.F. Randolph</i>	535
Influence of initial conditions on bearing characteristics of sand <i>K. Ueno, T. Nakatomi, K. Mito &amp; O. Kusakabe</i>	541
Verification of shape factors for shallow foundations on sands <i>S.A. Aiban</i>	547
Loading of shallow foundations: Importance of testing procedures <i>N.E. Bakir, J. Garnier &amp; Y. Canepa</i>	553
 9 <i>Embankments and slopes</i>	
Simulation of a sand column trial embankment <i>B.B.K. Huat &amp; W.H. Craig</i>	561
The behaviour of soft subsoil during construction of an embankment and its widening <i>A.G.I. Hjortnaes-Pedersen &amp; H. Broers</i>	567
Failure of embankments due to seepage flows and its countermeasure <i>J. Takemura, T. Kimura, A. Hiro-oka &amp; H. Muraishi</i>	575
Study of settlement of embankment <i>Z.R. Yue, X.M. Zhang &amp; S.T. Jing</i>	581
Embankments with base reinforcement on soft clay <i>M.D. Bolton &amp; J.S. Sharma</i>	587
Evaluation of the cut-off structures of a rockfill dam <i>L. Zhang, J. Zhang &amp; T. Hu</i>	593
Stability of decomposed granite soil slopes <i>S. Yoshitake &amp; K. Onitsuka</i>	599
Stability of cut slopes in Ariake clay <i>K. Onitsuka &amp; K. Yamamoto</i>	605
Effect of soil stress-strain characteristics on slope failure <i>M. Kitazume &amp; M. Terashi</i>	611
Bearing capacity of a foundation on protected slopes <i>M. Terashi, K. Saitoh, N. Katakami, Y. Yamamoto &amp; Y. Taniguchi</i>	617
Geotextile reinforced cohesive slopes on weak foundations <i>A. Porbaha &amp; D.J. Goodings</i>	623
Studies on the stability of model rock slopes <i>D.P. Stewart, D.P. Adhikary &amp; R.J. Jewell</i>	629

Studies of rock slopes for the Three Gorges Project <i>S.H.Han &amp; H.H.Wang</i>	635
 10 <i>Deep excavations and tunnels</i>	
Stability of deep excavations in soft clay <i>S.D.Zhang &amp; H.D.Zhang</i>	643
Excavation in soft clay using an in-flight excavator <i>T.Kimura, J.Takemura, A.Hiro-oka, M.Okamura &amp; J.Park</i>	649
Modelling diaphragm wall installation and excavation processes <i>W.Powrie, D.J.Richards &amp; C.Kantartzi</i>	655
Deformation and failure characteristics of vertical cuts and excavations in clay <i>Y.Toyosawa, N.Horii, S.Tamate, S.Hanayasu &amp; S.K.Ampadu</i>	663
Modelling the soil nailing – Excavation process <i>S.Frydman, A.Levy &amp; R.Baker</i>	669
Modelling of a large underground excavation in China <i>W.Liu, K.M.Lee &amp; S.D.Zhang</i>	675
The influence of a bored tunnel on pile foundations <i>A.Bezuijen &amp; J.van der Schrier</i>	681
Behavior of stacked-drift-type tunnels <i>A.Onoue, H.Kazama, H.Hotta, T.Kimura &amp; J.Takemura</i>	687
Response of a tunnel lining due to an adjacent twin shield tunneling <i>H.Yoshimura, K.Miyabe &amp; J.Tohda</i>	693
A miniature shield tunneling machine for a centrifuge <i>T.Nomoto, K.Mito, S.Imamura, K.Ueno &amp; O.Kusakabe</i>	699
Behaviour of a tunnel lining embedded in a Bentonite quartz flour water mixture in granular soil <i>D.König, H.L.Jessberger, P.Chambon &amp; P.Dangla</i>	705
Face stability of tunnels constructed using the mechanical precutting tunneling method <i>A.Skiker, P.Chambon, E.Leca &amp; J.Garnier</i>	713
Compensation grouting <i>M.D.Bolton, C.Y.Chin &amp; Y.C.Lu</i>	719
 11 <i>Pipes and anchors</i>	
FE elastic analysis of earth pressure on buried flexible pipes <i>J.Tohda, L.Li &amp; H.Yoshimura</i>	727
Soil structure interaction of partially buried flexible pipes <i>M.Javenmard &amp; A.J.Valsangkar</i>	733
Study of pipelines subjected to landslide conditions <i>M.J.Paulin, J.I.Clark, F.Poorooshab &amp; M.Rizkalla</i>	739

Performance of buried corrugated HDPE pipe <i>S.M.Sargand, T.Masada, B.Mao, V.S.R.Yalamanchili &amp; J.O.Hurd</i>	745
Uplift resistance of buried pipelines in granular materials <i>C.W.W.Ng &amp; S.M.Springman</i>	753
Performance of ground anchor models under repeated loading <i>J.M.Carey, W.H.Craig &amp; C.M.Merrifield</i>	759
Model testing and theoretical analysis of drag anchors in sand <i>S.R.Neubecker &amp; M.F.Randolph</i>	765
 12 <i>Miscellaneous topics</i>	
An examination of the integrity of stone columns in soft clay <i>D.P.Stewart &amp; M.Fahey</i>	773
Earth pressure change during rotational failure of retaining wall <i>K.Kawasaki &amp; R.N.Taylor</i>	779
Modeling the stress history of Pisa clay <i>M.Pepe &amp; R.Renzi</i>	785
Experiment and analysis of earth pressure on an axisymmetric shaft in sand <i>T.Fujii, T.Hagiwara, K.Ueno &amp; A.Taguchi</i>	791
Study of sinkholes in weakly cemented sand <i>W.A.Abdulla &amp; D.J.Goodings</i>	797
Ice scouring of the seabed <i>P.R.Lach &amp; J.I.Clark</i>	803
Collapse of cavities in sand and particle size effects <i>B.L.Kutter, J.-D.Chang &amp; B.C.Davis</i>	809
Effect of particle size on localisation development in model tests on sand <i>R.J.White, K.J.L.Stone &amp; R.J.Jewell</i>	817
Behavior of suction caissons under static uplift loading <i>M.J.Morrison, E.C.Clukey &amp; J.Garnier</i>	823
Displacement of gravity caisson resting on sand key <i>C.F.Leung, E.Khoo &amp; A.C.Toh</i>	829
Author index	835



## 1 Keynote lectures and VELACS report

## Modeling seismic problems in centrifuges

Hon-Yim Ko

*University of Colorado, Boulder, Colo., USA*

**ABSTRACT:** Techniques developed to simulate seismic forces in centrifuge testing are reviewed and their advantages and disadvantages compared. Particular attention is focused on the electro-hydraulic method which seems to have received universal acceptance in recent years due to its ability to produce the desired scaled motions in terms of frequency and wave form. Besides generating the appropriate input motion, complete scaling for seismic problems requires the resolution of several other issues, such as the effects of wave reflection from the boundaries of the finite soil model container, and the conflict in the time scaling for the coupled dynamic pore pressure generation and diffusive pore pressure dissipation phenomena. Attempts to resolve these and other issues are reviewed. Seismic simulation is being utilized for various purposes including the study of basic phenomena such as liquefaction, verification of seismic resistant design, and the validation of numerical models. Reference is made to the recently completed VELACS project as well as other projects to illustrate the advances made by this powerful dynamic testing technique.

### 1 INTRODUCTION

Since the revival of interests in the 1960's and 1970's in using centrifuges to model geotechnical systems, the technique has been applied to classical geotechnical problems, such as foundations and slopes, as well as problems which are nontraditional from the geotechnical sense, such as ground freezing and explosive cratering. The advances in this field of geotechnical physical modeling have been documented in the proceedings of the tri-annual conferences organized under the auspices of the Technical Committee on Centrifuge Testing of ISSMFE (Corte, 1988; Ko and McLean, 1991).

In recent years, no application in centrifuge modeling has received more attention than seismic simulation, especially in the United States and Japan, where earthquakes are common occurrences and earthquake hazard mitigation is a major challenge to the engineering profession, especially the geotechnical engineering community. The large earthquakes of Niigata and Alaska in 1964 have helped soil dynamics and geotechnical earthquake engineering become a recognizable sub-discipline and considerable

advances have been made in developing an understanding of the pertinent dynamic soil properties which influence the performance of soil deposits and soil structures under seismic loading.

Numerous analytical procedures, some of which are empirical while others are based on coupled theories of soil/water interaction incorporating elasto-plastic constitutive models, have been proposed to explain and correlate the observed earthquake-induced phenomena. However, due to a lack of quality field data, there remains a considerable gap in our understanding of the phenomena of permanent deformations, especially those occurring during liquefaction, and because of the inherent difficulties in orchestrating full scale seismic events, it has been increasingly obvious that physical modeling in the centrifuge is the best alternative for studying the seismic performance of earth structures. The fact that scale models can be prepared with prescribed soil property profiles and shaken in the simulated gravity environment in a centrifuge with controllable base input motion makes this approach particularly attractive as a means to study the

phenomena qualitatively and to obtain quantitative data for calibrating numerical procedures and validating specific prototype designs.

In this paper, the state of the art in earthquake simulation as related to centrifuge modeling is reviewed. The effects of boundary constraints and the conflicts in scaling relations between dynamic and diffusion phenomena are discussed and efforts to resolve these issues are discussed.

## 2 SEISMIC SIMULATION TECHNIQUES

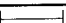



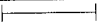
The recognition that physical modeling of seismic events on the centrifuge could produce a data base for a better appreciation of the effects of earthquakes on soil structures has, in the last 15 years, led to intense research to implement seismic simulation capabilities in centrifuge testing facilities. Many different techniques have been tried for generating ground motion on centrifuge models. Morris (1983) and Ortiz et al. (1983) employed the concept of releasing a cocked spring to produce free, damped vibrations on the soil model. The resulting motion depends on the mass of the model and the stiffness of the spring which cannot be easily altered to meet the requirement of a particular test. The bumpy road concept, described by Schofield (1981), was implemented on the Cambridge University centrifuge by Kutter (1983), in which the test package, while in flight, was allowed to make contact with a wavy track mounted on the wall of the centrifuge test chamber. Although the bumpy track was designed to produce 10 cycles of sinusoidal input motion at a single frequency to the soil model, the actual motion obtained is usually contaminated by other frequencies due to the dynamics of the motion transfer mechanism. Another drawback of this method is that the frequency of the input motion is dependent on the speed on the centrifuge which in turn determines the modeling scale. Thus, there is always a fixed relation between the scale factor and the frequency of the input motion, limiting the flexibility which is usually desired for modeling earthquakes of different frequencies and intensity of shaking. While it is theoretically possible to change tracks for different experiments, the costs of doing so have limited the bumpy road technique to one track and in one centrifuge facility only.

Arulanandan et al. (1982) described a system which uses the piezoelectric effects to produce motion by applying fluctuating voltages to a stack of piezoelectric ceramic elements buried in the soil. The main drawbacks of this method are that high voltages are required to produce sufficient amplitude of motion for earthquake simulations and that only high frequency motions are obtainable. Zelikson et al. (1981) used the detonation of explosives at the boundary of the soil container to generate soil motion which is transmitted to the test model. A similar method of boundary excitation was described by Prevost and Scanlon (1983) using a hydraulic hammer to strike a plate buried at the bottom of the soil model. Although the frequency of the input motion can be adjusted by changing the dynamic characteristics of the plate, only high frequency motion has been obtained so far. All three methods are handicapped by the fact that only one pulse could be set off at a time, and that the resulting motion is not particularly representative of earthquakes. More recently, the electromagnetic method of excitation was examined by Fujii (1991), but the large masses of the magnets cut substantially into the available payload capacity, and as a result, this method is not suitable for use on centrifuges with a limited payload capacity.

A more versatile method is the electro-hydraulic method which when utilized with servo-control methodologies can theoretically deliver any desired motion to the payload being tested. This technique has been widely applied in structural testing and in laboratory testing to obtain dynamic soil properties for many years. It was successfully applied by Aboim et al. (1983) to earthquake simulation in centrifuge testing. The key to their success lies in mounting accumulators on the centrifuge to serve as the main hydraulic power supply, thus bypassing the small, restrictive passages of the hydraulic rotary joints usually employed in geotechnical centrifuges. Over the relatively short duration of the earthquake to be triggered in the centrifuge test (time scale is compressed by the factor  $N$ ), the decompression of the hydraulic fluid in the charged accumulators is sufficient for driving the double acting actuator to deliver the pre-programmed input motion to the payload being shaken. The feedback signal is either the acceleration or the displacement of the payload. This method is superior to the others because of the large forces

which can be generated by the hydraulic actuators and because of the versatility in producing pre-programmed motion to match the desired frequency and amplitude.

A comparison of the different excitation methods is given by Whitman (1988) and is shown in Fig. 1.

	COST	SIMPLI- CITY	ADJUST- ABILITY	FREQUENCY RANGE
				Low High
COCKED SPRINGS	Very Low	Very Simple	Poor	
PIEZO- ELECTRIC	Low	Simple	Good	
EXPLOSIVE	Low	Simple	Moderate	
BUMPY ROAD	High	Complex	Moderate	
HYDRAULIC	Very High	Very Complex	Very Good	

**Fig. 1** - Comparison of various methods for simulating earthquake ground motions on centrifuge (From Whitman, 1988).

### 3 PERFORMANCE OF ELECTRO-HYDRAULIC SHAKE TABLES

To date, only one-dimensional shaking in the prototype horizontal direction has been attempted in the electro-hydraulic method of earthquake simulation. Whitman (1988) compared the response spectrum of the horizontal motion produced by Aboim et al. (1983) in the Caltech centrifuge with that of the record of the 1971 San Fernando earthquake and found that in general the method is capable of capturing the essential features of the motion of the prototype earthquakes.

In the ground motion simulator in the Caltech centrifuge and others which follow its design, the soil container is suspended from the payload platform by rods while the hydraulic actuator applies the driving force from below the container using the platform as the reaction mass. The base motion shakes the soil model in the circumferential direction in the centrifuge, which brings into question the effects of a divergent centrifuge acceleration field over the width of the soil model in the direction of shaking. To minimize these undesirable effects, some researchers using this type of ground motion simulators which shake the model in the centrifuge circumferential direction have

prepared the soil model with a curved base and surface conforming to the radius from the center of the rotating centrifuge (Arulanandan et al., 1988).

On the other hand, the electro-hydraulic method is applied at the University of Colorado in a manner different from the one previously mentioned in two aspects, Ketcham et al. (1988, 1991). First, the soil model container is placed on a slip table which is driven by the hydraulic actuator mounted below. Its modular design makes it possible to transfer the entire slip table system to other centrifuges if needed, Astaneh (1993). Second, in order to bypass the need to curve the base and the surface of the soil model, the slip table is mounted in such a way that it produces the shaking motion in the vertical direction in Earth's reference frame, or parallel to the centrifuge's axis of rotation. Thus, a parallel body force field prevails on the model equivalent to the prototype conditions, to which the superimposed slip table shaking motion will be perpendicular.

However, in most apparatuses employing the electro-hydraulic method of excitation, a vertical motion component is usually obtained along with the intended horizontal (base) shaking. This is due to the fact that when the driving force is applied by the hydraulic actuator mounted below the center of mass of the payload, as dictated by space limitations on the small centrifuges on which the technique has been implemented, a rocking motion is developed, which is superimposed on the horizontal motion desired by the experimenter. It has been argued that such coupled motion, although not purposely planned, produces a better simulation of actual earthquakes which usually have all three components of motion present. Irrespective of the desirability of this additional component of the shaking motion, it has to be measured and characterized along with the input horizontal motion, in order that the effects of both can be quantified. When similar shaking systems are designed for large centrifuges where space and payload limitations are less restrictive, such deficiencies should be corrected, so that any undesirable components can be eliminated, or at least minimized. To date, there has been no concrete suggestion to apply two or more axes of controlled shaking to a centrifuge model, perhaps due to the anticipated difficulties in designing such a complex system.

The electro-hydraulic actuation technique as described above is theoretically operable under closed-loop serve-control conditions. But because of the compression of the time scale for dynamics modeling and the resulting scaling up of the frequency of the input motion, it is beyond the capability of currently available servo-valves to operate beyond several hundred Hz with closed loop feedback. In addition, the dynamical shake table/container system tends to attenuate the input motion such that the motion transmitted to the soil is not necessarily identical to the input. Thus, a correction scheme has to be employed to eventually focus on delivering the desired motion to the payload. Borrowing from well developed algorithms used in servo-controlled structural testing, Ketcham et al. (1988, 1991) applied such a correction algorithm, as depicted in Fig. 2, in which the system transfer function (Fourier transform of an output divided by the Fourier transform of the input) is first determined and subsequently used to successively correct the input motion until the desired slip table motion is obtained. Similar concepts have been employed to produce desired shaking motion in ground motion simulation experiments on various centrifuges (Van Laak et al., 1994a; Nagura et al., 1994).

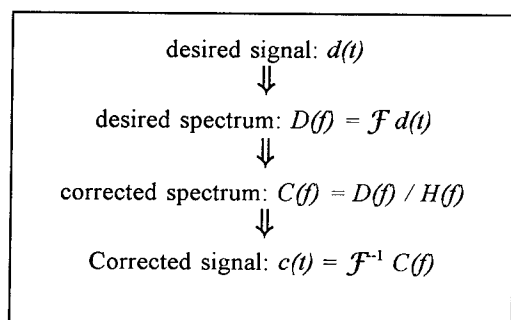


Fig. 2 - Single exciter correction algorithm for system with frequency response function  $H(f)$  (After Ketcham et al., 1988)

Shaking table systems are being designed and fabricated for use on large centrifuges (Kutter et al., 1994). Their goal of shaking large payloads requires the deployment of multiple actuators at several points below the table or along the edges of the table. The control of the simultaneous input motions from these actuators to produce a uniform base motion to the soil model is a

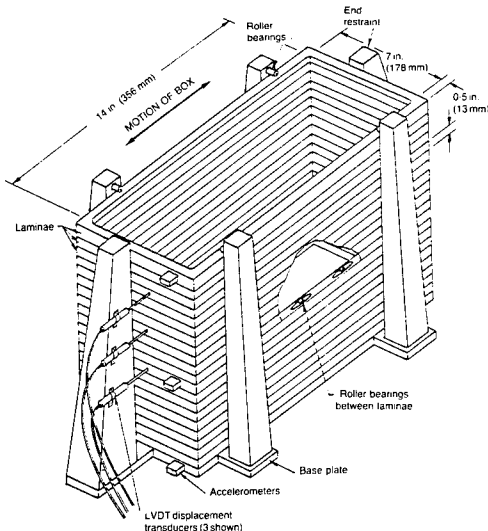
challenging problem whose solution will largely determine the success of the electro-hydraulic actuation technique to seismic simulation in centrifuge testing.

#### 4 CONTAINERS FOR DYNAMIC MODEL TESTING

The finite size of geotechnical centrifuges places a practical limit on the size of the container which can be used to carry the soil model. The container size is further limited by the actuator force, irrespective of the method of producing the input motion. This immediately brings into question the issue of the interaction of the soil mass with the container. When a container with rigid walls is used in the experiment, particular care is required to ensure that the stress waves reflected from the boundaries are either measured and quantified in regards to their effects on the model performance, or reduced by suitable absorption at the boundaries.

Coe et al. (1985) pioneered the use of Duxseal as a liner material for absorbing the stress waves at the boundary in dynamic experiments in rigid containers. The effects of such attempts have been evaluated by Cheney et al. (1988) and Lenke et al. (1991) for situations in which an embedded foundation was excited from above with small amplitude input motion at frequencies of several thousand Hz. It was found that there are indeed beneficial effects in using a boundary layer of absorbant material. Honda et al. (1994) used silicone rubber as the lining material between sand and the model container in studying the dynamic response of a vertical shaft subjected to base input motion. By analyzing the transfer function from the bottom to the surface of the sand layer, they concluded that with boundary treatment the sand layer behaved in a fashion as predicted by a one-dimensional lumped mass simulation.

On the other hand, a totally different approach has been taken in dealing with the boundary effects when large soil motion is involved in the experiment. Whitman and Lambe (1986) proposed a set of criteria for designing a model container to use in seismic simulation in which one-dimensional wave propagation through an infinite layer of soil is to be modeled. According to these criteria, the container should maintain a constant horizontal cross-section during shaking, have zero mass and zero



**Fig. 3 - Laminar container for simulating one-dimensional soil response** (From Hushmand et al., 1988)

stiffness to horizontal shear, and develop complementary shear stresses equal to those occurring on horizontal planes. Following these criteria, they fabricated a circular, stacked ring container, whose lateral flexibility allowed the soil column to move as a vertical shear beam. Improvements were implemented by Hushmand et al. (1988) who developed a rectangular laminar container as shown in Fig. 3. Numerous similar devices have been constructed by others. Law et al. (1991) described a systematic evaluation of the performance of the rectangular laminar container by measuring the uniformity of motion in a full bed of soil in the container and demonstrated the effectiveness of using such a container in dealing with boundary reflection problems. Further recent efforts have been expanded in improving the design of this type of containers, Van Laak et al. (1994b). A correction is suggested to account for the influence of the lateral inertia of the container on the soil response.

It is widely accepted that some form of a laminar container is an indispensable tool in earthquake simulation experiments in the centrifuge where stress wave reflections from the

end boundaries of the container are of concern when the input motion is supplied at the base of the model. However, there is no agreement on the optimal design of an ideal container. Fiegel et al. (1994) described a new type of container, called a hinged-plate container, for modeling properly prototype conditions. They compared the performance of this new device with that of the rigid container, and the laminar box of the type described by Hushmand et al. (1988) and the equivalent shear beam container (Schofield and Zeng, 1992), and concluded that different frequency and damping characteristics were observed with different containers which must be incorporated into the analysis of the experimental results.

In addition, it is not clear if such a container needs to be used in situations where the soil domain being modeled is not an infinite layer and does not stretch far enough to touch the end boundaries of the container. For instance, in the case of an embankment model, there is obviously no need for a laminar container. Even in the case of a retaining wall problem where only one end of the soil model touches the boundary, it is not clear if a laminar container should be used to create boundary conditions in the centrifuge test which do not necessarily correspond to any field conditions. For instance, Zeng (1994) used Duxseal lining on only one end of the container in testing models of retaining walls, but did not shown results to demonstrate the necessity of such measures to deal with wave reflections from the boundary so treated.

## 5 SUBSTITUTE MODELING MATERIALS

It is well known that there are conflicts in the scaling relations for the different time dependent phenomena occurring simultaneously in the soil model being testing at  $N.g$  in the centrifuge. The prototype time scale for diffusion (consolidation) phenomena is reduced by a factor of  $N^2$ . The dynamic time scale is reduced by a factor of  $N$ , while strain rate effects are unaffected by the gravity scaling. Thus, in centrifuge experiments where seismic simulation generates excess pore pressures leading to consolidation of a soil whose constitutive properties exhibit significant creep effects, the extrapolation of the model performance to the prototype scale becomes difficult unless the

conflicts in the time scaling relations is first resolved.

In the absence of strain rate effects, the conflict between dynamic and diffusion time scaling can be theoretical handled by slowing down the diffusion event with a substitute pore fluid which is  $N$  times more viscous than water (thus making the soil permeability  $N$  times smaller), without changing the soil skeleton structure itself. Silicone oils with the correct viscosities can be mixed to specification according to the demand of the dynamic centrifuge experiments. This technique was first employed at Cambridge University over 10 years ago, and has been adopted by many other researchers. See, for example, Koseki et al. (1994) and Pilgrim and Zeng, (1994). While it can be argued that the constitutive properties of soils are governed by effective stresses, the presence of an oily fluid on the constitutive properties of the soil produces unknown effects on intergranular friction in sandy soils, while the effects on fine grained soils like silts and clays are obviously much more complicated and must be evaluated thoroughly before such substitutions can be universally accepted. Not only the stress-strain and strength properties of a soil mixed with silicone oil need to be fully characterized and compared with those of the same soil mixed with water, the damping characteristics must also be quantified and shown to be unaffected.

Madabhushi (1994) undertook such a study to identify the effects of high viscosity silicone oil on the damping characteristics by testing tower models. After identifying the contributions from structural and radiation damping as small, he used the logarithmic decrement method to calculate the damping ratio due to material damping, and concluded that while the water saturated sand exhibited a slightly higher damping ratio than silicone oil saturated sand, the difference is insignificant in comparison to the change in viscosity.

Other recent efforts have focused on other types of substitute pore fluids. Liu and Dobry (1994) used mixtures of water and glycerin at different strengths as the substitute pore fluid. No data were shown on the constitutive properties of the soil. Allard and Schenkeveld (1994) discussed at great details the requirements for a suitable model pore fluid. It must behave like a Newtonian fluid with nearly the same mass density, compressibility and surface tension

as water, so that capillary effects will be properly scaled. In addition, it must be hygroscopic so that a film of it covering the soil grains will not alter the interparticle friction angle. It must also be chemically polar to enable its use with silts and in the making of clays. They reported on the characterization of a Delft Geotechnics model pore fluid which was obtained by mixing some chemical components to water, and evaluated its performance in light of the above requirements. Promising results were presented.

At the University of Colorado, experiments using a substitute pore fluid have been conducted on homogeneous soil embankment models. This substitute pore fluid is obtained by mixing hydroxypropyl methylcellulose, or metolose, which is a water-soluble cellulose ether, in water at concentrations up to several percent to obtain solutions with different viscosities. Ko et al. (1993) have shown that the constitutive properties of a granular soil are not affected by using metolose solutions as the pore fluid replacing water. Experiments were carried out by Astaneh (1993) on homogeneous embankments using metolose solutions as the pore fluid. Some of the results are shown in Fig. 4. One group of tests were conducted at the same 50 g level, with pore fluids with different viscosities (Test H7 with  $\nu = 50$  cps, Test H5 with  $\nu = 1$  cps). Different dynamic pore pressure and settlement histories were observed. In the second group of tests, a modeling-of-models approach was employed by testing  $N$ -th scale models of a hypothetical prototype at  $N$ -g, using pore fluids with  $N$  times the viscosity of water, where  $N = 50, 75$  and  $100$  for Tests H7, H15 and H14, respectively. The input shaking motion in these tests was also properly scaled in terms of intensity ( $N$  times) and duration ( $1/N$  times). It can be seen from these tests that the time histories of pore pressure generation and dissipation and crest settlement are similarly modeled at the different scales. Thus, with water as the pore fluid in seismic simulation experiments, the accumulation of dynamic pore pressure will be reduced by the rapid dissipation due to the improperly scaled soil permeability, and that the actual prototype response could not be observed on the model unless the soil permeability is reduced by increasing the viscosity of the pore fluid so that a common time scale is obtained for dynamic and diffusion phenomena.

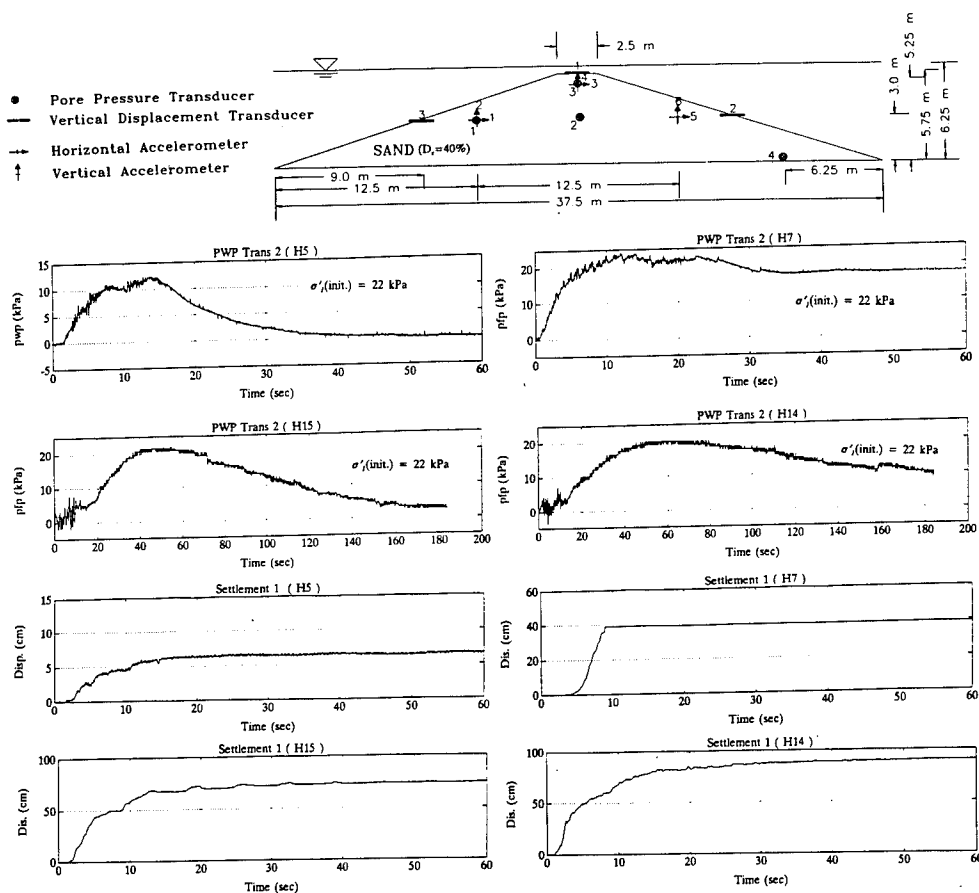


Fig. 4 - Embankment test results with pore fluids of different viscosities (After Astaneh, 1993).

## 6 CENTRIFUGE MODELING VERSUS NUMERICAL MODELING

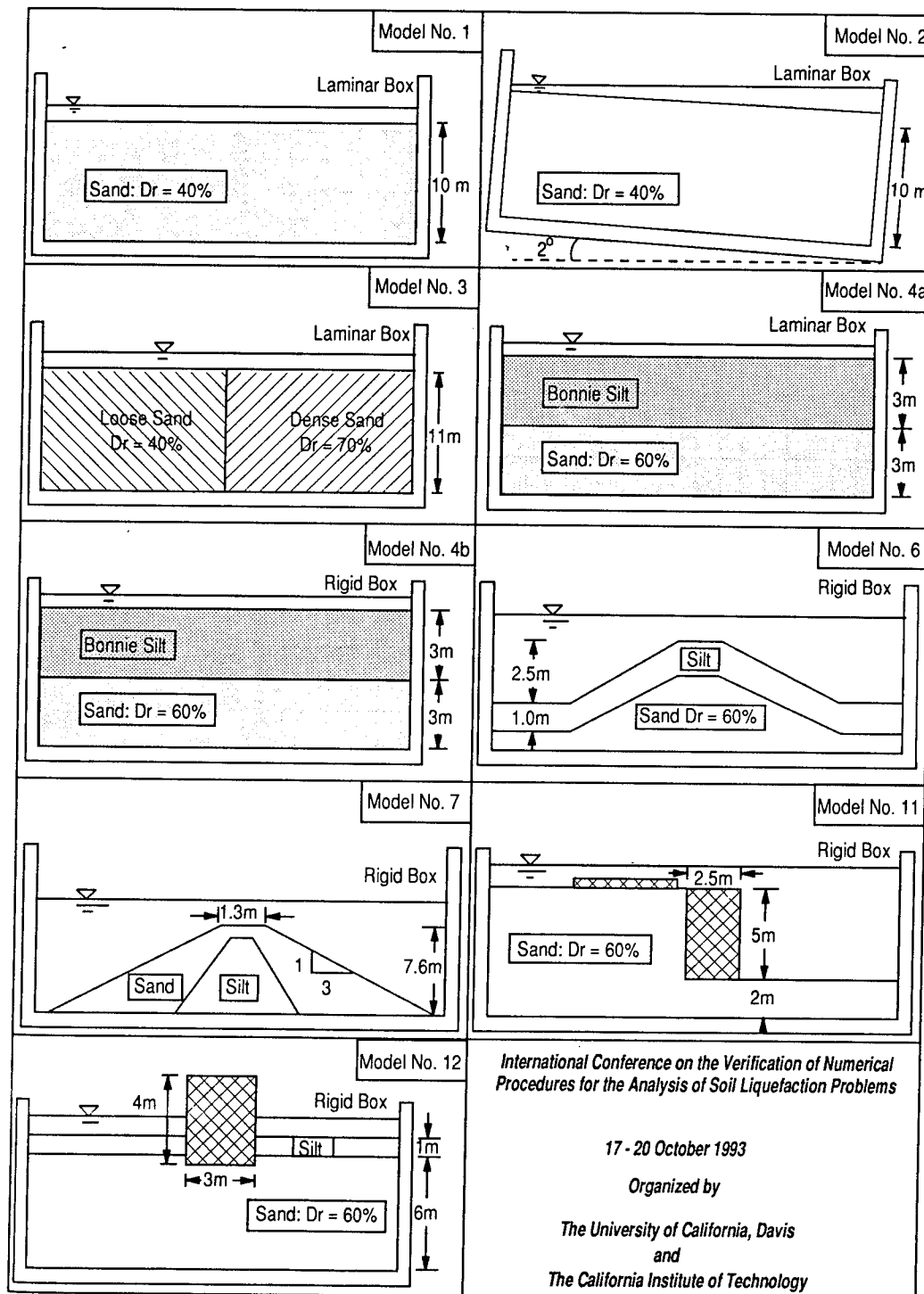
In recent years, it has been increasingly recognized that perhaps the most appropriate use of centrifuge modeling is to provide a data base for the validation of the numerical procedures employed for the analysis and design of earth structures. This is particularly true when the dynamic response to earthquake loading is concerned, since it is extremely difficult to obtain good field data for such validation purposes. The obvious need for data for the bench marking of numerical codes under conditions closely approximating those in the field has motivated the rapid development of the seismic simulation techniques in centrifuge testing, as described in this paper.

A cooperative research project called VELACS (Verification of Earthquake

Liquefaction Analysis by Centrifuge Studies), sponsored by the National Science Foundation in the U. S. was recently completed. It involved centrifuge testing of 9 kinds of models of earth structures (see Fig. 6) in 6 centrifuge laboratories in the U. S. and U. K. which have seismic simulation capabilities. These models, which were eventually shaken to produce large deformations caused by soil liquefaction, were used as the basis of Class A (before the event) predictions by 23 predictor teams. Results of centrifuge experiments and their predictions have been reported by Arulanandan and Scott (1993b).

Previous exercises involving the validation of constitutive models (Yong and Ko, 1980; Saada and Bianchini, 1987) have raised questions regarding the reliability of the test data used in the prediction. In VELACS, in anticipation of similar questions on the centrifuge model test results, the dependence of these results on the





**Fig. 5 - Centrifuge model configurations for Class A predictions - VELACS Project (From Arulanandan & Scott, 1993b).**

testing apparatus and the test team was investigated by first conducting a series of comparison tests at the participating laboratories. A standard container was used in testing a dry sand model and a saturated sand and silt layered model, following a common test procedure. The results of these tests, reported by Arulanandan and Scott (1993a), showed that in spite of the anticipated scatter arising from the different techniques used in generating the input base motion, the overall behavior in all of the tests was sufficiently similar to provide the confidence in using subsequent test data for the intended validation purposes. Most of the 9 models employed for the Class A predictions were duplicated at two or more laboratories to assure that similar results were obtained.

## 7 CONCLUSIONS

The desire to conduct centrifuge experiments to observe effects of earthquake loading on earth structures has spurred rapid developments in seismic simulation capabilities on geotechnical centrifuges worldwide. Judging from the increasing number of papers contributed to this conference and its predecessors, such experiments are now almost routine in many centrifuge facilities. For seismic simulation to produce maximum benefits, great care must still be exercised in controlling and characterizing the input motion to properly simulate a particular earthquake, while maintaining the proper boundary conditions in such experiments and the need to use a substitute pore fluid also require close attention. It appears that in the next several years, enormous amounts of data will be forthcoming from such centrifuge experiments, providing the earthquake geotechnical engineering community with an excellent opportunity to study earthquake induced effects on earth structures.

## REFERENCES

- Aboim, C., R. F. Scott, J. R. Lee & W. H. Roth (1983). Centrifuge Earth Dam Studies: Earthquake Tests and Analyses. Report to National Science Foundation, Grant No. CEE-7926691, Dames and Moore, Los Angeles.
- Allard, M. A. & F. M. Schenkeveld (1994). The Delft Geotechnics Model Pore Fluid for Centrifuge Tests. Paper submitted to this conference.
- Arulanandan, K. & R. F. Scott (1993a). Project VELACS - Control Test Results. J. Geotechnical Eng. Div., ASCE, 119, 1276-1292.
- Arulanandan, K. & R. F. Scott (1993b). Eds., Verification of Numerical Procedures for the Analysis of Soil Liquefaction Problems, Vol. 1, Balkema, Rotterdam.
- Arulanandan, K., C. Yogochandran, K. K. Muraleetharan, B. L. Kutter & G. S. Chang (1988). Seismically Induced Flow Slide on Centrifuge. J. Geotechnical Eng. Div., ASCE, 114, 1442-1449.
- Arulanandan, K., J. Canclini & A. Anandarajah (1982). Simulation of Earthquake Motions in the Centrifuge. J. Geotechnical Eng. Div., ASCE, 108, 730-742.
- Astaneh, S. M. F. (1993). Effects of Earthquakes on Saturated Soil Embankments. Ph. D. thesis, University of Colorado.
- Cheney, J. A., O. Y. Z. Hor, R. K. Brown & N. R. Dhat (1988). Foundation Vibration in Centrifuge Models. Centrifuge 88, J. F. Corte, ed., Balkema, Rotterdam, 481-486.
- Coe, C. J., J. H. Prevost & R. H. Scanlon (1985). Dynamic Stress Wave Reflections/Attenuation: Earthquake Simulation in Centrifuge Soil Models. Earthquake Engineering and Structural Dynamics, 13, 109-128.
- Corte, J. F. (1998). Ed., Centrifuge 88, Balkema, Rotterdam.
- Fiegel, G.L., M. Hudson, I. M. Idriss, B.L. Kutter & X. Zeng (1994). Effect of Model Containers on Dynamic Soil Response. Paper submitted to this conference.
- Fujii, N. (1991). Development of an Electromagnetic Centrifuge Earthquake Simulator. Centrifuge 91, H. Y. Ko and F. G. McLean, eds., Balkema, Rotterdam, 351-354.
- Honda, M., N. Ohbo, H. Hayashi, J. Zheng & R. F. Scott (1994). Dynamic Response of a Shaft in Dry Sands. Paper submitted to this conference.
- Hushmand, B., R. F. Scott & C. B. Crouse (1988). Centrifuge Liquefaction Tests in a Laminar Box. Geotechnique, 38, 253-262.
- Ketcham, S. A., H. Y. Ko & S. Sture (1988). An Electrohydraulic Earthquake Simulator for

- Centrifuge Testing. Centrifuge 88, J. F. Corte, ed., Balkema, Rotterdam, 97-102.
- Ketcham, S. A., H. Y. Ko & S. Sture (1991). Performance of an Earthquake Motion Simulator for a Small Geotechnical Centrifuge. Centrifuge 91, H. Y. Ko and F. G. McLean, eds., Balkema, Rotterdam, 361-368.
- Ko, H. Y. & F. G. McLean (1991). Eds., Centrifuge 91, Balkema, Rotterdam.
- Ko, H. Y., A. T. Stadler & M. M. Dewoolkar (1993). Metolose Testing. Internal report, University of Colorado.
- Koseki, J., Y. Koga & A. Takahashi (1994). Liquefaction of Sandy Ground and Settlement of Embankments. Paper submitted to this conference.
- Kutter, B. L. (1983). Centrifuge Modeling of the Response of Clay Embankments to Earthquakes. Ph. D. thesis, Cambridge University.
- Kutter, B. L., I. M. Idriss, T. Khonke, J. Lakeland, X. S. Li, W. Sluis, X. Zeng, R. C. Tauscher, Y. Goto & Kubodera, I. (1994). Design of a Large Earthquake Simulator at UC Davis. Paper submitted to this conference.
- Law, H., H. Y. Ko & S. Sture (1991). Development and Performance of a Laminar Container for Earthquake Liquefaction Studies. Centrifuge 91, H. Y. Ko and F. G. McLean, eds., Balkema, Rotterdam, 369-376.
- Lenke, L. R., R. Y. S. Pak & H. Y. Ko (1991). Boundary Effects in Modeling of Foundations Subjected to Vertical Excitation. Centrifuge 91, H. Y. Ko and F. G. McLean, eds., Balkema, Rotterdam, 473-480.
- Liu, L. & R. Dobry (1994). Seismic Settlements and Pore Pressures of Shallow Foundations. Paper submitted to this conference.
- Modabhushi, S. P. G. (1994). Effect of Pore Fluid in Dynamic Centrifuge Modelling. Paper submitted to this conference.
- Morris, D. V. (1983). An Apparatus for Investigating Earthquake-Induced Liquefaction Experimentally. Canadian Geotechnical Journal, 20, 840-845.
- Nagura, K., M. Tanaka, K. Kawasaki & Y. Higuchi (1994). Development of an Earthquake Simulator for the TAISEI Centrifuge. Paper submitted to this conference.
- Ortiz, L. A., R. F. Scott & J. Lee (1983). Dynamic Centrifuge Testing of a Cantilever Retaining Wall. Earthquake Engineering and Structural Dynamics, 11, 251-268.
- Pilgrim, N. K. & X. Zeng (1994). Slope Stability with Seepage in Centrifuge Model Earthquakes. Paper submitted to this conference.
- Prevost, J. H. & R. H. Scanlon (1983). Dynamic Soil Structure Interaction: Centrifugal Modelling. Soil Dynamics and Earthquake Engineering, 2, 212-221.
- Saada, A. & G. Bianchini, (1987). Eds., Constitutive Equations for Granular Non-Cohesive Soils, Balkema, Rotterdam.
- Schofield, A. N. (1981). Dynamic and Earthquake Geotechnical Centrifuge Modelling. Proc. Int. Conf. on Recent Advances in Geotechnical Earthquake Engineering and Soil Dynamics, 1081-1100.
- Schofield, A. N. & X. Zeng (1992). Design and Performance of an Equivalent Shear Beam Container for Earthquake Centrifuge Modeling. Cambridge University Report CUED/DSOILS/TR245.
- Van Laak, P. A., A.-W. Elgamal & R. Dobry (1994a). Design and Performance of an Electrohydraulic Shaker for the RPI Centrifuge. Paper submitted to this conference.
- Van Laak, P. A., V. M. Taboada, R. Dobry & A.-W. Elgamal (1994b). Earthquake Centrifuge Modeling Using a Laminar Box. Dynamic Geotechnical Testing II, ASTM STP, 1213.
- Whitman, R. V. (1988). Experiments with Earthquake Motion Simulation. Centrifuges in Soil Mechanics, W. H. Craig, R. G. James and A. N. Schofield, eds., Balkema, Rotterdam, 203-216.
- Whitman, R. V. & P. C. Lambe (1986). Effect of Boundary Conditions Upon Centrifuge Experiments Using Ground Motion Simulation. Geotechnical Testing Journal, 9, 61-71.
- Yong, R. N. & H. Y. Ko, (1980). Eds., Limit Equilibrium, Plasticity and Generalized Stress-Strain in Geotechnical Engineering, ASCE Publications.
- Zelikson, A., B. Devaure & D. Badel (1981). Scale Modeling of Soil Structure Interaction During Earthquakes Using a Programmed Series of Explosions During Centrifugation. Proc. Int. Conf. on Recent Advances in Geotechnical Earthquake Engineering and Soil Dynamics, 1, 361-366.
- Zeng, X. (1994). Seismic Response of Gravity Type Quay Wall. Paper submitted to this conference.

## Mechanical behaviour of intermediate soils

T. Kimura, J. Takemura, A. Hiro-oka & M. Okamura  
Tokyo Institute of Technology, Japan

**ABSTRACT:** An attempt is made to study mechanical behaviour of intermediate soils using artificial soils made by mixing clay with sand and its crushed component. Static and dynamic centrifuge model tests are carried out together with static and cyclic triaxial tests. The aims of this study are to investigate the effect of loading rate and plasticity on the bearing capacities and deformations of the intermediate soils. It is found that mechanical behaviour heavily depends on the plasticity of soils.

### 1 INTRODUCTION

Soils with mechanical properties with half way between those of sand and clay are often called intermediate soils (Nakase 1978). Sands generally have high static strength and high permeability, but are susceptible to liquefaction. On the other hand, majority of clays have low strength and high compressibility, particularly in undrained conditions, but are not susceptible to liquefaction. Naturally the intermediate soils have both advantages and disadvantages of these two soils. In actual static design, they are dealt with as clay, neglecting an advantage that they have considerably high angle of friction even in quick loading. In dynamic design, they are treated as sand because liquefaction of silty sands have been witnessed at several sites (Mori et al. 1991).

Consideration of safety of structures thus leads to conservative design in which intermediate soils are considered as soils with disadvantages of sands and clays. Nakase (1985) asked a question if this approach is reasonable. The importance of this question has been appreciated by some research workers, and a considerable number of studies have been conducted to investigate mechanical behaviour of intermediate soils. Most of them are, however, on the behaviour of soil elements (Georgiannou et al. 1990, 1991; Ishihara and Koseki 1989 for example) and very few works have been conducted to study behaviour of soil mass. After Nakase joined the soil mechanics group at Tokyo Institute of Technology, the group started comprehensive studies on mechanical behaviour of intermediate soils combining centrifuge model tests with triaxial tests. This paper introduces some of the results of static and dynamic centrifuge model tests together with the mechanical properties investigated with triaxial tests.

### 2 T.I.T. MIXTURES AND RESULTS OF TRIAXIAL TESTS

Physical properties of intermediate soils used in the tests are shown in Table 1. The figures after the character "M" represent the plasticity index of each soil. The soils other than M30 are artificial soils made by mixing Toyoura sand and its crushed component with M30 which is Kawasaki clay sampled at Tokyo bay. The soil mechanics group define

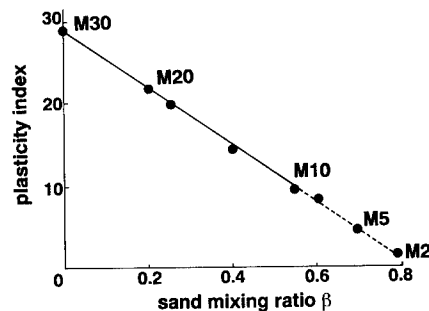


Fig.1 Relationship between plasticity index and sand mixing ratio

Table 1 Physical properties of TIT mixtures

Soil	M-2	M-5	M-10	M-20	M-30
specific gravity of soil particle ( $G_s$ )	2.65	2.65	2.65	2.65	2.65
liquid limit ( $w_L$ )	19.2	20.5	27.0	40.0	54.0
plastic limit ( $w_P$ )	-	-	15.8	20.2	25.5
plasticity index ( $I_P$ )	(2)	(5)	11.2	19.8	28.5
sand mixing ratio ( $\beta$ )	0.78	0.69	0.54	0.25	0
permeability coefficient (m/s) ( $k$ )	$1.3 \times 10^{-7}$	$2.0 \times 10^{-8}$	$8.7 \times 10^{-10}$	$6.0 \times 10^{-10}$	$6.0 \times 10^{-10}$

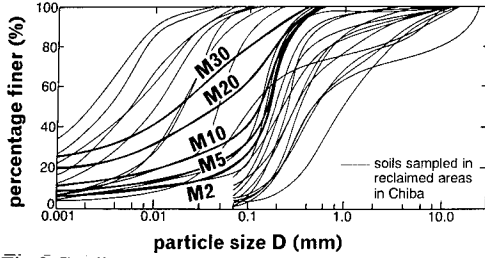


Fig.2 Grading curves of soils sampled at reclaimed area in Chiba and TIT mixtures

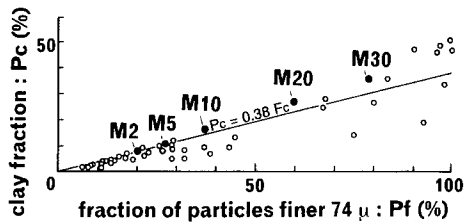


Fig.3 Relationships between Pc and Fc of soils sampled at reclaimed areas in Chiba and TIT mixtures

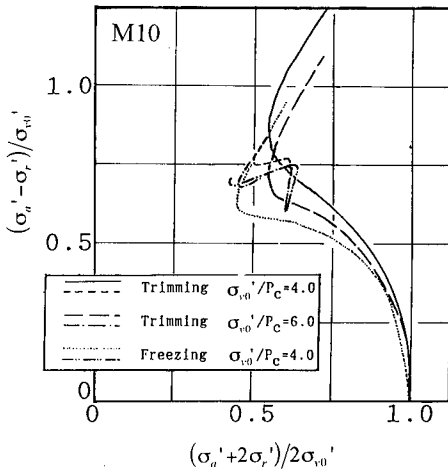


Fig.4 Differences in effective stress path for trimmed samples and frozen samples: M10

all the soils in Table 1 as T.I.T. mixtures.

A relationship between weight proportion of sand in a mixture  $\beta$  and plasticity index  $I_p$  is illustrated in Fig.1, which has been established by accumulating the results of numerous tests. Since this relationship holds only up to the point with  $I_p$  equal to 10 or so, the artificial soils with the proportion  $\beta$  on the extrapolated region were named as M5 or M2. For these two soils, the figures attached after "M" do not of course represent their real plasticity index. However, it is certain that the plasticity index of these soils is definitely smaller than that for the soils on the solid part of this line.

The grading curves of artificial soils are compared

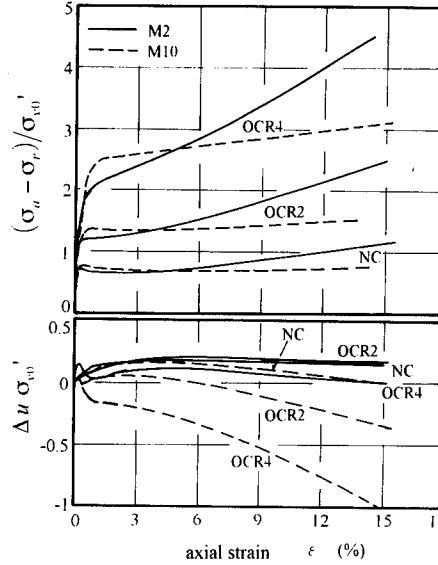


Fig.5 Results of  $K_0$  consolidated undrained compression triaxial tests: M2, M10

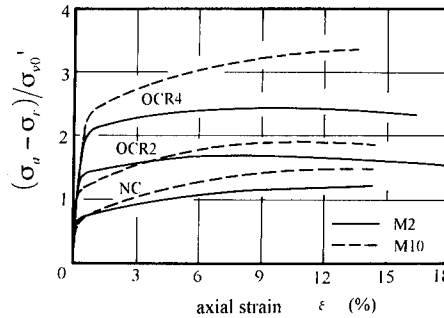


Fig.6 Results of  $K_0$  consolidated drained compression triaxial tests: M2, M10

Table 2 Conditions of cyclic triaxial tests

soil	M-30, M-10, M-5, M-2
type of consolidation	isotropic & anisotropic normally consolidation for all soils isotropic & anisotropic over-consolidation for M-2 & M-5
type of loading	sinusoidal frequency 1-0.01Hz

with those of real soils sampled in reclaimed areas near Tokyo in Fig.2(Harada et al.1990). It is seen that the artificial soils represent soils in situ reasonably well. The relationship between clay fraction (particles finer than  $5\mu m$  according to a convention in Japan) and fraction of soil particles finer than  $74\mu m$  for the soils at the same sites as in Fig.2 is illustrated in Fig.3. The T.I.T. mixtures fall very closely on to the average line, which also shows that the artificial soils are good representation of real soils.

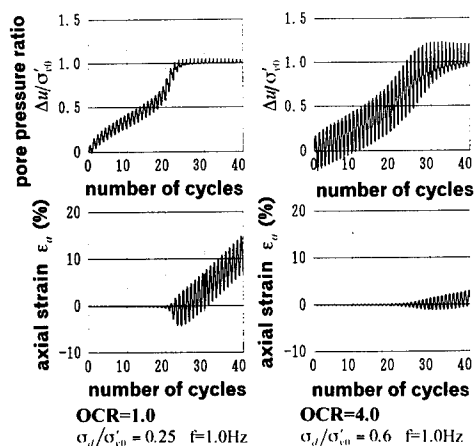


Fig.7 Results of cyclic triaxial test: M2, isotropic

Since it was not possible to trim specimens for triaxial tests from consolidated chunk of M5 and M2, the specimens were once frozen after preconsolidation in a mould designed particularly for this purpose. The frozen specimen was set on the pedestal in a triaxial cell, the specimen was thawed, consolidation was conducted, and then static or cyclic tests were carried out. The difference in normalized effective stress paths obtained for trimmed and frozen specimens of M10 in static undrained tests is illustrated in Fig.4, where  $p_c$  is preconsolidation pressure and  $\sigma'_{v0}$  is consolidation pressure. The paths for frozen specimens are more likely as normally consolidated soil. The effect of disturbance is clearly noticed for the trimmed specimens with the paths more like those of over-consolidated specimens. The difference in paths shown in the figure justifies the use of freezing method for preparing specimens of soils with extremely low plasticity.

The results of static triaxial tests on  $K_0$  consolidated specimens are shown in Fig.5 and 6, in which the vertical axis is observed deviator stresses normalized by consolidation pressure  $\sigma'_{v0}$ . Both in undrained and drained conditions, the normalized strength increases with the increase in overconsolidation ratio(OCR). In undrained conditions, M2 shows strain hardening, particularly for high overconsolidation ratio. It is noticed that high negative pore pressures are built up at high strains. This is clearly because dilation of sand parts in M2 is suppressed in undrained conditions. This explains strain hardening of M2. Strain hardening disappears in drained conditions, because sand parts are now allowed to dilate. One interesting conclusion derived from Fig.6 is that the drained strength of M2 is smaller than that of M10, implying that the magnitude of  $\phi'$  for sand parts in M2 is lower than that of clay parts for M10. This can be explained by considering the fact that M2 is extremely loose.

A series of cyclic triaxial tests were also conducted on these soils. The conditions of cyclic triaxial tests are given in Table 2. In this test series, M20 was not

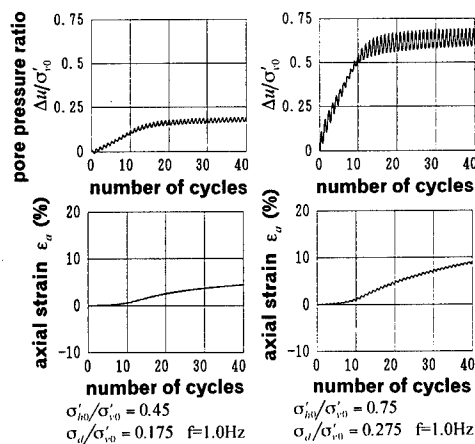


Fig.8 Results of cyclic triaxial test: M2, anisotropic

considered. Over-consolidated specimens were made only for M5 and M2. Sinusoidal waves with the frequency ranging between 1Hz and 0.01Hz were applied to the specimens.

Observed pore pressure ratios and axial strains are compared for normally consolidated and over-consolidated specimens of M2 in Fig.7, in which the vertical axis is observed pore pressure increments normalized by consolidation pressure  $\sigma'_{v0}$ . The over-consolidated specimen sustains a higher stress ratio  $\sigma'_d/\sigma'_{v0}$ , where  $\sigma'_d$  is input cyclic stress amplitude, but the way pore pressures are built up is very similar. There is a marked difference in the development of axial strains after initial liquefaction at about 20 cycles. The over-consolidated specimens clearly show higher ductility. Results obtained for anisotropically normally consolidated specimens are illustrated in Fig.8. Since these specimens are subjected to initial shear stresses, pore pressures generated do not reach the level where the effective stress becomes zero. It is, however, worthy to note that fairly large irrecoverable axial strains appear even in this case.

Differences in pore pressure response for a similar magnitude of stress ratio are shown in Fig.9 for different normally consolidated soils. Higher pore pressures are generated for the soils with smaller plasticity index. The degradation index defined by Idriss et al.(1978) was calculated for the same series of tests as in Fig.9 and it was plotted against the number of loading cycles in Fig.10. The reduction in stiffness is more marked for the soils with lower plasticity and liquefaction takes place at smaller numbers of loading cycles. Pore pressure response and degradation index for M2 with different overconsolidation ratio are illustrated in Fig.11 and 12 respectively. Generated pore pressures are smaller for over-consolidated specimens, although sustained stress ratios are higher. The reduction in stiffness is smaller for over-consolidated specimens, implying that liquefaction resistance is higher for them. Mori et al.(1991) showed a relationship between stress ratios

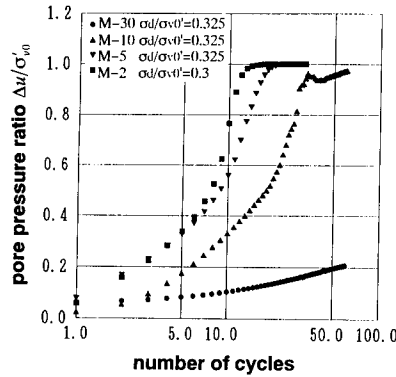


Fig.9 Variations of pore pressure ratio in cyclic triaxial test: NC, isotropic

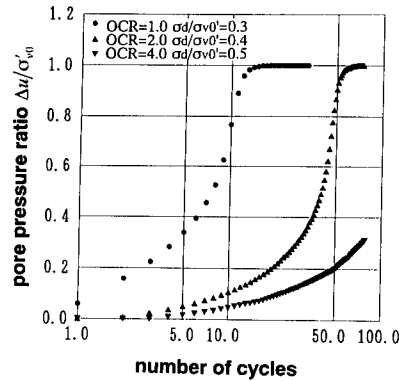


Fig.11 Variations of pore pressure ratio in cyclic triaxial test: M2, OC, isotropic

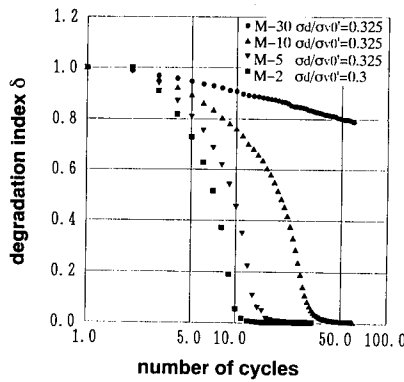


Fig.10 Variations of degradation index in cyclic triaxial test: NC, isotropic

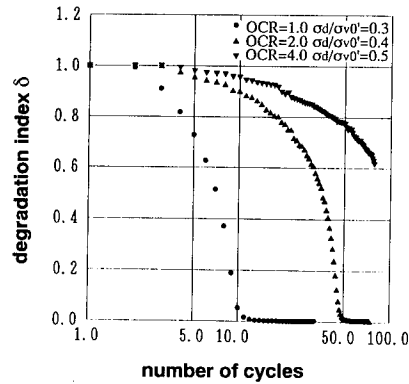


Fig.12 Variations of degradation index in cyclic triaxial test: M2, OC, isotropic

causing 5% double amplitude strain in 20 cycles and plasticity index as in Fig.13. The results of this study are added to this. It is seen that the data obtained with this study are consistent with those reported by Mori et al., although they are in the lower limit in this group, giving slightly smaller liquefaction resistance. The general trend is that the liquefaction resistance increases with the increase in plasticity index.

### 3 RESULTS OF CENTRIFUGE MODEL TESTS AND DISCUSSIONS

#### 3.1 Static behaviour

Since the permeability of intermediate soils is considerably higher than that of clays as shown in Table 1, it is possible that partial drainage takes place even in quick loading. This may give rise to different bearing capacities and deformations for intermediate soils from those of typical clays. In an attempt to study the effect of the ratio of loading rate to permeability coefficient on the bearing capacities and

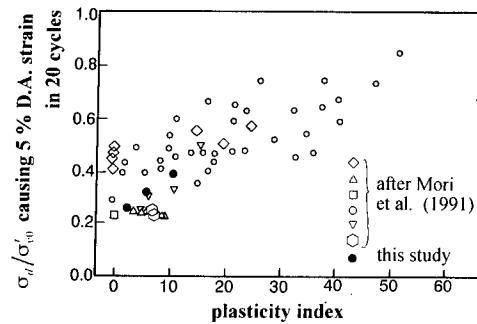


Fig.13 Relationship between stress ratio causing 5% D.A. strain in 20 cycles and plasticity index

deformations, a series of static loading tests were carried out in centrifugal field using M10 and M2.

Deaired slurry of artificial soils was first consolidated in a strong box on the lab floor under a pressure of 10kPa. Prior to consolidation rubber membranes

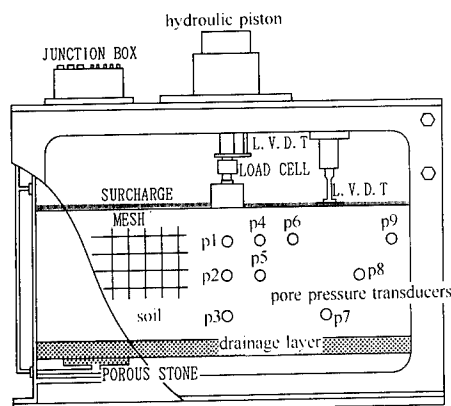


Fig.14 Setup for static loading test

Table 3 Conditions of static loading tests

Test code	soil	loading rate kPa/min	footing width mm	relative loading rate $\dot{q}/k$ kPa/m *	$c_0$ kPa	$\rho B/c_0$
NC1	M-2	210	60	$1.1 \times 10^4$	3.7	2.6
NC2	M-10	200	60	$1.6 \times 10^6$	3.9	2.6
NC3	M-2	190	30	$9.6 \times 10^3$	3.7	1.3
NC4	M-10	140	30	$1.1 \times 10^6$	3.9	1.3
NC5	M-10	2.2	60	$1.7 \times 10^4$	3.9	2.6
NC6	M-2	2.2	60	$1.1 \times 10^2$	3.7	2.6
OC1	M-2	170	60	$9.2 \times 10^3$	9.9	1.0
OC2	M-10	180	60	$1.4 \times 10^6$	13.7	0.8

\*: prototype scale

smeared with silicon oil were placed at the inside walls of the box in an attempt to reduce wall friction. Meshes were drawn on the membrane at the front wall so that deformations of soil can be measured by photographing the meshes during loading tests. On completion of consolidation, a model footing and brass rods were placed on the surface of soil so that this gives the surcharge pressure of either 10.8kPa or 43.2kPa in 50g field. A loading device was attached to the strong box as shown in Fig.14. The box was then mounted on a centrifuge and centrifugation was conducted at 50g. With this arrangement, soil layers with undrained strength increasing linearly with the depth, which is typical of young normally consolidated clays, can be made. For the cases with surcharge pressure 43.2kPa, centrifugal consolidation was carried out once again by reducing the pressure at the soil surface to 10kPa. This produces soil layers with overconsolidation ratio of 4 at the surface, which also have strength increasing linearly with depth.

Having confirmed dissipation of excess pore pressures in a model, stress-controlled loading tests were carried out by pushing a model footing with a hydraulic piston. Centrifuge models were instrumented with pore pressure transducers and LVDTs. The conditions of the tests are summarized in Table 3. The widths of model footing were twofold, 30 and 60mm. The bottom surface of the footing was roughened by

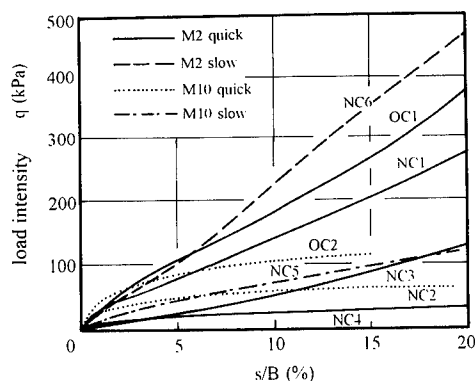


Fig.15 Load intensity and settlement curves

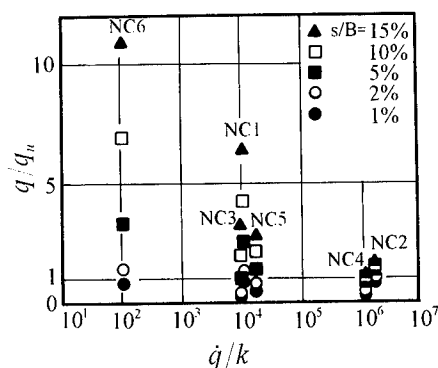


Fig.16 Relationship between load intensity and relative loading rate for different stages of footing settlements

gluing sand grains. Two types of loading tests, quick and slow, were conducted with loading rates of approximately 200 and 2kPa/min or 120 and 1.2kPa/day in prototype scale respectively.

Observed relationships between load intensity and settlements of footing normalized by footing width ( $s/B$ ) are illustrated in Fig.15. In all the cases, peaks do not appear and the load intensity increases almost linearly with the increase in settlements. The gradient of the linear portions is greater for M2 than for M10 and greater for slow loading than for quick loading.

Load intensity normalized by  $q_u$  is plotted against relative loading rate  $\dot{q}/k$  in Fig.16 for different stages of footing settlements, where  $q_u$  is an upper bound of bearing capacity calculated theoretically for undrained conditions (Takemura 1991),  $\dot{q}$  is the loading rate and  $k$  is the permeability coefficient determined at the vertical consolidation pressure of 48kPa. The horizontal axis  $\dot{q}/k$  is expressed in terms of prototype scale. Only the results for normally consolidated soils are plotted in the figure. The last column in Table 3  $\rho B/c_0$  denotes a non-dimensional parameter which determines the bearing capacities of soil layers with undrained strength increasing with the depth, where  $\rho$



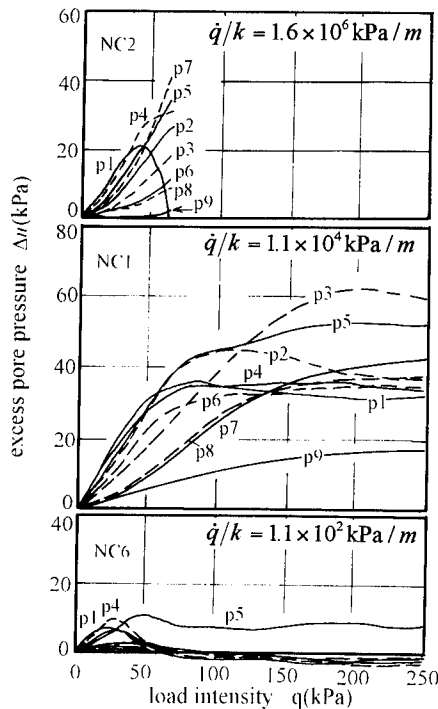


Fig.17 Observed pore pressures during static loading tests

is the gradient of strength increase,  $B$  the width of footing and  $c_0$  the strength at the surface. The two parameters  $\rho$  and  $c_0$  were calculated from stress history during the consolidation process. For the relative loading rates greater than  $10^3 \text{ kPa/m}$ , the normalized load intensity is very close to 1 with negligible differences for different footing settlements. This justifies the assumption of undrained conditions in the evaluation of bearing capacities for the loading rates in this range. For the relative loading rates less than  $10^3 \text{ kPa/cm}$ , however,  $q/q_0$  increases with increase in footing settlements, reaching the magnitude considerably greater than 1. The assumption of undrained conditions for this range of relative loading rates leads naturally to underestimation of bearing capacities.

Pore pressures measured at the locations indicated in Fig.14, are plotted against load intensity in Fig.17. For NC2 with the highest relative loading rate in this test series, pore pressures show linear increase with the increase in load intensity nearly at all the locations throughout the test, which implies that the undrained condition is satisfied in this case. On the contrary, only marginal pore pressures are observed at all the locations for NC6 with the lowest relative loading rate. This demonstrates that entire parts of soil is in the drained condition. For NC1 with the relative loading rate half way between that for NC2 and NC1, the pore pressures show linear increase at initial stages, approximately up to the load intensity of 50 kPa. At subsequent stages, those at shallow

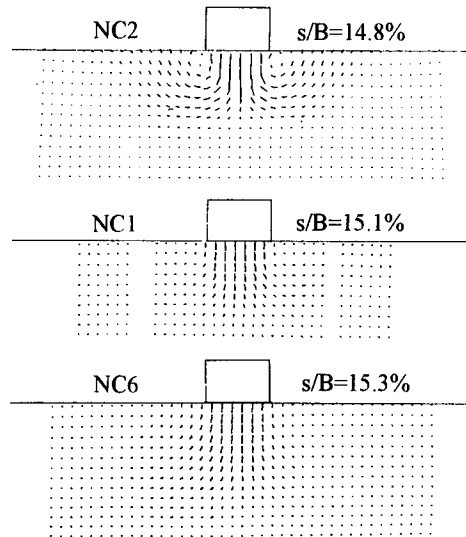


Fig.18 Observed deformations in normally consolidated soils with different relative loading rates

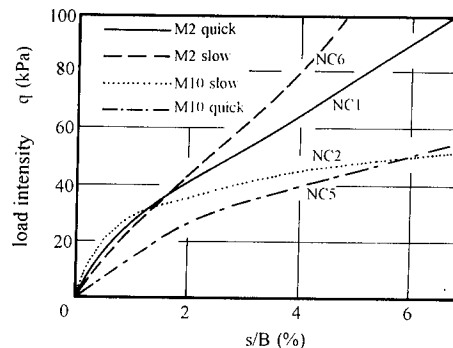


Fig.19 Load intensity and settlement curves of normally consolidated soils at initial stage of loading:  $B=60 \text{ mm}$

locations, P1 and P4, begin to reduce, indicating that local drainage takes place particularly in the areas near the surface in this case. This is consistent with the results shown in Fig.16.

Deformations observed at the stage with  $s/B$  equal approximately to 15% are illustrated in Fig.18. For NC2 with the highest relative loading rate, the pattern of deformations is similar to that of general shear failure which is typical of undrained deformations of clay, with an active wedge formed beneath the footing and upward movements in outer regions. For NC6, only limited lateral deformations are observed and vertical deformations prevail to the considerable depth. Hardening due to local drainage in the area beneath the footing is considered to be responsible for this. The pattern of deformations is that of local shear failure. Deformations for NC1 are half way between those of NC2 and NC6.

The relationships between load intensity and  $s/B$  up to the stage with  $s/B$  equal to 7% are replotted in

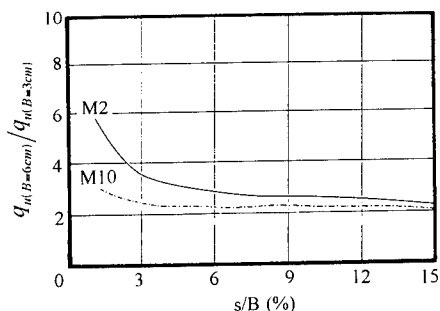


Fig.20 Ratios of load intensities between different footing widths: NC, quick loading

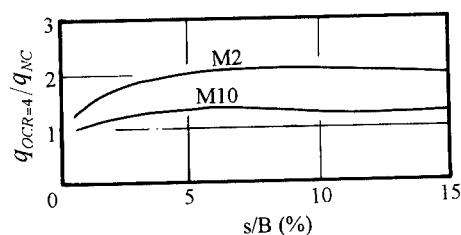


Fig.21 Ratios of load intensities between normally consolidated and over-consolidated soils: B=60mm, quick loading

Fig.19. The load intensity is greater for quick loading both for M2 and M10 when  $s/B$  is small. This relationship is reversed at later stages. A previous study by the group (Nakazono 1991) has shown that the undrained strength increases by 11 and 15% for M2 and M10 respectively for the increase of 100 times of loading rate. The difference in load intensity for M10 at initial stages of loading tests is by far greater than this increase. The amount of drainage is considered to be higher near the surface at initial stages of loading for lower loading rates, resulting in larger settlements. This gives smaller load intensities for lower loading rates at the initial stages.

Load intensities observed in quick tests are compared in Fig.20 for two different widths of footing, 3 and 6cm, for M2 and M10. Clearly at initial stage the ratio in the figure is much higher than 2 given by Terzaghi's theory for sandy soils, particularly for M2. Yamaguchi and Murakami (1978) demonstrated by their theoretical calculation that consolidation progresses faster for narrower footings. Since settlements at an identical load intensity are greater for faster consolidation, load intensities for an identical  $s/B$  are smaller for narrower footings. This explains the difference in load intensity for footings with different width. Since the amount of drainage is higher for M2, the ratio for M2 is greater than that for M10. Drainage takes place from the beginning of loading, with higher amount of drainage for narrower footings.

It is known that the strength of clay can be increased by preloading or overconsolidation. Load intensities observed for normally consolidated and

Table 4 Input parameters used in FEA

Soil	$\kappa$	$\lambda$	$e_{cs}$	M	k(m/min)	$\nu$
M-2	0.0064	0.035	0.748	1.43	$7.9 \times 10^{-6}$	0.30
M-10	0.0076	0.058	0.842	1.51	$5.2 \times 10^{-8}$	0.30

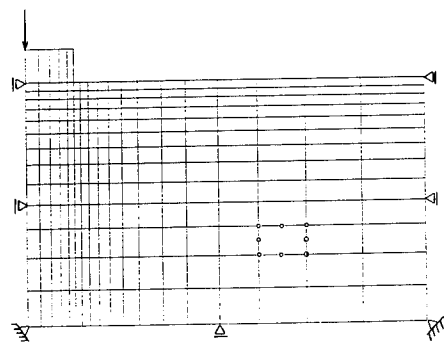
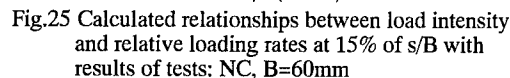
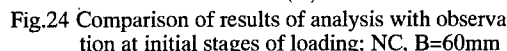
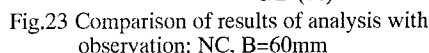


Fig.22 Meshes used in FEA

over-consolidated M2 and M10 are compared in Fig.21. The effect of preloading is certainly more marked for M10 which contains higher amount of clay fraction.

In this study, an attempt was made to investigate the applicability of finite element analysis to the prediction of mechanical behaviour of normally consolidated intermediate soils. A computer code used for the analysis is based on the modified Cam clay model. Input parameters are listed in Table 4 and meshes used for computation are shown in Fig.22. Relationships between load intensity and  $s/B$  obtained with the analysis are compared with the observation in Fig.23. Although the analysis somewhat underestimates the observation, it can predict the actual behaviour reasonably accurately. The load intensity increases nearly linearly with the increase in settlements, and the gradient of the linear portions is greater for M2 than for M10 and greater for slow loading than for quick loading, which agrees very well with the observed results shown in Fig.15.

The initial parts of the relationships given in Fig.23 are replotted in Fig.24. This again compares well with the observation shown in Fig.19. Since the effect of viscosity of soil is not incorporated into the computer code, the difference in load intensity for different loading rates is considered mainly because of difference in the amount of drainage. Calculated relationships between the load intensity at 15% of  $s/B$  and relative loading rates are shown in Fig.25 for M2 and M10. This also agrees with the observation reasonably well. It can be concluded from this that undrained conditions can be assumed for the relative loading rates greater than  $10^5$  kPa/m and that local or partial drainage takes place for the relative loading rates in the range between  $10^2$  and  $10^5$  kPa/cm. The relative loading rates less than  $10^2$  kPa/m yields nearly fully drained conditions. This finding compares well with Asaoka's conclusion that partial



drainage takes place in the range of permeability coefficient between  $10^{-6}$  and  $10^{-9}$  m/sec for soft clays (Asaoka et al. 1992).

### 3.2 Dynamic behaviour

In order to investigate the dynamic response of soil layers consisting of intermediate soils, dynamic cen-



Table 5 Conditions of dynamic tests

soil	ground condition	input motion	seismicity (Kh)	container
M-2	NC	sinusoidal	0.18	rigid box with damper
	NC	sinusoidal	0.28	
	OC	sinusoidal	0.15	
	NC	random	0.30	laminar box
M-5	NC	sinusoidal	0.20	
	NC	sinusoidal	0.20	rigid box with damper
	OC	sinusoidal	0.21	
	NC	random	0.15	
M-10	NC	sinusoidal	0.43	laminar box
	NC	sinusoidal	0.17	
	NC	sinusoidal	0.18	
	NC	random	0.43	rigid box with damper
M-30	NC	sinusoidal	0.22	
	NC	sinusoidal	0.19	laminar box
	NC	sinusoidal	0.18	
	NC	sinusoidal	0.18	
Toyoura sand	Dr=32%	sinusoidal	0.18	rigid box with damper
	Dr=28%	sinusoidal	0.18	
	Dr=40%	random	0.38	
	NC	sinusoidal	0.16	laminar box

centrifuge acceleration:50g

surcharge: 10 kPa

contact pressure at the base of caisson: 35 kPa

number of cycles of sinusoidal motion:20

frequency of sinusoidal motion: 70 Hz

trifuge model tests were carried out using a model shown in Fig.26, in which a model caisson sits on a consolidated soil layer. The model was instrumented with pore pressure transducers, accelerometers and LVDTs. The conditions of the tests are summarized in Table 5. The majority of the input waves were sinusoidal, but an attempt was made to input also random waves. A newly designed laminar box was used in some tests. Observed records of acceleration are illustrated in Fig.27. For soils with plasticity index greater than 5, the acceleration amplifies at initial stages and amplification is greater for soils with higher plasticity index. In all the cases, even for sand, the acceleration of caisson reaches a stationary magnitude at later stages, showing no evidence of liquefaction. Prior tests showed that level ground consisting of sand without a caisson completely liquefies under a similar input condition. This difference in dynamic response can be explained by the fact that the ground was subjected to initial shear stresses due to the existence of caisson. However, as shown in Fig.8, even when the specimens are subjected to initial shear stresses, irrecoverable displacements appear. Therefore the settlement is of

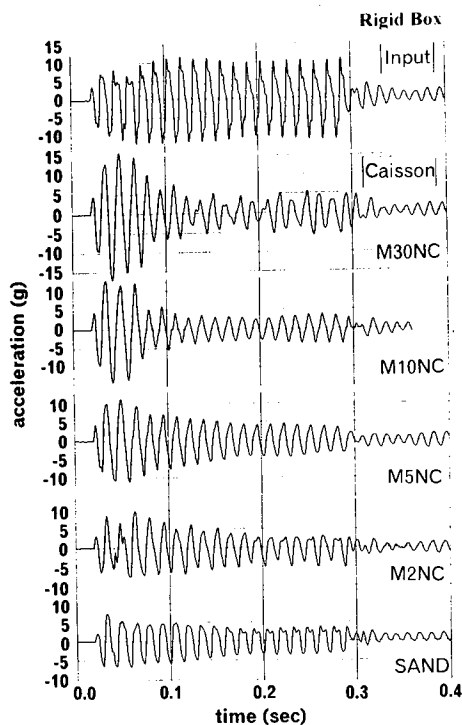


Fig.27 Input base acceleration and observed accelerations of caisson: NC, rigid box

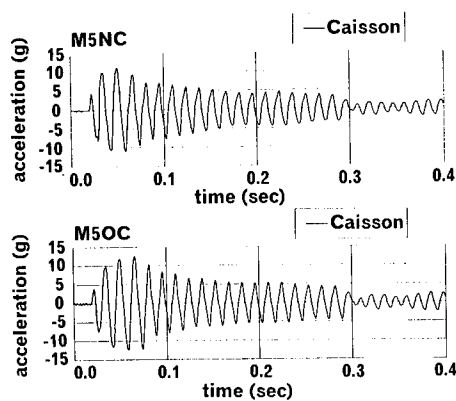


Fig.28 Comparison of observed accelerations of caisson between normally consolidated and over-consolidated M-5: rigid box

overriding importance in this type of case. Dynamic response for normally consolidated and over-consolidated M5 is compared in Fig.28. Although the response at later stages is similar for the two cases, amplification of acceleration is somewhat greater for the over-consolidated case. As shown in Fig.12, over-consolidated specimens have higher stiffness than normally consolidated specimens. The results in

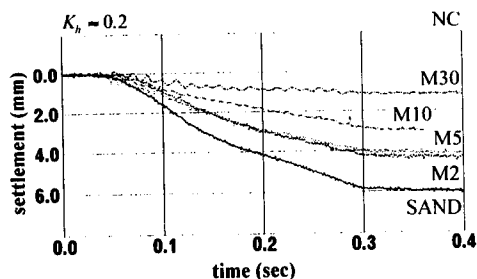


Fig.29 Observed settlements of caissons: NC, rigid box

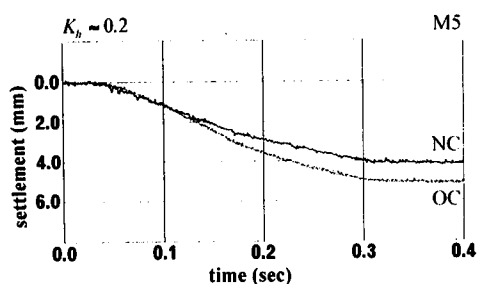


Fig.30 Comparison of observed settlements of caisson between normally consolidated and over-consolidated M-5: rigid box

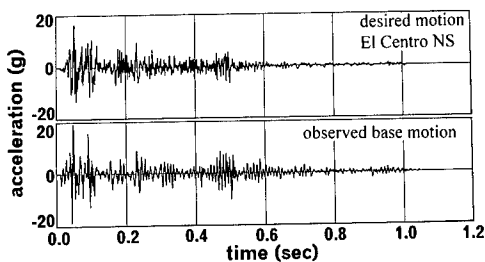


Fig.31 Comparison of desired and observed base motion

Fig.28 show that soils with higher stiffness are subjected to higher cyclic stresses. This leads to a speculation that the stability of soil layers consisting of soil with higher stiffness is not always greater when the soil-structure interaction comes into picture. Records of observed caisson settlements are compared for different soils in Fig.29. Clearly the settlements are greater for soils with smaller plasticity index. The settlements of caisson for normally consolidated and over-consolidated M5 are shown in Fig.30. The settlement is slightly greater for the over-consolidated case, justifying the speculation made concerning the stability of soil layers.

The well-known record of El-Centro NS acceleration is illustrated in the top figure of Fig.31. The one at the bottom is the record of base motions obtained with an earthquake simulator which the authors' group have developed (Takemura et al. 1989). Although high frequency components appear to be missing, the overall performance is fairly reasonable.

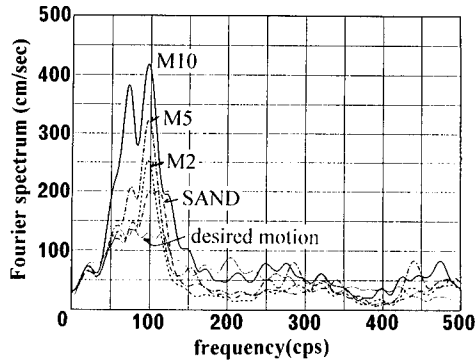


Fig.32 Fourier spectra of desired and observed base motions

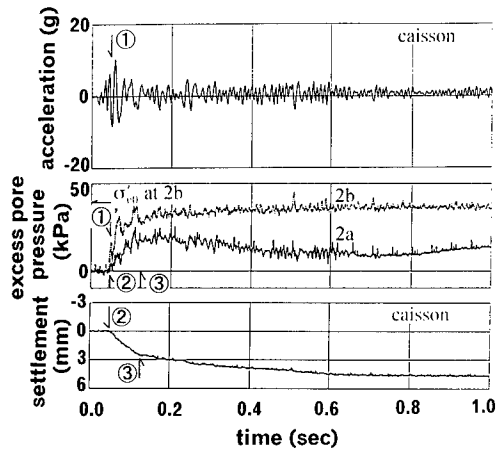


Fig.33 Variations of acceleration, settlement of caisson and excess pore water pressure: M2, NC, random motion

Fourier spectra calculated from the base motions for the tests using four different normally consolidated soils are illustrated in Fig.32, which shows that the performance becomes poorer as the plasticity index of soils increases. Shortage of driving power in the system is considered to be responsible. Tests after this series were very successfully conducted by replacing the servo-valve. In spite of shortage of power in the system, some relevant results were obtained in this test series. Observed accelerations and settlements of caisson for M2 are plotted in Fig.33 together with pore pressures measured at two locations, 2b and 2a shown in Fig.26. The pore pressures start to increase at the instance when the acceleration starts to amplify and the settlement shows a sudden increase at this point. At the point when the pore pressures become stationary, the increase in the caisson settlement begins to reduce. All these three records are consistent. Fourier spectra calculated from observed records for ground and caisson for M2 and M5 are given in Fig.34. The general trend is that dominant frequencies appear in the lower range than for the input base motion both

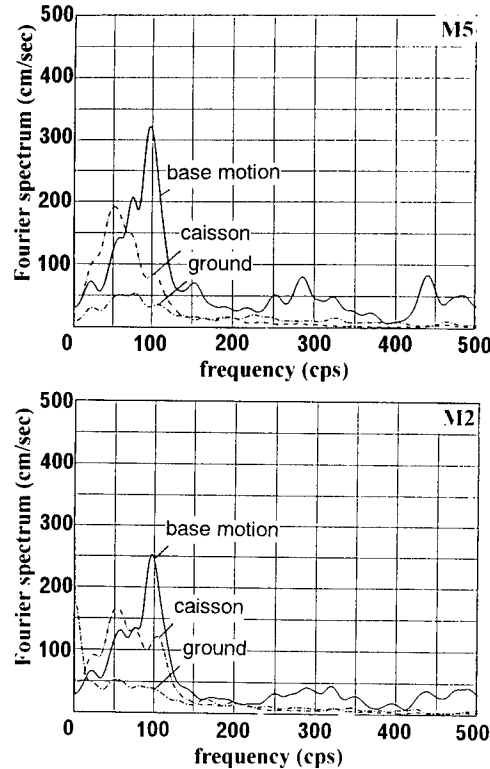


Fig.34 Fourier spectra of observed accelerations: M5, M2

for ground and caisson.

Settlements of caisson for sinusoidal and random waves are plotted against plasticity index in Fig.35, in which figures in the bracket represent horizontal seismicity. The horizontal seismicity is nearly identical for sinusoidal waves and the settlements of caisson recorded are larger for soils with smaller plasticity index. For random waves, the settlements are nearly identical irrespective of soil type, but it has to be noted that the horizontal seismicity increases with the plasticity index. Summarizing all these, it is concluded that when a structure on a soil layer consisting of intermediate soils is subjected to actual earthquake loading, larger settlement can take place for soils with lower plasticity index.

All the experimental data introduced so far are those obtained with a rigid soil box. Although a pair of dampers were installed at both ends of the box as shown in Fig.26 to avoid unfavourable reflection of waves, the authors are well aware that the rigid box has its limitation and that a laminar box has many advantages in carrying out dynamic tests in centrifugal field. A laminar box the authors have developed is shown in Fig.36. The box consists of aluminum frames which are supported by roller bearings placed in the groove of underlying frames. The size of the box is 400x220x150mm and it weighs only 6kg. Shaking tests with a caisson at the surface which are

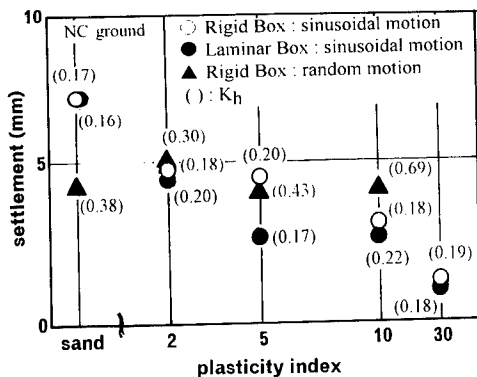


Fig.35 Relationship between observed settlements of caisson and plasticity index

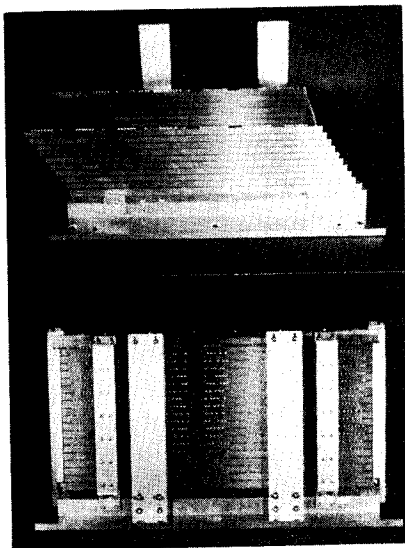


Fig.36 Laminar box used for dynamic tests

similar to the tests discussed above, were carried out with this new laminar box. Acceleration records observed with this laminar box are given in Fig.37. They are considerably different from those obtained with the rigid box shown in Fig.27. For M30 and M10, the acceleration record for the caisson in the laminar box is very similar to the input record, implying that the soil layer follows the input motion. For the rigid box, the acceleration amplifies at the initial stages, probably because the soil layer cannot follow the input motion due to the end constraint and the input acceleration is transferred directly to the caisson. This, in turn, damages the soil layer near the caisson, causing decoupling of motion at subsequent stages. The pattern of acceleration records is very different for M2 and sand. For the laminar box, deterioration of soil layer can clearly be recognized implying that the soil layer is subjected to fairly uniform shear strains. This is not the case with the

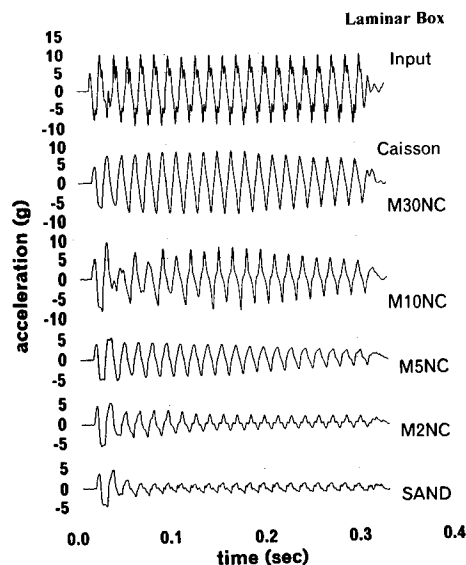


Fig.37 Input base acceleration and observed accelerations of caisson: NC, laminar box

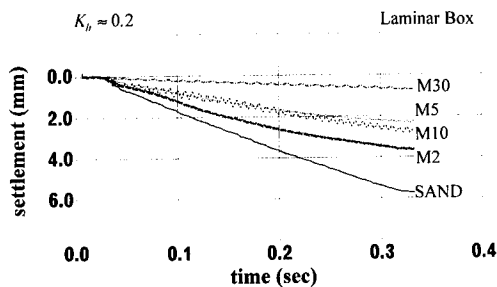


Fig.38 Observed settlements of caissons: NC, laminar box

rigid box, probably because of the end constraint.

The settlements of caisson observed with the rigid box and laminar box are shown in Fig.38. No settlements are observed at the initial stages for the rigid box as indicated in Fig.29. The end constraint seems to be responsible for this. This is followed by large settlements which seem to be caused by deterioration of soil layers near the caisson due to amplification of acceleration at the initial stages as explained above. For the laminar box, the settlement takes place even at the initial stages and the way the settlement progresses is fairly linear. This implies that the soil layer is subjected to uniform shear strains during shaking giving rise to deterioration of soil layers, which in turn results in settlements of caisson. The settlements observed with the laminar box shown in Fig.38 are added to Fig.35. The results do not change the overall trend discussed above, but it is interesting to notice that the settlements observed with the laminar box are slightly smaller than those with the rigid box.

#### 4 CONCLUSIONS

Following conclusions are drawn from this study on mechanical behaviour of intermediate soils as elements and mass.

##### Static triaxial tests

(1) Intermediate soils with extremely low plasticity index exhibits marked strain hardening in undrained conditions. This is considered to be the reflection of properties of sand in the soils. In drained conditions, these soils show characteristics close to those of loose sand.

##### Cyclic triaxial tests

- (1) Artificial soils the authors' group have made are good representation of real soils.
- (2) Higher pore pressures are generated for intermediate soils with smaller plasticity index.
- (3) Reduction in stiffness is more marked and liquefaction takes place at smaller numbers of loading cycles for intermediate soils with lower plasticity.
- (4) Pore pressures generated are smaller and liquefaction resistance is higher for over-consolidated intermediate soils.

##### Centrifuge model tests – Static

- (1) Relationships between load intensity and settlement of footing are linear, particularly at later stages of loading. The gradients of this portion are greater for intermediate soils with lower plasticity and greater for lower loading rate. Drainage in the soils is responsible for this.
- (2) The relative loading rate defined as the ratio of loading rate to the permeability coefficient of soils has turned out to be a useful parameter to judge the extent of drainage in intermediate soils. Undrained conditions can be assumed for the relative loading rate greater than  $10^5 \text{ kPa/m}$ . Partial or local drainage takes place at relative loading rates in the range between  $10^5$ – $10^2 \text{ kPa/m}$  and fully drained conditions are achieved at the rates less than  $10^2 \text{ kPa/m}$ . This is supported by the pore pressures observed in loading tests.
- (3) The pattern of failure shifts from general shear type to local shear type as the relative loading rate decreases or as the extent of partial or local drainage increases.
- (4) The effect of preloading is more marked for intermediate soils with higher plasticity.
- (5) Finite element analyses based on the modified Cam clay model gives reasonable prediction on the effect of loading rate on the deformations and bearing capacities of intermediate soils.

##### Centrifuge model tests – Dynamic

- (1) The dynamic stability of a soil layer consisting of soil with high stiffness is not always greater, when a structure exists on the layer.

(2) When a structure on a soil layer consisting of intermediate soils is subjected to an earthquake, larger settlements take place for the soils with lower plasticity.

(3) Reasonable response is obtained with a newly designed laminar box. It seems that the end effects can be eliminated with this laminar box to some extent.

#### REFERENCES

- Asaoka, A., Nakano, M. and Matsuo, M. 1992. Prediction of the partially drained behavior of soft clays under embankment loading. *Soils and Foundations*, Vol.32, No.1, 41–58
- Georgiannou, V.N., Burland, J.B. and Hight, D.W. 1990. The undrained behaviour of clayey sands in triaxial compression and extension. *Geotechnique*, Vol.40, No.3, 431–449
- Georgiannou, V.N., Hight, D.W. and Burland, J.B. 1991. The undrained behaviour of natural and model clayey sands. *Soils and Foundations*, Vol.31, No.3, 17–29
- Harada, M., Urasawa, Y. and Shirai, S. 1990. Liquefaction potential of fine-containing sands of reclaimed deposits. *Journal of JSSMFE*, Vol.38, No.6, 21–26 (in Japanese)
- Idriss, I.M., Dobry, R. and Singh, R.D. 1978. Nonlinear behaviour of soft clays during cyclic loading. *Journal of Geotech. Div. ASCE*, Vol.104, GT12, 1427–1447
- Ishihara, K. and J. Koseki (1989). Cyclic shear strength of fine-containing sands. *Proc. Discussion Session on Influence of Local Conditions on Seismic Response*, 12th ICSMFE, 101–106
- Mori, S., Numata, A., Sakano, N. and Hasegawa, M. 1991. Characteristics of liquefied sands on reclaimed lands during earthquakes. *Journal of JSSMFE*, Vol.38, No.6, 21–26 (in Japanese)
- Nakase, A. 1978. Personal correspondence with Osterberg, J.O.
- Nakase, A., Kusakabe, O., Nakanodo, F. and Ohneda, H. 1985. Case record of quaywall construction on a coral mixed cohesive soil. *Soils and Foundations*, Vol.25, No.4, 103–116
- Nakazono, H. 1991. Fundamental study on dynamic mechanical properties of intermediate soils. Master thesis Dept. Civ. Engrg. Tokyo Institute of Technology (in Japanese)
- Takemura, J., Kimura, T. and Suemasa, N. 1989. Development of earthquake simulators at Tokyo Institute of Technology. Technical Report of Dep. Civ. Engrg. T.I.T., No.40, 41–68
- Takemura, J. 1991. Bearing capacities and deformations of clay of which strength varies with depth. Doctoral Thesis Tokyo Institute of Technology (in Japanese)
- Ymaguchi, H. and Murakami, Y. 1978. Some analytical results of a plane strain consolidation problems of clay layer with finite thickness. *Soils and Foundations*, Vol.18 No.1, 98–104

## What the VELACS project has revealed

K. Arulanandan, M. Manzari, X. Zeng & M. Fagan  
*University of California, Davis, Calif., USA*

R. F. Scott  
*California Institute of Technology, Pasadena, Calif., USA*

T. S. Tan  
*National University of Singapore, Singapore*

**ABSTRACT:** The VELACS project was conducted in order to improve existing methods for the analysis of the consequences of soil liquefaction. The project showed that centrifuge studies are repeatable only under carefully controlled conditions. Most procedures were able to predict the onset of liquefaction in contractive soils, but only effective stress based fully coupled nonlinear procedures were able to predict deformations due to liquefaction. None of the currently available procedures could simulate the behavior of dilative soils adequately. Problems were attributed to improper constitutive model implementation and inadequate calibration.

### 1 INTRODUCTION

The VELACS (VERification of Liquefaction Analysis using Centrifuge Studies) project was a collaborative effort among seven universities: University of California, Davis; California Institute of Technology; Cambridge University; University of Colorado, Boulder; Massachusetts Institute of Technology; Princeton University; and Rensselaer Polytechnic Institute. From 1989 to 1993, extensive research was conducted at these universities to develop improved methods for experimentally simulating and numerically modeling the consequences of soil liquefaction. The project was coordinated by the University of Florida, North Carolina State University, and the University of Southern California as well as the Earth Technology Corporation (Arulanandan and Scott, 1993).

The main objective of the VELACS project was to provide the experimental data necessary to determine the efficiency of the various computer codes available for dynamic soil analysis. In order to attain this objective, nine centrifuge model tests with well defined boundary conditions were performed (see Figure 1). The soils used in these studies were extensively tested so that their material behavior could be properly characterized. The base motions used were selected prior to performing the actual tests. A priori or "Class A" numerical predictions of model response were made by over 30 numerical modelers using various numerical procedures. The project concluded that only fully coupled, nonlinear, effective stress based procedures are capable of properly capturing the consequences of soil liquefaction.

### 2 REPEATABILITY OF CENTRIFUGE TESTS

Centrifuge modeling is known to be a reliable tool for studying the mechanisms of soil behavior in boundary value problems. In order to gauge the errors inherent in centrifuge studies, each of the nine VELACS models was performed at three separate universities. Test results from different facilities showed good repeatability only when the centrifuge modelers followed identical methods of model preparation, and only when the centrifuge facilities were capable of producing simulated earthquake motions which accurately reproduced the entire range of frequency components specified.

In the VELACS project, Models 1, 2, 4a, and 4b all showed fairly good repeatability (Arulanandan and Scott, 1993). Model 4a illustrates reasonable centrifuge repeatability between universities. The measured excess pore pressures, and the horizontal and vertical accelerations were nearly identical among the Davis, Caltech, and RPI tests even though the input base motion achieved by Caltech did not contain precisely the correct frequency components. However, the surface settlement measured by the three universities did not agree all that well (Figure 2). Note that much greater repeatability may be attained by a single investigator using the same facilities to perform a number of centrifuge tests.

Although the centrifuge studies showed reasonable repeatability for models with simple geometry, the repeatability for more complex geometries was not very good. In Model 7, a silt core embankment was modeled at Davis, RPI, and Colorado. The specified input base motion had considerable high frequency components that were not captured by the hydraulic actuators used to simulate the base motion. This is



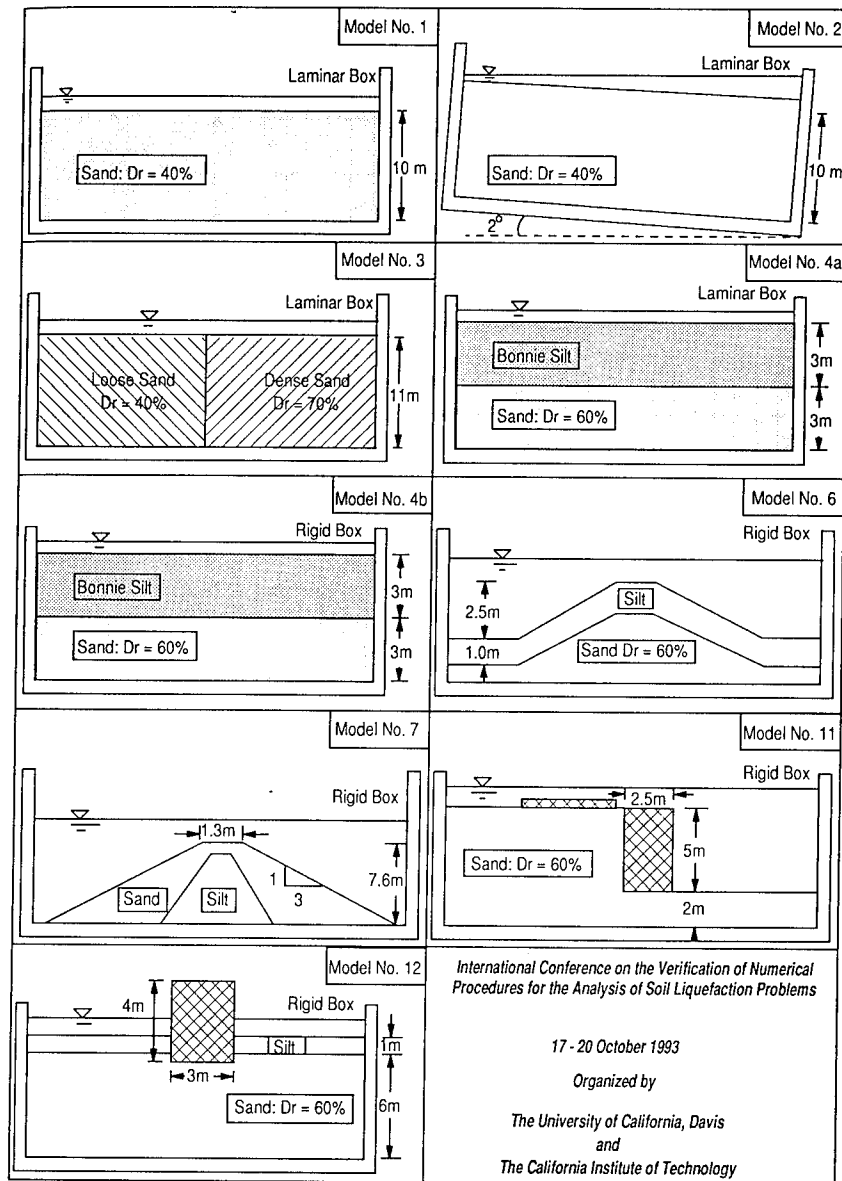
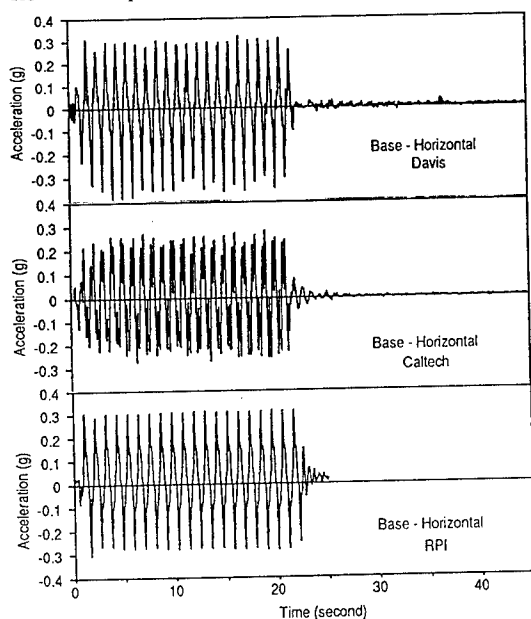
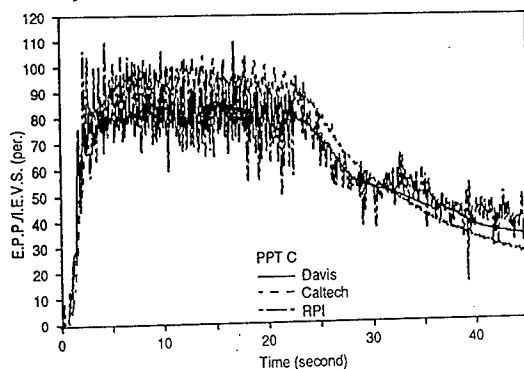


Fig. 1: Centrifuge Model Configurations for VELACS Project

#### Horizontal input motion



#### Excess pore pressure at mid-depth of sand layer



#### Settlement of the silt surface

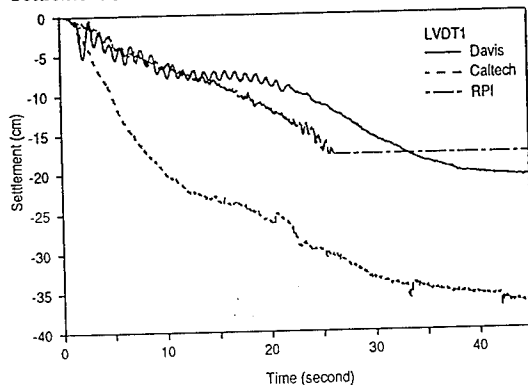


Fig. 2: Repeatability in Centrifuge Model 4a

the main reason that the accelerations, displacements, and pore pressures did not show good repeatability among the universities (Figure 3). Other issues which may have led to poor repeatability include human error in transducer placement, boundary effects of the model containers, and undesirable side effects such as unaccounted for vertical base motions. These phenomenon should be thoroughly studied in future applications of centrifuge modeling.

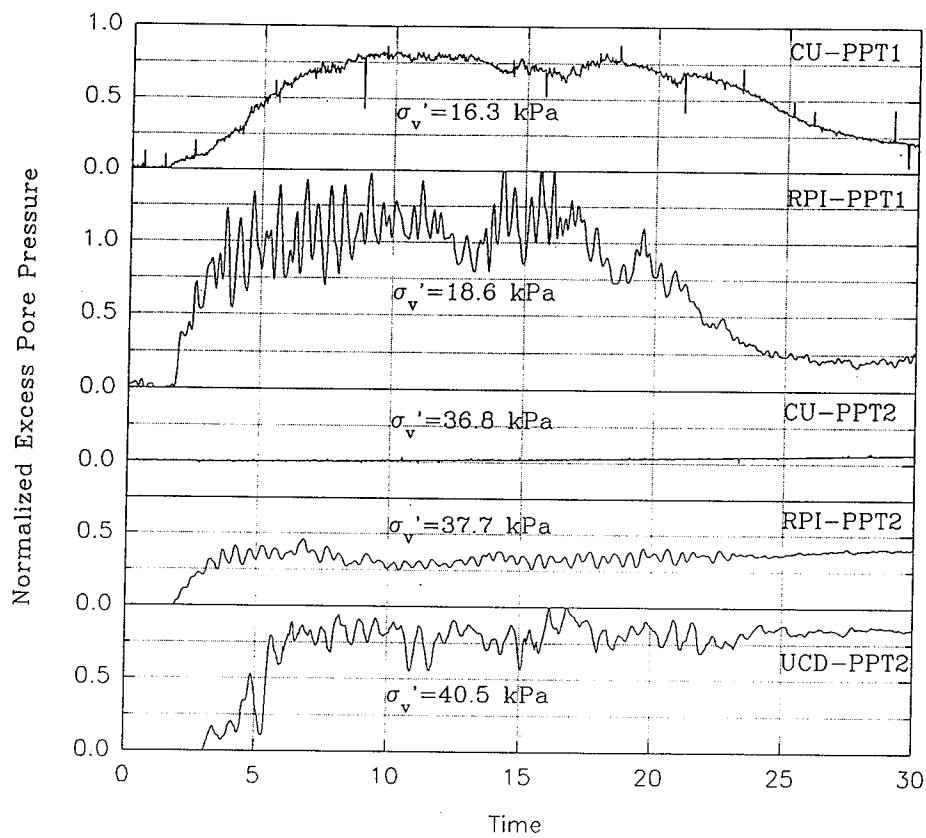
### 3 SOIL LIQUEFACTION ANALYSIS

In order to fully appreciate the significance of the VELACS findings, a brief summary of the different types of soil liquefaction analysis procedures currently available will be presented. Uncoupled, or total stress equivalent linear methods of analysis have been widely used in programs such as SHAKE, QUAD-4, FEADAM, LUSH, and FLUSH. The fundamental assumption of the equivalent linear methods is that nonlinear soil response can be approximated satisfactorily by a damped linear elastic model. The stress-strain properties of a soil are defined by strain-dependent shear moduli and equivalent viscous damping ratios. For saturated cohesionless soils, this method is used in conjunction with laboratory data from undrained cyclic loading tests to assess liquefaction potential at any part of the system. This method can not accurately calculate displacements, and consequently Newmark's Sliding Block method must also be used.

DESRA and TARA are the most representative codes that have been developed based on the indirect coupling methodology. Indirectly coupled methods assume that the material can be considered to behave elastically in small load increments. The bulk and shear moduli of the soil are changed in each load increment. The main improvement in this approach is the linkage of pore pressure generation to the nonlinear equations of motion. Both DESRA and TARA include a semi-empirical pore pressure generation model which relates the change in pore pressure to the change in the volumetric strain under drained conditions. The excess pore pressure generated during each load increment is used to calculate the current effective stress, which in turn is used to compute the pressure dependent elastic moduli for the next increment or iteration. To account for the possibility of pore pressure dissipation during dynamic excitation or after the event, a one dimensional diffusion mechanism is also built into these programs. However, the poor simulation of pore pressure dissipation leads to inaccurate displacement time histories.

DYSAC2, DYNAFLOW, and SWANDYNE are codes which have been developed using fully coupled effective stress based formulations. In fully coupled methods, the equations governing the motion of the solid and fluid phases are coupled with the mass balance equation resulting in fully coupled differential equations governing the problem. These

### Normalized Excess Pore Pressure



### Normalized Response Spectra

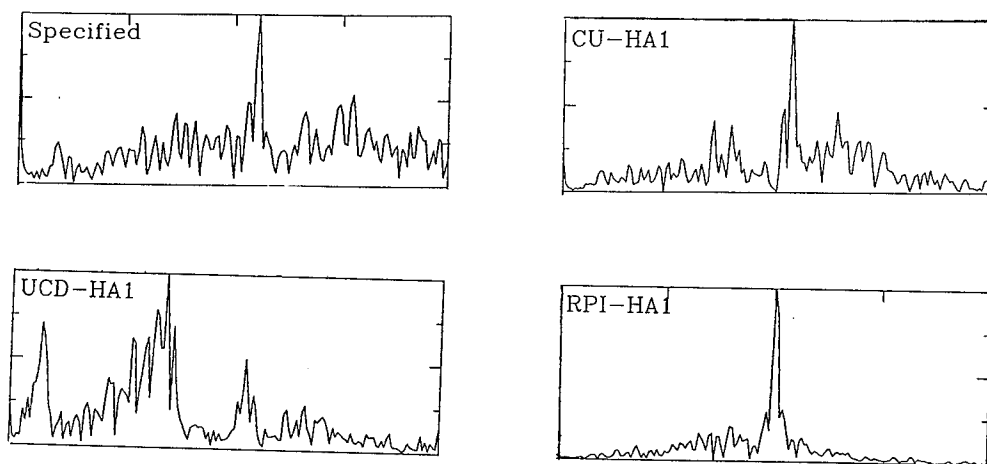


Fig. 3: Poor Repeatability in Centrifuge Model 7

differential equations are then approximated by a weighted residual method such as Galerkin's method. The approximate integral form is then discretized by the finite element technique. The final matrix differential equations are integrated by a temporal integration method such as the Hilbert-Taylor-Hughes method. In fully coupled methods, pore pressure generation and dissipation are directly linked to the soil skeleton deformation according to Biot's formulation, and consequently are also controlled by the constitutive relationship. This is potentially the most accurate method of analysis.

#### 4 CONTRACTIVE/DILATIVE SOILS

All existing numerical procedures for soil liquefaction analysis are generally effective in simulating the onset of liquefaction in contractive noncohesive soils. VELACS Model 1 modeled the simplest possible case: a single layer of level sand. All of the numerical procedures used in the VELACS project were capable of predicting liquefaction in the top of the sand column. However, a wide range of differences exist in the predictions of deformations induced by liquefaction. Predicted surface settlements in Model 1 ranged from less than 0 cm to more than 34 cm (whereas the centrifuge showed about 20 cm). Some of the predictions even showed surface swelling during liquefaction (Figure 4).

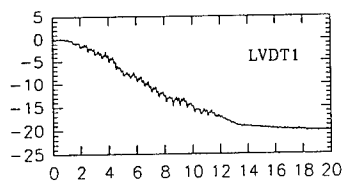
VELACS showed that fully coupled effective stress based numerical procedures predict deformation better than partially coupled or uncoupled procedures which utilize empirical relationships to correlate the pore pressure generation with the volumetric strain of the soil. The Class A VELACS predictions revealed that the latter procedures may produce unrealistic deformation trends during the shaking phase for contractive soils.

None of the available numerical procedures adequately simulate the behavior of dilative soils. VELACS Model 6 consisted of a heterogeneous embankment consisting of a relatively dense sand core overlain by a silt layer. An examination of the Class A predictions conducted on Model 6 reveals that predictions of pore water generation in the sand core (PPTD) generally do not agree with the experimental results (Figure 5). This discrepancy is expected due to the deficiencies in the existing constitutive models used to simulate the cyclic behavior of dense sands.

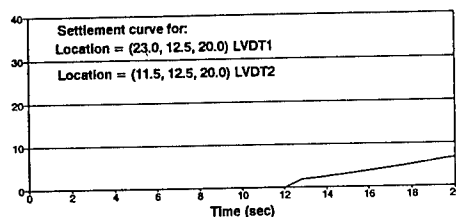
#### 5 PROPER CONSTITUTIVE MODELING

One of the major lessons learned from the VELACS project is that constitutive models play an essential role in any analysis of soil liquefaction and deformation. A comparison of the different Class A predictions made using effective stress based procedures shows a wide range of deficiencies. These are two main reasons for these deficiencies, namely, improper model calibration and improper numerical implementation.

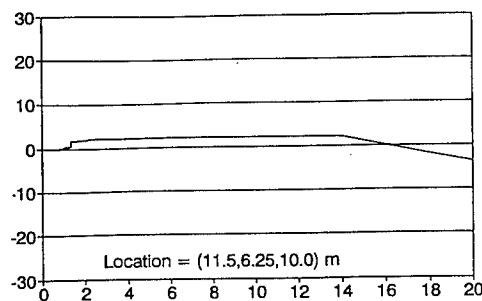
Settlement Measured by LVDT1



Settlement Predicted by Uncoupled Code



Settlement Predicted by Partially Coupled Code



Settlement Predicted by Fully Coupled Code

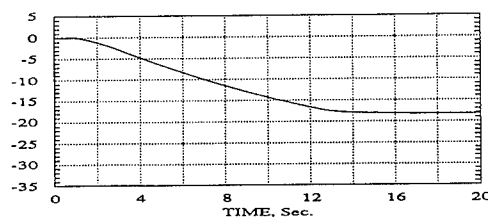
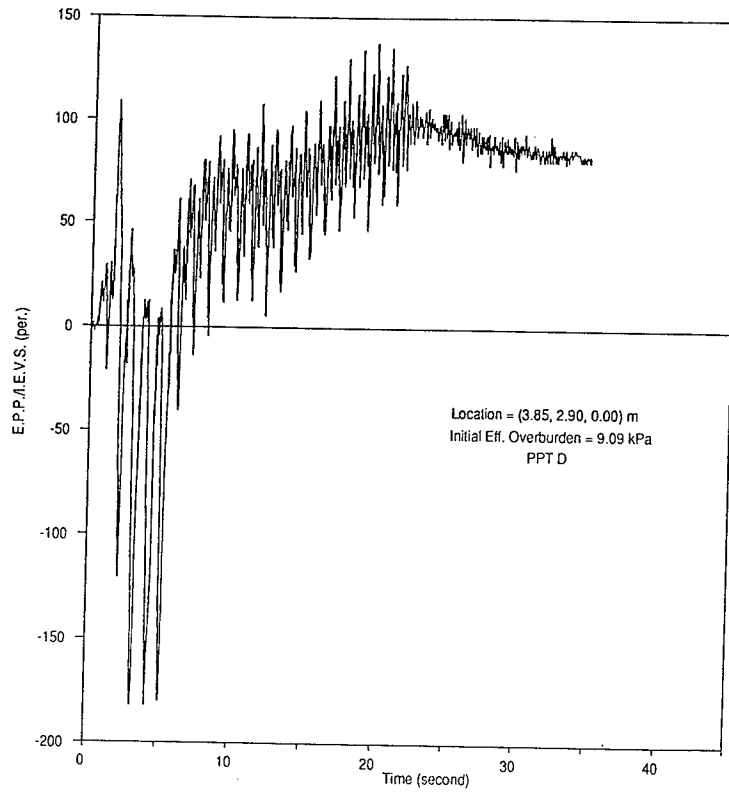


Fig. 4: Surface Settlement for Model No 1

Some existing models are incapable of simulating the stress-strain response of non-cohesive soils for different stress (or strain) paths using a unique set of parameters. In most of the models, a compromise must be made by choosing an average set of parameters which should approximate the stress path in the boundary value problem. This compromise involves considerable engineering judgement.

### Pore Pressure Measured by PPTD



### Pore Pressures Predicted with Fully Coupled Code

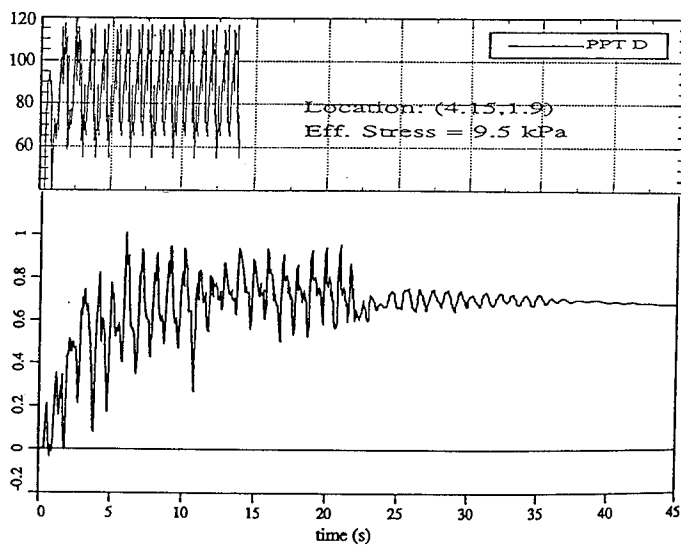


Fig. 5: Pore Pressure (PPTD) for Model 6

In general, predictors try to get a best fit to the results of laboratory tests. However, there is no standard procedure for achieving a best fit. Consequently, different sets of parameters may be attained by different users for the same problem, even if both predictors use the same code to predict the same problem.

The VELACS predictors used different methods to implement their plasticity based constitutive models in the computer codes. The accuracy and stability of these methods was not studied thoroughly. A close examination of the published materials on the constitutive models used in the VELACS project reveals that most of the constitutive equations were integrated using conventional integration procedures. In many cases, special features of the constitutive models such as pressure-dependent moduli were not properly implemented in the integration procedure. Recent studies show that even in the case of simplest soil plasticity model (the modified cam clay model) special integration is necessary if accurate and reliable results are to be obtained.

## 6 CONCLUSIONS

Centrifuge studies show repeatability between universities only if the shakers used are capable of reproducing the frequency components of the input base motion and if care is taken in model preparation. Most predictive methods are capable of predicting the onset of liquefaction for contractive soils, although only fully coupled nonlinear effective stress based numerical procedures can properly predict displacements for contractive soils. None of the presently available procedures can properly characterize dilative soils. Constitutive modeling is the most important factor in dynamic soil modeling, yet there is still considerable ambiguity in the calibration procedure. Constitutive models need to be properly implemented in order to give reasonable results.

VELACS showed that only effective stress based nonlinear numerical procedures are capable of producing reasonable predictions for soil liquefaction problems. These procedures are highly dependent upon the performance of their plasticity based constitutive models, and consequently it is important to properly characterize the soil and obtain a reliable set of material parameters. Analysis should include a priori evaluations of the site response to representative historical earthquakes. Such evaluations would require a thorough site characterization using non-destructive in situ methods (Arulanandan et al., 1977; 1990).

Future research efforts along these lines include the VELACS 2 project. The project will attempt to resolve the difficulties encountered in the Class A predictions of VELACS, and to isolate the main causes of these difficulties. Intense scrutiny will be placed on each step of the research in order to assure the acquisition of a reliable data base. It will attempt to identify reasons for poor numerical predictions

such as improper model calibration and implementation. It will also propose solutions to these problems. The ultimate accomplishment will be the recommendation of procedures for the analysis of geotechnical structures by professional engineers.

## 7 ACKNOWLEDGEMENTS

The National Science Foundation sponsored the VELACS project, and their funding is greatly appreciated.

## REFERENCES

- Adalier, K., Elgamal, A. (1993). "Experimental Results of Centrifuge Model No. 7" *Verification of Numerical Procedures for the Analysis of Soil Liquefaction Problems*, Vol. 1, Davis, CA, pp 799-808.
- Arulanandan, K. (1977). "Method and Apparatus for Measurement of Porosity and Fabric of Soils." Patent, University of California, Davis, Regents of University of California.
- Arulanandan, K. and Yogachandran, C. (1990). "A Preliminary Analysis of Ground Response and Soil Liquefaction of Sites in the Marina District of San Francisco Subjected to the Loma Prieta Earthquake of October 17, 1989." Technical Report No. 1990-1, Department of Civil Engineering, University of California, Davis, CA.
- Arulanandan, K., and Scott, R.F. (1993). "Verification of Numerical Procedures for the Analysis of Soil Liquefaction Problems." Volume 1, Experimental Results and Numerical Predictions, University of California, Davis, A.A. Balkema, Rotterdam.
- Arulanandan, K., Zeng, X., Rashidi, H. (1993). "Experimental Results of Model No. 4a." *Verification of Numerical Procedures for the Analysis of Soil Liquefaction Problems*, Vol. 1, Davis, CA, pp 595-600.
- Arulanandan, K., Zeng, X., Rashidi, H. (1993). "Experimental Results of Model No. 6." *Verification of Numerical Procedures for the Analysis of Soil Liquefaction Problems*, Vol. 1, Davis, CA, pp 737-744.
- Astaneh, S., Ko, H., Sture, S. (1993). "Experimental Results of Model No. 7" *Verification of Numerical Procedures for the Analysis of Soil Liquefaction Problems*, Vol. 1, Davis, CA, pp 783-798.

Manzari, M. and Arulanandan, K. (1993). "Numerical Prediction for Model No 1." *Verification of Numerical Procedures for the Analysis of Soil Liquefaction Problems*, Vol. 1, Davis, CA, pp 179-186.

Rollins, K. and Marks, M. (1993). "Numerical Prediction for Model No 1." *Verification of Numerical Procedures for the Analysis of Soil Liquefaction Problems*, Vol. 1, Davis, CA, pp 197-212.

Scott, R., Hushmand, B., Rashidi, H. (1993). "Duplicate Test of Model No. 4a: Horizontally Layered Soil in Laminar Box" *Verification of Numerical Procedures for the Analysis of Soil Liquefaction Problems*, Vol. 1, Davis, CA, pp 601-610.

Siddharthan, R., and El-Gamal, M. (1993). "Numerical Prediction for Model No 1." *Verification of Numerical Procedures for the Analysis of Soil Liquefaction Problems*, Vol. 1, Davis, CA, pp 221-246.

Taboada, V., Dobry, R. (1993). "Experimental Results of Model No. 1" *Verification of Numerical Procedures for the Analysis of Soil Liquefaction Problems*, Vol. 1, Davis, CA, pp 3-18.

Taboada, V., Dobry, R. (1993). "Experimental Results of Model No. 4a at RPI" *Verification of Numerical Procedures for the Analysis of Soil Liquefaction Problems*, Vol. 1, Davis, CA, pp 611-623.

Taboada, V., Dobry, R. (1993). "Experimental Results of Model No. 7" *Verification of Numerical Procedures for the Analysis of Soil Liquefaction Problems*, Vol. 1, Davis, CA, pp 809-817.

Yogachandran, C. (1993). "Numerical Prediction for Model No 6." *Verification of Numerical Procedures for the Analysis of Soil Liquefaction Problems*, Vol. 1, Davis, CA, pp 767-776.

## 2 Centrifuge facilities





## LXJ-4-450 geotechnical centrifuge in Beijing

Y. Du, S. Zhu, L. Han & L. Ru

*Institute of Water Conservancy and Hydroelectric Power Research, Beijing, People's Republic of China*

P. Jia & W. Wang

*Chinese Academy of Space Technology, Beijing, People's Republic of China*

**ABSTRACT:** The LXJ-4-450 geotechnical centrifuge has been operational since March 1991. This machine is 5.03 metres in radius and can carry a payload of 1500 kg to 300 gravities. The centrifuge main body consists of two symmetrical rotary arms and two swing baskets. The centrifuge facility includes a digital data acquisition and control system. The foundation of the centrifuge was designed to eliminate the potential for resonance and avoid transfer of vibrations to other parts of the laboratory during centrifuge operation.

### 1. INTRODUCTION

The centrifugal modelling technique, which is actively studied and adopted in many countries, is a versatile and powerful experimental approach in geotechnical engineering. The advantage of this modelling technique is that deformation and failure processes in geotechnical engineering can be studied and viewed under prototype stress conditions. In order to satisfy needs of high dam construction in China, development of the LXJ-4-450 geotechnical centrifuge was placed in the national key technologies R & D programme during the seventh five-year plan. This centrifuge has been operational since March 1991. Operation of the centrifuge has shown that the centrifuge main body runs smoothly, and the automatic control and data acquisition systems work reliably. The development of the centrifuge was jointly carried out by the following organizations: Institute of Water Conservancy and Hydroelectric Power Research; Beijing Institute of Science of Environmental Engineering, Chinese Academy of Space Technology; Nanjing Equipment Factory of Electric Power Automation and The First Heavy Machinery Works. In this paper the specifications, general construction of the centrifuge main body, drive system and data acquisition system are introduced, along with the building and layout of the laboratory.

### 2. SPECIFICATIONS

The LXJ-4-450 geotechnical centrifuge has the following specifications:

Max. rotary radius	5.03 metres
Max. acceleration	300 gravities
Max. rotary speed	259 rpm
Payload (under 300 g)	1,500 kg
Payload capacity	450 gt
Model basket	1.5 m * 1.0 m * 1.5 m
Onset time	
(up to max. acc.)	15-20 min.
Continuous	
operational time	24 h
Driving power	700 kW
There are 14 power sliprings, 100 signal sliprings and 2 pressure revolving adapters on the centrifuge.	

### 3. MAIN BODY OF CENTRIFUGE

The general structure of the centrifuge main body involves two symmetrical rotor arms and

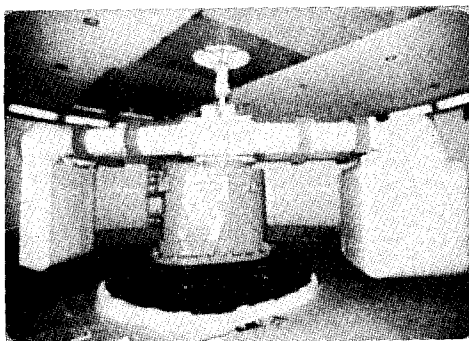
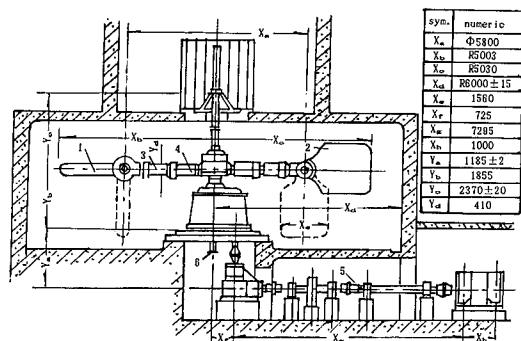


Fig.1. LXJ-4-450 Geotechnical Centrifuge

two swing baskets, as shown in Fig.1 and fig.2. The main components include the rotor arm, model basket, counterweight basket, turning platform, decelerator, drive shaft, slipping stacks and revolving pressure adapters. This structural form can automatically eliminate any unbalanced moment due to the 1g gravity field and mechanical friction during swing up. During the test, symmetry of the mass and centroid of the model and counterweight baskets are guaranteed by using specific counterweights.



- 1-Counterweight basket 2-Model basket  
3-Rotary arm 4-Turning platform  
5-Main drive 6-Adapter

Fig.2. The elevation view of the centrifuge and its drive system

The rotary arm is assembled by two circular hollow steel beams and five shackles. Because the overall structure of the arm has no welds, adverse stress concentrations are eliminated. The assembled arm has a length of 6.4 m, a width of 1.9 m and a height of 0.6 m. To streamline the arm, outer coverings are used. The model basket consists of a bottom plate and two side plates. Maximum deflection of the bottom plate is less than 1 mm under a 450 gt load. The structural form of the side plates was determined based on the objectives of maximizing model view and minimizing self weight while satisfying strength and stiffness requirements. The windows of the side plates are 1.0 m wide and 0.75 m high. The bottom plate is connected to the two side plates by a joggle joint, and fixed by using screws in the side direction. Thus the large shearing force at the joint is borne by the mortise and tenon; however, the screws only bear the tensile force in the side direction. According to the distributive specificity of the centrifugal force field, the model basket is swung in the long direction of the bottom plate, thus the accuracy of the two-dimensional model test can be increased.

There is the main shaft system in the turning platform, which consists of a hollow main shaft with varied diameters, a thrust roller bearing and two radial bearings. The main shaft has a length of 1.85 m, an internal diameter of 0.2 m and a maximum outer diameter of 0.4 m. The distance between the two radial bearings is 1 m. The thrust bearing is placed between the two radial bearings. The load-bearing and anti-overturning are respectively borne by the thrust and radial bearings. There is an oil box near the main bearing. If the power supply stops while the centrifuge is rotating, this oil box can automatically supply oil to the main bearing for about 15-20 min. to maintain safe operation. The overall size of the turning platform is 2 m long, 0.8 m wide and 1.3 m high.

#### 4. DRIVE SYSTEM

The drive system of the centrifuge involves a direct-current motor and a speed governor, which is a digital-analogue combination SCR governor with microcomputer automatic control subsystems. A block diagram of the drive system is shown in Fig.3. To meet the requirements of the power and rotatory speed of the centrifuge, a Z500-1A direct-current motor with 700 kW and GSFA22-1500A/660VF SCR governor were selected. The rated revolution, voltage and current of the direct-current motor are 1,000 rpm, 660 V and 1121 A, respectively. The regulating control circuit consists of double-closed loops, in which the external speed loop is the main regulator and the internal current loop is the subsidiary one. The advantage of this control circuit is that the dynamic difference is less, and thus the self-regulating ability is better. The regulated range of speed is 1:10 for the motor, namely, the revolution of 100- 1,000 rpm can be adjusted smoothly. The stabilized speed accuracy is better than 0.5% in the overall regulated range.

The digital-analogue combination SCR governor involves a digital external loop outside the double-closed loops of the above-mentioned speed governor. The digital feedback signal of the revolution is obtained by using a photoreader and a digital measuring circuit with the M/T method. There are four microcomputers, which are used as the controller, monitor, display and so on, in the automatic control subsystem. Besides the display, another three microcomputers are joined into the network, that automatically control the entire process of the centrifuge operation on the organized programs. The display is an autonomous device, to ensure elimination of any interference and correct indication of the parameters of the operation. The operational flow chart

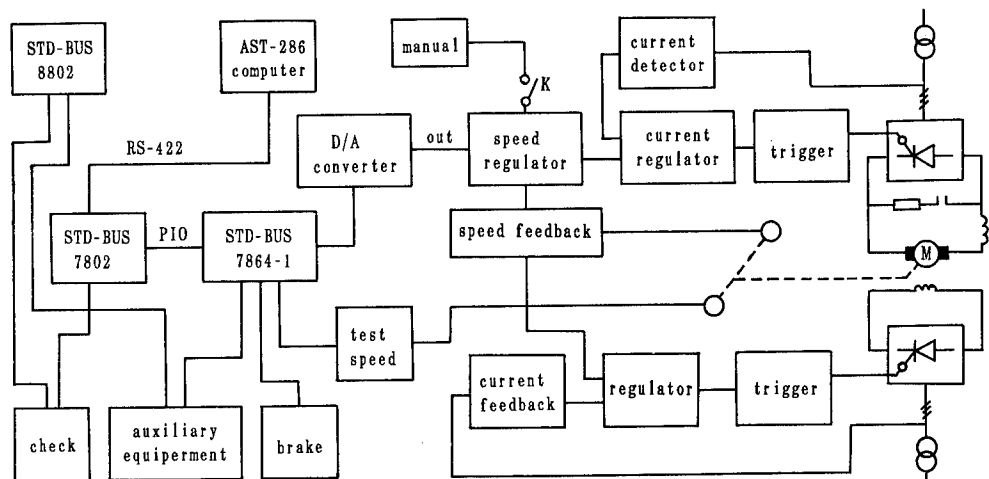


Fig.3. A block diagram of the drive system

of the system is shown in Fig.4. In order to ensure safety of the centrifuge operation, the hand control subsystem is added in this control system. The automatic and hand controls

can be interchanged without any disturbance.

## 5. DATA ACQUISITION SYSTEM

The data acquisition and control system consists mainly of the transducers, preprocessing element, and transmitting and data processing elements. Digital signal transmission was adopted for the data acquisition system, because of the operating environment of the centrifuge. This form of data transmission reduces system interference, allowing a reduction in the number of sliprings and accuracy requirements.

The HP3497A data acquisition/control unit is used as the preprocessing element. This data acquisition unit is able to measure voltage, resistance, frequency, pressure, strain, etc. The measuring accuracies are  $1\mu V$  for voltage,  $1m\Omega$  for resistance and  $1\mu\epsilon$  for strain. The microcomputer adopted is a HP standard industrial microcomputer with quasi 32 bit. The communication between the microcomputer and data acquisition unit adopts HP-IB parallel interface. A maximum transmission speed is 1Mb/s. The data acquisition unit is fixed on to the arm near the shaft. Generally, the output magnitude of the transducers, which measure the pore water pressure, earth pressure, acceleration, displacement etc, is on the order of mV. The strain gauge output is in  $\mu V$ .

In order to observe and record the model deformation at any time, a closed circuit television (CCTV) system is also installed. The CCD (charge coupled device) colour cameras are placed into the model basket. The scheme

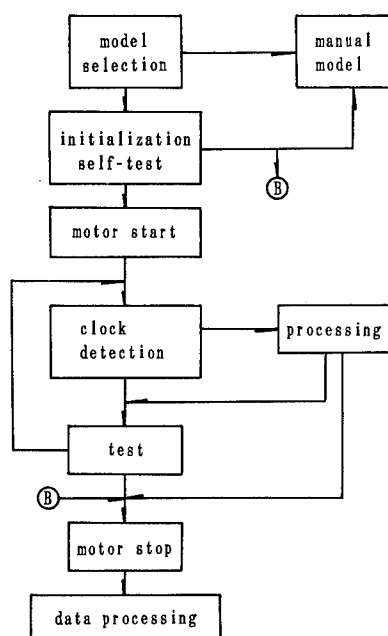
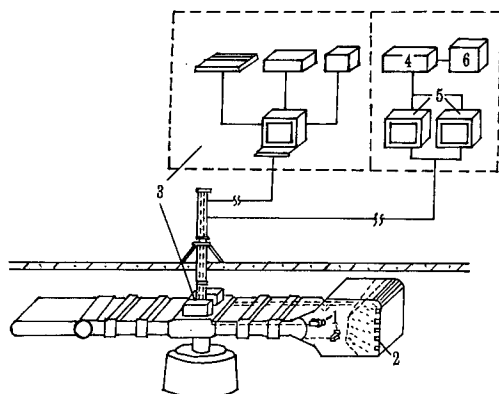


Fig.4. Flow chart of the system operation



- 1- Camera 2- Transducers  
3- HP data acquisition system  
4- Video recorder 5- Monitor  
6- Video graphic printer

Fig.5. Scheme of the data acquisition and CCTV system on the centrifuge

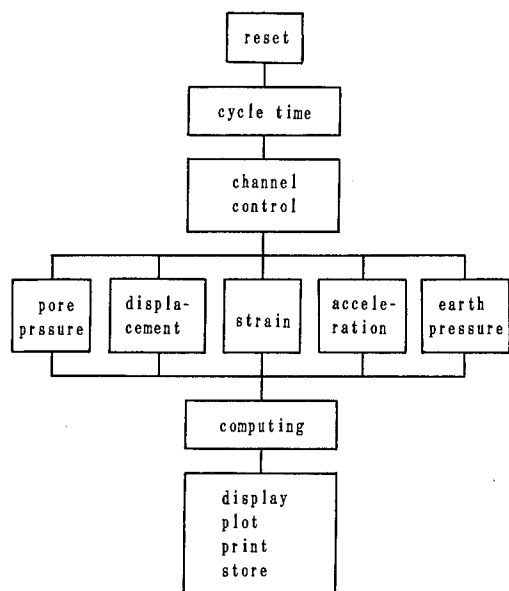
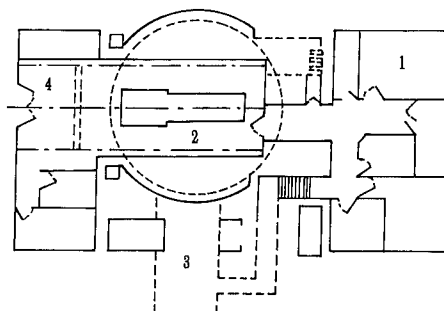


Fig.6. Flow chart of data acquisition programs

of the data acquisition and CCTV system is shown in Fig.5.

The data acquisition programs of this system are written in Basic and Pascal. The flow chart of the programs is shown in Fig.6. The transducers of all kinds can be installed simultaneously in a testing model. According to the transducer signal acquired, the corres-



- 1- Control room 2- Hoist room  
3- Drive system room  
4- Sample preparation areas

Fig.7. Layout of the centrifuge laboratory

ponding subprograms are automatically transferred and the corresponding physical quantities are computed and displayed by using the subprograms. At the same time, the testing results can be plotted by using the plotting subprograms.

## 6. LABORATORY

This laboratory has a building area of 554 m<sup>2</sup>. There are the monitor-control and data processing areas, sample preparation areas, workshop and office in the laboratory. The general arrangement of this laboratory is shown in Fig.7.

The centrifuge main body is placed in the basement of the building, whose foundation is treated by the replacement method. The subbase of the centrifuge main body and the foundation of the drive system are an integral reinforced concrete structure cast with high strength concrete. The subbase of the centrifuge main body is an integral circular hollow construction of 11.0 m in diameter and 2.9 m in height. The designed first and second natural frequencies of the foundation are  $f_1=11.05$  Hz and  $f_2=20.5$  Hz, respectively. The designed vertical and horizontal amplitudes are  $A_z=11 \mu\text{m}$  and  $A_z=58 \mu\text{m}$ , respectively. In order to measure the practical natural frequencies of the foundation, in situ shock tests were carried out by using a TQJ-4 synchronous shock machine. The test results show four natural frequencies: 11.2, 15.0 Hz (horizontal direction) and 15.0, 17.0 Hz (vertical direction). The designed natural frequencies of the foundation generally agreed with the measured values. Because the natural frequencies of the foundation are much higher than the frequencies of the centrifuge rotation, resonant phenomenon can not occur during centrifuge operation.

- 1- Stone replacement content of 50%
- 2- Stone replacement content of 40%
- 3- Stone replacement content of 30%
- 4- Stone replacement content of 0%

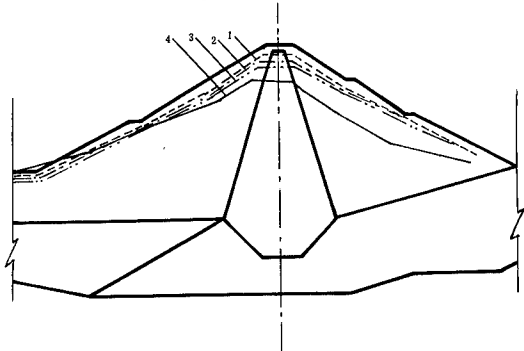


Fig.8. Variation of dam body deformation with different stone replacement contents

In order to avoid vibrational interaction with parts of the laboratory, the foundation of the centrifuge main body is separated from the other parts through the structural joints. Because the room of the centrifuge main body is placed in the basement, the rotational plane of the rotor arm and swing baskets during the centrifuge operation is also under the ground surface. Therefore if any unforeseen accidents occur, damage can be minimized.

## 7. APPLICATION

The LXJ-4-450 geotechnical centrifuge has been operational since March 1991. Tests for the projects of Wuping reservoir and Pucheng power station, as well as some theoretical research tests have been completed using this centrifuge. Currently, the following model tests are under way: the deep water cofferdam of Three Gorges project, the concrete-faced rockfill dam of Tianshengqiao hydropower station, the rockfill dam with earth impervious element of Xiaolangdi reservoir and the high slope of Longtan hydropower station, and others. It is thus clear that this geotechnical centrifuge will play an important role in water conservation and hydroelectric power development in China.

Tests for the projects of Wuping reservoir and Pucheng power station are to study the construction of a dam on soft foundation soil. The testing results of Wuping reservoir are briefly introduced as an example. The diversion dam of this reservoir is a rockfill dam with an impervious earth element. This dam, with a maximum height of 50 m, is constructed on a lacustrine soft foundation soil with a maximum depth of 33 m. The designers recom-

mended using vibroflotation to treat the foundation. Therefore, the objective of the project test is to demonstrate the feasibility of the treatment method and to determine the stone replacement contents in the foundation. Four model tests with crushed stone replacement contents of 50%, 40%, 30% and 0% were completed for this project. The dam body deformations corresponding to the above-mentioned stone replacement contents are shown in Fig.8. The testing results show that foundation treatment by vibroflotation is feasible. According to the stability analysis results, the stone replacement requirements in the foundation are determined to be 35-40%.

## Takenaka centrifuge facility

K. Suzuki, R. Babasaki & Y. Suzuki

*Takenaka Technical Research Laboratory, Chiba, Japan*

### ABSTRACT:

Takenaka installed a large geotechnical centrifuge in conjunction with the construction of a new laboratory. The centrifuge is capable of carrying out model tests for structures that Takenaka will actually build various construction projects. The payload dimensions of the centrifuge's platform are width 2.0m  $\times$  depth 2.0m  $\times$  height 1.1m, and its maximum capacity is 700g-ton. This paper describes the centrifuge specifications, the centrifuge facilities, and the data acquisition system.

### INTRODUCTION

Geotechnical centrifuges have been introduced in a number of Japan's public and private research institution in the past several years, and there has been an increased level of research focused on the stability of civil engineering structures.

Takenaka formulated plans to include a geotechnical centrifuge when it built its new laboratory. The centrifuge was designed with specifications that can accommodate model testing on structures that will actually be built by Takenaka in various construction projects.

It was designed and manufactured by Acutronic

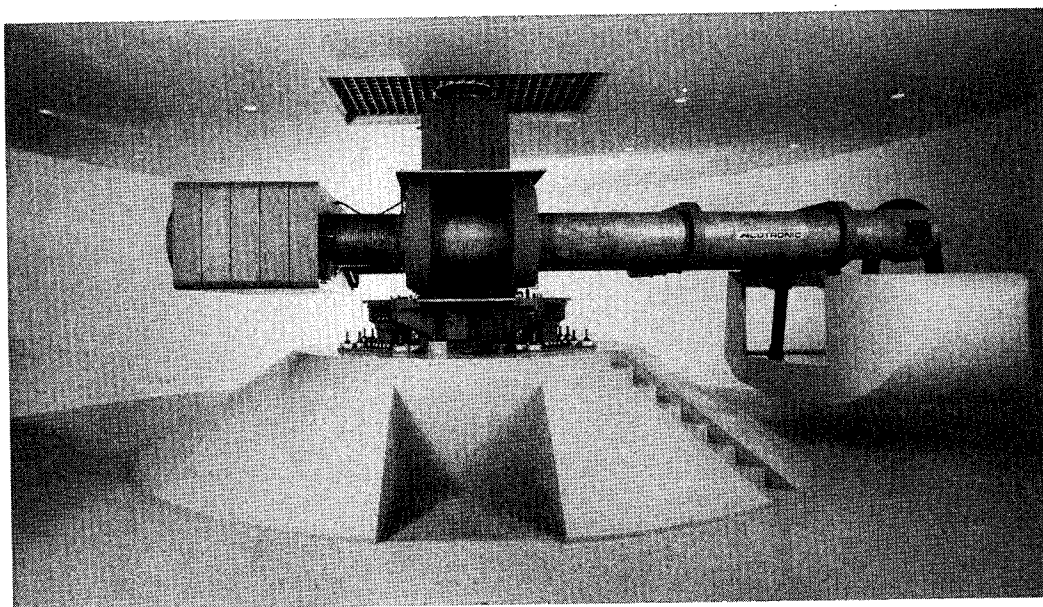


Figure 1 Takenaka centrifuge

France, a company that has the most experience in the field. After approximately two years of design and manufacture, the centrifuge was installed from late April through early May 1993.

The Takenaka centrifuge is the largest in Japan, and one of the strongest in the world.

## CENTRIFUGE SPECIFICATIONS

Takenaka's centrifuge is shown in Figure 1, which was manufactured by Acutronic France (Model 685). It is a larger version of Model 680 (LCPC, France). Its size and capacity were designed according to Takenaka's specifications.

Figure 2 shows the plan and side views of the Model 685 centrifuge, which consists of ; a) platform; b) centrifuge arm; c) balancing counterweight; d) hydraulic rotary joint; e) electrical slip-rings assembly; f) drive system; g) aerodynamic shrouds; h) in-flight balancing system and lubricating unit. Table 1 provides the centrifuge's specifications.

1. Centrifuge radius: The platform radius is 7.0m; the nominal radius is 6.5m
2. Usable payload dimensions: The dimensions of the platform are; width 2.0m  $\times$  depth 2.0m  $\times$  height 1.1m
3. Performance: Maximum payload is 5,000kg; acceleration at maximum payload is 100g; payload at maximum acceleration is 2,000kg; and acceleration range is between 10g and 200g. Figure 3 shows the centrifuge's performance envelope.
4. Electrical slip-rings; The centrifuge is equipped with 214 electrical slip-rings. Two-hundred of these are on the signal lines; 12 are on the power lines; and 2 are used for video signals.
5. Rotary joints : These are a total of 6 passages, with 2 rotary joints each for oil, air and water.

Table 2 provides additional specifications, including: run-up time; platform flatness; maximum acceptable imbalance; and power requirements.

Figure 4 shows the operating principle behind the in-flight automatic balancing feature. This option permits in -flight balancing that compensates for center-of-mass shift during centrifugal tests. In-flight balancing is achieved by the displacement, inside the boom tubes, of two heavy steel pistons. Each tube is filled with oil, except for the volume occupied by the free pistons, which divide each tube into two chambers. The heavy piston is moved into position by hydraulic actuation control, which is led by two proportional servo-valves driven by the automatic balancing control circuitry. The imbalance error sig-

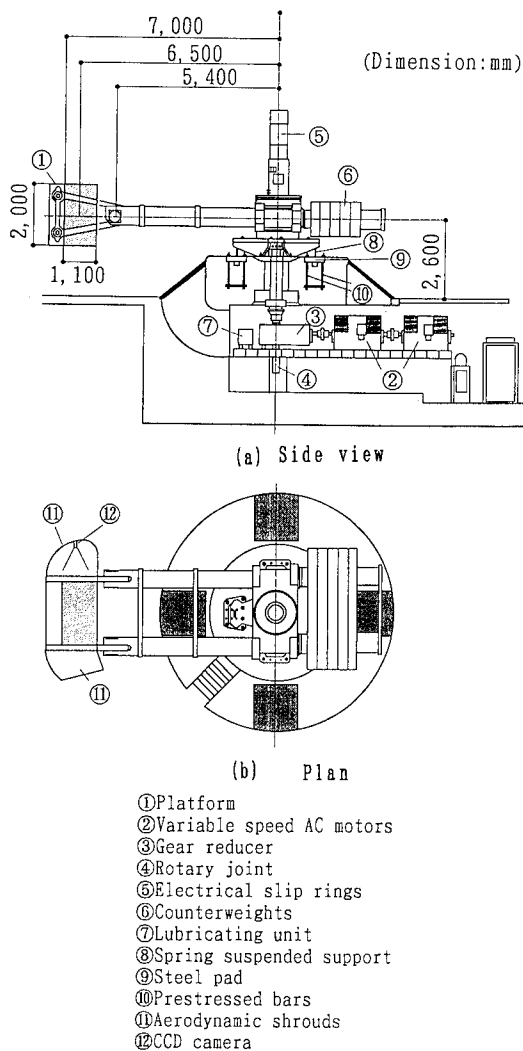


Figure 2 Plan and side views of centrifuge

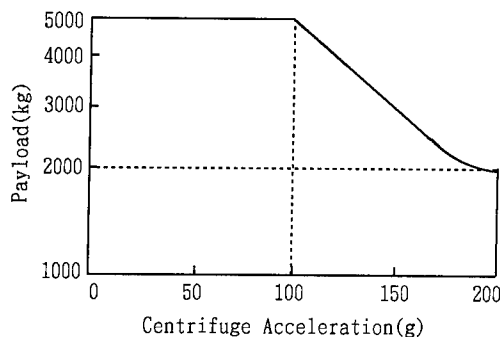


Figure 3 Centrifuge performance envelope



Table 2 Centrifuge specifications

Centrifuge Radius	Platform Radius		7. 0m
	Nominal Radius		6. 5m
Usable Payload Dimensions	Platform Width		2. 0m
	nominal Depth		2. 0m
	Max. Usable Height		1. 1m
Performances	Maximum Payload		5, 000kg
	Acceleration at Max. Payload		100g
	Payload at Max. Acceleration		2, 000kg
	Acceleration Range		10 to 200g
	Acceleration Accuracy		± 0. 2% F. S
Electrical Sliprings	Signal-line's Quantity		200
	Power-line's Quantity		12
	Video-line's Quantity		2
Rotary Joints	Oil	Quantity	2
		Working Pressure	20MPa
	Air	Quantity	2
		Working Pressure	1MPa
		Maximum Flow	110liter/min
	Water	Quantity	2
		Working Pressure	2MPa
		Maximum Flow	10liter/min

Table 1 Centrifuge specifications

Run Up Time	
0 - 100g	3minutes
0 - 200g	6minutes
Platform Flatness	
Static	0.5mm T. I. R (Total Indicated Runout)
Maximum Load	1.0mm T. I. R
Max Acceptable Imbalance	200,000N
Power Requirements	2,000KVA

nals are delivered from the dynamic imbalance monitoring circuitry. Any change in the payload's center-of-mass position is automatically compensated for by this circuitry. The hydraulic power supply and the accumulator are located in the power

room below the circular enclosure.

To accommodate the earthquake simulator on the platform, the Finite Element Method was used during the design phase to calculate the natural frequencies and stress that earthquake simulator would generate. The assumption used for the modeling of the Model-685 centrifuge was that it would be identical to the modeling of the LCPC Model-680 centrifuge, in which the computed modes showed a close correlation to the actual modes. The results of the analyses revealed that the maximum stress will not cause any serious limitation of use of the earthquake simulator.

The model created in the model preparation room is transported by air pallet to an area near the platform. The model is then lifted onto the platform with a crane installed on the top of the centrifuge enclosure's ceiling. The crane has fine inching control for both hoisting and lowering operations to ensure that the model is not damaged. There is a traveling crane installed in the upper portion of the preparation room. As shown in Figure 6, the control room contains a centrifuge control desk and a data acquisition system.

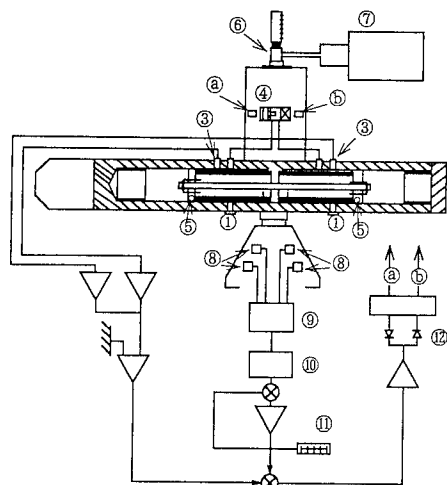
## CENTRIFUGE FACILITIES

As shown in Figure 5, the facilities comprise a centrifuge enclosure, man-protected area, model preparation room, centrifuge power room, control room, and data processing room. The centrifuge enclosure, man-protected area, and model preparation room all occupy the same underground level, and the power room is located beneath the centrifuge enclosure. The control room and data processing room are located above the model preparation room.

The circular enclosure, measuring 16.4m in diameter by 4.6m in height, was designed to meet aerodynamic requirements. An Eigen value analysis was conducted on the enclosure, and it was confirmed that there was no periodic excitation resulting from the rotating pressure wave.

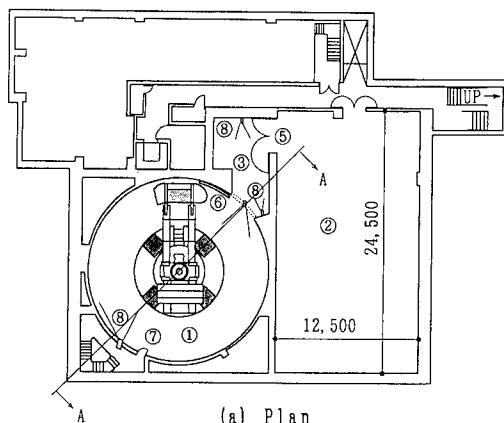
To satisfy safety requirements, the walls of the circular enclosure are made of reinforced concrete. As

shown in Figure 2, the centrifuge pedestal is attached to its reinforced concrete foundation through four spring-suspended supports connected to four steel pads. The foundation is preloaded with prestressed bars. The power room contains a gear reducer attached to the drive shaft, two variable speed AC motors, and a power control cabinet.

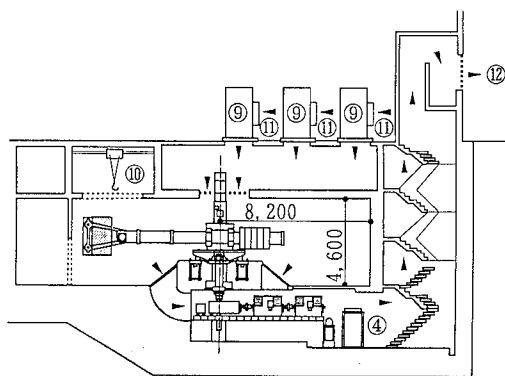


- ① Drain plugs
- ② Free piston
- ③ Pressure sensors
- ④ Proportional control valve
- ⑤ Balancing weight
- ⑥ Rotary joint
- ⑦ Hydraulic supply
- ⑧ Strain gages
- ⑨ Signal conditioning
- ⑩ Demodulation
- ⑪ Imbalance monitor
- ⑫ Hydraulic amplifier

Figure 4 Schematic of in-flight automatic balancing system



(a) Plan



(b) Side view (section A-A)

- ① Centrifuge enclosure
- ② Model preparation room
- ③ Man-protected area
- ④ Centrifuge power room
- ⑤ Door-A
- ⑥ Door-B
- ⑦ Door-C
- ⑧ TV-cameras
- ⑨ Air-ventilation fans
- ⑩ Crane
- ⑪ Air-flow input
- ⑫ Air-flow exhaust

Figure 5 Centrifuge facilities

Three fans are used for air ventilation in the circular enclosure. As shown in Figure 5, these fans are designed to maintain a temperature inside the enclosure that goes no higher than 10°C above the outside temperature. The airflow direction, from input to exhaust, is indicated on the diagram by arrows.

To ensure human safety and optimized operation, the centrifuge facilities are equipped with a safety management system (S. M. S.) that includes TV cameras and monitors, locks, detectors, emergency switches, horn, and intercommunication system. As shown in Figure 6, the control desk is equipped with four monitors. The set of locks requires a series of circulating keys. As shown in Figure 5, the doors are locked in order from Door C to Door A, using moving keys. It becomes possible to operate the centrifuge only after the final moving key has been used in a lock installed in the control desk. The safety management system also incorporates various environmental detectors, including a temperature and humidity sensor with display and alarm; smoke detector with alarm; centrifuge imbalance sensor; and centrifuge vibration meter. All alarms except those for temperature and humidity automatically stop the centrifuge's rotation. The horn is activated in the preparation room when the command for centrifuge rotation is given. Emergency stop buttons are installed in the circular enclosure, power room, man-protected area, and preparation room, making it possible to interrupt centrifuge control from these areas.

## DATA ACQUISITION SYSTEM

As shown in Figure 7, a data acquisition system is employed for centrifuge mode tests. The analog signals from the transducers pass through the slip-rings to the control room where they are digitized by high-speed, multi-channel AD converter interfaces and recorded on the internal disk of a workstation (EWS-I). Each channel of the converter interfaces operates at a 2μ sec sampling rate.

Results can be viewed on the workstation monitor, with various types of graph displays representing the data stores on the disk. For static experiments, the data is displayed during the experiment; for dynamic experiments, the data is displayed after the experiment is completed.

The video system incorporates a CCD (Charged Couple Device) camera and a high-speed video camera. The CCD camera is installed near the model on top of the platform. The high-speed video camera is installed on top of the centrifuge's arm, and records the model via a reflection mirror attached to the platform. The high-speed video camera can record up to

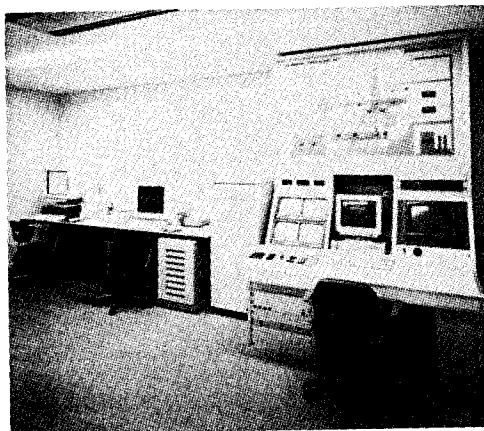


Figure 6 Centrifuge control desk and data acquisition system

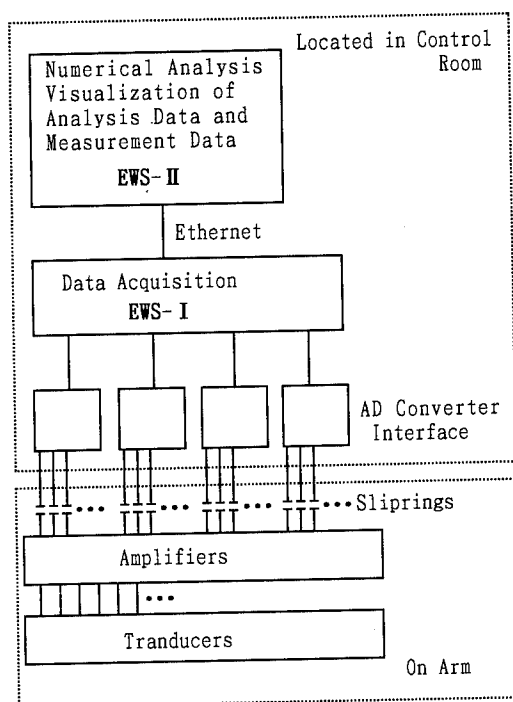


Figure 7 Configuration of data acquisition system

1000 frames per second. An image analysis system is used to analyze the gauge-mark movements in the model that are recorded on the video tape.

Data analyses and numerical analyses are conducted using another workstation (EWS-II) in the

---

control room. The workstation incorporates an Engineering Oriented Design Assistant System (EODAS) developed by Takenaka that makes it possible to view the analytical results on a visual display (T. Shiomi, et. al., 1992)

## CONCLUSION

At the time of writing this paper, installation of the centrifuge has been completed, and we are now conducting acceptance tests. Development is proceeding on the workstation-based data acquisition system and on the visual display system that will permit direct comparisons between experimental results and numerical analysis results; the completion target for these system is spring of 1994.

## REFERENCES

- Nicolas-Font, J. (1988), Design of Geotechnical Centrifuge, Centrifuge 88; Paris, France  
Shiomi, T., Ishikawa, Y. and Tsunekawa, H. (1992), Engineering Visualization for Seismic Structure Analysis, Earthquake Engineering, Tenth World Conference, Madrid, Spain

## The University of Delft geotechnical centrifuge

H.G.B. Allersma

*Delft University of Technology, Netherlands*

**ABSTRACT:** A geotechnical centrifuge with a diameter of two meters has been developed at the University of Delft. The design concept was to keep the device as simple as possible and to keep the weight of the samples so low that they could be handled by one person. To enable the performance of a large variety of tests, several miniature devices were developed. The limitation of space for sensors was neutralized by using image processing techniques to measure test parameters in flight.

### 1 INTRODUCTION

In 1988 the development of a small geotechnical centrifuge with a diameter of two meters was started at the University of Delft. The device was operational in 1990. Test models with a dimension of 300x400x450 mm<sup>3</sup> and a weight of 300N can be accelerated up to 300 g. A small geotechnical centrifuge is relatively cheap in use, and the development of the centrifuge and the equipment did not take so much time. To enable the performance of advanced tests in flight the carriers of the centrifuge are made just large enough to contain computer controlled test devices. Because the costs of operation are low the device is very suitable to perform trial and error tests. The modification of the centrifuge for different tests is relatively simple, so that a very flexible operation is obtained. The test containers and actuators are in general so small that they can be carried by one person. This is convenient during the preparation of the tests and the soil samples can be handled very carefully. Another advantage of small containers is, that it is rather easy to build automated sample preparation devices. Very good reproducible sand samples could be obtained in this way, so that the influence of small modifications of the test procedure can be investigated. A disadvantage of a small centrifuge is the limitation in the use of sensors during a test. This restriction, however, can be compensated partly by using image processing techniques applied to the video images of the on board video camera.

Several miniature devices have been developed to enable the performance of advanced tests in flight, such as: loading, displacement and the supply of sand, water and air. The devices operate under software control,

which runs in a small computer located in the spinning part of the centrifuge. The signals from load cells, pressure transducers and other sensors are received by the on board computer without interference of slip rings. Information with the outside world is exchanged via slip rings using the RS232 protocol. The test devices are driven by small dc motors, which are manipulated by the on board computer.

Several devices have been developed to prepare sand and clay samples. To improve the reproducibility the devices are automated as much as possible. A special centrifuge has been built to consolidate clay slurry, in order to obtain a very soft normally consolidated clay.

In 1993 five different research projects are being carried out in the centrifuge by graduate students, i.e.: sliding behavior of spudcan foundations, stability of dikes during wave overtopping, blowouts and cratering, stability of embankments during widening and shear band analysis. The flexibility of the device is demonstrated by the fact that on several day's three quite different model tests were performed.

### 2 THE UNIVERSITY OF DELFT CENTRIFUGE

#### 2.1 Mechanical part

The mechanical part of the centrifuge (Fig.1) consists of a frame which is fixed on the floor. The frame carries the bearing house of the vertical axis and the protection shield. A beam with a length of 1500 mm is connected to the axis, so that it rotates in the horizontal plane. A heavy machine was chosen, because this design minimizes the effect of imbalance, which can occur during tests, on the stability of the centrifuge.

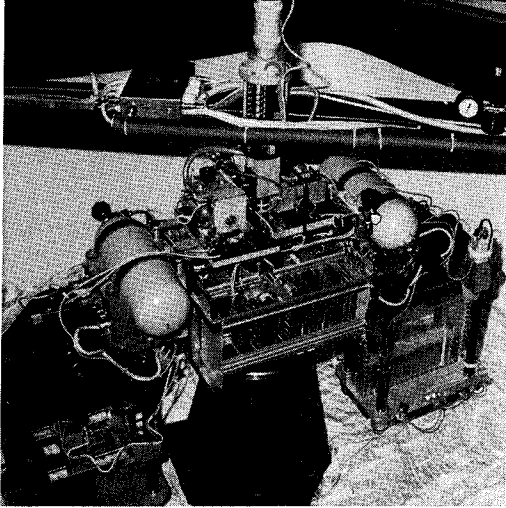


Fig.1 Photograph of the small centrifuge of the University of Delft.

Two swinging carriers are connected to the beam by means of brackets. The carriers are formed by two plates 450 mm apart, which are connected to each other by four cylindrical iron beams. The area of the plates is 400 x 300 mm<sup>2</sup>. More than six different types of boxes are designed in order to confine soil samples during testing. The maximum size of the boxes is limited by the working area of the carriers.

The potential danger of the spinning part of the centrifuge is minimized by a protection shield. The iron protection shield with a thickness of 5 mm forms a large cylindrical box. A second shield at a distance of 50 cm apart is made of wooden plates. The gap between the two shields is filled with concrete blocks and granular material. This fill gives additional safety against flying projectiles and the weight stabilizes the device.

The centrifuge is driven by an electric motor of 18 kW via a hydraulic speed control unit. The hydraulic speed controller can be manipulated from the keyboard of the control computer via a stepper motor. A computer program has been developed to adjust the speed of the centrifuge using the signal of a tachometer. Several options are available to control the speed in an advanced way. It is, for example possible to make the increment of the acceleration dependent on time or other test parameters, such as the pore water pressure in a clay sample or parameters obtained by processing video images.

## 2.2 Measuring facilities

To enable to perform computer controlled tests in flight, the centrifuge is equipped with an electronic

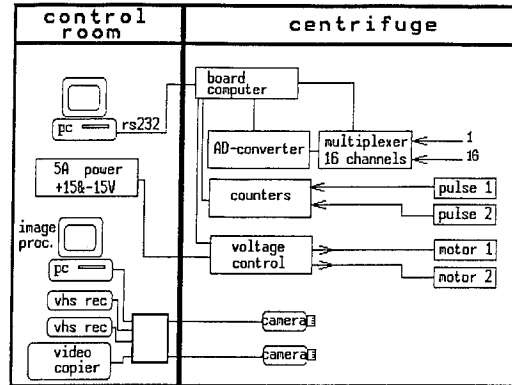


Fig.2 Diagram of the electronic control and measuring system.

system. The diagram of the system is presented in Fig.2. To minimize the number of slip rings the primary control units are placed in the spinning part of the centrifuge. The control unit contains a small one board computer, an analog to digital converter with a 16 channel multiplexer, two voltage controlled outputs of more than 5 Ampere each and two 16 bits counters. The signals from the sensors are conditioned by amplifiers. Eight power slip rings are available to feed the electronics and the actuators. Twelve high quality slip rings are used to transmit the more sensitive signals, such as, for example, two video lines and the RS232 connection between the board computer and the PC in the control room. During a test the relevant parameters are sent to the PC in the control room. Here the data are displayed in graphical form and stored on disk.

A special feature is that several phenomena can be measured by using video images. In this technique the video images are captured in flight by the frame grabber in the PC and processed until the relevant parameters are isolated. Image processing can be used to visualize and digitize the surface deformation of clay and sand samples or to digitize the consolidation of a clay layer (Allersma, 1990, 1991, 1994). This technique has proven to be very useful in several research projects.

## 3 TEST EQUIPMENT

The following miniature devices have been developed to perform tests in flight:

- Two dimensional loading system
- Sand sprinkler
- Vane apparatus
- Gas supply system
- Water supply system

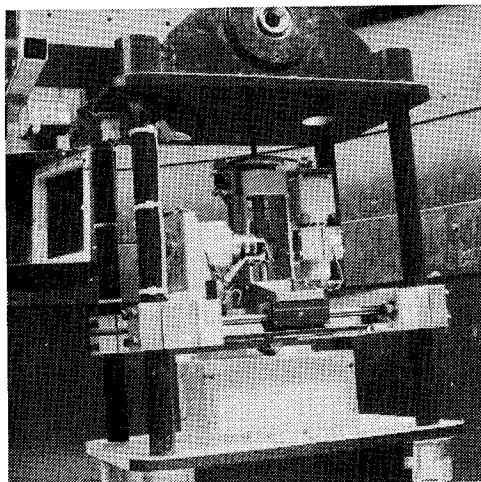


Fig.3 Photograph of the two dimensional loading system.

### 3.1 Two dimensional loading system

The two dimensional loading system (Fig. 3) can be considered as a universal tool, which can be used for several tests. Two guiding systems based on linear ball bearings and axes of tempered steel guarantee a more or less friction free translation in two perpendicular directions. The system is driven by two miniature dc motors. Translation is obtained by means of a screw spindle with a translation of 1 mm per revolution. The number of revolutions is counted by means of small pulse generators, which also detect the direction of rotation. One revolution is equivalent to 200 pulses. A special interface has been built with two 16 bit counters to make possible the number of pulses to be read in the control program in order to determine the displacements in the two perpendicular directions. The loads in the two perpendicular directions are measured by means of load cells. The output of the load cells can be read in the computer program via the multiplexer and the analog to digital converter. Sufficient information is now available to perform load or displacement controlled tests. Furthermore the device can be used as a simple robot to manipulate a test during flight. Loads of more than 5 kN can be applied by the system. The accuracy of the measurement of the displacements is better than 0.1 mm. The maximum vertical displacement is about 50 mm and the range in horizontal direction is 100 mm. The mass of the device is approximately 10 kg. It takes about ten minutes to install the loading system in the centrifuge. Up to now the device has been used at gravitation levels of more than 150 g.

As an example, the typical output of a spudcan test on

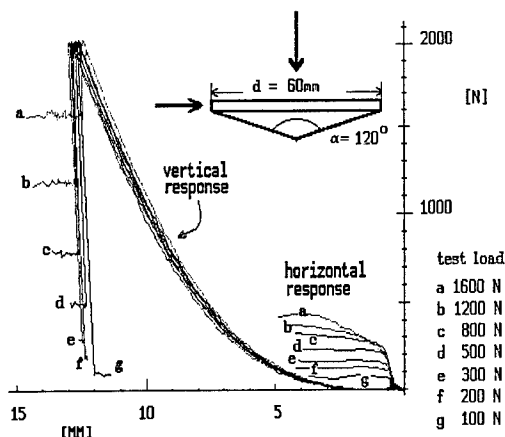


Fig.4 Graphical output of spudcan tests on dry sand at 100g (prototype diameter is 10m).

sand is shown in Fig.4. Initially the spudcan was pre-loaded in vertical direction up to 2 kN. Next the vertical load was decreased to the so called test load, indicated by a-g in Fig.4. The test load is kept constant, where the horizontal load on the spudcan is increased. This tests give information about the sliding resistance of the foundation. Spudcans with a diameter of more than 14 meters were simulated. Other tests that can be performed with the loading system are, for example: anchors, bulldozer, footing, excavation (Allersma, 1991).

### 3.2 Sand sprinkler

A computer controlled sand sprinkler has been developed in order to make embankments in flight. The device consists of a hopper, which can be translated easily by means of linear ball bearings and axes of tempered steel (Fig. 5). The mass of the device is approximately 10 kg. The translation (range is 150 mm) is obtained by means of a small electric dc motor. The sprinkler system is designed in such a way that no close seals are required. A shaft is located in the outlet of the hopper, so that the granular material flows only when the shaft is rotated (Fig.6). The mechanism has proven to be reliable up to 120g. The shaft of the sprinkler system is also driven by a small dc motor and the amount of lost sand is detected by counting the number of revolutions by means of a pulse wheel. Several options can be assessed in the control program. It is possible to sprinkle sand layer by layer or at one particular location. The disturbing effect of Coriolis forces is minimized by means of hinged sheets, which guide the sand grains. On the other hand the Coriolis effect can be used to build an embankment with a

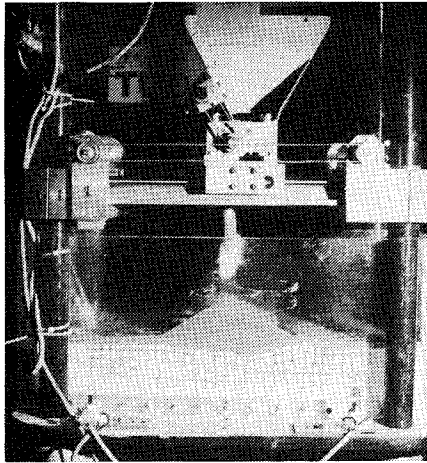


Fig.5 Photograph of the in flight sand sprinkler.

gradient in height over the width of the sample box. This can be used to investigate time effects in the failure of clay under an embankments. As an option the control program of the sand sprinkler also reads the output of pressure transducers, which can be placed in the clay layer. The pore water pressure is plotted on the screen. An automatic link can be made between the pore water pressure and the sand supply scheme. The arising of i.e. a dike during sand supply and the deformation of the clay can be monitored by a video camera. The deformation of the clay is made visible by means of a grid. Software has been developed (Allersma, 1990) to digitize the co-ordinates of the nodes of the grid automatically by image processing. In principle it is possible to make an automatic link between the program which controls the sand supply and the image processing system, so that an embankment can be built in flight where the images of the video camera are used to control the sand supply. The sand sprinkler system is used to investigate the stability of dikes (Fig. 5) and different methods of embankment widening, on soft soils. Since the centrifuge has two swinging platforms the loading system and for example the sand sprinkler can both be mounted in the centrifuge. In this way the centrifuge can be used very efficiently, because quite different type of tests can be performed close after each other.

### 3.3 Vane apparatus

In Fig.7 a photograph is shown of the developed vane apparatus. For a flexible operation the device has been automated in such a way that the depth ( range 100 mm) and penetration speed can be adjusted in flight.

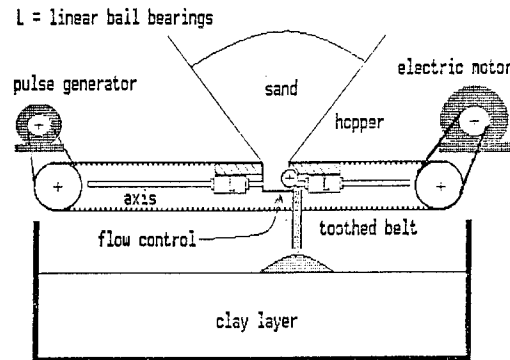


Fig.6 Schematic drawing of the sand sprinkler system.

The waiting time between penetration and rotation and the rotation speed of the vane can also be varied. Depending on the gear box used the rotation speed of the vane can be adjusted between less than 1 degree per second to approximately 20 degrees per second.

The horizontal position of the vane can be adjusted over a range of 250 mm during flight, so that several tests can be performed without stopping the centrifuge. A complete test procedure can be defined in advance in the control program. Three miniature dc motors are used to control the device. Up to now a vane is used with a diameter and height of 13 mm both. A sensor has been developed to measure the small torque. The sensitive measuring element has to be supported in order to eliminate the influence of the gravity. The mass of the vane apparatus is approximately 3 kg.

### 3.4 Gas supply system

In some tests it is required that gas can be supplied to a soil sample. Since the small centrifuge is not equipped with fluid slip rings gas has to be stored in the spinning section of the centrifuge. To make the storage as compact as possible, two high pressure (20 MPa) cylinders of 5 litres each are mounted on the centrifuge beam (Fig.1). Before a test is started the cylinders are filled with air by means of a high pressure compressor. A computer controlled air supply system has been developed in order to regulate the gas flow from a distance. The pressure of the supplied air is controlled by a normal pressure regulator, which is modified in such a way that it can be driven by a small dc motor. The output pressure of the regulator is detected by a pressure transducer, the signal of which is used in the computer program to control the dc motor. A modified valve, which is also driven by a small dc motor is used to start or stop the gas flow quickly. The gas flow per unit of time is known by measuring the pressure drop



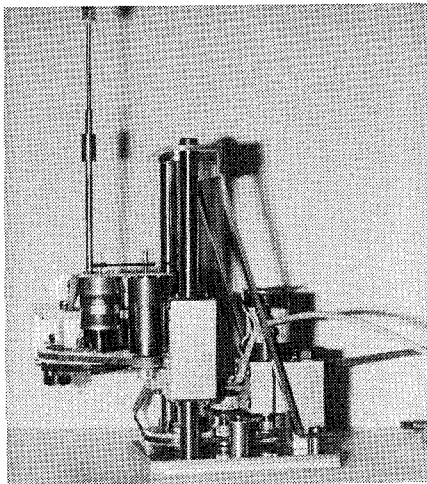


Fig.7 Photograph of the miniature vane apparatus.

of the gas cylinders during the test, where also the temperature of the gas is taken into account. A computer program has been developed to obtain an interactive control over the gas supply. During a test the cylinder pressure, the test pressure and the gas flow are plotted on the screen. With the actual system flow rates of 10 l/s can be reached. The gas in the high pressure cylinders represents a large amount of power, which can be used for tests in which large loads or energy are needed.

The gas supply system is used to simulate blowouts and cratering (Fig.8) in sand layers with a prototype thickness of approximately 20 - 30 meters (Allersma et al. 1994).

### 3.5 Water supply system

In several geotechnical problems it is required that a water flow be controlled in the spinning centrifuge. It is not so simple to obtain a smooth control because rather high pressures are required to overcome the gravity. Good results are obtained by a system where water is circulated by means of a gas jet. Here the gas supply system is used to control the jet. The advantage of this system is that the water supply can be controlled very smoothly from zero to the maximum flow and the system is very simple, at least if the air supply system is already available. The flow rate can be linked to the pressure by calibration, but it is also possible to detect the flow rate by a small turbine. A maximum flow of about 10 l/min at 0.15 MPa has been reached at 100g.

The water system was used to investigate the stability of dikes during water infiltration which can occur by wave overtopping (Fig.9).

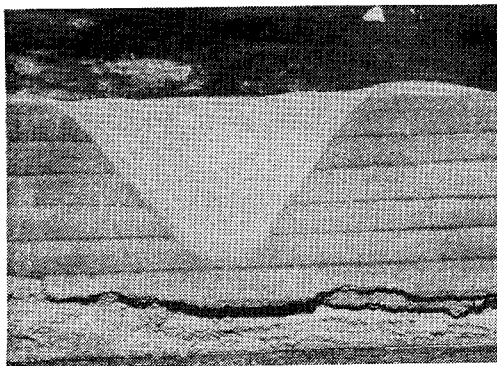


Fig.8 Photograph of the simulation of a blowout at 100g in a sand layer of 20 cm (20m prototype).

## 4 SAMPLE PREPARATION DEVICES

An important requirement is that the samples can be reproduced in a very accurate way, so that the results of similar tests can be compared with each other. Two different devices have been developed in order to prepare clay and sand layers.

### 4.1 Clay preparation

Up to now it was found that the best control over the samples was obtained by making artificial clay. In this technique clay powder is mixed with water, where the air content is kept as low as possible. A technique has been developed in which an air free slurry is obtained under normal atmospheric conditions. The device operates more or less automatically and is self cleaning. The principle of the device is that a thin layer of clay powder is poured continuously at the rotating water surface of the mixing basin. In this way no air bubbles are included due to differences in infiltration speed of the water. The water with a very low clay content is pumped to a basin where the clay is sedimented. The clay slurry, with a water content of 100 per cent, is homogenized in a mixer before it is put into the sample boxes. The best way to obtain a normally consolidated soil with a smooth and realistic gradient of water content and strength over the height of the sample is to consolidate the slurry in the centrifuge at the same g level as will be used in the tests. Consolidation will take several hours or even days when a low permeable clay is used. Because the centrifuge will be occupied all that time no other tests can be performed. Therefore a special centrifuge has been built which is only used to consolidate the clay layers. This centrifuge has a diameter of 1 meter and can accelerate sample boxes with a weight of approximately 200N up to 200g. The pore water pressure can be measured via slip rings.



Fig.9 Failure at the toe of a sand slope due to water infiltration at the top.

#### 4.2 Sand preparation machine

A computer controlled device has been developed to prepare sand layers in the test containers. Since this device is completely automated, very good reproducible samples can be made. The sand, which is stored in a hopper can be sprinkled in a curtain by means of a rotating shaft, following the same technique as the in flight sand sprinkler. The falling height of the sand can be adjusted over a range of more than 30 cm. The distance to the sand surface is measured by means of an optical sensor and the height of the test box is adjusted by a stepper motor in order to keep the falling height constant during raining. The sample box is moved back and forth by means of a second stepper motor, while a smooth acceleration is realized in the turning points to prevent shocks. The sand pluviation system can be adjusted with the computer program, so that sand is only sprinkled when the sample box is located under the outlet of the hopper. The wasted sand is transported back to the hopper by a conveying belt and a pneumatic system. By means of filters it is prevented fine material from separating from the sand used.

Sand samples with a ground surface of 300x300 mm<sup>2</sup> and a maximum thickness of approximately 150 mm can be made. The porosity, depending on the sand type, can be varied between 35% and 39%. The standard deviation of the mean porosity of medium dense dune sand was 0.18%. The reproducibility of the porosity is also demonstrated with the vertical response of the seven spudcan tests in Fig.4. For each test a new sand bed was prepared. The scatter is mainly caused by the fact that the initial height of the spudcan was adjusted by hand. The preparation of the sample with a thickness of 100mm takes about 20 minutes.

#### 5 CONCLUSION

The small geotechnical centrifuge at the University of Delft has proven to be very successful in operation.

The small size of the samples means that the machine is very flexible in operation and orientational tests can be performed in a short time after the idea has been arisen. Due to modern electronics, measuring techniques and the development of several miniature devices, advanced tests can be performed in flight. Since the control computer is located in the spinning part of the centrifuge only a few slip rings are required to interface the spinning equipment with the PC in the control room. The disadvantage of a small centrifuge, being the limitation in sensors, is partly neutralized by using image processing techniques. Several different types of tests can be performed in the small centrifuge. The flexibility in operation allows that the centrifuge can be used for several different type of tests on the same day. Good reproducible sand samples could be prepared, with the automated sand sprinkler device. In the case that very soft clay has to be used in test, in flight consolidation of the slurry is the best way to produce normally consolidated clay layers. The centrifuge, built to consolidate the clay samples, has increased the capacity of the main centrifuge significantly.

#### ACKNOWLEDGEMENT

The centrifuges, the electronics, the software, the soil preparation devices and the in flight testing equipment are designed in all details by the Geotechnical group of the Department of Civil Engineering of the University of Delft. Many thanks are given to the technicians of the laboratory, Mr. J. van Leeuwen, Mr. A. Mensinga and Mr. J.J. de Visser, for their contribution to this research. The specific research projects are supported by Shell, the Dutch Ministry of Public Works and the Dutch National Science Foundation.

#### REFERENCES

- Allersma, H.G.B., 1990: On line measurement of soil deformation in centrifuge tests by image processing. Proc. Int. Conf. on Experimental Mechanics, Copenhagen, pp.1739-1748.
- Allersma, H.G.B., 1991: Using image processing in centrifuge research. Proc. Int. Conf. Centrifuge, Boulder, pp. 551-558.
- Allersma, H.G.B., A.P. Kooijman, W.J. van Niekerk, 1994: Simulation of cratering in a small geotechnical centrifuge. Proc. Int. Conf. Centrifuge94, Singapore.
- Allersma, H.G.B., H.G. Stuit, P. Holscher, 1994: Using image processing in soil mechanics. Proc. XIII Int. Conf. on Soil Mechanics and Foundation Eng., New Delhi.

## Development of medium-size geotechnical centrifuge at Tsinghua University

J.L. Pu, F.D. Liu, J.K. Li, S.Q. Li, K.T. Yin & Y.S. Sun

*Department of Hydraulic Engineering, Tsinghua University, Beijing, People's Republic of China*

P.F. Jin

*CHREDI, People's Republic of China*

**ABSTRACT:** A medium size geotechnical centrifuge facility has recently been established at Hydraulic Engineering Department, Tsinghua University. The centrifuge has an effective radius of 2.0 m and capacity of 50 g-tons. This paper describes the features of the machine and subsidiary facilities.

### 1. INTRODUCTION

A new medium size geotechnical centrifuge was in operation in May 1993. The machine was designed and manufactured by Chinese Helicopter Research and Development Institute in 1990-1991. Engineering design of geotechnical centrifuge laboratory with an underground centrifuge enclosure and associated facilities was initiated in the summer of 1991. Construction of the laboratory started in June and completed in October 1992. The centrifuge was installed and commissioned in April 1993.

### 2. CENTRIFUGE LABORATORY

A review of the machine is shown in Fig.1. The layout of the geotechnical centrifuge laboratory and

the cross section of the centrifuge are shown in Fig.2 and Fig.3 respectively. The laboratory comprises a total 120 square meters of floor space on the ground floor by the existing building. The complete complex includes the centrifuge enclosure, a basement for the installation of a motor and a gear box, a model preparation room, a control room, a computer room and a graduate students' room. The circular enclosure for the centrifuge is 5.2 m in diameter and 1.7 m in height. It is designed to meet the aerodynamics requirements of the centrifuge and to reduce power consumption. The ferroconcrete shell of the enclosure is 45cm thick. The centrifuge foundation is designed to withstand horizontal unbalanced force due to the loss of the container when the centrifuge is operating at the maximum speed. A air ventilation system provides cooling within the enclosure. Figure 4 shows

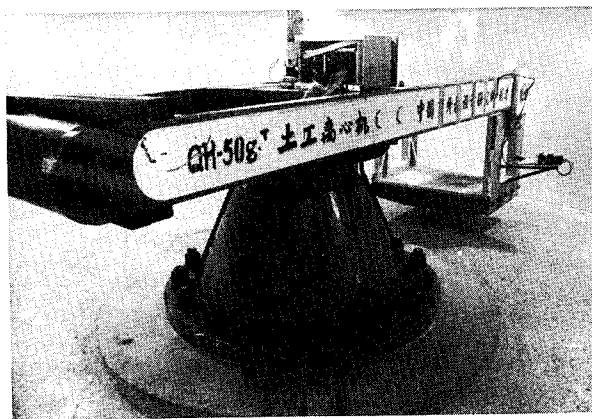


Fig.1 QH-50gt geotechnical centrifuge

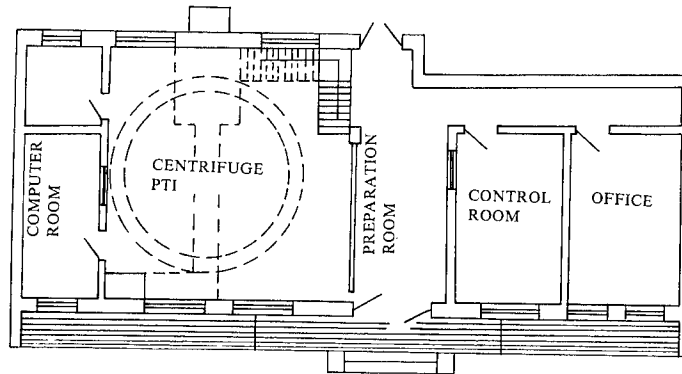


Fig.2 Layout of the geotechnical centrifuge laboratory

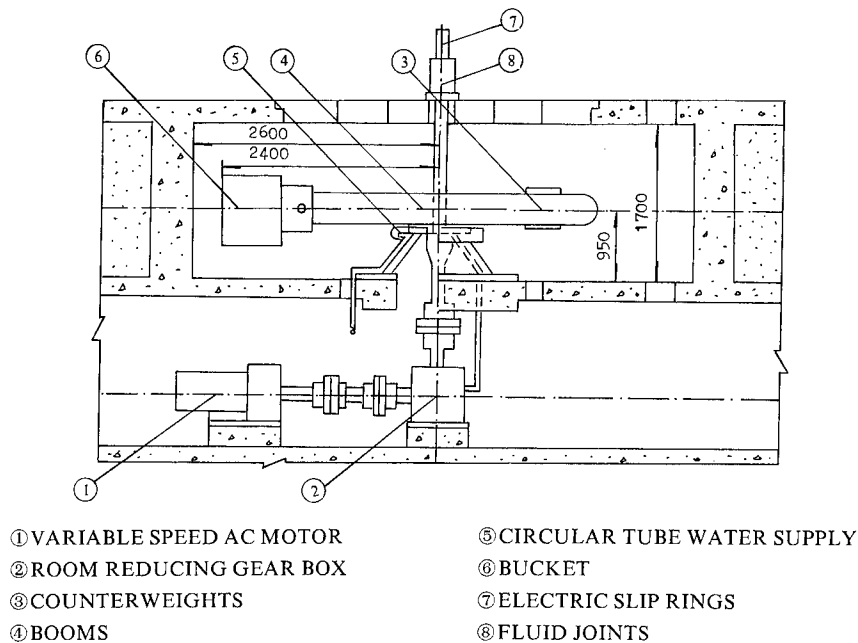


Fig.3 Cross section of the centrifuge

the relation between temperature in the enclosure and time during a long term testing with cooling. The room temperature is affected by the outdoor air temperature of the air flow passing through the rotunda. During 12 hours testing the outdoor air temperature increased about  $6^{\circ}\text{C}$  and the increase of temperature generated by centrifuge operating is only  $5^{\circ}\text{C}$ . The model preparation room is a general purpose laboratory area where the model can be built. An electric single-arm lift is used to transport the container with model from the preparation

room to the centrifuge platform. The control room adjacent to the preparation room houses the centrifuge controls and main data acquisition computer as well as TV monitor, cassette recorder. (see Fig.5)

### 3 GEOTECHNICAL CENTRIFUGE

A cross-section of the centrifuge is shown in Fig.3. The outer surface of the swing platform is at a radius of 2.4 m and has a working space 0.7m by 0.7m. A clearance of

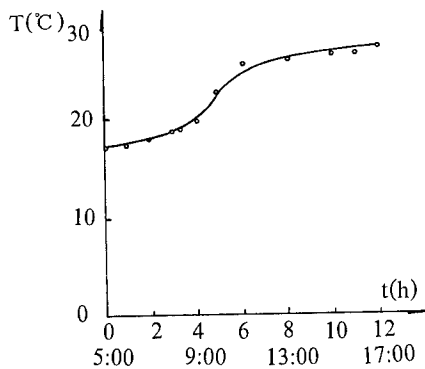


Fig.4 Temperature development during a long term test

1.30m can be used to mount equipment on the top of the container. The centrifuge can carry a maximum payload of 500 kg at 100 g or a payload of 200 kg at the maximum acceleration of 250g. The weight of swing bucket is 160 kg and the maximum platform deflection is 1 mm under full capacity condition. The centrifuge structure is designed to limit stresses to one-fifth of material yield stress. The centrifuge is driven by a 1320 rpm, 55 kw AC motor (JZTY 91-4) with JBIB-90 controller, whose speed can be changed smoothly between 440-1320 rpm. The motor is mounted horizontally on the floor below the centrifuge pit and drives the vertical axial shaft via a 3.9046:1 reduction gear box. The acceleration accuracy is within 0.8%. The power at 100g and 250g are 26 kw and 36kw respectively when the aerodynamics shrouds are removed from the bucket.

#### 4. SLIPRINGS AND FLUID JOINTS

There are 36 electric sliprings in a capsule mounted on an auxiliary shaft. The sliprings are made of silver and the brushes are made of graphite. In the capsule 26 sliprings can be used to transmit the signals of transducers of the model and the rest are for power transmission. Three passages of fluid joint are installed on the auxiliary shaft below the electric slip rings. The working pressure of the fluid joints is 10.0 MPa. In addition, a circular tube water supply system is fixed to the lower part of the booms to provide a large amount of water, 200 l/min, for such tests in geotechnical centrifuge as erosion testing.

#### 5. CCTV AND PHOTOGRAPHIC SYSTEM

The CCTV system makes a continuous observation during the testing. The video signal from the cameras can be sent to a video cassette recorder. The main TV camera with illuminating projector is fixed to the front side of the container in the aerodynamic shroud and gives a continuous view of the model cross-section. The other is located near the center of the rotating arm to monitor the upper surface of the model. A spark photographic system is mounted above a small observation window in the roof of the centrifuge pit to measure the displacement of the model surface. The shutter opening is synchronized with the passage of the rotor.

#### 6. DATA ACQUISITION SYSTEM

The centrifuge data acquisition system is developed to

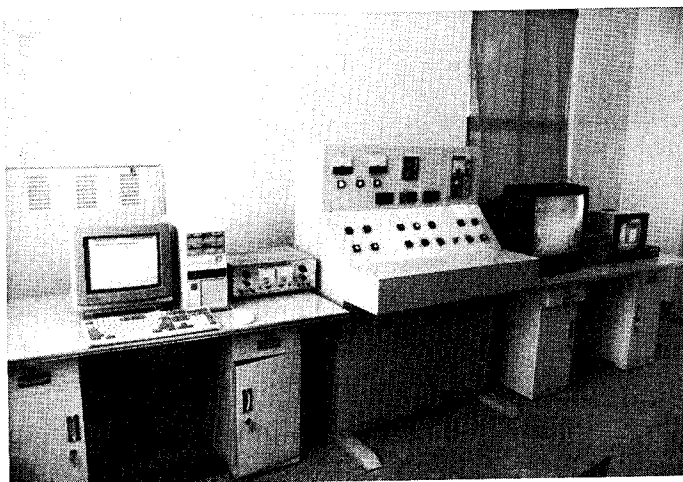


Fig.5 Control room

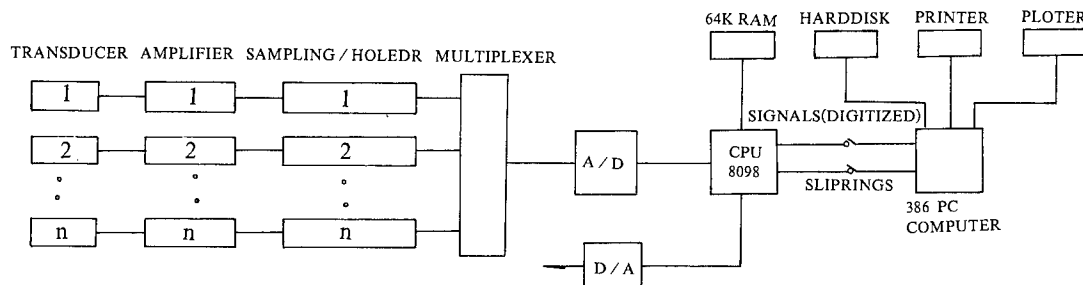


Fig.6 Configuration of data acquisition system

accommodate a wide variety of static and dynamic tests. The configuration of the data acquisition and control system is shown schematically in Fig.6. The data acquisition / control system is fixed on the rotary arm of the centrifuge near the vertical shaft. Transducers to measure displacement, pore water pressure and earth pressure are used. The analog signals from transducers are amplified individually and through sampling / holder, a multiplexer then converted into digital signals. The digital signals are either stored in single chip microcomputer (CPU 8098) as fast collection of data or transmitted through the sliprings to a main computer (386 / pc) which is housed in the control room. The computer is mainly used to perform timing, data collection, storing, processing and control. The digital communication on the sliprings is much better than the analog one.

## Canadian national centrifuge centre with cold regions capabilities

Ryan Phillips, Jack I. Clark, Michael J. Paulin, Rick Meaney, David E. L. Millan & Karl Tuff  
*Centre for Cold Ocean Resources Engineering, Memorial University of Newfoundland, St. John's, Nfld, Canada*

**ABSTRACT:** The C-CORE Centrifuge Centre, St John's, Newfoundland was completed and commissioned in June 1993. The C-CORE centrifuge is the first large centrifuge in Canada having a maximum payload capacity of 220 g-tonnes.

This paper describes the new centre, including the centrifuge and the ancillary equipment. The centrifuge will specialise in cold regions research using a custom-built 7 kW refrigeration unit connected to the test package and a purpose-built cold room for model preparation and examination.

### 1 INTRODUCTION

C-CORE, the Centre for Cold Ocean Resources Engineering, is an independently funded research institute located at Memorial University of Newfoundland in St. John's, Newfoundland, Canada. Funded by industry and government, the Centre has traditionally undertaken research, development and technology transfer that contribute to the safe and productive use of Canada's ocean resources. This research was conducted by three main groups at C-CORE: Ice Engineering, Seabed Geotechnics and Remote Sensing.

In 1992, a fourth group was formed at C-CORE: the Geotechnical Engineering Group. The creation of this group reflected C-CORE's growing expertise in geotechnical engineering and marked the culmination of a major initiative to acquire a technically advanced centrifuge modelling centre in St. John's.

The C-CORE Centrifuge Centre was established as a national centre to develop the industrial and academic centrifuge testing capability in Canada. Much of Northern Canada is covered annually by ice and has extensive permafrost. The cold regions modelling capability of the machine reflects national needs to manage the resources of Canada. C-CORE's major commitment is to Canadian and the

incorporation of centrifuge modelling into their business activities. The Centre's centrifuge education and training program are carried out across Canada to introduce the technique and the national facility to industry. C-CORE also provides 30% of its centrifuge time to Canadian universities for research and the training of graduate students.

### 2 THE C-CORE CENTRIFUGE CENTRE

The C-CORE Centrifuge Centre is a research facility located between the Captain Robert A. Bartlett building and the S.J. Carew building on the campus of Memorial University of Newfoundland. The centrifuge centre was constructed and equipped through funding from the Canada-Newfoundland Offshore Development Fund, the Technology Outreach Program of Industry Science Canada and the Natural Sciences and Engineering Research Council Canada.

The centre, shown in Figure 1, comprises a two-storey building and a containment structure housing the C-CORE centrifuge. The containment structure has three levels. The upper level provides a stiff ceiling to the main centrifuge chamber to resist the aerodynamic excitation imposed by the centrifuge in rotation.

The upper level also houses the electrical slipring capsule and associated interfaces. The intermediate level is the main centrifuge chamber which is accessible by forklift from the main building. The main chamber is 13.5m in diameter and 4.2m high. The 300mm thick reinforced concrete chamber wall is aerodynamically clean inside and retains a rockfill safety berm outside. The lower level is underground and contains the centrifuge drive unit with associated controllers, the refrigeration unit and the exhaust fan.

The two-storey building includes at ground level the centrifuge control room, sample preparation, investigation and storage areas, an x-ray bay, mechanical and electrical workshops and a coldroom. Upstairs, there are data processing areas, a soils testing laboratory and office space for visiting researchers and clients. The building is linked to Memorial University's computer capabilities.

### 3 THE C-CORE CENTRIFUGE

The C-CORE centrifuge, Figure 2, is an Acutronic 680-2 centrifuge similar to the centrifuge described by Corté (1984) at the Laboratoire Central des Ponts et Chaussées (LCPC) in Nantes, France. The C-CORE centrifuge has a radius of 5.5 metres to the swinging platform which can accommodate a payload of up to 1.1 by 1.4 metres in plan and up to 1.2 metres in height over the full platform plan area. The headroom increases in the centre of the platform to 2.1 metres. At the maximum rotational speed of 189 rpm, the acceleration at a radius of 5m is approximately 200g. The centrifuge carries a maximum payload of 2.2 tonnes to 100g at 5m radius which reduces to 0.65 tonnes at 200 g due to the increased self-weight of the platform.

The centrifuge arm consists of two parallel steel tubes held apart by a central drive box and spacers. The swinging platform is suspended on bushings at the ends of the steel tubes. The swinging platform is enclosed by an aluminium aerodynamic shroud to reduce drag. The platform and the payload are balanced by a 20.2 tonne mass counterweight. The position of this counterweight is adjusted by driving a series of gearwheels along screwthreads on the outside of the parallel steel tubes using an electric motor attached to the counterweight. This electric

motor is controlled from the 3-phase electrical switchgear located in the centrally mounted cabinet adjacent to the central axis. The other centrally-mounted cabinet contains the user interface to the slipring services and a PC-based monitoring system, which records the forces within the steel tubes and the platform support arms and vibrations of the centrifuge arm.

The centrifuge arm rotates on a set of tapered roller bearings inside the central drive box and mounted on a stationary shaft. This shaft is attached to the centrifuge containment through a four branch star support suspended on four springs. Each of the four springs is strain-gauged to sense centrifuge imbalance to within 10kN.

The centrifuge drive unit comprises a 450kW AC variable speed motor connected directly to a 9:1 gear reducer. The variable speed motor is energized through two 250kW invertors connected in parallel. Precision couplings and a hollow vertical drive shaft connect the hollow output shaft of the gear reducer to the central drive box. Two rotary joints which contain 6 passages are attached beneath the output shaft of the gearbox and are described below.

The power consumption is due mainly to aerodynamic drag within the centrifuge chamber. The centrifuge and the chamber are cooled by forced air ventilation. Air is drawn into the chamber through a ceiling vent around the central axis of the centrifuge. Air is drawn out of the chamber through a floor vent by an exhaust fan located in the lower level.

### 4 CENTRIFUGE SERVICES

#### 4.1 Rotary Joints

The C-CORE centrifuge is equipped with two rotary joints which permits fluids to flow through the central axis of the machine to the platform. These rotary joints contain a total of six passages; two are designed to accept high pressure hydraulic fluid; two are dedicated to the refrigeration unit; and the remaining two can carry either air or water. The rated capacity of the fluid passages are as follows:

High pressure joints, 2#:	
working pressure:	200bar (20MPa)
working temp:	10 to 50 °C
Cold fluid joints, 2#:	
working pressure:	20 bar (2MPa)



working temp: -30 to 50°C  
 Air/water joint, 2#:  
 working pressure:  
     air: 7 bar (725kPa)  
     water: 20 bar (2MPa)  
 working temp: 10 to 50°C

#### 4.2 Refrigeration Unit

To enable cooling of the experimental package, the C-CORE Centrifuge Centre is equipped with a refrigeration system which delivers 7kW of cooling to the platform. Cooling of the package will be accomplished by recirculating a cold fluid through the rotary joint between the package and the refrigeration unit. The refrigeration unit can deliver 10 l/min of glycol refrigerant with temperatures reaching -30°C. At the platform, a series of fluid to air or fluid to fluid heat exchangers will provide cooling of the package. The temperature control will be accomplished by varying the volume of refrigerated fluid passing through these heat exchangers. This system is depicted schematically in Figure 3.

#### 4.3 Electrical sliprings

The electrical slip rings are located in two capsules above the centrifuge. An Aeroflyte capsule contains the necessary sliprings for machine functions and presents for research usage:

64#	1 amp individually shielded signal lines;
8#	15 amp shielded power lines;
& 6#	coaxial channels.

The other slipring capsule contains a full 3-phase, 5 line, 380V, 80 amp power service, part of which is used to energise the counterweight motor. Provision is made for a fibre-optic link to be easily fitted through these slipring capsules to the centrifuge.

#### 4.4 Ancillary Equipment

Ancillary equipment are currently being developed to support operations within the centrifuge centre. These essential items include

strongboxes, consolidometers, an in-flight cone penetrometer, and a refrigerated strongbox. The rectangular strongboxes have an internal working area of 1.18m x 0.94m and a depth of 0.4m. The cold box is a customised rectangular strongbox used to house experiments requiring temperature control. Three small circular strongboxes are 0.3m internal diameter and 0.4m high. Larger circular 1m diameter strongboxes with extension pieces are under construction.

The hydraulic consolidometers apply pressures of up to 400 kPa onto samples contained within the existing rectangular strongbox. The cone penetrometer system consists of a 1cm<sup>2</sup> instrumented shaft and two linear actuators. The vertical actuator has a peak load capacity of 10 kN at a velocity of 20 mm/sec using a recirculating ballscrew and stepper motor drive. The second actuator is used to position the cone over the test package using a chain drive and stepper motor.

The cone penetrometer is shown in Figure 4. Typical cone resistance profiles obtained with this device are shown in Figure 5 for a mixture of 50% kaolin and 50% silt with the water table at depth. Profile A was obtained with no evaporation permitted from the surface by coating the soil surface with industrial-grade petroleum jelly. Evaporation of the surface was permitted in profile B. The shear strengths estimated from profile A are approximately 20 to 25% greater than for kaolin under similar conditions.

#### 4.5 Data Acquisition

The data acquisition and electrical power sub-system currently in place at the centrifuge centre is depicted in Figure 6. The system utilizes high quality custom designed signal conditioning (S/C) sub-system mounted on the strongbox. The individual S/C modules are dual channel printed circuit cards mounted in a 12 card chassis. Each chassis provides on board regulated excitation supplies for the attached instrumentation. Each individual channel/instrument is fed via a six pin circular-mil connector; the card/connector is configurable on the S/C card for a wide variety of instruments. The bulk power for the S/C cards and instrumentation is fed from a high quality power supply mounted on the drive box, via a bulk power umbilical. The power supplies

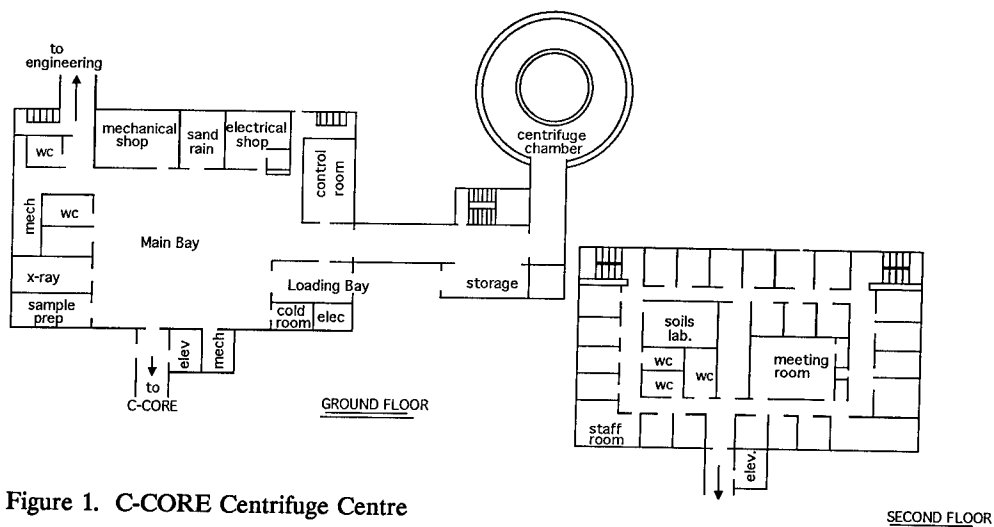


Figure 1. C-CORE Centrifuge Centre

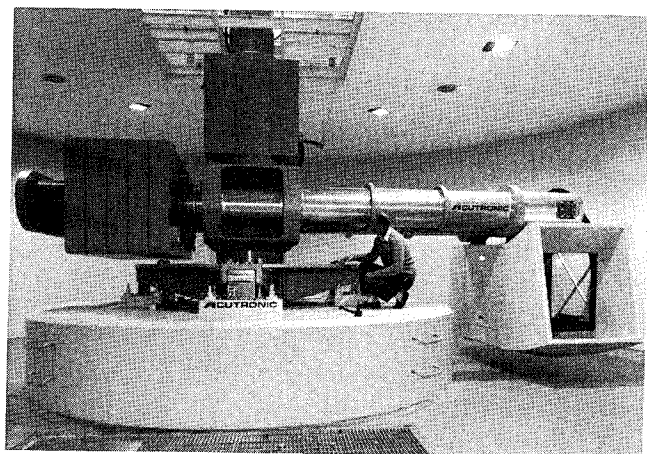


Figure 2. Acutronic 680-2 Centrifuge

are fed from a 220V single phase, 3-wire connection from the main 380V, 5-wire, 3-phase supply.

The signals from each chassis are fed back to a patch panel on the drive box where they are redistributed to suit the 2 x 32 channel arrangement of the sliprings. On the far side of the sliprings the signals run into a shielded cabinet and are attached to a 64 channel multiplexer, which then feeds a PC based ANALOG HSDAS-16 (16 bit A/D convertor). The Slipring Room data acquisition PC is currently running SNAP-Master data acquisition

software. This PC is connected via a thinwire ethernet to the Control Room Data Acquisition PC, and logs all its data to the CRDAS PC's Magneto-Optical drive. The various coaxial rings are rated to carry data-communications and high bandwidth analog signals.

The support equipment for maintaining, calibrating and repairing the elements of the data acquisition/power systems is mostly in place. The current data acquisition system is an intermediate step on the way to a state-of-the-art system. This system will be shortly upgraded by mounting the slipring room equipment at the centrifuge hub.

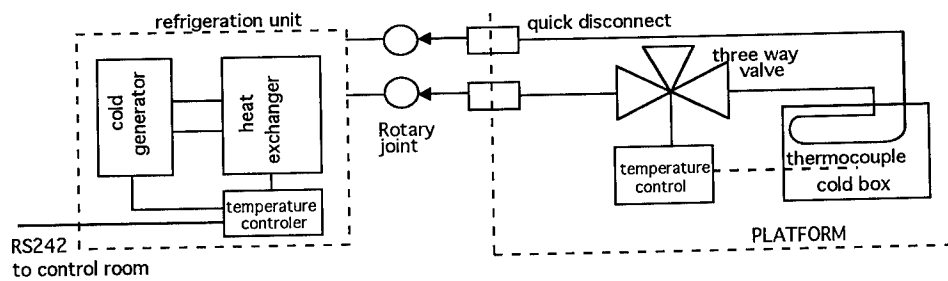


Figure 3. C-CORE Refrigeration System

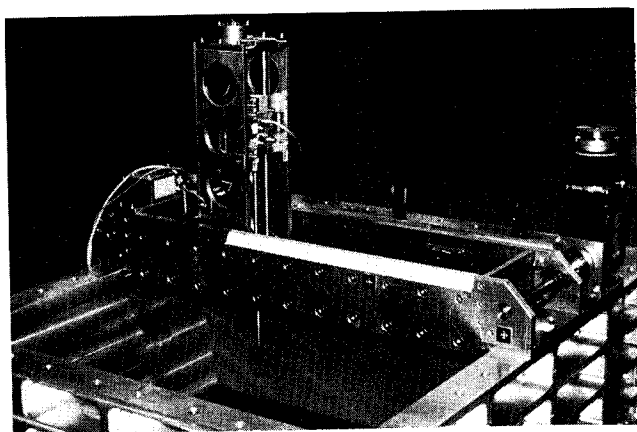


Figure 4. C-CORE Cone Penetrometer

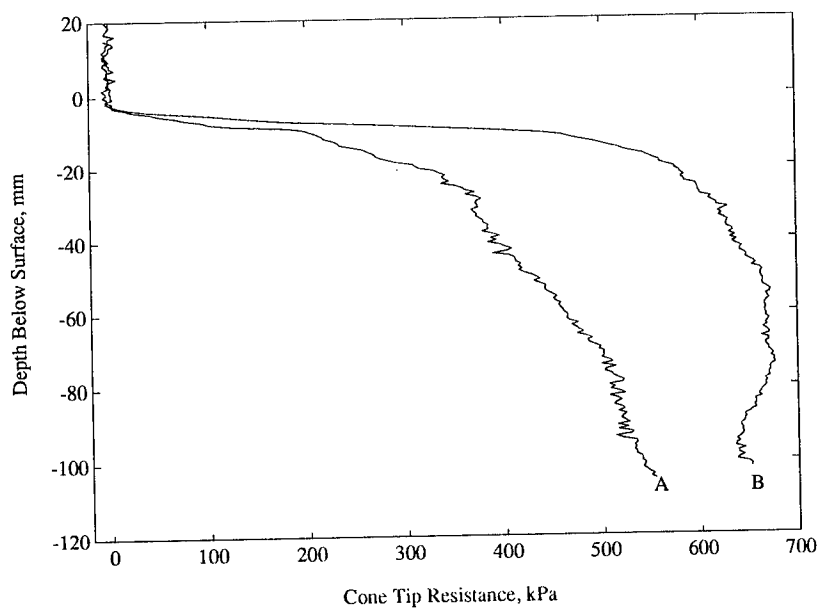


Figure 5. Typical Cone Penetration Resistance Profiles

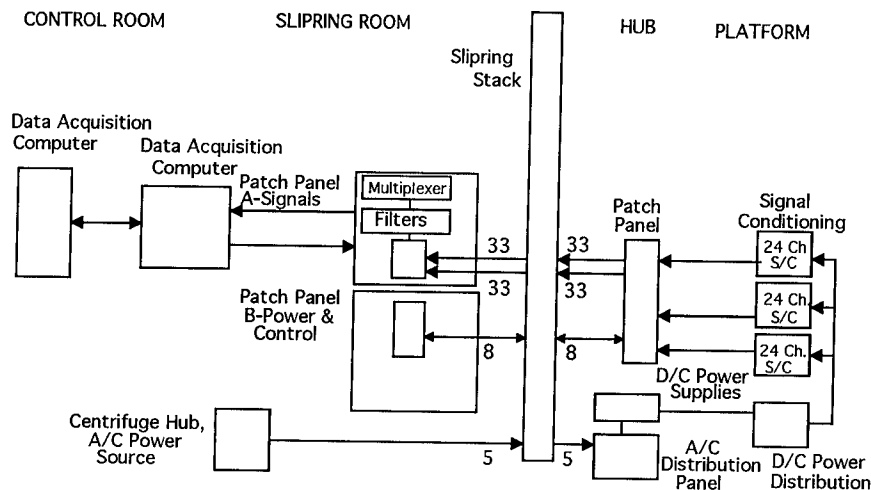


Figure 6. C-CORE Data Acquisition & Electrical Power Sub-System

## 5. SUMMARY

This paper has described the new C-CORE Centrifuge Centre in St. John's, Newfoundland which was commissioned in June 1993. The machine selected after international evaluation was an ACUTRONIC 680-2 centrifuge with a payload capacity of 220 g-tons. Most ancillary equipment for the facility is now in place and the data acquisition system is operational. Research has commenced in the area of soil/structure interaction. Work will commence shortly in the development of cold regions centrifugal research.

## 7. REFERENCES:

- Corté, J.F. (1984). Presentation of the L.C.P.C. Centrifuge, Int. Symp. Geotech Cent Model Testing Tokyo, pp. 120-126.

## 6. ACKNOWLEDGMENTS

The Authors are grateful to the Canada-Newfoundland Offshore Development Fund; Industry Science Canada and the Natural Sciences and Engineering Research Council (NSERC) of Canada for the funding to build, equip and establish the new C-CORE Centrifuge Centre. They are also grateful to the staff of C-CORE and Memorial University of Newfoundland for their support. The guidance and advice from other centrifuge centres, particularly at Cambridge University and the Laboratoire Central des Ponts et Chaussées in Nantes, are gratefully acknowledged.

## US Army's engineering centrifuge: Design

R. H. Ledbetter

*US Army Corps of Engineers, Waterways Experiment Station, Vicksburg, Miss., USA*

R. S. Steedman, A. N. Schofield & J. F. Corté

*Andrew N. Schofield and Associates Ltd, Cambridge, UK*

J. Perdriat & J. Nicolas-Font

*Acutronic France S.A., Les Clayes-sous-Bois, France*

H. M. Voss

*Acutronic USA Inc., Pittsburgh, Pa., USA*

**ABSTRACT:** In early 1992 the detailed design of a large and exceptionally powerful engineering centrifuge (1,144,000 g-kg) was initiated for the U.S. Army Corps of Engineers Waterways Experiment Station (WES) in Vicksburg, Mississippi. Although much of the recent world-wide interest in centrifuge modeling has concentrated on geotechnical problems, the new centrifuge facility will address research needs in physical modeling across the full range of civil engineering applications. The unique world class facility will be a key element in the development of new and novel research capabilities in physical modeling. This paper will discuss the centrifuge specifications, requirements, and the key design aspects. The centrifuge is expected to be in operation with its first research experiments in 1995.

### 1 INTRODUCTION

The WES is developing a unique powerful engineering centrifuge which will provide new and novel research capabilities for the U.S. Army Corps of Engineers. Development of research capabilities and test equipment are being undertaken by Andrew N. Schofield and Associates Ltd. (ANS&A). Detailed design and fabrication of the centrifuge is being carried out by Acutronic USA Inc. The centrifuge will have a radius of 6.5 meters and a maximum payload of 8000 kg to 143 g decreasing to 2000 kg at 350 g.

WES has a history of applying centrifuge techniques in the solution of high priority challenges to the Army. Early pioneering work on weapons effects in the mid 1970's was followed by research projects in liquefaction, erosion of dams, and earthquake engineering. In 1989, the WES accepted a proposal from ANS&A to provide novel research capabilities in physical modeling by developing a unique centrifuge facility at WES. A key feature of

these new modeling capabilities will be the wide range of engineering applications.

Recent world-wide interest in centrifuge modeling has concentrated on geotechnical applications; however, the WES centrifuge facility has a much broader mission. The WES centrifuge will address research needs in physical modeling across the full range of civil engineering applications. Research investigations in the fields of geotechnical, structural, hydraulic, environmental, cold regions, and coastal engineering are planned. Studies will be possible under climatic conditions ranging from desert to polar to ocean regions.

The centrifuge size and capability requirements are based on the research activities of WES which lie at the state of the art and typically involve field problems with large dimensions, depths and time scales.

At the core of the WES centrifuge center will be an Acutronic 684-1 model based on the design concept of the Acutronic 680 model installed at Laboratoire central des ponts et chaussée (LCPC) in Nantes, France, in 1985

and a dozen subsequent geotechnical engineering centrifuges installed or in the process of installation world-wide. However, the much higher payload and g specification and the factor of safety (2.7 to the elastic limit) required under design loads of the WES centrifuge placed great emphasis on the structural analysis. Of critical importance was the selection of appropriate high strength steels which could accept the high stresses using minimum weight.

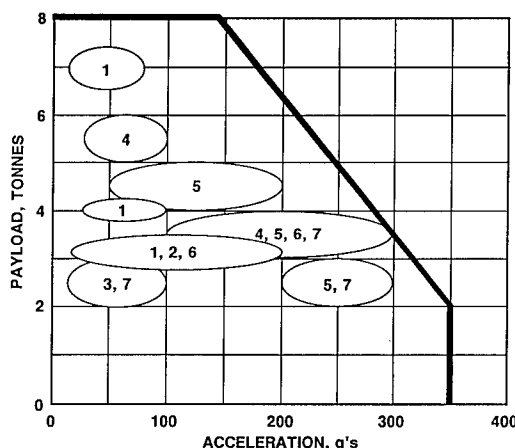
## 2 DESIGN REQUIREMENTS

The applications of centrifuge testing where it would greatly benefit research and development objectives were studied (Ledbetter 1991) in the technical areas representative of the research conducted by the five laboratories and the Coastal Engineering Center of the WES and the U.S. Army Cold Regions Research and Engineering Laboratory. Technical areas studied were (1) coastal, (2) environmental, (3) geotechnical, (4) hydraulic, (5) structural, and (6) cold regions. The study identified forty broad research thrust areas with the centrifuge operational requirements and specifications for each. These research thrust areas and centrifuge requirements address real world problems where structures and conditions can be on a large scale. It was found that large models were needed for research tests at low as well as high g levels.

The criteria for developing centrifuge operational requirements was centered on the needs of: (1) model size, (2) payload-platform dimensions, (3) payload, (4) acceleration, and (5) centrifuge capacity. There are several criteria that govern the choice of model size and acceleration when designing a centrifuge model testing program. These criteria include: (1) purpose of the experiments, (2) dimensions and mass of the prototype, (3) size and acceleration requirements for model validation tests, (4) resolution requirements for measuring small volume phenomena, (5) space required on the centrifuge payload-platform or in the model container for necessary test equipment, (6) size of measurement instrumentation and inclusions compared with the model and its materials and

components, and most importantly (7) model dimension limitations in order to minimize the boundary influences from the payload-platform and model container side walls as they affect the results for the specific purpose test.

Study results showed that to meet the needs of the research thrust areas, centrifuge requirements ranged as: (1) payload from 540 to 14,514 kg, (2) acceleration from 10 to 400 g, and (3) capacity from 18,144 to 816,466 g-kg.



- |                      |                        |
|----------------------|------------------------|
| 1-Cold Regions       | 5-Locks, Dams, Control |
| 2-Structures         | Structures             |
| 3-Pavement, Mobility | 6-Environmental        |
| 4-Blast effects      | 7-Hydraulics, Coastal  |

Fig. 1 Centrifuge design requirement operating envelope

The most economical centrifuge to meet the requirements resulted in the 1,144,000 g-kg machine to be described in the following sections. Figure 1 shows the design requirement operating envelope for the centrifuge with generalized research thrust areas superimposed.

Key centrifuge capabilities which will be provided include: (1) earthquake and vibration loading, (2) blast loading, (3) test package environment control, (4) in flight manipulation of model materials and fluids, (5) in flight site investigation, and (6) high speed data acquisition and control systems.

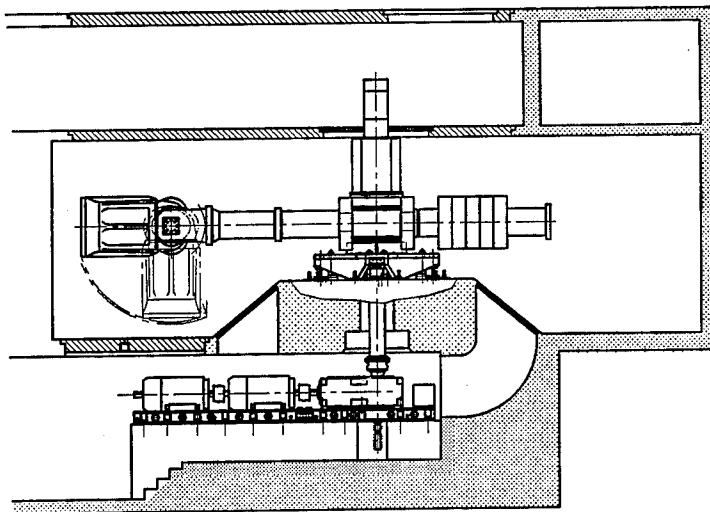


Fig. 2 Acutronic 684-1 centrifuge elevation

### 3 MECHANICAL DESIGN

Design of the WES centrifuge (Figure 2) was carried out by Acutronic France, with technical review by ANS&A working in the UK and in France. The objectives of the design review process were to ensure that the new centrifuge facility would be integrated into the overall WES research capabilities and to maximize the potential of the centrifuge within the specified design parameters.

The high payload and high g specification for the centrifuge led to a unique design which was governed (mechanically) by four criteria:

1. high payload-platform stiffness to minimize deflections under load.
2. high natural frequency to avoid resonance in rotation.
3. high safety factor on working loads to the elastic limit.
4. capacity to come to rest safely given loss of payload (ultimate limit state).

The payload-platform design was governed by the allowable deflections and by its mass, which is critical because of the forces it imposes under high g on the supporting straps, hinges and centrifuge arm. Payload-platform deflections were limited to less than 1 mm TIR under a

2000 kg load at 350 g distributed over a typical circular or rectangular package 'footprint'.

Two designs for the payload-platform were considered: (1) a system based on rectangular and circular hollow tubes forming a grillage structure, and (2) a welded honeycomb box structure. Although the tubular form had an important advantage in eliminating welds in critically stressed locations, this design was significantly heavier than the welded box structure and was therefore rejected.

Using high strength steel an immediate reduction in mass of 700 kg (around 20 percent of the original mass of the payload-platform slab) was made and further reductions of nearly 30 percent were then achieved by optimizing the design with finite element analyses.

The transfer of load from the payload-platform slab to the supporting straps was achieved via six high strength conical pins (three on either side of the payload-platform) which are located in bushings welded into the payload-platform box structure. Tensile forces arising from the tangential 'spreading' of the parallel booms are accommodated by bolts around the pins which connect the payload-platform slab to the straps. Figure 3 illustrates the finite element mesh of a quarter of the payload-platform honeycomb structure and pins.

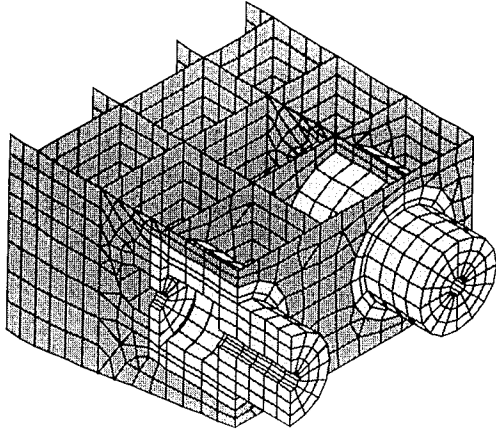


Fig. 3 Finite element mesh of one quarter of the payload-platform

Finite element analyses of the supporting straps resulted in an optimized design using 35 NCD 16 laminated steel plates, with heat treatment to achieve a yield strength of 1200 MPa.

Spherical sleeve bearings were used for the hinges at the connection between the straps and the booms. Teflon coated and made from high strength steel, the bearings provide a low

friction joint and protect the booms from stress concentrations caused by the high loads transferred by the supporting straps. (At 350 g each strap must transfer a force of around  $(8 \times 350)/2 = 1400$  tonnes to the booms.) Figure 4 shows a cross-section through the hinge.

The two parallel tubular booms, characteristic of Acutronic centrifuges, were fabricated from forged 35 NCD 16 solid steel rods 9.73 m long and 0.69 m in diameter, each initially weighing 30,700 kg. Each rod was machined to its final outer diameter of 0.64 m and length of 9.45 m with a central bore 0.3 m in diameter and 8.7 m long to provide for the automatic balancing mechanism.

The booms were subjected to a rigorous ultrasonic examination and to heat treatment to relieve internal stresses and ensure the required yield stress of 1000 MPa. The high quality of fabrication (Forgemasters of Sheffield, UK) allowed for an increase in length of the booms which was used to provide a corresponding increase in the fixed counterweight capacity.

Each boom weighs 17.6 tonnes. Their design was dictated by the requirement of a high natural frequency in rotation which led to a high bending stiffness requirement rather than the simple requirement of tensile strength.

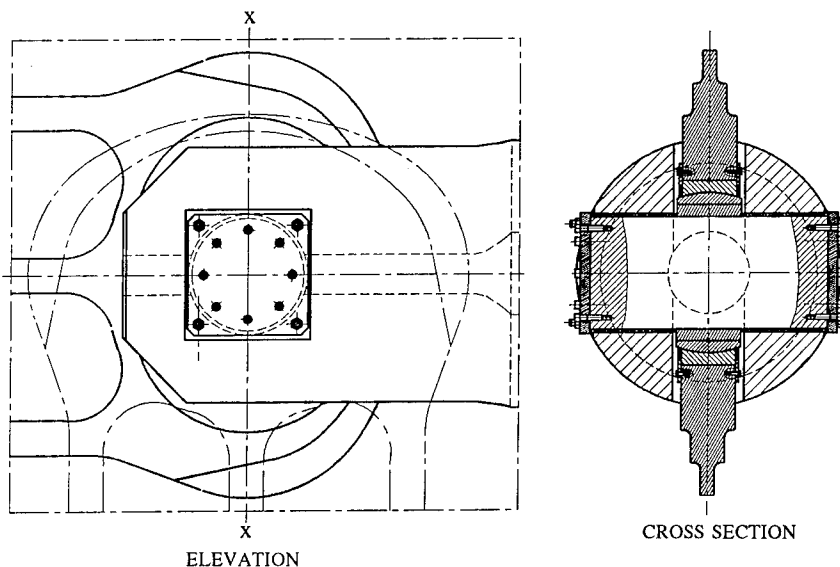


Fig. 4 Hinge connecting swinging payload-platform to the booms



The lowest resonant frequency of the arms is around 7.35 Hz, more than twice the maximum rotational frequency of 3.66 Hz (220 rpm).

The counterweight consists of five steel plates each 2.87 m wide, 2.2 m high and 0.32 m thick with a total mass of 32,000 kg. This permits the required range of centrifuge payloads (0 to 8000 kg) on the swinging payload-platform to be balanced without any additional mass. An electrical motor system can move the fixed counterweights over their extreme range in about 60 minutes. The automatic in-flight balancing system can accommodate up to 100 kg of imbalance using movable pistons inside the tubular booms.

The central section of the centrifuge provides anchorage and lateral support during rotation. The main shaft and the bearing size were also determined by the requirement for a high natural frequency, but the diameter of the bearings was limited by the available clearance between the booms. The final design resulted in the use of a set of bearings of 1 m outer diameter and a base suspension frequency of 32 Hz with a shaft natural frequency in the first mode of 8.8 Hz.

#### 4 AERODYNAMICS AND BUILDING DESIGN

Aerodynamic behavior is a critical aspect of centrifuge performance, Nicolas-Font (1988). In the design process, careful attention was given to the energy losses in the rotation of the centrifuge. The energy losses are caused by interaction between the rotating machine, the air in the chamber, and the containment structure.

Experimental data gathered from operating Acutronic centrifuges were used to validate the design method adopted for the WES centrifuge.

In particular, the efficient operation of large centrifuges depends on early consideration in the design of the centrifuge chamber. Four aspects dominate the chamber design process:

1. structural integrity and safety management systems.
2. aerodynamics of the rotating arm.
3. resonant frequency.
4. air quality (humidity and temperature).

The size and power of the WES centrifuge

required that level separation be achieved in the arrangement of centrifuge chamber and control room. This requirement was achieved at the site by locating the centrifuge in a natural valley adjacent to the main laboratory.

The structural specification of the centrifuge chamber was dictated by the dynamic requirement to achieve a fundamental natural frequency over four times the maximum rotational frequency of the centrifuge.

As the arm rotates in the centrifuge chamber the air in the chamber is also set in rotation, but at a slightly lower speed. The difference between these rotational speeds creates a pressure wave traveling with the arm. A pressure increase exists in front of the leading boom and a pressure reduction occurs behind the trailing boom. For the WES centrifuge, this pressure was computed to be equivalent to a cyclical pressure of up to 17 kPa at the maximum rotational frequency.

Power consumption is dramatically affected by energy losses caused by air drag in the centrifuge chamber. Experimental measurements in 1985 on the Acutronic 680 at LCPC showed that the centrifuge theoretical power consumption of 180 kW was increased by 75 kW as a result of air drag. The construction tolerances and air-tightness of the centrifuge chamber are of great importance in minimizing these effects.

The WES centrifuge chamber was designed to have a first natural frequency of 15 Hz, with circularity to within 10 mm on a chamber diameter of 15.45 m.

Environmental control of the air mass in the WES centrifuge chamber was specified as a function of ambient conditions. The large volume of air flowing through the chamber made it inefficient to attempt absolute control of the temperature and humidity while the centrifuge is in flight. Instead it was decided that environmental control of models would best be provided in individual model packages when necessary, such as during testing periods of long centrifuge operation.

Air flow downward through the chamber and out the motor room and access stairwell is controlled by two 110 kW fans. Each one of the fans is capable of delivering an air flow of

130,000 liters/sec. This capability meets the required specification of ambient temperature plus ten degrees Celsius and ambient humidity minus ten percent.

## 5 USER INTERFACES

The design review process placed considerable emphasis on the useability of the WES centrifuge and on the necessity for a wide range of services to be available on board the centrifuge. Central arm services, designed by ANS&A, will interface with the Acutronic slip ring stack and the optical and hydraulic rotary joints. Electrical power of 60 kW will be available to the user through power slip rings, together with two high pressure (200 bar) and four low pressure (10 bar) hydraulic lines for gases or fluids. The signal stack includes 65 low voltage lines, 6 video lines and 1 fibre-optic rotary joint incorporating a high speed IEEE modem. On-board data acquisition systems, under remote control by the user, are currently being designed for general application.

## 6 CLOSURE

A key feature of the design and development of the WES centrifuge was the close cooperative technical appraisal, quality assurance efforts, and partnership among WES, Acutronic, and ANS&A. Technical aspects of the WES centrifuge design were reviewed at frequent meetings between Acutronic and ANS&A and at regular meetings with WES throughout the design phase. These meetings ensured that the centrifuge design was, as far as possible, tailored to meet the likely requirements of its future users, without escalation of cost.

Although large high g centrifuges have been constructed in the past in the former Soviet Union, this is the most powerful centrifuge presently known to be designed using modern analysis techniques and advanced materials. The ability to use high strength steels and to conduct detailed numerical analyses of stress concentrations allowed the centrifuge performance to be optimized without compromising the safety of the facility.

This centrifuge is probably also unique in its intended application for research in the wide field of civil engineering as opposed to the more traditional geotechnical arena. The new capabilities that will flow from the centrifuge will depend on the ingenuity of its users and the design of its appurtenances. In this respect the design of the centrifuge itself, the subject of this paper, is merely one component of the development of new capabilities in physical modeling that will ultimately be the basis of the WES centrifuge center.

## ACKNOWLEDGEMENT

The authors acknowledge the support of the U.S. Army Engineer Waterways Experiment Station and the permission of the Chief of Engineers to publish this paper.

## REFERENCES

- Ledbetter, R.H., Ed. 1991. Large centrifuge: a critical army capability for the future. MP GL-91-12, U.S. Army Engineer Waterways Experiment Station, Vicksburg, Mississippi, USA.
- Nicolas-Font, J. 1988. Design of geotechnical centrifuges. *Proceedings of The International Conference on Geotechnical Centrifuge Modelling*, Paris, France: 9-15. Rotterdam: Balkema.

## Development of NHRI – 400g. t geotechnical centrifuge

Y. Dou

Nanjing Hydraulic Research Institute, People's Republic of China

P. Jing

602 Research Institute, The Ministry of Aeronautics and Astronautics Industry, People's Republic of China

**ABSTRACT:** In order to develop a geotechnical centrifuge, i. e. the type NHRI – 400 g. t geotechnical centrifuge, technical – economic evaluation and verification efforts were carried out at the Nanjing Hydraulic Research Institute during the period from October 1984 to December 1986. In January 1987 the Ministry of Water Resources and the Ministry of Communications agreed to make joint investment in the Project. In August 1987, through bidding a contract was signed with The 602 Research Institute of The Ministry of Aeronautics and Astronautics Industry for technical development of the 400g. t geotechnical centrifuge. As soon as the contract went into effect the 602 Institute began to undertake design, manufacture, installation and debugging activities. In December 1991 the centrifuge facility was put into service after being checked and accepted.

### 1 SPECIFICATION FOR NHRI – 400g. t GEOTECHNICAL CENTRIFUGE

The main specifications are as follows:

(1) Effective radius (from centre of gravity of model to centre of rotation) 5.0m, and 5.5m from platform of swinging basket to centre of rotation.

(2) clear swinging basket dimensions,  $1.2 \times 1.2 \times 1.1\text{m}^3$ , maximum deflection of bedplate when subjected to maximum loading, 1 ~ 2mm.

(3) Design standard acceleration (at 5.0m radius) 200g, and payload (model case plus model) 2000kg.

(4) Rate of change of centrifugal acceleration for 24 hours less than  $\pm 1\%$ .

(5) Starting duration for design standard acceleration (200g) does not surpass 10 minutes.

(6) In various constant speed conditions, vertical and tangential acceleration errors are controlled to about 0.2 % of the design acceleration.

(7) Maximum driving power < 500KW.

(8) An unbalance monitoring system is installed which has an auto – balance capacity of 5 % of the maximum load (i. e 200KN) . If unbalance exceeds the limit load of 200KN, the machine will stop automatically.

(9) Stop and braking devices are installed.

(10) A slipping with 100 channels and an electric ring with 10 channels are installed on

the spline shaft.

(11) An air conveyance or water conveyance joint (pressure = 20MPa), a water transfer joint

(discharge = 380l / min), and two oil transfer joints (pressure = 20MPa, discharge = 30L/min) mounted on the spline shaft.

(12) The swinging basket is capable of accommodating instrumentation weighing 100kg and affords room for a TV monitoring device, photographic apparatus and data acquisition system.

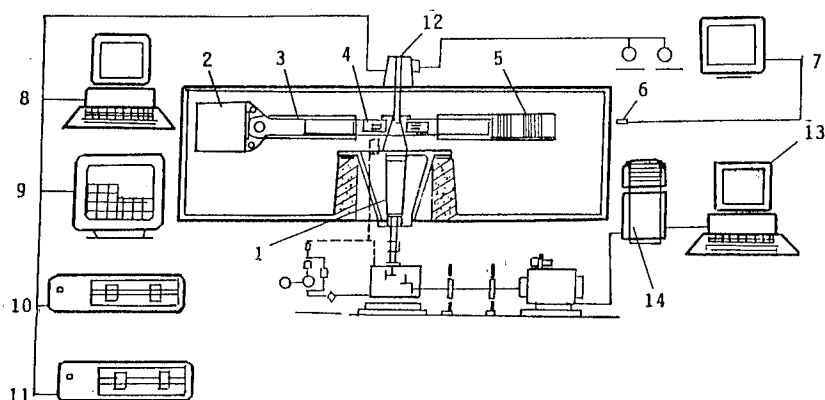
(13) In the design of the centrifuge, consideration has been given to the effects on the centrifuge of dynamic loading to be induced by future installation of earthquake simulation and vibrating devices. In the case of 200g, the frequency of the dynamic load is 500Hz, and the dynamic load (soil plus the model case) 500kg.

(14) Due to the fact that measurements are made by the use of low – frequency signals, it is necessary to get environment noise under control and prevent the electric trailing system from constituting a public nuisance to the electric network.

### 2 FEATURES OF MAIN MACHINE SYSTEM

#### 2.1 General layout

The general layout of geotechnical centrifuge is shown in Fig. 1.



1. Driving shaft 2. Swinging basket 3. Rotor arm 4. Force sensor  
5. Balancing counterweight 6. Observation camera 7. Observation monitor  
8. Control computer 9. Image 10. Plotter 11. Printer 12. Slipring  
13. Auto-control computer 14. Power supply control cabinet

Fig.1 General layout of NIIRI'S 400g.t Geotechnical centrifuge

The features of the main machine system include a rotararm, swinging basket, counterweight box, spline shaft, machine table, transmission system (comprising a speed reducer, coupling, braking device, rotation axis and lube pump), driving and speed - governing system, balancing system, safety monitoring system, etc. The main machine is installed in a round reinforced - concrete enclosed chamber 12, 200mm in diameter and 2,800m in height.

The electric motor, speed reducer, lube pump and braking device and so on are installed in its lower part, the slipring and hydraulic slipring, etc. are installed in its upper part. In addition, there are several rooms for controlling and operating, such as a control room, a operation room, a preparation room, and a pump room, etc.

## 2.2 Structure of components

**2.2.1 Rotorarm:** In view of the power supply conditions, an asymmetrical rotorarm, a monolithic load - bearing beam structure, is adopted. Its chief advantages are compact construction, small height (500mm), light weight (the total weight being not more than 10,000kg), small windage loss and small rotation inertia, a condition favorable to power reduction. Disadvantages are: relatively complicated structural stress conditions, low utilization of materials and high cost of manufacturing.

Connection of the rotorarm to the spline shaft is accomplished using a two - hinged mechanism, which is one of the major features of the main machine.

This type of connecting mechanism is structurally effective in hindering vibration forces from being transmitted to the spline shaft so as to reduce the vibrations of the global machine. The results of debugging tests showed that during operation of the centrifuge at its full capacity of 400g.t, the vertical and tangential accelerations of the swinging basket were not more than 0.1% of the design values, thus fully confirming, the usefulness of the two - hinged mechanism. This guarantees that a vibration exciter for earthquake simulation can be installed successfully in the second stage of project.

**2.2.2 Swinging basket:** The design of swinging basket has much influence on the global of the geotechnical centrifuge due to it set on the biggest position of centrifugal force field (nominal effective radius of machine  $R = 5m$ ), swinging basket mainly bears centrifugal inertia forces caused by its own weight, the weight of the model and frictional additional moment induced by swing at the hinges and others such as aerodynamic resistance, tangential inertia force occurring during acceleration and gravity, etc. Enough strength is needed, in particular for the hooker. Enough stiffness is also needed for the bedplate and deflection of the bedplate under a maximum load is 1~2mm. Its weight is not more than 2000kg.

## 2.3 Aerodynamic design and calculation of power

**2.3.1 Estimation of windage loss power in the enclosed chamber:** It is impossible to calculate windage loss power accurately. It is usually

calculated with the aid of an empirical formula and then verified by conducting small-scale model tests in similar conditions.

Power calculation is made mainly to determine the mean coefficient of windage loss of the swinging basket and rotorarm  $C_D$ , the coefficient of surface (walls, floor and ceiling) air friction resistance  $C_f$  in enclosed chamber and the ratio of rotational speed of air  $k$  ( $= \omega_a / \omega_c$ ), i. e. the ratio of rotational angular velocity of air  $\omega_a$  to that of the geotechnical centrifuge. By small-scale tests  $C_D$ ,  $C_f$  and  $K$  of 400g. t geotechnical centrifuge are measured as follows:  $C_D = 0.875$ ,  $C_f = 0.006298$ ,  $K = 0.5072$ . Calculated values of power are shown in Fig. 2.

2.3.2 Test of actual power loss: A power loss test was conducted under normal conditions of operation of the motor drive system, power supply system, transmission system, lubricating and cooling systems and auto-balance system, with current and voltage being measured for different rotational speeds (accelerations) and for no-load, 1,000kg, 1500kg, 2,000kg and 2,100kg without a rectifier hood and 2,000kg with a rectifier hood respectively. The results are shown in Fig. 2.

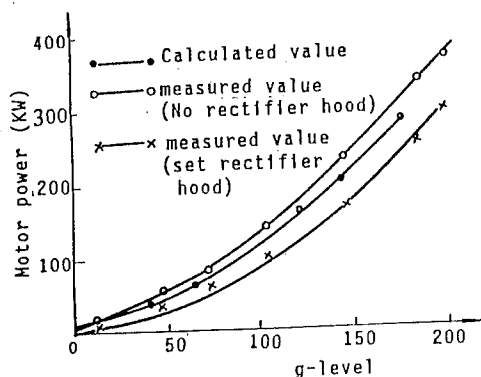


Fig.2 Relation between windage loss and Centrifugal acceleration

From the test results, it is clear that the variation of actual power loss with acceleration is close to the estimated value, particularly, when the power loss of the driving system is taken into consideration. When a rectifier hood is adopted, the power loss may be reduced by 20% ~ 25%, in particular, for low acceleration. It follows that the aerodynamic design is successful with good rectifying results.

#### 2.4 Speed regulating system

The speed regulating system utilizes a

digit-analog double enclosed ring, including a current regulator (LT) and a speed regulator (ST). The current regulator is similar to a conventional analog system. The difference are as follows: the original given potentiometer is replaced by a digital dial, the speed measuring motor is replaced by a photo-pulse generator (EMB), and the given integrator (SJ) and speed regulator (ST) (analogue and digital regulator) are both made up of digital integrated circuits. Besides continuous comparison between given and feedback frequencies, the system compares their phases, and the disadvantage of drift of an analog system is overcome. A particular feature is the ability of the system to simulate quantities when regulating signal output, thus overcoming the discontinuousness of the digital system. The accuracy of static steady velocity, given accuracy and linearity are better than 0.1%, thereby leading to better static and dynamic properties.

#### 2.5 In-flight balancing system

Because of an asymmetric rotorarm two kinds of balance are needed: 1) static balance, i. e., the weights of swinging basket and model are balanced by using fixed weights; 2) in-flight unbalance forces produced by the model mass during operation of the centrifuge and its moment. In order to eliminate the influence of in-flight unbalance forces on the centrifuge a balance system is provided. According to the technical specifications, the auto-balance capacity of the system is 5% of the maximum load (200kN), beyond which the centrifuge stops automatically.

2.5.1 Principle of balance system: The system is designed to accomplish dynamic balance by using the movement of the centre of gravity of the water mass. There are mainly an unbalance force measuring unit, an air source and a power supply for balance control.

The principle is as follows: unbalance force after being measured by a gauge installed on the rotorarm is sent to a computer for direction judgement through a quadratic instrument gauge and then order is given to relevant water and air valves. As the valves opened, water is pressed to some water tank, with changes in water volume, the centrifugal force changes and makes unbalance force shift toward the state of balance. The computer checks unbalance continuously. As soon as the equilibrium zone is reached, the computer cuts off water valve and air valve signals, and thus, balance regulating is finished.

2.5.2 Debugging results: Debugging test was conducted when the main machine had reached a normal state of operation and after the

force - measuring gauge had been calibrated. The test was conducted to determine the time<sub>m</sub> and response time<sub>r</sub> required to balance the unbalance force of 10kN for 400, 600, 700 and 800 rpm. as well as the time<sub>r</sub> required to automatically balance the unbalance force of 200kN for 800 rpm. For unbalance force > 200kN, an alarm is given and machine stops.

The debugging tests show that when the unbalance force  $10\text{kN} \leq F \leq 200\text{kN}$ , auto - balance can be realized (error is only 2.4%). The balance time for 10kN unbalance force is not more than 137s, if the maximum balancing capacity of 200kN is exceeded, an alarm is reported and the machine stops automatically. Therefore, the auto - balance system is a success with high accuracy and fast regulating speed.

## 2.6 Safety monitoring system

The system includes mainly the following parts:

(1) Safety monitoring of the driving system and its protection. If overflow, overload and no - phase appear, the control system gives a alarm and the machine stops automatically.

(2) The balance system is not only a in - flight balancing system, but a balance - lose check system. For an unbalance force < 200kN, balance can be reached automatically, and for an unbalance force > 200kN, it gives the alarm first and the control signal is cut off so as to stop the centrifuge.

(3) Safety measurement of temperature. sensors are installed on some key parts such as bearing and so on, as soon as temperature exceeds a certain allowable value, the machine reports an alarm and stops.

(4) Safety monitoring of the braking system. Once the brake is out of work, a fault signal is given out.

## 2.7 Functions of centrifuge software

The software is designed to meet performance requirement and guarantee safe operation. Its main functions are as follows:

(1) To specify rotational speeds and change a given rotational speed at any time as required

(2) To check and print the rotational speeds of the main machine and their corresponding accelerations.

(3) To check the magnitude and direction of unbalance forces, control auto - balance and send out alarm and stop orders.

(4) To check and print temperature changes at various parts and report alarm and stop orders.

(5) To control the brake devices.

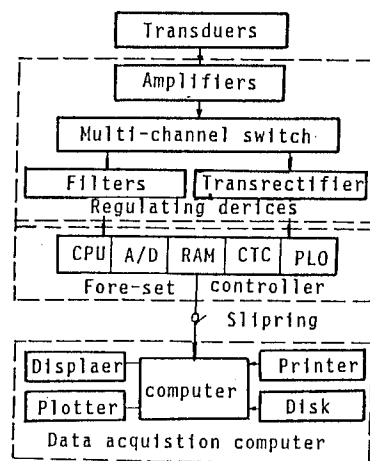


Fig.3 Block diagram of data acquisition system

## 3 DATA ACQUISITION AND PROCESSING SYSTEM

### 3.1 Hardware

The system is composed mainly of 3 parts, i. e., a signal regulating device, a fore - set controller and a computer. Amplification and setting of signals, A/D conversion of data and acquisition control, and operation and data management of the system are accomplished by means of the 3 parts respectively. Its working flow is shown in Fig. 3.

### 3.2 Development of software

The main program of the system was compiled on the basis of micro soft C 5.0 under UC DOS. The operator can choose different sub - programs to complete his measurement work according to the menu in the course of operation.

## 4 VIDEO SYSTEM

The centrifuge is equipped with two kinds of video devices, i. e., a closed circuit TV and an image processing system.

### 4.1 Closed circuit TV

The closed circuit TV is used to monitor the operating state of the centrifuge as a whole. The camera uses a wide - angle lens (WV-CL 300) and is installed at a port located on the wall of the centrifuge chamber. The monitor screen is in the controlling room.

### 4.2 Digital image processing system

In order to collect data on the whole course of

modelling test, a digital image processing system is introduced. The system is a product of the Erdas corporation of America, It is composed of a main computer and I/O devices. The in-flight configuration of the models deformation can be obtained by this system.

## 5 CIVIL ENGINEERING OF GEOTECHNICAL CENTRIFUGE

### 5.1 General layout

In accordance with the technical requirements and working conditions of centrifuge, the laboratory occupies a total area of 2,320 m<sup>2</sup>. There is a building of 565 m<sup>2</sup>, including 458 m<sup>2</sup> for the first floor and 107 m<sup>2</sup> the second floor. Arranged on the first floor are the centrifuge chamber, transformer, power distribution room, SCR, gas and oil pump room, model preparation room and so on. On the second floor are the monitoring room, office room etc.

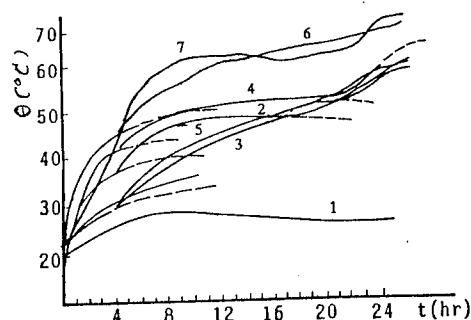
Due to the fact that centrifuge chamber is of the semi-cellar type, the antechamber of the laboratory is provided with a detachable roof in order to meet the assembling and overhaul requirement of the centrifuge. In the chamber there is a 5-tonne bridge crane for use in the assembling of the model and other equipment.

### 5.2 Design index of centrifuge chamber

The centrifuge chamber includes rotorarm, swinging basket (including model), shaft and rotation space. Its design index and accuracy requirement of size are determined by power loss and safety protection. The size requirements are 12, 200 ± 10 mm in diameter, roundness error of the inner cylindrical surface  $\geq 20$  mm; 2, 800 ± 5 mm high, perpendicular alignment of the top and bottom planes to the cylindrical surface  $\geq 5$  mm, unevenness of the inner surface of the cylinder  $\geq 3$  mm, 600 mm thick reinforced concrete wall that can bear the impaction of 2,000 kN force.

### 5.3 Temperature state in centrifuge laboratory

Based on the laws of conservation of energy and heat conduction and the assumption that the machine chamber is enclosed (no interchange with outside air), primary estimates have been made. The results of estimation show that heat transmission and heat evolution in the machine room depend mainly on the top coverplate. Only use of a 20 mm thick steel-plate cover can make it possible to obtain a steady temperature rise difference of 40°C in the machine chamber in



1. Temperature in the hall;
2. Temp. in the hole for electric motor;
3. Temp. of the centrifuge;
4. Temp. of lubricating oil;
5. Temp. of top bearing;
6. Temp. of low bearing;
7. Temp. of transformer.

Fig.4 Temperature change properties of 24 hours operation

1~2 hours, while use of a concrete cover may make the steady temperature rise difference reach 200°C over 20 hours (the coefficient of heat conduction of concrete is 1.28 W/m.K, while that of steel is 44.21 W/m.K). The latter is intolerable to the transmission system and measuring system of the centrifuge. Therefore, ventilation and temperature lowering measures are necessary for the enclosed machine room. In view of the fact that there is a difference between the assumed conditions and reality and that the temperature rise in the centrifuge chamber is about 40°C, devices for lowering temperature are not added in the room for the present.

During the stage of centrifuge debugging, 2-3 hours of continuous monitoring of the temperature indicated that the temperature in the machine room was between 20°C ~ 35°C (air temperature is about 15°C). The reason was that during operation, the centrifuge absorbed outside cold air from the orifice where the electric-slipring was installed in the middle part of the machine room, while the warm air exited through the access door gap in the cylinder wall and the movable steel coverplate gap, an resulting in exchange of cold and heat air. Power loss is needed to compensate for this condition.

The temperature change within 24 hours of operation of the key parts of the centrifuge are shown in Fig.4.

From Fig.4 it is clear that at a steady rotational speed, the change in temperature slowly approaches a state of balance as the operation time is increased. when acceleration is

changed sharply, the tendency of temperature rise is abrupt. Judging from the present situation, high temperature in the machine room (57°C) has much influence on data acquisition and sensors due to long time operation. This deserves careful attention. All the temperatures of other key parts are within the range of allowable values.

## 6 CONCLUSIONS

After scheme demonstration, design, manufacture and assembling, debugging tests were conducted on the complete set of devices of NHRI - 400g. t geotechnical centrifuge, they includes; 1) the test of maximum effective mass (model case plus model) at a maximum design acceleration; 2) the test of starting duration for the maximum design acceleration; 3) the stability accuracy test of centrifugal acceleration during 24 hours of operation; 4) the test of the vertical and tangential accelerations of the model at constant speed; 5) the maximum driving power test of the centrifuge; 6) the stop and braking capacity test; 7) the auto - balancing capacity test; 8) the 24 hr temperature change test of the key parts of the centrifuge and debugging of data acquisition system. Its technical indexes meet or are superior to the original design values. It is already in use. Now several centrifuge tests on the national key research project and engineering projects are being carried out.

To bring into play the features of centrifugal modelling dynamic tests, we are going to work energetically to develop second - stage dynamic devices.

## 7 ACKNOWLEDGMENTS

The NHRI - 400g. t centrifuge project was supported by a grant from Ministry of Water Resources and Ministry of Communications. This support is gratefully acknowledged. The project been made possible by enthusiastic support of Prof. Huang wenxi (Tsing hua University). The authors also wish to acknowledge the senior engineer Zhu weixing, Sun shuzu and engineer Liu shouhua, Cai zhengying et al are engaged together in the same project.



### 3 Equipment and instrumentation

## Cone penetration tests in the centrifuge: Experience of five laboratories

R. Renzi – ISMES, Bergamo, Italy

J.F.Corté & G. Rault – LCPC, Nantes, France

G. Bagge – DIA, Lyngby, Denmark

M. Gui – CUED, Cambridge, UK

J. Laue – RUB, Bochum, Germany

**ABSTRACT:** Trying to make the most of the potential of a centrifuge test, it is often necessary to know the soil properties under the state of stresses actually experienced during rotation. Up to now various laboratories have developed different small penetrometers for the centrifuge. These devices are not standardized and operate according to different procedures. No valid rules have been scientifically established for the interpretation of the results. Five European laboratories (LCPC France, ISMES Italy, RUB Germany, DIA Denmark, CUED United Kingdom), have combined their efforts in order to qualify experimental procedures on a common basis. Tests performed at the five laboratories on similar models allowed to assess inter-laboratory variability of tests results, both using sand and clay specimens. The influence of different experimental conditions (penetration rate, distance from wall, grain size) have been subsequently investigated.

### 1 INTRODUCTION

This note presents results of a research undertaken to improve the understanding of cone tests results performed in centrifuge models (for analysis of bearing capacity problems and simulation of field conditions). Firstly, a series of tests have been performed at the participating laboratories on similar models to assess inter-laboratory variability of tests results, both using sand and clay specimens. This effort intended to render the results obtained in analogous laboratory tests independently. Later on, depending on the potential of the different centrifuges and the interest declared by the different laboratories, each group accepted to take an active part in studying the influence of a particular experimental condition. During this phase, each lab was allowed to choose soils of major interest. Work on this topic is still in progress.

### 2 INTER-LABORATORY COMPARATIVE TESTS

To assess inter-laboratory variability of tests results, two soils have been selected for model preparation: Fontainebleau sand and Speswhite clay.

The sand is a medium-fine uniform sand

having a uniformity coefficient of 1.3 and an average particle size  $d_{50} = 0.22$  mm. Dry density is found to be ranging from 1415 kg/m<sup>3</sup> to 1681 kg/m<sup>3</sup>.

The clay has a liquid limit and a plasticity index equal to 51% and 28%, respectively. Grain size analysis indicated a prevalence of clay-size particles (65% by weight) with 33% silt-size particles and 2% sand.

#### 2.1 Tests in dry Fontainebleau sand specimens

Dry densities equal to 1530 and 1630 Kg/m<sup>3</sup> ( $I_p = 48\%$  and  $84\%$ , respectively) were selected for sand models preparation. At least two specimens at the recommended densities were prepared and tested by each lab in order to check the repeatability of the results. A minimum height of 350 mm was selected for model preparation.

It was recommended to measure the dry density of each specimen before acceleration in the centrifuge. It was suggested that this be calculated from weight and volume determinations of the total mass.

Tests have been performed in the centre of specimens adopting a rate of penetration equal to 2.5 mm/sec. The magnitude of the gravitational field was

70g at the surface of each model.

Records from the tests on specimens prepared at the recommended densities are compared in figures 1 and 2.

Table 1 presents the principal features of the tests executed on the specimens prepared at the higher density, including shape and size of the container used, technique employed for model preparation and diameter of the probes used.

Table 1. Comparative tests - Summary of tests performed on Font. sand specimens.

Laboratory	LCPC	DIA	RUB	CUED	ISMES
Test n.	SFS501	24/1/C	SBP1/FC2	SCP1/FC1	T1/FB2
Container <sup>1</sup>	R	C	C	C	R
Size (mm)	1200x800	0530	0750	0850	800x400
Method <sup>2</sup>	a	b	b	b	a
Density (Kg/m <sup>3</sup> )	1656	1630	1646	1663	1637
Diam. cone (mm)	12	10	11.3	10	11.3
Radius surf. (mm)	5117	2295	3160	3755	1846

<sup>1</sup> R Rectangular, C Cylindrical; <sup>2</sup> a) Travelling pluviation in air, b) Pluviation in air from a single hopper

Direct comparison shows that the total width of the band containing all cone profiles for both dense and medium dense specimens is on the order of 20% of the average measured cone resistance  $q_c$ . This difference is considered to be within acceptable limits.

## 2.2 Tests on saturated reconstituted speswhite clay specimens

A minimum of two specimens were to be prepared by each lab for repeatability.

For model preparation the following procedure was recommended:

1. Pluviate a 20 mm dry uniform sand into the test container and then fill it with deaired tap water.

2. Place the appropriate amount of tap water in a mixer and then add the dry clay powder to achieve an initial water content equal to 125%.

3. Once the appropriate amount of dry clay powder has been placed, mix the slurry for a couple of hours. It was highly recommended to do this operation under vacuum, if possible.

4. Just after mixing, transfer the slurry into the test container to get an unconsolidated specimen height of 400 mm.

5 After the slurry has been placed into the test container leave the slurry to consolidate under a total vertical stress of 10 KPa for 4 days, allowing top and bottom drainage. Then increase the vertical load on the clay until a uniform vertical stress of 200 KPa is reached and then leave the specimen to consolidate

under this final load for 3 to 5 days.

6. Unload the specimen in two steps. Firstly, reduce the total vertical stress from 200 to 100 KPa, leaving the specimen to swell under 100 KPa for 1 day. Later on, after removal of excess water from the

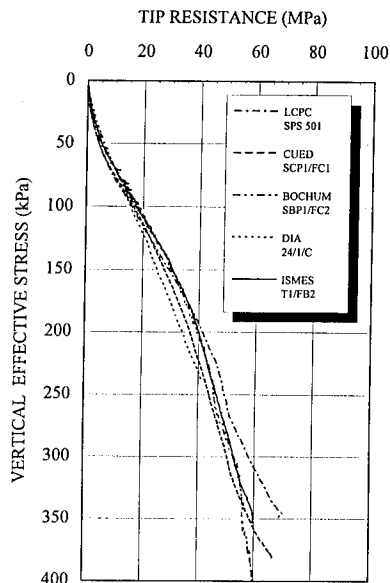


Fig.1 Comparative tests on dry Fontain. sand specimens (recomm.  $\rho_d = 1630 \text{ kg/m}^3$ )

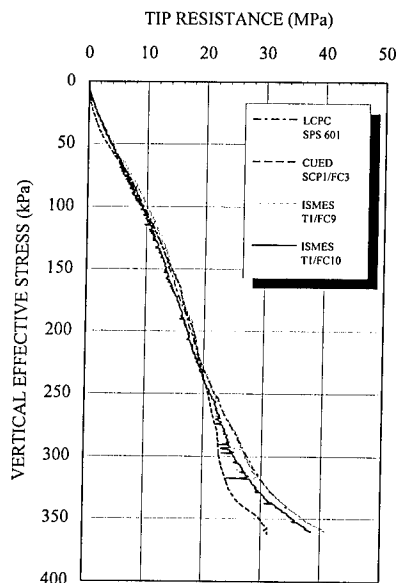


Fig.2 Comparative tests on dry Fontain. sand specimens (recomm.  $\rho_d = 1530 \text{ kg/m}^3$ )

top and closure of the base drain, reduce the vertical stress from 100 to 0 KPa.

A maximum delay between final unloading and flight was fixed to 1 day. 30 mm of free water was added just before accelerating the centrifuge. The magnitude of the imposed gravitational field was 70g at the surface of the clay. The clay was reconsolidated in flight for 7 hours.

Tests were performed in the centre of each specimen adopting a rate of penetration equal to 2.5 mm/sec.

Records from the tests are compared in figure 3, showing measured cone resistance,  $q_c$ , versus corrected prototype depth,  $z_{pc}$ , where:

$$z_{pc} = n z_m [1 + (z_m / 2R_s)]$$

$z_m$  = depth in the model

$R_s$  = radius at the surface of the specimen

Table 2 presents the principal features of the tests, including the shape and the size of the containers, the initial amount of slurry, the final specimens height and the probes diameter.

Direct comparison shows that the total width of the band containing all cone profiles is on the order of 30% of the average measured cone resistance  $q_c$ . This difference is considered to be large for engineering purpose. It is retained that it could be attributable to both departures from the recommended procedure

Table 2. Comparative tests - Summary of tests performed on clay specimens.

Laboratory	LCPC	CUED	ISMES
Test n.	SPK301	MWG4	T1/KC4
Container <sup>1</sup>	C	C	C
Size of container (mm)	Ø804	Ø850	Ø400
Init. height of slurry (mm)	358	413	400
Init. water cont. (%)	120	127	125
Final height (mm)	213	216	216
Delay unload-flight (days)	1.0	0.8	0.1
Diameter of cone (mm)	12	10	11.3
Radius at the surface (mm)	5242	3826	1974

<sup>1</sup> R Rectangular, C Cylindrical

inadvertently introduced during model preparation and/or differences in testing procedure.

### 3 FURTHER WORK

Despite the unsatisfactory discrepancies observed on clay specimens the groups considered profitable to enlarge the scope of the work. Each laboratory involved accepted to take responsibility for studying the effect of a particular experimental condition. In this way repetition of similar tests was avoided and it was possible to take advantage of the peculiarities of the different centrifuges.

#### 3.1 Tests in dry sand specimens

The work was carried out using Fontainebleau sand specimens. It was decided to concentrate on the following topics:

A1) effect of the ratio (diameter of container)/(diameter of cone) in cylindrical containers

B1) effect of the ratio (distance from wall)/(diameter of cone) in rectangular containers

C1) effect of the ratio (distance from wall)/(diameter of cone) in cylindrical containers

D1) grain size effects (variable cone diameter and variable g level)

Topic A1): CUED responsible.

Two test specimens were prepared in a 850 mm cylinder and two in a 420 mm cylinder. Four tests were performed at medium and high density and ratios of 85 and 42. Test results are shown in figure 4. The following observation can be made:

- for both medium dense and dense specimens there is no apparent increase in  $q_c$  for a test done at a ratio of 42, as compared to ratio of 85.

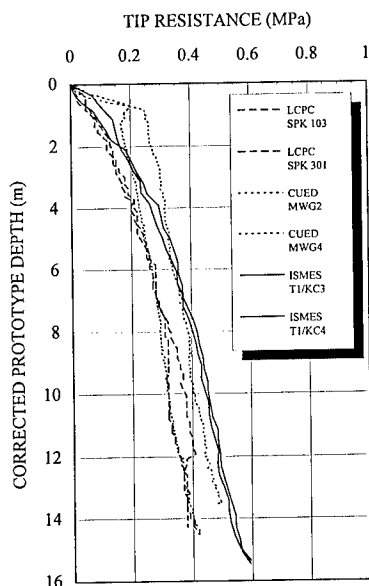


Fig.3 Comparative tests on saturated reconstituted speswhite clay specimens

Topic B1): LCPC responsible.

Two test specimens were prepared in a rectangular box having length and width equal to 1200 mm and 800 mm, respectively. Nine tests have been performed at medium and high density and ratios ranging from 33 to 2. The first test of each series was run in the centre of each specimen. A cone penetrometer drive which can be moved in flight was used. Test results are shown in figures 5 and 6. The following observations can be made:

- for the dense sand specimen a noticeable increase in  $q_c$  is seen when comparing the reference test at a ratio of 33 to the test done at a ratio of 7. The apparent increase of  $q_c$  values is about 10%.
- for the medium dense sand specimen a noticeable increase in  $q_c$  is seen when comparing the reference test at a ratio of 33 to the test with a ratio of 18. The apparent increase of  $q_c$  values is on the order of 10%.

Topic C1): DIA responsible.

Two test specimens at high density were prepared in a 530 mm cylinder. Three cone tests have been executed per specimen. A cone penetrometer which can be moved in flight was used. Test results and location of the tests are shown in figures 7 and 8. The following is observed:

- there is no apparent increase in  $q_c$  for subsequent tests executed at a ratio of 11, as compared to the reference test executed as first test at a ratio of 22.
- even after changing the order of execution of the tests the aforementioned statement remains valid (figure 8).

Topic D1): RUB responsible.

Two test specimens were prepared in a 1000 mm cylinder at high density. Two test were run per specimen using cones having diameters of 11.3 and 20 mm. Adopting 40 and 70g with one specimen and 70 and 125g

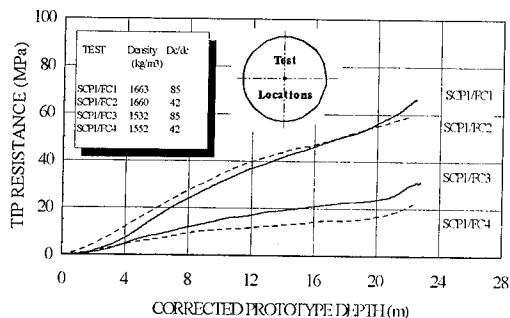


Fig.4 Investigation of the effect of the ratio (diam. of container)/(diam. of cone)

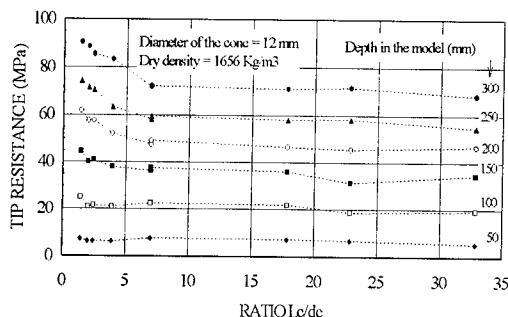


Fig.5 Effect of the ratio (distance from wall,  $L_c$ )/(diameter of cone,  $d_c$ )

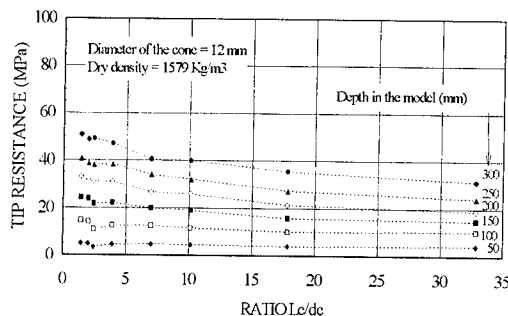


Fig.6 Effect of the ratio (distance from wall,  $L_c$ )/(diameter of cone,  $d_c$ )

with the other, two different prototype piles having diameters of 80 and 140 cm have been modelled. Test results are shown in figures 9 and 10. The following observations can be made:

- for the tests modeling the 80 cm diameter prototype pile there is no apparent increase in the normalized tip resistance,  $Q$ , when plotted versus normalized depth, with:

$$Q = (q_c - \sigma'_{v0}) / \sigma'_{v0}$$

- for the tests modeling the 140 cm diameter prototype pile the aforementioned statement remains valid.

- data from these modeling-of-models trials reveal that soil particle size does not affect the results for ratio  $d_c/d_{50}$  in the range of 90 to 50.

### 3.2 Tests on saturated reconstituted clay specimens

It was decided to concentrate the work on the following topics:

- A2) penetration pore pressure effects
- B2) penetration rate effects

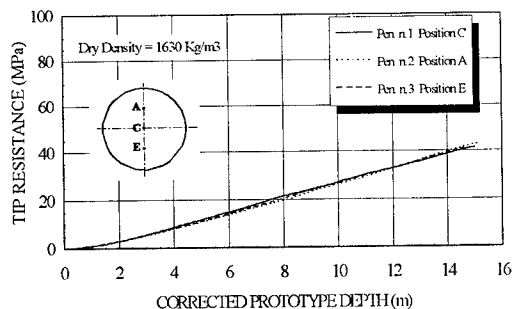


Fig.7 Investigation of the effect of the proximity of the wall in cylind. contain.

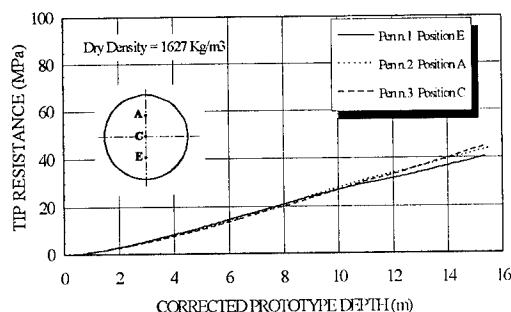


Fig.8 Investigation of the effect of the proximity of the wall in cylind. contain.

Work on topic A2) has been carried out using speswhite clay specimens. For topic B2) samples of silty clay obtained from a quarry of cohesive material located in Pontida, Italy, was used to prepare a reconstituted specimen. The latter clay has a liquid limit and a plasticity index equal to 24% and 11%, respectively. Grain size analyses indicates a prevalence of silt-size particles (53% by weight) with 30% clay-size particles and 17% sand.

Topic A2): ISMES responsible.

A mini-piezcone was used. Pore pressure is measured behind the tip at 11 mm from the apex. Two test specimens were prepared in a 400 mm cylinder. Model specimens were prepared following the procedure outlined in section 2.2. One cone test was performed per specimen. The tests were run in the centre of each specimen adopting a rate of penetration equal to 2.5 mm/sec.

Penetration pore pressure,  $u$ , versus depth are presented in figure 11 for both tests. Measured tip resistance values have been corrected to total stress because of unequal areas  $A_{ti}$  (net area) and  $A_{Tt}$  (total area) at the tip. A net area ratio  $A_{ti}/A_{Tt}$  equal to 0.785 has been introduced.

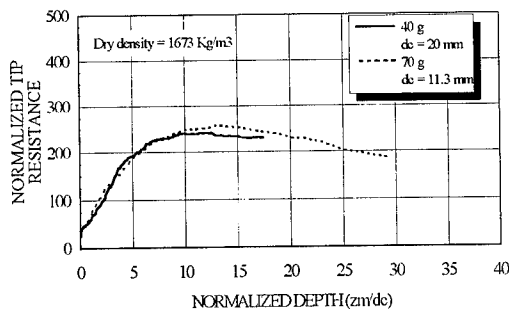


Fig.9 Modeling of models: investigation of grain size effects on Fontain. sand

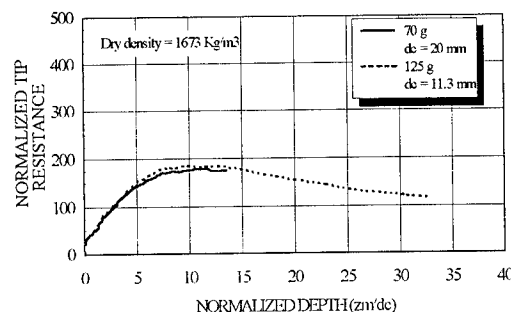


Fig.10 Modeling of models: investigation of grain size effects on Fontain. sand

$$q_c(\text{corr}) = q_c(\text{uncorr}) + \Delta u (1 - A_{ti}/A_{Tt})$$

Corrected and uncorrected tip resistance profiles recorded in both tests are compared in figure 12. The following can be observed:

- Applying the correction for the net area ratio using the measured pore pressure, tip resistance profile are about 15% greater than those measured without applying the correction.

Topic B2): ISMES responsible.

One test specimen was prepared in a 400 mm cylinder. The specimen was first subjected to a vertical effective stress of 30 kPa, allowing top and bottom drainage. Hydraulic gradient consolidation was then superimposed by applying a fluid pressure of 270 kPa to the top of the specimen. The final height was approximately 300 mm. Four piezocone profiles were performed adopting rates of penetration equal to 2 and 60 mm/sec. The sequence of operation is summarized as follows:

- 1 Allowance of 10 hours for full reconsolidation of the clay specimen under its own weight. In flight the soil specimen simulates a 30 m thick stratum of

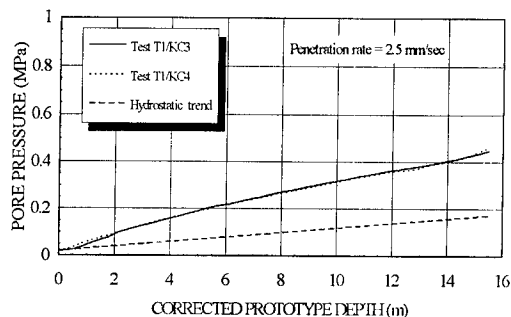


Fig.11 Pore pressure resulting from tests executed on speswhite clay specimens

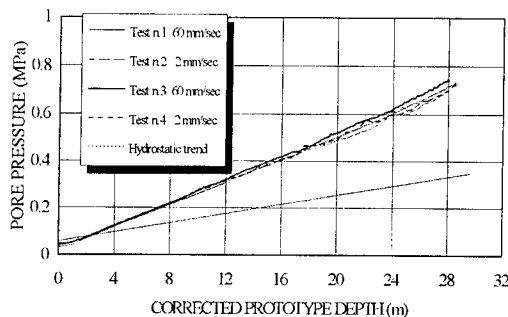


Fig.13 Effects of the rate of penetration using reconstituted Pontida clay specimens

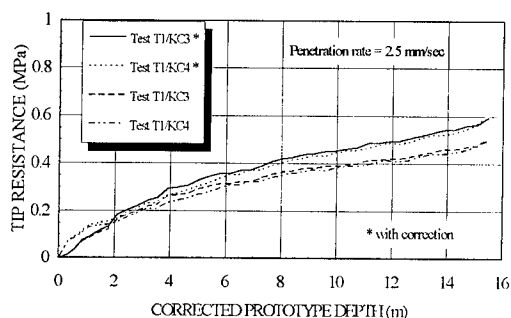


Fig.12 Effect of the correction for the net area ratio on speswhite clay specimens

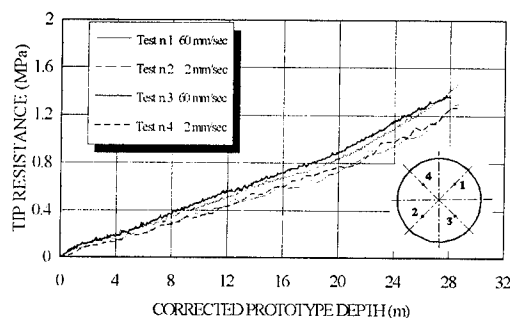


Fig.14 Effects of the rate of penetration using reconstituted Pontida clay specimens

normally consolidated clay.

2 Execution of a cone test and subsequent allowance of 2 hours for dissipation of penetration pore pressure with the cone withdrawn to its initial position.

3 Relocation of the piezocone, still in flight, using a rotation frame.

4 Repetition of steps 2 and 3 according to the scheme shown in figure 14 from test 1 to 4.

Records from the four tests are provided in figures 13 and 14, showing, respectively, pore pressure and tip resistance versus depth. The following can be observed:

- increasing the rate of penetration from 2 to 60 mm/sec, both the tip resistance and the pore pressure increase
- the apparent increase of  $q_c$  is on the order of 15%.

#### 4. CONCLUSIONS

Comparison have been made between cone penetration profiles obtained by different laboratories on sand and clay. Direct comparisons showed an inter-laboratory

variability of the tests results for both medium dense and dense specimens which was on the order of 20% of the measured cone resistance. This difference was considered within acceptable limits.

For clay specimens the inter-laboratory difference, on the order of 30% of the measured cone resistance, was not completely satisfactory. Factors linked to the history of the effective stresses experienced by models, like the stress applied during the last step of preconsolidation at 1g and the delay between final unloading and flight, may have affected tests results.

Taking advantage of the peculiarities of the different centrifuges, questions related to the influence of different experimental conditions have been subsequently investigated. Preliminary tests results from each laboratory have been presented.

#### REFERENCES

EEC Science Contract: n. SC1 - CT91 - 0626, "Improvement of model testing in the geotechnical field".

## Performance of a sand hopper

M.A.Allard, A.G.I.Hjortnæs-Pedersen & J.G.Out  
*Delft Geotechnics, Netherlands*

**ABSTRACT:** To simulate correctly in the centrifuge a prototype situation relating to the building of dikes and embankments, it is of great importance to perform the whole construction process in flight. Only in that way, both the initial stress and applied load histories of the foundation layer will reflect reality, allowing for the study of deformations and failures. The sand hopper is an equipment developed to answer this requirement.

Delft Geotechnics' sand hopper covers a great range of special features. The hopper allows for the building of a very large variety of embankment profiles and embankment combinations, with accuracy in the making of the various shapes. With the 1 m<sup>2</sup> size of the hopper in the 2 m<sup>2</sup> centrifuge container, large embankment profiles can be built. A predefined construction scheme can be followed accurately thanks to controllable time delays between stages. At any location of the embankment or next to it, cone penetration tests can be performed, before, during or after completion of the construction. The settlement of the foundation layer can be measured at various positions. The embankments can be built with coloured layers to locate failure circles.

### 1 INTRODUCTION

During the construction of embankments on soft soils, the stress history of the subsoil is determinant for the behaviour and stability of the completed structure. It is essential to be able to simulate in the model test the same stress history as in the prototype. Therefore it is needed, for centrifuge tests, to perform all the embankment construction steps in flight. The first hopper was developed at Cambridge, it allowed in flight construction of one type of embankment with successive "lifts", Beasley (1976). Since then, other centrifuge facilities have developed on-board sand hoppers with various characteristics.

In 1991 a sand hopper was designed and built at Delft Geotechnics for the 300 g centrifuge, Nelissen (1991). Taking advantage of the large size of the centrifuge, and answering requirements for quality, the hopper has extended possibilities, flexibility and accuracy in the making of embankments, compared to existing hoppers.

A description of the hopper is given, and it is explained how to take advantage of the possibilities of the hopper to achieve the construction of complex embankments with high accuracy. Then some examples of applications performed in the Delft Geotechnics geocentrifuge are given.

### 2 DESCRIPTION OF THE HOPPER

The hopper body, is made of 1118 thin wall tubes glued at the top and bottom to horizontal perforated plates to provide strength and light weight.

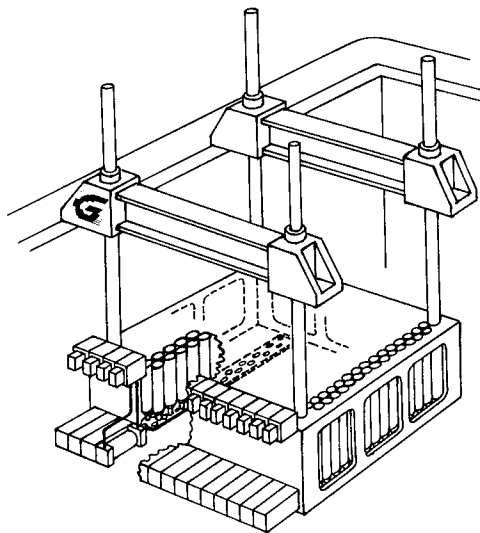


Fig.1 The fully assembled sand hopper mounted in the centrifuge container.

Each tube, or cell, is individually filled with sand to provide reservoir capacity, to build in flight embankments up to 150 mm height, and contribute to the definition of the profile (making slopes). The hopper has 36 rows of 31 or 32 cells and covers an area of about 1 m<sup>2</sup>. A total of 18 strips are mounted



directly beneath the cells to block their opening. Each strip has the same hole pattern as the one formed by two consecutive rows of cells. At one end of the strip sits a double acting hydraulic plunger. By activating the plunger, to which a strip is attached, the cells can be opened (allowing then sand raining) or closed (stopping the sand flow).

Each double acting plunger is connected to an electro-hydraulic valve for the control of oil flow. With these 18 valves each strip can be individually operated. The valves are activated in flight by computer control. It is therefore possible to have sand raining from selected rows (to create different shapes), for a limited time (to make layers), with variable time delay between valves actions (allowing staged construction). This gives then a lot of flexibility for the construction process and the resulting geometry of sand embankments.

The hopper support frame consists of two transversal beams attached across the 2 m \* 1 m centrifuge container, from which four vertical columns hang inside the container. The sand hopper body can slide up and down along these columns over 350 mm. For a test the hopper body is fixed on the columns, its position is adjusted according to the test set up requirements.

In order to slow down the raining of the sand from the cells during flight, special nozzles are fitted in the bottom of the cells to reduce the opening from 12 mm to 2 mm. This allows therefore better control in the building of layers and slopes throughout the construction of embankments.

The fully assembled hopper is shown mounted in the centrifuge container in Figure 1, and in the preparation hall with its filling system in Figure 2.

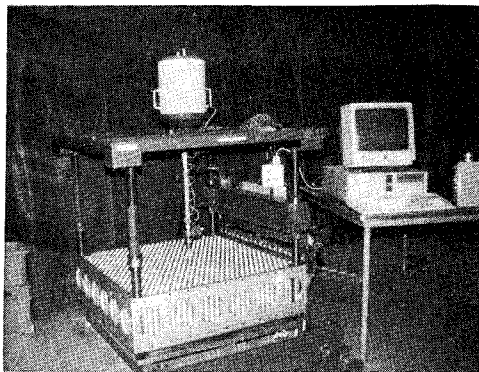


Fig. 2 The sand hopper and its filling system.

Holes are made through the hopper body and the strips, to allow the mounting of instrumentation at various locations above of the sand hopper, and providing direct connection to the model soil foundation. In this way, displacement transducers, DCDTs for example, can be used to follow the settlement of the foundation layer, Figures 4 & 7.

Devices such as a cone penetration equipment can be installed above the hopper, Figures 4 & 7, the

cone point goes then through the opening of a cell without nozzle. It is therefore possible to perform cone penetration tests any time before, during or after embankments construction.

### 3 HOPPER OPERATION

A great number of applications are made possible with this hopper, thanks to the very large flexibility given by the fact that rows of cells can be dealt with individually both for the filling and for the way the sand will be rained.

For making any profile, a scenario has to be defined. The scenario is a series of steps to be performed in order to recreate all the construction phases of the initial loading profile requirements. The scenario includes a number of items such as:

- The valves opening control table, which is the data for computer control during flight. The table defines for the test, step by step of the embankments construction, the valves that need to be open to create the required geometrical profile, the opening time needed for making the layers, and the waiting delay before the next construction step (e.g. for dissipation of excess pore pressure for stability).
- The filling of the hopper cell by cell, with variable sand quantity per row calculated according to the valve opening times and the making of the slopes, to get the required geometrical profile.
- The actual loading history which gives, for each step of the construction, the resulting loading profile on the foundation layer, calculated from the geometrical shape and the embankment density. The actual loading history is used as input for the numerical calculation model.

It is important to recall that a few parameters play a major role in the control of the hopper, and the definition of the scenario.

The RPM level of the test, or angular velocity of the centrifuge, is determinant in the calculation of the Coriolis effect which can be compensated for with this hopper. A sand particle released from the hopper and settling to form a sand embankment, in a container subjected to centrifugal motion, will describe a particular trajectory with respect to a reference frame fixed to the container, see Figure 3. Assuming no initial velocity of the particle, and no drag force (Delft Geotechnics centrifuge operates under 25 mbar), the equations of motion of the particle in the container reference frame reduce to:

$$\frac{d^2x}{dt^2} - \omega^2x = \omega^2R + 2\omega \frac{dy}{dt} \quad (1)$$

$$\frac{d^2y}{dt^2} - \omega^2y = -2\omega \frac{dx}{dt} \quad (2)$$

with  $\omega$  = centrifuge angular velocity, and  $R$  = radius at which the sand particle is released, Tan (1985).

Using Laplace transform method, the solutions are:

$$x = R(\cos \omega t + \omega t \sin \omega t - 1) \quad (3)$$

$$y = R(\omega t \cos \omega t - \sin \omega t) \quad (4)$$

Equations (3) and (4) fully define the trajectory due to Coriolis effect of the sand grain with respect to the container. The  $x$  and  $y$  coordinates are later called the falling height and the deviation. The shape of the sand trajectory during a test has been compared with the solution, given by equations (3) and (4). Very good agreement was obtained.

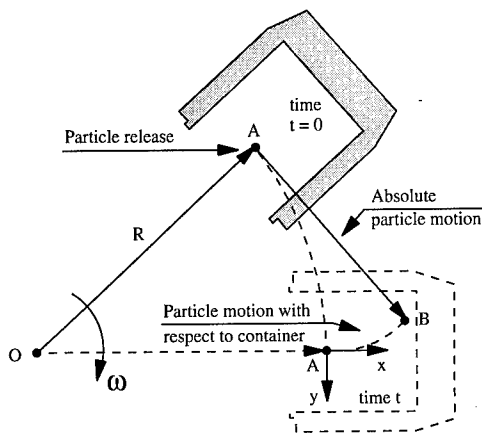


Fig. 3 Particle motion, in the container reference frame, due to the centrifugal gravity field.

Another important item is the vertical position of the sand hopper with respect to the embankment. To determine the position of the sand hopper, the maximum falling height is used. This falling height is defined as the vertical distance between the point of release of the sand grain in the sand hopper and the embankment foundation layer.

For any point in the embankment we know the coriolis deviation undergone by the sand grains using equations (3) and (4). Then the filling of the hopper will take into consideration the sand "destination". For example, special correction for the Coriolis effect is made when an embankment slope is obtained by adequate filling of the various rows of cells entering its composition. The slopes built in the hopper itself, or correction factors used, are different for an embankment slope going up in the direction of the Coriolis force, and one going down in the direction of the Coriolis force.

The falling height, at a given RPM level, will influence the embankment density. The density of the embankment, to be used for calculations, is determined by preliminary tests. If a given density is preferred, it is possible to adjust the falling height with the hopper support frame, to achieve it.

The characteristics of the sand are also important. In the applications presented, Eastern Scheldt sand is

used, with:

$$d_{50} = 0.15 \text{ mm}, d_{90} / d_{10} = 2.0, n_{\min} = 0.35, n_{\max} = 0.47, \phi_{n=0.41} = 37.5^\circ.$$

The embankment density or density profile, the rolling slope, the correction factor for shallower slopes will depend on the sand characteristics.

## 4 PRESENTATION OF SOME APPLICATIONS

### 4.1 Embankment and its widening

The hopper has been used to study the behaviour of soft subsoil during construction of an embankment and its widening, extended description of the test programme and results are given in Hjortnæs-Pedersen (1994).

A first embankment was built in flight in seven stages to recreate the existing road. Pore pressure dissipation in the soft subsoil was allowed after each layer to ensure stability. Then a second embankment, Figure 4 & 5, was built in nine stages, directly against the first one to provide widening of the existing embankment.

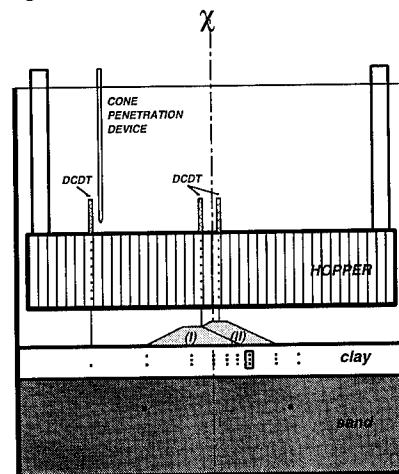


Fig. 4 Section of the full set up, in the centrifuge container, of the embankment widening test. Profile of embankments and position of pore pressure transducers in foundation layer.

In this case, all the slopes are 1:2.0. The left slope of embankment (I) and the right slope of embankment (II) were obtained by adjusting the filling of the cells, taking into account the necessary corrections for Coriolis effect, as mentioned above. The common slope of embankments (I) and (II) was in turn made by special actions of the valves. The slope was discretized by the number of rows of cells entering in its composition. By playing with the opening times of the valves, the valves to be opened, the sand natural rolling slope, the right slope of embankment (I) was achieved, and a good geometrical fit of it was obtained during construction

of embankment (II). Also the proper surface deck connection as shown in Figure 4 was achieved.

The complete scenario for a test was elaborated. The filling of the hopper was done accordingly, the valves opening control table was established and fed to the programme for computer control during flight, and the loading profile history was in turn used in numerical calculations.

Many pore pressure transducers were installed at various locations into the foundation clay layer, Figure 4, to monitor build up and dissipation of excess pore pressures during the embankments' construction. The readouts of some transducers versus time are given in Figure 5. The selected transducers placed almost under the right toe of embankment (I) are shown with a frame around them in Figure 4 & 5. This time history of pore pressures shows the response to the staged construction of the embankments. Each sudden increase in pore pressure corresponds to the placement of an embankment layer.

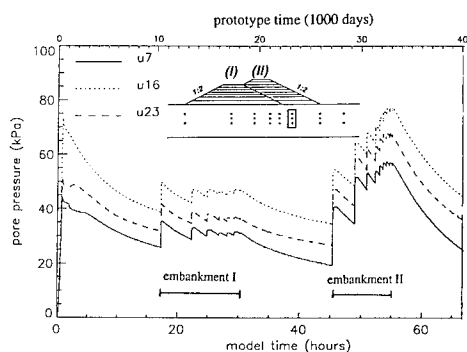


Fig. 5 Time history of pore pressures during the full embankment widening test. Evidence of staged construction of the two embankments.

Two tests were carried out at 120 g. The tests loading histories were calculated using two different construction factors of safety. The computed schemes gave various levels of excess pore pressure dissipation between the construction of each embankment layer, resulting in different time duration for construction stages. During the tests, it is taken advantage of the possibility to interact manually with the control of the hopper. The measured pore pressures are used to set the delays between the construction stages. In flight, the programme is paused after each stage, and resumed at the appropriate time to build the next one, when pore pressure dissipation reaches the prediction value.

In addition, DCDTs with their cores going in the special holes through the hopper gave settlement measurements of the foundation layer during the whole test. Also a cone penetration test was performed just before construction of the embankments; see the complete set up for such a test in Figure 4.

#### 4.2 Embankment and its widening by the "gap method"

In the case of very soft subsoil, another procedure to widen existing embankment on very soft soils is to follow what is called the "gap method" developed by Kuiter, Kruizinga (1989).

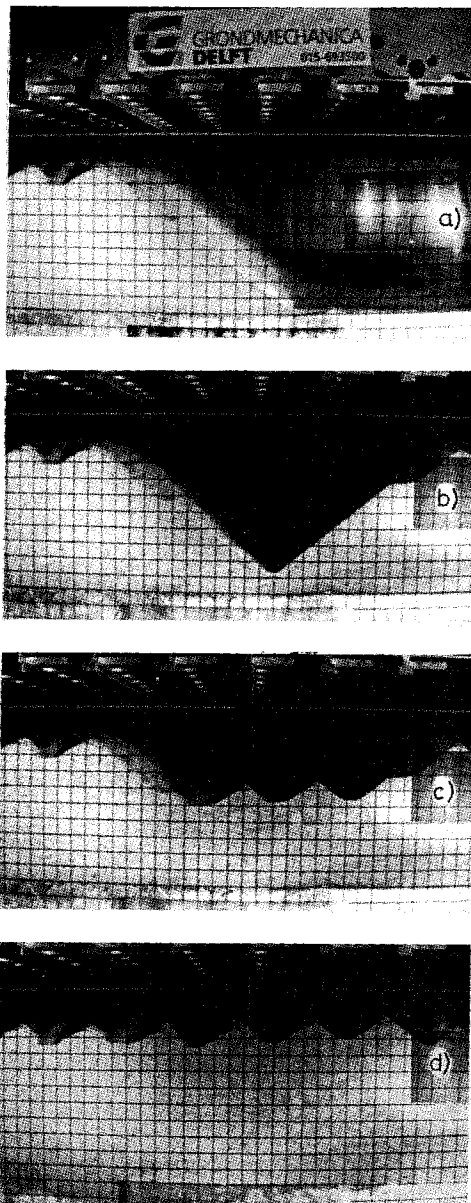


Fig. 6 Images of the widening of an embankment by the gap filling method.

In this case a second embankment is built next to the existing one. The toes of both embankments are touching or slightly overlapping to ensure stability.

During construction of the second embankment, the large settlements occur away from the region of the asphalt deck of the existing embankment. By minimizing the differential settlements in the existing embankment during the construction of the second one, damages such as large crack openings of the asphalt deck are prevented. Maintenance of the existing asphalt deck is therefore efficiently reduced. When the subsoil has consolidated sufficiently under the second embankment, the gap between the two is filled, giving then a resulting large deck. Because they are no more stability problems, the gap filling occurs very quickly. Important maintenance of the asphalt deck will then be needed only over a short period of time, in that last stage of the construction process of the widening.

In this test, performed at 100 g, it was chosen to create by adequate filling 1 : 2.5 slopes, on the outside, and by valve action 1 : 1.5 slopes, in the inside, for both embankments. The aim was to gain experience in building various slopes, and to define the steepest slope for this sand. In turn, it provided evidence for the possibility of creating slopes with very high accuracy. This is particularly essential when studying stability of embankments and dealing with small factors of safety, e.g. 1.05 or 1.1.

The main focus of the test is to show the ability with this sand hopper to perform the full construction process of the "gap method" in flight, in one continuous centrifuge run. That is, to create a first embankment, then a second one next to it, and finally being able to fill the gap in between them.

It was chosen to build the gap in six layers of 1.5 m (prototype scale). A sequence of images taken in flight, Figure 6, shows the evolution of the construction. In Fig. 6.a, the right toe of the completed first embankment is seen. In Fig. 6.b, the second embankment is completed, this give a view of the full gap. Then Fig. 6.c and 6.d give an intermediate stage (third layer) and the final stage of the gap filling.

#### 4.3 Two models in one test set up

The last application to be presented here, shows the possibility with Delft Geotechnics large centrifuge and sand hopper to perform two independent model tests in one centrifuge run. Two totally different embankments can be built to study two problems, still ensuring that boundary conditions for the two are fulfilled, Figure 7. The main advantages of this possibility being, first, to obtain two tests with fully similar conditions, allowing to eliminate the problem of parameters variations from one model foundation layer to the other during interpretation and simulation of tests results, and second, to reduce by two the number of centrifuge spinning hours for consolidation and excess pore pressure dissipation, which is considerable when dealing with very soft natural subsoil. This possibility has been used in a test series for the study of slope failures under various factors of safety.

To use one model foundation layer and perform two tests in one centrifuge run, a separation wall is made in the model container. In order to optimize embankments dimensions, a special shape is given to the separation wall over the height corresponding to the sand embankments, see Figures 7 & 8. This shape corresponds to the coriolis trajectory of a sand grain. The position of the wall is defined by the hopper cell arrangement, it allows for a good building up of the embankments.

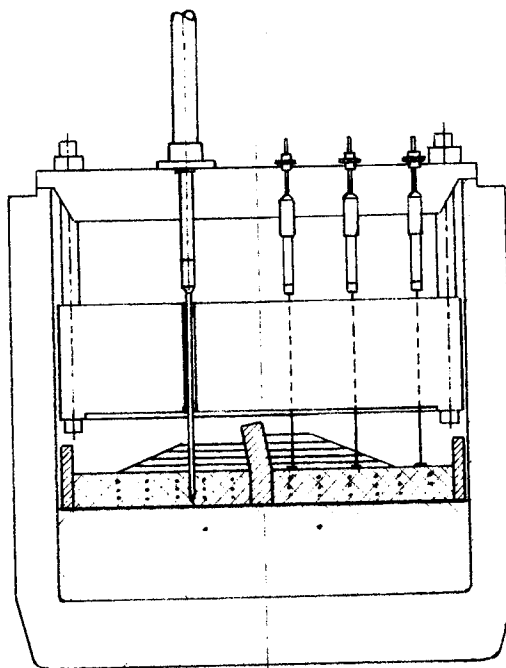


Fig. 7 Section of the full set up for the construction of two embankments on one foundation layer.

The tests of this series, performed at 100 g, aimed at obtaining failures of the embankments in flight. To visualize the position of the failure circle in the embankment itself, some coloured layers are made in each sand embankment. The solution to make such coloured layers, chosen from preliminary tests, is to alternate between layers of Eastern Scheldt sand, and thin layers of black coloured Eastern Scheldt sand, see Figure 8. In order to preserve the properties of the sand when coloured layers are made, the sand is mixed with a very small amount of a special black chalk powder. The correct amount of sand for each layer is successively manually filled into the few cells of the front line of the hopper which provide the sand coming in contact with the transparent wall used for image processing. Then the coloured layers are made visible, against the wall, during embankment construction.

For this test series, where the failure of embankments is studied with various safety factors, it is chosen to place the first several layers (1 m to 1.5 m height each, prototype scale), and then to

increase the embankment height to failure by placing a succession of thin layers (0.15 m to 0.20 m). The later are obtained using a small valve opening time (0.5 sec. for a 100 g test) giving accurate and reproducible layers. Also, it is possible to interact manually during flight with the hopper control, in order to wait after each thin layer to see if failure, which is usually delayed, will occur, and to stop the construction process once failure has occurred. The shape of the failed embankment is then preserved by preventing extra sand to be rained on top of it.

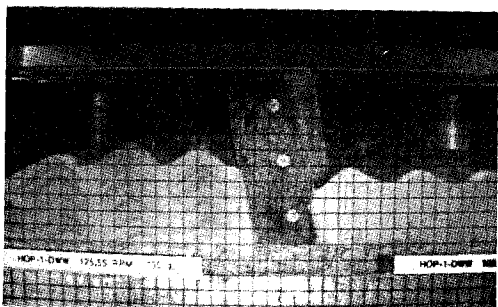


Fig. 8 Image of the two embankments with the separation wall and the coloured sand layers.

## 5 HOPPER FILLING SYSTEM

In addition to the hopper, a device to enable reliable and efficient filling of the hopper has been developed.

It consists of a 30 litres sand reservoir fixed on a double ball bearing beam arrangement set above the sand hopper, and allowing easy X-Y motion across the whole hopper area, see Figures 2 & 8.

The reservoir empties into a narrow tube with a special granular flow pinch valve to which a 7 mm nozzle is attached and set just above the top of the hopper cells. The on/off pinch valve is activated using computer control.

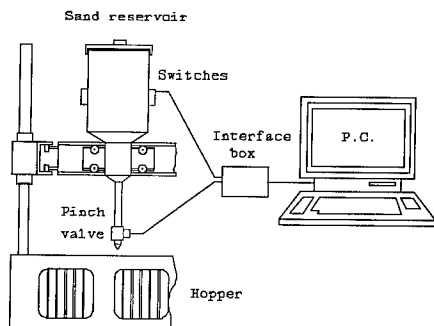


Fig. 9 Computer controlled hopper filling system.

With a specially built interface box and computer programme, it is possible to control the filling of the hopper. A hopper filling table, giving for each row

the weight of sand to be placed in a cell, is used as input for the programme. The sand weight is converted into valve opening time. A calibration of the pinch valve sand outflow is made regularly.

The reservoir is moved so that the nozzle is just above the centre of a cell. The cell is recognized by its row number and its line number in the row. Then the pinch valve is activated for the time stored in the computer programme for that row. Sand is rained into the cell. The programme updates the hopper filling status, and the reservoir is moved to the next cell. The programme can be stopped and resumed at a later stage. A LED-photo diode system set into the reservoir indicates when sand needs to be added. On the top of the reservoir sits a sieve so that all foreign material is taken away, to avoid blockage of the sand hopper 2 mm nozzles.

## 6 CONCLUSION

With the Delft Geotechnics sand hopper it is possible to simulate perfectly the construction of many embankment profiles and embankment combinations, with a large range of accurately defined slopes, and with precise reproduction of the construction process. This is due to the very large number of degrees of freedom given by the individual filling of the cells, the action of the strips in any kind of sequences, and the choice of valve opening times.

## ACKNOWLEDGEMENTS

The authors would like to thank the centrifuge operators T. van Dijk, F. Kop and W. Lönning and all the co-workers of Delft Geotechnics, who contributed to bring the sand hopper and its filling system to operation, and to perform the tests described herein.

## REFERENCES

- Beasley, D.H., and R.G. James (1976), "Use of a hopper to simulate embankment construction in a centrifugal model," *Geotechnique*, Vol. XXVI, March 1976, pp.220-226.
- Hjortnaes-Pedersen, A.G.I., and H. Broers (1994), "The behaviour of soft subsoil during construction of an embankment and its widening," *Proc. Int. Conf. Centrifuge 94*, Singapore Aug./Sept. 1994.
- Kruizinga, J. and J.W. Sip (1989), "Aardebaan bij Van Brienenoord over 10 kilometer verbreed," *Land and Water*, Nr.5, pp.26-28.
- Nelissen, H.A.M. (1991), "The Delft geotechnical centrifuge," in *Centrifuge 1991*, Ko and McLean Editors, Balkema Rotterdam Publishers, pp. 35-42.
- Tan, T. S. (1985), "Two phase soil Study. A- Finite strain consolidation. B- Centrifuge scaling consideration," *Soil Mechanics Laboratory Report No. 85-01*, California Institute of Technology.

## Development of a miniature piezocone

Edmundo Rogério Esquivel & Hon-Yim Ko  
*University of Colorado, Boulder, Colo., USA*

**ABSTRACT:** This paper presents a new miniature piezocone, developed for the centrifuge testing center at University of Colorado at Boulder, to perform penetration testing on centrifuge soil models. The design of the piezocone is described, as well as the complementary hardware necessary for performing the tests. Emphasis is given on the testing procedures, and on the techniques used for data collection and interpretation.

### 1 INTRODUCTION

In the last decade, in-situ testing has gained considerable popularity among geotechnical engineers as a means of ascertaining soil profiles and of measuring soil properties. Much attention has been devoted to the piezocone (QCPT), which represents a new generation of in-situ testing devices. Their applications fall into two categories: soil profiling and assessment of soil properties.

In order to obtain the various engineering properties of soil tested by cone penetration, investigators have relied almost exclusively on empirical relations between the cone resistance  $q_c$  and the various stiffness and strength parameters. This is necessitated by the fact that a precise theoretical solution of the complex phenomena occurring around the cone tip during the penetration process has not been developed. The usefulness of empirical relations in interpreting cone penetration data has to be verified by their ability to correlate with field measurements.

However, field calibration tests have many limitations and disadvantages due to soil inhomogeneities and uncertainties regarding the properties, the in-situ stresses and the stress history of the deposit. Furthermore, it is practically impossible to study the influence of a

particular parameter by varying it independently in the field. The lack of quality field data has frustrated further development of a sound theoretical basis for these empirical methods. To overcome these limitations, calibration tests should be done in the laboratory, where reproducible soil specimens can be prepared and tested under known and controlled conditions.

Different authors have performed laboratory calibration chamber tests for calibrating cone penetrometers. However, almost all of these tests are related to cohesionless soil specimens. Only a few are related to compacted or preconsolidated cohesive soils (Kurup, 1993). This is mainly due to the difficult and time-consuming process necessary for the preparation of large cohesive soil samples used in calibration chambers.

### 2 CENTRIFUGE MODELS

In recent years, centrifuge testing has become a useful tool for testing models under conditions that approximate those in the field in terms of the in-situ stress profile (Ko, 1988). In centrifuge models, using different preparation procedures, it is possible to build different soil property profiles

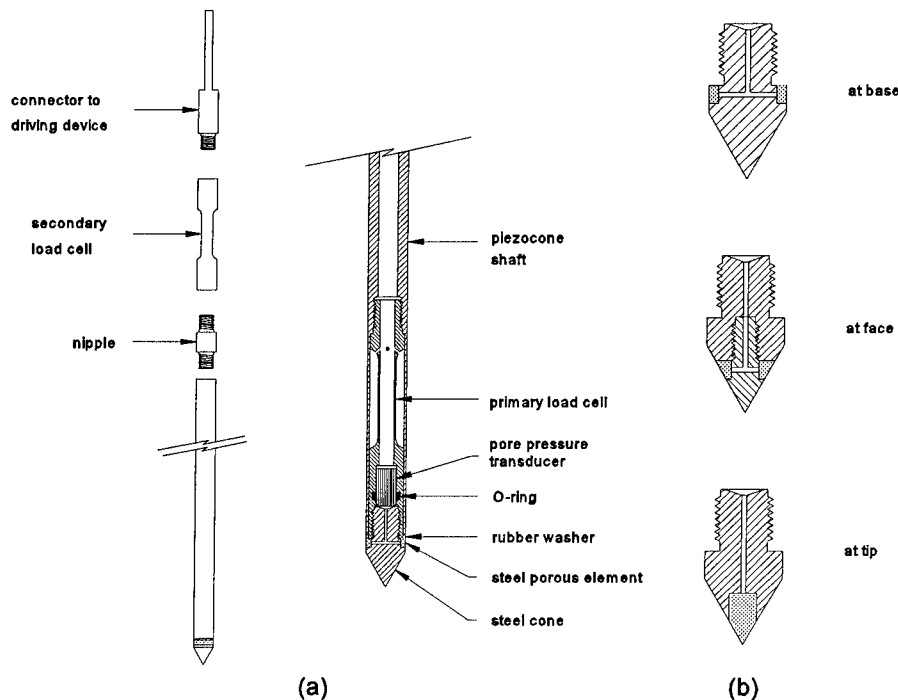


Figure 1 - (a) Piezocone; (b) cones with different filter locations.

to simulate normally consolidated as well overconsolidated conditions. This technique is very promising in piezocone calibration tests.

In contrast to calibration chamber tests, in centrifuge models it is possible to incorporate some aspects, such as the effect of overburden pressure on the cone penetration resistance and the vertical stress gradient. Also, by using centrifuge modeling scaling relations, miniature piezocone tests can simulate full scale tests, or in other words, they can represent standard piezocone penetration tests in several meters high soil deposits.

### 3 MINIATURE PIEZOCONES

A miniature piezocone CUB1, suitable for centrifuge tests, has been developed recently at University of Colorado at Boulder (Fig. 1). This piezocone is able to measure simultaneously point resistance and pore pressure during penetration.

Also, the total load including side friction is measured during penetration. The piezocone CUB1 (Fig. 1) is 305mm long and 12.7mm in diameter. The cone has a projected area of 127mm<sup>2</sup> and apex angle of 60°. There are two load cells mounted at its extremities. The primary load cell, located inside the shaft, measures the point resistance. The secondary load cell, located at base of the shaft, measures the total load applied to the piezocone. The secondary load cell makes it possible to evaluate skin friction  $f_s$  along the piezocone shaft.

Because one of the major applications of piezocone tests is assessing properties of soft and very soft clays, a main concern is the sensitivity of the load cells. Considering this fact, the CUB1 primary load cell was designed for measuring the relatively low penetration resistance of soft clays. It has a resolution of 0.0005 kN for the range 0-0.5 kN. The high sensitivity was achieved by using two semiconductor strain gauges in each arm of the fully active bridge.

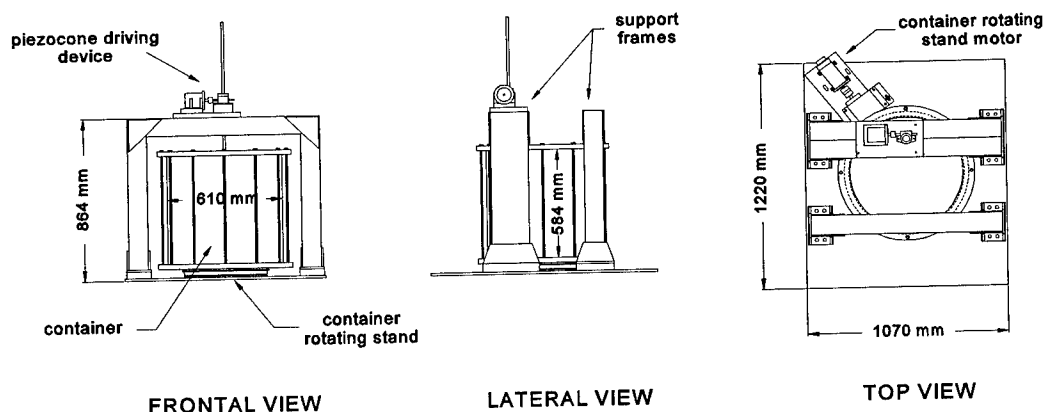


Figure 2 - Penetration testing apparatus

The pressure transducer used in the piezocone is a Druck pressure transducer, model PDCR81, with a silicon diaphragm which ensures very fast response time. It is placed inside the primary load cell, as shown in Fig. 1a. There are three different cone options with different filter locations. The cones can be easily replaced because they are simply threaded to the primary load cell (Fig. 1b). Whereas the piezocone shaft and load cells are made of aluminum, the cones are made of stainless steel, and the filters are made of sintered stainless steel. The filter pore size that has shown the best results in penetration tests in soft clays is  $5\mu\text{m}$ .

The saturation of the piezocone tip (filter plus pressure transducer) is done under vacuum, using glycerin as saturating fluid.

#### 4 THE PENETRATION TESTING APPARATUS

The penetration testing apparatus has dual purposes. In a first phase during the tests, the setup serves as a slurry consolidometer. In a second phase, it supports the equipment necessary for penetration tests (Figure 2).

The basic framework of the penetration testing apparatus consists of a steel base, two welded steel support frames and a rotating stand (turntable) which supports the model container. The steel frames are used for supporting the

pneumatic loading system during the consolidation process, for helping to place the whole apparatus on the centrifuge platform, and for supporting the piezocone driving device.

The cylindrical model container consists of a large diameter tube, a base plate, a top flange, and a top cover. All these parts are made of aluminum, except the tube which is made of PVC. The top cover and top flange are connected to the base through 12 threaded bars. Both the base and the top flange are provided with grooves for fitting the tube properly. To prevent water leakage at the base plate groove, a second groove with a rubber O-ring is provided. A gasket seal is inserted at the contact between the tube and the top flange. The threaded bars are tensioned by means of nuts, causing compression at contacts between the tube and the aluminum parts.

At the container base plate, a bottom drainage system allows for uniform downward flow of water through the soil during the seepage induced consolidation phase of sample preparation. This drainage system consists of a sheet of porous plastic filter overlaying a sheet of corrugated aluminum mesh. To prevent clogging by fine clay particles, the plastic filter is covered with a sheet of filter paper. The water is drained to outside the container through radial conduits drilled in the bottom plate. These conduits are connected together with plastic tubes and connected to a common line. During the seepage induced consolidation phase, the water coming from the



drainage system is collected and its flow rate is measured for comparing with theoretically predicted values. During centrifuge runs, the common line is connected to the layer of free water existing above the soil sample to ensure that the pressure at bottom of the sample is hydrostatic.

On the wall of the container, various holes are drilled for installation of PDCR81 Druck pressure transducers. These pressure transducers are used for monitoring the excess pore water pressure generated during the consolidation process and during the penetration tests. Also, a Data Instruments (Model AB) pressure transducer is installed at bottom of the container to monitor the static water pressure.

The piezocone driving device consists of a Duff Norton linear mechanical actuator, model PKM-2500-16. The actuator is driven by an Electro-craft servo motor (model 644-36-012). The position and the motion of the piezocone are controlled from a computer located in the centrifuge control room.

The purpose of the container rotating stand is to allow different penetration tests at different sites in the same tub of soil, without stopping the centrifuge for changing the position. The rotating stand consists of a steel disk pivoted in the center and supported by ball bearings. For keeping the ball bearing in place, grooves are made in the upper disk and in the base plate. The rotating stand is driven by an Electro-craft servo motor, through a Boston gear reducer, a chain and sprockets.

## 5 VANE APPARATUS

It is known that the undrained shear strength  $s_u$  is not a unique property of a specific clay, and that when  $s_u$  is determined experimentally, different values for this characteristic can be found (Wroth, 1988). Because of this, the cone factor  $N_k$  in expression (1), in which  $q_c$  and  $\sigma_o$  represent the penetration resistance and the total mean stress respectively, is dependent on the type of the undrained test used to obtain  $s_u$ . Thus, great care must be exercised in using any correlation for interpreting cone penetration tests.

$$q_c = N_k \cdot s_u + \sigma_o \quad (1)$$

According to Campanella and Robertson (1988), the reference  $s_u$  should be taken as the field vane value (FVT) and should be clearly stated. This is one of the reasons, in this research, for calibrating the piezocone against vane tests which are performed concomitantly with penetration tests.

The 400g-ton centrifuge at University of Colorado is equipped with a vane shear test apparatus for testing in flight. The dimensions of the blades are 12.7mm long and 6.3mm wide, giving a total width of 12.7mm. A Slo-Syn Synchronous DC-stepper motor (model M062-LF-402), controlled by a pre-programmed indexer (model 3180PI/125), transmits the necessary torque to the vane blades. At a distance of about 40mm above the vane blades, a torque cell measures the applied torque to the vane blades. A system similar to the piezocone driving device is used to provide the linear motion for inserting the vane into the soil sample in flight.

## 6 DATA ACQUISITION SYSTEM AND MOTION CONTROL SYSTEM

The data acquisition system of the centrifuge facility at University of Colorado is based on Tektronix/CDS data acquisition hardware. The TEKDAF program controls all data acquisition and storage. All of the test data is stored into standard ASCII data files. TEKDAF also allows plotting in real time the collected data on the computer screen.

A modular motion control system remotely controls the operation of the piezocone driving device, the container rotating stand and the vane apparatus. The basic system is made up of four components: (1) the host computer, from which the commands to the drive system originate; (2) the indexer, which receives commands from the host computer and generates the pulse stream required to control the motor and drive systems; (3) the servo amplifier, which provides the necessary power amplification to maintain the operation of the motors; and (4) DC servo motors and optical encoders with two channels in

quadrature. The optical encoders connected to the motors, provide feedback signal for controlling position, speed, acceleration, direction and range of the movement.

A menu-driven program MOTOP is used for operating the motion control system. Through this software, the user selects the option to be executed and is prompted for inputs that define the direction, range and speed of motion.

The electric-mechanical piezocone driving device is of very simple construction and has shown very good performance and accuracy.

## 7 TESTING PROCEDURE

Clay specimens are prepared in such way as to obtain a certain specified undrained shear strength profile. The samples are prepared by consolidating a slurry made of Speswhite kaolin clay and water at an initial water content of 137%, which is approximately two and a half times the liquid limit of the material. From previous experience (Znidarcic, et al., 1991), this is the appropriate initial water content required to produce a uniform soil paste that can be placed in the container without entrapping a large quantity of air in the slurry.

The first stage of the consolidation process consists of applying a combination of seepage forces and surcharge load to the clay sample. The values for this combination of loads are determined by the desired undrained shear strength profile. The second stage consists of a self weight consolidation process at the increased gravity level in the centrifuge. This latter stage is controlled by monitoring the excess pore pressure developed during the centrifugation. When the pore pressure readings reach steady values, the sample is considered fully consolidated and ready for penetration testing.

Before each penetration test, the container is properly positioned by rotating the turntable. Penetration tests usually are performed 45° to 60° apart, corresponding to a distance of 10 to 15 piezocone diameters between penetration sites. The range and the rate of penetration are selected through the program MOTOP. Although the equipment allows a variable rate of penetration for studying its effect on penetration test results,

usually penetration tests are performed at standard penetration rate of 20 mm/sec (Campanella and Robertson, 1988).

Besides cone penetration tests, vane shear tests are also performed in the same specimen without stopping the centrifuge.

When the series of tests is completed and the centrifuge is stopped, a cylindrical sample is extracted from the soil specimen for determination of the void ratio profile.

## 8 TEST RESULTS

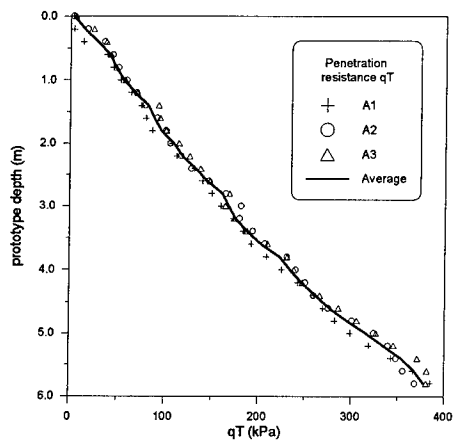
Some examples of results obtained from penetration tests performed in the centrifuge environment are shown in Figures 3, 4 and 5. Figures 3 and 4 depict the variation of the corrected penetration resistance  $q_T$  and the pressure  $u_T$  acting behind the cone, with depth, respectively. Figure 5 shows the variation of  $N_{KT}$  and OCR with depth. The values of  $N_{KT}$  were obtained using expression (2), where  $\sigma_v$  is the total vertical stress and  $s_u$  is the undrained shear strength obtained from vane tests, and from the void ratio profile using an empirical correlation (3) between undrained shear strength and void ratio (Znidarcic, et al., 1991).

$$s_u = \frac{q_T - \sigma_v}{N_{KT}} \quad (2)$$

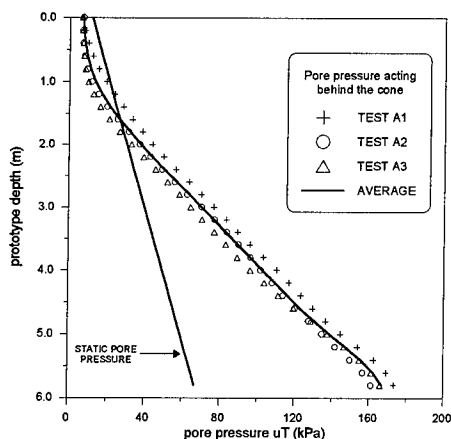
$$e = 1.945 - 0.435 \log s_u \quad (3)$$

For this particular case, the sample was prepared by applying to the slurry at 1 g, a combination of a surcharge load of 37 kPa and a seepage gradient of 185 kPa. The sample was reconsolidated in the centrifuge at 20 g's, resulting in an overconsolidation profile as shown in Figure 5.

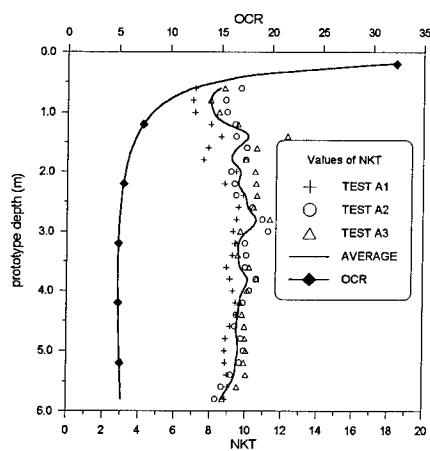
Preliminary tests have show that the soil specimens are reproducible and confirm the good repeatability of the penetration tests. Performing penetration testing on centrifuge soil models is producing two major benefits. First, an experimental data base is being developed, in which the full scale field stress conditions are



**Figure 3** - Corrected penetration resistance  $q_T$  versus prototype depth.



**Figure 4** - Pore pressure  $u_T$  acting behind the cone versus prototype depth.



**Figure 5** - Cone factor  $N_{KT}$  and overconsolidation ratio  $OCR$  versus prototype depth.

properly simulated, for the validation of existing cone penetration interpretation methods and for the development of new methods. Second, the technique itself can be used for ascertaining the properties of the soil model constructed for centrifuge testing, so that the results of the centrifuge test can be interpreted with a full knowledge of the in-situ conditions for comparison with numerical calculations.

## 9 ACKNOWLEDGEMENT

The development of this research has been made possible by a grant from National Science Foundation (NSF).

## 10 REFERENCES

- Campanella, R.G., and Robertson, P.K. (1988). Current status of the piezocone test. Proc. First International Symposium on Penetration Testing, ISOPT-1, Orlando, Florida.
- Ko, H.Y. (1988), Summary of the state-of-the-art in centrifuge model testing. Centrifuges in Soil Mechanics, Craig, James and Schofield (eds), Balkema, Rotterdam, The Netherlands.
- Kurup, P.U. (1993), Calibration chamber studies of miniature piezocone penetration tests in cohesive soil specimens. Ph.D. Dissertation, Louisiana State University, Baton Rouge, Louisiana.
- Wroth (1988), Penetration testing - A more rigorous approach to interpretation. Proc. First International Symposium on Penetration Testing, ISOPT-1, Orlando, Florida.
- Znidarcic, D., et al. (1991), Drag Anchor Tests in Clay. Report submitted to Exxon Production Research Company, under contract PR-11714, University of Colorado, Boulder, Colorado.

## Earth pressure distribution on sheet pile walls

A. Schürmann & H. L. Jessberger

*Institute for Soil Mechanics and Foundation Engineering, Ruhr-University Bochum, Germany*

**ABSTRACT:** A second centrifuge, Acutronic model 661, has recently been established at the Ruhr-University Bochum. In this paper the installation of the facility and the development of the equipment like data acquisition system and strong boxes are described. One of the first test series is a study of sheet pile walls in dry sand. One aim of these investigations is to get the possibility of measuring lateral earth pressure on flexible structures in incohesive soil. The distribution of the earth pressure is calculated in double derivation of the measured bending moment. To increase the number of data points and to select a fitting curve through these points, a local spline function is used. The paper describes test design, instrumentation of the model and methods of transformation. A comparison between the calculated distribution and curves proposed in standard design methods is presented.

### 1 INTRODUCTION

The new centrifuge ZII has recently been established at the Ruhr-University Bochum. The centrifuge was set up in February 92, the inauguration took place in June 92. To mark this occasion, a seminar was held about the practical use of the centrifuge model technique in foundation, tunneling, deep shaft construction and environmental technology. (Geotechnik Sonderausgabe 1992)

In addition to the centrifuge ZI with a capacity of 2 tonnes at 250 g, which is described by Jessberger and Güttler (1988), an Acutronic model 661 with a capacity of 40 g-tonnes is installed. The installation of this second quite small centrifuge was required by two main reasons. The first reason is the full utilization of the centrifuge ZI. This centrifuge is nearly daily in operation. Another advantage of the small centrifuge ZII is the easy handling and quick installation of models, which is suitable for parametric studies of model behaviour. At least there are lower costs for operation of the centrifuge according to the preparation of models, the power supply, and the manhours. One of the first test series in this small containers on sheet pile walls in sand is described in the second part of this report.

### 2. THE SECOND BOCHUM CENTRIFUGE ZII

#### 2.1 The centrifuge building

The Acutronic centrifuge is located in an inground chamber inside the laboratory building. The chamber has a height of 2.5 m and a diameter of 4.6 m. The walls, floor and ceiling are made of reinforced concrete. The dimensions of the chamber are shown in Fig.1.

The whole chamber is separated from the laboratory building by a run down expansion joint to avoid harmful vibrations on the rest of the building. The hydraulic power supply and the power cabinet are located in a separate room beside the centrifuge chamber. The centrifuge is loaded by opening of two concrete plates in the ceiling.

#### 2.2 Centrifuge specifications

The centrifuge ZII is a well-known Acutronic Model 661, which is also installed at the City University London and the University of Western Australia. The distance between axis and platform is 1.8 m. The platform offers a useable area of 500 mm by 700 mm

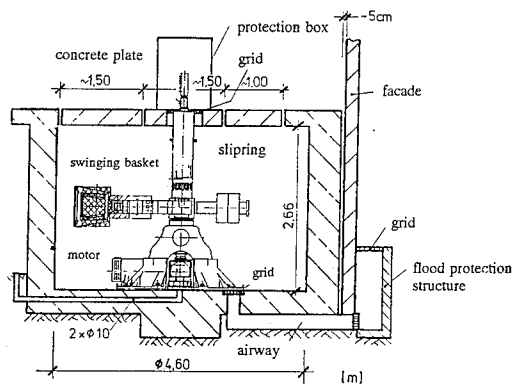


Fig.1. Cross section of the centrifuge and its chamber.

with a maximum package height of 500 mm. The maximum payload up to an acceleration of 100 g is 400 kg. There is a linear decrease of payload to 200 kg at the maximum acceleration (200 g = 340 rpm).

The centrifuge ZII is equipped with an automatic balancing system, which can equalize a maximum imbalance in a range of  $\pm 25000$  N within 60 sec. To provide a model with hydraulic, air or water pressure, there are 6 fluid joints. The two hydraulic oil sliprings have a working pressure up to 200 bars, the 4 other sliprings for water and air have a working pressure up to 20 bars.

To cool the air in the chamber during long tests, there is a 4 kW low speed fan, which is controlled by a thermostat. To prevent low temperatures under  $10^{\circ}\text{C}$ , a floor heating is applied.

### 2.3 Data Acquisition

For the data transfer from the platform to the control room there are 60 electrical sliprings. Electrical measurements are transmitted by a set of 46 sliprings (1 Amp., 150 V DC), the electrical power by 12 sliprings (5 Amp., 220 V) to provide actuators or other equipments. Continuous observation of the model is possible by a video system, which is connected by two video sliprings to the control room.

To guarantee a high speed data transmission with extreme noise immunity, a fiber optic rotary joint is installed. This performs a bi-directional transmission of data up to 50 Mbps.

All sliprings are housed within the main axis, with the fixed cables in the inner part. All cables are conducted downward through the floor. The data lines are special metal shielded to reduce electrical noise.

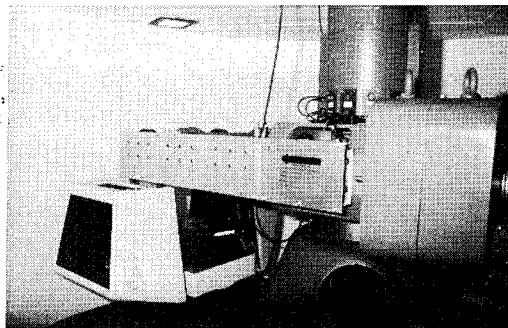


Fig.2. The centrifuge ZII (ACUTRONIC 661) after installation

The main power lines are installed in a maximum distance to data lines and consist of a 5 wire twisted cable with a steel shield and is routed independently to a local stepdown transformer.

The data lines are connected in control room with the data acquisition system, which is also used for the centrifuge ZI. This system consists of four data acquisition boards with independent processors, placed in the slots of a PC. Each board makes maximum number of 16 channels available for single ended, analogue input and two channels for analogue output. This boards are synchronized to make a simultaneous record of data by the boards up to 64 channels possible. For the operation of 16 channels per board a maximum scan rate of 14.7 kHz is reached. Scan rates, number of channels, number of readings, filter parameters, triggers etc. can be changed easily by a software package. During the operation all data are stored in a file on the hard disk.

### 2.4 Model equipment

Inflight-amplifiers and most of the transducers are used in both centrifuges ZI and ZII. Due to the limitation of payload and the small working area in the centrifuge ZII a total new design for the strong boxes was necessary.

The sheet pile wall tests have been performed in a rectangular box, which is made of aluminium. The side units consist of a honeycomb construction with a high stiffness and less weight. The container has internal dimensions of 360 by 560 mm by a 300 mm height and a weight of 73 kg.

A FE-calculation of the long-side units results a maximum deflection of 0.8 mm with the hypothesis of full earth ( $k_0 = 0.75$ ) and water pressure at the maximum acceleration level.

### 3. EARTH PRESSURE MEASUREMENTS ON FLEXIBLE RETAINING STRUCTURES

#### 3.1 General

A main geotechnical problem is the exact horizontal pressure distribution in cohesionless soil on a retaining structure. The earth pressure is influenced by the direction and quantity of the wall deflection. Related to this deformation a real prediction of the earth pressure at a special depth is rendered more difficult. Due to this problem a research project is going on at the Ruhr-University Bochum supported by the German Research Foundation (DFG). One of the topics of this research is the measurement of earth pressure behind retaining structures under consideration of wall deflection. In this paper the investigation method and first test results are presented.

To solve the problems of measurements, centrifuge model tests are performed. A vertical measuring device is applied with strain gauges, which are measuring the bending moment caused by the different edge fibre strain.

By means of the bending moment, the acting earth pressure is calculated by the theory of elasticity. This method is used in the centrifuge model techniques by King et al. (1984) for the earth pressure computation on a horizontal loaded sheet pile wall.

The authors report on problems in the derivation of the bending moments to determine the earth pressure distribution. If the bending moment is described by a polynomial with ten coefficients, the second derivation, which expresses the earth pressure distribution, results in some perturbation of the bending moment at depth, with rather large oscillations in pressure distribution. Lower order polynomials give moment equilibrium if the zero pressure condition at the sheet pile head is ignored.

According to this experience a modified method is used at Ruhr-University Bochum. To determinate the resultant earth pressure, the following equation (1) can be used:

$$M''(z) = -p(z) \quad (1)$$

The double derivation requires high quality of original data and high standard measuring devices and data transfer. To compensate inevitable measuring errors, the moment distribution is interpolated with cubic spline functions between the measuring points. The missing data are approached by polynomial with three coefficients, so that the curvature is zero in these places.

Table 1. Soil properties of the model sand

Parameter	Value
Compactness $\rho_{min/max}$ [g/cm <sup>3</sup> ]	1.41/1.70
density index [%]	100
unit weight $\gamma$ [kN/m <sup>3</sup> ]	17.0
angle of internal friction $\phi$ [°]	40

Spline functions have a smooth course between the measured datas, which is suitable for the application to measuring techniques. The method has advantages over the polynomial interpolation, which uses high order polynoms. These polynomial incline to oscillate after the derivation disturbing the earth pressure distribution.

The bending moment distribution is twice numerically differentiated after the spline interpolation. The result is the earth pressure distribution on the retaining structure. A double integration results in the deflection of the wall.

These numerical methods are combined in a computer program, which is developed at the Institute for Soil Mechanics and Foundation Engineering at the Ruhr-University Bochum.

#### 3.2 Earth pressure tests

##### 3.2.1 Test design and performance

The sheet pile wall is modelled by three aluminium plates. Each plate has a height of 22 cm and a width of 11.6 cm with a thickness of 0.3 cm. The acceleration level was choosen to 30g. The sheet pile model corresponds to a Larssen pile 607 with an equivalent bending resistance. The prototype height is 6.6 m. The central wall is instrumented with 10 strain gauges distributed over the whole height at a spacing of 21 mm (Fig. 3). The use of three sections overcome the effects of wall friction. A rectangular box with internal dimintions ( $h/b/t=0.56/0.36/0.30$ ) is used. For the first tests, Bochum model sand is rained with a high density. The soil properties are discribed in Table 1.

The embedded lenght of the sheet pile wall amounts to 6 cm, the vertical distance to the bottom of the container is 4 cm.

To reduce side friction at the container walls, glass panes are put in. A rubber membrane is located in front of the sheet pile wall, creating a water basin with a servo valve controlled outlet.

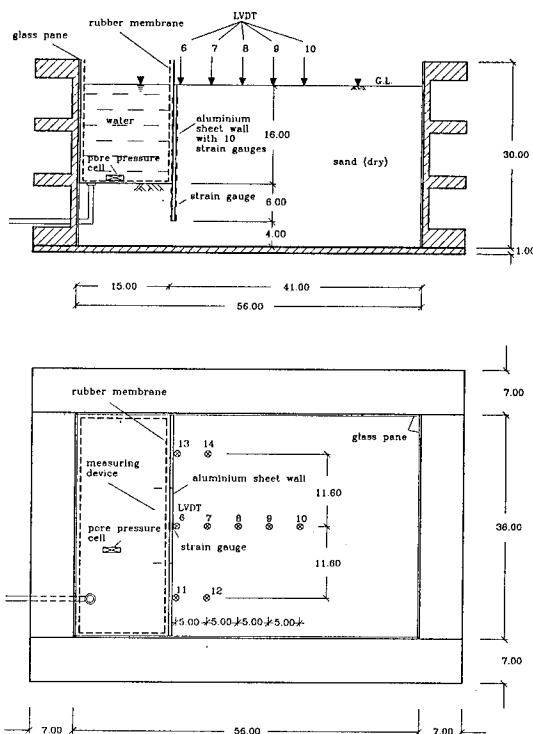


Fig. 3. Schematic test set-up to the earth pressure tests (cross section and plan view)

As the backfill is pluviated with sand, the membrane on the frontside is filled with water. The water is drained off in flight in three steps approaching a simulation of the excavation.

At last 9 LVDT's are placed on the ground level, measuring the vertical displacements on the backfill behind the wall. A schematic test set-up is shown in Fig. 3.

After increasing the g-level up to 30 g, the water will be drained out of the basin in steps. The water level inside the basin is controlled by a pore pressure transducer on the bottom of the basin.

When the water is drained off completely, the unpropped wall height amounts to 16 cm. During the whole test a continuous data acquisition of the bending moments, displacements and water pressure takes place.

### 3.2.2 Test results and comparison with the classical earth pressure distribution

To make an assessment on the test-method, a compa-

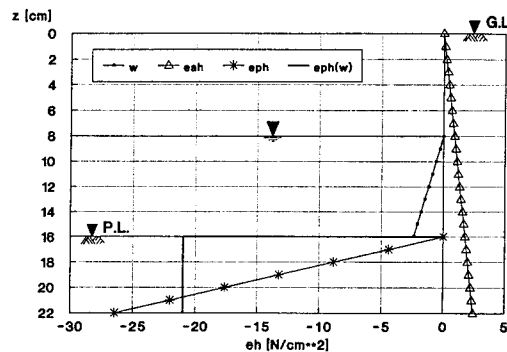


Fig. 4. Calculated loads on the sheet pile wall at 8 cm draining off the water in the basin

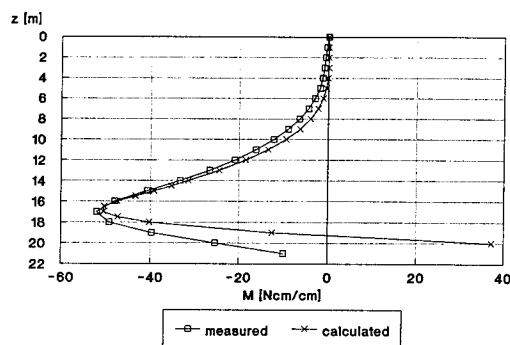


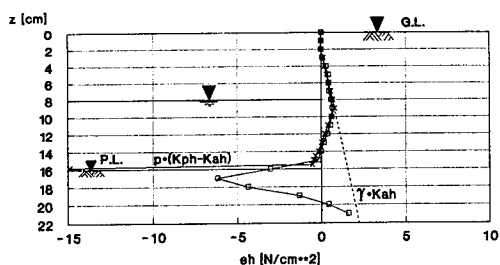
Fig. 5. Comparison between the calculated and measured moment distribution at 12 cm water in front of the wall.

relative calculation was undertaken, in doing so the different design loads were calculated after Coulomb. Fig. 4 shows the calculated loads on the sheet pile wall resulting from active and passive earth pressure distribution. An increasing of the passive earth pressure results from water loads in the basin; the water pressure on the wall is represented likewise. A comparison between the calculated and measured bending moments is shown in Fig. 5.

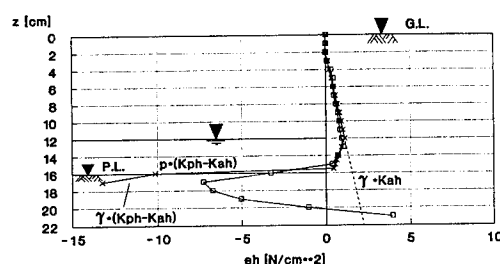
Estimating an angle of wall friction of  $\delta = 2/3\phi$  a quite good correspondence between the calculated and the measured data is obtained.

The earth pressure distribution resulting from the bending moment lines are shown in Fig. 6.

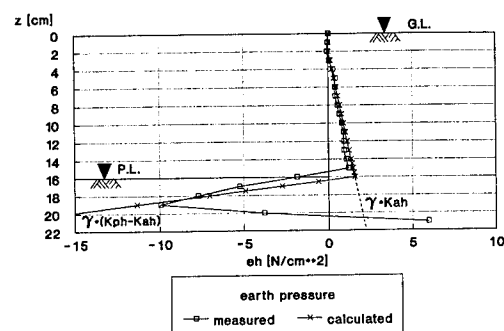
The supporting pressure of the sheet pile wall by the different water levels on the excavation side is established obviously (Fig. 6a and 6b). In Fig. 6c the water level in front of the wall is completely drained



a)



b)



c)

Fig 6. Resulting earth pressure distribution

- a) water level - 8 cm
- b) water level - 12 cm
- c) complete excavation

off, the passive earth pressure is reduced for the value  $p_w \cdot K_{ph}$ .

The strain gauge at the bottom of the wall is located at a level of 21 cm below the ground surface resulting in a completion of the earth pressure distribution at the bottom of the wall (22 cm). The completion must give an equilibrium of the acting forces in horizontal direction.

A comparison of the earth pressure distributions with the calculated data after Coulomb's method indicates a slight oscillating of the differentiated

values. This might be attributed to an increasing of the wall rigidity at the strain gauge locations and a predeformation caused by the wire weights. By improving the measuring techniques with substantially smaller wires and application of the strain gauges by using a softer glue, the measurement inaccuracies might be reduced.

The bending moments and displacements, caused by the water pressure in direction to the backfill side before the water is drained off, can be neglected on account of the small values. The resulting deformations do not suffice to activate passive earth pressure. But the method of fluid supporting offers the possibility to keep an equilibrium state at the start of the test after reaching the g-level.

### 3.3 Evaluation of the test results

The results of the centrifuge model tests will be evaluated, according to the coefficient of active earth pressure  $K_{ah}$ , which is calculated dependent on the height and the deformation of the wall. Calculating the coefficient of active earth pressure  $K_{ah}$  on base of the earth pressure distribution and deflections of the wall, a decreasing of the coefficient down to a minimum value of  $K_{ah} = 0.18$  is observed (Fig.7).  $u_i$  stands for the horizontal displacement at the location  $i$  and  $h_i$  describes the vertical distance from this location to the centre of rotation. Applying the values in this mode a consideration of the deflection figur of a flexible retaining wall is carried out, through which all local displacements are related to their distance to the rotation centre.

The maximum value for the coefficient  $K_{ah}$  reaches for small displacements  $u_i/h_i = 0.006$  at an excavation level of -8 cm about  $K_{ah} = 0.31$ . At an excavation level of -12 cm and a dimensionless displacement of  $u_i/h_i = 0.009$  the maximum value is  $K_{ah} = 0.28$ . The  $K_0$ -value for this sand is approximately calculated to  $K_0 = 1 - \sin \phi = 0.357$ . Due to this observation the soil on the active side of the wall is near to a  $K_0$ -condition caused by the water pressure support, while in a state of full excavation, the coefficient  $K_{ah}$  decreases to a minimum value of  $K_{ah}$ .

For the decrease of the active earth pressure to a coefficient  $K_{ah}$  an ultimate value of displacement is required according to a rotation round the base of the wall. This value is exceeded at several tests in a state of excavation at -8 and -12 cm, because of the water pressure support in front of the wall. This water pressure support obstructs a relaxation of the soil in the lower part of the wall.

In contrast to this observation, calculation and test



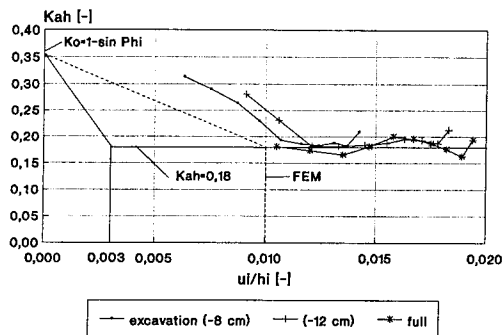


Fig 7. Coefficient of active earth pressure  $K_{ah}$  versus relative deformation  $u_i/h_i$

results in literature can be found, which mention larger ultimate displacements. For example a FE-calculation of Ziegler (1987) gives a value for the active ultimate displacement at a rotation of  $u_i/h_i > 0.01$ . To make this evident the value is connected straight lined with the  $K_0$ -value in Fig 7.

#### 4. CONCLUSIONS

The increasing number of centrifuge tests at the Institute for Soil Mechanics and Foundation Engineering in Bochum made an installation of a new centrifuge necessary. A second centrifuge was installed with advantages in easy handling and quick installation of models. For that reason the facility is very suitable for parametric studies of model behaviours.

In the second part of this paper a first test series to the measurement of lateral earth pressure on flexible retaining structures is described. It has been turned out, that only a few centrifuge model investigations were performed to this topic because of the difficulties in the measuring technique.

One method to determinate the horizontal earth pressure is the measurement of the bending moment distribution and to differentiate numerically these data twice. Unfortunately this method is very sensitive to measuring inaccuracies. According to this the inaccuracies are adjusted by a special interpolation and the development of the function is interpolated between two points. For this interpolation cubic splines are used.

The investigations with sheet pile models show the general aptitude of this method in centrifuge model technique. A comparative calculation after Coulomb results in a satisfactory correspondence.

With regard to the dependence of deformation due to the magnitude of the active earth pressure it was demonstrated, that the evaluation of fully controlled centrifuge tests can lead to new findings to the problem of earth pressure. By a further improvement of the measuring technique and an increasing of the measuring points, increased quality of data is expected.

#### ACKNOWLEDGEMENTS

We like to thank the German Research Foundation (DFG) for the support to install this second geotechnical centrifuge in Bochum hoping to get with this new facility a centre of geotechnical research in Germany. We also like to acknowledge the good cooperation with Acutronic France and Germany during the installation.

#### REFERENCES

- Franke, D. (1980). Die Berechnung des Erddrucks in der Baupraxis. Mitteilungen der Forschungsanstalt für Schiffahrt, Wasser- und Grundbau, Berlin, Heft 42
- Geotechnik Sonderausgabe (1992). Sonderheft: Praxisbezogene Anwendung der Zentrifugenmodelltechnik in Grundbau, Tunnel- und Schachtbau und Umwelttechnik
- Jessberger, H.L., Güttler U. (1988). Bochum geotechnical centrifuge, Centrifuge 88 Paris, Balkema Rotterdam
- King, G.J.W., Dickin, E.A., Lyndon, A. (1984): The development of a medium size centrifuge testing facility. The Application of Centrifuge Modelling to Geotechnical Design. University of Manchester, Engineering Department
- Ziegler, M. (1987). Berechnung des verschiebungsabhängigen Erddrucks in Sand. Veröffentlichung des Instituts für Bodenmechanik und Felsmechanik der Universität Karlsruhe, Heft 101

## Pore pressure measurement during centrifuge model tests: Experience of five laboratories

D. König & H.L. Jessberger – *Ruhr-Universität Bochum, Germany*

M. Bolton & R. Phillips – *Cambridge University, UK*

G. Bagge – *Danmarks Ingenior Akademi, Lyngby, Denmark*

R. Renzi – *Istituto Sperimentale Modelli e Strutture SpA, Bergamo, Italy*

J. Garnier – *Laboratoire Central des Ponts et Chaussées, Nantes, France*

**ABSTRACT:** The five laboratories are involved in a cooperation with the aim to improve experimental procedures and instrumentation. This paper presents the results of investigations on pore pressure measurements under static conditions in an overconsolidated clay specimen (Speshwhite Kaolin). Recommendations for the handling of the pore pressure transducer PDCR 81, produced by DRUCK, England, were formulated and each laboratory performed centrifuge model tests under definite boundary conditions. The presented results show the high standard of pore pressure measurement during the preconsolidation phase as well as during reconsolidation of the model soil inside the centrifuge. The pore pressure measurements in different depths offer the facility to determine the consolidation conditions at each state of a centrifuge model test.

### 1 INTRODUCTION

Centrifuge model technique requires a high standard of measurement technology. Different boundary conditions make several, sometimes conflicting, demands on measuring instruments.

Classical tasks are the measurement of displacement and force values. Displacement values are generally measured by LVDT's, in some cases by gap sensors or flexible strips provided with strain gauges. Forces acting between a loading device, for example a pneumatic cylinder, and a structure can be registered by load cells. To determine the stress and strain of a structure, for example a tunnel lining, strain gauges are used. Stress measurement in the soil is more complex.

It is not possible to measure effective stress directly neither in situ nor in model tests. The effective stress is determined by the difference of the total stress and the pore water pressure. Using dry soil the task is reduced to the measurement of the total stress. In saturated soft soil both are necessary.

One aim of the cooperation between Cambridge University (CUED), Danmarks Ingenior Akademi (DIAB), Istituto Sperimentale Modelli e Strutture S.p.A. (ISMES), Laboratoire Central des Ponts et

Chaussées (LCPC) and the Ruhr-Universität Bochum (RUB) is to collect the experience of each laboratory about pore pressure measurement, to rate the current state and to initiate new developments. The exchange of experiences shows that all laboratories use the pore pressure transducer PDCR 81, fabricated by Druck, England. Detailed discussions demonstrated many differences in the handling of the transducer. Due to that, recommendations for the use of the PDCR 81 under static conditions were formulated, to make sure that the results of pore pressure measurement are reproducible and comparable.

The applicability of the recommendations and the comparability of pore pressure measurement with the PDCR 81 taking account of the recommendations were demonstrated by a centrifuge model test under definite boundary conditions. This test was carried out by all five laboratories and the results were compared.

In section 2 of this paper the pore pressure transducer PDCR 81 is described and some basic information about the handling is given. Section 3 presents the experimental procedures followed by each laboratory. The test results are shown and discussed in section 4.

## 2 THE PORE PRESSURE TRANSDUCER PDCR 81

### 2.1 Geometry and function of the transducer

The PDCR 81 transducer measures the differential pressure between the reference atmospheric air pressure and a fluid pressure. Figure 1 shows the geometry of the pore pressure transducer (PPT). Strain gauge circuits are etched on the thin silicon diaphragm, which is fixed on a glass ring placed in a strong steel tube. To resist the effective stress of the soil a porous filter plate or stone is placed in front of the diaphragm. The gap between the porous filter and the diaphragm is 0.13 mm.

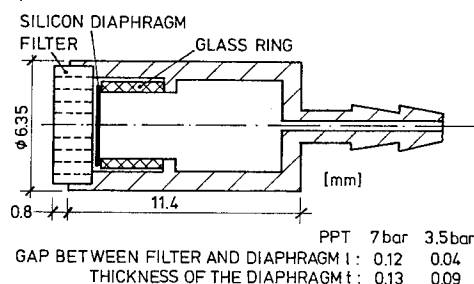


Figure 1: Geometry of the pore pressure transducer PDCR 81

The fluid pressure acts through the porous stone on the silicon diaphragm while the atmospheric air pressure is communicated along the PTFE sleeve lead, which also houses the electric wires. The PTFE sleeve lead is inserted at the back of the transducer. The sealing between the steel tube and the lead is realized by adhesive and protected by an additional rubber tube.

Druck produces the PDCR 81 transducer for different operational pressure ranges: 75 mbar, 350 mbar, 1, 3, 7, 15, 35 bar.

### 2.2. Electrical connection

The PDCR 81 has to be connected with a power supply. It is recommended to energise the transducer at -5V. Thermal problems are recognized at higher voltage levels. The negative voltage is important, as water is in direct contact with the silicon diaphragm. A negative voltage reduces the rate at which the

silicon diaphragm is attacked by the water, increasing the life of the PDCR 81.

### 2.3. Porous filter

Druck supply the PDCR 81 with a ceramic filter stone 2 mm thick. Different laboratories found that these stones get blocked with successive usage, which causes uncertainty about the degree of saturation of the stone and also an unacceptable increase in the response time of the transducer. It is recommended to use new filters for every test and to discard the old filters. LCPC in Nantes protects the porous stone by surrounding the transducer with filter paper.

The permeability of the filter is checked by the speed of the transducer's response, as a result of quickly increasing the fluid pressure. The pressure increase and the reaction of the transducer are plotted against time. The differences between the two curves is a reference for the permeability of the filter. This test is used for applications under static conditions.

Filter stones supplied by Druck are not used in Cambridge. Ceramic filter stones are made from Porcelain Mullite Cellton V1 material manufactured by Fairey Industrial Ceramics, Stone, Staffordshire for use in clay. These stones are machined to a thickness of 1.7 mm and a diameter of 5.82 mm +/- 0.01 mm. Sintered bronze filters are used in sand. These filters are 2 mm thick and are made from Porosint Bronze sheet manufactured by GKN Sheepbridge Limited, Sutton in Ashfield, Nottinghamshire. Their diameter is machined also to 5.82 mm. The filter increases the response time and causes less restriction to saturation of the PDCR 81.

The ceramic and bronze filters are slightly larger than those supplied by Druck, so they can be push-fitted directly into the steel tube of the transducer.

### 2.4 Saturation of the porous filter

The saturation of the porous filter is a precondition to get good results with the PDCR 81. Bronze filters cause less restriction to saturation. The following procedure is recommended for the use of ceramic filter stones.

The porous stone is separated from the transducer. The stone is placed into water and is de-aired by boiling the water for about 15 minutes, until air bubbles are no longer coming from the stones. After cooling the porous stone, the transducer can be

It is important to take care that no particles are on the diaphragm. The gap between the stone and the diaphragm is very small and a thin particle could cause a connection between the stone and the diaphragm.

To remove the stone without damaging of the transducer the stone has to be dug out with a cutter. Generally, it is not possible to remove the stone supplied by Druck without breaking them.

## 2.6 Sources of error at the transducer and checking the transducer

Another source of error is the porous filter. The problems of blocking the ceramic stone and of particles between the diaphragm and the filter have been discussed above.

First, the PDCR is visually checked for damage, including closure of the sleeve by crushing of the lead and cuts in the sleeve, to ensure the integrity of the air passage. The seal between the head and the lead is checked by the calibration procedure. If a vacuum is applied in the calibrator, air bubbles show defects at the seal or the diaphragm.

Before placing the transducer in the soil it is connected to a power supply and a digital volt meter. The porous filter is pressed careful by hand into the transducer. If the transducer reacts on this test, a connection must exist between the filter and the diaphragm, usually caused by particles on the diaphragm.

Within the bounds of another part of the cooperation, which involves cone penetration tests, some centrifuge model tests were performed with soft clay. To verify the recommendations for the use of the pore pressure transducer PDCR 81, and to demonstrate the comparability of the pore pressure measurements, pore pressure transducers were installed inside the clay. The transducers detected the pore pressure during the preconsolidation phase of the clay outside the centrifuge and during the reconsolidation inside the centrifuge.

103

Table 1: Absolute dimensions of the centrifuge models prepared of each laboratory

Laboratory	CUED	DIAB	ISMES	LCPC	RUB
Test	MWG4	Nr.29	KC3	Sp.3	PENKAO
D [mm]	850	534	400	894 <sup>1</sup>	750
r [mm] <sup>2</sup>	3800	2402	1974	5207	3805
hw [mm]	36	26	36	45	30
hk [mm]	207	204	216	233	216
h1 [mm]	36	54	64	83	86
h2 [mm]	95	104	104	133	131
h3 [mm]	180	154	144	183	176
h4 [mm]	112	104	104	133	131

<sup>1</sup> The pore pressure transducer were placed in a distance of about 120 mm from the container wall

<sup>2</sup> Radius from centrifuge axis to model surface

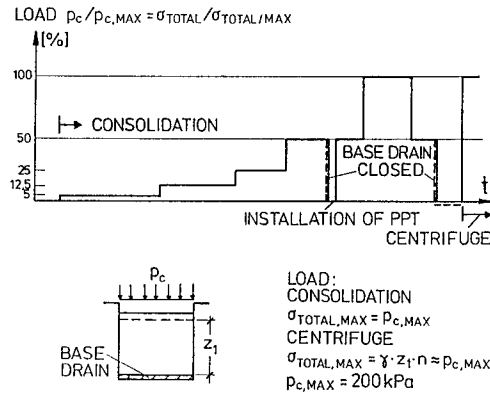


Figure 3: Loads steps of the preconsolidation phase

Table 2: Properties of Speshwhite Kaolin from English China Clay (ISMES)

Density of solid particles [g/cm <sup>3</sup> ]	2.640
Liquid limit [%]	50
Plastic limit [%]	29

### 3.1 Preparation of the sample

The clay sample was prepared from a dry clay powder and water. Each laboratory used clay from the same batch of Speshwhite Kaolin (Table 2). The clay powder was added step by step to the measured mass of water to achieve an initial water content of 125 %. The slurry was mixed under vacuum for several hours and then placed in the strong box up to a height of 400 mm above the lower sand layer (base drainage). The surface of the slurry was covered by a filter paper.

During the consolidation phase outside the centrifuge the consolidation pressure was applied in different load steps by a hydraulic jack. The recommended sequence of load steps and their duration is shown in Figure 3.

After the first 2 days of the 100 kPa load step the clay was unloaded to install the pore pressure transducer. During unloading the base drainage was closed.

### 3.2 Calibration of the PPT

It was found that the calibration of the PDCR 81 is the same with and without a porous filter when the filter is unblocked by fine particles and well saturated.

Two different methods are used to calibrate the transducer. The first one is to run a calibration test in the centrifuge. The transducer is put on the bottom of a tube or box filled with water. This tube is placed on the centrifuge basket and the level of gravitation is increased step by step. The real water pressure acting on the transducer is calculated and evaluated in relation to the reaction of the transducer.

The second way is to calibrate the transducer outside the centrifuge in a separate apparatus. In this case visual checking of the transducer under water pressure is possible. The transducer is placed in a calibrator. The calibrator is a strong closed box, in most cases a clear plastic tube.

The system is filled with water and de-aired by applying a vacuum. If the transducer is damaged, air will be seen as bubbles at the back of the transducer, as mentioned above, or sometimes air is drawn through or around the edges of the diaphragm.

During the calibration procedure the water pressure inside the calibrator is increased in increments up to about 150 % of the maximum hydrostatic pressure expected during the centrifuge test. At each pressure increment the applied water pressure and the reaction of the transducer is recorded. The results of this calibration procedure depend on the quality of the pressure cell measuring the applied water pressure.

The details of the calibrator depend on the equipment of the laboratory (data acquisition system, air pressure system, air/water interface etc.).

In all cases it is necessary to insert the lead of the transducer into the calibrator and to ensure a seal between the lead and the strong wall of the calibrator.

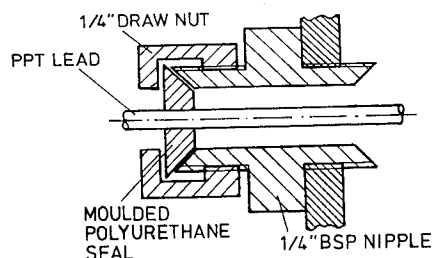


Figure 4: Outlet with seal for the PPT lead

A special seal is developed to guarantee the air passage through the lead of the transducer to the back of the silicon diaphragm. The principle of the seal is shown in Figure 4. An 1/4" nipple (male - male thread) is screwed into the wall of the calibrator. The nipple is large enough to pass over the head of the transducer. A special moulded polyurethane split seal is then placed around the transducer lead and pushed into the 60 degree end of the BSP nipple. A standard draw nut is then tightened by hand to compress the seal onto the lead.

### 3.3 Installation of the PPT

The installation of the PPT's was carried out through holes which were drilled in the side wall of the strong box before the preparation of the model started. During the first part of the consolidation these openings were sealed by 1/4" BSP nipples and caps.

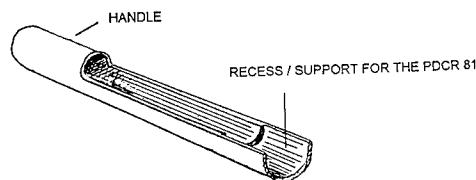


Figure 5: Semi-circular guide for placing the PPT in clay

When the consolidation was nearly finished and the consolidation pressure was released a horizontal hole was drilled into or cut out of the clay with a diameter of about 7 mm through the openings mentioned above. The end of the hole is about 5 mm in front of the final position of the transducer stone. With the help of a semi-circular guide (Figure 5) the

transducer is inserted into the hole and pushed through the last 5 mm of undisturbed clay to its final position. Later the hole is filled with a thick clay slurry. The insert of the lead of the transducer was sealed as with the calibrator described above.

### 3.4 Test procedure

After unloading the clay the strong box was placed in the swinging basket of the centrifuge. On the surface of the clay 30 mm of water was added. Then the model was accelerated up to a g-level of 70 g. The maximum delay between final unload and accelerating the model was one day. During the time of seven hours the pore pressure was detected by the PPT's and a data acquisition system.

## 4 PRESENTATION AND DISCUSSION OF THE TEST RESULTS

### 4.1 Preconsolidation phase

Figure 6 shows the typical development of the pore pressure during the last part of the preconsolidation phase outside the centrifuge. Just after installation the PPT's into the unloaded clay, the transducers detected a negative pore pressure due to the unloading of the clay from 100 kPa to 0 kPa before the installation. On applying a consolidation pressure  $p_c$  a new total stress level was reached. Simultaneously the pore pressure increased by about the magnitude of the change of the total stress level. Under constant consolidation pressure the pore pressure decreased with time. During unloading at the end of the preconsolidation negative pore pressures were observed.

The pore pressures during laboratory testing by DIAB are almost ideal. Note in particular that on final removal of the 100 kPa surcharge, the pore pressure immediately reduces to about -100 kPa (gauge), or zero (absolute). This can only happen if the clay and the transducer are perfectly de-aired. Other laboratories showed final pore pressures not as negative as this indicating cavitation, gassing or air entry.

The time settlement curves of different laboratories are shown in Figure 7 for the 200 kPa load step, on a logarithmic scale. The 100 % line of the primary consolidation and the time factor  $T = 1$  are clear by these curves. With this information the theoretical pore pressure profile over the depth of the clay stratum is calculated.

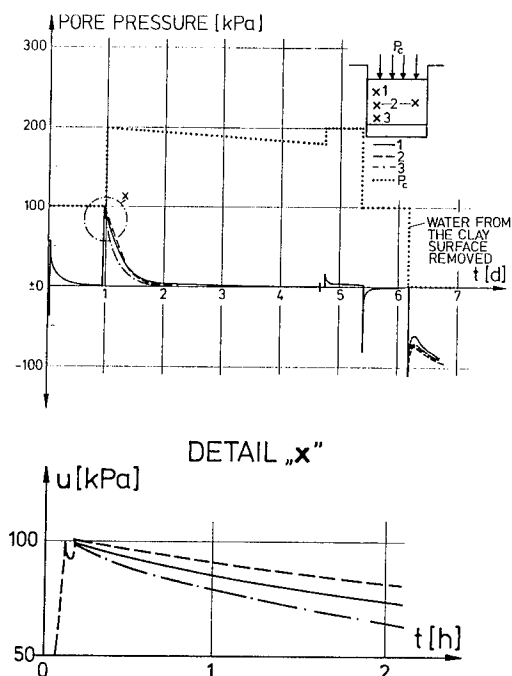


Figure 6: Typical pore pressure development during the last part of the preconsolidation phase (DIAB)

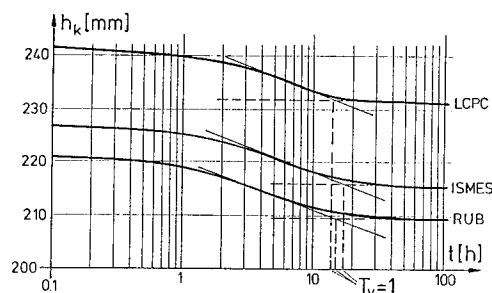


Figure 7: Time settlement curves from the 100 kPa to 200 kPa load step of the preconsolidation

Figure 8 shows the measured pore pressure  $u/\Delta p_c$  ( $\Delta p_c$ : Additional consolidation pressure of the actual load step) in comparison to the expected pore pressure profile over the dimensionless depth  $z/h_k$  at time factors of  $T = 0.2$  and  $T = 0.5$ . The measured values corresponded very well to the expected profile. It is obvious to see, that the pore pressure detected by the transducers placed more close to the top and the bottom of the clay stratum decrease faster than the pore pressure in the middle of the stratum. This is also demonstrated in the detail enlargement of Figure 6.

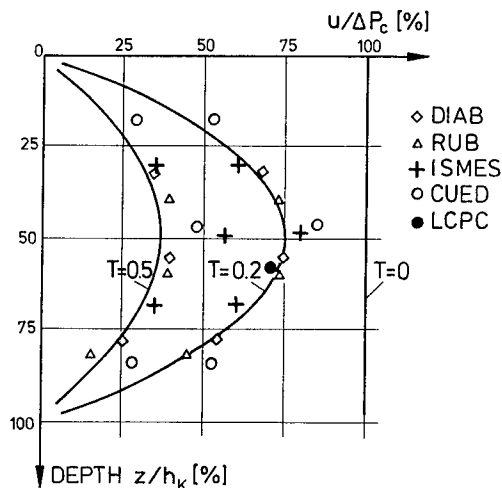


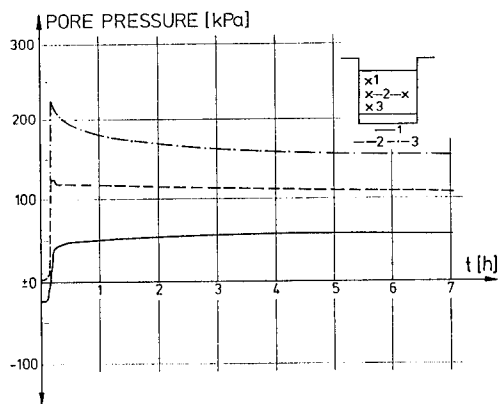
Figure 8: Pore pressure profile over the depth of the clay stratum during the 100 kPa to 200 kPa load step of the preconsolidation as a function of time

#### 4.2 Reconsolidation in the centrifuge

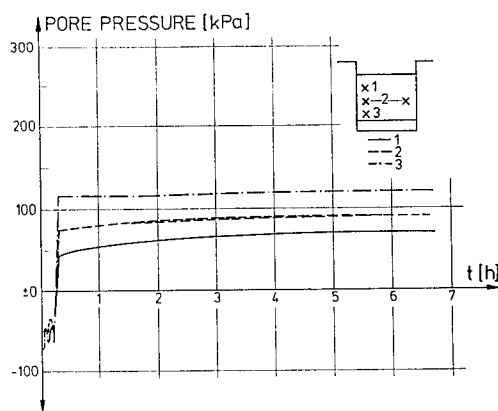
Test results from CUED and ISMES are shown in Figure 9. The pore pressure measured during the reconsolidation of the clay in the centrifuge is plotted versus time. In both cases the pore pressure increased on accelerating the model in the centrifuge and reached an initial value. With time the pore pressure converged towards the hydrostatic water pressure. The initial pore pressure measured by ISMES was at each depth smaller than the hydrostatic pressure and approached the final hydrostatic pressure from below. The results of CUED show initial pore pressures higher than the hydrostatic pressure. In this case the pore pressure approached the hydrostatic pressure from a higher level.

Figures 10 shows the measured pore pressure profiles over the depth of the clay stratum prior to centrifuging and just after reaching the selected g-level for the tests carried out by CUED, DIAB and ISMES. The following features of the shown pore pressure data should be noted:

- The initial values prior to centrifuging range from strongly negative (e.g. DIAB, circa -80 kPa) to weakly negative (e.g. CUED, circa -25 kPa).
- The immediate increment of pore pressure due to centrifuging is almost the same in every case. This leaves the pore pressure at the start of centrifuge consolidation either smaller than hydrostatic (e.g. DIAB) or larger than hydrostatic (e.g. CUED).
- The final hydrostatic pore pressure are almost the same in every case as shown in Figure 11. The



a



b

Figure 9: Development of the pore pressure during the centrifuge test (a: CUED; b: ISMES)

average difference between the expected pore pressure and the measured pore pressure is less than 10 %. The maximum difference is 20 %.

The differences in the pore pressure development are due to the delay between unloading of the clay and accelerating the model in the centrifuge and to the degree of saturation as mentioned above. At DIAB and ISMES the delay was limited to 0.2 or 0.1 days. During this time only a part of the negative pore pressure impressed by the unloading disappeared and high negative pore pressures were measured at the beginning of the centrifuge test. In this case the sum of the additional total stresses due to the increasing self weight of the soil during accelerating the centrifuge and the initial negative pore pressure was lower than the hydrostatic pressure.

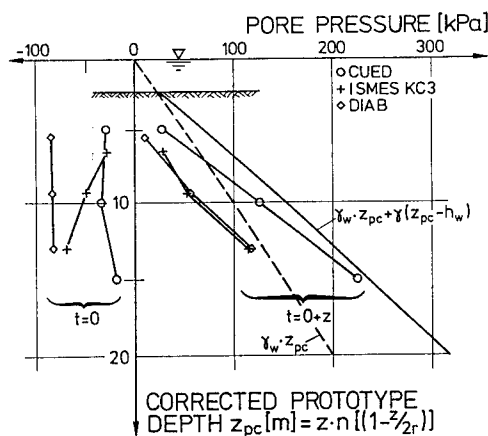


Figure 10: Pore pressure profile over the depth of the clay stratum before centrifuging ( $t = 0$ ) and after reaching the selected  $g$ -level ( $t = 0 + z$ )

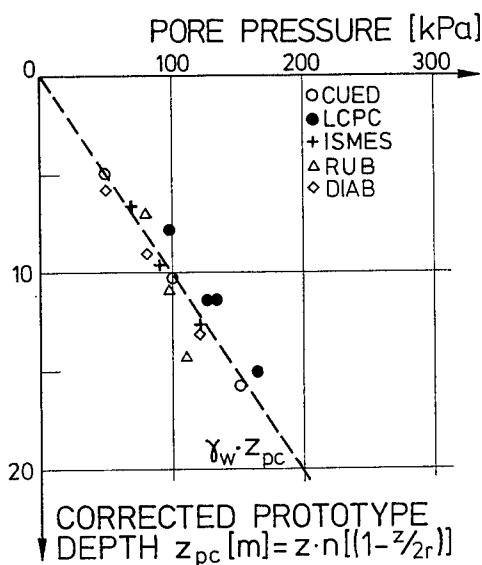


Figure 11: Comparison of the pore pressure measurement after 7 hours in centrifuge test

If the delay between unloading the clay and starting the centrifuge was longer (CUED: 0.8 d), most of the negative pore pressure disappeared before the model was accelerated in the centrifuge. The sum of the total stress and the remaining negative pore pressure got higher than the hydrostatic pressure. Only in this case a reconsolidation of the clay took place during the centrifuge test.



The strong presumption is that the clay in the test at DIAB was almost perfectly de-aired, whereas other laboratories achieved less complete saturation. An explanation might lie with the degree of vacuum actually achieved during mixing of the clay powder with water. The main practical consequence of the lack of the saturation and different consolidation paths would be:

- Unloading events (excavation, tunnelling etc.) would be accompanied by gassing and cavitation. This may or may not be equivalent to the behaviour in the field, depending on saturation in the field.
- Loading events would be accompanied by rather faster dissipation of excess pore pressures, due to compression and dissolution of the air bubbles.
- Initial strain paths would not be correctly initialised since even overconsolidated samples would tend to consolidate in the centrifuge, instead of swelling. This would place the soil on the wrong branch of its hysteresis loop of swelling and reconsolidation.

## 5 SUMMARY AND CONCLUSION

Five European laboratories collected experiences about pore pressure measurement and formulated in a first part of their cooperation recommendations for the use of the Druck pore pressure transducer PDCR 81. The main parts of the recommendations are presented in this paper.

The applicability of the recommendations and the comparability of pore pressure measurement with the PDCR 81 taking account of the recommendations were demonstrated by a centrifuge model test under definite boundary conditions. The test was carried out by all five laboratories.

The comparison of the results of the pore pressure measurement during the preconsolidation phase of the clay sample outside the centrifuge and during the centrifuge test shows a good agreement with the expected values following consolidation theory. The initial pore pressure just after accelerating the model in the centrifuge up to the constant g-level is highly influenced by the delay between unloading the clay and starting the centrifuge and by the degree of saturation of the soil. The readings of the pore pressure transducers are a good tool to determine the state of consolidation during each part of a centrifuge model test.

## ACKNOWLEDGEMENT

The cooperation of the five laboratories was made possible by the financial support of the European Community (SCIENCE contract SC1-ST91-0626). J.-F. Corté (LCPC), who was one of the initiators of the project, acted as coordinator. The participation of F. Smits (ISMES) during the application phase is also acknowledged. F. Smits died in autumn 1991 just before the cooperation started.

## Performance of an automated centrifuge control system

K.L.Goh

*Department of Civil Engineering, National University of Singapore, Singapore*

**ABSTRACT:** An automatic closed-loop control system has been developed to automate the flight control of the geotechnical centrifuge at the National University of Singapore. The control system employs a Proportional-Integral-Derivative (PID) software controller primarily to provide precise flight control over the centrifuge's angular speed and acceleration. Performance tests have shown that it is significantly precise. Consequently, prototype soil stresses can be modelled more accurately. Secondary responsibilities of the software include temperature monitoring of the centrifuge system and enclosure and the system pressure of the hydraulic drive system. The system requires minimum supervision during flight. Centrifuge users can now exploit these features for applications such as long period in-flight consolidation.

### 1. INTRODUCTION

An automatic closed-loop control system is essential for precise control over a centrifuge's angular velocity and angular acceleration. The design of the centrifuge in terms of size, payload capacity, and the drive system would determine the appropriate type of automatic control system required. To date, some of the institutions that have implemented automatic controllers are the University of California, Davis (Kutter et al. 1991) and Delft Geotechnics (Nelissen 1991). At Davis, a Proportional-Integral (PI) closed-loop software controller controls the 80 g-ton centrifuge, which is driven by a DC motor. The controller was modelled from a mathematical formulation of the equation of motion involving various factors such as inertia and speed dependent drag force. The software performs background tasks like data acquisition, monitoring machine instrumentation; foreground tasks include speed setting and emergency handling. The 16.5 g-ton centrifuge at Delft is driven by a hydro-electro system. A programmable logic controller (PLC) controls the drive system, automatic balancing system, temperatures, oil pressures, imbalance forces, structural stresses in the arm and the container, and the stability of the rotation. With manual control, it was observed that a skilled

operator was required to ensure precise control over the angular velocity and acceleration. Also, should a centrifuge user desire to run his test continuously for hours, an operator had to be present at the control console to periodically correct for changes in speed and to constantly monitor the various plant parameters. Hence, to improve this situation, an automatic closed-loop control system has been developed recently for the 40 g-ton centrifuge at the National University of Singapore. The whole system is extremely versatile: it was conceptualized to provide more precise control over the angular velocity and acceleration and is designed to handle the tasks of monitoring various plant parameters like the temperature of the centrifuge bearings and the surroundings and the hydraulic drive pressure (system pressure). Should any of these parameters exceed the desirable safety limits, the software controller will automatically terminate the flight. Consequently, the control system requires minimum supervision during operation. From geotechnical centrifuge engineering point of view, centrifuge users can exploit the built-in capabilities of the control system to model the prototype soil stresses more accurately, reduce supervision required for in-flight consolidation over long periods, and even execute several stages of g-levels within precise time intervals per run to simulate varying loading forces.

The primary objective of this paper is to present a comprehensive account of the automated centrifuge control system that is actually an extended modification from a manual control system and how the control system instrumentation may be exploited to suit centrifuge modelling purpose.

## 2 THE CLOSED LOOP CONTROL CIRCUIT

Figure 1 shows the closed-loop control system. In implementing the control circuit, the hardware consideration was straightforward because many of the available components for manual control could be used for the automatic control system and the additional components are relatively simple to install. On the software aspect, a computer program was developed in-house. The software incorporates a controller that serves as an extension to the existing manual controller so that should the former fails, the latter can take over the job. From a wide range of controllers, the PID controller was selected for two reasons. Firstly, the controller is an attractive choice of use when the formulation of a mathematical model of the centrifuge control system was not readily available. Secondly, the PID controller is relatively robust, i.e., can withstand plant parameter variations and reasonable nonlinear operation.

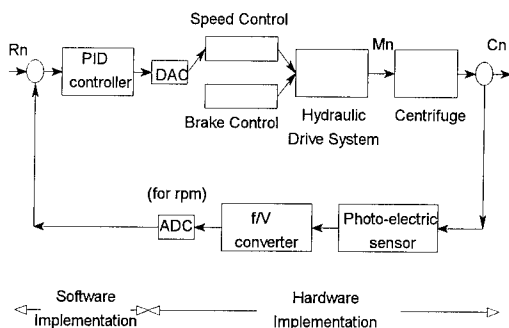


Figure 1. The Closed-loop Control System. Only the ADC for rpm is shown.

The closed-loop software controller, (i.e., the PID controller) is incorporated in a menu-driven user-interface software, CFGCTRL. The controller essentially monitors and maintains the centrifuge's speed at the designated g-level.

The hardware of the computer controller system consists of a Metrabyte DAS16 data acquisition card housed in a 80386DX33 PC. On-board the data

acquisition card, there are two Digital-to-Analog-Converters (DAC) and eight Analog-to-Digital Converters (ADC) of which six are used. Each DAC has a specific task: (1) Ramp-accelerates and maintains the centrifuge's speed, (2) Controls the deceleration of the centrifuge. Monitoring the centrifuge's speed and system pressure each involves one ADC and temperature sensors involve four ADCs. The sampling throughput was set at 10000 Hz. Each DAC and ADC has a voltage signal resolution of 0.002V (12 bits). For the pair of DAC and ADC that are involved in the speed control, the corresponding resolutions of interest are 0.08 rpm and 0.06g.

The hydraulic drive system employs proportional swash-plates for speed control and proportional valves for deceleration. These proportional valves are electronically controlled by on-board proportional amplifier cards, Rexroth VT2000S40, housed in a control box in the centrifuge control room. Each amplifier (connected to one DAC) receives stepped (discrete) voltage signals from the DAC and converts them into slowly rising or falling output electric currents that flow out of the card and into the proportional solenoids of the hydraulic drive system. The essential component in the amplifier is a ramp generator that provides smooth acceleration or deceleration of the centrifuge.

The hydraulic drive system comprises of a 3-phase induction AC-motor driving a Mannesmann Rexroth variable displacement hydraulic pump. This hydraulic drive system operates by means of high pressure piping which enables the hydraulic oil to flow into the radial piston hydraulic motor coupled to the base of the rotor shaft causing the latter to rotate due to the flow action. The rotation of the shaft drives the variable displacement hydraulic pump, causing the pump to be displaced. The degree of the displacement is controlled by the swivel angle of a swashplate inside the pump. This angle is solenoid-adjusted by varying the electric current output from a Speed Control card that flows through the solenoid. Changing the displacement will affect the flow rate of the oil and hence the speed of the centrifuge.

The centrifuge (Lee et al., 1991) has a radius of 1.87m and a maximum speed of 300 rpm (5Hz). Each end of the rotor arm supports a hinged steel swing platform. Each platform has a working area of about 750 mm by 700 mm and a model headroom of around 1200 mm. The centrifuge rotates about a

vertical rotor shaft that is coupled to the hydraulic motor located at the base of the centrifuge.

The speed of the centrifuge during flight is monitored directly by the photoelectric retro-reflective transmitter and sensor that is installed at the base of the centrifuge at roughly a foot away from the rotor shaft. The transmitter is oriented such that it generates an infra-red beam towards the centrifuge's rotor shaft. At the surface of the shaft is attached a reflective strip that reflects off the beam and sends it to the sensor. The sensor converts each signal received to a pulse and is output to a frequency to voltage (f/V) converter.

The f/V converter converts in-coming pulses, at a frequency ranging from 0.001Hz to 20Hz into electrical voltage ranging from 0 to 10V. The output voltage resolution of the DAC on the f/V converter is 0.01V (10 bits). The outgoing signal is received by an ADC on the DAS16 card. Signal degradation is minimized in this instance because the voltage resolution of the ADC is one order of magnitude smaller than the DAC on the f/V converter.

### 3 CONTROL SOFTWARE

Figure 2 illustrates the features of CFGCTRL. CFGCTRL was conceptualized for ease of use during normal and emergency times. It is a menu-driven user-interface program written in QuickBasic Version 4.5, compiled with the QuickBasic compiler

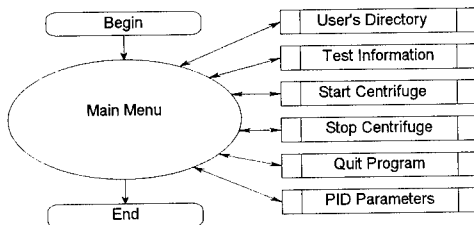


Figure 2. Flowchart of CFGCTRL

and linked to a firmware library (DASG16.LIB) supplied by Metrabyte Inc.. This library contains essential subroutines for driving the data acquisition card Metrabyte DAS16. A 80386DX33 PC is used to run CFGCTRL. CFGCTRL controls the entire centrifuge operation. Before a test commences, the operator logs the essential flight and test information, i.e., ramp-controlled acceleration, effective radius and payload, g-levels and elapsed

time, into the program which then interprets this information for command generation and control operations. All input data, including PID control gains, are saved in the files created by CFGCTRL for future retrieval. During flight, CFGCTRL essentially performs automatic control of the speed and monitoring of temperature sensors on-board the centrifuge and in the room and the system pressure of the hydraulic drive system. The test is terminated automatically when any of these parameters exceeds the desirable safety limits.

An interrupt service is available to allow the flight to be interrupted either during acceleration or steady-state g-level and let the operator log in a new set of data to override the current set. Multi-stage g-level execution capability (maximum 15 stages) within a test run enables centrifuge users to simulate varying loading forces within specified scaled time intervals set for each stage. Ramp-controlled acceleration time can also be preset for all stages.

### 4. PID CONTROLLER ALGORITHM

An introduction to the use of the PID controller can be found in Bollinger and Duffie (1988). Figure 3 shows the flow-chart for the PID algorithm.

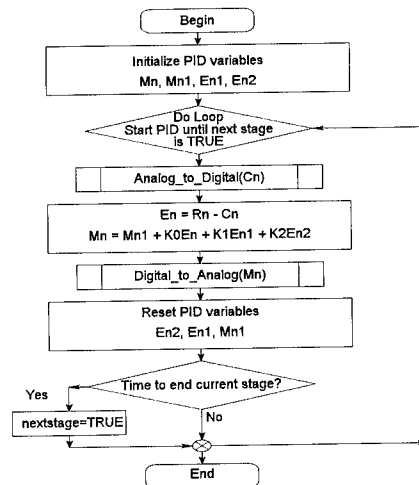


Figure 3. Flow-chart of the PID controller for one stage

The PID controller operates on an iterative scheme. The controller constantly adjusts the variables (in real time) to optimize the system's performance.  $R_n$

is the reference (or desired) value stored in the computer.  $M_n$  is the manipulated process input (in this case, the input into centrifuge).  $C_n$  is the process output (i.e., output from the centrifuge);  $E_n$  is the error, or steady state error, i.e.,

$$E_n = R_n - C_n \quad (1)$$

The PID controller is of the form,

$$M_n = M_{n-1} + K_0 E_n + K_1 E_{n-1} + K_2 E_{n-2} \quad (2)$$

where

$$K_0 = K_p + K_i T + K_d / T$$

$$K_1 = -K_p - 2K_d / T$$

$$K_2 = K_d / T \quad (3)$$

$K_p$  is the proportional parameter that performs correction to  $C_n$ , the feedback speed, in proportion to the error  $E_n$ .  $K_i$  is the integral parameter that performs correction to  $C_n$  proportionally to the time integral of  $E_n$ . The derivative parameter,  $K_d$ , performs correction to  $C_n$  proportionally to the derivative of  $E_n$  with respect to time.  $T$  is the sample period, defined as

$$T \approx T_s + T_c + T_o \quad (4)$$

$T_s$  is the time required to sample the feedback and is dependent on the sampling rate (10000Hz) of the DAS16 data acquisition.  $T_c$  is the time required to compute the manipulation.  $T_o$  is the time required to output the manipulation.  $K_p$ ,  $K_i$  and  $K_d$  need not be found analytically but can be obtained empirically. The method involves a simple tuning process that requires inputting an arbitrary initial non-zero value for  $K_p$  while fixing the rest at zero value (except  $T$  which can take any non-zero value when  $K_d=0$ ).  $C_n$  is closely monitored for the degree of instability or fluctuation at one or more designated g-level during flight. The operator either increases or decreases  $K_p$  to minimize the instability, in other words, optimizes the value of  $K_p$ , up to a point before  $K_i$  is introduced to further minimize the instability which may not be possible with  $K_p$  alone. The process of obtaining an optimised value for  $K_i$  is similar to  $K_p$ .  $T$  can be found approximately by calculating  $T_s$ ,  $T_o$  and  $T_c$ . Currently,  $K_p=1.067$ ,  $K_i=1.001$ ,  $K_d=0$  (disabled) and  $T(\text{approx.})=0.01\text{sec}$ . From instrumentation point of view, the advantage of this

empirical method is that it demands very little skill from a centrifuge operator.

## 5. PERFORMANCE OF THE CONTROL SYSTEM

The performance of the centrifuge's automatic closed-loop control system and the outcome of centrifuge modeling is determined by the steady state error  $E_n$  during flight.  $E_n$  gives an indication of the precise speed control (stability) of the centrifuge during steady g-level. The performance test described in the following paragraphs measured  $E_n$  for various designated g-levels (multi-stages) within one entire flight for different payloads (0kg, 130kg, 170kg). The choice of the last two payloads served as typical examples as many centrifuge models here were designed with payloads ranging from 100kg to 200kg. A typical run at 50g for manual control with 0kg payload was conducted to illustrate the problems encountered with manual mode.

For manual control, speed control was executed by turning a thumbwheel located on the centrifuge control box console. To monitor and record the feedback rpm ( $C_n$ ) and instantaneous time of flight, the f/V converter of the speed monitoring system was directly wired to a computer controlled data acquisition system located in the control room.

For automatic control, a modified CFGCTRL program was used to record the feedback rpm ( $C_n$ ) and the error feedback ( $E_n$ ) and saved into a data file. The entire flight involved ten different designated g-levels. Each stage of flight lasted 2 minutes. There was no need to run the test for long period (i.e., > 2 min.) to observe instability because from past experiences of running long hours, the PID controller was observed to be relatively robust (stable). From mechanical engineering point of view, any sudden surge or drop in speed attributing to the resistive torque of the centrifuge is not expected to occur.

Figure 4 shows three typical problems encountered with manual control: overshoot, non-uniform acceleration, decreasing speed. Overshoot arisen when, having accelerated up to the designated g-level, the large momentum propelled the centrifuge forward and hence bypassed the designated g-level. To correct for this demanded the skill of re-adjusting the thumbwheel in small turns with much caution. Hence, applications that require simulating varying

loading forces within a single run cannot be precisely executed. Non-uniform acceleration is attributable to the operator's skill. Decreasing speed at designated g-level is a stability problem owing to the centrifuge's high resistive torque which tended to slowed down the spin. The operator had to periodically monitor the speed and re-adjust the thumbwheel to correct the deviation. Consequently, in-flight consolidation requiring as many as 12 hours of continuous run demands the operator to be at the control console all the time to correct for any change in speed in addition to monitoring the temperature of the bearings and surroundings and the hydraulic pressure.

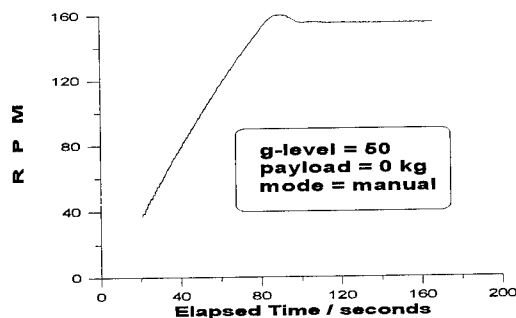


Figure 4. Graph of Cn versus Time at 50g for payload 0kg by manual control

Table 1 shows the performance results of the automatic closed-loop controller. The quantities calculated were fractional overshoot (in terms of g), time to reduce the overshoot, and mean fractional oscillatory amplitude (in terms of g). The fractional overshoot gives the g ratio of the overshoot to the designated g-level. The mean fractional oscillatory amplitude gives the g ratio of the fluctuations to the designated g-level long after overshoot had decayed.

Figure 5 shows a typical multi-stage's flight-control with payload 130kg. The controller was adept in handling overshoots problem by keeping the overshoot magnitude small within the shortest possible time. In comparing the overshoot for 0kg and 130kg payloads, it was observed that the overshoot decreased significantly with increased payload. One possible reason for this could be that the additional payload contributed to a higher inertia to counter overshoot. With 170kg payload, the overshoot appeared unchanged with respect to 130kg payload because the difference in the

additional weight was not sufficient to effect a further significant change.

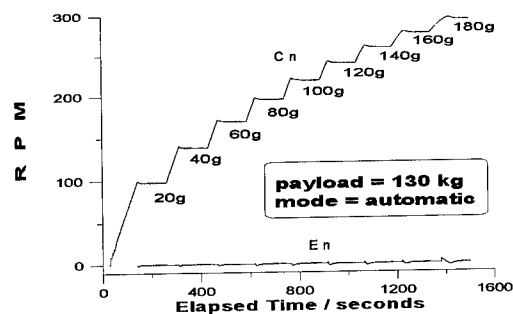


Figure 5. Graph of Cn & En versus time for payload 130kg by automatic control

The time to reduce the overshoot appeared to increase with increasing g. It was suggested that the presence of a large angular momentum at high g imposed a longer delay period to correct the overshoot. The time to reduce the overshoot was also observed to increase with increase payload. Intuitively, this is evident because a heavier payload presented a larger angular momentum and hence a longer delay period to correct the overshoot.

Speed fluctuations at designated g-level were observed to be small. Between 0kg and 130kg, it was further observed that the oscillatory amplitude decreased with the increase in payload. The additional payload counteracted and hence minimized this degree of freedom of motion. Between 130kg and 170kg, the difference in the payload was insufficient to effect any further significant change in the oscillatory amplitude. It was also observed that the oscillatory amplitude also decreased with increasing g value. This is evident because at high g, a large proportion of the momentum from the oscillatory motion was transferred to the forward momentum to maintain the high angular velocity.

In conclusion, without loss of generality, performance results indicated that: (1) Overshoot decreased significantly with increased payload, (2) Time to reduce the overshoot increased with increasing g value and with increased payload, (3) Oscillatory amplitude decreased with increased in payload and with increased in g value. For a centrifuge user, these conclusions could serve as

Table 1. Performance results of the automated centrifuge control system

g-level	20	40	60	80	100	120	140	160	180
<b>Payload = 0 kg</b>									
Overshoot $\Delta g/g$	0.019	0.022	0.018	0.015	0.014	0.030	0.030	0.025	0.015
Time (seconds) to reduce overshoot	5.16	5.34	5.71	13.57	8.45	24.49	37.07	40.60	48.00
Mean oscillatory amplitude $\Delta g/g$	0.0160	0.0060	0.0020	0.0070	0.0050	0.0010	0.0010	0.0010	0.0020
<b>Payload = 130 kg</b>									
Overshoot $\Delta g/g$	0.009	0.008	0.005	0.006	0.005	0.005	0.004	0.003	0.003
Time (seconds) to reduce overshoot	9.45	35.21	36.85	40.81	37.74	46.84	41.36	44.05	52.07
Mean oscillatory amplitude $\Delta g/g$	0.0004	0.0005	0.0004	0.0003	0.0002	0.0002	0.0003	0.0002	0.0003
<b>Payload = 170 kg</b>									
Overshoot $\Delta g/g$	0.009	0.006	0.005	0.006	0.005	0.005	0.004	0.004	0.004
Time (seconds) to reduce overshoot	19.61	31.42	34.77	38.55	33.34	44.55	41.19	49.54	67.61
Mean oscillatory amplitude $\Delta g/g$	0.0004	0.0005	0.0004	0.0003	0.0003	0.0002	0.0003	0.0002	0.0003

important considerations in the payload design and g-level when developing his centrifuge test model should he wish to ensure that there is an optimum trade-off between accuracy in the loading forces and his test requirements.

Lastly, stability of the controller sometimes degenerate with changes in the plant parameters. On the basis of experience and from the results shown in the table, to achieve good stability results during tuning would require one to ensure that: (1) Overshoot is less than 1.5g near the end of ramp-controlled acceleration, determines by  $C_n$ , (2) Maximum oscillatory amplitude is less than 0.5g at designated g-level, determines by  $E_n$ .

## 6. CONCLUSION

The foregoing is an overall presentation of an automated centrifuge control system. The PID controller is robust and has been shown to be able to execute precise control over the angular speed and angular acceleration. The software, CFGCTRL, performs secondary functions like monitoring the temperature of the surroundings and the bearings and the system pressure and automatically terminates the entire flight when these parameters exceeded desirable safety limits. Hence, centrifuge modelling applications such as long period in-flight consolidation and multi-stage g-levels simulating varying loading forces can be executed with minimum supervision. The conclusions drawn from the performance results regarding the payload design and desired g-level serve as important considerations

to the user should he require greater accuracy in modelling prototype soil stresses. Future modifications to the software to further improve the controller's performances by introducing an even more robust adaptive controller have been planned.

## ACKNOWLEDGMENTS

The author wishes to thank Drs F H Lee, C F Leung and T S Tan for initiating and supporting the development of the automated control system, Dr G S Hong for the advice on the technical design of the system, Mr C Y Wong for the feedback obtained from operating the system and Mr S H Goh for advice on the computing problems.

## REFERENCES

- Kutter, B.L., X.S. Li, W.F. Sluis & J.A. Cherney 1991. Performance and instrumentation of the large centrifuge at Davis. *Proc. Centrifuge 91*: 19-26. Rotterdam: Balkema.
- Nelissen, H.A.M. 1991. The Delft geotechnical centrifuge. *Proc. Centrifuge 91*: 35-42. Rotterdam: Balkema.
- Lee, F.H., T.S. Tan, C.F. Leung, K.Y. Yong, G.P. Karunaratne & S.L. Lee 1991. Development of geotechnical centrifuge facility at the National University of Singapore. *Proc Centrifuge 91*: 11-17. Rotterdam: Balkema.
- Bollinger, J.G. & N.A. Duffie 1988. *Computer Control of Machines and Processes*. New York: Addison-Wesley.

## Side friction effects in plane strain models

E. Khoo

*Engineering Division, Port of Singapore Authority, Singapore*

T. Okumura

*Department of Civil Engineering, Aichi Institute of Technology, Toyota-shi, Japan*

F.H. Lee

*Department of Civil Engineering, National University of Singapore, Singapore*

**ABSTRACT:** An important consideration in centrifuge modelling of plane strain problems is the minimisation of side friction and its spurious effects on model results. In the past, several researchers have reported on the need to eliminate side friction at model boundaries and the appropriate width to height (W/H) ratio of the model needed to eliminate the side friction effects. This paper examines the effectiveness of a proposed method to eliminate side friction in granular soil models. The proposed method consists of lining the sides with grease-treated polyethylene sheets. The study consists of two parts. In the first part, 1-g laboratory tests were carried out to determine the amount of side friction at the sand-concrete and sand-steel interfaces. In the second part, 100-g centrifuge model experiments were conducted to assess the effectiveness of the grease-treated polyethylene sheets to reduce side friction.

### 1 INTRODUCTION

In physical modelling, the model is invariably bounded by the container walls. These artificial boundaries can impose stress and displacement constraints on the model which do not exist in the prototype. To simulate plane strain conditions in centrifuge experiments, the two important boundary conditions of zero out-of-plane normal strain and zero in-plane shear stress must be fulfilled. Errors in the boundary conditions may have significant influence on the behaviour of model on granular soils.

Leung (1981) reported that failure lines in centrifuge model tests of continuous anchor tend to curve inward along the interface between the sand and glass. This effect was attributable to side friction between sand and glass. In addition, side friction introduced errors in the estimation of shape factors and rendered comparison of 1g model and centrifuge test results less definitive. Lee (1985) reported that, for sand embankment models subjected to earthquake loadings, side friction resulted in some differences between the response of the mid-span of the embankment and that of a section near the ungreased side window. The application of silicone grease appeared to reduce the friction somewhat resulting in closer agreement in response between the mid-span

and the side-span of the embankment. Santamarina and Goodings (1989) also observed side boundary friction effects in reinforced sand retaining wall models loaded to failure by increasing self-weight in a centrifuge. They recommended that, in order to minimise side friction effects, the appropriate model width (W) should be of the order of 4 times the model wall height (H) or more. From the above, it is evident that under certain circumstances, side friction can adversely affect the reliability of model results and significant improvement to the quality of data can be derived by minimising this friction.

In order to minimise side friction effects, Taniguchi et al. (1988) lubricated the side walls of the model container with a 100 µm thick layer of silicone grease. Furthermore, to prevent the soil from penetrating into the grease, a 0.2 mm thick latex membrane was placed between the greased wall and the soil model. This arrangement created a nearly frictionless interface between the rubber membrane and the wall. As the soil deforms, so does the rubber membrane. If the soil is stiff, the reinforcing effect of the rubber membrane is unlikely to be significant. However, if the soil is soft, the stiffness of the rubber membrane may significantly alter the deformation pattern of the soil near the sides. This paper examines a proposed interface arrangement for minimising side friction in a long and narrow plane



strain model. The study consists of two parts. In the first part, 1-g laboratory tests were performed to determine the angles of friction of different interfaces. This allows the interface with the lowest angle of friction to be identified. In the second phase, the selected interface was used in a series of centrifuge tests involving caisson models and its effects observed.

## 2 DETERMINATION OF ANGLE OF FRICTION VIA 1-G TESTS

Fig 1 shows the centrifuge container which will be used in the caisson experiment. As can be seen, three sides of the container are steel surfaces while the remaining side is a perspex window. In addition, the caisson model consists of concrete walls which will come into contact with the sand during the centrifuge experiments. Fig 2 shows the experimental setup used to determine the angles of friction of concrete-sand, steel-sand and perspex-sand interfaces. A shallow tray containing 50 mm of medium fine sand with properties shown in Table 1 was overlain by a concrete caisson whose weight can be adjusted by changing the amount of lead shot infill. By applying a horizontal load to the caisson and measuring this load at incipient continuous sliding, the angle of static friction at the interfaces can be determined. To measure friction at steel-sand interface, a steel caisson model was substituted for the concrete caisson. Similarly, the same applies for measuring friction at perspex-sand interface.

There is a slight difference between the conventional sliding block analysis of a mass slipping over a rigid base and this experimental setup. A rigid base will not deform and the total displacement observed is solely due to the sliding displacement at the interface. However, the sand layer at the base is not rigid and it will deform under the applied shear stresses transmitted from the model caisson via the interface. Uesugi and Kishida (1986) showed that the total displacement which occurred in such test consists of two components; namely the displacement due to the shearing deformation of sand mass ( $\delta_2$ ) and the sliding displacement along the contact surface ( $\delta_1$ ) before yield, see Fig 3. Thus lateral movement of the caisson will occur even before the interface static friction is fully mobilised. In order to account for this effect, the maximum resisting force is recorded at the onset of continuous lateral caisson movement. This is taken to be the static limiting frictional force at the interface.

Fig 4a shows the friction angles of concrete-sand, steel-sand and perspex-sand interfaces respectively. As can be seen, the friction angles of the concrete-sand, steel-sand and perspex-sand interfaces are about 20.3°, 14.3° and 11.8° respectively. Fig 4b shows the results from a complementary set of tests in which a layer of grease is applied directly on the base of concrete, steel and perspex to lubricate the surfaces. As can be seen, the use of grease alone to eliminate friction is relatively ineffective. This is attributable to the fact that sand particles can penetrate the grease and come in direct contact with the concrete/steel/perspex surfaces. To prevent this, the sand was separated from the surfaces by two layers of ultra-thin polyethylene sheets with a coating of grease in between. Whereas the rubber membrane possesses a certain degree of stiffness which may significantly affect the model behaviour under low effective stresses, the polyethylene sheets will tear easily under stresses to allow model deformation. This difference is likely to be significant near the soil surface where the effective stresses are low.

Fig 4c shows the corresponding 1-g test results for the proposed grease treated polyethylene sheet interface. As can be seen, the friction angle is reduced significantly with the proposed interface, thereby indicating that this interface is effective in reducing interface friction by a factor of about 2 from 20° to 10°. During these tests, it was observed that high normal stresses will cause the grease in the polyethylene sheets to be squeezed out. To reduce the expulsion of grease, a filler consisting of talc powder was added into the grease. This was found to be effective in reducing the expulsion of grease. However, as shown in Fig 4c, it also increases the friction angle somewhat.

## 3 100-G CENTRIFUGE MODEL TEST

Two centrifuge model configurations were tested for the effectiveness of the greased-polyethylene arrangement. One consist of dry sand and the other which is saturated with water under which both untreated sides and treated sides of the container walls were tested. Data of the two treated and untreated models were compared to study the effects of side friction on model behaviour.

Fig 5 shows the schematic of the centrifuge model which was used to study the effects of side friction under dry conditions. A model concrete caisson [B2] was founded on a layer of 150 mm-thick of sandbed [B1]. Sand backfill was pluviated behind the caisson from a sand-hopper at 100g. The side walls of the

Table 1 : Properties of sand

Minimum void ratio	0.64
Maximum void ratio	0.99
D <sub>10</sub>	0.23
Coefficient of Uniformity	1.83

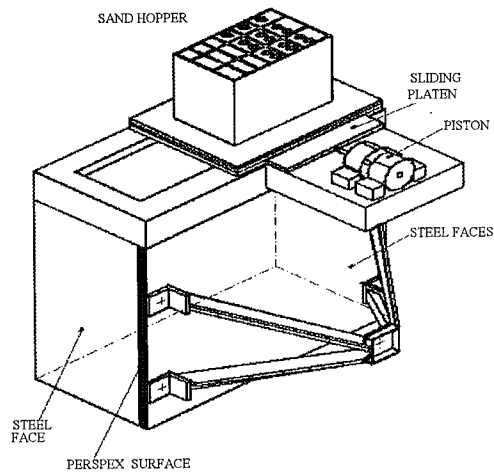


Fig 1 : Isometric View of Strongbox

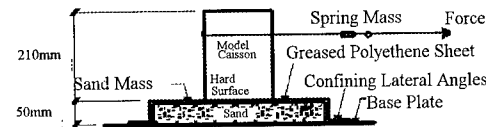
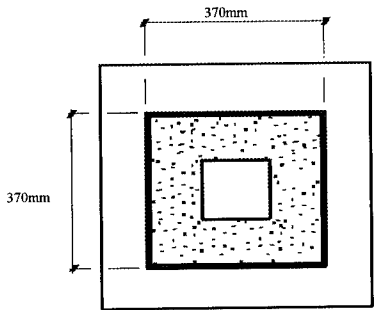


Fig 2 : Apparatus Setup to determine side friction

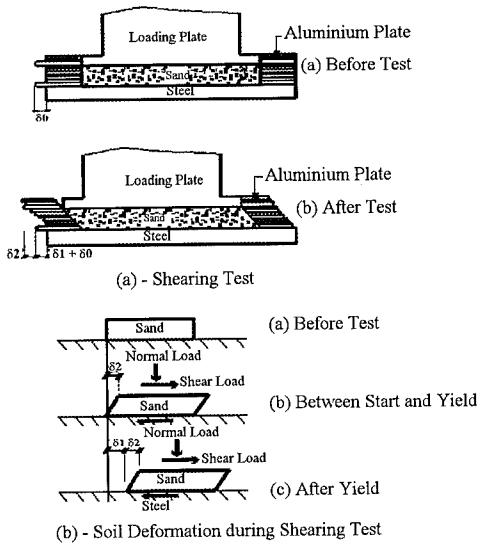


Fig 3 : Schematic Diagram of Shearing Process

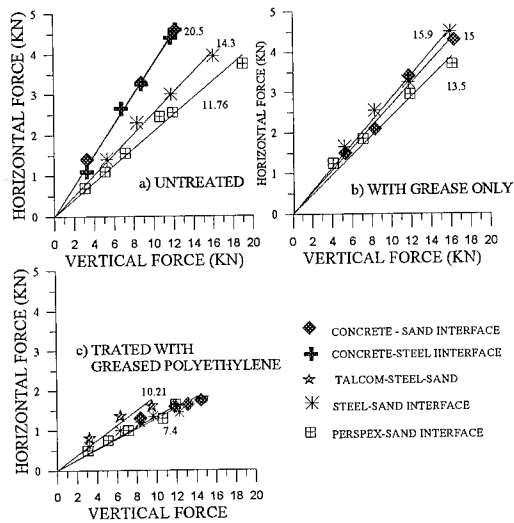
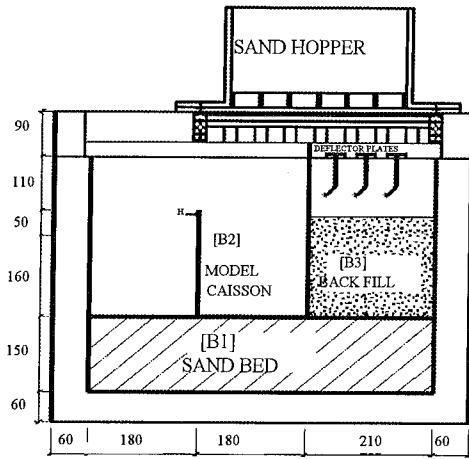
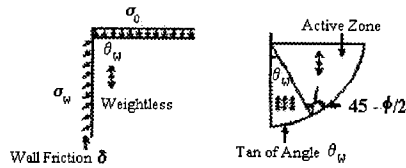


Fig 4 : Friction Angles of Various Interfaces



H : HORIZONTAL DISPLACEMENT TRANSDUCER

Fig 5 : Setup of Centrifuge Experiment for Testing with dry sand



Lower Bound To Plastic Collapse

$$\begin{aligned} \text{Eqn 1} \quad \theta_w &= 1/2 (\sin^{-1}[\sin \delta / \sin \phi] - \delta) \\ \text{Eqn 2} \quad K(\delta, \phi) &= \left[ \frac{1 - \sin \phi \cos 2\theta}{1 - \sin \phi} \right] e^{(-2\theta_w \tan \phi)} \\ \text{Eqn 3} \quad K_n &= K(\delta, \phi) \cos \delta \end{aligned}$$

Fig 6 : Schematic of Free Body Diagram showing the forces acting on Caisson (After Bolton 1993)

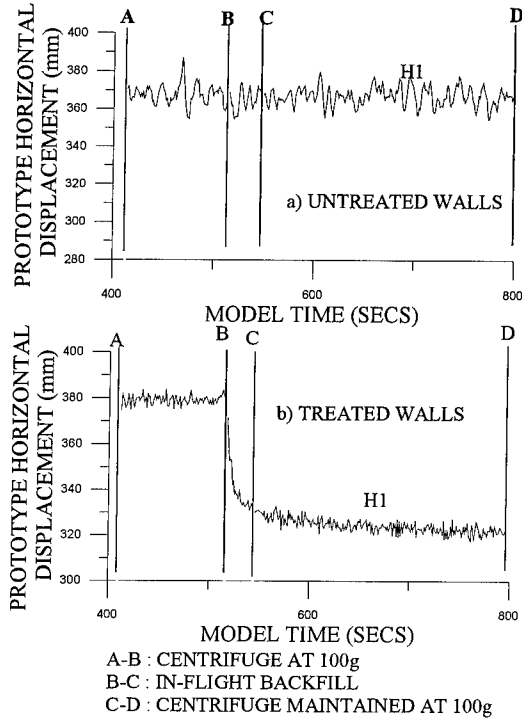
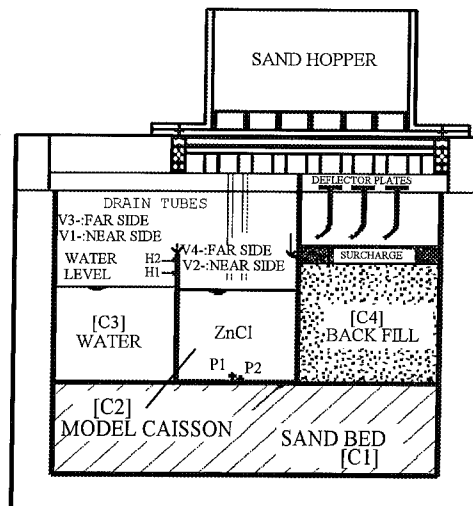
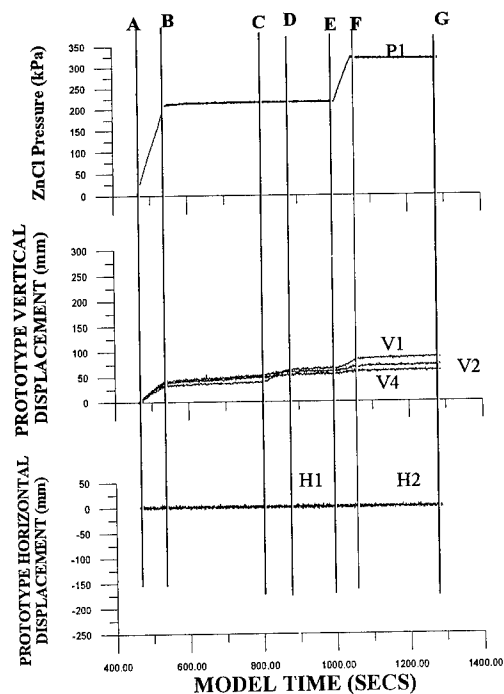


Fig 7 : Model Response for Untreated and Treated sidewalls (Relative Density = 70%)



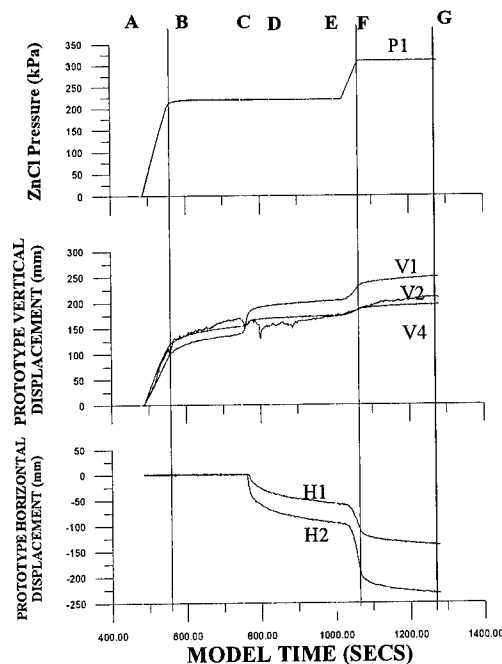
P : PRESSURE TRANSDUCER  
V : VERTICAL DISPLACEMENT TRANSDUCER  
H : HORIZONTAL DISPLACEMENT TRANSDUCER

Fig 8 : Setup of Centrifuge Experiment for testing with Saturated Sand



A-B : INFILLING OF CAISSON  
C-D : BACKFILLING BEHIND CAISSON  
E-F : LIVE-LOAD ON CAISSON

Fig 9 Model Response for Untreated Sidewalls  
(Relative Density = 50%)



A-B : INFILLING OF CAISSON  
C-D : BACKFILLING BEHIND CAISSON  
E-F : LIVE-LOAD ON CAISSON

Fig 10 : Model Response for Treated Sidewalls  
(Relative Density = 50%)

strongbox were then either treated with the greased polyethylene interface or left untreated respectively. The sandbed was prepared dry by pluviating sand into the container. The empty caisson was then placed on top of the sandbed. A rubber gasket was placed behind the caisson to seal the gap between caisson walls and container side wall so as to prevent leakage of sand from the backfill into the gap between the container and side walls. A LVDT was placed in front of the caisson on the seaward side. Deflector plates for controlling the trajectory of the sand backfill during the in-flight pouring were placed behind the caisson and positioned directly below the sand hopper. The container was placed onto the centrifuge platform and the sand-hopper frame was attached to the container. The centrifuge was then accelerated to the 100g model gravity. Sand was then released from the sand hopper into the backfill area behind the caisson to simulate the creation of landfill behind the prototype caisson. The movements of the caisson during the in-flight construction were monitored and recorded by a horizontal LVDT.

Based on plasticity methods, Bolton (1993) obtained a lower bound solution for the plastic collapse as shown in Fig 6. Using this solution, the model factor of safety was estimated to be about 1.14. As the factor of safety is quite close to unity, caisson movements are to be expected. Fig 7 shows the horizontal movements of the caisson converted to equivalent prototype values. The release of sand backfill into the container is depicted by the segment [CD]. As can be seen, almost negligible horizontal movement was recorded in the test for the untreated walls while 55 mm of horizontal displacement was recorded in the test for the treated walls.

Fig 8 shows the schematic of the centrifuge model which was used to study the effects of side friction under saturated conditions. The geometry and dimensions of the sandbed, caisson and backfill are identical to those of the dry model. An additional 30 mm thick layer of sand is pluviated on top of the backfill in-flight to account for the imposition of surcharge loads. The free water surface extends 160 mm from the top of the sandbed [C1]. The saturated

sandbed [C1] was prepared by pluviating sand through de-aired water. The degree of saturation is not significant in this test as the loading rate is slow enough for drained conditions to prevail. The model caisson [C2] was then gradually lowered onto the sandbed. De-aired water was then siphoned into the model container until the water level was 160 mm above the top of the sandbed [C3]. Three stages of loading were applied to the caisson in-flight as shown in Fig 8 and 9. The first was the ballasting of the caisson [CD] by in-filling it with heavy zinc chloride solution (ZnCl<sub>2</sub>). This was followed by the in-flight release of sand backfill behind the caisson [EF] to simulate the reclamation of land behind the caisson. Finally, additional ZnCl<sub>2</sub> was released into the caisson [GH] to simulate the imposition of live loads on the caisson during service.

As shown in Fig 9 and Fig 10, caisson movements of the model with treated walls are much greater than those of the model with untreated walls during all three stages of loading. The results show that there were significant differences in behaviour between model caissons with the greased treated polyethylene interface and those without.

#### 4 CONCLUSION

Based on the findings of the 1-g tests, it is concluded that the use of grease alone is ineffective to eliminate friction between concrete-sand, steel-sand and perspex-sand interfaces. The proposed greased polyethylene interface was found to reduce significantly the friction at the respective interfaces. The findings of the 100-g tests confirmed that side friction at the container walls may affect the results of narrow plane strain models significantly. The proposed greased polyethylene interface herein appears to be effective in reducing the side wall friction substantially.

#### ACKNOWLEDGEMENT

The authors would like to express their gratitude to the Port of Singapore Authority for the permission to publish this paper. They would also like to acknowledge Dr. C.F. Leung and Mr. C.Y. Wong for their contributions during these experiments.

#### REFERENCES

- Bolton, M.D. 1993. Private Communications
- Khoo, E. Leung, C.F., Lee, F.H. and Toh, A.C. 1993. Centrifuge model study of caisson foundation. Proc. of 11th Southeast Asia Geotechnical Conference, Singapore, pp.559-564, Singapore.
- Lee, F.H. 1985. Centrifuge modelling of earthquake effects on sand embankments and islands, PhD Thesis, University of Cambridge.
- Leung, C.F. 1981. The effects of shape, size and embankment on the load-displacement behaviour of vertical anchors on sand, PhD Thesis, University of Liverpool.
- Leung, C.F., Khoo, E. and Toh, A.C. 1994. Displacement of gravity caisson resting on sandbed, Proc. of the International Conference Centrifuge 1994, Singapore.
- Santamarina, J.C. and Goodings, D.J. 1989. Centrifuge modelling: a study of similarity. Geotechnical Testing Journal, ASTM, Vol. 12, pp. 163-166.
- Taniguchi, E., Koga, Y., Morimoto, I., and Yasuda, Y. 1988. Centrifugal model tests on reinforced embankments by non-woven fabric. Proceedings of the International Conference on Geotechnical Centrifuge Modelling, Paris. pp 253-258.
- Uesugi, M. and Kishida, H. 1986. Influential factors of friction between steel and dry sands, Soils and Foundations, Vol 26, No.2, pp.33-46.

## Techniques for saturating sand with oil

Y.S. Hsu, C.H. Collison & E.T.R. Dean  
*University of Cambridge, UK*

R.G. James  
*Andrew Schofield and Associates, Cambridge, UK*

**ABSTRACT:** To ensure consistency of inertial time scaling and pore pressure dissipation time scaling in sand models tested at  $N_g$  centrifuge gravities, oil of viscosity  $N$  times that of water may be usefully employed as a pore fluid. In preparing an oil-saturated sand sample it is essential to ensure that all air is removed from the dry sample and from any instruments within it before introducing the oil, and to ensure that oil entry is sufficiently slow that it does not do mechanical damage to the sample. This paper describes an apparatus developed at Cambridge to achieve this, involving a new procedure of heating under vacuum of both the sand sample and the oil prior to saturation.

### 1. INTRODUCTION

Numerous centrifuge modelling studies into the drained response of circular spud footings have been conducted in Cambridge University. Model foundations both on sand and clay have been subjected to vertical, horizontal and moment loading, by applying a horizontal monotonic or cyclic loading to a model jack-up structure or an individual spud-can foundation. The work includes studies performed by Silva Perez (1982), Lau (1988), Shi (1988), Tan (1990) and more recent industrially sponsored work, Murff, Hamilton, Dean, James, Kusakabe, and Schofield (1991), Dean James, Schofield and Tsukamoto (1992). These numerous projects are related to jack-up platforms. These are offshore structures not piled to the sea bed or equipped with a bottom mat. They usually consist of a hull and three legs, or a multi-pod with spud cans as foundations. A typical large spud geometry is shown in Fig. 1.

These studies suggest that the bottom fixity provided by spud-can foundations could possibly justify economies in the use of certain jack-up structures in deeper or/and more exposed water. However, these were not studies in which there were excess pore pressures generated under the spud-cans. Pore pressures in the foundation soil

under extreme wave loading conditions may be:

1. positive excess pore pressure, leading to weakening of the soil and in severe cases causing partial liquefaction, or alternatively

2. suction, especially in dense soil, that will temporarily strengthen the foundation soil.

Presently, numerical models are used to predict pore pressure generation. It is very difficult to place pore pressure transducers under spud-cans in the field.

The most practical way of verifying pore pressure generation is the use of centrifugal modelling. A preliminary study by Dean (1991) provided an initial framework of analysis, which suggested that there should be some further experimental studies of the effect of pore pressure transients on spud fixity. The main objective of the centrifuge tests is to produce pore pressure data of the behaviour of scaled model jack-up spud-cans founded on sand and subjected to cyclic loading. Under normal circumstances, in which the same soil and the same pore fluid occurs in both model and full-size prototype, drainage time in the centrifuge occurs  $N^2$  times faster than the prototype (where  $N$  is the geometric scale factor i.e. the g-level applied to the model). For these tests, however, we need to slow down the diffusing process in the model, so that practical loading rates can be achieved. Thus,

we employ viscous oil as the pore fluid instead of water. The oil viscosities required for these tests, and the volumes of soil involved, were significantly greater than for previous tests in which oil had been used (Lee for example, Lee and Schofield (1988)). This paper outlines the apparatus developed at Cambridge, involving a new procedure of heating under vacuum of both the sand sample and the oil prior to saturation.

## 2. DESCRIPTION OF APPARATUS

Fig.2 illustrates the general arrangement of the apparatus for the saturation of a sand sample with oil, related to the study of excess pore pressure under model spud-can foundations.

### 2.1 Silicone oil

The oil used in this series of centrifuge tests is 200 centistokes (at 25°C) silicone oil. Silicone oil is a relatively inert fluid with a specific gravity of 0.97 (at 25°C/15.6°C). The viscosity remains constant at a given temperature. However, the viscosity of silicone oil varies significantly with temperature. Tests were thus conducted using a viscometer to ascertain the effect of the temperature on the viscosity. This was also checked with the specification provided by the supplier. Generally, the more viscous the oil, the slower would be the rate of saturation. To increase the rate of saturation to a practical level, the temperature of the soil sample and the oil entering the sample is heated up to 75°C with the use of a water bath. At that temperature, the viscosity of the 200 centistokes (at 25°C) silicone oil will have fallen to about 70 centistokes.

### 2.2 850 mm diameter tub and water tank

An 850 mm diameter tub (400 mm depth) is used for this particular series of centrifuge tests. A pressure lid is available such that when sealed against the top of the tub a vacuum can be applied to the tub and its contents. The tub and pressure lid were designed to safely resist the external pressure exerted when a vacuum of 30" mercury is applied inside the tub. A water tank made up of steel plates welded together lagged with rock

wool and hardboard acts as a water bath accommodating the tub during saturation. Industrial convection water-heaters with three phase AC voltage supply are installed near the bottom of the water bath.

### 2.3 Sand

The sand used is 100/170 Leighton Buzzard sand. A summary of the properties of the sand is shown in Table 1. Comparison triaxial tests between water and oil saturated sand was conducted by Eyton (1982) and Bielby (1989). It was concluded that oil saturated sample show maximum shearing angles ( $\phi_{max}$ ) of around 2° lower and critical shearing angles ( $\phi_{crit}$ ) of around 1.5° lower than the corresponding water saturated specimens.

Table 1 Summary of the properties of 100/170 Leighton Buzzard sand.

<u>Leighton Buzzard 100/170 Sand</u>	
D <sub>10</sub> grain size	0.095 mm
D <sub>50</sub> grain size	0.14 mm
D <sub>60</sub> grain size	0.15 mm
Specific Gravity G <sub>s</sub>	2.65
Minimum Voids Ratio e <sub>min</sub>	0.613
Maximum voids Ratio e <sub>max</sub>	1.014
Permeability to water (e=0.72)	0.98E-4 m/s
Estimated Angle of Shearing Resistance at	
Critical State $\phi_{crit}$	32°

### 2.4 Pore pressure transducers

Miniature pore pressure transducers manufactured by Druck Ltd were used to measure the variations in the fluid pressure. It is essential to position the pore pressure transducers under each spud-can in such a way that the characteristics of the pore pressure generation in the soil surrounding the spud can are captured. The leads for the pore pressure transducers are often coiled into a circular bundle after each centrifuge test, resulting in the leads having the tendency to curl up when resting on a flat surface. Thus it was difficult to place the pore pressure transducer at a specified position. In the first centrifuge test, one of the pore pressure transducer positioned about 30 mm below the sand surface floated up to the surface.

In the subsequent tests, to ensure that the pore pressure transducers will remain in the intended positions, some steps were taken to reduce this effect. Instead of coiling the leads into a circular bundle after a centrifuge test, the pore pressure transducer leads are straightened and strapped to an open slot trunking with cable ties.

## 2.5 Pressure vessel, oil container and other accessories

The oil flows from a container, which is open to the atmosphere, to an evacuated pressure vessel, and then via pipes to oil inlet holes at the base of the 850 mm diameter tub. The function of the evacuated pressure vessel is to remove all the air from the silicone oil before the oil enters the tub. A pressure gradient is created between the pressure vessel and the tub using a fine vacuum tuner.

The oil container is open to the atmosphere and the weighing machine allows measurement of the amount of oil entering the pressure vessel. It is used to supply oil to the pressure vessel via a needle valve which controls the pressure difference between the pressure vessel and the tub.

Vacuum gauges are used to monitor the pressures at the different components of the vacuum system. They are also used to ensure that the appropriate pressure gradient between the tub and pressure vessel is maintained. This also allows the rate of oil flow in to the tub to be controlled.

## 3. OIL SATURATION PROCEDURE

Fig. 3 shows a flowchart illustrating the oil saturation procedure.

### 3.1 Placing of sand and pore pressure transducers

In this experiment, fine sand is pluviated from a hopper into the 850 mm diameter tub. The height of pluviation and the flow rate of hopper are adjusted depending on the sand density required. The pouring of sand is interrupted only by the placing of pore pressure transducers at the appropriate depth from the top of the tub. As mentioned in section 2.4, the leads are

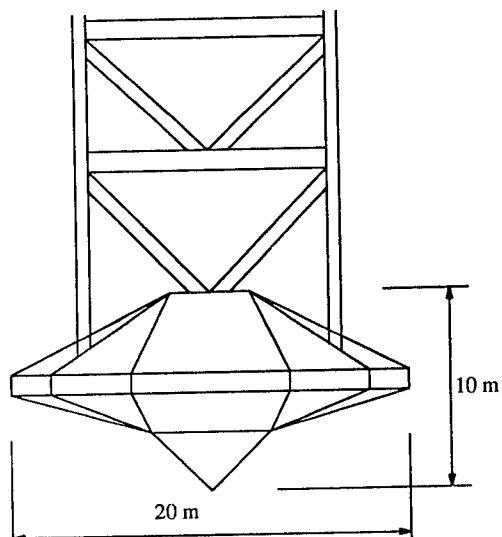


Fig. 1 Spud-can Geometry

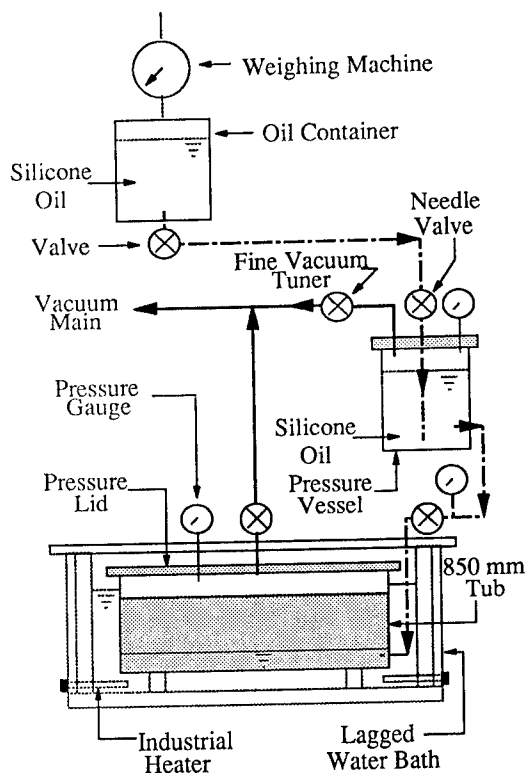


Fig. 2 General Arrangement of Apparatus



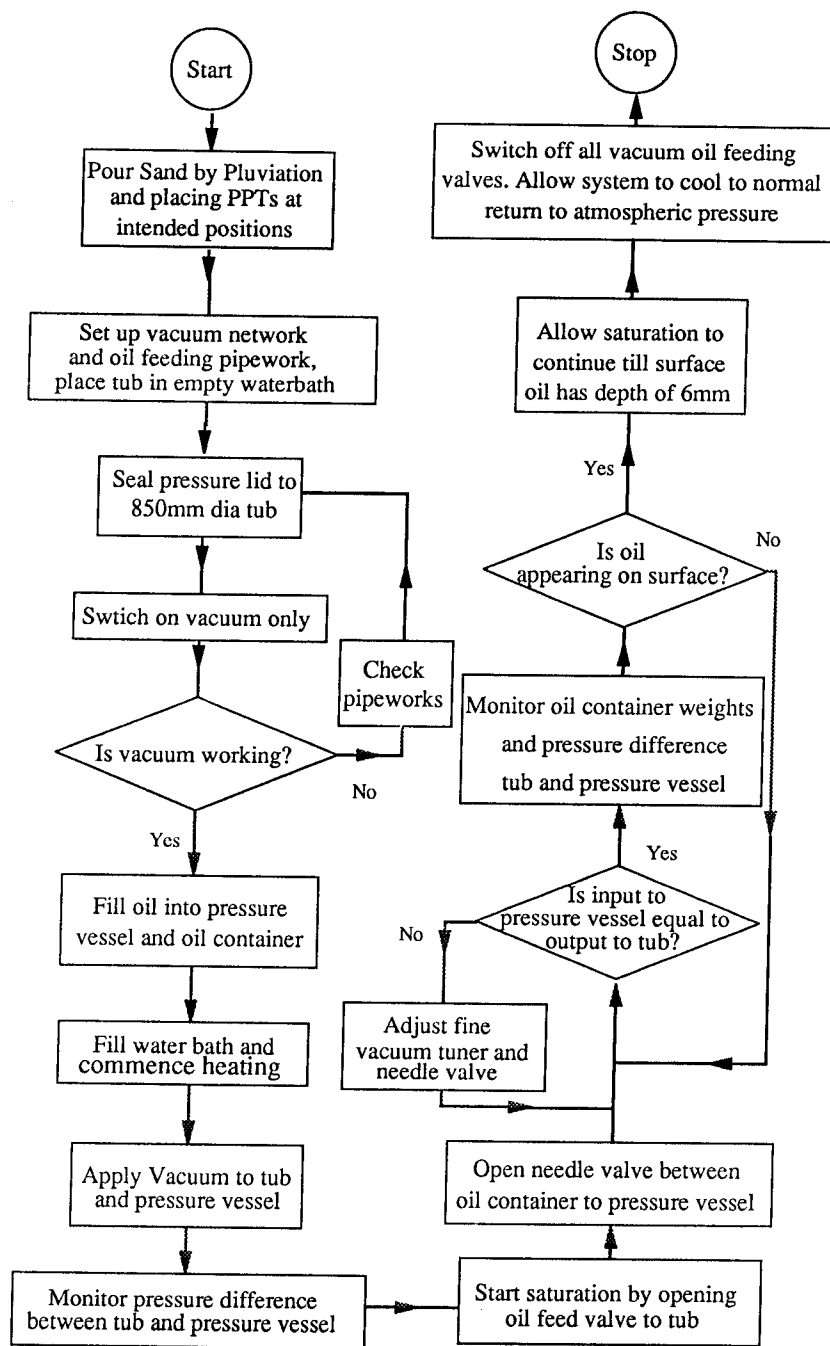


Fig. 3 Flowchart of Oil Saturation Process

straightened using an open slot trunk. The lead will still curl a bit, the part of the lead closest to the tub wall is moved until the transducer is stationary over the intended position, a cable tie is attached and the lead held firmly to the wall. When all pore pressure transducers at the specified depth are placed, the sand pouring operation continues.

### 3.2 Initial check

The plugs of the pore pressure transducers are put into a plastic bag which is then sealed. This is then placed into a container which rests on the sand sample at a location remote from the model jack-up test site. The pressure lid is sealed over the mouth of the tub and the vacuum system is then set up. Isolating the pressure vessel, a vacuum is applied to the tub to check for leaks. When inspection shows no leak, the tub pressure is allowed to return to atmospheric very slowly.

### 3.3 Saturation process

Subsequently, the oil feeding system is connected up as shown in Fig.2. The tub with the sample and pressure lid is moved into the water tank. The water tank is then filled with water and the temperature raised to 75°C. The pressure vessel is filled with silicone oil and the vacuum for both the tub and pressure vessel is initiated to evacuate all air before oil feeding. The fine vacuum tuner is used to control the vacuum so as to ensure that there is a pressure gradient between the tub and the pressure vessel. It is adjusted such that the rate of flow from the pressure vessel to the tub is maintained at constant practical level and also to prevent partial or localised liquefaction of the sand sample.

The needle valve is opened to fill the pressure vessel, ideally, the valve should be adjusted to ensure that quantity entering the tub is equivalent to that entering the pressure vessel. However, this is difficult to achieve. The oil feeding process is monitored by the weighing the oil container feeding the pressure vessel. If there is no leakage, the oil feeding process could be left unattended except when refilling of the oil container is required. The oil feeding is stopped when the oil surface (seen through laminated polycarbonate

windows in the lid of the 850 mm diameter tub) is more than 6 mm above the sand surface. Then the vacuum is switched off and all the valves are closed. The tub and pressure vessel are allowed to slowly return to atmospheric pressure.

It is also helpful to preheat the oil before entering the tub by circulating hot water through a pipe work system with the oil pipes fastened to it.

## 4. RESULTS AND DISCUSSION

The vacuum system evacuates the air from the silicone oil before the oil enters the tub and flows into the sand. This allows a high degree of saturation to be achieved. In all the tests conducted, the estimated degree of saturation attained from the sand sample is about 98%. This is calculated from the measured volumes and measured weights of sand particles and silicone oil used.

All the pore pressure transducers are also sufficiently de-aired ensuring the sensitivity of the pore pressure transducers are not affected by the presence of air.

To prevent partial and local liquefaction, the rate of flow has to be sufficiently slow. The temperature is raised to 75°C to ensure that period of saturation can be reduced to a week without causing 'piping' of the sand specimen.

This method of saturation is suitable for both loose and dense samples. Post test investigation shows that the positions and depths of the pore pressure transducers were close to the intended locations. The effect of drawing air out of the sand specimen did not cause any significant settlement. However, in the case of loose samples, there is a significant settlement after the saturation process. This is most probably be due to the vibration and movements induced when moving the tub into the water tank. To investigate the possible problem of induced settlement due to application of vacuum in loose samples, a brass container 85 mm diameter and 122 mm depth is filled with a loose sand sample. A rigid rig with a linear variable displacement transducer (LVDT) attached, is then placed over the container so as to measure the settlement when a vacuum is applied. The container and its accessories are then placed in a desiccating glass chamber and a vacuum is applied at different rates. The results showed no settlement of the sand sample.

## 5. CONCLUSION

In the preparation of saturated soil samples for a centrifuge test, it is an essential requirement to ensure that the air within the dry soil samples, and in any instruments installed like pore pressure transducers, and in the pore fluid, is evacuated satisfactory before introduction of the pore fluid. In many cases, where the study of excess pore pressure generation, like beneath spud-can foundations, or in earthquake tests, viscous silicone oil may be employed as the pore fluid to slow down the rate of diffusion and dissipation. By doing so, the fluctuations and possible build-up of pore pressure can be captured and analysed. This paper describes a process of heating and saturating the sand sample with silicone oil under vacuum. This method produced samples with a high degree of saturation, ensuring that the instruments would be satisfactorily de-aired and that the oil entry was sufficiently slow to prevent partial or local liquefaction of the samples. The process is effective for both loose and dense sand samples. In the case of loose samples, the method of transporting and placing the tub in the heater has to be free from shocks and vibrations to ensure that the sample will not settle significantly.

## ACKNOWLEDGEMENTS

We would like to thank Professor A.N. Schofield for his comments and the Cambridge University Engineering Department (CUED) staff members involved in the oil saturation process, in particular J.A. Chandler, A. Else and P. Ford. We would also like to thank J.A. Curtis of Andrew N. Schofield and Associates Ltd. (ANS&A) and R. Philips of the Centre of Cold Ocean Research Engineering (C-Core), Canada.

## REFERENCES

- Bielby, F. 1989. Triaxial tests on oil saturated sand. Part 2 Project Report. Cambridge University Engineering Department
- Dean, E.T.R. 1991. Some Potential Approximate Methods for the Preliminary Estimation of Excess Pore Pressures and Settlement-Time Curves for Submerged Circular Spud Foundations subjected to Time-Dependent Loading. Technical Report CUED/D-Soils/TR240. Cambridge University Engineering Department.
- Dean, E.T.R., James, R.G., Schofield, A.N., and Tsukamoto, Y. 1992. Combined Vertical, Horizontal, and Moment Loading of Circular Spuds on Dense Sand Foundations: Data Report for Drum Centrifuge Model Tests YT1-1L-A thru-G and YT2-1L-G thru-V. Technical Report CUED/D-Soils/TR244. Cambridge University Engineering Department.
- Eyton, D.G.P. 1982. Triaxial Tests on Sands with Viscous Pore Fluid. Part 2 Project Report. Cambridge University Engineering Department.
- Lau, C.K. 1988. Scale Effect in Tests on Footings. Ph.D. Thesis. Cambridge University.
- Lee, F.H. and Schofield, A.N. 1988. Centrifuge Modelling of Sand Embankments in Earthquakes. *Geotechnique* 38(1): 45-58.
- Murff, J.D., Hamilton, J.M., Dean, E.T.R., James, R.G., Kusakabe, O. and Schofield, A.N. 1991. Centrifuge Testing of Foundation Behaviour using Full Jack-up Rig Models. Paper OTC6516. *Offshore Technology Conference*.
- Shi, Q. 1988. Centrifugal Modelling of Surface Footings subject to Combined Loading. Ph.D. Thesis. Cambridge University.
- Silva Perez, A.A. 1982. Conical Footings under Combined Loads. M.Phil. Thesis. Cambridge University.
- Tan, F.S.C. 1990. Centrifuge and Theoretical Modelling of Conical Footings on Sand. Ph.D. Thesis, Cambridge University.

## Effect of pore fluid in dynamic centrifuge modelling

S.P.Gopal Madabhushi

Wolfson College, Department of Engineering, Cambridge, UK

**ABSTRACT:** In the last decade dynamic centrifuge modelling has emerged as a powerful technique for studying the seismic response of various civil engineering structures. In a dynamic centrifuge test involving saturated soil modelling of the pore fluid is very important. Use of high viscosity silicone oil as the pore fluid models the inertial effects and the consolidation effects satisfactorily. In this paper the effect of the change in pore fluid on the dynamic characteristics like damping will be considered. A pair of centrifuge tests on a model tower structure founded on saturated sand bed with identical geometry but with different pore fluids will be studied. The components of damping involved in such a centrifuge model will be explained. By comparing the damping in such a pair of centrifuge tests it is possible to isolate the effect of the pore fluid on damping. Based on the results obtained from two pairs of such tests it will be concluded that the damping is rather less sensitive to the viscosity of pore fluid thus justifying the use of high viscosity pore fluids in the centrifuge tests.

**KEYWORDS:** centrifuge modelling, earthquakes, excess pore pressures, pore fluid, damping, tower structures

### 1 INTRODUCTION

Use of geotechnical centrifuges to study the dynamic behaviour of complex soil structure interaction problems has been established as a powerful technique in the past decade. At the Cambridge University a wide variety of soil-structure interaction problems were studied using the 10 m diameter beam, Schofield (1981) and Steedman (1991). The bumpy road actuator described by Kutter (1982) was used to simulate earthquake loading on the centrifuge model in flight. One of the problems that has been investigated was the generation of excess pore pressures in saturated sands subjected to earthquake loading. The cyclic shear stresses induced by strong ground motion will result in the densification of an initially loose soil deposit. In the absence of sufficient time as in an earthquake episode this will lead to generation of excess pore pressures in a saturated soil layer resulting in the lowering of effective stress. During a sufficiently strong ground motion this may result in a very low effective stress causing one or other phenomena of liquefaction. The mechanisms leading to failure during strong ground motion have been studied for various engineering problems. For example, Schofield and Lee (1988) have observed the decoupling of the crest of the embankment on a saturated sand bed from the base motion due to large excess pore pressures. Schofield and Steedman (1988) suggested that the excess pore pressures may lead to a degradation in soil stiffness which may bring a soil structure system close to its resonant frequency. Madabhushi and Schofield (1993) have observed that the excess pore pressures under a tower structure may result in the lowering of the natural frequency of the tower-soil system to one of the driving frequencies of the earthquake where its energy is concentrated.

In many of these studies it was important to use a pore fluid which was more viscous than water to satisfy the scaling laws of the centrifuge modelling accurately. At the Cambridge University the pore fluid of a saturated soil in a centrifuge test conducted at 'ng' would be silicone oil which is blended to have a viscosity of 'n' centistokes. More recently high viscosity glycerine was used as pore fluid in the centrifuge tests conducted at the RPI, USA. In this paper the effect of using high viscosity pore fluid on the dynamic characteristics like damping in soil will be investigated.

### 2 SCALING LAWS

A set of scaling laws were established to relate the centrifuge model behaviour and the prototype behaviour, Schofield (1980, 81). In table 1 some of the scaling laws applicable to dynamic centrifuge modelling are presented. In a centrifuge model the stresses and strains will be the same as in an equivalent prototype giving the model to prototype ratio for these quantities of 1 in table 1. The frequency of a dynamic event like an earthquake episode in a model must be 'n' times that of a prototype event that we seek to model. Thus an earthquake which has a frequency range of 1 to 5 Hz in the field can be represented in a centrifuge test at 80g by a model earthquake with a frequency range of 80 to 400 Hz. In Cambridge the bumpy road actuator can fire earthquakes with a frequency of 120 Hz in a 80 g which represents a prototype earthquake with a frequency of 1.5 Hz. As a result of the frequency scaling law the time in a dynamic event must have its scaling law as '1/n' (see table 1).

A different time dependent phenomenon is the dissipation of pore pressure in a consolidation process governed by the

Table 1 Scaling laws

Parameter	Ratio of model to prototype
Length	1/n
Area	1/n <sup>2</sup>
Volume	1/n <sup>3</sup>
Stress	1
Strain	1
Force	1/n <sup>2</sup>
Velocity	1
Acceleration	n
frequency	n
time (dynamic)	1/n
time (consolidation)	1/n <sup>2</sup>

differential equation

$$\frac{\partial^2 u}{\partial^2 x} + \frac{\partial^2 u}{\partial^2 x} + \frac{\partial^2 u}{\partial^2 y} = \frac{1}{C_v} \frac{\partial u}{\partial t} \dots (1)$$

where  $C_v$  is the coefficient of consolidation. This coefficient is same for the model and the prototype if the same soil is used. Considering the left hand side of Eq.1 we can derive that

$$\frac{\nabla^2 u_{\text{model}}}{\nabla^2 u_{\text{prototype}}} = n^2 \dots (2)$$

The right hand side of Eq.1 must be equal to  $n^2$  to satisfy Eq.1 for the prototype and the model.

$$\left( \frac{1}{C_v} \frac{\partial u}{\partial t} \right)_{\text{model}} = n^2 \dots (3)$$

$$\left( \frac{1}{C_v} \frac{\partial u}{\partial t} \right)_{\text{prototype}}$$

which gives the scaling law for time during a consolidation process as  $1/n^2$ . In fact this scaling law is exploited in a large number of centrifuge tests involving clays to model events lasting up to 6 years in the field. However in a dynamic centrifuge test this scaling law is in conflict with the scaling law for the time of a dynamic event. This discrepancy can be avoided

- i) either by using a pore fluid whose viscosity is 'n' times the normal viscosity
- ii) or by using reduced size particles to make the model soil less permeable than the prototype soil.

If reduced size particles were to be used in a centrifuge model then the effect of this on the stress-strain behaviour of soil must be investigated. At the Cambridge University the method suggested in item i) is preferred and high viscosity silicone oil was used as explained earlier. Eyton (1982) conducted laboratory tests on different soils with silicone oil as pore fluid

and based on his study stated that the change of pore fluid has insignificant effect on the stress-strain behaviour of soil. However there was some concern that the use of high viscosity silicone oil may alter some of the dynamic characteristics of the model such as damping. Bolton and Wilson (1990) have carried out resonant column tests on sands saturated with the silicone oil and water. They have suggested that the material damping in the soil can be considered as hysteretic and viscous damping.

In this paper the effect of pore fluid on damping will be investigated. Identical centrifuge tests with a model tower founded on a saturated sand bed with water and silicone oil as pore fluids will be considered. Such a pair of centrifuge tests may be termed as conjugate centrifuge tests. In Fig.1 the schematic diagram representing the centrifuge model for all the tests considered in this paper is presented. The structure is a top heavy model tower. The rocking mode of vibration is induced in such a tower when the centrifuge model is subjected to lateral shaking. The horizontal sand bed constituted of medium dense Leighton Buzzard 52/100 sand with a nominal particle size of 0.225 mm.

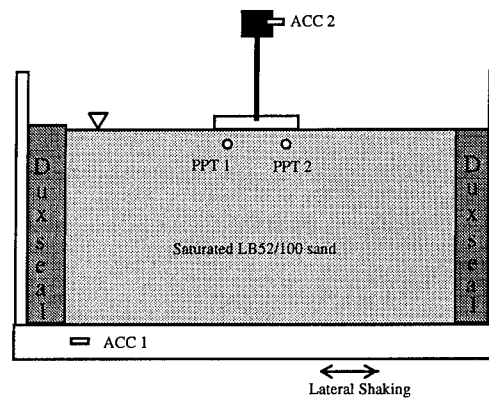


Fig.1 Schematic diagram showing the section of the centrifuge model

A large body of data exists concerning the laboratory behaviour of this sand, Stroud (1971), Mak (1984). In all the centrifuge tests the pore fluid level was maintained at the surface of the horizontal sand layer. The damping associated with the response of the structure in a pair of conjugate centrifuge tests will be compared. Before presenting the results from the centrifuge tests the components constituting the damping in the centrifuge model.

### 3 COMPONENTS OF DAMPING

For a centrifuge model described above the following components constitute the damping;

- i) damping present in the structure itself, due to air resistance etc.,
- ii) material damping in the soil participating in the rocking vibrations with the tower structure,
- iii) radiation damping accounting for the dissipation of energy into the far field.

The material damping in the soil can be divided into two components following Bolton and Wilson (1990). These will be the hysteretic damping in the sand when the sand is subjected to earthquake loading and the viscous damping due to the pore fluid. The hysteretic damping is realised as the energy dissipated in taking the soil through one complete stress cycle. The viscous damping arises from the energy dissipated in the pore fluid. Thus the total damping may be expressed as

$$\eta_{total} = \eta_{structure} + \left[ \underbrace{\eta_{hysteretic} + \eta_{viscous}}_{\eta_{material}} \right] + \eta_{radiation} \dots (4)$$

### 3.1 Structural damping

The damping in the structure itself was small. For the low and high frequency structures used in the present centrifuge tests this was determined based on lab floor impulse tests as about 0.05% and 0.1% respectively. For a conjugate pair of centrifuge tests this component will be the same as the same structure is used in both the tests.

### 3.2 Material damping

As explained above the material damping consists of two components namely the hysteretic damping and the viscous damping. The hysteretic damping will be same for a pair of conjugate centrifuge tests as the same soil is used for both the tests. Further the intensity of the earthquake was approximately the same in the pair of conjugate tests. However, the viscous damping will be dependent on the pore fluid used.

### 3.3 Radiation damping

Radiation damping will be the same in a pair of conjugate centrifuge tests as the model geometry is identical for both the tests. However it is necessary to show that the magnitude of this damping is small compared to the total damping if we wish to compare the damping in the conjugate centrifuge tests. Following Hall (1967) the radiation damping for a rigid structure in rocking mode may be estimated as

$$\eta_{radiation} = \frac{0.15}{(1+B)\sqrt{B}} \dots (5)$$

where B is a non dimensional quantity given by

$$B = \frac{3(1-\nu)I}{8\rho r^5} \dots (6)$$

where  $\nu$  is the Poisson's ratio for sand, I is the mass moment of inertia,  $\rho$  is the density of sand and r is the equivalent circular radius. Using Eq. 6 the radiation damping in the first pair of conjugate tests with a low frequency structure was estimated to be 0.18%. In the second pair of conjugate tests with a high frequency structure this was estimated to be 0.94%. Further, Morris (1979) has observed that the radiation damping associated with his model was extremely small.

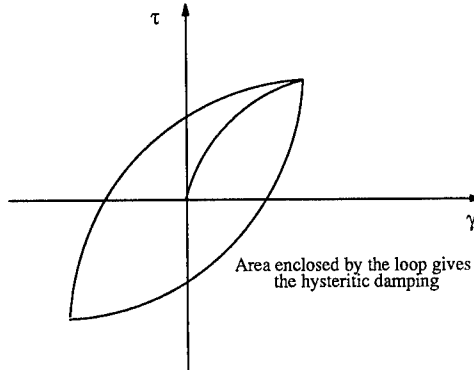


Fig.2 Hysteretic damping in the soil

Based on the argument outlined in the above section we can say that by comparing the damping associated with tower-soil systems in a pair of conjugate centrifuge tests we are in fact comparing the effect of pore fluid on damping.

## 4 LOGARITHMIC DECUREMENT

The logarithmic decrement can be used to estimate the damping associated with a time trace. By definition the logarithmic decrement is expressed as

$$\delta = \frac{1}{n} \ln \left[ \frac{A_1}{A_{n+1}} \right] \dots (7)$$

where  $A_1$  is the amplitude of the first cycle and  $A_{n+1}$  is the amplitude in the  $n^{th}$  cycle of the trace. If the damping ratio of the dynamic system is defined as  $\eta$  we have

$$\eta = \frac{c}{C_c} \dots (8)$$

where  $C_c$  is the critical damping given by  $2\sqrt{KM}$  in which K is the stiffness and M is the mass of the system. The logarithmic decrement is related to the damping ratio as given below

$$\delta = \frac{2\pi\eta}{\sqrt{1-\eta^2}} \dots (9)$$

## 5 RESULTS FROM THE CENTRIFUGE TESTS

Two pairs of the conjugate centrifuge tests were conducted during the present study. All the tests were performed at a centrifugal acceleration of 80g. In the first pair of tests (MS4 with silicone oil as pore fluid and MS8 with water as pore fluid) a low frequency tower was used. The natural frequency of this tower in the rocking mode was 55.0 Hz which represents an equivalent prototype with a natural frequency of 0.7 Hz. In the second pair of conjugate tests (MS1 and 3) a high frequency tower was used. The natural frequency of this tower in the rocking mode was 380 Hz which represents an equivalent prototype with a natural frequency of 4.75 Hz.

### 5.1 First pair of conjugate centrifuge tests MS4 and MS8

The results from the first pair of tests are presented in Figs.3 and 4. In these figures the input acceleration is given by ACC 1 and the response of the structure is recorded by the ACC 2. The pore pressures under the structure were recorded by the pore pressure transducers PPT 1 and 2 which were buried under either side of the structure (see Fig.1). As indicated by the vertical lines in Fig.3 the traces recorded by these PPT's are almost  $180^\circ$  out of phase confirming that the rocking mode of vibration of the structure. The magnitude of the excess pore pressure generated in the centrifuge test MS4 was 5.5 kPa. This is comparable to the excess pore pressure of 6.2 kPa observed in the centrifuge test MS8. It must be pointed out that the excess pore pressures generated in test MS8 dissipate rapidly compared with its conjugate test MS4. The response of the tower structure in both the tests compares satisfactorily.

From the response of the structure recorded by ACC 2 we can estimate the logarithmic decrement and hence the damping using Eqs.7 to 9. In the case of centrifuge test MS4 with silicone oil as pore fluid this was estimated as 1.6%. Using the response of the structure in test MS8 with water as pore fluid shown in Fig.4b the damping was estimated to be 2.85%.

### 5.2 Second pair of conjugate centrifuge tests MS1 and MS3

The end response of the high frequency structure after the end of the earthquake in the second pair of conjugate tests is presented in Figs.5 and 6. The magnitude of excess pore pressures in both the tests was comparable. The excess pore pressures in the water saturated test dissipated rapidly. These pore pressure traces are not shown here but a complete set of results of these tests are described by Madabhushi (1992). From these figures the damping was estimated for the test MS1 with silicone oil as pore fluid as 4.0%. For the conjugate centrifuge test MS3 with water as pore fluid the damping is estimated as 5.85%.

Based on the results from these centrifuge tests we may conclude that the damping in a centrifuge test with water as pore fluid is slightly higher than in the test with silicone oil as pore fluid. Also the high frequency structure has a higher damping compared to the low frequency structure.

## 6 CONCLUSIONS

Modelling of the pore fluid is important in dynamic centrifuge

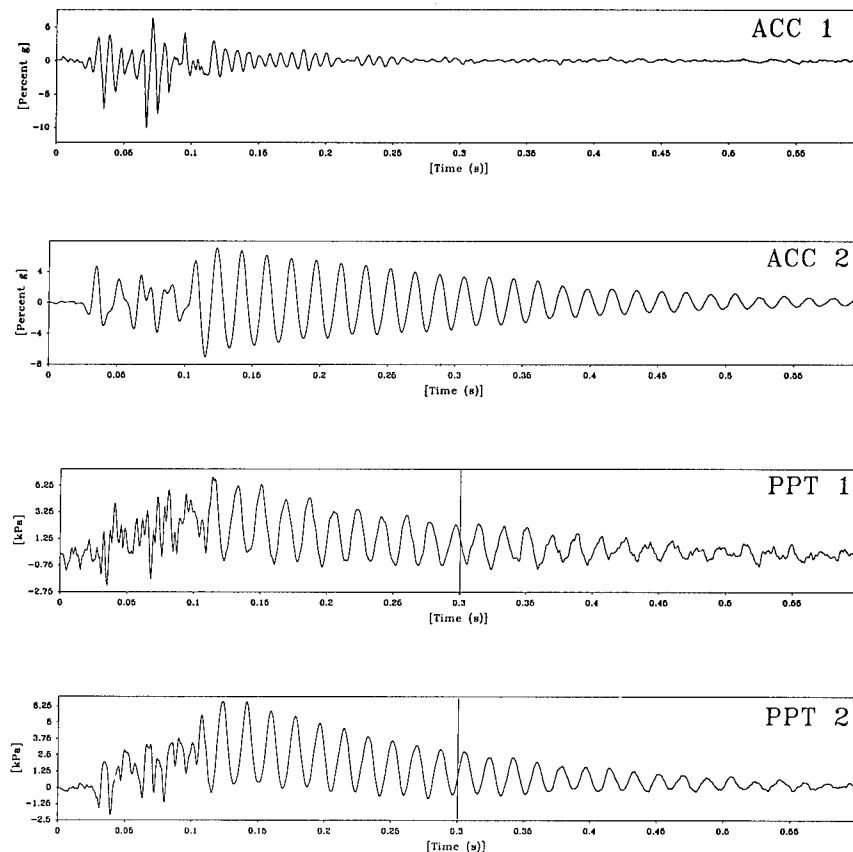


Fig.3 Time histories recorded during the centrifuge test MS-4

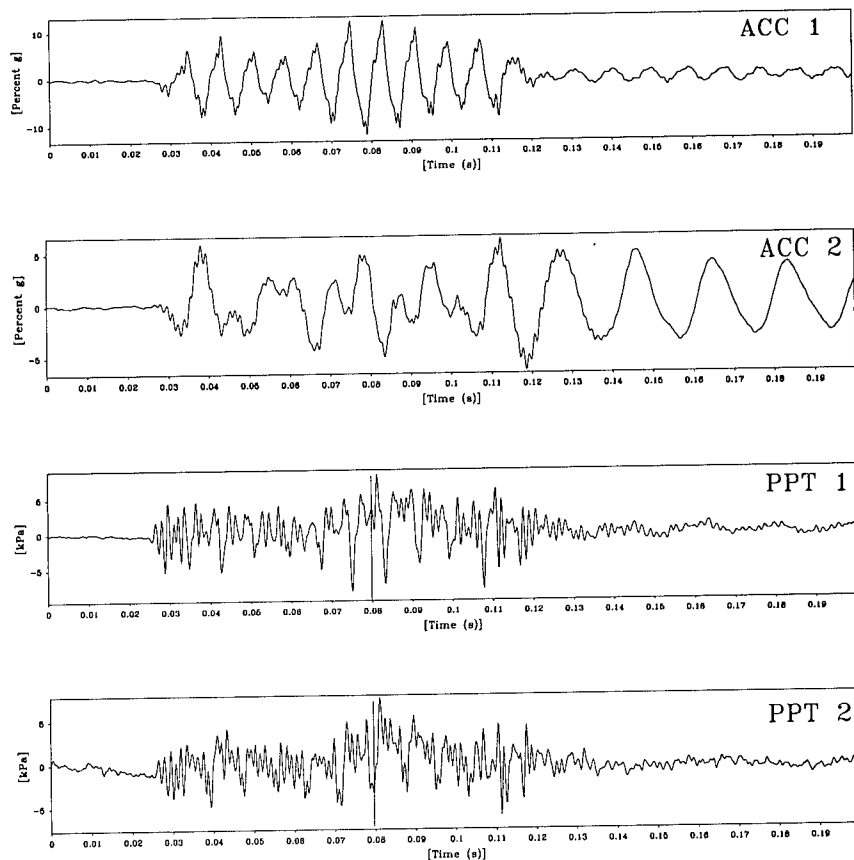


Fig.4a Short term time histories recorded during the centrifuge test MS-8

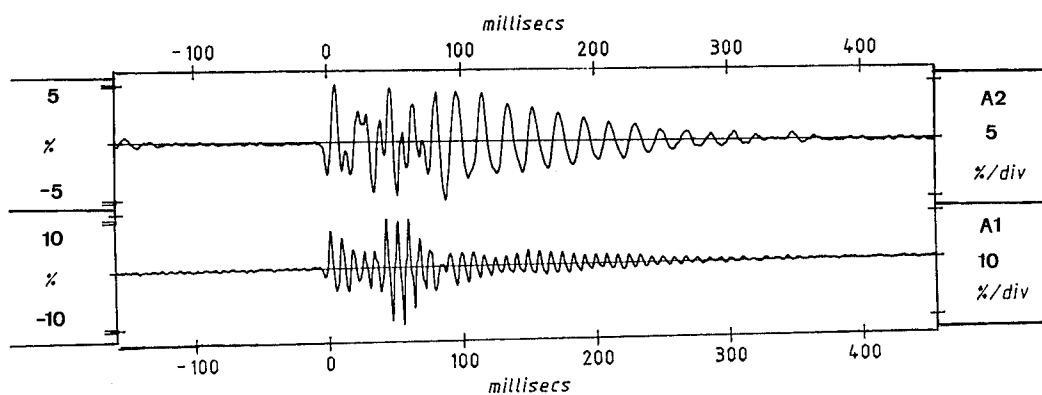


Fig.4b Long term response of the structure in the centrifuge test MS-8



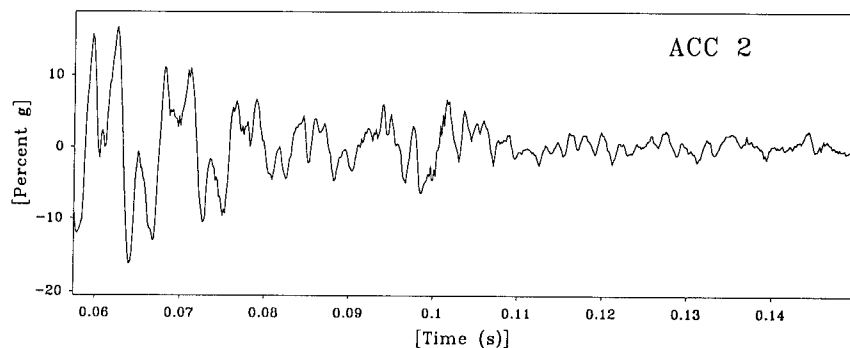


Fig.5 End response of the structure in the test MS1 after the earthquake

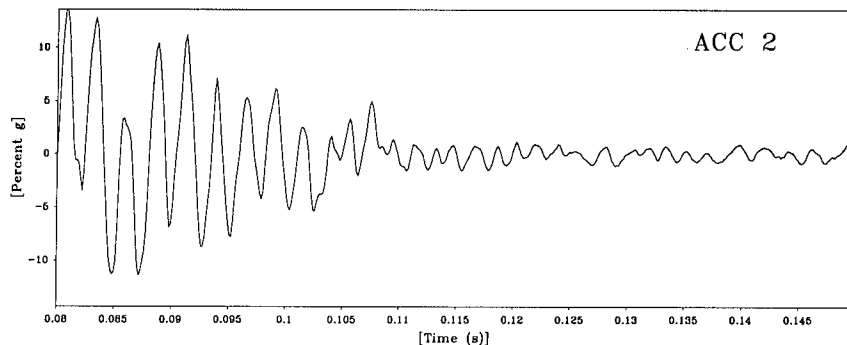


Fig.6 End Response of the structure in the test MS3 after the earthquake

tests with saturated soils. Use of high viscosity pore fluids models the inertial effects and the consolidation effects satisfactorily. The effect of the change in pore fluid on the dynamic characteristics like damping was investigated. Conjugate centrifuge tests of a tower structure founded on saturated sand bed which have identical geometry but with different pore fluids were conducted. The components of damping involved in such a centrifuge model are explained. By comparing the damping observed in a pair of conjugate centrifuge tests it was possible to isolate the effect of the pore fluid on damping. Based on the results from two pairs of such conjugate tests it was concluded that the damping is rather less sensitive to the viscosity of the pore fluid thus justifying the use of high viscosity pore fluids in centrifuge tests.

#### REFERENCES

- Bolton, M.D. & Wilson, J.M.R., (1990), Soil stiffness and damping, Proc. Eurodyn'90, Bochum, Germany.
- Eyton, D.G.P., (1982), Triaxial tests on sands with viscous pore fluids, Part II project report, Cambridge University.
- Kutter, B.L., (1982), Centrifugal modelling of the response of clay embankments to earthquakes, Ph.D. thesis, Cambridge University, England.
- Madabhushi, S.P.G., (1991), Response of tower structures to earthquake perturbations, Ph.D. thesis, Cambridge University, England.
- Madabhushi, S.P.G. and Schofield, A.N., (1993), Centrifuge modelling of tower structures on saturated sands subjected to earthquake perturbations, *Geotechnique* Vol.43, No.4.
- Mak, K.W., (1984), Modelling the effects of strip load behind rigid retaining walls, Ph.D. thesis, Cambridge University.
- Morris, D.V., (1979), The centrifugal modelling of dynamic soil-structure interaction and earthquake behaviour, Ph.D. thesis, Cambridge University, England.
- Schofield, A.N., (1980), Cambridge geotechnical centrifuge operations, *Geotechnique*, Vol.25, No.4, pp 743-761.
- Schofield, A.N., (1981), Dynamic and Earthquake geotechnical centrifuge modelling, Proc. Rec. Adv. in geotech. earthquake eng., Soil dynamics and earthquake eng., Univ. of Missouri-Rolla, Rolla.
- Schofield, A.N. and Lee, F.H., (1988), Centrifuge modelling of sand embankments and islands in earthquakes, *Geotechnique*, Vol.38, No.1.
- Schofield, A.N. and Steedman, R.S., (1988), Recent development of dynamic model testing in geotechnical engineering, Proc. IX WCEE, pp 813-824, Tokyo-Kyoto, Japan.
- Steedman, R.S., (1991), Centrifuge modelling for dynamic geotechnical studies, Proc. II Intl. Conf. on Rec. Adv. in Geo. and earthquake eng., St. Louis, USA.
- Stroud, M.A., (1971), The behaviour of sand at low stress levels in the simple shear apparatus, Ph.D. thesis, Cambridge University, England.

## The Delft Geotechnics model pore fluid for centrifuge tests

M.A. Allard & F.M. Schenkeveld  
Delft Geotechnics, Netherlands

**ABSTRACT:** Delft Geotechnics has developed a model pore fluid for centrifuge tests in various types of soils, that can be several hundred times more viscous than water. This fluid offers physical and chemical properties similar to those of water. Extensive laboratory tests as well as centrifuge tests have shown that similarity in the constitutive behaviour of sand models is preserved. High accuracy, repeatability and stability have been obtained in preparing this pore fluid and in making fluid saturated model soils. This special centrifuge model pore fluid enables scaling following similitude equations in order to perform meaningful dynamic centrifuge model experiments.

### 1 INTRODUCTION

The need for a centrifuge in experimental geotechnics arises from the non-linear behaviour of soil, and the gravity-induced nature of the soil stresses. When doing model scale experiments, similarity between the model and the chosen prototype problem has to be established. When the governing differential equations, together with constitutive conditions of the material are known, similarity laws can be derived in a straightforward manner by specifying the equation invariability in the change of units from prototype to model.

The choice for a centrifuge, with increased gravitational acceleration for decreased model length is made, starting from the equilibrium equation of continuum mechanics:

$$\nabla \sigma + b - \rho (d^2u / dt^2) = 0 \quad (1)$$

For dynamic events, velocity will then be same in the centrifuge model and the prototype.

Now, for flow and dissipative events (pore pressure dissipation phenomena are governed by the flow regime in the soil), following the macroscopic flow equation for soils, proposed by Darcy:

$$v = k i \quad (2)$$

the seepage velocity through a centrifuge model, subjected to an increase of self-weight of  $N$  times, will be  $N$  times greater than that in the prototype, if identical soil and pore fluid are used, and identical gradient applied.

This apparent inconsistency on velocity or time scale, when same soil and pore fluid are used in model and prototype, only means that using these materials do not allow for simultaneous similitude of dynamic and diffusion events. This can be expressed by the fact that the scale factor for the weight and inertia forces is different from the scale factor for seepage forces, and therefore the proportionality of

forces is not preserved.

From the original definition of similitude in which the proportionality of all the forces acting on similar systems is required, one must choose a model soil and pore fluid, such that the dynamic and inertial effects, and the flow and dissipative effects do occur simultaneously in the model. Then the saturated centrifuge model soil in the  $N g$  field, and prototype soil in the  $1 g$  condition, have the same Darcy coefficient of permeability.

One approach used by Rowe and Craig (78) and many others since, consists of using the same soil and using a model pore fluid with higher viscosity than, but similar density to, the prototype fluid. This practice is the current one used for modelling some dynamical events in the centrifuge. Change of permeability has been accomplished by altering the viscosity of the pore fluid. From the literature this has been done by adding glycerol to the pore water or by using silicone oil (decreasing permeability by factors of about 100), or later, using water solutions with various chemical components.

Difficulties encountered in the making of some of the soil models, in the analysis of test results, and the limitation to sand models when using silicone oil, brought Delft Geotechnics (DG) in the 80's to look into the development of a new model pore fluid for centrifuge testing. The aim in this research was to obtain a centrifuge model fluid that could be used to represent different prototypes with accuracy. To accomplish this goal, the requirements were to create a fluid that in the centrifuge environment, would be as similar as possible to water, the prototype pore fluid. The aim included the fact that the fluid could be used in various types of soils, to model dynamic problems under different soils conditions and in layered soils for example.

## 2 DESCRIPTION OF THE CONCEPT

The first requirements in the design of the model pore fluid were to provide a set of fluid solutions covering a wide range of viscosity and offering a density very close to the one of water. To make full use of the 300 g capacity of DG' geocentrifuge, the dynamic viscosity ranges, at a temperature of 20 °C, from 1 mPa.s for water to 500 mPa.s. Providing the same density for the fluid and water, the inertia and seepage forces scaling is correct and does not necessitate correction such as needed when using silicone oil which has 10% lower density than water.

A second set of requirements is motivated by the fact that the constitutive behaviour of the soil with the model pore fluid in the centrifuge environment must be the same as the soil with water in the 1 g field. The soil-fluid interaction must be preserved and the stress-strain properties of the soil unaltered. These requirements correspond to physical/chemical properties of the model pore fluid:

- The fluid must be, like water, a Newtonian fluid. The dynamic viscosity  $\eta$  of a fluid is the ratio between the applied shear stress and the rate of shear, and it is a measure of the resistance to flow of the fluid. For water this ratio is constant for all shear stress levels. It must be the same with the model pore fluid so that the soil-fluid interaction is unaltered.
- It must have the same compressibility as water so that the soil skeleton - fluid interaction during loading and unloading is preserved.
- The model pore fluid must be chemically polar to enable its use not only with sands but with silts and clays.
- If the fluid has the same density as water, the surface tension and capillarity are properly scaled, Fuglsang and Ovesen (1986).

Finally there are some operational requirements for the making and handling of the model fluid.

- The fluid should be non-toxic, environmentally sound, and soluble in water, to ensure safety in handling and to ease cleaning operations.
- The components coming into its composition should be readily available to allow the making of the fluid when needed.
- The fluid should be obtainable in an accurate, reliable and repeatable way to ensure high quality in testing.
- The fluid should be stable so that its properties will be preserved throughout a whole test series, allowing then accuracy, reliability and repeatability to be ensured.
- It should be non-corrosive, in the time scale of experiments, to provide workability with the various equipment and materials commonly used for testing.
- It should have a low vapour pressure, to have low evaporation, when for example, the Delft Geotechnics centrifuge is operated under 25 mbar vacuum at full acceleration level (300 g).

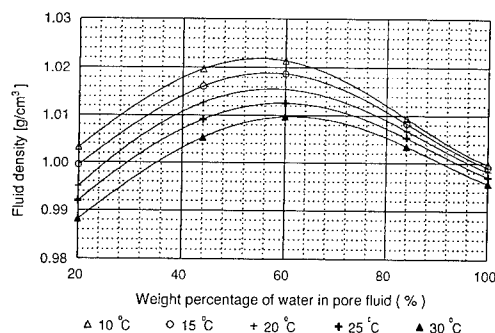


Fig. 1 Density of different pore fluid solutions at different temperatures.

## 3 CHARACTERISTICS OF THE MODEL FLUID

Delft Geotechnics' model pore fluid is a water based chemical solution. The proportions used in the composition are varied to obtain solutions, recognized by their amount of water (% per weight), covering a wide range of dynamic viscosity.

All the requirements mentioned in section 2 are fulfilled by the model fluid solutions.

The principal physical characteristics of the fluid: dynamic viscosity and density, have been measured with precision over the full range of solutions. Because temperature has a very large effect on viscosity, and some on density, a complete series of measures has been performed to define the change of viscosity, and of density, over the full range of fluid solutions, for temperatures varying from 10° C to 30° C, which are the minimum and maximum expected temperatures for a test run in the DG centrifuge under normal conditions.

Within the temperature range mentioned above, and for all the solutions, the density  $\rho$  (mass per unit volume) of the fluid, measured using hydrometers, varies between 0.9882 g/cm<sup>3</sup> and 1.0214 g/cm<sup>3</sup>, while the density of water varies between 0.9957 g/cm<sup>3</sup> and 0.9997 g/cm<sup>3</sup>, see Figure 1. The maximum errors in density are then - 0.75% and + 2.2%. The temperature accuracy is 0.1 °C. The measurements are made following the standard practice for density by hydrometer method, ASTM standards D1298-85. In conclusion, for any test, any fluid density can be considered the same as the one of water.

In this development project it was chosen to perform measurements of kinematic viscosity rather than dynamic viscosity to have more flexibility and obtain higher accuracy. The kinematic viscosity  $\nu$  is a measure of the resistive flow of a fluid under gravity, the pressure head being proportional to the density  $\rho$  of the fluid. For Newtonian fluids:

$$\nu = \eta / \rho \quad (3)$$

A complete set of glass capillary kinematic viscometers has been used to cover the full range of viscosity. Each viscometer is calibrated using viscous fluids from the Dutch Measurement and

Normalization Institute. Calibration measurements lead to an accuracy of  $\pm 1\%$ . Repeated measurements both on the calibration fluids and the model pore fluid solutions gave a measurement reproducibility within  $\pm 0.1\%$ . Repeated preparation of a fluid solution in small (below 1 liter) and in large quantity (above 10 liters) gave a reproducibility in solution viscosity well within  $\pm 1\%$ . The measurements are made following the standard test method for kinematic viscosity of transparent and opaque liquids, ASTM standards D445-88, and specifications and operating instructions for glass capillary kinematic viscometer, ASTM standards D446-89a.

Using equation (3) the dynamic viscosity is derived using the kinematic viscosity and density values, and is presented in Figure 2.

Measurements of solutions viscosities were performed at various times spread over a full year. No changes of viscosity were observed, the solutions are stable and are not affected by ageing.

With the measurement database fed in a surface fit program, one can get within 0.3 % accuracy:

- the viscosity for any given solution definition and temperature. This allows the recalculation of the viscosity of the fluid during any experiment for which temperature is monitored;
- the solution to use to obtain a given viscosity at a given temperature. This enables the choice of the mixture to use for a given experiment when the temperature has been established and a given viscosity is required.

#### 4 SOIL-FLUID INTERACTION

Series of laboratory tests have been conducted on sand samples saturated with water and with various model fluid solutions to investigate the model pore fluid influence on the soil behaviour. The sands used were: washed Eastern Scheldt sand, commonly used at DG for model testing, and Baskarp sand, provided by the Norwegian Geotechnical Institute (NGI) for the project mentioned in section 5. Some properties of both sands are given in Table 1.

##### 4.1 Presentation of laboratory test results with sand

###### 4.1.1 Permeability tests

A standard permeameter was used. Some additions were made in the set-up to facilitate the saturation of the sand sample with various model pore fluid solutions. It was chosen to make only one sand sample that was tested successively saturated with, as pore fluid, water and various solutions. In doing so the soil skeleton of the sample is preserved, and only the characteristics of the fluid are changed.

In the laboratory (1 g environment) the permeability tests were performed as follows: one dense Baskarp sand sample ( $D_r = 80\%$ ) was built in the modified permeameter, initially fully saturated with water.

A first test series at a constant temperature  $T = 20^\circ\text{C}$  and with a constant head was performed with 100%

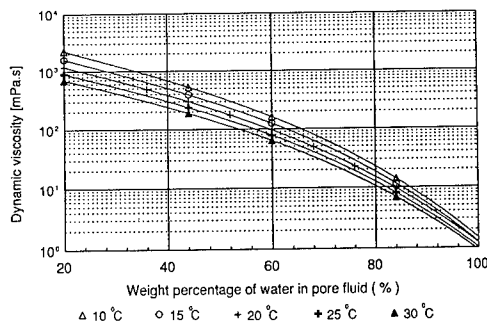


Fig. 2 Dynamic viscosity of different pore fluid solutions at different temperatures.

Table 1 Properties of Washed Eastern Scheldt sand and Baskarp sand.

Sand type	$\gamma_s$ ( $\text{kN/m}^3$ )	$n_{\min}$ (%)	$n_{\max}$ (%)	$d_{50}$ (mm)	$d_{90}/d_{10}$
W. E. S.	26.0	35.1	47.0	0.15	2.0
Baskarp	26.0	33.6	46.3	0.15	2.3

Table 2 1-g permeability test results.

Fluid solution (% water)	Temp ( $^\circ\text{C}$ )	$v$ ( $10^{-6}$ $\text{m}^2/\text{s}$ )	$k$ ( $10^{-5}$ $\text{m/s}$ )	$k_f \cdot v_f$ ( $10^{-11}$ $\text{m}^3/\text{s}^2$ )	error %
100	20	1.035	8.670	8.97	0
76	20	22.4	0.395	8.86	1.26
60	20	95.7	0.0912	8.73	2.74
44	20	294.7	0.0297	8.75	2.51
44	11	196.3	0.0478	9.26	-3.19
44	29	486.6	0.0177	8.62	3.91
100	21	1.014	8.68	8.80	1.91

water as pore fluid, the same sample was then saturated successively with a 76%, 60%, and 44% water pore fluid solution.

A second series was performed with one pore fluid: the 44% water solution, but with various temperatures, which implied a change in the viscosity values of the fluid.

The same sample was finally saturated back with 100% water as pore fluid, and tested again.

The results are presented in Table 2.

The coefficient of permeability  $k$  can be expressed as follows:

$$k_{m,f} = \rho_f \cdot g \cdot \kappa_m / \mu_f = g \cdot \kappa_m / v_f \quad (4)$$

with:

$\rho_f$  = fluid density

$\mu_f$  = fluid dynamic viscosity

$v_f = \mu_f / \rho_f$  = fluid kinematic viscosity

$g$  = gravitational acceleration

$\kappa_m$  = material intrinsic permeability

For permeability tests performed on a given soil

Table 3 Isotropic and drained axial compression test results with Eastern Scheldt sand samples.

$n_{ini}$ (%)	B (MPa) 50-100 kPa	B (MPa) 100-200 kPa	$v$ (mm <sup>2</sup> /s)	$\phi$ (°)
39	22.2	34.1	1	40.5
39	20.9	37.3	90	41.0
39	21.6	37.9	230	40.2
39	20.7	35.6	350	40.0

sample (same material) with various pore fluids, at a fixed 1 g environment we have from equation (4):  
 $k_f \cdot v_f = g \cdot \kappa = \text{constant}$  (5)

Equation (5) is verified with the laboratory test results. The intrinsic permeability  $\kappa$  of the sand sample is not altered by the model fluid, and the coefficient of permeability  $k$  is inversely proportional to the kinematic viscosity.

#### 4.1.2 Triaxial compression tests

Various triaxial tests have been performed on both Eastern Scheldt sand and Baskarp sand samples saturated with water or various model pore fluid solutions. Presented here are some results of two test series, one on each sand type, including a drained axial compression test was performed.

For the Eastern Scheldt sand test series, all the specimens, with an initial porosity  $n = 39\%$ , were compressed isotropically to 50 kPa, 100 kPa, 200 kPa and finally to 220 kPa where the drained axial compression test was started. The results are presented for samples saturated with water and three pore fluid solutions. The bulk moduli,  $B$ , for consolidation between 50 and 100 kPa, and between 100 and 200 kPa, the kinematic viscosity of the various pore fluids, and the friction angle calculated for maximal deviatoric stress, are given in Table 3.

For the Baskarp sand test series, all the specimens with initial porosity  $n = 36.4\%$  or  $n = 41.4\%$ , were first consolidated to a stress level of  $\sigma'_v = 250$  kPa and  $\sigma'_h = K_0 \cdot \sigma'_v = 112.5$  kPa, then submitted to undrained cyclic loading (see section 4.1.3), and further consolidated to a stress level of  $\sigma'_v = 300$  kPa and  $\sigma'_h = 162.5$  kPa where a drained compression test was performed. The results are presented in Table 4, where the initial sample porosity, the pore fluid viscosity and the friction angle calculated at maximum deviatoric stress are given. The undrained compression test results of the denser Baskarp sand samples are shown in Figure 3. Agreement between the two tests is very good.

All the results obtained are in very good agreement with one another, the model pore fluid interaction with sand samples is satisfactory, there is no alteration of the sand behaviour due to the model pore fluid.

Table 4 Compression test results with Baskarp sand.

$n$ (%)	$\sigma'_v$ (kPa)	$\sigma'_h$ (kPa)	$v$ (mm <sup>2</sup> /s)	$\phi$ (°)
36.4	300	162.5	1	43.7
36.4	300	162.5	299.5	44.0
41.4	300	162.5	1	40.0
41.4	300	162.5	299.5	40.0

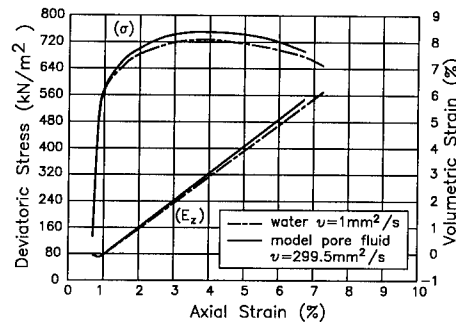


Fig. 3 Drained axial compression test results on Baskarp sand samples,  $n_{ini} = 36.4\%$ .

#### 4.1.3 Triaxial undrained cyclic tests

Several sets of triaxial undrained cyclic tests have been done on Eastern Scheldt sand and Baskarp sand samples. Cyclic loadings were performed at different consolidation levels, with various cyclic stress amplitudes, and on samples of different porosities. Presented in Figures 4a and 4b are tests performed on loose,  $n = 41.4\%$ ,  $D_r = 38\%$ , and dense,  $n = 36.4\%$ ,  $D_r = 78\%$ , Baskarp sand samples saturated with water and a fluid solution of  $299.5$  mm<sup>2</sup>/s kinematic viscosity. The tests are done in a temperature-controlled room because of the large influence of temperature on the fluid viscosity. The samples are first consolidated to a stress level of  $\sigma'_{vc} = 250$  kPa, and  $\sigma'_{hc} = K_0 \cdot \sigma'_{vc} = 112.5$  kPa. Then only for the dense samples, pre-cyclic loading is applied to the samples. It consists of 4 series of 100 cycles undrained loading with a single cyclic amplitude of  $\tau_{cy} = 0.10 \cdot \sigma'_{vc} = 25$  kPa. Full pore pressure dissipation is allowed after each loading series is executed. Finally cyclic loading is applied, with 500 cycles of single cyclic shear stress amplitude:  $\tau_{cy} = 0.275 \sigma'_{vc} = 68.75$  kPa.

Very good reproducibility is obtained for dense samples for mean axial strain, axial strain cyclic amplitude, mean pore pressure build up and cyclic pore pressure amplitude. The soil behaviour for dense sand is perfectly preserved when using the model fluid as pore fluid. For the loose samples saturated with the model pore fluid, higher mean axial strains are obtained after about 100 cycles, while axial strain cyclic amplitude are comparable. Slightly higher mean pore pressure build up is also observed, while cyclic amplitude is somewhat larger than for the sample with water. After 100 cycles

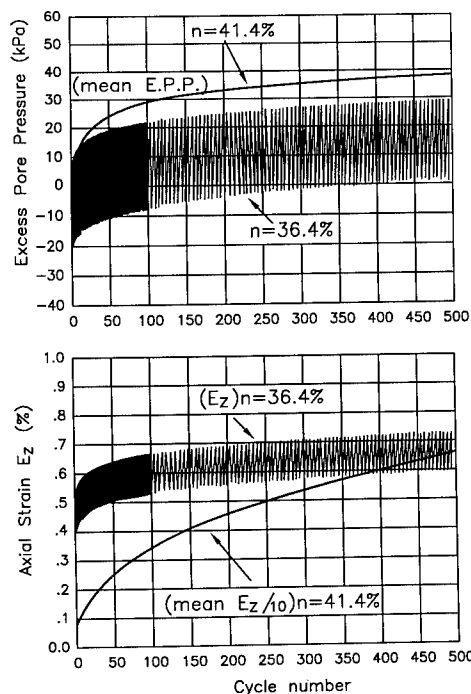


Fig. 4a Pore pressure generation and axial strain during undrained cyclic loading, for Baskarp sand sample saturated with water.

already 3.5 % mean axial strain is reached. The samples are well deformed. Laboratory testing might not be a representative way to test the sample saturated with the model pore fluid which should be tested in the centrifuge environment. Under drained compression, it was seen in the previous section that, also for loose samples, a good reproducibility for the friction angle was obtained. Similar behaviours are observed for loose samples saturated with water or the model pore fluid under drained conditions, or undrained conditions provided not too large axial strains are developed.

#### 4.2 Presentation of centrifuge test results with sand

Because the model pore fluid is to be used in the centrifuge and not in the laboratory, it appeared important to test it directly in the centrifuge. It was made use of existing equipment to perform testing.

##### 4.2.1 Settlement of medium loose saturated sand

A test series was performed in DG table centrifuge. Loose ( $n = 43\%$ ) Eastern Scheldt sand samples, 66 mm diameter and 69 mm high, were built and saturated with water and various model pore fluid solutions. The sample cups were instrumented with two pore pressure transducers at different depths and a LED-photo diode strip system to follow the settlement of the sample during centrifugation.

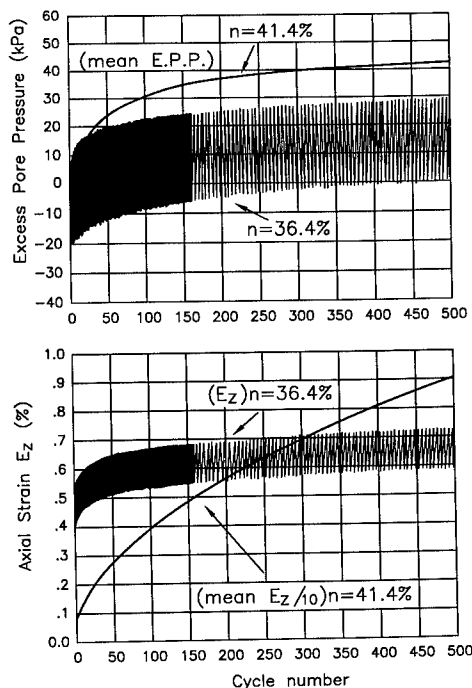


Fig. 4b Pore pressure generation and axial strain during undrained cyclic loading, for Baskarp sand sample saturated with model pore fluid solution.

The accuracy of the LED-diode system is in hundredth of mm. All the samples spun up to an average acceleration of 205 g, did undergo the same settlement. The time to reach maximum settlement increased with the viscosity of the model pore fluid. By checking the properties of the fluid before and after the test, no alteration was observed, even for the more viscous fluid which run for 5 consecutive days in the centrifuge. No effect of the centrifuge field can be observed on the fluid solutions. Also, pore pressure measurements were good, confirming the procedure to use these instruments in model saturated with the model pore fluid.

##### 4.2.2 Centrifuge permeability test

A special set up to study slurry self weight consolidation and clogging effect of underlying filter material, has been built for the large centrifuge, Schenkeveld (1993); it allows to perform constant head centrifuge permeability tests. This set-up permits the testing in parallel of four soil samples, 100 mm diameter, 300 mm height, with 100 mm top fluid layer. The bottom drain of each sample can be set to provide anything between 1 mm and 100 mm head. The fluid permeating a sample is recovered in a thin graded column with a pore pressure transducer at the bottom. The outflow volume is then continuously monitored. A fluid pump, that can be started once the test acceleration is reached, will

bring up the fluid layer above the samples, which is then maintained at a constant level by the outflow outlet. A pore pressure transducer placed in the fluid layer above the samples allows continuous monitoring of the head.

The dependence of the coefficient of permeability on acceleration level was checked. Two Baskarp sand samples were made, and similar philosophy as for the 1 g test was followed. The acceleration being  $N \cdot g$ , the following equation holds:

$$k_{f,N} \cdot v_f / N = g \cdot \kappa = \text{constant} \quad (6)$$

The samples were first saturated with water and tested at 1 g and 40 g. The samples were successively saturated with a 40 mm<sup>2</sup>/s solution, and tested at 40 g and 200 g, and with a 200 mm<sup>2</sup>/s solution and tested at 160 g and 200 g. Finally the samples were saturated back with water and tested at 1 g. During testing, temperature transducers placed directly above the samples indicate changes in fluid temperature. Correction of the fluid viscosity can then be done. Samples of the fluids, to check viscosity, were made after each saturation and each test. Once again the results are very good, well within the  $\pm 5\%$ , which indicates good interaction between the fluid solutions and the sand samples.

The sample saturated with the model pore fluid, itself  $N$  times more viscous than water, has in the model environment (gravity field =  $N \cdot g$ ), the same permeability coefficient as the water saturated prototype sample in the prototype environment ( $1 \cdot g$ ).

## 5 APPLICATION: CYCLIC LOADING OF A GRAVITY PLATFORM ON SAND

Centrifuge model tests have been successfully used to verify numerical calculation procedures and to bring reliability and accuracy in the design of foundations of offshore structures on clays. Analyses of offshore foundation behaviour on sand has been more limited, and more insight is needed in order to improve the current design procedures.

A geotechnical centrifuge provides the environment where stresses are modelled properly. Provided a model pore fluid is used in the model soil, the similitude between model and prototype, for gravity stresses, dynamic loading, and drainage conditions for pore pressure dissipation, is fulfilled.

The Delft Geotechnics model pore fluid has been successfully used in a centrifuge test series as part of a project with the Norwegian Geotechnical Institute (NGI). The investigation dealt with the behaviour of an offshore gravity platform on a very dense sand layer under almost undrained monotonic and cyclic loading, Allard & al. (1994). The results show that high negative pore pressures, induced by dilatancy of the very dense sand under shearing, and the limited drainage occurring during each loading cycle could provide platform foundation bearing capacity considerably higher than normally allowed in design. The results also indicate that displacements rather than bearing capacity would govern the allowable wave loads on an offshore gravity platform on very dense sand, Andersen & al. (1994).

## 6 CONCLUSIONS

The analysis of test results in this study demonstrates that the constitutive behaviour of sand is not altered by the use of Delft Geotechnics model pore fluid. This, together with the high accuracy, repeatability and stability obtained in preparing the fluids and in making the sand samples, concludes the validity of the use of the fluid solutions for centrifuge testing.

Thanks to the use of this model pore fluid, and the quality reached in model preparation and testing, valuable experimental data on the cyclic interaction between an offshore gravity structure and its dense sand foundation have been acquired. These very promising centrifuge tests results have shown the feasibility and reliability in using Delft Geotechnics operational model pore fluid in centrifuge tests.

The experience gained gives new openings for accurate and valuable centrifuge model testing: cyclic, transient, or dynamic loading of structures in sands, and liquefaction problems, are some of the possible applications for new investigations.

Preliminary tests have been performed on clay consolidation with the model pore fluid. To enlarge the scope of applications, the laboratory and centrifuge test investigation on the interaction between the model pore fluid and silts and clays, has to be completed.

## ACKNOWLEDGEMENTS

The authors are grateful to Aad Schapers, who performed all the laboratory tests and adapted procedures for the use of the model pore fluid. His expertise in laboratory testing was very valuable. Also thanked are the members of the centrifuge team and all the colleagues of Delft Geotechnics who contributed in developing the model pore fluid and in performing measurements and tests.

## REFERENCES

- Allard M.A., K.H. Andersen, and J. Hermstad (1994), "Centrifuge model tests of gravity platform on dense sand; I Testing technique and results," proc. BOSS'94, Boston, July 1994.
- Andersen K.H., M.A. Allard, and J. Hermstad (1994), "Centrifuge model tests of gravity platform on dense sand; II Interpretation," proc. BOSS'94, Boston, July 1994.
- Fuglsang L.D. and N.K. Ovesen (1986), "The application of the theory of modelling to centrifuge studies," Centrifuges in Soil Mechanics, Craig, James & Schofield, Balkema, Rotterdam, 1988.
- Rowe P.W., and W.H. Craig (1978), "Prediction of caisson and pier performance by dynamically loaded centrifugal models," Int. Symp. Soil Mech. Res. and Found. Design for the Oosterschelde Storm Surge Barrier, Vol. 2, IV.3, Oct. 78.
- Schenkeveld F.M. (1993), "Centrifugeproeven slipdepot Geuzenhoek, Belgie," Delft Geotechnics Report BO-338950/8, December 1993.

## Design and performance of an electrohydraulic shaker for the RPI centrifuge

P.A. Van Laak, A.-W. Elgamal & R. Dobry  
*Rensselaer Polytechnic Institute, Troy, N.Y., USA*

**ABSTRACT:** An electrohydraulic shaker for earthquake model testing has been developed for use with the Acutronic 100 g-ton centrifuge at Rensselaer Polytechnic Institute. The shaker is designed to provide 1-dimensional base input motions for centrifuge models of up to 90 kg. An outline of the design approach is presented. Salient features concerning the slip table bearings and the servo-hydraulic system are discussed. A number of calibration experiments are conducted and discussed in order to characterize both the performance of the shaker and the response of soil models to shaking. Shaker performance is illustrated using measurements of quality of input motion in terms of wave shape and frequency content. A linearized dynamic model of the mounted shaker is developed using frequency-domain analysis of measured input-output data. It is shown how this linearized model is used to pre-condition signals to be applied to the shaker in order to obtain the desired input motion. Data obtained from shaking tests on soil models are presented, demonstrating the utility of the shaker for geotechnical centrifuge research.

### 1 INTRODUCTION

In 1989 Rensselaer Polytechnic Institute (RPI) installed a 100 g-ton geotechnical centrifuge with funds provided by the National Center for Earthquake Engineering Research (NCEER), the State of New York, and the National Science Foundation (Elgamal et al, 1991). Initially the centrifuge was equipped only for static tests, and in order to permit study of earthquake problems, RPI has developed an earthquake simulator for the centrifuge.

Prior to designing the shaker, the target performance objectives were defined. These objectives were largely based upon recommendations put forth in a National Science Foundation workshop (Cheney and Whitman, 1983), upon information gathered from existing simulation facilities, and upon consideration of the research objectives at RPI. A partial list of these objectives includes:

- Capability for producing input motions having arbitrary shape,
- Matching as closely as possible the performance envelope developed in the NSF workshop for a centrifugal acceleration of 50 g,
- Capability for operation at up to 100 g centrifugal

acceleration with a maximum payload of 90 kg.,

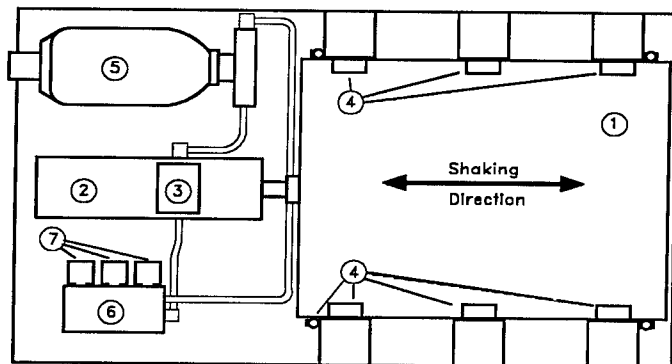
- Base excitation in one direction only, with constraints to prevent uncontrollable vertical and transverse horizontal motions,
- Easy installation and removal,
- Low maintenance and high reliability,
- Capability for multiple successive shakings without stopping the centrifuge.

Based upon these and other considerations, it was determined that an electro-hydraulic shaker was the best choice for meeting the performance objectives. Servo hydraulic technology has been shown to be readily adaptable to centrifuge shaker applications (Ketcham et al, 1991; Kimura et al, 1988; Kutter et al, 1987; Scott, 1983).

### 2. DESCRIPTION

The basic layout of the shaker is shown schematically in Fig. 1. The supporting frame is made from welded structural steel channel, thermally stress-relieved and ground flat after welding. A 600 mm x 460 mm x 12.7 mm thick steel plate is screwed to the frame at one end and serves as the attachment point for the hydraulic subassemblies. Nine steel 75





#### LEGEND

- 1 Slip Table
- 2 Hydraulic Linear Actuator
- 3 Electrohydraulic Servo valve
- 4 Bearing Assemblies
- 5 Hydraulic Accumulator
- 6 Hydraulic Manifold
- 7 Solenoid Valves

Fig. 1. Schematic plan view of shaker

mm x 75 mm bearing posts are screwed into the frame at the other end. These posts transmit the static centrifugal loads from the model to the frame. All components of the frame are designed to be very stiff to prevent excessive flexing of the structural components under load and to avoid structural resonances at shaking frequencies.

Shaking is produced by a double-acting linear hydraulic actuator. The actuator is a standard unit, type 242.02 manufactured by MTS Corp., and is designed for high frequency structural testing applications. It has a peak displacement of 1.27 cm., a piston area of 5.9 cm<sup>2</sup> and a nominal dynamic force capacity of 10 kN at a 20.6 MPa system pressure. It incorporates a high performance two-stage servo valve for modulating oil flow and controlling displacement of the actuator piston. The servo valve attaches directly to the actuator housing. This minimizes the volume of oil situated between the servo valve and the actuator piston, thereby minimizing losses due to compliance of the oil and maximizing the frequency response. An LVDT displacement transducer is mounted internally for measuring the relative displacement between the actuator piston and housing. This LVDT is a high frequency unit designed to provide accurate displacement measurements over the frequency range 0 - 500 Hz, the nominal frequency range of the shaker. The body of the actuator is bolted to the

steel mounting plate on the shaker frame, and the piston is rigidly connected to the slip table. The slip table is made from 38 mm thick 6061 T6 aluminum alloy plate. To reduce weight, 350 recesses, each 20mm W x 20mm L x 25 mm deep, are machined into the underside of the slip table in a honeycomb pattern. The slip table can accommodate model containers up to 558 mm long by 381 mm wide. It is supported and guided at the edges and along the centerline by 19 bearings. The bearings used are McGill cam-follower roller bearings with crowned rollers, eccentric studs and oil seals. The bearing's mounting stud is manufactured with a 0.75 mm eccentricity. This design permits adjustment of bearing alignment and/or application of a bearing pre-load during assembly using a torque wrench. The 16 bearings situated at the edges of the slip table are mounted in opposing pairs, and during shaker assembly a pre-load is applied to these bearings, constraining the slip table to move in the specified shaking direction. The studs of the cam-followers are mounted in the steel bearing posts screwed into the shaker frame, and the rollers bear on hardened steel pads attached to the softer aluminum alloy slip table.

Pressurized oil is supplied by a hydraulic pump located in a room adjacent to the centrifuge and having a flow capacity of 20 liters per minute. A rotary joint mounted atop the centrifuge is used for passage of oil to and from the centrifuge during

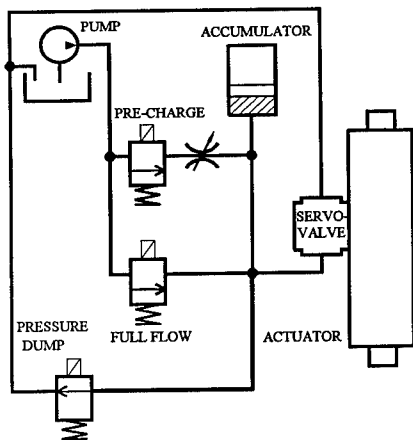


Fig. 2. Schematic of the hydraulic supply system

spinning. Flexible hydraulic hoses equipped with quick-connect fittings connect between the shaker and the supply tubes on the centrifuge. Oil is routed to the shaker via the hydraulic control manifold. This manifold is constructed from A36 steel and incorporates three screw-in cartridge-style solenoid directional control valves. A switch console manufactured at RPI and located in the centrifuge control room is used to operate the solenoid valves. A two-liter hydraulic accumulator is mounted adjacent to the actuator to prevent transients when the actuator is pressurized.

A schematic drawing of the hydraulic supply system is shown in Fig. 2. Before starting the pump, the pre-charge and full flow valves are closed and the pressure dump valve is opened to prevent transient shaker motions during pump startup. After the pump is switched on and nominal operating pressure is developed at the pump outlet, the pre-charge valve is opened, permitting a small flow of oil to pass through the shaker system without pressurizing the actuator. This mode is useful for warming the hydraulic oil prior to shaking, since the servo valve performs best with hydraulic oil at a temperature of 45° C. Just prior to shaking, the pressure dump valve is closed, filling the accumulator with oil and pressurizing the actuator. With the actuator pressurized, the full flow valve is opened and shaking can be initiated.

A MOOG model 121A132 servo controller mounted on the centrifuge powers the servo valve and provides feedback control of the shaker (Fig 3). A signal generator located in the control room sends a voltage signal proportional to the desired shaker displacement to the input terminal T1 of the MOOG

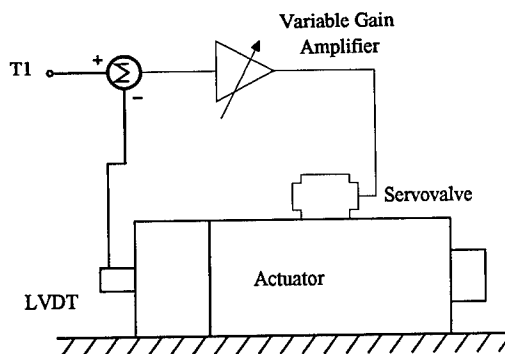


Fig. 3. Schematic of the shaker feedback control system

servo valve amplifier. The input voltage is compared with the feedback signal from the LVDT at the summing junction, and the resulting error signal is amplified and sent to the servo valve. The servo controller has provisions for scaling the input and feedback signals and for adjusting the loop gain.

### 3. KINEMATIC PERFORMANCE

Throughout the rest of this paper, all performance data are described using actual measured (i.e. model) units unless otherwise noted.

A series of tests was performed to determine the nature of the slip table motions and, in particular, to ascertain the performance of the bearing design. A dry sand model in a rigid rectangular container weighing a total of 45 kg was mounted on the shaker, and accelerometers were mounted on the slip table in horizontal and vertical directions. The centrifuge was spun to 50 g and several sinusoidal input signals of various amplitudes and frequencies were applied. Some typical results, plotted in prototype units, are shown in Fig. 4, where it can be seen that the vertical accelerations of the slip table are small in comparison to the acceleration in the direction of shaking, demonstrating the efficacy of the pre-loaded bearing design. Prototype units are used in Fig. 4; that is, the actual accelerations have been divided by 50 and the actual time multiplied by 50.

### 4. DYNAMIC PERFORMANCE

The theoretical performance envelope of the shaker for a payload consisting of a 35 kg rigid mass is

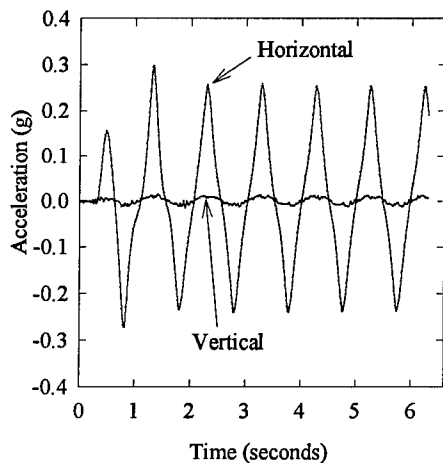


Fig. 4. Comparison of measured horizontal and vertical accelerations (prototype units)

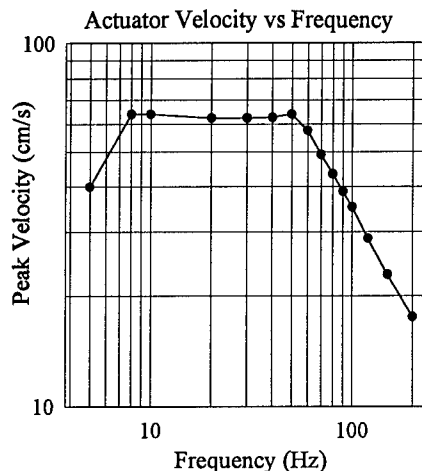


Fig. 5. Theoretical performance envelope of shaker

plotted in Figure 5. In the absence of structural and hydraulic resonances, and assuming that the shaker motion is sinusoidal, this graph demonstrates how sizing of the various hydraulic components used for the shaker limits the maximum theoretically achievable shaker performance. In this figure the maximum velocity of the slip table relative to the shaker frame is plotted as a function of shaking frequency. At very low shaking frequencies the 2.54 cm travel of the actuator limits the shaker performance, and in this region the shaker is said to be displacement- (or stroke-) limited. For frequencies greater than 8 Hz and less than 50 Hz the shaker is no longer constrained by the stroke limitation but by the flow capacity of the hydraulic supply (consisting of the pump, tubing, accumulators, and servo valve). For frequencies greater than 50 Hz, the shaker is constrained by its force limit, with the maximum attainable acceleration equal to the force capacity of the actuator divided by the shaken mass.

Graphs such as shown in Figure 5 are extremely useful for sizing various parts of the hydraulic system during the design phase. They do not, however, give a complete picture of the dynamic performance of the shaker. The shaker is a feedback control system, having dynamic characteristics which depend upon the inherent structural and hydraulic resonances of the shaker itself, as well as upon the type of input signal used (e.g. its amplitude, frequency, duration, etc.), the nature of the payload (its mass, stiffness, and damping during shaking), and the operating conditions (the centrifugal acceleration of the test).

These dynamic characteristics impose additional limitations on the achievable shaker performance.

The shaker dynamics are strongly influenced by the settings of the servo controller. It is important to fine-tune the control system parameters, especially for shakers having modestly sized actuators, in order to achieve actual shaker motions which closely approximate target input motions. Proper adjustment of the loop gain is an important factor in determining the frequency response of the shaker and the overall system accuracy. Increasing loop gain yields higher bandwidth and accuracy while reducing system stability; very high values of loop gain can bring about instability.

Loop gain for the shaker control system is set by adjusting a potentiometer on the MOOG servo controller board. To perform the calibration, a dry sand model in a rigid container weighing 35 kg total was placed on the shaker and spun up to 50 g, and a two-channel dynamic signal analyzer was used to provide a random excitation signal to the shaker and to measure the gain and phase margins while the gain potentiometer was adjusted. Because centrifuge models exhibit wide variations in dynamic response properties depending upon level of shaking, centrifugal acceleration, type of container, type of soil, etc., the shaker has been adjusted for slightly conservative gain and phase margins of 8 dB and 45 degrees, respectively, to prevent system instability. All data presented herein were obtained with this value of loop gain.

In order to produce a target displacement (or

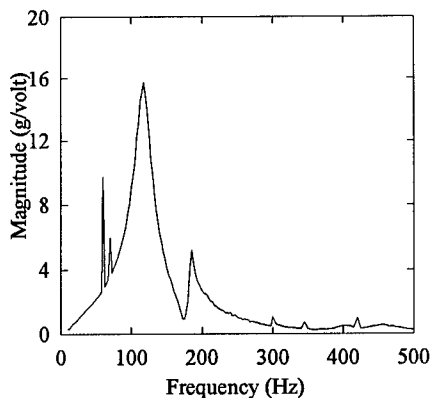


Fig. 6. Measured frequency response function (FRF) of shaker

velocity or acceleration) time history, the relationship between input voltage and the corresponding output motion must be known. Hence the shaker dynamics must be taken into account when preparing an excitation signal for the shaker.

Over a broad range of operating conditions, the shaker behaves in a nearly linear fashion, so that a linear model may be used to approximate its dynamic response characteristic. This simplifies the problem of determining the input voltage to the shaker, since for a linear system, the system input is equal to the system output divided by the transfer characteristic. Figure 6 shows the measured acceleration/voltage frequency response function (FRF). For this measurement, a dry sand model weighing a total of 35 kg was spun at 50 g and excited with a 1 volt rms random noise input while the slip table acceleration was measured using an accelerometer. In order to improve the signal-to-noise ratio of the measurement, twenty measurement records were averaged.

This linear model provides useful and important information about the behavior of the shaker. The resonance peak at 119 Hz corresponds to the fundamental hydraulic resonance, caused by the interaction of the shaken mass and the compliant hydraulic oil within the shaker; the pole dominates the time-domain response of the shaker; the associated fundamental time constant is approximately 19 ms. The peaks (i.e. poles) in the magnitude plots at 119 Hz and 184 Hz indicate that the shaker responds strongly and is therefore capable of producing large accelerations at these frequencies. The shaker produces only limited accelerations at very low frequencies, very high frequencies, and at the system zero at 174 Hz.

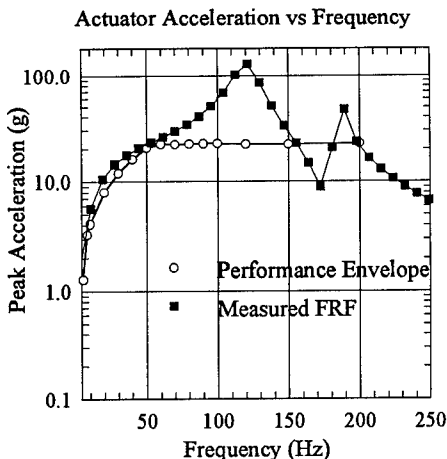


Fig. 7. Graph showing range of shaker operation

More generally, the transfer function together with the performance envelope give an indication of the range of shaker operation, that is, the class of target motions which the shaker can feasibly produce. For instance, the  $\pm 10$  volt input limitation of the servo controller multiplied by the acceleration transfer characteristic is plotted together with the performance envelope in Figure 7. The region beneath both curves constitutes the approximate range of the shaker.

If the target acceleration time history can be satisfactorily approximated by a finite Fourier series and lies within the range of shaker operation, the corresponding input voltage signal can be approximated. The Fourier transformed target input acceleration  $Y(j\omega)$  is divided by the system FRF  $H(j\omega)$  to obtain the Fourier transform of the shaker input voltage  $X(j\omega)$ . This can be inverse transformed to obtain the actual voltage signal  $x(t)$  needed to produce the target motion. This technique is particularly effective for producing periodic motions that are of relatively long duration compared to the time constant of the shaker system.

## 5. TEST RESULTS

The shaker has been used to perform tests at centrifugal accelerations of up to 100 g on soil models. Figure 8 shows a comparison of target and measured input accelerations, in prototype units, for a 35 kg total weight dry sand model tested at 50 g centrifugal acceleration. In this case, the input voltage signal was obtained from the target motion

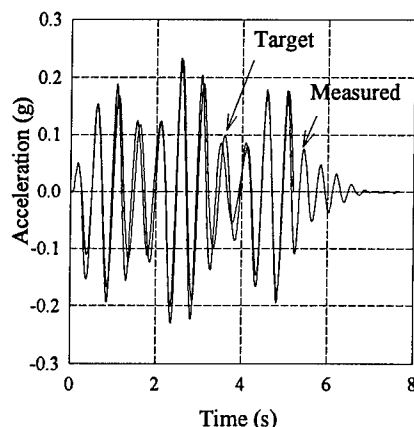


Fig. 8. Comparison of target and measured input motion (prototype units)

and shaker transfer function using the procedure described above. The figures demonstrate that the measured shaker motion closely approximates the target motion.

## 6. CONCLUSIONS

A servo hydraulic centrifuge shaker has been developed for dynamic centrifuge testing at RPI. The design, construction and operation have been described. Measurements of the shaker's time- and frequency-domain dynamic characteristics have been used to quantify performance. Tests on representative soil models have demonstrated that the a-priori performance objectives have been achieved satisfactorily.

## 7. ACKNOWLEDGMENTS

The authors wish to acknowledge the National Center for Earthquake Engineering Research (NCEER), the National Science Foundation (NSF), and the State of New York for their continuous support of the development and operation of the RPI Centrifuge Center. Special thanks are due NCEER for its support of the electrohydraulic shaker project.

## 8. REFERENCES

- Arulanandan, K., and Scott, R., Eds. 1993. *Verification of Numerical Procedures for the Analysis of Soil Liquefaction Problems*. Rotterdam: Balkema
- Cheney, J. A., and Whitman, R. V., 1983. Workshop for development of specifications for a ground motion simulator for centrifuge modelling in geotechnical engineering. National science foundation division of civil and environmental engineering.
- Dobry, R., and Liu, L., 1992. Centrifuge modelling of soil liquefaction. *Post Conf. Proc. 10th World Conf. on Earthquake Eng'g*.
- Elgamal, A.-W., Dobry, R., Van Laak, P., and Nicolas-Font, J., 1991. Design, construction and operation of a 100 g-ton centrifuge at RPI. *Centrifuge 91*: 27-34. Rotterdam: Balkema
- Liu, L., and Dobry, R., 1994. Seismic settlements and pore pressures of shallow foundations. Submitted for publication to *Centrifuge 94*
- Ketcham, S., Ko, H.-Y., and Sture, S., 1991. Performance of an earthquake motion simulator for a small geotechnical centrifuge. *Centrifuge 91*: 361-368. Rotterdam: Balkema
- Kimura, T., Takemura, J., and Saitoh, K., 1988. Development of an electrohydraulic centrifuge earthquake simulator. *Centrifuge 88*: 103-106. Rotterdam: Balkema
- Kutter, B. L., Chang, G. S., Cheney, G. A., Arulanandan, K., and Sluis, W., 1987. Hydraulic shaker for the Schaevitz centrifuge report and operations manual. U. C. Davis
- Schran, U., Ting, N.-H., and Whitman, R. V., 1992. Dynamic centrifuge testing of a tilting retaining wall with saturated backfill; 1. Summary of results and preliminary interpretation. Research report R92-12 Dept. of Civil and Environ. Engg. MIT
- Scott, R. F., 1983. Centrifuge model testing at Caltech. *Soil Dynamics and Earthquake Engineering, Vol 2, No. 4*: 188-198
- Van Laak, P., Taboada, V., Dobry, R., and Elgamal, A.-W., 1994. Earthquake centrifuge modelling using a laminar box. *Dynamic Geotechnical Testing: Second Volume, ASTM STP 1213*, to be published in 1994
- Vucetic, M., Tufenkjian, M., and Doroudian, M., 1993. Dynamic centrifuge testing of soil-nailed excavations. *Geotechnical Testing Journal, Vol. 16, No. 2*: 172-187

## Effect of model containers on dynamic soil response

Gregg L. Fiegel, Martin Hudson, I. M. Idriss, Bruce L. Kutter & X. Zeng

*Department of Civil and Environmental Engineering, University of California, Davis, Calif., USA*

**ABSTRACT:** Four different types of model containers used for dynamic geotechnical centrifuge testing are discussed. A new type of container, termed a hinged-plate container (HPC) has been developed to properly model prototype boundary conditions. As part of this study, centrifuge experiments have been performed with the hinged-plate container using dry, moist, and saturated sand models; various levels of dynamic excitation have been used. In addition, similar experiments have been performed using a fixed-end container, Caltech's laminar box, and Cambridge's equivalent-shear-beam container (ESB). Results indicate that each container has its own dynamic properties or characteristics. Knowledge of these dynamic characteristics and how they can affect soil response is essential if test results are to be evaluated properly.

### INTRODUCTION

In dynamic centrifuge testing it is sometimes desirable to simulate prototype deposits of infinite lateral extent in the direction parallel to shaking. The ability to model this type of deposit is important, for example, if one is to study site response, liquefaction, or soil-structure interaction problems.

In order to properly model an infinite soil layer, the walls or boundaries of the centrifuge model container should not influence the response of the soil. Whitman and Lambe (1986), Campbell et al. (1991), and Schofield and Zeng (1992) have summarized the ideal boundary conditions necessary for minimizing adverse soil-container interaction. Some important qualities of an ideal model container are listed below:

1. The container should allow for development of complementary shear stresses during shaking.
2. The container should maintain a constant horizontal cross-section during shaking.
3. The container end and side walls should be stiff enough to maintain a  $K_0$  condition.

4. Container walls should have small mass to minimize dynamic lateral forces at the boundary.

It is important that the container be allowed to develop complementary shear stresses and deform as a shear beam. If these stresses do not develop then unrealistic bending stresses may occur in the soil in response to the overturning moment created during shaking.

In recent history, several container designs have been used in order to eliminate the adverse boundary effects created by using a fixed-end or "rigid" model container. Liquefaction or laminar containers have been constructed and tested by Hushmand et al. (1988), Law et al. (1991), and Van Laak et al. (1994). For these containers, rectangular frames were stacked with bearings in between; this permitted relatively free movement of the soil and frames during shaking. A second type of model container, termed an equivalent-shear-beam, has been designed at Cambridge University; this container, built with alternating rectangular layers of rubber and aluminum, is designed to act as a shear beam with dynamic stiffness similar to that of an average or typical prototype soil deposit (Schofield and Zeng 1992).

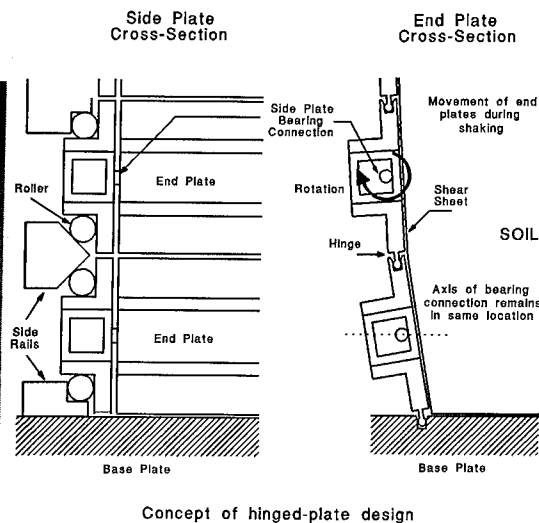
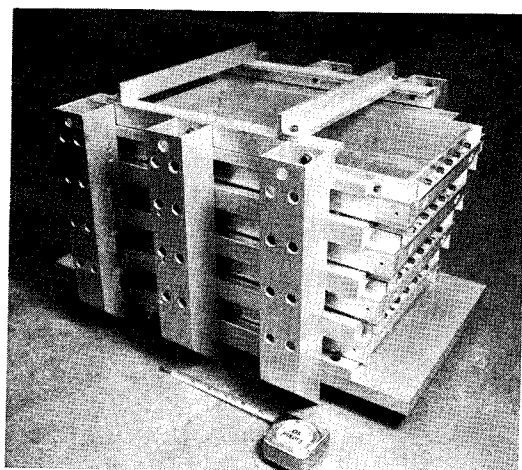


Fig. 1 Photograph and sketch of the hinged-plate model container

## THE HINGED-PLATE CONTAINER

A centrifuge model box, termed a hinged-plate container (HPC), has recently been constructed at the University of California, Davis. Goals of the container design were to: 1.) offer little if any resistance to horizontal shear deformation, 2.) sustain dynamic complementary shear stresses in order to prevent bending deformation of the soil column, 3.) provide adequate stiffness in the side and end walls to prevent lateral strains during spin-up and shaking, 4.) keep the mass of the side and end walls low, and 5.) provide displacement continuity along each end wall.

The new model container is pictured in Fig. 1. The container consists of four rectangular aluminum frames with the following inside dimensions: 5.7 cm (2.25 in.) tall, 38.1 cm (15.0 in.) long, and 21 cm (8.25 in.) wide. As shown in Fig. 1, a cross-section of a typical end or side plate consists of two angle sections and a square tube; the angles and tube are bolted together at several points along the length of the section. The built-up section was designed to resist significant deflection while minimizing mass. Aluminum angle and tube sections were used in

the design to keep the mass of the container walls low.

The side plates of the rectangular frames rest on steel balls which are supported by a rail system; thus, each level of the container is free to move back-and-forth during shaking. The rails, attached to external columns, provide support for each of the individual levels so that the top level of the container does not rest on the bottom level. Thus, the friction between the steel balls and the rails for a lower level does not depend on the weight of other levels above.

Confinement or continuity at the end walls is provided by a hinge between the end plates of each level. The concept is illustrated in Fig. 1. The end plates are connected to the side plates with a bearing type joint and are free to rotate 360°. Each end plate, however, is interconnected by the hinge system shown thus providing displacement continuity at the end boundary. This design allows for horizontal displacement of the soil mass during shaking without the stair-type displacement pattern that exists in laminar model containers.

To account for dynamic complementary shear stresses that occur during shaking, a shear sheet has been incorporated into the design (Schofield

Table 1: Dimensions for the four model containers used in this study

Container Type	Inside dimensions L x W x H (cm)	No. levels or laminae	Degrees of freedom per level	Mass of container walls (kg)	Wall-to-soil mass ratio
ESB	38.1 x 21.0 x 22.9	8	1	19	0.52
HPC	38.1 x 21.0 x 22.9	4	2	8	0.22
Laminar	35.6 x 17.8 x 25.4	20	1	9	0.28
Fixed	55.9 x 27.9 x 17.8	N/A	N/A	N/A	N/A

and Zeng 1992). As shown in Fig. 1, a thin aluminum sheet lies next to each end wall; the sheet, which is fixed to the base of the model container, is roughened by the use of glue and sand. In compression and extension, the sheet is intended to transfer complementary shear stresses directly to the base of the container.

#### INITIAL CENTRIFUGE EXPERIMENTS

As part of this study, four model containers were used in centrifuge experiments. The four included Davis' hinged-plate and fixed-end containers along with replicas of the Cambridge equivalent-shear-beam (ESB) and Caltech's laminar box. Dimensions of the four containers are included in Table 1. To calculate the wall-to-soil mass ratio, the mass of the container walls was divided by the mass of soil ( $2.0 \text{ g/cm}^3$ ) required to fill the model container volume.

Initial experiments were carried out using the hinged-plate container and the fixed-end or "rigid" box. In these tests, a 12 cm high uniform layer of Nevada sand was subject to base shaking. The tests were performed at a centrifugal acceleration of  $50g$ ; therefore, the prototype deposit was 6 m in height. It is noted that the Nevada sand was placed at a relative density ( $D_r$ ) of 60%; the mean grain size of this material is 0.13 mm, and the coefficient of uniformity is about 2.

In numerous centrifuge experiments, dry, saturated, and moist deposits of this sand were

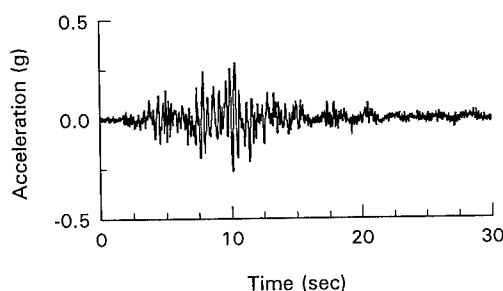


Fig. 2 Example of the base input motion used in centrifuge experiments.

subjected to a base motion corresponding to the Santa Cruz motion recorded during the Loma Prieta Earthquake of 1989; the motion is shown below in Fig. 2. This motion was scaled to produce time histories with approximate peak accelerations of 0.1, 0.3, and  $0.6g$ 's prototype. For each experiment, a sand deposit was shaken by each of the three scaled motions in order of increasing intensity.

Results of several tests involving dry and moist sand are shown in Fig. 3. In this figure, shown in prototype terms, peak acceleration at the surface of the deposit is plotted against peak acceleration at the base. As indicated, peak surface acceleration values measured in the hinged-plate container were amplified at low levels of shaking; however, this amplification was much less for higher levels of shaking. The trend is consistent with nonlinear soil response observed in the field. Contrary to these HPC observations, peak surface acceleration values



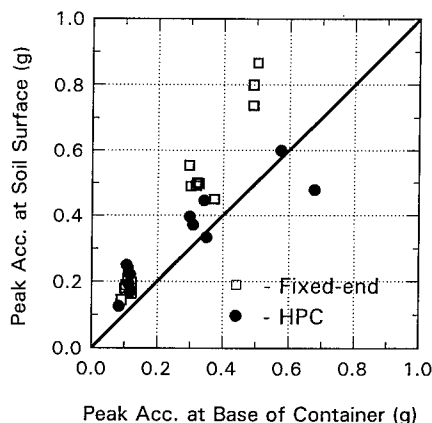


Fig. 3 Centrifuge test results on Nevada sand using hinged-plate and fixed-end containers

measured in the fixed-end container were highly amplified at the higher levels of shaking. It appears that the fixed-end container tends to inhibit nonlinear soil response.

A separate series of tests were conducted using the same Nevada sand and both the hinged-plate and fixed-end model containers. In these tests, dry sand was placed in a very dense state ( $D_r = 95$  to  $100\%$ ); models were then shaken with an impulse type motion corresponding to a square wave input displacement. Acceleration was measured at the base of each container, and an approximate free vibration acceleration response was measured at the surface. The results from these tests are shown in Fig. 4.

Fig. 4(a) shows the response measured in the hinged-plate container. A  $0.25g$  acceleration spike was recorded at the base of the model, and a relatively smooth acceleration response was measured at the soil surface. However, as indicated in Fig. 4(b), response in the fixed-end container was much different. The surface acceleration record included a high frequency component absent in the hinged-plate test; this high frequency response was likely caused by P-waves generated due to interaction of the fixed container walls and the soil during shaking.

In addition to the surface acceleration record, the base acceleration record measured in the fixed-end test was different than that measured during the hinged-plate test. After a  $0.26g$

acceleration peak, continued low period response was measured at the base. It appears that for the fixed-end container an interaction may take place between the soil and the container. This would suggest that an input base motion can be affected by the model container used.

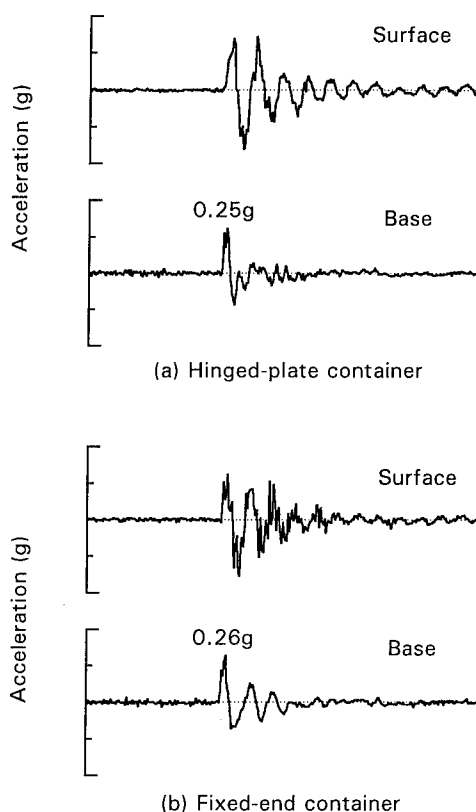


Fig. 4 Base and soil surface acceleration response of dense sand layers

#### "FLEXIBLE" CONTAINER EXPERIMENTS

Three model experiments were conducted using the hinged-plate, equivalent-shear-beam, and laminar containers. Each test was performed at  $50g$  using a dry Nevada sand layer  $20.6$  cm high ( $D_r = 60\%$ ). A typical model configuration included instrumentation to measure horizontal acceleration throughout the height of the model. It is noted that additional experiments were performed using saturated sand models;

however, these results are not presented.

Each dry sand model was subjected to the Santa Cruz input motion; again the motion was scaled to produce events with peak accelerations of approximately 0.1, 0.3, and 0.6g. These three motions were applied to the models in order of increasing intensity. Shown in Table 2 are prototype surface settlements measured in all three experiments. For these settlements, it can be shown that the maximum increase in relative density experienced after the 0.1 and 0.3g shaking events was fairly small at 3%.

Table 2. Prototype surface settlement measured during dry sand experiments

Container	Surface settlement measured for each event (cm)		
	0.1g	0.3g	0.6g
ESB	1.3	3.6	6.4
HPC	1.4	5.1	7.7
Laminar	1.3	3.5	7.1

In Fig. 5 peak acceleration at the surface of the sand is plotted as a function of peak base acceleration for each model test. The curves show a non-linear trend which is consistent with field observations for sandy soils (Seed and Idriss 1982); however, surface accelerations measured in the ESB and laminar containers seem to be high and low, respectively.

It is noted that the ESB container was originally designed to have a dynamic stiffness similar to that of a 10 m prototype deposit of sand ( $D_r = 50\%$ ). Since the stiffness of the ESB container is fixed, the container was designed for use in low to moderate shaking environments where a change in soil stiffness is minimal. Centrifuge results appear to confirm this design restriction. The higher measured accelerations indicate that the ESB container, although designed with a dynamic stiffness similar to that of the Nevada sand model, may not accurately take into account soil non-linearity (stiffness and damping) especially for moderate to higher levels of shaking. The aluminum-rubber wall

design and the high wall-to-soil mass ratio cause the ESB container to control soil response to some degree at these higher shaking levels.

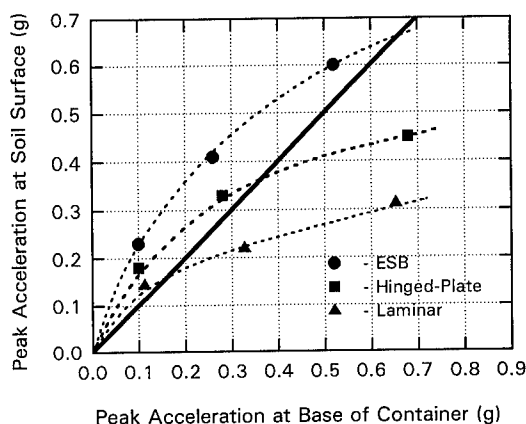


Fig. 5 Summary of peak surface accelerations for dry sand experiments

Acceleration response spectra are shown in Fig. 6 for surface accelerations recorded during the 0.3g shaking events; it is noted that the spectral shape of the input base motion was nearly identical for each test. As shown, surface acceleration response is similar to that presented in Fig. 5. However, despite differences in the absolute values, spectral ordinates normalized with respect to peak ground surface acceleration are similar for each container.

Additional tests were performed using dense dry sand ( $D_r = 95$  to  $100\%$ ) in each of the three flexible containers. In these tests, each model was subject to a series of 0.15g sinusoidal input motions with different periods. Response at the surface of the sand was measured so that an amplification ratio relating surface to base acceleration could be calculated for each base input period. The results are presented in Fig. 7.

As shown, the ESB container had the highest amplification ratio; this peak corresponded with an input period of 0.4 seconds. The HPC also peaked at this period, but the curve for the laminar box was shifted to the right. The shift indicates that the laminar box might not be as stiff as the other containers. This could explain the low accelerations shown in Figs. 5 and 6.

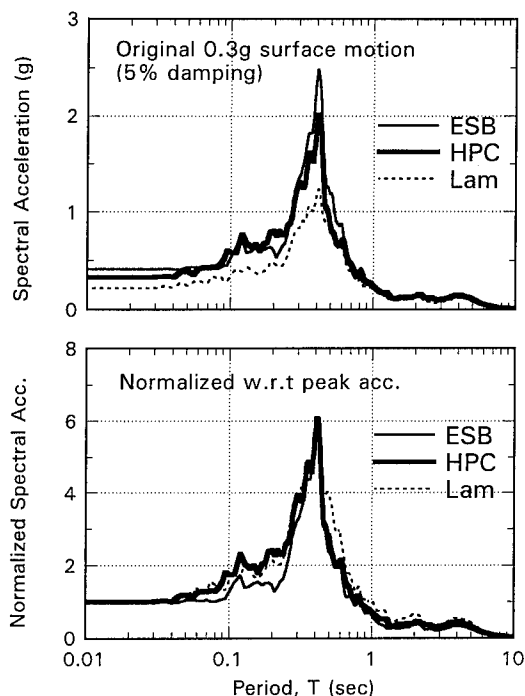


Fig. 6 Dry sand surface response spectra

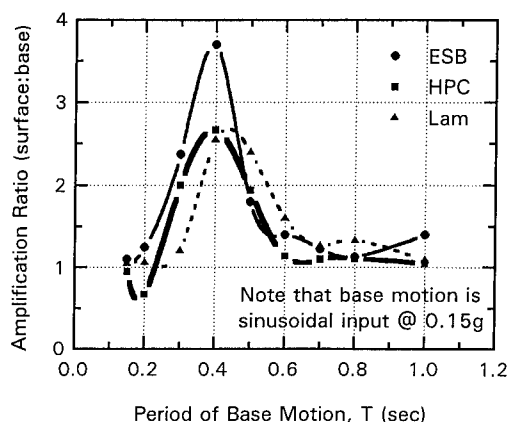


Fig. 7 Acceleration amplification ratio as a function of period of sinusoidal input motion

## CONCLUSIONS

Different model containers each have their own mass, stiffness, and damping. Results show that soil response was similar for models tested in each of the flexible containers; soil response in

the fixed-end container differed from the flexible containers for stronger levels of shaking. With regard to flexible containers, dry sand tests showed that the HPC and ESB operated at nearly the same natural period; the higher accelerations measured in the ESB may be attributed to its limited ability to model soil non-linearity especially at higher shaking levels. A higher natural period (lower system stiffness) was found for the laminar container; this could have led to the small measured accelerations. Overall, differences in soil response show that it is essential that a model container's dynamic characteristics be fully incorporated when evaluating centrifuge test results and when making comparisons with other experiments.

## ACKNOWLEDGEMENT

The authors gratefully acknowledge Caltrans for sponsoring the research described in this paper.

## REFERENCES

- Campbell, D., Cheney, J., and Kutter, B.L. 1991. Boundary effects in dynamic centrifuge model tests, *Proc. of Centrifuge 91*, pp. 441-448.
- Hushmand, B., Scott, R.F. and Crouse, C. 1988. Centrifuge liquefaction tests in a laminar box, *Geotechnique*, Vol. 38, No. 2, pp. 253-262.
- Law, H., Ko, H.Y., Sture, S., and Pak, R. 1991. Development and performance of a laminar container for earthquake liquefaction studies, *Proc. of Centrifuge 91*, pp. 369-376.
- Schofield, A.N. and Zeng, X. 1992. Design and performance of an equivalent-shear-beam container for earthquake centrifuge modeling, *Cambridge Report: CUED/DSOILS/TR245*.
- Seed, H.B. and Idriss, I.M. 1982. Ground motions and soil liquefaction during earthquakes, *EERI Monograph Series*, EERI.
- Van Laak, P.A., Taboada, V.M., Dobry, R., and Elgamel, A.W. 1994. Earthquake centrifuge modeling using a laminar box, *Dynamic Geotechnical Testing II*, ASTM STP 1213.
- Whitman, R.V. and Lambe, P.C. 1986. Effect of boundary conditions upon centrifuge experiments using ground motion simulation, *ASTM GTJODJ*, Vol.9, No. 2, pp. 61-71.

## Development of an earthquake simulator for the TAISEI centrifuge

K. Nagura, M. Tanaka, K. Kawasaki & Y. Higuchi  
*Taisei Corporation, Yokohama, Japan*

**ABSTRACT:** A geotechnical centrifuge has been in operation at Taisei Corporation since February 1991. It was initially designed for dynamic model tests. An electrohydraulic servocontrolled shaking table system has been fabricated and its control has been achieved by providing a close approximation of the magnitude spectrum of the Fourier transform of a scaled motion earthquake record, using the inversed transfer function from trial testing. Furthermore the data acquisition system by means of an optical transmission has been developed to eliminate noise. This paper introduces the Taisei centrifuge and illustrates the earthquake simulator and the data acquisition system.

### 1 INTRODUCTION

Authors has been engaged in various research and technical development projects to support increasing large-scale and diverse underground development projects. These include predicting soil behavior during excavation, stabilizing soil, preventing from liquefaction of soft soils and investigating geological structures. In such back-ground, TAISEI centrifuge was developed to simulate the complex behavior of underground up to 100m deep by model experiments and the ground motion during earthquakes.

### 2 GENERAL SPECIFICATION

The main parts of the centrifuge are housed in the underground reinforced concrete enclosure for safe operation. The inner size of the enclosure is founded on the hard clay layer having approximately  $80\text{N/cm}^2$  unconfined strength. The main parts of the centrifuge weighs approximately 240kN and whose diameter is 6.9m. As shown in Fig.1, two types of swinging baskets hinged to the rotating arm are prepared. One of them is delivered the radial force under high acceleration to the end plate of the arm by means of the special system (Touch-Down System) for dynamic and earthquake geotechnical model tests mainly. The other basket for static geotechnical model tests swings up freely corresponding to the centrifugal acceleration.

The platform on the basket provides an area of 100 cm by 90 cm on which any type of model package could be mounted.

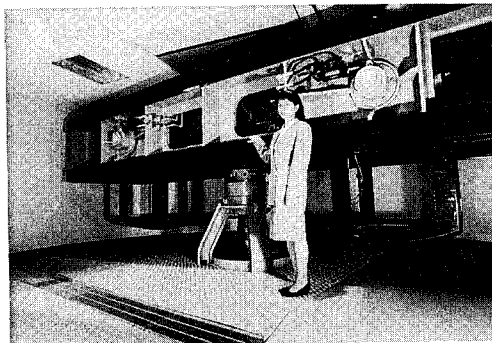
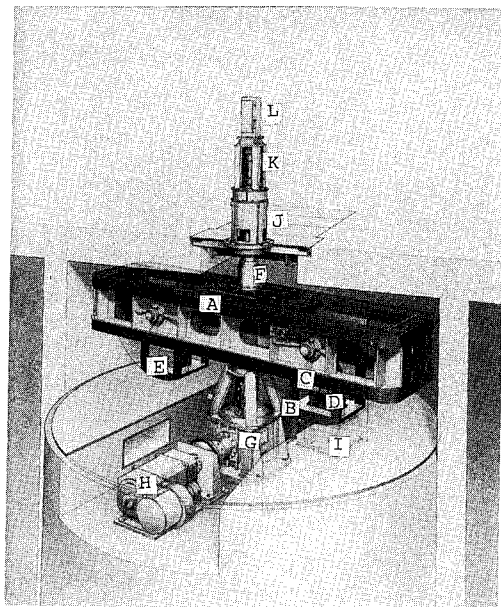


Fig.1 Photograph of Taisei centrifuge

As shown in Fig.2, 300kW direct current motor is mounted as a drive unit for the centrifuge in the pit under the bottom floor of the enclosure and generates steady acceleration up to 200g at the effective radius. The control of the centrifuge is carried out in the operation room on the upper floor. Important conditions, such as rocking of the main shaft, temperature of the air in the enclosure, pressure of the lubricant and so on, are always displayed on the control panel. Safety function is equipped to stop the machine automatically in the case of severe trouble.



A:Rotating arm  
B:Basket  
C:Specimen container  
D:Shaking table  
E:Counter weight  
F:Main shaft  
G:Beveled gear (Reduction gear)  
H:300kW direct current motor  
I:Hydraulic supply unit  
J:Hydraulic rotary joint  
K:Slip ring riggings  
L:Multiport fiberoptic rotary joint

Fig.2 Descriptions for the centrifuge

Photo-instrumentation and TV monitoring are carried out through the openings of the side wall or the upper floor of the enclosure. Electricity and hydraulic pressure are supplied to the baskets through the slip ring riggings and hydraulic rotary joints respectively. Signals from transducers are transmitted to the computer through the newly developed optic transmission system.

Major specifications of the TAISEI centrifuge are the followings.

Diameter of arm	: 6.90m
Effective radius	: 2.65m
Main motor	: 300kW
Maximum speed of rotation	: 260rpm
Maximum acceleration	: 200g
Maximum capacity	: 80g-ton
Space of platform	: 1000mm* 900mm
Electric slip ring	: 45poles
Fiber-optic rotary joint	: 1system
Number of hydraulic joints	: 5

### 3 TOUCH-DOWN SYSTEM

There are two pivots on the arm, which are incorporated with bearings to swing up the basket and are equipped with four jacks in dynamic testing side. The center of the bearings is 5mm eccentric from the center of the pivots. When centrifuge acceleration reaches at a predetermined value, the jacks controlled by the computer revolve the pivot 90 degree and the basket seats on the end plate of the arm. Fig.3 shows photograph of the basket seated on the end plate and the principle of the "Tough-Down System" is illustrated in Fig.4.

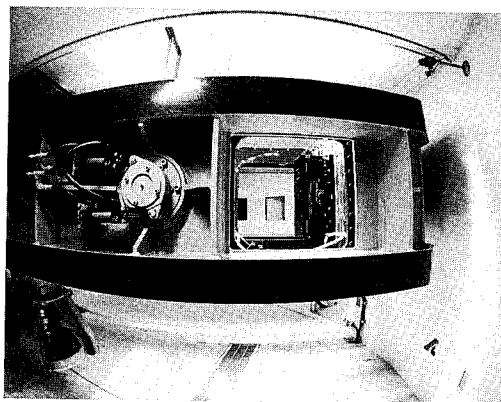


Fig.3 Basket seated on the end plate of arm

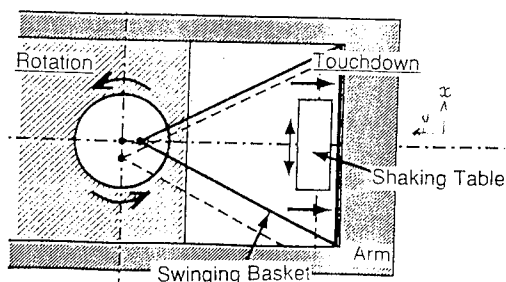
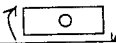
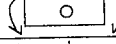
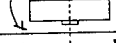
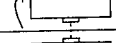
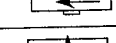

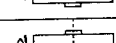




Fig.4 Principle of "Touch-Down system"

### 4 RESONANT FREQUENCY OF THE ROTATING ARM

Fig.5 shows resonant frequencies and mode shapes of the rotating arm corresponding to each mode, which are calculated by means of NASTRAN (3 dimensional dynamical finite element analysis without considering centrifugal force). It is considered from this results that response frequency of the specimen mounted on the basket will be affected by a 35Hz resonant frequency corresponding to the 4th mode of the arm, in the dominant frequency bandwidth of the shaker.

mode	resonant frequency	mode shape
1st	18.4	
2nd	18.6	
3rd	23.9	
4th	35.0	
5th	42.6	
6th	55.0	
7th	57.5	
8th	59.8	
9th	106.3	

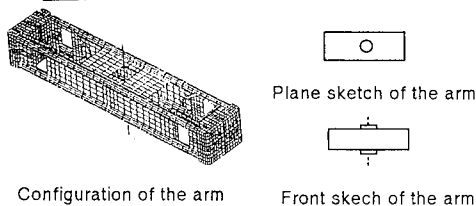


Fig.5 Resonant frequency of the arm

#### 5 EARTHQUAKE SIMULATION SYSTEM

An electrohydraulic servocontrolled shaking table has been developed to simulate centrifuge earthquake motions. It is fairly easy both to control amplitude of horizontal displacement and to create high power. Fig.6 shows photograph of the shaker. Specifications of the shaker are the followings.

Centrifuge acceleration : 50 g  
Horizontal acceleration : 20 g  
Shaking mass : 180 kg  
Frequency range : 30Hz-300Hz  
Max.amplitude of horizontal displacement :  $\pm 2\text{mm}$

Base excitation of the shaker is not always in coincidence with desired signal because the shaker is mounted on the structure having complex mechanism. Therefore the signal correction system was adopted to account for the deficient frequency response of the shaking table. Transfer function obtained from the results of experiments with comparative motions is necessary for calculating a corrected input signal from the desired signal.

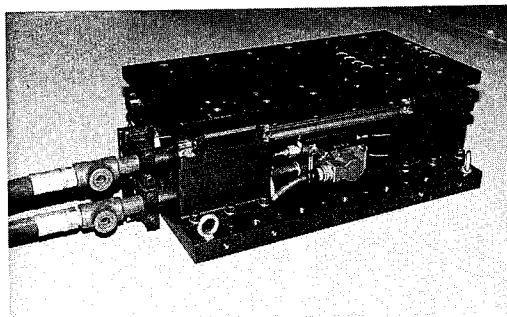


Fig.6 Overview of the shaker

Experiments are carried out as trial shaking tests by generating very small vibration which cause little change to the soil structure in the model container. Outline of this procedure is shown in Fig.7. This procedure implies that an iterative scheme is required to estimate a corrected input signal.

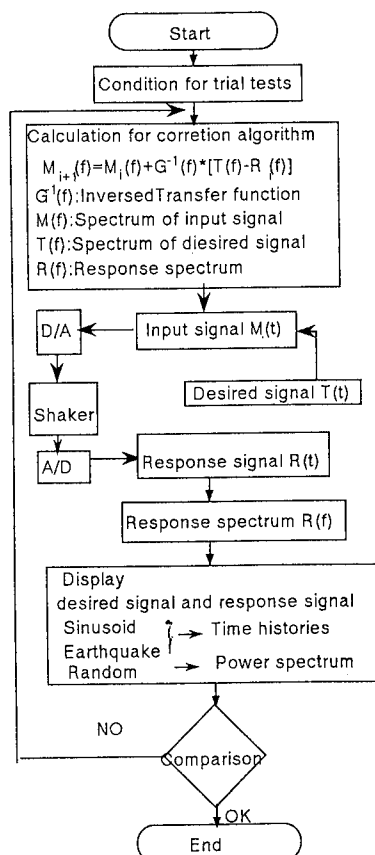
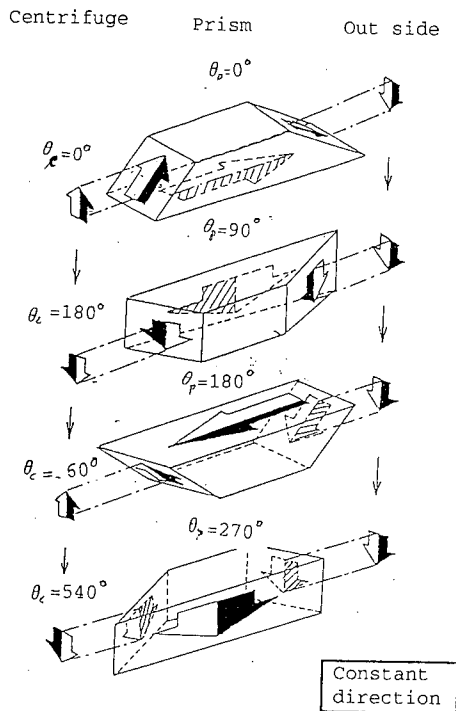


Fig.7 Signal correction system

## 6 DATA ACQUISITION SYSTEM

For dynamic testing events, the sampling rate of the data acquisition system has to be very fast because the frequency of the loading in centrifuge modeling is scaled to be  $N$  times higher than that experienced by prototype. Therefore it is very important to eliminate the noise in the transmission system from sensors to a computer. Brush and slip ring riggings are common method of providing a signal path from the centrifuge shaft to the outside. Noise is chiefly caused by dynamic vibration during which brush is in contact with slip rings. The transmission system incorporated with multiport fiber-optic rotary joint has been developed as a non-contact transmission system. Principle of that is shown in Fig.8a. The axis of the trapezoid prism and the optical fiber in the centrifuge side are in coincidence with the outside optical fiber axis. The trapezoid prism rotates in the same



$\theta_c$ : Angular displacement of centrifuge shaft  
 $\theta_p$ : Angular displacement of prism  
 $\dot{\theta}_c$ : Angular velocity of centrifuge shaft  
 $\dot{\theta}_p$ : Angular velocity of prism  
 $\dot{\theta}_p = 1/2 * \dot{\theta}_c$

Fig.8a. Principle of multiport fiber-optic rotary joint

direction as the centrifuge shaft but with a half angular velocity of the centrifuge shaft. Then the rotating portrait in the centrifuge side is projected in the constant direction of the outside optical fiber.

The outline of this system is shown in Fig8b. Analog signals obtained from sensors are amplified in the signal conditioning unit and converted to digital signals through A-D converter mounted on the rotating arm. Subsequently digital signals are converted to optical signals through the electric-optic (E/O) converting unit. Furthermore through the optic rotary joint, optic signals are sent to the optic converting unit located in the control panel. After converting to electrical signals through the optic-electric (O/E) unit, the signals are sent to the computer for data acquisition. Specifications of the data acquisition system are shown below.

Max. of signal channels: 32  
 Sampling rate  
 for 32 channels : 10,000 samples/sec  
 Capacity of  
 buffer memory : 1,000,000 samples  
 Signal-noise ratio : < 0.2%

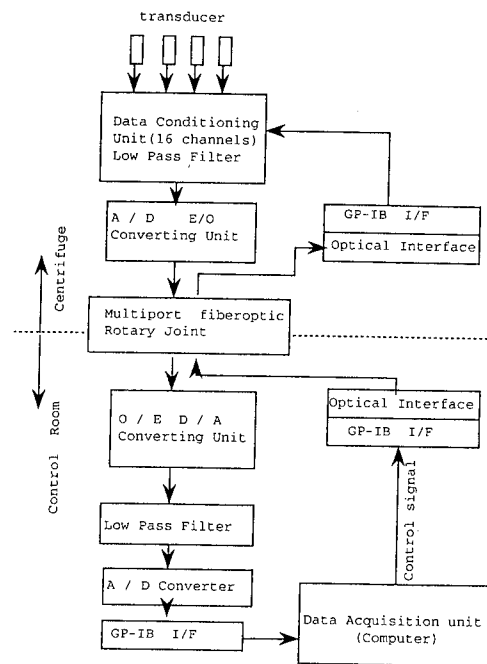


Fig.8b. Data Acquisition System

## 7 RESULTS OF PROOF TESTS

Several preliminary tests were carried out at a 50g centrifuge acceleration to investigate performance of the developed shaking system. Fig.9 shows the response acceleration waves of the shaking table mounted with a 1750N package at 30Hz frequency and 3g amplitude for non-correction and correction of input signal, respectively. Fig.10 shows those at 100Hz and under 3g, and Fig.11 shows at 30Hz and under 5g, respectively. It can be said from these results that the acceleration waves compensated by the correction algorithm is not distorted compared with those from non-correction method. In the case of high frequency bandwidth as seen in Fig.10, response waves with non-correction method is slightly distorted.

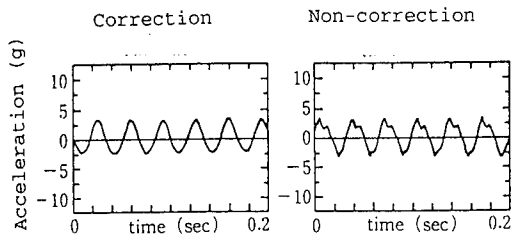


Fig.9 Response waves of shaking table  
( $f=30$  Hz,  $a=3$  g)

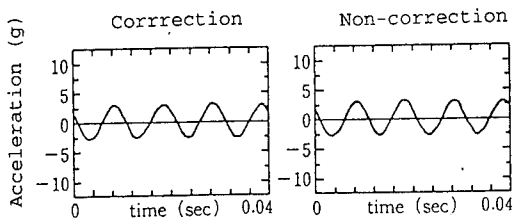


Fig.10 Response waves of shaking table  
( $f=100$  Hz,  $a=3$  g)

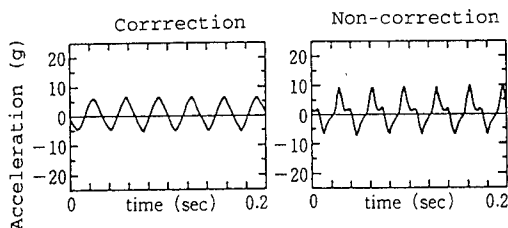


Fig.11 Response waves of shaking table  
( $f=30$  Hz,  $a=5$  g)

Fig.12 shows response acceleration of the shaking table mounted with a 1750N package targeting at 3g amplitude in the designed frequency bandwidth by means of the correction and non-correction methods, respectively. It can be concluded from the results that the response acceleration for the correction system is constant, but for the non-correction method it varies corresponding to frequency.

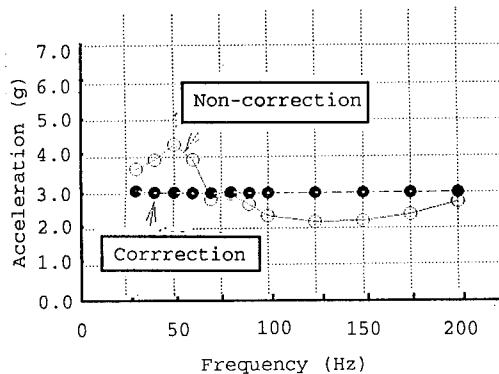


Fig.12 Response acceleration of shaking table

The top of Fig.13 shows the acceleration time histories observed at Hachinohe in the 1968 Tokachi-oki earthquake, whose seismic magnitude is 7.9, as the desired signal. The bottom of Fig.13 shows the response acceleration time histories measured on the shaking table. As seen in Fig.13, it appears that the response wave of the shaking table almost coincides with the desired wave.

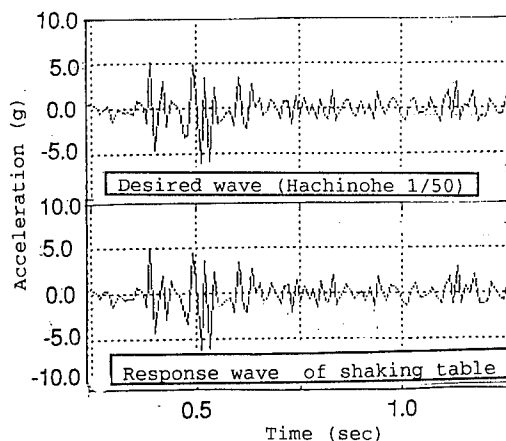


Fig.13 Comparison with desired wave and response wave of shaking table



The top of Fig.14 shows the response acceleration of the shaking table again, generated by the above mentioned earthquake. The middle of Fig.14 shows the negligible coupled acceleration time histories of the shaking table in the vertical direction (y direction shown in Fig.4). The bottom of Fig.14 shows, similarly, the negligible coupled acceleration of the basket in the horizontal direction (x direction shown in Fig.4). In order to obtain a precise response wave, it is important that the coupled motion of the shaking table is very small and negligible during x direction excitation of the shaking table. From these results, it can be said that the vertical excitation of the shaking table and horizontal excitation of the basket are very small, compared with the response wave of the shaking table in the horizontal direction. These results show the developed earthquake simulation system can simulate earthquake motions precisely.

## 8 CONCLUSIONS

In order to simulate earthquake motions precisely, operational in gravity force, the new shaking system was developed with the following features.

(1) Due to seating of the basket on the end plate of the rotating arm by means of the "Touch-Down System", low level of undesirable excitation on the basket and in a vertical direction of the shaking table, which is normal to the centrifugal and gravitational force fields, can be detected during centrifuge dynamic testing.

(2) It was proved that application of the signal correction system accounting for the deficient frequency response of the shaking table was succeeded by comparison of the response signals and the target signals, using sinusoidal waves and earthquake records.

(3) As the sampling rate of the data acquisition system in centrifuge modeling has to be fast, the signal transmission system incorporated with multipoint fiber-optic rotary joint was adopted.

## REFERENCES

- Ketchaman, S.A., Ko, H.Y., Sture, S. 1988. An electrohydraulic earthquake simulator for centrifuge. *Centrifuge 88*, pp.97-102.
- Ketchaman, S.A., Ko, H.Y., Sture, S. 1991. Performance of an earthquake motion simulator for a small geotechnical centrifuge. *Centrifuge 91*, pp.361-367.
- Nagura, K., Tanaka, M., Kawasaki, H., Higuchi, Y. 1992. A study on the centrifuge model testing. *Taisei Technical Report*, Vol.25, PP.141-148.
- Terashi, M. 1985. Development of PHRI geotechnical centrifuge and its application. *Report of the Port and Harbor Research Institute*, Vol.24, No.3, pp.73-122.

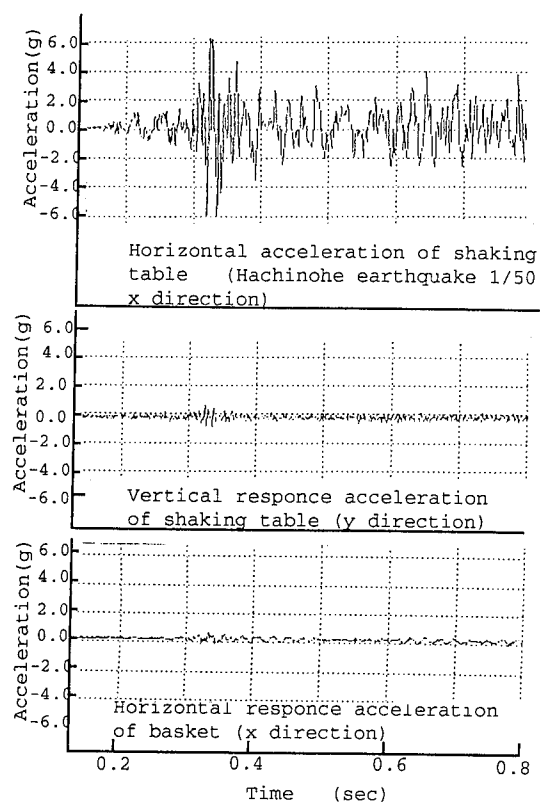


Fig.14 Response acceleration of shaking and of basket

## A new dynamic geotechnical centrifuge and performance of shaking table tests

Masayoshi Sato  
Shimizu Corporation, Tokyo, Japan

**ABSTRACT:** This paper introduces a new dynamic geotechnical centrifuge facility at Shimizu Corporation. The facility consists of a shaking table mounted on a centrifuge having a radius of 3.11 m to the shaking table top; a digital feedback control system; and a laminar container, 74 cm long, 34 cm wide and 50 cm deep, fabricated from square steel tubing. The results of preliminary shaking table tests show that (1) the digital feedback control system can excite the shaking table to closely reproduce acceleration histories of actual earthquakes under elevated gravity field; (2) the distribution of accelerations in the model ground of dry sand is relatively uniform within the laminar container; and (3) the model ground of sand saturated with a viscous liquid can be liquefied by applying scaled earthquake record to the shaking table.

### 1 INTRODUCTION

In order to faithfully reproduce the dynamic behavior of soil structures and sand deposits such as seismic liquefaction-induced displacements, many researchers have recently paid their attention to dynamic model tests on a geotechnical centrifuge. However, there exists a problem that the size of soil model is generally too small because the centrifuge cannot provide sufficient space and payload capacity. Because the boundary effect of soil container is extremely important in centrifuge

experiments, particularly in the case of liquefaction tests, one must pay special attention to the large inertia and possibly very large displacement of a soil container. Accordingly it is necessary to make a laminar container as large as possible.

The aim of this paper is to describe a new geotechnical centrifuge facility shown in Fig.1, and two kinds of shaking table tests on model sand deposit by using a large payload shaking table with a electro-magnetic earthquake simulator and a large laminar container.

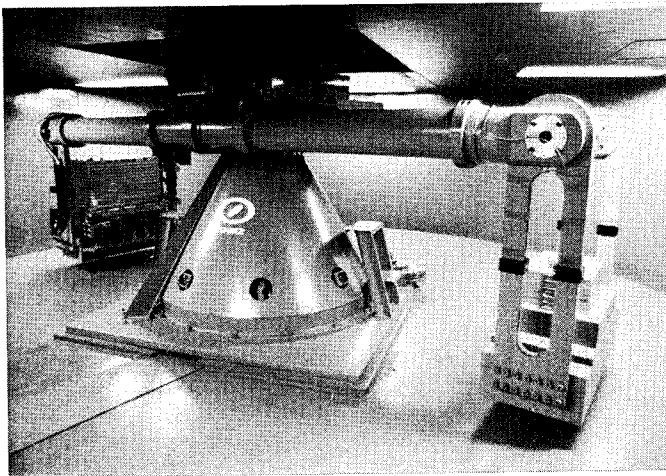
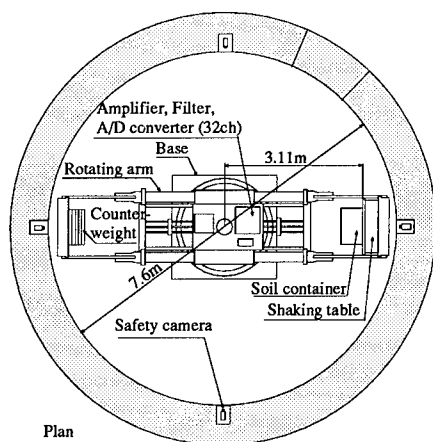
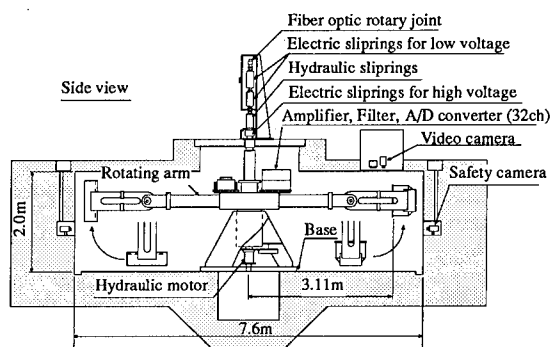


Fig. 1 Geotechnical centrifuge at Shimizu Corporation



Plan



Side view

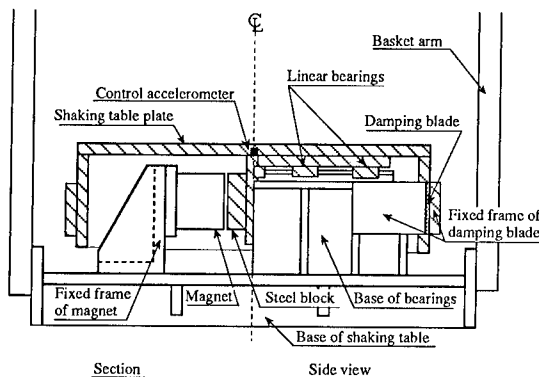
Fig. 2 Centrifuge in underground pit

## 2 TEST EQUIPMENT

### 2.1 Main feature of centrifuge

The centrifuge has been fabricated at the Institute of Technology, Shimizu Corporation, Japan, in 1991. It is housed in a heavily reinforced underground pit, 7.6 m in diameter and 2.0 m deep. Fig. 2 shows the plan and side view of the centrifuge. The centrifuge apparatus is comprised of two symmetrical swing platforms, a rotating arm, a swing counterweight, a driving system, an in-flight balancing system, and fiber optic rotary joint and electric slipring assemblies. In addition, a shaking table and a laminar container are available for dynamic tests.

A model container is mounted on one of the swing platforms, and an adjustable counterweight on the other. There are two types of swing platform for the model container. One of them accommodates a rigid container for static tests, and the other a shaking table driven with an electro-magnetic shaker for dynamic tests. The arm radius of the



Section

Side view

Fig. 3 Shaking table

Table 1 Specifications of shaking table test

Radius of rotation	3.11m
Size of shaking table	95cm×65cm
Centrifuge acceleration	5~50g
Maximum payload	300kg
Shaking acceleration	
: Sine wave	5g
: Random wave	10g
Range of frequency	50~350Hz

centrifuge to the basket platform is 3.35 m for static tests and 3.11 m for dynamic tests. The centrifuge accommodates a maximum payload of 750 kg at the maximum acceleration of 100 g for static tests and 300 kg at 50 g for dynamic tests. The centrifuge is driven by a hydraulic motor with a closed loop control system which enables close control of centrifuge acceleration, even at small accelerations of less than 10 g.

For safety reasons, four video cameras are mounted on the wall of the underground pit.

### 2.2 Shaking table

Specifications of the shaking table test are shown in Table 1. Although an electro-hydraulic excitation system has been popular for dynamic model tests on a centrifuge, an electro-magnetic excitation system is adopted here because it has an advantage over an electro-hydraulic systems in that it is able to produce and control large accelerations over a wide range in frequencies in the same way as in tests in 1 g field. The shaking table as shown in Fig. 3 is a modified version of the one designed previously by Fujii (1991).

The shaking table shown in Fig. 3 is symmetrical

about the centerline, the left half of the figure showing the cross-section and the right half the side view. The movable parts are hatched. The shaking table is supported with ten linear springs in two rows allowing the table to move in one horizontal direction only. There is a 1 mm gap between the thick steel block fixed to the underside of the table and each of the magnets fixed to the basket.

A test was conducted to confirm a limit

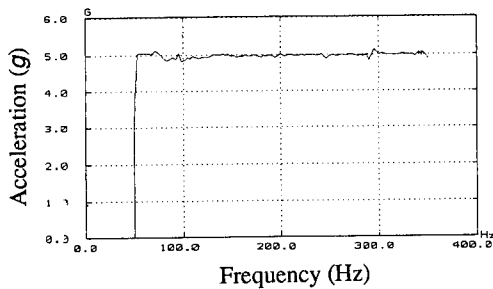


Fig. 4 Result of limit performance test for shaking table

performance of the shaking system. The test conditions are maximum payload 300 kg, sine wave, shaking acceleration 5 g, and range of frequency 50~350 Hz under centrifuge acceleration 50 g. The test result illustrated in Fig.4 shows that the shaking system can excite at acceleration 5 g.

### 2.3 Earthquake simulation system

The shaking table motion should simulate scaled earthquake records in order for the model ground to simulate prototype behavior during actual earthquakes. This is achieved here by digital feedback correction by computer control as shown in Fig. 5. The shaking table motion is controlled with an accelerometer mounted on the shaking table. The first step correction, ① through ④, is similar to the method by Ketcham et al. (1991) in which averaged frequency response function is used. If necessary, additional correction, ⑤ through ⑨, is repeated until simulation becomes satisfactory. Two iterations are usually sufficient to

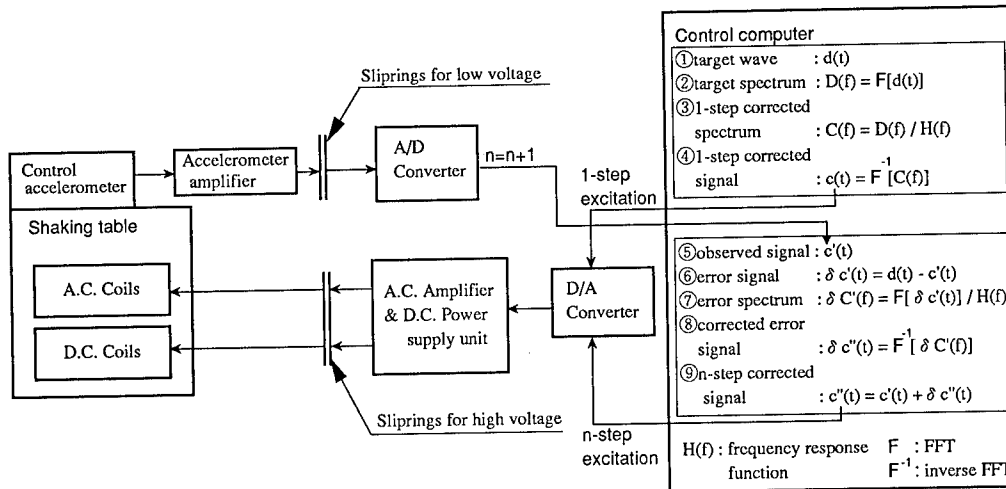


Fig. 5 Control system for shaking table

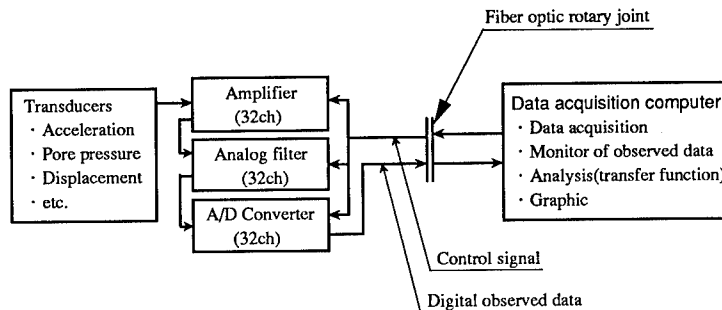


Fig. 6 Data acquisition system

satisfactory. Two iterations are usually sufficient to achieve good simulation of target records as described later in 3.2.

#### 2.4 Data acquisition system

The data acquisition system shown in Fig. 6 consists of transducers; an amplifier, a filter and an A/D converter capable of recording 32 channels of data which are installed on the rotating arm near its axis as shown in Fig. 2; and a data acquisition computer in a control room located on the first floor. The analog signals measured with the transducers are amplified, filtered and finally digitized in the real time. The data are then sent through fiber optic rotary joint into the computer and recorded. This system can record data with high precision by filtering out noise.

### 3 SHAKING TABLE TEST ON CENTRIFUGE

#### 3.1 Design of laminar container

A laminar container is designed as shown in Figs. 1 and 7. The container consists of 14 rectangular frames made of square steel tubing. Linear bearings 2 mm high are installed between these frames. The inside dimensions of the model container are 74 cm long, 34 cm wide and 50 cm deep. The container is lined with 1 mm thick rubber membrane to provide waterproofing for saturated soil and to protect the bearings from the soil. The

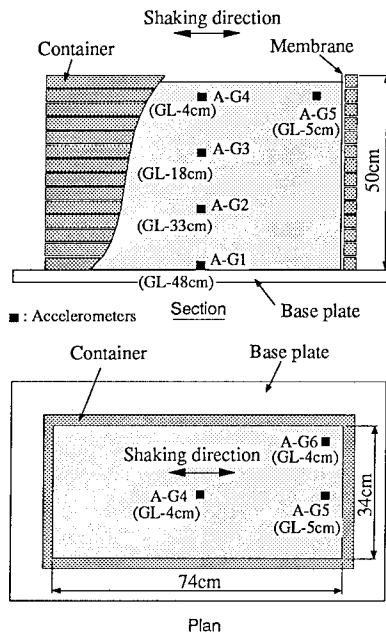


Fig. 7 Dry sand model and location of accelerometers

model ground can be saturated by supplying pore fluid through eight small holes in the base plate.

In addition to being strong and rigid, the model container needs to be light to minimize its inertia effects. In the current design using 1.2 mm thick hollow steel tubing, the ratio between the mass of the container and that of the model ground is 1:4.6 for dry Toyoura sand of 85% relative density, and 1:6.0 for saturated Toyoura sand of 60% relative density. These ratios are better than those in previous designs for centrifuge tests, although they are not as good as the usual ratio of about 1:20 for shaking table tests in 1 g field.

#### 3.2 Shaking table test with dry sand

Shaking table tests on 48 cm deep dry Toyoura sand in the laminar container were performed under 25 g to study the dynamic response of the model ground. Oven-dried sand was poured through a funnel from a constant height to control the density

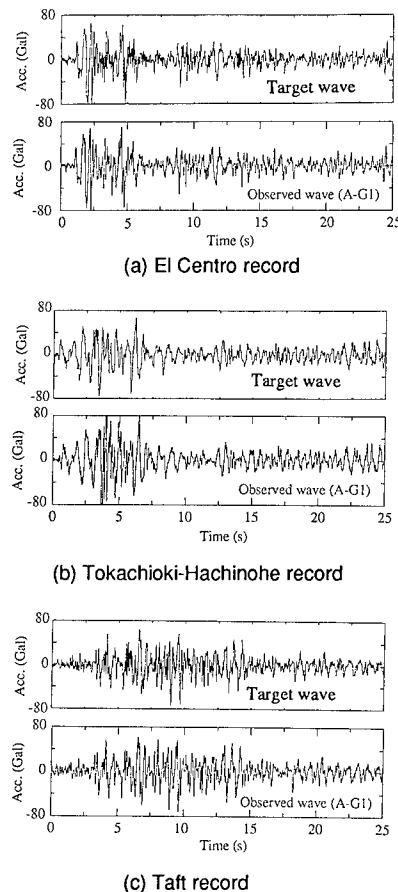


Fig. 8 Comparison between target wave and observed wave at base of model container

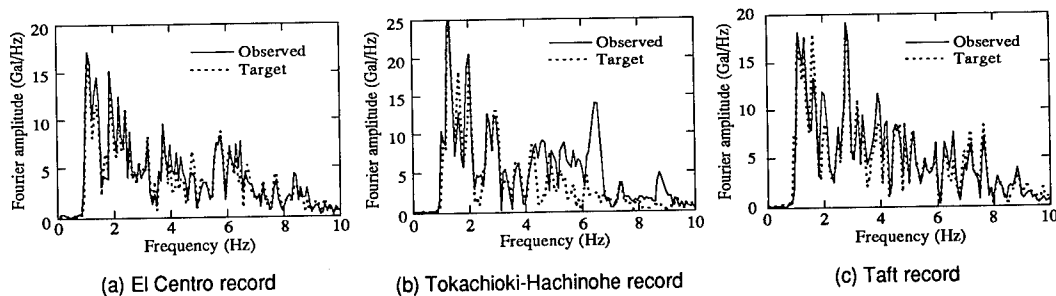


Fig. 9 Comparison between Fourier spectrum of observed wave and target wave

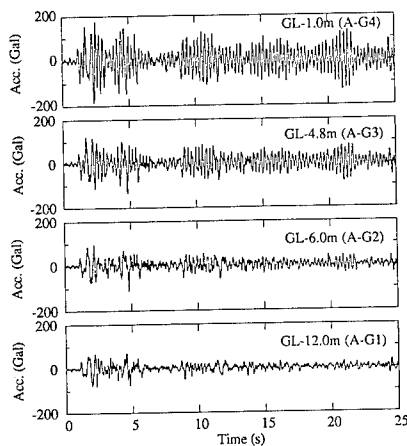


Fig. 10 Acceleration histories for dry test

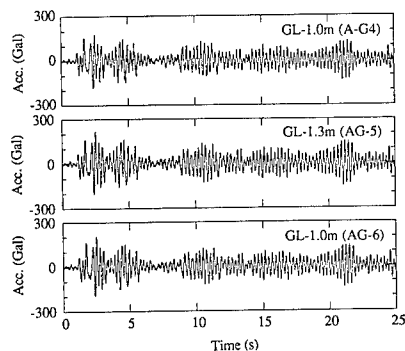


Fig. 11 Comparison of acceleration histories at three locations in model ground (see Fig. 7)

shown in Fig. 7. Three kinds of earthquake records usually used in the aseismic design of important structures in Japan were selected: the NS component of the El Centro record, the EW component of the Tokachioki-Hachinohe Harbor record, and the NS component of the Taft record. Each of the target acceleration histories was scaled so that its maximum acceleration was 80 gals that is

compatible with the 1:25 scale for the model ground.

In Fig. 8 are compared the acceleration histories observed at the base plate of the container and the target earthquake acceleration histories. The input signals were corrected with the feedback control system shown in Fig. 5. Fig. 8 shows that the target acceleration histories are reproduced at the base of the shaking table with satisfactory fidelity. In Fig. 9 are compared the Fourier spectrum of the observed acceleration and the target acceleration for three kinds of earthquake records, both of them almost agree with each other. So, it can be confirmed that the new digital feedback control system can excite a shaking table to closely reproduce acceleration histories of actual earthquakes.

Fig. 10 shows the acceleration histories at different depths for the El Centro record. The predominant frequency contained in the acceleration response at shallower depths of 1.0 m and 4.8 m is equal to the natural frequency of the model ground.

In Fig. 11 are compared the acceleration histories at three locations near the surface: A-G4, A-G5 and A-G6. The maximum accelerations at the three locations are 195 gals, 212 gals and 206 gals, respectively, i.e., the maximum accelerations near the container wall are only 6 to 9 % larger than that at the center of the model ground.

### 3.3 Shaking table test on saturated sand (liquefaction test)

A shaking table test on saturated Toyoura sand under 25  $g$  was conducted to check the applicability of this system to liquefaction studies. The sand was saturated with silicon oil 30 times as viscous as water. The liquid was allowed to seep upwards from the base plate at a very slow rate that required about 30 hours. Fig. 12 shows the location of accelerometers and pore pressure transducers. The EW component of the Tokachioki-Hachinohe record was selected as the target earthquake acceleration.

Figs. 13 and 14 show the acceleration histories and pore pressure histories, respectively, at different

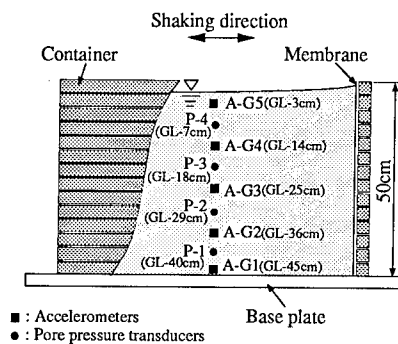


Fig. 12 Saturated sand model and location of transducers

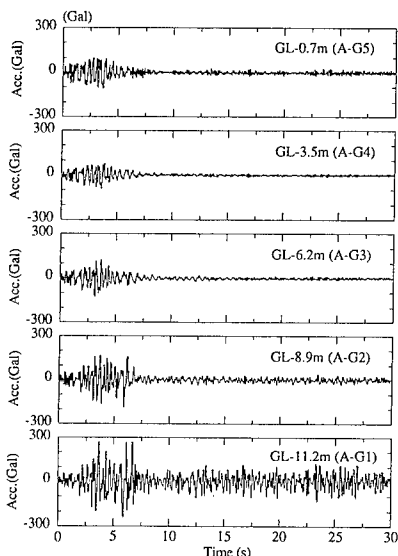


Fig. 13 Acceleration histories for saturated test

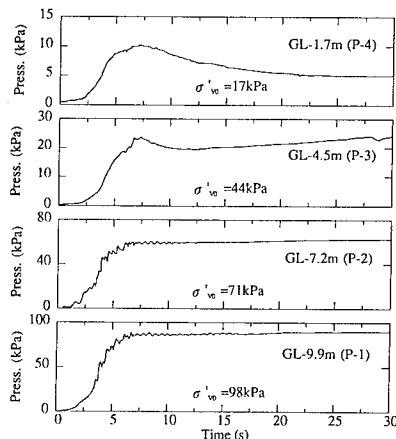


Fig. 14 Pore pressure histories for saturated test

depths of the sand. Note that the base acceleration is much greater than that in the dry test described in 3.2 to insure that the sand liquefies. The amplitude of acceleration decreases and the frequency increases after the pore water pressure has peaked at about 7.5 seconds. The high-frequency component in the acceleration histories may have been caused by the cables fixed on the container wall. Further study is needed to clarify this point.

The relatively low pore pressure ratios at shallower depths may be attributed to the fact that the response accelerations begin to decay early as shown in Fig. 13.

#### 4 CONCLUSIONS

The new digital feedback control system can excite a shaking table to closely reproduce acceleration histories of actual earthquakes under elevated gravity field.

The distribution of accelerations in the model ground of dry sand is relatively uniform within the laminar container fabricated from square steel tubing.

The new system enables one to perform shaking table tests on sand saturated with a viscous fluid.

#### 5 ACKNOWLEDGMENT

The author is grateful to Professor N.Fujii at Chuo University for his valuable advice, and to Dr. Y.Yoshimi, Mr. Y. Shamoto and Dr. K.Tamaoki at Shimizu Corporation for their support.

#### 6 REFERENCES

- Fujii N. 1991. Development of an electromagnetic centrifuge earthquake simulator. CENTRIFUGE 91: 351-354
- Ketcham, S. A., H-Y Ko & S. Sture. 1991. Performance of an earthquake motion simulator for a small geotechnical centrifuge, CENTRIFUGE 91: 361-368.

## A device for cyclic displacement-controlled actuation of an integral bridge abutment

Sarah M. Springman & Alison Norrish  
*Cambridge University, UK*

Keith Wilkinson  
*A.N. Schofield & Associates, Cambridge, UK*

**ABSTRACT:** Economic considerations are leading to widespread use of joint-free 'integral' bridges around the world. Eliminating expansion joints will reduce maintenance costs associated with corrosion and mechanical disruption. However, thermal strains induced in the deck will cause cyclic loading on the soil behind the abutments. The design of a cyclic actuator, which can deliver small scale displacement controlled deformations in a centrifuge to the top of an abutment wall retaining dry sand, will be described.

### 1 INTRODUCTION

Recent investigations into the performance of bridge deck expansion joints have identified various problems which are leading to excessive maintenance costs (Johnson and McAndrew, 1993). Primarily, it is the combination of corrosion (induced by the use of rock salt for de-icing) and deficiencies in terms of design, construction or maintenance which cause unsatisfactory performance. Similar problems are experienced at the bearings (Lund, 1993). Pritchard (1992) argues a convincing case for continuity on these grounds and points out additional benefits in terms of various reductions in first time construction costs.

Integral 'joint free' bridges have been designed as rigid portal frames so that expansion joints and bearings are no longer required. This construction method has been popular overseas, particularly in winter affected countries such as Sweden (Paterson, 1993) and North America (Burke, 1990) for continuous spans less than 100 m. The subsequent maintenance has been highly cost-effective.

However, this rigid frame design will cause a varying range of lateral cyclic motion at the bridge abutment as the deck expands and contracts with diurnal and seasonal temperature fluctuations.

Current design methods (Hambly (1991) and Pritchard (1992)) are quite crude, largely because the complicated mechanisms of deformation and volume change are not well understood. Centrifuge modelling offers an attractive medium in which to investigate such behaviour.

Recently, the Department of Transport (DoT) have established that the few integral bridges under their care, in the span range of 35-50 m, have performed surprisingly well (Paterson, 1993). They are now recommending the use of continuous integral bridges for spans up to 70 m, and are in the process of publishing a Departmental Standard.

Through the UK Transport Research Laboratory, DoT have commissioned a series of centrifuge model tests to examine this behaviour of full-height 'rigid frame' or 'integral' bridges retaining cohesionless soil. Of particular concern is the likelihood of a build-up in lateral pressure behind the wall over successive cycles, leading to excessive wall bending moments, and the possibility of apparent 'ground loss' behind the abutment.

This paper will focus on the development of a cyclic actuator which is capable of delivering repeatable displacement-controlled deformations to a bridge deck which is rigidly connected to an abutment wall. The equipment will be described, and some preliminary results will be presented.

### 2 TEST SPECIFICATIONS

Two different types of abutment will be investigated: a relatively flexible embedded wall with a stiff deck (Fig. 1a), or a stiffer spread base abutment combined with the same deck (Fig. 1b). In the first case, the mode of behaviour is anticipated to be flexure of the pile wall combined with a rigid wall-deck connection which forces



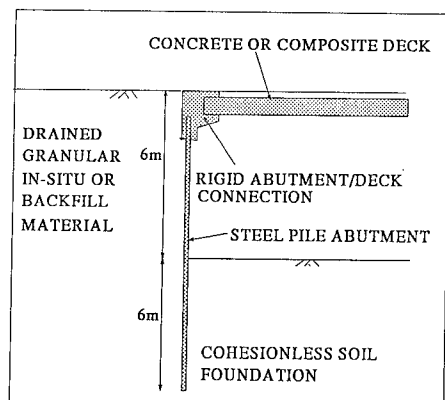


Figure 1a. Prototype piled integral abutment

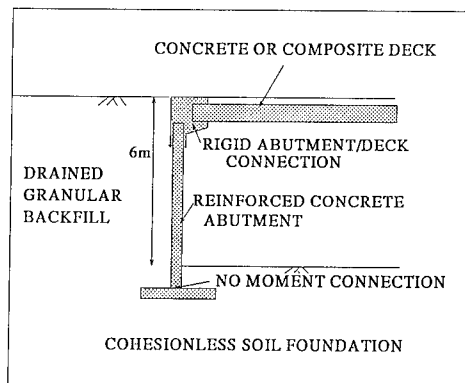


Figure 1b. Prototype spread base integral abutment

Table 1. Prototype specification and scaling factors

Variable	Field prototype	Scale	Centrifuge model
Bridge span	50-150 m	1/60	200 mm
Cyclic movement	+/- 6 mm diurnally, +/- 30 mm annually	1/60	+/- 0.1 mm diurnally, +/- 0.5 mm annually (also test +/- 1 mm)
Retained height of fill	6 m	1/60	100 mm
Embedment for piled wall	6 m	1/60	100 mm
Piled wall flexural stiffness	$1.5 \times 10^5 \text{ kNm}^2/\text{m}$	$1/60^3$	$0.69 \text{ kNm}^2/\text{m}$
Spread base wall flexural stiffness	$1.5 \times 10^6 \text{ kNm}^2/\text{m}$	$1/60^3$	$6.9 \text{ kNm}^2/\text{m}$
Deck flexural stiffness	$4.5 \times 10^6 \text{ kNm}^2/\text{m}$	$1/60^3$	$20.8 \text{ kNm}^2/\text{m}$
Particle size of retained fill	5.4-9 mm	1/60	0.09-0.15 mm
Piled wall thickness		1/60	4.92 mm
Depth of deck		1/60	18.2 mm
Bending moment / m width		$1/60^2$	
Shear force / m width		1/60	
Lateral pressure		1	

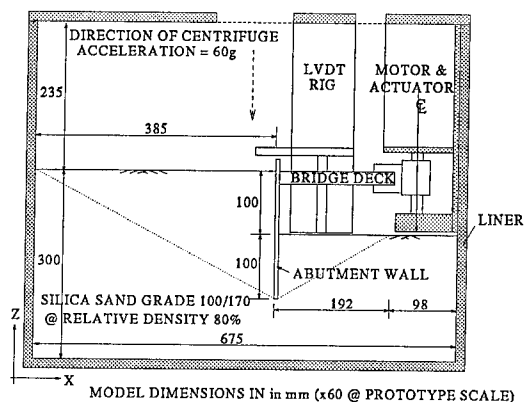


Figure 2. General arrangement: centrifuge model

rotation at this joint and zero tip displacement and rotation. In the second example, the displacement at deck level will be accommodated by a combination of rotation, translation and a lesser degree of flexure.

The dimensions of the field prototype and the scaled centrifuge model are shown in Table 1. Given the range of deformations +/- (6 - 30 mm) specified for 50 - 150 m span bridges, it was necessary to consider carefully the acceleration level  $n g$  to be adopted, given the need to reduce this deformation range by a factor of  $1/n$ .

A nominal acceleration of 60 gravities was selected for these tests, so the displacements required were from +/- 0.1 mm to +/- 0.5 mm. In order to examine the soil behaviour at relatively

large strains and to allow for compliance in the system, the nominal range was extended to  $\pm 1$  mm.

### 3 ARRANGEMENT OF CENTRIFUGE MODEL

The general arrangement of a centrifuge model of the embedded wall is shown in Fig. 2. A strongbox of plan dimension, 200 x 675 mm, and height 535 mm was used. A perspex window was fitted to the front of the box.

A 6 m height of cohesionless soil was to be retained by a 12 m embedded wall (Fig. 3a) made from 6061/T6 grade Dural, which was instrumented with pressure cells and strain gauged bending moment transducers (BMTs). There was a rigid moment-carrying connection at the wall-deck joint. The deck (Fig. 3b) was made from a block of mild steel with the three 'beams' milled to a universal section of the required flexural stiffness, and gauged (Fig. 3c) to measure bending and axial load (ALC).

The relative rigidity between the deck and wall were defined, from recommendations of bridge designers, to be 30 for the embedded wall or 3 for the spread base wall. The scaling factors for flexural stiffness, bending moment and shear force per metre length of wall are quoted in Table 1.

The deck would remain the same in both cases. It was designed to transfer the cyclic displacement from the actuator, which was located at the extreme right hand edge of the package, as viewed through the perspex window. It was not intended that the entire span of the deck should be modelled, simply that the fixity and the cyclic displacements at the wall-deck connection were to be replicated.

### 4 DESIGN OF THE CYCLIC ACTUATOR

The displacement cycles were initiated by a 7 Nm torque stepper motor (Compumotor SX8), which drove an eccentric vertical drive shaft connected into a vertical pin joint (Fig. 4). Sets of concentric, tapered roller bearings of bores varying from 20 mm to 30 mm were adjusted to minimise any linear play or backlash in the system, and also to cope with the additional weight of the device under 60 g. Lip seals and circlips prevented sand ingress. Clearly, there should be minimal lateral play in any of the mountings of the eccentric drive shaft, and also at the pin joint connection with the bridge deck if repeatable cycles of movements as small as  $\pm 0.1$  mm are to be applied.

The 17.5 kg actuator was both hung from a 19 mm

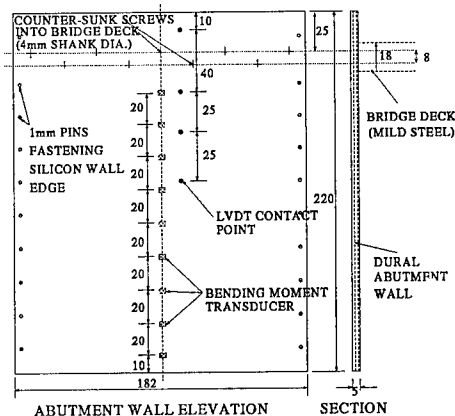


Figure 3a. Instrumented flexible abutment wall

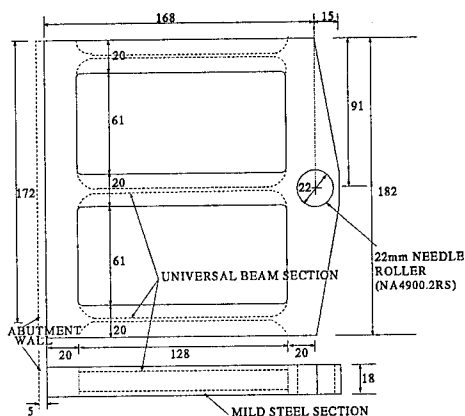


Figure 3b. Model bridge deck

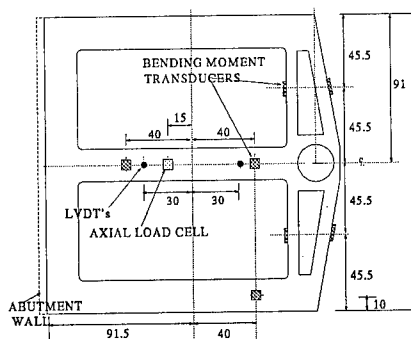
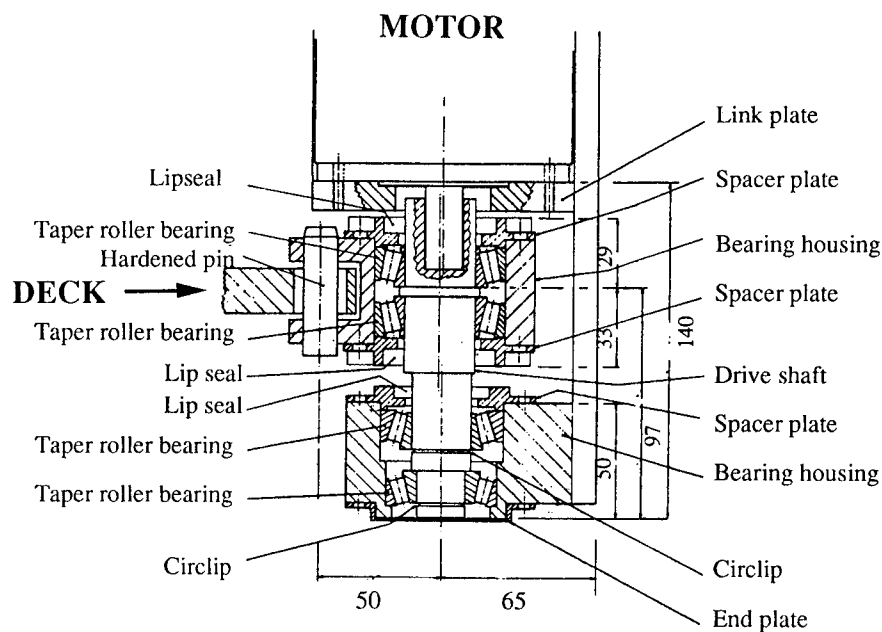


Figure 3c. Instrumented bridge deck



All dimensions in millimetres

Figure 4. Cyclic actuator

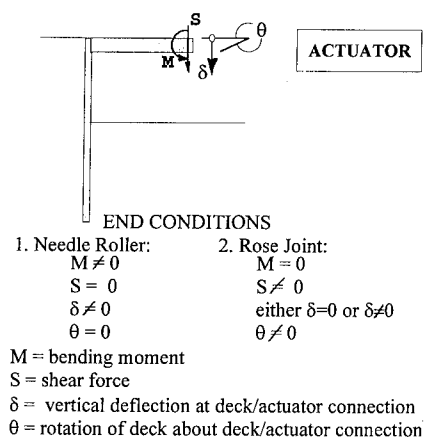


Figure 5. Boundary conditions: deck-actuator joint

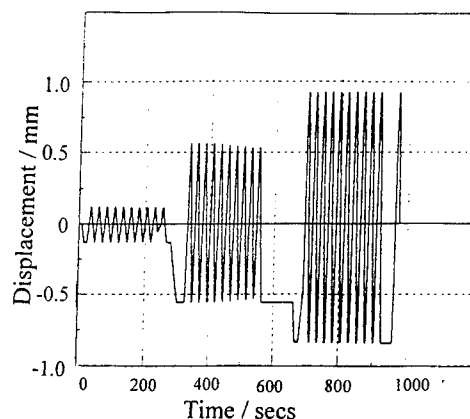


Figure 6. Proof test of displacement actuator

steel plate which was bolted into the top of the strongbox, and fixed onto the right hand sidewall.

Various modes of support were tried at the edge of the deck adjacent to the 22 mm needle roller. Eventually, restraint was provided against vertical movement downwards (but not upwards) (Fig. 5). Initially, there was no support, but the weight of the deck at 60 g caused excessive vertical displacement.

## 5 CONTROL OF THE CYCLIC ACTUATOR

A dedicated 386 PC controlled the stepper motor through commercial XWARE software (1992), which allowed both user-interactive and pre-determined sequences to be specified. An SX8 digital controller was configured as a serial driver to produce pulsed output (via an RS232 link) to drive

the motor a number of steps in either direction, and was mounted at the centre of the beam arm.

25,000 steps were equivalent to one revolution ( $360^\circ$  rotation) of the drive, which, without allowing for the small degree of backlash, gives nominal peak to peak displacements of  $\pm 1$  mm at model scale ( $1/60$ ), varying sinusoidally, which become  $\pm 60$  mm at prototype scale. For rotations less than  $360^\circ$ , e.g. for  $\pm 0.1$  mm ( $\pm 6$  mm prototype) and  $\pm 0.5$  mm ( $\pm 30$  mm prototype), the 'waveform' was expected to be sawtooth in shape.

Given the nature of the dry cohesionless soil backfill to the abutment wall, strain rate was not considered to be important. In the event, between 10 - 25 seconds were allowed per cycle.

## 6 EVALUATION OF PERFORMANCE

Preliminary tests were carried out on the deck-actuator system at 1 g to calibrate the expected displacements from the stepping programs against those measured using linear variable displacement transducers (LVDTs) mounted against the wall. These proved to be very successful, and, when plotted at greater intervals of time scale than in Fig. 6, sinusoidal displacement plots were observed for the full revolutions of the shaft, and sawtooth waveforms for the smaller displacements. The cycles appear to be uniform and repeatable at each set of nominal displacement. The maximum range of movement is of the order of  $\pm 0.8$  mm.

However, during the first centrifuge test at 60 g, the actuation system jammed due to a combination of insufficient support at the deck-actuator joint and maladjustment of the drive shaft bearings. Consequently, the shaft was able to move downwards under 60 g, increasing friction to unacceptable levels.

The roller bearings were tightened and a subsequent proof test produced similar data to that shown in Fig. 6.

## 7 PRELIMINARY TEST RESULTS

Early tests followed a prescribed sequence of cyclic displacements, with deck level initiation either into (passive) or away from (active) the fill by an initial displacement of the same amount as the subsequent displacement cycles which were at prototype (model) scales:

- (a)  $N = 50$  cycles at  $\pm 6$  mm ( $\pm 0.1$  mm)
- (b)  $N = 75$  cycles at  $\pm 30$  mm ( $\pm 0.5$  mm)
- (c)  $N = 100$  cycles at  $\pm 60$  mm ( $\pm 1.0$  mm).

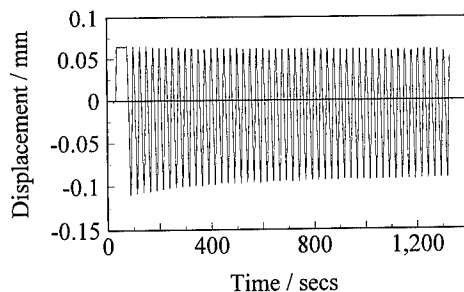
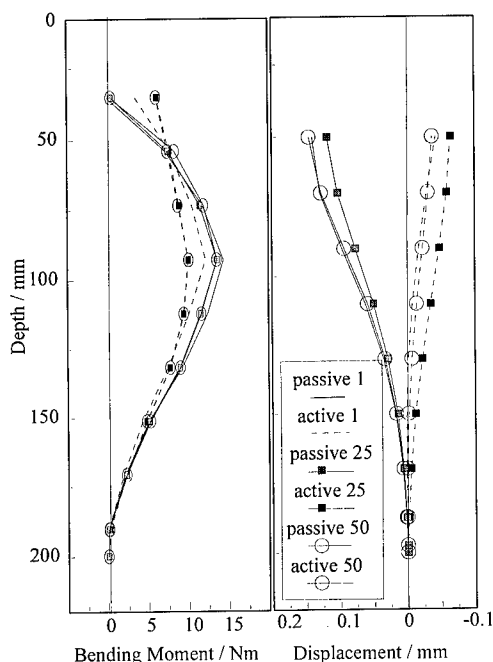


Figure 7. 50 cycles of  $\pm 0.1$  mm displacement



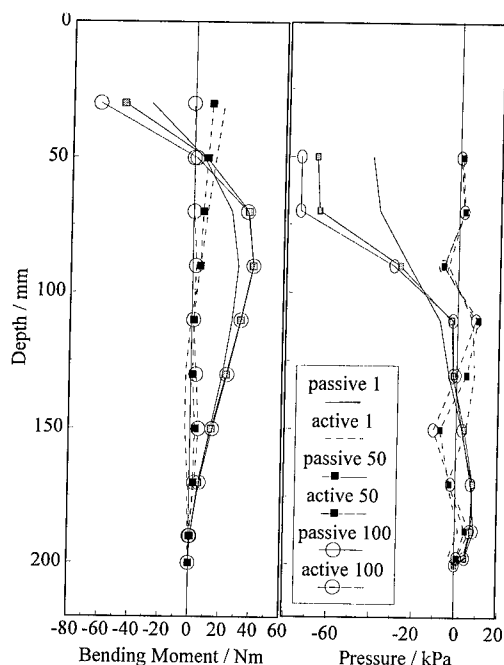
(a) Bending moment (b) Displacement

Figure 8. Data from 50 cycles of  $\pm 0.1$  mm

Typical data for the smallest displacement, (a) (Fig. 7) shows that a regular and repeatable cycle has been established. Subsequently, 100 cycles were used for (a) and (b), and an additional range was introduced as  $\pm 12$  mm ( $\pm 0.2$  mm).

BMTs, ALC and LVDTs were monitored, and some results are plotted here at model scale. Values of bending moment for both active and passive wall positions as a function of  $N$  (Fig. 8a) show slight changes with increasing  $N$ . For case (c), these values increase with  $N$ .

This bending moment diagram may be integrated



(a) Bending moment (b) Lateral pressure

Figure 9. Data from 100 cycles of  $\pm 1.0$  mm

twice to give a profile of displacement down the wall, and fitted to boundary conditions obtained from LVDTs to check internal consistency of the data (Fig. 8b). Comparisons are generally encouraging.

Minimal change was observed in the bending moments with increasing  $N$  (Fig. 8a). However, contrasting behaviour was noted for  $\pm 1$  mm range, (Fig. 9a), from which crude estimates of lateral pressure obtained by double differentiation also showed increasing pressure with  $N$  (Fig. 9b).

## 8 CONCLUSIONS

Repeatable small scale cyclic displacements between 0.1 - 1 mm may be reproduced in the centrifuge to model the temperature-induced actuation of an integral abutment. Initial data derived from instrumentation has shown internal consistency with the applied displacements.

## 9 ACKNOWLEDGEMENTS

These activities would have been impossible with-

out Messrs N.H. Baker, S.G. Chandler, C.H. Collison, P. Ford, J. Chandler, A. Brand, T. Ablett, Prof. Schofield and Dr M.D. Bolton.

## 10 REFERENCES

- Burke, M.P. 1990. Integrated bridge design on the rise. *Modern Steel Construction*. AISC.
- Hambly, E.C. 1991. *Bridge Deck Behaviour*. 2nd ed. London: E & FN Spon.
- Johnson, I.D., McAndrew, S.P. 1993 Research into the Condition and Performance of Bridge Deck Expansion Joints. *TRL*. PR. 9 E434A/BC.
- Lund, J. 1993. Bearing Performance. *Henderson Colloquium*. London: E&FN Spon.
- Paterson, G.A. 1993. DoT Attitude to Continuity / Integral Bridges. *Henderson Colloquium*. London: E&FN Spon.
- Pritchard, B. 1992. *Bridge Design for Economy & Durability*. Thomas Telford. pp. 7-13.

## Design of a large earthquake simulator at UC Davis

Bruce L. Kutter, I. M. Idriss, Thomas Khonke, John Lakeland, X. S. Li, William Sluis & X. Zeng  
*University of California, Davis, Calif., USA*

Robert C. Tauscher  
*Team Corporation, Seattle, Wash., USA*

Yozo Goto & Iemitsu Kubodera  
*Obayashi Corporation, Tokyo, Japan*

**ABSTRACT:** A new earthquake simulator, about an order of magnitude larger than existing servo-hydraulic centrifuge shakers, is being constructed at UC Davis. The model container will accommodate 1.75 m long models, and provide 15 g shaking accelerations to about 2700 kg payloads. The hydraulic power supply, servo-actuators, bearing system, model containers, and the control system have unique features that are described. Finite element analysis of the interaction of the shaker and the centrifuge indicate that the dynamic loads transferred to the centrifuge spindle bearings will be low. Results from finite element analysis, used to assist in the design of a laminar soil container is also described.

### 1 INTRODUCTION

The large centrifuge at Davis, in terms of radius (9.2 m to bucket floor), maximum payload mass (4500 kg), and available bucket area (4.0 m<sup>2</sup>) is believed to be the largest geotechnical centrifuge in the world. Recently, the allowable payload of the centrifuge has been increased by 1000 kg. At present, the centrifuge is limited to centrifugal accelerations below 53 g. The centrifuge capacity in terms of the maximum acceleration multiplied by the maximum payload is 53 g x 4500 kg = 240 g-ton. The maximum speed of the centrifuge is limited by available drive torque, thus there is a potential to increase the maximum acceleration by streamlining the enclosure or the arm itself. The centrifuge facility has already been described in some detail by Kutter et al (1991).

Most of the testing that has been conducted on the large centrifuge has involved large models and low centrifugal accelerations. For example, 1/8 scale tests at 8 g were conducted to study automobile impact on highway guardrails (Bartlett and Kutter, 1992). The purpose of this work was to investigate the effect of a nearby slope on the capacity and energy absorbing characteristics of the guardrail posts. In another series of experiments (Maroney et al, 1993), a pair of 1/2 scale bridge abutments were tested off the centrifuge at one g, and now 1/12 scale models of the one g tests are being conducted on the centrifuge. The purpose of this work is to determine the longitudinal and transverse stiffness and load capacity of abutments to provide some input data for dynamic analysis of bridges. Based on our experience with large models tested at small centrifugal accelerations, the 53 g limit is not perceived as the critical limitation of the machine.

Considering the difficulty in analyzing the behavior of geotechnical structures during earthquake loading, the expense associated with upgrading the seismic resistance of geotechnical structures in California, and the expertise and research interests of the faculty at UC Davis, development of a large shaker has been the highest priority activity for the large centrifuge over the last couple years.

### 2 SPECIFICATIONS FOR THE LARGE SHAKER

Table 1 lists some specifications of the shaker which is now under construction. The first part of the table lists general specifications of the shaker system, and the second part lists specifications of

Table 1. Specifications of Large Shaker

Mass of Model and Container (kg)	2700
Max Shaking Acc'n for 2700 kg (g)	15
Max Absolute Velocity (m/s)	1.0
Max Relative Displacement (cm)	2.5
Useful Frequency Range (Hz)	20 to 200
Length of Container (m)	1.75
Width of Container (m)	0.7
Height of Container (m)	0.6
Number of Actuators	2
Actuator Area (m <sup>2</sup> )	0.0081
Hydraulic Pressure (MPa)	35
Servo-valve flow rate (l/s)	13
35 MPa Supply Reservoir Vol. (l)	70
1.3 MPa Exhaust Reservoir Vol. (l)	55

the servo-hydraulic system. In terms of payload mass, container volume, actuator capacity and servo-valve flow rate, the shaker is roughly an order of magnitude larger than existing centrifuge shakers. Several novel features have been incorporated in the design, and this paper will describe a few of these.

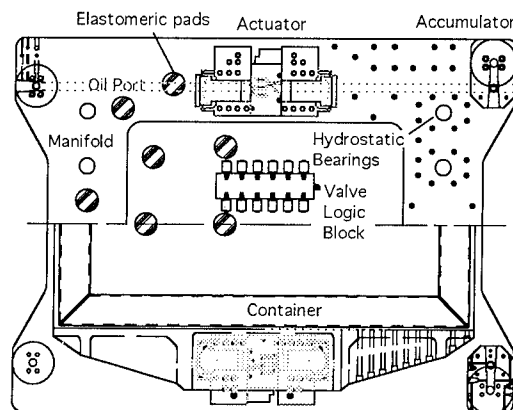
### 3 OVERVIEW OF THE DESIGN

#### 3.1 Design Concepts

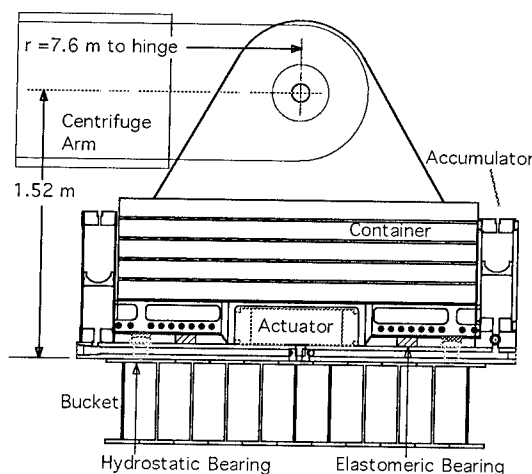
A plan view showing the layout of the actuators, accumulators, and manifold on the centrifuge bucket is shown in Fig. 1a. One servo-actuator will be mounted on each side of the container, which will be shaken in the direction that the bucket swings during spin up. The location of the actuators on the sides of the containers has two advantages over the use of actuators under the container: (1) overturning (rocking) moments are minimized, and (2) vertical space is conserved. The side view (Fig. 1b) looking through the side walls of the swing bucket shows an actuator reacting against the stiff drive frames attached to the side of the container base plate.

Figure 2 shows a schematic of the hydraulic system. A 15 kW, 700 kPa air compressor outside the centrifuge is the source of energy to charge the accumulators and provide lubrication to hydrostatic bearings. This air is fed through a rotary joint to a 700 kPa air / 35 MPa nitrogen pressure multiplying pump, which charges the 35 MPa nitrogen reservoir mounted near the centrifuge axis. To shake the sample, the valve in Fig. 2 is opened to pressurize the oil in the supply accumulators. Oil then flows from the supply accumulator along a pathway through the manifold, servovalve, actuator, and then back through the servovalve and manifold to the exhaust accumulators.

While the centrifuge is spinning, without shaking, a compressed air driven oil pump is used to circulate oil to continuously lubricate the servo-actuators. Also shown in Fig. 2 are hydrostatic bearings and a hydrostatic bearing pressure regulator. The hydrostatic bearings mounted near each corner of the manifold are part of a hybrid bearing support system. Elastomeric bearing pads are used to support the majority of the centrifugal loads. The hydrostatic bearings are mounted on actuators so that the load felt by the hydrostatic bearings can be regulated. The orifices feeding the hydrostatic bearing actuators are designed restrict the flow rate to provide a stiff support during high frequency shaking (minimizing rocking), and an adjustable height, pressure regulated support during the relatively slow changes in centrifugal acceleration. Due to the significant bucket deflections that are expected due to centrifugal loads, it was necessary to develop a bearing system that was flexible during slow changes in centrifugal acceleration, but stiff during high frequency shaking.



(a)



(b)

Fig. 1. (a) Plan view, and (b) Side view of shaker and container mounted on the centrifuge bucket.

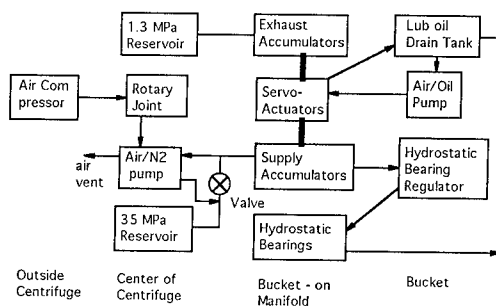


Fig. 2. Schematic of pneumatic / hydraulic systems

### 3.2 Dynamic Analysis of the Centrifugal Shaker/Model System

Before developing a detailed design, it was considered important to show that the large shaker would not damage the centrifuge. The main centrifuge spindle bearings were considered to be the most critical concern. The actuators, with combined capacity of 540 kN acting at a radius of 9 m, could potentially transmit substantial moments to the spindle.

A 1-D finite element program including the main structural components of the centrifuge (shaker/swing bucket, tension straps, beam weldment as shown in Fig. 3) has been developed to investigate the response of the centrifuge under shaking. (See Kutter et. al., 1991 for a more detailed description of the centrifuge structure). The program considers the stiffening effect due to centrifugal force and the influence of non rigid foundation. The swing bucket angle is set to be a function of the centrifugal acceleration. Two situations are considered for the hinge that connects the bucket and the tension straps: one assumes no friction ( $M_h = 0$ ) so that the bucket can freely rotate relative to the tension straps; the other assumes that the friction is so large that the bucket and tension straps are effectively locked together during shaking. Figure 3 shows the forces and moments acting on the bucket, tension strap, and weldment, respectively. In the figure,  $N_{sp}$ ,  $Q_{sp}$ , and  $M_{sp}$  are the forces and the bending moment transferred to the foundation through spindle.  $u$  and  $y$  denote the displacements in horizontal and vertical directions, respectively.

To experimentally verify the finite element model, the response of the arm to forced sinusoidal vibrations and the impulse response were measured using accelerometers at several locations. Sinusoidal excitations of different frequencies were applied using a small electromagnetic shaker attached to the centrifuge bucket. Impulse

excitation was generated by dropping a large steel weight onto the arm at the connection between the arm beam weldment and the tension strap. Figure 4a shows the Fourier amplitude spectrum of vertical acceleration measured at the point of application of the impulse load. Figure 4b shows the Fourier spectrum of the impulse response predicted by the finite element model. It can be seen that the calculated response agrees remarkably with the experimental results.

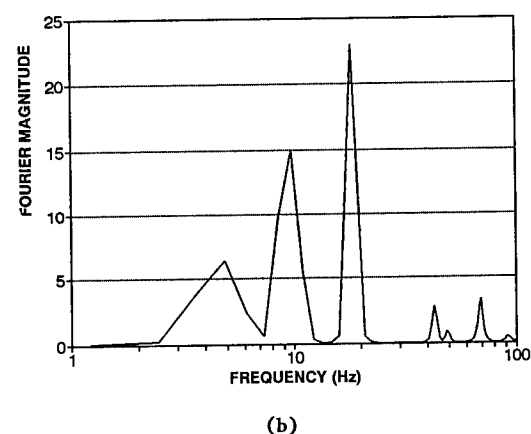
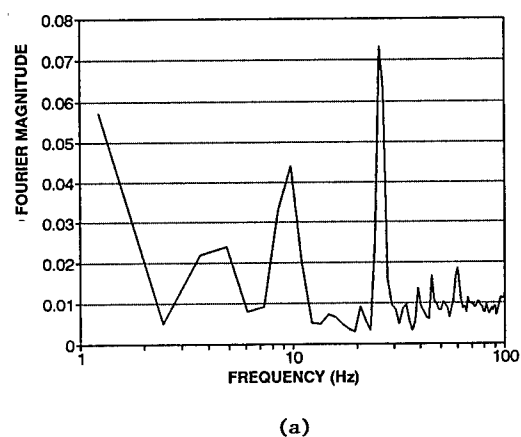


Fig. 4 (a) Measured, and (b) predicted impulse response of the centrifuge arm.

Once verified, the numerical model was used to analyze the interaction of the shaker and the centrifuge. Four cases were studied as shown in Table 2, with typical expected input motions applied to the shaker. The numerical analysis indicates that if the spindle is assumed to be rigid and the bucket pivot is locked during shaking, the moments transferred to the spindle would be about

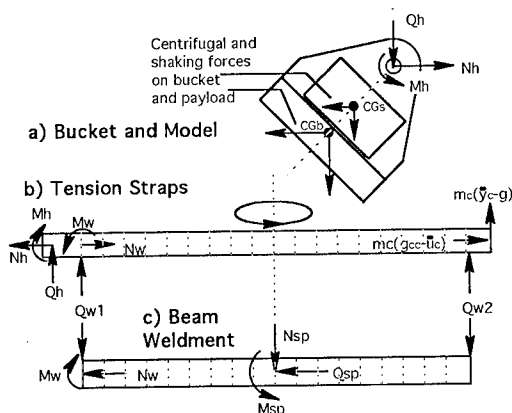


Fig. 3. Models of the Bucket/Shaker, Tension Strap, and Beam Weldment.



Table 2. Predicted Spindle Moments for Different Boundary Conditions in Numerical Model.

Case	Bucket Hinge	Spindle Stiffness	Maximum Spindle Moment (kN-m)
1	Locked	Rigid	675
2	Free	Rigid	225
3	Locked	$k = k_{static}$	125
4	Free	$k = k_{static}$	28

twice the allowable spindle moment. By introducing the statically measured spindle stiffness and allowing the bucket hinge to slip (calculations based on measured friction in the bucket hinge indicate that the journal bearings are likely to slip during shaking), the calculated dynamic moments transmitted to the spindle reduce to 28 kN-m, 8% of the allowable. The bucket hinge and the spindle flexibility were found to have beneficial vibration isolation properties which are expected to protect the spindle bearings.

Separate dynamic analyses using commercial finite element codes were also conducted to study the suitability of the existing swing bucket to act as a reaction mass for the shaker. These analyses provide the natural frequencies and mode shapes of the bucket/shaker system. It was determined that the I-beam weldment with which the bucket floor is constructed is not as stiff as would be desired. The webs of the I-beams (see Fig. 1) run in a direction perpendicular to the direction of shaking. This orientation is optimal for transmission of centrifugal loads to the side plates of the bucket, but not for providing a stiff reaction mass. Several natural frequencies, with mode shapes similar to those of a drum, were computed in the range of 200 to 300 Hz. We believe that this will be the primary factor which determines the upper limit of shaking frequencies. Concepts for improving the stiffness of the bucket/reaction mass were considered:

1. Replacing the bucket floor with a nearly solid block of magnesium alloy,
2. Cutting the bucket into pieces to permit installation of transverse webs,
3. Welding transverse stiffeners onto the outside of the bucket,
4. Stiffening the top of the bucket using a thick aluminum manifold.

The first option was determined to be the most desirable; natural frequencies of a solid block of magnesium were found to be roughly two times larger than for the existing bucket structure. The first option was also determined to be the most expensive. The second option was thought to be impractical, and the third was found to have little benefit. The final option has been implemented. A 90 mm thick aluminum plate is bolted to the top flanges of the bucket, providing some stiffening, while serving as a manifold for hydraulic oil.

### 3.3 Description of Servo-Actuators

As indicated in Fig. 1, two synchronized actuators will be used to shake the centrifuge models in one direction. The servo-actuators are implementations of unique concepts in hydraulic actuation. Each double acting actuator consists of two single acting actuators ported to a high frequency servo valve mounted cross axially to the piston's motion, Fig. 5. The single acting actuators are externally tied together by the stiff drive frames on the sides of the model container. In other words, the shaker moves back and forth pushing first on one side of the drive frames and then the other, see Fig. 1.

On the end of each piston is a segmented spherical hydrostatic bearing as well as a sliding bearing. This "Pad Bearing" connection means that shear and bending deflections, caused by centrifuging the bucket and stressing the surrounding structure, are eliminated. The pistons self align to the table structure eliminating any locked in transverse static loads.

Hydrostatic bearings are also used to provide lateral support to the pistons. The pistons float on a fluid film even while being subject to the forces of the centrifuge. The use of hydrostatic bearings eliminates the need for high pressure seals thus eliminating "stick slip" and other sources of non-linear forces. Future expansion to two or three directions of shaking could be implemented by using additional sets of actuators. The pad bearings on the existing actuator would permit the table to slide freely in a cross axis motion.

### 3.4 Model Container

The container, inside dimensions 1.7 x 0.7 x 0.6 m (length x width x height), is a "Flexible Shear Beam" (FSB). It consists of a stack of rings with alternating layers of soft rubber and welded rectangular aluminum tubing. The rubber is designed to allow the FSB container to deform

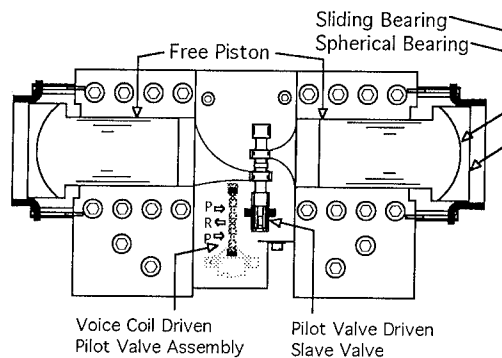


Fig. 5 Servo-actuator concept (patented)

laterally with the soil layer, with minimal shear stiffness. The design is very similar to the "Equivalent Shear Beam" (ESB) type container described by Zeng and Schofield (1992), except that for the ESB, the stiffness of the rubber is designed to make the natural frequency of the container similar to the natural frequency of a soil layer. In liquefaction studies, the natural frequency of the soil layer changes dramatically as the pore pressures build up. It is not feasible to develop an ESB that matches the non-linear, changing soil properties. Thus, it was concluded that, for liquefaction studies, a box with small mass and small stiffness would be preferable to a box with a fixed natural frequency. The mass of the flexible container is about 25% of the mass of the soil, assuming the container is filled to the top with soil.

An ESB type of container has been studied and experimentally compared to other flexible soil containers in a separate paper to this conference (Fiegel et al., 1994). The ESB/FSB type container is a relatively straight forward mechanical design and it appears to provide reasonable results.

To clarify the end wall effects of ESB or FSB type containers on a centrifuge shaker system, liquefaction analyses on soil in containers were carried out. An FEM code named "EFFECT1" based on effective stress and a non-linear constitutive model was used (Kimura et al, 1993). Table 3 shows physical properties of soil.

Table 3. Physical properties of FE container model

Soil:	Toyoura sand ( $D_r = 60\%$ )
Pore Water:	30cs silicon oil
Soil Profile:	Simple uniform layer
Bulk Modulus of Grains	$1.0 \times 10^{40}$ kPa
Unit weight of Grains	25.8 kN/m <sup>3</sup>
Porosity	0.432
Permeability	$5 \times 10^{-5}$ m/s
Bulk Modulus of Fluid	$1.1 \times 10^6$ kPa
Unit weight of Fluid	9.36 kN/m <sup>3</sup>

Analytical models are as follows:

- M1: Free field model (ideal model having no effects of container)
- M2: Rigid soil container model
- M3: Laminar soil container model

Figure 6 shows the FEM model. A 60 Hz sinusoidal wave with 35 m/s<sup>2</sup> amplitude under 30 g centrifugal acceleration was used as input motion.

In the case M3, we considered the inertia force of the rings by increasing the unit weight of side wall. Both ends of model at the same elevation move at the same amplitude.

Figures 7 to 9 show time history of the excess pore water pressure ratio (denote as P.R., hereafter). In Fig. 7(a) each model produces nearly same P.R. in the center area of model ground. On the contrary, in Fig.7(b), P.R. near the side wall clearly shows a boundary effect. In Fig. 8, P.R. shows

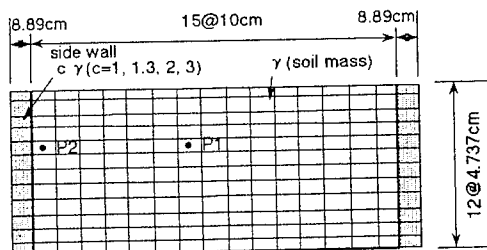


Fig. 6 Finite Element Mesh of Laminar Container

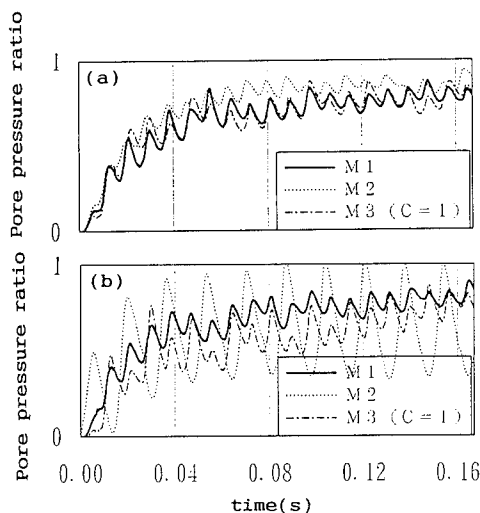


Fig. 7 Computed pore pressure ratios of each model at P1(a) and P2(b). (C is the ratio of the unit weight of rings to unit weight of soil.)

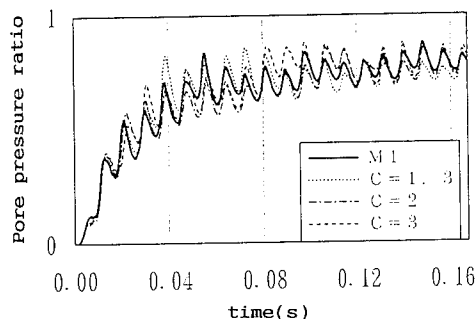


Fig. 8 Comparison of pore pressure ratio at P1 for analysis M1 and M3.

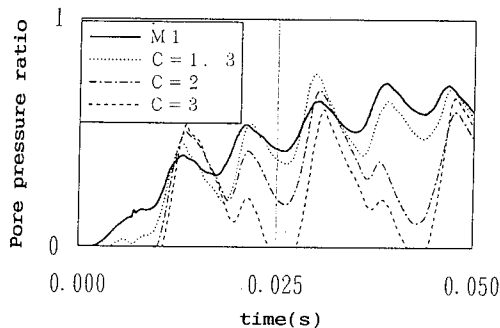


Fig. 9 Comparison of pore pressure ratio at P2 for analysis M1 and M3.

quite slight differences between M1 and the others. This result indicates that the weight of the stacked rings does not affect the pore pressure at the center of model. However, in Fig. 9 the weight of stacked ring affects the P.R. of the ground adjacent to the wall in the beginning of shaking. If the weight of the stacked rings is less than 30% of the weight of the soil there appears to be only slight differences between M1 and M3. Additional analyses (not shown) indicate that the frequency of excitation affects the magnitude of the box effect. Analyses with 90 Hz or 120 Hz excitation showed smaller box effects than the 60 Hz results presented here. In all cases, the maximum deviation of computed pore pressure peaks (compared to computed free field response) at a distance of 37 cm or more from an end wall was in error by less than 25% of the overburden pressure. If the cyclic peaks in pore pressure are neglected, the errors are significantly smaller. The middle half of the container seemed to provide reasonably good results.

### 3.5 Data Acquisition

In the existing data acquisition system for the centrifuge, the instrumentation signals are transmitted by shielded twisted pairs to 32 channels of signal conditioning amplifiers, then fed through the slip rings to an A to D converter in the control room.

This system is being upgraded to include an onboard IBM compatible 486 computer with a Data Translation model DT 2839, 32 channel data acquisition board. Two 16 channel anti-aliasing filter boards will be used in conjunction. This arrangement allows the data to be digitized before going over the slip rings, which will improve data quality by eliminating slip ring noise. The onboard computer is to be remotely controlled via an Ethernet link through the sliprings to the control room computer.

### 3.6 Shaker Control

Considerable research has gone into the design of a control system for this new shaker. Development of design concepts has been accompanied by assembly of different types of controllers and testing them on the existing servo-hydraulic shaker on the small centrifuge at UCD.

For the large shaker, it is critical that the actuator pistons do not slam into ends of the cylinders; therefore, it is considered necessary to use relative displacement of the piston as the primary feedback signal. On the other hand, displacement signals are small at high frequencies, and they are not especially good for controlling high frequency vibrations.

In a conventional closed loop feedback controller, the excitation to the servo-valve is proportional to the difference between the command and the feedback signal. A fundamental problem arises in feedback control systems when the feedback signal lags more than  $90^\circ$  behind the command signal. If the feedback signal is lagging by  $180^\circ$ , the subtraction of the feedback amounts to addition of an in-phase signal! An instability arises if damping is insufficient. Even with sufficient damping, the out of phase feedback introduces erroneous excitation to the servo-valve.

Theoretically, if the shaker system and model response was linear, it would be possible to pre-condition the command signal to compensate for the poles and zeroes that develop in the feedback control system. But on centrifuge shakers, we tend to face constraints in allowable payload space and mass. We tend to minimize container and reaction masses (and stiffness) while maximizing the mass of the non-linear soil payload, and we are interested in studying highly non-linear problems like soil liquefaction. In addition, it is desirable to use the actuators up to their pressure limit, where the actuator characteristics are themselves non-linear. It seems to be not feasible, therefore, to rely on a pre-conditioning scheme that is based on linear control theory.

In our current plan, we intend to use an closed loop analog feedback to control the low frequencies of vibration, where the feedback signal is lagging less than about  $60^\circ$  behind the command signal. We expect this frequency to be at about 50 Hz, yet we desire to excite the shaker at frequencies up to 200 Hz or more.

The phase lag of the feedback signal is caused by mechanical inertia and flexibility (e.g., payload mass and oil column compressibility) as well as instrumentation and conditioning of the feedback signal. We have found that 10 kHz LVDT's themselves introduce a time delay with a minimum value of about 0.001 s. This corresponds to a  $18^\circ$  phase delay at 50 Hz, just due to instrumentation. We have discovered that "Hall Effect" transducers are capable of essentially eliminating the

instrumentation component of the phase delay, and they will increase the frequency at which we can accomplish closed loop control.

Beyond about 50 Hz, we plan to run the shaker "open loop". To accomplish the transition to open loop control while eliminating erroneous feedback signals with large phase delay, a high order filter must be used to remove the higher frequency feedback signals. Conventional filters are self defeating in this regard since they introduce phase delay in the feedback signals; they cannot eliminate high frequency feedback without increasing phase delay of the desirable low frequency feedback signal. A design effort is under way to utilize real time digital filters, which have the potential to perform this filtering task with insignificant phase delay in the passband.

Such a system would maintain closed loop displacement control of the large amplitude, low frequency motions, while passing high frequency command components directly to the shaker, unaltered by summing with erroneous feedback. The likelihood of successfully pre-conditioning the command signal is improved if it is not necessary to compensate for the amplification of errors that would be introduced by out-of-phase feedback.

#### 4 CLOSURE

A large earthquake simulator is now under construction. The large models that may be tested using this shaker will enable testing of models at low scale factors so that scale effects can be minimized and more details can be included in the models. Alternatively, a single test bed may contain several structures which are tested simultaneously. For example, one of the first projects to be conducted using the large shaker will involve measuring the response of stiff piles in soft soils. We envision that we may place several pile groups each with a different superstructure in a single test bed. It will then be possible to obtain several data points in a single test. Working at a larger scale, it will also be possible to construct more accurate models of complicated structures such as pile supported bridge abutments.

#### ACKNOWLEDGMENTS

The US National Science Foundation (Grant No. BCS-9106503) supported the design studies for the large shaker. The construction of the shaker is being funded by the California Dept. of Transportation, the Obayashi Corporation and matching funds from the University of California. K Cappel was instrumental in development of the servo actuator concept. Yie Ruey Chen, Dr. Matsuda, and Doug Lund conducted some of the analyses presented in this paper. R Scott, R Calvet, and J Beck served on an NSF appointed design oversight committee.

#### REFERENCES

- Bartlett, R. and Kutter, B.L. (1993), Lateral Load Capacity of Posts and Footings for Metal beam Guardrails Located Close to Slopes, Final Report #FHWA/CA/TL-93-02, Calif. Dept. of Transp.
- Fiegel, G.F., Hudson, M. Idriss, I.M., Kutter, B.L., and Li, X.S. (1994) Proc. Centrifuge 94, Singapore.
- Kimura, T., Takemura, J., Hirooka, A., Ito, K., Matsuda, T., and Toriihara, M., (1993) Numerical Prediction for Model No 1, Proc Symp. on Verification of Numerical Procedures for the Analysis of Soil Liquefaction Problems, Arulanandan and Scott (eds), Balkema, Rotterdam, pp. 141-152.
- Kutter, B.L., Li, X.S., Sluis, W. and Cheney, J.A. (1991) Performance and Instrumentation of the Large Centrifuge at Davis, Proc. Centrifuge 91, Ko and McLean, eds., pp.19-26.
- Maroney, B.M., Romstad, K.M., and Kutter, B.L. (1993) Struct. Eng. in Natural Hazards Mitigation, Vol. 1, Proc. ASCE Structures Congress '93, A. H-S. Ang and R. Villaverde, eds., pp. 1065-1070, April 19-21.
- Schofield, A.N., and Zeng, X. (1992) Design and Performance of an Equivalent-Shear-Beam (ESB) Container for Earthquake Centrifuge Modelling, Department of Engineering Report No. CUED/D-SOILS/TR245, University of Cambridge.

## Dynamic capabilities of the Wright Laboratory geotechnical centrifuge facility

K. Brownell, M. Purcell & C.A. Hollopeter  
Wright Laboratory, Tyndall Air Force Base,  
Panama City, Fla., USA

R. Frigaszy  
Watkinsville, Ga., USA

T. Taylor  
University of Washington, Seattle, Wash., USA

K.L. Olen  
GeoSyntec Consultants, Atlanta, Ga., USA

**ABSTRACT:** The Wright Laboratory geotechnical centrifuge located at Tyndall Air Force Base Florida, has undergone major renovations in the last three years. Instrumentation, mechanical operation, and physical capabilities have all been improved to allow dynamic testing of soil models. A state-of-the-art geotechnical centrifuge is now available for use by universities, industry, and military researchers.

### 1 INTRODUCTION

Due to an increasing interest in the modeling of dynamic events in the centrifuge, the geotechnical centrifuge facility at Tyndall Air Force Base has been improved over the past three years to facilitate the modeling of dynamic events. This paper presents a brief summary of projects conducted at the facility through which these dynamic capabilities evolved, and a summary of the specific improvements made to the facility to allow for the testing and analysis of dynamic problems.

### 2 BACKGROUND

The geotechnical centrifuge facility operated by Wright Laboratory is located at Tyndall Air Force Base in Panama City, Florida. The facility contains a 133 g-kG Genisco Model E-185 centrifuge enclosed in a concrete housing (shown in Figure 1). The centrifuge was originally built to test avionic equipment and mechanical devices subjected to high-g loads.

The centrifuge radius is 1.83 m, and the payload platforms located at the end of each cantilever arm measure 760 mm x 760 mm. The capacity of the centrifuge is 133 g-kG (i.e., the product of the g-level and payload may not exceed 133 g-kG); however, the maximum load on the cantilever arm is 227 kg and the maximum operating level is 100 g. Both hydraulic and electrical services are available on the centrifuge. Compressed air and fluids can be fed in via the control console. Primary electric

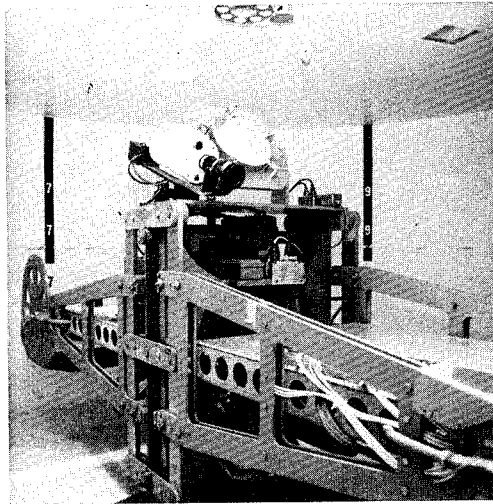


Figure 1. Wright Laboratory geotechnical centrifuge

signals for controlling servo motors, lights, cameras, and the explosive firing system are provided by means of a stacked slip ring. In all, 28 slip rings with shielded cable are available for data collection purposes. Also associated with the centrifuge facility are a machine shop, carpentry shop, state-of-the-art video editing area and dark room, soils laboratory, and an image analysis system including a scanning electron microscope.

### 3 RECENT DYNAMIC STUDIES

In the past three years, several dynamic problems have been studied with the aid of the Wright Laboratory geotechnical centrifuge. Three such studies are summarized below.

#### 3.1 Stress wave propagation in moist sand

Stress wave propagation in unsaturated sands was studied by Dr. Wayne Charlie and colleagues at Colorado State University. As part of the research effort, explosives were detonated in partially saturated sand samples to investigate the influence of moisture content on stress wave transmission through the soil and on apparent crater dimensions (Walsh, 1993 and Villano, 1993; Brownell, 1993).

#### 3.2 Dynamically loaded reinforced soil walls

One thirtieth scale reinforced soil wall models subjected to blast loading were studied by GeoSyntec Consultants Inc. and Applied Research Associates. Replica scaling laws were used to design small scale reinforced soil wall systems. Cubed root scaling laws were used to design a model detonator, which was buried in the backfill behind the model reinforced soil walls. An initial centrifuge test series was conducted in which ten nominally identical reinforced soil walls were subjected to a buried explosive charge, to investigate reproducibility of centrifuge test results. As shown by Fragaszy et al. (1993), reinforced soil wall facing panel deflections and measured wave speeds were very reproducible in the centrifuge. A photograph of a typical model wall is presented in Figure 2. A parametric study was then conducted to investigate the effects of individual components of the reinforced soil wall system on the overall system response to blast loading (Olen et al., 1993).

#### 3.3 Deep dynamic compaction of granular soil

A study on deep dynamic compaction has just been completed under a Cooperative Research and Development Agreement (CRDA) by Dr. Teresa Taylor of the University of Washington. This study required construction of a unique, heavy-duty

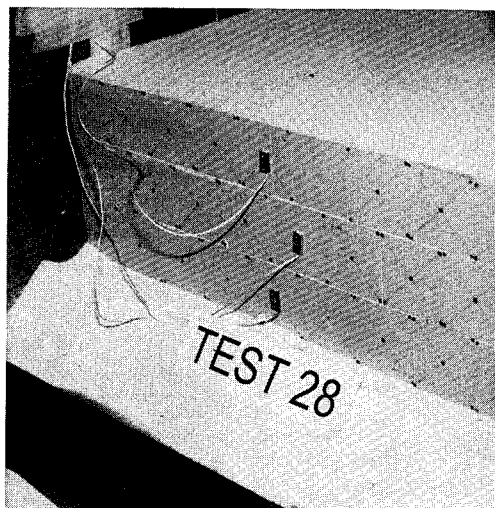


Figure 2. Reinforced-soil wall model, 1:30 scale

electro-mechanical system capable of dropping and retrieving different weights to and from any x-y location in the plane of the sample surface (Taylor and Demchak, in progress). The system has been operated successfully up to 89 g. Tests conducted to date have addressed soil improvement associated with variables such as multiple drops at a single location and at adjacent locations, as well as different drop energies, contact pressures, fall heights, etc.

### 4 CONTROL SYSTEM

A major modification recently made to the centrifuge was the replacement of the hydraulic control system with an electro-hydraulic control system manufactured by Oil Gear Company, and installed by Applied Research Associates. All operations can now be controlled from a computer console. Not only is the operating g-level accurate to 0.001 g, but accelerations and decelerations can be customized for each test.

In addition, all electronic equipment is now integrated. The operator needs only to select the desired g-level; all other operations are performed automatically. Once the centrifuge stabilizes at the selected g-level, a high speed shuttered video camera and a high speed rotating prism camera (described in Section 7) are initiated. When the high speed camera reaches a pre-set operating speed, the data

acquisition system is activated and the dynamic event (e.g., detonation of an explosive) is triggered. Thus, all of the recording equipment is fully operational before the dynamic event takes place. Should the equipment not become operational, the test may be held or stopped prior to triggering the dynamic event.

## 5 INSTRUMENTATION

An on-board data acquisition system was installed on one arm of the centrifuge to minimize electrical noise which commonly corrupts channel signals when slip rings are used. The system is a Pacific Instrument Model 5700 Transient Data Recorder (TDR). This particular TDR has 16 channels and is shock-hardened to withstand 50 g along any axis. Each channel is individually programmable for different sampling rates. The digitizer is programmable for both pre-trigger and post-trigger memory segments for sampling rates ranging from 1 MHz to 10 MHz. Also available is an excitation power supply programmable from 0 to 12 volts in one volt increments.

Pacific Instrument's data acquisition and data reduction software (PACMON), is now used to reduce the centrifuge data to graphical form. Depending on the instrumentation used for a given test, pressure-, acceleration-, or strain-time histories can be recorded. Such a capability is critical in the study of dynamic events.

Wright Laboratory recently purchased a commercially available data acquisition software package from S-Cubed in La Jolla, California. Named Vu-Point, the package is described as "a digital data processing system for IBM PC/XT/AT and compatible personal computers." This menu-driven program allows several different data sets to be analyzed in a number of ways. To date, the most frequently used functions have included scaling, integration, smoothing, and filtering.

In an effort to find low cost instrumentation, one thousand ohm, 1/8 watt, carbon resistors manufactured by Allen Bradley (model RCRO5) have been used to obtain crude estimates of blast wave pressure in dynamic centrifuge modeling tests (Walsh, 1993 and Bachus et al., 1993). The Allen Bradley resistors measure 0.368 mm in length and 0.157 mm in diameter. Prior to using the resistors in actual testing they were placed through a cyclic loading. The preparation consisted

of placing 3 inches of sand in a 2 inch diameter mold. Densification of the soil was performed with a Proctor hammer. The resistors were placed in the mold, with the lead wires protruding through an orifice on the side of the mold. The resistors were orientated with the long axis horizontal. A second three inch soil lift was placed over the resistors and compacted with a proctor hammer. The mold was placed onto a load frame and the soil was pre-loaded several times to maximize flexibility, and thus sensitivity of the carbon inside the resistor. The soil was then compressed to various load levels. The measured voltage levels were plotted against the corresponding calculated stress levels (i.e., load divided by cross-sectional area of the soil specimen) resulting in a voltage-stress calibration curve. When voltages were subsequently measured in the dynamic centrifuge tests, they were converted to stresses using the calibration curve.

In an effort to improve the quality of pressure and acceleration data, miniature pressure transducers and accelerometers (Figure 3) were used during the reinforced soil wall tests. Endevco piezoresistive accelerometers (model 7270A) were placed in the soil surrounding the detonator to record peak particle accelerations. The accelerometers are 7.1 mm high x 14.24 mm long x 2.79 mm wide and require extremely careful placement.

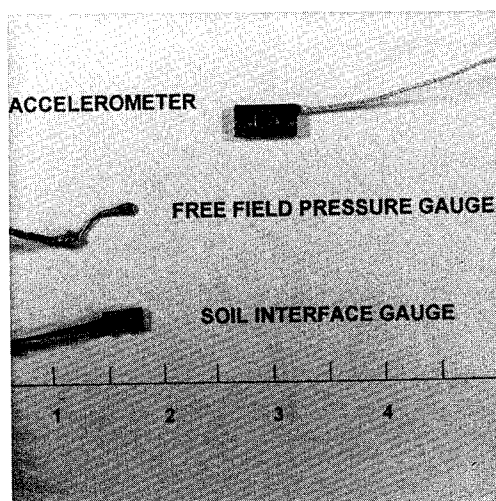


Figure 3. Miniature pressure transducers and accelerometers

Miniature pressure transducers manufactured by the Precision Measurements Company in Ann Arbor, Michigan were selected for the reinforced soil wall test program. Model 105S gauges were used to measure the free field blast pressure. This gauge is a 1/4 bridge design having a diameter of 2.6 mm and a thickness of 0.35 mm. Model 156F gauges were affixed to the facing of the wall panels and were used to determine the pressure and impulse transferred to the wall panels. These gauges measure 3.96 mm x 9.5 mm x 1.55 mm.

#### 6 EXPLOSIVE MODELING

Although explosives have been modeled on the centrifuge for some time, commercial detonators have not been used extensively. The Wright Laboratory Centrifuge Facility is licensed to store and use explosives. Explosive charges manufactured by Reynolds Industries Systems Inc. (RISI), a subsidiary of Reynolds Industries Inc., are used for most dynamic events. These include the RP series detonators, and the specially designed detonator described below. Figure 4 shows the complete line of charges currently available for use at the centrifuge facility.

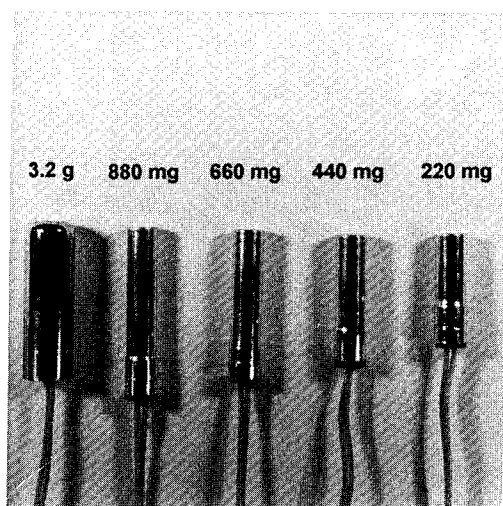


Figure 4. Modified RP-83 detonators and specially designed 3.2 g RISI detonator

For the stress wave propagation study, the RP-83 detonator was selected as the explosive source. The RP-83 detonator is

7.11 mm in diameter by 39.62 mm in length. Various PBX9407 output charge weights (220, 440, 660, and 880 mg) were used in this study.

The test plan for the stress wave propagation study utilized the modeling of models technique in which different sizes of explosives were detonated at various g-levels to model the same prototype event. To accomplish this, the 220 mg pressings of PBX9407 were singularly removed from the output charge creating RP-83 detonators of four different output charge sizes; 880 mg, 660 mg, 440 mg, 220 mg. Based on similar pressure readings from the different size detonators, the modifications were considered successful.

From the cube root scaling law, the reinforced soil wall model required 3.2 grams of PBX9407 at one thirtieth scale. Initially, three RP-83 detonators were bundled together to make-up a total output charge of 3.2 grams. This temporary technique was improved upon with the manufacture of a new explosive charge containing a single pressing of 3.2 grams of PBX 9407 and a 23 mg initiating charge housed in an aluminum casing. The single pressing insured an instantaneous explosive event modelling a 500 pound general purpose weapon containing 198 lbs of explosives.

#### 7 PHOTOGRAPHIC SUPPORT

A high speed shuttered video camera (Nisus, model N-2000), operating at 60 exposures per second with an exposure time of 1/10,000 of a second, has been mounted on the centrifuge to visually record experiments. The camera is controlled from the centrifuge control room through slip rings. In this manner, test recordings can be limited to any desired length. The camera is also connected to a monitor so that tests can be viewed in real time.

Realizing the limitations of the video camera when used to record dynamic events lasting only tens of milliseconds, a high speed rotating prism camera (Photec, model PSI-164-8-132VDC) has also been installed in the centrifuge facility. Adequate space for the camera was not available on the centrifuge itself, so the camera was mounted on top of the centrifuge housing. The lens is directed through a hole in the housing directly above the center of rotation of the centrifuge arms. A 254-mm diameter parabolic mirror is mounted on the centrifuge at the center of rotation, so that the line of sight of the camera is directed into the specimen bucket at the end of the centrifuge arm. The camera uses



a rotating prism to transfer images onto 16 mm film.

To increase the luminescence inside the centrifuge housing, high intensity lights were set into the ceiling of the housing in a circular pattern around the camera lens. The luminescence from the lights is sufficient for 3000 pictures to be taken each second. Thus far, the high speed camera has been used to analyze the travel path of crater ejecta and the displacements explosively induced in a reinforced-soil wall. Neither of these events could be observed in the test videos where the framing rate was 60 pictures per second.

#### 8 FUTURE IMPROVEMENTS

Future improvements to the Wright Laboratory Geotechnical Centrifuge Facility will begin with the data acquisition system. As revisions and upgrades to the PACMON and Vu-Point software become available, they will be incorporated into the system. The same approach will also be used for the computers themselves.

A General Purpose Interface Bus (GPIB) extender has recently been obtained for the Pacific Instruments data acquisition system. Once this system is installed, all instrumentation used for centrifuge testing will be monitored from the control room in real time throughout each test. Also, the calibration of the miniature pressure transducers will be performed under dynamic as well as static conditions. The transducers will be calibrated using a pressure step apparatus available at Wright Laboratory.

Photographic improvements to the centrifuge facility will begin with increased lighting for the high speed camera. With additional luminescence, the camera may be used to its full capacity of 10,000 pictures per second.

Lastly, the addition of earthquake modeling capability is planned for the centrifuge facility. The design requirements for a shaker table are currently being investigated. The shaker table will be designed so that both frequency and amplitude in the x and y direction can be controlled and manipulated.

#### ACKNOWLEDGEMENTS

Funding for this research was provided by the United States Air Force. The authors wish to thank Capt. Richard Reid, USAF, Mr. Carl Hollopeter, and Mr. Dale Whalstrom,

Applied Research Associates, for their tremendous assistance throughout all dynamic centrifuge studies.

#### REFERENCES

- Brownell, K., 1993. Centrifuge modeling of explosion-induced craters in unsaturated sand. DTIC, HQ AFCEA, Suite 2, Tyndall AFB, Florida.
- Fragaszy, R. J., Olen, K. L., Purcell, M., and Brownell, K., 1994. Assessing reliability of results in a dynamic centrifuge test, in Proceedings, Centrifuge 94.
- Purcell, M., Hollopeter, C. R., 1993. The AFCEA centrifuge, ESL-TR 9275, Tyndall AFB, Florida.
- Taylor, T. and Demchak, S., "Equipment Design for Modeling Deep Dynamic Compaction in the Centrifuge", to be submitted to Geotechnical Testing Journal, ASTM.
- Villano, E., 1993. Stress wave propagation in unsaturated sands: Volume II, DTIC, HQ AFCEA, Suite 2, Tyndall AFB, Florida.
- Walsh, A., 1993. Stress wave propagation in unsaturated sands: Volume I, DTIC, HQ AFCEA, Suite 2, Tyndall AFB, Florida.
- Bachus, R.C., Fragaszy, R.J., Jaber, M., Olen, K.L., Yuan, Z., and Jewell, R., 1993. Dynamic Response of Reinforced Soil Systems Volumes I and II, CEL-TR-92-47, HQ AFCEA, Suite 2, Tyndall AFB, Florida.
- Olen, K.L., Fragaszy, R.J., Purcell, M., and Cargill, K.W., 1993. Dynamic Response of Reinforced Soil Wall Systems: Phase II, in Press.

## Development of a dynamic loading device for model foundations

T.G.Ng, F.H.Lee, C.Y.Liaw & E.S.Chan

*Department of Civil Engineering, National University of Singapore, Singapore*

**ABSTRACT:** In order to achieve correct scaling of the inertial effects in dynamic centrifuge model tests, the spectral contents of the forcing function and their corresponding amplitudes and relative phase angles have to be properly scaled and applied to the model. This paper discusses the development and applications of a closed-loop servo-controlled electro-hydraulic loading system for shallow foundations. User-prescribed forcing functions can be preprogrammed into a computer and then applied onto the foundation. Preliminary test results show that the system is able to reproduce the amplitudes of forcing functions with frequency up to 10 Hz at 100 g acceleration. However, more significant distortion is observed in the phase relation. The phase lag between the programmed function and actual forcing function imposed by the actuator increases from 0° to 180° as the excitation frequency varies from 0.1 Hz to 10 Hz.

### 1 INTRODUCTION

In dynamic model centrifuge tests involving forced oscillations, correct modelling of the inertial effects requires the frequency and amplitude of the forcing function to be scaled by  $N$  and  $1/N^2$  respectively, in which  $N$  is the geometric as well as gravity scale factor. For instance, offshore foundations in Southeast Asian waters are usually subjected to wave loadings with wave period between 6 s and 10 s. To model the dynamic effects of such wave loadings in a 1/100th scale model would require a model loading frequency between 17 Hz and 10 Hz.

Cyclic loading devices have been developed by researchers (Craig, 1981; Tan, 1990; Hjortnaes-Pedersen & Nelissen, 1991; and Dean et al., 1993) to simulate the wave loading on offshore structures. However, not all of them have sufficiently high frequency response to simulate the dynamic effects of wave loading. For example, Tan (1990) used pneumatic jacks controlled by a system of solenoid valves and timing mechanism to apply one directional cyclic loading to a single spudcan model. The highest frequency which can be applied by this system is 1 Hz. Dean et al. (1993) used an electrically-operated servomotor to drive a central threaded carriage backward and forwards to produce horizontal cyclic forces onto a 3-leg jackup model. The maximum operating frequency reported was 3.2 Hz. To overcome the scale

distortion, the viscosity of the model pore fluid is artificially raised according to the relation:

$$N^* = N^2(T_m/T_p) \quad (1)$$

in which,

$N^*$  - Ratio of model to prototype pore fluid viscosity

$T_m$  - Model consolidation time scale

$T_p$  - Prototype consolidation time scale

By using a pore fluid of viscosity  $N^*$  times the viscosity of water, where  $N^* > N$ , the ratio of model to prototype frequency required to model consolidation events will be less than  $N$ . This allows consolidation events to be simulated by lower model frequency than is otherwise needed. However, the inertial effects are still not scaled. The system reported by Craig (1981) and Hjortnaes-Pedersen & Nelissen (1991) are capable of producing high frequency dynamic loading of up to 10 Hz and 300 Hz, respectively. Nonetheless, performance test results on this class of dynamic loading device and centrifuge test results of shallow foundations remain relatively scarce.

In addition to the requirement of correct inertial scaling, the loading system should be able to apply vertical, sliding and rocking modes of loadings onto the foundation. This is necessary because horizontal loads are often imposed on the structures above foundation level. For instance, the wave and wind forces are

applied at a distance above the jackup foundation, they will not only impose dynamic horizontal forces and moments to the footing but also dynamic vertical forces to its foundation soil. During a design storm, overturning moments caused by wave and wind forces may increase the vertical load at a footing by as much as 35%-50% of the gravity load, whilst, the lateral load may range from about one-tenth to one-third the magnitude of the total vertical footing load (McCelland et al., 1981).

This paper discusses the development, performance as well as preliminary test results on a closed-loop servo-controlled electro-hydraulic loading device which has been developed on the NUS Geotechnical Centrifuge. The ultimate objective of this exercise is to develop a device which can apply vertical and horizontal forces as well as rocking moment onto the model footing. At the time of writing, this device can apply dynamic vertical loadings on a variety of foundations. The development of the loading device used in this study will first be described. This will be followed by the model preparation and testing procedures. Finally, some results on the dynamic response of the loading system and dry sand model tests will be presented.

## 2 SYSTEM CONFIGURATION

### 2.1 Centrifuge model configuration

The working area of the swing platform on the NUS Geotechnical Centrifuge measures 750 mm x 700 mm. The maximum allowable height of the payload is 1187 mm. Details of the NUS Geotechnical Centrifuge can

be found in Lee et al. (1991) and Lee (1992). The model configuration used in the centrifuge tests is shown in Fig. 1. The soil model is contained in a cylindrical steel container measuring 550 mm internal diameter and 400 mm high. The maximum thickness of the soil bed [1] that can be accommodated by this setup is 350 mm. As shown in Fig. 1, the actuator controlling vertical motion consists of a servo-controlled hydraulic cylinder [9] mounted on top of a loading frame [8] overhanging the model. The loading frame [8] was made from standard steel channel sections. The two columns of the loading frame were fastened onto the flange of the model container. Stiffeners [7] were welded onto the exterior of the model container to strengthen the flange. A miniature close-circuit TV camera (CCTV) [12] was attached to the flange of the model container to monitor the motion of the footing. An aluminium shaft [3] was used to transfer the force from the cylinder piston to the foundation. A horizontal cross bar [5] is mounted to the end of the piston rod of the cylinder. This cross bar slides on linear bearings [6] at both ends to facilitate vertical movement. Electrical feedback to the servo-control system was generated by an in-line load cell [4] and a linear variable displacement transformer (LVDT) [10] measuring the shaft load and displacement. Three different model footings were fabricated, viz a circular footing, a conical footing with a vertical angle of  $120^\circ$  and a 1/100th scale spudcan footing with an upper cone angle of  $154^\circ$  on top of a tip with an angle of  $76^\circ$  (Fig. 1(c)). All of them were circular in plan with a diameter of 100 mm. When they are tested under 100g centrifuge gravity, their behaviour would correspond to that of prototype footings having diameter of 10m.

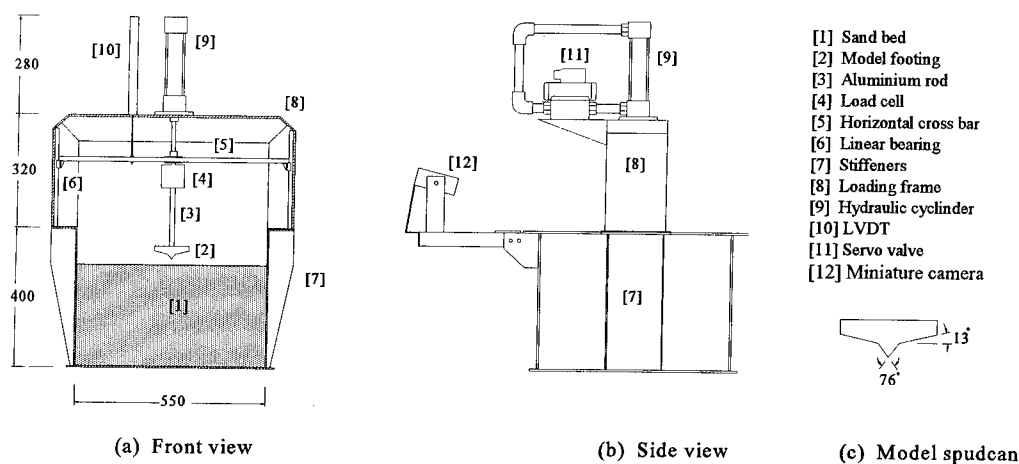


Fig. 1 Centrifuge model setup

## 2.2 Closed-loop control system

Fig. 2 shows a schematic diagram of the electrical and hydraulic circuits. As shown in this figure, the loading or displacement function is fed from a computer signal generator into a servo amplifier. The latter in turn generates the necessary electrical signals to control the pressure or flow rate variation in the hydraulic cylinder through a servo valve. The output from the hydraulic cylinder, in the form of displacement or load, is continuously monitored by the LVDT or load cell and fed back to the servo amplifier to be compared with the input signal. The error resulting from comparing these two signals is amplified and converted into a correcting signal which is then sent back to the servo valve. By so doing, errors are continuously corrected within the margin of acceptance.

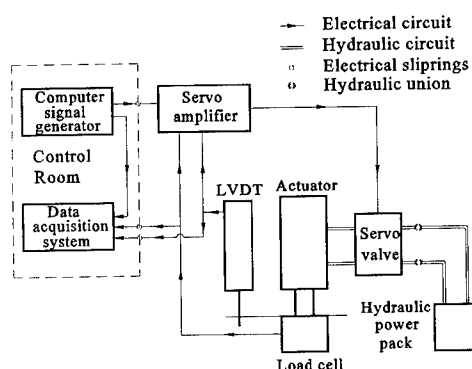


Fig. 2 Schematic diagram of the electrical and hydraulic circuits

Digital data of the loading functions for the initial installation, preloading and subsequent dynamic loading of the model footing were preprogrammed into a personal computer prior to the test. During the test, these digital data were converted into an analogue command signal using an Advantech PCL 726 digital-to-analogue (D/A) output card running on the software Labtech Notebook.

The analogue command signal was fed into a Nobel Elektronik H-4-ASM servo amplifier. Within the servo amplifier, the signal was sign-inverted by an inverter after it has been passed through a ramp generator. The feedback signal was compared with the command signal in a summation amplifier. The resulting discrepancy or error is then fed to a proportion amplifier and integrator. The signal outputs from proportional amplifier and integrator were added in another summation amplifier before the correcting signal was sent out to the servo valve through a power

amplifier. Normally, a dither generator is used to reduce the hysteresis effect in a servo system. In this instance, the hysteresis effect was found to be acceptably small even without dither. Furthermore, the dither was found to give rise to a small fluctuating dynamic load on the foundation. For this reason, the dither generator was not used in this system.

The servo amplifier was housed in an earthed enclosure with the load cell and LVDT amplifiers. In order to eliminate slipping noise and minimize length of signal path within the closed-loop system, the enclosure was mounted on the centrifuge rotating arm instead of the control room. Calibration was carried out on the servo amplifier before every test.

An ULTRA 4685 mechanical feedback two-stage servo valve was used. The electrical signal applied to a torque motor in the electro-magnetic first stage is converted into the movement of a four way valve spool in the hydro-mechanical second stage. The spool is positioned proportionally to the applied electrical signal thus enable a high accuracy and fast response control in a closed-loop control system. The manufacturer's specifications and frequency response for this valve are shown in Table 1 and Table 2 respectively.

Table 1: Technical specifications of servo valve

Nominal rated flow	85 l/min at 70 bar pressure drop
Supply pressure:	
minimum required to effect	
spool movement	3.5 bar
minimum recommended	15 bar
maximum continuous	210 bar
Hysteresis	Less than 5% without dither
Threshold	Less than 2% without dither

Table 2: Frequency response at rated pressure of 70 bar

Frequency (Hz)	Amplitude ratio (dB)	Phase Lag(°)
1	0	0
5	-0.25	10
10	-0.8	22.5
20	-3	42
30	-7	60

The hydraulic pressure was supplied from a hydraulic power pack outside the centrifuge through a set of hydraulic union mounted on the rotor shaft. The maximum pressure that can be transmitted through the hydraulic union was 60 bar at 100g operation. Owing to this limitation the operating pressure was set to 56 bar.

The actuator consists of a double acting hydraulic cylinder with a bore diameter of 40 mm and a maximum stroke length of 150 mm. Based on the maximum allowable pressure of 56 bar, a maximum force of about 7 kN could be exerted by the actuator.

In order to reduce the pressure losses and optimize high frequency response, it is preferable to mount the servo valve on the cylinder. However, it was found that the manifold of the servo valve is larger than the external diameter of the cylinder. Thus it became impractical to mount the servo valve on the hydraulic cylinder. As a compromise, the servo valve was mounted on the loading frame, and connected to the vertical cylinder by high pressure steel pipes.

A load cell with a full-scale range of 11 kN was used to measure the applied load on the footing. It was installed below the horizontal cross bar so that the measured force will include the self weights of the piston and horizontal cross bar. Tensile force arising from the self weight of aluminium shaft and model footing was offset during calibration.

Vertical displacement was measured by a Phillips RP 9350 LVDT. The transducer body was mounted on the loading frame, while the end of the slider was attached to the horizontal bar. If the whole setup is sufficiently stiff, the displacement experienced by the model footing will be equal to the displacement measured at the horizontal bar.

### 3 PERFORMANCE TESTS

Performance tests were conducted at 1g condition to evaluate the frequency response of the loading system. Due to the low soil strength under 1g condition, these tests cannot be carried out on the original sand foundation without causing a bearing capacity failure. As a result, the load was applied onto a rectangular steel beam simply supported on the flange of the model container. The same model configuration shown in Fig.1 was used except that the aluminium shaft connected to the load cell was omitted. A rubber pad was placed under the load cell to prevent it from knocking against the steel beam. Sinusoidal loading functions with frequency ranging between 0.1 Hz and 10 Hz were used. The feedback from the load cell was captured and compared with the command signal. Supply pressure was set to 56 bar so that the results can be compared with those obtained from 100g tests later. Fig. 3 shows typical loading time history records and response with frequencies of 5 Hz and 10 Hz. A summary of frequency response for the system at 1g condition is shown in Table 3.

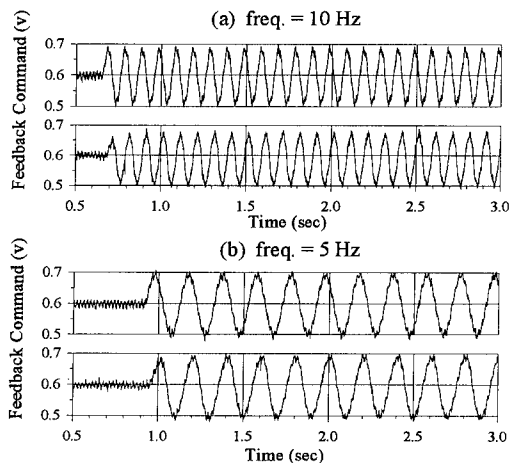


Fig. 3 Frequency response of load control at 1g

Table 3: Frequency response at 1g performance tests

Frequency (Hz)	Amplitude ratio (dB)	Phase Lag( °)
0.1	-0.22	17
0.5	-0.22	25
1	-0.22	30
5	-0.445	72
10	-1.0	108

Comparing the test results from Table 3 with the manufacturer's specification in Table 2, apparently a good amplitude response is achieved at 1g condition although the phase lag shows some deviations. The difference in phase lag could be due to the lower supply pressure used compare to the rated pressure. From Fig. 3, it is also noted that even though the phase lag increases with frequency, the shape of the input wave form is still preserved.

### 4 DYNAMIC MODEL TESTS

#### 4.1 Model preparation

The foundation soil used consists of greyish silica dry sand with properties as shown in Table 4. The soil beds were prepared by pluviation through air. Dry sand was poured into the cylindrical tub directly from a sand hopper suspended from the arms of a fork lift. The rate of pouring is fixed by the small openings at the bottom of the hopper. By keeping the height of fall constant, fairly uniform relative density was found to be obtained throughout the sand sample. By changing the height of

Table 4: Properties of sand (after Yet et al., 1994)

Classification	Fine sand
Gradation	
0.150 mm < d < 0.3 mm	76%
0.063 mm < d < 0.15 mm	22%
Grain size	
D <sub>60</sub>	0.22 mm
D <sub>10</sub>	0.09 mm
uniformity coefficient	0.2
Dry density	
maximum	1660 kg/m <sup>3</sup>
minimum	1332 kg/m <sup>3</sup>
Void ratio	
maximum	0.98
minimum	0.59
Specific gravity	2.63

falling, samples with different relative density can be obtained.

#### 4.2 Testing procedure

The actuator was first set to displacement control with the piston fully retracted during the swing-up stage. When the centrifuge had reached the required acceleration, the system was switched to load control. The preprogrammed loading time history was then streamed from the computer to the servo amplifier.

Output signals from load cell and LVDT were passed across the centrifuge slirings to the control room for analysis. All analogue signals were first passed through a low-pass filter before being converted to digital data. Two 486 PCs were used for low and high speed data acquisition respectively. The former utilized Burr Brown PCI-20098C-1 A/D converter with the sampling rate preset at 100 Hz. The latter utilized Data Translation 2839 A/D converter with the sampling rate preset at 200 kHz.

Real time displays of command and feedback signals were presented on computer monitor using the low speed data acquisition system. All data were saved directly into the hard disk and processed after the test.

#### 4.3 Test results

In this series of tests, the footing was first loaded to a predetermined level which was then maintained for a short period of approximately 10 seconds. This is followed by a sinusoidal dynamic loading time history of prescribed frequency and amplitude to simulate the effect of wave loading on footing without preloading.

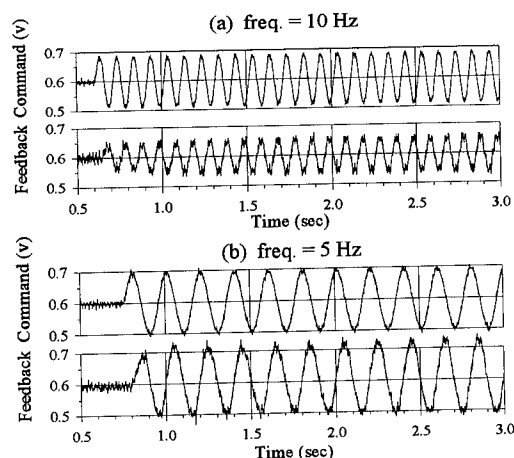


Fig. 4 Frequency response of load control at 100g

Fig. 4 shows results of two sets of loading and feedback time history records captured from dynamic tests with frequencies of 10 Hz and 5 Hz, respectively. As shown in this figure, the frequency response seem to be more sensitive to the excitation frequency at 100g "gravity". The 100g tests show a larger reduction in amplitude ratio and increases in phase lag (up to 180° for freq.=10Hz) compared to the 1g tests. The difference in system response may be attributed to the following reasons,

- (1) In the 1g tests the load was applied onto a steel beam whereas, at 100g, it was applied onto a sand bed. Since the steel beam is stiffer than the sand bed, it allows better closed-loop force control to be imposed.
- (2) The noise caused by oil leakage into the electrical slirings has contaminated the command signal sent into the servo amplifier. This was reflected in Fig. 4 as smooth command signals compare to the erratic feedback signals.
- (3) A higher friction was expected between the spool and the sleeve under 100g condition. At a higher excitation frequency, the drop of efficiency will be more significant. Therefore the frequency response shows more dependent on the excitation frequency under high-g application.

Fig. 5 shows the settlement curve for one of the tests using spudcan footing on dense sand sample. The dynamic loading was applied at frequency of 10 Hz for a total period of about 1000 cycles at 100g. This corresponds to a storm of about 2.8 hours assuming a

prototype wave period of 10 seconds. As shown in Fig. 5, some progressive settlement of the footing occurred during the dynamic loading stage. The rate of progressive settlement reduces with cycle number, as the footing finally settles into a stable state. Similar progressive settlement were also observed by Tan (1990).

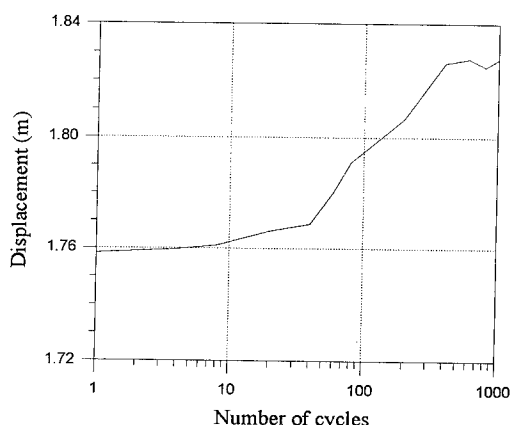


Fig. 5 Displacement under dynamic loading

## 5 CONCLUSIONS

A closed loop loading device has been developed using servo controlled hydraulic actuator in NUS Geotechnical Centrifuge. It is switchable between load and displacement control. Experimental setup, frequency response tests and preliminary test results on dry sand model are presented.

In the performance tests under 1g condition, the amplitude ratio of the system shows a good response conforming to the technical specifications given by the manufacturer. However, the phase lag does not show the same response. This could be attributed to the lower supply pressure used compared to the rated pressure in the specifications. To overcome this problem, a new hydraulic union with maximum operating pressure of 70 bar at 100g operation is being installed.

In the 100g dynamic tests, the frequency response appears to be more sensitive to the excitation frequency than in the 1g tests. The phase lag increases and the wave amplitude decreases as the excitation frequency increases toward 10 Hz.

Dynamic tests on spudcan footing without preloading had been carried out. The test results show that

progressive settlement occurred under constant amplitude dynamic loading. A lateral actuator is being added to the system. When fully completed the device will allow dynamic vertical and lateral loads as well as rocking moments to be applied to foundations.

## ACKNOWLEDGMENTS

The authors are grateful to the National University of Singapore for the funding provided under research grant RP910667, and to all the staff working in the Geotechnical Centrifuge laboratory of NUS.

## REFERENCES

- Craig, W.H. 1981. Cyclic Loading Equipment for Offshore Foundation Model. *Offshore Structures: The Use of Physical Models in Their Design*, eds. Armer, G.S.T. and Garas, F.K. pp 327-334, Construction Press, NY.
- Dean, E.T.R., Hsu, Y.S., James, R.G., and Schofield, A.N. 1993. Development of a New Apparatus for Centrifuge Testing of Offshore Jackup Platform Models and Data Report for Centrifuge Test YSH1: 3-leg Jackup Model with Flat Spuds on Dense Water-Saturated Sand. Technical Report CUED/D-Soils/TR267. University of Cambridge, London.
- Hjortnaes-Pedersen, A.G. & Nelissen, H.A.M. 1991. Applications of Hydraulic Actuators in the Delft Geotechnical Centrifuge. *Centrifuge 91*. pp 385-390, Balkema, Rotterdam.
- Lee, F.H., Tan, T.S., Leung, C.F., Yong, K.Y., Karunaratne, G.P. and Lee, S.L. 1991. Development of Geotechnical Centrifuge Facility at the National University of Singapore. *Centrifuge 91*. pp. 11-17, Balkema, Rotterdam.
- Lee, F.H. 1992. The National University of Singapore Geotechnical Centrifuge - Users' Manual. Research Report No. CE 001. July 1992.
- McClelland, B., Young, A.G. and Remmes, B.D. 1981. Avoiding Jack-up Rig Foundation Failures. *Geotechnical Aspects of Coastal and Offshore Structures*. pp 137-157, Balkema, Rotterdam.
- Tan, F.S.C. 1990. Centrifuge and Theoretical Modelling of Conical Footings on Sand. Ph.D. Thesis, Cambridge University, Jan 1990.
- Yet, N.S., Leung, C.F., Lee, F.H. 1994. Pile behaviour in sand during installation and load test. *Proc. of the Int. Conf. Centrifuge 94*. Singapore.

## 4 Earthquake effects



## Seismic response of gravity type quay wall

X. Zeng

Department of Civil Engineering, University of Kentucky, Lexington, Ky, USA

**ABSTRACT:** Failure of gravity type quay walls induced by earthquakes was widely observed in the field. This paper studies the seismic response of gravity type quay walls using the data of centrifuge tests. Failure mechanisms similar to that happened in the field were replicated in centrifuge tests. It is shown that for a gravity wall with dry backfill, Newmark's sliding block method can be used to estimate the lateral displacement. When sliding occurs the vibration of a wall is de-coupled from the base shaking. However for a retaining wall with saturated backfill the influence of excess pore pressure makes the calculation difficult. Data of centrifuge tests clearly show the degradation of soil stiffness under cyclic loading, which has strong influence on the seismic response of a retaining wall.

### 1 INTRODUCTION

Failure of quay walls was reported during many earthquakes in coastal areas, such as during the Niigata Earthquake in 1964. Details about the retaining structures, site conditions and extents of damage were described by the Bureau of Ports and Harbors (1989). Characteristic damage of gravity type quay walls was a large displacement of the retaining wall (outward movement, rotation and settlement) and substantial ground deformation in the backfill. This type of damage was very expensive to repair since it had to be done against an intense and extensive ground subsidence.

There have been considerable research activities to study the seismic response of quay walls. For instance a finite element analysis of the seismic response of a gravity wall was reported by Pitilakis *et al.* (1989) and the results of wall displacement and ground settlement were compared with the data in the field. An experimental study using a shaking table at normal gravity was conducted by Lai *et al.* (1991). It was concluded that resistance of a quay wall to earthquake loading can be improved by introducing drainage and ground compaction in the backfill. Theoretical analysis based on the data of centrifuge tests on an anchored sheetpile wall by Zeng *et al.* (1993) showed that amplification of vibration induced by stiffness deterioration of backfill can initiate failure of a quay wall.

The current design practice for gravity type quay walls considers three major factors: stability of a gravity wall against sliding along the base; bearing capacity at the base; and the overall stability of the foundation soil.

Extensive research work has been carried out on the dynamic earth pressure on a retaining wall following the early work of Okabe (1924) and Mononobe *et al.* (1929). It is widely proved by experiments that the Mononobe-Okabe equation gives a reasonable estimation about the magnitude of dynamic earth pressure, although the acting point is higher than one third of wall height above the base.

During base shaking hydrodynamic pressures are induced on both sides of a quay wall. The magnitude of hydrodynamic pressure on the seaward side depends on the interaction between fluid and structure and, in the case of a rigid wall, is given by Westergaard's formula (1933). The estimation of hydrodynamic pressure on the backfill side is complicated by the existence of the soil particles which restrict the movement of fluid. As a result the magnitude of dynamic fluid pressure depends on not only the dynamic interaction between fluid and wall but also the restriction on the movement of pore fluid imposed by soil. Matsuo *et al.* (1965) proposed an analytical method to calculate the hydrodynamic pressure, which showed a clear dependence on permeability and porosity of soil.

The lateral displacement of a gravity type retaining wall can be estimated using a Newmark (1965) sliding block method. It is assumed that a rigid wall would slide along a planar surface which has a rigid-plastic friction resistance. The wall will start sliding when the base shaking has reached the level of threshold acceleration and relative displacement will accumulate until the block and ground have the same velocity again.

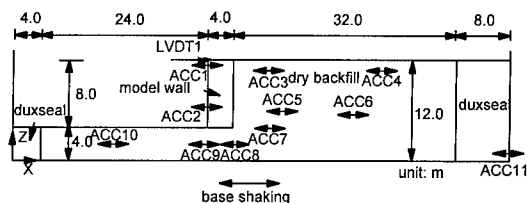


Fig. 1 Cross-sectional view of centrifuge model XZ7

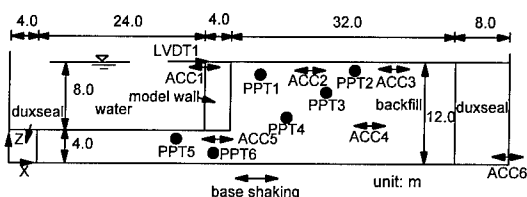


Fig. 2 Cross sectional view of centrifuge model XZ9

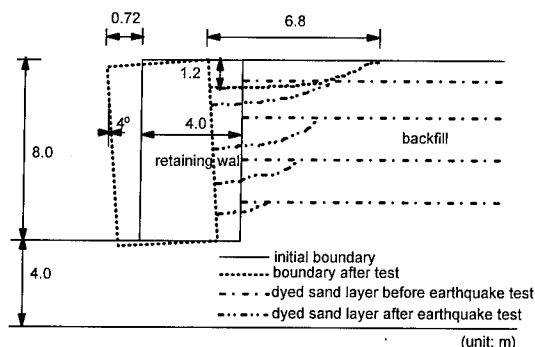


Fig. 3 Failure of gravity wall after earthquakes, test XZ7

## 2 CENTRIFUGE MODEL TESTS

Centrifuge tests reported here were performed at the Cambridge Geotechnical Centrifuge Center between 1990 and 1991 as part of the Cambridge contribution to the VELACS Project, Arulanandan *et al.* (1993). The operation of the beam centrifuge was reported by Schofield (1980). The model earthquakes were generated by the Bumpy Road Actuator, Kutter (1983). A total of four centrifuge tests were performed on a gravity wall 8 meter high, 4 meter wide in prototype scale. Soil used in the models was Nevada sand. Properties of the sand were reported by the Earth Technology Corporation (1991). The gravity wall model was made of aluminum. The critical friction angle between the sand and aluminum was measured to be 18 degrees. Specifications of two centrifuge tests reported here are summarized in Table 1. Cross-sectional views of the two centrifuge models are shown in Figs. 1 & 2. The two tests were conducted at a centrifugal

acceleration of 80g. All the data here is presented in prototype scale. Details of the models and all the data of the tests were reported by Zeng (1992).

Table 1 A summary of centrifuge tests

Model No	XZ7	XZ9
Void ratio	0.79	0.764
Relative density	25.8%	32.7%
Pore fluid	dry	water
Water table	—	top of wall
Wall displacement	lateral	lateral
	rotation	rotation
		settlement
Backfill deformation	subsidence	subsidence

## 3 FAILURE MECHANISM

During the centrifuge test, failure of the retaining wall models was observed, which included lateral displacement, settlement and rotation of the wall, and ground settlement in the backfill.

In test XZ7 the retaining wall had a loose dry backfill (relative density 25.8%). In this test colored sand layers were placed in the backfill to observe the size of failure wedge and the location of the sliding surface. Two relatively large earthquakes were applied to the model with peak intensities of 0.155g and 0.224g respectively. After the earthquakes the retaining wall showed a clear failure mechanism, Fig. 3. The wall moved out by 0.72 meter and rotated by 4 degrees but there was little settlement. The ground in the backfill suffered large settlement of up to 1.2 meter right behind the wall, which covered an area of up to 6.8 meter away from the wall. The movement of dyed sand layers showed an approximately planar sliding surface with a wedge angle of about 40 degrees.

Severe failure occurred during test XZ9. The backfill was water saturated loose sand (relative density 32.7%). One large earthquake with a peak intensity of 25.5% was applied to the model. During this earthquake pore pressure transducers in the backfill recorded high excess pore pressures of up to full liquefaction level at several locations. The recording of some transducers during the earthquake is shown in Fig. 4. That had led to a large outward movement (0.81 meter), rotation (7 degrees) and settlement (0.8 meter) of the wall, severe ground settlement (up to 1.44 meter) in the backfill which affected an area as far as 9.6 meter away from the wall, Fig. 5. In the backfill far away from the wall there was uniform ground settlement of 0.8 meter.

The failure mechanism was similar to that observed in the field. Therefore the centrifuge tests have replicated the field events. Moreover, the transducers used in the tests recorded important information about the seismic response of the structure which would help the understanding of such complex soil-fluid-structure interaction problems.

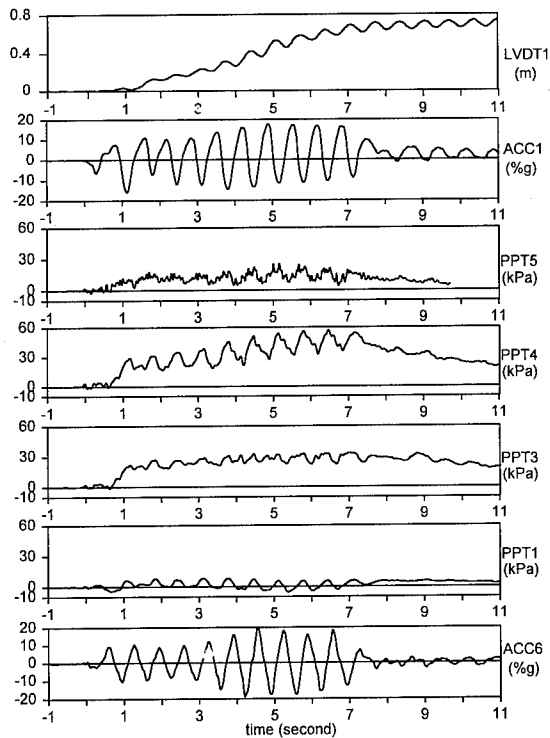


Fig. 4 Recording of some transducers during EQ1, XZ9

#### 4 LATERAL DISPLACEMENT OF GRAVITY TYPE QUAY WALL

Displacement of a retaining wall induced by an earthquake can be divided into three categories: elastic, plastic residual and sliding displacement. Under base shaking, soil deformation will result in displacement of a retaining wall. After a base excitation is over, part of the soil deformation will recover, which can be regarded as elastic deformation. However large proportion of the displacement remains as residual displacement even without sliding of a retaining wall. That displacement is caused by plastic deformation of soil. The residual deformation may also cause an increase in lateral earth pressure on a retaining wall after an earthquake, as has been observed in many experiments, Seed *et al.* (1970). On the other hand, if dynamic loading is so large that the equilibrium of the wall cannot be satisfied, sliding displacement will occur. The magnitude of this type of displacement depends on the intensity and duration of base shaking. In most cases it is this type of displacement that is the major concern for engineers.

##### 4.1 Sliding displacement of a gravity wall

Newmark's sliding block method has been widely

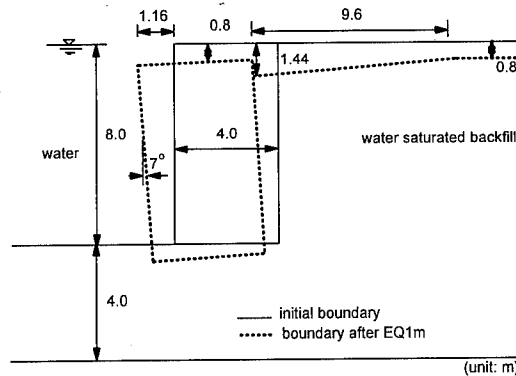


Fig. 5 Failure of the model after earthquake, test XZ9

used to estimate sliding displacement of gravity walls. There are two important assumptions behind this type of calculation. First the block is assumed to move as a single rigid body with shear resistance mobilized along a planar sliding surface. The second assumption is that the sliding surface is free draining. There is no excess pore pressure. This can be applied to either dry soil or saturated soil but with high permeability. In the application of the analysis, three aspects need to be considered: strain softening, amplification of vibration, and influence of excess pore pressure

For a gravity wall with dry backfill the influence of the first two factors can be estimated. For example, if there is strain softening during base shaking the threshold acceleration will be reduced gradually as shown in centrifuge tests reported by Steedman (1984). However, in the case of saturated backfill the combined effect of these three factors is very difficult to estimate by simple calculations. Since the magnitude of excess pore pressure is difficult to predict, the threshold acceleration is varying with time and cannot be derived directly.

##### 4.2 Experimental data

Test XZ7 was conducted on a gravity retaining wall with dry sand backfill. The recordings of some transducers during a model earthquake are shown in Fig. 6. ACC11 was fixed at the base and its recording can be regarded as the input motion. ACC2 was fixed on the wall beneath mid-height and hence it recorded the lateral vibration of the retaining wall. Compared with the input motion there were obvious differences. Firstly the phase of the wall vibration was slightly behind the base shaking input. Secondly, while in the negative half cycle the amplitude of base shaking and wall vibration was approximately the same, the acceleration recorded on the wall in the positive half cycle had a flat peak started from the fifth cycle and this flat peak lasted for a period of time. During that period the base acceleration was first larger and later smaller than the acceleration on wall,

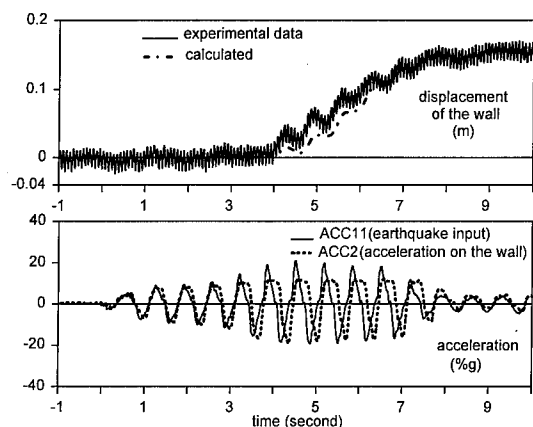


Fig. 6 Response of the wall during EQ2, test XZ7

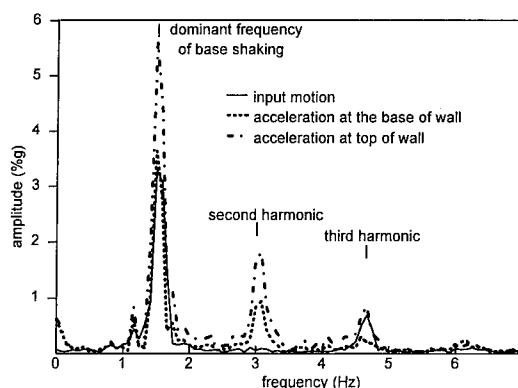


Fig. 8 Fourier amplitude spectra of accelerations

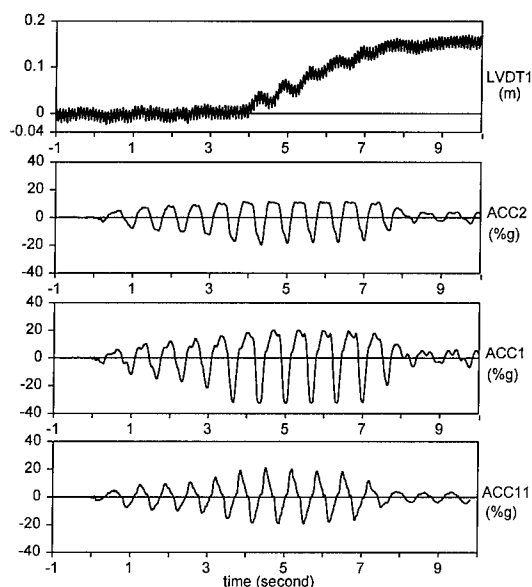


Fig. 7 Response of the wall during EQ2, test XZ7

indicating the buildup and decline of a relative velocity between the wall and its base. As a result, displacement of the wall relative to the base was accumulated.

The threshold acceleration recorded on the wall had a magnitude of 12.5%. From equilibrium of forces on the wall, the threshold acceleration calculated is 14.8% which agrees well with the experimental result. The displacement of the retaining wall can be derived by integrating twice the difference in the accelerations, which is also shown in Fig. 6. It shows a good agreement with experimental data.

As discussed above, for a gravity retaining

wall with saturated backfill excess pore pressures have strong influence on the displacement. Test XZ9 was conducted on a wall with saturated backfill. The recordings of some transducers during an earthquake are shown in Fig. 4. During this earthquake pore pressure transducers in the backfill recorded considerable excess pore pressures. As shown in Fig. 4 there was not a unique threshold acceleration recorded on the wall. Displacement of the wall was recorded during both large cycles and small cycles as excess pore pressure continued to build up. The magnitude of permanent displacement under such circumstance is difficult to estimate by using the sliding block method.

## 5 AMPLIFICATION AND PHASE SHIFT OF VIBRATION

Under cyclic loading, the increase in shear strain and the buildup of excess pore pressure will lead to deterioration of soil stiffness. Test XZ7 was conducted on a gravity retaining wall with dry sand backfill. The response of the wall to a large earthquake is shown in Fig. 7. ACC2 was fixed on the wall near the base and hence recorded predominantly horizontal vibration of the wall. ACC1 was fixed near the top of the wall and hence its recording was the combined effect of rocking and horizontal vibration of the structure. The Fourier amplitude spectra of accelerations on the wall and that of input motion are shown in Fig. 8. Firstly the amplification of vibration recorded by ACC2 was around the second harmonic suggesting that the natural frequency for horizontal vibration was dropped from an estimated value of 4.66 Hz at the beginning of shaking to around 3.0 Hz. This amplification was also shown in the acceleration recorded at the top. On the other hand, the spectrum of acceleration at the top had clear amplification around the dominant frequency of base shaking indicating the natural frequency of rocking had

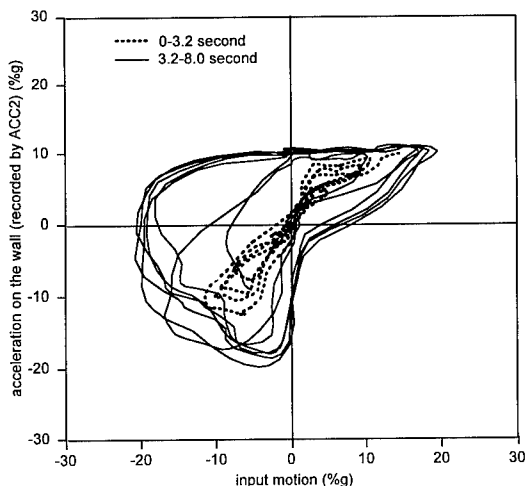


Fig. 9 Lissajous figure for accelerations, test XZ7

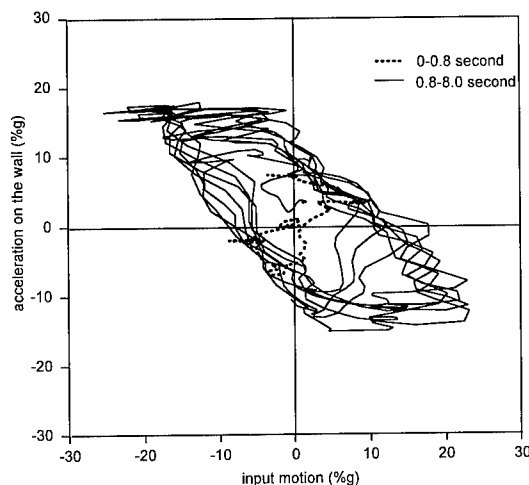


Fig. 10 Lissajous figure for accelerations, test XZ9

dropped from an estimated value of 3 Hz at the beginning of shaking to around 1.5 Hz. The phase relation shown by the Lissajous figure also showed the deterioration of the soil stiffness, Fig. 9. During the first four small cycles (0 - 3.2 second) the vibration of the wall was roughly in phase with the base shaking. However with increasing amplitude of vibration the phase shift was gradually increased. Another important result is that the diagram is strongly non-symmetric. There is a flat top on the positive side for the acceleration of the wall indicating the sliding of the wall. During that period, the vibration of the wall was decoupled from base shaking.

In test XZ9 the gravity retaining wall with

loose backfill was subjected to a large earthquake. The recordings of some transducers during the earthquake are plotted out in Fig. 4. Pore pressure transducers in the soil recorded high excess pore pressures during this earthquake. For example the peak magnitude recorded by PPT1 and PPT3 was close to the initial vertical effective stresses at those locations, indicating liquefaction of sand. Thus the deterioration of soil stiffness was expected to be severe. That was shown in the phase relation of Lissajous figure, Fig. 10. Between 0 and 0.8 second (the first cycle of vibration) the phase shift was smaller than 90 degrees. However in the followed larger cycles the phase shift was increased and eventually close to 180 degrees, indicating that the natural frequency of the wall had dropped to lower than the dominant base shaking frequency. During the earthquake the wall suffered large displacement, settlement and outward rotation as shown in Fig. 5. The consequence of deterioration of soil stiffness is clear.

## 6 CONCLUSIONS

Centrifuge tests have replicated that happened in the field and generated useful data about the seismic response of gravity type quay walls. In the case of a gravity retaining wall with dry backfill the current design practice can be used to estimate the displacement. However for a wall with saturated backfill the generation of excess pore pressure increases the loading on a wall, deteriorates the stiffness of soil and may initiate failure of the structure. Under such circumstances conventional analysis cannot generate satisfactory results. To limit the magnitude of excess pore pressure is hence important in design.

## ACKNOWLEDGMENT

The work reported here is funded under the VELACS grant of the National Science Foundation; the program manager is Dr. C. Astill. The author would like to express his gratitude to the advice of Prof. Schofield and Dr. Steedman in the research. The author acknowledges the financial support of Churchill College, Cambridge University through the William and Barbara Hawthorn Fellowship.

## REFERENCES

- Arulanandan, K. and Scott, R.F. (1993): Project VELACS - Control test results, *Jrn. of Geotech. Eng., ASCE*, Vol. 119, No. 8, pp.1276 - 1292.
- Bureau of Ports and Harbors (1989): Earthquake resistant design for quay walls and piers in Japan, Ministry of Transport, Japan.
- Earth Technology Corporation (1991): VELACS laboratory testing program soil data report, National Science Foundation, USA.

- Iai, S. and Matsunaga, Y. (1991): Soil improvement area against liquefaction, Proceedings of International Conference on Geotechnical Engineering for Coastal Development, Vol. 1, pp.453-458, September, Yokohama, Japan.
- Kutter, B.L. (1983): Centrifuge modeling of the response of clay embankments to earthquakes, Ph.D thesis, Department of Engineering, Cambridge University.
- Matsuo, H., and Ohara, S. (1965): Dynamic pore water pressure acting on quay walls during earthquakes, Proc. of 3rd World Conf. on Earthquake Engineering, Vol. 1, pp. 130-140, New Zealand.
- Mononobe, N. and Matsuo, H. (1929): On the determination of earth pressure during earthquakes, Proc. World Eng. Congress, Vol. 9, pp.177-185.
- Newmark, K.M. (1965): Effect of earthquakes on dams and embankments, *Geotechnique* 15, No. 2, pp.139-160.
- Okabe, S. (1924): General theory of earth pressure and seismic stability of retaining wall and dam, *Jrn. Japan Civil Engng. Society*, Vol. 10, No. 6, December.
- Pitilakis, K. and Moutsakis, A. (1989): Seismic analysis and behavior of gravity retaining walls - the case of Kalamata Harbor Quaywall, *Soils and Foundations*, Vol. 29, No. 1, pp.1-17.
- Schofield, A.N. (1980): Cambridge geotechnical centrifuge operations, *Geotechnique* 30, pp. 227-268.
- Steedman, R.S. (1984): Modeling the behavior of retaining walls in earthquakes, Ph.D Thesis, Cambridge University.
- Westergaard, H.M. (1933): Water pressure on dams during earthquakes, *Transactions of the ASCE*, Vol. 98, pp.418-472.
- Zeng, X. and Steedman, R.S. (1993): On the behavior of quay walls in earthquakes, *Geotechnique* 43, No.3, pp.417-431.
- Zeng, X. (1992): Dynamic centrifuge tests on quay wall models, Technical Report TR251, Department of Engineering, Cambridge University.

## Comparison of 1g and centrifuge models of a dynamic earth pressure problem

M. Kazama

*Tohoku University, Sendai, Japan*

T. Inatomi & E. Iizuka

*Port and Harbor Research Institute, Ministry of Transport, Yokosuka, Japan*

**ABSTRACTS:** An experiment of a dynamic earth pressure acting on the caisson foundation both in the 40g centrifugal field and in the ordinary 1g field is performed. To examine the difference in the model tests both experimental results are fed back, based on the law of similarity to the prototype size structure, and the results are compared with a numerical analysis. The adaptability of the law of similarity is investigated. The quantitative coincidence of the dynamic acceleration response between model test and numerical calculation was good for both in the 1g and 40g field test. On the other hand, regarding the quantitative coincidence of the dynamic earth pressure there are double or half differences between the test and the numerical results. It is also found that the dynamic response in the 1g field test was more sensitive than that in the 40g centrifuge test.

### 1 INTRODUCTION

The behavior of ground and structure systems during earthquakes is investigated by a model vibration test. Previously, when actual soil was used in a 1g model vibration test, the law of similarity could not be strictly adapted because the dynamic properties of soils are affected by the confining pressure. As a result, such experiments have rarely been conducted to estimate the behavior of an prototype size structure.

The law of similarity of a model vibration test using earth material in a normal gravitational field has been studied by Kagawa(1978) and Kokusho(1979). In these studies, the similitude was obtained under an assumption (Rocha's assumption 1975) that the stress-strain relationships are similar for grounds with different confining pressures. Iai(1988) introduced an overall law of similarity in the 1g field which can be applied to model vibration tests on the ground, structure and fluid system. Then Iai examined the validity of "Rocha's assumption" with respect to sandy soil. The authors (1993) introduced the similitude in model vibration tests for the ground, structure and fluid system, which can be applied to an arbitrary gravitational field. The portion used in this study is shown in Table 1.

In this study the experimental results for the 1g and the 40g fields are converted to prototype size structures on the same scale, and the adaptability of the similitude is investigated.

### 2 MODEL VIBRATION TESTS IN A 1G FIELD AND IN A CENTRIFUGAL FIELD

The tests in a centrifugal field were performed by using PHRI geotechnical centrifuge developed by Terashi (1981) with an effective radius of 3.8m. The actuator used in the centrifuge test was second version electro hydraulic type shaker developed by the authors in 1989. Its table dimensions were 70cm by 40cm. The first version shaker was introduced by Inatomi et al (1988). On the other hand, the shaking table used in 1g tests was an electro magnetic type of 3.5m by 4m table in PHRI. The details of the test apparatus and the procedure were described by the authors (1990).

Fig.1 shows the cross section of the caisson to ground system and the sensor layout. The caisson was provided with a pressure receive plate to measure the earth pressure using three bi-axial load cells. The load cells measured the static and the dynamic earth pressure as a resultant force directly. The model grounds of both tests were made by dry sand sampled from Akita Port. Both tests used the input acceleration wave forms (NS

Table 1 Similitude for model vibration test

Notations	Items	scaling factors (model/prototype)		
		A)General Scaling law	B)Scaling law for 1g field	C)Scaling law for centrifugal field
$N_l$	length	$N_l$	$1/N$	$1/N$
$N_\rho$	density of saturated soil	$N_\rho$	1	1
$N_\epsilon$	strain of soil	$N_\epsilon$	$N_\epsilon$	1
$N_g$	acceleration	$N_g$	1	N
$N_t$	time	$(N_l N_g / N_\epsilon)^{1/2}$	$(N_\epsilon / N_g)^{1/2}$	$1/N$
$N_f$	frequency	$(N_l N_g / N_\epsilon)^{-1/2}$	$(N_\epsilon / N_g)^{-1/2}$	N
$N_u$	absolute displacement of soil skeleton	$N_l N_g / N_\epsilon$	$N_\epsilon / N_g$	$1/N$
$N_\sigma$	stress of soil	$N_\rho N_l N_g / N_\epsilon$	$1/N$	1
$N_D$	stiffness of soil	$N_\rho N_l N_g / N_\epsilon$	$1/(N_\epsilon N_g)$	1

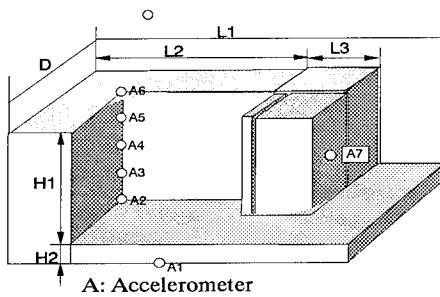


Fig.1 Model caisson and backfill

Table 2 Model dimensions

	1G-Model	40G-Model
H1	80	20
H2	20	6
L1	300	60
L2	200	37
L3	48	12.5
D	150	18

component) recorded at Hachinohe Port during the Tokachi-oki earthquake (1968). Table 2 shows the model dimensions. The symbols in the Table correspond to Fig.1. The model caisson in the centrifuge test is 20cm high. This means that the ratio of the models is 1: 4 .

### 3 FEEDBACK OF THE MODEL TO THE PROTOTYPE SIZE STRUCTURE BASED ON THE SIMILITUDE

To examine the difference in the model tests between a 1g field and a centrifugal field both test results are base on the similitude to the scaled prototype size. According to the similitude,the centrifuge model has a length scale factor of 1/40, and the 1g model has a length scale factor of 1/10. In the similitude of the model tests,the similarity

in the stress strain relationship of soils is assumed. The confining pressure of the 1g model ground with a reduced scale of 1/N is 1/N of the prototype ground and therefore,the validity of this assumption can be discussed by studying the dependence of the dynamic deformation property of soil on the confining pressure. According to the experiments conducted by Kong(1986) and Tatsuoka (1978) the strain dependency curves of the shear modulus and the damping ratio of the sandy soil coincide with each other,if the strain axis is scaled by the square root of the confining pressure. If the scaling factor of the strain is assumed to be 0.5th power of the reduced scale in length,then the similitude in a 1g field can be derived as shown in Table 3.

Table 4 shows scaled values of both models. For the 1g model,the conversion to the prototype used the similitude given in Table 3,while for the centrifuge,it used the similitude in the centrifugal field (Table 1c).The maximum resultant force of dynamic earth pressure is the value converted to the unit depth per meter. The apparent density of caisson is the whole weight that contains sand in the caisson divided by the whole volume. The shear wave velocity of the backfill is the average shear wave velocity obtained by the natural frequency of the backfill

In this Table,it has to be noted that there are several different items. The coefficient of earth pressure at rest before excitation is 0.359 for the 1g model and 0.166 for the centrifuge model,and that 1g model ground is softer and its density is lower than expected. It is found that the maximum resultant force of the dynamic earth pressure converted to the prototype is twice as great in the 1g prototype than in the 40g prototype, reflecting the softness of the backfill. These results seem to express a good qualitative agreement between the test conditions and the experimental results.



Table 3. 1G Scaling factors (model/prototype)

Items	N=N	N=10
length	1/N	1/10
stress	1/N	1/10
strain	$N^{-1/2}$	0.316
time	$N^{-3/4}$	0.178
frequency	$N^{3/4}$	5.62
stiffness	$N^{-1/2}$	0.316
shear wave velocity	$N^{-1/4}$	0.562
acceleration	1	1
density	1	1
force over unit meter	$N^{-2}$	1/100

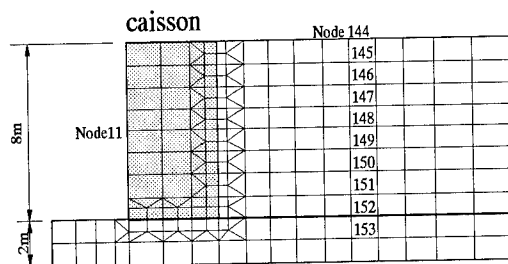


Fig.2 FEM mesh corresponding to prototype

#### 4 NUMERICAL CALCULATION OF MODEL TESTS

The two dimensional finite element program FLUSH was used to study the quantitative validity of the acceleration response and the maximum dynamic earth pressure. for these two prototype size model. Fig.2 shows the finite element mesh used for the calculation. The

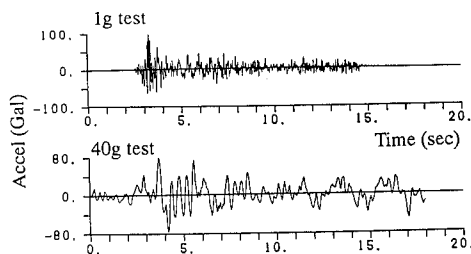


Fig.3 Scaled input motions at -10m.

calculation assumed a Poisson's ratio of 0.33 for the ground elements. The input acceleration motion used in the analysis is the scaled motion as it is obtained from each test shown in Fig.3, because it is considered that the frequency content of input motion will considerably affect the dynamic behavior of the system.

#### 4.1 Physical properties of the backfill ( $G_0$ , $G/G_0$ to $\gamma$ , and $h$ to $\gamma$ curves)

The essential point of the centrifuge test is to make the ground's stress state identical to the prototype. In this paper, to study how the results are affected by the dependence of the dynamic properties of the ground on the confining pressure, the properties were calculated for two cases: the backfill considered to be uniform, and the two backfills, one divided into 5 layers and the other divided into 10 layers. The properties were determined as follows:

Table 4 Conversion of model into prototype

Quantity	1G-Model	1G-Prototype	40G-Model	40G-Prototype
Initial Static Coefficient of Earth Pressure	0.359	0.359	0.166	0.166
Density of Backfill Ground (Relative density)	1.56t/m (53%)	1.56t/m (53%)	1.66t/m (81%)	1.66t/m (81%)
Apparent Density of Caisson	1.574t/m	1.574t/m	1.524t/m	1.524t/m
Shear Wave Velocity	122m/s	217m/s	260m/s	260m/s
Max. Input Acceleration	96Gal	96Gal	31.3m/s	78Gal
Duration of Input Motion	3.0s	16.8s	1.0s	40s
Filtering Frequency	250Hz	44.5Hz	300Hz	7.5Hz
Max. Resultant Force of Dynamic Earth Pressure	70kgf/m	7.0tf/m	68kgf/m	2.7tf/m

1g scaling law  
(scaling factor=10)

centrifuge scaling law  
(scaling factor=40)

(1) When the backfill is considered to be uniform  
The backfill is considered to be homogeneous with an uniform shear wave velocity. At this time, the initial shear modulus  $G_0$  of the ground is obtained from the shear wave velocity shown in Table 4. The  $G/G_0$ - $\gamma$  curve and  $h$ - $\gamma$  curve are the average curves obtained from a previous sand element test (Kitazawa et al 1986).

(2) When the dependence of the backfill on the confining pressure is considered

The backfill is divided into horizontal 5 and 10 layers. The initial shear modulus of each layer is obtained from the shear wave velocity structure calculated in advance from the multiple reflection theory so that each initial shear modulus is proportional to the square root of the confining pressure at the intermediate depth of each layer, and so that the dominant first frequency of the backfill coincides with the case described in Table 4. Also, the  $G/G_0$ - $\gamma$  curve and  $h$ - $\gamma$  curve are assumed to be dependent on the confining pressure. This means that when these curves used in the conditions outlined in (1) are considered to be the curves corresponding to a confining pressure of 1 kgf/cm<sup>2</sup>, their ratio to the confining pressure for each layer at the intermediate point can be calculated. The curves used in each layer were obtained by reducing the ratio of the strain axis at the square root of the confining pressure

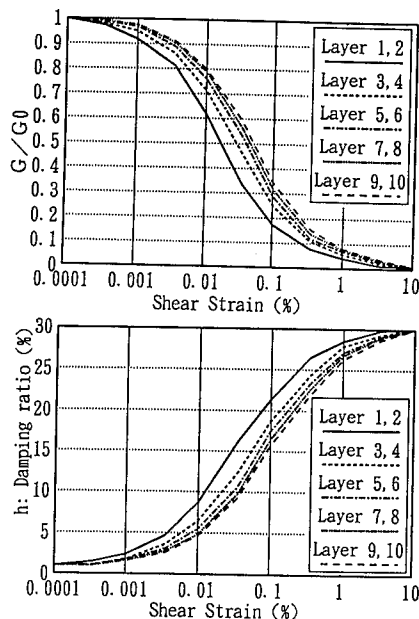


Fig.4 Strain dependency of shear modulus and damping ratio used in FEM calculation.

ratio, and were thus determined as shown in Figure 4.

#### 4.2 Comparing the calculation results to the experiment results

Fig.5 shows the time histories of acceleration and the dynamic earth pressure of all cases.

(1) Maximum acceleration response of the backfill.

Fig.6 shows the maximum acceleration distribution of the backfill in vertical direction along the vertical line at node 144. The maximum acceleration obtained from the calculations are greater in the 1g model than in 40g model coinciding qualitatively with the test results. It is found that the distribution in depth direction tends to approximate the test values by making the layer division finer by considering the dependency of the shear modulus on the confining pressure.

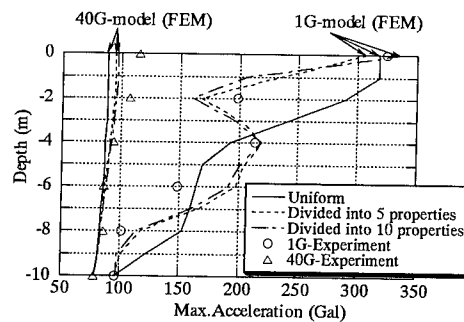


Fig.6 Distribution of the maximum acceleration response in backfill.

(2) Maximum caisson acceleration response

Fig.7 shows the maximum caisson response at node 111. The results in 40g model calculation is well consistent with the test results compared with that in the 1g model. It is inferred from Fig.6 that the caisson response is influenced by the backfill response distribution.

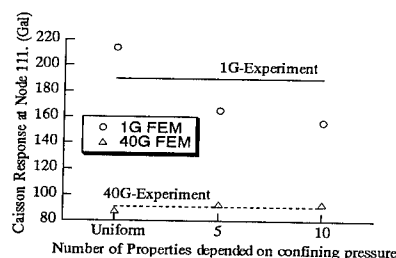


Fig.7 Comparison of the maximum caisson response at Node 11 between the test and the FEM.

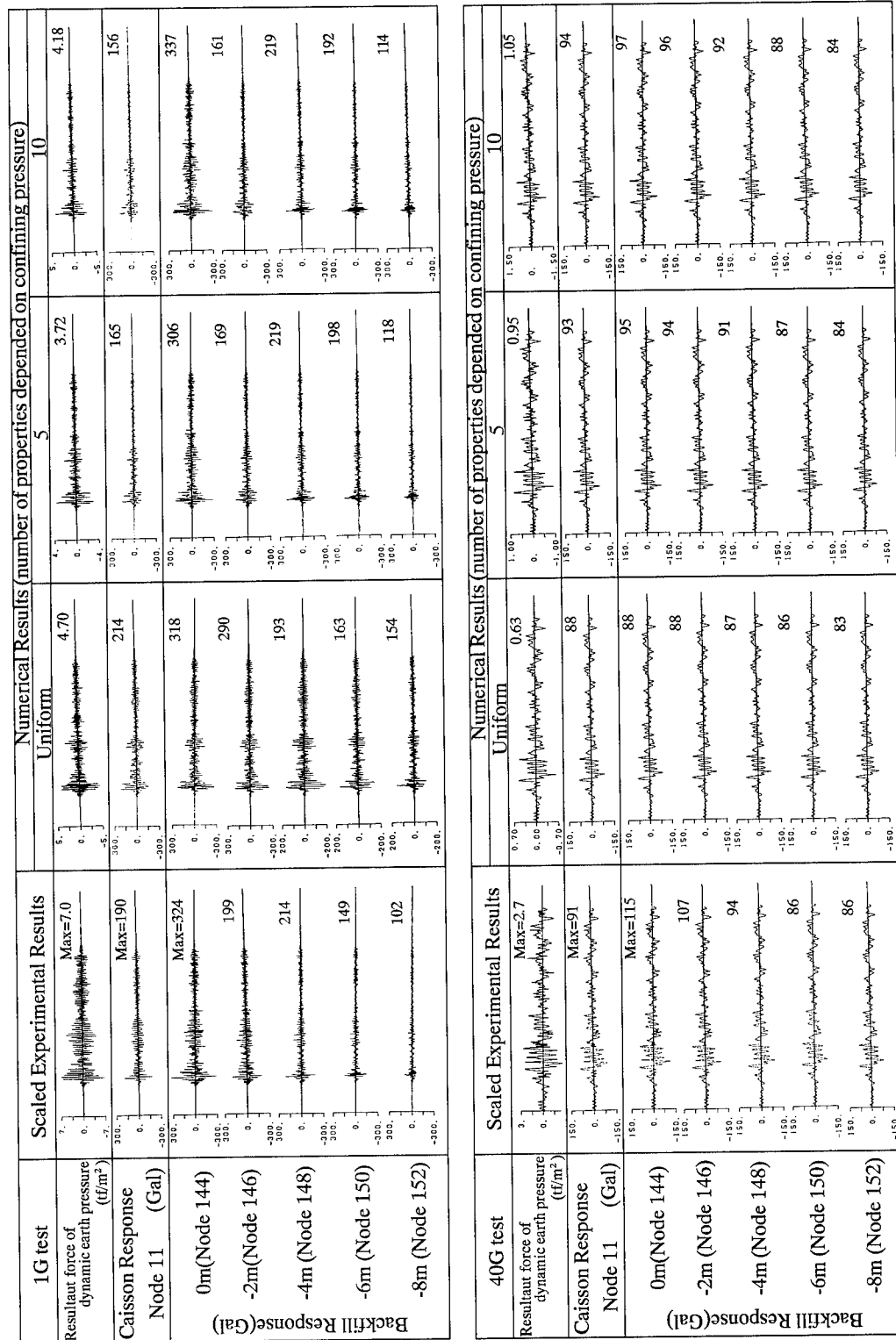


Fig.5 Comparison of time histories between experiment and numerical calculation

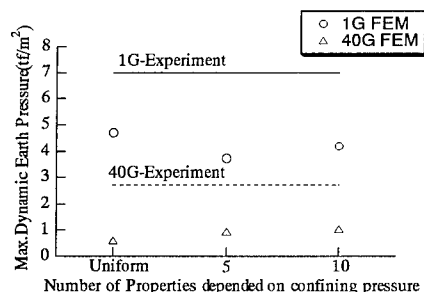


Fig.8 Comparison of the maximum dynamic earth pressure between the test and the FEM.

### (3) Maximum resultant force of the dynamic earth pressure

Fig.8 shows a comparison of the maximum resultant force of the dynamic earth pressure. The calculated force was obtained as the maximum value when the horizontal stress of the ground elements near the caisson was converted to forces and its time histories was superimposed. Unless the properties are given more fine that is, the dependence of the ground's physical properties on the confining pressure is more precisely considered, the calculation results are not always close to the test results.(solid line and broken line). These values, however, are half of the test data or even less than that.

The reason for the poor agreement for dynamic earth pressure between the calculation and the test seems to be: 1) the difference in the nonlinearity of the interface between the caisson and the backfill, 2) the initial stress state affects the dynamic earth pressure behavior considerably, 3) the uncertainty of the curves used for the calculation to express the dependency of the shear modulus on the strain, and 4) the limit of the law of similarity in the 1G field. With regard to whether the equivalent linear analysis used here is right or not, the effective shear strain in this calculation was within a range of 0.01% and 0.04% or less, which is the proper range for an equivalent linear calculation.

### CONCLUSION

Using the law of similarity, the model test results in the 1g and the 40g centrifugal fields were converted to prototype size structures of nearly the same size and the results were compared with

numerical calculations. The acceleration responses of the caisson and the backfill of the calculation express a good agreement with the test data. When numerical calculations are used to study the maximum acceleration, it was necessary to consider the dependence of the ground physical properties on the confining pressure in the depth direction especially for the looser ground subjected to the lower confining pressure. The resultant force of the dynamic earth pressure in the calculation, however, was half of test value or less.

### REFERENCES

- Iai, S. 1988. Similitude for shaking table tests on soil-structure-fluid model in 1g field, Report of the PHRI, Vol.27, No.3, pp.3-24.
- Inatomi, T., Kazama M. and Othuka K. 1988. Development of earthquake simulator in PHRI centrifuge and its application, Proc. of 9th WCEE, Vol.8, SI-3, pp.831-836.
- Kagawa, T. 1978. On the similitude in model vibration tests of earth structures. Proc. of JSCE, No.275, pp.69-77(in Japanese).
- Kazama, M. & Inatomi, T. 1990. Model vibration tests for the seismic earth pressure acting on the rigid caisson foundation, Proc. of JSCE, No.416/I-13, pp.419-428(in Japanese).
- Kazama, M. & Inatomi, T. 1993. Application of centrifuge model testing to dynamic problems, Proc of JSCE, No.4 /I-25, pp.83-92(in Japanese).
- Kitazawa, S. Higaki, N. & Noda, S. 1986. Estimation of the maximum ground acceleration in Okinawa prefecture and Amami islands, Technical note of PHRI, No.396, pp.23-25(in Japanese).
- Kokusho, T. & Iwatate, T. 1979. Scaled model tests and numerical analyses on nonlinear dynamic response of soft grounds, Proc of JSCE, No.285, pp.57-67(in Japanese).
- Kong, X. J., Tatsuoka, F. & Pradhan, T.B.S. 1986. Dynamic Deformation properties of sand at extremely low pressures, Proc. of 7th Japan Earthquake Engineering Symposium, pp.631-636.
- Tatsuoka, F., Iwasaki, T. & Takagi, Y. 1978. Hysteresis damping of sands under cyclic loading and its relation to shear modulus, Soil and Foundations, Vol.18, No.2, pp.25-40.
- Terashi, M. 1985. Development of PHRI Geotechnical centrifuge and its application. Report of PHRI, Vol.24, No.3, pp.73-122.
- Rocha, M. 1957. The possibility of solving soil mechanics problems by the use of models, Proc. 4th

## Validation of a computer code for the analysis of dike retaining structures

K. K. Muraleetharan, K. Arulmoli & S. V. Jagannath  
*The Earth Technology Corporation, Irvine, Calif., USA*

R. C. Wittkop & J. E. Foxworthy  
*Port of Los Angeles, San Pedro, Calif., USA*

**ABSTRACT:** As a part of the Port of Los Angeles' Pier 400 dredging and landfill design project, a fully-coupled, nonlinear, dynamic finite element code called DYSAC2 was used to study the dynamic performance of rock-dike retaining structures. This paper presents the validation of the computer code DYSAC2 for the analysis of rock-dike retaining structures using the results from a dynamic centrifuge testing program.

### 1 INTRODUCTION

The Ports of Los Angeles (POLA) and Long Beach (POLB) in conjunction with the United States Army Corps of Engineers have conducted a long-range planning study to determine the Ports' facilities and infrastructure needs through year 2020. This planning effort indicates that over 400 hectares of new land will be needed for POLA by the year 2020 encompassing 20 new liquid bulk, dry bulk, container, automobile and general cargo terminals. This land will be created by dredging and landfilling in the outer harbor. The initial phases of land creation involve dredging of over 45 million m<sup>3</sup> of materials, placing the material behind approximately 6 km of rock-dike or containment structure creating approximately 235 hectares of new land. The new land will be called Pier 400.

For the Pier 400 dredging and landfill project's conceptual design phase, a fully-coupled, nonlinear, dynamic finite element code called DYSAC2 (Muraleetharan et al. 1988, 1991; Muraleetharan 1990) was used to study the dynamic performance of Pier 400 containment structure/landfill configurations. As a part of the above project, dynamic centrifuge tests were also performed to acquire data for the validation of DYSAC2 and to study the potential deformation mechanisms of Pier 400 containment structures subjected to base shaking.

Several model configurations consisting of, uniform and layered foundation soil overlain by a gravel dike retaining a fine sand backfill, were tested in the centrifuges at University of California, Davis (UCD) and California Institute of Technology (Caltech). Both the UCD and Caltech centrifuges have an effective radius of 1 m.

Selected results from one of the above centrifuge tests and the corresponding predictions made by DYSAC2 are presented in this paper.

### 2 COMPUTER CODE DYSAC2

DYSAC2 is a finite element computer code for the dynamic analysis of two-dimensional geotechnical engineering structures. DYSAC2 is based on the finite element solution of the fully-coupled dynamic governing equations of saturated porous media (Biot 1962). The development of the governing equations and numerical approximations used by DYSAC2 is similar to that of Zienkiewicz and Shiomi (1984). Specifically, the U-u approximation of Zienkiewicz and Shiomi (1984) is used in the current version of DYSAC2, where U is the displacement of the fluid and u is the displacement of the soil skeleton. Four-noded isoparametric elements with reduced integration for the fluid bulk modulus terms are used in DYSAC2.

To integrate the spatially discrete finite element equations, a three-parameter time integration scheme called the Hilber-Hughes-Taylor  $\alpha$ -method (Hilber et al. 1977) and a predictor/multi-corrector algorithm is used in DYSAC2 instead of the widely-used Newmark's method (Newmark 1959). In dynamic analyses resulting from a computational discretization process (e.g., finite element models), many of the high frequency modes actually correspond to spurious artifacts of the discretization process instead of representing real physical behavior of the actual continuous system. Therefore, it is desirable for the time integration algorithm to possess some form of numerical dissipation capable of damping out spurious participation of the higher frequency modes, while permitting the accurate low-frequency behavior of the actual system to emerge without attenuation. The time integration scheme used in DYSAC2 provides quadratic accuracy and the above mentioned desirable numerical damping characteristics.

In DYSAC2, stress-strain behavior of soils can be described by isotropic linear elastic model and

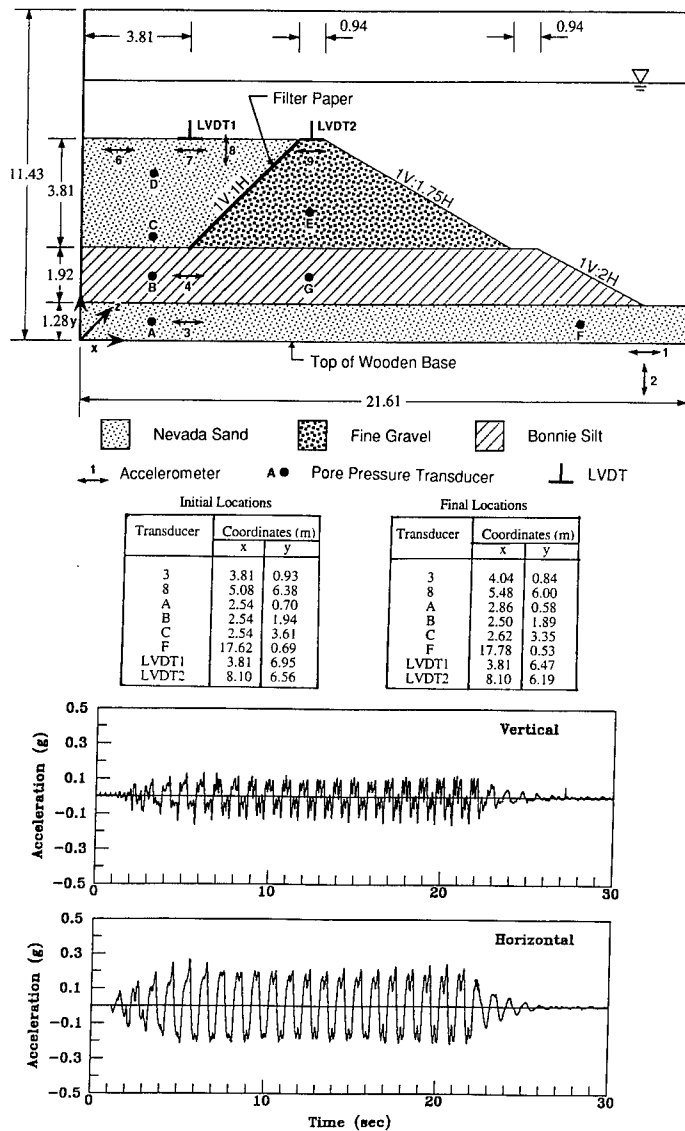


Fig. 1 Configuration of the centrifuge model (all dimensions are given in meters and in prototype scale) and the input base acceleration - time histories.

bounding surface elastoplastic constitutive models. Two constitutive models based on bounding surface plasticity theory are used in DYSAC2. One for cohesive soils (Dafalias and Herrmann 1986) and another for non-cohesive soils (Yogachandran 1991) are used.

Predictions made by DYSAC2 for dynamic behavior of embankments containing stratified soils have been validated using centrifuge test results (Muraleetharan 1990, Muraleetharan and Arulanandan 1991).

### 3 CENTRIFUGE TESTING AND NUMERICAL PREDICTIONS

One of the centrifuge model configuration tested at Caltech (Scott et al. 1993a), the initial and final locations of the selected instruments, and the input base acceleration - time histories used in the test are shown in Figure 1. The test was performed at a centrifugal acceleration of 50 g, however, all the quantities are reported in prototype scale in this paper. All of the model configurations used and the centrifuge tests performed at Caltech and UCD were in general accordance with the guidelines given by

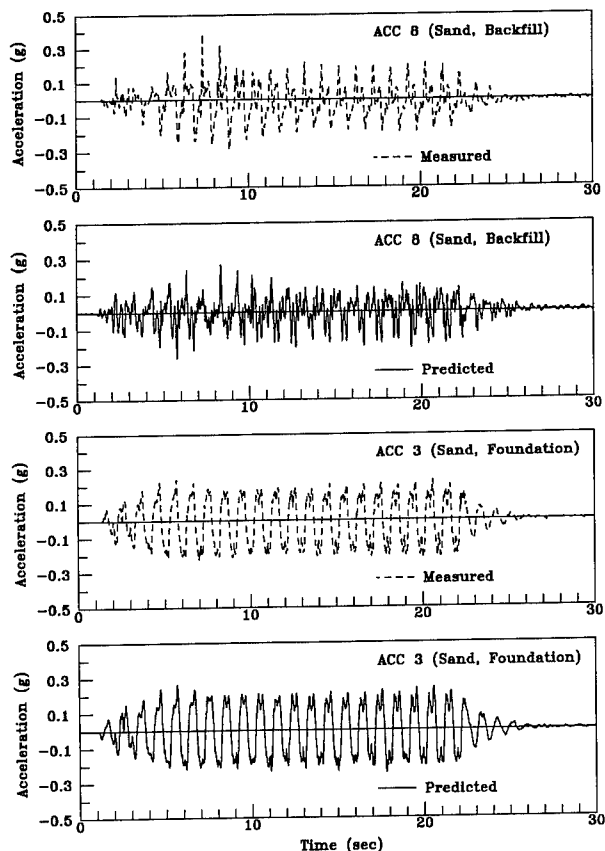


Fig. 2 Measured and predicted vertical acceleration - time histories at location 8 and horizontal acceleration - histories at location 3.

The Earth Technology Corporation (Earth Technology 1993a).

Nevada Sand ( $D_{50} = 0.15$  mm,  $e_{\max} = 0.887$ ,  $e_{\min} = 0.511$ ), Bonnie Silt (Liquid Limit = 29 %, Plasticity Index = 15 %,  $D_{50} = 0.03$  mm), and a fine gravel ( $D_{50} = 5.5$  mm, uniformly graded and angular) were used as model materials in all the tests. These materials were also distributed to UCD and Caltech by The Earth Technology Corporation. Other model configurations, in addition to the one shown in Figure 1, consisted of: (i) a gravel dike; (ii) a configuration similar to the one shown in Figure 1, but, without the bottom sand layer; (iii) a configuration similar to the one shown in Figure 1, but, without the bottom sand layer and with a horizontal foundation silt layer instead of a silt layer with a slope outside the toe.

Bonnie Silt was prepared as a slurry at a water content of 30 % and then consolidated in the centrifuge. The gravel dikes were placed at a dry unit weight of approximately  $15 \text{ kN/m}^3$ . In all the model configurations, except one, Nevada Sand was placed at a relative density ( $Dr$ ) of 60 % and water was used as the pore fluid. In one test, a horizontal foundation layer of Nevada Sand prepared at a relative density of

60 % underlaid a Nevada Sand backfill placed at a relative density of 40 %, retained by the gravel dike. The above test was performed using a 55 % glycerol/45 % water (by weight) mixture as the pore fluid. All the model tests were conducted in a rigid box.

In DYSAC2, Nevada Sand, Bonnie Silt, and fine gravel were modeled using bounding surface plasticity model for non-cohesive soils. Bounding surface plasticity model parameters for the above materials were obtained directly from the laboratory tests and by calibrating the model against the laboratory test results. Coefficient of permeability values (at 1 g) of  $5.6 \times 10^{-5} \text{ m/s}$ ,  $1.0 \times 10^{-8} \text{ m/s}$ , and  $0.065 \text{ m/s}$  were also measured for Nevada Sand ( $Dr = 60$  %), Bonnie Silt, and fine gravel, respectively, in laboratory tests. Values of all the bounding surface model parameters are given elsewhere (Earth Technology 1993b).

At the time that DYSAC2 predictions were made, most of the centrifuge tests had been completed and the results known. However, the constitutive model parameters used for Nevada Sand, Bonnie Silt and fine gravel were selected independent of the centrifuge

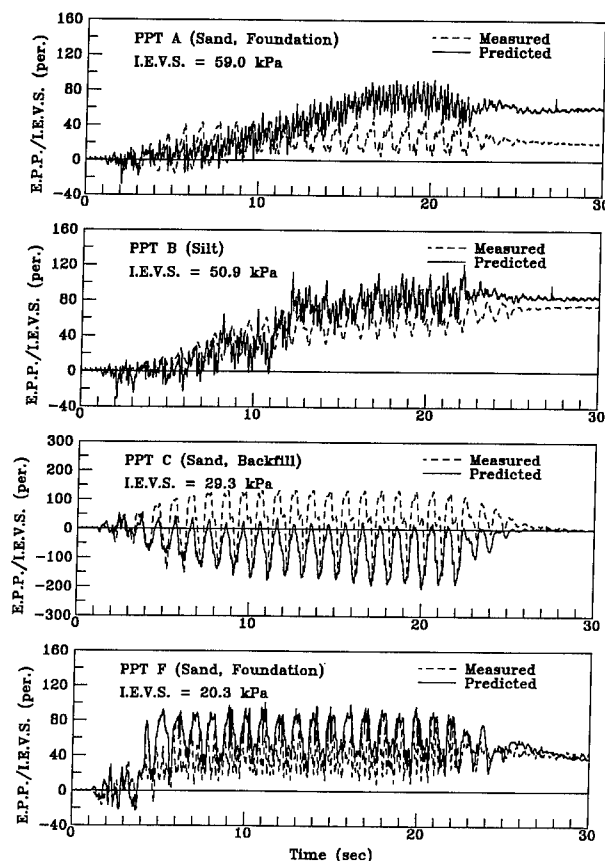


Fig. 3 Measured and predicted excess pore pressure ratio - time histories at locations A, B, C, and F (E.P.P. - Excess Pore Pressure, I.E.V.S. - Initial Effective Vertical Stress).

tests and were not subsequently altered to match the centrifuge test results.

Due to limitations of the length of the paper, only the measured quantities at selected locations of the centrifuge model shown in Figure 1 and the corresponding predictions are given in this paper. Comparisons between measured and predicted quantities at other locations as well as in other centrifuge models are given in Earth Technology (1993b).

Measured and predicted vertical acceleration - time histories at location 8 and horizontal acceleration - time histories at location 3 are shown in Figure 2. Measured and predicted excess pore pressure ratio - time histories at locations A, B, C, and F are given in Figure 3. Measured and predicted settlement - time histories at locations LVDT1 and LVDT2 are compared in Figure 4. Tracings of the model profile before and after shaking on the side transparent polycarbonate window of the model box are shown in Figure 5. A deformed mesh predicted by DYSAC2 at  $t = 28.8$  s and selected lines of the original mesh are shown in Figure 6.

#### 4 DISCUSSION

It can be seen from Figure 2 that the trends in acceleration - time histories are predicted very well by DYSAC2. From the excess pore pressure ratio - time histories shown in Figure 3 it can be concluded that the general trends seen in the measured data are predicted well by DYSAC2. However, positive excess cyclic pore pressures measured at location C is missing in the predictions. One possible explanation for this discrepancy is that the centrifuge box might have undergone a rocking motion (which was not modeled in DYSAC2) in addition to the vertical and the horizontal shaking imposed by the shaker and this rocking motion could have imposed some additional compressive stresses in the backfill sand. Some evidence of this rocking motion in the Caltech centrifuge can be deduced from the responses of pore pressure transducers P1 and P2 of the VELACS (Verification of Liquefaction Analyses by Centrifuge Studies) project's Model No. 3 centrifuge test results (Scott et al. 1993b).

Settlement - time histories shown in Figure 4 and the measured and predicted deformation patterns shown



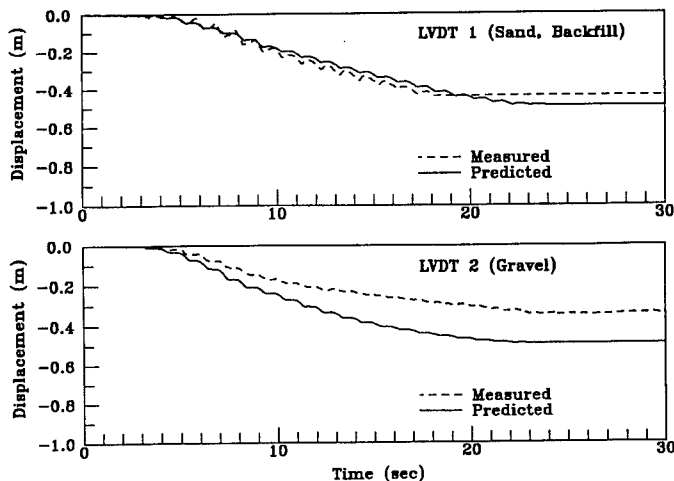


Fig. 4 Measured and predicted settlement - time histories at locations LVDT1 and LVDT2.

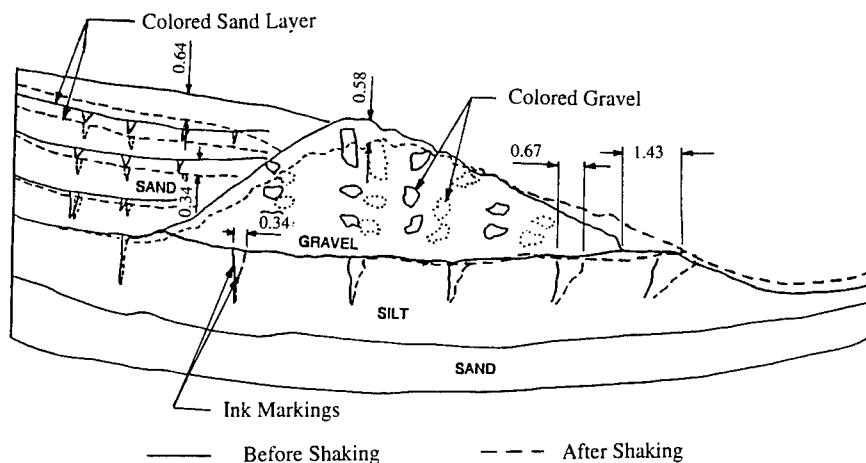


Fig. 5 Cross-section of the model before and after shaking near the window of the model box (all dimensions are in meters).

in Figures 5 and 6, respectively, indicate that DYSAC2 predicts deformations and deformation mechanisms very well. The measured deformation mode shows larger settlements of the backfill near the dike as compared to away from the dike (Figure 5), whereas the predicted deformation mode shown in Figure 6 indicates more or less uniform settlement of the backfill. The larger settlements seen near the dike in Figure 5 were caused by the intrusion of sand through some weak spots in the water soaked filter paper during shaking as evident from photographs taken before and after shaking. This might also explain somewhat larger settlement of the backfill as shown in Figure 5 as compared to the measurement at LVDT1 shown in Figure 4. At LVDT2 a settlement of 0.3 m was measured (Figure 4), however, from

the final deformed configuration shown in Figure 5 it can be seen that the gravel dike settled about 0.58 m (a value closer to the prediction by DYSAC2 at location LVDT2, Figure 4). Settlement caused by a gravel particle at 50 g ( $D_{50} = 5.5$  mm) moving down is equivalent to a prototype settlement of approximately 0.28 m. This shows the difficulty of measuring settlements using LVDT's (Linear Variable Differential Transformer) for coarse grained materials such as gravel in centrifuge tests.

The lateral displacement of the toe of the gravel dike shown in Figure 5 (1.43 m) is higher than the predicted value (0.85 m) shown in Figure 6. A couple of particles which rolled down the slope would explain the above discrepancy. This points out to the difficulty in modeling the gravel as a continuum in a

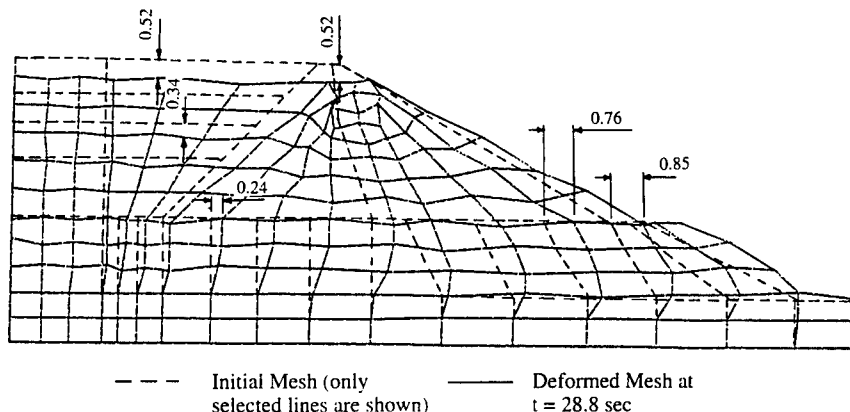


Fig. 6 Predicted deformed mesh at  $t = 28.8$  seconds (all dimensions are in meters, deformation magnification factor = 1).

finite element analysis. However, the overall behavior has been predicted well by DYSAC2 in spite of the above difficulty; perhaps, the presence of other soils for which a continuum assumption is good, makes the effects of modeling coarse-grained gravel particles relatively insignificant.

The fine gravel used in the centrifuge tests described above were selected for two reasons: (i) to retain the backfill; (ii) to act as a drainage boundary without generating any excess pore pressures within the dike (pore pressure transducers within the dike confirmed this by showing only cyclic pore pressures and no sustained excess pore pressures). These are, in fact, two important functions of a prototype dike; however, no attempt was made to model a prototype dike exactly in the centrifuge.

## 5 SUMMARY AND CONCLUSIONS

A fully-coupled, nonlinear, dynamic finite element code DYSAC2 is validated for the analysis of rock-dike retaining structures using a dynamic centrifuge model test results. In the design of rock-dike containment structures, prediction of deformations of the dike and adjacent landfill under earthquake loading is a key consideration. Measured and predicted settlement - time histories as well as the deformation mode predicted by DYSAC2 in comparison with the measured deformation mode, suggest that DYSAC2 can be used with confidence to guide the design approach for rock-dike retaining structures.

## 6 REFERENCES

- Biot, M.A. 1962. Mechanics of deformation and acoustic propagation in porous media. *J. Appl. Phys.* 33: 1482-1498.
- Dafalias, Y.F. & L.R. Herrmann. 1986. Bounding surface plasticity II: Application to isotropic cohesive soils. *J. Engrg. Mech. Div., ASCE* 112(12): 1263-1291.
- Earth Technology .1993a. Pier 400 dredging and landfill project; Specifications for the base centrifuge testing program. *Report*, Prepared for Pier 400 Design Consultants.
- Earth Technology .1993b. Pier 400 dredging and landfill design project; Report on geotechnical numerical modeling to study the performance of dike retaining structures. *Report*, Prepared for Pier 400 Design Consultants.
- Hilber, H.M., T. J. R. Hughes & R. L. Taylor. 1977. Improved numerical dissipation for time integration algorithms in structural dynamics. *Earthquake Engineering and Structural Dynamics* 5:283-292.
- Muraleetharan, K.K. 1990. Dynamic behavior of earth dams. *Ph.D. Dissertation*, University of California, Davis, California.
- Muraleetharan, K.K. & K. Arulanandan. 1991. Dynamic behavior of earth dams containing stratified soils. *Proceedings*, International Conference Centrifuge 1991, Hon-Yim Ko & Francis G. McLean (Eds), Boulder, Colorado, 401-408, Rotterdam, Balkema.
- Muraleetharan, K.K., K.D. Mish, C. Yogachandran & K. Arulanandan. 1988. DYSAC2: Dynamic soil analysis code for 2-dimensional problems. *Computer Code*, Department of Civil Engineering, University of California, Davis, California.
- Muraleetharan, K.K., K.D. Mish, C. Yogachandran & K. Arulanandan. 1991. User's manual for DYSAC2: Dynamic soil analysis code for 2-dimensional problems. *Report*, Department of Civil Engineering, University of California, Davis, California.
- Newmark, N.M. 1959. A method of computation for structural dynamics. *J. Engrg. Mech. Div., ASCE* 85(3): 67-94.
- Scott, R.F., B. Hushmand & H. Rashidi . 1993a. Results of the centrifuge tests for Pier 400 project - Port of Los Angeles, Phase I; Tests on Model (configuration) No. 3. *Report*, Prepared for Bing Yen & Associates.
- Scott, R.F., B. Hushmand & H. Rashidi . 1993b. Model No. 3 primary test description and test results. *Proceedings (Volume I)*, International Conference on the Verification of Numerical Procedures for the Analysis of Soil Liquefaction Problems, K. Arulanandan & R.F. Scott (Eds), Davis, California, 435-462, Rotterdam, Balkema.
- Yogachandran, C. 1991. Numerical and centrifugal modeling of seismically induced flow failures. *Ph.D. Dissertation*, University of California, Davis, California.
- Zienkiewicz, O.C. & T. Shiomi. 1984. Dynamic behavior of saturated porous media; the generalized Biot formulation and its numerical solution. *Int. J. Numerical and Analytical Methods in Geomechanics* 8: 71-96.

*Massachusetts Institute of Technology, Cambridge, Mass., USA*

209

input ground motions are usually very high in such tests (e.g., 100 ~ 200 Hz). Under such circumstances, the pore pressure transducers within the model can reliably record the dynamic pore pressure responses only when they are properly saturated. The requirements for saturating pressure transducers are more stringent than for saturating most sand skeletons. This paper presents a low-absolute-pressure saturation technique to prepare highly saturated sand models for dynamic centrifuge testing. The amount of air within the dry sand prior to saturation is minimized by maintaining the absolute pressure below 25 mTorr in the sand container for several hours. Highly saturated sand specimens can be produced by following the procedures and principles described in this paper. Special care is also taken to prevent piping conditions when the pore fluid starts to saturate the sand.

This paper focuses more upon the key features in designing and performing dynamic centrifuge tests of the model: (1) the preparation of highly saturated sand models for centrifuge testing; (2) the design of the test model in Figure 1; and (3) the testing program. Two aspects of the results are also presented: (1) the characteristics of liquefaction and quasi-liquefaction of soils; and (2) the estimations of dynamic earth and pore water thrusts with Mononobe-Okabe and Westergaard equations. Mononobe-Okabe equation together with total unit weight of the soil proved to give reasonable estimates for the amplitude of the dynamic lateral earth force. Some other important aspects of the test results, such as features of the behavior of sand during cyclic shearing as well as the interaction between the backfill soil and the retaining wall, are discussed by Ting (1993) and Whitman and Ting (1993).

## 2. IDEALIZED MODEL RETAINING WALL

The wall, a 9.5mm thick aluminum plate, is hinged at the base and supported by a tie-back system with an elasto-plastic force-displacement relationship. This arrangement allows the wall to tilt about its toe during earthquakes. It resembles retaining walls in a very rough way but does contain important aspects of actual full-scale problems.

The tie-back is connected at one end to the retaining wall and at the other end to the wall of the testing box via a load cell. The elastic and plastic behaviors of the tie-back are provided by the spring and the slider respectively. The spring in the tie-back is a stack of eight Bellevue spring washers. The stiffness of this spring was calibrated to be 605 kN/m (actual units) statically. The slider provides the possibility of plastic elongation in the tie-back. The frictional slider allows the tie-back to fail temporarily when the load in the tie-back exceeds the shear resistance of the slider. The shear resistance of the slider can thus be viewed as the yield load of the tie-back. The slider consists of an aluminum center piece sliding between two phenolic side pieces. A normal force across the sliding interfaces controls the shear resistance of the slider. This force can be adjusted

by tightening or loosening the threaded rods extending through the assembly.

A permanent slip along the sliding interfaces accompanies a temporary failure at the slider during each load cycle in which shear resistance is exceeded. Such slip results in a plastic elongation of the tie-back and thus a permanent tilt in the retaining wall. The slider was designed to allow for a maximum tilt in the retaining wall to be 2.8%, thus preventing possible damages to the testing apparatus (see Figure 1).

Two stops installed to test box near the top of the wall prevent the wall from tilting past the vertical toward the backfill. Prior to placing the soil, the wall is kept vertical with a temporary strut on the outer face away from the backfill. The tie-back is installed after the soil is prepared. Then a preload is applied in the tie-back to hold the wall against the stops under 1-g conditions. The preload is set to be smaller than the earth thrust against the wall developed during the centrifuge spin-up. Therefore, the wall always tilts off the stops by the end of spin-up.

## 3. PREPARATION OF SAND MODELS

### 3.1 Pluviation of Dry Sand

Uniform beds of dry sand were prepared by pluviation using a diffusive rainer with several sieves within a raining chimney. This technique was reported effective by Al-Douri et al. (1990). By adjusting the sieves within the rainer, the raining rate, and therefore the relative density of the sand, can be controlled. To ensure homogeneity, the sand was mixed thoroughly prior to the placement of the sand models. The pluviation process was interrupted frequently for installing transducers within the sand. The nominal thicknesses of the final sand stratum and of the sand below each transducer are reached through over-pluviation followed by removal of the extra sand using a vacuum cleaner. This test program used a vacuum cleaner with an elephant trunk, extended to 3mm above the expected sand surface, traveling all over the sand surface. This technique to bring the sand to the nominal thickness has been applied to preparing large sand specimens at MIT for many years (Ting, 1993).

### 3.2 Saturation of Sand Specimens

In dynamic centrifuge tests with pore pressure measurements, it is necessary to saturate the pressure transducer, in addition to saturating the sand. Miniature pressure transducers (e.g., Druck PDCR 81) are widely used in centrifuge testing. Each transducer has a protective ceramic filter in front of its pressure diaphragm. The pores in the ceramic porous stone are much finer than those in most sand skeletons. Therefore, saturating the pressure transducer ensures the saturation of the sand skeleton. A low-pressure-saturation technique (Ting, 1993) was developed to saturate both the sand and the pressure transducers.

Figure 2 shows the schematic diagram of the saturation technique. The sand was first evacuated by vacuum pump No. 1 to an absolute pressure below 25 mTorr (1 atm = 760 Torr). This very low absolute pressure ensures the quality of saturating fine ceramic porous stones. Regular vacuum pumps in geotechnical laboratories can bring down the absolute pressure to about 50 to 125 Torr (corresponding to 94 to 84 kPa vacuum). Some vapor of the vacuum pump oil starts to migrate into the chamber at such pressures. The oil vapor prevents further lowering of the pressure in the system. It is therefore necessary to connect an oil trap between the vacuum pump (No. 1) and valve No. 1 in order to reduce the absolute pressure further. The vapor trap (not shown in the figure) is surrounded by liquid Nitrogen and can catch the migrating oil vapor by crystallization at low temperatures. This trap prevented the oil vapor from entering into the soil through the evacuation route. Such

technique can effectively bring down the absolute pressure to less than 20 mTorr (0.02 Torr).

The sand was then allowed to be saturated with de-aired water through the bottom inlet (valve No. 6 in the figure). However, at these very low absolute pressures, water would vaporize instantly (due to a large pressure gradient) when it started entering into the dry sand from the bottom. This would cause a type of piping damage to the sand stratum. To avoid such a disastrous condition, the absolute pressure in the sand container was, prior to saturation, brought up to a point above the vaporization pressure of water. This was done by introducing a vapor pressure of water, 12 Torr, above the sand surface (through valve No. 3 at the top) prior to saturating the sand from the bottom. The flow rate of the water into the container was controlled small to ensure a small gradient. The total time required for saturating the sand model was about four hours.

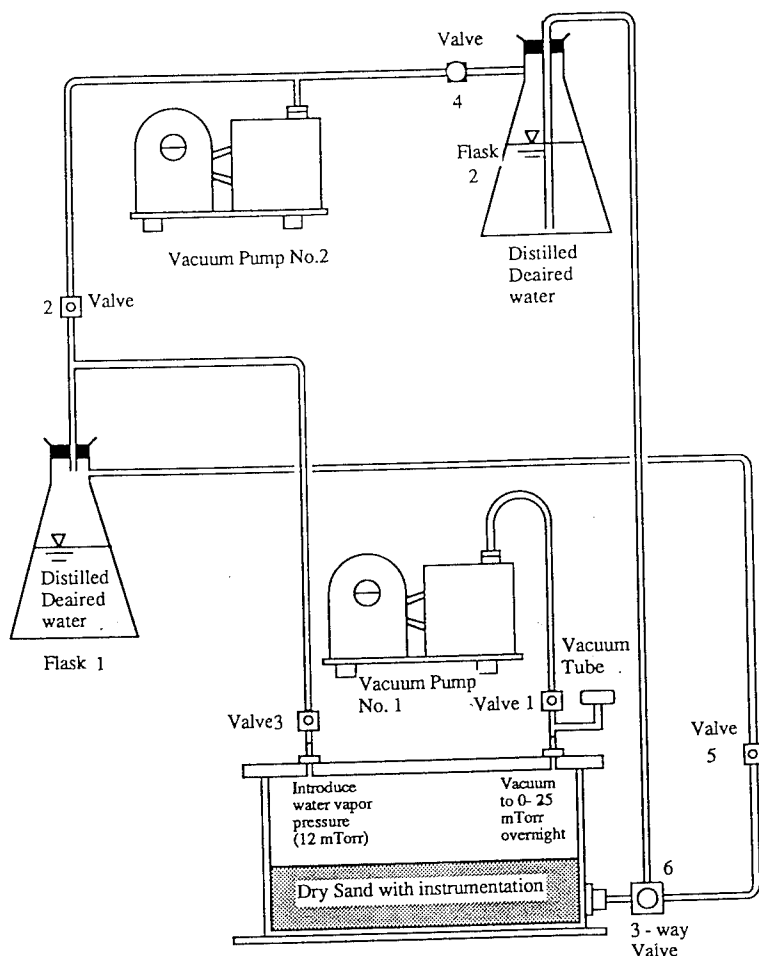


Figure 2: Saturation of sand and pore pressure transducers

#### 4. TESTING PROGRAM

Table 1 displays the testing program. Eighteen tests were performed on six soil models prepared at two relative densities: 60% and 75%. The primary factor that varies from test to test was the intensity of the earthquake (input base shaking). The dynamic tests were all performed at a nominal centrifugal acceleration of 50g (at the mid-depth of the model). Each test involved ten cycles of more-or-less sinusoidal excitation at 100 Hz (2 Hz in prototype earthquake) in the horizontal direction, which is perpendicular to the rotation surface of the centrifuge arm. The general form of the input base shaking was similar in all tests, with only the intensity of shaking varied. Figure 3 shows the typical form of the horizontal excitation. It also demonstrates that the vertical component was small. The letters a, b etc. in Table 1 indicate the sequence of shakings applied to each model. Full dissipation of the excess pore pressure was reached prior to all subsequent tests on each testing model.

The purpose of using centrifuge to perform dynamic geotechnical tests is to down-scale the model dimensions. However, the permeability, a key parameter of the soil in liquefaction studies, remains unchanged with scaling. Water, in this testing program, represents a pore fluid 50 times more permeable in prototype scales. Therefore, one series of tests was performed using a 55% glycerol solution as pore fluid. The permeability of this pore fluid was ten times less permeable than water. Nevertheless, results of the tests on this model have demonstrated substantial differences from similar tests performed on water-saturated models (Ting, 1993).

The less permeable pore fluid did not affect the rate or pore pressure generation. However, it had substantial influences on dissipation-related pore pressure variations. Comparison of results from two similar tests (2b and 3a) using water and glycerol solution as pore fluid shows three effects: (1) the rate of pore pressure accumulation decreased gradually larger during the earthquake in 2b but not in 3a; (2) the pore pressure ratios at P5 and P6 stayed at 100% much longer in 3a, as a result of slower pore pressure propagation from larger depth; and (3) the time required to dissipate 80% of excess pore pressure in Test 3a was about ten times of that in Test 2b.

Table 1: Summary of the testing program

Dr	Pore Fluid	Peak Input Acceleration (g)					
		0.05	0.10	0.13	0.25	0.30	0.35
60%	Water	1a	1b		1c		
		4b	4c		4a		
75%	Water	2a	2b	2c	2d	2e	2f
			5b				5a
	55%Glycerol Solution		6b		6a		
		3a			3b		

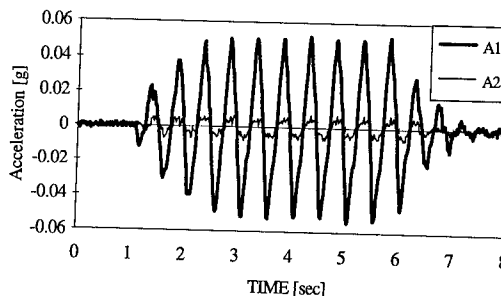


Figure 3: Input acceleration in Test 2a

#### 5. LIQUEFACTION AND QUASI-LIQUEFACTION

Liquefaction is the most important feature of the dynamic tests on saturated sand. It can be indicated by two types of data: the pore pressures and accelerations within the sand stratum. For the purpose of identifying liquefaction of soil, the excess pore pressure is usually converted to excess pore pressure ratio which is the excess pore pressure normalized by the initial effective stress. Liquefaction is possible when the excess pore pressure ratio reaches 100%, i.e., when the excess pore pressure essentially reaches the initial effective stress.

Liquefaction of soil is defined as a soil, with zero effective stress, which can not transmit ground acceleration during earthquakes. Soils usually lose their effective stresses before they lose the capability to transmit ground acceleration. Within a saturated sand bed, liquefaction usually initiates at the ground level. The liquefaction front (an imaginary surface within the stratum above which the soil is liquefied) moves down to the deeper soil as the earthquake continues. Figure 4 shows the pore pressure and acceleration data in Test 5a, a strong earthquake, as an example. When the excess pore pressure reaches 100% at the mid-depth, the upper soil was really liquefied and behaves like a fluid. The ground acceleration can not be transmitted to the upper part of the soil after two cycles of excitation.

Quasi-Liquefaction of soil is defined as a soil in which effective stress reduced to zero one or two times during a cycle of excitation, but can still transmit ground acceleration. Figure 5 shows the data in Test 2c, a moderately strong earthquake, to illustrate quasi-liquefaction. The excess pore pressure ratios reached 100% near the surface (P5 and P6), but did not reach 100% at the mid-depth (P3 and P4). The acceleration data show that the ground accelerations were still transmitted to the surface of the soil even though the upper soil had zero effective stress. The acceleration data show that the history of acceleration near the surface was amplified and there was a phase lag, compared to the input acceleration. These two features are mainly due to the damping in the soil and the soil-wall interaction in the model during earthquakes. Such acceleration data indicate that the soil skeleton was not fully destroyed and

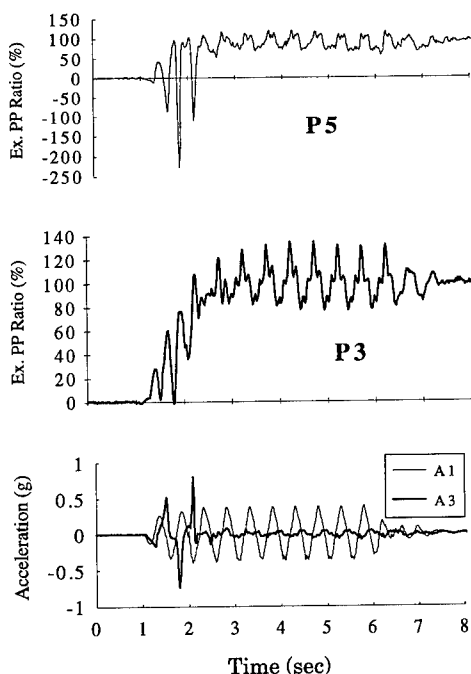


Figure 4: Excess pore pressure ratio and acceleration response in backfill in Test 5a

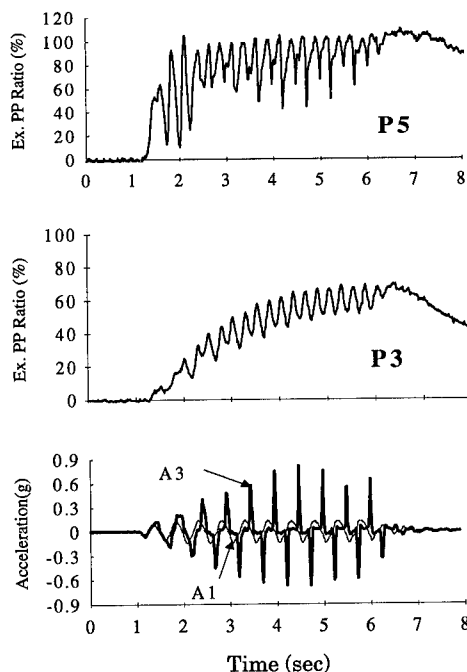


Figure 5: Excess pore pressure ratio and acceleration response in backfill in Test 2c

therefore the soil was not constantly fluidized during cyclic shaking. The soil is recognized as quasi-liquefied in this test.

## 6. DISCUSSION

Seed and Whitman (1970) proposed to estimate the dynamic amplitude of earth thrust from dry sand using Mononobe-Okabe equation with simplified coefficient. Eq. (1) is a possible adaptation of the S-W equation to estimate the (double) amplitude of the dynamic thrust from the soil skeleton part only in saturated sands:

$$2\Delta P_p = \gamma_b w H^2 \left( \frac{3}{4} K_h \right) \quad (1)$$

with the thrust acting at  $0.5H$ . In Eq. (1),  $w$  is the width of the retaining wall;  $H$  is the thickness of the backfill;  $\gamma_b$  is the buoyant unit weight of the sand; and  $K_h$  is the ratio of the horizontal acceleration to the gravitational acceleration. Westergaard (1933) developed an approximation for the dynamic water thrust during earthquakes on a straight dam with a vertical up-stream face. This approximation sometimes is used to estimate the dynamic thrust from pore water behind a vertical retaining wall while it is applied here to estimating the double amplitude of the thrust from pore water:

$$2\Delta U = 2 \left( \frac{7}{12} \gamma_w w H^2 K_h \right) \quad (2)$$

with a height of the thrust acting at  $0.4H$ .

The above two equations did not correctly estimate the dynamic thrusts from the soil skeleton and water pressures in this study. Figure 6 shows the test results and estimations; all results are from tests without slip at the slider. However, an equation combining these two equations gave reasonable estimations for the amplitude of total earth thrust fluctuations by calculating the amplitude of the total moment about the base from the earth pressures:

$$\Delta M_{\text{earth}} = \frac{1}{2} \gamma_b w H^2 \left( \frac{3}{4} K_h \right) \frac{H}{2} + 2 \left( \frac{7}{12} \gamma_w w H^2 K_h \right) (0.4H) \quad (3)$$

The test results and estimations with this equation are plotted in Figure 7. The reason that Eq. (3) works for dynamic amplitudes of total earth thrust is because it generates results similar to the one using Mononobe-Okabe equation with  $\gamma_t$ , the total unit weight of the soil; that is, from a macro point of view, the pore water was accelerating more or less with the mineral skeleton.

The reason that Eqs. (1) and (2) did not work was due to interaction between the backfill and the retaining wall during the earthquakes. The study of phase relations provided significant information supporting the above findings (Ting, 1993). Based upon the analyses by Mononobe (1929) and Okabe (1926) for lateral (dry) earth pressures on the retaining walls, and Westergaard's (1933) analyses for water pressures during earthquakes, the minimum and maximum in the fluctuations of the

thrust from the backfill soil are expected to be observed when ground is at the positive and negative peaks, respectively. However, such expectations were not fulfilled in this study. Ting and Whitman (1993) studied the phase lags of the various thrusts from the input accelerations and showed that: (1) the phase lag of the soil skeleton thrust was associated with the lag of the ground acceleration transmission through the sand stratum; and (2) the phase lag of pore water thrust was a result of the interaction between the backfill and the wall.

## 7. FINAL REMARKS

This study has examined the behavior of one saturated sand and the retaining wall that supports it during earthquakes. It also accomplished two major achievements regarding the dynamic centrifuge testing:

- (1) developing a technique for preparing highly saturated sand models for dynamic centrifuge testing;
- (2) building an idealized earth retaining wall and performing dynamic centrifuge tests on it.

Three major conclusions have emerged from test results:

- (1) Soil may still transmit ground accelerations when it loses its effective stress temporarily during earthquakes. This condition is classified as quasi-liquefaction. Liquefaction of a soil is defined as a soil that can not transmit ground accelerations when it loses its effective stress during an earthquake.
- (2) Mononobe-Okabe-Westergaard equation proved to be effective in estimating the total dynamic earth thrust on a retaining wall in a saturated sand during earthquakes.
- (3) Tilt in the wall as a result of slip at the slider can be estimated using a lumped-mass-sliding-block model (Ting, 1993). This study proposes to estimate the earth's contribution towards the dynamic load applied to the tie-back using the Mononobe-Okabe-Westergaard equation in Eq. (3).

The centrifuge model tests in this study are carried out with quality controlled procedures and the results of which are suitable for verifying numerical procedures predicting soil performances during earthquakes. The predictability of one numerical model is examined with results of this test program (Bouckovalas et al, 1993).

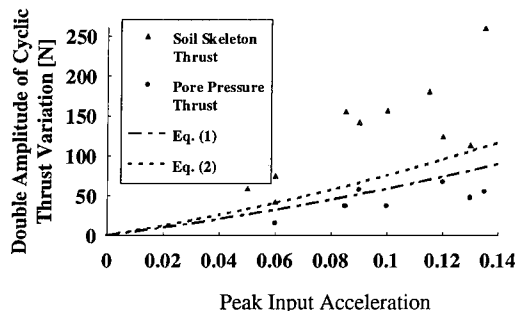


Figure 6: Double cyclic amplitudes of thrusts from pore pressure and soil skeleton in non-slip tests

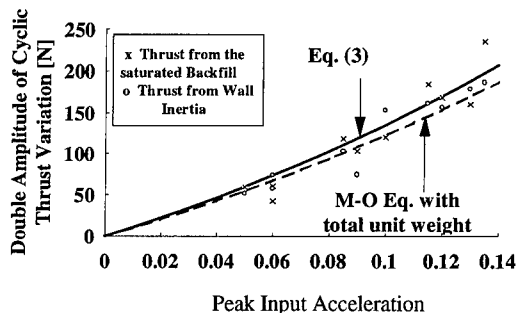


Figure 7: Double cyclic amplitude of thrusts from wall inertia and soil backfill in non-slip tests

## REFERENCES

- Al-douri, R. H., Hull, T. and Poulos, H. G. (1990) *Preparation and Measurement of Uniform Sand Beds in the Laboratory*, Research Report No. R609, March 1990, The University of Sydney, Department of Civil and Mining Engineering.
- Bouckovalas, G., Ting, N-H and Whitman, R. V. (1993) *Analytical Predictions for an Anchored Bulkhead with Liquefiable Backfill*, Proceedings. International Conference on the Verification of Numerical Procedures for the Analysis of Soil Liquefaction Problems, Arulanandan and Scott (eds), Vol. 2, Davis, California, USA, 17-20 October.
- Mononobe, N. and Matsuo, H. (1929) *On the Determination of Earth Pressures During Earthquakes*, Proceedings, World Engineering Congress, Vol. 9.
- Okabe, S. (1924) *General Theory of Earth Pressure and Seismic Stability of Retaining Wall and Dam*, Japan Society of Civil Eng. Journal, Vol. 10, No. 6.
- Seed, H. B. and Whitman, R. V. (1970) *Design of Earth Retaining Structures for Dynamic Loads*, 1970 Specialty Conference on Lateral Stresses in the Ground and Design of Earth Retaining Structures, Cornell University, Ithaca, NY; State of the Art Papers, 103-147.
- Ting, N-H (1993) *Earthquake-induced Tilt of Retaining Wall with Saturated Backfill*, Ph.D. Thesis, Department of Civil and Environmental Engineering, Massachusetts Institute of Technology, Cambridge, MA, USA.
- Westergaard, H. M. (1933) *Water Pressures on Dams during Earthquakes*, Transactions ASCE, Vol. 98, 418-472.
- Whitman, R. V. and Ting, N-H (1993): *Experimental Results for Tilting Wall with Saturated Backfill*, International Conference on the Verification of Numerical Procedures for the Analysis of Soil Liquefaction Problems, Arulanandan and Scott (eds), Vol. 2, Davis, California, USA, 17-20 October.



# Liquefaction of sandy ground and settlement of embankments

J. Koseki, Y. Koga & A. Takahashi

Public Works Research Institute, Ministry of Construction, Tsukuba-shi, Japan

**ABSTRACT:** Dynamic centrifugal model tests of embankments on a liquefiable sand layer were conducted at 30g and 50g using models of the same prototype size. Each model was subjected to sinusoidal shakings of the same prototype frequency. Comparisons were made between the 30g models and the 50g models on the liquefaction strength of sand layers and the settlement of embankments. The effects of shaking history on these characteristics were also investigated by comparing the results of virgin models and preshaked models.

## 1. INTRODUCTION

Liquefaction of sandy ground causes settlement of an embankment founded on the ground. Many model tests have been conducted using shaking tables to reveal the seismic behavior of the embankment. However few tests have been performed using dynamic centrifuges. Schofield and Vantor (1984) investigated the behavior of excess pore pressure in a saturated sand foundation of a coastal dyke. Koga et al. (1991) examined the effect of Deep Mixing Method as a countermeasure against liquefaction of the foundation below an embankment. In these studies sinusoidal waves were used as input acceleration. Koga et al. (1992) used irregular shakings to study the effect of the shape of the shaking acceleration on the excess pore pressure in the foundation and on the settlement of the embankment.

This paper deals with dynamic centrifugal model tests of an embankment founded on a liquefiable sand layer. The tests were conducted to investigate the effects of a scale factor and a seismic history using sinusoidal waves as input acceleration.

## 2. TEST PROCEDURE

Fig.1 shows a cross section of test models and the location of transducers. The effect of a scale factor was investigated using 30g models and 50g models. The model dimensions were determined for both models so that their prototype size in a 1g field would coincide

with each other.

A sand layer was prepared by pouring Toyoura sand through air in a rigid soil container. The surface of the layer was rounded in accordance with a rotational radius. A colored sand mesh was drawn to observe the deformation of the sand layer through a transparent front glass of the container.

An embankment was made of a mixture of Toyoura sand and a clay-sand with a ratio of 4:1 in weight and a water content of 15%. After setting the container in a vacuum box the sand layer was saturated with silicone oil which is 30 times as viscous as water for the 30g models and 50 times for the 50g models.

A sinusoidal shaking of 20 cycles was conducted after applying a centrifugal acceleration. It was repeated several times with increased amplitude. The prototype wave frequency in the 1g field was 2Hz for both the 30g models and the 50g models.

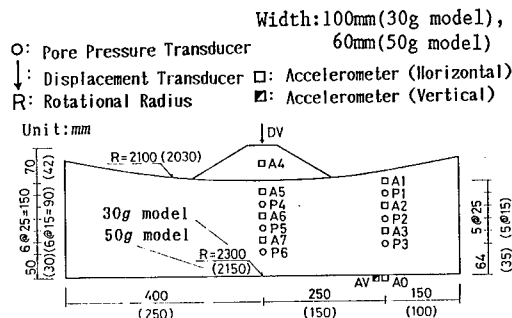
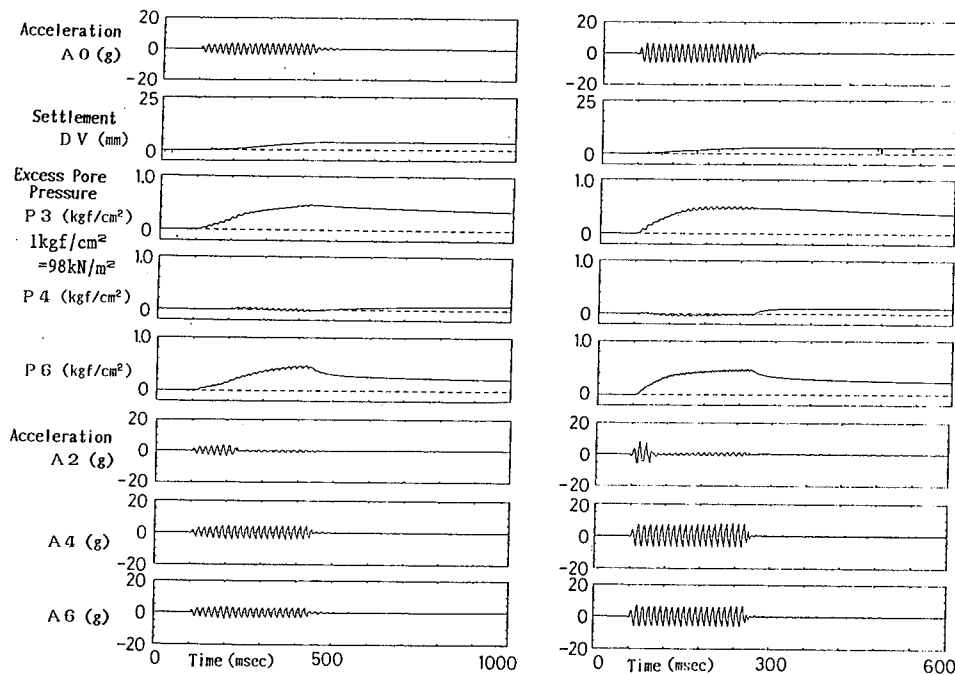


Fig.1 Cross section of test model

Table 1 Test cases and conditions

Year	Case	Centrifugal Acc. (g)	Input Sinusoidal Wave	Input Acc. (g)						Dr of Sand Layer (%)
				1st	2nd	3rd	4th	5th	6th	
1988	63-1-1	30	60Hz, 20cycle	1.2						*
	63-1-2			2.5	4.1	5.2	7.3	8.7	12.7	*
	63-1-3			3.7	5.6	7.1	8.3	12.5		*
	63-1-4			5.5						*
	63-1-5			7.3						*
	63-1-6			9.0						*
1991	63-1-7	30	60Hz, 20cycle	5.8						62
1992	63-1-8	30	60Hz, 20cycle	7.9						63
	63-1-9			4.9						62
1988	1-5-3	50	100Hz, 20cycle	7.0						52
	1-5-4			5.8						60
1992	1-5-1	50	100Hz, 20cycle	9.8						61
	1-5-2			6.5						67

\* The relative density of the sand layer for model 63-1 in 1988 is not known due to incorrect measurement. It is assumed to be almost the same as others, because the sand layer was prepared in the same way.



(1) Case 63-1-3 (30g) in the 1st shaking

(2) Case 1-5-4 (50g) in the 1st shaking

Fig.2 Measured data

A summary of the test cases and the test conditions are shown in Table 1. The first series of the tests started in 1988, and the other series were conducted in 1989, 1991 and 1992.

### 3.EFFECT OF SCALE FACTOR

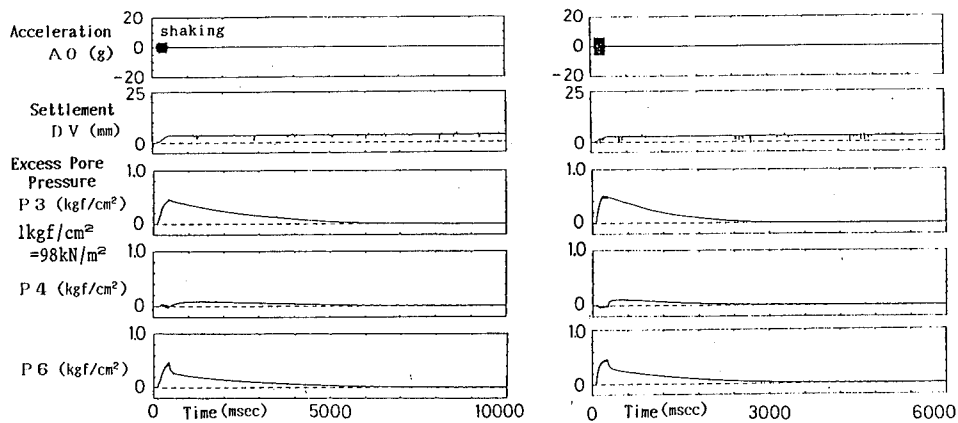
#### 3.1 Comparison of time histories

Fig.2 compares some of measured data between

the 30g model and the 50g model in the first shaking step. Time axes in the figure are arranged to have the same prototype length in the 1g field. In Fig.3 the time axes are shortened to show changes after the shaking.

There were qualitative agreements between the result of the 30g models and that of the 50g models as follows:

(1) Beneath the embankment, the excess pore pressure (P4) did not accumulate during the shaking, but it increased after the shaking. In a deeper part the accumulation of the



(1) Case 63-1-3 (30g) in the 1st shaking (2) Case 1-5-4 (50g) in the 1st shaking  
Fig.3 Measured data (Changes after the shaking)

excess pore pressure was almost similar at the same depth (P3 and P6), however the dissipation proceeded faster below the embankment (P6) than in the side layer (P3).  
(2) A rapid reduction of a response acceleration due to liquefaction occurred in the side layer (A2), while it did not occur in or below the embankment (A4 and A6).  
(3) A crest settlement of the embankment proceeded at a nearly constant rate during the shaking, but it stopped after the shaking.

The dissipation of the excess pore pressure finished in about 5second in the 30g models and in about 3second in the 50g models. They are equivalent to 150second in the 1g field.

In this study the viscosity of the silicone oil used as a pore fluid of the sand was determined assuming that it is in inverse proportion to an apparent permeability of the sand although Inatomi et al. (1989) showed another relationship experimentally. Within the limits of this test it may well be adequate to use the simple assumption, because the duration of the dissipation was almost equivalent.

### 3.2 Resistance against liquefaction

Fig.4 shows the relationship between the prototype input acceleration and the number of cycles until the excess pore pressure at P2 and P3 reaches a limiting value which is maintained during liquefaction in the first shaking steps. Different notations were used based on the model scale and the year when the test was performed.

Although the data was scattered, the resistance of the sand layer against liquefaction was generally lower in the 50g

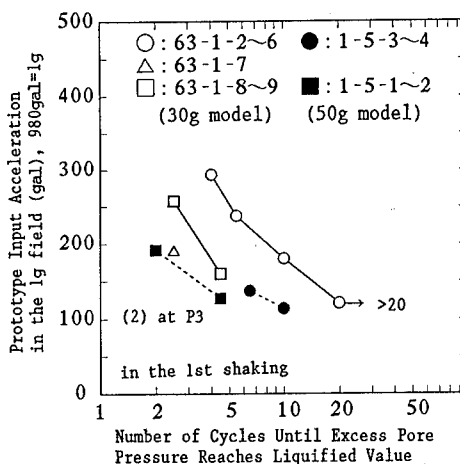
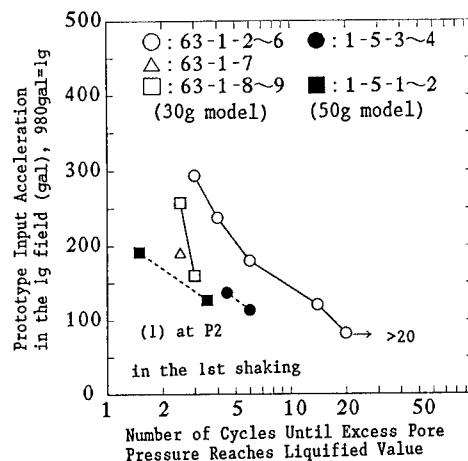


Fig.4 Input acc. vs. number of cycles until excess pore pressure reaches liquified value

models than in the 30g models.

The reason is not known yet, but it may be due to the different degree of volume change in the sand layer at the process of saturation which is caused by the high viscosity of the silicone oil.

The results also showed some dependency on the test year, which may be caused by unnoticeable change in the condition of model preparation.

### 3.3 Crest settlement

Fig.5 shows the relationship between the prototype input acceleration and the induced prototype crest settlement of the embankment in the first shaking steps. On the whole the prototype settlement was slightly larger in the 50g models than in the 30g models at the same prototype input acceleration.

Fig.6 shows the relationship between the induced prototype crest settlement and the number of cycles until the excess pore pressure at P2 and P3 reaches the limiting value in the first shaking steps. At the same number of cycles the prototype settlement was smaller in the 50g models than in the 30g models.

Figs.4 and 6 indicate that in the 50g models at the same prototype input acceleration the excess pore pressure accumulated faster before liquefaction and that the crest settlement proceeded slower after the liquefaction. Although both of these differences affected the induced settlement as shown in Fig.5, the difference in the liquefaction resistance had a relatively larger effect.

## 4.EFFECT OF SEISMIC HISTORY

The effect of a seismic history was investigated based on the result obtained in the six cases of the 50g models performed in 1988. The shaking amplitude was changed in the first step of each case and was increased gradually in the following steps.

### 4.1 Crest settlement

Fig.7 shows the relationship between an input acceleration and an induced or accumulated crest settlement. The induced settlement in the first step of each case without the seismic history was larger than the one in the following steps of cases 63-1-2 and 63-1-3 with the seismic history, and it was smaller than the accumulated settlement of the pre-shaken cases.

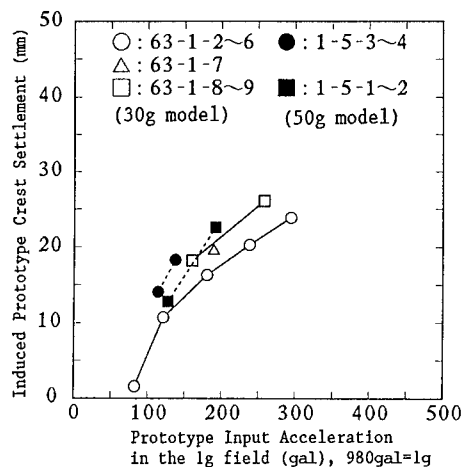


Fig.5 Input acc. vs. crest settlement

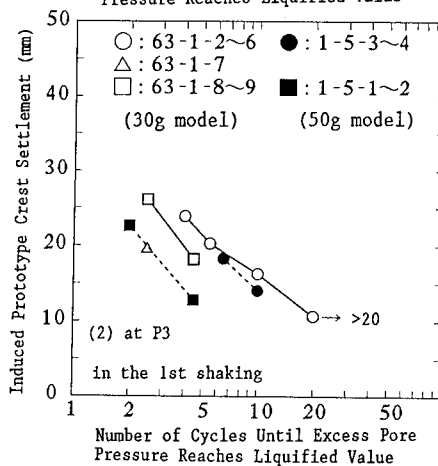
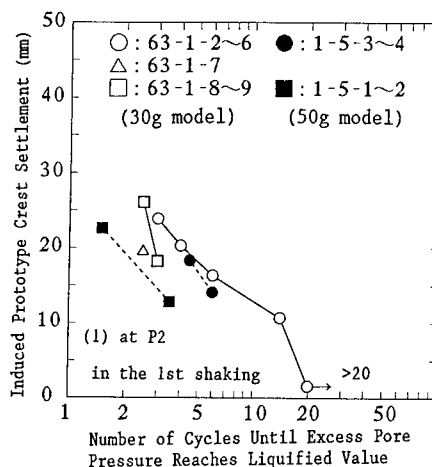


Fig.6 Crest settlement vs. number of cycles until excess pore pressure reaches liquified value

The difference in the accumulated settlement was small between these cases, therefore the case 63-1-2 is used as a representative case with the seismic history in the following comparisons.

#### 4.2 Excess pore pressure

Fig.8 shows the relationship between the input acceleration and a maximum excess pore pressure ratio at a depth of 10cm (P2 and P5). An initial effective vertical stress is calculated one-dimensionally using a unit weight of the sand layer and the embankment.

With or without the seismic history the ratio in the side layer (P2) was nearly 1.0 when the input acceleration was about 4g, but the ratio was higher with the seismic history when the input acceleration was more than 7g. Below the embankment (P5) the ratio was higher with the seismic history than without it over a whole range of the input acceleration.

It is considered that with the seismic history densification of the sand layer due to reconsolidation after the liquefaction reduces the generation of the excess pore pressure,

and the rate of the densification seems to be larger below the embankment than in the side layer.

Seismic History (Case)	Location	
	P 2	P 5
Virgin (63-1-1~6)	—○—	—●—
Pre-shaked (63-1-2)	- -△- -	- -▲- -

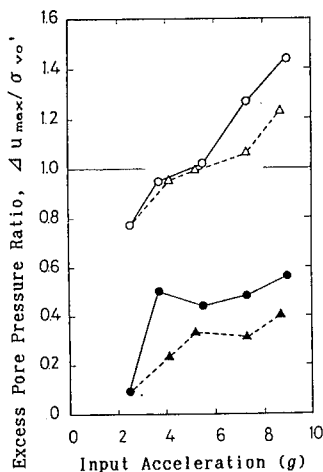


Fig.8 Input acc. vs. excess pore pressure ratio (model 63-1-2~6)

Seismic History (Case)	Type of Settlement	
	Induced	Accumulated
Virgin (63-1-1~6)	—○—	
Pre-shaked (63-1-2)	- -△- -	- -▲- -
Pre-shaked (63-1-3)	- -□- -	- -■- -

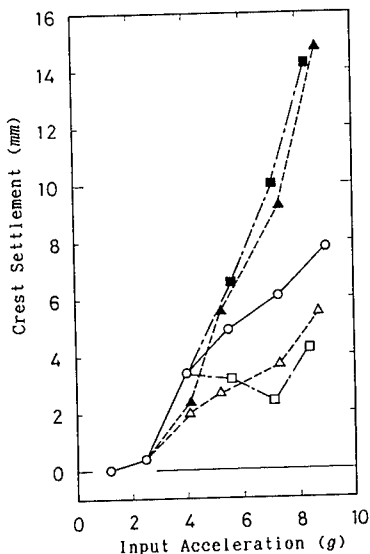


Fig.7 Input acc. vs. crest settlement (model 63-1-2~6)

Seismic History (Case)	Location		
	A 2	A 4	A 6
Virgin (63-1-1~6)	—○—	—●—	—●—
Pre-shaked (63-1-2)	- -△- -	- -▲- -	- -▲- -

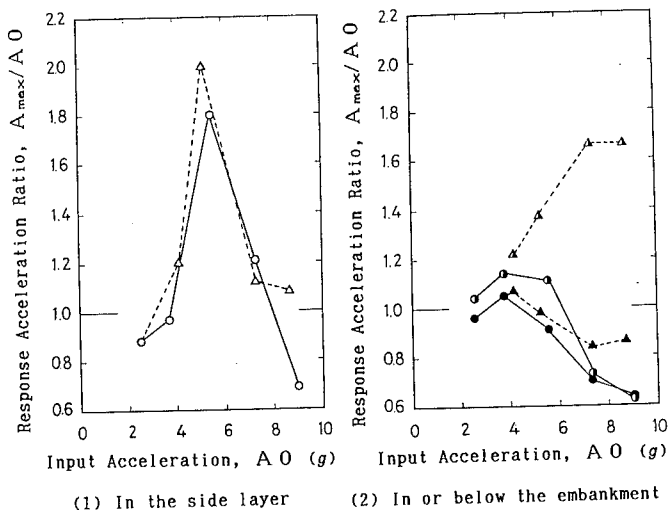


Fig.9 Input acc. vs. response acc. ratio (model 63-1-2~6)

#### 4.3 Response acceleration

Fig.9 shows a relationship between the input acceleration and a ratio of a maximum response acceleration to the input one. With or without the seismic history the ratio was almost the same in the side layer (A2). Below the embankment (A6) it was higher with the seismic history when the input acceleration was more than 7g. In the embankment (A4) the ratio increased as the input acceleration increased with the seismic history, and it decreased without the seismic history.

These results agree with the consideration that the effect of the densification due to the seismic history is higher below the embankment than in the side layer. The difference in the induced crest settlement between the virgin cases and the pre-shaken cases may be caused by both the densification and the residual deformation of the pre-shaken cases as shown in Fig.10.

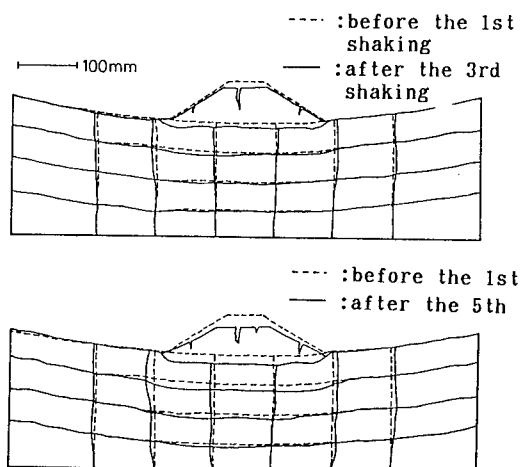


Fig.10 Observed deformation in Case 63-1-3

#### CONCLUSIONS

The result of dynamic centrifugal tests of an embankment founded on a liquefiable sand layer with a centrifugal acceleration of 30g or 50g is summarized as follows:

(1) A comparison of the measured data of the 30g models and the 50g models showed that there were several qualitative agreements between them on a dynamic response characteristics. A lower resistance against liquefaction in the 50g models resulted in a slightly larger prototype crest settlement although at the same number of cycles until liquefaction the settlement was smaller in the 50g models. The different degree of volume

change in the sand layer at the process of saturation which is caused by the high viscosity of the silicone oil may affected the resistance of the sand layer against liquefaction.

(2) To investigate the effect of a seismic history a comparison was made between the results obtained in the first shaking steps and those obtained in the following steps. The effect on the excess pore pressure and the response acceleration was larger in or below the embankment than in the side layer. It is considered that the rate of a densification of the sand layer due to a reconsolidation after the liquefaction is larger below the embankment than in the side layer. A smaller induced crest settlement with the seismic history was obtained, and it may have been caused by both the densification and the residual deformation.

#### REFERENCES

- Inatomi, T., Kazama, K., Noda, S. and Tsuchida, H. 1989. Centrifugal dynamic model tests in PHRI. Proc. of the 21st Joint Meeting of U.S.-Japan Panel on Wind and Seismic Effects, US/JAPAN Natural Resources Conference.
- Koga, Y., Matsuo, O., Koseki, J., Goto, Y., Kubodera, I., Suzuki, K., Fukuda, H. and Okumura, R. 1991. Applicability of the dynamic centrifuge model test method in developing countermeasures against soil liquefaction. Proc. of International Conference CENTRIFUGE 1991: 431-438.
- Koga, Y., Koseki, J. and Takahashi, A. 1992. Model tests of embankments on liquefiable ground using dynamic centrifuge. Proc. 10th World Conference on Earthquake Engineering: 1299-1304.
- Schofield, A. N. and Vantor, K. 1984. Earthquake induced pore pressures in the foundation of a sea dyke. Proc. of International Symposium on Geotechnical Centrifuge Model Testing: 157-163.

## Assessment of earthquake effects on soil embankments

S.M.F. Astaneh, H.-Y. Ko & S. Sture  
*University of Colorado, Boulder, Colo., USA*

**ABSTRACT:** The response of embankment dams subjected to dynamic loads was investigated experimentally. Saturated models of homogeneous and zoned soil embankments were subjected to earthquake-like base excitation in the centrifuge. Two different densities of sand,  $D_r = 40\%$  &  $60\%$ , were used. The models were tested in a submerged state and were instrumented with acceleration, pore water pressure, and displacement transducers. The experiments were performed using a servo-controlled electro-hydraulic shaker installed on the centrifuge platform. The actual horizontal and vertical acceleration records measured on the base of the model container were very close to the intended motions. The rise in excess pore water pressure at some locations was high enough to cause liquefaction. In some experiments liquefaction was followed by structural degradation and local failure of the embankment's slope. Evidence of sudden soil movement and the inability of the soil to transmit the motion in the liquefied zones were successfully captured by the accelerometers located in those areas.

### 1 INTRODUCTION

The increasing use of the centrifuge in geotechnical laboratory studies around the world and the development of new equipment and techniques have generated widespread interests in the actual behavior of earth structures. Dynamic response of earth embankments during earthquakes or any other dynamic loadings, especially in the presence of water, has been the focus of many studies in recent years. This paper describes the experimental research work conducted at the, Department of Civil, Environmental, and Architectural Engineering, University of Colorado at Boulder, on saturated models of soil embankments. Two general types of homogeneous and zoned dams were studied. The models were tested in a submerged state and were instrumented with acceleration, pore pressure, and displacement transducers. The experiments were performed using the servo-controlled electro-hydraulic shaking system of CU Boulder. Configurations of models are shown in Figure 1.

### 2 MODEL CONTAINER AND SOIL MATERIALS

The model container has internal dimensions of  $75 \times 34 \times 15$  cm and is made of 1.27 cm thick aluminum. Features of the container include passages in the base for transducer wires, sealed joints, plumbing accommodations, and a plexiglass lid, which allows the evacuation of the air from the container and the flow of water into the container during model saturation. The container base is covered by a thin layer of a sand and glue mixture to provide a rough base for good contact between the base and the model in order to assure good transmission of shear motion to the test embankment.

Nevada No. 120 sand and Bonnie silt, both with specific gravities ( $G_s$ ) of 2.67, were used to construct the models. The maximum and minimum dry densities of the sand are  $17.33 \text{ kN/m}^3$  and  $13.87 \text{ kN/m}^3$ , respectively. Deaired distilled water was chosen to be the pore fluid.

### 3 SAMPLE PREPARATION AND INSTRUMENTATION

In the preparation of zoned models, the silt core was constructed first. Air dried Bonnie silt was mixed with water at an initial water content of 35% to form a slurry. This slurry was poured into a mold that defined the shape of the core in the embankment. The whole container was then spun in the centrifuge at 50 g for 0.5 hr. to speed up the settlement process while the material was still completely wet. The container was then taken out from the centrifuge and accumulated water on the top and the sides of the core was removed. The water content of the silty core at this stage had been reduced to 28%. After removing the mold the core was slightly trimmed to the desired final shape. Two acceleration transducers (one horizontal and one vertical) were placed on top of the core at this stage and sandy shoulders were constructed. In order to construct the shoulders, air-dried sand was pluviated through air into the container using an automated raining device with the capability of controlling the height, speed, and the traveling distance of the sand to obtain the desired density. Sand was rained in the form of thin sheet layers. In order to assure a good degree of saturation the container was initially filled with carbon dioxide.

The extra sand was then removed, with the help of a special vacuum system, from both shoulders to form the embankment slopes. Carbon dioxide was continuously supplied into the container during the whole process of raining and trimming. The container was then closed and air was evacuated, while distilled deaired water was introduced into the container from the bottom corners. After the whole specimen was submerged the water valves were closed and vacuum was maintained for 12 hours to obtain a high degree of saturation. Preparation of homogeneous models was exactly the same as preparation of zoned models except that the step of constructing the core was skipped. Also, the 12 hr vacuum time at the end was shortened to 6 hours, since the finer silt did not exist in this case.

The placement of transducers was done mostly before and during raining. Pore water pressure transducers were placed in the empty container with the wires secured and sealed in the base passages. Accelerometers, however, had to be placed during raining after reaching the desired

levels of sand. The targets for the displacement transducers were placed on the top and on the slope of the embankment as the very last step of instrumentation. The displacement transducers are of the noncontacting type made by Kaman Instrumentation Corporation. They work in a certain small range but with high sensitivity and accuracy. The transducer system measures the gap between the probe tip and a target metal surface. The targets are made of a 0.2 mm thick aluminum plate, and have a diameter of 3.5 cm, and a mass of 2 g. The pore pressure transducers are Druck model PDCR 81. They are cylindrical with a diameter of 5.8 mm, a height of 11.4 mm, and a mass of 2 g. The transducers are available in various pressure ranges and sensitivities. 100 kPa and 300 kPa range options were used for this study. The accelerometers are PCB Piezotronics model 303A11. They are quartz piezoelectric accelerometers with a diameter of 7 mm, a height of 12.2 mm, and a mass of 2g.

### 4 TESTING PROCEDURE

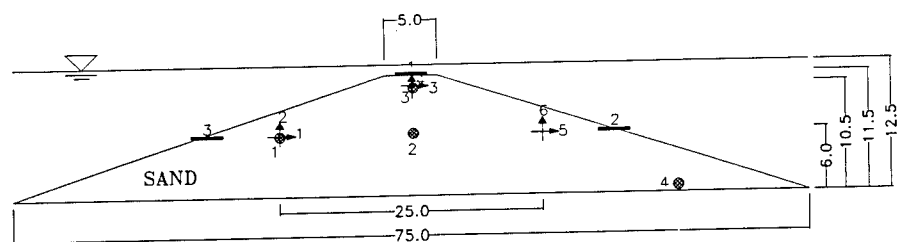
After completion of instrumentation and saturation the models were transferred to the centrifuge and spun up until an acceleration level of 50 g was reached at the mid-height of the embankments. The acceleration increase from 1 to 50 g took place gradually in 10 minutes.

The 50 g acceleration level was maintained for another 10 minutes to make sure that the centrifuge and the model were in steady state. The models were then shaken with several different earthquakes in different experiments. In most experiments data was collected for a period of time twice as long as the shaking time in order to capture possible post-shaking events. A total of 19 tests on homogeneous embankment models were conducted. In addition, 8 zoned embankment models were tested under different conditions, of which one was presented for Class A predictions in the VELACS project.

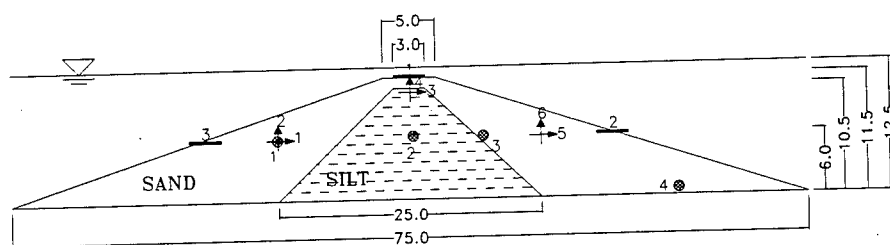
### 5 TEST RESULTS

Typical results of an experiment on a homogeneous model without occurrence of liquefaction are presented in Figure 2. Typical results of an experiment on a zoned model with occurrence of liquefaction are presented in





( side view of a homogeneous embankment model )



( side view of a zoned embankment model )

#### LEGEND

- Horizontal Accelerometer
- ↑ Vertical Accelerometer
- Pore Pressure Transducer
- Vertical Displacement Transducer

NOTE: The model dimensions are in centimeter

**FIGURE 1** - Configurations of homogeneous and zoned embankment models

Figure 3. All the records are plotted in terms of prototype values. To have complete information about the acceleration records, they are all presented in both time and frequency domains.

In order to have a good assessment of the occurrence of liquefaction, variation of the strength of soil, and the stability of the embankment during and after the earthquake, the acceleration, pore water pressure, and displacement records have to be evaluated together. As shown in Figure 2, the periodic-like motion applied to the base of the model could not cause any significant damage to the embankment. This claim is supported by the following observations:

(1) The horizontal and vertical base motions were transmitted throughout the whole structure from the bottom to the top and recorded by horizontal accelerometer 3 and vertical accelerometer 4 placed close to the crest. Other

accelerometers like 5 and 6 placed in other locations of the model also recorded similar behavior. The similarity between the base motions and the motions transmitted into the body of the embankment is especially evident in frequency domain in which locations of the peaks and their relative magnitudes match very closely.

(2) The excess pore water pressures were not high enough to reduce the effective stresses to zero and make the soil grains lose contact (compare the maximum excess pore pressures of 7.5 kPa and 12.5 kPa at locations 1 and 4, respectively, with the initial normal effective stresses of 11 kPa and 17 kPa at the corresponding locations).

(3) The less than 20 cm settlements at locations 1 and 2 compared to the 6 m and 3 m initial heights of those points are not big enough to be considered as signs of a catastrophic failure

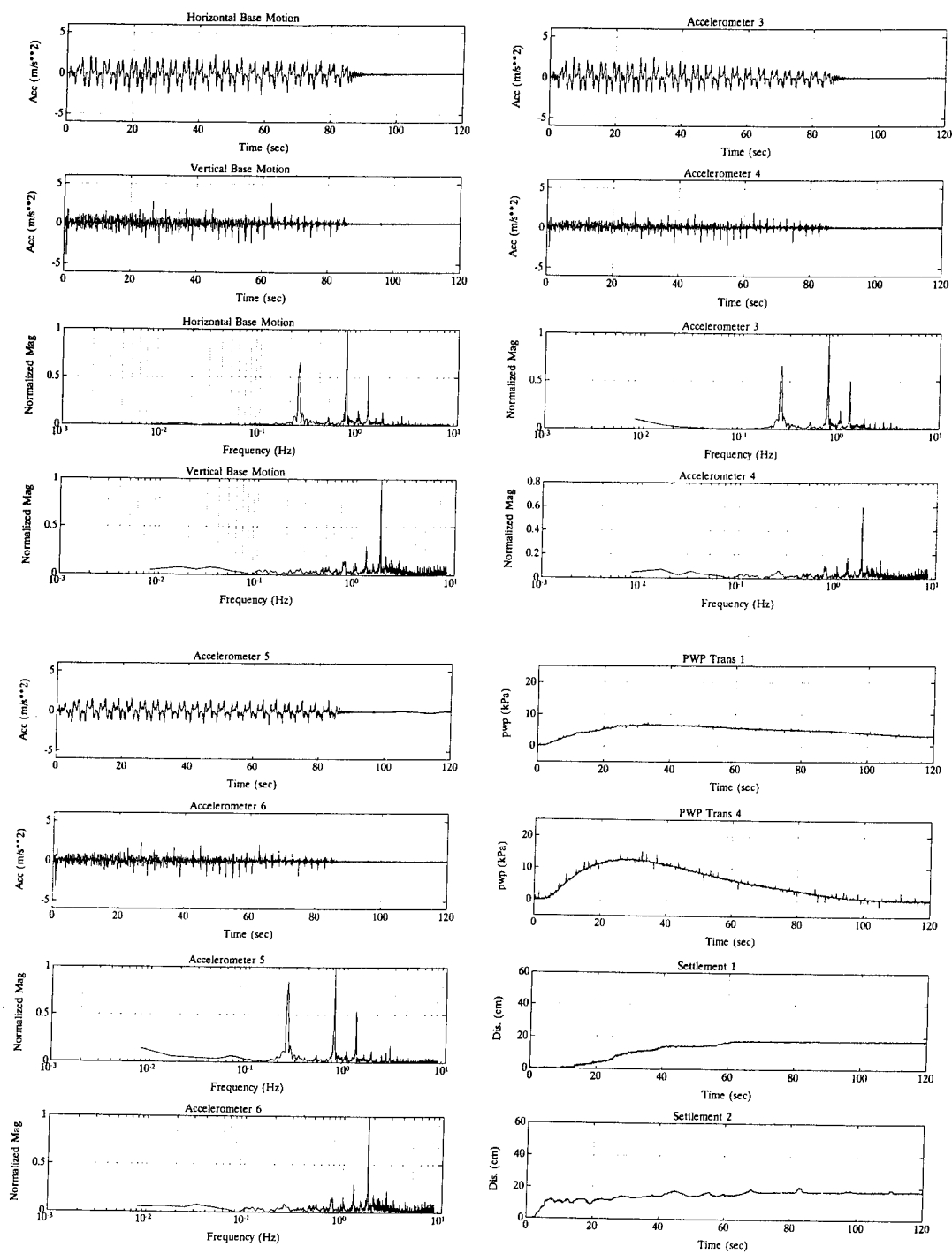


FIGURE 2 - Results of an experiment on a homogeneous model without occurrence of liquefaction

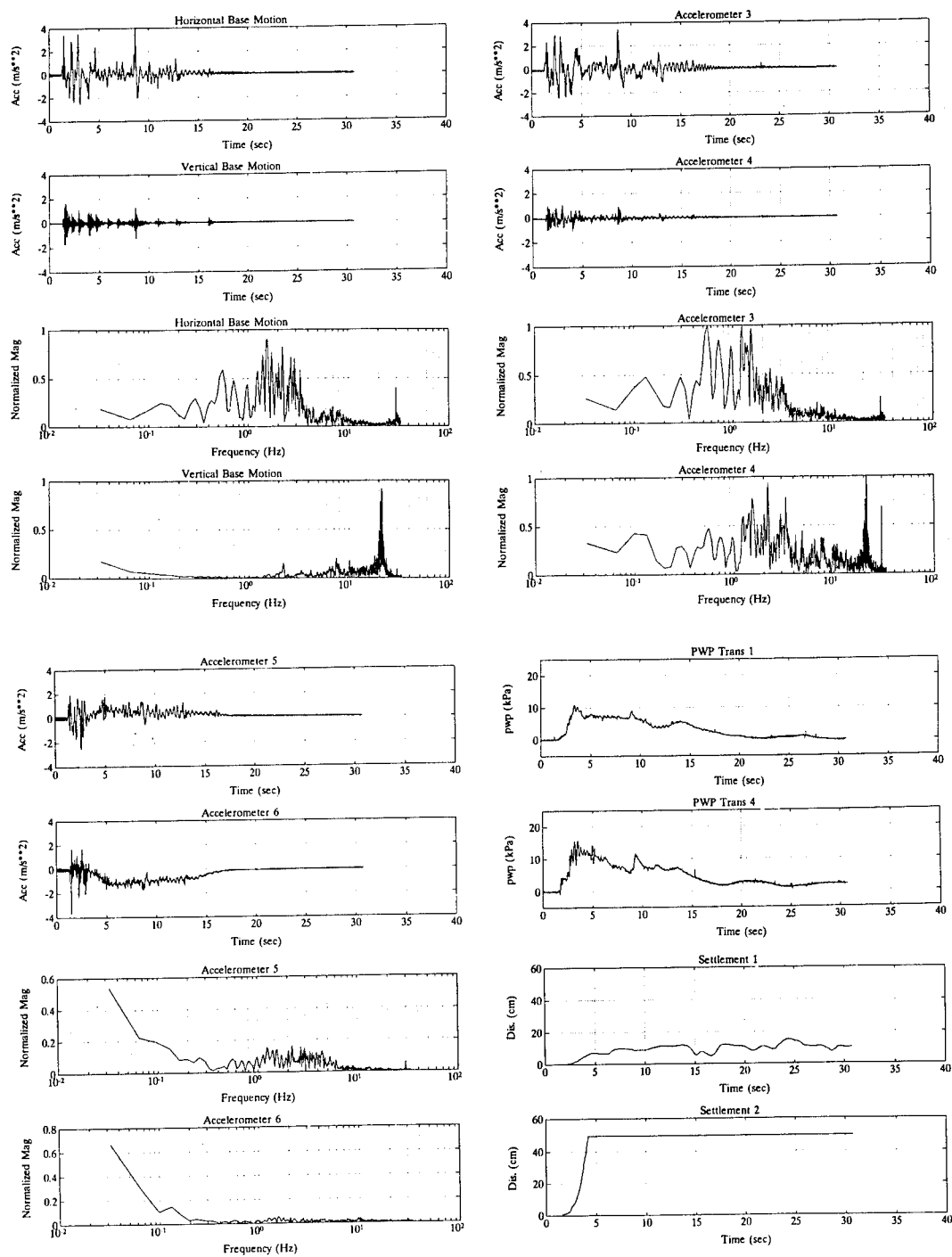


FIGURE 3 - Results of an experiment on a zoned model with occurrence of liquefaction

(which is usually the case when the soil mass liquefies).

A typical example of a zoned embankment which shows clear signs of liquefaction and subsequent structural degradation and failure of the embankment is given in Figure 3. The excess pore pressures at locations 1 and 4 rise quickly in the first three cycles of the random-like base motions until they reach the maximum initial effective stresses at those points. At this stage, the soil structure loses its integrity and the sandy shoulders collapse. From this point on, several decreases and increases in the pore pressures happen until the earthquake stops. Coincidence of pore pressure increases with acceleration peaks and pore pressure dissipations with quiet motions prove good consistency among the results.

The failure phenomenon in the zoned model was captured clearly by the vertical displacement transducers located on the crest and the mid-height of the slopes as well. Displacement transducer 2 recorded a quick settlement of 50 cm in less than 3 seconds from the start of the earthquake and then went out of range. The target for displacement transducer 1 moved about 10 cm and then was stopped by the stiff core. Horizontal accelerometer 5 and vertical accelerometer 6 also recorded the flow failure of the embankment by their movements towards the toe and the bottom. These movements are clear in the overall deviation of the acceleration records from zero axis in time domain and the very low dominant frequencies of the motions in frequency domain. These acceleration records show also a big reduction in the soil's ability to transmit the strong motions, once liquefaction starts.

There was no significant excess pore pressure generated in the silt, and the cores stayed undamaged during the earthquakes in all zoned embankments. Strong base-motion-like accelerations captured by accelerometers 3 and 4 mounted on top of the core are clear indications of the silt's good integrity.

From the totality of zoned and homogeneous embankments, the following significant findings can be summarized:

(a) Liquefaction and subsequent failure of the soil mass was observed in the sand in several experiments.

(b) The acceleration, pore pressure, and displacement records were found to have good consistency with each other.

(c) Liquefaction in models with 40% relative density of sand was observed to happen faster

and more easily than in models with 60% relative density.

(d) Having the same density of sand and being subjected to the same excitation, the zoned models failed more easily than the homogeneous ones. This could be explained by the facts that in zoned models: (1) the base motions could be transmitted more easily into the structures with the help of stiff cores, and (2) the much less permeable cores would limit the internal dissipation and redistribution of excess pore pressures, therefore, allowing them to build up more easily.

(e) Magnitude and frequency of the base motions were found to have significant impact on the stability of soil embankments against liquefaction. A periodic motion similar to the one presented in Figure 2 but with a frequency twice as high made the same homogeneous model fail.

## 6 CONCLUSIONS

Submerged saturated homogeneous and zoned embankments scaled down 50 times were shaken with different excitations in 50 g gravitational acceleration in the centrifuge. Several important features of the soil behavior regarding liquefaction due to earthquake loadings were investigated. These features include the general observation on liquefaction, effect of soil density, effect of embankment's type, and effect of loading's magnitude and frequency.

## ACKNOWLEDGMENT

The financial support of this work by National Science Foundation under grant No. BCS9000390 is gratefully acknowledged.

## Seismic settlements and pore pressures of shallow foundations

L. Liu & R. Dobry

*Rensselaer Polytechnic Institute, Troy, N.Y., USA*

**ABSTRACT:** A series of model tests were conducted at the RPI centrifuge to investigate the seismic behavior of shallow foundations on saturated cohesionless soil deposits, with and without foundation soil improvement by vibrocompaction. The soil permeability and compaction depth were varied in the tests. The pattern of excess pore pressure buildup and redistribution, and the mechanism of foundation settlement, are reported and discussed.

### 1 INTRODUCTION

Liquefaction-induced unacceptable structure settlement and tilting are among the most destructive foundation failures during strong earthquakes. According to the field investigation along Perez Blvd. in Dagupan City after the 1990 Philippines earthquake (Adachi, et al., 1992), the settlements of damaged buildings ranged from 0.2 m to as much as 2.5 m or more, with much of the settlements falling in the 0.5 - 0.7 m range. These buildings had shallow spread foundations founded on a loose uniform fine sand deposit ( $D_{50} \approx 0.2$  mm). It is estimated that the soil liquefied to a depth of 6 - 10 m and that the maximum ground acceleration was about 0.2 g at the site (Adachi, et al., 1992).

Liquefaction-induced building settlement is a complex phenomenon involving dynamic and post-shaking static interactions between the building, the foundation, the soil skeleton and pore fluid within the soil. This makes it quite difficult to analyze. A further complication may be introduced if the liquefiable soil is treated under/or near the foundation. The roles of a number of important parameters of this interaction process such as soil density, permeability, foundation width, as well as the extent to which the liquefiable soil around the foundation was treated, are poorly understood.

This paper presents some results from two series of centrifuge tests: Series A consisting of three tests focused on soil permeability effects; and Series B, including five tests with focus on the effectiveness of soil improvement by vibrocompaction. The centrifugal acceleration was 50g for Series A tests and 80g for Series B tests. All of the tests were conducted at the RPI centrifuge earthquake simulation system.

### 2 TEST FACILITIES AND MODEL CONFIGURATIONS

The RPI centrifuge and earthquake simulation system consists of an Acutronic Model 665-1 centrifuge with a 3.0 m radius and 100 g-ton capacity. An electro-hydraulic shaker is installed on the centrifuge platform to produce earthquake-like shaking at the base of the soil or soil-structure model. More information about this system can be found in Elgamal, et al. (1990).

The model container used in the Series B tests is a rigid rectangular bucket, of dimensions  $457 \times 204 \times 241$  mm<sup>3</sup>. The container used in the Series A tests is slightly smaller. The model response was measured by miniature transducers including accelerometers (303A03 PCB from Piezotronics), pore pressure transducers

(PDCR81 from Druck Inc.) and linear variable differential transformers (LVDT MHR100 from Schaevits Engrg.). Two PC computers were employed to control the shaker excitation and the data acquisition from the response of the model. The response data was collected at 50 KHz.

The soil tested is a fine uniform sand, Nevada No. 120, with  $D_{50} = 0.1$  mm and permeability  $k = 2.3 \times 10^{-3}$  cm/s at 1g. The model time in these tests was scaled to prototype by multiplying a factor of  $N$  to meet the dynamic conditions ( $N$  is the centrifugal g-level). Therefore, according to the scaling laws, in the Series B tests where water was used as pore fluid, the simulated prototype soil permeability was actually  $1.84 \times 10^{-1}$  cm/s, corresponding to a coarse sand rather than a fine sand. On the other hand, in the Series A tests a variation of the soil permeability was implemented by using aqueous solutions with different glycerol content as pore fluid (water-glycerol mixture). The symbol GC is used here to represent glycerol content by weight in the pore fluid solution. The three tests G0, G55 and G85 in Series A, used GC = 0 (water), GC = 55% and GC = 85%, respectively. If the usual assumption is made that  $k$  is proportional to  $(\text{viscosity})^{-1}$ , the permeabilities in Tests G55 and G85 were, respectively, 10 and 100 times smaller than the permeability of the soil in Test G0. That is, these two tests bracket the correct factor of 50 required by the scaling law for  $N = 50$ .

Figure 1 depicts the model configuration used in Series A. All three models consist of a medium dense sand deposit. The deposit

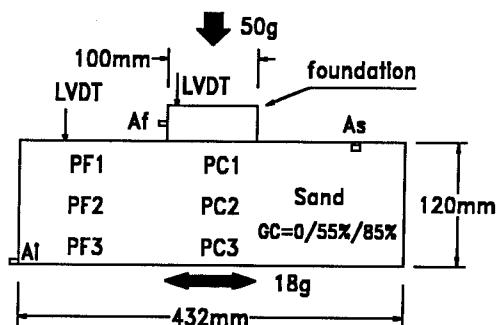


Figure 1. Model profile for Series A tests

Table 1. Series A tests

Tests	$D_r$ (%)	GC (%)	$a_{av}$ (g)	$q_{av}$ (KPa)
G0	53	0	0.35	125
G55	51	55	0.36	122
G85	45	85	0.39	119

GC: glycerol content by weight in pore fluid

$a_{av}$ : average amplitude of input acceleration

$q_{av}$ : average foundation contact pressure

thickness is in the range  $120 \pm 5$  mm, corresponding to about 6 m in prototype at 50g. The model foundation is a rigid circular footing with a diameter of 100 mm. Horizontal accelerometers were installed at the model base and foundation and are labelled  $A_i$  and  $A_f$ , respectively. A third horizontal accelerometer,  $A_s$ , was located at the soil surface away from the foundation to monitor what is believed to be approximately the free field response. The foundation settlement and the settlement of the soil surface away from the foundation were measured by two LVDTs. Typically two sets of three pore pressure transducers were installed at depths under the center of the footing and away from the foundation, labelled respectively PC and PF. Some specifications for the Series A tests are summarized in Table 1. The term  $a_{av}$  in the table corresponds to the average amplitude of the uniform sinusoidal base input acceleration, while  $q_{av}$  is the average contact pressure of the footing during centrifuge flight. The term GC is the glycerol content in the pore fluid as explained earlier.

The model configuration of Series B is shown in Fig. 2. The instrument layout is similar to that in Series A. All five models in Series B

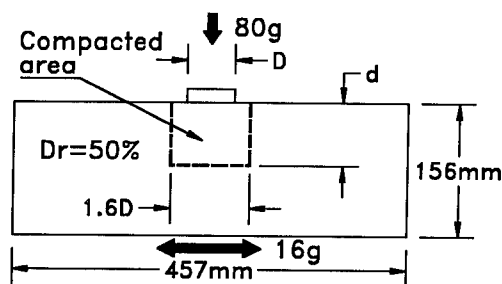


Figure 2. Model profile for Series B tests

Table 2. Series B Tests

Tests	$D_r$ (%)	$d$ (m)	$d/D$	$D_{rc}$ (%)
C0	54	0.00	0.00	-
C1	51	3.22	0.71	>100
C2	55	6.72	1.47	88
C3	49	9.45	2.07	91
C4	51	12.58	2.76	89

$d$  : prototype compaction depth

$D$  : prototype footing diameter

$D_{rc}$ : relative density in the compacted area

were built at medium relative density ( $52 \pm 3$  %). The soil deposit thickness in this series was  $156.5 \pm 2.5$  mm, corresponding to about 12.5 m in prototype at 80g. The diameter of the rigid circular model foundation was 57 mm, corresponding to a prototype diameter of 4.56 m. The major parameters of the models in this series are listed in Table 2. In these tests the soil was compacted around and under the foundation. The soil compaction was done over a diameter equal to 1.6 the footing diameter (Fig. 2) and to depth  $d$  which changed between tests. The values of  $d$  for all tests are listed in Table 2. Also given in the table are the ratios of compaction depth to footing diameter,  $d/D$ , and the soil relative density in the compacted area,  $D_{rc}$  (88% to > 100%).

### 3 MODEL PREPARATION AND TEST PROCEDURE

In the Series A tests the soil models were constructed through a dry sand raining process followed by application of vacuum at -101 KPa for an hour to saturate the model. The transducers were installed at the desired locations during the sand raining process. Then the pore fluid was slowly supplied into the soil with the vacuum on. After saturation the model foundation was placed on top of the soil deposit and the model was spun to 50g for consolidation. The shaking signal was applied to the shaker controller after the model had been consolidated and all transducer outputs had reached steady state.

For the Series B tests the procedure was essentially the same, except that a compaction process was conducted after raining the dry sand. Also, the saturated soil deposit was first spun to 80g to consolidate it, and then it was brought back to 1g to install the foundation. The foundation-soil model was spun and consolidated again to 80g, and was then shaken.

The compaction diameter in these tests is equal to 1.6 times the footing diameter; this factor 1.6 will be varied in future investigations. Overall, the compaction was implemented at 19 points across the compacting area, using a 19-hole guide to locate the compacting points in each test. The compactor used was a 6.5 mm diameter aluminum tube with a vibrator clamped on top. During the compaction operation, the vibrating tube was first inserted to the desired compaction depth,  $d$ , and was then subjected to several withdraw-insert cycles with an approximate 40 mm (in model units) insert stroke and slightly longer withdraw stroke, until the tube was finally withdrawn out of the soil. Also, the relative density in the compacted area ( $D_{rc}$ , see Table 2) was estimated by backfilling the compacted area with sand to the initial height, and by assuming that the effect of compaction is limited to within 1.5 times the tube diameter around the compacting tube. The compaction relative densities,  $D_{rc}$ , obtained this way, were in the range 88-91%, except for Test C1, where  $D_{rc} = 106\%$  was calculated. This error was probably due to the fact that this was the test with the shallowest compaction depth, and thus even a small error in the estimation of the compaction volume results in a large error in the calculated relative density. Nevertheless these estimated  $D_{rc}$  give an idea of the consistency of the compaction operation.

### 4 TEST RESULTS AND DISCUSSION

Some selected records from Test G0 in Series A is plotted in Fig. 3. Deaired water was used in this test as a reference for the other two tests. The units used in all plots as well as in the following text are in prototype scale, except otherwise indicated.

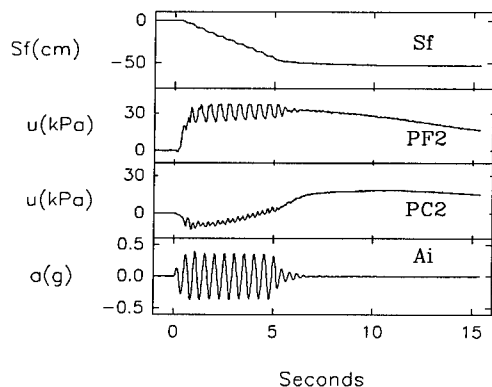


Figure 3. Selected records from Test G0

The base input acceleration  $A_i$  as shown in Fig. 3 was a 10 cycle, uniform sinusoidal signal, 2.0 Hz in prototype. This same signal was used in all three Series A tests. As the shaker used can reproduce input signals very well, all input accelerations actually measured in these tests were fairly close. The average amplitudes of the input accelerations in Series A were in the range  $0.37 \pm 0.02$  g.

The base input acceleration in Series B tests was also a 10 cycle uniform sinusoidal signal, but with a frequency of 1.5 Hz and an average amplitude of 0.2 g.

Typically the excess pore pressures away from the foundation, PF1, PF2 and PF3, developed rapidly during shaking, and by the end of shaking the 100% pore pressure ratio condition (initial liquefaction) had been reached down to a

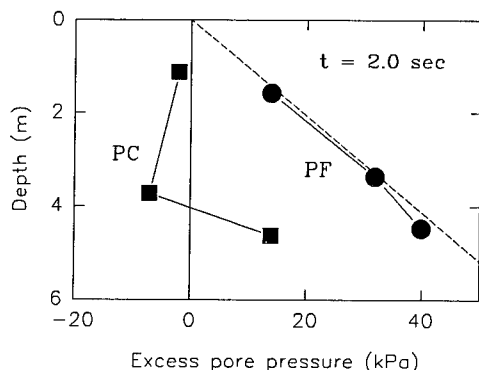


Figure 4. Excess pore pressure distribution in Test G0 at  $t = 2.0$  seconds

depth of more than half of the total depth of the soil deposit. These measurements may be used to approximate the free field response. The right line in Fig. 4 is the excess pore pressure distribution curve in Test G0 at  $t = 2.0$  seconds (total duration of shaking = 5.0 seconds), along transducers PF1, PF2 and PF3. The dashed line shown is the calculated overburden effective stresses versus depth assuming a 1D condition.

In contrast to the free field response, negative excess pore pressures developed temporarily under the foundation to a depth of about 3/4 of the footing diameter, as shown by the left curve in Fig. 4. This suggests that a dilation tendency took place during shaking in the granular soil due to permanent shear straining caused by the driving shear stress.

Generally the excess pore pressures during and following an earthquake are the result of two major components. One is the locally generated excess pore pressure due to cyclic straining of the soil skeleton, which occurs exclusively during shaking. A densification tendency in the skeleton induces a positive pore pressure buildup, while any dilating tendency leads to a negative pore pressure generation. The second component is the redistributed excess pore pressure which occurs wherever and whenever a hydraulic gradient has been established; this can happen during or after shaking. In the tests reported here a high positive excess pore pressure developed in the surrounding soil and under the dilation zone where negative pore pressures had developed

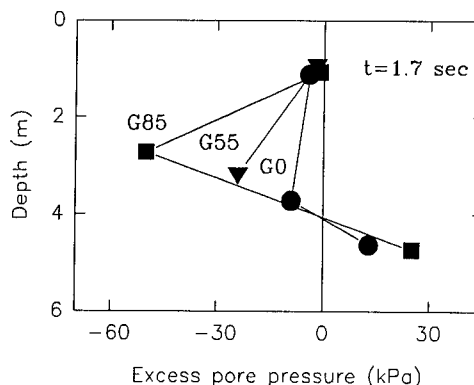


Figure 5. Distribution of excess pore pressures under the foundation at  $t = 1.7$  seconds



due to the shaking; thus, a pore pressure redistribution was inevitable. Because the dilative zone under the footing was relatively small compared with the zone of positive pore pressures, the left line in Fig. 4 moved toward the right before the end of and shortly after shaking. As this latter component of excess pore pressure is soil permeability dependent, it redistributed more slowly in models with lower soil permeabilities (larger GC). It can be seen in Fig. 5 that larger negative excess pore pressures were measured in models having larger GC, because the measured excess pore pressures are now dominated by the first component of excess pore pressure generated by the shaking.

In the Series B tests, where the soil was compacted to different depths, the excess pore pressures away from the footing were very similar in all cases, suggesting that initial liquefaction ( $r_u = 100\%$  condition) had developed to depths of 6 to 8 m in the free field by the end of shaking. The compaction depth had only a minor influence on the free field pore pressures, because the compaction was restricted to the central part of the deposit. The influence of compaction depth on the pore pressures under the foundation is shown in Fig. 6. Some reduction was observed in the rate of pore pressure development in the early stage of shaking under the foundation, as the compaction depth increased. However, because these tests were run at 80g with water as pore fluid, and thus the redistribution of the excess pore pressures was very rapid, by the end of shaking the excess pore pressures along the axis of the

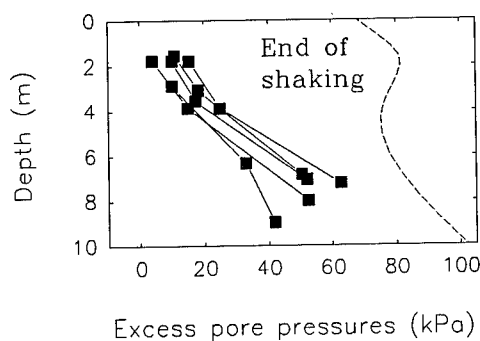


Figure 6. Distribution of excess pore pressures under the foundation in Series B tests.

Table 3. Foundation settlements

Tests	GC (%)	S <sub>f</sub> (cm)	S <sub>fd</sub> (cm)	S <sub>fa</sub> (cm)
G0	0	53	48	5
G55	55	34	27	7
G85	85	36	24	12

GC: glycerol content

S<sub>f</sub>: total foundation settlement

S<sub>fd</sub>: foundation settlement during shaking

S<sub>fa</sub>: foundation settlement after shaking

footing in these tests were located in a narrow band, which was in turn close to the free field excess pore pressures (Fig. 6). The dashed line here represents the effective overburden stresses along the axis of the foundation estimated using elastic theory. Based on the observations in the Series A tests, a lower permeability should slow down the pore pressure redistribution and thus enhance the differences between free field pore pressures and the pore pressures under the foundation, as well as the differences between pore pressures under the footing between tests with different compaction depths.

As shown later, the compaction depth had a substantial effect on the foundation settlement, while the pore pressures were not so different among these tests (Fig. 6). This suggests that the level of excess pore pressure is not a significant factor in determining foundation settlement, at least in the tests reported here.

The shaking-induced foundation settlement in Test G0 was 53 cm, developed almost linearly with time and occurring mostly during shaking. When the soil permeability was decreased by adding glycerol into the pore fluid in Tests G55 and G85, less final settlements and during-shaking settlements were observed but with more post-shaking settlements (Table 3). It can be speculated that in the more pervious medium (Test G0) the foundation settlement is mainly caused by the development of cyclic shear strains due to inertia forces, while in the less pervious medium (Test G85) the contribution to foundation settlement of the soil volumetric strain associated with the slow pore pressure dissipation becomes relatively more important.

In the Series B tests, the foundation settlement decreased as the compaction depth increased.

As plotted in Fig. 7, there is a consistent relationship between the ratio of foundation settlement over free field settlement,  $S_f/S_s$ , and the ratio of compaction depth to footing diameter,  $d/D$ . This relation shows that compaction down to a depth of 1.5 the footing diameter can reduce the foundation settlement  $S_f$  to a value similar to the free field soil settlement,  $S_s$ , which in this test series fell in the range 20 - 28 cm, corresponding to an average volumetric strain in the soil of 1.6 - 2.5 % for an assumed 1D condition.

Compared with the foundation failure investigation in Dagupan City, Philippines mentioned at the beginning of the paper, this conclusion from the tests means that compacting the soil down to a depth of about 1.5 footing diameter may bring the foundation settlement from 50 cm - a clearly destructive value - down to less than 20 cm - the lower bound of damaging settlement. It is also seen from Fig. 7 that the decrease of foundation settlement  $S_f$  from  $d/D = 0$  to  $d/D = 1.5$  is quite fast. Beyond  $d/D = 1.5$ ,  $S_f$  stabilizes or increases very slowly with  $d/D$ . This suggests that a compaction deeper than 1.5 footing diameters may have essentially no effect on foundation settlement. However, this conclusion may be limited to a compaction diameter of about 1.6 footing diameters, as well as to the other factors kept constant in these tests, such as the total thickness of the liquefied layer, the depth to bedrock, etc. These factors should be investigated in future studies.

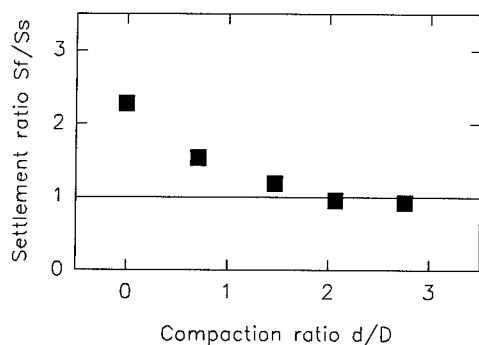


Figure 7. Normalized foundation settlement versus compaction ratio in Series B tests.

## 5 CONCLUSIONS

It was observed in these centrifuge tests that the soil permeability has a significant effect on the pattern of pore pressure distribution near the foundation. The dilatancy of the granular soil under the shallow foundation may temporarily cause negative excess pore pressures down to a depth of approximately three quarters of the footing diameter during shaking. However, the equalization of the excess pore pressures was very rapid, especially for conditions corresponding to a coarse sand deposit.

The soil permeability seems to have a minor effect on the total foundation settlement, but a lower permeability can increase the post-shaking settlement.

When the medium dense soil was vibrocompacted to a diameter of 1.6 footing diameter, the foundation settlement decreased significantly with increasing compaction depth down to about a depth equal to 1.5 footing diameters. Below  $d/D = 1.5$ , no settlement reduction or very little reduction was observed.

## REFERENCES

- Adachi, T., Iwai, S., Yasui, M. and Sato, Y. 1992. Settlement and inclination of reinforced concrete buildings in Dagupan City due to liquefaction during the 1990 Philippine earthquake, Proc. 10th World Conf. on Earthquake Engineering, Vol. 1, pp. 147
- Elgamal, A.-W., Dobry, R., Van Laak, P. and Nicolas-Font, J. 1991. Design, construction and operation of 100g-ton centrifuge at RPI, Proc. Int. Conf. Centrifuge 91, Hon-Yim Ko and Francis G. McLean (eds.), pp. 27-34
- Whitman, R. V. and Lambe, P. C. 1982. Liquefaction: Consequences for a Structure, Proc. Conf. Soil Dynamics and Earthquake Engineering, pp. 941-949
- Yoshimi, Y. and Tokimatsu, K. 1977. Settlement of Buildings on saturated sand during earthquakes, Soils and Foundations, Vol. 17, No. 1, pp. 23-38

## Slope stability with seepage in centrifuge model earthquakes

N.K. Pilgrim

Engineering Department, Cambridge University, UK

X. Zeng

Department of Civil and Environmental Engineering, University of California, Davis, Calif., USA

**ABSTRACT:** Some results from an investigation of the response of sand slopes with seepage during centrifuge model earthquakes are presented. The objective of this investigation was to establish the nature of deformation observed beneath slopes of different gradient. The model gradients reproduce stress conditions in which both an inertial loading effect and the effects of transient pore pressure increase are apparent.

### 1 INTRODUCTION

In Characteristic State Theory the response of saturated sand to earthquake loading depends on both the initial effective stress ratio,  $\tau/\sigma'_n$  or  $q/p'$ , and the amplitude of the cyclic shear stress,  $\tau_{cy}$  or  $q_{cy}$ .

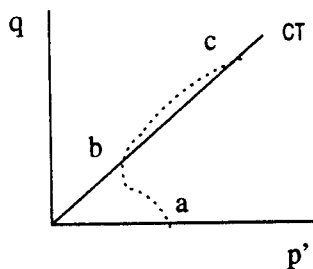


Fig. 1: Undrained shear loading

Figure 1 shows the schematic stress path of a sand sample subject to monotonic shear loading in an undrained tri-

axial test. As shear strains are applied the grain assembly begins to unlock allowing particles to settle (generate positive pore pressures) such that the stress path moves towards the Characteristic Threshold. Then, with increasing shear strain, the grain assembly starts to relock with a tendency to dilate (generate negative pore pressures) as particles override. The period in which the effective stress path reverses is associated with the onset of a higher strain rate (Luong and Sidaner 1981).

### 2 CENTRIFUGE MODELS

Models were constructed to a scale of 1/80 and tested at 80g. The Bumpy Road facility at Cambridge simulates earthquakes by providing ten cycles of horizontal, unidirectional acceleration. At 80g the fundamental frequency is about 120 Hz. All the models were made from Nevada sand. In order to satisfy scaling relationships for time, 80 cs sili-

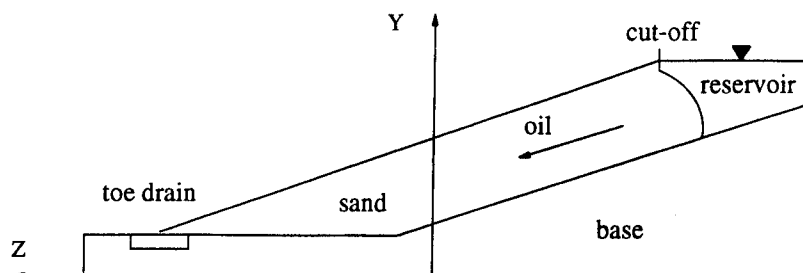


Fig. 2: Centrifuge package

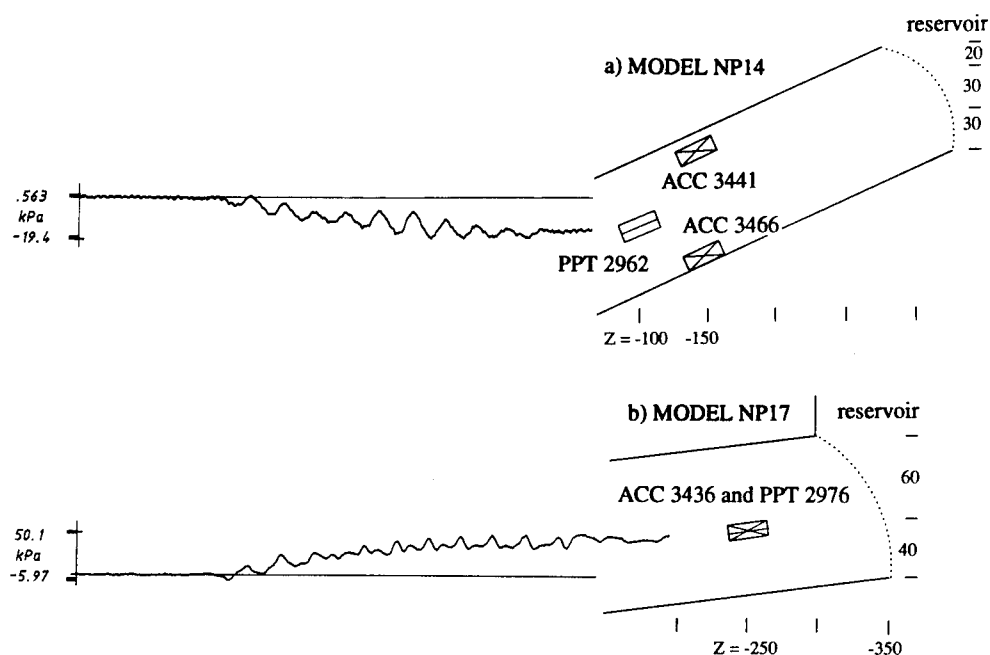


Fig. 3: Transducers and excess pore pressure

con oil was used. The density of silicon oil is  $960 \text{ kg/m}^3$  which is similar to water and so pore pressures are correctly modelled.

The experimental package is shown in Figure 2. Air pressure is used to raise oil at a constant flowrate from a tank at the side of the slope to the reservoir at the top of the slope. The supporting structure is made of marine plywood. To improve the transmission of base shaking to the sand layer, sand was glued to the

plywood base. Stainless steel side plates were fitted to reduce side friction.

### 3 EXPERIMENTAL DATA

A relative density of about 40 % was obtained by pouring sand from a suspended hopper. The location of transducers is shown for Tests NP14 ( $18^\circ$  slope, 40 % relative density) and NP17 ( $6^\circ$ , 40 %) in Figure 3, together with records of excess

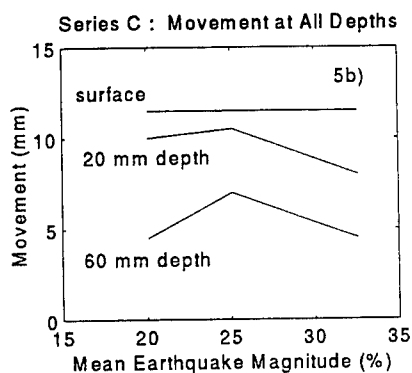
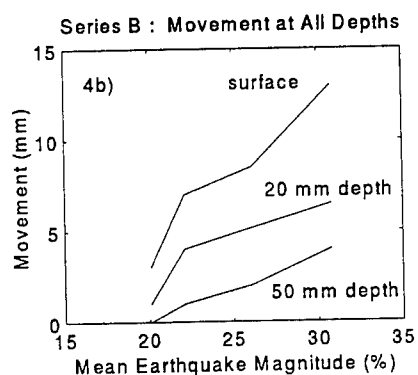
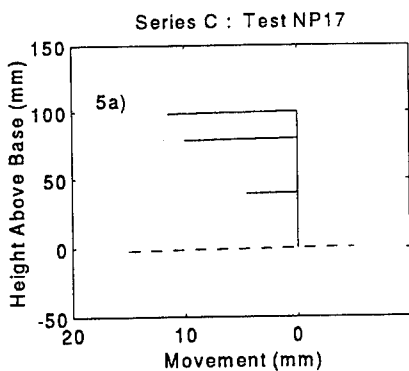
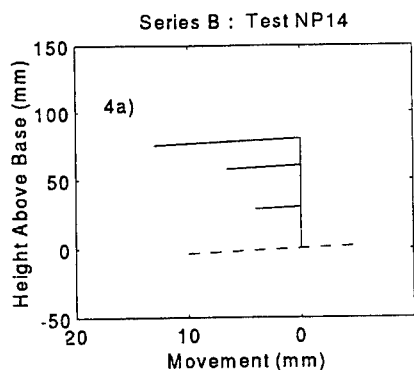


Fig. 4: Series B deformation

Fig. 5: Series C deformation

pore pressure. In Test NP14 the magnitude of the earthquake was 30.8 % of  $g$ , and in Test NP17 the magnitude was 20.1 %.

The profile of line marker movements for Test NP14 is shown in Figure 4a. Figure 4b shows the movement of line markers plotted for four Series B models (18°, 40 %) against earthquake magnitude. Deformation depends on earthquake magnitude. Figure 4b suggests a limiting earthquake magnitude of between 18 and 20 % below which no deformation will take place at any depth.

The profile of line marker movements for Test NP17 is shown in Figure 5a. Figure 5b shows the movement of line markers plotted for three Series C models (6°, 40 %) against earthquake mag-

nitude. Deformation is independent of earthquake magnitude.

#### 4 COMPUTATIONAL MODELLING

##### 4.1 Inertial loading effects on steeper slopes

Relative movement between base and surface layers is examined by inspecting velocity records from below (input) and above (output) a hypothetical sliding plane. As shear stresses propagate through the sand layer the motion is modified in both magnitude and phase (the surface layer lags the base layer and has a larger amplitude of motion); since the acceleration records used in the

analysis are recorded a finite distance apart, their magnitude and phase must be adjusted to account for this effect. The comparison of velocity records is not therefore intended as an exact measurement of surface displacement.

The acceleration and velocity records for cycle 6 of Test NP14 are presented in Figure 6. A phase shift of  $25.8^\circ$  has been made, the base acceleration has been amplified by a multiplication factor of 1.135 and the surface acceleration has been attenuated by a multiplication factor of 0.865. The downslope deformation indicated by these results is consistent with centrifuge test data (the recorded movement of mid-depth line markers) shown in Figure 4a.

When considered with the effective stress path (presented below) these results provide some useful insights into the behaviour of the sand layer.

#### 4.2 Dynamic loading conditions

By considering the forces parallel and perpendicular to the plane shown in Figure 7, the shear stress,  $\tau_{sdy n}$ , and normal stress,  $\sigma'_{sdy n}$ , are established. If it is assumed that total stresses on the opposite vertical faces of the section cancel out, then the relationships are as follows:

$$u = \gamma_s \cdot (z - z_w) \cdot \cos^2 \beta$$

$$\tau_{sdy n} = W \cdot (\sin \beta + K \cdot \cos \beta)$$

$$\sigma'_{sdy n} = W \cdot (\cos \beta - K \cdot \sin \beta) - u - u_e$$

in which  $W$  is the total weight,  
 $u$  is the static state pore pressure,  
 $u_e$  is the excess pore pressure,  
 $K$  is the dynamic seismic coefficient.

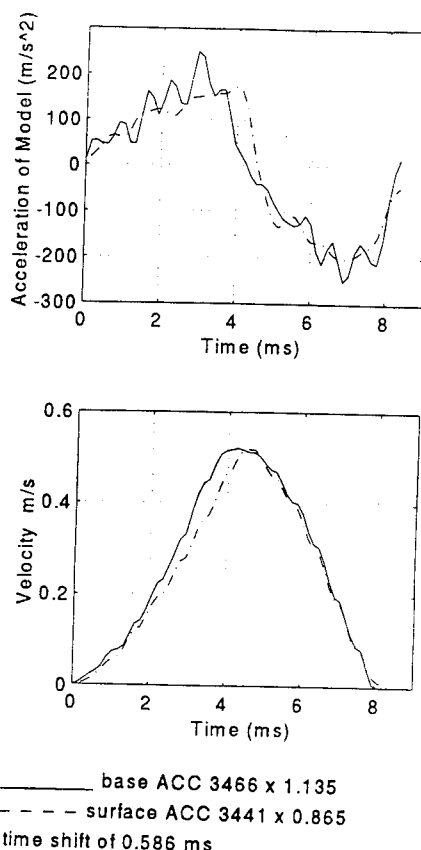


Fig. 6: NP14, cycle 6: Acceleration and Velocity

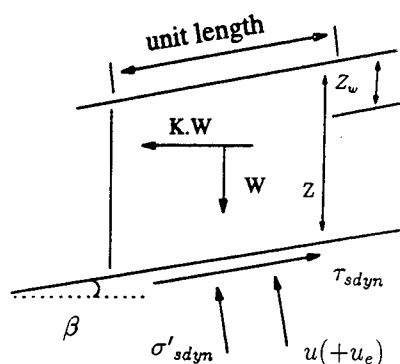


Fig. 7: Forces on a section of slope

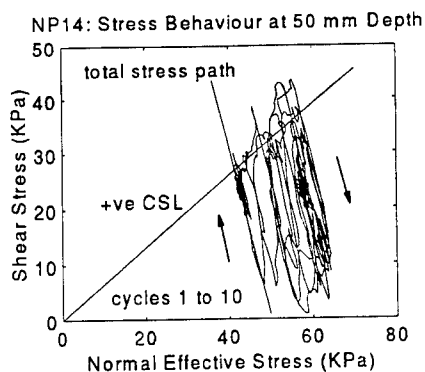


Fig. 8: NP14: Effective stress path

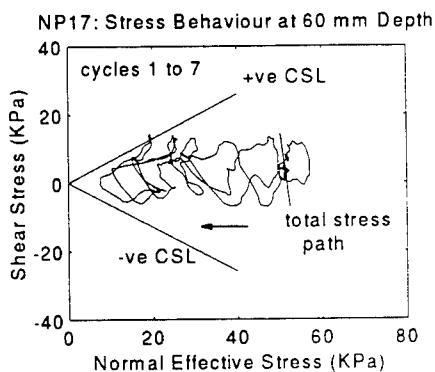


Fig. 9: NP17: Effective stress path

In Series B tests the accelerometer at mid-depth failed and in Test NP14 the effective stress path is investigated by coupling the records of ACC 3441 ( $K$ ) and PPT 2962 ( $u_e$ ). In Test NP17 the records of ACC 3436 ( $K$ ) and PPT 2976 ( $u_e$ ) are coupled. In both tests it is apparent that during the earthquake the slope loses contact with the reservoir. The hydraulic force from the reservoir is therefore zero. Since PPT 2976 is close

to the reservoir, the assumption that total stresses on opposite vertical faces of the section cancel out no longer holds. From consideration of maximum active force (for a section of slope taken 100 mm to either side of the transducer), the total stress resisting downslope movement on the mid-depth plane is 6.3 KPa.

The effective stress paths at mid-depth recorded in Models NP14 and NP17 are shown in Figures 8 and 9.

## 5 RESULTS AND DISCUSSION

Inertial loading effects are predominant in the mechanism associated with the deformation of the steeper Model NP14. Downslope deformation is characterised by partial decoupling and recoupling of base and surface layers during each cycle: the positive acceleration peaks of the surface layer are truncated followed by an acceleration spike. However, this deformation does not take place on a discrete plane between layers, but accumulates through the sand layer. The phase lag increases as motion propagates through the sand layer.

As the effective stress path crosses the Characteristic Threshold there is a tendency for the sand to dilate and negative pore pressures cause the sand to stiffen. The shear strength increases as a function of the mobilised angle of shearing resistance (Characteristic friction angle) and the effective stress (excess pore pressure) (Lambe and Whitman 1979). Although some shear strain takes place, the base and surface layers are able to recouple and the acceleration spike is seen in the record of the surface layer.

With the accumulation of negative pore pressure, the effective stress path migrates into a region in which the cyclic

effective stress is no longer sufficient to cross the Characteristic Threshold and cause large shear strains. As a result, later cycles in the record of surface acceleration do not exhibit truncation.

The loading condition in the mechanism associated with the deformation of the gentle slope, NP17, is dominated by transient pore pressure effects. The sand mass softens as positive pore pressures accumulate and the stress path migrates towards initial liquefaction and the region in which large strains will occur. Inspection of Figures 4b and 5b shows that, for earthquakes of magnitude less than 2.5 % of  $g$ , the more gentle Series C slopes suffer greater deformation.

A condition of cyclic mobility is apparent. As the shear stress increases, the sand exhibits an initial tendency to contract, creating positive pore pressures. As beneath the steeper slope, the sand then tends to dilate creating negative pore pressures and the shear strength increases as a function of the mobilised angle of shearing resistance and the increasing effective stress. As a result of the small, static shear stress, displacement accumulates in the downslope direction.

## 6 CONCLUSION

Discrete slip planes associated with Mohr-Coulomb type rupture are not observed. The predominant form of instability is through shear strain deformation.

The deformation observed in Model NP14 ( $18^\circ$ ) is predominantly due to inertial loading effects. At all depths, the sand has retained some capacity to dilate and the limiting shear strength is not mobilised even for the largest of the cyclic stress peaks. This prevents the develop-

ment of a discrete slip plane.

The deformation observed in Model NP17 ( $6^\circ$ ) is a result of transient pore pressure increase, and indicates the mechanism by which more sensitive soil structures, such as wind blown loess or minewaste, collapse to give extensive flow failures. In Model NP17 the sand was able to regenerate strength following initial liquefaction. This suggests that the sand was relatively dense (Ishihara 1985). In a sample of very loose sand, particles are left in a suspended state during initial liquefaction and the tendency to override, generating negative pore pressures, is reduced. In this case the sand's shear strength is not regained, dynamic shear stresses are not transmitted from the base, and static shear stresses result in a more extensive failure of the slope.

## REFERENCES

- Ishihara, K. 1985. Stability of natural deposits during earthquakes. *Proc. 11th ICSMFE*, 1:321-376
- Lambe, T.W. & R.V. Whitman. 1979. *Soil Mechanics SI Version*, p442-443. John Wiley.
- Luong, M.P. & J.F. Sidaner. 1981. Undrained behaviour of cohesionless soils under cyclic and transient loading. *Proc. Int. Conf. Recent Advances in Geotechnical Earthquake Engineering and Soil Mechanics*, 2:215-220.
- Newmark, N.M. 1965. Effects of earthquakes on dams and embankments. 5th Rankine Lecture. *Geotechnique*, 15:139-160.



## Permanent displacement of sloping ground due to liquefaction

H. Nagase

*Kyushu Institute of Technology, Kitakyushu, Japan*

H.-Y. Ko, H. K. Law & R. Y. S. Pak

*University of Colorado, Boulder, Colo., USA*

**ABSTRACT:** In order to investigate an effect of confining pressure on permanent displacement of sloping ground, several shaking table tests were conducted under centrifugal condition. In the tests, the permanent ground displacement occurred in the whole liquefied layer even under 20 g and 80 g. Furthermore, an important relationship was confirmed between the permanent ground displacement and the thickness of the liquefied layer.

### 1. INTRODUCTION

A series of shaking table tests under 1 g condition have been previously performed by Yasuda et al. (1992), in order to clarify the mechanism of permanent displacement of sloping ground, which is a huge land slide in sand deposit liquefied by an earthquake. These tests showed that the permanent ground displacement did not occur at the boundary between the liquefied layer and the non-liquefied layer, but occurred in the liquefied layer with a constant shear strain. However, it was clarified by Ishihara et al. (1991) that sand behavior in a region of large deformation is considerably affected by confining pressure. Therefore, it is necessary to perform a shaking table test using centrifuge apparatus to clarify the mechanism of the displacement, because it is not easy to examine the effect of confining pressure on the characteristics of sand in dynamic loading in the shaking table test under 1 g condition.

In the present study, several shaking table tests using a centrifuge apparatus were conducted to investigate the effect of confining pressure on the permanent ground displacement, in a procedure similar to the test proposed by Yasuda et al. (1992).

### 2. SAMPLE AND TEST APPARATUS

The sand used in this study is F-75 sand with a grain size distribution as shown in Fig. 1. The sand is a rounded and clean quartz sand and white in color. The specific gravity of the sand is 2.65, the mean particle size is 0.185 mm and the uniformity coefficient is 1.79. The maximum and minimum

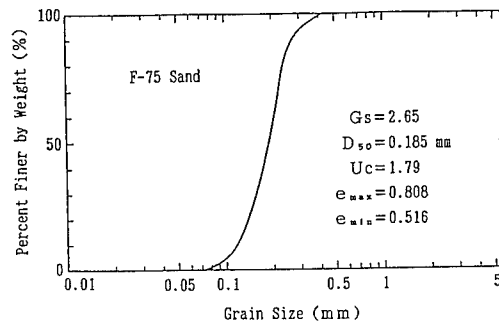


Fig. 1 Grain size distribution curve of F-75 sand

void ratios are 0.808 and 0.516, respectively.

The 400 g-ton centrifuge facility installed at the University of Colorado at Boulder was used in the present study. The top of the swing platform is at a radius of 5.49m. A maximum payload with a mass of 2tf can be carried on the platform. The centrifuge apparatus is capable of accelerating the payload to a maximum of 200 g. An in-flight shaking table, which is mounted on the swing platform was used to simulate earthquakes. The system is based on the development of electro-hydraulic servo valves and its description can be found elsewhere (Ketcham, 1989).

A laminar soil container was used in the centrifuge experiments. This device was previously described by Law et al. (1991) and is shown schematically in Fig. 2. Its inside dimensions are 58cm in length, 24cm in width and 17cm in depth. The container is composed of 12 rectangular aluminum plates

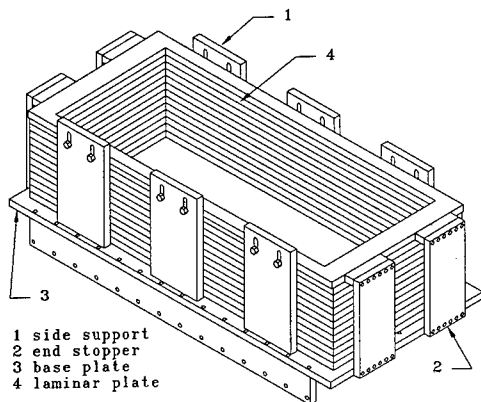


Fig.2 Schematic orthogonal view of the laminar container

stacked on the base plate, as shown in Fig.2. The laminar plates are guided by the side and end supports, and several linear bearings are inserted between adjacent laminar plates, in order to reduce the friction between them. Inside the container, a double-layer latex membrane was installed to prevent leaking of water from the laminated layers.

### 3. TEST PROCEDURES

Fig.3 shows the model ground used for the tests. The following procedure is used to make the ground and to conduct the shaking table test. (1) The base ground with a desired slope angle is made by compacting F-75 sand under moist conditions. (2) The dry F-75 sand contained in a relatively large funnel is air-pluviated through a sieve with an opening of 2.0mm. The height for the air-pluviation was determined to obtain the model ground with a desired relative density of 30 %. Thus, the liquefied

layer shown in Fig.3 can be defined as a loose sand layer which is supposed to be sensitive to liquefaction. (3) During pluviation, several accelerometers and pore pressure gauges are installed in the ground. (4) After the model ground is saturated by slowly supplying water from a stand pipe at a corner near the lower end of the slope, the surface of the model ground is flattened to form a desired sloping angle. (5) The soil container is moved on to the shaking table, after letting it stand for about 15 hours. It is considered that the models were nearly saturated by thus steeping sand in water for about 15 hours, with no vacuum pressure. Then, eleven thumbtacks are placed at regular intervals to measure the permanent ground displacement on the surface. (6) Eleven dry chinese noodle sticks are inserted into the ground at regular intervals and the positions of the eleven thumbtacks are measured. (7) The centrifuge is operated at a desired spinning acceleration, after one hour is allowed for the noodles to be softened. (8) The spinning is continued for 5 to 10 minutes and the shaking table test is performed. The centrifuge is stopped 5 minutes after the shaking table test. (9) The soil container is removed and the positions of the thumbtacks are measured. (10) The positions of the noodles are examined carefully by digging into the ground.

The test conditions are shown in Table 1. Two spinning accelerations of 20 g and 80 g are adopted, and either sloping angle of 5% or 10% is used for both the ground surface and the bottom surface of the liquefied layer. A sine wave motion with about ten cycles is introduced to the model ground during the shaking table test.

For the similitude rule, the scaling relations indicated by Ko (1988) were applied to the test results. Therefore, it is necessary to keep the shear stress ratio,  $\tau/\sigma_v' (= \alpha/g)$ , constant for such liquefaction problems, and to increase the frequency of

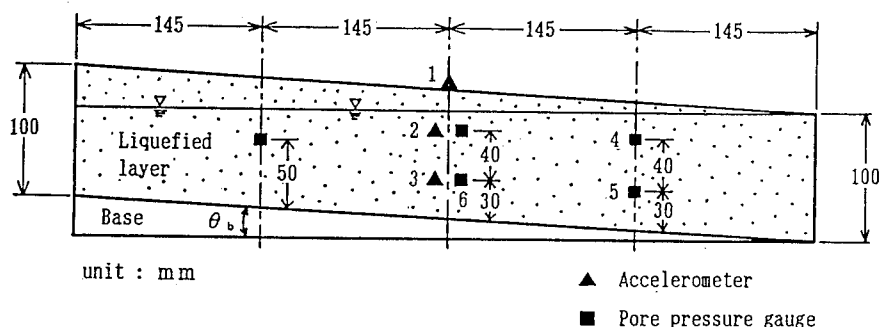


Fig.3 Soil model and location of transducers

Table 1 Test conditions

Test No.	Slope angle $\theta$ , (%)	Spinning acceleration (g)	Relative density $D_r$ (%)
1	5	20	34.0
2	10	20	17.7
3	10	20	41.4
4	5	80	27.9
5	10	80	31.7
6	5	20	43.6
7	10	80	30.0
9	10	20	36.6

base motion introduced under  $n$  g condition by  $n$  times that under 1 g, where  $\tau$  is shear stress,  $\sigma_v$  is vertical effective stress,  $\sigma$  is horizontal acceleration and  $g$  is gravitational acceleration. From the similitude rule, the amplitude and the frequency of the base motion used in the centrifuge experiments were targeted to be 5 g and 60 Hz under a spinning acceleration of 20 g, and 20 g and 240 Hz under that of 80 g, respectively, if prototype 10-cycle sinusoidal stress, having stress ratio of 0.25 at a frequency of 3 Hz is imposed on the models.

#### 4. TEST RESULTS

Time histories of the data obtained by Test 1 are shown in Figs.4(a) to (g). The figures (a) to (c) and (d) indicate the time histories of acceleration recorded at points 1 to 3 shown in Fig.3 and acceleration

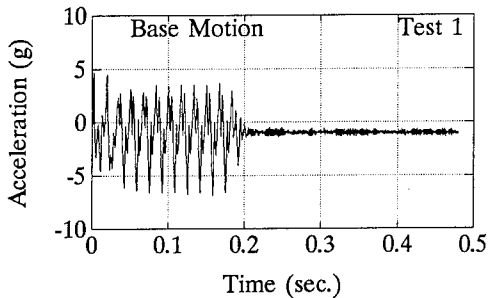
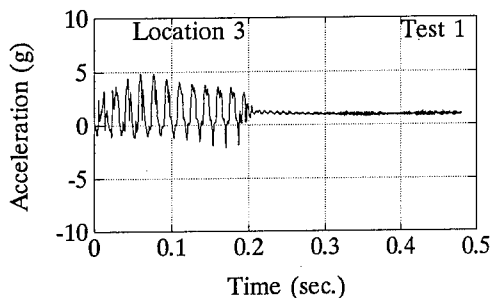
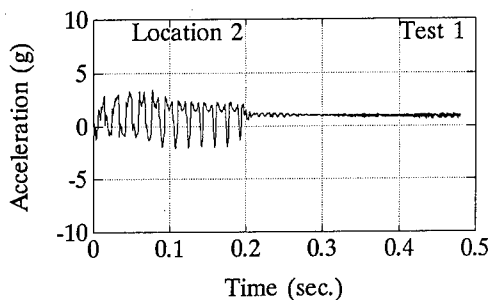
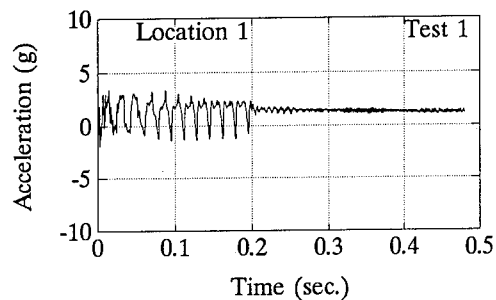
of the shaking table, which is considered to be the base input motion. The time histories of pore water pressure measured at points of 4 to 6 as shown in Fig.3 are also demonstrated in the figures of (e) to (g).

In Test 1, the magnitude of the maximum pore water pressure ratio almost becomes 1.0, because the applied base motion is relatively large and close to the desired amplitude of 5 g as shown in Fig.4(d). However, it seems to be caused by a small amount of floatation of pore pressure gauges during liquefaction that the magnitude of the maximum pressure ratio is not equal to 1.0 exactly. Therefore, it can be seen that liquefaction occurred approximately in the entire loose sand layer of the model ground. Moreover, the accelerations propagated to the liquefied layer from the base are prominently biased to the positive direction, as shown in Figs.4(a) to (c). It is supposed that the accelerometers used to measure those data could not catch up with the movement in that one direction during shaking. The test results are summarized in Table 2. Liquefaction occurred under 20 g spinning acceleration, although liquefaction did not occur under 80 g. The latter seemed to be due to the fact that the amplitudes of the accelerations introduced to the shaking table were smaller than the desired value and the similitude rule on drainage time was not satisfied with the test condition, in which water was used as the pore water in the model ground.

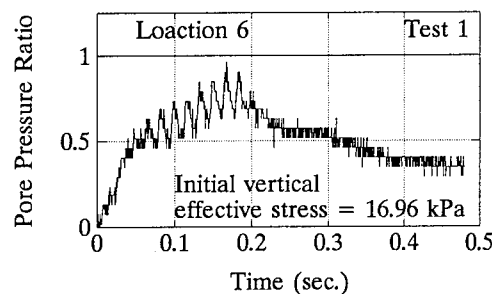
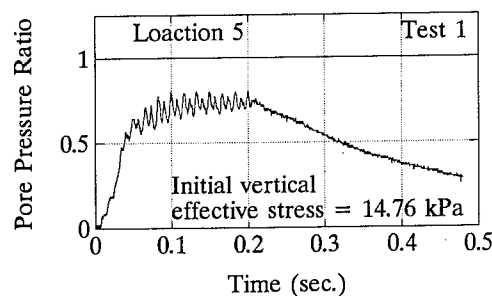
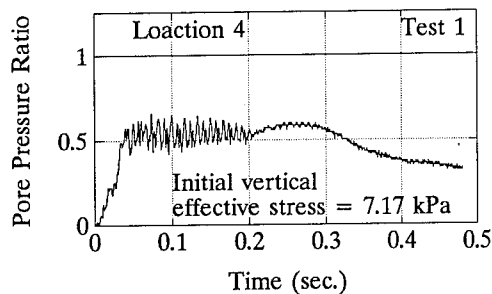
Fig.5 shows the deformation profiles measured by the final positions of the chinese noodles in Test 1, 4, 7 and 9. In test 1, the permanent ground displacement in the center of the container occurred upslope at the ground surface and downslope in the middle of the liquefied layer. However, the permanent ground displacement did not

Table 2 Test results

Test No.	Average value of acceleration of the base motion (g)	Liquefaction occurred or not	Average value of permanent displacement measured by thumbtacks on the ground surface (mm)	Average value of settlement measured by thumbtacks on the ground surface (mm)
1	5.0	occurred	4.3	1.7
2	2.9	not	9.3	3.3
3	9.2	occurred	12.7	3.0
4	12.0	not	1.0	1.0
5	12.7	not	2.7	2.0
6	3.5	occurred	1.8	2.0
7	16.6	not	6.3	1.5
9	6.5	occurred	21.5	8.0



Figs.4(a)-(d) Time histories of acceleration measured during and after shaking



Figs.4(e)-(g) Time histories of pore water pressure ratio measured during and after shaking

occur at the boundary between the liquefied layer and the non-liquefied layer. In the vicinity of the edge of the container, the displacement was restricted especially at the lower end. In Test 9, the permanent ground displacement with a relatively constant shear strain seem to occur due to liquefaction of a whole layer, except in the vicinity of both ends. Thus, it seems that the displacement in the center of the container occurred without the restriction of both ends of the slope, because the displacement in that region took place almost uniformly. On the contrary, liquefaction did not occur sufficiently to induce large

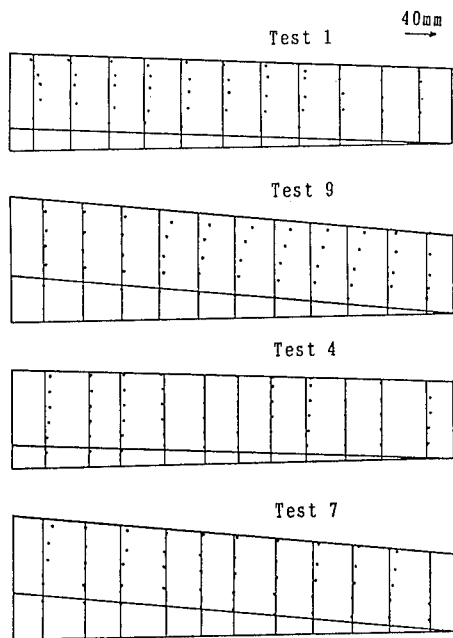


Fig.5 Final positions of chinese noodles in the liquefied layer in Test 1, 4, 7 and 9

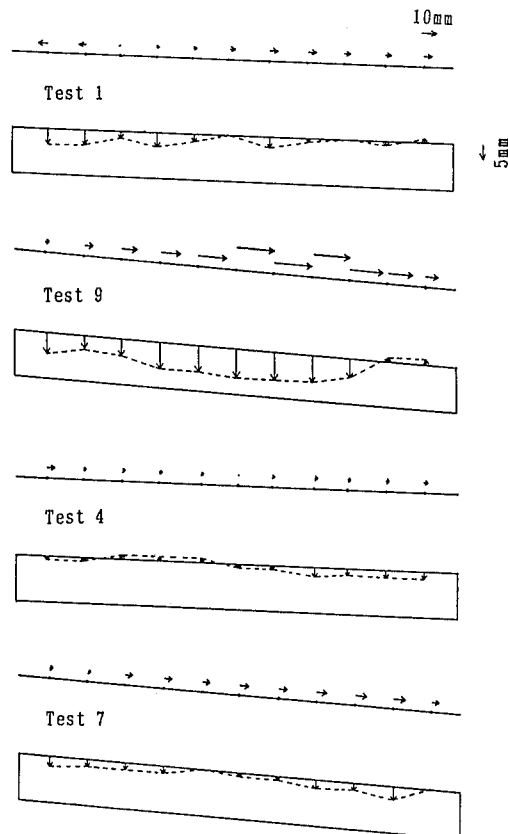


Fig.6 Permanent ground displacements and settlements at the ground surface observed by thumbtacks in Test 1, 4, 7 and 9

permanent ground displacements in Tests 4 and 7 under 80 g. However, it seems that the permanent displacement in those tests were induced by shear deformation in the whole liquefied layer. It can also be observed in Tests 4 and 7 that several permanent displacements sections shown in Fig.5 indicate the deformations in the upslope direction. This could be the results of the back-and-forth motion, induced by the sinusoidal excitation, that happened to stop during the upslope motion. Permanent displacements and settlements measured by the thumbtacks on the ground surface are shown in Fig.6. The permanent displacement at the ground surface was large, if the loose sand layer was liquefied, as shown in the data of Test 9. The settlement at the ground surface was large in the upper area of the slope, while it was small or negative value in the lower area in the case of the tests where liquefaction occurred. On the contrary, the settlement took place uniformly if liquefaction did not occur as in Tests 4 and 7.

Fig.7 indicates the relationship between the amount of the permanent ground displacement,  $D_s$ , measured by thumbtacks and the thickness of the liquefied layer,  $H$  on a log-log graph paper. The permanent ground displacement plotted is the average

value of 6 data points obtained from the center of the container. The average value of the permanent ground displacement and the thickness of the liquefied layer are shown in prototype scale in Fig.7. B-1 to B-4 and G-3 to G-4 are the data obtained by Yasuda et al. (1992). A straight line is drawn on the basis of the data of B-1, B-3 and B-4. In Fig.7 are also shown the test conditions in terms of relative density,  $D_r$  and slope angle,  $\theta_b$ . The data obtained by the present tests are shown with the test numbers in parentheses. It can be seen from this figure that straight lines parallel to the line obtained by Yasuda et al. (1992) can be drawn through the data points of G-3 and (1) obtained under the condition with a relative density of 35 % and a slope angle of 5%, and through G-4 and (9) obtained under the condition with a relative density of 35 % and a slope angle of 10 %. This result means that there is a relationship between the permanent displacement and the

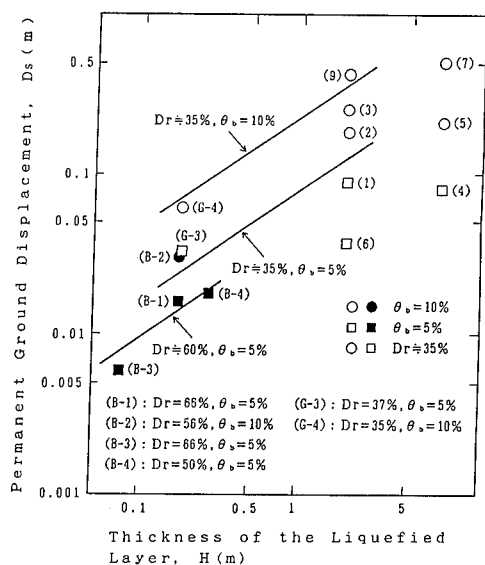


Fig.7 Permanent ground displacement and thickness of the liquefied layer shown in prototype scale

thickness of the liquefied layer as follows

$$D_s \propto a \cdot H^b \quad \text{----- Eq.1}$$

where  $a$  and  $b$  denote material constants. The magnitude of the permanent ground displacement can be considered to be the maximum value, because liquefaction occurred in both tests of (1) and (9). It can be considered that the formula is identified with the empirical equation obtained by Hamada et al. (1986a,b). Furthermore, " $a$ " in Eq.1 is supposed to be a material constant determined by the values of relative density and slope angle. However, in the tests of G-3 and G-4, the model ground was subjected to the horizontal acceleration in the direction perpendicular to the slope. For the effect of the shaking direction, it was shown by Sasaki et al. (1992) that the direction of the permanent displacement is independent of the direction of the seismic inertia force. Moreover, it may be noted that the permanent ground displacement does not generally occur with a constant shear strain in the liquefied sand layer, because " $b$ " in Eq.1, which indicates the inclination of the straight line shown in Fig.7, is not equal to 1.0.

## 5. CONCLUSIONS

In the present study, the effect of confining pressure on the permanent displacement due to liquefaction was investigated by performing several shaking table tests using

a centrifuge apparatus. Several conclusions are obtained as follows.

- (1) The permanent displacement occurs in the whole liquefied layer with a shear strain even under 20 g and 80 g condition.
- (2) The relationship between the permanent ground displacement and the thickness of the liquefied layer indicates a straight line on log-log graph paper, if the relative density and the slope angle of the model ground are constant.
- (3) The permanent ground displacement does not generally occur with a constant shear strain in the liquefied sand layer, because the inclination of the straight line is not equal to 1.0.

## REFERENCES

- Hamada, M., Yasuda, S., Isoyama, R. and Emoto, K., "Study on Liquefaction Induced Permanent Ground Displacement," Association for the Development of Earthquake Prediction, 1986a, Tokyo, Japan.
- Hamada, M., Yasuda, S., Isoyama, R. and Emoto, K., "Observation of Permanent Ground Displacement Induced by Soil Liquefaction," Proc. of Japan Society of Civil Engineering, No.376, III-6, 1986b, pp.211-220 (in Japanese).
- Ishihara, K., Verdugo, R. and Acacio, A. A., "Characterization of cyclic behavior of sand and post-seismic stability analyses," IX Asian Regional Conference on Soil Mechanics and Foundation Engineering, Bangkok, Thailand, 1991.
- Ketcham, S., "Development of an Earthquake Motion Simulator for Centrifuge Testing and the Dynamic Response of a Model Sand Embankment," Ph.D. Thesis, University of Colorado, Boulder, CO, 1989.
- Ko, H. -Y., "The Colorado Centrifuge Facility," Centrifuges in Soil Mechanics, 1988, pp.73-75.
- Ko, H. -Y., "Summary of the State-of-Art in Centrifuge Model Testing, Centrifuges in Soil Mechanics, 1988, pp.11-18.
- Law, H., Ko, H.-Y., Sture, S., and Pak, R., "Development and Performance of a Laminar Container for Earthquake Liquefaction Studies," Centrifuge 91, Balkema Publ., 1991, pp.369-376.
- Sasaki, Y., Towhata, I., Tokida, K., Yamada, K., Matsumoto, H., Tomari, Y. and Saya, S., "Mechanism of Permanent Displacement of Ground Caused by Seismic Liquefaction," Soils and Foundations, Vol.32, No.3, 1992, pp.79-96.
- Yasuda, S., Nagase, H., Kiku, H. and Uchida, Y., "The mechanism and a simplified procedure for the analysis of permanent ground displacement due to liquefaction," Soils and Foundations, Vol.32, No.1, 1992, pp.149-160.

## Simulation of O'Neill Forebay Dam, California, subjected to the 1989 Loma Prieta Earthquake

Hubert K. Law & Hon-Yim Ko

University of Colorado, Boulder, Colo., USA

Robert Scavuzzo

Science Application International, Lakewood, Colo., USA (Formerly: Bureau of Reclamation, Denver, Colo., USA)

**ABSTRACT:** On October 17, 1989, a magnitude 7.1 earthquake that occurred in a sparsely settled portion of the Santa Cruz mountains triggered several transducers embedded in the near-by dams that are owned and operated by the Bureau of Reclamation. The information collected by the event provides excellent opportunities for centrifuge modeling which, in many cases, lacks comparisons with field data especially in the case of earthquake loading. Four model embankment dams were tested to simulate the field event of the earthquake and the tests were conducted under three different  $g$  levels and model sizes. In the comparison among the model tests, it was found that the modeling-of-models was achieved satisfactorily and thus reliability of the test data was ascertained. The model results were then compared with the field data from the O'Neill Forebay Dam. A good agreement was found between the centrifuge model tests and the prototype dam.

### 1 INTRODUCTION

This research program studied the effects of the October 17, 1989 Loma Prieta earthquake ( $M_s = 7.1$ ) on water-storage dams in central California. During the earthquake, several accelerometers which were placed in the structures as a part of the instrumentation program of the Bureau of Reclamation were triggered and recorded motions. The instruments were located at four water storage facilities; namely Martinez Dam, San Justo Dam and Diike, O'Neill Forebay Dam, and San Luis Dam. Peak horizontal acceleration on the crest of the dam closest to the epicenter (San Justo) reached nearly 0.5  $g$ . This field data provided valuable information which could be compared with centrifuge model test results. Fig. 1 is a map showing the location of the epicenter, instrumented sites, and geographic features. On the basis of the available records of the structure during the earthquake as well as the size of the structure itself in regards to our ability to model

it on the centrifuge, O'Neill Forebay Dam was chosen for the simulation. This structure is 60 ft. tall, 400 ft. wide at the toe, and 35 ft. wide at the crest. Fig. 2 shows the cross-section of O'Neill Forebay Dam and locations of instruments (sm-1 through sm-4). The dam is a homogeneous structure. Even though instrument sm-4 was not

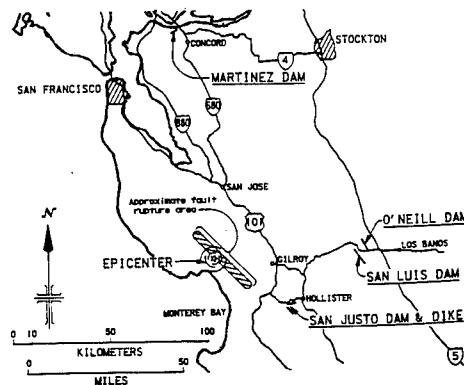


Fig. 1 Site location map. Source: Wood et. al., 1991.

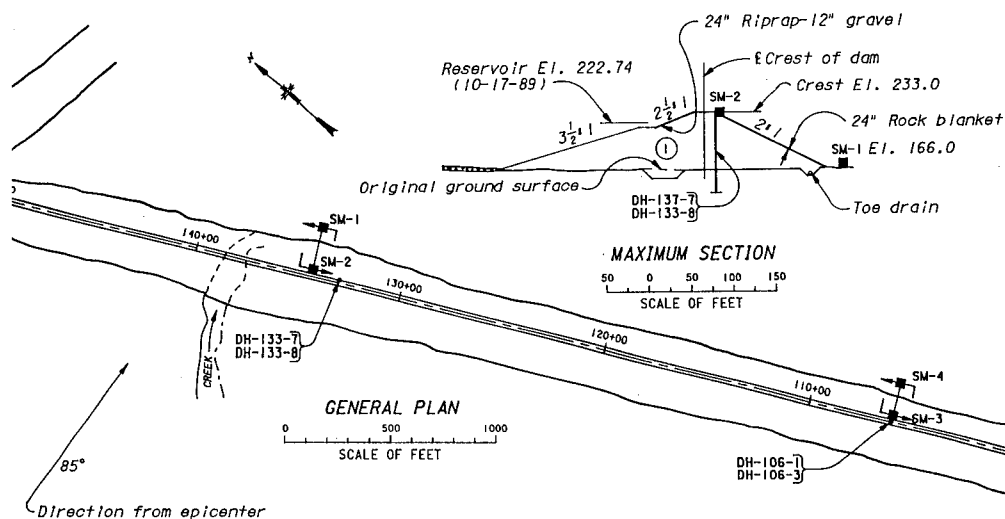


Fig. 2 Cross section of O'Neill Forebay Dam and transducer locations. Source: Wood et al., 1991.

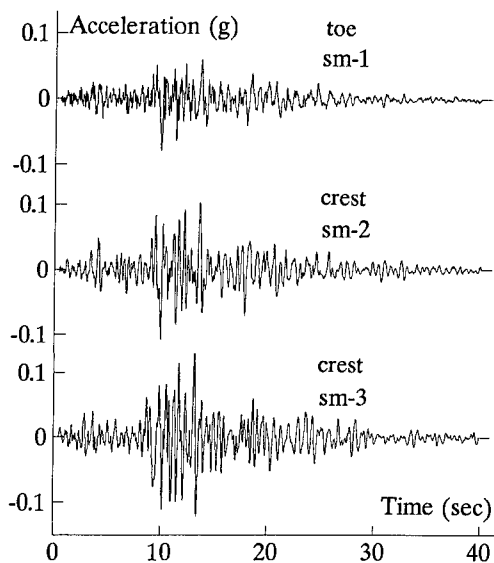


Fig. 3 Field measurements. Source: Wood et al., 1991.

Table 1 Summary of the experiments.

Test	G level	Peak base acceleration	Duration of earthquake
Test A	100	7.59 g	0.56 sec
Test B	125	11.54 g	0.45 sec
Test C	125	9.15 g	0.45 sec
Test D	150	12.34 g	0.37 sec

triggered during the earthquake, others did produce useful data which are shown in Fig. 3.

## 2 EXPERIMENTAL PROGRAM

We have conducted four model experiments in the 400 g-ton centrifuge at the University of Colorado. The experimental program is summarized in Table 1 indicating G level of the operation, peak base acceleration, and the duration of earthquake in the experiment. Since three different centrifugal acceleration levels (100, 125, and 150 g) were involved, the physical dimensions and the input base accelerations of the models were scaled for each centrifugal g level according to the scaling relations generally applied in modeling of earthquake problems. An attempt was made to reproduce the motion recorded by the field accelerometer sm-1 during the 1989 Loma Prieta Earthquake on the centrifuge shake table for each scale test. The shake table which is now mounted on the 400 g-ton centrifuge is an electro-hydraulic servo-controlled system and is described by Ketcham and others (1991). Fig. 4 shows the results of this attempt to generate the motion of the shake table for the 100th scale. Because of the limited space, those for the 125th and 150th scales are not presented here. The model base motions were compared with the prototype base motion in terms of response spectra and Fourier magnitudes, and the comparison was reasonably good. The



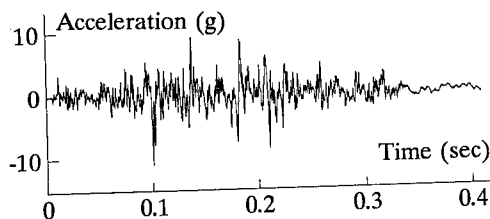


Fig. 4 Motion of the shake table.

detailed comparison is described by Ko and Law, 1993.

To accommodate the scaled model of the 400 ft wide embankment dam, a container having inside dimensions of 48 in. long, 12 in. wide, and 9 in. high was constructed. Three different sizes of wooden molds which serve as the casts for the model dams were prepared; all provided the same shape as the O'Neill Forebay Dam. By stacking wooden blocks, the mold eventually forms the outer shape of the model dam. The soil was the natural material obtained from the field and was used to construct O'Neill Forebay Dam. It is classified as clayey sand with gravel, SC group, and PI of 8; but only the portion passing no. 4 sieve was used in the model. The soil was premixed at 15.2 % moisture content corresponding to 85 % saturation and the mixture was placed in the mold and was compacted in layers by tamping with a steel block. The weight of each layer was calculated to produce a uniform wet density of 134 pcf. These moisture content and soil density were based on the bore hole information obtained near station sm-3 in order to reproduce the properties in the field. Transducers were embedded at the designated layer during the model construction. Upon the completion of the model construction, the wooden blocks of the mold were removed.

After the model was placed on the shake table in the centrifuge, the machine was slowly accelerated to the targeted G level (100, 125, or 150 g) to allow time for consolidation to take place under the soil's own weight. After about 2 to 3 hours of spinning, the centrifuge was stopped for a short period of time for filling the upstream side of the dam with water. The water levels are shown in Fig. 5 which correspond to the field condition when the 1989 Loma Prieta Earthquake shook the structure. The centrifuge was again accelerated to the designated G level and the

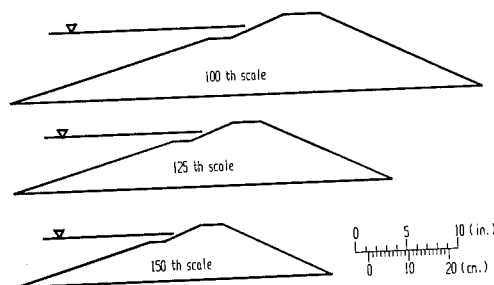


Fig. 5 Model dimensions.

earthquake was triggered to shake the model. There was no sign of failure of the dam model after the earthquake in any experiment.

The question arose regarding the development of steady state seepage conditions in the dam. To examine the feasibility of modeling such conditions, a separate centrifuge experiment was carried out to determine the time needed to reach steady state flow in the dam model. The results indicated that it was impossible to obtain the condition in any reasonable laboratory time frame, due to the low permeability of the soil ( $10^{-9}$  m/sec). Therefore, no attempt was made to achieve the steady state seepage flow in the model dam prior to shaking of the structure.

### 3 RESULTS

Since the measurements in the first test (Test A) indicated that no measurable pore pressures were generated during the shaking, primarily due to the fact that the soil was only about 85 % saturated, no pore pressure transducers were used in the subsequent experiments. There were several accelerometers (up to 11) employed in each model test. However, only the data from the base and crest motions are discussed in this paper, because the field measurements which will be used to compare the test results, are available only at those locations.

The prototype cross section at which accelerographs sm-1 and sm-2 are located is designated as section S-1-2, and section S-3-4 for accelerographs sm-3 and sm-4. During the earthquake, sm-4 failed to trigger, therefore section S-1-2 was selected as a primary candidate for the comparison with the models despite the

fact that the material properties of the models were based on the drill hole data at section S-3-4. Fig. 6-a shows the peak values of the base and crest accelerations from the field and lab results plotted against g levels. The dashed line, having a slope N (the modeling scale), is the extrapolation of the field result from sm-1 according to the scaling laws. For ideal experiments, the maximum base accelerations of the model experiments would have plotted on the dashed line. The results shown in Fig. 6-a demonstrate that the targeted maximum base accelerations were obtained with reasonable accuracy in the four model experiments. Similarly, the solid line is the extrapolation of the field results from sm-2 according to the scaling law. It can be seen that the maximum crest accelerations measured on the four models were higher than the values expected from extrapolation of sm-2. In order to take into account the discrepancy of input accelerations from the ideal case, amplification factors (crest acceleration divided by base acceleration) were calculated and plotted as shown in Fig. 6-b. These amplification factors of the four model experiments are consistent, with an average value of 1.65, which however is higher than the value of 1.35 for the prototype obtained from the measurements of sm-1 and sm-2. This makes us believe that all the model dams were somewhat softer and more flexible than the prototype structure at section S-1-2.

In addition to defining the amplification factor by using a single maximum value from the entire time history, the response spectra of the various motions can also be utilized. The response spectra of base and crest motions were computed for each case including the field measurements from section S-1-2. Fig. 7 shows these response spectra presented in the prototype scale with 5 percent damping. The reason for presenting them in the prototype scale is that the response spectra is a tripartite plot showing displacement, velocity and acceleration together; each of these quantities has a different scaling factor and, therefore, the figure would be highly distorted if presented in the model scale. The response spectra of the crest motions (Fig. 7-b) were then compared with those of the base motions (Fig. 7-a). For all the model experiments, the spectral velocities of the crest motions are about 2 to 3 times higher than those

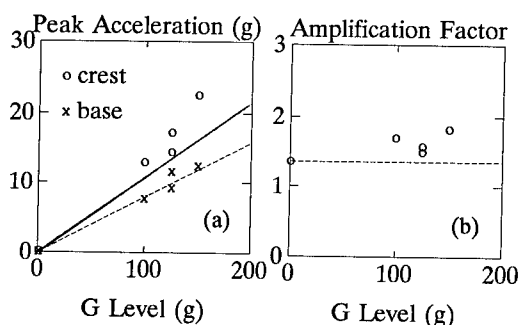


Fig. 6 Comparisons of the peak accelerations of the model tests with section S-1-2.

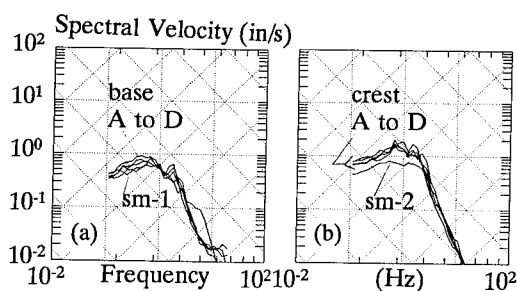


Fig. 7 Comparisons of the response spectra of the models test with section S-1-2.

of the base motions in the range of 0.1 to 3 Hz, and the model tests are consistent with each other. However, for the field measurements of sm-1 and sm-2, the ratio of spectral velocities of the crest motion to base motions is only about 1.3.

In the comparison of section S-1-2 with the model tests, the assumption of a homogeneous material along the dam's longitudinal direction and throughout the cross section was made. The geologic log data from the drill hole near station sm-3, which is the only drill hole data available in the region, indeed shows a homogeneous cross section, and therefore the soil density and moisture content from this information were used to construct the test models in all the experiments. But it is not entirely appropriate to compare the responses of the models, whose properties matched with prototype section S-3-4 to those of section S-1-2, because we later realized that there were variations of soil properties from one cross section to another in the prototype dam. The variations of soil properties were indeed confirmed by the in-situ shear wave velocity profiles obtained by the crosshole method for

sections S-1-2 and S-3-4, as shown in Fig. 8. These profiles clearly show much higher velocities, and hence higher stiffness, at section S-1-2 than section S-3-4. Therefore, the comparison of the model responses should be made with section S-3-4. Unfortunately, sm-4 which is located at the toe of the dam section S-3-4 did not give useful data during the Loma Prieta Earthquake. However, it is not unreasonable to assume that the motions at sm-4 and sm-1 would be similar since the two stations are only 3000 ft. apart and underlain by an alluvium formation and there is no superstructure near the stations.

Assuming the prototype base motion of section S-3-4 to be the same as the measurement of sm-1, the behaviors of section S-3-4 were compared with the performances of the model tests. Fig. 9-a is a plot showing the peak crest accelerations of sm-3 (prototype) and the scaled model tests along with a dashed line of a slope  $N$ , the scaling factor, to express an ideal modeling-of-models situation. From this the plot, it is evident that the models simulate the field behavior reasonably well at S-3-4 since the model crest accelerations are close to the solid line. The crest amplification factors of section S-3-4 and models were computed and are plotted on Fig. 9-b. The average amplification factor of the four model tests is 1.65, and the value of the prototype section is 1.7. The response spectra of the model test results are compared with sm-3 (Fig. 10) and it can be seen that the spectral velocity of sm-3 is more similar to those of model tests than sm-2 is in Fig 7-b. It appears that the model test results agree better with the prototype dam at section S-3-4.

The transfer functions between base and crest motions were computed, as shown in Fig. 11, for the prototype (section S-1-2 and S-3-4) and the four model tests. They are only plotted in the frequency range where significant energy of the base motion is present. A smooth curve is drawn on each of these plots to curve fit the transfer function. The curve fitting was not done numerically, but rather it was hand-drawn based on the authors' engineering judgement. There is a peak on the fitted curve which indicates the natural frequency of the fundamental mode of the structure. We expect the peak of the transfer function to be broad and, if there is more than one peak present, they are far apart because earth materials have high damping ratio and low

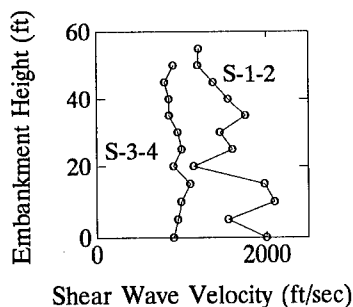


Fig. 8 Shear wave velocity profiles at sections S-1-2 and S-3-4. Source: Wood et. al., 1991.

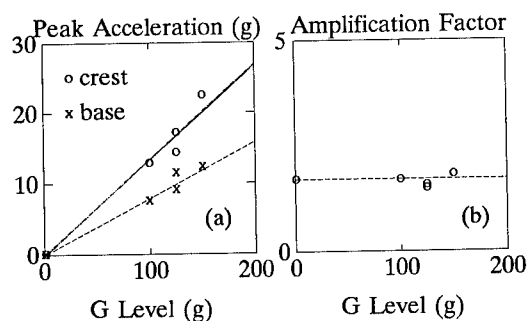


Fig. 9 Comparisons of the peak accelerations of the model tests with section S-3-4.

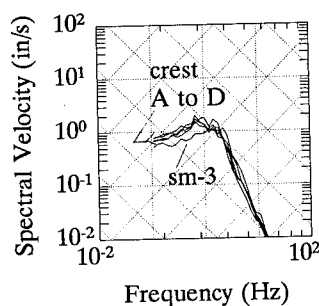


Fig. 10 Comparisons of the response spectra of the models test with section S-3-4.

stiffness. The corresponding frequencies of the transfer function peaks for the 100th, 125th, and 150th model tests are at 155 Hz, 180 Hz, and 195 Hz, respectively. These values reflect fundamental natural frequencies of 1.55 Hz, 1.44 Hz, and 1.3 Hz in the prototype scale. These values are close to the value of section S-3-4 (1.6), but they are significantly lower than the fundamental natural frequency of section S-1-2 which occurred at 2.3 Hz.

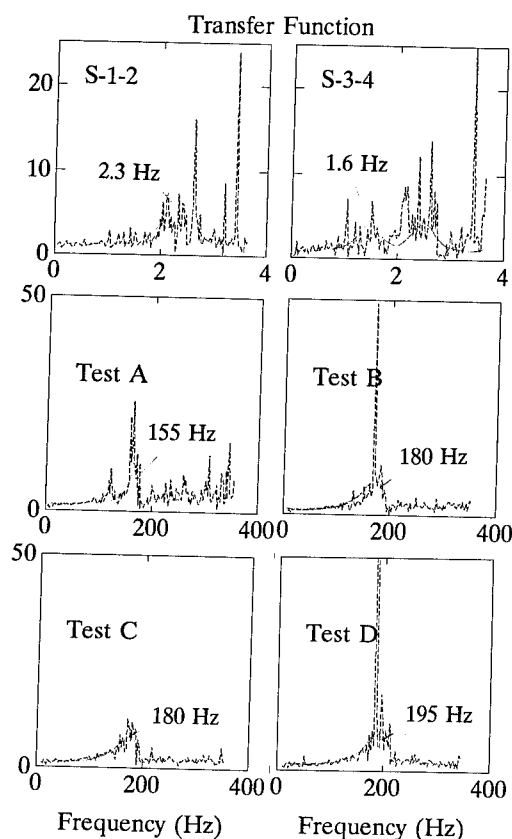


Fig. 11 Transfer functions.

#### 4 CONCLUSIONS

Comparing the model experiments from three different  $g$  levels, the results were very consistent and the modeling-of-models was considered to be successful. Regarding modeling of the prototype, there are two instrumented cross sections in the prototype dam embankment; neither of the cross sections has a complete set of information for comparison with the models, i.e., one does not have a soil property profile, and the other does not have the record of base motion during the earthquake. Field data indicate that soil properties are different in these two sections. Assuming that the base motion at the embankment's toe is the same everywhere, the model behaviors compare reasonable well (for practical purpose) with the prototype responses at one of the sections whose

properties matched those of model dams. The other cross section which the model tests failed to simulate, however, seems to be considerably stiffer according to the shear wave velocity profile; it may contain significant amounts of gravel and boulders, but this information is not available. In general, both modeling-of-models and modeling-of-prototypes were successful, and thus the measurements at other locations in the models which are not presented here can be used to study the prototype responses that are not available in the field otherwise.

#### REFERENCE

- S. Ketcham, H. Ko, and S. Sture, "Performance of an Earthquake Motion Simulator for a Small Centrifuge," Centrifuge 91, Boulder, CO, 1991, pp-361-368.
- H. Ko and H. Law, "Simulation of Field Performance of Earth Structure under Earthquake Loading by Centrifuge Testing," Final Report to the Bureau of Reclamation, Denver, CO, 1993.
- The Governor's Board of Inquiry on the 1989 Loma Prieta Earthquake, "Competing Against Time", Report to Governor George Deukmejian of California, May 1990.
- C. Wood, D. Copeland, and A. Veksne, "Strong Motion Data: Loma Prieta Earthquake of October 17, 1989", Bureau of Reclamation, Denver, CO, August 1991.

## Liquefaction of the ground reclaimed by urban refuse ash

H. Akamoto, M. Miyake, M. Wada & A. Maruyama

Technical Research Institute, Toyo Construction Co., Ltd, Hyogo, Japan

**ABSTRACT:** A series of centrifuge model tests was carried out to investigate the liquefaction of urban refuse ash ground. In order to investigate the influence of the hard surface layer, model tests were carried out for two conditions of ground. One condition of model ground consisted of five loose layers and the other consisted of a compacted surface layer (4cm) and four loose layers. The model tests were carried out under 50g, and 50Hz sinusoidal waves were applied. The duration of the vibration was 2 seconds and 0.5 seconds. There seems to be influence of a compacted surface layer on the process of dissipation of excess pore water pressure. No useful relationship was discovered between the vertical distribution of excess pore water pressures and the duration of the vibration.

### 1 INTRODUCTION

Recently in Japan, urban refuse has been incinerated and disposed of by coastal reclamation. The characteristics of urban refuse ash ground have not been previously investigated, so we have carried out electronic cone penetrometer tests and density logs with radio isotope on the reclaimed ground in the offing of Amagasaki. The reclaimed ground was found to be very loose and soft except for its

surface layer (at depth of 1 to 1.5m), which was dense and hard. Cyclic triaxial tests were conducted on isotropically-consolidated specimens of urban refuse ash. The volumetric strain of urban refuse ash subjected to vertical cyclic loading was very large and its liquefaction resistance was small (Iwatani, et al. 1992).

The purpose of this study is to investigate with centrifuge model tests how the urban refuse ash ground behaves when it is subjected to an earthquake.

### 2 CENTRIFUGE MODEL TESTS

#### 2.1 Earthquake simulator

The earthquake simulator consists of a double-acting oil cylinder, a piston and an electro-hydraulic servo valve (Akamoto, et al. 1989). An input wave is memorized in Read Only Memory (ROM). The servo valve then receives electrical signals from the ROM. A platform with a soil container is supported by a pair of linear bearings as shown in Fig.1. Table 1 shows the major specifications of the electro-hydraulic shaker.

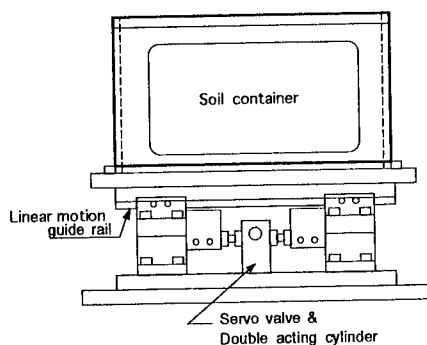


Fig.1 Electro-hydraulic shaker

Table 1 Major specifications of the electro-hydraulic shaker

Maximum shaking force	$\pm 2000 \text{ kgf/cm}^2$
Maximum displacement	$\pm 2.5 \text{ mm}$
Maximum frequency	100Hz
Maximum oil pressure	$210 \text{ kgf/cm}^2$

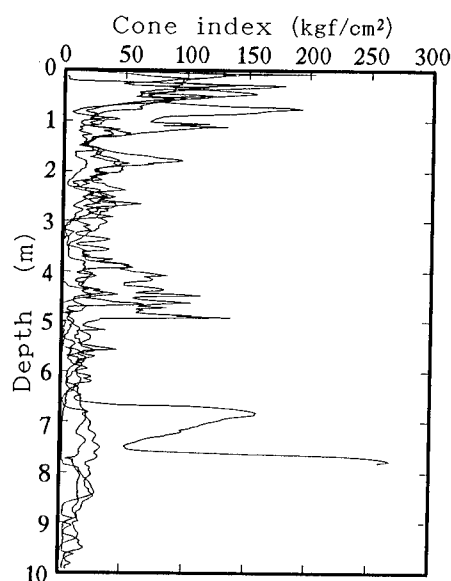


Fig.2 Vertical distribution of cone index

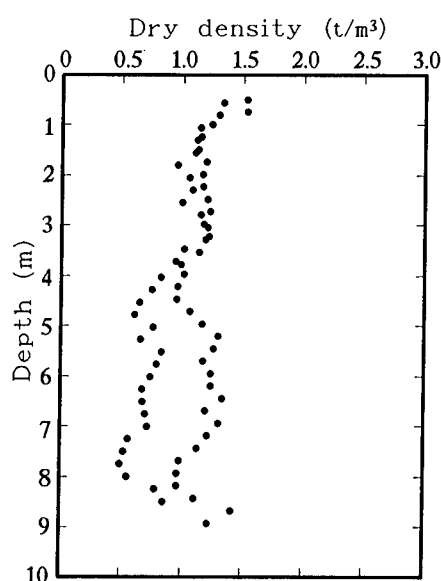


Fig.3 Vertical distribution of dry density

## 2.2 Characteristics of urban refuse ash ground

Electronic cone penetrometer tests were carried out at 4 locations on the reclaimed ground in the offing of Amagasaki in order to investigate the characteristics of urban refuse ash ground. Fig.2 shows the vertical distributions of the resulting cone index. It was seen in Fig.2 that the ground surface layer (1 to 1.5m) was very hard and the values of its cone index ( $q_c$ ) were 100 to  $200 \text{ kgf/cm}^2$ . Density logs with radio isotopes were carried out at 2 locations at the same site. The vertical distributions of dry density are shown in Fig.3. The average value of dry density to 2m depth was  $1.214 \text{ t/m}^3$ . Below 2m, the average dry density decreased to  $0.987 \text{ t/m}^3$ .

## 2.3 Test conditions and procedures

The sample material was the urban refuse ash which constitutes the reclaimed ground in the offing of Amagasaki. Before model tests were performed, the ash was passed through a 4.76mm sieve, and the fraction not passing was discarded. The physical properties of the ash

Table 2 The physical properties of ash

Specific gravity	2.600
Maximum grain size (mm)	4.76
Mean grain size (mm)	0.58
Gravel fraction (%)	22.4
Sand fraction (%)	54.5
Silt fraction (%)	14.8
Clay fraction (%)	8.3

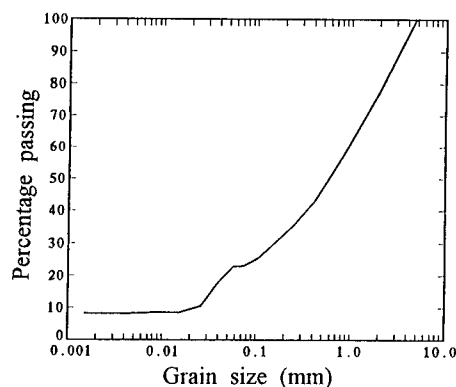


Fig.4 The grain size accumulation curve

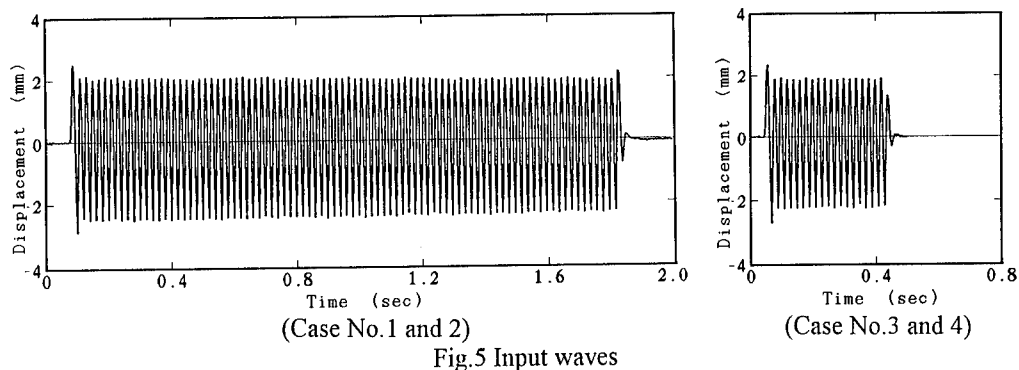


Fig.5 Input waves

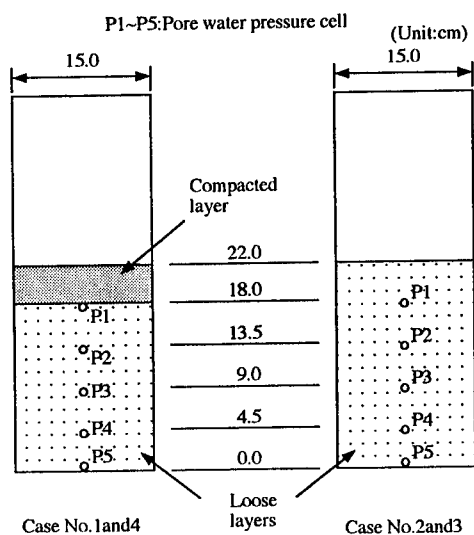


Fig.6 Model ground

thus prepared are shown in Table 2, and its grain size accumulation curve is shown in Fig.4.

The soil container for the model test is an aluminum box 600mm in length, 150mm in breadth and 400mm in depth. The front face contains a viewing window made of a high-strength plastic plate. In the model tests, 50Hz sinusoidal waves were applied under centrifugal acceleration of 50g. For the cases No.1 and No.2 the duration of the vibration was 2sec, and for the cases No.3 and No.4 it was 0.5sec. The input waves are shown in Fig.5.

The ash was mixed with a solution of Methylcellulose (coefficient of viscosity = 50cP); air was pulled out of the mixture in a vacuum tank. The ash was then poured into the soil container.

Table 3 Test conditions

Case No.	Ground condition	Duration of vibration(sec)
1	one compacted layer	2
2	five loose layers	2
3	five loose layers	0.5
4	one compacted layer	0.5

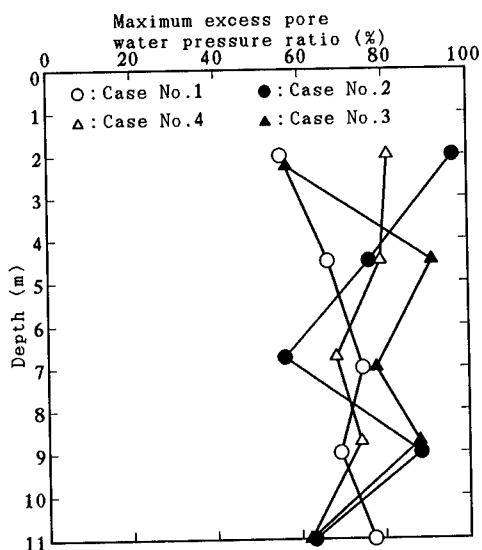


Fig.7 Vertical distribution of maximum excess pore water pressure ratios

The model ground consisted of five layers (each layer's height is 4 to 5cm), with a total height of 22cm. A preconsolidation pressure of 0.1kgf/cm<sup>2</sup> was applied to each layer, and a preconsolidation pressure of 0.2kgf/cm<sup>2</sup> was applied to the full-height model ground. In cases

No.1 and No.4 the model ground consisted of a compacted surface layer (4cm thick, with a dry density of  $\rho_d=1.2\text{t/m}^3$ ) and four loose layers (average dry density  $\rho_d=1.0\text{t/m}^3$ ). In the other cases the condition of the model ground consisted of five loose layers. In order to investigate the process of upturn and dissipation of excess pore water pressure, five pore pressure cells were installed at locations shown in Fig.6. The test conditions are summarized in Table 3.

### 3 TEST RESULTS AND CONSIDERATION

Fig.7 shows the vertical distribution of maximum excess pore water pressure ratios. In Fig.7, the depth is indicated in prototype scale. Fig.7 shows that the maximum excess pore water pressure ratios are distributed between 60 and 100% in any case. There appeared to be no distinction of the vertical distribution between the model ground conditions, and between the

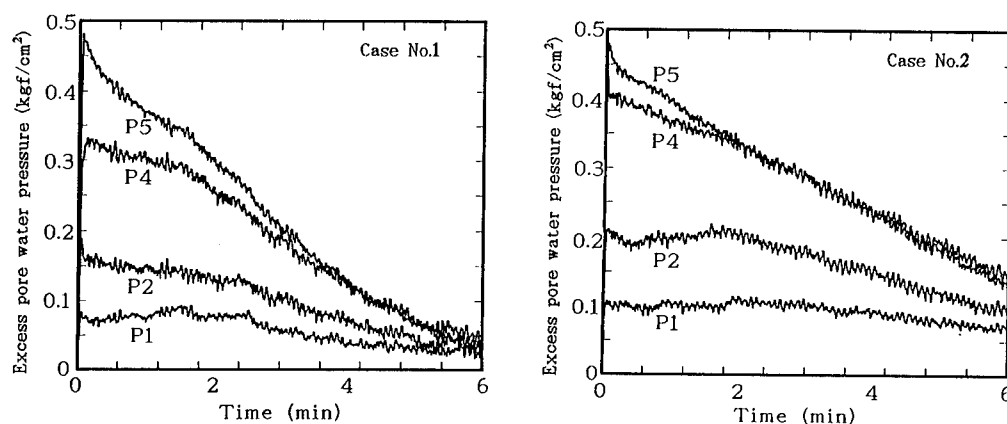


Fig.8 Time histories of excess pore water pressure

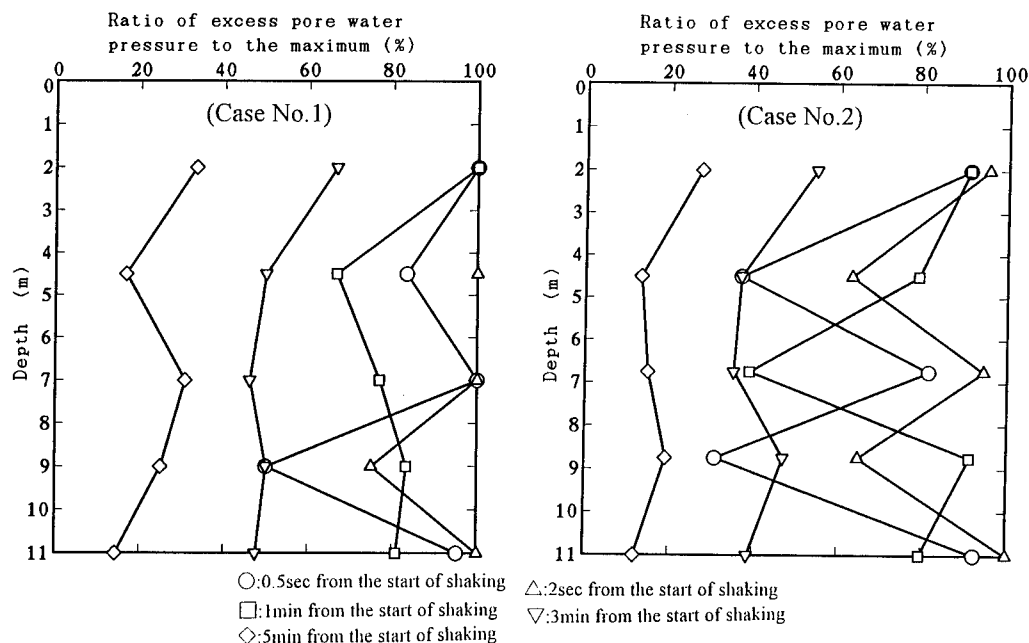


Fig.9 Isochrones of the ratio of excess pore water pressure to the maximum excess pore water pressure



durations of the vibration.

Fig.8 shows the time histories of excess pore water pressure in cases No.1 and No.2. Many small jumps contained in the time histories are noise. It could be seen from Fig.8 that the compacted surface layer had an influence on the process of dissipation of excess pore water pressure. This may be because the compacted surface layer is a partially saturated layer.

Fig.9 shows the isochrones of the ratio of excess pore water pressure to the maximum excess pore water pressure in cases No.1 and No.4. In case No.1 the excess pore water pressures observed at all layers reached their maximums at the end of the vibration. In case No.4 the excess pore water pressures did not reach their maximums after 2sec from the start of the vibration. The excess pore water pressures in case No.4 upturned a little slower than in case No.1. However, the excess pore water pressures in case No.4 dissipated somewhere faster than in case No.1. The excess pore water pressure at 9m depth upturned much slower than at other depths.

Amagasaki. Tsuchi-to-Kiso. JSSMFE. Vol.40, No.6, pp.5-10 (in Japanese).

#### 4 CONCLUSIONS

In this study, an attempt was made to investigate the liquefaction behavior of ground reclaimed by urban refuse ash. Some understanding derived from this study can be summarized as follows :

(1) There seems to be influence of a compacted surface layer on the process of dissipation of excess pore water pressure.

(2) No useful relationship was discovered between the vertical distribution of excess pore water pressures and the duration of the vibration.

Some more study is necessary to investigate the influence of the compacted surface layer on the process of dissipation of excess pore water pressure.

#### REFERENCES

- Akamoto, H. & Miyake, M. 1989. Development of a centrifuge earthquake simulator. Proc. 44th ACJSCE, 3, pp.14-15 (in Japanese).  
Iwatani, F., Miyake, M., Wada, M. & Maruyama, A. 1992. Mechanical Properties of Trash Ashes Dumped in Phoenix Area in the Offing

## Dynamic response of a shaft in dry sands

M. Honda, N. Ohbo, H. Hayashi & J. Zheng  
*Kajima Technical Research Institute, Tokyo, Japan*

R. F. Scott  
*California Institute of Technology, Pasadena, Calif., USA*

**ABSTRACT:** In order to study the dynamic behavior of a shaft in soil during earthquakes, dynamic centrifuge tests were carried out. Two types of models were taken up; (1) level ground of sand; and (2) a hollow shaft of two different depth embedded into the level ground. An effective boundary treatment method was presented so that the semi-infinite ground condition can be satisfied approximately. The effects of input level and shaft geometry on the response of shaft-soil system were discussed.

### 1 INTRODUCTION

The behavior of underground structures during earthquakes can be simulated on a centrifuge much more realistically compared with conventional model test. In view of the above, the seismic behavior of hollow shaft embedded in a dry sand deposit was modeled experimentally on a centrifuge at 1/50 scale in order to investigate the dynamic behavior of shaft-soil system during earthquakes. Main attention were given to the following two aspects: (1) to propose a boundary treatment method; (2) to study the effects of input motion level and shaft geometry on the response of shaft-soil system.

### 2 PRELIMINARY CENTRIFUGE TEST ON THE BOUNDARY TREATMENT

One of the problems in physical modeling of dynamic phenomena is that the model is bounded by the container walls, and the artificial boundaries at the end and side walls can significantly affect the response of ground model. Thus it is important to reduce both the end wall effects and the friction between side wall and the ground model<sup>(1)</sup>. In this section, a method to treat the boundary at the container walls is proposed. The verification of the proposed

boundary treatment method is also presented through both dynamic centrifuge tests and the 1-D numerical analysis<sup>(2)</sup>.

#### 2.1 Experiment arrangement

Silicone rubber was placed between sands and end wall, as shown in Fig.1, so that the shear deformation of the ground model would not be greatly affected by the end wall. The stiffness of silicone rubber is determined by preliminary numerical analysis. The Young's modulus of silicon rubber is 2.4kgf/cm<sup>2</sup>, and the damping ratio is 4.8%(at the first peak). These values

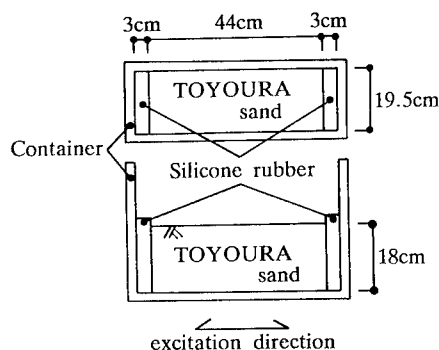


Fig.1 Outline of preliminary test

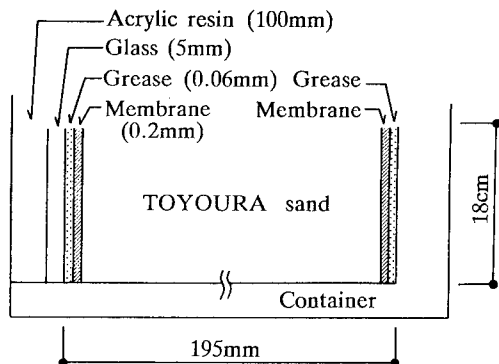


Fig.2 A section of container

Table.1 Preliminary test condition

	height of ground model h	relative density of ground model Dr	maximum acceleration of input motion
with boundary treatment	18.4cm	95.2%	1.5g
without boundary treatment	17.4cm	97.9%	1.8g

were obtained from 1g excitation tests of the silicone rubber. Rubber membrane was set up between sands and side walls with grease pasted along the interface between them, as shown in Fig. 2. The rubber membrane is supposed to move with the ground model, and the grease reduces the friction between rubber membrane and side walls.

To verify the proposed boundary treatment method, two types of the boundary conditions(with treatment and without treatment) were considered. Fig.1 shows the cut view of the experiment model. Table 1 shows the model condition and the maximum acceleration of input motion for two test cases with different boundary conditions. All tests were carried out under 50g centrifugal condition. The input signal for the shaker was intended to simulate the 1940 El Centro NS wave. The TOYOURA standard sand was pluviated through air directly into the container to be the model ground. Fig. 3 and Table 2 show the physical properties of TOYOURA standard sand.

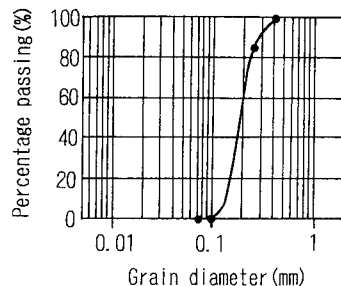


Fig.3 Grain size distribution of TOYOURA standard sand

Table.2 Physical properties of TOYOURA standard sand

Specific gravity	2.648
Bulk density - compacted	1.645 g/cm <sup>3</sup>
- uncompacted	1.335 g/cm <sup>3</sup>

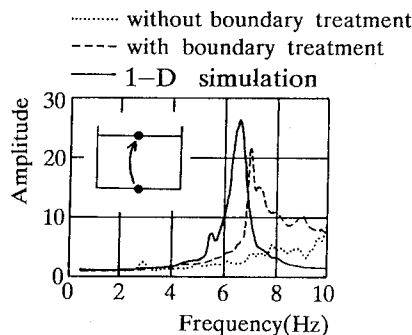


Fig.4 Effects of boundary condition on transfer function

## 2.2 Test results

Fig.4 for the preliminary test shows the transfer functions for two cases of different boundary condition computed from the ratio of Fourier spectra of response at the surface to those at the bottom. The frequency shown in these figures is at prototype scale. The result of 1-D non-linear simulation using lumped mass model is also shown in the same figure. The input motion in 1-D simulation is the acceleration observed at the bottom.



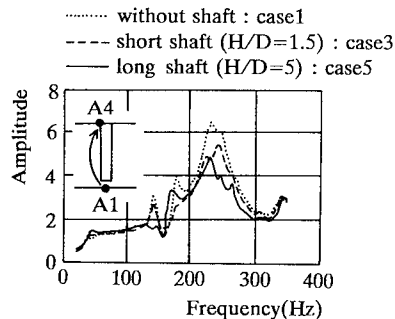


Fig.6 Transfer function at A4 in the case with small amplitude input

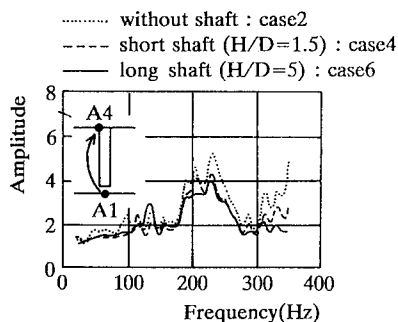


Fig.7 Transfer function at A4 in the case with large amplitude input

same. Two types of shaft conditions, short shaft( $H/D=1.5$ ) and long shaft( $H/D=5$ ), are considered. The shaft models are made of aluminum. Table 3 also shows the density of ground model and the maximum acceleration of input motion. All tests were carried out under 50g centrifugal condition. The model ground, composed of the dry TOYOURA standard sand, was made by air-pluviation.

El Centro 1940 NS record was used as the input signal for shaker. The shaking time was shortened to 1/50 of the original one in accordance with similitude. The sine acceleration waves with frequency of 100Hz and 250Hz were also used as input motions in separate tests. The first natural frequency of the ground model is 225Hz(see Fig.6).

Fig. 5 shows the location of the sensors. In order to observe the acceleration response of the ground model and shaft, accelerometers were set up at various locations. To measure the horizontal earth pressure acting on the shaft, pressure transducers were instrumented at the outer

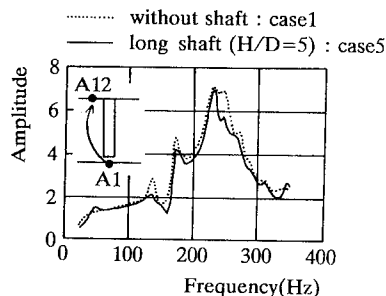


Fig.8 Transfer function at A12 in the case with small amplitude input

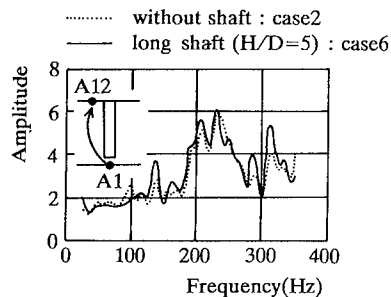


Fig.9 Transfer function at A12 in the case with large amplitude input

face of shaft. Eight and four pressure transducers were used at long and short shafts, respectively. In order to observe the strain in axial direction of the shaft during excitation, pairs of strain gauges were bounded at both ends of a diameter to the inner face of shafts. Eight and six gauges were used at long and short shafts, respectively.

### 3.2 Test results and analysis

Responses of shaft and ground are first investigated through the analysis of transfer function. In order to study the effects of the input amplitude level, the transfer functions subjected to input motions of small and large amplitudes are compared. Fig.6 and Fig.7 show the transfer functions at the A4(see Fig.5)for the case with short shaft, long shaft and without shaft under low and high excitation levels. All the transfer functions are computed from the ratio of Fourier spectra of acceleration response at A4 to those at the bottom. It can be seen that, the

predominant period becomes longer and the amplification ratio decreases with the input level. As this tendency does not depend on the shaft condition, it is believed to be due to soil non-linearity.

To study the effects of the shaft conditions, the transfer functions for the cases with different shaft conditions are compared. It can be seen from Fig.6 and Fig.7 that the transfer functions of the shaft(at the surface, point A4) have smaller amplitudes compared with that of the ground at the same position at the non-shaft case. Fig.6 and Fig.7 show that the transfer functions for the case with long shaft have smaller amplitude compared with that for the case with short shaft. These tendencies don't depend on the input level. Hence, the shaft, which is much stiffer than the ground, restrains the shear deformation of the ground model, and the long shaft has a stronger effect than the short one. Fig.8 and Fig.9 show the transfer functions at the point A12 for the cases with and without shaft, under low and high excitation levels. Transfer functions of the ground point A12, which is 100mm away from the shaft center, are quite similar in all cases. This tendency doesn't depend on the input level. Therefore, it could be concluded that the extent of the ground to which the shaft could restrain is less than  $1.5D$  ( $D$ : diameter of the shaft) from the shaft center.

The distribution of relative displacement amplitude(peak to peak) between shaft and ground, which could be calculated from accelerations, is also studied. Fig.10 shows the results for the cases under sine wave excitation. The relative displacement is very small in the case of 100Hz wave excitation regardless of the shaft condition. This excitation frequency is lower than  $f_0$  (the natural frequency of the ground model), which is around 225Hz (see Fig.6). Therefore the shaft and ground move together when the excitation frequency is lower than  $f_0$ . However, in the case of 250Hz wave excitation, which is close to  $f_0$ , relative displacement in the region near the ground surface is large, and the relative displacement in the case with long shaft is larger than that in the case with short shaft. Thus, when the excitation frequency is close to the  $f_0$ , the response at ground surface is largely amplified, resulting in

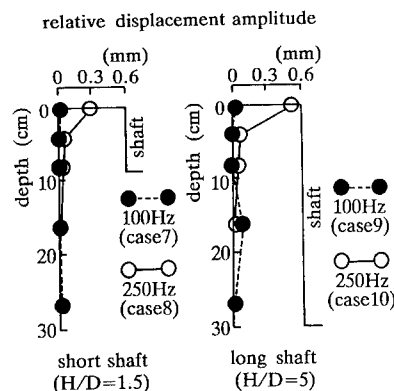


Fig.10 Distribution of relative displacement amplitude

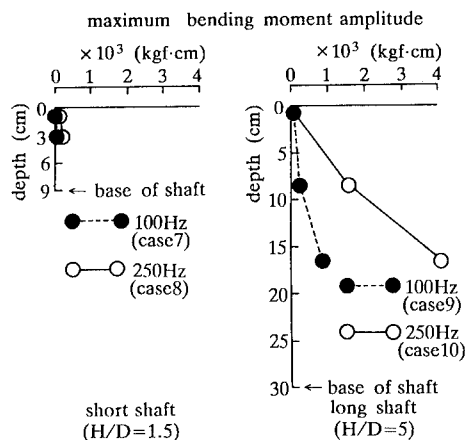


Fig.11 Distribution of dynamic bending moment amplitude

significant different response between shaft and ground. As the shaft is longer, the difference between responses of ground and shaft tends to be larger.

The bending moments of shaft during shaking are calculated using the record of the strain gauges. Fig 11 shows the distributions of dynamic bending moment amplitude (peak to peak) during sine wave excitation. In the case of short shaft, bending moment is very small, which suggests that the short shaft vibrates as a rigid body during shaking. In the case of long shaft, on the other hand, as the depth of shaft increases, the bending moment becomes larger, and bending moments at each depth change all in phase. Therefore, the vibration mode of the long shaft could be considered as the deformation of a

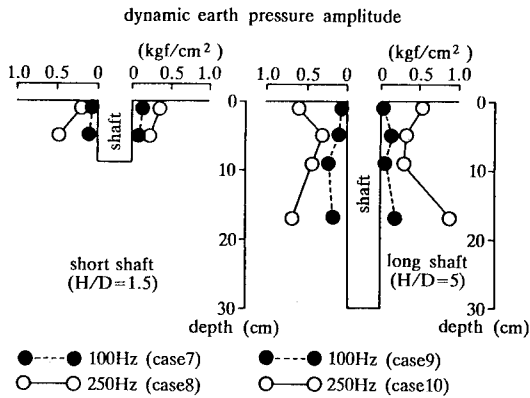


Fig.12 Distribution of dynamic earth pressure amplitude

cantilever under distributed load around tip.

The distribution of dynamic earth pressure amplitude(peak to peak), observed in the experiment under sine wave excitation, is shown in Fig.12. In the case with long shaft under 250Hz sine wave excitation, the dynamic earth pressure acting on the top and middle part of the shaft have larger amplitudes. This distribution tendency results from the distribution of the relative displacement between shaft and ground. At the depth near the ground surface, the relative displacement between ground and shaft becomes significant, which results in large earth pressure. To balance the large pressure at the top, large reaction force is needed at around the middle of the shaft where the soil is stiffer. It can be also seen that the distribution pattern of dynamic earth pressure amplitude varies as shaft condition is changed. Therefore, the distribution of dynamic earth pressure depends on the shaft vibration mode and the distribution pattern of the relative displacement, which is determined by the shaft geometry.

#### 4 CONCLUSIONS

In order to reveal the earthquake response characteristics of a shaft in dry sand, dynamic centrifuge tests have been successfully carried out. Following are the main conclusions drawn from this study:

1)The proposed boundary treatment method is shown to be very promising

through both dynamic centrifuge test and the 1-D numerical analysis;

2)The acceleration response of shaft-ground system is significantly affected by the amplitude level of input motion;

3)Shaft condition has large effect on the transfer function at the shaft, but little effect on that at the ground surface;

4)Short shaft vibrates in almost the same way as ground. However, in the case of long shaft, large response difference between the shaft and ground is observed near the ground surface;

5)Short shaft vibrates as a rigid body. Long shaft deforms during shaking, and its vibration mode is very similar to the deformation mode of a cantilever under distributed load around tip;

6)The distribution of dynamic earth pressure depends on the shaft vibration mode, which is determined by the shaft geometry.

#### REFERENCES

- 1)Campbell D. J., Cheney J. A. & Kutter B.L. 1991. Boundary effects in dynamic centrifuge model tests. *Centrifuge 91* :441-448
- 2)Hayashi H., Honda H., Yamada T. & Tatuoka F. 1992. Modeling of nonlinear stress strain relations of sands for dynamic response analysis. *10th World conference on Earthquake Engineering* : 19-24

## 5 Dynamic problems



## Behaviour of foundation systems in sand with dynamic sinusoidal loadings

J. Laue & H.L. Jessberger

*Institute for Soil Mechanics and Foundation Engineering, Ruhr-University Bochum, Germany*

**ABSTRACT:** With a new loading device and a fast data acquisition system, centrifuge model tests are carried out on the soil structure interaction of cyclic and dynamic vertically loaded circular shallow foundations in fine grained dry sand. These tests have been executed in the geotechnical Centrifuge Centre at the Ruhr-University Bochum in the 10 m Centrifuge (Z1). The possibilities of a new hydraulic loading device are described. The soil-structure interaction of vertically loaded circular shallow foundations are presented, with varying depth of embedment, different load amplitudes and frequencies.

### 1. INTRODUCTION

The description of dynamic soil structure interaction is a special problem in soil mechanics. Of special interest is the description of the elasto-plastic behaviour of the subsoil due to cyclic and dynamic loadings and its dependency on the frequency and the number of load cycles. To get a deeper knowledge of this behaviour, centrifuge model tests on vertically loaded circular shallow foundations are carried out in the Bochum geotechnical centrifuge (Z1) described by Jessberger and Güttler (1988). The strain distribution in the subsoil and the time-dependent increasing of the acceleration due to decreasing deformation is investigated. The behaviour can be measured by LVDT's and acceleration transducers. The measured deformations are divided into elastic and plastic portions.

For these tests, a new loading device and a fast data acquisition system were installed. Also a test control system was developed.

### 2. LOADING DEVICE AND DATA ACQUISITION SYSTEM

The basis for inflight tests on cyclic and dynamic problems is to have an effective and fast loading and data acquisition system. The high g-level causes high standards for all components. This leads to strong demands, especially for the dynamic loading device.

#### 2.1 LOADING DEVICE

The cyclic and dynamic loading of the foundations has been achieved by using hydraulic jacks. A standard hydraulic package with a maximum pressure of 23 MPa is installed outside the centrifuge close to the sliprings. To safeguard the sliprings during the dynamic loading, each jack has an additional storage tank. With this additional tank, a fast flow of the pressurized oil can be guaranteed without forcing the sliprings.

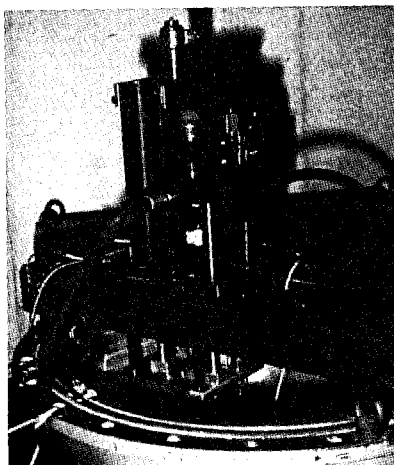


Fig. 1: Hydraulic jack used for vertical dynamic loadings

The jacks were specially constructed by R.D.P. Howden, Warwickshire U.K., which guarantees the dynamic abilities of the jacks at 100 g up to 100 Hertz for small amplitudes. The stroke is 72 mm. The jacks can be controlled by an internal LVDT or a force transducer. Specially constructed servo-valves are placed directly on the jacks, so that they resist the elevated g-levels as well. Fig. 1 shows one of the hydraulic jacks used for vertical loadings.

Using the control panel of the hydraulic unit, up to three cylinders can be controlled in parallel to apply different loads at the same time.

## 2.2 DATA ACQUISITION

For data acquisition and test controlling, a new data acquisition system was installed. This system consists of four independent processors, placed in the slot of a PC. Each board has as maximum 16 channels for single-ended, analogue input, 2 channels for analogue output and one channel for a trigger. With this system, a maximum of 64 channels can be recorded simultaneously. Operating with 16 channels per board, a maximum scan rate of 14.7 kHz is reached. Using only one channel per board, the practical scan rate reaches 235.2 kHz by measuring 4 channels at exactly the same time. In addition to the four processors placed in one PC, another processor with 16 channels is placed in a second PC, to have a continuous measurement of selected values especially during dynamic tests.

## 2.3 COMBINATION OF THE LOADING AND THE DATA ACQUISITION

To optimize the loading and the data acquisition for tests under cyclic and dynamic conditions using the hydraulic system, a special control system was developed, which is shown in Fig. 2.

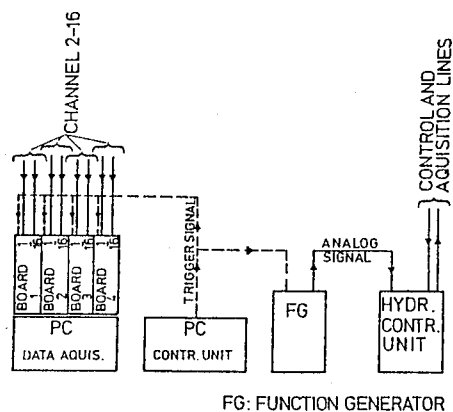


Fig. 2: Control system for loading and data acquisition [Kotthaus et al 1993]

A second PC sends trigger signals at specified times to the data acquisition system and to a function generator. This ensures, that the data acquisition and the loading start exactly at the same time. The next signals sent by the second PC are only used to control the data registration at specified times. It allows the measurement of distinct load cycles to reduce the length of the data file. More details of this system are described by Kotthaus et al (1993).

## 3. CENTRIFUGE MODEL TESTS

### 3.1 TEST SETUP

All tests presented are carried out in the Bochum Geotechnical Centrifuge ZI. A typical section of the model set up is shown in Fig. 3. A ground plan is given in Fig. 4.

The centrifuge tests are carried out in a circular container with a diameter of 100 cm. Six tests can be carried out in

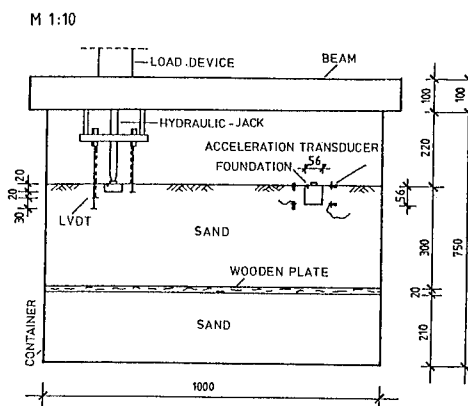


Fig. 3: Cross section of the model set-up of the tests series DFF.

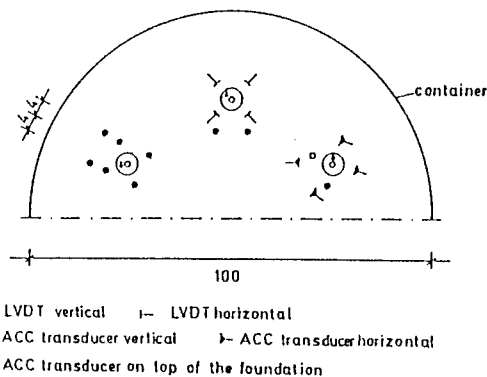


Fig. 4: Ground plan of the half of the model container

one container, when six foundations were placed at the quarter line of the diameter with a center angle of 60°. It was shown by running penetration tests at several stages of the test, that the influence of the vibrations at one location for a neighbouring location is neglectable. A test to determine the rupture load of a foundation adjoined to the vibrated footing shows additionally, that this test set up does not lead to interference between single foundations.

Bochum model sand, a fine grained sand, is used as the model soil. The parameters of the sand are given in Tab. 1. The grain-size distribution curve is shown in Fig. 5.

Tab. 1: Parameters of the Bochum standard sand

Parameter	Value
$\rho_s$ [g/cm <sup>3</sup> ]	2.66
Compactness $\rho_{min}/\rho_{max}$ [g/cm <sup>3</sup> ]	1.41 / 1.70
Porosity $n_{min}/n_{max}$	0.36 / 0.47
$d_{50}$ [mm]	0.23
$d_{10}$ [mm]	0.12
Uniformity coefficient $d_{60}/d_{10}$	2.08
Angle of friction $\phi$ [°]	38

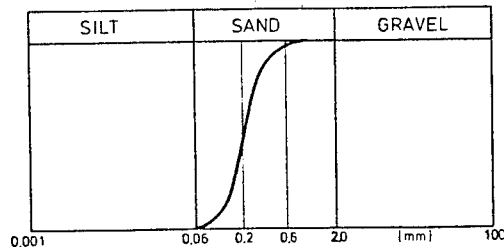


Fig. 5: Grain size distribution curve of the Bochum standard sand.

The sand is placed in the container by pluviation. To control the reached density, small boxes are placed in the soil at different layers in depth and at different locations. At the end of the tests the boxes were taken out of the container in a specified method and the reached density can be defined. A high density of about  $D_r = 98\%$  was reached in all tests.

Three different kinds of circular model foundations are used. Two of them with diameters  $D = 5.6$  cm and  $D = 7.5$  cm are made of steel with a thickness of  $d = 2$  cm. The third is made of aluminum with a thickness of  $d = 5.6$  cm and a diameter of  $D = 5.6$  cm. In a hole on top of the foundations an acceleration transducer can be placed. A construction to assure the exact placement for guaranteeing the comparability of all tests is used. The placement of all transducers is shown in Fig. 6.

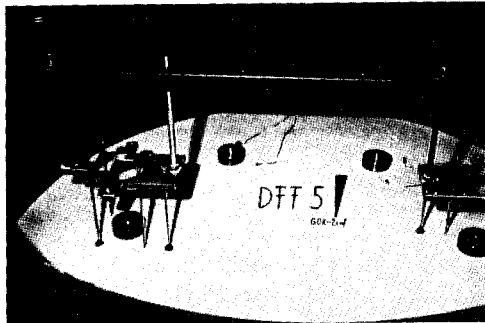


Fig. 6: Photo of the installation of LVDT's and acceleration transducers at the defined depth for the tests on dynamically loaded foundations

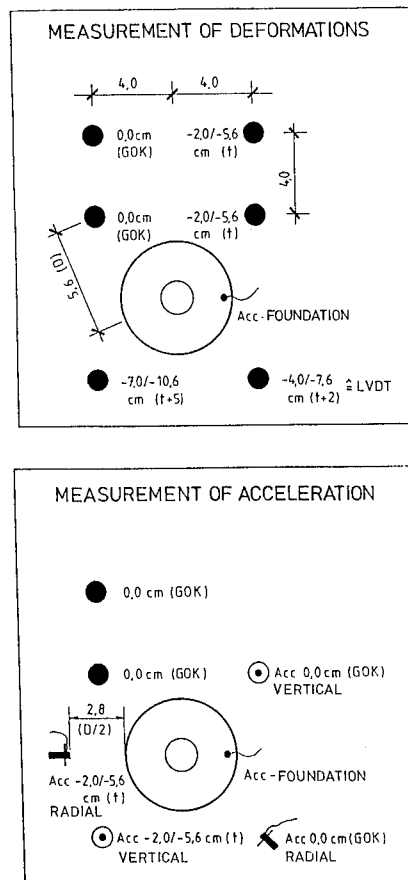


Fig. 7: Plan view of an observed foundation with the indication of the measuring points

Reaching a specified layer of the sand, the first transducers were placed at specified heights in the half-space. To get the influence of the static and cyclic loading, LVDT's and acceleration transducers were placed at the measuring points shown in Fig. 7 in a distance of  $D/2$  and  $D$  from the edge of the foundations to observe the behaviour in the half-space in all three possible directions, vertical, radial and tangential to the area of the footing. It was observed that the tangential values were very low in comparison to the others and therefore are neglected in this paper. Several tests are carried out under the same loading conditions to check the reproducibility of the results and to measure the reactions with different placements of the transducers. Six measurements can be done in the half-space at the same time because of restrictance in space.

### 3.2 TEST PROCEDURE

After placing the container in the basket of the centrifuge, the centrifuge is swing up to a  $g$ -level of 30. To assure the same conditions for all six tests done in one container, the centrifuge is raised before the first tests up to the  $g$ -level three times. The loading on the footings has been applied with a hydraulic jack. The load function is shown in Fig. 8.

At first a dead load of half of the failure load ( $V/V_r$ ) was applied to the foundation. After this, 1000 cycles of a sinusoidal load function were applied to the foundation. This sinusoidal loading increases from  $\Delta V/V = 0.2$  over 0.5 to 1.0. The measurement takes place for the first four cycles and afterwards for specified cycles (10, 20, 50, 100, 200, 500 and 1000) which assures a data file of less than 200 kB.

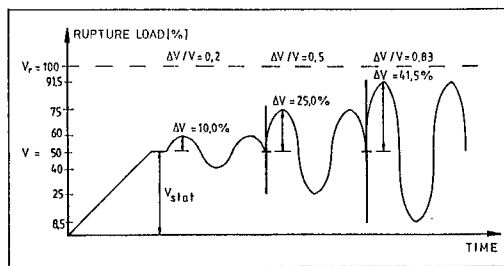


Fig. 8: Load function applied on the footings

A complete test matrix of all tests is too large to be presented here. Variations in the tests include: the geometrical conditions, the depth of embedment, the kind of the measurement, horizontal displacements, vertical displacements and accelerations, and changings of the load history by changing in a first step only the frequency. Fig. 9 shows as an example a test matrix to observe the influence of the embedment depth on the dynamic behaviour.

load frequency	data acquisition			
	deformation		acceleration	
	$t = 2,0$	$t = 5,6$	$t = 2,0$	$t = 5,6$
stat.	X	X		
10 Hz	X	X	X	
30 Hz			X	
60 Hz	X	X	X	X

Fig. 9: Test-matrix for the observation of the influence of the embedment depth

### 3.3 TEST RESULTS

The tests presented here are carried out with model foundations with a diameter of 5.6 cm representing a foundation in the prototype scale of 1.68 m. Three different embedment conditions, foundations on the surface and embedment depths of  $t = 2$  cm ( $0.60$  m =  $0.4$  D) and  $t = 5.6$  cm ( $1.56$  m =  $D$ ) were observed under three different dynamic loadings of  $f_m = 10$  Hz; 30 Hz; 60 Hz, representing prototype frequencies of  $f_p = 1/3$ ; 1 and 2 Hz.

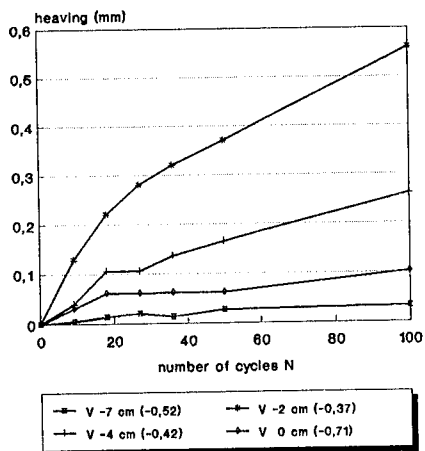
Additional dynamic loading after reaching the values of half the failure loads leads to lifting in most of the points in the halfspace. Fig. 10 shows the additional irreversible deformation for the measuring points in the half-space. For one test on a foundation with an embedment depth of  $t = 0.4$  D and a load frequency of 60 Hz the lifting at the surface shows the same values at both observed distances of  $D/2$  and  $D$  to the edge of the foundation.

The maximum additional lifting can be observed at the locations of the LVDT at the bottom height of the foundation. It can be seen that the main depth of influence on the layers is from the top up to a depth of about 7 cm ( $t = 1,3D$ ) below the foundations.

Fig. 11 shows a slightly different behaviour. Especially in the depth of the bottom of the foundation no great influence on the irreversible behaviour can be seen. A frequency of 10 Hz implies a smaller zone of influence around the foundation in the subsoil. The main zones of interest in depth remain the same. The behaviour of the layer at -7 cm shows an almost ideal elastic force settlement curve due to the cyclic loadings.

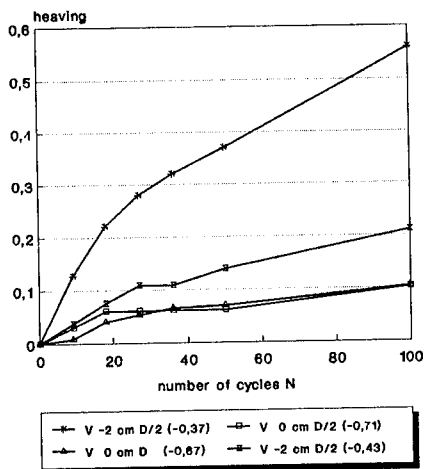
Fig. 12 shows the reaction of the LVDT's in the half-space for a foundation with an embedment depth of  $t = D$ . Although the loading conditions are the same as for foundations with an embedment depth of  $t = 0.4D$ , other effects can be observed. The surface shows an increasing settlement during cyclic loading. This is due to the spreading angle which operates from the bottom edge of the foundation. The accelerations in the half-space increase with time. Fig. 13 shows the acceleration in the radial direction for different frequencies under the same loadings

irrev. deformations ( $t=2 \text{ cm}$  ;  $f=60 \text{ Hz}$ )  
 $V=1543,2 \text{ N}$  ;  $dV=308,6 \text{ N}$  ;  $dV/V=0,2$   
 distance of  $D/2$  to the edge



( ) settl. due to the dead load

irrev. deformationen ( $t=2 \text{ cm}$  ;  $f=60 \text{ Hz}$ )  
 $V=1543,2 \text{ N}$  ;  $V'=308,6 \text{ N}$  ;  $V'/V=0,2$



( ) settlement due to the dead load

Fig. 10: Irreversible deformation in the half-space

a) comparison of all measuring points at a distance of  $D/2$  from the edge of the foundations

b) comparison of the heaving at measuring points at the surface and at the layer of the bottom of the foundation

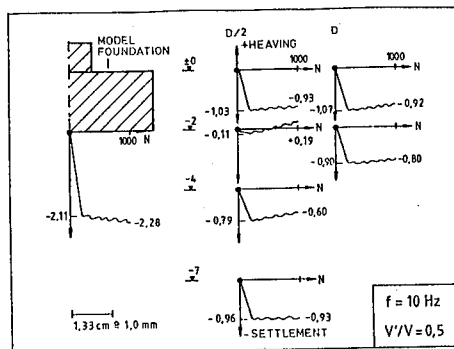


Fig. 11: Deformation behaviour at several parts of the half-space due to a cyclic loading of 10 Hz and a load value of  $\Delta V/V = 0.5$ .

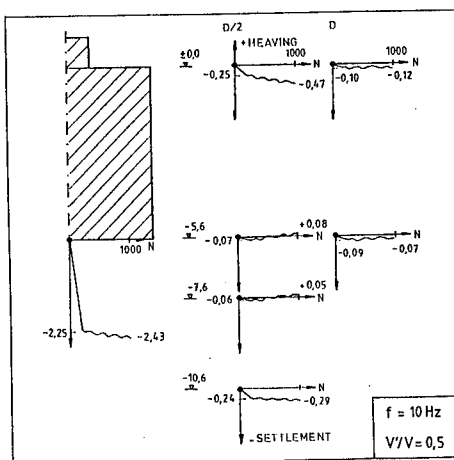


Fig. 12: Observation of the additional plastic settlement/heaving for a foundation with  $t = D$

at equal foundations. It can be seen that the radial acceleration at the surface is as double as high as at the surface of the layer.

This behaviour is obvious due to the increasing stiffness of the soil in the half-space. The cyclic energy introduced by the loading on top of the foundation is partly absorbed by the movement of the surrounding soil. This can be termed as frictional damping. The evaluation of the hysteretical (elastic) part of the settlement of the foundation leads to a development of the damping coefficient. This damping coefficient decreases with the number of load cycles. (Fig. 14). The values of the damping shown in fig. 14 are determined for a thickness of the soil layer of 1 cm as a reference value. This had to be done because the zone of influence couldn't have been defined exactly in opposite to the evaluation in element tests.

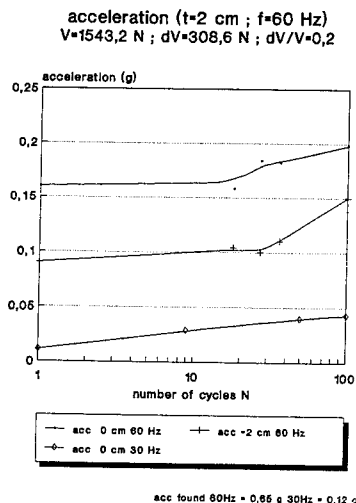


Fig. 13: Development of the acceleration due to the number of load cycles in one test

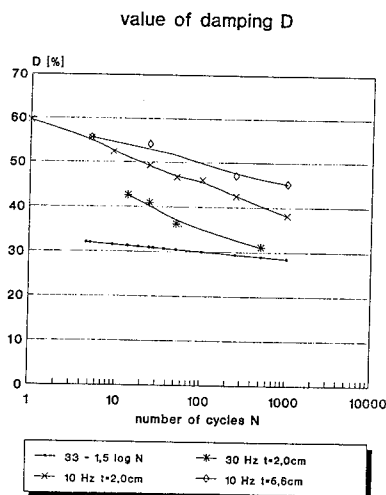


Fig. 14: Estimated damping of two tests in comparison to an empirical equation

$$D_{\max} = D_1 - 1,5 \cdot \log N \quad (\text{eq. 1})$$

with  $D_1 = 33$  for dry sand  
 $N$  number of cycles

Comparing the results of the tests with a damping behaviour shown in equation 1 (Thiel, 1988, according to Hardin), it can be seen, that the observed stiff system ( $t = 1D$ ) behaves in the same way. For smoother systems, like the researched foundations with embedding depths of  $t = 2$  cm, this equation could not describe the observed behaviour.

#### 4. CONCLUSION

Several tests have been done on the time-settlement behaviour on circular shallow foundations with different embedment conditions under varied loading and frequency conditions. With these investigations the influence of the observed parameters on the settlement of a foundation and also on the deformation and strain distribution in the half-space can be described. The aim of further tests will be the additional determination of critical points: for example the time in dependancy on the frequency and the load amplitude, at which an elasto-plastic behaviour turns into an ideal elastic, and also the observation over longer periods of time.

In addition, the above mentioned test results have to be compared with results of shaking table tests, where the foundations are not loaded directly by an actuator, but indirectly using a vertical shaking direction.

#### 5. ACKNOWLEDGEMENTS

The investigations presented in this paper are carried out within the scope of the research project SFB151 "Structural Dynamics" sponsored by the German Research Foundation (DFG) at the facility of Civil Engineering at the Ruhr-University Bochum.

#### REFERENCES

- Jessberger, H.L. & Güttler, U. (1988); Bochum geotechnical centrifuge; Centrifuge 88 Paris, Balkema Rotterdam
- Kotthaus, M., Lauc, J. & Jessberger, H.L. (1993); Centrifuge model tests on the interaction behaviour of deep and shallow foundations; Structural Dynamics - EURO DYN 93, Moan et al. (Eds.), Balkema Rotterdam
- Thiel, G. (1988); Steifigkeit und Dämpfung von wassergesättigtem Feinsand unter Erdbebenbelastung; Dissertation (in German), Schriftenreihe des Institutes für Grundbau, Wasser und Verkehrswesen; Serie Grundbau Heft 14, Bochum

## Physical simulation of dynamic soil-foundation systems on unbounded media

R.Y.S. Pak & B.B. Guzina

Department of Civil Engineering, University of Colorado, Boulder, Colo., USA

**ABSTRACT:** Recent experimental progress on the centrifuge modeling of dynamic soil-foundation interaction problems is presented. By virtue of large soil models, absorbing boundaries and signal processing techniques, the physical simulation of the three-dimensional wave propagation problem of a footing in vertical motion is shown to be both feasible and effective. Through a systematic study, comprehensive data is obtained which illustrates the influence of foundation contact pressure, footing dimension and soil density on the dynamic response of foundations on a granular soil.

### 1 INTRODUCTION

One of the fundamental problems in dynamic soil-structure interaction (SSI) is the characterization of surface foundations resting on a soil medium under time-dependent loads. Despite its apparent importance to both research and practice in soil dynamics and earthquake engineering, a clear understanding of the problem has not been achieved because of the complexity of real soil behavior and its constitutive modeling, the insitu and stress-induced heterogeneity in the soil's stiffness, and the three-dimensional nature of the underlying wave propagation phenomena. To provide a basis for improvement, a comprehensive experimental data base which can permit a direct identification of key physical parameters for the problem would clearly be desirable. Notwithstanding the useful purpose full-scale testings serve as a direct check of the applicability of relevant theories to practice, they are inherently limited for fundamental studies owing to the expenses and difficulties in performing parametric variations on aspects such as those involving soil and site formations. Scaled modeling on the centrifuge on the other hand does not present such problems. By increasing the effective body-force field in the soil model through centrifugal acceleration, the correct in-situ gravity-induced stress condition which is intimately related to the soil's mechan-

ical response can be replicated. Owing to the small scale of centrifuge models, numerous tests with well-defined conditions can be performed at a fraction of the cost of a full-scale test. For the dynamic problem of interest, however, centrifuge simulation is not without challenges, the major one of which is the boundary effects (see Coe et al. 1985, Cheney et al 1990, Weissman 1989, and Lenke et al. 1991).

In what follows, a series of centrifuge studies on the dynamic characteristics of surface foundations on sand will be presented. Apart from highlighting the combination of experimental techniques developed which renders the dynamic simulation successful, the paper describes an experimental data base which illustrates the effects of foundation contact pressure, footing dimension, and soil density on the soil-structure interaction problem.

### 2 EQUIPMENT AND INSTRUMENTATION

#### 2.1 *Experimental Apparatus*

The experiments presented in this investigation were conducted using the 440 g-ton centrifuge at the University of Colorado centrifuge facility. Detailed description of this facility can be found in Ko (1988).

The soil model container was chosen to have a rectangular geometry, with dimensions 1.0m

Table 1: Dimensions of Soil Samples Tested

Duxseal Linings	Soil Sample	
Thickness [m]	Base [m <sup>2</sup> ]	Depth [m]
0.035	0.93 × 1.13	0.46

by 1.2m by 0.61m height. The shape of the bucket is important because a cylindrical boundary will cause a severe wave focusing effect which can distort the foundation response (see Lenke et al. 1991). A large container was also found to be helpful in simulating a prototype half-space environment. To achieve the non-wave-reflecting characteristics of a semi-infinite medium more closely, a viscous oil-based material called Duxseal was also placed at the side-walls whose treatment was found to be pivotal for this class of problems (Lenke et al. 1991). Duxseal was first used as an absorbing boundary in dynamic centrifugal modeling by Coe et al. (1985). Later, Cheney et al. (1990) and Lenke et al. (1991) have also tested this material and confirmed its usefulness in wave absorption in their centrifuge models. As part of this study, a similar material called Duct Seal (see Campbell et al. 1991) was also tested and found to be useful as an absorbing boundary. Owing to the compressibility of both Duxseal and Duct Seal, however, the side-wall linings have shown some undesirable settlements under centrifugal forces, causing small failure wedges to appear around the side of the soil sample. To maintain a homogeneous soil model and to provide a stronger lateral wall stiffness, a supporting grid was designed and constructed to shore up the Duxseal linings. The final thickness of the reinforced Duxseal walls is given in Table 1.

All the model footings used in the investigation had a circular base. To ensure the model footings were rigid, they were designed to have a truncated conical shape, as shown in Figure 1. A total of five footings were tested, with their basic parameters presented in Table 2. As can be deduced from Tables 1 and 2, the minimum ratio of the soil depth to footing radius was about 12. The first three footings were used successfully in a series of modeling-of-model tests to verify the internal consistency of the scaled modeling. For that purpose, their dimensions

Table 2: Geometric and Inertial Properties of Model Footings

Footing #	Model Radius, $a$ [m]	Model Mass, $m$ [kg]
1	0.0162	0.038
2	0.0216	0.091
3	0.0270	0.178
4	0.0381	0.319
5	0.0381	0.700

and masses were designed according to the scaling relations, with  $a_3 = 1.25a_2 = 1.67a_1$  and  $m_3 = 1.95m_2 = 4.66m_1$ . Note that the model masses presented in Table 2 include the masses of the attached accelerometers and the belonging portions of the transducer cables. In order to produce a wider range of average contact bearing stresses, two steel discs were fabricated to be attached to the model footings, resulting in the increase of the vibrating mass. These two steel discs, henceforth referred to as 'Mass #1' and '#2', had masses of 0.1485 kg and 0.3935 kg, respectively.

The excitation system consisted of an electromagnetic shaker, a power amplifier and a random signal generator. A Brüel & Kjær 4809 vibration exciter with a low armature weight (60 gr) and a force rating of 44.5 N was used in this study. The system can provide acceleration, velocity and displacement over the frequency band of 10 to 20,000 Hz. A random signal, provided by a Tektronix 2630 Fourier analyzer, was fed to the exciter which can provide a load with a uniform frequency spectrum over the specified frequency range.

To monitor the loading and the response, all model footings were instrumented with a washer-shaped Kistler 9001 dynamic load cell and a pair of PCB 303A11 accelerometers. The instrumentation-model assembly is shown in Figure 1. The output signals were amplified by the programmable signal conditioner on board the centrifuge and passed through the slip rings to the Tektronix 2630 Fourier analyzer which is an analog data acquisition and signal processing unit. Together with a personal computer, the unit can be used to digitize multi-channel analog time signals and process them in the frequency domain.



Table 3: Densities of F-75 Silica Sand Tested

Mass Density $\rho$ [kg/m <sup>3</sup> ]	Void Ratio $e$	Relative Density
1730	0.532	86%
1687	0.571	74%
1628	0.628	56%

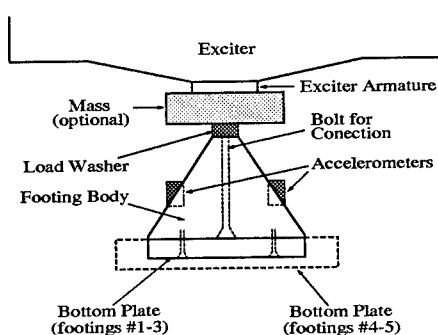


Figure 1: Typical Footing Design with Transducer Locations

## 2.2 Soil samples

The soil tested was a uniform, dry, fine silica sand designated as F-75 by the U.S. Silica Company. In the investigation, three different sand densities ranging from high to medium as shown in Table 3 were used in the centrifuge testing. During all tests, the sand was kept dry, with water content  $w < 0.1\%$ . To construct a homogeneous sample, the method of pluviation through air was employed with satisfactory results. Existing raining devices were calibrated to yield relative densities of 86, 74 and 56%. The variety of densities was obtained by varying the raining height and the flux of the sand.

## 2.3 Measurement approach

As discussed previously, during the random excitation of the model footings, analog signals from the transducers are sampled, digitized and analyzed in the frequency domain by means of the Fast Fourier Transform. In terms of the transformed input ( $X(f)$ ) and output ( $Y(f)$ ) signals, various frequency transfer functions characterizing the dynamic soil-foundation response can then be calculated. Due to the presence of

noise, however, the alternative representation of a transfer function

$$H(f) = \frac{G_{xy}(f)}{G_x(f)} \quad (1)$$

in terms of the cross-spectral density ( $G_{xy}$ ) and auto-spectral density ( $G_x$ ) functions of the input and output signals  $x(t)$  and  $y(t)$  is more useful (see Bendat and Piersol, 1986). By means of spectral averaging and windowing functions, the desired transfer function can be determined experimentally. Generally referred to as the acceleration function  $A(f)$ , the particular transfer function of interest is defined as the ratio of the acceleration of interest at the soil-foundation interface to the dynamic load applied to the footing in the frequency-domain. As will be illustrated in the ensuing presentation, the acceleration function is an item of fundamental relevance in this kind of study.

## 3 CENTRIFUGE EXPERIMENTS

### 3.1 Scope of the study

For linearized dynamic soil-structure interaction analysis, the foundation response can be completely characterized by the *dynamic interfacial compliance function* which is defined as the ratio of the displacement response to the total interfacial load at the soil-foundation interface as a function of frequency. For the vertical mode of interest, the compliance function can be denoted by  $C_{vv}(f)$ . Owing to the stress-dependent behavior of granular soils, such compliance function has been found to depend on the average contact stress  $p$  between the foundation and the soil, as well as the foundation radius  $a$ . As discussed in Pak and Guzina (1992), the experimental data on the foundation compliance can be approximated by the power law in the form of

$$C_{vv}(f) = g(e)a^{-\gamma}p^{-\beta}[F_1(f) + iF_2(f)]. \quad (2)$$

Here  $a$  is the characteristic radius of the foundation,  $p$  is the average soil bearing pressure,  $e$  is the void ratio,  $f$  is the frequency,  $g$  is a function which depends on the soil's void ratio, and  $F_1$  and  $F_2$  are related to the dimensionless frequency functions of the uniform half-space solution in, e.g., Pak and Gobert (1991). According

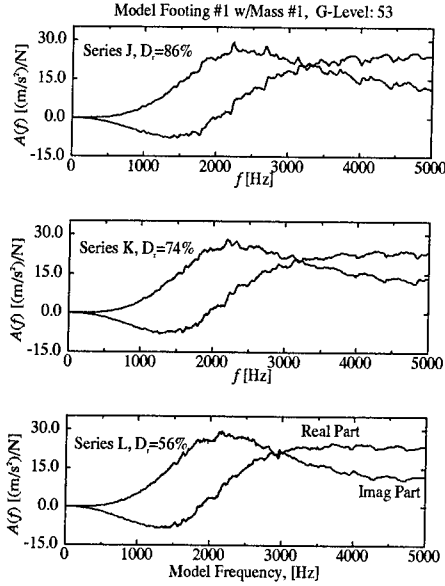


Figure 2: Experimental Accelerance Functions

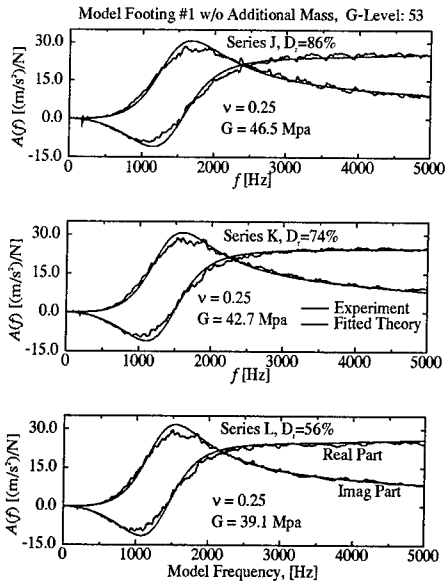


Figure 3: Experimental and Theoretical Accelerance Functions

to the current data, typical values for  $\gamma$  and  $\beta$  for the dense sand under consideration were found to be around 1.1 and 0.5, respectively.

From the experimental data, it was found that the Poisson's ratio  $\nu$  of the sand tested can be

reasonably well approximated by 0.25. In the format of the theoretical solution in elastodynamics, (2) can be re-cast as

$$C_{vv}(f) = \frac{1-\nu}{4Ga} [F_1(f) + iF_2(f)], \quad (3)$$

where

$$G = G(e, a, p) = G_0(e) a^\alpha p^\beta. \quad (4)$$

Here  $G$  and  $\nu$  are the equivalent shear modulus and the Poisson's ratio of the soil, respectively. Comparison of (3) with (2) reveals that  $\alpha = \gamma - 1$  and therefore has a typical value of 0.1.

### 3.2 Experimental results

In what follows, three series of tests performed on soils of 86, 74 and 56% relative densities will be presented. Each of these series consisted of 26 centrifuge experiments with a variety of prototype footing radii ranging from 0.5 to 3m and static contact pressures from 30 to 250kPa. The testing matrix was achieved by varying the g-level as well as the model footing's radius and mass. Typical experimental accelerance functions with both the real (in-phase) and imaginary (out-of-phase) parts are presented in Figure 2. Regardless of the soil density, the measured experimental soil-foundation response were considerably smoother than those in Cheney et al. (1990) and Lenke et al (1991). Together with the consistency demonstrated by the results from modeling-of-models, the foregoing observation has confirmed the usefulness of the combination of centrifuge modeling, Duxseal boundary, large container and signal processing technique for this class of dynamic soil-structure interaction problems.

To avoid confusion between the model and the prototype values, all variables in the ensuing presentation are referred to the model size. Extrapolation to the prototype scale can be achieved noting that  $f_{pr} = \frac{1}{n} f_{model}$  and  $C_{vvpr} = \frac{1}{n} C_{vvmodel}$ .

## 4 ANALYSIS OF RESULTS

As discussed in the preceding presentation, a function describing the soil-foundation response which is experimentally evaluated in the present study, is the accelerance function  $A(f)$ . It is re-

lated to the dynamic interfacial compliance function  $C_{vv}(f)$  through

$$C_{vv}(f) = -\frac{1}{(2\pi f)^2} \left[ \frac{1}{A(f)} - M \right]^{-1}, \quad (5)$$

where  $M$  denotes the footing mass. As a result, by calibrating the analytical solution (3) against the experimental data, an equivalent shear modulus of the soil can be determined. Some typical results of the calibration procedure are presented in Figure 3. Upon collecting the values of  $G$  calibrated for equation (3), it was found that for the whole range of densities tested, the equivalent shear modulus of the soil can be well approximated by formula (4), with parameters  $\alpha$  and  $\beta$  being within previously stipulated ranges. Setting  $\alpha = 0.1$  and  $\beta = 0.5$ , it was found from the experimental data that the mean values of  $G_0(e)$  for the void ratios tested are as given in Table 4. As can be seen, function  $G_0(e)$  is a monotonically decreasing function of the void ratio.

Table 4: Variation of  $G_0(e)$  ( $\alpha = 0.1$ ,  $\beta = 0.5$ )

Series	Void Ratio $e$	Mean Value Value $G_0(e)$ [MPa]	Standard Deviation [MPa]
J	0.532	6.33	0.014
K	0.571	6.05	0.016
L	0.628	5.55	0.010

## 5 CONCLUSIONS

In this study, an experimental investigation was conducted to further the understanding of dynamic soil-structure interaction aspects pertaining to granular soils. First, it was confirmed by the experimental results that the dynamic foundation response on a uniform granular soil could be approximated by the analytical solution for a homogeneous half-space with a proper choice of the equivalent shear modulus of the soil. The dependence of such a shear modulus on the characteristic foundation dimension and the average contact stress between the soil and the foundation was shown to be significant. As expected, experimental data also indicated that the equivalent shear modulus was a decreasing function of the soil's void ratio.

## 6 ACKNOWLEDGMENT

The support from the U.S. National Science Foundation and the help of Tom Weiss of Tektronix are greatly appreciated.

## REFERENCES

- J. S. Bendat and A. G. Piersol (1986). *Random Data*. Wiley Interscience, New York.
- D.J. Campbell, J.A. Cheney and B.L. Kutter (1991). Boundary Effects in Dynamic Centrifuge Model Tests. *Centrifuge 91*. A. A. Balkema, Rotterdam, 441-448.
- J. A. Cheney, O. Y. Z. Hor, R. K. Brown and N. R. Dhat (1988). Foundation Vibration in Centrifuge Models. *Centrifuge 88*. A. A. Balkema, Rotterdam, 481-486.
- J. A. Cheney, R. K. Brown, N. R. Dhat and O. Y. Z. Hor (1990). Modeling Free Field Conditions in Centrifuge Models. *J. Geot. Eng.*, Vol.116, No.9, 1346-1367.
- C. J. Coe, J. H. Prevost and R. H. Scanlan (1985). Dynamic Stress Wave Reflections/Attenuation: Earthquake Simulation in Centrifuge Soil Models. *Earth. Eng. Struct. Dyn.*, Vol.13, 109-128.
- H.Y. Ko (1988). The Colorado Centrifuge Facility *Centrifuge 88*. A. A. Balkema, Rotterdam, 73-76.
- L.R. Lenke, R.Y.S. Pak and H.Y. Ko (1991). Boundary Effects in Modeling of Foundations Subjected to Vertical Excitation. *Centrifuge 91*. A.A. Balkema, Rotterdam, 473-480.
- R. Y. S. Pak and A. T. Gobert (1991). Forced Vertical Vibration of Rigid Discs with Arbitrary Embedment. *J. Eng. Mech.*, Vol. 117, No. 11, 2527-2548.
- R. Y. S. Pak and B. B. Guzina (1992). Experimental and Theoretical Dynamic Compliances of Foundations. *Proc. 9<sup>th</sup> Eng. Mech. Conf., ASCE*, 596-599.
- K. Weissman (1989). Centrifugal Modeling of Dynamic Soil-Structure Interaction. *Ph.D. Thesis, Princeton University, Princeton*.

## Experimental study of dynamic soil-pile interaction in sand

A.T.Gobert

*Electricité de France, Engineering and Construction Division, Villeurbanne, France*

R.Y.S.Pak

*Department of Civil, Environmental and Architectural Engineering, University of Colorado, Boulder, Colo., USA*

**ABSTRACT :** The dynamic response of an axially-loaded pile embedded in a uniform granular soil is studied. By means of the centrifuge scaled modeling technique and an absorbing boundary, the dynamic compliance function for the foundation is obtained experimentally by a random vibration method. The effects of the superstructure weight, pile geometry, pile-soil relative stiffness on the dynamic behavior are examined as a function of frequency. On the basis of the experimental records, an evaluation of the relevance and accuracy of existing analytical methods is presented.

### 1. INTRODUCTION

The effects of dynamic soil-pile interaction have received considerable attention because of their importance in the design of foundations and structures which are required to support vibrating machinery and resist seismic loads. The behavior of pile foundations is often difficult to predict as it can be influenced by pile-soil contact, possible soil heterogeneity, non-linear stress-strain relationships and pile-soil-pile interaction in pile group problems. In view of the difficulty to model such phenomena, the need and importance of experimental data has been well recognized. Owing to the expenses and difficulties associated with full-scale field tests, small-scale laboratory tests and centrifuge modeling have seen increasing recognition as a powerful tool for such purposes (Scott et al., 1982, Finn et al., 1987). In this paper, a parametric centrifuge experimental study aimed at the characterization of the dynamic response of an axially-loaded pile under a variety of pile and soil conditions typically encountered in the field is presented.

### 2. EXPERIMENTAL PROCEDURE

A brief description of the centrifuges facilities, soil samples, foundation models,

instrumentation, and the measurement techniques is presented in the following.

#### 2.1 Centrifuge facilities

Two geotechnical centrifuges in operation at the University of Colorado are used in the test program. The smaller one, a Genisco Model 1230-5 accelerator rated to 15 g-ton can perform up to 100 g. The larger one, rated to 440 g-ton can perform up to 200 g. The scaling relations relevant to dynamic tests are listed in Table 1, in which the acceleration and the compliance are defined as acceleration over load and displacement over load ratios, respectively.

#### 2.2 Soil samples

To minimize the dynamic boundary effects, rectangular soil containers both have lateral boundary panels packed with an oil-based absorbing viscous material called Duxseal to reduce wave reflection and simulate the radiation damping of semi-infinite media. The width, length and height of the bucket used in the small centrifuge tests is 0.40 m., 0.35 m. and 0.30 m., respectively and, for the large centrifuge, 1.10 m., 1.60 m. and 0.47 m., respectively. The thickness of the lateral absorbing panels ranges from 25 to 50 mm.

Table 1 Scaling relationships relevant to dynamic tests on scaled models

	prototype	model at n g
stress	1	1
strain	1	1
frequency	1	n
acceleration	1	n
force	1	1/n <sup>2</sup>
displacement	1	1/n
accelerance	1	n <sup>3</sup>
compliance	1	n

The details of Duxseal can be found in Lenke et al. (1991).

The granular soil used throughout the test program is a quartz dry uniform fine sand from the U.S. Silica Company, designated as the Ottawa F-75 sand (see Table 2). The samples are prepared using a carefully calibrated pluviation through air technique and three uniform soil relative densities are used in the experimental program as indicated in Table 3.

As noted by Hardin and Drnevich (1972) the small-strain shear modulus of granular materials generally depends on the effective confining stress through

$$\mu_s^{\max} [MPa] = \frac{78.2(2.973 - e)^2}{1 + e} (\sigma_o [MPa])^{0.5} \quad (1)$$

with  $\mu_s^{\max}$  small-strain shear modulus  
 $\sigma_o$  effective confining stress

In this study, the profile with depth of the soil shear modulus is evaluated through Equation (1) with a value of the coefficient of earth pressure at rest of 0.33.

Table 2 Characteristics for the Ottawa sand

D <sub>10</sub> = 0.12 mm	max. weight 17.5 kN/m <sup>3</sup>
D <sub>30</sub> = 0.16 mm	min. weight 14.4 kN/m <sup>3</sup>
D <sub>50</sub> = 0.19 mm	max. void ratio e <sub>max</sub> = 0.805
D <sub>60</sub> = 0.21 mm	min. void ratio e <sub>min</sub> = 0.489

Table 3 Relative density, void ratio and mass density for the Ottawa F-75 sand

Relative density	void ratio	mass density
D <sub>r</sub> = 86 %	e = 0.532	1730 kg/m <sup>3</sup>
D <sub>r</sub> = 74 %	e = 0.570	1688 Kg/m <sup>3</sup>
D <sub>r</sub> = 57 %	e = 0.623	1633 Kg/m <sup>3</sup>

## 2.3 Foundation models

Seven pile models are built for the exper-

imental study. They are made from stock drawn aluminium 6061-T6 tubings and rods. The letters T or R refer to tube-like or full rod-like pile models. Each cross section type is available with three sizes (1,2 and 3) as described in Table 4. For the tubings, the ratio between the internal and external radii is 0.75 for all sizes. Parameters for the foundation models are given in Table 4, in which a and l are the external radius and length of the model, respectively and  $\bar{l} = l/a$  and  $\bar{r} = 2a/D_{50}$

Table 4 Foundation models

	a(mm.)	l (mm.)	$\bar{r}$	$\bar{l}$
TL1	3.175	133.3	33	42
T1	3.175	88.9	33	28
T2	4.762	133.2	50	28
TS2	4.762	95.2	50	20
TS3	6.350	127.0	66	20
R1	3.175	88.9	33	28
R2	4.762	133.2	50	28

## 2.4 Instrumentation and measurement techniques

The measurement system is composed of (i) a host personal computer, (ii) a four-channel Tektronix Fourier analyser, Model 2630, used as a random signal generator, analog data acquisition system, digitizer and Fourier analyser, and (iii) a programmable signal conditioner. The excitation is provided by an electro-magnetic vibration exciter manufactured by Bruel&Kjaer, Model 4809, mounted on a massive reaction frame. The foundation response is measured using three quartz pie-zoelectric accelerometers, from PCB Piezo-electronics, Model 303A, and a quartz load-cell washer from the Kistler Corporation, Model 9901, as shown in Figure 1.

In this investigation, the method of random vibration is employed. With the forced random excitation used (less than 1 N rms), the response of the piles are verified to be linear. As a result, the determination of the transfer function can be achieved by DSP techniques for linear systems (Bendat and Piersol, 1986). In particular, it can be shown that, in the presence of noise due to the various electrical connections, the accelerance function can be computed using

$$A(f) = \frac{G_{af}(f)}{G_{ff}(f)} \quad (2)$$

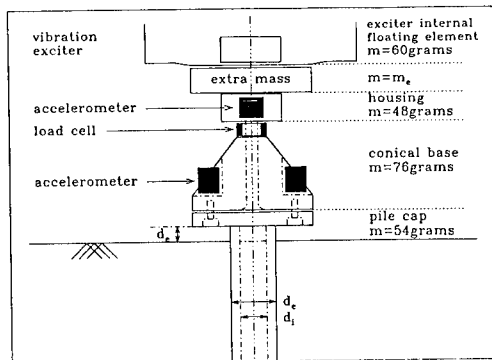


Fig. 1 Experimental configuration of the pile and its cap

with  $G_{af}(f)$  being the cross spectral density function of the force and acceleration signals and  $G_{ff}(f)$  being the autospectral density function of the force signal. These spectral densities functions are average over 30 time-windows. The extent of noise and the presence of non-linearities in the system response can be assessed by computing coherence functions between the different signals via

$$\gamma_{af}^2(f) = \frac{\|G_{af}(f)\|^2}{G_{af}(f)G_{ff}(f)}, \quad 0 \leq \gamma_{af}^2(f) \leq 1 \quad (3)$$

with them being unity across the frequency band in the absence of noise and for a perfectly linear system.

Typical values for the frequency of the excitation induced by rotating machinery go up to about 100 Hz. This implies that the frequency band of a model foundation tested at for instance 50 g should extend to 5 KHz. The selected frequency band for all tests performed between 20 g and 60 g is DC to 5 KHz. The sampling frequency of the digitizer is set to 12.8 kHz and 4096 samples are recorded per time-window. This in turn provides a transfer function with 1600 alias free points and a frequency resolution of 3.125 Hz.

From the acceleration function, the dynamic compliance of the pile at the ground level can be determined once the inertial contribution of the pile cap is determined. To obtain the latter, vibration tests are performed with the conical base and the pile cap mounted onto the exciter and without any soil contact.

### 3. EXPERIMENTAL RESULTS

#### 3.1 Pile-soil parameters

In the characterization of the foundation system, one of the important parameters is the pile-soil stiffness ratio which may be defined by

$$\bar{K} = \frac{A_p E_p}{2 \pi a^2 \mu_s} \quad (4)$$

with  $A_p E_p$  axial stiffness of the pile  
 $\mu_s$  representative shear modulus of the soil sample

Practical values are found in the 200 to 2000 range. Likewise, the pile-soil inertia ratio is defined as

$$\bar{\rho} = \frac{A_p \rho_p}{\pi a^2 \rho_s} \quad (5)$$

with  $A_p \rho_p$  lineal density of the pile  
 $\rho_s$  soil mass density

Typical values of the inertia ratio ranges from 0.70 to 1.70.

In what follows, experimental results in the foregoing ranges will be presented to highlight some of the fundamental aspects of the dynamic soil-pile interaction problem.

#### 3.2 Coherence functions

To illustrate the quality of the results, a typical coherence function between acceleration and force signals for a test performed at 60 g is shown in Fig. 2. One can see that the coherence function is virtually unity for all frequencies from 500 to 5000 Hz. The degradation of the coherence function as one approaches the static condition for this type of force-controlled tests is due to weaker

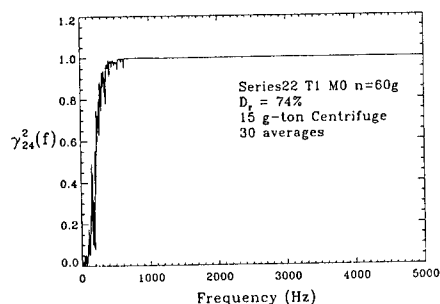


Fig. 2 Typical coherence function between the acceleration and the load signals

acceleration signals accompanied by a progressive increase in the noise to signal ratio as the frequency tends to zero.

### 3.3 Verification of the scaling laws

To ensure that the results obtained from small-scale tests can be extrapolated to prototype field cases, the validity of the scaling relationships must be verified. This can be achieved by a method commonly referred to as the technique of modeling of models (Ko, 1988). It involves the testing of several scaled models at different g-levels and all corresponding to an identical prototype foundation. In Table 5 are presented two examples of such a procedure. As the weight of the superstructures can influence the dynamic system response, pile caps with different masses are installed on the pile head so as to generate a static force  $F$  corresponding to a prototype static force  $F_p$ .

Table 5 Modeling of model Tests

Models	Example 1	Example 2
model 1	T1 at 60g $a_1=3.175$ mm $F_1 = 140$ N	R1 at 45g $a_1=3.175$ mm $F_1 = 105$ N
model 2	T2 at 40g $a_2=4.762$ mm $F_2 = 315$ N	R2 at 30g $a_2=4.762$ mm $F_2 = 236$ N
prototype at 1g	$a_p = 190.5$ mm $F_p = 504$ KN	$a_p=142.9$ mm $F_p = 213$ KN

In Figures 3 and 4 are presented (a) the magnitude of the model massive axial acceleration and (b) the prototype pile-top compliance for example 1 and example 2, respectively. From the graphical displays, it can be observed that the use of the scaling relationships to compute the prototype pile-top compliances leads to a good agreement between the model responses for both the real part and the imaginary part of the compliances.

As can be deduced from Table 1, the prototype dynamic compliance  $C_{AA}^p$  is related to the model-scale compliance  $C_{AA}^m$  through

$$C_{AA}^p = 1/n C_{AA}^m \quad (6)$$

as the function is defined as the ratio of the pile-head displacement to the applied loading in the frequency domain. For the comparison with theoretical results, it is also useful to

cast the results in a dimensionless form with the definition of

$$\bar{C}_{AA}(\bar{\omega}) = 2 \pi a \mu_s C_{AA}^m(f^m) \quad (7)$$

$$\bar{\omega} = \frac{2 \pi f^m a}{\sqrt{\mu_s/\rho_s}} \quad (8)$$

where  $\mu_s$  is a representative shear modulus of the soil and the superscript "m" refers to the model scale.

### 3.4 Effects of the testing sequence

The effects of the testing chronology on the system response is studied. A typical sequence consists of testing a model at 30 g, test (a), 40 g, test (b), 60 g, test (c), and then at 40 g, test (d), 30 g, test (e) etc.. Various testing sequences are implemented in the study, it is found that the foundation response at a g-level  $n_1$  can be altered if it has previously experienced a higher g-level  $n_2$ . This effect is found to be independent of the number of cycles used in the sequence and a function of the ratio  $n_2/n_1$  only. The stresses existing in the soil (i.e. residual stresses) may depend on whether or not the model has experienced a higher g-level than the one it is tested at.

## 4. INTERPRETATION OF EXPERIMENTAL RESULTS

In view of the difficulties to model analytically all relevant pile-soil interaction phenomena, a simplified approach is adopted herein to compare the experimental data with a fundamental analytical solution. To this end, the comparison uses the dynamic solution of a deformable floating pile embedded in a homogeneous half-space (Gobert, 1992). The representative shear modulus needed for the comparison is defined as the modulus (henceforth called "peak modulus") for which the resonant frequency of the experimental data and the one predicted by the analysis can be made to coincide. Typical back-calculated values for the peak modulus are presented in Table 6 for a dense sand. It can be seen that the pile properties (i.e. deformability and inertia), superstructure weight, and the testing sequence have a significant effect on the dynamic system response and thus on the value of the peak modulus. Arithmetic averages of the shear modulus over the pile embedment ("average modulus") are computed with Equation (1)

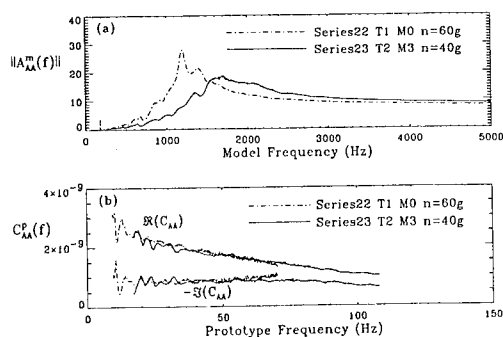


Fig.3 The modeling of models technique ; example 1: (a) magnitude of the model accelerance function in  $m/s^2/N$ , (b) prototype pile-top compliance in  $m/N$ ,  $D_r = 74\%$

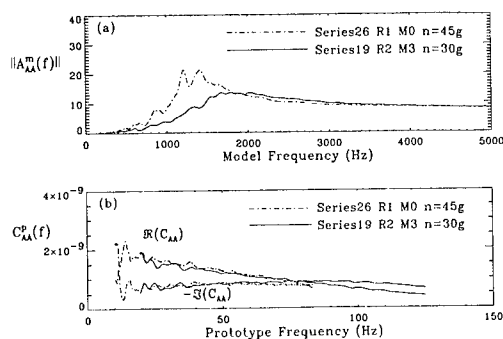


Fig.4 The modeling of models technique ; example 2: (a) magnitude of the model accelerance function in  $m/s^2/N$ , (b) prototype pile-top compliance in  $m/N$ ,  $D_r = 86\%$

and given in Table 7. These values are consistent with the peak moduli. However, they obviously do not incorporate effects such as the testing sequence, pile deformability and superstructure weight.

In Figure 5 are presented the comparisons between experimental and theoretical pile-top dimensionless compliances. Some discrepancies between the two solutions remain as the variation of the shear modulus in sand is not captured by the homogeneous solution. The agreement however is quite good across the frequency band for the stiffer piles (Model R2). The experimental data seem to yield a real part for the compliance consistently higher by 10 to 25 % than the theoretical ones, when the imaginary parts are reasonably well matched.

## 5. CONCLUSIONS

A parametric experimental study on the dynamic behavior of an axially-loaded pile has shown the complexity of this fundamental soil-structure interaction problem. By means of the centrifuge modeling technique, small-scale pile foundations have been tested and similitude laws relevant to vibration tests have been verified by the technique of modeling of models. An interpretation of the experimental records is given with respect to the homogeneous half-space solution. The data reveal the importance of pile properties, superstructure weight and loading path on the dynamic system response.

Table 6 Peak shear modulus expressed in MPa for a dense sand with  $D_r = 86\%$ .

Foundation model	Superstructure mass	Test (a) n = 30 g	Test (b) n = 40 g	Test (c) n = 60 g	Test (d) n = 40 g	Test (e) n = 30 g
T2-Mass0	m = 238 gr.	41.3 *	47.1	55.9	51.6	45.4
T2-Mass2	m = 638 gr.	46.2	51.9	60.8	58.3	54.0
T2-Mass3	m = 803 gr.	49.7	55.7	66.2 *	63.5	60.5 *
R2-Mass0	m = 238 gr.	49.6	54.8	63.3	60.5	58.3
R2-Mass2	m = 638 gr.	52.6	58.3	67.0	63.9	60.5
R2-mass3	m = 803 gr.	55.1 *	60.5	70.7 *	65.6	62.8 *

\* test results presented in Figure 5

Table 7 Average shear modulus expressed in MPa for a dense sand with  $D_r = 86\%$

Foundation model	Superstructure mass	Test (a) n = 30 g	Test (b) n = 40 g	Test (c) n = 60 g	Test (d) n = 40 g	Test (d) n = 30 g
T2 and R2	all	52.8	61.0	74.3	61.0	52.8



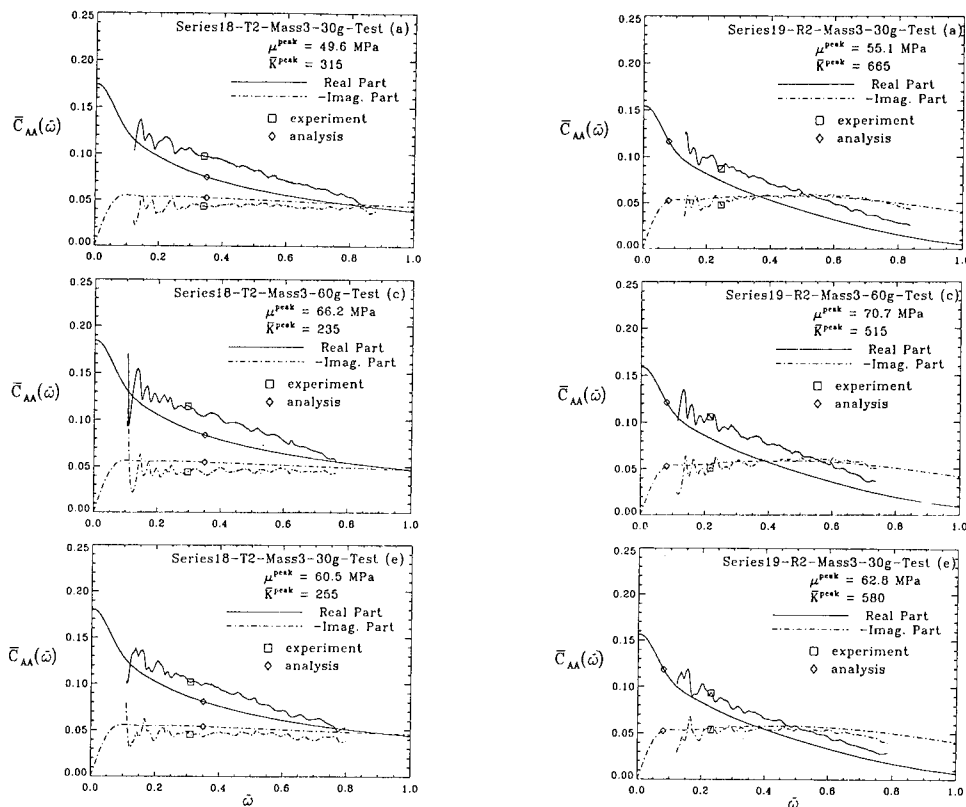


Fig.5 Comparison of the experimental and theoretical dimensionless pile-top compliances for a dense sand with  $D_r = 86\%$

## ACKNOWLEDGMENTS

The financial support for this work by the U.S. National Science Foundation through Award BCS 8958402 is gratefully acknowledged.

## REFERENCES

- Bendat, J.S. and Piersol, A.G., 1986, "Random data, analysis and measurement procedure", John Wiley and Sons, Inc.
- Finn, W.D. and Gohl, B., 1987, "Centrifuge model studies of piles under simulated earthquake lateral loading", Dynamic response of pile foundations, Geotechnical special publication, Nogami (Ed.)
- Gobert, A.T., 1992, "Dynamics of a pile under axial loading : analysis and experiment", Ph. D. Dissertation, University of Colorado
- Hardin, B.O. and Drnevich, V.P., 1972, "Shear modulus and damping in soils", Journal of Soil Mechanics and Foundation Division, ASCE, Vol.98, No.SM7, pp.667-692
- Ko, H.Y., 1988, "Summary of the state-of-the-art on centrifuge model testing", Centrifuge in soils mechanics, Craig, James and Schofield (Eds), Balkema, Rotterdam
- Lenke, L.R., Pak, R.Y.S. and Ko, H.Y., 1991, "Boundary effects in modeling of foundations subjected to vertical excitations", Ko and McLean (Eds), Balkema, Rotterdam
- Scott, R.F., Ting, J.M. and Lee, J., 1982, "Comparaison of centrifuge and full-scale dynamic tests", Proceedings Conference on Soil Dynamics and Earthquake Engineering, Southampton, Vol.1, pp.299-309

## Efficiency of a stress-wave mitigation barrier

M.P. Luong

CNRS-LMS, Ecole Polytechnique, Palaiseau, France

**ABSTRACT:** The presented experimental procedure describes a drop-ball arrangement, able to generate in-flight stress waves propagating through a centrifugal soil mass. It has been used to study the efficiency of a stress wave mitigation barrier. The screening principle of this new type of energy-dissipating barrier has been suggested by the dissipative behaviour of sandy soils, evidenced by infrared vibrothermography.

### 1 INTRODUCTION

A problem of practical importance for the foundation engineer in urban areas is the protection of structures against ground-transmitted waves generated by earthquake hazards and other vibrations such as external traffic, machinery, blasting, which result in ground amplitudes, causing disturbances to adjacent structures.

Most of the vibratory energy affecting structures nearby is carried by surface (Rayleigh) waves that travel in a zone close to the ground surface. The soil may act as a vibration transmitter, thereby modifying the intensity, frequency content and spatial distribution of ground shaking and therefore the structural damage. It is then possible to reduce the ground-borne vibrations significantly by placing a suitable wave barrier in the ground around the structure. The usefulness of such wave barriers is directly associated with the proper isolation of the Rayleigh wave energy. Traditionally, ground vibration isolation, based on the principles of scattering and diffraction of elastic Rayleigh waves, uses rows of cylindrical obstacles installed in the ground, concrete barriers or open and in-filled trenches.

In seismic zones, foundations of civil engineering structures must be designed to resist the effects of strong earthquakes and to undergo substantial deformations without suffering excessive damage or loss of strength in face of subsequent load applications. This is also the cases for isolation of vibrations caused by traffic, vibrating machines, blast, shock or impact loadings.

### 2 CENTRIFUGE TESTING

In dynamic geotechnical engineering, the best approach is to observe the behaviour of the actual structure and check the accuracy of the existing procedure or to

establish a new design technique abstracting new assumptions from observations of the full-scale structure.

Unfortunately, full-scale tests to observe the behaviour of an actual structure are almost always very costly, time consuming and they sometimes may be very dangerous. Furthermore, it is impossible to carry out a parametric study and to check the reproducibility of the test results. Therefore the need for scaled modelling arises to replace full-scale observations.

The scaled reproduction of wave propagation is advantageous for several reasons :

- a) the problem at hand is too complex or too little explored to be amenable to an analytical solution ; empirical information on relevant physical phenomena is needed.
- b) Scale models permit transformation of systems to manageable proportions and investigation of model size effects.
- c) Scaled modelling shortens experimentation.
- d) It promotes a deeper understanding of the phenomenon under investigation : failure mechanisms and analyses.
- e) It verifies numerical models.
- f) Direct modelling can be used to check the design of full scale structures.

In order to predict the prototype behaviour correctly from observation, scaling laws must be established for the model and the prototype, taking into account three groups of equations governing the physical phenomena : balance equations or general laws, constitutive relations or rheological laws, and boundary conditions or initial references and boundary values. In centrifuge testing, the scaling relationship emphasises the relevant effect of self-weight induced stresses appropriate to the prototype earth structures.

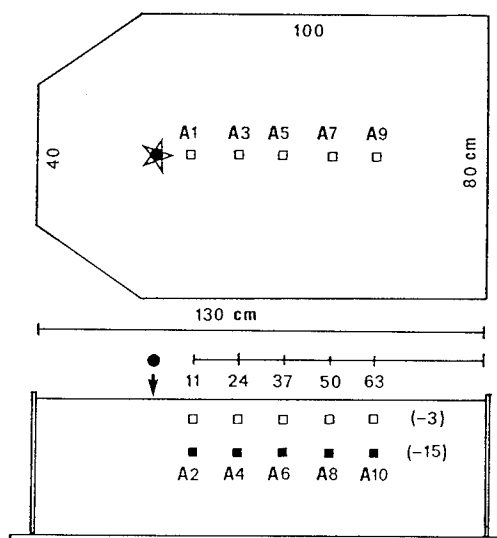


Fig. 1 - Location of accelerometers in soil mass.

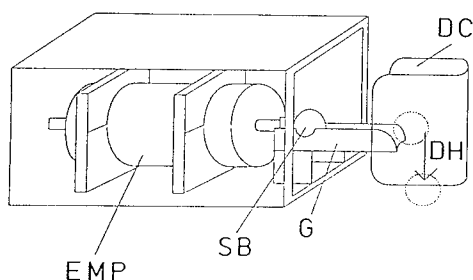


Fig. 2 - Drop-ball arrangement in centrifuge.

### 3 EXPERIMENTAL SET-UP

The experiments were carried out in the 200g-ton centrifuge built by Latecoere in 1964 at the CEA-CESTA-centre near Bordeaux France. The arm has a radius of 10.5 m to the centre of the swinging platform. The centrifuge is equipped with 108 low noise electrical slip rings. The motor drive unit comprises 4 suspended motors (350 HP each) and 4 Ward Leonard groups (250 kVA each). The run-up time to 100g is 60 s.

The rotating container of internal dimension length = 1.30 m by width = 0.80 m by height = 0.40 m, mounted on the swinging platform, was filled with Fontainebleau sand rained to the density of  $1520 \text{ kgm}^{-3}$ . The tests were run at 100g, respecting the usual scaling relationships (Centrifuge 88 and 91 conferences) (Corté 1988, Ko and McLean 1991).

The motion was detected by 3D piezo-electric accelerometers which provided data on the horizontal (x), transverse (y) and vertical (z) movements at

different locations in the soil mass (Fig. 1) : A1, A3, A5, A7, A9 and A2, A4, A6, A8, A10 respectively installed at 3 cm (three metres) deep and 15 cm (fifteen metres) deep. Charge amplifiers delivered a tension proportional to electric charge and independent of the capacity of the lines.

All the signals were recorded on magnetic tapes. With the same magnetic tape recorders, all the signals have been read again and sent to analog channels with programmable low pass anti-aliasing filter, a hold circuit and a multiplexer. Each sample is weighted by an Hanning window. The frequency response function resolution is about 1.25 Hz. The measurement error has been evaluated at 2.5 per cent.

A drop-ball arrangement (Fig. 2) has been installed in a large swinging container to produce Rayleigh shear waves. An electromagnetic motor (EMP) pushes horizontally the steel ball (SB - mass = 0.5 kg) along a guide (G) toward a thin steel wall (DC) that controls its vertical drop (DH - height = 0.1 m).

The use of impact excitation together with a Fast Fourier Transform (FFT) based spectrum analyser to determine the dynamic characteristics of soil is potentially a very attractive technique as attested the dynamic studies presented at Centrifuge 88 and 91 conferences.

An impact technique may readily generate high stress wave energies. The frequency content due to a ball drop can be theoretically controlled by varying ball size and drop height as defined by the Hertz elastic solution for impact; the size of the impacting ball is the most significant factor for controlling input frequency content. The resulting frequency distribution will be essentially broadband, and control of input frequency bandwidth is limited.

An impact usually gives excitation across a relatively broad frequency range and the upper limit of this range can be tailored to suit the particular test by varying the ball material. Therefore it is frequently possible to investigate the whole low frequency range of interest in a single test. The test is also very quick to set up since the need for connecting and aligning a shaker is eliminated.

The conventional shear modulus can be deduced from the velocity of Rayleigh waves :

$$G = \rho V_R^2$$

### 4 ATTENUATION WITH DISTANCE

The body waves propagate radially outward from the source along a hemispherical wave front and the Rayleigh wave propagates radially outward along a cylindrical wave front. All of the waves encounter an

increasingly larger volume of material as they travel outward; thus, the energy density in each wave decreases with distance from the source. This decrease in energy density or decrease in displacement amplitude is called geometrical damping.

For a vertical oscillating, uniformly distributed, circular energy source on the surface of a homogeneous, isotropic, elastic half-space, Miller and Pursey (1955) determined the distribution of total input energy among the three elastic waves to be 67 per cent Rayleigh wave, 26 per cent shear wave, and 7 per cent compression wave. The facts that two-thirds of the total input energy is transmitted away from a vertically oscillating footing by the Rayleigh wave and that the Rayleigh wave decays much more slowly with the distance than the body waves indicate that the Rayleigh wave is of primary concern for foundations on or near the surface of the earth.

The amplitude of the body waves decreases in proportion to the ratio of  $r^{-1}$  ( $r$  is the distance from the input source) except along the surface of the half-space, where the amplitude decreases as  $r^{-2}$ . The amplitude of the Rayleigh wave decreases as  $r^{-1/2}$ . The decrease in amplitude of the vertical component of the R-wave with distance due to geometry alone or geometrical damping can be expressed as :

$$w = w_1 (r_1/r)^{-1/2}$$

where  $r_1$  is the distance from source to point of known amplitude,  $r$  the distance from source to point in question,  $w_1$  the amplitude of the vertical component of the R-wave at distance  $r_1$  from source, and  $w$  the amplitude of the vertical component of the R-wave at distance  $r$  from source.

Because soil is not perfectly elastic, there is another consideration which influences the attenuation of R-waves. In real earth materials, energy is lost by material damping. The existence of material damping in soils is demonstrated by the fact that amplitude attenuation measured in the field is greater than would be predicted by geometric damping alone. Both geometrical and material damping is included in an expression for R-wave attenuation as follows :

$$w = w_1 (r_1/r)^{-1/2} \exp [-\alpha(r - r_1)]$$

where  $\alpha$  is the coefficient of attenuation, having dimensions of (distance) $^{-1}$ .

This equation implies that the total energy on two concentric circles at radii  $r_1$  and  $r$  from a point energy source is constant except for the energy lost through material damping. Although material damping occurs in real soils, it is geometrical damping which contributes most to the attenuation of R-waves (Fig. 3).

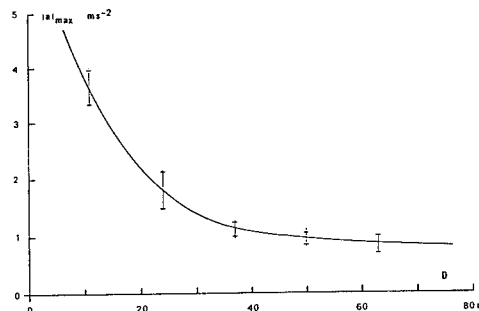


Fig. 3 - Attenuation of Rayleigh waves when using the drop-ball arrangement.

Thanks to the large size of the used swinging container (Fig. 1), the decrease in amplitude of the generated stress waves with depth and distance, measured by accelerometers, has been found sufficiently important to allow the assumption of negligible boundary effects.

## 5 ENERGY-DISSIPATING MECHANISM

When a siliceous sand grain slides against another one, there occurs a motion resistance called friction. What is the cause and what really happen on the contact surface ?

Bowden and Tabor (1959) demonstrated that when quartz or glass surfaces slide over another in the dark, small sparkling points of light can be seen at the interface. The friction between grains generates heat in the same fashion as when prehistoric man used silex stones to generate fire.

A consideration of the forces and deformations at each contact surface (Mindlin & Deresiewicz 1953) may serve as one starting point in interpreting the thermomechanical coupling of sand behaviour under vibratory shearing.

For the simplest case of two like spheres compressed statically by a force which is directed along their line of centres, normal to their initial common tangent plane, the contact theory caused by Hertz predicts a plane, circular contact radius. When an additional tangential force is applied in the plane of contact, the Mindlin's solution shows that the tangential traction is parallel to the displacement and increases without limit on the bounding curve of the contact area.

In accordance with Coulomb's law of sliding friction, slip is assumed to be initiated at the edge of the contact and to progress radially inward, covering an annular area. An annulus of counter-slip is formed and spreads radially inward as the tangential force is gradually decreased. The inelastic character of the unloading

process appears evident since the annulus of the counter-slip does not vanish when the tangential force is completely removed.

Under oscillating tangential forces, the load-displacement curve forms a closed loop traversed during subsequent force oscillations between the limits providing that the normal force is maintained constant. The area enclosed in the loop represents the frictional energy dissipated in each cycle of loading. Thus at small amplitudes of the tangential force, energy is dissipated as a result of plastic deformation of a small portion of the contact surface, whereas, at large amplitudes, the Coulomb-sliding effect predominates.

In the conventional triaxial test, if the load is cycled within the subcharacteristic domain below the characteristic threshold  $\eta_c$  (Luong 1980), the intergranular contacts remain stable. Small slips lead to a maximum entanglement caused by the relative tightening of constituent granules. The dissipated work given by the hysteresis loop is relatively small. The corresponding heat production is relatively low and negligible.

On the contrary when the shear load is cycled at large amplitude exceeding the characteristic thresholds (compression and extension), the intergranular contacts become unstable, leading to significant slidings caused by interlocking breakdown. A large frictional energy is dissipated and is transformed almost entirely into heat owing to the thermomechanical conversion. If the stress peaks in triaxial compression and extension are not exceeded, the resultant effect is densification because the high amplitude loading benefits in partial loss of strain-hardening during the dilating phase in the supercharacteristic domain leading to a breakdown of the granular interlocking assembly. On each reload, the tightening mechanism induces new irreversible volumetric strains and recurs each time with a renewed denser material. This case is particularly interesting when energy needs to be dissipated without risk of soil failure.

The theoretical background of the energy-dissipating mechanism is based on the coupled thermo-visco-elastic-plastic analysis (Kratochvil & Dillon 1969). This leads to a coupled thermomechanical equation where the intrinsic dissipation term is predominant in this case. The work done to the system by plastic deformation is identified as the major contribution to the heat effect.

In the framework of thermo-elastic-plasticity, there exists a general acceptance that not all the mechanical work produced by the plastic deformation can be converted to the thermal energy in the solid. A larger portion of the work is believed to have been spent in the change of material microscopic structure. The work done in plastic deformation per unit volume can be evaluated by integrating the material stress-strain curve. This internal dissipation term constitutes an important part of the nonlinear coupled thermomechanical effect.

The quantification of this intrinsic dissipation for soils is an extremely difficult task if infrared

thermography is not used. This paper emphasizes the advantages of the infrared thermographic technique for the detection of this effect.

## 6 INFRARED VIBROTHERMOGRAPHY

Infrared thermography has been successfully employed as an experimental method for detection of plastic deformation during crack propagation under monotonic loading of a steel plate or as a laboratory nonintrusive technique for investigating damage, fatigue, creep, and failure mechanisms. The heat dissipation evidenced here is associated with a plastic work of distortion.

This technique is sensitive, nondestructive and noncontact, thus ideally suited for records and observations in real time of heat produced by the heat transformation of energy caused by friction between grains of sheared sandy soil. No interaction at all with the specimen is required to monitor the thermal gradient.

The quantity of energy emitted by infrared radiation is a function of the temperature and the emissivity of the specimen. The higher the temperature, the more important is the emitted energy. Differences of the radiated energy correspond to differences of temperature.

Soils present a very low thermomechanical conversion under monotonic loading. However plastic deformation, whereby sliding between grains occurs creating permanent changes globally or locally, is one of the most efficient heat production mechanisms. Most of the energy that is required to cause such plastic deformation is dissipated as heat. Such heat generation is more easily observed when it is produced in a fixed location by reversed or alternating slidings because of vibratory reversed applied loads. These considerations define the use of vibrothermography as a nondestructive method for observing the energy-dissipating ability of granular material (Fig. 4).

A scanning camera is used which is analogous to a television camera. It utilizes an infrared detector in a sophisticated electronics system in order to detect radiated energy and to convert it into a detailed real time thermal picture in a video system both colour and monochromatic. Response times are shorter than a microsecond. Temperature differences in heat patterns as fine as  $0.1^\circ\text{C}$  are discernible instantly and represented by several distinct hues. The quantity of energy  $W$  ( $\text{W m}^{-2} \mu\text{m}^{-1}$ ) emitted as infrared radiation is a function of the temperature and emissivity of the specimen. The higher the temperature, the more important is the emitted energy. Differences of radiated energy correspond to differences of temperature.

The AGA 782 SW infrared scanner unit in use comprises :

- a set of infrared lens which focusses the electromagnetic energy radiating from the object being scanned into the vertical prism,

- an electro-optical scanning mechanism which discriminates the field of view in 10 000 pixels by means of two rotating vertical (180 rpm) and horizontal (18 000 rpm) prisms with a scanning rate of 25 fields per second,
- a set of relay optics containing a selectable aperture unit and a filter cassette unit which focusses the output from the horizontal prism onto a single element point detector, located in the wall of a Dewar chamber,
- a photovoltaic SW short waves infrared detector composed of Indium Antimonide InSb which produces an electronic signal output varying in proportion to the radiation from the object within the spectral response  $3.5 \mu\text{m}$  to  $5.6 \mu\text{m}$ ,
- a liquid nitrogen Dewar which maintains the InSb detector at a temperature of  $-196^\circ\text{C}$  allowing a very short response time ( $1 \mu\text{s}$ ),
- and a control electronics with preamplifier which produces a video signal on the display screen.

## 7 STRESS-WAVE MITIGATION BARRIER

The dynamic response of buildings due to soil vibration can be mitigated by various different techniques :

- use of friction elements at appropriate locations within a structure to increase the structural damping through energy dissipation at these locations.
- change of the vibration behaviour of a building by changing the soil around the foundation.
- mounting of special devices such as rubber bearings, springs or a combination of springs and dampers at the foundation of the building.
- reduction of the spreading waves by installing a wave barrier like a trench, a concrete wall or a wall consisting of air cushions.

The barrier disturbs the natural spreading of the waves and so screens the buildings at a certain region behind the barrier. Isolation of structures and machine foundations from ground transmitted vibrations by installation of wave barriers has been attempted many times. However this technique has met with varying degrees of success (Barkan 1962, Dolling 1966, Woods 1968, Aboudi 1973, Haupt 1977, Liao & Sangrey 1978 and Ahmad & Al-Hussaini 1991). Several numerical, experimental and analytical techniques have been applied to study the surface wave propagation across different types of barriers or in-filled trenches.

This paper presents some experimental results obtained with a new type of wave barrier, designed to dissipate seismic energy by friction between soil particles. It is suggested by a theoretical idea concerning the stability of the soil element in the presence of wave propagation. For geomaterials, experimental evidence of mechanical behaviour that contradicts Drucker's stability postulate, has been shown by a great number of geotechnical researchers (Lade et al 1987, 1988).

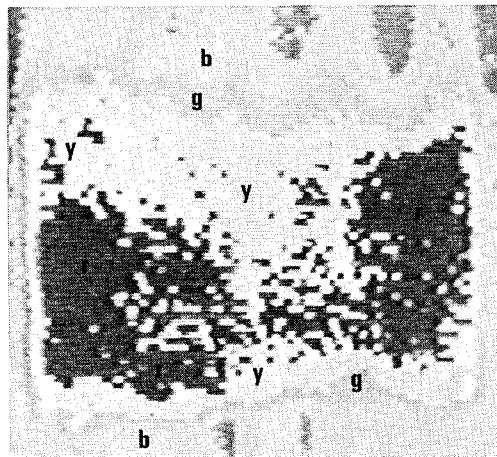


Figure 4. Infrared thermography of the energy dissipation of a siliceous fine sand subject to shear loadings ( $10^\circ\text{C}$  for each colour hue).

Within the theory of plasticity, using wave propagation considerations, Mandel (1964) showed that Drucker's postulate was a sufficient but not a necessary condition for a material to be stable, due to the frictional nature of sliding between soil particles (Hardin 1978).

Based on the assumption that a stable material is able to propagate a small perturbation in the form of waves, Mandel (1964) proposed a necessary condition for stability. He showed that a wave can propagate in a material with an elastic-plastic matrix  $\mathbf{A}$ , along the direction  $\alpha$ , if and only if all the eigenvalues  $\lambda$  of the matrix  $\mathbf{M}$  are positive.

$$d\epsilon_{ij} = A_{ijkl} \cdot d\sigma_{kl}$$

$$M_{ik} = A_{ijkl} \cdot \alpha_j \cdot \alpha_l$$

where  $k = 1, 2, 3$  and  $\lambda_k > 0$ .

If one of the eigenvalues  $\lambda$  is  $\leq 0$ , one of the corresponding components of the perturbation cannot propagate. This implies instability, and the possible appearance of strain localisation along a shear band or sliding zone along a certain direction.

This phenomenon occurs when the stress state reaches the supercharacteristic domain where the frictional mechanism is very active between soil particles, or when the loading is cycled near the characteristic threshold. A very important amount of mechanical energy (several tens of  $\text{kJ.m}^{-3}$ ) can then be dissipated in soil mass by heat as evidenced by infrared vibrothermography (Luong 1986).

In the centrifuge, a dissipating wave barrier has been simulated by applying on the soil mass an additional

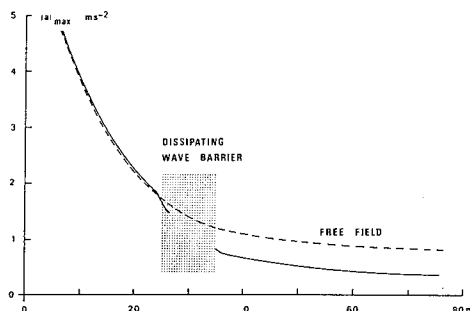


Figure 5. Efficiency of the proposed dissipating wave barrier.

loading such that the stress state locally reaches the supercharacteristic threshold. This loaded region will mitigate the wave energy as shown by the decreased amplitude of acceleration records (Fig. 5). The first centrifuge results were very promising. However these results must be validated by field tests.

## 8 CONCLUSION

Centrifuge simulation of wave propagation in soils is very useful for a realistic evaluation of the dynamic soil properties involved in the interpretation of the geotechnical performance of earthquake-resistant and vibration-isolating structure models.

This technique provides a reliable representation of :

- (1) soil modulus varying with depth,
- (2) frequency variability of the soils resulting from soil inertia, damping reactions caused by elastic wave radiation and internal friction and
- (3) both kinematic and inertial soil-structure interactions. It aims to elucidate the relevant parameters influencing the rheological behaviour of geotechnical structures subjected to transient and dynamic loadings.

The proposed technique of in flight falling-weight source offers a very simple means of applying a substantial transient force normal to the ground surface during the impact.

Artificially generated seismic waves provide useful information about the mechanical characteristics of soil in flight, facilitating the analysis of dynamic centrifuge test results. Such centrifuge model experiments offer promise for future application on seismic or vibratory isolation of geotechnical structures.

## REFERENCES

- Aboudi, J. 1973. Elastic waves in half-space with thin barrier. *J. Engng Mech. Div.*, ASCE, 99(1): 69-83.
- Ahmad, S. & T.M. Al-Hussaini 1991. Simplified design for vibration screening by open and filled trenches. *J. Geot. Engng*, ASCE, 117(1): 67-88.
- Barkan, D.D. 1962. *Dynamics of basis and foundations*. Mc Graw Hill, New York.
- Bowden, F.P. & D. Tabor 1959. *Friction and lubrication*. Monographies, Dunod, Paris.
- Corté, J.F. ed. 1988. *Centrifuge 88*. Rotterdam: Balkema.
- Dillon, O.W.Jr 1963. Coupled thermoplasticity. *J. Mech. Phys. Solids*, 11, 21-23.
- Dolling, H.J. 1966. Efficiency of trenches in isolating structures against vibrations. *Proc. Symp. Vibration in Civil Engineering*, Butterworths, London, 273-276.
- Hardin, B.O. 1978. The nature of stress-strain behavior of soils. *Proc. Conf. Earthquake Engineering and Soil Dynamics*, 1, ASCE, Pasadena, USA, 3-90.
- Haupt, W.A. 1977. Isolation of vibration by concrete core walls. *Proc. 9th ICSMFE*, Jap. SMFE, Tokyo, 2: 251-256.
- Ko, H.Y. & F.G. McLean ed. 1991. *Centrifuge 91*. Rotterdam: Balkema.
- Kratochvil, J. & O.W. Dillon 1969. Thermodynamics of elastic-plastic materials as a theory with internal state variables. *J. Appl. Phys.*, 40, 3207-3218.
- Lade, P.V., Nelson, R.B. & Y.M. Ito 1987. Nonassociated flow and stability of granular materials. *J. Engng Mech.*, ASCE, 113(9): 1302-1318.
- Lade, P.V., Nelson, R.B. & Y.M. Ito 1988. Instability of granular materials with nonassociated flow. *J. Engng Mech.*, ASCE, 114(12): 2173-2191.
- Liao, S. & D.A. Sangrey 1978. Use of piles as isolation barriers. *J. Geot. Engng Div.*, ASCE, 104(9): 1139-1152.
- Luong, M.P. 1980. Stress-strain aspects of cohesionless soils under cyclic and transient loading. *Proc. Int. Symp. on Soil under Cyclic and Transient Loading*, Rotterdam: Balkema, 315-324.
- Luong, M.P. 1986. Characteristic threshold and infrared vibrothermography of sand. *Geotechnical Testing J.*, GTJODJ, 9(2): 80-86.
- Mandel, J. 1964. Conditions de stabilité et postulat de Drucker. *Proc. IUTAM Symp. Rheology and Soil Mechanics*, Grenoble, 58-68.
- Miller, G.F. & H. Pursey 1955. On the partition of energy between elastic waves in a semi-infinite solid. *Proc. Royal Society*, London, A, 233, 55-69.
- Mindlin, R.D. & H. Deresiewicz 1953. Elastic spheres in contact under varying oblique forces. *J. Appl. Mech.*, 20, 327-344.
- Woods, R.D. 1968. Screening of surface waves in soils. *J. Soil Mechanics and Foundations Div.*, ASCE, 94(SM4): 951-979.

## Simulation of failure of dikes by water infiltration by waves

H.G.B. Allersma & I.A.G. Ligtenberg  
*University of Delft, Netherlands*

B.A.N. Koehorst  
*Ministry of Public Works, Delft, Netherlands*

**ABSTRACT:** A test program has been carried out in the small geotechnical centrifuge at the University of Delft in order to investigate the stability of dikes during water infiltration due to wave overtopping. This research was very helpful to get insight in the mechanism during failure of the dikes.

### 1 INTRODUCTION

In 1953 several dikes, which protect the low-lying parts of the Netherlands against the sea, were broken during a heavy storm in combination with spring tide. A large area in the south-west part of the country was covered by sea water several meters deep. About 1900 people were killed during this disaster. It appeared that several dikes were not damaged in the first instance on the sea side by the mechanical forces of the waves, but on the land side. The water of the sea had reached such a high level that it flowed over the top of the dikes due to the wave action. The amount of water itself was not very critical because a polder has sufficient capacity to store this water. The point was, however, that the water infiltrates into the dike. This was possible because the top of the dike and the slope on the land side were not covered with a waterproof layer. The water flow in the soil dramatically reduces the stability of the slope on the land side, which causes failure of the dike.

In order to estimate the potential danger, several theoretical analyses have been made for determining the stability of dikes when wave overtopping occurs. It appeared that the steepness of the slope and the appearance of different soil layers are important parameters. Tests are required to get more insight into the contribution made by these parameters. Since it is very difficult to perform real scale tests under controlled conditions a test program has been carried out in the small geotechnical centrifuge of the University of Delft. A pumping system has been developed to enable an accurate control of a water flow at high  $g$  levels. The flow of the pore water and the behavior of the dikes could be observed in flight with a video camera. The images could be analyzed in more detail by image processing. Tests on dikes of cohesive material are reported also by Liu et al., 1988 and

Kimura et al., 1991. In this test program, however, only dikes of non-cohesive material were investigated.

Several different profiles of dikes were tested and numerical calculation methods applied to predict the effect of the water flow through the body of the dike and to calculate the safety factor. Failure mechanisms which were not understood during evaluation of the failed dikes in 1953 could be simulated in the centrifuge. The small centrifuge has proved to be very convenient for performing these tests.

### 2 EQUIPMENT

The test program was carried out in the small geotechnical centrifuge (Fig.1) of the University of Delft (Allersma, 1994). This centrifuge has a diameter of two meters, which can accelerate samples with a weight of approximately 300N up to 300g. A small centrifuge is extremely suitable for performing trial and error tests. Because the size and weight of the samples are low, a large number of tests can be performed, so that the influence of several test conditions can be investigated in a short time. The application of up to date electronics permits the performance of advanced computer controlled tests. To enable the performance of stability tests of slopes due to water infiltration, a well controlled flow of liquid has to be available during spinning. Because the centrifuge is not equipped with fluid slip rings, the liquid flow has to be generated in the spinning part of the centrifuge.

For this test program a simple water supply system has been developed, in which water circulation is obtained by means of an air jet (Fig.2). The advantage of this technique was that the water supply could be controlled very smoothly between zero and the maximum flow rate (approximately 10 l/min). The



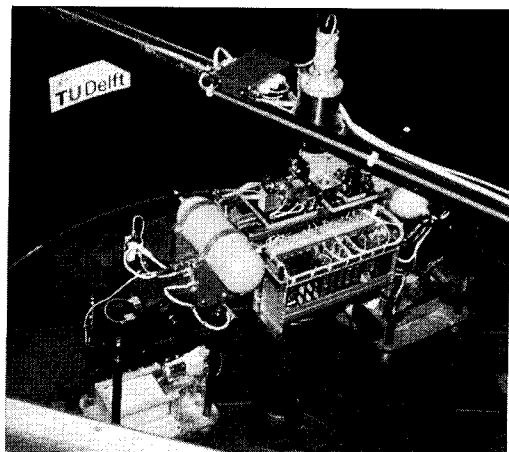


Fig.1 University of Delft geotechnical centrifuge.

measurement of the flow rate was based on calibrations which were made in advance and estimations can be made from the observed water table in the tested soil sample. In this test program the maximum water flow was 1 l/min.

The air required to perform the tests was stored in two high pressure (200 bar) cylinders with a total volume of 10 litres. The cylinders are mounted on the beam of the centrifuge. Before the centrifuge was started the cylinders were filled with air by means of a high pressure compressor. The air supply during a test was controlled by a pressure regulator and a valve. The pressure regulator and the valve are standard devices which are equipped with small dc motors to enable interfacing with the on board computer. The on board computer is connected, using the rs232 protocol, with a pc via slip rings. A program in the pc permits effective control over the water flow during spinning of the centrifuge. During the test the process parameters are plotted on the screen, where it is possible to combine the plots with the real time video image.

### 3 TEST TECHNIQUE

The tests are performed in plane boxes with transparent walls at a distance of 50 mm apart. The dimension of the box is 36x40 cm<sup>2</sup>. The model of a dike was located on a metal platform. The space which was left under the platform was used as a water reservoir. Many tests have been performed in which the behavior of a sand layer on a slope of very strong clay was investigated. Because no deformation of the clay layer was assumed the clay body was simulated by a metal block (Fig.2).

Up to now the tests have been performed at gravities of 80g and 120g, so that dikes with a prototype height

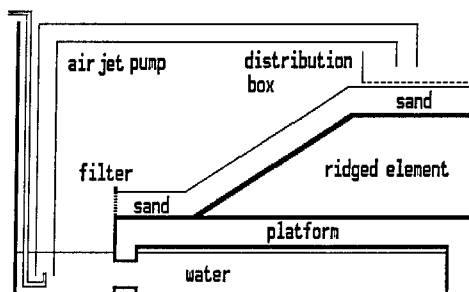


Fig.2 Diagram of the test box with the air jet pump.

of approximately 2 to 7 meters were simulated. The water was supplied at the top of the dike through a small box with a filter bottom to distribute the water equally. A good distribution of supplied water prevents erosion due to locally high flow rates. The water flow in the sand layer was visible due to the difference in contrast between wet and dry sand. The tests were recorded on video tape, so that it was possible to study the failure mechanism in more detail afterwards, i.e. by using thin layers of black sand and image processing techniques (Allersma, 1991).

Due to the higher g level the stresses, induced by the capillary forces (36 cm water at 1 g) could be ignored. On the other hand the flow rate of the pore water in the dune sand during tests at 80 g was still low enough (maximum flow rate in the test series was 0.016 m/s) to keep the Reynolds number (the estimated max. value was 1.6) below the value which indicates turbulence. If the flow can be assumed to be steady state and laminar, the flow rate of the water is linear with the acceleration of the centrifuge. The self weight stresses and the flow induced stresses can then be assumed to be in close agreement with the prototype situation. It appeared in most tests that failure of the slope is initiated by local instability due to seepage. Because flow problems in the centrifuge have to be interpreted with care at critical Re numbers (Goodings, 1984) orientating tests have been performed to investigate if the failure mechanism in the centrifuge models is representative. Small scale tests at 1g, centrifuge tests with different grain sizes and the analyses of a video tape of a real scale test gave support that the initial failure mechanism in the centrifuge models may not expected to be very different from reality. In reality, during overtopping, the water infiltrates not in the crest only, but also in the slope of the dike. Tests in which the whole body of the dike has to be infiltrated require a coating of the sand surface to prevent failure by erosion, in order to investigate whether other mechanisms are responsible for failure. It appeared, however, that the infiltration pattern in dikes with and without a coating were nearly the same. Therefore it

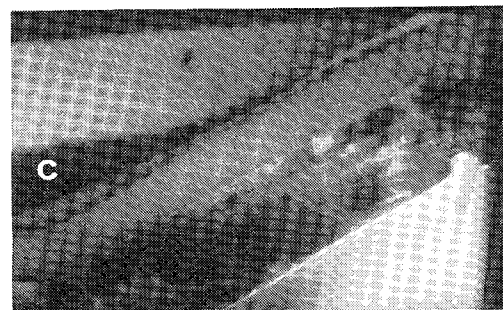
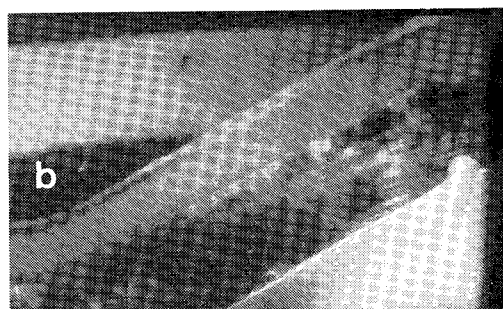


Fig.3 Infiltration of a sand dike with an impermeable core.

was assumed that overtopping was sufficiently well simulated in a centrifuge by infiltration of the water in the crest of the dike only.

In the tests, the water was supplied continuously. Since not every wave will induce overtopping in reality the infiltration varies in time. It was supposed, however, that circumstances of constant water supply did not simulate the problem in a safer way.

#### 4 TEST PROGRAM

The aim of this test program is to investigate the mechanism which leads to failure of dikes of non-cohesive material during water infiltration and to compare the result with numerical calculations. In this paper centrifuge tests on three different dike profiles

were presented.

The first profile was a dike with an impermeable core and a permeable top layer. This configuration simulates the improvement of an old clay dike by increasing the height with sand. Dikes with different slope angles (5:7, 1:2, 1:3) were tested at 80g.

The second profile were dikes of which the slope was covered with a thin impermeable top layer of clay. Homogeneous dikes and dikes with an impermeable core with shape angles of 1:2 and 1:3 were tested at 120g. To prevent erosion by surface flow, in reality a sand dike is covered with a clay layer for growing grass on. In several cases the clay layer appeared to be cracked, so that there is a potential danger that water can penetrate into the dike during wave overtopping.

In the third case a homogeneous dike profile of sand with a critical slope angle (5:7) was tested at 80 g.

The slopes are made of dune sand, characterized by

Unit weight	16 kN/m <sup>3</sup>
Permeability	0.01 cm/s
Friction angle	36°
D <sub>10</sub>	0.1 mm
D <sub>50</sub>	0.2 mm

#### 5 RESULTS

In the first case the thickness of the top layer on the impermeable core was 1 and 2 cm and the tests were performed at 80g. It appeared that the thickness of the top layer did not affect the mechanism significantly. The water supply was increased smoothly, so that the level of the phreatic line increased in time. By means of drainage, the horizontal part of the dike at the toe was prevented from flooding. Three stages of a test with a slope angle of 1:2 are shown in Fig. 3. Due to the difference in contrast between saturated (dark) and dry sand, the development of the infiltration pattern can be seen in time. The maximum infiltration stage is shown in Fig.3<sup>b</sup>. It appeared that the permeable layer could be saturated almost completely. Even a dike with an impermeable core and a top layer with a critical slope can be almost totally saturated. It can also be observed in the series that the flow of the pore water is initially parallel to the core. In Fig.3<sup>c</sup> failure has taken place. The failure was initiated by local instability at the surface of the slope. It was expected that the maximum level of the phreatic line, which could be reached in a test was strongly dependent on the slope angle. It appeared however that it was possible, in several tests, to saturate the sand layer almost completely. The failure finally started at the location where seepage occurred. At this point a thin layer of sand at the surface of the slope is displaced by the forces due to seepage, the progression of this mechanism finally resulted in total failure of the dike. The seepage occurs at a lower level for steeper slopes. In the centrifuge tests, the initial failure mechanism of a

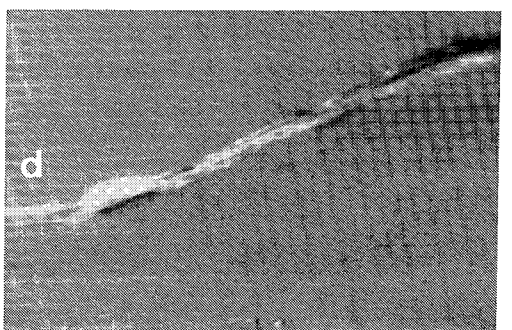
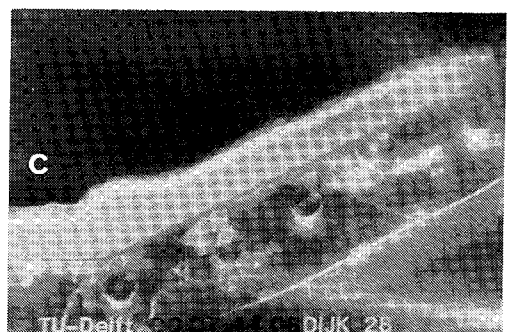
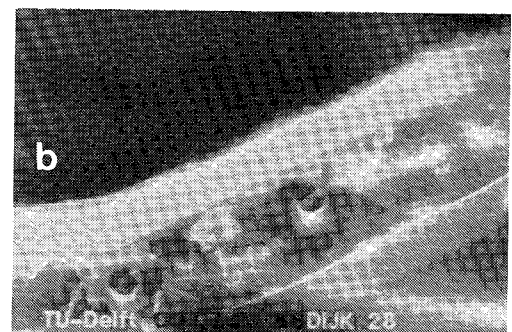
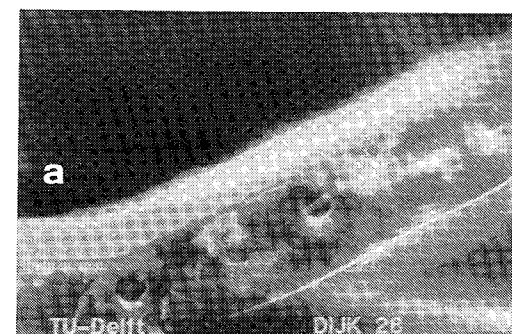


Fig.4 Sand dike with an impermeable core and a sand slope covered with a thin clay layer.

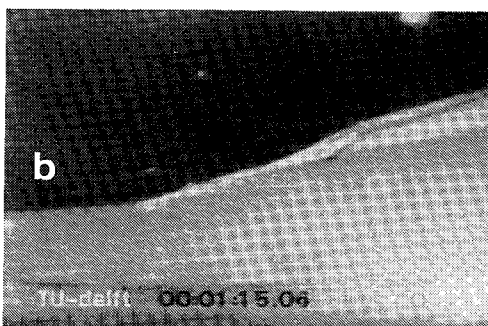
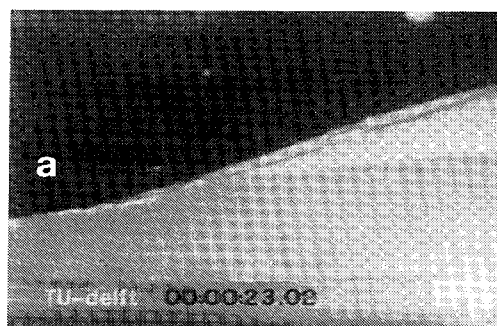


Fig.5 Homogeneous sand dike covered with a thin layer of clay.

dike with an impermeable core and a permeable top layer was a shallow phenomenon and not a shear band mechanism as assumed in some calculation methods.

An example of case two is shown in Fig.4. Three stages are shown of a test at 120g, in which an impermeable core (1:2) with a sand layer of 2 cm was covered with an impermeable top layer. The cover was made of a clay layer with a thickness of 4 mm and a cohesion of 20 kPa. The tests were also performed on dikes with a slope of 1:3. It appeared that failure was caused in these tests by pore water pressure generation under the clay cover near the toe of the slope. First, the clay layer was lifted up near the toe and then local

deformation in the sand under the clay cover could be observed. The failure in the sand layer remained only local near the toe (Fig.4<sup>c</sup>), where the whole clay layer slides over the sand slope. The displacement of the top layer is made visible by subtracting two exposures (Fig.4<sup>d</sup>), one before and one after failure.

The infiltration of a dike with a homogeneous core of sand covered with a thin clay layer can be seen in Fig.5. The water flow under the crest was in the vertical direction. The flow became horizontal when the water reached the impermeable base. The angle between the phreatic line and the slope of the dike is larger than in the dike with the impermeable core. Because of the smaller hydraulic gradient the uplift force of the clay layer near the toe is smaller, which probably results in smaller deformations of the clay layer than in the previous test series. In Fig.5<sup>c</sup> the failure zone is visualized by subtracting the previous stages. The rising of the water level, needed to initiate failure is visible also.

Finally a test series is shown in Fig.6 where a homogeneous dike of sand with a critical slope was tested in the centrifuge at 80g. The failure of the dike started near the toe due to local instability caused by seepage. Contrary to dikes with an impermeable core the homogeneous dike could not be completely saturated before failure started. This can be explained by the fact that the phreatic surface is not so steep as in the tests with the impermeable core, so that the seepage in the toe starts at a more earlier stage. The initial failure of a homogeneous dike in this test (Fig.6<sup>a</sup>) also appeared to be a surface phenomenon. In Fig.6<sup>d</sup> the images of two stages are subtracted. The black area represents the displaced sand near the toe, where the bright area shows the rising water level. As can be seen in this figure, no significant deformation took place in the upper part of the slope. The local instability proceeds with increasing water flow, which results finally in a total failure of the embankment.

## 6 DISCUSSION

The failure of the homogeneous dikes and the dikes with a permeable top layer and an impermeable core started at the location on the slope where seepage occurs. At this location the forces of the flowing water exceeded the weight of the grain and instability appeared. The initial failure mechanism is a shallow mechanism. In a later stage the stability decreased to such an extent that total failure occurred.

Dikes with an impermeable core and a permeable top layer show very stable behavior. Even dikes with a critical slope can be saturated to a high level.

In geometries with an impermeable top layer, the failure is caused by pore pressure generation under the clay layer near the toe of the slope. The result is that the clay layer is lifted up at the toe followed by

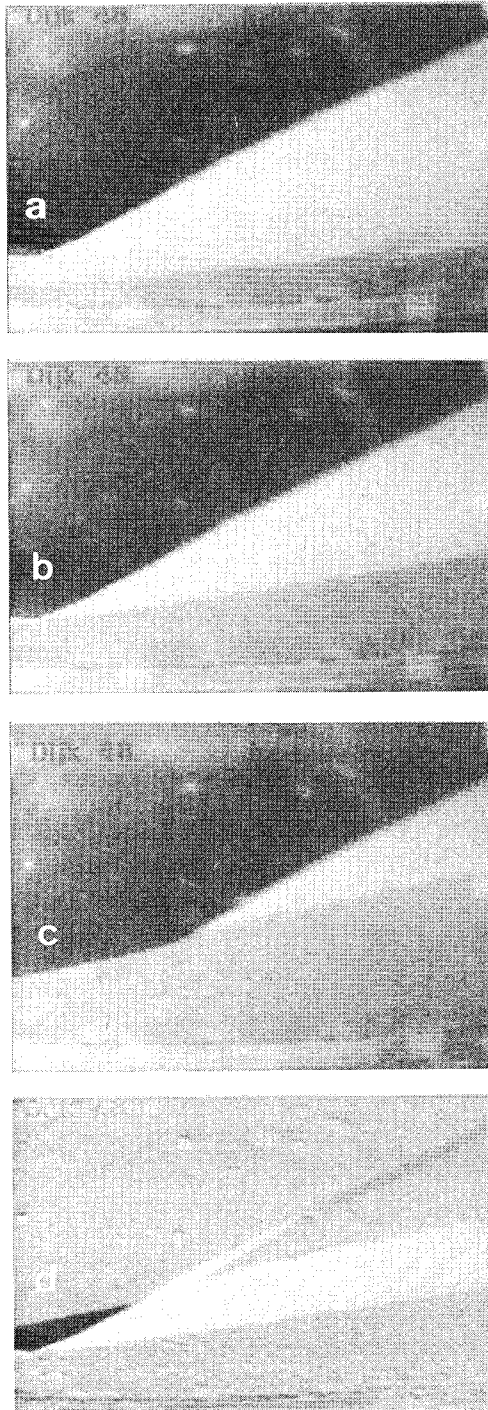


Fig.6 Infiltration of a homogeneous sand dike with a critical slope.

deformation in the sand under the clay layer. This is a local failure mechanism where the clay slides over the sand core.

In practice the water supply by wave overtopping is given in litres/s/m. In these tests the water infiltration at failure varies between 0.1 and 0.3 l/s/m. There are no measurements available from practice. In the design rules the permitted quantities lies between 0.1 and 10 l/s/m, depending on the protection of the slope.

The stability factor of some configurations is calculated with a finite element computer program (Vermeer, 1991). A finite element program is used because the flow induced pore pressure should be taken into account. This procedure is to be preferred above using hydrostatic pore pressure derived from a phreatic line as, for example, used in the slip circle method of Bishop. The stability factor for dikes with a core and for homogeneous dikes are calculated by a  $c-\phi$  reduction and the results are given in Table 1. The calculated results are more or less in agreement with the test results, because also in the calculations the homogeneous dikes show a lower safety factor than the

## 7 CONCLUSION

The small geotechnical centrifuge was very convenient for investigating this problem. In a relatively short time a large number of test conditions could be investigated.

The moment of failure of a sand dike during wave overtopping is dependent on the saturation and the slope angle of the sand body. Critical slopes with an angle of  $36^\circ$  show failure if the phreatic line has reached the soil surface at a height of  $1/3$  of the slope. Non-critical slopes can be completely saturated before failure occurs. It appeared that the failure of sand dikes during water infiltration at the crest is initiated by local instability due to seepage. This is in contradiction with some theoretical hypotheses, which assume that failure starts with a slip circle mechanism, like Bishop.

Finite element calculations show a tendency for a more shallow failure mechanism at a lower cohesion. A problem was that cohesion could not be set to zero in the finite element program used. Probably the cohesion plays a very important role in the failure mechanism.

The observations in this research are supposed to be useful in optimizing the monitoring system of a real scale test, which will be performed in the near future.

Table 1 Calculated safety factors.

slope	dike with core	homogeneous dike
1:2	1,02	smaller than 1
1:3	1,5	1,14

dikes with an impermeable core. In the calculations the same boundary conditions concerning the water infiltration at the crest are taken into account, which means the same hydraulic head and infiltration area. The program does not work for soils with a cohesion of zero. Therefore the results of the calculations and the test results (in which  $c=0$ ) are not perfectly comparable. Furthermore local instability can not be simulated by the program. In contradiction with the time dependent progression of the failure as observed in tests the program gives the final stage at once. The friction angle of the sand used was  $36^\circ$  and the top layer had a thickness of 2 meters.

We have to consider that real dikes are in general not homogeneous as they are built of locally available materials and have usually been reconstructed over the past number of years. The heterogeneity in permeability affects the process of infiltration, while stability is affected by the distribution of strength. Therefore, performing tests on dikes with a soil structure, which is more representative of the reality, has to be considered.

## 8 ACKNOWLEDGEMENT

Many thanks are devoted to the technicians of the laboratory for their assistance in this project. This research was sponsored by the Ministry of Public Works.

## REFERENCES

- Allersma, H.G.B. 1991: Using image processing in centrifuge research. Proc. Int. Conf. Centrifuge91, Boulder, Balkema Rotterdam:551-558.
- Allersma, H.G.B. 1994: The University of Delft geotechnical centrifuge. Proc. Int. Conf. Centrifuge94, Singapore, Balkema, Rotterdam.
- Goodings, D.J. 1984: Relationships for modelling water effects in geotechnical centrifuge models. Proc. Symp. Application of Centrifuge Modelling to Geotechnical Design, Manchester: 1-24.
- Kimura, T. and Takemura, J., 1991: Failure of fills due to rain fall. Int. Conf. Centrifuge91, Boulder, Balkema:509-516.
- Liu, L. and Jiang, S.W., 1988: Centrifugal model tests for stability of ash soil composite dams. Int. Conf. Centrifuge88, Paris, Balkema, Rotterdam:135-140.
- PLAXIS manual, version 4.0, editor P.A. Vermeer, Delft University of Technology, A.A. Balkema, Rotterdam, 1991.

## Wave-induced instability of sand beds

H. Sekiguchi & K. Kita

Kyoto University, Japan

O. Okamoto

Ministry of Transport, Japan

**ABSTRACT:** This paper focuses on the centrifuge modelling of wave-induced instability of seabed deposits. The features of the experiments are : (1) quasi-standing waves were generated by a flap-type wave actuator; and (2) viscous scaling was introduced to satisfy the similitudes of dynamics and consolidation simultaneously. Significant development of residual pore pressure was observed at a shallow depth in a loose sand deposit, approximately below an antinode, bringing the soil into temporal liquefaction. The measured pore pressure response was found to compare favourably with an analytical solution with cyclic plasticity allowed for in a simplified fashion.

### 1 INTRODUCTION

One of the important factors in causing damage to offshore facilities such as pipelines, is the wave-induced liquefaction of the surrounding seabed soils. There have been various experimental attempts to investigate the mechanisms of liquefaction due to wave loading. They may be divided into four categories as illustrated in Fig.1.

Wave tank experiments under 1 *g* conditions are the most common in dealing with progressive water waves (Fig.1(a)). The associated sediment trench cannot, however, be long or deep enough in many cases, due to practical reasons. Another common 1 *g* experiment is to use an "oscillatory pressure column", with the focus on phase-lag related instability of gassy sediments (Fig.1(b)). Even when the sediment is only slightly unsaturated, there will be a substantial lag in the response of excess porewater pressures relative to the input pressure waveform, say  $f(t) = a \cdot \sin \omega t$  (cf. Zen and Yamazaki, 1990.)

The centrifuge wave experiment illustrated in Fig.1(c) may have a potential advantage over the conventional wave-tank experiment of Fig.1(a), in studying flow slides of sediments. The point is that the drum centrifuge would permit unrestrained lateral flow of soil to occur, in its circumferential direction, if the soil underwent complete loss of strength by liquefaction. The present

study featured by Fig.1(d) was motivated by the drum-centrifuge wave experiment that has been put forward at Cambridge University (Sekiguchi and Phillips, 1991; Phillips and Sekiguchi, 1992). Phillips and Sekiguchi (1992) generated progressive wave trains and observed that the surface of a submerged sandy causeway underwent significant settlement due to the passage of the wave trains. However, no residual pore water pressure was observed in their wave tests. This may indicate that consolidation took place more rapidly compared

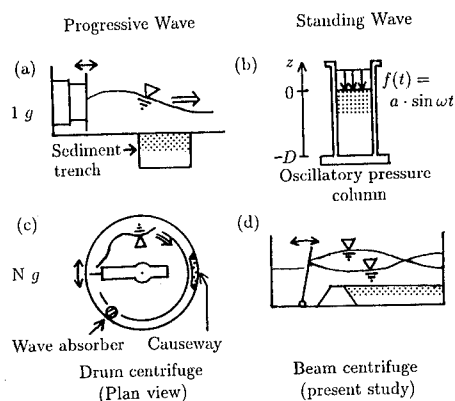


Fig.1 Four categories of wave/seabed experiment

with the corresponding field situation, since water was used as the pore fluid in their experiment.

In fact, the above-mentioned led the authors to introduce viscous scaling in their wave experiment. It was then decided to make full use of standing waves, in such a way that the facilities of a balanced-beam centrifuge may be utilized conveniently. Note that the standing wave experiment is important in its own right, since the stability of the toe of composite breakwaters has often been affected by standing waves occurring there.

In what follows, a theoretical account relevant to the present experimental program will be outlined first. This is followed by a description of the experimental apparatus and experimental procedure. The experimental results obtained will then be discussed in the light of the theoretical framework.

## 2 THEORETICAL CONSIDERATIONS

### 2.1 Wave-induced effective stresses by poro-elasticity

A proper design of the wave/seabed experiment necessitates the estimation of effective stress changes that might be induced in the soil due to anticipated waves. The poro-elastic solutions by Yamamoto(1981) have conveniently been used for this particular purpose.

Yamamoto's solutions are concerned with poro-elastic, finite layers subject to regular water waves. The solutions for a standing wave can readily be obtained by adding up the solutions for two oppositely travelling waves (Sekiguchi et al., 1993). The principal feature of such wave-induced stress changes may be represented in a form shown in Fig.2. Each of the three lines in the figure indicates the decay of the cyclic stress ratio  $\Delta\tau_{max}/\sigma'_{v0}$  along a vertical line below the seabed, for a given wave regime. This particular calculation was done under the following assumptions: the centrifugal acceleration = 50g; the input pressure amplitude  $a = 2.5kPa$ ; the wave length  $L = 0.52m$ ; the wave frequency  $f = 8.8Hz$ .

Note that in the case of a standing wave, the cyclic stress ratio  $\Delta\tau_{max}/\sigma'_{v0}$  tends to decrease with  $z$  differently, depending on the horizontal location of the soil element relative to the input spatial waveform. The cyclic stress ratio below the node takes a value of 0.055 immediately be-

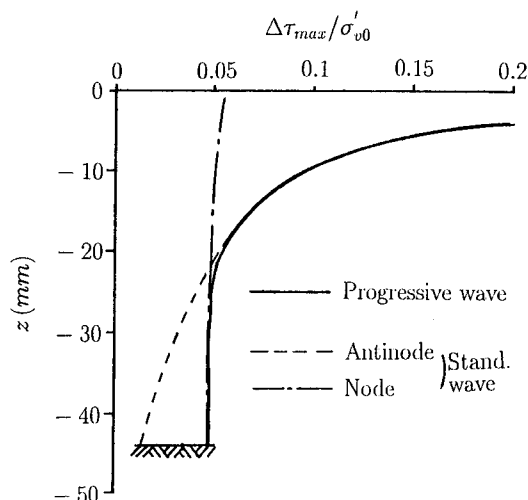


Fig.2 Profiles of cyclic stress ratio with elevation

low the seabed and then decreases only gradually with  $z$ . In contrast, the cyclic stress ratio below the antinode at shallow depths has much larger values than those occurring below the node. For instance, the cyclic stress ratio at  $z = -5mm$  is as high as 0.2. The value of the cyclic stress ratio then decreases rapidly with  $z$  and becomes smaller, compared with the chain-dotted line associated with the node. It is also interesting to observe that the  $\Delta\tau_{max}/\sigma'_{v0}$  versus  $z$  relation for the antinode of the standing wave is essentially the same as that for the progressive wave, at depths up to  $z = -20mm$  in this particular case.

### 2.2 Poro-elastoplastic modelling of pore pressure response

This subsection provides one-dimensional poro-elastoplastic formulation of wave-induced pore pressure response.

Consider that a sand bed with a thickness  $D$  is underlain by an impervious rigid base, and is subjected at the surface  $z = 0$  to the oscillating fluid pressure,  $f(t) = a \cdot \sin \omega t \cdot H(t)$ , where  $H(t)$  represents Heaviside's step function. Let  $p_e$  be the pore pressure at a given elevation  $z$ . By introducing the "transformed pore pressure  $P$ " defined by  $P = p_e - B \cdot f(t)$ , one can prove that the governing equation for this problem takes the following form

(Sekiguchi et al., 1994):

$$\frac{\partial P}{\partial t} = C \frac{\partial^2 P}{\partial z^2} + \frac{\dot{v}^p}{m_v + n\beta} \quad (1)$$

$$B = \frac{1}{1 + n\beta/m_v}, \quad C = \frac{k}{\gamma_f(m_v + n\beta)}$$

where  $m_v$  is the volume compressibility of the soil skeleton,  $n$  is the porosity,  $\beta$  is the volume compressibility of the pore fluid,  $\gamma_f$  is the unit weight of the pore fluid,  $k$  is Darcy's coefficient of permeability, and  $v^p$  is the volumetric strain due to cyclic plasticity.

The plastic volumetric strain,  $v^p$ , is assumed here to accumulate with the number of wave repetitions,  $\xi = (2\pi/\omega)t$ , according to:

$$v^p = v_\infty^p(z) \cdot (1 - \exp[-\alpha\xi]) \quad (2)$$

Here  $v_\infty^p(z)$  indicates the plastic volumetric strain attained after an infinite number of wave loadings.

In view of the results from the oscillatory pressure column tests done by Zen and Yamazaki (1990), one can assume the following specific form for  $v_\infty^p(z)$ :

$$v_\infty^p(z) = v_\infty^p(0) \cdot \frac{\cosh \lambda(z + D)}{\cosh \lambda D} \quad (3)$$

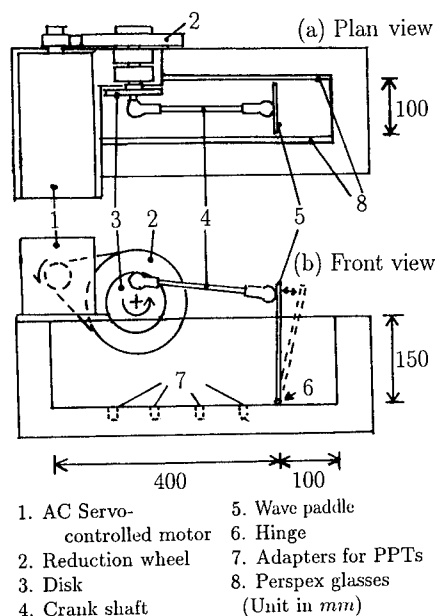


Fig.3 Wave channel with wave actuator

where  $v_\infty^p(0)$  stands for the plastic volumetric strain at the seabed  $z = 0$ , and  $\lambda$  is a parameter representing the rate of decrease in  $v_\infty^p$  with decreasing  $z$ .

With a given set of material parameters and wave parameters, one can obtain a closed-form solution with the aid of a Laplace transform, and express it in the form:

$$p_e = p_e^{(1)} + p_e^{(2)} \quad (4)$$

The first term on the right-hand side of eq.(4) stands for the elastic part of the pore pressure response, whereas the second term represents the contribution of cyclic plasticity which is responsible for the development and dissipation of residual pore pressure with time. The theoretical performance relevant to this experimental program will be shown later in this paper in graphical form. The concrete analytical expressions of the  $p_e^{(1)}$  and  $p_e^{(2)}$  terms, will be given elsewhere (Sekiguchi et al., 1994).

### 3 EXPERIMENTATION

#### 3.1 Wave channel and wave generator

The wave tank with a wave generator used in the present experimental program is shown in Fig.3. The effective channel length of the wave tank is 0.4m, the width is 0.1m and the height is 0.15m. These correspond to the wave channel of 20m in length, 5m in width and 7.5m in height under the elevated centrifugal condition of 50g. The side walls (8) are transparent to enable the optical observation with a video camera in flight. Four adapters (7) are available at the channel base to accommodate miniature pore pressure transducers. No wave absorber is equipped at the end of the channel.

A flap-type mechanism was adopted for wave generation. An AC servo-controlled motor (1) of 1.5kW capacity drives a reduction wheel (2) through a rubber belt. At the opposite side of the reduction wheel, a crank shaft (4) is connected onto a disk (3), with some offset from the center of rotation. The rotational motion of the reduction wheel is converted to the linear motion of the crank shaft through the rotation of the disk. The other end of the crank shaft is attached to a wave paddle (5) with a universal joint. The wave pad-



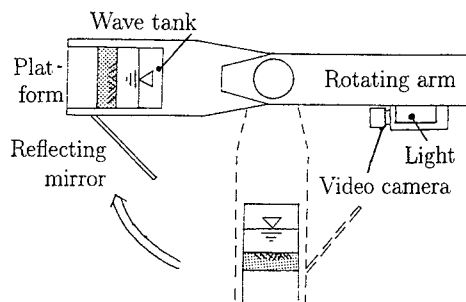


Fig.4 Optical observation system - side view -

dle is hinged at the channel base (6). The linear motion of the crank shaft (4) is thus converted to the back-and-forth motion of the wave paddle around the hinge, and the fluid on both sides of the plate is oscillated.

The wave channel and the wave generator are installed on the balanced-beam centrifuge of 2.5m in effective arm length. The frequency of oscillation of the wave paddle is specified by a potentiometer in the observatory room. A servo-control unit on the rotating arm regulates the revolution rate of the motor (1) by combining the driving signal from the potentiometer with the feed-back electric signal. The wave height is adjusted by the eccentricity of the crank shaft.

### 3.2 Optical observation system and experimental configuration

A CCD camera with a lighting system is attached on the rotating arm for the in-flight optical observation (Fig.4). A mirror is fixed to the platform with an angle of 45 degrees, to reflect pictures of the experiment to the video camera. The video signal is transferred through slip rings to a monitoring and recording system in the observation room. The optical information is later retrieved to quantify the spatial waveform of the fluid surface by means of a video digitizing system.

The model configuration adopted is shown in Fig.5, together with the typical spatial waveforms depicted with the video digitizing system. A sandy deposit was formed by pluviating Leighton Buzzard sand through the 'sea of silicone oil'. The physical properties of the sand are as follows: the specific gravity  $G_s = 2.65$ , the mean grain size  $D_{50} = 0.15\text{mm}$ , the maximum void ratio  $e_{max} = 1.07$ , and the minimum void ratio

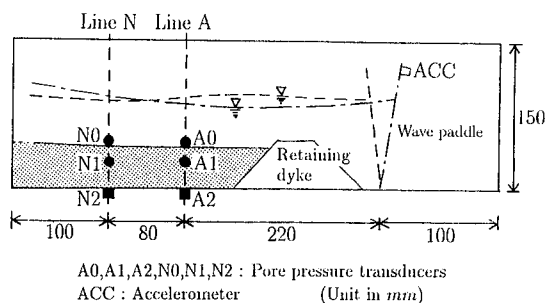


Fig.5 Experimental configuration

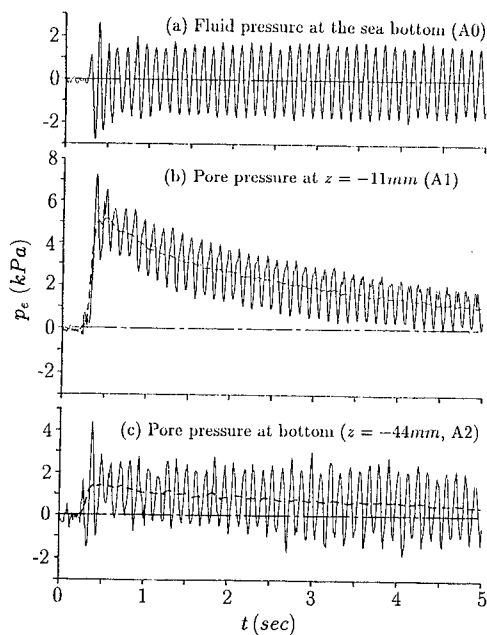


Fig.6 Measured fluid pressure-time histories

$e_{min} = 0.64$ . The silicon oil of 50cSt viscosity was employed as the pore fluid, allowing the consistent time scaling for consolidation and dynamics (viscous scaling).

Miniature pore pressure transducers (Kyowa BP-DS) were located at three different depths in the deposit, along the two vertical lines A and N. The line N was located approximately below the node of the standing wave and was 300mm away from the wave paddle. The line A was located at the middle point between the node and the antinode, with a distance of 220mm from the wave paddle.

#### 4 OBSERVED PORE PRESSURE RESPONSE

All the experiments were carried out under the centrifugal acceleration of  $50g$ . The well-defined standing waves of first mode were generated under the conditions of the fluid depth  $h = 47mm$  and the frequency of oscillation  $f = 8.8Hz$ .

##### 4.1 Pore pressure-time histories

The most remarkable response was obtained in the experiment on the loosest deposit with a relative density  $D_r = 13\%$  ( $e = 1.01$ ). The pore pressure-time histories measured with the transducers on line A are shown in Fig.6. Fig.6(a) shows the input fluid pressure measured with the transducer A0, at the surface of the sediment. The amplitude,  $a$ , of the input fluid pressure is equal to  $1.7kPa$ . Fig.6(b) shows the pore pressure-time history measured with A1 which was embedded at a depth of  $11mm$  below the sand surface. The broken line in the figure represents the averaged variation of pore pressure with time. One can notice the significant build-up of residual pore pressure at  $t = 0.5sec$ . In fact, the residual pore pressure developed up to  $p_{max} \approx 5kPa$ , which is practically equal to the initial effective vertical stress ( $\sigma'_{v0} \approx 4.7kPa$ ). This indicates the occurrence of liquefaction at this particular instant of time, at the horizon  $z = -11mm$ .

Fig.6(c) depicts the pore pressure-time history at the base of the sediment ( $z = -44mm$ ). The residual pore pressure there is seen to develop only moderately ( $p_{max} \approx 1.5kPa$ ).

##### 4.2 Variation in maximum residual pore pressure with depth

The variation of the maximum residual pore pressure,  $p_{max}$ , with elevation,  $z$ , obtained in the series of experiments, are summarized in Fig.7. It is seen that the maximum residual pore pressure decreases with increasing depth. The rate of attenuation is larger along the line A than that along the line N. This performance generally conforms to the profiles of the cyclic stress ratio estimated from the theory of poro-elasticity (cf. Fig.2).

#### 5 DISCUSSION

This section discusses the effect of partial drainage on the evolution of residual pore pressure.

The one-dimensional analytical solution is applied to analyze the pore pressure response observed in the experiment with the loosest deposit (cf. Fig.6). The parameters used for the analysis are summarized in Table 1.

The calculated pore pressure-time histories for  $z = -11mm$  are shown in Fig.8. Fig.8(a) shows

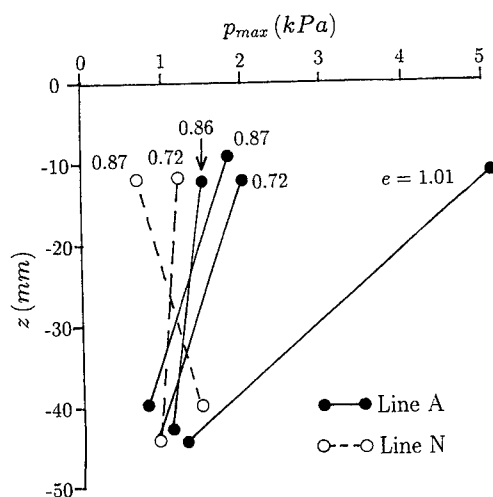


Fig.7 Profiles of maximum residual pore pressure with elevation

Table 1 Parameters for one-dimensional analyses

Pressure amplitude, $a$	$1.7 \times 10^3 N/m^2$
Angular frequency, $\omega$	$55.3 rad/sec$
Layer thickness, $D$	$4.4 \times 10^{-2} m$
Porosity, $n$	0.5
Coefficient of volume compressibility, $m_v$	$7.0 \times 10^{-7} m^2/N$
Plastic parameter, $v_{\infty}^p(0)$	0.01
Plastic parameter, $\lambda$	$68.2 m^{-1}$
Plastic parameter, $\alpha$	1.4
Coefficient of permeability*, $k$	
to silicone oil	$2.0 \times 10^{-5} m/sec$
to water	$1.0 \times 10^{-3} m/sec$
Unit weight of pore fluid*, $\gamma_f$	$4.8 \times 10^5 N/m^3$
Compressibility of pore fluid, $\beta$	$3.6 \times 10^{-7} m^2/N$

\* Values correspond to the centrifugal acceleration of  $50g$ .

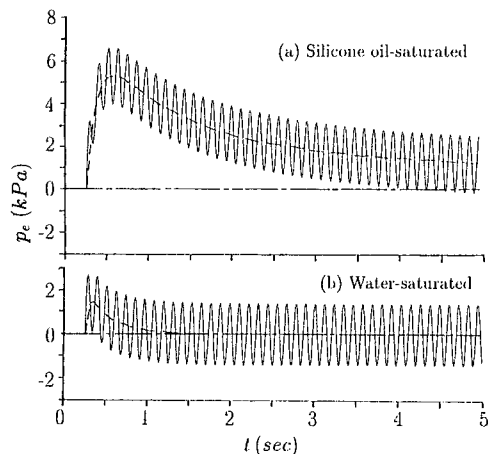


Fig.8 Calculated pore pressure-time histories for  $z = -11\text{mm}$

the pore pressure-time history calculated from the analysis in which the viscous scaling is taken into consideration. It is seen that the theoretical waveform compares favourably with the experimental curve shown in Fig.6(b).

Fig.8(b) illustrates the theoretical pore pressure response for  $z = -11\text{mm}$  when the pore fluid was water. The effect of the viscous scaling will be evident by comparing the two waveforms shown in Figs.8(a) and (b).

The theoretical performances obtained for  $z/D = -0.25$  are summarized in a form shown in Fig.9. Here, the vertical coordinate represents the maximum residual pore pressure,  $p_{max}$ , divided by a reference pressure,  $p_u(0) = v_\infty^p(0)/(m_v + n\beta)$ . The normalized, maximum residual pore pressure is drawn against the characteristic time factor,  $T_v^* = (2\pi/\omega) C/D^2$  for three different values of  $\alpha$ . The solid circle in the figure indicates the measured data point from Zen and Yamazaki (1990). It should be emphasized that they observed significant, permanent settlements of the sand deposit, while no residual pore pressure was detected in their test. This experimental result is compatible with the theoretical performance shown in Fig.9.

## 6 CONCLUDING REMARKS

- The centrifuge wave experiment with viscous scaling has proved to be successful, in the sense that it reproduced wave-induced liquefaction for

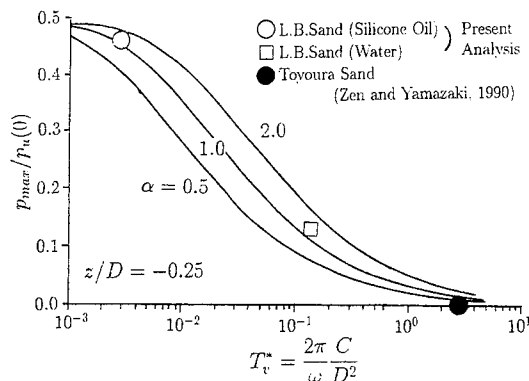


Fig.9 Variations of normalized, maximum residual pore pressure with characteristic time factor

a loose deposit of sand.

- The pore pressure response predicted from the one-dimensional poro-elastoplastic theory showed good agreement with the measured pressure waveform.
- The analytical solutions presented in the form of Fig.9, provide a means for readily assessing the effect of partial drainage upon the development of wave-induced residual pore pressure.

## REFERENCES

- Phillips, R. and Sekiguchi, H. 1992. Generation of water wave trains in drum centrifuge. Proc. Int. Symp. Techno-Ocean 92: 29-34.
- Sekiguchi, H., Kita, K. and Okamoto, O. 1993. Centrifuge modelling of wave-induced instability of sand beds. Proc 3rd NTU-KU-KAIST Trilateral Seminar/Workshop on Civil Engineering: 199-204.
- Sekiguchi, H., Kita, K. and Okamoto, O. 1994. Response of poro-elastoplastic beds to standing waves. Soils and Foundations: Submitted.
- Sekiguchi, H. and Phillips, R. 1991. Generation of water waves in a drum centrifuge. Proc. Int. Conf. CENTRIFUGE 91: 343-350.
- Yamamoto, T. 1981. Wave-induced pore pressures and effective stresses in homogeneous seabed foundations. Ocean Engineering 8: 1-16.
- Zen, K. and Yamazaki, H. 1990. Oscillatory pore pressure and liquefaction in seabed induced by ocean waves. Soils and Foundations 30-4: 147-161.

## Study of geosynthetic interface friction

Thomas F. Zimmie, Anirban De & Mahadzer B. Mahmud

*Department of Civil and Environmental Engineering, Rensselaer Polytechnic Institute, Troy, N.Y., USA*

**Abstract:** The applicability of centrifuge modeling to the problem of dynamic friction at geosynthetic interfaces has been studied. The dynamic friction angle was calculated on the basis of the magnitude of shake table acceleration necessary to induce sliding. Prototype stress conditions on the interfaces (e.g. in landfill liners and embankments) were simulated at higher *g* levels on the centrifuge. The values of dynamic friction angles obtained agree well with those reported in the literature.

### 1 INTRODUCTION

The use of geosynthetic materials (e.g. geomembranes, geotextiles, geogrids) in geotechnical engineering practice has increased considerably in recent years. Geosynthetics serve a variety of functions, such as separation, filtration, soil reinforcement, slope stabilization, drainage, impermeable barriers, and etc., in a wide variety of geotechnical systems [Koerner (1990)]. In many of these cases different layers of geosynthetic surfaces are used consecutively in layered arrangements. In structures where the potential for sliding is present, the friction angles between various interfaces are important design considerations.

Normally the angle of friction at a geosynthetic-geosynthetic interface is much lower than that at a geosynthetic-soil interface or the internal friction angle of soil. Hence a knowledge of the correct friction angles for all the geosynthetic interfaces included in a structure is of critical importance in the design.

To date most of the research on geosynthetic interface friction is limited to cases under static conditions. The dynamic friction behavior of geosynthetic-geosynthetic interfaces is important in the design of structures such as landfills and embankments against dynamic loadings caused by earthquakes, blasts, and etc. Many regulatory

agencies currently require landfills to be designed for earthquake type loading.

The paper presents an experimental study of dynamic interface friction in geosynthetics. The experiments were performed on a shaking table apparatus installed aboard a 100 g-ton centrifuge. The interface friction angle is calculated on the basis of the acceleration level that induced sliding. Experiments were performed at different *g*-levels in a modeling of models study to understand the scaling laws involved. The effects of frequency of vibration and normal stress on interface friction were studied. The values of dynamic friction angles obtained in this study were found to agree with those published by other authors.

### 2 DYNAMIC FRICTION

The use of a direct shear type device to determine the interface friction angles for geosynthetics has been reported by various authors. However there have been very few attempts to determine the friction angle under dynamic loading conditions. Notable work in this respect has been done by Yegian and Lahlaf (1992) and Kavazanjian et al (1991). These studies utilized shaking table apparatus to provide sinusoidal and earthquake like

vibrations of different frequencies to the interface under various normal stress conditions.

### 3 TESTING PROGRAM

The experiments reported here studied the dynamic friction at the interface of a smooth HDPE geomembrane (Gundle HD60) and a nonwoven geotextile (Polyfelt TS700). The tests were performed on the 100 g-ton centrifuge at Rensselaer, and a servohydraulic shaker was utilized to provide the vibrations to the sample. Detailed descriptions of the centrifuge and the shaker is provided by Elgamal et al (1991).

#### 3.1 Experimental Setup

Figure 1 shows the setup used in the tests. The geomembrane (560 mm x 355 mm in area) was laid in contact with the shaking table surface and fixed to it by means of a frame. A geotextile layer was laid flat over the geomembrane and a concrete block (445 mm x 292 mm base area) was placed on top of the geotextile.

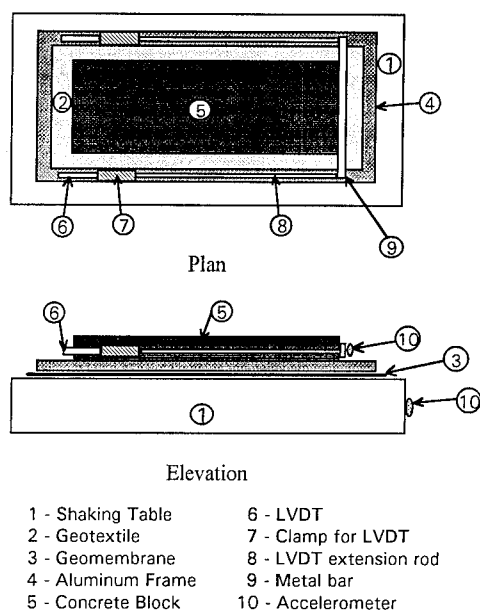


Figure 1. Experimental setup

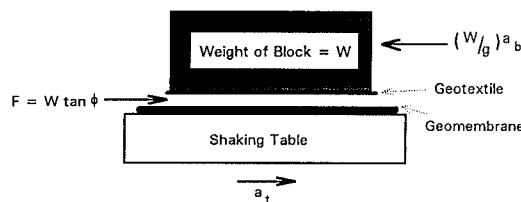


Figure 2. Freebody diagram

The instrumentation used in this series of experiments consisted of accelerometers to record the accelerations developed at the geomembrane and the geotextile surfaces and LVDT's (Linear Variable Differential Transformers) to measure the relative displacement (slip) between the two materials.

Two accelerometers were placed on the shaking table and the concrete block to observe the accelerations in the direction of motion in the geomembrane and the geotextile, respectively. Two LVDT's, mounted on the frame, were used to observe the relative displacement between the geomembrane and the geotextile.

#### 3.2 Principle

Figure 2 shows a free body diagram for the experimental setup used. The frictional resistance between the concrete block (which had a very rough surface) and the geotextile is significantly larger than that between the geosynthetic surfaces (geomembrane and geotextile). Thus any slip that was observed during the test occurred due to a relative displacement between the two geosynthetic layers.

As the table accelerates with an acceleration  $a_t$ , it transmits a frictional force,  $F$  to the block. This frictional force cannot exceed the interface shearing strength between the two layers of geosynthetics. In terms of dynamic friction angle,  $\phi_d$  at the geosynthetic interface and the weight of the concrete block,  $W$  the value of  $F$  may be expressed as

$$F = W \cdot \tan \phi_d \quad (1)$$

This limiting shear force will induce a limiting block acceleration referred to as  $a_b$  and given by

$$W \cdot \tan \phi_d = \left(\frac{W}{g}\right) \cdot a_b \quad (2)$$

or

$$a_b = \tan \phi_d \cdot g \quad (3)$$

Equation 3 implies that, starting from at-rest position, as the acceleration of the table ( $a_t$ ) is increased, the block and the table will move together for as long as the table acceleration is smaller than the limiting block acceleration ( $a_b$ ), given by equation 3. When the acceleration of the table,  $a_t$ , exceeds the limiting value,  $a_b$ , relative movement will be induced between the block and the table. Thus the dynamic interface shear properties between the geosynthetic layers is provided by the block acceleration measurements. The dynamic friction angle at the geosynthetic interface can be expressed as

$$\phi_d = \tan^{-1}\left(\frac{a_b}{g}\right) \quad (4)$$

### 3.3 Test procedure

During each test a sinusoidally varying horizontal acceleration was provided to the geomembrane layer through the shaking table. This acceleration was passed on from the geomembrane to the geotextile by means of the frictional resistance at their interface. The amplitude of vibration was varied using a dynamic signal analyzer. At low amplitudes of acceleration the interface friction was sufficient to pass the entire vibration to the geotextile and hence the two geosynthetics moved together. Under such conditions the accelerometers mounted on the shaking table (to which the geomembrane was fixed) and the block (placed on the geotextile) gave the same readings for acceleration with time. The LVDT's also showed no relative displacement between the shaking table and the block (indicating no movement of the geotextile with respect to the geomembrane).

The shaker vibration was increased gradually and at each level of acceleration the amplitude was held constant for a certain time span. The acceleration at the shaker and the block

increased together until the entire frictional resistance at the interface was mobilized. Any increase in the amplitude of acceleration of the shaking table beyond this point caused sliding to occur. The amount of relative displacement between the shaker and the block was indicated by a change in the LVDT readings. Also, because the dynamic friction at the interface of the two geosynthetics was not able to transfer the entire shear force any longer, the amplitude of acceleration of the block was smaller than that of the shaker. This was evident on the plots of acceleration versus time for the shaking table and the block.

The above procedures were followed in tests performed at 1 g and at four different higher g levels. As the results presented in the next section show, the response obtained at the interface was identical in each case. Plots obtained from a test at 1 g with frequency of vibration 5 Hz are used in this section to illustrate the test process.

Figure 3 shows the plots of relative displacement between the shaking table and the block with time. The two curves in the figure indicate the displacements measured by the two LVDT's mounted on either side of the concrete block. The portion of the curves shown here include the time when slip between the block and the table was actually initiated.

The initial values of relative displacements of 20 mm and 11 mm on the two LVDT's respectively, indicate the initial positions of the setup before any sliding occurred. During the first part of the plots (up to 11 seconds from the start), shown in Figure 3, there is no relative displacement (i.e. constant LVDT reading), indicating that the block and the table moved together. Beyond 11 seconds, a gradual change

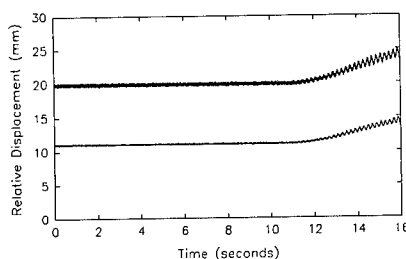


Figure 3. Relative Displacement vs. Time at 1g (frequency 5 Hz)

in the curve occurred, indicating that sliding had initiated at that time. The two LVDT's were placed on the two sides of the concrete block, in the direction of motion (as shown in Figure 1). The plots of the two lines in Figure 3 are parallel to each other, indicating that the displacement of the block occurred in the direction of the shaking excitation, with no measurable rotation.

The plots of acceleration versus time for the block and the shaking table are shown in Figure 4. As mentioned previously, the vibration is sinusoidal in nature with a gradually changing amplitude. The plots shown here represent the same time frame as Figure 3, i.e. the time sliding between the two materials begins to occur. Thus it may be seen that initially both plots have the same amplitude of acceleration indicating transfer of the entire shear force at the interface. As the amplitude of acceleration increased a point is reached when the acceleration of the table exceeds that of the block, and continues to increase. This point represents the value of acceleration at which sliding ensued and corresponds exactly to the point, on Figure 3, where relative displacement started.

In the experiments the acceleration of the shaking table was gradually increased, from a very low amplitude to a point when sliding started and then beyond, until the movement of the block went beyond the range of the LVDT's, or was obstructed by the frame. The curves of acceleration versus time provided the amplitudes of acceleration developed at the shaking table and the block at any given instant of time. The plots of these results are presented in the following section of the paper. All experiments reported here were performed on the same pair of geosynthetic materials. The samples used in the test were changed after every few tests.

Tests were performed at five different g-levels: 1g, 5g, 10g, 20g and 40g. A prototype frequency of 5 Hz was simulated by using suitably scaled model frequencies. The normal stresses were applied using the same blocks in each case. Thus at higher acceleration levels a higher prototype normal stress was represented.

In order to understand the effects of frequency and normal stress on the dynamic interface friction, tests were performed at 1g using different frequencies of vibration and normal stresses.

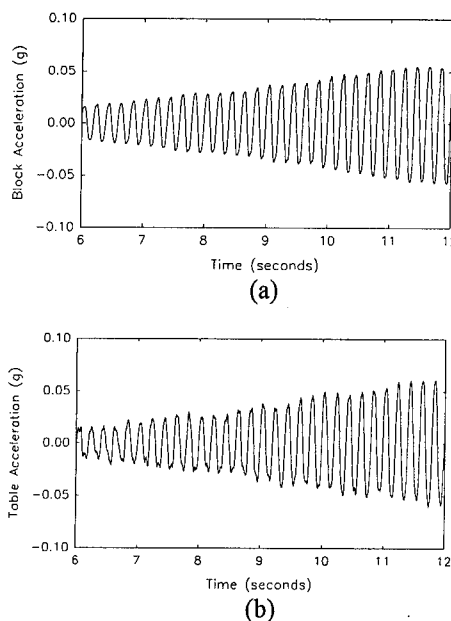


Figure 4. Block & Table Accelerations vs. Time at 1g (frequency 5 Hz)

#### 4 RESULTS & DISCUSSIONS

The first results presented in this section are from 1g tests performed to understand the effects, if any, of frequency of vibration and the magnitude of normal stress on the dynamic friction behavior at the geosynthetic interface. Figure 5 shows results from 1g tests performed with different frequencies of vibration. The amplitudes of block accelerations are plotted with respect to the amplitudes of table accelerations at the same instant of time. At the beginning of a test the amplitude of acceleration was relatively low and the concrete block (with the geotextile attached to it) moved together with the shaking table (and the geomembrane fixed to it). Thus the accelerations developed in the block and in the table have the same magnitude. This can be seen in the first part of the plot. The amplitude of acceleration is gradually increased and the block and the table move together up to the point when the entire dynamic friction at the interface is mobilized.

The formulation presented earlier can be utilized to obtain the value of dynamic friction angle for the interface. Following equation 4 the

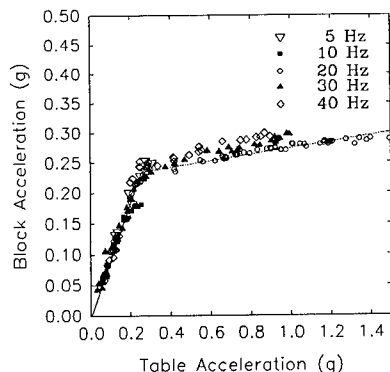


Figure 5. Table Acceleration vs. Block Acceleration for different frequencies at 1g

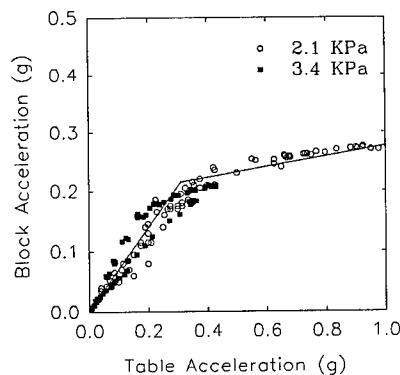


Figure 6. Table Acceleration vs. Block Acceleration for different normal stresses at 1g

maximum value of block acceleration,  $a_b$  at the point before slip occurs is 0.22 g.  
Thus

$$\phi_d = \tan^{-1}(a_b/g) \\ = 12.4^\circ$$

As the amplitude of table acceleration is increased beyond this point, the amplitude of acceleration for the block remains less than that of the shake table. This is represented by the dotted portion of the curve. The LVDT reading under such conditions shows a slip happening between the block and the table. As the acceleration of the shaking table is increased beyond the point where slip was initiated, the block acceleration also increases, though at a much slower rate. This is shown by the gradual rising trend in the dotted line in the curve.

In Figure 5 the plots for vibrations with three different frequencies are shown. It may be seen from the curves that for the range represented the frequency of vibration has no effect on the friction behavior at the interface. This has also been noted by other researchers using shaking table apparatus [Yegian and Lahlaf (1992)].

Figure 6 shows plots for experiments conducted at two different stress levels and it can be seen that the magnitude of normal stress has no effect on the friction behavior. The conclusions drawn from Figures 5 and 6 were utilized in the subsequent tests using the same experimental setup at different acceleration

levels aboard the centrifuge. The independence of dynamic friction on frequency of vibration and normal stress allows comparison of the results obtained at different g levels.

Figure 7 shows plots of results obtained from tests performed at five different g levels: 1g, 5g, 10g, 20g and 40g. The plot from each g level shows the same trend as seen at 1g, viz. a first part when accelerations in the block and the table are the same, followed by a much gentler rising curve after slip has occurred. The LVDT reading in each case matched with the point of initial slip, as seen on the acceleration plots. The magnitude of acceleration at which slip starts is found to increase with the g level of the test. These values are separately shown in Table 1. It can be seen from the table that the magnitudes of acceleration were properly scaled at higher g levels and the values of dynamic friction angles in each case lie within reasonable limits.

## 5 CONCLUSIONS

Centrifuge tests were performed to model the dynamic friction behavior at interfaces of geosynthetic layers. The results from centrifuge model tests performed at different g-levels has shown that the dynamic friction at the interface is correctly simulated at high acceleration fields and the same value of dynamic friction angle (as obtained in 1g tests) is obtained. The results indicate that, for the interfaces used, dynamic friction angle is independent of the frequency of



Table 1. Dynamic friction angles at different g-levels and under different normal stresses

g level	Normal Stress (KPa)	Model frequency (Hz)	Model acceleration at slippage (g)	Prototype acceleration (g)	Dynamic Friction Angle
1	2.1	5	0.215	0.215	12.1°
		10	0.22	0.22	12.4°
		20	0.22	0.22	12.4°
		30	0.22	0.22	12.4°
		40	0.225	0.225	12.7°
	3.4	5	0.22	0.22	12.4°
		10	0.215	0.215	12.1°
		20	0.2175	0.2175	12.3°
5	10.5	25	1.10	0.22	12.4°
10	21	50	2.1875	0.21875	12.3°
20	42	100	4.50	0.225	12.7°
40	84	200	8.75	0.21875	12.3°

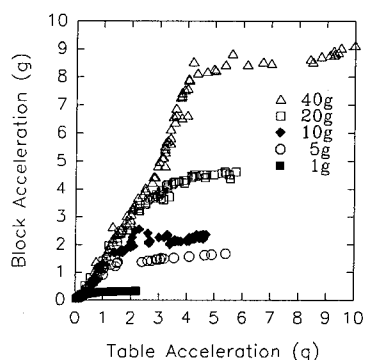


Figure 7. Table Acceleration vs. Block Acceleration for tests at different g-levels

vibration (testing range 5 - 40 Hz), and appears to be independent of normal stress applied on the surface (at least for low values of normal stress, up to 84 KPa).

The use of model tests on a centrifuge permits application of high normal stresses simulating conditions at geosynthetic interfaces used in landfill liners and retaining walls. The interface friction angle may not be constant in the case of some particular liner materials, e.g. textured geomembranes, geogrids and geosynthetic clay liners. In such cases it will be important to perform tests under prototype stress conditions. The application of geotechnical centrifuges will be important in simulating such conditions. In

the tests reported here a shaking table apparatus located on the centrifuge platform was used to provide the dynamic excitation to the interface.

The shake table apparatus used here is capable of simulating actual earthquake type shakings to study interface response. Also more complex field situations, such as a soil-geosynthetic interface can be simulated with a suitable physical model. In such cases the use of a centrifuge will also help simulate realistic prototype soil conditions.

## REFERENCES

- Elgamal, A-W., Dobry, R., Van Laak, P. and Nicolas-Font, J.(1991),"Design, construction and operation of 100 g-ton Centrifuge at RPI", *Centrifuge 91*, Ko (ed.), Balkema, Netherlands, pp. 27-34.
- Kavazanjian, Jr., E., Hushmand, B. and Martin, G. R. (1991), "Frictional base isolation using a layered soil-synthetic liner system", *Lifeline Earthquake Eng.*, Proc. of the 3rd U. S. Conf., ASCE, pp. 1140-1151.
- Koerner, R. M. (1990), *Designing with Geosynthetics*, 2nd Ed., Prentice Hall, USA.
- Yegian, M. K. and Lahlaf, A. M. (1992), "Dynamic Interface Shear Strength Properties of Geomembranes and Geotextiles", *J. of Geotechnical Eng.*, ASCE, Vol. 118, No. 5, pp. 760-779.

## Wave propagation and active vibration control in sand

Th. Siemer & H. L. Jessberger  
*Ruhr-University Bochum, Germany*

**ABSTRACT:** For the description of the soil structure interaction due to dynamic loads it is first important to assess the dynamic soil properties. Experiments are carried out to determine the pressure and shear wave velocities which are related to the dynamic soil stiffness. A new method is investigated where a concrete block, substituting a natural bedrock is built beneath a foundation to decrease soil wave amplitudes due to outgoing waves. The waves arise from an impact loaded foundation. The experiments are carried out in the Bochum geotechnical centrifuge ZI.

### 1 INTRODUCTION

Machine foundations transmit vibrations through the ground. The energy input is transported in the direction of other structures by waves. If the wave reaches the foundation it will also be excited to vibrations. This effect causes disturbances at sensitive buildings or machines and the environment in general.

For that reason, the reduction of the vibration of buildings and soil wave amplitudes is getting more and more important in engineering design. A reduction of surface wave amplitudes or foundation vibrations can be reached by a number of different methods.

Steel springs, especially helical springs, are standard elements for vibration control (Heiland 1992). Another possibility to reduce the propagation of waves is to install wave barriers in form of open trenches (Woods 1968) or trenches filled with styrofoam and sand (Sridharan et al. 1981) or concrete (Haupt 1986). The barrier impedes the wave and shields the building depending on the location of the trench.

This approach is based on a theoretical calculation (Schmid 1991). The transmitting behaviour of a soil stratum over an infinitive stiff bedrock is used to hinder the spreading of waves at the load source (active isolation) or the incoming waves at a neighbouring structure (passive isolation).

In most cases it is not possible to find a natural bedrock at the place and the depth where it is needed. Therefore an artificial bedrock has to be build.

The tests which are carried out in the Bochum geotechnical centrifuge ZI show the effects of an artificial bedrock which is simulated by a concrete block. A stiff foundation is placed the surface at a certain height over the block. The dynamic load source is a falling-weight which hits the foundation.

It is important for any studies of the soil structure interaction to assess the physical properties of the model ground. One of the most valuable information is the wave velocity which is directly related to the stiffness of the soil. The results of other centrifuge tests towards the development of the pressure wave velocity show strong dependency on the confining pressure and the void ratio.

### 2 DETERMINATION OF PRESSURE WAVE VELOCITIES

#### 2.1 Experimental system

The technique used in the centrifuge ZI to investigate the wave spreading velocities is very similar to the well known "Down-Hole-Method" (Telford et al. 1985). A foundation at the surface is excited dynamically by a falling mass. This weight is hold at a certain height by an electromagnetic system. If the current is adjusted down, the contact between the mass and the magnetizing system is removed and the falling-weight is triggered.

Accelerometers of piezo-electric type, B&K 4374 and B&K 4393 with a resonance frequency of

85kHz and 55kHz are placed in the soil beneath the foundation (figure 1) to registrate the wave passing the transducers, especially the first arrival time.

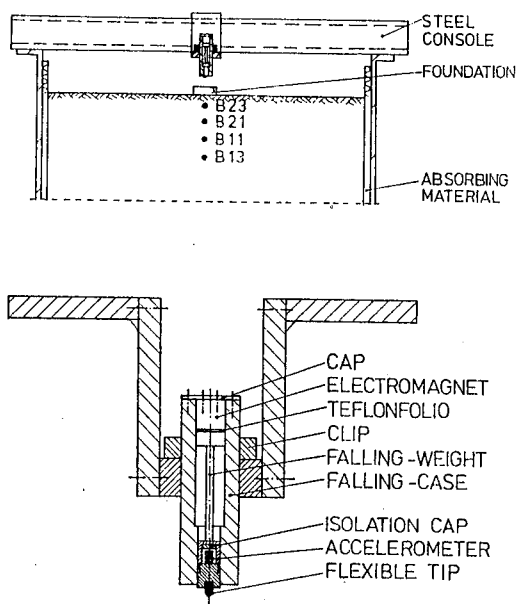


Fig.1 Experimental system

- Cross section of the model container
- Detail of the load device

The distance between the two detection points is set at 130 and 94mm.

In comparison to the "Down-Hole-Method", the method introduced in this paper is able to work without the complicated bore hole technique. The accelerometers are carefully embedded in the sand. The difficulties of coupling a pick-up in the bore hole to the surrounding soil does not occur.

Signals from the accelerometers are converted and first amplified by small charge amplifiers, type B&K 2634. A second amplification takes place in an amplifier as shown in figure 2. The measurement system in figure 2 is used for the tests described in section 3, but is also applicable to the tests in section 2. The difference is that only two accelerometers are used and only cartridge A with 2 channels in connection with the data acquisition board 1, is needed.

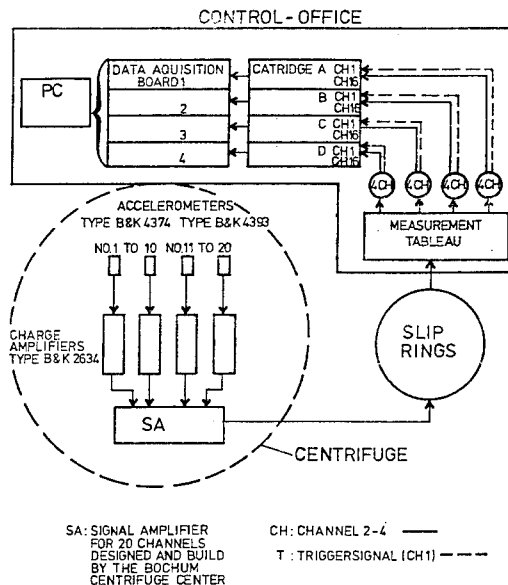


Fig.2 Measurement system

The signals are transferred through slip rings to the data recording system in the control office. For data acquisition four data acquisition boards with independent processors are used. Each board has 16 channels. It is possible to use them simultaneously. The first channel is used as the trigger channel. For the investigation of the pressure wave velocity always three channels in different tests are in use with a scan rate of 66,7kHz. A parallel measurement with an oscilloscope (scan rate of 500kHz) makes sure by comparing the signals that the sampling rate is sufficient.

The model ground is rained by hand in a cylindrical model container 1000mm in diameter and 750mm high. A sand with the following properties is used:

$\rho_s = 2,66 \text{ g/cm}^3$ ,  $\rho_{\min} = 1,41 \text{ g/cm}^3$ ,  $\rho_{\max} = 1,70 \text{ g/cm}^3$ ,  $e_{\min} = 0,89$ ,  $e_{\max} = 0,56$ ,  $d_{50} = 0,23 \text{ mm}$ ,  $U = 2,08$ ,  $\phi = 38^\circ$ . All the tests are run with air-dried sand. The density index  $D_d = (\rho - \rho_{\min}) / (\rho_{\max} - \rho_{\min})$  is 98% on average. The pressure wave velocities are measured under various centrifugal accelerations up to 90g.

## 2.2 Experimental results

The pressure wave velocity is determined by the travel time difference of the p-wave between two accelerometers. A pressure wave occurs as the first

### Accelerometer Signals In The Time Domain

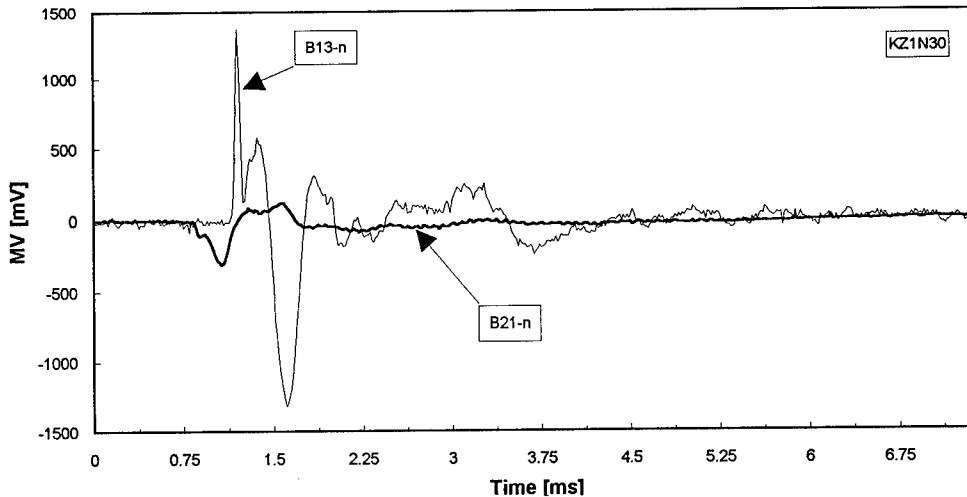


Fig.3 Accelerograms in the 30g centrifugal acceleration field

peak in the time history of a recorded signal. The measured accelerograms in a 30g field are shown in figure 3.

The model time distance between the two marked lines is found to be  $dt=0,302\text{msec}$  and if the distance between the two detection points B21 and B13 is  $ds=0,130\text{m}$ , the pressure wave velocity is obtained as follows:

$$c_p = ds/dt = 430\text{m/s} \quad (2.2.1)$$

If the p-wave velocity is plotted against the g-level or respectively against the prototype depth, it is seen that the pressure wave velocity raises with depth (figure 4).

A semi-empirical equation is proposed by Iwasaki et al. (1977). They describe the dynamic soil stiffness  $G_{dyn}$  as a function of the confining pressure and the void ratio, as Richart et al. (1970) have found before:

$$G_{dyn} = 83,4 \frac{(2,17 - e)^2}{(1 + e)} (\sigma_0)^{0,44} \quad (2.2.2)$$

with  $G_{dyn}$  [MN/m<sup>2</sup>] and  $\sigma_0$  [kg/cm<sup>2</sup>]

The confining pressure  $\sigma_0$  depends on the dynamic poisson ratio  $\nu_{dyn}$ . This value can be calculated with the following equation:

$$\nu_{dyn} = \frac{c_p^2 - 2 \cdot c_s^2}{2(c_p^2 - c_s^2)} \quad (2.2.3)$$

With the double impulse technique the shear wave velocity  $c_s$  at the sand surface is experimentally identified to  $c_s=130\text{m/s}$ . The corresponding p-wave velocity is  $c_p=225\text{m/s}$ . Inserting the two velocities into equation (2.2.3), the dynamic poisson ratio is calculated to  $\nu_{dyn}=0,25$  which is an acceptable result compared with values in the literature.

## 3 WAVE PROPAGATION

### 3.1 Experimental system

The effects of an artificial bedrock on the transmitting behaviour of waves due to transient loading is being investigated by means of geotechnical centrifuge model tests.

A description of the load device is already given in section 2.1. An accelerometer of the type B&K 4374 is inserted into the tip of the falling-weight. This tip is made of synthetic material. A little thread at the tip guarantees an easy exchange. It's signal is used to trigger the measurement.

The tests are run at 30g. All system parameters which are specified in the following text are values

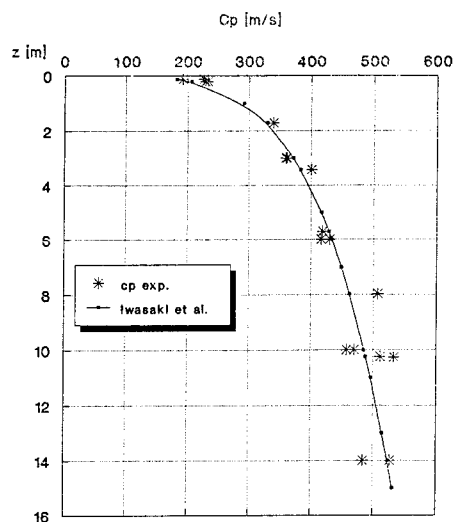


Fig. 4a Experimental results and calculated values for the pressure wave velocity  $c_p$

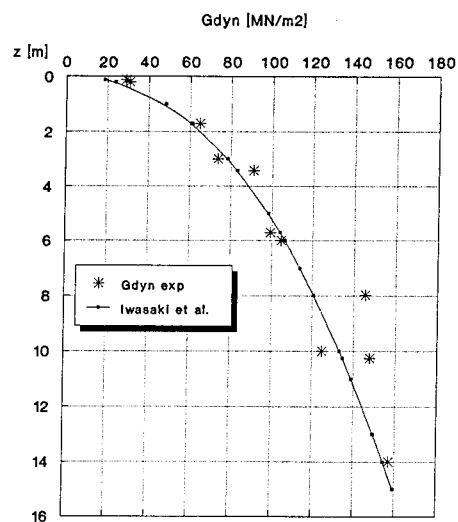


Fig. 4b Experimental results and calculated values for the dynamic soil stiffness  $G_{dyn}$

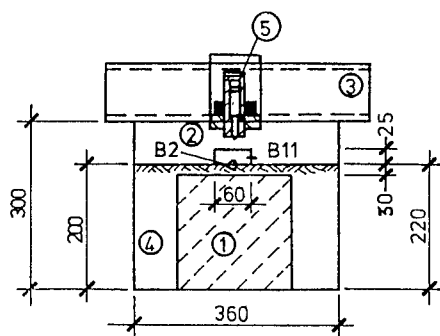


Fig. 5a Cross section

Fig. 5 Model container with details of the experimental system with

- 1 Concrete block 200/200/200mm
- 2 Foundation 60/60/25mm
- 3 Steel console
- 4 Model sand
- 5 Load device (see. fig.1)
- B Accelerometers

related to the prototype and include the scaling relationship.

If the mass is impacted on the foundation at 30g centrifugal acceleration the energy is equal to

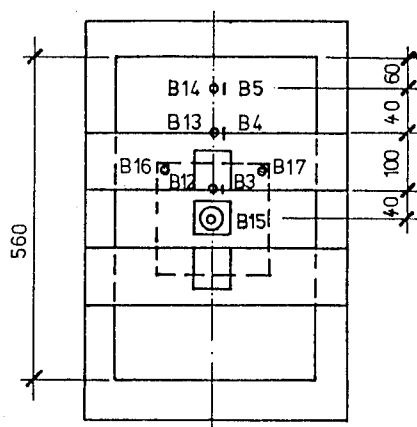


Fig. 5b Plan view

0,002Nm. This energy corresponds to a prototype energy of 53Nm. The mass falls from a height of 0,15m. Three accelerometers are connected to the concrete block, the others are applied to the foundation and to the sand surface as shown in figure 5. Dimensions are given in model scale. The concrete block is placed 0,90m beneath the foundation.

An overview of the measurement system is given in figure 2 of section 2.1. The model soil is the same sand chosen for the tests to measure the wave velocities and even the density is the same.

### 3.2 Selected experimental results

In this study the active isolation in form of a concrete block 0,90m beneath a single foundation as shown in figure 5 is applied. Both the horizontal and the vertical acceleration time histories of the accelerometers placed in a distance of 4,20m from the axis of the foundation are recorded.

In figure 6 the vertical response at the surface with and without concrete block and in figure 7, the horizontal response at the same distance as mentioned before, are presented.

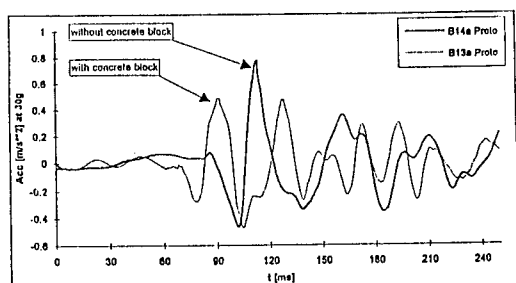


Fig.6 Comparison of the vertical response time histories due to vertical loading for a system with and without concrete block

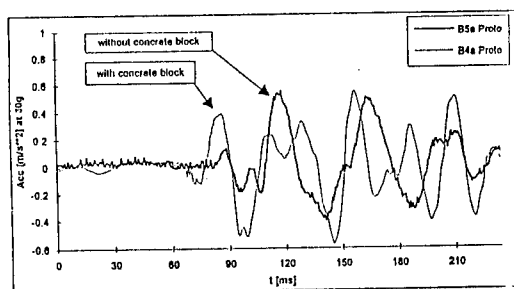


Fig.7 Comparison of the horizontal response time histories due to vertical loading for a system with and without concrete block

In figure 8 the acceleration of the falling-weight is plotted versus time as a multiple of the amount of the acceleration of gravity, with 0,15m height of fall. After triggering, an acceleration of 1g aligned downwards is observed. A large increase in acceleration in the opposite direction identifies the impact on the foundation.

If the maximum acceleration of approximately 30g is reached, a straight decrease in acceleration is observed followed by a rebound of the falling-mass.

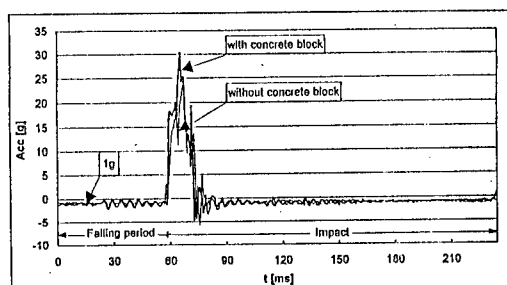


Fig.8 Acceleration time history of the falling-mass during the event of fall and impact

After about 0,3 seconds of recording of the falling process, a second impact is observed. The duration of the bouncing time shows that approximately an elastic system is involved, comparable e.g. with the physical process using the compaction technique of heavy tamping. In the investigations presented here the actions before the second impact are of interest.

One criterion to assess the effectiveness of the block as a wave impediment is to compare the acceleration amplitudes at the surface outside the region of the concrete block. The reduction factor can be written as

$$RF = \left(1 - \frac{A_b}{A}\right) \cdot 100 [\%] \quad (3.2.1)$$

with  $A_b$  = Maximum response with concrete block caused by a vertical excitation  
and  $A$  = Maximum response without concrete block caused by a vertical excitation

The experimental results show, that the block can reduce the vertical accelerations. The reduction factor is calculated to  $RF_v = 36\%$ . In the case of the horizontal response caused by a vertical dynamic impulse, no clear difference between the systems with and without the concrete block is detected.

According to the results of Chouw et al. (1991) it seems to be important to investigate a larger part of the surface, because the displacements are varying irregularly at greater distances from the load source, especially in the case of horizontal movement.

It is conspicuous that although the foundations are

loaded at the same time, the accelerometers at the sand surface respond with a phase difference (see fig. 6 and 7). The reason for the unequal arrival time can not be a different wave velocity, because the boundary conditions for the tests are the same, as are the model sand and soil properties. These findings can be interpreted as follows:

- The waves are running faster at the interface between sand and concrete block
- The waves are multiple reflected at the surface of the impediment

So, the wave velocity at the interface (equal to the wave velocity of concrete) is greater and respectively the path covered by the waves is shorter, if a concrete block is used to screen the surrounding area from outgoing waves.

#### 4 CONCLUSIONS AND FURTHER WORK

The pressure wave velocity of a dry sand with constant density increases with depth depending on the confining pressure and the void ratio. Centrifuge model tests in a high acceleration field show that the travel time of a wave between two accelerometers is reduced corresponding to the g-level. The experimental results are in good agreement to the statements given in the literature.

Experimental investigations show that the propagation of waves can be influenced by an active isolation system using a concrete block beneath a transient vertically loaded foundation. The acceleration amplitudes at the surface caused by the transported energy through the wave, are measured. In the first stage the maximum amplitudes with and without concrete block are compared. A reduction of about 36% for the vertical direction is observed.

In future work the transfer functions of the measurement points as a relation of the output signal spectrum to the input power spectrum will be ascertained. The results for the experiments with and without the artificial bedrock will be compared.

#### REFERENCES

- Chouw, N., Le, R., Schmid, G. 1991. Verfahren zur Reduzierung von Fundamentschwingungen und Bodenerschütterungen mit dynamischem Übertragungsverhalten einer Bodenschicht. Bauingenieur 66 (1991) S.215-221.
- Haupt, W. 1986 (ed.). Ausbreitung von Wellen im Boden. Bodendynamik Grundlagen und Anwendung. Braunschweig: Vieweg Verlag
- Heiland, D. 1992. Comparison of vibration structure-borne noise control efficiency for elastic systems. Elsevier Science Publishers LTD. Oxford. Mayfield House. 256 Banbury Road.
- Iwasaki, T., Tatsuoka, F. 1977. Effects of Grain size and grading on dynamic shear moduli of sands. Soils and foundation. Vol.17. No.3, pp.19-35
- Richart, F.E., Hall, J.R., Woods, R.D. 1970. Vibrations of soils and foundations (eds.). Prentice Hall. Inc. Englewood Cliffs. N.J.
- Schmid, G., Chouw, N., Le, R. 1991d, G., Chouw, N., structures from Soil Vibrations. Soil Dynamics and Earthqu. Eng. V. IBF Univ. Karlsruhe.
- Sridharan, A., Nagendra, M.V., Parthasarathy, T. 1981. Isolation of Machine Foundations by Barriers. Int. Conf. on Rec. Adv. in Geotechnical Earthqu. Eng. and Soil Dyn. pp.279-282.
- Telford, W.M., Geldart, L.P., Sheriff, R.E., Keys, D.A. 1985. Applied Geophysics (eds.). Cambr. Univ. Press Syn. Univ. of Cambr.
- Woods, R.D. 1968. Screening of Surface Waves in Soils (ed.). Jour. of the Soil mech. and Found. Div. ASCE. Vol.94. No.SM4. pp.951-979.

## Assessing the reliability of results in a dynamic centrifuge test

R.J.Fragaszy  
Watkinsville, Ga., USA

K.L.Olen  
GeoSyntec Consultants, Inc., Atlanta, Ga., USA

M.Purcell  
Applied Research Associates, Inc., Tyndall AFB, Fla.,  
USA

K.C.Brownell  
US Air Force, WL/FIVCS, Tyndall AFB, Fla., USA

**ABSTRACT:** Ten nominally identical centrifuge tests were conducted on a model reinforced soil wall subjected to explosive loading in the backfill behind the reinforced soil mass. The results of these tests were used to evaluate the reliability of the test data. Statistical analysis of data on wall panel displacements and peak free-field and interface pressures show a high degree of reliability.

### 1 INTRODUCTION

Centrifuge tests are often conducted to determine the effects of specific soil and/or structural parameters on the behavior of a complex geotechnical system. For example, soil density, layer thickness, footing size and bearing pressure may be varied in a parametric study of the development of dynamic pore water pressure under a footing during earthquake loading. In any physical modeling program there will be some variation in system response to nominally identical loading, no matter how much care is taken to build identical models. Therefore, to evaluate differences in system response due to intentional variation of parameters, it is necessary to have knowledge of the magnitude of random variation of response under fixed parameters (i.e., the reliability of results).

To some extent, the expected variability can be estimated by analyzing individual components of the system. For example, when Steedman (1990) conducted centrifuge tests on the effects of blast loading on pipe piles, he calculated the expected error in measured bending moment in the piles by summing the expected errors resulting from: (a) the variability of Young's modulus for the pile material; (b) the manufacturer's tolerance on variability in the pile dimensions; (c) the accuracy of the strain gages; and, (d) the accuracy of strain gage placement. Steedman's analysis indicated a maximum error of 20.2%. This calculation, however, does not include the variation in bending moment arising from variation in blast characteristics, soil properties or test geometry. Therefore, if a specific test

parameter such as soil water content is changed, it would take considerably more than a 20% difference in system response before one could state that water content significantly affects system response. How much difference is required cannot be determined unless a sufficient number of tests are conducted to allow statistical analysis of the data. Unfortunately, time and financial constraints often make such a test series difficult, if not impossible, to include.

### 2 BACKGROUND

During the past two years, the authors have been involved in an investigation of the response of a reinforced soil wall to blast loading (Bachus et al, 1993). During Phase I of this research effort, a series of centrifuge tests were conducted to determine if the centrifuge modeling technique was an appropriate and valuable tool for this investigation. A comparison of the results of 9 centrifuge tests with numerical modeling results and full-scale tests showed considerable similarity (Bachus et al, 1992). For example, reinforcement length, within certain bounds, did not appear to have a significant influence on wall deformations. However, based on limited replication testing, it was not clear if the reliability (repeatability) of the centrifuge data was sufficient to determine, with any degree of confidence, the influence of system parameters on wall behavior, especially wall displacement. Therefore, it was decided that a reliability testing program would be conducted during Phase II of the research before a parametric study was undertaken.



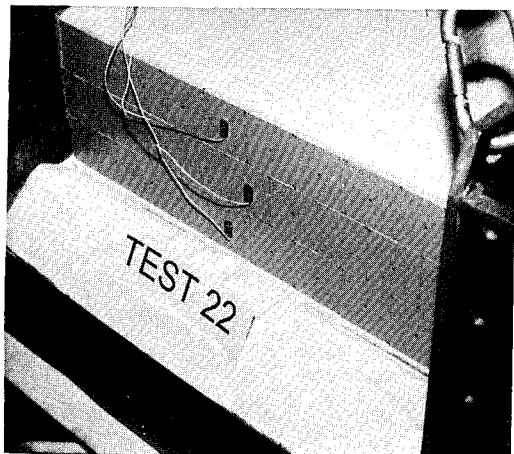


Fig. 1. Typical wall before testing

Wall displacement and soil-wall interface pressure data from this reliability test series are presented below.

### 3 DESCRIPTION OF TESTING PROGRAM

#### 3.1 Model description

After 6 preliminary tests to develop modeling techniques, 10 reliability tests were conducted. Each model wall was prepared by the same individuals using the same techniques, equipment and instrumentation. The dimensions of the model wall were 152 mm high and 508 mm long, with three rows of 51 mm square facing panels. Each facing panel had two strips of nylon netting, 152 mm long by 51 mm wide, attached at the one-third points, to simulate geogrid reinforcement. A photograph of the model before testing is presented in Fig. 1. Dry Tyndall beach sand, a clean quartz sand, at a density of  $1.65 \text{ Mg/m}^3$ , was used. All tests were conducted at the Wright Laboratory centrifuge facility at Tyndall Air Force Base, Florida. Tests were conducted at 30g, thereby modeling a 4.56m high prototype wall with 1.53m square facing panels. The model explosive was a made-to-order cylindrical detonator containing 3.8 gm of PBX9407. At the test acceleration of 30g, this detonator modeled 89.4 kg of the explosive H-6.

#### 3.2 Model Construction

The experimental package was contained within a 508 mm square, 508 mm deep aluminium bucket with a removable front panel. To begin construction of the model, a 153 mm

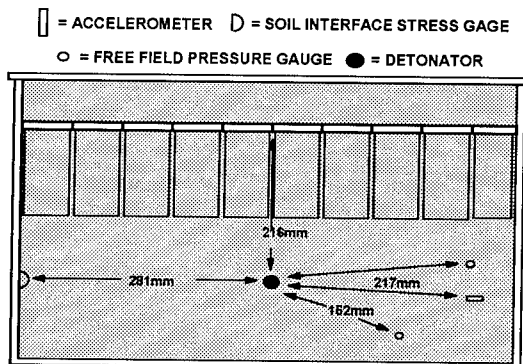


Fig. 2. Top view of test package

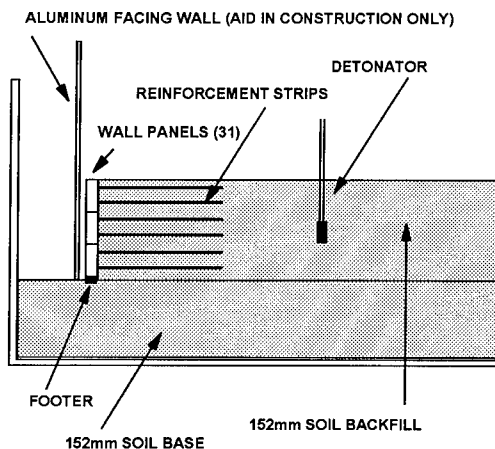


Fig. 3. Side view of test package

thick foundation was placed by pluviation of the Tyndall beach sand. A thin wood footing and an aluminum facing wall were then placed on the foundation soil. The first row of facing panels, with the attached reinforcement folded up off the soil, was then placed up against the aluminum facing wall. The backfill was constructed by pluviating behind the facing panels up to the elevation of each reinforcement layer. The reinforcement was then placed on the soil surface, slack was removed by pulling on the reinforcement while sand was pluviated on top of it. The second and third rows of facing panels were placed in the same manner. At mid-height of the wall, free-field pressure gages, accelerometers and the detonator were placed, as shown in Figs. 2 and 3. The three center panels, one each on the top, middle and bottom rows each had an accelerometer attached to the outside face and an

interface pressure gage attached to the inner face, prior to construction of the wall. The wires from the instrumentation package were attached to an on-board data acquisition system which has a sampling speed of 1 MHz. The wires from the detonator were attached to an on-board firing system connected through a slip ring to the control room. Details of the data acquisition system are presented in Brownell et al (1994).

An interface pressure gage was placed on the bucket wall after completion of the fifth reliability test. Because of its location and size, it is assumed that the use of the gage for only half of the tests did not significantly affect the behavior of the wall. No other changes were made during the reliability testing and each of the ten tests are considered to be nominally identical.

### 3.3 Test Procedure

After construction of the model, the aluminum facing wall and the front panel of the centrifuge bucket were removed. Using a digital micrometer with an accuracy of  $\pm 0.125$  mm, the distance from the front edge of the centrifuge bucket to the corner of each wall panel was measured. The front panel of the bucket was then replaced and the model package placed on the centrifuge. After connecting the instrumentation wires to the data acquisition system, but before the detonator was connected, the model package was accelerated to 30g, maintained at 30g for 60 seconds, then decelerated back to 1g. The front panel was removed and measurements of the distances from the front edge of the bucket to the corners of each wall panel were made again. After the measurements were taken, the detonator was connected to the firing system and the model package accelerated to 30g. When the g-level stabilized at 30g, the firing system was activated, causing the detonator to fire. The centrifuge was immediately decelerated after the explosion. The entire centrifuge test was recorded using a shuttered video system described by Brownell et al (1994). A photograph of a typical test wall after detonation is shown in Fig. 4.

Measurements of the distances between the front edge of the bucket and the corners of all the wall panels were made immediately after the test. The dimensions of the crater behind the wall were also recorded and the data from the on-board acquisition system were downloaded to the centrifuge computer system for analysis.

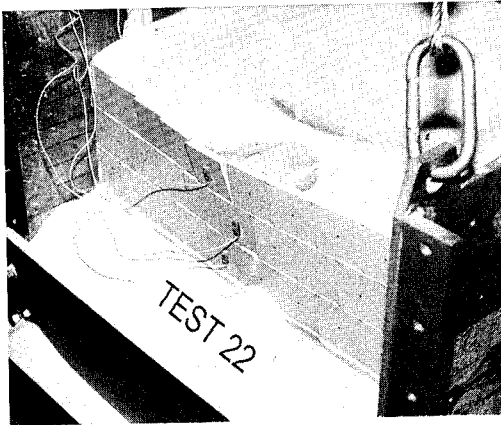


Fig. 4. Typical wall after detonation

### 3.4 Data Analysis

Each set of distance measurements was entered into a spreadsheet for analysis. The average distance from the front edge of the bucket was calculated for each panel by averaging the four corner distances. Panel displacements under static load only, under dynamic load only, and total displacement were calculated. Also, the mean displacements for each row of panels and the mean displacement of the entire wall (static, dynamic and total) were calculated for each of the tests.

Statistical analyses of the data included calculation of mean, standard deviation, variance, coefficient of variation, mean plus and mean minus two standard deviations.

In addition to information on wall displacement, data from the free-field pressure gages and accelerometer, and from the soil interface gages and accelerometers located on the panels were obtained for each reliability test. Peak values from each of these instruments were also entered into a spreadsheet for analysis.

## 4 RESULTS

### 4.1 Displacements

Displacement data for the reliability series (tests 7-16) are presented in Table 1. The panel numbers refer to Fig. 5 which shows the locations of the panels. For each test, the total displacement is shown for each panel. At the bottom of the table below the individual panel displacements are the average total, static and dynamic displacements for each wall and the average total displacements for the top, middle and bottom

Table 1. Reliability test data and statistics

Panel	Displacement (mm)										Mean	Stand. Dev.	Coeff. of Variation	Mean + Two SD	Mean - Two SD	Panel
	Test 7	Test 8	Test 9	Test 10	Test 11	Test 12	Test 13	Test 14	Test 15	Test 16						
T1	4.41	3.48	4.24	3.84	3.78	3.46	4.17	3.97	4.12	3.55	3.90	0.34	8.6%	4.57	3.23	T1
T2	8.24	7.37	7.42	8.24	7.18	7.00	7.84	7.63	8.02	7.22	7.62	0.45	5.9%	8.51	6.72	T2
T3	12.93	12.48	11.64	13.23	11.54	10.05	11.72	11.63	13.12	11.48	11.98	0.97	8.1%	13.92	10.04	T3
T4	19.09	18.49	16.62	18.97	16.17	14.88	16.17	16.25	18.37	17.09	17.21	1.43	8.3%	20.08	14.34	T4
T5	23.96	23.22	20.98	23.71	21.26	20.85	20.85	20.14	22.59	22.19	21.97	1.35	6.1%	24.67	19.28	T5
T6	25.84	28.88	28.12	29.76	24.06	24.48	23.51	24.48	24.80	25.30	25.92	2.20	8.5%	30.32	21.53	T6
T7	18.68	17.51	17.72	20.80	15.21	16.81	15.91	15.77	16.01	16.69	17.11	1.66	9.7%	20.44	13.78	T7
T8	11.44	10.06	10.48	12.03	9.82	8.90	10.01	10.05	10.63	10.80	10.42	0.88	8.4%	12.17	8.67	T8
T9	7.32	6.62	7.92	7.94	6.17	5.85	5.46	6.74	6.88	6.28	6.72	0.83	12.3%	8.38	5.06	T9
T10	3.09	2.51	2.79	2.83	2.57	2.44	2.44	2.79	2.31	2.14	2.59	0.28	10.9%	3.16	2.03	T10
M1	2.41	2.61	2.41	2.49	2.47	2.50	2.35	2.22	1.95	2.41	2.38	0.18	7.7%	2.75	2.01	M1
M2	4.50	4.51	4.03	4.42	4.24	3.32	4.10	4.16	4.18	4.01	4.15	0.34	8.3%	4.83	3.46	M2
M3	7.14	7.13	6.34	7.23	6.48	4.88	6.13	6.63	7.00	6.48	6.54	0.70	10.7%	7.94	5.15	M3
M4	10.75	10.57	9.33	10.82	9.28	7.04	8.94	9.71	10.57	9.79	9.68	1.15	11.9%	11.97	7.38	M4
M5	14.64	14.43	12.58	14.93	12.46	10.22	11.98	12.77	14.71	13.45	13.22	1.51	11.4%	16.23	10.20	M5
M6	17.02	16.29	14.53	16.91	14.00	13.33	13.72	13.94	16.14	15.11	15.10	1.39	9.2%	17.88	12.32	M6
M7	14.50	13.87	13.77	14.92	12.62	10.94	12.01	12.45	13.09	12.70	13.09	1.20	9.2%	15.49	10.69	M7
M8	9.57	8.72	8.27	9.89	8.57	7.07	7.75	7.99	9.00	8.90	8.57	0.84	9.9%	10.26	6.88	M8
M9	5.77	5.66	5.21	6.19	5.35	4.48	5.10	5.01	5.49	4.88	5.31	0.49	9.2%	6.30	4.33	M9
M10	3.11	3.68	3.00	3.59	2.98	2.91	3.09	2.99	3.18	2.77	3.13	0.29	9.3%	3.71	2.55	M10
M11	1.56	2.06	1.54	1.93	1.56	1.64	1.49	1.28	1.68	1.21	1.60	0.26	16.3%	2.12	1.07	M11
B1	2.22	2.74	2.11	2.20	2.28	2.28	2.10	2.01	2.10	2.14	2.22	0.20	9.2%	2.63	1.81	B1
B2	3.64	3.96	3.15	3.44	3.49	3.10	3.23	3.31	3.43	3.33	3.41	0.25	7.4%	3.92	2.90	B2
B3	5.04	5.18	4.64	5.01	4.18	3.61	4.40	4.64	5.19	4.76	4.67	0.50	10.7%	5.66	3.67	B3
B4	6.90	6.79	6.01	7.21	5.99	4.61	5.87	5.97	6.90	6.39	6.26	0.75	12.0%	7.77	4.76	B4
B5	8.66	8.40	7.56	8.69	6.92	5.98	7.19	6.89	8.85	7.70	7.68	0.96	12.4%	9.59	5.77	B5
B6	8.54	8.19	7.59	8.44	6.84	6.02	7.20	6.44	8.36	7.36	7.50	0.88	11.8%	9.27	5.73	B6
B7	6.38	6.13	6.03	6.89	5.49	4.62	5.90	5.20	6.48	5.87	5.90	0.66	11.2%	7.22	4.58	B7
B8	4.08	4.48	4.39	4.61	3.93	3.44	4.28	3.85	4.51	3.92	4.15	0.37	8.9%	4.89	3.41	B8
B9	2.87	3.21	3.19	3.28	3.11	2.77	3.07	2.82	3.31	2.60	3.02	0.24	8.0%	3.51	2.54	B9
B10	1.42	1.99	2.39	2.12	2.17	1.86	2.05	1.81	2.10	1.61	1.95	0.28	14.6%	2.52	1.38	B10
Total	8.89	8.75	8.26	9.24	7.81	7.14	7.74	7.79	8.55	8.07	8.23	0.64	7.8%	9.50	6.95	Total
Static	-0.05	0.41	0.58	0.41	0.65	0.58	0.60	0.50	0.37	0.60	0.46	0.21	44.3%	0.88	0.05	Static
Dynamic	8.95	8.34	7.68	8.83	7.17	6.56	7.14	7.30	8.18	7.47	7.76	0.79	10.1%	9.33	6.19	Dynamic
Top	13.50	13.06	12.79	14.14	11.78	11.47	11.81	11.94	12.69	12.27	12.55	0.85	6.8%	14.25	10.84	Top
Middle	8.27	8.14	7.37	8.48	7.27	6.21	6.97	7.20	7.91	7.43	7.52	0.69	9.1%	8.90	6.15	Middle
Bottom	4.98	5.11	4.71	5.19	4.44	3.83	4.53	4.29	5.12	4.57	4.68	0.43	9.3%	5.54	3.81	Bottom

row of panels for each wall. To the right of the individual panel displacements are columns showing the mean, standard deviation, coefficient of variation, and the mean plus and minus two standard deviations for each panel. These statistics are also given for the data on the average total, static and dynamic displacement for each wall and for each row of panels.

The mean and standard deviation for static loading only (0.46 mm and 0.21 mm, respectively) are very small compared to that for dynamic loading. However, the coefficient of variation of the static displacement is quite high compared to the total displacement. For these reasons it

was decided that only the total displacements would be used in analyzing the reliability and production tests.

Looking first at the repeatability of individual panel displacements, Table 1 shows a range in the coefficient of variation from 5.9% - 16.3%. Excluding the end panels, where boundary effects are most severe, the range is 5.9% - 12.4%. These data show that individual panel displacements vary very little from test to test. The pattern of displacements is also very consistent. For the top and middle row of panels, displacement increases monotonically from the end of the wall (panels 1 and 11) to a peak at the same two panels (5 and

Table 2. Reliability pressure data and statistics

		Pressure (psi)										Stand. Coeff. of			Mean -	Mean +		
		Gage	Test 7	Test 8	Test 9	Test 10	Test 11	Test 12	Test 13	Test 14	Test 15	Test 16	Mean	Dev.	Variation	Two SD	Two SD	Gage
Wall	P1	187	106	179	197	111	105	142	164	136	212	154	40	26%	75	233	P1	
	P2	82	40	195	157	191	228	239	200	244	270	184	73	40%	38	331	P2	
	P3	117	21	119	143	130	189	220	142	141	186	141	54	38%	33	248	P3	
	Ave.	129	56	164	166	144	174	200	169	174	222	160	45	28%	70	249		
Free-Field	P4	82	106	104	FAIL	141	130	136	152	111	151	124	24	20%	75	172	P4	
	P5	286	329	233	291	354	269	FAIL	FAIL	276	383	303	49	16%	205	401	P5	
Bucket	P6	NA	NA	NA	NA	NA	137	153	177	198	164	166	23	14%	120	212	P6	

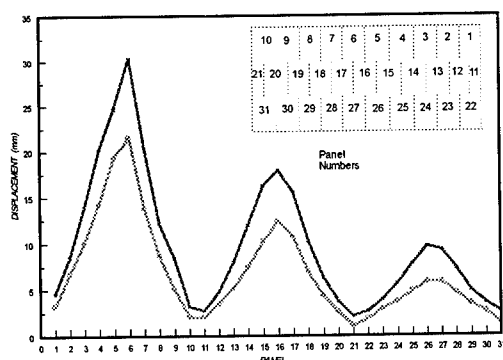


Fig. 5 Mean panel displacements and 95% confidence range for all tests

16), then decreases monotonically. This pattern is followed in the bottom row in all but two tests (9 and 12). In these tests the maximum displacement is in panel 27, rather than panel 26. However, in Tests 9 and 12 the displacement of panel 27 is only 0.03 mm and 0.04 mm, respectively, greater than that of panel 26.

The average total displacement of each of the walls is remarkably consistent, considering the complexity of the model. The standard deviation of average total wall displacement (0.64 mm) is only 7.8% of the mean wall displacement (8.23 mm). The data appear normally distributed; there are 5 tests above the mean and 5 below, 7 fall within 1 standard deviation and all 10 tests fall within 2 standard deviations of the mean. The range of average total wall displacement for the 95% confidence interval (mean plus or minus two standard deviations) is 6.95 - 9.50 mm. This is shown graphically in Fig. 5.

The consistency of the average displacement for each row of panels is also very high. The coefficient of variation ranges from 6.8% for the top layer to 9.3% for the bottom layer. In every test but one, the

average displacements for the three rows were either all above or all below the mean. The exception was Test 9 where the middle row has an average displacement below the mean, while the top and bottom displaced more than the mean. However, the average displacement for each row is within 2% of the mean.

#### 4.2 Pressures

The peak pressures measured by the free-field and interface pressure gages are shown in Table 2, along with the mean, standard deviation, coefficient of variation and mean plus and minus two standard deviations for each gage. The predicted prototype pressures are the same as the model pressures. The variability of the peak pressures is considerably higher than for the displacements. The coefficient of variation ranges from 14% to 40%. This variability compares favorably with that found in full-scale testing. Also, there is a consistency in the way variability differs, depending on the type of measurement made. The interface pressure on the bucket wall is most consistent (coefficient of variation = 14%). Significant factors influencing this pressure are the explosive, the soil between the explosive and the gage and the distance to the explosive. (The location of the gage is not a factor as it was not removed between tests). The next most consistent measurements are from the free-field gages (coefficient of variation = 16 and 20%). These gages are influenced by the factors listed above plus the additional factor of gage location. The least consistent measurements are the interface pressures on the wall panels (coefficient of variation for average pressure = 28%). These measurements are influenced by the same factors which influence the free-field gages, plus the additional factor of wall stiffness. Interface pressure is strongly affected by the

rigidity of the surface upon which the pressure wave is impinging. Small, unavoidable differences in wall construction result in wall stiffness differences that can strongly influence interface pressure. While the range for the 95% confidence interval may seem large, it is a consequence of the inherent variability of the construction process and a similar range might be expected in full-scale reliability testing.

## 5 DISCUSSION

The results of the reliability test series described above provide useful information regarding centrifuge modeling of explosive events in general, as well as invaluable help in the interpretation of the results of the specific parametric investigation for which it was designed. The very narrow range of displacements observed in the tests demonstrates that a high degree of reproducibility is possible for displacements caused by high strain rate events. This is in agreement with work by Taylor et al (1991) on projectile penetration in sands, which also showed very high reproducibility.

Peak dynamic pressures are much more variable (approx. 3.5 times) than displacements. The large variability in pressure measurements may be due to instrumentation, data acquisition and data reduction, rather than true variability in the amplitude of the blast wave. However, the pressure gages were recalibrated frequently and no evidence of gage problems was found. The higher reliability of the interface gage on the bucket suggests that the variability found in peak pressures is real.

Another interesting observation regarding peak pressures is the relationship between peak interface pressure and average wall displacement. The tests with the 3 highest average wall displacements (7, 8, 9) had 3 of the 4 lowest average peak interface pressures. Rather than indicating high displacement, high peak interface pressure correlates well with low wall displacement. This implies that design methodologies that aim to reduce peak pressure on the wall may not be the way to minimize wall displacement.

The data from the reliability test series are currently being used to analyze the results of the production tests. A clear criterion has been established to determine if the variation of a specific parameter produces a significant increase or reduction in wall displacement or wall interface pressure. A difference of more than 1.5 mm above or below the mean for the average wall displacement is sufficient to show the

probability is less than 5% that the variation is due to random factors. It also will be possible to determine if a given change in the model affects a specific row of panels differently.

Without the results of the reliability testing, it is difficult to imagine that 15-20% differences in wall displacement (< 2 mm) would be taken as significant. It is also possible that a difference of 40-50% in peak interface pressure would be seen erroneously to be significant.

## 6 SUMMARY AND CONCLUSIONS

A series of 10 centrifuge tests modeling the response of a reinforced soil wall to blast loading was conducted to evaluate the reliability of the test data. Statistical analyses of the data show that the average displacement of the wall, as well as individual wall panels, are very reproducible. Peak interface pressures on the wall vary considerably more and correlate inversely with wall displacement. The results of this reliability investigation can be used to determine the significance of variations in displacement and interface pressure measured in a parametric study of wall behavior.

## ACKNOWLEDGEMENTS

Funding for this research was provided by the United States Air Force. The authors thank Capt. Richard Reid, USAF, and Carl Hollopeter for their assistance.

## REFERENCES

- Bachus, R.C., Fragaszy, R.J., Jaber, M., Olen, K., Yuan, Z. & Jewell, R. 1992. Dynamic response of reinforced soil systems, Volume I. CEL-TR-92-47, Air Force Engineering Support Agency. Tyndall AFB, Florida
- Brownell, K.C., Purcell, M.R., Hollopeter, C.A., Fragaszy, R.J. Taylor, T. & Olen, K.L. 1994. Dynamic capabilities of the Wright Laboratory centrifuge facility. Proceedings, Centrifuge 94.
- Steedman, R.S. 1990. Centrifuge modeling of the effects of blast loading on piles Volume II: Data analysis. 1990 Air Force Weapons Laboratory Report WL-TR-90-33 Vol.II. Kirtland AFB, New Mexico.
- Taylor, T., Fragaszy, R.J. & Ho, C.L. 1991. Projectile penetration in granular soils. J. Geotech. Engrg., ASCE, 117(4):658-672.

## Dynamic soil structure interaction resulting from blast loading

M.C.R. Davies

*School of Engineering, University of Wales, Cardiff, UK*

**ABSTRACT:** A study, centred on a series of centrifuge model tests, has been conducted to investigate the effects of ground shock - initiated by a buried explosion - on buried structures. The study was in two parts. The first phase was a fundamental investigation of cratering, resulting from explosions, attenuation of stress waves propagating through soil, and the soil structure interaction resulting from the interaction of the propagating stress wave with a buried structure. In the second phase of the study the feasibility of protecting buried structures from the effects of buried explosives by the use of barriers was investigated. The effectiveness of each barrier concept was assessed using the results of strain gauges and accelerometers to compare the response to loading of protected structures with similar unprotected structures.

### 1 INTRODUCTION

There are situations when buried structures, or building foundations and basements, may be subjected to impulsive loading resulting from blast. Buried explosions might be caused by construction or quarrying activities; alternatively blast loading can be the result of terrorist activity or act of war. Two major aspects should be considered when assessing the effect of blast loading (Davies 1991). First, the level of stress reaching the structure, which is a function of the size of the blast the distance from the buried structure and the soil type through which the stress wave is propagating. Secondly, the response of the structure to the imposed loading, which is a function of the nature of the impulse and the relative stiffnesses of the soil and loaded structural element.

Extra protection may be provided to buried structures if the stress wave propagating towards it may be attenuated by means of a barrier. Woods (1968) conducted field trials to investigate the isolation of machine foundations by placing a trench around the oscillating source. The results indicated effective screening of surface (R) waves. Analytical studies conducted by Al-Hussaini and Ahmad (1991) have also indicated that such barriers are effective for surface wave screening. However, for trenches filled with media such as concrete the latter study indicated that vertical components of the incident wave transferred to a greater depths and horizontal components

were not effectively attenuated.

When considering the protection of buried structures from propagating body (P and S) waves it may not be practical to surround the structure with a void which may require support, become inundated with water or restrict access. A barrier constructed from a material which provides attenuation without some of these disadvantages might be more desirable. Practical means of providing this were investigated in the study described herein.

A consequence of centrifuge scaling laws is that when a model is accelerated at  $n$  g the mass of explosive scales by  $n^3$ ; thus very small quantities of charge may be used to model large explosives. For example, in the tests described herein which were conducted at 20 g a charge totalling 0.002 kg was equivalent to a 16 kg charge at prototype scale. When considering the effect of blast close to buried structures it is important that any influences of crater geometry on the soil/structure interaction are correctly modelled. This can satisfactorily be achieved at elevated gravity. The technique has previously been used by other workers to study blast effects on buried structures and the effect of blast loading on buried structures (Kutter et al 1988) and deep foundations (Steedman et al 1989).

The experiments described herein were conducted using the geotechnical centrifuge at the University of Manchester, UK. This has a diameter of 6.4 m and is capable of carrying a soil package 2 m x 1 m x 0.6 m. For the test programme described herein, the models were

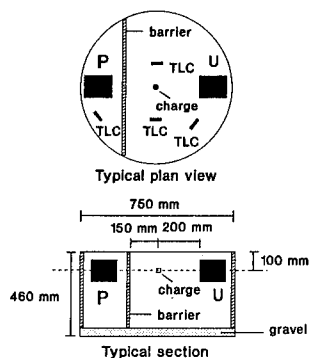


Fig. 1 Centrifuge model package

contained in a strong box 0.75 m diameter and 0.46 m deep. All tests were conducted at a centrifuge acceleration of 20g.

## 2 CENTRIFUGE MODEL TESTING

A general arrangement of the models may be seen in Fig. 1. Two structures were subjected to blast loading in each experiment. One, the "protected" structure, was located behind a protective barrier and the other, the "unprotected" structure, was placed at the same distance from the charge and acted as a control specimen. The sides and base of the strong box were lined with a 12 mm thick polystyrene sheet to reduce the reflection of stress waves as they reached the boundaries of the model. Measured stresses indicated that the peak amplitude of reflected waves was negligible compared to the values at the soil/structure interface. A 40 mm drainage layer of pea gravel was placed in the bottom of the box.

The soil used in the tests was a fine Mersey River Sand ( $D_{50} = 0.22$  mm,  $C_U = 1.5$ ). Sand was placed in the box by pluviation; resulting in a density of  $16.68 \text{ kN/m}^3$ . The model structures and instrumentation were installed at the required depth during formation of the soil model. Layers of dyed sand were placed at regular intervals during the pluviation process. The layers enabled discontinuities to be observed in the foundation layer when it was sectioned following the test. On completion of the model the soil was saturated and then allowed to drain thus producing a damp sand exhibiting negative pore pressures.

The structures used in the experiments consisted of a cubical steel box of internal dimensions  $90 \text{ mm} \times 90 \text{ mm} \times 90 \text{ mm}$  and side wall thickness 5.0 mm. Steel plates, either 0.5 mm or 2.0 mm thick were located on the front and back faces of the structure. These plates were fixed to the side walls only (i.e. spanning

one way) and are considered as encastre for analysis purposes. The plate facing the charge was instrumented with strain gauges on both its outside and inside face. At prototype scale the face plates of the model structures represented a steel plate either 10 mm or 40 mm thick with a span of 1.8 m. The mid-height of the structures was located at a depth of 100 mm beneath the ground surface, i.e. 2 m at prototype scale.

Four barrier concepts were investigated in the model tests. These were:

(i) a low acoustic impedance barrier - a 12 mm thick sheet of expanded polystyrene (equivalent to 0.24 m a prototype scale),

(ii) a stiff barrier - a 15 mm thick reinforced concrete wall (equivalent to 0.3 m a prototype scale) fabricated using "micro concrete", having a strength,  $f_{cu} = 30 \text{ N/mm}^2$ , and reinforced on its centreline with 1 mm (0.02 m) diameter bars at 5 mm (0.1 m) centres both vertically and horizontally,

(iii) a composite barrier - polystyrene and reinforced concrete barriers (each having the same dimensions as the barriers in concepts i and ii) placed together with the polystyrene facing the charge

(iv) an air void - a 15 mm wide trench excavated to the inverse level of the structures and supported in sand models by cantilever sheet piled walls but unsupported in clay models

The barriers spanned the full width of the strong box and extended to the full depth of the box or the invert level of the structures as determined by the requirements of each experiment.

In tests conducted in sand models the charge consisted of 0.0015 kg of plastic explosive plus a detonator equivalent to 0.0005 kg. This corresponded to 16 kg at prototype scale. In the clay models the charge was a detonator with 0.0010 kg of plastic explosive - i.e. 12 kg prototype. The charge was placed in a borehole with its centre of gravity at a depth of 100 mm, the same level as the mid-height of the structures. The borehole was backfilled following placement of the charge.

In addition to the strain gauges located on the structures, accelerometers were placed in each structure and earth pressure transducers (TLC in Fig. 1) located in both the free field (i.e. unprotected) and protected zones of the models. The accelerometers were manufactured by Kulite (model GS-500, 2500g) and had dimensions 23 mm long and 12.7 mm in diameter.

The pressure cells were manufactured at University of Wales, Cardiff. These were strain gauge diaphragm type earth pressure cells, 40 mm in diameter and 12 mm deep. Signals were recorded using a data acquisition system capable of scanning 32 channels at a rate of 500 kHz. These were

conditioned and stored digitally on the centrifuge arm, the amplified signals being passed through the slip rings for storage on disk and analysis following the test.

A total of 21 tests were conducted in a programme which included repeat testing of each barrier concept. Modelling of models was not conducted in this testing programme. A comparison of full scale prototype behaviour with centrifuge model response is the subject of a current research project and will be reported at a later date.

### 3 RESULTS

#### 3.1 Crater Profile

Investigations into cratering phenomena in centrifuge models (e.g. Serano et al 1988) have indicated that scaled crater volumes agree closely with those measured in full scale field tests. In both centrifuge and field studies empirical correlations between crater volume,  $V$  and charge mass,  $W$  indicate that

$$V \propto W^n \quad (1)$$

where  $0.75 < n < 1.0$ .

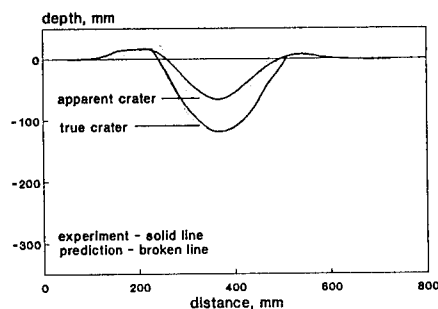


Fig. 2 True and apparent crater profiles - measured and predicted using TM-5-855

Typical sand crater profiles measured in the centrifuge tests are shown in Fig. 2. An advantage of these centrifuge models was that it is possible to section the model following the test to locate the outline of the true crater profile in addition to that of the apparent crater. The diameter of the craters in the experiments was typically 300 mm, the apparent depth 80 mm and the true depth 120 mm. This corresponding to 6 m, 1.6 m and 2.4 m at prototype scale, respectively. Measured

dimensions are in excellent agreement with predictions using the method proposed in the most widely used design code TM 5-855-1 (US Army 1986) which are also shown in Fig. 2.

As Fig. 2 shows, the protective barrier and hence the structures were located outside the true crater. The soil/structure interaction therefore resulted from the effects of stress waves propagating through soil and not from ejecta interacting with the structure or barrier.

#### 3.2 Stress Attenuation

Measurements of peak stress amplitude at varying distances from the charge in the free-field (i.e. in the unprotected region of a model) are shown in Fig. 3 and Fig. 4 for sand and clay models respectively. Also plotted are the

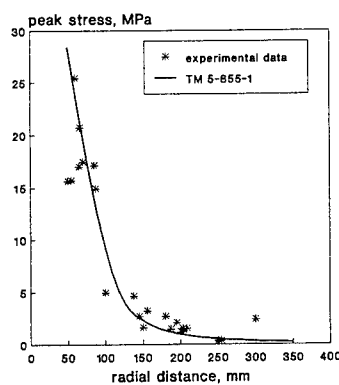


Fig. 3 Stress wave attenuation in sand - measured and predicted using TM-5-855

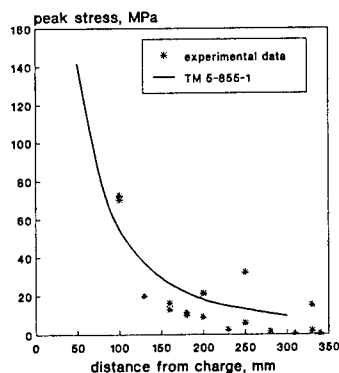


Fig. 4 Stress wave attenuation in clay - measured and predicted using TM-5-855



predicted stress attenuation calculated using the attenuation formula suggested in TM 5-855-1 7(U.S. Army) using values of soil density and stress wave velocity measured in the experiments where possible. Figure 3 shows very good agreement between measured and predicted values of peak stress amplitude in sand. Despite difficulties in measuring propagating stress waves in the clay models, caused by excessive signal noise, there is a reasonable correlation between predicted and experimentally obtained values, Fig. 4. There is undoubtedly scatter in the experimental results, but the trends are in good qualitative agreement with the predicted behaviour. It should be noted that much higher stress levels were achieved in the clay tests despite the smaller charge size.

The results of these comparisons are very encouraging and provide confidence in the quality of data obtained in the experiments. In addition, since the predictions in TM 5-855-1 are obtained empirically from a large body of filed test data these good correlations further validate the use of the technique of centrifuge modelling for studies of the type described herein.

The effect of screening the propagating stress wave by placing a polystyrene barrier in its path was a reduction in its peak amplitude. At a distance of approximately 200 mm from the blast (i.e. the location of the structure) the peak amplitude was reduced from a free field value of 1.17 MPa to 0.08 MPa. Using the theory of wave propagation in an elastic medium the attenuation provided by a barrier may be quantified by the value of the "transmission coefficient" i.e. the ratio of the intensity of the incident wave on the barrier to the wave transmitted through the barrier (Davies and Ismail 1991). The average value of this coefficient was measured to be 0.027 in the centrifuge models which compares with a predicted value of 0.013. Thus measured and predicted values were in close agreement.

### 3.3 Soil-Structure Interaction

A comparison of strain gauges located at the mid-span of the front face in the protected and unprotected structures is shown for each of each barrier type located in sand models in Figs. 5, 6, 7 and 8 (N.B. in these figures tensile strains are negative).

The plots indicate that:

(i) As the stress wave arrived at the two structures the mid-span gauges displayed tension - indicating bending. The gauges on the unprotected structure and the structure protected by the reinforced concrete barrier initially recorded a compressive strain - indicating hogging - prior to tension. During

this phase the protected structure displayed higher values of tensile strains. The period of this loading phase, about 550  $\mu$ s, corresponded with the length of the compressive wave impulse at this distance from the blast.

(ii) Following this first phase of deformation there is a continued increase in strain development in both structures. Both reach a peak some time after the propagating wave passed the structure.

These observations indicate that there are two distinct loading mechanisms operating on the structures. In the first phase the dominant loading of the structures resulted from interaction with the propagating stress wave - "stress wave loading". This was highly attenuated by the low acoustic impedance materials in the polystyrene and composite barriers and by the open trench, Figs. 5, 7 and 8, but not by the high acoustic impedance reinforced concrete barrier, Fig. 6.

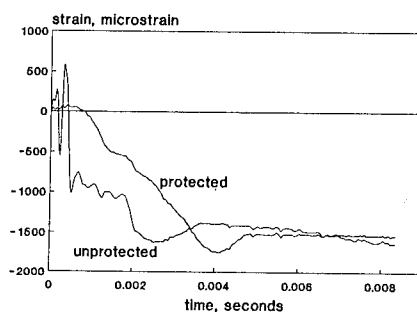


Fig. 5 Response of mid-span strain gauge on protected and unprotected structures - polystyrene barrier

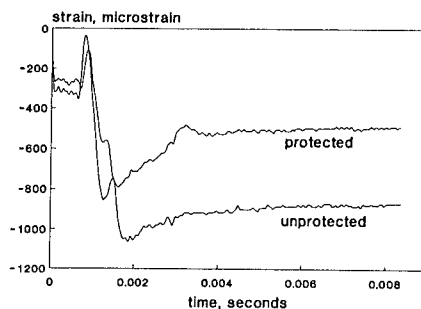


Fig. 6 Response of mid-span strain gauge on protected and unprotected structures - reinforced concrete barrier

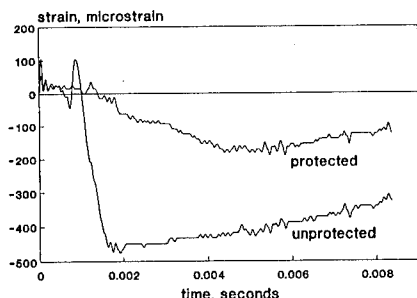


Fig. 7 Response of mid-span strain gauge on protected and unprotected structures - composite barrier

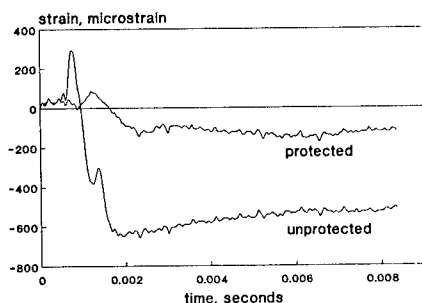


Fig. 8 Response of mid-span strain gauge on protected and unprotected structures - open trench

The increase in deformation with time after the wave front had passed the structure indicated a continued loading. This resulted from the acceleration of the soil located between the structure and the edge of the crater. The response of the structure develops over a relatively longer time because of the inertia of this mass of soil - loading in this second phase is thus referred to as "inertial loading". Similar behaviour has also been observed in other series of centrifuge tests where buried structures have been subjected to impulse loading (Kutter et al 1988, Davies 1991a).

Although the polystyrene barrier was demonstrated to be highly effective in reducing the stress wave loading on the structure, the results show that it provided limited, if any, resistance to inertial loading. This is because the location of the barrier in relation to both the crater and the structure was such that significant inertial force could be developed by the acceleration of the soil between the crater and the barrier. Since the barrier was highly flexible this loading was not distributed over a

large area, but was transferred to the soil in the zone immediately behind the barrier and hence to the structure.

In contrast, although there was only limited attenuation of the stress wave loading by the reinforced concrete barrier, Fig. 6, significantly less strains were developed in the protected structure than in the unprotected structure during the inertial loading phase. This was because the barrier had a significantly greater bending stiffness than the polystyrene barrier and thus acted to distribute the loading over a greater area. The most efficient barrier concept was obtained by combining both polystyrene and reinforced concrete to optimise the favourable properties of both materials, i.e. the low acoustic impedance of the polystyrene and the stiffness of the reinforced concrete, Fig. 7.

The best protection was afforded by an open trench, as indicated by the lowest protected structure strains measured in the series of tests shown in Fig. 8. Loading of the protected structure resulted from distribution of stress due to inertial loading on the embedded portion of the cantilever sheet pile walls.

Although the open trench resulted in the lowest structural response this concept may not be the best practical means of protection. Should the trench become inundated with water (which has a high acoustic impedance) this will facilitate the transmission of stress waves. In clay medium tests in which protection was provided by unsupported trenches the collapse of the trench during loading resulted in "inertial loading" of the structure.

### 3.4 Structural Accelerations

The presence of the barrier reduced the frequency of vibration and magnitude of the acceleration experienced by the structure. Figure 9 shows typical acceleration history

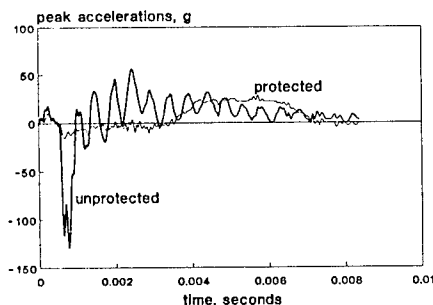


Fig. 9 Acceleration response - protected and unprotected structures

plots for a structure protected by a polystyrene barrier and the unprotected structure from the same test; the peak acceleration was reduced from 130 g to 25 g. This type of barrier would therefore be effective in reducing the magnitude of shock loading to buried structures and the foundations of surface structures.

#### 4 CONCLUSIONS

The following conclusions can be made from the results of the series of centrifuge tests:

1. Measured model crater dimensions in sand models corresponded well with predicted prototype values.
2. The recorded values of peak stress amplitude reduced with distance from the source of the blast. Predictions of attenuation agreed very well with the experimental results.
3. Barriers containing low acoustic materials were highly effective in attenuating propagating stress waves and reducing the magnitude of shock loading on structures.
4. The soil structure interaction revealed that there were two distinct loading mechanisms. The first resulting directly from the propagating stress wave and the second due to inertial loading from the soil located between the crater and the structure. Although a low acoustic medium barrier was highly effective in reducing peak stresses and accelerations it only provided limited resistance to inertial loading. Stiff barriers distributed the inertial loading providing greater protection for the buried structures.

#### ACKNOWLEDGEMENTS

The study described herein has been carried out with the support of Procurement Executive, Ministry of Defence, on behalf of Defence Research Agency, RARDE (Christchurch). The authors wish to thank Dr W.H Craig, Mr M. Cruickshank and Dr C.M. Merrifield and their colleagues in the centrifuge modelling group at Manchester University for their help in conducting the experiments.

#### REFERENCES

- Al-Hussaini, T.M. and Ahmad S. 1991. Design of Wave Barriers for Reduction of Horizontal Ground Vibration. *Journal of Geotechnical Engineering*, ASCE, Vol 117, No. 4: 616-639.
- Davies, M.C.R. 1991. Buried structures subjected to dynamic loading, Chapter 8, *Structures Subjected to Dynamic Loading*, Eds. R. Narayanan and T.M. Roberts, Elsevier: 271-302.
- Davies M.C.R. 1991a. Modelling of Dynamic Soil Structure Interaction resulting from impulsive surface loading. Centrifuge 91, (Eds.) H-Y Ko and F.G. McLean, *Proceedings International Conference Centrifuge 91*, Boulder, Colorado, Balkema: 487-493.
- Davies, M.C.R. and Ismail, A.B. 1991. Retro-Fitting of Expedient Protection for Buried Structures. *Rapidly Assembled Structures*, (Ed.) P.S. Bulson, *Proc. Int. Conf on Mobile and Rapidly Assembled Structures*, Southampton: 163-174.
- Kutter, B.L., O'Leary, L.M. Thompson, P.Y. and Lather R. 1988. Gravity-scaled tests on blast-induced soil-structure interaction. *Journal of Geotechnical Engineering*, Vol 114, No. 4: pp 431-447.
- Serano, C.H. Dick, R.D., Goodings, D.J. and Fournery, W.F. Centrifuge modelling of explosion induced craters. 1988. Centrifuge 88, (Ed.) J-F Corte, *Proc. International Conference Centrifuge 1988*, Paris, Balkema: 445-450.
- Steedman, R.S., Felice, C.W. and Gaffney E.S. 1989. Dynamic response of deep foundations. *Proc. 4th Int. Conf. on the Interaction of Non-nuclear munitions with structures*, Panama City, USA, Vol 2: 80-84
- U.S Army. 1986. *Fundamentals of protective design for conventional weapons*, TM 5-855-1, Engineering Waterways Experimentation Station, Vicksburg, Miss.
- Woods, R.D. 1968. Screening of Surface Waves in Soils, *Journal of Soil Mechanics and Foundations Division, ASCE*, Vol. 94, SM4: 951-979.

## Simulation of cratering in a small geotechnical centrifuge

H.G.B. Allersma & W.J. van Niekerk  
*Delft University of Technology, Netherlands*

A.P. Kooijman  
*Shell Research b.v., Rijswijk, Netherlands*

**ABSTRACT:** A research program has been carried out in the small geotechnical centrifuge at the University of Delft to investigate the formation of craters during an internal blowout. Several different conditions have been simulated and the knowledge about this phenomenon has been increased significantly. The results of this project contribute to safer drilling practices and better assessment of risk of an internal blowout.

### 1 INTRODUCTION

A very hazardous situation that can be encountered during the drilling or completion phase of oil/gas wells is the loss of well control after an influx of highly overpressurized formation fluids (kick). The unsuccessful control of a kick, with further influx of formation fluids, may lead to a blowout. The process of a blowout with high pressure hydrocarbons finding their way to the surface may culminate in the fluidization of a considerable volume of soil near the surface (cratering) (Walters, 1990).

Crater size and especially crater depth predictions have a direct bearing on the setting depth requirements of sub-surface safety valves in wells. The safety valves can prevent escalation of such disasters by closing in already completed wells. For this purpose they should be set at the correct depth, i.e. below the crater bottom. Further prediction of the crater size is important for determining the probability of the crater undermining an offshore platform.

The physical processes occurring during the formation of a crater are very complex. In order to obtain a better understanding of these processes, model tests have been performed in a geotechnical centrifuge. In these experiments cratering is simulated by injecting gas under pressure at the bottom side of the soil sample. The gas required to simulate the blowout was stored under high pressure in the spinning section of the centrifuge. The gas flow rate and pressure could be measured and controlled during flight.

Cylindrical models as well as plane models were used to investigate the behavior of the soil during gas injection. The processes occurring in flight were monitored during testing in a plane model by means of a video camera. The phenomena in several tests were studied in more detail using a pc based image processing system (Allersma, 1991). The crater

formations in cylindrical models were analyzed by using a technique in which small slices were cut from the preserved sample and by X-ray computer tomography, which enables visualization of the crater without damaging the sample.

A large number of tests were performed to investigate the behavior of a soil layer under different conditions of gas supply. Significant progress was made in understanding the process that controls crater initiation and development.

### 2 EQUIPMENT

The test program was carried out in the small geotechnical centrifuge (Fig.1) of the University of Delft (Allersma, 1994). This centrifuge has a diameter of two meters, which can accelerate samples with a weight of approximately 300N up to 300g. A small centrifuge is extremely suitable for performing trial and error tests. Because the size and weight of the samples is low, a large number of tests can be performed, so that the influence of several test conditions can be investigated in a short time. The application of modern electronics permits the performance of advanced computer controlled tests. To perform blowout tests a well defined gas flow must be available during spinning. Because the centrifuge is not equipped with fluid slip rings, two high pressure (200 bar) cylinders with a total volume of 0.01 m are mounted on the beam of the centrifuge. Before the centrifuge is started the cylinders are filled with air by means of a high pressure compressor. The gas flow during a test is controlled by a pressure regulator and a valve. The diagram of the control system is shown in Fig.2. The pressure regulator and the valve are standard devices which are equipped with small dc motors to enable interfacing with the on-board computer. The on-board

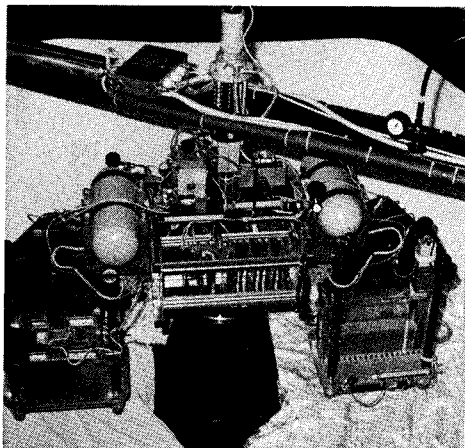


Fig.1 The University of Delft geotechnical centrifuge.

computer is connected using the rs232 protocol with a pc via slip rings. A program in the pc permits advanced control over the gas flow during spinning of the centrifuge. During a test the process parameters are plotted on the screen, where it is possible to combine the plots with the real time video image. The maximum flow rate of the gas is approximately 10 l/s at 1 bar. The actual gas flow is derived from the pressure drop in the cylinders during a well defined time interval.

### 3 TEST TECHNIQUE

Centrifuge tests are the best way to perform small scale simulations of the cratering process. If the small scale tests are performed at 1 g level several conditions are not in agreement with the real situation. In the first instance the cohesion due to capillary forces appeared to be very significant, so that quite different behavior of the sand layer can be observed. Because the soil stress is very low at 1 g it is not really possible to investigate the influence of the flow rate of the gas on the depth of the crater.

The centrifuge tests are performed in plane boxes with transparent walls at a distance of 40 mm apart and in cylindrical containers with a diameter of 240 mm. The advantage of plane tests is that the crater formation can be made visible in flight. The three dimensional tests performed in the cylindrical containers, however, are closer to reality. The height of the sand samples was approximately 200 mm. Up to now the tests have been performed at a gravity of 100 to 150g, so that a maximum prototype height of 30 meters could be simulated. The gas was supplied in the center at the bottom of the sample by means of a nozzle (Fig.3).

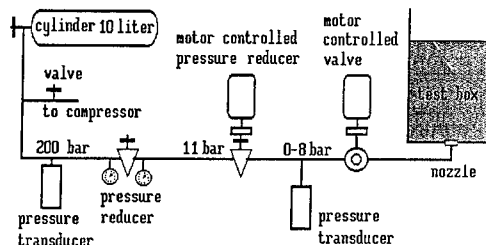


Fig.2 Layout of the gas control system.

The nozzle is covered with a sieve to prevent sand from plugging the gas supply tube. The flow rate of the gas was controlled by adjusting the pressure in the supply tube. The actual flow rate of the gas depends on the resistance of the nozzle and the permeability of the soil layer. The computer controlled valve makes it possible to start the gas flow either suddenly or gradually.

In most tests fine sand was used with the following properties:

Unit weight	15 kN/m <sup>3</sup>
Permeability	0.001 cm/s
Friction angle	34°
D <sub>50</sub>	0.095 mm
D <sub>90</sub>	0.12 mm

Fine sand was used in order to keep the Reynolds number as low as possible. The sand sample was prepared by hand. The container was filled first with water. Subsequently dry sand was poured on the water surface. When a layer of approximately 3 cm has formed, the sand was made more dense by vibration. To improve the visibility of the process, thin layers of dark colored sand were poured at different depths during sample preparation. In the plane tests the crater shape could be measured simply by observing the sand sample through the transparent boundary. The color of the sand in the crater is always different from the sand in the undisturbed sample. The measurement of the crater in the cylindrical samples is more time consuming. The water was drained first making the unconfined sample stable due to capillary forces. Then the sand sample is extracted from the container by means of compressed air. The crater can now be found by removing slices of sand. Drawings of the crater shape can be made at different cuts, so that afterwards the total shape and e.g. the volume of the crater can be derived. In several cases the image processing system has been used to improve and analyze the images.

Some experiments were performed to investigate the influence of a clay layer on the crater formation. To ensure good contact between the clay and the boundary, clay slurry was added to the sand surface. The clay was sedimented in flight and next the final

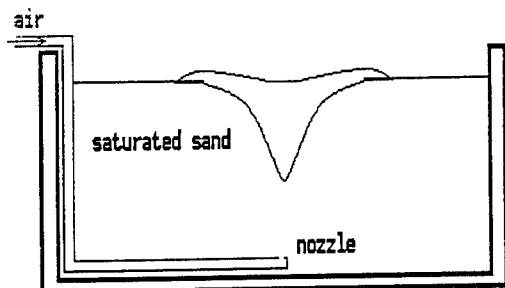


Fig.3 Diagram of the test box.

sand layers were poured in the container. The test was performed when the clay layer had been completely consolidated.

#### 4 TEST RESULTS

In the first instance two dimensional tests were performed on fine sand. Because the active zone of the sample was visible during the tests the effect of the different parameters could be observed in real time. Whether the gas was supplied gradually or suddenly soon appeared to be very important. In the case of a gradual gas supply the pore water in the sand was displaced first in a more or less conical soil volume. This process is visible due to a slight difference in contrast between the saturated and unsaturated sand. If the gas flow is increased, the conical soil volume in which the pore water is displaced becomes larger. Because this area, which is more permeable for gas increases, the flow rate of the gas does not increase sufficiently to cause a large crater. Only some fluidization at the surface could be observed, with a prototype depth of approximately 2 meters. The maximum flow rate of the gas in this test was 4 l/s at 1 bar. A photograph of the test result is presented in Fig.4. This picture is obtained by subtracting the initial and final stage of the sample, using the image processing system. The black areas represent the changes in the sample. The conical region in which the water is displaced is also visible.

In Fig.5 the result is shown of a test in which the gas is supplied suddenly. In this case the pressure in the supply tube is adjusted to some value first and next the valve is opened. In this test a crater is formed in less than 0.5 sec. The first stages of the test are presented in time steps of 0.04 sec. It is shown that in the first instance, the upper sand layer is lifted up. Next a breach can be observed, which finally results in a stable crater. The soil in the crater is in circulation due to the continuous gas flow. The crater depth appeared to be highly dependent on the start pressure of the gas.

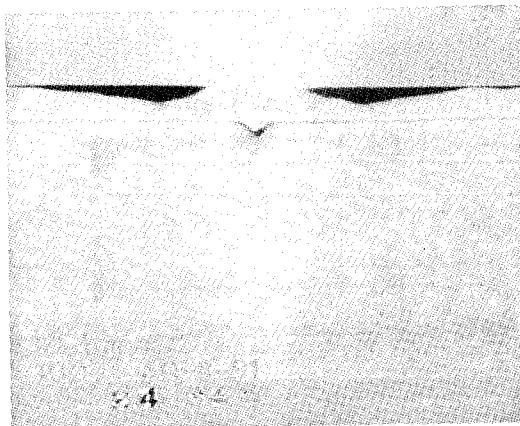


Fig.4 Photograph of a plane sand sample, subjected to a gradual gas supply.

A few tests on plane sand samples have been performed where a clay layer of approximately 1 cm was inserted half way the height of the sand sample. The phenomena in these tests are rather complicated. It appeared that a crater was formed also if the gas was supplied gradually. The explanation for this is that the gas is accumulated just beneath the clay layer in the first instance. If the pressure becomes too high the clay layer collapses. Because the gas escapes suddenly a crater is formed (Fig.6).

In Fig.7 a test result is shown in the case that cylindrical samples are used to simulate cratering. The sand sample was cut layer by layer to visualize the crater shape at the center. What is typical is the complicated shape of the crater.

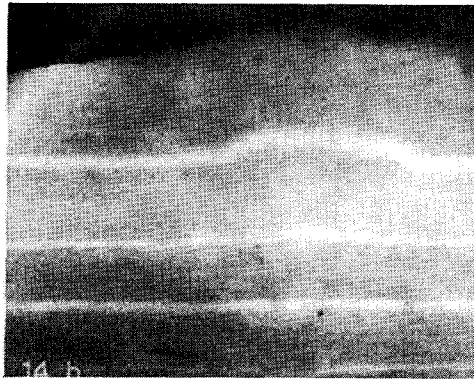
#### 5 DISCUSSION

The two dimensional tests show clearly the interaction between the gas and the sand body. When the gas flow is increased gradually the development of discrete canals is visible in the first instance. Later on a slight difference in contrast shows clearly that the pore water is displaced in a more or less conically shaped soil volume. This region could be visualized very well, also, in cylindrical samples by means of X-ray computer tomography (Fig.8). If the gas flow is increased gradually, only shallow fluidization at the surface of the sand sample can be observed. The depth of the disturbed region is about 2 meters in prototype conditions.

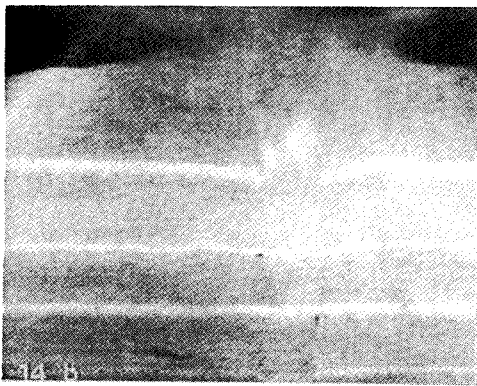
Craters with larger depth were formed if the gas flow is started suddenly. The initiation of the crater is probably a result of the liquid flow caused by the displacement of the pore water. If the crater is formed



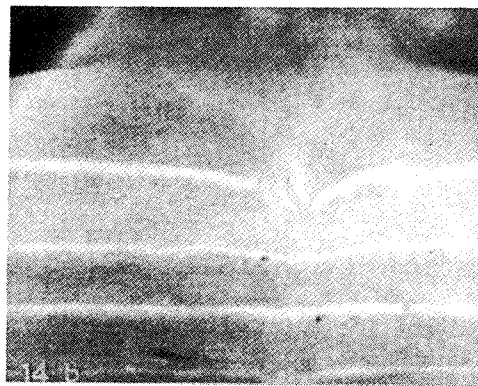
$t = 0 \text{ s}$



$t = 0.04 \text{ s}$



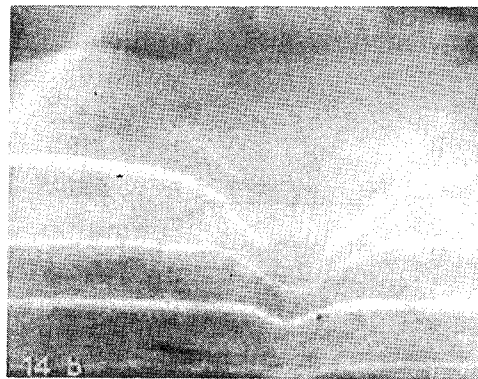
$t = 0.08 \text{ s}$



$t = 0.12 \text{ s}$



$t = 0.16 \text{ s}$



$t = 0.36 \text{ s}$

Fig.5 Formation of a crater at 100g, shown in time units of 1/100 sec.

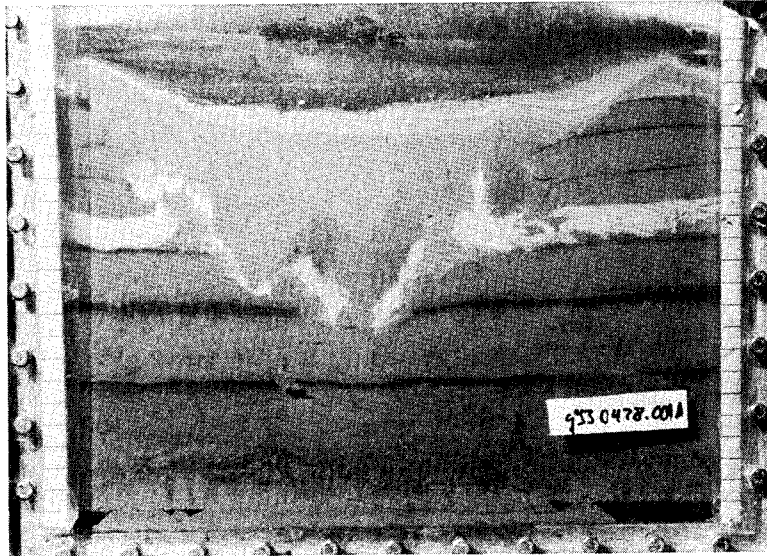


Fig.6 Simulation of cratering in soil with a clay layer; width of the box is 320 mm.

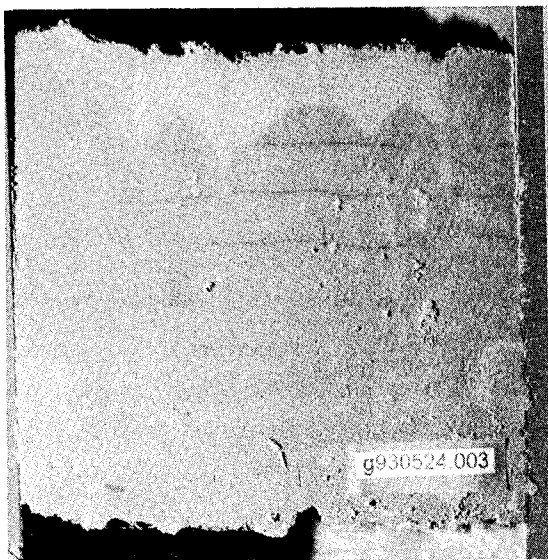


Fig.7 Typical result of cratering experiments in cylindrical samples; diameter is 240 mm.

the gas flow is capable of keeping the crater active. At the first moment when the water has not yet been displaced the system behaves very rigidly. At this stage the gas pressure in the supply tube is probably of great importance on the depth of the initial crater. Once the crater is formed the gas flow causes the crater

volume to increase with time.

The tendency could be observed that a clay layer causes a crater in the case that the gas flow was increased gradually. The explanation for this is that a significant amount of gas is accumulated in the first instance under the clay surface. If the clay layer



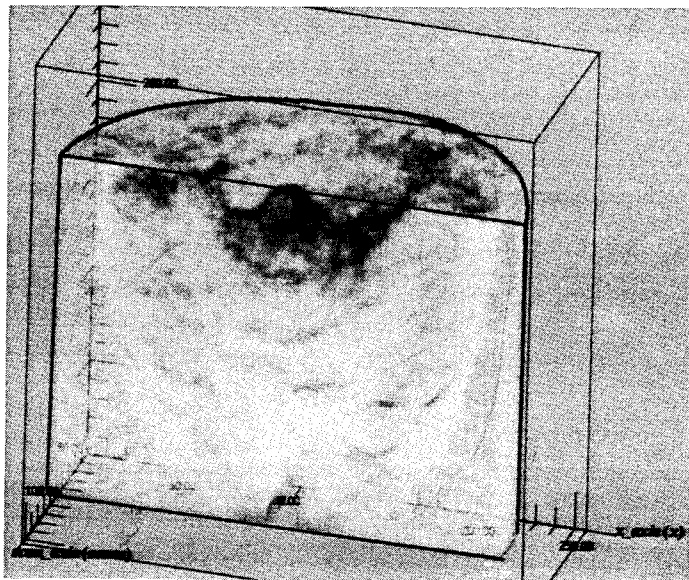


Fig.8 Interior of a cylindrical sample showing the displaced pore water, obtained by X-ray tomography.

collapses the gas escapes suddenly, causing a crater.

The cylindrical tests give a more realistic representation of real cratering phenomena. The measurement of the crater depth in a cylindrical sample is much more complicated, because the shape is very irregular. The major advantage of plane samples is that the phenomena are visible during the test. This is particularly important if time dependent phenomena have to be observed.

## 6 CONCLUSION

A small centrifuge appeared to be very convenient for performing the blowout tests. It appeared to be possible to influence the crater depth by means of the gas supply. Because the samples are small a large number of test conditions could be investigated in a relatively short time. The adjustment speed of the gas flow was extremely important. If the gas flow was started suddenly a crater was formed, where a gradual increase of the flow rate gives only shallow surface phenomena.

The tendency for a clay layer to cause a crater if the gas flow is increased gradually has been observed.

Three dimensional tests in cylindrical samples show a more unstable behavior than plane tests. In the plane tests the crater shape was well defined. In the cylindrical samples, however, the shape of the disturbed region was very irregular.

The tests have led to a better understanding of the

phenomena that play a role in cratering.

The results of this project contribute to safer drilling practices and better assessment of risk of an internal blowout.

## ACKNOWLEDGEMENT

Many thanks is devoted to the technicians at the laboratory for their assistance in this project. The authors are grateful to Shell Internationale Research Maatschappij, Shell UK Exploration and Production and Esso Exploration and Production UK Ltd. for permission to publish this paper.

## REFERENCES

- Allersma, H.G.B. 1991: Using image processing in centrifuge research. Proc. Int. Conf. Centrifuge91, Boulder, Colorado, June 1991, pp. 551-558.
- Allersma, H.G.B. 1994: The University of Delft geotechnical centrifuge. Proc. Int. Conf. Centrifuge94, Singapore, Balkema, Rotterdam.
- Walters, J.V. 1990: Internal blowouts, cratering, casing setting depth and the location of sub surface safety valves. Europec 90, The Hague, Netherlands, Oct.1990:SPE20909.

## Moisture content effects on explosion-induced craters in sand

Kenneth C. Brownell

US Air Force, Tyndall AFB, Fla., USA

Teresa Taylor

University of Washington, Seattle, Wash., USA

Wayne A. Charlie

Colorado State University, Fort Collins, Colo., USA

**ABSTRACT:** This paper presents results of a centrifuge study undertaken to provide additional insight into the influence of compaction saturation on high strain rate loading response of sands, by comparing geometries of surface craters generated from detonation of buried charges. Both magnitude and geometry of craters were influenced by compaction saturations. Apparent crater dimensions increased from minimum values for dry samples, to maximum values as the compaction saturation was increased to approximately residual saturation and beyond. Changes in crater shape (defined by aspect ratio) were also observed at similar threshold values of compaction saturation; higher aspect ratios were associated with dry craters, while lower aspect ratios were observed for samples compacted moist.

### 1 INTRODUCTION

Considerable scatter exists in crater dimensions reported for 1-g explosive tests (e.g. Strange et al., 1973; Rooke et al., 1974); however, data trends indicate that the dimensions are influenced by soil type and soil saturation; specifics regarding how these variables influence crater dimensions have not been reported.

This research involved a program of centrifuge tests studying the influence of saturation on explosive-induced craters in sand. Both crater dimensions and material strength attributes were investigated.

### 2 BACKGROUND

In centrifuge tests conducted to study effects of water content on apparent crater dimensions, Schmidt and Holsapple (1979) found small differences in moisture content produced large differences in crater size and structure. Higher moisture contents resulted in more hemispherical craters, whereas lower moisture contents were associated with flatter crater shapes. They attributed the flatter craters to reduced cohesions at the lower water contents.

Analysis of the centrifuge cratering test results using the material strength cratering model developed by Schmidt and Holsapple (1978, 1979) indicates that explosive-induced crater dimensions scale differently for moist, cohesive soils than for dry, cohesionless soils. The dif-

ference in model:prototype scaling is observed when cohesion is large compared to the total shear strength.

The objective of this research was to determine the influence of compaction saturation on apparent crater dimensions and material strength for explosives detonated in sand.

### 3 EXPERIMENTAL APPROACH

The centrifuge facility at Tyndall Air Force Base, Florida was utilized for this research. The facility contains a 133 g-kN centrifuge with 1.83 m radius. Four sizes of specially manufactured RP-83 detonators were used to model different explosive weights, as described by Brownell (1993).

Table 1 presents the test matrix for this research. The g-levels presented in the matrix are calculated at the center of mass of the detonator. Detonators were buried at a normalized depth of charge burial,  $\lambda$ , equal to  $0.73 \text{ m/kg}^{1/3}$  to maximize transfer of explosive energy into the soil.

The Florida beach sand used in this research is a fine-grained quartz sand with a nearly uniform particle size distribution ( $D_{50} = 0.24 \text{ mm}$ ,  $C_u = 1.53$ ,  $C_c = 0.95$ ). The characteristic shape of the sand is classified as subrounded to subangular. Samples were compacted through a top-down, vertical vibration technique to a dry density of  $1522 \text{ kg/m}^3$  ( $D_r = 39\%$ ,  $e = 0.74$ ).

Crater depth (measured at the deepest point) and inside diameter were directly measured immediately after the centrifuge was decelerated (no changes in apparent crater shape were observed during centrifuge deceleration). Volume measurements were indirectly obtained by preparing a concrete cast of the crater, forming a clay mold of the cast, and measuring the volume of water required to fill the cast.

#### 4 DISCUSSION

The current research differs from previous centrifuge cratering studies in soil type, density, and saturation, as well as depth of charge burial ( $\lambda$ ). Fig. 1 shows scaled apparent crater volume vs. scaled explosive mass results obtained for this research and in work by other researchers (Goodings, et al., 1988; Schmidt and Holsapple, 1978, 1979; Strange, et al., 1961, and Rooke, et al., 1974). The different soil type and, in particular, lower relative densities of test specimens used in the current research are reflected in larger crater volumes compared to those obtained by other researchers.

Differences in  $\lambda$  between the current research and work by previous centrifuge investigators arise in development of the

Table 1. Test matrix ( $\lambda = 0.83 \text{ m/kg}^{1/3}$ )

No. of tests	Scaled explosive (kg TNT)	Detonation g-level	Compaction saturation, $S_c$
2	.00062 (b)	1	20
2	.00062 (b)	1	60
1	7 (c)	19	0
2	7 (a)	26	0
1	7 (c)	19	17
1	7 (a)	26	17
1	49 (a)	49	20
1	124 (a)	67	20
1	7 (c)	19	35
1	7 (a)	26	35
1	49 (a)	49	40
1	124 (a)	67	40
1	7 (c)	19	53
1	7 (a)	26	53
1	49 (a)	49	60
1	124 (a)	67	60
2	7 (c)	19	70
2	7 (a)	26	70

(a) RP-83 detonator, 220 mg PBX

(b) RP-83 detonator, 440 mg PBX

(c) RP-83 detonator, 880 mg PBX

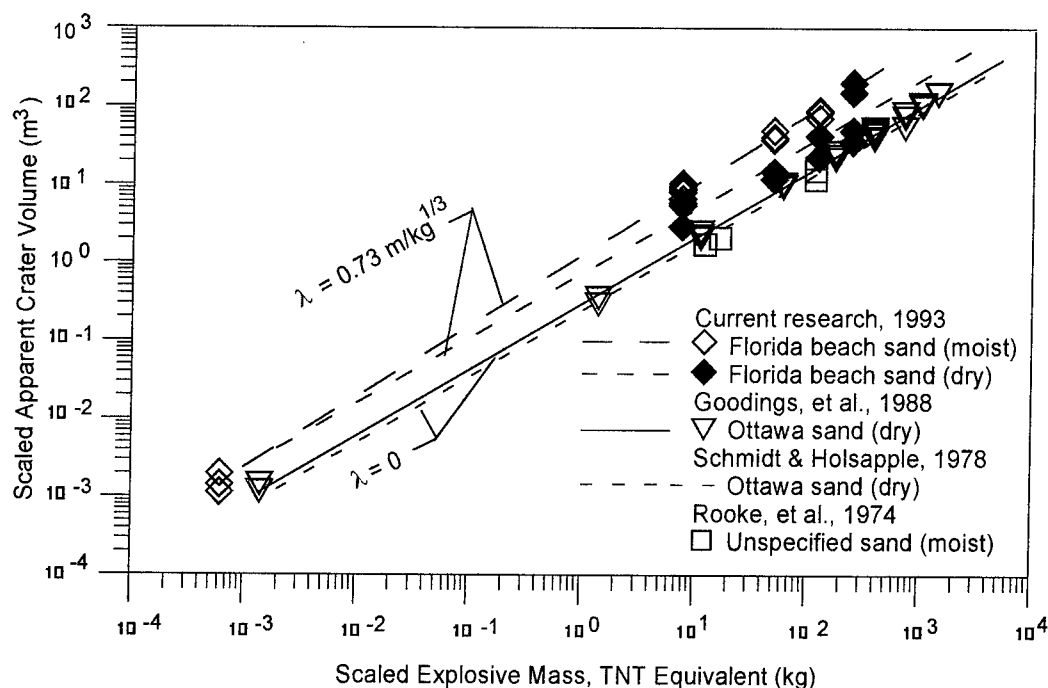


Figure 1. Scaled apparent crater volume vs. scaled explosive mass, TNT equivalent (after Brownell, 1993).

best-fit equations for the data presented in Fig. 1. Both Goodings, et al. (1988) and Schmidt and Holsapple (1978, 1979) used half-buried charges (placed at the soil surface), which were subject to zero confining pressures at all g-levels. Thus, these investigators were able to correlate 1-g tests using half-buried charges with results of their centrifuge tests; correlations are shown in Fig. 1.

In contrast, use of charge burial depths proportional to explosive mass in the current research resulted in significant confining pressures acting on the buried charges in the high-g tests. Consequently, it was not reasonable to correlate centrifuge crater data with 1-g crater data for tests in dry sand. For the tests in moist sand, however, it appeared that the apparent cohesion resulting from capillary forces controlled crater formation at all g-levels; consequently, 1-g data are included in the correlation for moist Florida beach sand shown in Fig. 1.

The best-fit lines through the log-log data plots in Fig. 1 yield  $Y$  proportional to  $W^n$ , where the slope,  $n$ , is the yield exponent,  $W$  is the explosive mass, and  $Y$  is the scaled apparent crater dimension. The yield exponents are tabulated in Table 2 for comparison.

Table 2. Summary of yield exponent,  $n$ , for cratering tests, various researchers;  $n_1$  = volume exponent,  $n_2$  = radius exponent,  $n_3$  = depth exponent.

Year	$S_c$ (%)	g level	$\rho_d$ , kg/m <sup>3</sup>	$n_1$	$n_2$	$n_3$
1993(a)	0	19-26	1522	.831	.297	.279
1993(a)	20-70	1-67	1522	.914	.308	.297
1988(b)	0	1-100	1704	.84	.29	.28
1979(c)	15	1-520	1572	.974	.316	.326
1978(d)	0	1-463	1779	.842	.280	.279
1974(e)	---	1	---	.951	.306	.335
1974(f)	---	1	---	.863	.305	.238
1961(g)	---	1	---	---	.270	.240

- (a) Current research, Florida beach sand  
 (b) Goodings et al., Ottawa sand  
 (c) Schmidt & Holsapple, Desert alluvium  
 (d) Schmidt & Holsapple, Ottawa sand  
 (e) Rooke et al., Unspecified sand (moist)  
 (f) Rooke et al., Desert alluvium (moist)  
 (g) Strange et al., Unspecified sand (dry)

Fig. 2 is a plot of crater aspect ratio  $r/d$  (radius/depth) vs. compaction saturation,  $S_c$ , for the current research. Results of a limited modeling-of-models program are shown for the test series conducted at 19-g and at 26-g, both of which modeled the same prototype of 7 kg

TNT using, respectively, 880 and 220 mg PBX. As can be seen, apparent crater dimensions are the same within the bounds of experimental error, and no charge size effect is evident. This is in agreement with results obtained by Goodings, et al. (1988) and Schmidt and Holsapple (1978, 1979) for half-buried charges.

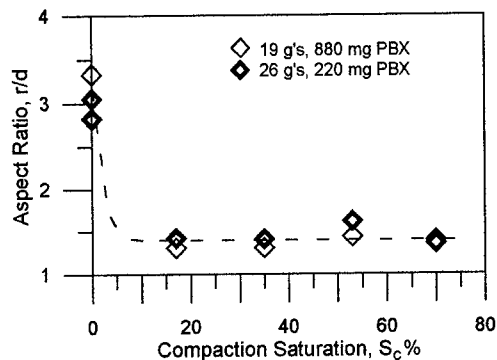


Figure 2. Aspect ratio vs. compaction saturation--modeling of models test results for 7 kg TNT equivalent prototype.

To achieve appropriate scaling of the buried charges in the current research,  $\lambda$  was held constant for all tests, regardless of charge size. This was accomplished during sample preparation by varying the thickness of the top compacted layer (immediately overlying the target location for charge placement) to achieve the desired scaled burial depth at the test g-level.

Also apparent in Fig. 2 is a noticeable decrease in aspect ratio between the dry tests and the moist tests. Similar trends were observed for all test series in this research effort; for clarity, Fig. 2 illustrates only results for the 7 kg prototype. The exact nature of the general trend indicated in Fig. 2 could not be adequately defined by the test data obtained in this research. Extremely high capillary pressures that developed at compaction saturations less than around 20% effectively prevented compaction of test specimens to the target density. Thus, the lowest compaction saturation for the test program was arbitrarily set at 20%, based on practical feasibility considerations. At all compaction saturation values in excess of 20%, essentially the same aspect ratio was obtained. It is reasonable to expect that comparable aspect ratios would apply to the range between residual saturation (approximately 10% for Florida beach sand) and 20%; at values less than residual, the aspect ratio would increase toward the values obtained for dry test specimens. Additional work is necessary to verify this.

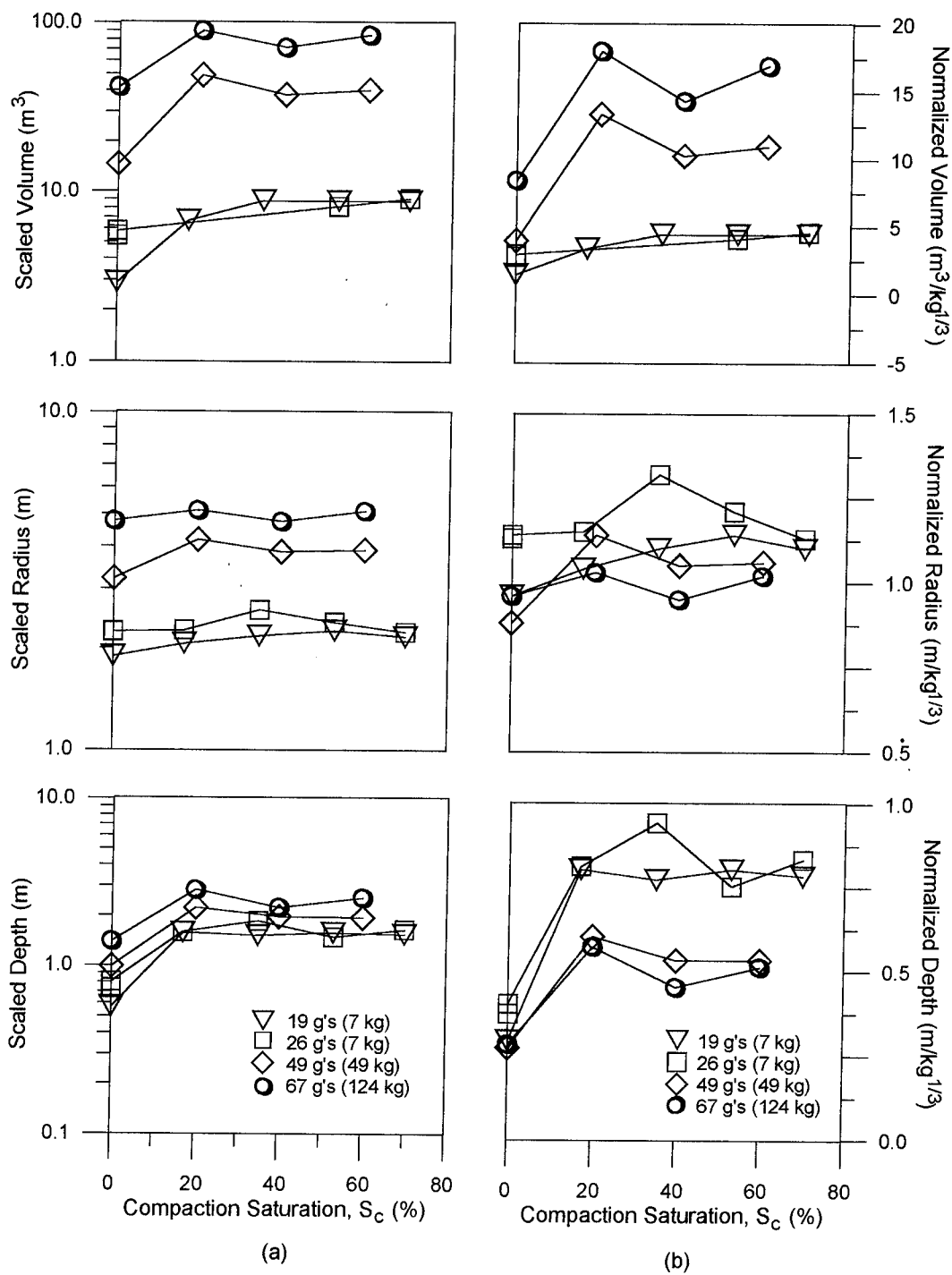


Figure 3. Apparent crater dimensions vs. compaction saturation,  $S_c$ : (a) scaled dimensions; (b) normalized dimensions.

Fig. 3 presents plots of scaled and normalized apparent crater volume, radius, and depth vs. compaction saturation for the current research. It is clear from this figure that these apparent crater dimensions increase with g-level. When the g-level is multiplied by a factor of 2.5 (increased from 26-g to 67-g), corresponding to an increase in prototype charge from 7 to 124 kg, apparent crater volume increases by an order of magnitude (from 7 m<sup>3</sup> to 70 m<sup>3</sup>) and apparent crater radius doubles (from 2.3 m to 4.6 m). Table 3 is a compilation of average aspect ratio and apparent crater wall angle,  $\alpha$  ( $\tan \alpha$  = crater radius/depth). Also included in this table are results from centrifuge tests by other investigators (Goodings, et al. 1980; Schmidt and Holsapple, 1978, 1979).

Table 3. Summary of average aspect ratios (r/d) and apparent crater wall angles ( $\alpha$ ), various researchers.

Year	S <sub>c</sub> (%)	g level	$\lambda$	r/d	$\alpha$
1993(a)	0	19	1.43	3.2 <sup>(1)</sup>	17.5
	0	26	2.67	3.2	17.5
	0	49	2.67	3.2	17.5
	0	67	2.67	3.2	17.5
	17-70	19	1.43	1.3	37.6
	17-70	26	2.67	1.4	35.5
	20-60	49	2.67	1.9	27.8
	20-60	67	2.67	2.0	26.6
1988(b)	0	10	0	3.8 <sup>(1)</sup>	14.8
	0	20	0	3.7 <sup>(1)</sup>	15.2
	0	50	0	4.0 <sup>(1)</sup>	14.1
	0	65	0	4.2 <sup>(1)</sup>	13.5
1979(c)	0	10	0	5.1 <sup>(1)</sup>	11.2
	0	451	0	4.4 <sup>(1)</sup>	12.7
1978(d)	4(2)	10	0	3.6 <sup>(1)</sup>	15.5
	4(2)	10	0	3.9 <sup>(1)</sup>	14.3
	4(2)	451	0	2.4 <sup>(1)</sup>	22.8

(a) Current research, Florida beach sand

(b) Goodings et al., Ottawa sand

(c) Schmidt & Holsapple, Ottawa sand

(d) Schmidt & Holsapple, Desert alluvium

(1) average values

(2) moisture contents

The observed differences in crater shape between values tabulated for these investigators compared to those for the current research are expected, based on differences in charge placement, as discussed in reference to Fig. 1.

In analyzing current test results as listed in Table 3, it is evident that

higher aspect ratios are obtained for craters in dry sands compared to craters in moist sand. One possible explanation involves slope failure; slumping of side walls would decrease crater depth and increase crater radius (and thus aspect ratio). Evidence supporting this possibility lies in the calculated value for  $\alpha$  of 17.5°, which is much lower than the angle of repose for Florida beach sand (approximately 30° to 35°).

The higher crater walls and larger values for  $\alpha$  observed for the moist sand tests conducted at 19-g and 26-g (37.6° and 35.5°) are likely associated with apparent cohesion developed due to capillary forces. These larger values of  $\alpha$ , coupled with the deeper craters (and corresponding lower aspect ratios) observed for these tests compared to tests in dry sand, suggest that slope failure was not likely to have occurred. As the g-level increases to 49-g and 67-g, the apparent cohesion component of shear strength becomes a smaller percentage of the total strength, and slope failure may occur. The smaller measured apparent crater depths for tests at 49-g and 66-g (which are less than the depth of charge burial), as well as the lower values of crater wall angles (27.8° and 26.6°) are significantly lower than the values of  $\alpha$  for tests at 19-g and 26-g, and lend support to this hypothesis.

## 5 CONCLUSIONS

The yield exponent,  $n$ , exhibits little variation (approximately 10%) with the addition of moisture, for the tests reported herein. Larger craters were produced in sample specimens prepared at lower relative densities compared to craters produced in higher density soil specimens as reported by other investigators. The scaled apparent crater dimensions of radius, depth, and volume increase, respectively, by 20%, 100%, and 150% between 0% and 20% compaction saturation. An increase in scaled apparent crater dimensions is observed as saturation increases from 0% to some value less than 20%, and likely associated with the residual saturation. Between 20% to 70% compaction saturation, no change in apparent crater dimensions is observed.

Craters in dry Florida beach sand have aspect ratios of approximately 3.2, while craters in moist sand have aspect ratios from 1.3 to 2.0, with the larger values associated with higher g-levels. The decrease in apparent crater depth for tests performed at 49-g and 67-g, and the relatively low crater wall angles of craters measured in dry sand (17.5°) and in partially saturated sand at 49-g and 67-g (27.8°, 26.6°), support slope failure as a contributing mechanism to the larger aspect ratios.

#### REFERENCES

- Brownell, K. C. 1993. *Centrifuge modeling of explosion-induced craters in unsaturated sand*. M.S. thesis, Colorado State University, Fort Collins, CO, USA.
- Goodings, D. J., W. L. Fourny, & R. D. Dick 1988. Geotechnical centrifuge modeling of explosion-induced craters-- a check for scaling effects. U.S. Air Force Office for Scientific Research, Washington, D.C., Report No. AFOSR-86-0095, July.
- Rooke, A. D., B. L. Carnes, & L. K. Davis 1974. Cratering by explosives: a compendium and an analysis. U.S. Army Engineer Waterways Experiment Station, Vicksburg, Mississippi, Technical Report B024-657, January.
- Schmidt, R. M. & K. A. Holsapple 1978. Centrifuge cratering experiments I: dry granular soils. Defense Nuclear Agency Report DNA 4568F, Washington, D.C.
- Schmidt, R. M. & K. A. Holsapple 1979. Centrifuge crater scaling experiment II, material strength effects. Interim Report for Period 31 January 1978 - January 1979, prepared for Defense Nuclear Agency, Washington, D.C., Contract No. DNA 001-78-C-0149, May.
- Strange, J. N., C. W. Denzel, & T. I. McLane 1961. Analysis of crater data, cratering from high explosive charges. U.S. Army Engineering Waterways Experiment Station Technical Report No. 2-547, Vicksburg, Mississippi, June.

## Comparison between field and centrifuge model tests of heavy tamping

Naotoshi Takada & Akihiko Oshima  
Osaka City University, Japan

**ABSTRACT:** A field test of heavy tamping was simulated with a centrifuge model under an acceleration field of 50 g. An actual field test was carried out to investigate ground deformation and earth pressure beneath the tamping hole. The ground was a loose and homogeneous sandy fill, 10 × 10 m in area and 6.5 m in height. Ground deformation and earth pressure were measured with markers and earth-pressure cells installed in the fill during embankment and excavated after tamping to measure their displacement. Ground deformation measured in the model was compared with that in the field. The earth pressure measured in the field and the ground strength measured by the cone penetration test in the model also reveal the detailed behavior of ground subjected to heavy tamping.

### 1. INTRODUCTION

Heavy tamping is a ground-compaction method using the impact force of a ram blow. This method has been successfully applied to sandy and gravelly ground and waste landfill. In the current design procedure, however, the work conditions are determined empirically. Although field measurement of ground deformation has often been attempted with settlement gages and inclinometers, current instrumentation has not been successful in obtaining accurate measurements due to the large ground deformation and tremendous impact force involved. The centrifuge model is the most effective alternative for investigating the compaction mechanism of this heavy compaction technique.

The authors have conducted several series of centrifuge model tests to investigate the effects of ram blows on ground deformation and on increase in ground strength under various tamping conditions (Mikasa et al. 1988; Mikasa et al. 1989; Oshima et al. 1993). They have suggested that the effects of tamping on sandy ground are governed by the ram momentum rather than the kinetic energy of the ram; specifically, the ram mass has the dominant effect, followed by ram drop height and number of blows. A theoretical consideration, based on field measurement of ram penetration of the ground, supported this tendency (Oshima et al. 1994).

This paper presents a simulation of a field test in

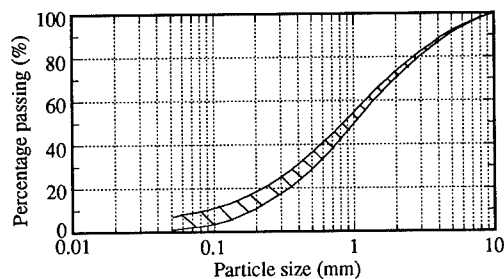


Fig. 1 Particle size distribution of fill

the centrifuge model (Takada et al. 1993). In this field test, markers and print-type pressure cells comprising an aluminum plate and a steel ball were installed in the fill during embankment and were excavated after tamping of the ground. This instrumentation revealed the ground deformation and the maximum earth pressure during tamping.

### 2. FIELD TEST

The test field was a fill ground, 10 × 10 m in area and 6.5 m in height, with a 1:2 slope. The fill material was decomposed granite; the particle size distribution is shown in Fig. 1. The maximum and minimum dry densities were 2.03 t/m<sup>3</sup> and 1.39 t/m<sup>3</sup>, respectively. The fill ground was homogeneous; SPT values were



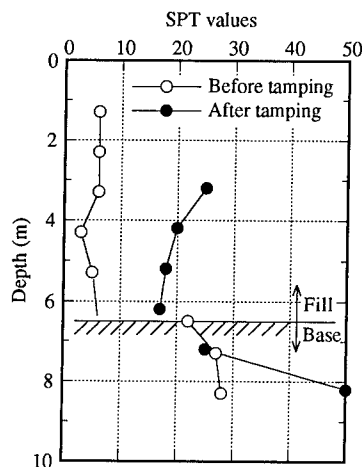


Fig. 2 SPT values in the fill

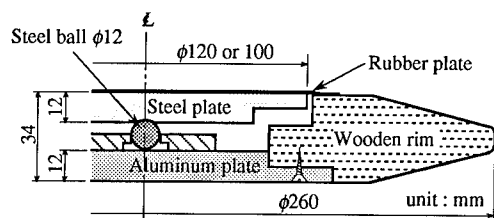


Fig. 3 Earth pressure cell

from 4 to 6 as shown in Fig. 2; the dry density was  $1.66 \text{ t/m}^3$ . Ground water was not observed in the fill. The tamping conditions were as follows: ram mass, 20 t; ram base area,  $4 \text{ m}^2$  (2.26 m in diameter); ram drop height, 20 m; and number of blows, 20. The ram blow was applied to the center of the fill.

Ground deformation was measured with markers. Three kinds of markers were used: soft balls (9.5 cm in diameter); circular steel plates (30 cm in diameter and 6 mm thick); and square wooden plates (30 cm long and 3 mm thick). They were installed at predetermined depths and distances from the center of the fill during embankment.

The earth-pressure cell as shown in Fig. 3 was of the imprint type, comprising a soft aluminum plate and a steel ball. Earth pressure acting on the surface of the steel plate is transmitted to the steel ball, which imprints a circular mark on the surface of the aluminum plate. The force on the steel ball is proportional to the square of diameter of the circular mark imprinted. The pressure cell is equipped with a wooden rim to avoid stress concentration and to give

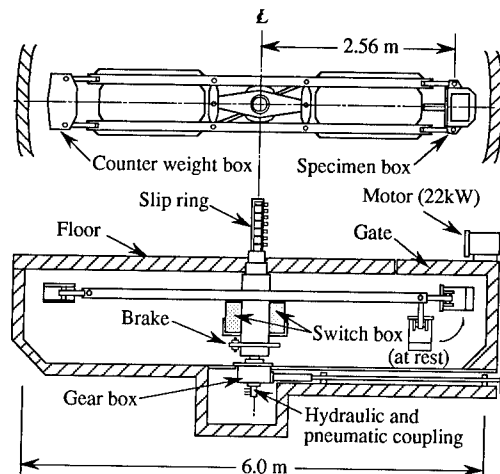


Fig. 4 OCU Mark-V centrifuge

it the same unit weight as the surrounding soil. Seven earth pressure cells for measuring vertical earth pressure were installed beneath the center of the fill; six for measuring vertical and horizontal earth pressure were installed 4 m from the center. The earth pressure measured by these pressure cells is considered to be the maximum pressure occurring during tamping.

Settlement of the ground surface, ram penetration and the diameter of the tamping hole at the ground surface were measured after each ram blow. After tamping, the ground was excavated to retrieve the markers and pressure cells and to measure their locations.

### 3. CENTRIFUGE MODEL TEST

Fig. 4 shows the main components of the OCU Mark-V centrifuge, which has a rotor 2.56 m in nominal radius and a maximum centrifugal acceleration of 200 g. The rotation speed is controlled with a frequency controller. The model ground is an axisymmetrical cylindrical column 30 cm in diameter, half of which is prepared as a semicylindrical column as shown in Fig. 5. The ram is a semicylindrical wooden column positioned to strike the center of the model ground. The vertical cross-section of the model ground, including its center axis, is supported by a glass plate through which the ground deformation can be observed. To eliminate friction between the glass plate and the model ground, the glass plate was coated with a 1-mm thick wet agar film. Two-hundred pieces

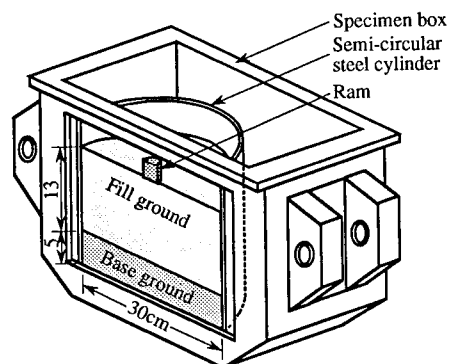


Fig. 5 Model ground

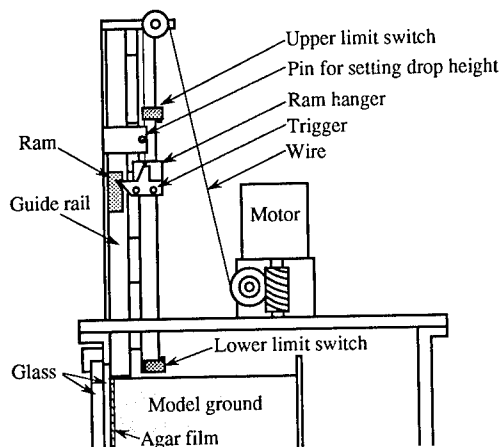


Fig. 6 Ram operating device

of cross marker 2 mm in diameter were pasted on the film to facilitate observation of the ground deformation.

The model material was the same as the field material, but finer than 2 mm; the maximum and minimum dry densities were  $1.82 \text{ t/m}^3$  and  $1.37 \text{ t/m}^3$ , respectively. A 13-cm thick model ground was prepared by compacting the material to a relative density  $D_r$  of 30%, the value of which was estimated from the SPT value in the field, while the 5-cm thick base ground was compacted to  $D_r = 95\%$ . Under a centrifugal acceleration field of 50 g, this model simulates a prototype fill 15 m in diameter and 6.5 m thick.

The ram blow was applied under simulated conditions: the ram mass was 80 g, the ram base area was  $16 \text{ cm}^2$  and the drop height was 43.8 cm. The drop height was corrected to generate the same ram

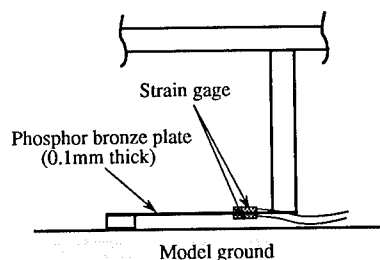


Fig. 7 Cantilever-type settlement gage

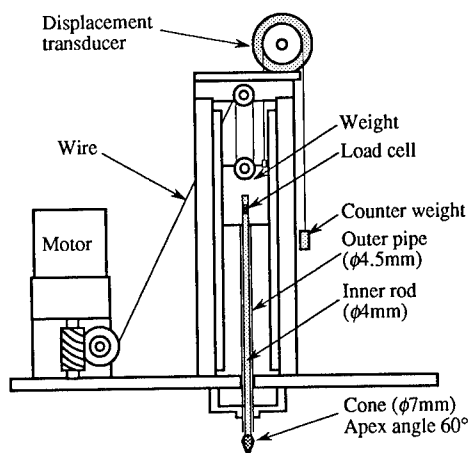


Fig. 8 Cone penetraion device

velocity occurring in a 1-g gravity field (Mikasa et al. 1989).

The model was allowed to settle under its selfweight at 50 g for 1 hour. The ram blow was then applied to the model ground with a ram operating device as shown in Fig. 6. During the ram blow, the ram penetration was measured visually with the aid of a stroboscope, and the ground surface settlement was measured with cantilever-type settlement gages as shown in Fig. 7 at distances of 4.5, 6.5, 8.5, 10.5, 12.5 and 14 cm from the center. Photographs were taken after every fifth blow.

After tamping, the cone point resistance was measured at distances of 2.5, 6.0 and 9.5 cm from the center with a cone penetration device as shown in Fig. 8. This cone is a double-tube type that reduces friction between the ground and cone rod; the penetration force is provided with a weight suspended by a wire and geared motor set.

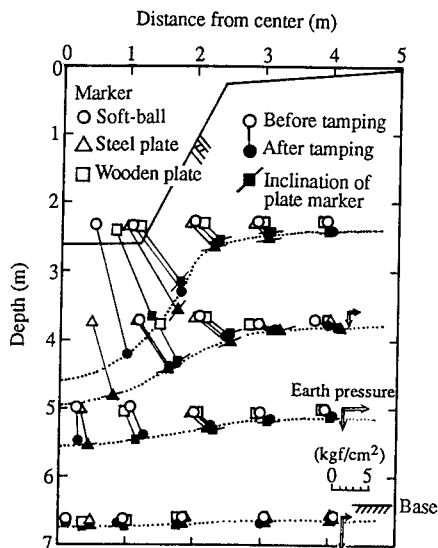


Fig. 9 Displacement of markers and ground deformation (Arrows indicate measured earth pressure)

#### 4. FIELD TEST OF GROUND DEFORMATION AND EARTH PRESSURE

Fig. 9 shows the displacement of the markers and the ground deformation after tamping. There was no difference in behavior among the three kinds of markers. Ground deformation concentrates beneath the tamping hole. The inclinations of the steel and wooden plate markers measured during excavation correspond to ground deformation. Vertical and horizontal earth pressures from the ram blow recorded 4 m from the center are also shown in the figure. The vertical earth pressure increases with depth, while the horizontal earth pressure at a depth of 5 m is greatest where the horizontal displacement is greatest.

Fig. 10 shows the distribution of the vertical earth pressure at the center. Since the earth pressure cells move with the ground deformation of the ram blow, their locations before and after tamping are indicated by the marks ○ and ●, respectively, although the exact locations of the earth pressure cells at 1 and 2 m (△) could not be determined during excavation. The earth pressure rises to 38 kgf/cm<sup>2</sup> at a depth of 1 m and decreases rapidly with depth. The maximum ram acceleration  $\alpha$  can be roughly estimated from the recorded earth pressure at a depth of 1 m, as follows:

$$\alpha = p \times A/W = 380 \times 4/20 = 76 \text{ g}$$

where  $p$  is the vertical earth pressure (tf/m<sup>2</sup>),  $A$  is the

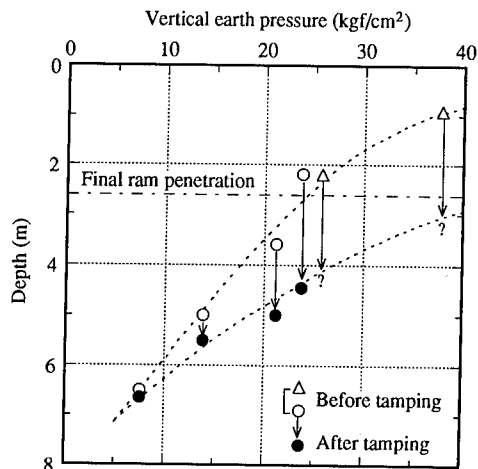


Fig. 10 Vertical earth pressure at center

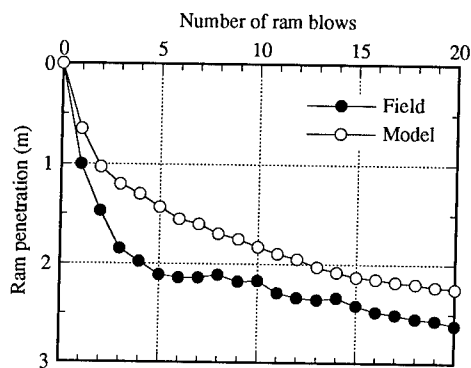


Fig. 11 Ram penetration

ram base area (m<sup>2</sup>), and  $W$  is the ram weight (tf). This value is comparative with the measured ram acceleration of 50 - 110 g.

#### 5. CENTRIFUGE MODEL SIMULATION

The results of the centrifuge model test at prototype scale are presented and compared with those of the field test.

##### 5.1 Ram penetration and ground compression

Fig. 11 plots ram penetration against number of ram blows. The ram penetration measured in the field is greater than that of the model. The diameter of the

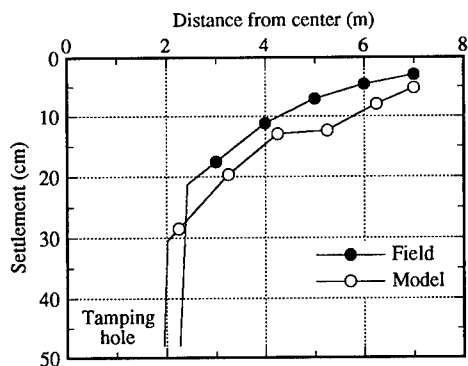


Fig. 12 Settlement of ground surface after tamping

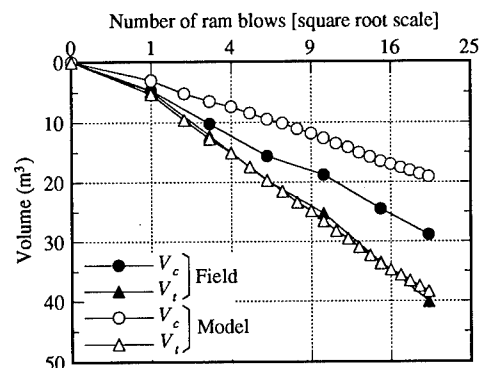


Fig. 13 Volume of tamping hole  $V_c$  and total ground compression  $V_t$

tamping hole at the ground surface was 4.8 m in the field, but 4.1 m in the model. Fig. 12 shows the settlement of the ground surface after tamping. The settlement of the model is a slightly greater than that measured in the field.

Fig. 13 shows the volume of the tamping hole and the total ground compression. The former is calculated using the ram penetration and the diameter of the tamping hole; the latter is obtained by integrating the ground surface settlement, including the volume of the tamping hole. The volume of the tamping hole in the field is greater than that of the model, whereas the total ground compression is approximately the same.

## 5.2 Ground deformation

Fig. 14 shows a comparison of the ground deformation in the field (Fig. 9) and in the model. They are very similar, although the horizontal displacement in

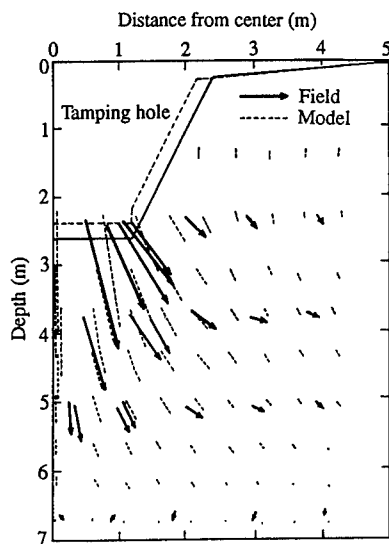


Fig. 14 Ground deformation

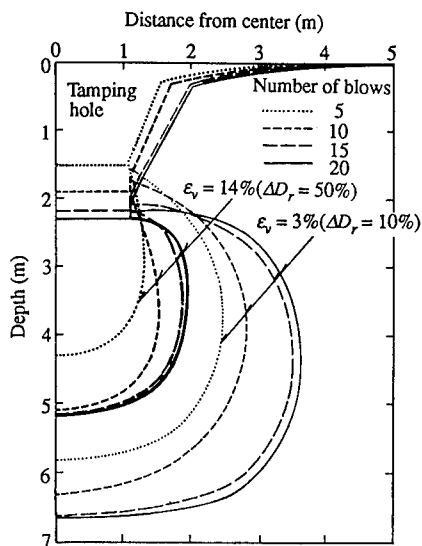


Fig. 15 Propagation of volumetric strain

the field is greatest at the mid-depth of the outer area of the tamping hole.

Fig. 15 shows the propagation of volumetric strains  $\epsilon_v$  of 3 and 14% in the model, calculated from the displacement of the markers following every fifth ram blow. The propagation rate of the contour lines decreases when the number of ram blows reaches 15. The volumetric strains  $\epsilon_v$  of 3 and 14% correspond to increases in the relative densities  $\Delta D_r$  of 10 and 50%,

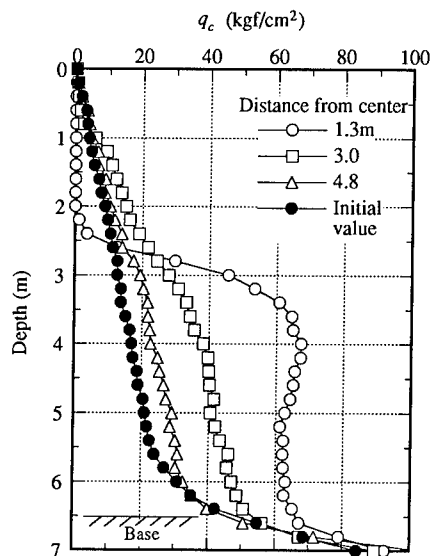


Fig. 16 Cone point resistance before and after tamping

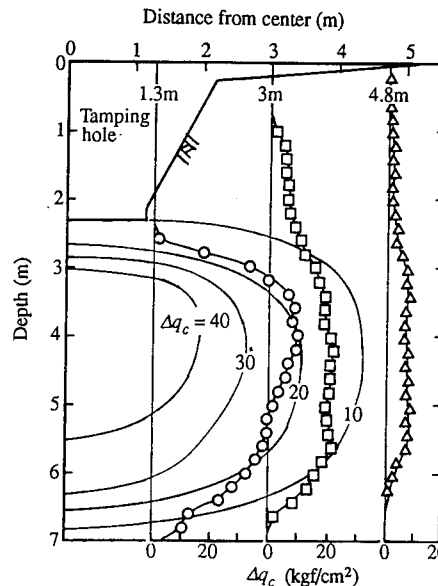


Fig. 17 Distribution of rate of increase of cone point resistance

respectively, resulting in the relative densities  $D_r$  of 40 and 80%, respectively. The spherical areas surrounded by the contour lines of  $\varepsilon_v = 14$  and 3% are regarded as heavily compacted and effectively compacted areas, respectively.

### 5.3 Cone penetration test

Fig. 16 shows the cone point resistance before and after tamping along the depth at various distances from the center of the ground. The rate of increase of the point resistance  $\Delta q_c$  at each location is presented in Fig. 17, where possible contour lines of several  $\Delta q_c$  values are also presented. The contour lines of  $\Delta q_c = 10$  and 40 kgf/cm<sup>2</sup> occupy locations similar to those of  $\varepsilon_v = 3$  and 14%, respectively, which appear in Fig. 15.

## 6. CONCLUSIONS

The comparison of the centrifuge model test with field measurement of heavy tamping leads to the following conclusions: 1) the field measurement revealed the detailed behavior of ground subjected to heavy tamping; 2) ram penetration in the centrifuge model was slightly greater than that measured in the field; 3) both tests showed similar ground deforma-

tion and generated similar ground compression due to the ram blows; and 4) the distribution of volumetric strain due to the ram blows was similar to that of the rate of increase of the cone point resistance.

## REFERENCES

- Oshima A. and Takada N. 1994. Effect of ram momentum on compaction by heavy tamping. Proc. of 13th ICSMFE, Vol.3, pp. 1141-1144.
- Oshima A., Takada N. and Tanaka Y. 1993. Effect of tamping conditions on density increasing area by heavy tamping. Proc. of 28th Annual Convention of JSSMFE, Vol. 2, pp. 2355-2358 (in Japanese).
- Mikasa M., Takada N., Ikeda M. and Takeuchi I. 1988. Centrifuge model test of dynamic consolidation. Centrifuge 88, Balkema, pp.185-192.
- Mikasa M., Takada N. and Oshima A. 1989. Dynamic consolidation test in centrifuge. Proc. of 12th ICSMFE, Vol. II, pp. 947-950.
- Takada N., Oshima A., Watanabe A. and Ikeda M. 1993. Field and centrifuge model tests of heavy tamping. Proc. of Japanese Society of Civil Engineers, Vol. 469, pp. 127-134 (in Japanese).

## 6 Contaminant transport and flow problems

## LNAPL penetration into porous media

R.J. Mitchell & B.C. Stratton  
*Queen's University, Kingston, Ont., Canada*

**ABSTRACT:** A 3 m radius geotechnical centrifuge has been used to model an instantaneous 2000 l surface spill of a light oil on dry medium sand at scales between 19 and 50 gravities. After one year, the 2000 l of oil was found to contaminate about 20 m<sup>3</sup> of sand to a depth of about 4 m. The maximum oil content was close to 7 percent by weight. The complete data set is made available in this paper for numerical model validation purposes.

### INTRODUCTION

Numerical modelling of the transport of light non-aqueous phase liquid (LNAPL) spills into soils has been the subject of recent research (see, for examples, Faust, 1985; Allen, 1985). Physical modelling is an alternative method of producing data and this paper presents results obtained from the infiltration of a circular surface spill on dry sand.

Centrifuge modelling of pollutant transport in unsaturated soils has been presented by several authors (see, for example; Cooke and Mitchell, 1991) and the scaling laws for fluid flow in centrifuge models has been described by Arulanandan et al. (1988).

The movements of a 2000 litre surface spill of a non volatile, non toxic oil (silicon oil) into a dry medium sand was modelled at four scales between 19 and 50 using a 3m radius geotechnical modelling centrifuge. The sand models were prepared in 100mm and 200mm diameter perspex cylinders which were fabricated in 2cm and 4cm ring thicknesses, respectively. The large cylinder is shown on Figure 1. Each ring assembly represents, at the respective scale factors, a one meter prototype depth. Stainless steel cutting rings, shown on Figure 2, were used to

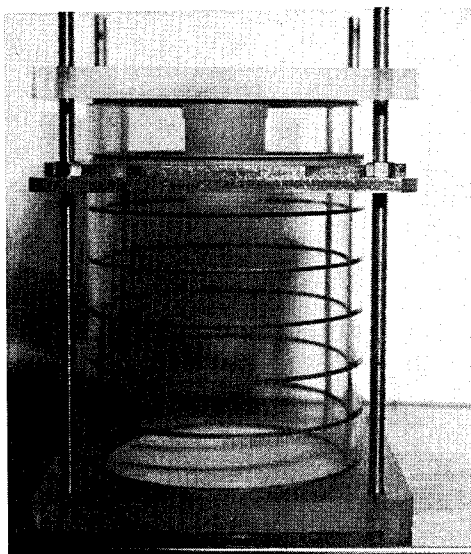


Fig. 1 The 200mm diameter sectioned cylinder

dissect each "model meter" of the soil profile into five annular rings. Models were dissected after 2 months, 6 months and one year of prototype infiltration time. The oil concentration in each of the sampled zones was determined by oil evaporation at 280°C and an oil balance was carried out to confirm the results.

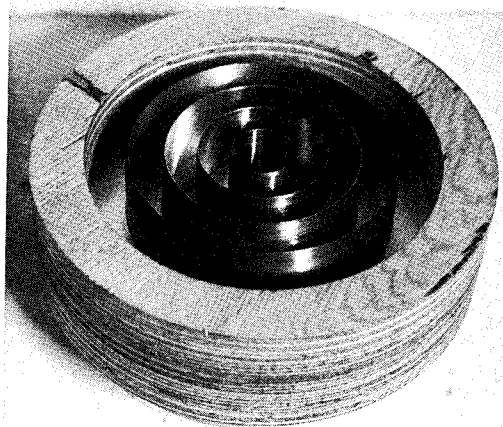


Fig. 2 Cutting rings for model dissection

#### MODELLING MATERIALS AND METHODOLOGY

A clean quartz and feldspar sand, having  $D_{10} = 0.07$  mm and a uniformity coefficient of about 3 was selected for this study because it has a sufficiently high permeability ( $k = 7 \times 10^{-6}$  m/s) to allow LNAPL penetration in a reasonable time frame and yet has a sufficiently small pore size that the Reynolds number, even at accelerated scales of up to 50 gravities, will be less than 0.2, so that Darcy flow can be assumed. Silicon oil, having a dynamic viscosity of 100 cs and a specific gravity of 0.96 was selected as the LNAPL because it is very stable at room temperature (low evaporation rates, high flash point) and is non-toxic when oxidized. Calibration tests showed that surface evaporation effects were negligible and that small quantities of the LNAPL would be 99% evaporated after 48 hours in a 280°C oven. This allowed easy and accurate determination of the LNAPL contained in sand samples.

Sand models were prepared by vibrating the sand in a sectioned sand column to a porosity of about 0.3. A cylindrical LNAPL spill container, shown on Figure 1, with a cutting edge and a perforated bottom plate was pressed into the sand surface so that the LNAPL spill would be confined to

penetrate a circular central area of  $1.8 \text{ m}^2$  (prototype). The equivalent of 2000 prototype litres of silicon oil was released into the receiving container shortly after the centrifuge was brought up to the required speed. Table 1 provides information of the scaled dimensions for different scale factors.

Table 1 Scaled dimensions

g level	1	19	25	50
spill volume	2000 litre	290 ml	128 ml	16 ml
typical infiltration times	2 mo 1 yr	4.1 hr 24.2 hr	2.3 hr 14.0 hr	0.6 hr 3.5 hr

After a predetermined prototype time, a model was removed from the centrifuge and dissected to determine the LNAPL distribution. Because the LNAPL wetted sand appeared darker in colour than the dry sand, the "LNAPL disk" could be measured at each horizontal section. Figure 3 shows a typical photo of the LNAPL wetted sand.

The average LNAPL mass percentage of each of the five concentric rings removed from each section were obtained from evaporation for

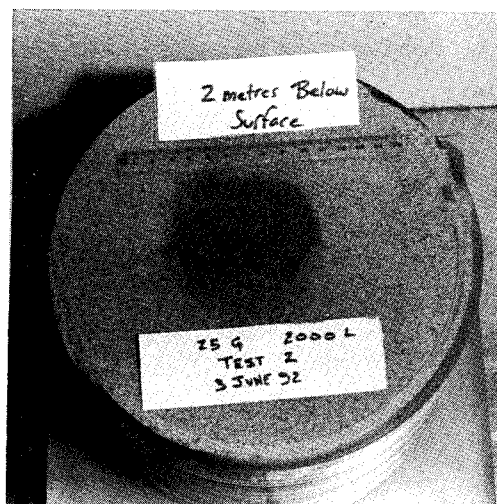


Fig. 3 Photo of LNAPL wetted sand



48 hours in a fume hood ventilated convection oven at 280°C. Thus, the LNAPL front and contours of LNAPL mass percentage could be established for the volume of sand penetrated by the LNAPL.

#### MODELLING RESULTS

Surface ponding of LNAPL was allowed to occur and the LNAPL level within the central containment vessel was monitored using a very accurate pressure transducer. Prototype LNAPL heights as derived from 25 g and 50 g scale models are shown on Figure 4 and confirm that the modelling dimensions and LNAPL spill volumes were correctly scaled such that similar prototype heads were being applied.

The LNAPL visible plumes and LNAPL mass percentages for the 50 g scale model at each of the three infiltration times is plotted in Figure 5. Standard laboratory permeability tests and laboratory capillarity tests were carried out using the medium sand and silicon oil. It was determined that the flow of LNAPL into dry sand is largely gravity driven but lateral transport does develop due to capillary suctions.

Results from scaled models at the four different scale factors were found to be in good agreement, indicating that centrifuge modelling does correctly model prototype transport phenomenon. This is illustrated in Figure 6 where a typical comparison is given for the LNAPL mass percentages. Data from 15 models are available in Stratton (1993). Table 2

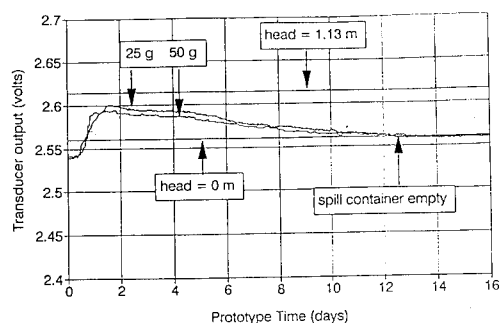


Fig. 4 LNAPL ponding height in models

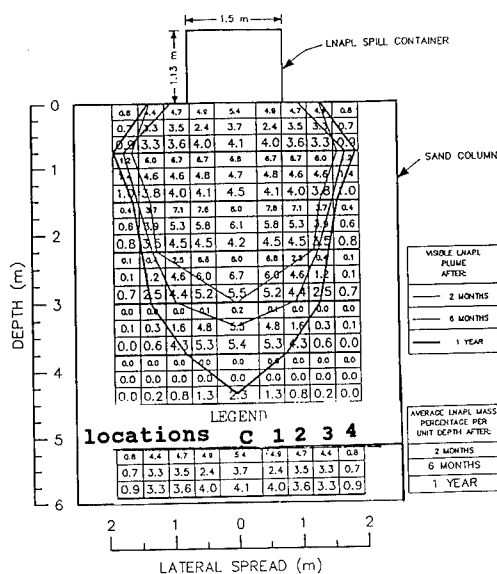


Fig. 5 Visible plume and LNAPL distribution in 38 g model

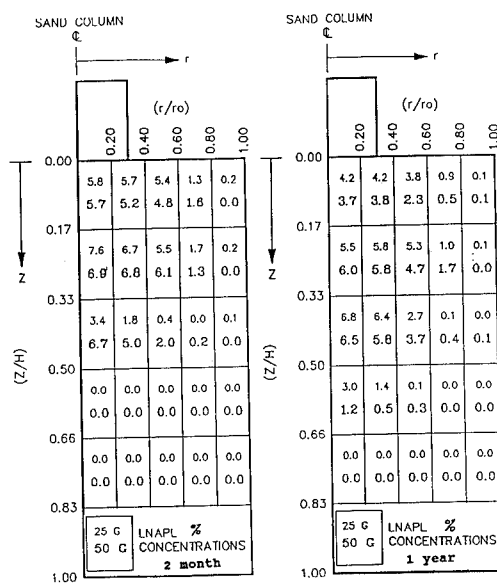


Fig. 6 LNAPL concentrations in typical 25 and 50 g models

provides a complete summary of the LNAPL mass percentages obtained.

#### DISCUSSION

It would seem reasonable to expect the shape of the model and prototype plumes to be similar if

Table 2 Mass percentages data

G level		19				25				38				50			
Time		2 m.	6 m.	1 y.	2 m.	6 m.	1 y.	2 m.	6 m.	1 y.	2 m.	6 m.	1 y.	2 m.	6 m.	1 y.	2 m.
Location*																	
Soil	4	1.5	...	3.0	0.2	0.1	0.1	0.8	0.7	0.9	0.0	0.1	0.0				
Slice	3	5.6	...	3.4	1.3	0.9	1.1	4.4	3.3	3.3	1.6	0.5	1.2				
1	2	5.7	...	1.6	5.4	3.8	3.3	4.7	3.5	3.6	4.8	2.3	2.7				
	1	5.8	3.5	3.3	5.7	4.2	3.4	4.9	2.4	4.0	5.2	3.8	3.1				
	c	5.7	3.6	3.6	5.8	4.2	3.8	5.4	3.7	4.1	5.7	3.7	3.2				
2	4	0.8	1.4	2.7	0.2	0.1	0.0	1.2	1.4	1.0	0.0	0.0	0.0				
	3	6.4	4.6	4.3	1.7	1.0	1.5	6.0	4.6	3.8	1.3	1.7	1.4				
	2	7.5	5.2	4.3	5.5	5.3	4.5	6.7	4.6	4.0	6.1	4.7	3.9				
	1	7.3	5.2	4.2	6.7	5.8	4.4	6.7	4.8	4.1	6.8	5.8	4.2				
	c	7.2	5.0	4.0	7.6	5.5	4.2	6.8	4.7	4.5	6.9	6.0	4.3				
3	4	0.0	0.1	1.1	0.1	0.0	0.0	0.4	0.6	0.8	0.0	0.1	0.0				
	3	1.8	4.5	3.8	0.0	0.1	0.4	3.7	3.9	3.5	0.2	0.4	0.1				
	2	7.0	6.4	5.0	0.4	2.7	3.6	7.1	5.3	4.5	2.0	3.7	2.0				
	1	8.7	6.2	5.6	1.8	6.4	5.3	7.8	5.8	4.5	5.0	5.8	5.2				
	c	8.9	4.4	5.2	3.4	6.8	5.5	8.0	6.1	4.2	6.7	6.5	5.4				
4	4	0.0	0.0	0.3	0.0	0.0	0.0	0.1	0.1	0.7	0.0	0.0	0.0				
	3	0.0	1.3	0.9	0.0	0.0	0.0	0.4	1.2	2.5	0.0	0.0	0.0				
	2	0.6	5.3	3.9	0.0	0.1	0.3	2.5	4.6	4.4	0.0	0.3	0.4				
	1	2.5	6.7	5.6	0.0	1.4	2.0	6.8	6.0	5.2	0.0	0.5	4.0				
	c	3.8	6.8	5.9	0.0	3.0	2.9	8.0	6.7	5.5	0.0	1.2	5.9				
5	4	0.0	0.0	0.1	0.0	0.0	0.0	0.0	0.1	0.0	0.0	0.0	0.0				
	3	0.0	0.0	0.0	0.0	0.0	0.0	0.0	0.3	0.6	0.0	0.0	0.0				
	2	0.0	0.0	0.6	0.0	0.0	0.0	0.0	1.6	4.3	0.0	0.0	0.0				
	1	0.0	0.7	2.6	0.0	0.0	0.0	0.1	4.8	5.3	0.0	0.0	0.2				
	c	0.0	1.5	4.1	0.0	0.0	0.0	0.2	5.5	5.4	0.0	0.0	2.6				
6	4	0.0	0.0	0.0	0.0	0.0	0.0	0.0	0.0	0.0	0.0	0.0	0.0				
	3	0.0	0.0	0.0	0.0	0.0	0.0	0.0	0.0	0.2	0.0	0.0	0.0				
	2	0.0	0.0	0.0	0.0	0.0	0.0	0.0	0.0	0.8	0.0	0.0	0.0				
	1	0.0	0.0	0.0	0.0	0.0	0.0	0.0	0.0	1.3	0.0	0.0	0.0				
	c	0.0	0.0	0.0	0.0	0.0	0.0	0.0	0.0	2.3	0.0	0.0	0.0				

\* locations C, 1, 2, 3, 4 are shown on Figure 5

contaminant transport in the vertical (gravitational) direction is modelled correctly. There are no lateral gravitational effects (advective/dispersive flows) in either, only diffusive and matrix suction effects. The similarity of diffusion transport is easily understood because diffusion is driven by concentration gradients which are identical in model and prototype. Because both the ground area and the time of transport are decreased, in models, by the square of the linear scale (i.e.  $N^2$ ), the lateral (radial) distance of contaminants diffusion is similar in model and prototype. The similarity, between model and

prototype, of the diffusion number is, thus, supported by logic.

Matrix suction effects are rather more complex but, because the volume of contaminant is reduced by the cube of the modelling scale and the holding capacity of the soil is similarly reduced, the ultimate distance of lateral (radial) migration by matrix suction will be similar if the vertical transport is similar. The fact that time is modelled as  $N^2$  and lateral matrix suction gradients are similar at similar fluid contents means that the area contaminated (also at  $N^2$  scale) will be similar in model and prototype, at any given time. Thus, the rate of lateral (radial)

contaminant movement by matrix suction will be similar in model and prototype, as expected from the similarity in the capillary effect.

It should be noted that the oil front propagation data presented in this paper was not obtained by monitoring a single model but by comparing similar models, each of which was dissected after a given time period of infiltration. It is further noted that the model scales used vary from 19, where 1 day of centrifugation models one year of prototype infiltration, to 50, where 1 prototype year is modelled in 3.5 hours. The continuity and consistency of the data, as represented by information on Figures 5 and 6 and in Table 2, indicates that the dissection methodology is satisfactory. The modelling of models technique also provides some confidence in the prospect of extrapolating such data to the field (prototype) scale. It is interesting to note, however, that the data is published primarily for use in validating numerical models, for which neither g levels nor physical sizes need be restricted. If a numerical model can correctly predict the transport in a model, confidence in that numerical model is increased. It, too, might be able to make satisfactory prototype predictions.

#### CONCLUSIONS

A geotechnical modelling centrifuge has been used to create data on the infiltration of 2000 litres of LNAPL into a dry medium sand. Four scaling factors, between 19 and 50 gravities, were used to demonstrate that the contaminant movement is independent of the model scale.

Although the lateral spread of LNAPL into the sand is increased by surface ponding, the effect of capillary suction in increasing the lateral spread is apparent. The 2000 l volume of LNAPL penetrated about 4m into the sand and contaminated close to 25m<sup>3</sup> of sand with oil percentages up to 7 percent by weight. The data set, from which time rates of contaminant movement can be derived, are presented for use in the validation of numerical predictions.

#### ACKNOWLEDGEMENTS

The research reported in this paper was jointly financed by grants from the Ontario Ministry of the Environment and the Natural Sciences and Engineering Research Council of Canada.

#### REFERENCES

- Allen, M.B. 1985. Numerical modelling of multiphase flow in porous media. *Advances in Water Resources* 8:162-186.
- Arulanandan, K., Thompson, P.Y., Kutter, B.L., Neegoda, N.J., Muraleetharan, K.K. and Yogachandran, C. 1988. Centrifuge modelling of transport processes for pollutants in soils. *ASCE Journal of Geotechnical Engineering*. 114:2: 185-205.
- Cooke, B. and Mitchell, R.J. 1991. Physical modelling of a dissolved contaminant in an unsaturated sand. *Canadian Geotechnical Journal* 28:6: 829-833.
- Faust, C.R. 1985. Transport of immiscible fluids within and below the unsaturated zone. *Water Resources Research* 21:4: 587-596.
- Stratton, B.C. 1993. Physical modelling of LNAPL releases into dry medium sand. M.Sc. Thesis, Queen's University, Kingston, Canada.

## A flexible, no lateral strain apparatus for clay liner-leachate testing

R.J. Mitchell

Queen's University, Kingston, Ont., Canada

**ABSTRACT:** An apparatus has been developed for use in a centrifuge to model a clay liner section which might be undergoing physical alteration by chemical or bacterial action. The in-flight lateral boundary condition applied to the model can be described as flexible, no lateral strain. Thus, should the liner section change volume due to physical alteration, the lateral stress would change in a manner similar to the changes that would occur in a prototype liner. The vertical stresses in the model, as with all centrifugal modelling, also simulate prototype stresses. Thus this flexible, no lateral strain ( $F\delta_0$ ) apparatus is capable of realistic clay liner-leachate compatibility modelling.

### INTRODUCTION

The true potential of physical modelling using a centrifuge is often found by the process of research development. Mitchell (1990) developed a confining cell for use in centrifuge testing of clay permeability and concluded that centrifuge permeability testing had advantages over bench permeability testing, mainly because tests could be carried out in quite short time periods (8 to 24 hours) under realistic prototype effective stress conditions.

Further development of the early test cell has produced the basic design for a flexible, no lateral strain ( $F\delta_0$ ) apparatus, as shown on Figure 1.

### FLEXIBLE, NO LATERAL STRAIN CELL

Two sizes of  $F\delta_0$  cells are currently in use at the Queen's University Centrifuge Modelling Laboratory. The first was a small (demonstration) cell that can accommodate a model clay liner thickness of 50 mm and is used in a 1.0 m diameter centrifuge

(Mitchell, 1993). The larger sized cell is 100 mm in diameter and can accommodate up to a 200 mm model thickness and is used in the 6.0 m diameter centrifuge at Queen's University. A typical modelling condition and a model pressure balance calculation are given in Table 1.

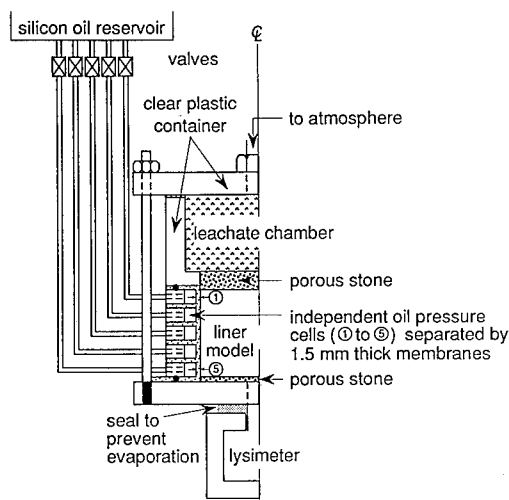


Fig. 1 Schematic of the flexible no lateral strain cell

Table 1 Typical Modelling Condition

<u>Scales</u>	<u>Model</u>	<u>Prototype</u>	<u>Unit weights</u>
linear	1/19 (N=19)	1	N/A
time	1	361	N/A
liner thickness	100mm	1.9m	19.5 kN/m <sup>3</sup>
sand cover	porous stone	0.6m	20.3 kN/m <sup>3</sup>
leachate height	80mm	1.52m	9.9 kN/m <sup>3</sup>
hydraulic gradient	1.8	1.8	N/A

Model pressure balance calculation (at 19 gravities,  $K_0 = 0.66$ )

Leachate pressure:  $U_L = 0.08$  (19)  $9.9 = 15.0$  kPa  
 effective stress at top of liner:  $\sigma'_v = 0.06$  (19)  $10.5 = 12.0$  kPa  
 horizontal stress at top of liner:  $K_0 \sigma'_v + U_L = 23.0$  kPa  
 height of oil cell valve above cell (1):  $23.0/19$  (9.4) = 0.13m  
 effective stress at base of liner:  $\sigma'_v = 27.0 + 0.08$  (19)  $19.5 = 64.0$  kPa  
 horizontal stress at base of liner:  $64.0$  (0.66) = 42.0 kPa  
 height of oil cell valve above cell (5):  $42.0/19$  (9.4) = 0.23m  
 Since elevation difference between cell (1) and cell (5) is 0.10m, no tilt is needed on the base of the silicon oil reservoir for  $\rho_{oil} = 0.96$ .

To fully understand the advantage of the  $F\delta_0$  cell, one must closely examine possible effects under alternative boundary conditions used in clay liner-leachate compatibility testing, being rigid boundaries and flexible (constant cell pressure) boundaries. It is clear that the flexible constant pressure boundary condition is not suitable for compatibility testing because volume shrinkage in the test specimen is easily mitigated by lateral consolidation. For this reason, many researchers recommend using a rigid boundary (see, for examples, Yanful et al., 1990; Budhu et al., 1991). Certainly a rigid boundary will not compensate for lateral shrinkage but close examination indicates that this boundary condition also has potential negative effects, as discussed below.

Installation of a field compacted specimen into a rigid walled apparatus is done by pushing a sharp cylindrical cutting tool through the sample, the cylinder then forming the rigid boundary. This technology suffers from all of the problems of field sampling (edge distortion, possible edge scour by downdrag on pebbles, etc.) plus one extra: if the cutting ring is pushed without the aid of a

mechanical guide system, slight rotation of the ring can cause sample disturbance and poor boundary contact. In addition, samples prepared by this method are usually relatively thin (compared with their diameter) and may not be representative of the bulk field compacted material. These potential negative effects are eliminated in the  $F\delta_0$  apparatus because the test specimen can be trimmed using a wire saw and the flexible membranes assures intimate boundary contact.

After a specimen is fitted into a rigid walled test cell, a vertical stress is applied in order to develop the lateral (sealing) stress against the rigid wall. Some one-dimensional consolidation will occur, with accompanying specimen distortion; more importantly, unless the specimen is relatively thin (with respect to diameter), boundary stress rotation and soil arching is likely to occur such that the applied vertical stress may not be uniform throughout the specimen and the lateral stress may not be representative of the field (prototype) conditions. These factors could affect the behaviour of the clay liner sample. In contrast the  $F\delta_0$  boundary condition allows the lateral confining pressure to develop with the

vertical effective stress as the specimen is accelerated in the centrifuge, reaching an in-flight equilibrium at the modelling speed. The vertical effective stress and leakage pressures are, of course, modelled after the prototype during centrifuge compatibility testing because effective stress has been shown to be a factor in determining whether clay shrinkage will, or will not, affect the observed permeability. (see for example, Fernandez and Quigley, 1991). These referenced permeability observations were not made under  $F\delta_0$  conditions and are, of course, subject to the potential problems outlined above.

The  $F\delta_0$  centrifuge model offers the significant advantage that effective stresses throughout the prototype liner are modelled so that, should clay shrinkage occur only under the lower effective stresses in the top half of the liner, for example, the resulting effects would be observed in the model. A number of separate tests, under varying effective stresses, would be needed to delineate this effect from normal bench testing.

#### PREPARATION AND MODELLING USING THE $F\delta_0$ APPARATUS

As noted earlier, a model liner may be trimmed from a large tube or block sample using a wire saw and guide. The model liner can be sufficiently thick to be representative of the field compacted liner. The model is installed inside the 1.5mm thick latex membranes of the  $F\delta_0$  apparatus and lateral confining pressures, equal to the calculated prototype horizontal effective stress at each cell level are applied. The valves to the silicon oil reservoir are then closed leaving saturated pressurized oil pressure cells surrounding the model. One or more porous stones are used to model a sand cover layer and the leachate is placed to any desired level in the leachate chamber. The "locked in" confining pressures affect a seal on the cylindrical model boundary while the cell is installed in the centrifuge. As the centrifuge is accelerated to the

design speed, the leachate pressure, effective stresses and oil cell sealing pressures all increase in proportion to the simulated gravity, reaching the prototype values calculated on Table 1 when the simulated gravity level is numerically equal to the model scale (i.e.  $a = Ng$ , where  $N$  is the linear scale factor).

A value of the insitu lateral at rest pressure coefficient,  $K_0$ , is needed to estimate the desired final in-flight pressures in the oil cell surrounding the model. Fortunately, the value of  $K_0$  for a clay soil is very sensitive to small strains and, thus, the no lateral strain condition, created by closing the valves to the silicon oil reservoir, is compatible with any reasonable assumption of  $K_0$ . Figure 2 shows how the oil cell pressures, as monitored by transducers, increase with simulated gravity level at the top and bottom of the liner model (levels 1 and 5 on Figure 1) during the initiation of a modelling sequence. The closed points are for cell 5 and the open points are for cell 1 on Figure 1. If transducer measurements had not indicated compatibility (final pressures about equal to estimated values), solenoid valves, controlled remotely through slip rings, could be closed to create the no lateral strain condition following initiation of the modelling sequence.

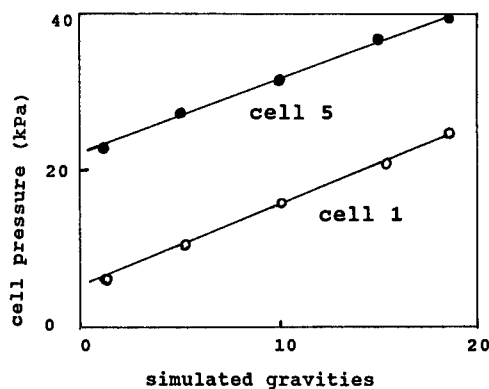


Fig. 2 Cell pressures developed in-flight

When in-flight with all valves closed, the pressures can change along the boundary of the model in sympathy with lateral strains in the model. If, for example, the top layer of the model tends to shrink laterally due to some chemical or bacterial action, there will be a reduction in the lateral confining pressure in the cell around this layer. If the shrinkage is sufficient, the effective lateral stress may approach zero (i.e. the lateral pressure is reduced close to the leachate pressure) and the permeability of the layer may increase. Indeed, it is possible for the sample to shrink away from the membrane or crack internally. Model distortion, due to the increased effective stress difference, may help to maintain some active level of lateral effective stress (less than  $K_0 \sigma'_v$ ) but this will develop in the model only if it would also develop in the prototype liner.

Should the permeability of the upper layer increase, the gradient across the rest of the liner would increase (as it would in the prototype) and the liner leakage would increase. The present  $F\delta_0$  apparatus has independent stress cells of 20 mm thickness. Thus, a 100 mm high model, as depicted on Figure 1 and Table 1, has five independent  $F\delta_0$  cells. This apparatus was constructed by modifying the segmented soil column described by Cooke and Mitchell (1991). A larger apparatus, with additional cells could, of course, be constructed if larger models are needed to ensure that the compaction of the prototype liner is well represented.

The present model is at a scale of 19 and operated, as noted on Table 1, at an acceleration equivalent to 19 gravities. This scale is selected because the time scale is  $(19)^2$  such that one day of centrifugation is equivalent to one year of prototype operation. The lysimeter is removed daily and the leachate level is adjusted to the initial levels (i.e. if 50 cc of fluid is obtained in the lysimeter, 50 cc of leachate is added to the leachate container. The Queen's University 6m diameter centrifuge is a user designed and built (in

1984/5) facility costing \$60K (Can.) and is allowed to operate continuously for days on such projects. To date, only permeability testing has been carried out in the larger (100 mm high) models and some permeability data, collected over several days is shown on Figure 3.

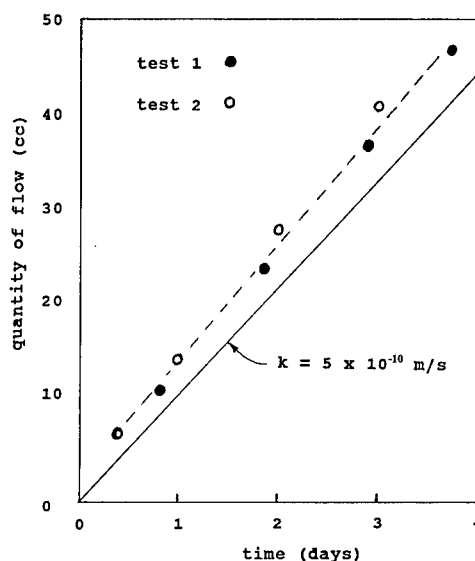


Fig. 3 Permeability test results

Compatibility modelling in a much smaller  $F\delta_0$  cell used in a 1.0 m diameter centrifuge, reported by Mitchell (1993), indicates that some household cleaning compounds may cause increased leakage in compacted clay liners. The  $F\delta_0$  apparatus, described in this paper, is currently being used in a 6.0 m diameter centrifuge to collaborate and extend that data.

The  $F\delta_0$  apparatus is also useful for investigating diffusive contaminant transport phenomenon in clay liners. Although diffusion is not gravity dependent and, hence, the rate of diffusion does not increase under centrifugation, the results of advective-diffusive modelling can be projected to predict prototype behaviour. Diffusive concentrations,  $C$ , are given, in the simple case of constant diffusion rate,  $D^*$ , as  $\delta C / \delta t = D^* \delta^2 C / \delta z^2$ , where  $t$  = time and  $z$  = distance. Thus the

diffusion time in a model is related to the diffusion time in the prototype as  $t_m = t_p (Z_m^2/Z_p^2) = 1/L^2 = 1/N^2$ , where  $L$  is the linear scaling factor which is equal to  $N$ , the gravitational scaling factor. This is the same time scaling relationship that is known to apply to advective concentrations in contaminant transport (see, for example, Cooke and Mitchell, 1991). In other words, advective and diffusive contaminant transport are compatibly modelled in a centrifuge.

The main reason to use a centrifuge for studying diffusive transport, then, is to maintain prototype effective stresses during the diffusion process. There, is no evidence, to date, that diffusion is stress dependent but it is known that diffusion rates are dependent on volumetric water content and this is influenced by the effective stress in a clay liner. The  $F\delta_0$  apparatus is, as noted earlier, designed to model the liner effective stresses under contaminant transport conditions.

Contaminant concentrations through a model liner following centrifugation with a known leachate can be determined by analyses of pore water extracted from clay layers, trimmed from the model liner after removing individual  $F\delta_0$  cells. By comparing results from models done at the same scale but using different leachate heads, the advective and diffusive components of transport can be differentiated. By comparing data from similar models at different scales (different  $g$  levels), the effect if any, of sorption can be identified. The  $F\delta_0$  apparatus will be used for these types of studies in the future.

## CONCLUSIONS

Centrifuge testing has led to the development of a flexible, no lateral strain ( $F\delta_0$ ) cell which has been further refined to create the  $F\delta_0$  apparatus described in this paper. The  $F\delta_0$  apparatus has been shown to reproduce, in one day, compacted clay permeability values

that took several days to establish in falling head bench permeability tests. The present  $F\delta_0$  apparatus is made up of five separate and relatively independent  $F\delta_0$  cells and is currently being used to model clay liner-leachate compatibility in a 6m diameter modelling centrifuge.

## ACKNOWLEDGEMENTS

The work reported in this paper was carried out under financial support from the National Sciences and Engineering Research Council of Canada and the Ontario Ministry of the Environment.

## REFERENCES

- Budhu, M., Giese, R.F., Campbell, G. and Baumgrass, L. 1991. The Permeability of Soils with Organic Liquids. *Can. Geotech. J.* 28:140-147.
- Cooke, A.B. and Mitchell, R.J. 1991. Physical Modelling of a Dissolved Contaminant in Unsaturated Sand. *Canadian Geotech. J.* 28:6:829-833.
- Fernandez, F. and Quigley, R.M. 1991. Controlling the Destructive Effects of Clay-Organic Liquid Interactions by Application of Effective Stress. *Can. Geotech. J.* 28:388-389.
- Mitchell, R.J. 1990. Clay Liner Leakage Evaluation. *Proc. 43<sup>rd</sup>. Canadian Geotech. Conf., Quebec.* Vol. 1, 365-369.
- Mitchell, R.J. 1993. A Novel Method for Clay Liner Compatibility Testing. *46<sup>th</sup> Canadian Geotech. Conf., Saskatoon.* In Press.
- Yanful, E.K., Haug, M.D. and Wong, L.C. 1991. The Impact of Synthetic Leachate on the Hydraulic Conductivity of a Smectite till Underlying a Landfill near Saskatoon, Saskatchewan. *Can. Geotech. J.* 27:507-519.



## A study of contaminant transport involving density driven flow and hydrodynamic clean up

E.E. Hellawell & C. Savvidou  
*University of Cambridge, UK*

**ABSTRACT:** This paper describes an experiment performed on the Cambridge Geotechnical Centrifuge investigating the migration of a contaminant plume under the influence of density gradients. The conceptual prototype was a landfill leaking a non-sorbing dense pollutant into a homogeneous silt layer. The formation of the plume was followed by clean up using hydrodynamic techniques. The concentration of pollutant throughout the soil was monitored by miniature insitu resistivity probes.

The work demonstrates the effectiveness of the geotechnical centrifuge in modelling transport processes involving dense pollutants. This paper presents the theory governing the transport of a dense pollutant through soil, outlines the relevant scaling laws, describes a typical centrifuge test and compares the results with a numerical prediction.

### 1. INTRODUCTION

Contamination of groundwater is an issue of major concern in residential areas in the vicinity of landfills and waste disposal repositories. The extent of contamination and the mechanisms responsible for the transportation of contaminants in the underlying groundwater system is a central issue in cases where municipal water supplies depend on the utilisation of the groundwater resources.

It has recently become apparent that there is a lack of physical observations of pollutant behaviour in soils. This information is vital to evaluate existing theoretical models and develop improved conceptual models of transport processes. The high costs, large time scales and lack of control over the boundary conditions have prevented the development of field scale experiments. Column tests are of limited use and difficult to apply to full scale problems. Thus researchers have recently come to recognise that a geotechnical centrifuge can provide a powerful testing tool for modelling the transport of contaminants in soils ( Hensley 1989, Cooke and Mitchell 1991, Hensley and Savvidou 1993, Hellawell et al 1993).

The research presented in this paper investigated the transport of a non-sorbing dense pollutant from a landfill into a homogeneous saturated silt layer and the subsequent hydrodynamic clean up.

The results of the tests were compared with theoretical predictions from the finite difference computer code HST3D ( Kipp 1987).

### 2. THEORY

Contaminant transport in porous media can be described by the conservation of fluid mass and contaminant mass in the macroscopic continuum. A comprehensive review of the governing equations can be found in Hensley and Savvidou 1993. The equations are linked through the coupling of velocity, density and viscosity terms and their dependence on fluid pressure and contaminant mass fractions. Fluid density is assumed to be a linear function of pressure and contaminant concentration over the ranges of these parameters encountered in this paper. Thus

$$\rho(p, w) = \rho_o + \rho_o \beta_p (p - p_o) + \rho_o \beta_w (w - w_o) \quad [1]$$

where  $\rho_0$  is the density at the reference pressure  $p_0$  and mass fraction  $w_0$ ,  $\beta_p$  is the fluid compressibility and  $\beta_w$  is the slope of the fluid density as a function of mass fraction, divided by the reference fluid density.

Darcy's law in one-dimensional form describes fluid motion as the sum of two convective terms:

a) piezometric head differences and b) density gradients causing free convection.

$$u_z = -\frac{k}{n\mu} \rho_0 g \frac{\partial}{\partial z} \left( \frac{p}{\rho_0 g} + z \right) - \frac{kg(\rho - \rho_0)}{n\mu} \quad [2]$$

The vertical direction of fluid motion due to free convection depends on the arrangement of the different density fluids.

The dominant convective mechanism is determined by the ratio of the forced and free convection terms (Bear 1972).

$$R = \frac{|\Delta\rho/\rho_0|}{|\Delta\phi_0/L|} \quad [3]$$

where  $\Delta\rho = \rho - \rho_0$ ,  $\phi_0 = (p/\rho_0 g + z)$  and  $L$  is the characteristic macroscopic length of the system.

Stable equilibrium of the system may be obtained even if the density gradient increases vertically upwards due to the damping effects of viscous resistance and diffusivity. This occurs provided the density gradient has not exceeded a critical value. The 'solute' Rayleigh number derived by Wooding (1959) determines the ratio between the driving buoyancy force and two resistive processes.

$$R_{as} = \frac{\frac{\partial w}{\partial z} g k H^2 \beta_w}{D_a^* \nu} \quad [4]$$

where  $\partial w/\partial z$  is the vertical concentration gradient at any given  $z$ ,  $D_a^*$  is the effective diffusion coefficient,  $\nu$  is the kinematic viscosity of the fluid and  $H$  is a typical linear dimension of the problem. At a critical value of the solute Rayleigh number buoyancy forces dominate and contaminant migration will occur. (Wooding 1959, Neild 1967)

### 3. CENTRIFUGE MODELLING

The simulation of identical effective stress states in scaled centrifuge model and equivalent prototype ensures the modelling of soil properties including hydraulic conductivity. Centrifuge modelling is particularly applicable in replicating the physical transport of dense pollutants due to gravitational gradients. The increased acceleration field is essential to correctly study such phenomena in reduced scale models (Savvidou and Hensley 1992, 1993).

#### 3.1 Scaling Laws

The correct scaling of physical parameters relating to contaminant transport is essential for similitude of these processes in the centrifuge model and prototype. Dimensional analysis (Laut 1975, Arulanandan et al 1988) and inspectoral techniques (Bachmat 1967, Hensley 1988) have been used to derive the general scaling laws for centrifuge modelling of contaminant migration. The relevant laws are

$$t_p = n^2 t_m \quad [5]$$

$$u_p = \frac{1}{n} u_m$$

$$c_p = c_m$$

where  $n$  is the scaling factor,  $u$  is the pore fluid velocity ( $L/T$ ),  $t$  is the time factor ( $T$ ),  $c$  is the concentration of pollutant ( $M/L^3$ ) and  $m$  and  $p$  symbolise the model and prototype respectively.

These laws assume that the dispersive processes are identical in model and prototype, and the adsorption of contaminant obeys a rapid linear equilibrium model. These assumptions are applicable to this study where dispersion does not dominate and a non-sorbing contaminant is used.

The same pollutant was used in the model and prototype, ensuring that  $\rho_m = \rho_p$  and  $\mu_m = \mu_p$ . For density driven flow it is also important to consider the replication of potential hydraulic instability. Hensley and Savvidou (1993) recently showed that for centrifuge models

$$R_{asp} = R_{asm} \quad [6]$$

which reinforces the argument for the need for the accelerated gravitational field in a reduced scale model.

### 3.2 Centrifuge test

The prototype considered was a 10m wide landfill leaking dense pollutant through its base into a homogeneous soil layer (figure 1). The level of fluid in the landfill was constant at the same height as the water table in the surrounding soil. Two sampling wells were positioned 28m apart on either side of the landfill.

The soil used was 180 grade silica flour mixed under vacuum to 40% moisture content. 1M sodium chloride solution was used as the model pollutant. Miniature 4 pin resistivity probes designed and manufactured at CUED monitored the progress of the contaminant plume through the soil. These were calibrated in the laboratory in soils samples prepared in the similar manner

to the tests containing known concentrations of sodium chloride. The accuracy of the resistivity measurement at these high saline concentrations was achieved by increasing the supply current and the signal amplification.

Thermocouples were attached to the resistivity probes to record variations of the soil temperature. Other instrumentation included Druck miniature pore water pressure transducers buried in the model and a linear variable differential transformer (LVDT) recording the settlement of the landfill.

The wells were constructed from moulded vyon and filled with coarse sand. They were supplied with fresh water from two standpipes attached to the package. Figure 2 illustrates the service arrangements for the test. Initially air valve B was shut and thus the water level in the wells and package was constant. A wave gauge determined the fluid depth in the landfill. A control loop from the gauge signal operated a peristaltic pump and solenoid valve which controlled the contaminant supply from an overhead reservoir. Thus constant fluid head in the landfill was maintained automatically.

Initially the centrifuge was started with a small amount of contaminant in the landfill. The speed was increased in stages to 100 gravities. The control loop operating the feed of pollutant to the landfill was then switched on and the landfill filled to the set height with contaminant. The sample consolidated under self weight and after about 15 minutes the pore water pressure had reached equilibrium.

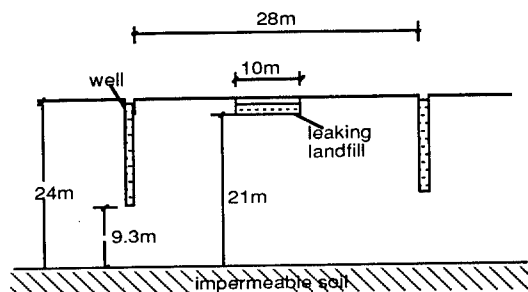


Figure 1 - Prototype of centrifuge test

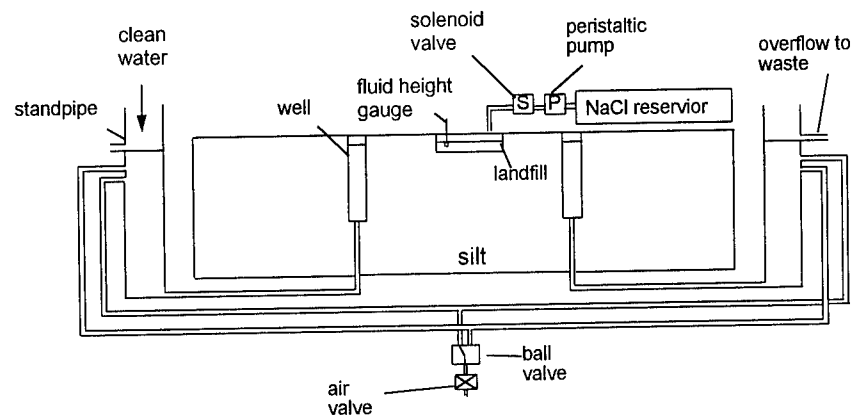


Figure 2 - Service arrangements for the centrifuge tests

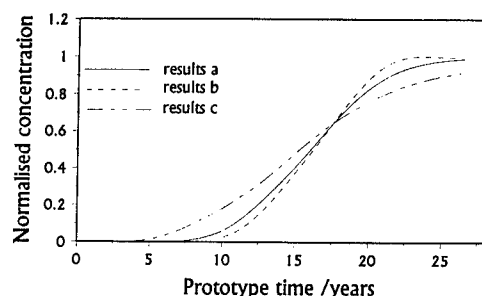


Figure 3 - Comparison of finite difference solutions, a) forward difference in time and backward difference in space, b) centre difference in time and space, c) centre difference in time and space with  $\alpha_L = 0.326\text{m}$

Table I - parametric values for analysis

Parameter Description	Value
Porous medium porosity	0.45
Hydraulic conductivity	$2.3 \times 10^{-7} \text{ m/s}$
Longitudinal dispersivity	$3.26 \times 10^{-4} \text{ m}$
Transverse dispersivity	$3.26 \times 10^{-5} \text{ m}$
$c_{\text{well}}$ ( 0-10.5 yrs)	0.6675 Mols
$c_{\text{well}}$ ( 10.5-30 yrs)	1.0 Mols
$\rho$ pore fluid	998.62 Kg/m <sup>3</sup>
$\rho$ contaminant (1M)	1041.9 Kg/m <sup>3</sup>
$\mu$ pore fluid	$1.001 \times 10^{-3} \text{ Kg/m}$
$\mu$ contaminant (1M)	$1.087 \times 10^{-3} \text{ Kg/m}$
$D_d^*$	$7.3 \times 10^{-10} \text{ m}^2/\text{s}$
$R_{as}$ (1-10.5)yrs)	167.5
$R_{as}$ (10.5-30yrs)	250.8
Isothermal temperature	18°C
<b>Clean up</b>	
Hydraulic gradient ( 0 -0.68yrs)	0.021
(0.68 - 5.7yrs)	0.125

Once the plume was created, valve B was opened and the clean up phase begun. The plumbing of alternate high and low overflows caused a hydraulic gradient to be established between the two wells. Ball valve A enabled flow reversal during clean up.

The test was performed at 100g with plume creation lasting, at model time, approximately 26.5 hours followed by 5 hours of clean up. The

instrumentation was monitored throughout the test recording the development of the contaminant plume. After the end of the test the centrifuge was stopped and the model inspected. The soil was then X-rayed and finally excavated to reveal the position of each probe.

#### 4. COMPARISON BETWEEN CENTRIFUGE TEST DATA AND THEORETICAL PREDICTIONS

The results from the centrifuge test were compared with theoretical predictions using computer code HST3D (Heat and Solute Transport in 3 Dimensions). The program uses finite difference techniques and can be adapted to consider isothermal density driven flow in 2 dimensions (Kipp 1989). In this form the program solves the saturated groundwater equation ( formed from the conservation of fluid mass and Darcy's law ) and the solute transport equation. The equations are linked through velocity density and viscosity coupling terms. Table I summarises the input parameters which were determined by laboratory tests. Prototype test values are considered and all results are presented in prototype test times.

The very low dispersivities representative for the homogeneous silty soil used in the centrifuge test caused difficulties in obtaining an accurate numerical solution. Trials using various differencing techniques, larger dispersivities and mesh refinements were performed in an effort to eliminate instabilities and numerical dispersion errors. Figure 3 presents a comparison of solutions for the movement of a concentration front at a point below the landfill. It was concluded that a solution using forward differencing in time with backward differencing in space with a 55x45 node mesh minimised the numerical dispersion and produced the optimum results. All theoretical solutions presented here have been produced in this manner.

The above table includes values for the solute Rayleigh numbers, which exceed the critical value of 27.1 suggested by Neild (1968) for porous/impermeable boundary conditions. Thus buoyancy forces dominated resulting in density driven contaminant migration.

At the start of the test the concentration of contaminant in the landfill varied as the short

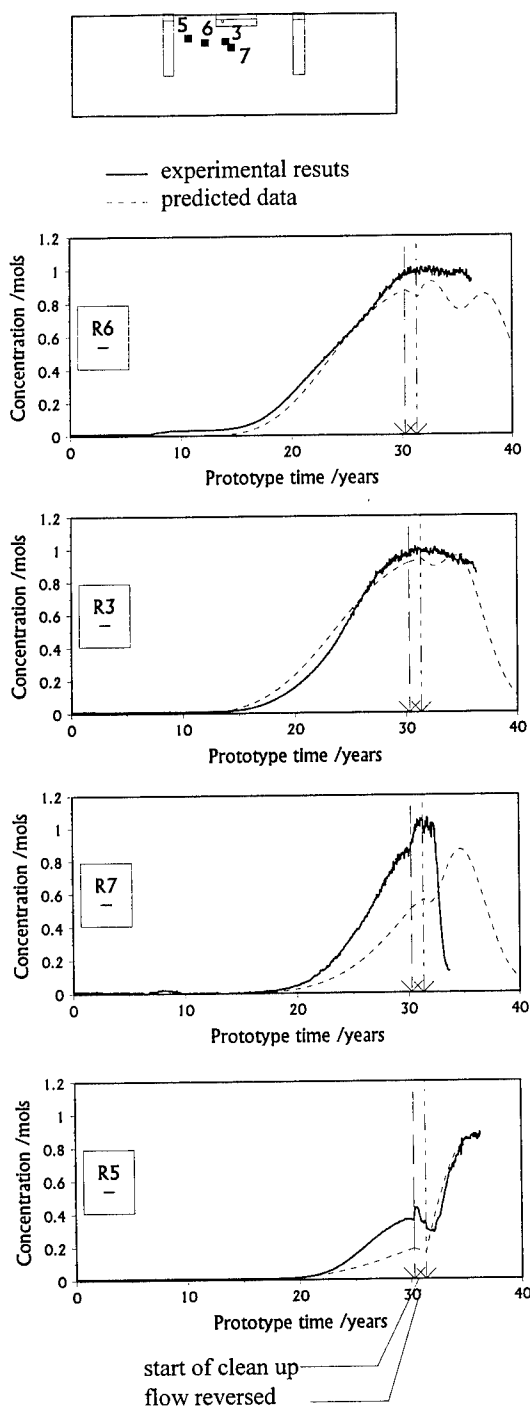


Figure 4 - Comparison of experimental and predicted results for the movement of the contaminant front at various positions

period of consolidation caused dilution of the solute. Thus the program was run in two stages with the landfill contaminant concentration set to the average value for that time period. HST3D considers a rigid porous matrix and therefore does not take into account consolidation. However this is fairly insignificant in the silt model where equilibrium was achieved shortly after the start of the test.

A comparison between the theoretical and measured contaminant front migration and later clean up at four positions in the soil model is shown in figure 4. Probes 3 and 6 lie at almost the same depth, yet the latter detected the plume first. This can be explained by a contour plot showing the predicted progress of the plume after 30 years (figure 5). The contaminant travels further at the edges of the landfill than beneath its centre. The plume is also predicted to show greater dispersion at the edges of the landfill where the contour spacing increases. A comparison of concentration profiles measured at the probes shows good agreement with this prediction.

The clean up phase was started about 26.5 hours (30 years of prototype time) after the initial leakage of dense pollutant. A hydraulic gradient was initially imposed to flush the plume towards well 2. However a blockage occurred in a standpipe overflow, thus the flow was reversed after 0.6 hours. The contaminant plume was then flushed towards well 1 for the remaining 5 hours of the test. All stages followed in the test were considered in the input to the numerical program.

The movement of the plume during clean up is shown by the effects of the flushing on probes 7, 3 and 5. At the end of the test probe 3 is beginning to detect the clean front, whereas high concentrations of contaminant are being detected at probe 5. Thus after 5.7 years of pumping, half the site is clean. Probe 7 showed a larger variation between the predicted and measured values. This is probably due to a lateral error in the positioning of the probe.

Reasonable agreement is obtained between the theoretical and measured values during the plume creation and clean up phases. The slight discrepancy in the slopes of the curves can be attributed to small numerical dispersion.

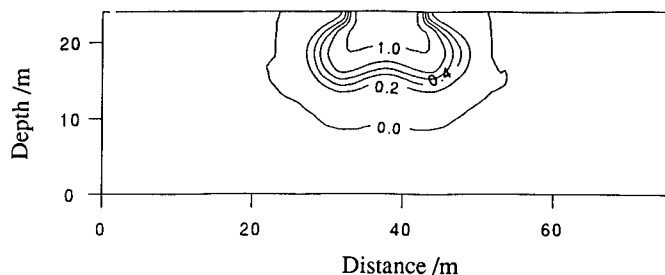


Figure 5 - Predicted progress of the contaminant plume after 30 years

## 5. CONCLUSIONS

The geotechnical centrifuge was used for modelling the migration of dense pollutants from a landfill. The accelerated gravity field enables correct scaling of density gradients in the reduced scale model.

The solute Rayleigh number implied that density forces were dominant over any viscous forces. Hydraulic instability occurred between the pollutant and saturated porous media resulting in density driven flow.

The hydrodynamic clean up of a dense contaminant plume was demonstrated. Although a high hydraulic gradient was imposed between the wells, at prototype time of 5 years after pumping only half the site was clean. The results highlight that hydrodynamic clean up is not satisfactory except in highly permeable soils.

Reasonable agreement was obtained between the theoretical model HST3D predictions and the centrifuge test results for both the plume development and clean up processes.

## 6. REFERENCES

- Arulanandan, K., Thompson, P.Y., Kutter, B.L., Meegoda, N.J., Muraleetharan, K.K. and Yogachandran, C., 1988 Centrifuge modeling of transport processes for pollutants in soils, *Journal of Geotechnical Engineering, ASCE*, 114, (2), February, 185-205
- Bachmat, Y., 1967 on the similitude of dispersion phenomena in homogeneous and isotropic porous media, *Water Res Res.* 3(4), 1079-1083
- Hellawell, E. E., Savvidou C. and Booker J. R., 1993 Modelling contaminated land reclamation, submitted for publication in *Soils and Foundations*, Japan and CUED report TR 250
- Hensley, P.J., 1988 Geotechnical centrifuge modelling of hazardous waste migration, in *Land Disposal of Hazardous Waste: Engineering and Environmental Issues*, Gronow, J. R., Schofield, A. N. and Jain, R. K. Eds. Ellis Horwood Ltd., Chichester, 139-151
- Hensley, P. J., Savvidou, C. 1992 Modelling pollutant transport in soils, *Australian Geomechanics*, 22 (July 1992)
- Hensley, P.J., Savvidou, C. 1993 Modelling coupled heat and contaminant transport in groundwater, *Int J. for Num. and Analyt. Methods in Geomechanics*, vol. 7, 493-527
- Laut, P., 1975 Application of centrifuge model tests in connexion with studies of flow patterns of contaminated water in soil structures, *Geotechnique*, 25(2), 401-407
- Kipp, K. L., 1987, HST3D: A computer code for simulation of heat and solute transport in three-dimensional groundwater flow systems, U.S. Geological Survey, Water-Resources Investigations Report 86-4095
- Neild, D. A., 1968, Onset of thermohaline convection in a porous medium, *Water Resources Res.*, 4, 553
- Wooding, R. A., 1959, The stability of a viscous liquid in a vertical tube containing porous material, *Proc. of the Royal Soc. of London, Series A*, Vol. 252, 120-134

## Experimental aspects of modelling of migration phenomena

H.P.Villar

*Universidade de Pernambuco, Recife, Brazil (Formerly: Department of Engineering, University of Manchester, UK)*

C.M.Merrifield & W.H.Craig

*Department of Engineering, University of Manchester, UK*

**ABSTRACT** - The study of solute migration in the centrifuge requires the maintenance of steady-state flow conditions over periods exceeding eight hours. The adoption of established methods and commercially available equipment in a unique way to provide and monitor water flow is described along with the use of miniature robust instrumentation controlled by a data acquisition system designed specifically for these studies. Results are presented which suggest discrepancies between measured and deduced values of flow are less than 5%.

### 1 INTRODUCTION

A recent application of centrifuge modelling is the study of pollutant migration through soil columns (Gronow et al., 1988; Arulanandan et al., 1988; Hensley, 1989; Cooke and Mitchell). The advantage of using the centrifuge lies in the acceleration of the processes in the model associated with fluid flow allowing the results thus obtained to be compared, using well-established scaling laws, with the same processes which occur over a much longer time period in a field-scale prototype.

The mass transport of solute in a porous medium is influenced by processes such as advection, molecular diffusion, hydrodynamic dispersion and adsorption. Diffusion is a spreading agent at the molecular level caused by the random thermal motion of the solute molecules and thus independent of the movement of the solvent, whilst dispersion, on the other hand, is directly related to the mass transport of the solute and a consequence mainly of the distribution of velocities of the solvent in the flow channels and of the differential flow paths around the grains. Adsorption is a phenomenon which may be of physical or chemical origin and corresponds to an interaction between a molecule of the solute and the reactive components of the porous medium, such as clay particles and organic matter, with the apparent result that the movement of the solute is retarded relative to the solvent.

Due to the dominance of one or more of the above processes within a particular environment, the

migration of solutes in porous media is complex even in uniform materials studied under laboratory conditions. The results from the modelling of migration patterns should, therefore, be seen as approximations (Smettem, 1986). The natural complexity of actual soils makes the analysis of migration phenomena an even more difficult task. In order to study the influence of diffusion, dispersion and adsorption in the migration patterns of different solutes in porous media it is essential to establish and maintain well-controlled experimental conditions. As one of the main spreading agents, hydrodynamic dispersion may dominate and therefore mask other processes. It is not only a consequence of the movement of the solvent, but its effect is dependent on the migration velocity (Bear, 1972; Fried, 1975). The experimental methods adopted for these studies should therefore include the following elements:-

- a) The maintenance in the model of a uniform downward flow of constant seepage velocity for the duration of each experiment.
- b) The precise monitoring of the movement of the solute in the model regardless of changes in environmental parameters such as temperature and soil solution pH.
- c) The estimation of the solvent velocity from a source other than through an assessment based on the migration rate of the solute.

Well-controlled experiments for the study of 2-D migration of selected solutes through a soil column conforming to the above criteria were performed

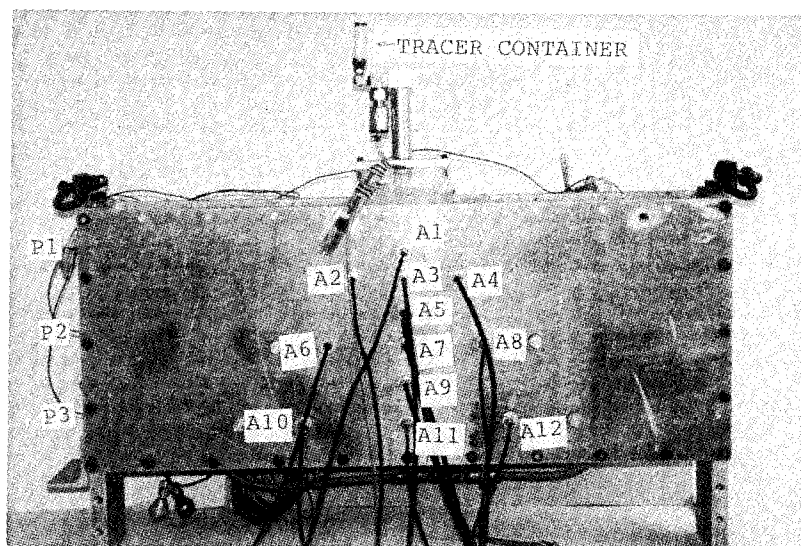


Fig. 1. Model container showing location of Geiger tubes (A1-A12) and porewater pressure transducers (P1-P3)

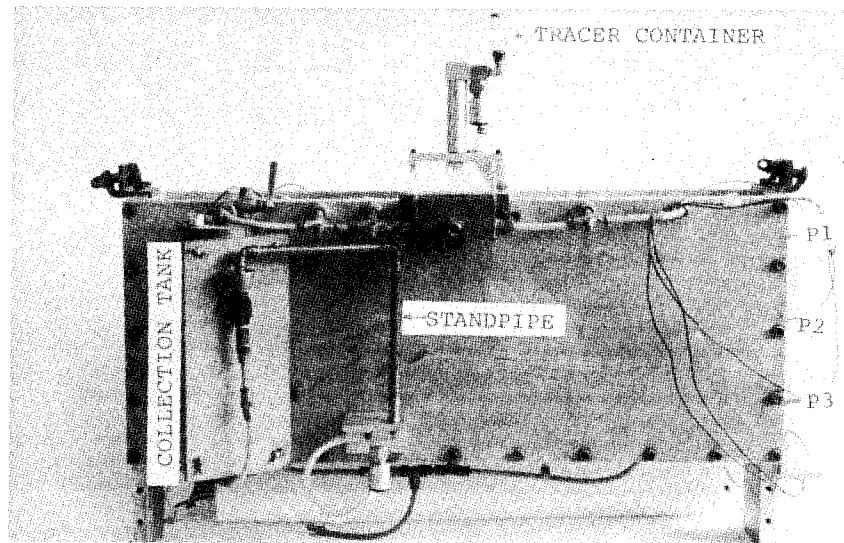


Fig. 2. Model container showing outflow arrangement



adopting relatively simple and inexpensive techniques.

## 2 EXPERIMENTAL ASPECTS

### 2.1 Description of the soil model

A soil model was prepared in an open aluminium box (see Fig. 1 and 2) 950mm long, 150mm wide and 325mm deep. Three holes in the base, connected through a remotely-operated valve to a single standpipe, shown in Fig. 2, allowed drainage of the model. The height of the standpipe dictated the hydraulic gradient through the model. In order to ensure vertical flow through the model the pore fluid drained through a 25mm thick layer of pea gravel at the base separated from the soil by a sheet of geofabric.

An instantaneous failure of a repository was modelled by releasing a volume of radioactive tracer into the soil bed via a rectangular perspex box with a perforated base.

The hydraulic head needed to generate flow at a constant rate through the model was obtained by supplying water through a weir adjacent to the model that maintained the water level at 15mm above the surface of the soil (see Fig. 3). A constant flow of distilled water was supplied to the weir from a source outside the centrifuge via a rotating open topped ring main mounted concentric with the axis of the beam and immediately above it. At a radius of 650mm this ring main was subjected to approximately 20g during tests run at 100g, sufficient to force water through a 9mm diameter outlet via a pipe to the weir. (See Fig. 4)

The assessment of the retardation effect by adsorption reactions required steady-state flow conditions prior to the injection of the solute. This was verified by three Druck miniature porewater pressure transducers inserted into the soil bed (see Figs. 1 & 2). The water pressure measured by the transducers was compared throughout the experiment with that which would have been expected for steady-state flow, based on the hydraulic gradient.

### 2.2 Solute monitoring

A method for precise monitoring of the solute movement was an essential requirement for this project. Characterised as follows, the method chosen was:-

i) sensitive enough to allow the use of a wide range of solute concentrations,

ii) immune from temperature fluctuations and to changes in the chemical properties of the solute or the solvent,

iii) based on small sensors capable of withstanding the high pressure associated with multigravity modelling (650kPa at 100g).

The method involved the use of miniature geiger tubes to monitor the passage of radioactive tracers. The presence of short-lived tracers was determined at concentrations under  $1 \times 10^{-6}$ ppm. The readings of emitted radiation were not affected by any physical or chemical agent, and sturdy Geiger tubes 12mm long and 5mm in diameter were commercially available. Tracers were obtained with short half-lives such that the model could be reused, even in the case of tracer retention, a few days after a previous experiment.

The tracer, usually 20MBq of a water-soluble salt or organic substance in about 8ml of distilled water, was released into the model via a remotely operated pneumatic valve from a perspex vial fitted above the box simulating the repository.

The data acquisition was rationalised by the incorporation of a specially designed on-board processor controlled by an external computer. Data were collected simultaneously from the twelve Geiger tubes over a period of one minute at predetermined intervals, processed and stored in a buffer prior to transmission to the controlling computer via a RS232 link. Further processing to allow for radioactive decay of the tracer during the test, manipulation of data and display was then undertaken.

### 2.3 Determination of the outflow rate

Distilled water was supplied to the ring main (see Fig. 4) by means of an electric pump the output of which was accurately controlled and used as an indicator to establish the water flow rate through the model. This was considered inaccurate, however, due to the inevitable water loss at the weir.

As the position of each Geiger tube was known, the time required for the radioactive plume to travel between contiguous tubes was used to determine the migration velocity of the tracer. Under non-sorptive conditions, this velocity was also the seepage velocity of the distilled water. The occurrence of retardation, however, could only be evaluated if an independent method to determine this flow rate was available.

Water emanating from the model through the outlet standpipe was directed to a collection tank.

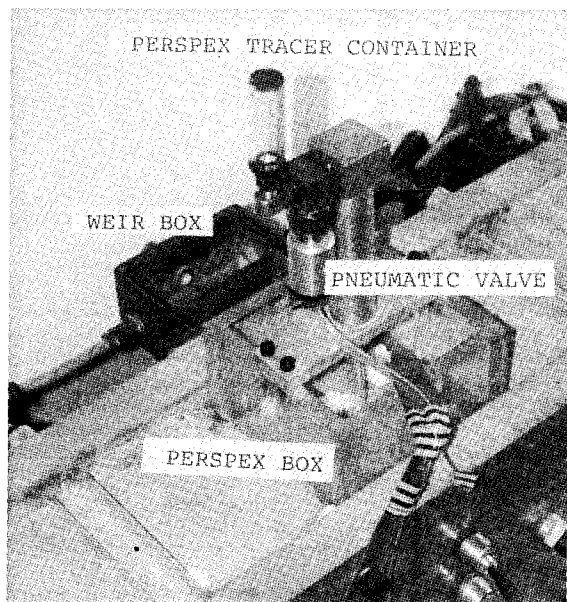


Fig. 3. Tracer dispensing mechanism and model of repository

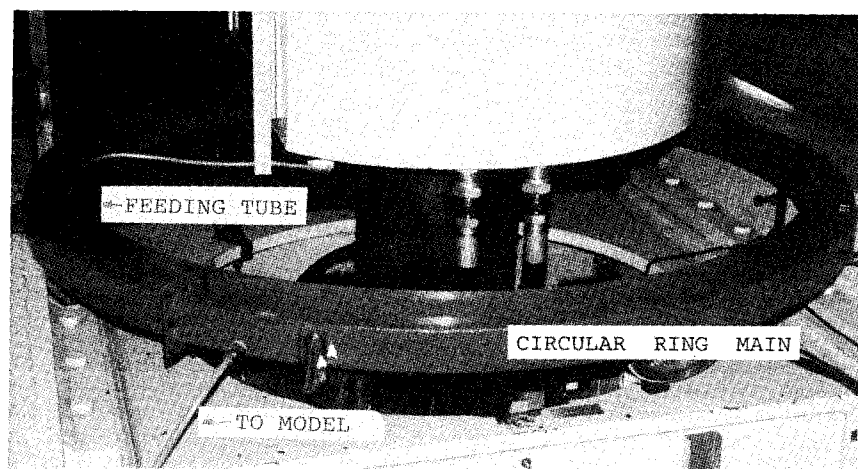


Fig. 4. Detail of ring main

The outflow rate was estimated from the rate of water pressure increase monitored within the tank. Since it was unable to accommodate the volume of water used throughout the experiment it was necessary to empty the tank periodically by displacing the water with compressed air.

### 3 RESULTS

The application of the system described above is shown for an experiment in which a soil bed of fine sand and illite clay was used to study the migration behaviour of iodine as NaI. As Iodine (I<sup>-</sup>) is among the most mobile ions in soils, only limited adsorption was expected. A solution of Na<sup>123</sup>I was used under a centrifugal acceleration of 50g.

The excess heads measured by the Druck transducers (P1, P2 and P3) within the model are shown in Fig. 5. Time  $t=0$  corresponds to the moment the tracer was released to the soil, at which time steady-state flow conditions had already been achieved. The excess heads remained constant until the test was stopped at  $t=230$ min. The height of the outlet standpipe was set to give a hydraulic gradient across the model of 0.33. This compared well with the hydraulic gradient deduced from the transducer measurements of 0.32. Fig. 5 also shows the change in pressure and thus water level in the collection tank. The uniform gradients of the pressure measurement against time suggest that the flow rate was generally constant at 65ml/min throughout the experiment. The steep gradient of pressure reduction at the end of each measuring cycle represents the evacuation of the tank.

The response of the centre-line Geiger tubes is displayed in Fig. 6. The time required for the tracer front to reach each detector may be estimated from

the location of the peak count rate in each case. On this basis the solute migration velocity was calculated as 1.4mm/min. Previous tests indicated the porosity of the soil bed to be 32%. On the assumption that the bulk of the tracer was not being retarded a flow rate of 65ml/min was estimated. This agreed well with the flow rate estimate based on the collection of the water. Tests with Iodine and another conservative tracer, Technetium, showed that measurement of the flow rate by the two methods generally agreed within 5%. This suggests that the assessment of retardation, whenever it occurs, may be possible.

Since the estimated flow rates for the solute and the water were found to be very similar it can be assumed that the solute was travelling with the same velocity as the water. Inspection of the count rates at 230 minutes in Fig. 6 suggests that some of the solute was retarded by the soil mass. This mechanism and its effect on irreversible sorption is the subject of further study.

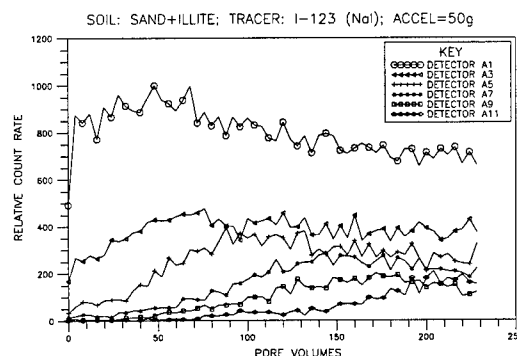


Fig. 6. Evolution of centreline count rates

### 4 CONCLUSIONS

The following conclusions are drawn:-

1. The methods proposed are shown to be appropriate for the multigravity study of solute migration patterns.
2. Control may be exercised over the flow regime during the experiment, and changes in conditions which may influence the processes under study are verified in flight.
3. The method adopted for dispensing water into the model allows the introduction of changes in the soil solution through the use of substances dissolved in the water.

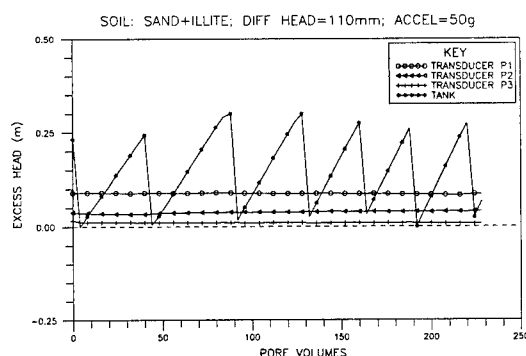


Fig. 5. Excess heads relative to outlet and water pressure in tank

4. The use of radioactive tracers has proved to be an effective and flexible means to monitor migration processes, as short-lived radioactive isotopes of many elements of concern for environmental studies are available, and the possibility of reuse of the model allows comparison of the behaviour of different solutes whilst maintaining the same soil bed conditions.

#### ACKNOWLEDGEMENT

The support given to Dr. Villar by Brazil's CIPq is gratefully acknowledged.

#### REFERENCES

- Arulanandan, K. P. Thompson, B. Kutter, J. Mergoda, K. Muraleetharan and C. Yogachandran 1988. Centrifuge modelling of transport processes for pollutants in soils, *J Geot. Eng, ASCE* 114:2, p. 185
- Bear, J. 1972. *Dynamics of Fluids in Porous Media*. American Elsevier
- Cooke, A.B. and R.J. Mitchell 1991. Evaluation of contaminant transport in partially saturated soils, *Proc. Int. Confr. Centrifuge 1991*, Boulder, Co., 503-508.
- Fried, J. 1975. *Groundwater Pollution*. Elsevier, Amsterdam
- Gronow, J., R. Edwards and A. Schofield 1988. *Drum Centrifuge Study of the Transport of Leachate from Landfill Sites*. Report CUED D-Soils/TR214, Cambridge University
- Hensley, P. 1989. *Geotechnical Centrifuge modelling of Hazardous Waste Migration*. PhD thesis, Cambridge University
- Smettem, K. 1986. Solute movement in soils. in *Solute Processes*, p.141, S. Trudgill (ed.), Wiley, New York, p.141

## Studies on groundwater transport of radioactive waste

H.P.Villar

Universidade de Pernambuco, Recife, Brazil (Formerly: Department of Engineering, University of Manchester, UK)

C.M.Merrifield

Department of Engineering, University of Manchester, UK

**ABSTRACT:** A novel approach is presented to study the problem of radioactive pollutant behaviour in soils following groundwater intrusion to a repository through a two-dimensional soil model in the geotechnical centrifuge. The radiotracers ( $^{99m}\text{Tc}$  and  $^{90}\text{Y}$ ) were used due to their similarity with the waste elements  $^{99}\text{Tc}$  and  $^{90}\text{Y}$  as a daughter of  $^{90}\text{Sr}$  and the ease of their detection, even when present in minute quantities. Three different soil beds were used and two acceleration levels, 50 and 100 gravities, were imposed on the models. The effects of dispersion and adsorption on solute migration were assessed. The movement of the tracers was monitored by Geiger tubes in the soil. Conclusions are drawn regarding the feasibility of the methods proposed for the study of pollutant migration.

### 1 INTRODUCTION

Growing awareness of environmental problems has prompted the detailed study of the impact on the biosphere of all human activities. This includes the disposal of hazardous wastes and attracts research from many areas, in view of the spectacular worldwide growth in the chemical and nuclear industries. For many types of toxic waste, such as radioactive waste, the main contamination pathway is the transport of waste components by groundwater intrusion into a deep repository (Krauskopf, 1988). Toxic materials are spread throughout the aquifer by advection, diffusion and dispersion. This progress, however, can be checked by adsorption of the solutes by the soil, i.e., the occurrence of physico-chemical reactions between the solutes and colloidal soil particles.

The governing differential equations describing the contribution of the above process are used in the analysis of pollutant migration problems. A modified advection-dispersion equation, which includes a coefficient  $R$  to account for retardation, can be used to describe the behaviour of retarded solutes. It is commonly assumed that there is a linear relationship between  $R$  and the distribution coefficient  $K_d$  with;

$$R = 1 + K_d \gamma_b / n$$

where;  $\gamma_b$  is the bulk density of the soil,  $n$  is the

porosity of the soil and  $K_d$  is defined as the ratio between the concentration of the solute in the soil solids and in the soil solution, once chemical equilibrium is achieved in a batch test. Assuming a linear adsorption isotherm and one dimensional flow the advection-dispersion equation becomes;-

$$\frac{\partial C}{\partial t} = D_l \frac{\partial^2 C}{\partial x^2} - v \frac{\partial C}{\partial x} - \frac{K_d \gamma_b}{n} \frac{\partial C}{\partial t}$$

or rearranging;-

$$\frac{\partial C}{\partial t} = \frac{D_l}{R} \frac{\partial^2 C}{\partial x^2} - \frac{v}{R} \frac{\partial C}{\partial x}$$

where;-

$C$  = Concentration of solute in the solvent ( $\text{kg/m}^3$ )

$x$  = Displacement coordinate (m)

$t$  = Time (s)

$D_l$  = Longitudinal dispersion coefficient ( $\text{m}^2/\text{s}$ )

$v$  = Average fluid velocity (m/s)

The application of the linear retardation assumption thus presupposes that equilibrium between the

concentrations of the solute in the solid and liquid phases of the soil can be maintained during the migration process. Such a condition cannot always be taken for granted (James and Rubin, 1979). Nevertheless, theoretical analyses based on the linear retardation assumption are commonly adopted (De Marsily, 1986; Domenico and Schwartz, 1990).

Solutions to the migration equations can be obtained either analytically (Van Genuchten and Wierenga, 1986) or numerically (Crank et al, 1981; Abriola, 1986). The validation of the mathematical and numerical models is difficult, due to the scarcity of production field repository data and the expense of constructing large field trials which would require very long term monitoring (tens or hundreds of years) to observe migration phenomena.

Modelling in the centrifuge circumvents this problem. It can be demonstrated (Arulanandan et al., 1988; Hensley, 1989) that in a 1/n scale repository model accelerated to  $ng$  the time scale factor for fluid flow is  $n^2$ . Every hour of experimental data gathered with a model accelerated to 100g would correspond to almost 14 months of observation in the field.

In the present work an analysis was attempted of migration patterns of selected radioactive waste components in three soils. Two acceleration levels (50 and 100g) were imposed on the model, and flow conditions induced such that markedly different dispersion conditions, as expressed by the Péclet number ( $P_e$ ), were achieved. The Péclet number for dispersion is expressed by:-

$$P_e = \frac{vd}{D_0\theta f_i}$$

where:

$D_0$  = Diffusion coefficient for solute

$d$  = Representative particle size (m)

$\theta$  = Volumetric moisture content of the soil

$f_i$  = Impedance factor, incorporating decrease in the concentration gradient caused by tortuosity and other factors within porous media.

The solutes employed were radioisotopes with short half-lives (under three days).

## 2. MATERIALS AND METHODS

### 2.1 Soil model

The soil model was contained in a rigid aluminium box of internal dimensions 950mmx150mmx375mm(H). The base was covered with a 25mm layer of pea gravel, separated from the

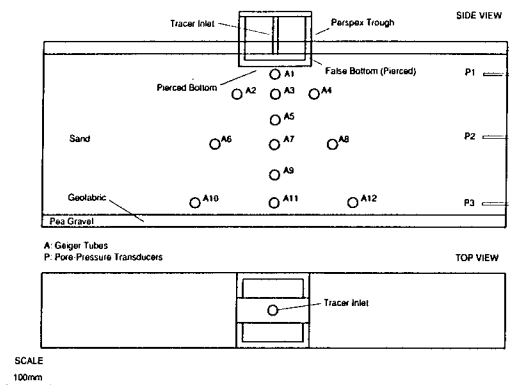


Fig.1: Diagram of Model

overlying soil bed by a sheet of geofabric. The soil bed itself was 325mm deep. A rectangular perspex box with an internal cross section of 150mmx150mm and 120mm high was embedded in the soil with its base 25mm below the soil surface simulating a repository as shown in Fig.1. The base was perforated to allow solute flow into the soil, simulating a leak.

The soil beds were characterised as follows:

Test bed A - Fine grained, sand- sized silica flour, to simulate non-sorptive conditions at high Péclet numbers.

Test bed B - Silt-sized silica flour, to simulate non-sorptive conditions at medium to low Péclet numbers.

Test bed C - As Test bed A but with 6% by weight of Illite clay, thoroughly mixed to simulate a sorptive environment.

A continuous downward vertical flow was established through the model by application of a constant hydraulic head which was varied between experiments. Miniature Druck transducers monitored the porewater pressures at three heights in the soil (see Fig. 1), to determine flow rate.

### 2.2 Tracers

The radioactive tracers were chosen on the basis of their half-lives, availability and similarity with radwaste components. Table 1 summarises the tracers employed and their characteristics. The tracer, typically 20MBq in 8ml of solution, was released into the model repository as a slug.

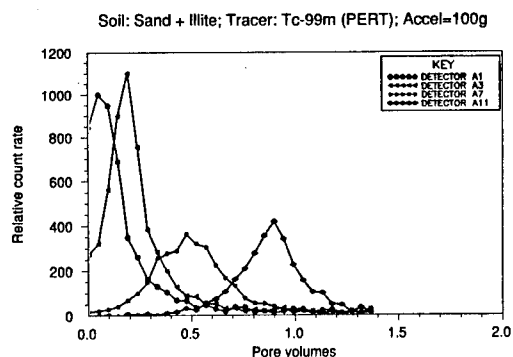


Fig.2: Evolution of centre-line count rates for Test No.1

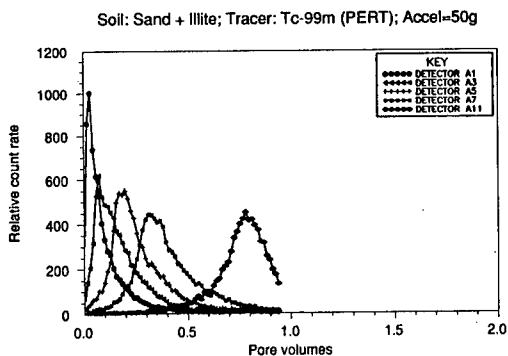


Fig.4: Evolution of centre-line count rates for Test No.2

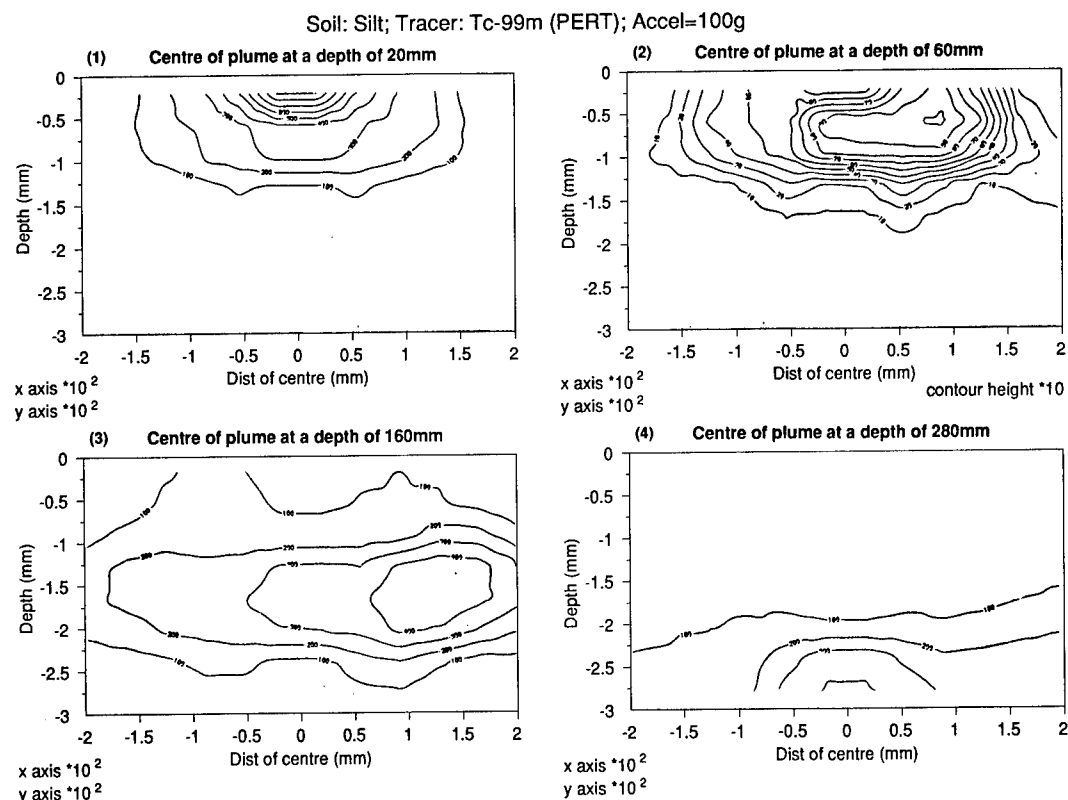


Fig.3: Count rate contours at various depths for Test No.1

### 2.3 Radiometric data acquisition

The evolution of the radioactive plume in the model soil bed was monitored by 12 miniature Geiger tubes placed in the soil as shown in Fig.1. This measurement technique was developed so that different chemical forms of the same radioisotope

could be studied without affecting the measurement of its flow rate.

All radiometric data were corrected for decay whilst the time base for flow rate data was normalised as units of model pore volume exchange. These units proved a convenient basis for the

Soil: Silt; Tracer: Tc-99m (PERT); Accel=50g

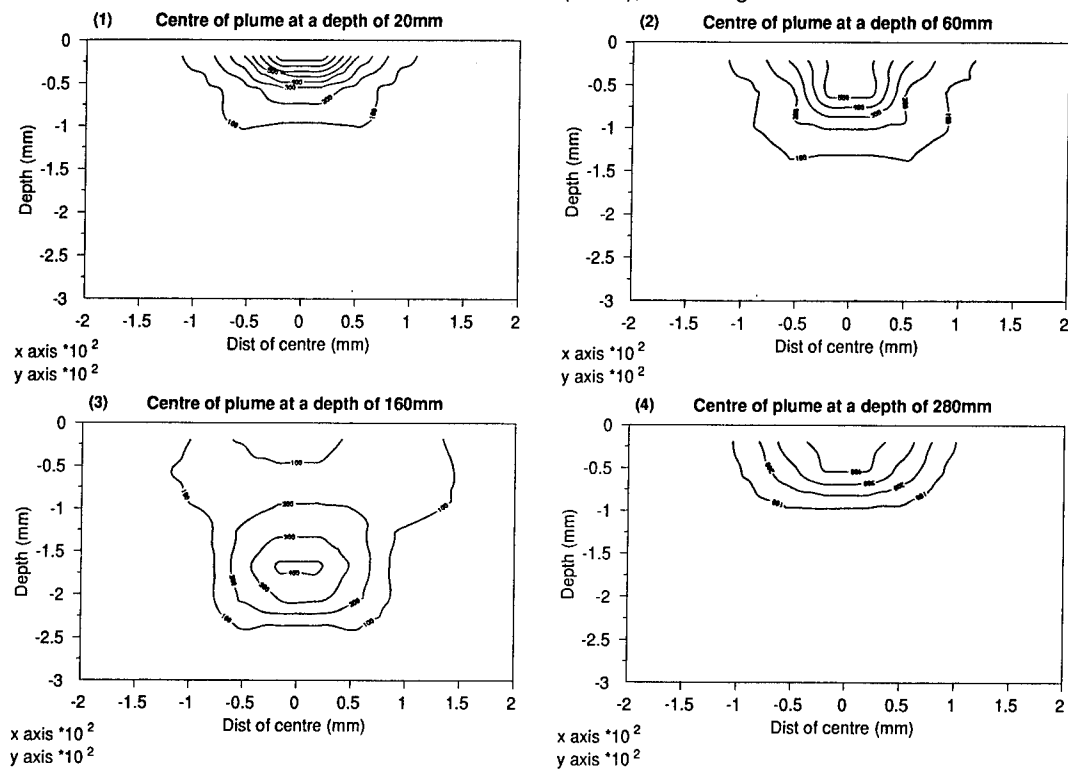


Fig.5: Count rate contours at various depths for Test No.2

Soil: Sand + Illite; Tracer: Tc-99m (PERT); Accel=50g

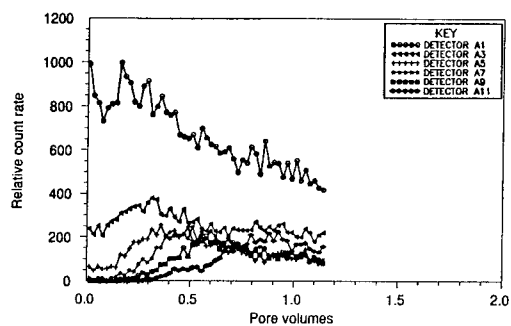


Fig.6: Evolution of centre-line count rates for Test No.3

Soil: Sand + Illite; Tracer: Tc-99m (PERT); Accel=100g

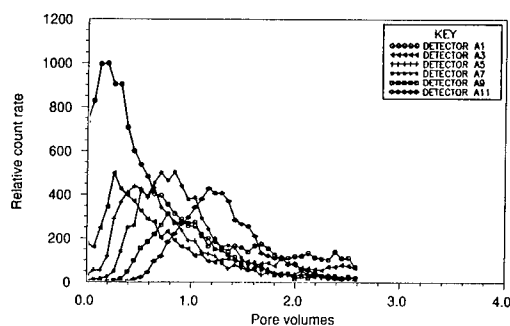


Fig.7: Evolution of centre-line count rates for Test No.4



comparison of tests with varying flow rate hence time required for complete pore volume exchange of solvent. Migration velocities of the radiotracer were deduced from the peak count-rate data from the Geiger tubes located accurately within the model. The development of the radioactive plume within the model was based on interpolated data from the Geiger tube array.

### 3. RESULTS

A total of 26 experiments were carried out with the three test beds. Two acceleration levels, 50 and 100g, were employed. Six of the tests are discussed in this paper. A summary of the tests is given in Table 2.

### 4. DISCUSSION AND CONCLUSIONS

In tests 1 and 2 the effect of hydrodynamic

Table 1. Summary of tracers employed with their characteristics

TRACER	T <sub>1/2</sub>	CHEMICAL FORM	SIMILAR WASTE COMPONENT
<sup>99m</sup> Tc	6h	TcO <sub>4</sub> , Tc <sup>4+</sup>	<sup>99</sup> Tc
<sup>123</sup> I	13.2h	I <sup>-</sup> (org + inorg)	<sup>129</sup> I, <sup>131</sup> I
<sup>90</sup> Y	2.67d	Y <sup>3+</sup>	<sup>90</sup> Y, <sup>91</sup> Y

dispersion is clearly demonstrated. This is seen in the change in the ratio of the full width of the peak count rate at each counter at half maximum of the count rate peak height (FWMH) between tests 1 and 2. In test 1 where the Péclet no. was of the order of 14 the FWMH for each counter was at 50% greater than that for the same counter in test 2 where the Péclet no. was about unity. (See Figs. 2 and 4) The migration velocity in test 2 was 30% of that in test 1.

The contours of count rates from the array of geiger tubes in tests 1 and 2 are shown in figs. 3 and 5 respectively. Whilst the development of the plume in test 1 suggests a chaotic behaviour the opposite is suggested in test 2 where the flow is much slower.

In tests 3 and 4 a mobile isotope <sup>99m</sup>TcO<sub>4</sub> was percolated through the soil bed containing 6% by weight of Illite clay. Here the shape and magnitude of the peak count rates from the geiger tubes on the vertical centreline of solute flow suggest that the adsorption behaviour was dependent on the seepage velocity. (Figs 6 and 7) From the shape of the peaks it is seen that a fraction of the tracer was retained and that this fraction decreased with increasing velocity.

In the case of the sorbed tracer (<sup>90</sup>Y<sup>3+</sup>) which was investigated in tests 5 and 6 the seepage velocity strongly influenced the sorption potential. Fig 8 shows the tracer hardly reached the first counter below the model repository when the seepage velocity was 1.75mm/min, whilst in test 6 (Fig 9) where the seepage velocity was 12.5mm/min only a fraction of the tracer was retained.

Table 2. Summary of tests highlighting the main characteristics.

Test No.	Soil Bed	Radiotracer	g Level n	Migration Vel. (mm/min)	Péclet No.	Figure No.
1	Silica sand	Na <sup>99m</sup> TcO <sub>4</sub>	100	7.64	14	2 & 3
2	Silica silt	Na <sup>99m</sup> TcO <sub>4</sub>	50	2.3	1	4 & 5
3	Silica silt + Illite	Na <sup>99m</sup> TcO <sub>4</sub>	50	1.75	4	6
4	Silica silt + Illite	Na <sup>99m</sup> TcO <sub>4</sub>	100	10.5	17	7
5	Silica sand + Illite	<sup>90</sup> YCl <sub>3</sub>	50	1.75	4	8
6	Silica sand + Illite	<sup>90</sup> YCl <sub>3</sub>	100	12.5	28	9

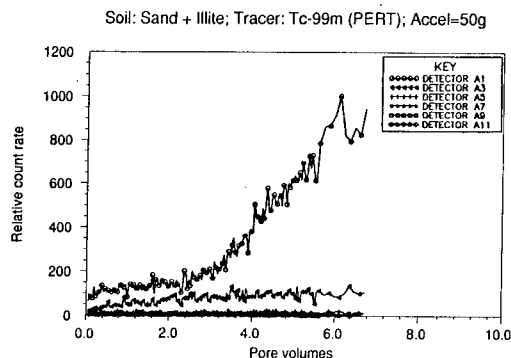


Fig.8: Evolution of centre-line count rates for Test No.5

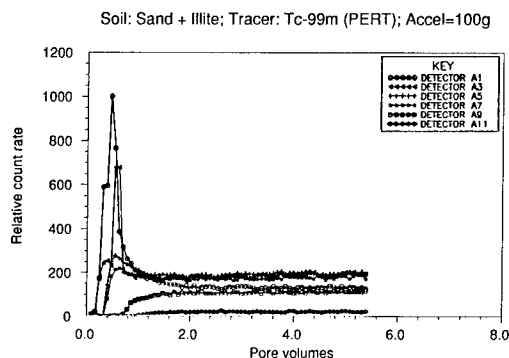


Fig.9: Evolution of centre-line count rates for Test No.6

## 5. CONCLUSIONS

a. Although in the preliminary stages of development the technique described has been shown to be capable of replicating, at least qualitatively, the influence of at least two processes that take place during the migration of solutes in groundwater. The movement of the solute has been measured independently of the flow of the solvent in a repeatable and reliable way.

b. The effect of dispersion on the solute flow has been clearly demonstrated - the higher the Péclet no. the greater the dispersion effects.

c. The degree of sorption is influenced substantially by the seepage velocity of the solvent. The higher the velocity the lower the sorption of the solute in a potentially sorptive environment. These experiments have also shown that the adsorption phenomenon does not comply with the generally

accepted linear retardation assumption. Therefore the mathematical representation should be modified to account for the effects of migration rate and hydrodynamic dispersion.

## ACKNOWLEDGEMENTS

The support given to Dr. Villar by Brazil's CNPq is gratefully acknowledged.

## REFERENCES

- Abriola, L. 1987. Modeling contaminant transport in the subsurface: an interdisciplinary challenge, *Reviews of Geophysics* 25:2, p215.
- Arulanandan, K., P. Thompson, B. Kutter, J. Meegoda, K. Muraleetharan and C. Yogachandran 1988. Centrifuge modeling of transport processes for pollutants in soils, *Jnl Geotech Engrg ASCE* 114:2, p.185
- Crank, J., J. McFarlane, G. Paterson and J. Peddey 1981. *Diffusion Processes in Environmental Systems*: MacMillan
- De Marsily, G. 1986. *Quantitative Hydrology*: Academic Press, New York
- Domenico, P. and F. Schwartz 1990. *Physical and Chemical Hydrogeology*: Wiley, New York
- Hensley, P. 1989. *Geotechnical Centrifuge Modelling of Hazardous Waste Migration.*, PhD Thesis, Cambridge University
- James, R. and L. Rubin 1979. Applicability of the local equilibrium assumption to transport through soils of solutes affected by ion exchange, *Chemical Modeling in Aqueous Systems*, E. Jenne ed., ACS, Wash., p225.
- Krauskopf, K. 1988. *Geology of high-level nuclear waste disposal*. *Ann Rec Earth Planet Sci* 16, p.173
- Van Genuchten, M. and P. Wierenga 1986. Solute dispersion coefficients and retardation factors: in *Methods of Soil Analysis, Part 1. Physical and Mineralogical Methods*, ASA-SSSA, Madison, p.1025.

## Simulation of long term performance of landfill covers

Thomas F. Zimmie, Mahadzer B. Mahmud & Anirban De

*Department of Civil and Environmental Engineering, Rensselaer Polytechnic Institute, Troy, N.Y., USA*

**Abstract:** A series of centrifuge model tests was performed to study the long-term behavior of different types of landfill cover materials, including the potential use of paper sludge as the impermeable barrier for landfill covers. The models were instrumented to monitor water infiltration levels, surface settlements and excess pore water pressures at various points in the models. The results were used to compare the performance of proposed paper sludge covers to conventional clay covers. The paper sludge was found to be highly compressible, and observed settlements were about an order of magnitude higher than in clay. The void ratio of paper sludge decreases rapidly during consolidation, resulting in a significant drop in permeability as the test progressed. These tests indicate that paper sludge is a good candidate for landfill cover material.

### 1 INTRODUCTION

This paper describes the centrifuge tests performed to study the long term behavior of different types of landfill cover materials. Two paper sludge samples were tested and their performance was compared with clay, which is currently considered as conventional impermeable barrier material. The long term behavior of paper sludge covers was found to be different from that of clay covers in several significant ways. The paper sludge tends to be highly compressible, and settlements are about an order of magnitude higher than in clay. The high compressibility of the sludge causes a large decrease in void ratio with time, with a resultant large drop in permeability. This behavior is unlike a conventional clay cap, which undergoes little strain under the typical stresses induced by cover materials. Thus, there is little change in void ratio and permeability, and for all practical purposes the initial and final clay permeabilities are the same.

A paper sludge may not initially meet the low permeability requirements for a cover barrier material, but after settlements occur may decrease in permeability sufficiently to meet the requirements.

### 2 LANDFILL COVER DESIGN

The specific purpose of the tests described in this paper was to secure approval for the use of paper sludge as the impermeable barrier layer for the cover of a municipal solid waste landfill located in New York State (NYS). New York State's Municipal landfill regulations (NYS Part 360 Regulations, 1993) do differ from federal landfill regulations promulgated by the United States Environmental Protection Agency (USEPA, 1988). However it is not the intent of this paper to discuss regulations in great detail. For the purposes of this paper, it will suffice to say that both the state and federal regulations are similar in philosophy, and the general philosophy will be discussed only as it affects

the use of paper sludge as the impermeable layer in landfill covers.

Basically, the intent of the regulations is to ensure that the permeability of the final cover should not be more than that of the liner system, to avoid the "bathtub" effect. In addition, the cover should be tolerant to settlement and subsidence of the underlying waste, and should be able to function with minimum maintenance.

The regulations generally recommend the use of a three-layer cap design, consisting of a vegetative top cover, a drainage layer and an impermeable barrier layer system as depicted in Figure 1.

The detail of the impermeable barrier layer system will vary, dependent on specific regulations. For example, the barrier layer for a hazardous waste landfill will typically consist of a composite system, comprising a layer of flexible membrane liner (FML), placed over a layer of compacted low permeability soil with a maximum saturated hydraulic conductivity of  $1 \times 10^{-7}$  cm/sec. Commonly the barrier layer for non-hazardous municipal landfill covers may consist of either a FML or a layer of compacted low permeability soil. In general the regulations do not specify the required design of material for the final cover, and allow the design engineers to develop their own design such that the final cover be 'no more permeable than' the liner system. The flexibility in designing the final cover allows the application of other types of material such as paper sludge in place of compacted low permeability soil, provided that the requirement for permeability is met. However, since clay is considered as conventional capping material for the impermeable barrier layer of landfills, the use of non-conventional material such as paper sludge must meet the approval of the specific regulatory agency involved.

Approval for the use of paper sludge as capping material has been obtained from the State of Massachusetts (Zimmie et al, 1993) and from the State of New York for a municipal landfill closure (the tests reported herein are part of that project). At the federal level, the USEPA has supported several

thk. (cm)	MATERIALS	k (cm/sec)
min 60.0	Vegetative Cover	not specified
min 30.0	Drainage Layer	min $1 \times 10^{-2}$
min 60.0	*Compacted Low Permeability Layer	max $1 \times 10^{-7}$

\* Compacted low permeability barrier layer or a minimum of 20 mil thick FML

Figure 1 Typical three-layer cap design for a municipal waste landfill.

research grants investigating the use of paper sludge as landfill cover material.

In addition to permeability and settlement studies, an important part of this project was to investigate the chemical compatibility and toxicity of the paper sludge leachate. Due to the relatively large model size used, it was possible to collect the several liters of leachate needed to perform the required chemical analyses. This would have been a very difficult task in a 1 g environment. A discussion of the chemical analyses is beyond the scope of this paper, but the leachate did pass chemical compatibility and toxicity requirements.

### 3 TEST PROCEDURES.

Three models (A1, A2, and A3) were tested in the centrifuge at 105 g's. The consolidation of the cover materials and seepage quantities were observed for 24 hour periods. Since the ratio of model time to prototype time is equal to  $g^2$  ( $t_m/t_p = 1/N^2$ ) for flow phenomena, the test simulated 30 years of prototype cover behavior. The tests were performed on the 100 g-ton centrifuge at Rensselaer using a sample box, 91 cm x 61 cm x 36 cm in size. Detailed descriptions of the centrifuge is provided by Elgamal et al (1991).

#### 3.1 Experimental Setup

In tests A1, A2 and A3, the test sample consisted of a 7.62 cm thick layer of the cover

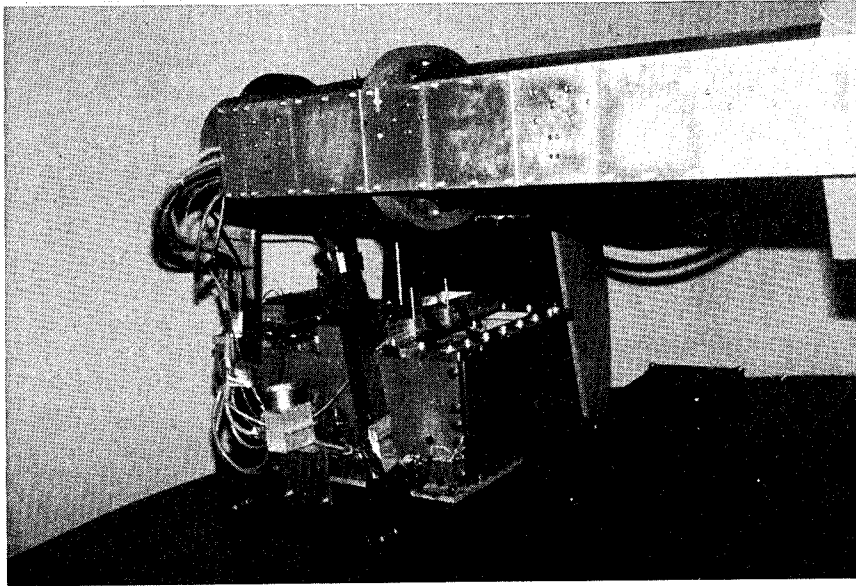


Figure 2. The actual setup of the model prior to centrifuge testing

material: clay in test A1 (same exact material currently utilized as cover material on site), and paper sludge in tests A2 and A3. For tests A2 and A3, paper sludge 1 (10-14 years old) and paper sludge 2 (2-4 years old) were used respectively. The cover material was placed over a 15.24 cm layer of clean sand and separated from the sand by a layer of geofabric. The sand layer was compacted to maximum density and was designed to capture the leachate flowing through the cover material throughout the duration of the test. The experimental setup used for these tests is shown in Figure 2. Bentonite slurry, about 5 cm wide and 6 cm deep, was placed between the wall of the box and the cover material to prevent sidewall leakage due to the high stress fields and hydraulic heads induced in the centrifuge.

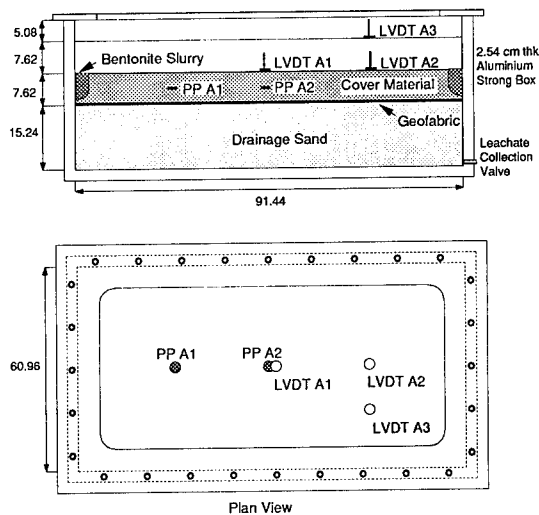


Figure 3. Experimental setup and instrumentation for tests A1, A2 and A3.

### 3.2 Instrumentation

At the beginning of each test, 7.62 cm of water was impounded on top of the cover material and the water level was monitored using a floating device attached to LVDT (Linear

Variable Differential Transformer) A3. Two other LVDTs, LVDT A1 and LVDT A2, were placed on the surface of the cover material at half and quarter span respectively (Refer to Figure 3). Pore pressure transducers, PP A1

and PP A2 were used to measure the pore water pressure at the mid-depth of the sample.

#### 4 RESULTS & DISCUSSIONS

The results from the tests are summarized in Figures 4, 5 and 6. Figure 4 shows the change in water level versus time for the first six hours of the test for all three covers. These curves were corrected for evaporation since some water was also lost due to evaporation while spinning the model at 184 rpm in the centrifuge. A separate test was run at the same g-level with only water in the model box and the changes in water level with respect to time due to evaporation alone were measured.

The results presented in Figure 4 are indicative of the seepage characteristics of the three cover materials under identical conditions such as compaction, thickness of sample and head of water. As expected the clay cover was the least permeable, with an observed permeability of  $4 \times 10^{-8}$  cm/sec, which remains almost constant throughout the test. However for the two sludge covers the drop in water level varies significantly with time as evidenced by the steeper slopes at the beginning of the test. These slopes correspond to coefficients of permeability of  $6 \times 10^{-7}$  cm/sec for Sludge 1 and  $2.5 \times 10^{-6}$  cm/sec for Sludge 2. The slope of the curves change significantly with time and towards the end of the tests the permeability of Sludge 1 and Sludge 2 are found to be  $2 \times 10^{-7}$  cm/sec and  $4.7 \times 10^{-7}$  cm/sec respectively. This demonstrates that the permeability of sludge covers will decrease considerably with time due to large decreases in void ratio and the high compressibility of the sludge, whereas in clay covers the permeability remains virtually constant.

The initial permeabilities for paper sludges in the centrifuge tests were above the  $1 \times 10^{-7}$  cm/sec requirement, but after 360 minutes of the test, which simulated about 7.5 years of prototype seepage time, the permeability values decreased to the order of about  $10^{-7}$  cm/sec. One of the goals of the tests was to illustrate

the relatively large decreases in permeability that occur with time in the sludges, compared to the clay which experiences little decrease in permeability. Thus it was not necessary to achieve exact initial permeability values of  $1 \times 10^{-7}$  cm/sec for the centrifuge tests. By varying the compactive effort and number and thickness of compaction lifts in the models, initial permeability values of  $10^{-7}$  cm/sec can be obtained. In the construction of the prototype landfill cover, the goal is to achieve initial sludge permeability values close to  $1 \times 10^{-7}$  cm/sec. This was successfully done on a landfill in Hubbardston, Massachusetts which used a similar paper sludge as cover material (Zimmie et al, 1993). The initial permeability values averaged about  $1 \times 10^{-7}$  cm/sec, and after one year decreased about an order of magnitude to about  $10^{-8}$  cm/sec.

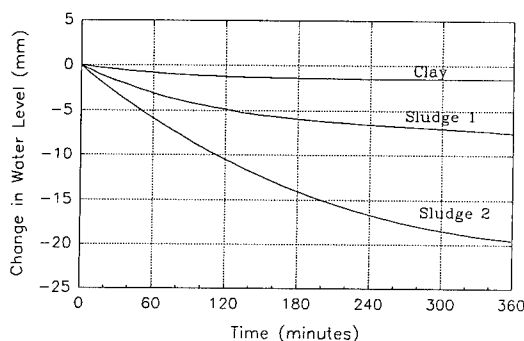


Figure 4. Change in water level (corrected for evaporation) for the first six hours of test.

Typical settlement versus time curves for the three cover materials are shown in Figure 5. The spikes at the tail end of the curves were caused when the centrifuge was stopped to add water and to correct machine imbalance. Consequently the samples were returned to the 1 g level, causing the surface to rebound. Once the centrifuge restarted and the model returned to 105 g's, the settlement proceeded as a continuation of the previous curve.

This figure shows that the two sludge covers are more compressible than the clay cover. The final settlement strains for clay, sludge 1 and

sludge 2 were observed to be 2.5%, 17.1% and 15.1% respectively. For typical values of effective stresses that the barrier materials are subjected to in landfill covers, final settlement strains in clay will be quite low, 2 - 3%, whereas the paper sludge will experience strains on the order of 20 - 30%. The high strain values predicted by the centrifuge tests have been observed in an actual landfill cover consisting of paper sludge. The paper sludge layer, approximately 0.9 m thick, has experienced about 16.2 cm of settlement in two years (17.7% strain). Final settlement strains are predicted to be on the order of 20% (Moo-Young, 1992 and Zimmie et al, 1993).

Figure 6 presents the value of the pore water pressure at mid-depth of the cover. As with the plots in Figure 5, the spikes in the curves indicate times when the centrifuge was stopped during the run and consequently, the pore pressure reduced.

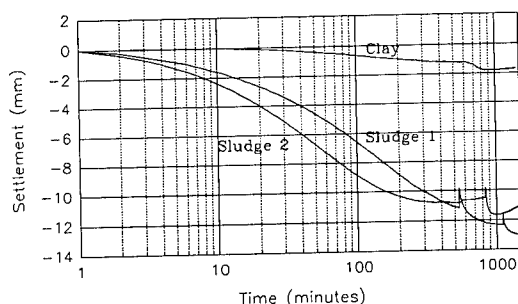


Figure 5. Settlement vs. Time at 105g

There is a rapid rise in pore pressure as the centrifuge spins up from one-g to 105 g. This startup time is typically several minutes, and is not shown in Figure 6. When the centrifuge reaches 105 g, the pore pressure reaches a maximum value, and starts to decrease, i.e. consolidation begins. The main objective of measuring pore water pressure was to validate the fact that the theory of one-dimensional consolidation was valid for the sludges, since simple one-dimensional analysis was utilized to estimate settlements as discussed previously. The results shown in Figure 6, indicate that the

dissipation of pore pressure with time is essentially following classical one-dimensional consolidation theory both for the sludges and the clay. This is best seen in the first 600 minutes at 105 g.

## 5 CONCLUSIONS

The results of the tests indicate that the paper sludge can be a good substitute for conventional clay impermeable barrier layers in landfill caps. The paper sludge can meet the hydraulic conductivity requirements for an impermeable barrier layer (typically  $10^{-7}$  cm/sec). However, unlike clay caps where initial and final permeability values remain virtually constant under the low effective stresses inherent in covers, the paper sludge permeability may decrease considerably from the initial placement value. This has important practical considerations for landfill closure, since the paper sludge may not initially meet a regulatory maximum permeability value, but will do so after consolidation. Decreases of about an order of magnitude in paper sludge permeability have been observed.

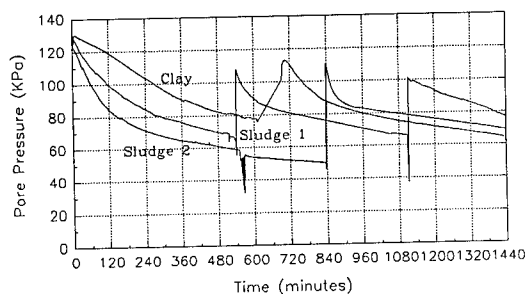


Figure 6. Pore water pressure vs. time at the center of cover at 105 g

The paper sludge is highly compressible relative to clay, about an order of magnitude higher. Strains of 2 - 3% were observed in clay, whereas strains of 20 - 30% were observed in the paper sludges. Similar values have been observed in the field.

The use of the centrifuge allows the simulation of long prototype times, which enables the prediction of the future behavior of paper sludge as landfill cover material, for example, consideration of settlements, leaching, chemical compatibility and toxicity. This proved to be an important consideration in obtaining regulatory agency approval for the use of sludge in landfill covers. The tests described herein subjected the clay and paper sludge models to 105 g for 24 hours, thus simulating 30 years of prototype behavior.

The biodegradation that occurs in the sludge over a period of 30 years cannot be modeled in a 24 hour test on the centrifuge. However biodegradation causes the percentage of organic in the sludge to decrease and the paper sludge to become more soil-like in character. Because of this the coefficient of permeability of the sludge decreases with the progress of biodegradation (Zimmie et al, 1993). Thus the tests presented here are useful since they yield conservative permeability values, i.e. the in-situ permeabilities after 30 years are expected to be lower than those measured in the centrifuge test.

It was also possible to secure a sufficient amount of leachate that infiltrated through the sludge to complete the extensive amount of chemical testing required by the regulatory agency. This would have been an extremely difficult task in a 1 g environment.

The test also confirmed that the use of classical one-dimensional consolidation theory appears to be adequate for settlement analyses of the paper sludge layer.

## REFERENCES

- Elgamal, A-W., Dobry, R., Van Laak, P. and Nicolas-Font, J. 1991. Design, construction and operation of 100 g-ton centrifuge at RPI, *Centrifuge 91*, Ko (ed.), Balkema, Netherlands, pp. 27-34.
- Moo-Young, H. K. Jr. 1992. Evaluation of the geotechnical properties of a paper mill sludge for use in landfill covers. MS thesis Rensselaer Polytechnic Institute, New York.
- New York State 1993. 6 NYCRR Part 360, Solid waste management facilities, NYS Dept. of Environmental Conservation, Albany, New York.
- USEPA. 1988. Lining of waste containment and other impoundment facilities. US Environmental Protection Agency. EPA-600/2-88/052, Cincinnati, Ohio, U.S.A., September 1988.
- Zimmie, T. F., Moo-Young, H. K. Jr. and LaPlante, K. 1993. The use of waste paper sludge for landfill cover material. Proceedings of Green '93. Waste disposal by landfill symposium. Bolton Institute, Bolton, UK., vol. 2, pp. 11-19.



## Contaminant migration through clay in a mini-drum centrifuge

D.C. Evans, C. Savvidou & A.N. Schofield  
University of Cambridge, UK

**ABSTRACT :** Physical observations of phenomena related to groundwater pollution are rare and difficult to obtain from field experiments. These observations are essential for the understanding of the coupled processes involved and for the evaluation of current predictive methods of such phenomena.

In this paper, experimental and theoretical investigations of the progression of a contaminant pulse through a clay layer are reported. In the experimental investigation, the type R Mini-Drum centrifuge was commissioned and established as a useful tool in studying problems related to Environmental Geotechnics. A downward hydraulic gradient caused advective flow through a layer of clay in which water content varied with depth. In the theoretical investigation, a simple model was used to predict the interstitial velocity which was then used in a simple one-dimensional, finite difference program to predict the contaminant profile in the layer. The experimental profiles of contaminant in the soil were compared to the predicted distributions.

### 1 THE MINI-DRUM CENTRIFUGE

Figure 1 shows a schematic diagram of the mini-drum with the axis of the drum in the vertical position. The machine is designed with a pivot system which when actuated through a hand operated, self locking worm gear box, permits the axis of the drum to be rotated through 90° into a horizontal position. The purpose of tilting into the horizontal mode is to facilitate the loading and preparation of soil models.

Figure 2 is a section diagram of the main rotating components of the centrifuge. The following items of equipment comprise the principal units of the drive system. The identification numbers correspond to the numbers on figure 2.

The rotating face plate, (item 1) has two main functions : it supports and drives the soil model and its associated container, and it, in two compartments, houses the electrical components associated with the instrumentation. A computer compartment is sealed by a cover, (item 2) and there is a junction box to which these

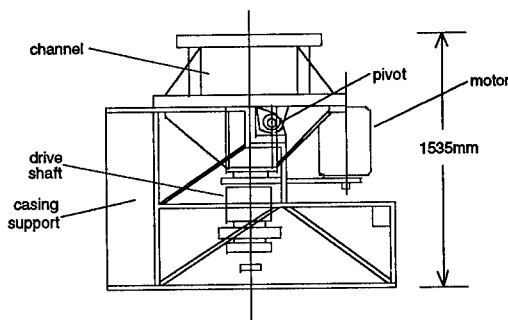


Fig.1 Elevation of mark I mini-drum with drive shaft vertical

instruments can be connected, (item 3).

The face plate is permanently secured to a shaft, (item 4) which transmits the driving force from the electric drive motor. The maximum spindle speed of the drive motor limits the face plate to a maximum speed of 1000 rpm. The diameter of the face plate is 800 mm.

Concentric with the face plate drive shaft are two further shafts: the drive shaft for the

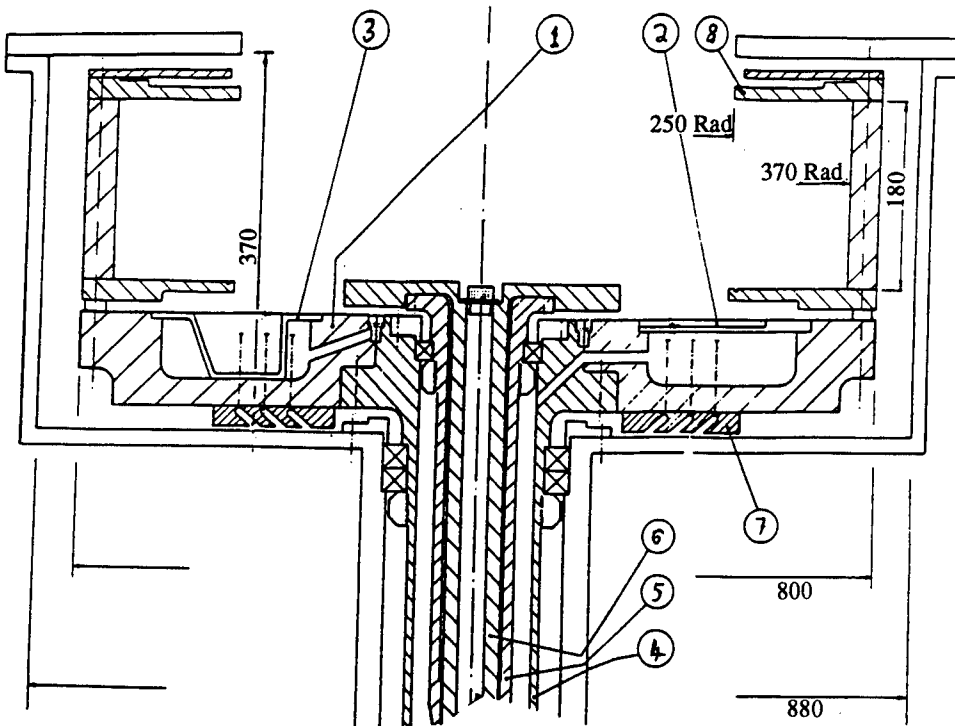


Fig.2 Section diagram of mini-drum

turntable, (item 5) and a spindle, (item 6) which supports and locates the turntable.

Three independent hydraulic slip ring channels are mounted on the back face of the face plate (item 7). These slip rings provide for the supply of fluids to the front of the face plate.

The soil sample drum container, (item 8) is a channel of depth 120 mm and width 180 mm formed by a cylindrical ring of 30 mm depth and 180 mm width and two flat circular plates with outer diameter 800 mm, each with a central hole of 500 mm diameter. The face plate, the channel and the surface of the soil or water can be viewed in flight with a stroboscope.

The junction box, housed in a compartment in the face plate, has sixteen 4-pin sockets. The power supply to each socket can be varied to accommodate pore pressure transducers, resistivity probes or linear velocity displacement transducers, which measure displacement. A multiplexer system is used, under computer control, to power up and record from each device in turn.

## 2 MODEL PREPARATION AND TESTING PROCEDURE

During model preparation, a bottom drainage layer was placed in the drum channel comprising a 10mm depth of coarse 25/52 Leighton Buzzard sand overlain by 5mm of finer 100/170 L.B. sand. During that stage, the channel was maintained with its axis horizontal and was rotated at 211 rpm. It was found that a satisfactory speed for smooth operation during model making was 211 rpm, which is 18g at the channel wall. With the axis horizontal and the drum channel in a vertical plane, it was a simple matter to pour sand carefully into the channel, where it was immediately subject to 18g and did not fall out of the top of the channel as it was carried over the top of the ring channel in continuing flight. When the layer was complete, it was smoothed in flight with a stationary tool. The layer was then saturated via a tapping which ran through the channel wall and connected the coarse sand with an outer supply channel.

Then, while the specimen was still in flight at 18g, speswhite kaolin slurry at a moisture content of 120 % was then gradually placed into the channel. In the first test, it was poured onto a fixed paddle which was positioned in such a way that the slurry ran down the inclined surface and dropped about 1 mm onto the current soil surface where it was immediately subject to 18g. The end of the paddle was slowly raised as the clay level rose.

In the second test, five layers of clay were poured and each was allowed to consolidate in stages. The first layer was placed using the paddle technique described above. The layer was consolidated and it was then possible to stop the centrifuge, with its axis vertical, without the clay layer falling down from the ring channel. With the drum stationary, a pore pressure transducer was positioned on top of this layer and the lead was fixed to the channel wall. The drum was then brought back to 18g and the clay slurry used for the following four layers was poured down a metal chute and onto the channel wall. The centrifugal force caused the slurry to move up the channel and bury the resistivity probes which were placed on each consolidated layer. It is believed that the staged construction technique resulted in an undisturbed model with resistivity probes at various depths throughout the clay layer.

The model was tested with a downward hydraulic gradient from a pool of water on the upper (inner) surface, to the base drain. The water was added onto the clay surface through two hydraulic slip-ring supplies. This ensured that the surface water level remained above the water level in the outer supply channel and hence the downward hydraulic gradient was ensured at all times. Preliminary tests using a "Mistral" bench-top centrifuge had showed that, in the absence of a downward hydraulic gradient, pock-mark formation may occur in a soft consolidating clay slurry. Pock-marks are the surface evidence of piping originating in the depth of the clay when the hydraulic gradient exceeds the critical hydraulic gradient.

In test 1, the speed of rotation was increased to 266 rpm, the channel was rotated to the horizontal position and then taken up to 730 rpm (corresponded to a g-level of 200 at two-thirds of the final depth of the sample), in steps

of 10g. In test 2, the sample was consolidated at 730 rpm after each layer was poured.

On reaching 730 rpm in test 1, the speed was reduced to a nominal 30g and a standpipe connected to the sand drain was shortened to promote downward advective flow. The channel was then returned to 730rpm. In test 2, the standpipe was not present and so a downward advective flow existed at all times. In both tests, hydraulic-gradient consolidation proceeded for about 2 hours after which the drum channel was stopped and the soil was left overnight.

Twelve hours later, each model was again centrifuged at 730rpm for 2 hours to ensure almost full consolidation. For model 1, the clay depth decreased from 95mm as slurry to 47.5mm when fully consolidated. The final fully consolidated depth of test 2 was also 47.5mm. After final consolidation, the machine was stopped and the water on the surface drained away. The clay layer was then ready for the start of the experiment.

In test 1, a 0.1 M salt solution was introduced onto the clay surface. The pulse of contaminant was supplied for 167 minutes, which, at 1/200 scale, corresponds to 13 years of prototype contaminant migration. After the salt exposure phase, fresh water was placed onto the clay surface. The exposure time of the clay to fresh water was 162 mins.

In test 2, the exposure times to 0.07 M NaCl, 0.14 M NaCl and fresh water were 159, 100 and 188 minutes respectively. During test 2, the pore pressure transducers and resistivity probes were monitored continuously.

At the end of both tests, the machine was stopped and a sampling, scraper tool was connected to the inner turntable which was rotated manually whilst the channel remained stationary. The metal scraper of 20mm width took samples at 0.5 to 1.0 mm increments through the depth of the clay, which were then stored in moisture content bottles. For test 2, the resistivity probes were excavated from the clay and their position within the model was carefully measured. In order to measure the salinity, water was added to the samples to produce a slurry. Unicam conductivity probes were then used to measure the concentration of chloride within the slurry samples and hence produce a pollutant profile curve.

### 3 THEORY

#### 3.1 Governing Equations

The one-dimensional advection-dispersion equation based on the approximation of a Fickian-type dispersion law, for the case of a rigid porous matrix and non-reacting solute, (see Gillham and Cherry, (1982)) has the form:

$$\frac{\partial^2 C}{\partial X^2} - U \frac{\partial C}{\partial X} = \frac{\partial C}{\partial T}, \quad (1)$$

in which the first term on the left represents dispersive transport and the second term advective. The variables have been non-dimensionalised;  $U$  is the average pore fluid velocity,  $C$  is the concentration (mass/unit volume of fluid). It was solved numerically using a forward difference formulation, where :

$$C = \frac{c}{c_0} \quad X = \frac{x}{L}$$

$$U = \frac{uL}{D_{hL}} \quad T = \frac{D_{hL}t}{L^2},$$

where  $c_0$  is the initial concentration of the contaminant,  $L$  is the overall length and  $D_{hL}$  is the longitudinal hydrodynamic dispersion coefficient.

### 4 RESULTS

#### 4.1 Numerical calculations for pollutant transport

In the programme "Mindrum", the clay stratum was divided into layers of 0.5mm depth. Assuming an initial void ratio for the top layer corresponding to 120% moisture content and allowing for a variable g-level with depth, then

$$\sigma'_v = \sigma'_v + \frac{(\rho_s - \rho_w)\omega^2(r+d)d_i}{1000(1+e)} + \frac{\rho_w i_{ave}\omega^2(r+d)d_i}{1000} \quad (2)$$

and

$$e = (2.48 - 0.25 \log(0.793 \sigma'_v))B, \quad (3)$$

where the middle term of equation (2) is the vertical effective stress due to the self weight of the solids and the last term is the seepage pressure acting on the solids due to the hydraulic gradient. Here  $\sigma'_v$  is the vertical effective stress, and features on both sides of the equation because of its summation with increasing depth.  $\omega$  is the rotational velocity of the channel,  $r$  is the radius to the upper surface of the clay,  $d$  is the depth of the layer being considered,  $d_i$  is the incremental depth,  $e$  is the void ratio,  $i_{ave}$  is the hydraulic gradient and  $\rho_s$  and  $\rho_w$  are the density of solids and water, respectively.  $B$  is a factor which was used to correct the average void ratio without changing its distribution with depth. The average void ratios given by the programme "Mindrum" are 1.415 and 1.413 for tests 1 and 2, respectively. The average void ratio of the clay in the model was 1.210 and 1.217. Factors  $B = 0.855$  and  $0.861$  were used, respectively.

The average void ratio,  $e_{ave}$ , is used to calculate a value of hydraulic gradient for each layer :

$$i = \frac{(1+e_{ave})}{(1+e)} i_{ave}, \quad (4)$$

and this was then used to calculate a value of Darcy velocity for each layer :

$$v_{Darcy} = \frac{k i \omega^2 (r+d)}{9.81}, \quad (5)$$

where  $k$  is the coefficient of permeability at unit gravity calculated from the empirical relationship  $k = 0.5e^{3.25}$  for speswhite kaolin, (Al-Tabbaa, (1987)). The average value of Darcy velocity was then used to calculate the pore fluid velocity for each layer.

Programme "Polluz" : A finite difference formulation was used to calculate the pollutant profile within the model.

The boundary condition,  $C(0, t)$ , at the clay surface is fixed according to the stage of the test. For example, in test 1, the initial surface boundary condition is  $C(0, t=0.167 \text{ mins}) = 1.0$ . The boundary condition at the base of the clay, in both tests, assumes  $C(L, t) = 0$ .

The clay depth was divided into 5 layers and an average pore fluid velocity and porosity was calculated for each layer by programme "Mindrum", as described above.

The effective diffusion coefficient was calculated from the relationship (see Andrews and Bennett, (1981)) :

$$D_d^* = \frac{D_d}{nF}, \quad (6)$$

where  $D_d = 1.5 \times 10^{-9} \text{ m}^2/\text{s}$  for chloride in solution.  $n$  is the porosity and  $F$  is the formation factor. An average value of  $F = 3.6$  is used (Hensley, (1989)).

The Peclet number, in the samples, was of the order of  $5 \times 10^{-4}$  and hence it could be assumed that mechanical dispersion was negligible.

For the time scales used in the experiment, adsorption could also be ignored, (Gronow et al., (1988)).

#### 4.2 Contaminant profiles

Figure 3 shows that, for both tests, the experimental and theoretical profiles, of final concentration, are in good agreement with each other. Relative depth is the depth divided by the total depth. Self weight consolidation results in a variation in void ratio which must be accounted for in the calculation of the dispersion coefficient. This is particularly important when considering the formation factor which shows different profiles when using an average value as opposed to values appropriate to individual layers. A formation factor of 3.6, together with the average porosity, was used to find a value of the empirical number,  $m = 2.10$  in the equation proposed by Archie (1942) :

$$F = n^{-m}. \quad (7)$$

The formation factor increases with decreasing porosity and hence increases with depth. Therefore the effective dispersion coefficient decreases with depth. However, if a constant value of  $F=3.6$  is used throughout the depth of the sample, the dispersion coefficient increases with depth. Figure 4 compares the theoretical profile of figure 3a with profiles calculated using constant formation factors,  $F = 3.6$  and  $5.0$ . They highlight the importance of dividing the sample into layers to account for the decreasing porosity with depth.

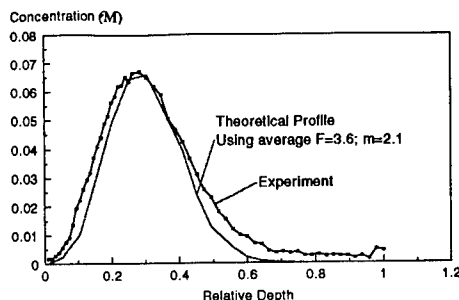


Fig.3a Experimental and theoretical concentration profile for test 1

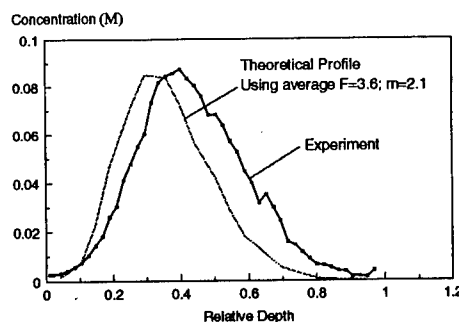


Fig.3b Experimental and theoretical concentration profile for test 2.

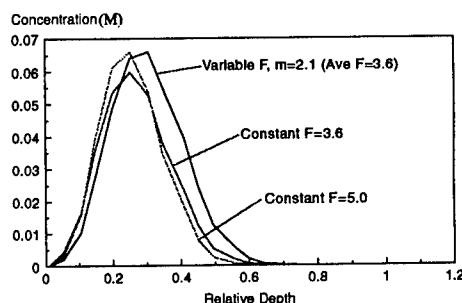


Fig.4 Effect of constant and variable formation factors on contaminant profile for test 1

Program 'Polluz' was also used to predict the contaminant profile at specified depths throughout the duration of test 2. The numerical and experimental profiles of four resistivity probes at various depths are shown in figures 5a to 5d. The relative depth of each probe is shown.

The resistivity probes were calibrated at a constant temperature in soil saturated with five salt solutions ranging in concentration from

0.001 to 0.1 M. Corrections were applied for the void ratio of the clay around each probe and the test temperature. The concentration values were normalised to the maximum value,  $C_{\max}$ , obtained in each case.

The shape of the experimental and theoretical profiles, in figures 5a to 5d, are in good agreement. The discrepancy in the profiles of probe 7, up to 159mins, is associated with the inability of the normalisation procedure to reduce the experimental values when exposed to the 0.07 M salt solution.

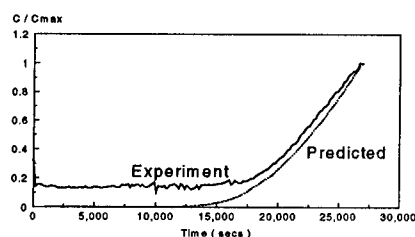


Fig.5a Response of probe 1; Rel. depth = 0.505

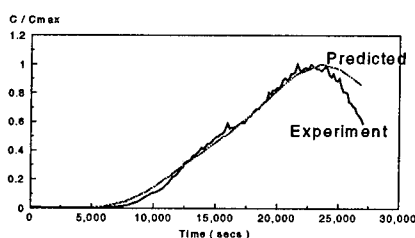


Fig.5b Response of probe 4; Rel. depth = 0.274

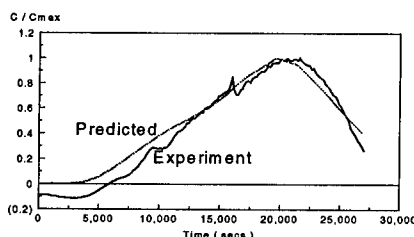


Fig.5c Response of probe 6; Rel. depth = 0.189

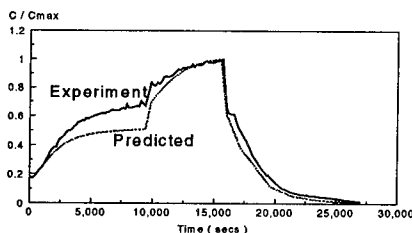


Fig.5d Response of probe 7; Rel. depth = 0.032

## 5 CONCLUSIONS

A new type R mini-drum centrifuge has been used to study the migration of contaminants through low permeability soils. The data obtained highlighted the potential of using this new machine for modelling accelerated transport processes involved in problems of Environmental Engineering.

In the theoretical investigation, a simple model, which accounted for the varying gravity level with depth, was used to predict the interstitial velocity. This was used in a simple one-dimensional, finite difference program which divided the clay into layers to account for the varying interstitial velocity and porosity with depth. The theoretical prediction is in good agreement with the experimental results.

## REFERENCES

- Al-Tabbaa, A. 1987. Permeability and stress strain response of speswhite kaolin. Ph.D. Thesis; CUED.
- Andrews, D. & Bennett, A. 1981. Measurements of diffusivity near the sediment-water interface with a fine-scale resistivity probe. *Geochimica et Cosmochimica Acta*, 45, 2169-2175.
- Archie, G.E. 1984. The electrical log as an aid in determining some reservoir characteristics. *Trans. Amer. Inst. Mining and Metallurgical Engrs.*, 146, 54-62.
- Gillham, R.W. & Cherry, J.A. 1982. Contaminant migration in saturated unconsolidated geological deposits. *Geophysical Society of America, Special Paper* 189 pp31-62.
- Gronow, J.R., Edwards, R.I. & Schofield, A.N. 1988. A report to the US Army Development and Standardisation Group (UK). University of Cambridge, CUED/D-SOILS/TR214.
- Hensley, P.J. 1989. Accelerated physical modelling of transport processes in soil. Ph.D. Thesis; CUED.

## Scaling concerns for immiscible multiphase flow in porous media

S.E. Petersen & B. Cooke

*Department of Civil Engineering, The University of Western Australia, Nedlands, W.A., Australia*

**ABSTRACT :** Centrifuge modelling appears to be a tool which could be used to study the flow of light non-aqueous phase liquids (LNAPL's) through the subsurface, as it has proved useful in other contaminant hydrogeological applications. However there are some aspects of immiscible multiphase systems which have not been analysed in the context of centrifuge modelling. This paper presents results of scaling analysis as it pertains to the phenomena of fingering and residual entrapment. Analysis of fingering indicates that at increased gravities fewer fingers will form, with those that do being larger and propagating more rapidly than would be required for modelling similitude. For analysis of trapping mechanics, the dimensionless variables the Bond number and Capillary number, which characterise entrapment mechanics, are not invariant. The variability in these numbers indicates that the degree of residual entrapment at increased gravities will be much lower than at one g.

### 1 INTRODUCTION

Despite the apparent suitability of geotechnical centrifuge modelling for the study of immiscible multiphase flow, there is to date a dearth of literature on the subject.

In a series of column tests on the centrifuge, Illangasekare et al. (1991) found the flow of a light non-aqueous phase liquid (LNAPL) through a dry sand and a sand at 2% residual saturation was modelled correctly. Meegoda et al. (1989) modelled gasoline leakage from underground storage tanks on the centrifuge, however offered no theoretical or experimental validation of the modelling exercise other than standard analysis of the stable flow equations.

The aim of this dissertation is to present the results of centrifuge scaling analysis on unstable flow in both the vadose zone (wetting) and the capillary fringe (non-wetting), and trapping mechanics exhibited in the capillary fringe and below.

### 2 CENTRIFUGE SCALING LAWS

The scaling laws for flow phenomena in the centrifuge are well established (Goodings (1984),

Schofield (1980)). For flow of water through soil, similitude is achieved with an N-fold increase in flow velocity and an reduction in time, where N is the model scale factor.

### 3 SCALING OF UNSTABLE WETTING DISPLACEMENTS

#### 3.1 Unstable Wetting Displacements

Unstable flows are defined as those in which a random perturbation to the front will grow in time. These perturbations can result from viscous instabilities or spatial and temporal variations in soil hydraulic properties. Unstable flow in porous media arises when perturbations to a moving front cause it to break down into a series of spatially discrete fingers. Averaged flow equations do not apply to the front, so it must be characterised by parameters detailing the geometry and growth rate of the front.

Wetting displacements originating at the surface are inherently resistant to viscous instability, however initiation due to spatial and temporal variations in soil hydraulic properties cannot be disregarded. Kueper and Frind (1988)

note:

'...[the] severity of permeability variation required to invalidate the homogeneous model is unclear, but experiments seem to indicate it is very slight'.

In the absence of any explicit data on the magnitude of the permeability variation required to initiate fingering, the analysis that follows assumes its presence in the model.

The stability analysis applied in this paper is that of Glass et al. (1991) for a three-dimensional axi-symmetric perturbation to an initially planar wetting front. The front can be assumed initially planar as it is stabilised by capillary forces. It must be remembered that the following analysis pertains only to the onset of fingering.

The analysis details three parameters of interest to the unstable flow phenomenon:

- i. the critical wavelength for the system
- ii. the width of the fastest growing finger
- iii. the growth factor of the disturbance.

The minimum wavelength is defined as the smallest wavelength that cannot be stabilised by imbibition from the sides of the finger. The growth factor defines the degree of instability, being a measure of the rate at which finger growth occurs at the onset of fingering.

Denoting the penetrating and penetrated fluids by the subscripts 1 and 2, and the prototype and model parameters by the subscripts p and m, the relevant relationships are as follows:

Minimum (or Critical) Wavelength:

$$\lambda_p^{crit} = 2\pi \left( \frac{\sigma^* k_f}{U_p q_f \Delta \mu_{21} + k_f g \Delta \rho_{12}} \right)^{\frac{1}{2}} \quad (1)$$

where  $\lambda_p^{crit}$  is the critical wavelength,  $\sigma^*$  is the macroscopic interfacial tension,  $U_p$  is the velocity of the unperturbed front,  $q_f$  is the conductivity at the front,  $\Delta \mu_{21}$  is the viscosity contrast ( $\mu_1 - \mu_2$ ) across the front,  $k_f$  is the effective permeability of the fingering fluid at the front, and  $\rho_{12}$  the density contrast ( $\rho_1 - \rho_2$ ) across the front.

Finger Width (specialised to oil-air system):

$$d_p = 4.8 \left( \frac{3\sigma^*}{\rho_1 g \left( 1 - \frac{q_p^s}{K_p^f} \right)} \right)^{\frac{1}{2}} \quad (2)$$

where  $d_p$  is the width of fastest growing finger,

$q_p^s$  is the flux through the system, and  $K_p^f$  is the hydraulic conductivity at the front.

Exponential Growth Factor:

$$\omega_p = \left( \frac{\kappa_p}{\Sigma \mu_{12} q_f} \right) (g k_f \Delta \rho_{12} + U_p q_f \Delta \mu_{21} - \sigma^* k_f \kappa_p^2) \quad (3)$$

where  $\omega_p$  is the exponential growth factor,  $\kappa_p$  is the Bessels function equivalent of a wave number, and  $\Sigma \mu_{12}$  is the viscous dissipation ( $\mu_1 + \mu_2$ ).

### 3.2 Scaling Results

Although it might seem possible for both soil and fluid parameters to be included in the analysis, the sensitivity of soil-fluid properties to these parameters precludes the possibility. In a paper on contaminant retention, Kia (1988) concluded that the sensitivity of retention characteristics to these properties necessitated "the use of undisturbed soil samples and the actual contaminant."

Accordingly, the critical wavelength can be expressed as:

$$\lambda_m^{crit} = 2\pi \left( \frac{\sigma^* k_f}{(NU_p) q_f \Delta \mu_{21} + k_f (Ng) \Delta \rho_{12}} \right)^{\frac{1}{2}} \quad (4)$$

because and  $U_m = NU_p$  and  $g_m = Ng$ .

This can be simplified to:

$$\lambda_m^{crit} = \frac{\lambda_p^{crit}}{\sqrt{N}} \quad (5)$$

The prototype wavelength,  $\lambda_p$ , is directly proportional to the source diameter. In accordance with the scaling laws presented earlier, correct scaling in the model requires that:

$$\lambda = \frac{\lambda_p}{N} \quad (6)$$

Consequently, the wavelength observed at the model scale is  $\sqrt{N}$  larger, implying the enhanced gravity acts to stabilise the flow by reducing the range of perturbations to which it is unstable.

Similarly, direct substitution of the scaled gravity into the equation for finger diameter and



rearranging yields:

$$d_m = \frac{d_p}{\sqrt{N}} \quad (7)$$

The diameter of the fastest growing finger is also increased by  $\sqrt{N}$ , which is apparent as the finger diameter is half the wavelength of the disturbance.

As stated above the wavelength is increased by  $\sqrt{N}$  in the model, thus logically the wave number is reduced by  $\sqrt{N}$ :

$$\kappa_m = \frac{\kappa_p}{\sqrt{N}} \quad (8)$$

Accordingly, substitution gives:

$$\omega_m = \sqrt{N^3} \omega_p \quad (9)$$

This growth factor is an exponential term which determines the rate at which the fingers grow. The  $\sqrt{N^3}$  scaling factor that arises therefore indicates that the fingers that form in the model are more unstable when compared with those that form in the prototype.

Consequently, although the displacement is stabilised with respect to wavelength, it is destabilised with respect to the exponential growth factor. Therefore in the model a smaller number of larger, more unstable fingers form.

As it is assumed that fingering occurs in the model, and is induced by permeability variations, two possibilities arise:

- i. fingering occurs in the prototype but not in the model, and
- ii. fingering occurs in the prototype and in the model.

In the first case, modelling of prototype events would not be possible simply because similitude of the model and prototype behaviour is not observed. Additionally, the model behaviour would underestimate contaminant loading at the water table. The second case allows for modelling provided the effects of the enhanced gravity on the fingering mechanism are not too severe. The possibility of no fingering in the prototype and the model is not considered, as the probability of encountering a homogeneous medium at the prototype scale is considered minimal.

## 4 SCALING OF THE TRAPPING MECHANICS

### 4.1 Trapping Mechanics

Trapping is the process by which the impinging pore fluid is occluded within the pore space. This pore-scale process depends on fluid density contrast, fluid viscosity contrast, applied pressure gradient, and gravity.

Entrapment is caused by capillary forces, and can be overcome by buoyant forces or viscous pressure gradient. The degree of trapping exhibited in a particular porous medium can be qualitatively assessed by measuring the ratio of both the buoyant forces to the capillary forces, and the viscous to the capillary forces. These ratios are known as the Bond number (Bo) and Capillary number (Ca) respectively, and are determined by the following relationships:

$$Bo = \frac{\Delta \rho g R^2}{\sigma} \quad \text{and} \quad Ca = \frac{\mu U}{\sigma} \quad (10)$$

where R is the characteristic pore size (taken as the  $D_{10}$  particle size), and  $\sigma$  is the liquid-liquid interfacial tension.

### 4.2 Scaling Results

Obviously the centrifuge variables that control the trapping process are the fluid velocity and the gravitational acceleration.

Accordingly the Bond and Capillary numbers scale as:

$$Bo_m = N Bo_p \quad \text{and} \quad Ca_m = N Ca_p \quad (11)$$

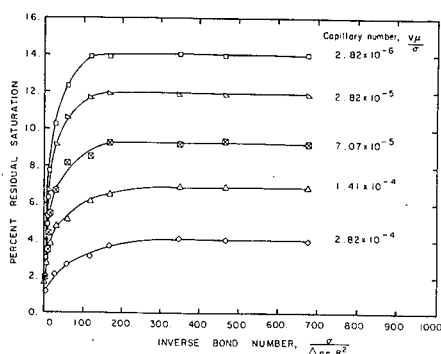
Before the effect of the change in Bond and Capillary number can be determined, average values for the fluid parameters and soil pore characteristics are required. As oil trapping only occurs for water saturations above 70% (Morrow & Songkran, 1981), water is the reference fluid. For BP LM<sup>®</sup> aviation kerosene used in the current research programme, the fluid parameters are given below.

$$\begin{aligned} \Delta \rho &= 175 \text{ kg m}^{-3} \\ \sigma &= 0.04 \text{ kg s}^{-2} \\ \mu &= 4 \times 10^{-3} \text{ kg m}^{-1} \text{ s}^{-1} \end{aligned}$$

The Bassendean sands characteristic of the Perth area typically have hydraulic conductivities of  $3 \times 10^{-4} \text{ m s}^{-1}$  and  $D_{10}$  sizes of approximately 225  $\mu\text{m}$ . Assuming the driving pressure gradient is hydrostatic, the saturated pore velocity is the same as the hydraulic conductivity, and a lower bound to fluid velocities.

Substituting these values yields a Capillary number of  $3 \times 10^{-5}$  and a Bond number of  $2 \times 10^{-3}$  for the 1 g prototype.

Plots of residual saturation versus inverse Bond number for varying Capillary numbers in random packings of regular sized spheres are given in Figure 1 (Morrow & Songkran, 1981). For the example cited above, at 1g the residual saturation is approximately 12%. At 20g the associated Bond and Capillary numbers yield a residual saturation of less than 2%, indicating the altered capillary and buoyant forces produce a significant deviation from prototype behaviour even at low g levels.



**Figure 1.** Residual saturation vs  $1/Bo$  for varying  $Ca$  (Morrow & Songkran, 1981)

Assuming that a 5 to 10% deviation in residual saturation is acceptable for modelling purposes, Figure 1 indicates a maximum acceptable g-level of 3 to 4g. Although it is somewhat misleading to use these plots to directly estimate effects of g-level, the trend they indicate is apparent.

Morrow and Songkran (1981) also combined the Capillary and Bond numbers to give a "total effects" number which can be correlated with hydraulic properties.

The relationship provided is:

$$Te = Ca + 0.001412 Bo \quad (12)$$

Table 1 correlates, among other things, the "Total Effects" number ( $Te$ ) to the relative permeability at the advancing front. As the Capillary and Bond numbers used do not correspond to the values estimated for 20 g acceleration, it is used to correlate the conditions in the model with the relative permeability at the front.

**Table 1:** Total Effects number ( $Te$ ) versus Relative Permeability at the Front (after Morrow & Songkran, 1981)

$Ca$ ( $10^{-6}$ )	$Bo$ ( $10^{-3}$ )	$Te$ ( $10^{-5}$ )	$k_{wf}$
2.82	6.67	1.22	0.13
16	15	3.72	0.34
36	24	6.99	0.47
60	37.8	11.34	0.50
94	55.6	17.25	0.53
136	79.4	24.81	0.54
195	110	35.03	0.56
265	150	47.68	0.56
360	194	63.39	0.59

At 1 g the total effects number is  $4.4 \times 10^{-5}$ . From the table this corresponds to a relative permeability at the front of 0.37. At 20 g the total effects number rises to  $8.9 \times 10^{-4}$  indicating a relative permeability at the front of greater than 0.59.

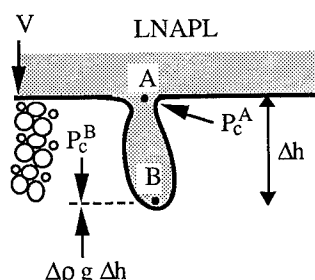
The result of the increase in the saturations and relative permeabilities in the capillary fringe is a more pronounced lateral flow of the LNAPL. This is due to the absence of trapping, which results in a piston-like displacement, increasing local permeability to the LNAPL

#### 4.3 Ganglia Size Distributions

Because the model and prototype are identical at the microscopic level, changes that occur at

At the pore level, these shifts in hydraulic properties indicate a change in the geometry and spatial distribution of the entrapped fluids, due to their gravity dependence when variable gravity is incorporated.

Figure 2 shows a typical ganglion. They are generally less than ten pore diameters long.



Trapping occurs when the imbibition pressure at A is greater than the sum of the hydrostatic pressure of the finger and the imbibition pressure at B:

$$P_c^A > P_c^B + \Delta \rho g \Delta h \quad (13)$$

Conversely, mobilisation is maintained when the imbibition pressure at A is less than the sum of the hydrostatic pressure of the finger and the imbibition pressure at B, for the simple reason that the resisting pressures can prevent imbibition at A.

$$P_c^A > P_c^B + \Delta P^S \quad (14)$$

where  $\Delta P^s = \Delta \rho g \Delta h$ .

$$\begin{aligned} P_c^A - P_c^B > \Delta P^S & \quad \text{TRAPPING} \\ P_c^A - P_c^B < \Delta P^S & \quad \text{MOBILIZATION} \end{aligned}$$

$$\Delta P_m^s = N \Delta P_n^s \quad (15)$$

In the prototype the distribution of ganglia is determined by the supplementary pressure and the geometry of the ganglia. The proportion of ganglia mobilised is that part with a capillary pressure contrast less than the buoyant pressure.

391

The source of the gravity dependence of the multiphase soil hydraulic properties is therefore capillary trapping phenomenon. The result is a set of hydraulic properties unique to each g-level. As modelling is predicated on the invariant nature of these very properties it seems that modelling is irrevocably compromised.

## 5 CONCLUSIONS

LNAPL contamination of the subsurface is subject to instabilities and depends strongly on microscopic trapping mechanisms exhibited within the three phase zone and below the capillary fringe. These processes are sensitive to density and viscosity contrasts between the fluids in the pore space, and the velocities of the pore fluids.

The geotechnical centrifuge utilises enhanced gravity and enhanced fluid velocities to effect a reduced scale accelerated time modelling of phenomena. As a result the hydraulic properties of the soil are altered, and the gross macroscopic behaviour of the LNAPL varies with g-level.

The result is that, in theory, both the microscopic and macroscopic behaviour is severely compromised, leading to a divergence of the phenomena exhibited at the prototype and model scale. Consequently, the centrifuge is not considered a suitable tool for the modelling of immiscible multiphase flows or any two-phase water-LNAPL displacements.

## 6 REFERENCES

- Glass, R.J., Parlange, J.-Y., & Steenhuis, T.S. (1991). Immiscible displacement in porous media: stability analysis of three-dimensional, axi-symmetric disturbances with application to gravity-driven wetting front instability. *Water Resources Research*, 27(8), 1947-1956.
- Goodings, D.J. (1984). Relationships for modelling water effects in geotechnical centrifuge models. In: W.H. Craig (ed.) *Application of Centrifuge Modelling to Geotechnical Design*, 1-24.
- Illangasekare, T.H., Znidarcic, D., Al-Sheridda, M., & Reible, D.D. (1991). Multiphase flow in porous media. *Proceedings of the International Conference Centrifuge 1991*, Boulder, Colorado, 517-523, Balkema, Rotterdam.
- Kia, S.F. (1988). Modeling of the retention of organic contaminants in porous media of uniform spherical particles. *Water Research*, 22(10), 1301-1309.
- Kueper, B.H. & Frind, E.O. (1988). An overview of immiscible fingering in porous media. *J. Contam. Hydrol.*, 2, 95-110.
- Meegoda, N.J., Gunasekera, S. & Hyjack, R. (1989). A new method to model transport and fate of gasoline from leaking underground storage tanks. *Proceedings of the 21st Mid-Atlantic Industrial Waste Conference*, 582-595.
- Morrow, N.R. & Songkran, B. (1981). Effect of viscous and buoyancy forces on non-wetting phase trapping in porous media. *Surface Phenomena in Enhanced Oil Recovery*. Plenum Press, New York.
- Schofield, A.N. (1980). Cambridge geotechnical centrifuge operations. *Géotechnique*, 30(3), 227-268.

## Implications of changes in seepage flow regimes for centrifuge models

Deborah J. Goodings

University of Maryland, College Park, Md., USA

**ABSTRACT:** Centrifuge models can simulate prototype seepage conditions governed by Darcy's law, including pore pressures and unconfined phreatic surfaces, even though the increase in self-weight causes a corresponding increase in laminar seepage velocity. Experimental results show this to be the case for seepage velocity Reynolds numbers up to about 3 which is large for hydraulic gradients at 1g but small for hydraulic gradients at 100g for granular soils. At higher seepage velocity Reynolds numbers, transitional and turbulent conditions develop, and these flow velocities affect pore pressure and position of unconfined phreatic surfaces. For those flow regimes, model and prototype flow velocities must be equal for similitude. This can be achieved with model grain size  $N$  times smaller than the prototype. This provides new opportunities for modelling geotechnical conditions with non-Darcy by a factor of  $N$  in the centrifuge model flow not usually achievable in 1g models.

### 1 INTRODUCTION

Laut (1975) considered the scaling laws for laminar seepage through a small soil model when the model is subjected to an increase in self-weight by a factor of  $N$  on the geotechnical centrifuge. For constant flow boundary geometry, that increase in self-weight (subscript  $m$ ) should cause a corresponding and directly proportional increase in seepage velocity,  $v$ , when compared to flow in the geometrically similar prototype (subscript  $p$ ), provided the flow can be considered to remain laminar in nature and to be governed by Darcy's law:

$$v_{m_{1g}} = N v_p, \quad (1)$$

For this laminar flow, dominated by viscous forces, losses in velocity head are considered to be negligible. Since all gross dimensions of the model are  $1/N$  those in the prototype, then times,  $t$ , for seepage events in the model and prototype are related as:

$$t_m = t_p / N^2 \quad (2)$$

The likely physical reality is that laminar,

transitional, and turbulent flow exist simultaneously in varying balances in most seepage through granular soils, unless seepage is very slow, because of the nature of the tortuous and changing pore sizes in a flow path. Bear (1979) noted that most groundwater flow occurs well within the laminar flow regime dominated by viscous forces, defined by values of Reynolds number,  $R_n$ , below an upper limit somewhere between 1 and 10. Flow with larger values of  $R_n$  up to about 100 may still be laminar, but inertial forces begin to govern flow and Darcy's law no longer applies. This is the transitional flow regime and losses in velocity head are no longer negligible. In a centrifuge model where seepage velocity can become significantly greater than exists in situ at 1g, an assumption of the continued applicability of Darcy's law may be incorrect.

Departure from viscous laminar flow has two consequences. The first is that volumes of seepage per unit time are no longer a linear function of acceleration, and the second, and more radical geotechnical consequence, is that the geometry of an unconfined phreatic surface changes, dropping dramatically as transitional flow begins to develop, since losses in velocity

head became significant. Goodings (1984) reviewed flow rules concluding that for both fully turbulent and transitional seepage flows, phreatic surfaces in centrifuge models will be geometrically similar to prototypes only if:

$$V_{mHg} = V_p, \quad (3)$$

which can be achieved if model grain size,  $D$ , is reduced as:

$$D_m = D_p/N \quad (4)$$

This requirement for a change in grain size can produce several potential difficulties for the modeller who wishes to use the same permeant in model and prototype. To ensure similar stress and strain in model and prototype, this change in grain size must not cause significant differences in mechanical properties, nor in capillary tension, which is a function of grain size, although that will be less of an issue in modelling effects in coarse grained soils. This means also that a given centrifuge model with unconfined flow and constant upstream and downstream boundary flow geometry will have an unconfined seepage surface that changes with changes in acceleration once outside the laminar regime governed by viscous forces. This increase, however, in velocity and change in flow regime may present an opportunity to model transitional and turbulent seepage, otherwise unattainable in 1g reduced scale models. In either case, this can have a bearing on selection of model size and test acceleration, and on the possibility that model grain size may have to be reduced. One purpose of this work was to examine systematically transitions in flow regime to guide modellers in their planning of models that simulate the flow effects central to the geotechnical problem at hand.

## 2 EARLIER RESEARCH

Muskat (1937) examined high velocity flow in porous media applying dimensional analysis to his results of flow through sand and lead shot. His application was petroleum engineering. Stephenson (1979) was concerned about flow through rockfill dams, and he used crushed rock, gravel, and marbles in his laboratory tests. Both researchers worked at 1g, relating Reynolds number,  $R_n$ :

$$R_n = \rho \frac{vD}{n\mu} \quad (5)$$

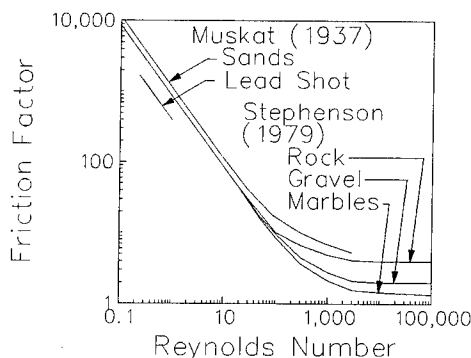


Fig.1  $R_n$  vs.  $F_f$  by Muskat(1937) and Stephenson (1979)

to a Friction Factor,  $F_f$ :

$$F_f = \frac{iDgn^2}{v^2} \quad (6)$$

where  $\rho$  = fluid density,  $n$  = porosity (and  $v/n$  is assumed to approximate pore seepage velocity),  $\mu$  = viscosity and  $g$  = gravitational acceleration. Their results are shown together in Figure 1.

The initial linear portion with slope equal to -1, describes laminar flow dominated by viscous forces where  $v$  is directly proportional to increases in  $i$ , all other parameters being held constant. At  $R_n > 10$ , there is a departure from that linearity which marks the upper limit for the applicability of Darcy's equation. That departure and approach to a constant value for Friction Factor independent of Reynolds number, occurred at successively larger values of  $R_n$  for crushed rock, gravel, and marbles in Stephenson's experiments. When  $F_f$  is a constant, fully turbulent flow can be said to dominate behavior and velocity becomes a function of  $i^{1/2}$  rather than  $i^1$ , as it was for laminar flow. Stephenson's data show  $F_f$  becomes equal to about 4 for crushed rock, and about 1.35 for marbles. Muskat did not obtain data at such large values of  $R_n$ .

## 3 EXPERIMENTAL METHOD

The intention of the research which is the subject of this paper was to conduct tests both on and off the centrifuge at high seepage velocities. As it turned out, all tests were conducted at 1g on the laboratory bench because of problems with water supply to the

models at the end of the centrifuge arm. It was also intended to extend testing into the fully turbulent flow regime for the three porous media used, but this was not feasible with this laboratory set-up with these materials. However, departures from the laminar flow regime described by Darcy's law, into the transitional flow, regime were identified.

In this research three uniformly graded particulate materials were used: copper shot with  $D = 2.8$  mm; glass marbles with  $D = 15.6$  mm; and one medium to fine granular soil, #30/#40 Ottawa sand, with  $D_{50} = 0.5$  mm. Special permeameters were fabricated for each of the three materials, and the internal cell diameters and sample lengths are given in Table 1. Ample supplies of the Ottawa sand meant that a large cell could be used for those tests, but a small supply of copper shot and glass marbles meant that those permeameters had to be smaller, although this was not ideal for testing.

Due to the enormous volumes of water required to develop and maintain steady state flow, non-deaired water was used in all tests. In the low hydraulic gradient tests on sand ( $i < 2$ ) water manometers were used to measure pore pressure, whereas in the higher gradient tests on sand, and all tests on the other materials, pressure transducers were used, operating through the same manometer ports, and recorded using automated data acquisition. The gage lengths, that is the distance between manometer ports, for the three cells are also given in Table 1.

All three materials were placed into their permeameters in lifts, with each lift being vibrated by blows to the side of the cell from a rubber mallet, in order to create a dense uniform packing which would be unaffected by large downward seepage pressures. In the case of the Ottawa sand the resulting void ratios were between 0.484 and 0.490 ( $n=0.33$ ). The sand was then tested under 41 hydraulic gradients ranging from 0.38 to 171.0.

The void ratio using this method of placement for the copper shot was 0.614 ( $n=0.38$ ) and for the glass marbles  $e$  varied from 0.655 to 0.658 ( $n=0.40$ ). The copper shot was tested under 12 hydraulic gradients ranging from 2.2 to 188.1 and the glass marbles over 25 hydraulic gradients from 0.08 to 4.58. The minimum Reynolds numbers achieved exceeded the maximum achieved in the sand, because the voids were larger and the smooth particle

Table 1. Permeameter Cells

Material Tested	Cell Diameter mm	Sample Length mm	Gage Length mm
Ottawa Sand	102	298	200
Copper Shot	52	154	102
Glass Marbles	76	711	508

Table 2. Maximum and minimum flow characteristics.

	Ottawa Sand	Copper Shot	Glass Marbles
Maximum			
$R_n$	122.9	3692	12691
$F_f$	11.9	1.7	1.3
$V_{seepage}$	26.33cm/s	172.6cm/s	70.5cm/s
$V_{discharge}$	8.69cm/s	65.6cm/s	28.2cm/s
Minimum			
$R_n$	0.39	278	808
$F_f$	2380	3.8	3.0
$V_{seepage}$	0.09cm/s	12.6cm/s	7.0cm/s
$V_{discharge}$	0.03cm/s	4.8cm/s	2.8cm/s

surfaces offered less resistance to flow. The maximum and minimum seepage and discharge velocities and corresponding Reynolds numbers and Friction Factors are given in Table 2 for all three materials. All experimental techniques, including results are given in detail in Babendreier (1991).

#### 4 RESULTS

A plot of the Reynolds numbers vs Friction Factors for the Ottawa sand is shown in Figure 2. At Reynolds Numbers less than or equal to 3.3 the data plot at a slope of -1, indicating flow governed by Darcy's equation. This line lies between the two lines Muskat and Stephenson plotted for their data for flow through sands and crushed rock, shown in Figure 1. At the next higher Reynolds number tested,  $R_n = 10.8$ ,

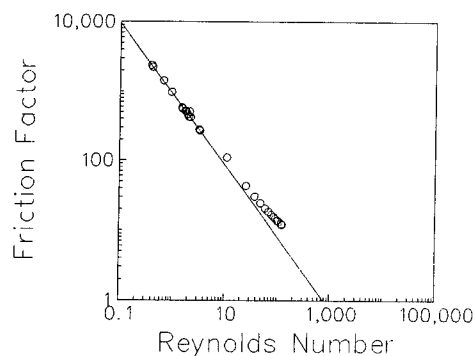


Fig.2  $R_n$  vs.  $F_f$  for Ottawa sand

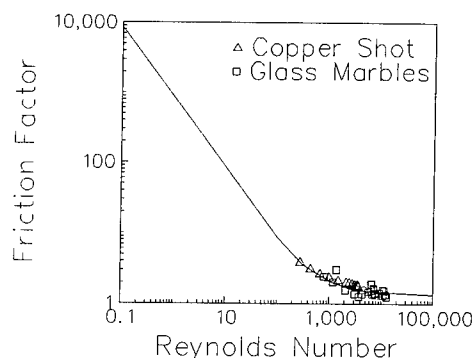


Fig.3  $R_n$  vs.  $F_f$  for copper shot and glass marbles

there is departure from that initial slope, meaning that Darcy's law is no longer valid, and velocity head loss begins to influence flow. This defines the end of the viscous laminar regime. The departure continues and increases at all larger Reynolds numbers to the maximum value of  $R_n$  achieved, which was 122.9.

The smallest Reynolds number achieved in either the copper shot or the glass marbles was 278, in spite of the low hydraulic gradients applied. This meant that there was no overlap with the data for sand. Figure 3 shows data for the copper shot and the glass marbles plotted together, overlapping and giving a single picture of  $F_f$  vs  $R_n$ . The initial linear portion in Figure 3 is that taken from the data for the sand in Figure 2 and is not from experimental data on these media. The curved portion of the line drawn through those data is the line Stephenson defined from his work on marbles, which seems to fit well, here.

Because the slope of these data is much less than 1- it is apparent that flows through these media at even these low hydraulic gradients were not described by Darcy's seepage equation. This is in spite of the fact that the particles are regular in size, so that void sizes are expected to be more uniform, and the particles are smooth on their surfaces, so that surface turbulence will be less. Velocity related head loss, then, influenced all flow in these tests. It appears that the beginning of the condition of fully turbulent flow, where  $F_f$  is no longer a function of  $R_n$ , may also have been achieved.

Figure 4 shows all data plotted together. The behavior identified by Stephenson with asymptotes to  $F_f = 4$  for crushed rock, and to  $F_f = 1.35$  for marbles, identified by Stephenson, are shown. For sand,  $F_f = 4$  could be considered as a possible, but unverified, value developing, perhaps, at  $R_n = 3000$ . Similarly the plot of the data of behavior of the copper shot and the glass marbles in this study falls into line with Stephenson's data for marbles. Even though laminar flow was not achieved for either the copper shot or the glass marbles, it seems likely, that the smooth regular spheres of those media cause laminar flow to prevail for larger values of  $R_n$  than is the case for flow through soils which have irregular pores. The relative positions of the sand data departure from linearity and of the data for copper shot and glass marbles suggest this also.

## 5 DISCUSSION

The consequences of these results for centrifuge modellers using granular soils are on the one hand, that departures from flow governed by Darcy's law may occur in models constructed at typical scales with typical model geometries, and tested at typical accelerations before that departure is desirable. But, on the other hand, centrifuge modelling presents opportunities to model seepage flow regimes usually unattainable in 1g models.

For Reynolds numbers up to, perhaps, at least 3 in this work, Darcy's law is an acceptable predictor of flow in sand. Since velocity head loss is too small to be significant in this flow regime, this means that in predicting geometries of steady state unconfined phreatic surfaces, seepage velocity is not directly considered. For this medium to fine Ottawa sand with  $D_{50} = 0.5$



mm and  $k = 0.08$  cm/s defined at 1g in the viscous laminar flow regime, flow was described by Darcy's law for hydraulic gradients of up to and including 3 at 1g, corresponding to a pore seepage velocity of 0.73 cm/s and a discharge velocity of 0.24 cm/s. This is a large hydraulic gradient in the context of conventional geotechnical seepage conditions. It is not large, however, in the context of centrifuge modelling where this upper limit to laminar flow means that in a model of this soil, tested at 10g, the largest hydraulic gradient (defined by model geometry) for flow governed by Darcy's law will be 0.3, and at 100 g, the largest hydraulic gradient will be 0.03. In a coarser soil, these limits will be even more problematic.

Consider, however the case where fully turbulent flow is the desired regime. Bear (1979) noted that this occurs when  $R_n > 150$  or 300. The conservative estimate from this work might be  $R_n > 3000$ . Then the pore seepage velocity in the Ottawa sand of this work would have to exceed 6m/s. Only then would head losses and pore pressures be correctly developed. Back calculation of  $i$  from  $F_t=4$  predicts a threshold hydraulic gradient of about 30,000 would be necessary to achieve that value of  $R_n$ .

But using coarser sands, with, for example,  $D = 2$ mm, presents special opportunities to model fully turbulent flow. A pore seepage of 1.5 m/s (or a discharge velocity of 0.5 m/s, assuming a porosity of 0.33), would produce a value of  $R_n = 3000$ . This should require a minimum hydraulic gradient of 460 at 1g, or 4.6 at 100g, for  $F_t = 4.0$ . In modelling a fully turbulent prototype phreatic surface in unconfined flow, equation 3 noted that seepage velocities must be equal in the model and the prototype. This will be achieved for equal values of  $i$ , when model grain size is  $N$  times smaller than in the prototype, as noted in equation 4. In this case, then, a model of unconfined fully turbulent flow through coarse sand with  $D = 2$ mm and  $i = 4.6$  at 100g, will correctly simulate unconfined fully turbulent prototype flow at 1g with  $i = 4.6$  through prototype rockfill with  $D = 200$  mm. At higher accelerations and/or in models with larger grain sizes, fully turbulent flow becomes even easier to achieve.

In transitional flow, which was observed in this uniformly graded sand for  $R_n$  greater than some threshold value greater than 3 but less than 11, velocity head losses also begin to affect both phreatic surface position in unconfined flow and

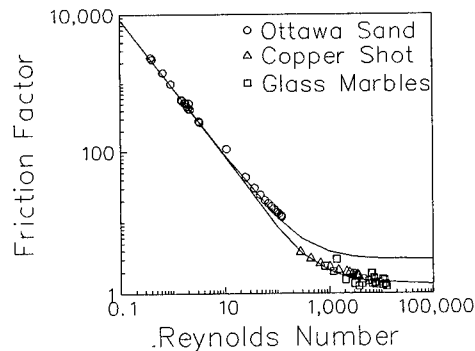


Fig.4  $R_n$  vs.  $F_f$  for all experimental data

pore pressure calculations. For similitude model and prototype seepage velocities must again be equal. This also requires a reduction in grain size by a factor of  $N$  when designing a model. This change to transitional flow occurs at much smaller, more easily achieved accelerations and hydraulic gradients.

Goodings (1987) identified evidence of different flow regimes developing in unconfined phreatic surfaces in a model of a homogeneous embankment dam described in Al-Hussaini et al. (1981). The model soil was 92% sand and 8% silt. At 66g, the observed phreatic surface corresponded closely to that predicted assuming Darcy's law. Calculated Reynolds numbers for the 66g model were of the order of 2 or less. This meant that for the geometry of that embankment dam at 66g, the phreatic surface, and thus the pore pressure and stability conditions, were considered to be unaffected by seepage velocity. That model, then, simulated a full scale 1g prototype 66 times larger with soil having identical mechanical properties. Seepage related time dependent events are considered to occur  $N^2$  times faster in that model, if model and prototype soil are the same.

At 75g, and 100g, however, the phreatic surfaces in the same model were much lower than predicted using conventional assumptions based on Darcy's law. This means that the pore pressures, and thus slope stability were also affected by seepage velocity. Exit Reynolds numbers were very large and could not be realistically calculated. For this model at 75g and 100g these conditions simulated flow only for prototypes with equal seepage velocities, which would have geometrically similar upstream and downstream water levels, but grain sizes  $N$  times larger than those in the

model. Seepage related time events when seepage velocities are equal in model and prototype are then scaled as  $t_m = t_p/N$ .

## 6 CONCLUSIONS

For seepage governed by Darcy's law, flow velocity itself does not affect the positions of unconfined phreatic surfaces. Centrifuge models, then, can model such prototype flow events at other velocities, even though velocity increases in direct proportion to  $N$  for geometrically similar boundary conditions. The upper limit of Reynolds number for the applicability of Darcy's law was found to be between 3 and 11. This means that for a 100g model of the medium fine Ottawa sand used in this research, the maximum hydraulic gradient (defined at 1g) for which laminar flow is ensured is 0.03, which can be quite restrictive when considering many geotechnical engineering cases.

For transitional and turbulent seepage, correct modelling of head loss and the position of unconfined phreatic surfaces can only be achieved if void seepage velocities are equal in model and prototype. In models using coarse sand or gravel this is quite achievable at typically available centrifugal accelerations. In this case, prototype grain sizes simulated are  $N$  times larger than in the prototype. This presents new possibilities to model high velocity seepage prototype flow conditions, such as occur in rockfill dams, which were hitherto difficult, if not impossible, to achieve.

Because of the early onset of transitional flow in the context of centrifuge models, attention to possible changes in flow regime and the resulting consequences of those changes is important and must be considered in selecting model scale, and thus acceleration, along with considering any changes required to model grain size, compared to that existing in the prototype.

## 7 ACKNOWLEDGMENT

This paper was based on experimental work by C.A. Babendreier, and was prepared with his assistance.

## REFERENCES

- Al-Hussaini, M.M., D.J. Goodings, A.N. Schofield, and F.C. Townsend 1981. Centrifuge modeling of coal waste embankments. *J. of Geotechnical Eng.*, ASCE, Vol. 107, No. GT4:481-499.
- Babendreier, C.A. 1991. Grain size effect on the time scales in centrifuge modelling of saturated steady state seepage in particulate media. M.S. thesis, University of Maryland, 56p.
- Bear, J. 1979. *Hydraulics of Groundwater*. New York: McGraw-Hill.
- Goodings, D.J. 1982. Relationships for centrifugal modelling of seepage and surface flow effects on embankment dams. *Geotechnique* 32:149-152.
- Goodings, D.J. 1984. Relationships for modelling water effects in geotechnical models. *Proc. Applic. of centrifuge modelling to geotechnical modelling*. Univ. of Manchester, 1-23.
- Goodings, D.J. 1987. Unexpected scaling effects in flow through centrifuge models, *Ninth European Conference on Soil Mechanics and Fdn Engg.*, Aug. 31-Sept. 3, 1987, Dublin, Ireland.
- Laut, P. 1975. Application of centrifugal model tests in connection with studies of flow patterns of contaminated water in soil structures. *Geotechnique* 25: 401-406.
- Muskat, M. 1937. *The flow of homogeneous fluids through porous media*. New York: McGraw-Hill.
- Stephenson, D. 1979. *Rockfill in hydraulic engineering*. Amsterdam: Elsevier.

## Initial stage of soft soil consolidation

Zhixian You & Dobrosław Znidarčič  
University of Colorado, Boulder, Colo., USA

**ABSTRACT:** The initial stage of consolidation of Speswhite china clay at very high initial void ratios is studied. The time scaling exponent based on sedimentation and consolidation theories is derived. Tests are conducted under one g and elevated g levels to verify the derived time scaling exponent. The material sampling after the centrifuge tests show that in the lower effective stress range the soil has different compressibility characteristics at elevated g levels than at the normal gravity. Test results show that such change in the compressibility characteristics only affects the initial portion of the settlement curves so that a unique time scaling exponent does not exist in this range. This is also shown to be the case from analysis based on the finite strain consolidation theory.

### 1 INTRODUCTION

Model testing in the centrifuge is based on the assumptions that the material behaves similarly in an  $N_g$  field as it does in 1g environment and that the centrifuge is capable of producing a uniform  $N_g$  field (Tan and Scott, 1985). Similitude is sought between the material behavior in an ideal  $N_g$  field and that in 1g field. The scaling relations are then verified in the centrifuge by "modeling of models tests", when, in most cases, 1g data are not available.

In this paper, the initial stage of soft soil consolidation is studied. Specifically, the time scaling exponent,  $x$ , is derived based on theoretical considerations and then verified in 1g and centrifuge tests. The scaling exponent can be obtained by noting particular average solids contents or percentage consolidation (in terms of settlement) and the corresponding elapsed times to achieve them. The scaling exponent,  $x$ , is then determined as

$$t_A(N_a)^x = t_B(N_b)^x \quad (1)$$

where  $t$ =time to achieve a specific solids content and  $N$  is the acceleration level in tests a and b.

### 2 SCALING RELATIONS

For the consolidation process in the centrifuge, Croce et al. (1984) derived the time scaling exponent,  $x$ , to be 2. Their derivation is based on the forces that play the key role in the consolidation processes. The same result is

obtained by considering the governing equation for consolidation (e.g. Gibson, England, and Hussey, 1967) and the principles of the dimensional analysis (You, 1993). The value has been experimentally verified by the modeling of models experiments (Croce et al., 1984) and there is a general agreement among researchers that the time scaling factor of  $N^2$  is appropriate for the consolidation processes. For the sedimentation process scaling relation is derived from Stoke's law that describes the process:

$$v = \frac{2}{9} \frac{\gamma_s - \gamma_f}{\eta} \left(\frac{D}{2}\right)^2 \quad (2)$$

where  $v$ =velocity of fall of spheres

$\gamma_s$ =specific weight of the sphere (specific weight=density x  $g$  = mass/unit volume x gravity)

$\gamma_f$ =specific weight of fluid (usually water)

$\eta$ =absolute, or dynamic, viscosity of the fluid

$D$ =diameter of sphere

If the same soil is used in both prototype and the centrifuge, as is normally done in the centrifuge tests, then  $D$  is the same.  $\eta$  is considered a material constant which is not gravity level dependent, as, for example, in the scaling derivations shown by Croce et al. (1984). The specific weights are the only gravity dependent variables in the Stokes' law. Therefore

$$V_m = NV_p \quad (3)$$

where the subscripts m and p designate 'model' and 'prototype', respectively. The same result was reported by Davidson and Bloomquist (1980), Bloomquist (1982) and later referenced by Scully et al. (1984). Velocity  $v=u/t$ , where u is the displacement which scales as  $u_m=u_p/N$ , thus

$$t_m = \frac{t_p}{N^2} \quad (4)$$

which is the same relation as that derived based on the consolidation theory. It is interesting to note that Davidson and Bloomquist (1980) did not carry their derivation for sedimentation to the time scale but stopped at the scaling factor for the settling velocity. However, in the later part of the report they state: "As noted previously, Section 4.6, sedimentation time models by a factor n while consolidation time models as  $n^2$ ." Their experimental results seemed to confirm the statement since for the soft soil the scaling exponents between 1 and 2 were obtained in their test analysis. As will be shown later we have a different explanation for these findings and our data indicate that the soft soil characteristics change in the increased gravity environment.

Kynch (1952) introduced a sedimentation theory to deal with "hindered settling" of particles. He made an assumption that the settling velocity depends only on local concentration of solids. No derivation was made based on considerations of the forces acting on the particles. Here, in order to derive scaling exponent for time, one has to assume how the velocity scales. If the scaling exponent for velocity is 1, the scaling exponent for time is 2, which is the same as that obtained based on consolidation theory and the Stokes' law. If the scaling exponent for velocity is 0, however, the scaling exponent for time is 1 which means in spite of the g levels in the centrifuge, the velocities remain the same among the various tests in a series of modeling of models tests, including the prototype, if 1g data are available.

It can be seen that some insight is gained through the scaling of Stokes' equation for settling particles. Thus, in the early stage of the test (when effective stress is zero everywhere), either it is considered a consolidation process or a sedimentation process, the same scaling exponent for time,  $x=2$ , is expected.

### 3. TESTING PROGRAM

To verify the scaling relations derived above, centrifuge tests were conducted in both the 15 g-ton and the 400 g-ton centrifuges at the University of Colorado. Long column tests were also conducted to provide one g prototype data. The test setup consisted of a column, a ruler

attached to the side of the column for settlement reading from a in-flight camera, and a differential pressure transducer for monitoring the dissipation of the excess pore pressure at the bottom of the sample. Test data were used to verify the time scaling exponent in the early stage of consolidation, to check if there was any change in soil compressibility characteristics under elevated g levels and to verify the scaling exponent in the later stage of soft soil consolidation.

#### 3.1 Test results and discussions

In the first series of tests the settling velocity in the early stage of soft soil consolidation was examined. Two sets of modeling of models tests were conducted with prototype heights of 1.20m and 2.40m. The results are plotted in Figure 1 and they include initial settling velocities for the centrifuge experiments at 10 and 20 g as well as for the prototype experiment for the 1.2 m high soil column. The results show small velocity variation with the column height and with the gravity level in the centrifuge. However, the initial settling velocities in the centrifuge were much higher than in the prototype and they were higher than the derived scaling relations would predict from the prototype behavior. Clearly there was no similarity between the prototype and the centrifuge experiments. If only the centrifuge experiments were analyzed the time scaling exponents of 1.21 and 1.04 would have been determined for 1.2 m and 2.4 m high prototypes, respectively. These values are comparable to the results reported by Davidson and Bloomquist (1980) obtained in the similar modeling of models experiments in the centrifuge.

The second series of tests was designed to clarify the noted lack of scaling between the prototype and centrifuge experiments. In a previous research project we have studied the properties of a soft soil created from the suspension (Liu, 1990). It was found that the void ratio at the soil surface (zero effective stress) depended on the water content at which the suspension was prepared unless the water content was so low that no sedimentation prior to the consolidation took place. Similar experiments were performed in the centrifuge at 10, 20, and 40g. The Speswhite china clay was mixed at the initial void ratio of 3.6, 6, 8, and 15 and placed in graduated cylinders that were spun in the centrifuge until full consolidation was reached. Water content samples were taken after the test from the surface of each column and the void ratio at the zero effective stress calculated.

The zero effective stress void ratio is plotted against the initial mixing void ratio in Figure 2. The 1g data obtained by Liu (1990) are also included. It is seen that for the soft material, the

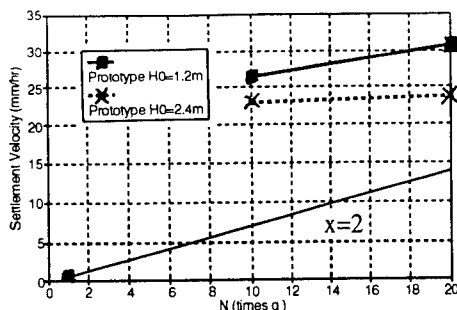


Figure 1 Settlement velocity versus gravity level

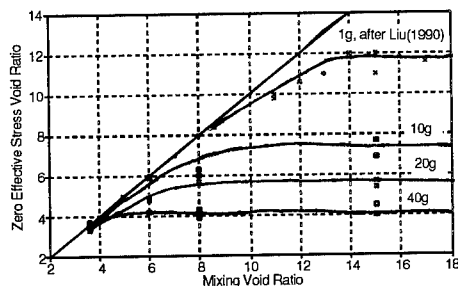


Figure 2 Gravity level dependency of void ratio corresponding to zero effective stress

zero effective stress void ratio is gravity level dependent. The higher the  $g$  level, the lower the void ratio. This relation is valid as long as the mixing void ratio is higher than the void ratio at which no sedimentation takes place which in turn is gravity dependent. For example at 1g the zero effective stress void ratio is equal to the mixing void ratio for the values below 8 while at 40g sedimentation takes place even when the mixing void ratio is as low as 4. It is clear that the materials with different mechanical properties are created in the centrifuge when compared to the lab samples as long as their preparation starts from a diluted suspension. While at normal gravity an increase in the effective stress is needed in order to compress the soil the same compression will be achieved in the centrifuge at the zero effective stress. Since the basic assumption of centrifuge modeling, same constitutive relations for the model and prototype materials, is violated in this case it is not surprising that the experiments show the break up of the scaling relations.

The previous results are not surprising when one considers that a soft soil structure in the soil formation process is the result of the balance among gravity forces causing particles to compress and the attractive and repulsive forces between particles. While the primarily electrostatic forces between the particles remained the same in the centrifuge, the gravity

body forces on the particles increased leading to a different equilibrium condition. The different structure and different zero effective stress void ratio were created as long as the individual particles had sufficient freedom of movement, i.e. as long as the soil suspension was relatively diluted. For the Speswhite clay tested, the freedom of movement for the individual clay particles was restrained at the void ratio of 4 for the gravity levels of up to 40g. For other soils and higher gravity levels this threshold would have to be determined experimentally in a similar testing program.

While the lack of proper scaling is found for the early stage of soft soil consolidation a scaling exponent of 2 is consistently verified for the later part of the process. The settlement records for the 10g and 20g experiments for the same prototype are shown in Figure 3 together with the prototype results of a long column test with initial sample height of 1.2m. The scaling exponent of 2 was assumed to plot the results in the prototype time. The lack of agreement in the beginning of the process is apparent but the curves coincide in the later stage of the self weight consolidation. In the later part of the process the two samples still had different surface void ratios but the thickness of the layer having that void ratio was smaller than at the beginning of the process. The effect can be further demonstrated by performing numerical simulation of the self weight consolidation of two columns having the same amount of solid material but different zero effective stress void ratio. The constitutive properties for the two columns are presented in Figure 4 showing a substantial difference in the low effective stress compressibility characteristics. Uniform initial void ratio distributions equal to the corresponding zero effective stress void ratios were assumed in the analysis. The results presented in Figure 5 show that despite the difference in the zero effective stress void ratio the settlement curves coincide towards the end of consolidation. The lower curve includes a vertical segment at time zero which indicates an instantaneous settlement due to change in the zero effective stress void ratio. In reality there will be a gradual change from the upper to the lower curve as shown in the experimental results (see Figure 3).

### 3.2 Centrifuge test results by other researchers

The presented results are in agreement with those reported by other researchers though they shed a different light and provide different explanation for some of the reported observations. Croce et al.(1984) obtained a time scaling exponent of 2 in the self weight consolidation centrifuge tests of Georgia kaolinite samples. The samples were mixed at an initial void ratio of 2.86 which was apparently

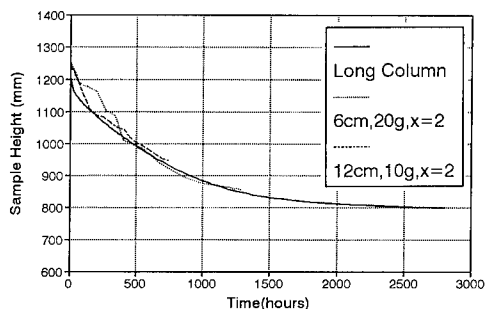


Figure 3 Comparison of results from centrifuge tests ( $x=2$ ) and the long column tests

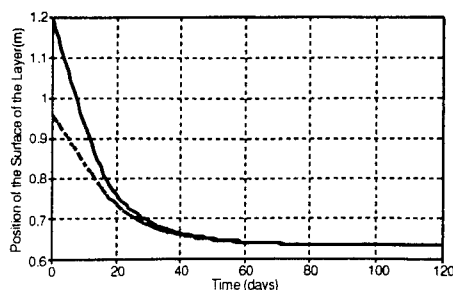
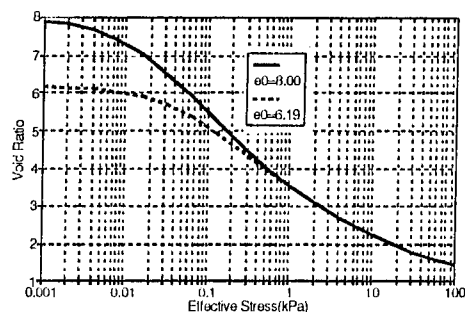
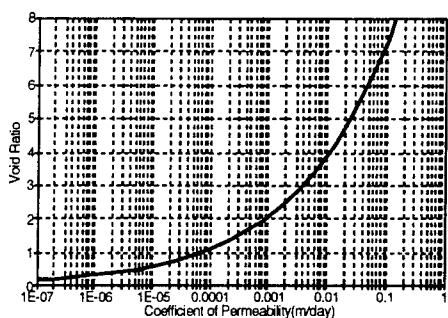


Figure 5 Numerical simulation of two long columns having the same amount of solids but different zero effective stress void ratio



(a)



(b)

Figure 4 Consolidation characteristics of the Speswhite clay used in the analysis

low enough to prevent any reduction in the zero effective stress void ratio due to centrifugation of up to 88g. In addition, prior to placing the sample in the centrifuge the material was allowed to consolidate under its own weight in the laboratory. Thus the soil was formed under 1g condition and a theoretically derived scaling exponent was experimentally confirmed.

Scully et al. (1984) showed an exponent around 2 for time scaling of a phosphatic clay at the void ratio of 15 (15% solids). Davidson and

Bloomquist (1980) and Bloomquist and Townsend (1984) reported for a phosphatic clay at 14% solids values ranging from 1.6 in the initial stage of consolidation to 2.0 in the later part when the average solids content exceeded 20%. These results are in agreement with our findings but our interpretation is quite different. The apparent change in the time scaling exponent should be viewed as the complete breakdown of the scaling law due to the change in the material characteristics caused by the high gravity environment. It should not be attributed to the transition from the sedimentation to the consolidation process since for both processes the time scaling exponent is 2.

#### 4 CONCLUSIONS

The scaling exponent for time in centrifuge modeling of both sedimentation and consolidation processes is 2. It is not 1 for sedimentation as previously reported in the literature. The previously reported apparent deviations from the theoretical value of 2 in the early stages of consolidation of soft soils in the centrifuge is caused by the change of the compression characteristics under the influence of the increased gravity. Thus, a different material is created from a thin slurry in the centrifuge than under normal gravity. This phenomenon violates the basic postulate of centrifuge modeling of soil: the model and prototype materials have the same constitutive properties. The breakdown of the scaling law is not surprising in this case.

When studying the consolidation processes of soft soils in the geotechnical centrifuge the researchers must first confirm, by experiments similar to ones reported here, that the material created in the centrifuge has the same relevant constitutive properties as in the prototype. The critical initial void ratio at which such a condition will be achieved will depend on the material properties and on the gravity level at which the tests will be performed.

## ACKNOWLEDGEMENT

The research presented in this paper was partially supported by the U.S. National Science Foundation. This support is gratefully acknowledged. The authors also thank Hon-Yim Ko, Frank Townsend and David Bloomquist for constructive discussions and for the assistance in getting the critical references needed for this paper.

## REFERENCES

- Bloomquist, D.G. 1982. *Centrifuge modeling of large strain consolidation phenomena in phosphatic clay retention ponds*. Ph.D. dissertation, University of Florida, Gainesville.
- Bloomquist, D.G. & F.C. Townsend 1984. Centrifuge modeling of phosphatic clay consolidation, *Sedimentation consolidation models, predictions and validations*, R.N.Yong & F.C. Townsend (eds) ASCE, New York:565-580.
- Croce, P., V.Pane, D.Znidarčić, H.Y.Ko, H.W. Olsen, & R.L.Schiffman 1984. Evaluation of consolidation theories by centrifuge modeling. *Proceedings of International Conference on applications of centrifuge modeling to geotechnical design*:380-401.
- Davidson, J.L. and D.Bloomquist 1980. *Centrifuge modeling of consolidation/sedimentation process in phosphatic clays*, Research Report 245\*W65, Department of Civil Engineering, University of Florida, Gainesville.
- Gibson, R.E., G.L.England, & M.H.L.Hussey 1967. The theory of one-dimensional consolidation of saturated clays, I. Finite nonlinear consolidation of thin homogeneous layers. *Geotechnique* 17:261-273.
- Kynch, E.J. 1952. A theory of sedimentation. *Transactions of Faraday Society* 48:166-176.
- Liu, J.C. 1990. *Determination of soft soil characteristics*, Ph.D. Dissertation, University of Colorado, Boulder.
- Scully, R.W., R. L. Schiffman, H.W. Olsen, & H.Y. Ko 1984. Validation of consolidation properties of phosphatic clay at very high void ratios. *Sedimentation consolidation models, predictions and validations*, R.N.Yong & F.C.Townsend (eds), ASCE, New York: 158-181.
- Tan, T.S. & R.F.Scott 1985. Centrifuge scaling considerations for fluid-particle systems. *Geotechnique* 35:461-470.
- You, Z. 1993. *Flow channeling in soft clays and its influence on consolidation*, Ph.D. dissertation, University of Colorado, Boulder.

## Study of sedimentation and flow in thickener tanks

R.G.Campbell & M.F.Randolph

*Department of Civil Engineering, The University of Western Australia, Nedlands, W.A., Australia*

**ABSTRACT:** Thickener tanks are used in the production of alumina from bauxite, in order to remove spent liquor from the processing plant. Liquor, consisting of alumina hydrate particles suspended in caustic soda at a solid content of about 100 grammes per litre (gpl), enters at the top of a 20 m high tank which has a conical lower section. The solid particles sediment out towards the base of the tank, where an underflow valve permits extraction of material at increased solids contents in the range 500 - 1000 gpl. Recurring problems in the operation of such tanks is the build up of solid material at the edges of the conical section of the tank, together with central (or funnel) flow of low solid content liquor through to the underflow. Periodically, collapse of the solid material can lead to complete blockage of the underflow, disrupting the process plant. The paper describes a centrifuge-based study of the sedimentation and underflow processes with the ultimate aim of devising improvements in the operation of the thickener tanks. A full discussion is included of the appropriate scaling relationships, together with a description of special instrumentation and flow-visualisation techniques that were developed. Results from a series of tests are presented.

### 1 INTRODUCTION

The production of alumina from bauxite involves the precipitation of alumina hydrate in a liquor of caustic soda. At the end of the precipitation cycle, spent liquor must be separated from the hydrate particles. The larger hydrate particles are passed on to the next stage of processing, while the smaller particles are mixed with fresh liquor and re-injected as seed into the start of the precipitation cycle.

Removal of the spent liquor is accomplished in a two stage 'thickener' process involving sedimentation of the particles in tall tanks, followed by extraction of thickened product from the base of the tanks (referred to as 'underflow'). This paper describes centrifuge modelling of the sedimentation and underflow processes in what are known as the 'secondary' thickener tanks. Background information is presented describing the operation of these tanks. The paper then describes the modelling techniques employed (including a discussion of the scaling relationships) and the results from a series of tests.

### 2 BACKGROUND

The secondary thickener (ST) tanks are 20 m high and 13 m in diameter, with a conical base section (see Figure 1). Liquor consisting of (spent) caustic soda and particles of alumina hydrate at a solid content of approximately 100 grammes per litre (gpl) is injected at the top of the tank. The solid particles sediment out towards the base of the tank, and the resulting thickened liquor is then extracted through an underflow valve of diameter 0.25 m at the base of the cone.

Different plants operate either as a batch process, where a time delay of 3 - 5 hours is allowed for sedimentation before extracting a batch of thickened liquor, or as a continuous underflow process. In either case, average throughput is some 250 m<sup>3</sup>/hr, and the target solid content of the underflow is in the range 500 - 800 gpl. The higher the solid content of the liquor, the less spent caustic soda is extracted, and the more economic is the overall process. Efficient thickener operation is therefore of utmost importance to the industry.



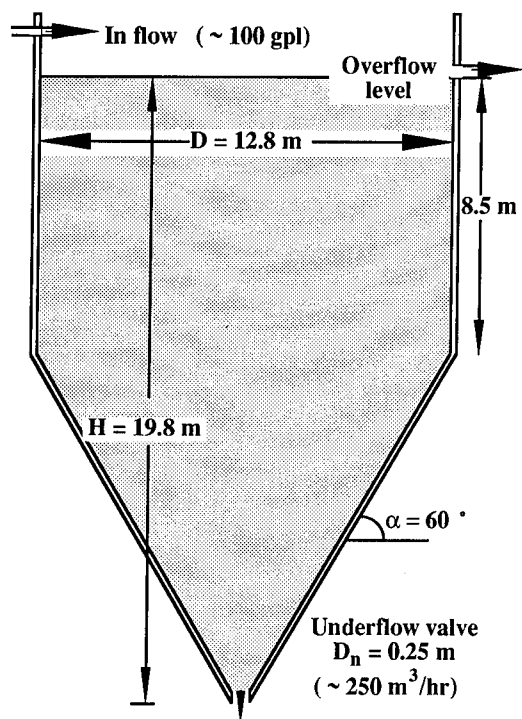


Figure 1 Prototype secondary thickener tank

The alumina hydrate particles have a specific gravity of 2.42, and the fraction that arrives at the inflow of the ST tank is relatively uniformly graded, with a mean diameter of 120  $\mu\text{m}$  and coefficient of uniformity of 2. The particle size distribution is shown in Figure 2.

The target solid content of 800 gpl at the underflow should be viewed in terms of the loosest packing of the dry hydrate, which gives a minimum dry density of  $\rho = 1100 \text{ kg/m}^3$ . Since the dry density in  $\text{kg/m}^3$  is equivalent to the solid content in gpl, the target solid content is only about 70 % of the density at which full particle contact may be expected. Thus, in principle, the underflow liquor should behave more as a viscous fluid than a weak soil.

In practice, however, operational problems occur with the ST tanks which appear to be associated with a build up of fully sedimented (and consolidated) material on the conical sides, accompanied by 'funnel' flow of liquor of low solid content close to the central axis of the tanks. Periodically, the sedimented material at the sides collapses into the centre, leading to complete blockage of the underflow, which may only be rectified by blasting.

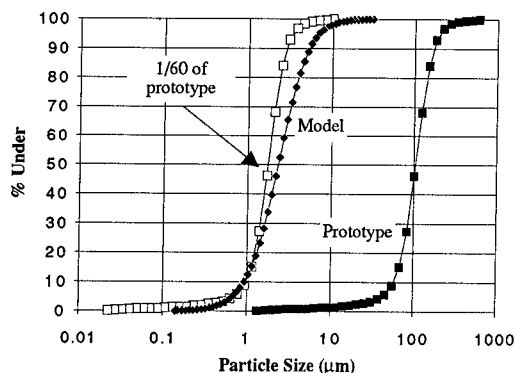


Figure 2 Particle size distributions of prototype and model material

### 3 MODELLING

In order to investigate the sedimentation and flow processes within the ST tanks, a series of centrifuge model tests were undertaken, at an acceleration level of 60 g. The rationale for centrifuge modelling, and relevant dimensionless scaling relationships are discussed here.

With reference to Figure 1, the solid content of the underflow,  $S_u$ , may be written as a function of the other key variables, as

$$S_u = f(S_i, H, D, D_n, \alpha, \rho_f, \mu_f, \rho_s, d_{50}, v, g) \quad (1)$$

where:

$S_i$  is the solid content at the inflow

$H$  is the overall height of the tank

$D$  is the diameter of the upper part of the tank

$D_n$  is the diameter of the underflow valve

$\alpha$  is the cone angle (from horizontal)

$\rho_f$  is the density of the fluid

$\mu_f$  is the viscosity of the fluid

$\rho_s$  is the density of the solids

$d_{50}$  is the mean particle diameter of the solids

$v$  is the mean downward velocity in the upper part of the tank (this may be expressed alternatively in terms of a sedimentation time,  $t = H/v$ , for batch operation).

$g$  is the gravitational acceleration.

The variables may be arranged in eight independent non-dimensional groups (numbered  $\pi_1$  to  $\pi_8$ ) as:

$$S_u = f\left(S_i, \frac{H}{D}, \frac{D_n}{D}, \frac{D_n}{d_{50}}, \alpha, \frac{\rho_f}{\rho_s}, \frac{(\rho_s - \rho_f)gd_{50}^2}{v\mu_f}, \frac{v}{\sqrt{gH}}\right) \quad (2)$$

The first six groups are self-explanatory. The

final two groups correspond to (a) the ratio of sedimentation velocity to throughput velocity, and (b) the Froude number for the flow.

Two additional groups may be obtained by combinations of the other groups. The first of these is  $\pi_9 = \rho_f g H D / \nu \mu_f$  which corresponds to the ratio of fluid stress to the viscous shear stress; the second is  $\pi_{10} = \rho_f D v / \mu_f$ , the Reynolds number for the tank flow, which will determine whether the flow is turbulent or laminar. The dimensionless groups that involve velocity will vary through the conical section of the tank. These groups may be evaluated in terms of the upper velocity,  $v$ , and the underflow velocity,  $v_u$ .

The two key groups among  $\pi_7$  to  $\pi_{10}$  are (a) the ratio of sedimentation velocity to the mean flow velocity in the tank ( $\pi_7$ ), and (b) the ratio of total stress to viscous shear stress ( $\pi_9$ ). In order to achieve similarity of both of these ratios, it is necessary that the model tests are carried out at an elevated  $g$  level, using model material where the particle size is reduced by the same ratio as the increase in  $g$  level.

The increase in  $g$  level can be achieved by centrifuge modelling, and a convenient scaling ratio on the linear dimensions is 1:60. In order to simplify the experimental conditions, it was decided to use water as the fluid, rather than the more viscous caustic soda (viscosity 2.5 times that of water, specific gravity 1.22).

The particle size of the prototype alumina hydrate was reduced by wet-grinding in a small ball mill. Figure 2 shows the resulting particle size distribution, which was found to be remarkably consistent from batch to batch. It may be seen that the mean size of the model material is still rather too large (at 3.5  $\mu\text{m}$ , rather than 2  $\mu\text{m}$ ). However, it was considered that this was sufficient for initial modelling purposes. Effectively, the use of a less viscous fluid, and particles that are oversize, will entail that the timescale of sedimentation will be reduced. Combining the effects of imprecise modelling of the fluid and the particle size leads to an overall decrease in timescale by a factor of about 9. Table 1 provides a summary of the key dimensionless groups at model and prototype scales.

It must be emphasised that the time scaling by a factor of 9 is that between centrifuge model test and true prototype. The paper also presents results from sedimentation tests where the model was tested in the laboratory at 1  $g$ . The time scaling between those tests and the centrifuge tests is by a factor of 60.

Table 1 Summary of dimensionless groups

Group	Description	Prototype	Model
$\pi_1$	Inflow solid content	0.05	0.05
$\pi_2$	Aspect ratio	1.55	1.55
$\pi_3$	Underflow ratio	51.2	30
$\pi_4$	Underflow/particle ratio	2080	2080
$\pi_5$	Cone angle	60°	60°
$\pi_6$	Density ratio	0.50	0.41
$\pi_7$	Sedimentation velocity ratio	125	125
$\pi_8$	Froude No.	$39 \times 10^{-6}$	$6 \times 10^{-6}$
$\pi_9$	Stress ratio	$2 \times 10^{12}$	$5 \times 10^{11}$
$\pi_{10}$	Reynolds No.	3400	1700

The above values are based on (a) increasing the diameter of the model underflow valve from the true scaled value of 4 mm, to 7 mm in order to maintain the same ratio of diameter to particle size, and (b) adjusting the mean throughput velocity in order to achieve equal sedimentation velocity ratios in model and prototype. As mentioned above, this will reduce the timescale of the model experiment by one order of magnitude.

A consequence of using particles of reduced size in the model tests is a change in the consolidation and general packing response. Thus, the model hydrate has a minimum density of 740  $\text{kg/m}^3$  (compared with 1100  $\text{kg/m}^3$  for the prototype material). Thus the target solid content at the underflow should be reduced to around 500 gpl, rather than the prototype value of 800 gpl.

### 3.1 Apparatus and Instrumentation

An important aspect of the model tests was to obtain visual information on the flow pattern within the tanks. As such, it was decided to model half of a complete tank, with a flat acrylic plate on the diametral plane. For fabrication purposes, two tanks were machined together, and the finished tanks are shown in Figure 3.

Two novel instrumentation procedures were developed for assessing the sedimentation and flow within the tank. In the initial experiments, a method presented by Baker (1966) was adapted. This method uses a pH indicator in the model liquor, together with an electrically

induced local change of acidity (and resulting colour change). Electrode wires were placed across the inside of the front face of the tank. Thymol blue indicator was added to the liquor (0.1 gpl) which was then titrated to the end-point using a small amount of dilute hydrochloric acid (0.6 ml per litre). This left a solution which was a pale yellow colour, compared with the pure white of the hydrate mix.

At appropriate points in the test, an electric current was passed along the exposed wires in the tank, resulting in a local colour change from yellow to blue in the vicinity of each wire. The movement of the blue markers then allowed the flow patterns to be observed. Figure 4 shows the resulting pattern, with clear evidence (in the original colour photo) of central funnel flow.

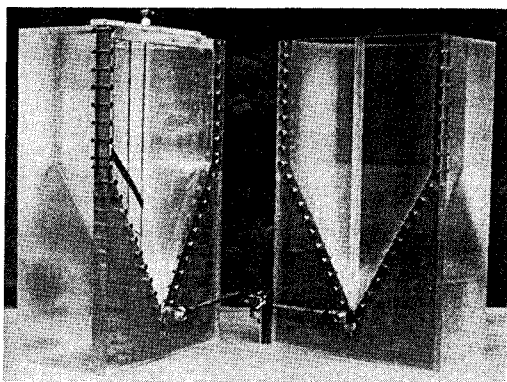


Figure 3 Model secondary thickener tanks

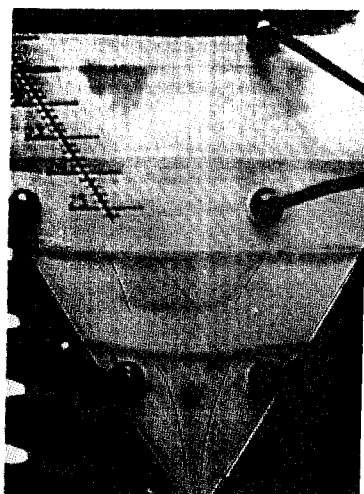


Figure 4 Observed funnel flow using pH indicator.

The other primary piece of instrumentation comprised resistivity gauges. These were fabricated directly from printed circuit boards, with pairs of gold electrodes, 2 mm apart, at spacings of either 9 mm or 18 mm along the board, as shown in Figure 5. Note, the wedge shape is to accommodate the increasing number of connections along the board. Generally, one probe was placed vertically on the inside of the front face, and one probe was placed against the sloping face of the base cone.

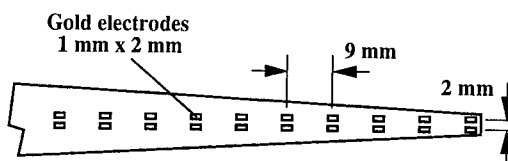


Figure 5 Resistivity probe

The resistivity probes were found to be particularly sensitive at relatively high solid contents, but less accurate at solid contents below about 100 gpl. They were therefore excellent at detecting an increase in solid content near the base of the tank, but less reliable for detecting any reduction of solid content in the upper part of the tank.

A resistivity gauge was also positioned in the outlet pipe from the underflow, allowing the underflow solid content to be measured directly.

Pore pressure transducers were placed in the face of the tank (see Figure 4) in order to measure the pressure distribution down the tank. In principle, the sedimentation process will lead to a change in the liquor density at each level, and hence a change in the pressure distribution. However, these changes are small, and are difficult to separate with confidence from changes in zero offset of each transducer due to small changes in temperature. A pore pressure transducer placed within the upper half of the tank allowed an accurate measurement of the liquor level within the tank, and hence the volume of underflow.

In addition to tests carried out in the model ST tanks, centrifuge and laboratory floor sedimentation tests were undertaken in a cylindrical tank, 130 mm in diameter and 325 mm high. These tests provide background information on the sedimentation performance of the hydrate.

## 4 TEST RESULTS

The model tests were conducted on the centrifuge at the University of Western Australia (Randolph et al, 1991). For each test, a batch of ground alumina hydrate was prepared to a solid content of 100 gpl, and sufficient dispersant was added to prevent any flocculation of the small hydrate particles.

The liquor was added to the tank immediately prior to starting the centrifuge. In interpreting and presenting the results, zero time was taken when the centrifuge was started, and the time during spin-up was factored by the ratio of current g-level to the final value (60 g) in order to provide an equivalent time at 60 g.

The results below are divided into two main sections, dealing respectively with sedimentation in a cylindrical tank and in the model ST tank, and performance during regulated underflow from the ST tank.

### 4.1 Sedimentation

Profiles of solid content at different times after the start of the test are shown in Figure 6 for sedimentation in a cylinder and in the model ST tank. The key features are:

- (1) More rapid increase of solid content in the ST tank than in the cylinder.
- (2) A tendency for the interface between sedimented material and the liquor to become very sharp as the surface area increases.
- (3) Gradual zero drift of the resistivity probes with time so that the solid content in the upper liquor appears to drop to zero and below.

The progress of the sedimentation front with time is shown in Figure 7. Interestingly, for a given time, the height of the sediment interface is very similar for both the vertical probe and the probe on the sloping side of the tank, if anything with a tendency for the interface to be higher on the central axis. Thus the paths of the downward moving particles must curve inwards, following the contours of the tank, rather than be vertical (the latter situation would give rise to high solid content at small times over the full length of the probe on the sloping face).

Also shown in Figure 7 for comparison is the sediment build up in the 1 g experiment, where the time has been factored by 1/60. The sediment build up in the 1 g experiment is a little slower than in the centrifuge test, and also, the

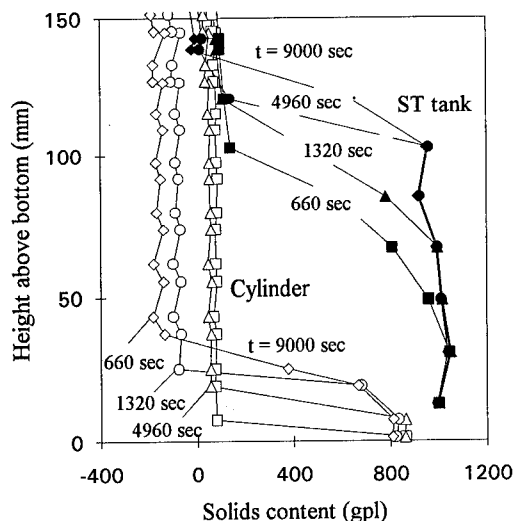


Figure 6 Profiles of solid content during sedimentation

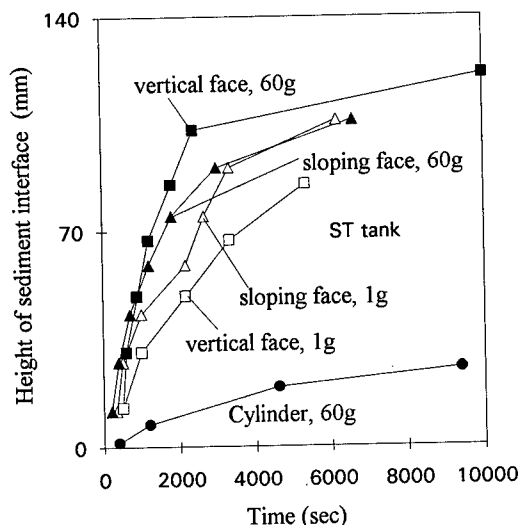


Figure 7 Variation of sediment interface height  
sediment tends to build up more rapidly on the sloping face than on the vertical probe.

### 4.2 Flow Performance

Underflow from the ST tank was controlled by means of a solenoid operated valve. Initially, this was a simple open/closed valve, but in the later experiments, a variable opening valve was incorporated, in order to improve control. Early

experiments showed that the underflow valve could become blocked very easily, once the solid content near the base of the tank exceeded the critical value at which particle contact was established (700 - 800 gpl for the model material). The aim of the tests was therefore to maintain a solid content of about 600 gpl near the base of the tank, while maintaining a relatively uniform underflow rate.

Figure 8 shows the variation of solid content obtained from one of these tests. Initially, the solid content at the base of the tank built up to about 1000 gpl, and the underflow blocked. The blockage was cleared by injecting air under pressure, and then more uniform underflow was achieved for the rest of the test (times after 800 sec). The control of the flow-rate was rather coarse, resulting in fluctuation of solid content measured by the resistivity gauge near the tank base. However, the underflow pipe maintained an even solid content of about 450 gpl.

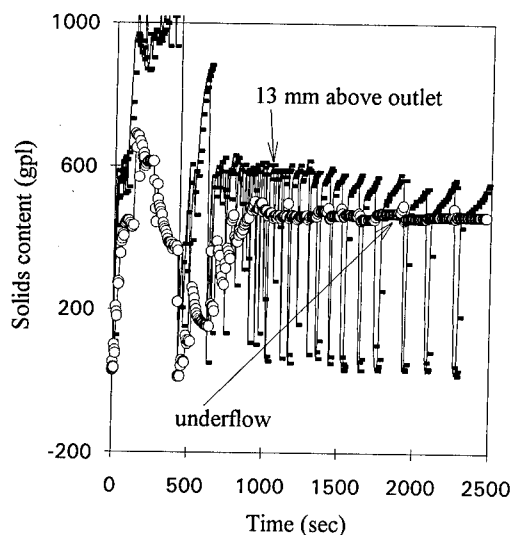


Figure 8 Variation of solid content near base of tank and in underflow pipe during underflow

Figure 9 shows the cumulative volume of underflow measured during the test. Once conditions had stabilised, the average underflow rate over a period of just under 2000 seconds was about 0.8 ml/s. Interestingly, there was no evidence of any additional build up of solid content on the conical face of the tank during the above experiment. Thus, although funnel flow had been observed in a previous test (Figure 4) the flow regime from this later test indicated

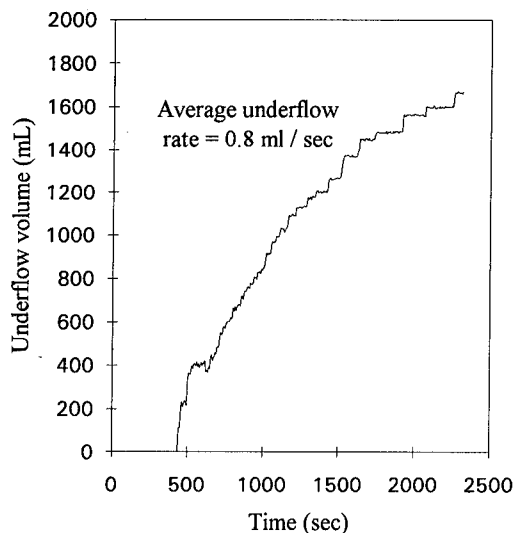


Figure 9 Underflow volume versus time

uniform flow across the full area of the tank.

## 5 CONCLUSIONS

This paper has described centrifuge model tests undertaken to explore the sedimentation and flow of alumina hydrate in thickener tanks. The tests showed that the underflow could become blocked very easily if the solid content was allowed to build up. However, process control using resistivity gauges to quantify the solid content in the vicinity of the underflow valve, led to relatively uniform and extended underflow at moderately high solid contents.

## REFERENCES

- Baker, D.J. 1966. A technique for precise measurement of small fluid velocities. *J. fluid Mech.* Vol 26(3), pp 573-575.
- Randolph, M.F., R.J. Jewell, K.J.L. Stone & T.A. Brown 1991. Establishing a new centrifuge facility, *Proc. Centrifuge 91*, Colorado, Ed. Hon-Yim Ko, Balkema, pp 3-9.

## ACKNOWLEDGMENT

The work described in this paper was funded by Alcoa of Australia; the authors would like to express their appreciation for permission to publish this paper and for input to the work from Mr Greg Mills and Mr Trevor Osborne.

## Determination of soil hydraulic properties

Brian Cooke

Department of Civil Engineering, The University of Western Australia, Nedlands, W.A., Australia

**ABSTRACT:** Modelling flow phenomena through the unsaturated zone requires the establishment of the relationships among soil suction, moisture content, and hydraulic conductivity. Current techniques for measuring or estimating these functions in the laboratory are difficult, time consuming, and somewhat uncertain. This paper proposes a technique of determining these relationships using parameter estimation, based on measurement of cumulative outflow under gravity drainage from an initially saturated soil column. The effectiveness of this technique has previously been demonstrated theoretically, but not implemented due to the inordinately long times required to drain a suitably tall soil column at one *g*. The increased gravity field of the geotechnical centrifuge permits application of these techniques to model columns representing much longer prototypes than are attainable in the laboratory.

### INTRODUCTION

Much of the current research effort into migration of contaminant plumes through soil is directed towards understanding and predicting flow through the unsaturated zone. Among the required inputs into numerical models used to study these processes are the functions describing the dependence of soil volumetric water content on capillary pressure head ( $\theta=\theta(h)$ ), and hydraulic conductivity on capillary pressure head ( $k=k(h)$ ).

Currently, the most common means of determining the  $\theta(h)$  relationship is through pressure extraction tests, a procedure which requires between 24 and 72 hours to determine each point on the curve. The  $k(h)$  relationship is usually determined indirectly through measurement of the soil diffusivity, itself a painstaking procedure involving either considerable time (volumetric measurement of water outflow as the pressure on a soil sample is increased incrementally) or elaborate and expensive equipment (e.g., tracing the advance of a wetting front through gamma radiation techniques). Furthermore, different methods of measuring the  $k(h)$  function yield different

results, and it is unclear which technique best represents the actual soil characteristics (Dane, 1980; Ragab *et al.*, 1981).

Because of the difficulty in establishing the true  $k(h)$  relationship, a frequently used option is to not measure this relationship at all, but to assume that it can be defined by the same parameters defining the  $\theta(h)$  relationship. Using this approach, a number of points on the  $\theta(h)$  curve are determined experimentally, and fitted to an assumed functional form defined by two or three curve fitting parameters. The best fit values of these fitting parameters are then substituted into another function which is assumed to describe the  $k(h)$  relationship. Two of the most often used models of this type are that introduced by Brooks and Corey (1964) and the van Genuchten (1979) model. The Brooks-Corey model is defined by:

$$\theta = \begin{cases} \left( \frac{h_D}{h} \right)^\lambda & h > h_D \\ \theta = 1 & h \leq h_D \end{cases} \quad (1)$$

$$k = k_s \Theta^{2+3\lambda} \quad (2)$$

Where  $h_D$ , the displacement or air entry pressure head, and  $\lambda$ , the pore size distribution index, are fitted parameters.  $k_s$  is the saturated hydraulic conductivity.  $\Theta$  is the effective saturation, defined as:

$$\Theta = \frac{\theta - \theta_R}{\theta_s - \theta_R} \quad (3)$$

where  $\theta$  is the volumetric water content, and  $\theta_R$  and  $\theta_s$  are the residual and saturated water content, respectively.  $\theta_R$  may be a fitted parameter, or may be determined or assumed based on other tests.

The van Genuchten model is:

$$\Theta = (1 + (\alpha h)^n)^{\frac{1}{n}-1} \quad (4)$$

$$k = k_s \sqrt{\Theta} (1 - (1 - \Theta)^{1/n})^{1-1/n} \quad (5)$$

where  $\alpha$  and  $n$  are curve fitting parameters, and other terms are as defined previously.

The problem with this approach is that, although the connection between the  $\theta(h)$  and  $k(h)$  relationships is theoretically valid, in fact it is frequently the case that the values of the fitting parameters which give the best fit for the  $\theta(h)$  curve, when substituted into the assumed  $k(h)$  function, do not give a very good fit to the actual  $k(h)$  relationship (Alexander and Skaggs, 1986; Valiantzas and Kerkides, 1990). For low degrees of saturation, the error in the value of hydraulic conductivity as determined by this technique can be a number of orders of magnitude. Thus it has long been apparent that there is a need for a quick, accurate method of determining these relationships, and particularly the  $k(h)$  function.

The idea of determining these relationships through inverse, or parameter estimation techniques has been discussed in the technical literature for more than a decade. Zachmann *et al.* (1981) proposed parameter estimation as an effective means of determining soil hydraulic properties from data collected by observing the gravity drainage of an initially saturated column of soil. However, the practical applicability of this technique is severely limited by the restrictions on column lengths

attainable in the laboratory under normal gravity, and the time required for drainage to occur in relatively fine-grained soils. These problems were addressed in companion papers by Kool *et al.* (1985) and Parker *et al.* (1985), who introduced three methods of determining hydraulic properties from one-step outflow experiments. Unfortunately, each of these methods suffers from some shortcomings, and the developers concede that the test is inferior to the standard stepwise method in terms of accuracy, but provides considerable advantage in speed.

Using a geotechnical centrifuge, the techniques of Zachmann *et al.* (1981) could be applied to model columns representing much longer prototypes than are attainable in the laboratory. In accordance with well-established centrifuge scaling relationships (Goodings, 1984; Schofield, 1980), the time required for drainage of the column to take place would be reduced by the square of the scale factor. Thus centrifuge modelling at 100g, for example, allows duplication in 1 hour of flow processes which would take 10000 hours in real time.

## PARAMETER ESTIMATION

The parameter estimation technique is based on the assumption that the  $\theta(h)$  and  $k(h)$  relationships are defined by mathematical expressions with a small number of parameters, such as the Brooks-Corey and van Genuchten expressions given above. The problem is to determine the relationships by determining the best values of these unknown parameters. Experimentally, this involves measurement of some flux controlled attribute during transient flow. The flow process is then simulated numerically, using guessed initial values of the parameters; simulations are repeated with improved guesses of the parameters until the difference between the simulated and experimental data is minimized. The potential value of this method to determine  $\theta(h)$  and  $k(h)$  functions using data from column drainage experiments has been demonstrated by Zachmann *et al.* (1981) through numerical simulations. Their results indicated that the most useful experimental data for this purpose is a record of cumulative discharge from the initially saturated column versus time.

It is desirable to minimize the number of unknown parameters in order to improve the "well-posedness" of the problem. Thus the models already discussed are well suited to this technique in that there are only two unknown parameters to determine in order to define both the  $\theta(h)$  and  $k(h)$  relationships. However, as mentioned above, using the same parameters to describe both relationships does not result in a very good fit for either. Simply put, when using these interdependent models in parameter estimation some of the error in  $k(h)$  is forced into the  $\theta(h)$  relationship, and vice versa. Experience has shown that a much better fit to the data can be obtained by using parameters in the  $k(h)$  relationship which are independent of those in the  $\theta(h)$  relationship. In order to do this, while still maintaining a low number of parameters, it has been found that a convenient form of the  $k(h)$  relationship is a power function similar to the Averjanov-Irmay model:

$$k = k_s \Theta^\beta \quad (6)$$

with the fitting parameter  $\beta$  being a function of the pore size distribution, rather than a universal constant as suggested by Irmay (1954). Note that this is of the same form as the Brooks-Corey model, but the exponent of  $\Theta$  is independent of the  $\theta(h)$  relationship.

For the current research the Averjanov-Irmay  $k(h)$  model was used together with the van Genuchten  $\theta(h)$  model. The latter was selected because it has the advantage of providing a continuous differentiable function, which eliminates the programming problems associated with models displaying discontinuity at the air entry value, such as the Brooks-Corey model. Thus there are three parameters to be determined from the data resulting from partial drainage of an initially saturated column -  $\alpha$  and  $n$  for the  $\theta(h)$  function, and  $\beta$  for the  $k(h)$  function.

It is possible to adapt the technique to provide a more accurate estimate of  $k(h)$  by determining  $\theta(h)$  by means other than parameter estimation, thus reducing the problem to one of estimating a single parameter. One method of achieving this is to allow the column drainage to proceed for a time sufficiently long that the column's moisture content profile approaches equilibrium. In this case, the  $\theta(h)$  relationship

can be determined at the end of the test by sectioning the column into horizontal slices and measuring the water content of each slice. The plot of water content versus elevation is equivalent to the  $\theta(h)$  relationship, since at equilibrium the elevation potential is equal to the soil suction, or capillary potential.

For lower permeability soils it is frequently not possible to drain the column to equilibrium, even in the accelerated time frame simulated by the geotechnical centrifuge. An option in this case is to establish  $\theta(h)$  by standard laboratory techniques. Otherwise it is necessary to determine both  $\theta(h)$  and  $k(h)$  by parameter estimation, which performance reduces the accuracy with each individual relationship is determined.

## EXPERIMENTAL METHOD

Two different soils were used to demonstrate the parameter estimation technique; Shirley Bay sand and UWA sand, both fine grained silty sands. Gradations for the two soils are shown in Figure 1. Saturated hydraulic conductivity and  $\theta(h)$  relationships were determined by standard techniques for both sands, but  $k(h)$  was only determined experimentally for the UWA sand.

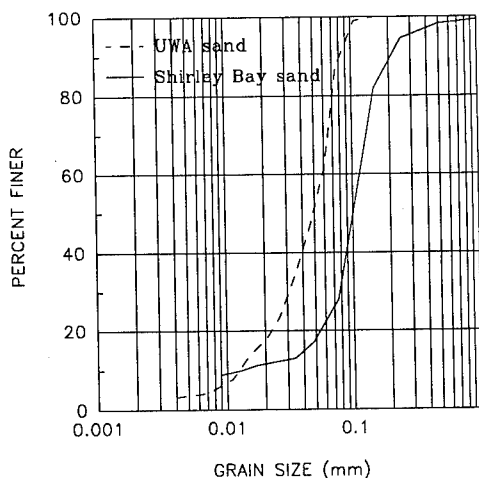


Figure 1. Soil grain size distributions.

For the drainage tests a column of saturated soil was placed in the centrifuge and accelerated to the target  $g$  level. Drainage was



Table 1. Model and prototype details

Sand	$k_{sat}$ (cm/s)	$g$	Column height (cm)		Drainage time (hours)	
			Model	Prototype	Model	Prototype
UWA	$3.0 \times 10^{-4}$	80.0	30.2	2418	3	19200
Shirley Bay	$3.3 \times 10^{-5}$	48.7	27.6	1342	12	28460

then allowed to begin by opening a valve at the base of the column. Throughout the test the condition of a constant water level at the base of the column was maintained. The water draining from the column ran into a tank mounted on pressure transducer, providing a continuous plot of cumulative outflow with time. The test was run for a predetermined length of time, considered sufficient to permit substantial completion of the column drainage. At the completion of the test on the Shirley Bay sand, the column was sectioned to establish the final moisture content profile. Unfortunately, the apparatus for the test on the UWA sand was not configured to permit sectioning of the column.

The models represented prototype soil columns between 13 and 24 meters deep, draining for up to 28000 hours. Model and prototype details are shown in Table 1.

#### COMPUTER MODEL

The computer program "PARMEST" comprises two modules; a parameter estimation routine based on the method of steepest descent, and "RICHARDS", a finite difference implementation of the Richard's equation for a draining soil column. The parameter estimation routine repeatedly calls "RICHARDS" as a subroutine during the estimation process. Upwards of 30 calls may be involved, resulting in lengthy computer runs. In some cases the parameter estimation computation process took over eight hours on a 33MHz 486 computer.

"PARMEST" was used with the centrifuge data in a number of different ways. Firstly, it was used to estimate the three parameters which define the two required relationships. It was then used with the same data to determine only the  $k(h)$  function, with the  $\theta(h)$  relationships input using known parameters

determined from the pressure plate tests. Thus the second determination was of the one parameter defining the Averjanov-Irmay model. For the Shirley Bay sand, a third determination was made, again to establish only  $k(h)$ , but this time with the input  $\theta(h)$  as determined from sectioning the column at the end of the drainage test.

#### RESULTS

For evaluation of the effectiveness of the techniques in establishment of the  $\theta(h)$  function it is most useful to look at the tests with the Shirley Bay sand, where there are three different determinations, as shown in Figure 2. It can be seen that the function fitted to the results of sectioning the column at the end of the test approximates quite closely the true relationship as determined by pressure plate tests. The curve determined by parameter estimation gives a somewhat poorer fit to the actual relationship at higher suctions.

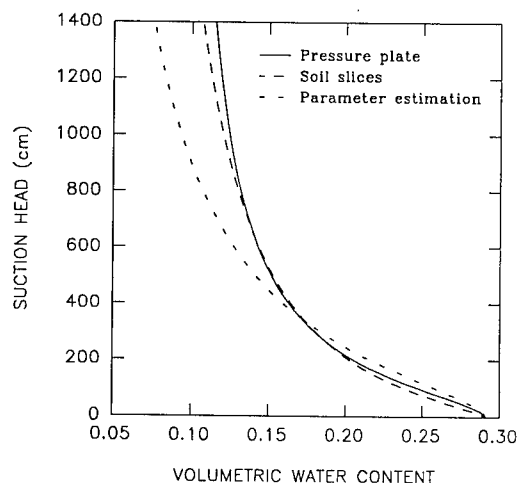


Figure 2. Shirley Bay sand  $\theta(h)$  determinations.

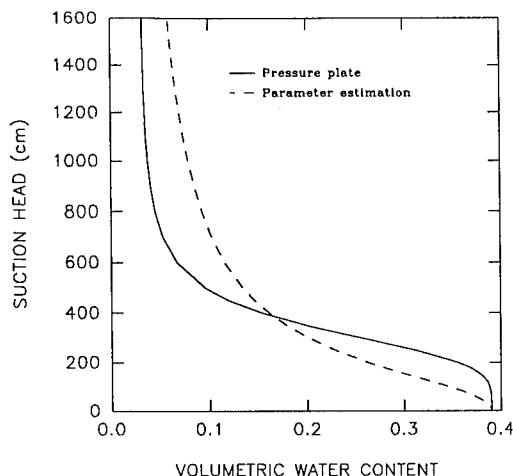


Figure 3. UWA sand  $\theta(h)$  determinations.

For the UWA sand it again appears that using the three parameter estimation routine gives only a rough approximation to the actual  $\theta(h)$  relationship as determined by pressure plate tests (Figure 3).

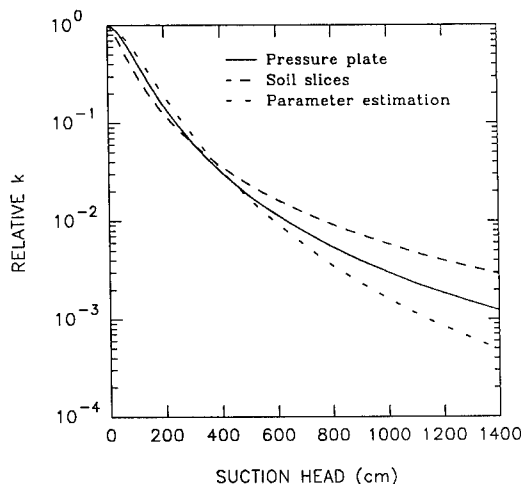


Figure 4. SB sand  $k(h)$  determinations.

For the Shirley Bay sand there are also three estimations of the hydraulic conductivity function, as shown in Figure 4. Relative  $k$ , plotted on the vertical axis, is the hydraulic conductivity at a given pressure divided by the saturated hydraulic conductivity. The two plots in which only one parameter was estimated are labelled according to the source of the  $\theta(h)$

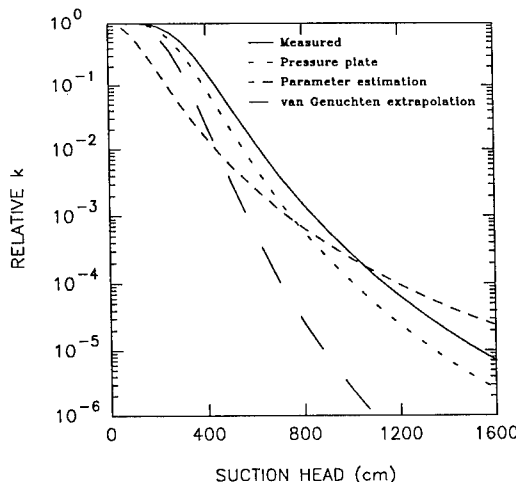


Figure 5. UWA sand  $k(h)$  determinations.

data, while the plot labelled "parameter estimation" represents the result of estimating all three parameters. The agreement among the three methods is remarkably good, with a difference of less than an order of magnitude among them at the highest suction head encountered in the test.

To evaluate the significance of the hydraulic conductivity functions, it is necessary to examine the results of testing using UWA sand, for which  $k(h)$  was experimentally determined prior to centrifuge testing. Figure 5 shows the curves determined by laboratory diffusivity tests, three parameter estimation, and one parameter estimation with the  $\theta(h)$  data from pressure plate extraction tests. Also shown is the curve extrapolated by using the parameters established by the pressure plate testing in the van Genuchten  $k(h)$  model; this is the curve which would be used if no centrifuge testing were done, as described in the introduction.

It is apparent that the one parameter estimation method gives good agreement with the laboratory values, whereas the three parameter technique gives somewhat poorer, but still reasonable, results. The agreement of these three curves within an order of magnitude over the test range compares very well with the curve extrapolated from pressure plate  $\theta(h)$  data using the van Genuchten model, which departs from the measured values by over four orders of magnitude at 1600 cm of suction.

## CONCLUSIONS

A method of determining the hydraulic properties of soils by centrifuge testing and parameter estimation has been presented, with experimental results indicating that the parameter estimation aspect is particularly useful for determining the  $k(h)$  relationship alone. Rough approximations of both  $\theta(h)$  and  $k(h)$  can be determined as well, although the degree of uncertainty in each of the parameters increases with increasing number of parameters.

The most promising use of the combination of centrifuge testing and parameter estimation is in working with soil columns which will drain to near equilibrium in a reasonable length of time (say, 10000 hours prototype time, or 4 hours at 50g). In this case, if the column apparatus is configured to permit rapid determination of the moisture profile at the end of a test,  $\theta(h)$  can be determined by direct measurement and  $k(h)$  by parameter estimation. This permits in one day a fairly accurate determination of two relationships which currently can take months of testing to establish.

## REFERENCES

- Alexander, L., and R.W. Skaggs (1986). "Predicting unsaturated hydraulic conductivity from the soil water characteristic." *Transactions of the ASAE*, 29(1), 176-184.
- Brooks, R.H., and A.T. Corey (1964). "Hydraulic properties of porous media." Hydrology Paper No. 3, Colorado State University, Fort Collins, Co.
- Dane, J.H. (1980). "Comparison of field and laboratory determined hydraulic conductivity values." *Soil Science Society of America Journal*, 44(2), 228-231.
- Goodings, D.J. (1984). "Relationships for modelling water effects in geotechnical centrifuge models." In: W.H. Craig (ed.) *Application of Centrifuge Modelling to Geotechnical Design*, 1-24.
- Irmay, S. (1954). "On the hydraulic conductivity of unsaturated soils." *Transactions of the American Geophysical Union*, 35, 463-468.
- Kool, J.B., J.C. Parker, and M.Th. van Genuchten (1985). "Determining soil hydraulic properties from one-step outflow experiments by parameter estimation: I. Theory and numerical studies." *Soil Science Society of America Journal*, 49(6), 1348-1354.
- Parker, J.C., J.B. Kool, and M.Th. van Genuchten (1985). "Determining --soil hydraulic properties from one-step outflow experiments by parameter estimation: II. Experimental studies." *Soil Science Society of America Journal*, 49(6), 1354-1359.
- Ragab, R., J. Feyel, and D. Hillel (1981). "Comparative study of field and laboratory methods for determining the hydraulic conductivity function of a sand." *Soil Science*, 131(6), 375-388.
- Schofield, A.N. (1980). "Cambridge geotechnical centrifuge operations." *Geotechnique*, 30(3), 227-268.
- Valiantzas, J.D., and P.G. Kerkides (1990). "A simple iterative method for the simultaneous determination of soil hydraulic properties from one-step outflow experiments." *Water Resources Research*, 26(1), 143-152.
- van Genuchten, M.Th. (1979). "Calculating the unsaturated hydraulic conductivity with a new closed form analytical model." Research Report no 78-WR-08, Princeton University, Princeton, N.J.
- Zachmann, D.W., P.C. DuChateau, and A. Klute (1981). "The calibration of the Richards flow equation for a draining column by parameter identification." *Soil Science Society of America Journal*, 45(6), 1012-1015.

## Moisture migration and stability of iron ore concentrate cargoes

J.H. Atkinson & R.N. Taylor

*Geotechnical Engineering Research Centre, City University, London, UK*

**Abstract:** A research programme has been undertaken investigating the behaviour of iron ore concentrate cargoes during transportation by ship. It has been shown that drainage can be significant during the course of a voyage and there is close correspondence between centrifuge test data, numerical simulations and measurements from a ship's cargo after a voyage. It was observed that the cargo material quickly became saturated near its base. Simple tilt tests have revealed mechanisms of cargo shift and the influence of initial loading geometry.

### 1 INTRODUCTION

Iron ore concentrate and other mineral ores are regularly transported in large bulk carrier ships and these cargoes are known to be liable to shifting. Incidents involving shift of bulk granular cargoes could lead to serious damage or loss of a ship. The Lloyd's Register returns for 1992 listed 13 losses of ships, totalling 580,000 tons, carrying bulk mineral ores and similar figures have been reported for previous years back at least to 1980. While some of these incidents may have been due to other causes some certainly involved cargo shifting.

Iron ore concentrates, and many other mineral ores, are essentially fine to medium sand sized and are liable to liquefaction when saturated and subjected to cyclic or dynamic loading. Most mineral ores have relatively high specific gravity and the bulk materials have relatively high unit weight so that loading of iron ore concentrate into bulk carrier ships should be carefully controlled. It is impossible to fill the holds completely and, furthermore, cargoes are usually left untrimmed; common practice is to load cargo from conveyors more or less equally into each hold. As a result iron ore concentrate and other heavy mineral ore cargoes are loaded as cones at their angle of repose and with their base just covering the floor area of each hold.

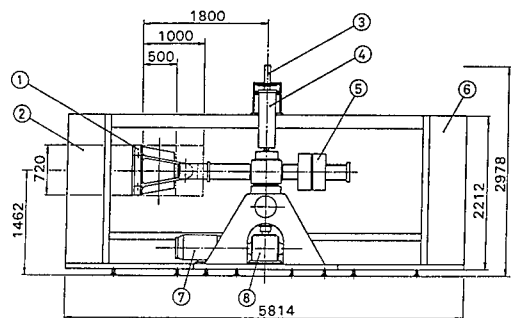
The International Maritime Organisation (IMO) recognise the hazardous nature of these cargoes and gives guidelines for safe stowage (IMO, 1989). The principal feature of these guidelines is restriction of the maximum moisture content at which the cargo should be loaded, the intention being to avoid liquefaction. The IMO guidelines describe tests to determine the flow moisture point (FMP) at which the material flows in a plastic manner when vibrated and they define a

transportable moisture limit (TML) as 90% of the FMP. The IMO method does not allow for drainage which may occur in a cargo during a voyage. A consequence of drainage would be that the moisture content near the base of the cargo would increase while the moisture content higher up in the cargo would reduce. In both cases suctions in unsaturated cargo could reduce so the strength and resistance to shifting would be lowered. If loose cargo becomes saturated near the base of the hold there is the possibility that excess pore pressures could be generated by rapid shearing so causing liquefaction. There are a number of possible mechanisms in which cargo may shift including failure of untrimmed slopes and sliding of the whole cargo over the base of the hold. The latter would involve sliding between the cargo and the steel plates which make up the base of the hold.

A programme of research into instability of iron ore concentrate cargo has been carried out at City University, London in collaboration with the Warren Spring Laboratory. Part of this research consisted of centrifuge model tests to investigate drainage in a cargo and to investigate the mechanisms of instability. Additional laboratory work included triaxial, direct shear and oedometer tests to determine the basic mechanical properties of iron ore concentrate and to investigate moisture content - suction relationships. In addition, observations were made of iron ore concentrate in the hold of a ship after a voyage from Canada to England.

Model tests to investigate drainage and instability of iron ore concentrate cargoes were carried out on the Acutronic 661 geotechnical centrifuge at City University. The essential features of the machine are shown in Figure 1 and further details of the City University centrifuge facility were given by Schofield and Taylor, 1988. The tests to model drainage were carried out in

a simple cylindrical tub and the tests to investigate cargo instability during rolling motions were carried out in a specially constructed model ship hold.



- 1 swinging platform
- 2 power supply cabinet
- 3 hydraulic joint
- 4 slip-ring assembly
- 5 counterweight
- 6 instrumentation cabinet
- 7 motor
- 8 reduction gearbox

Figure 1 Geotechnical centrifuge at City University.

## 2 CHARACTERISTICS OF IRON ORE CONCENTRATE

The material tested, and also the material examined in the ship's cargo, was a Canadian iron ore concentrate. The grading of the material is shown in Figure 2. It is essentially a uniform medium sand with 80% in the size range 0.1 to 1.0mm. It differs from soil in that the specific gravity of the grains is about  $G_s = 5.3$  and typically the bulk unit weight exceeds  $30\text{kN/m}^3$ . The

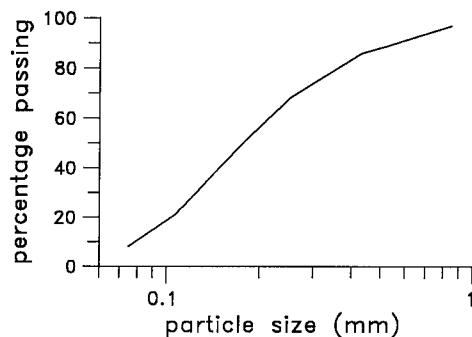


Figure 2 Grading of iron ore concentrate tested.

flow moisture point is about 9% and the transportable moisture limit is about 8% (Kruszewski, 1989). The average moisture content as loaded into bulk carriers is usually in the range 2 to 4% depending on the weather conditions at the loading port. (Following the

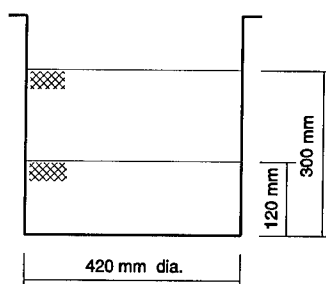
conventional practice in bulk cargo handling the moisture content is defined on the basis of the wet weight.) The low values of moisture content are a consequence of the relatively high values of specific gravity of the grains.

Drained triaxial and shear box tests on dry and saturated samples showed that the critical friction angle of the iron ore concentrate was  $\phi' = 34^\circ$  and the critical friction angle for iron ore concentrate sliding on steel plate was about  $20^\circ$ . These values remained unchanged when silicon oil was used as the pore fluid instead of water.

## 3 DRAINAGE EXPERIMENTS

Centrifuge model tests were carried out to investigate vertical drainage of iron ore concentrate using the simple cylindrical tub shown in Figure 3. Tests were carried out at two scales ( $n = 40$  and  $n = 100$ ) both modelling a prototype approximately 12m deep.

Material was loaded at an initially uniform water content and allowed to drain to an impermeable base under centrifugal acceleration. At appropriate times the centrifuge was stopped and a core of material extracted in a 20mm dia. thin wall tube. In some tests the model was allowed to drain to an equilibrium moisture content before the centrifuge was stopped while in other tests the centrifuge was stopped and restarted at intermediate times and the progress of drainage with time investigated. The cores were divided into sections about 25mm long and the moisture content determined for each section. In tests in which the scale factor was  $n = 40$  each 25mm long moisture content sample represented a layer in the prototype 1m deep.



- 300 mm at 40g = 12m prototype
- 120 mm at 100g = 12m prototype

Figure 3 Dimensions of drainage models.

Drainage and water retention in unsaturated granular materials involves a number of phenomena including self weight forces and surface tension and the appropriate scaling laws are not clear. For the present work the normal scaling laws for geotechnical modelling were

adopted so that the scale factors for dimension and loading rate (in the tilting tests) were taken as  $n$  and the scale for rate of drainage was taken as  $n^2$  where  $ng$  is the centrifuge acceleration. The scaling for dimension was investigated by carrying out tests at two different scale factors and the results of these tests will be discussed later. The scaling for rate of drainage is further complicated by the run-up and run-down times which were significant compared to the total run time. The equivalent drainage times were calculated using an approximate method which allowed for the drainage during the speed changes (Atkinson et al, 1991).

#### (i) Equilibrium moisture content profile

Figure 4 shows the variation of equilibrium moisture content with depth for a typical drainage test in which the scale factor was  $n = 40$  to model a depth of about 12m of cargo. The initial moisture content, shown by the broken line was about 4.2%. After drainage on the centrifuge the moisture contents in the upper portion reached a constant value of about 1.5% while the moisture content near the base reached a value of about 10% and there was a relatively well defined transition. A value of moisture content of 10% corresponds closely to full saturation at the voids ratio measured near the base of the model while a moisture content of 1.5% corresponds closely to the equilibrium moisture content of iron ore concentrate.

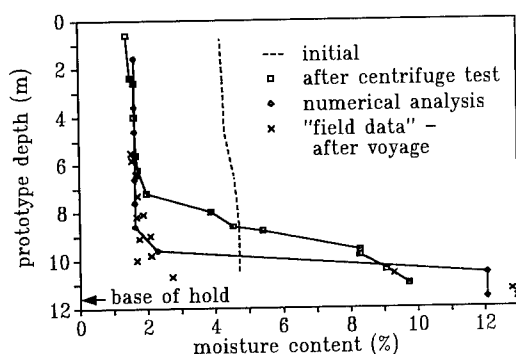


Figure 4 Variation of equilibrium moisture content with depth in model cargo.

#### (ii) Effect of initial moisture content

Figure 5 shows equilibrium moisture content profiles for three initial moisture contents of 2.8%, 4.2% and 6.2%. In all cases the moisture content in the upper layer was about 1.5%, there was a region at the base in which the moisture content was considerably larger and there was

a relatively well defined transition between the two regions. For the two larger initial moisture contents the moisture content near the base was about 10% corresponding to full saturation and the principal influence of initial moisture content was to change the level of the transition. For the lowest initial moisture content the equilibrium moisture content measured at the base was about 5.5%. (It should be noted that this represents the average moisture content in a layer about 1m deep in the prototype and the moisture content close to the base may have been larger.)

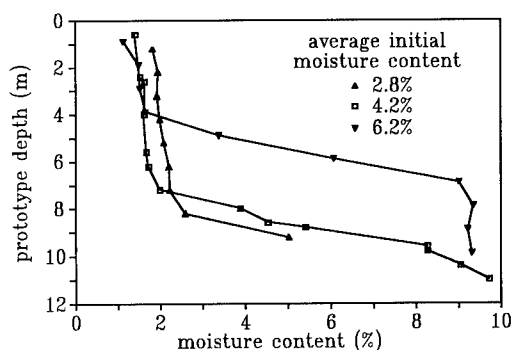


Figure 5 Influence of initial moisture content.

#### (iii) Effect of scale factor

Figure 6 shows profiles of equilibrium moisture content with depth for two tests modelling the same prototype with a depth of 12m but with different scale factors  $n = 40$  and  $n = 100$ . Both profiles have the characteristic features shown in Figure 4 and there is no significant difference between the data obtained with the different scale factors. These results indicate that the linear scaling rule adopted for the tests was reasonable.

#### (iv) Variation of drainage with time

Figure 7 shows the variation of moisture content with depth at various times for a typical drainage test in which the scale factor was  $n = 40$  to model a depth of 12m of cargo. The initial moisture content, shown by the broken line was about 4.2%. The equivalent prototype times were calculated from the centrifuge run times including allowances for the run-up and run-down times. As noted above the prototype times shown on Figure 7 should be regarded as approximate. At equilibrium the moisture contents shown in Figure 7 are similar to those in Figure 4: the moisture contents in the

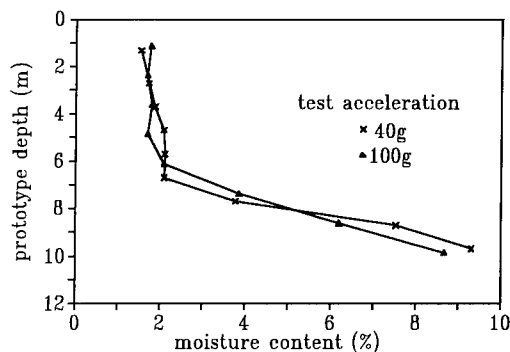


Figure 6 Influence of scale on equilibrium moisture content for the same prototype depth.

upper portion reached a constant value of about 1.5% while the moisture content near the base reached a value of about 10% and there was a relatively well defined transition. The data shown in Figure 7 show the progress of drainage with time from the initial condition of uniform moisture content to the final equilibrium condition.

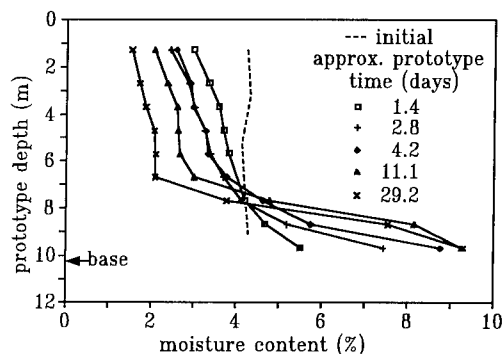


Figure 7 Variation of moisture content with time.

Figure 4 also shows the variation of moisture content obtained from a numerical analysis by Kruszewski (1993). The numerical analysis was based on relationships between moisture content and suction measured in a number of laboratory tests. The moisture contents in the upper region of about 1.5% observed in the model tests and calculated from the numerical analyses are in close agreement. Near the base of the hold the calculated values of 12% are greater than the

values of about 10% measured in the centrifuge model tests. The reason for this is that in the model tests the material was compressed by the weight of the overlying material while the laboratory samples were not compressed so that the voids ratio and saturated moisture content in the models were smaller than those in the laboratory tests used to develop the numerical analyses.

Also shown in Figure 4 are two profiles of moisture content with depth measured in a cargo of iron ore concentrate in the hold of a large bulk carrier ship after a voyage from Canada to England. These field moisture contents correspond well with those observed in the centrifuge model tests.

#### 4 STABILITY EXPERIMENTS

A second series of centrifuge model tests was carried out to investigate mechanisms of instability of iron ore concentrate cargo with different initial loading configurations during rolling motions. Real ships' motions involve complex cyclic and dynamic oscillations in three dimensions but with the equipment available it was only possible to apply a simple, relatively slow one-way roll about an axis close to the centre of mass of the model. Consequently the tests illustrate the mechanisms of cargo shift but they do not necessarily model qualitatively roll angles at which shift would occur in practice.

The apparatus used was a plane section model hold supported on a trunnion bearing as shown in Figure 8. The front wall of the model container incorporated a perspex window so movements of the cargo could be observed by closed circuit TV and recorded on video tape. As an aid to observation a grid of coloured sand was placed against the window. Settlements of the surface of the cargo were measured using displacement transducers (LVDT type) placed as shown in Figure 8. The tests were carried out at a constant centrifuge acceleration of 100g so the models represent a section of a hold about 35m wide and 16m deep. Following the usual practice, silicon fluid with a viscosity 100cs was used for the pore fluid in these 100g tilting tests to ensure the same time scaling factor ( $t_m:t_p = 1:100$ ) for pore fluid drainage and rate of loading.

Rotation of the model hold was controlled by bleeding oil from the hydraulic cylinder. With the available equipment it was not possible to control the rate of roll precisely and the time to achieve a roll angle of about 40° was typically 20s. With a scale factor of  $n = 100$  this represents a single one-way 40° roll in about 2000s (about 1° per min) at prototype scale. This is considerably longer than the 10s period for a typical one-way ship roll.

Iron ore concentrate was loaded into the model hold in one of the geometrical configurations shown in Figure 9. Cases A and B represent cargo trimmed level over a central area below the loading hatches and, in practice,

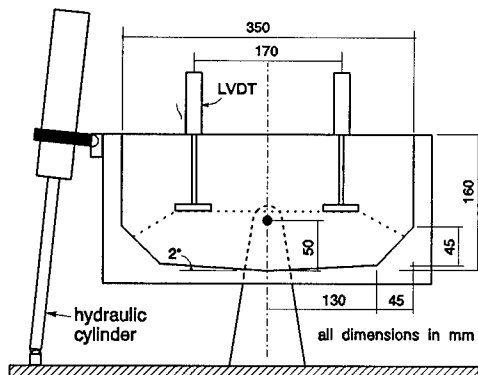


Figure 8 Model hold for instability experiments.

these profiles could be achieved by moving the discharge point of the loading conveyor. Case A represents a deep layer in which the angled haunches of the base of the hold are buried while case B represents a relatively shallow layer in which the cargo covers the base of the hold and extends only a little way up the angled haunches. Case C represents an untrimmed cargo and it only covers the base of the hold. In practice case C is the most common as it avoids the need for trimming and all holds can be loaded equally. In case A some holds would remain empty or only partly filled to avoid exceeding the overall capacity of the ship.

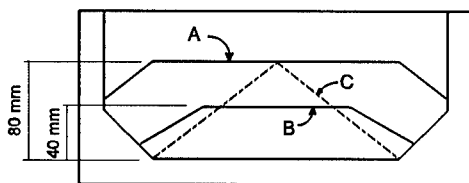


Figure 9 Loading geometry.

The model hold with its cargo loaded was placed in a level position on the centrifuge and maintained at constant acceleration of 100g until drainage of the pore fluid was complete. Then, still under constant centrifuge acceleration, oil was bled from the hydraulic cylinder allowing the model hold to rotate about the bearing axis at approximately constant rate to a maximum angle of about 40°.

## 5 MECHANISMS OF CARGO INSTABILITY

In all cases the cargo became unstable and shifted. Examination of the video tapes obtained from the closed circuit TV showed that the cargo shifting consisted of a combination of steady and unsteady movements both through the cargo and between the cargo and the base of the hold. At the end of most tests the final profile of the cargo approximated to that illustrated in Figure 10 with the surface at a uniform angle (beta) about 32° to 34° to the horizontal. This is close to the critical friction angle for the material.

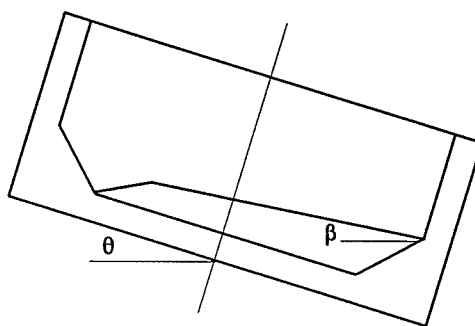


Figure 10 Typical cargo profile after movement in instability test.

Figure 11 shows the settlements recorded by the up-hill LVDT plotted against roll angle for three tests with the initial loading conditions shown in Figure 9. While these settlements record vertical movements of the surface of the cargo they indicate the progress of the horizontal shift of the cargo. In particular, a smooth gradient indicates steady flow of material and, from the closed circuit TV recordings this was due principally to flow in the upper levels of the cargo. The occasional sharp steps in the settlement records indicate bulk

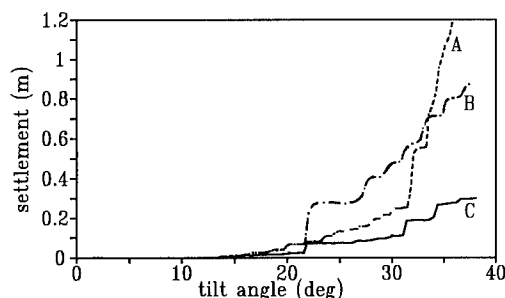


Figure 11 Typical variations of surface settlement with roll angle.



movement of the cargo and, from the closed circuit recordings these were due principally to slipping between the cargo and the base of the hold. In cases B and C these distinct slips between the cargo and the base of the hold occurred at roll angles a little in excess of 20° which is close to the critical friction angle for shearing of iron ore concentrate against steel plate.

These centrifuge model tests indicate that there were two principal mechanisms of instability. One mechanism consisted of flow in the upper material which had relatively low moisture content after drainage. In this case the shift of the cargo was progressive. The other mechanism consisted of bulk movement between the cargo and the base of the hold. In this case the shift was discontinuous and took place in distinct increments.

A simple limit equilibrium stability analysis based on a single straight slip plane indicates that the shift occurred with essentially zero pore pressures. This is reasonable considering the relatively slow rates of roll at prototype scale (about 1° per minute). In practice cyclic and dynamic oscillations experienced by ships at sea may generate excess pore pressures in bulk granular cargoes which would have the effect of allowing shift at smaller angles of roll than those observed in the model tests.

## 6 SUMMARY AND CONCLUSIONS

The work demonstrates an application of geotechnical centrifuge modelling to a problem of drainage and stability in a granular material which is not strictly within the normal range of geotechnical engineering. The model tests clearly demonstrated that drainage will occur in iron ore concentrate cargo within the period of a typical voyage. They also revealed the mechanisms of cargo shift during relatively slow rolling motions.

Figures 4 to 7 show variations of moisture content with depth observed in centrifuge drainage tests on an iron ore concentrate. In all cases the equilibrium moisture contents in the upper layers were about 1.5% and those near the base of the hold were about 10% irrespective of the initial uniform moisture content provided that this was not less than about 4%. There was a distinct transition between the drier upper region and the wetter lower region and the position of this transition depended principally on the initial moisture content. The rates of drainage and the times required to achieve the equilibrium moisture contents were subject to uncertainties but the results indicated that iron ore concentrate cargoes would be expected to drain fully in a period of a few days or weeks and usually within the period of a normal voyage.

The equilibrium moisture contents observed in the centrifuge models corresponded well with the moisture content measured in a cargo of iron ore concentrate after a trans-Atlantic voyage. They also corresponded well with numerical analyses by Kruszewski (1993) based on simple laboratory determinations of the moisture content

suction relationships for the iron ore concentrate material provided that an allowance was made for the smaller voids ratios in the material at the base of the centrifuge models. These results demonstrate that iron ore concentrate cargo drains relatively rapidly so that the cargo is likely to become saturated near the base of the hold and it will have a low moisture content in its upper layers. In both cases the strength of the cargo will have been reduced from its original value.

Simple limit equilibrium stability analyses indicated that in the model tests both types of shift occurred under conditions of approximately zero pore pressure. In practice cyclic and dynamic loadings could cause increased pore pressures so reducing the stability of the cargo.

## ACKNOWLEDGEMENTS

The work described in this Paper was carried out under contracts with the Department of Transport in collaboration with the Warren Spring Laboratory of the Department of Trade and Industry. The Authors are grateful to Dr Andrew Kruszewski for his contributions to the work and particularly for making available some of the results of his laboratory tests and numerical analyses.

## REFERENCES

- Atkinson, J.H., Coop, M.R. and Taylor, R.N. (1991). Drainage of iron ore concentrate cargoes and the effects upon cargo stability. Report to Warren Spring Laboratory and Department of Transport. The City University Research Report GE/91/05.
- International Maritime Organisation, (1989). Code of Safe Practice for Solid Bulk Cargoes; 7th edition. IMO, London.
- Kruszewski, A. (1993) Iron Ore Concentrate Cargo Tests: Part Two. Warren Spring Laboratory Report; LR 846 (MP/BM).
- Schofield, A.N. and Taylor, R.N. (1988). Development of standard geotechnical centrifuge operations. Proc. Centrifuge '88, Paris. Balkema, pp. 29-32.

## 7 Deep foundations

## Effects of repeated stress on toe resistance of cast-in-place concrete piles

F. Okumura

*Railway Technical Research Institute, Tokyo, Japan*

S. Mokutani, M. Okamura, J. Takemura & T. Kimura

*Tokyo Institute of Technology, Japan*

**ABSTRACT:** Stress release and disturbance of ground at pile toes make end bearing resistance of cast-in-place concrete piles weaker than that of driven piles. A new method has been developed for improving this shortcoming, whereby concentric-circle divided concrete rings are intruded at pile toes by hydraulic jacks repeatedly before concrete casting. In order to evaluate this piling method, two series of centrifuge model tests of piles in a sand layer were conducted. Simple undivided pile models and divided pile toe models were utilized for simulating this piling method. Overburden pressures and relative density of the sand were varied in these tests. Model pile diameters used were 20mm and 40mm. Test results were analyzed from the point of parameters effect. As well as centrifuge model tests, two full scale loading tests were carried out for comparing two piles constructed by the developed method and the conventional one. Diameter and length of test piles were 1m and 14.2m, respectively. Centrifuge test results were compared with these from the full scale loading test.

### 1 INTRODUCTION

From an environmental point of view, noise and vibration during construction of a driven pile, especially in urban areas, make a cast-in-place concrete pile more acceptable than a driven pile. But, because of stress release and disturbance of ground at pile toe, the cast-in-place concrete piles usually have smaller toe resistance than that of the driven concrete piles. Small toe resistance may cause differential settlement of foundation, causing heavy damage to superstructures. According to Foundation Design Standard for Railways (JSCE, 1986), in order to reduce the differential settlement of the piled foundations, the settlement of individual piles should not exceed 2cm for 95% reliability in design. Because of the displacement limitation, design load of cast-in-place pile is mainly borne by shaft resistance. Compared with a driven pile, toe resistance of a cast-in-place pile is usually not mobilized well within a settlement of 2cm.

In order to improve the resistance mechanism of a cast-in-place pile, a new construction method has been developed. (Okumura et al. 1992) In this method, between excavation and concrete casting, concentric-circle divided concrete rings are intruded at the pile toe by hydraulic jacks repeatedly into the soil. The concrete rings are 20cm high with diameters of 40, 60 and 80cm and shown in Fig. 1. Repeated normal stress will cause shear strain in the ground and the strength of the loosened ground is recovered or improved. Using divided rings, large intrusions can be introduced into the soil

under the limitation of capacity of the hydraulic jacks. From preliminary analysis, preloading makes the toe resistance of the developed pile 50% higher than that of conventional one.

In order to evaluate this piling method, two series of centrifuge model tests of pile in sand were conducted. The first series utilized a simple undivided pile model. In the second series, divided pile toe models ("ring" pile) were utilized for simulating this piling method. Load-settlement behavior of the tests are examined and compared. Elastic moduli at the initial loading and at each loading cycle are obtained from load-settlement curves. Elastic moduli are normalized by the initial elastic modulus of the test and compared in the parameter study.

As well as centrifuge model tests, two full scale loading tests were carried out for two piles

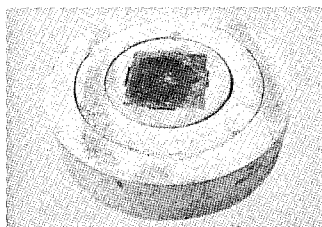


Fig. 1 View of concrete ring

constructed by the developed method and the conventional method. Diameters and length of test piles were 1m and 14.2m, respectively. Centrifuge test results were compared with the result of the comparative loading test.

## 2. FULL-SCALE LOADING TESTS OF CONVENTIONAL PILE AND DEVELOPED PILE

The full-scale loading test of the conventional pile and the developed pile was conducted. The soil profiles near the piles are shown in Fig. 2. Ground strength near the conventional pile toe is higher than that near the developed pile.

Load-displacement curves of these piles are shown in Fig. 3. These curves are drawn without shaft resistance. In this paper "load" means load intensity, that is, applied load divided by the base area of the pile. At settlement of 2% and 10% of pile diameter, toe resistance of the developed pile is 30% and 12% larger than those of the conventional pile, respectively.

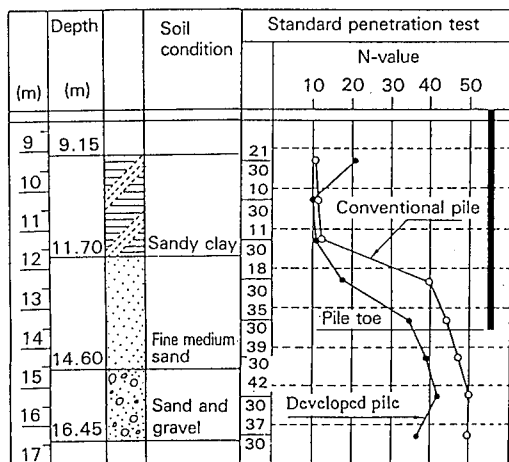


Fig. 2 Soil profile of comparative loading test site

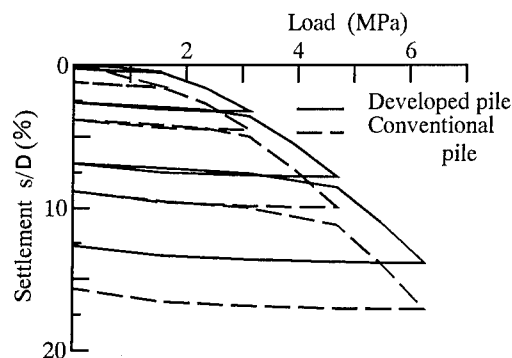


Fig. 3 Load-settlement curves (Prototype)

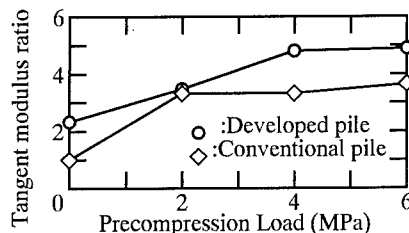


Fig. 4 Tangent modulus ratio v.s. precompression load (Prototype)

Fig. 4 shows the relationship between the tangent modulus ratio and precompression load. The ratio is the tangent modulus normalized by the initial tangent modulus of the conventional pile and the precompression load the maximum applied load before each repeated loading. The effect of the repeated stress at pile toe may be seen in the higher toe resistance and elastic modulus of the developed pile compared with the conventional pile, especially at initial loading.

## 3. CENTRIFUGE MODEL TEST

### 3.1 Test series and testing procedure

Conditions of the centrifuge model tests and the full-scale tests are summarized in Table 1. The parameters varied in the centrifuge tests are the relative density of the sand, overburden pressure, centrifugal acceleration and diameter of model pile. The general view of the test apparatus is shown in Fig. 5. The container is 500mm wide, 400mm high and 300mm long.

Table 1 The list of centrifuge tests

test code	D (mm)	pile shape	loading procedure	Dr (%)	p (kPa)	n (G)
2605	20	undivided	repeated	60	49	50
2605T	20	undivided	monotonic	60	49	50
2610	20	undivided	repeated	60	98	50
2620	20	undivided	repeated	60	196	50
2620T	20	undivided	monotonic	60	196	50
4610	40	undivided	repeated	60	98	25
2805	20	undivided	repeated	80	49	50
2805T	20	undivided	monotonic	80	49	50
2810	20	undivided	repeated	80	98	50
2820	20	undivided	repeated	80	196	50
2820T	20	undivided	monotonic	80	196	50
4810	40	undivided	repeated	80	98	25
R605	40	ring	repeated	60	49	25
R610	40	ring	repeated	60	98	25
R805	40	ring	repeated	80	49	25
R810	40	ring	repeated	80	98	25
R610T	40	ring	monotonic	60	98	25
T810T	40	ring	monotonic	80	98	25
P1*	1000	ring	repeated	--	102	1
P2**	1000	undivided	repeated	--	102	1

p1\*: the developed pile

p2\*\*: the conventional pile

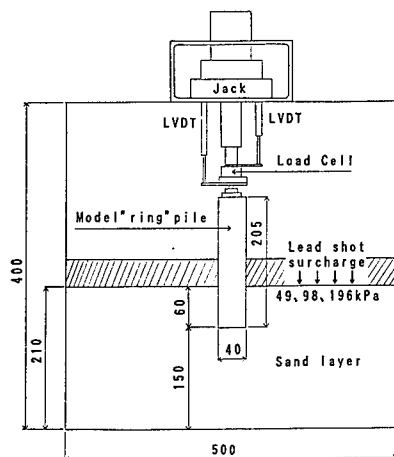


Fig. 5 General view of test apparatus

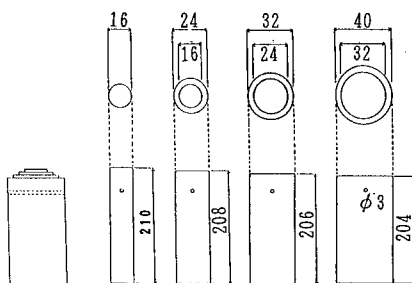


Fig. 6 Schematic image of ring pile

The diameters of the model piles are 20mm and 40mm and centrifugal accelerations 50g and 25g, respectively. The pile diameter in the prototype scale is 1m for all tests. A combination of concentric cylinders is used for simulating the pile toe of the developed method. This pile is called "ring" pile in this paper. The structure of ring pile is shown in Fig. 6.

The thicknesses of the sand layer beneath the pile toe are 150 and 100mm for pile diameters of 40 and 20mm, respectively. It is considered to be desired that the ratio of the thickness of sand layer to the pile diameter should be enough large, maybe more than 5, for eliminating the boundary effect of the base of the container. Because of the limitation of the dimension of the container, however, the ratio was 3.75 in the case of the pile diameter of 40mm. According to the calculation for circular loading on an elastic body, the vertical stress at the depth of 3.75 times as the diameter of loading area is about 10% of the applied load. From this it may be said that this shortage of the depth of the sand layer does not lead much differences in settlement behavior of the pile from that of the case with the ratio of 5.

The sand used in the model is Toyoura sand, a poorly graded fine quartz sand. The sand layer is prepared by air-pluviation. The hopper and the height of pouring are adjusted for each relative

density according to the specification determined by a proof test. After pouring, the surface of the sand layer is leveled by vacuuming. The model pile is set to be perpendicular to the sand surface very carefully, and is held by a guide. The sand is again poured around the pile for making 60mm embedment. The pile guide holds the pile until the embedded part is completed. Lead shot is laid on the sand surface in the cases of overburden with 98kPa and 196kPa, and the loading jack is set up on the container. The load applied on the top of the piles is measured by a load cell.

The pile is pushed vertically by a loading rod attached at the loading jack along with the guide arranged at the top of the pile. The loading is done by displacement control at the rate of 1mm/minute. 2 LVDTs were used for displacement measurement.

There are two series of the test. One is monotonic loading and the other is repeated loading. For the monotonic loading cases, the pile is pressed to the settlement of the half of pile diameter(D) monotonically. For the repeated loading cases, the model pile was unloaded at arbitrary settlements and reloaded cyclically until the settlement of 0.5D.

The set-up procedure of the ring pile is very similar to that of the undivided model pile. The ring pile consists of four rings including the center core. Each ring has a length 2mm longer than that of the next outer ring. At the initial arrangement of the rings the bottom surface is flat as shown in Fig. 6. This pile is loaded by a loading rod with flat surface attached at the loading jack. This rod has a diameter of 40mm. Firstly the center core of the ring pile is pressed by 2mm, and then the next outer ring is pressed together with the core by 2mm and more 2mm intrusion of the three inner rings is done into the sand. After this series of intrusions, although the most outer ring has not experienced any vertical movement, the top surface of the ring pile becomes flat. In the tests with the ring piles, monotonic and repeated loading were also conducted. In the former loading test, loading is conducted continuously on the whole pile and in the latter loading test, the model pile is once unloaded after the above mentioned intrusions and then loaded until the settlement of 0.5D.

### 3.2 Test results and discussion

#### 3.2.1 Load-settlement behavior

The results of modeling of models of cases of 60% relative density are shown in Fig.7, in which 20mm and 40mm diameter piles were used under 50 and 25 g centrifugal acceleration respectively, giving the same pile diameter; 1m in the prototype scale. Even for the some difference in the ratio of the thickness of sand layer to the pile diameter between the two models, the results of these two tests agree fairly well. From the test cases of 80 % relative density, almost identical results are obtained. These facts make the authors believe the testing procedure is

proper and centrifuge testing is quite beneficial for simulating the prototype tests.

Load-displacement curves of repeated loading cases and monotonic loading tests with the undivided and ring piles are shown in Fig. 8 and 9 respectively. While load is in virgin area, both curves agree reasonably well. Compression behavior of

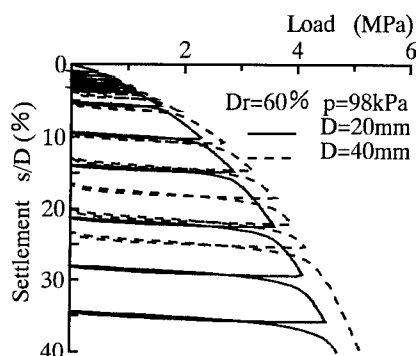


Fig. 7 Results of modeling of models

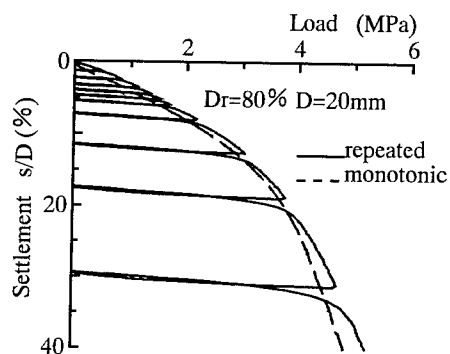


Fig. 8 Comparison of load settlement curves between monotonic and repeated loading tests with undivided pile

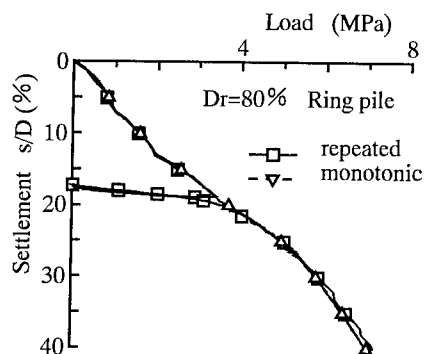


Fig. 9 Comparison of load settlement curves between monotonic and repeated loading tests with ring pile

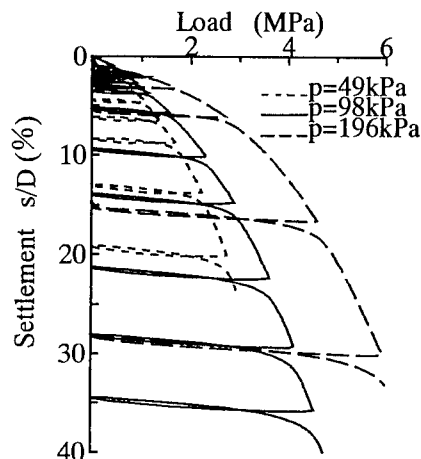


Fig. 10 Load settlement curves of undivided piles: Dr=60%,

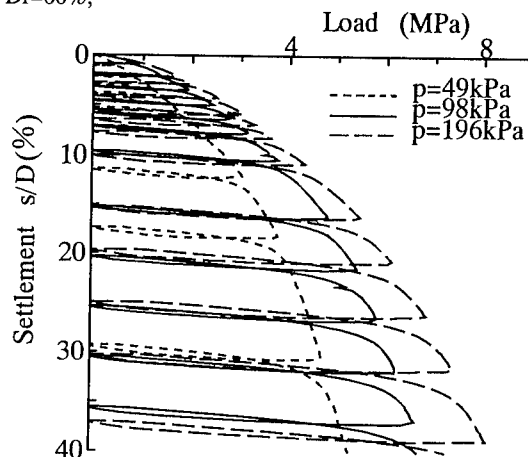


Fig. 11 Load settlement curves of undivided piles: Dr=80%,

ground at pile toe is not affected by precompression load. Test results of undivided and ring piles show the same tendency. From these comparison, it may be said that the test results with undivided piles can reflect the effect of the repeated stress on the toe resistance by intruding the divided piles.

Load-settlement curves of the undivided rings for the cases of 60% and 80% relative densities are shown in Fig. 10 and 11. Relationship between the load at the settlement of 10% pile diameter and overburden pressure is given in Fig. 12. For the ring pile, this 10% settlement is one measured from the reloading point in the repeated loading test. Load at settlement of 0.1D is specified as the standard bearing capacity of piles in Foundation Design Standard for Railways.(JSCE,1986) For cases of 60% relative density, load at 0.1D increases in direct proportion to overburden pressure, but for 80% cases, it is not in direct proportion.

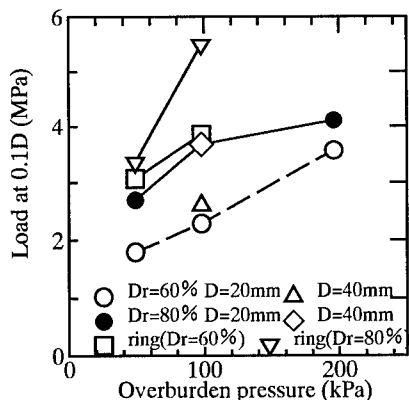


Fig. 12 Relationship between Load at settlement of 0.1D and overburden pressure

Considerable improvement in bearing capacity improvement by ring intruding may be seen in Fig.12. Compared with the cases of undivided pile with the same density and overburden pressure, the ring piles produce 20 to 70% bearing capacity increase, which is a little higher than that of full-scale loading test.

### 3.2.2 Elastic modulus

From load-settlement curves, secant and tangent moduli of elasticity are calculated at initial loading and at each repeated loading cycle. The tangent modulus is calculated from each reloading curve. The secant modulus is calculated at the settlement of 1% pile diameter from each restarting point. In the design of railway foundation, the coefficient of subgrade reaction of pile foundations is determined from the secant modulus at the settlement of 10mm, that is, 1% of the pile diameter of the prototype in this tests.(JSCE,1986)

Relationships between the tangent modulus and the precompression load are shown in Fig.13. The tangent moduli increase with the precompression load in the range of small precompression load and approach to steady values around the precompression load of 2MPa. There are not much differences in the steady values between the cases of 60% and 80% relative densities. In the cases of overburden pressure more than 98kPa, the increase of the overburden pressure does not bring a substantial increase on the steady value. The tangent moduli on the reloading curves of the cases with the ring pile are also given in the figure. In the cases of the ring pile the tangent moduli are almost same for all cases, irrespective of relative density and overburden pressure.

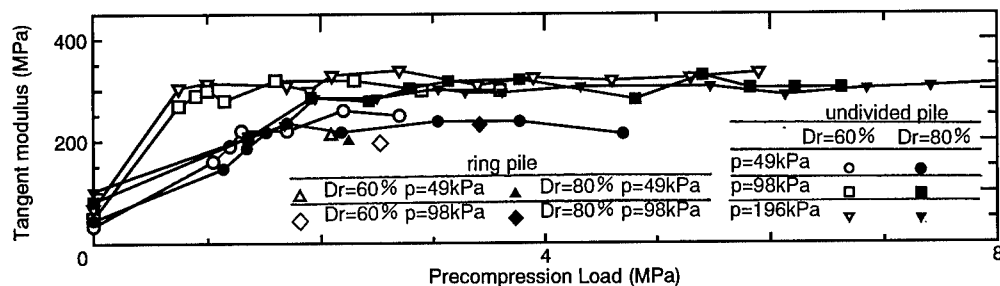


Fig.13 Tangent modulus v.s. precompression load

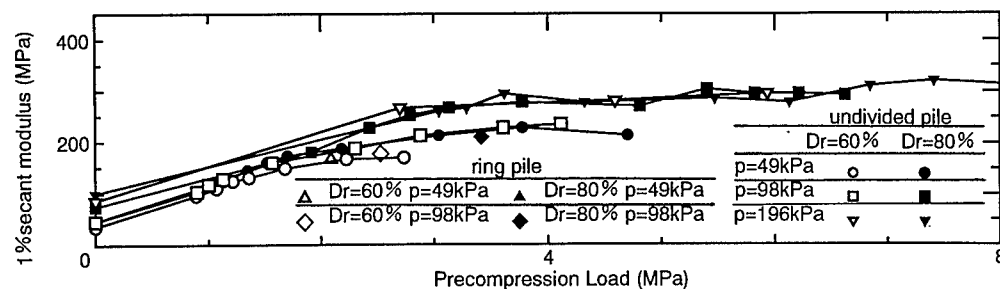


Fig.14 1% secant modulus v.s. precompression load

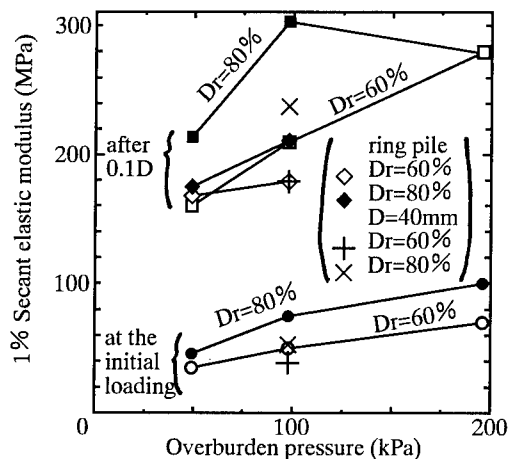


Fig.15 1% secant modulus at the initial loading and after settlement of 0.1D v.s. overburden pressure

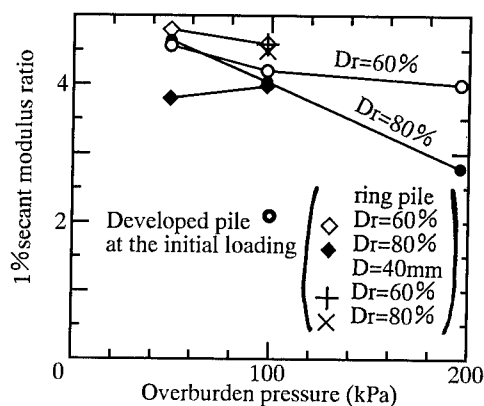


Fig.16 Increase rate of 1% secant modulus

Fig.14 shows relationships between 1% secant modulus and precompression load. The secant modulus increases gradually with precompression load. For small precompression loads, the settlement of 1%D is sufficient to cause yielding. As the increase of the precompression load, the elastic portion in the settlements of 1%D increases and then the secant modulus also increases. In the cases of 80% relative density, the settlement of 1%D from the restarting point is finally within the previously loaded area and the secant modulus approaches to a steady value which is almost same as that of tangent modulus. On the other hands in the cases of 60% relative density, the secant moduli for the overburden pressure less than 98kPa continuously increase until the end of loading, which giving such results that the higher the relative density, the higher the 1% secant modulus.

Relationships between 1% secant modulus and overburden pressure at the initial loading and after settlement of 0.1D are shown in Fig.15. The secant moduli of the ring pile in the reloading curves are also given in the figure. The higher relative density and the larger overburden pressure, the higher secant moduli, except of the modulus after 0.1D settlement in the cases of 80% relative density with the overburden pressure larger than 98kPa.

Fig.16 shows the rate of the 1% secant modulus increase after 0.1D settlement in the tests with the undivided piles, together with the results in the tests with the ring pile and the full-scale loading tests on the developed pile. The increasing rate for the tests with the ring is defined as the ratio of the 1% secant modulus to that of undivided pile at initial loading with the same prototype condition and the rate for the test of the full scale developed pile the ratio of the modulus between the developed and conventional piles. In the cases of 80% relative density, the increasing rate decreases with the overburden pressure mainly due to the difference of initial modulus. Both for undivided piles and ring piles, similar increasing rates of about 4 were obtained. The increasing rate in the full-scale developed pile is about half of that of centrifuge tests. The difference in the soil profiles at sites of the two full scale tests may be responsible to this. The site of the conventional pile has higher N-value than that of the developed pile as shown in Fig.2.

#### 4 CONCLUSIONS

In this study, the authors were trying to investigate the effect of repeated stress on the toe resistance of pile with centrifuge model tests.

The following conclusions were derived from this study.

1. Centrifuge tests can simulate the ring intruding of the large-scale prototype test reasonably well. Ring intruding at the pile toe produces an increase of both bearing capacity and elastic modulus.
2. Load-settlement behavior of monotonic loading and repeated loading coincide with in the virgin load area.
3. Tangent moduli and secant moduli increase with precompression load and finally approach to a steady value. The higher relative density and the larger overburden pressure, the higher secant moduli. On the other hand these parameters have not much effect on the steady value of tangent modulus.

#### REFERENCES

- Japan Society of Civil Engineers 1986. Foundation Design Standard for Railway Structures (in Japanese), Tokyo: JSCE
- Okumura, F. et al. 1992. Development of new cast-in-place concrete pile. Journal of JSCE, (in Japanese) Vol.77 No.14: 10-13



## Pullout resistance of steel pipe piles in improved ground

M. Miyake, M. Wada, T. Satoh & Y. Katoh  
Toyo Construction Technical Research Institute, Hyogo, Japan

**ABSTRACT:** The pullout resistance of raking steel pipe piles installed in ground improved by the Deep Mixing Method was studied using results from a series of centrifuge model tests. The pullout resistance of steel pipe piles can be determined by the unconfined compressive strength of cement treated soil, independent of the differences in length and diameter of the piles. A field test to confirm the pullout resistance obtained from the centrifuge model tests was performed at the construction site in Tokyo Bay, and the stability of the bulkheads was confirmed.

### 1 INTRODUCTION

The construction of a bulkhead composed of steel sheet piles and coupled steel pipe piles is planned in ground improved by the Deep Mixing Method (DMM) at a reclaimed land site in Tokyo Bay. Steel pipe piles are installed into the improved ground using water jets, and are fixed in place by grouting cement milk into the spaces between piles and the improved ground, as illustrated in Fig. 1. There are few precedents for this method in Japan.

port and harbour areas of Japan, equation (1) is recommended with regard to the maximum pullout load of a pile in clay strata.

$$R_{ul} = \bar{C}_a \cdot A_s \quad (1)$$

where  $R_{ul}$  (tf) is the maximum pulling load of a pile,  $\bar{C}_a$  (tf/m<sup>2</sup>) the average adhesion between the clay and an embedded pile,  $A_s$  the surface area of an embedded pile.

It is recommended to adopt the following relations (Tomlinson 1971) for  $\bar{C}_a$ :

$$\bar{C}_a = C \quad \text{for } C < 10 \text{ tf/m}^2 \quad (2.a)$$

$$\bar{C}_a = 10 \text{ tf/m}^2 \quad \text{for } C > 10 \text{ tf/m}^2 \quad (2.b)$$

where  $C$  is the undrained shear strength of clay.

It can be realized that cement treated soil has an intensively anisotropic strength. The relations obtained by Terashi et al. (1980) for the tensile strength of cement treated soil improved by the DMM are

$$\sigma_t = 0.15 q_u \text{ tf/m}^2 \quad \text{for } q_u < 133 \text{ tf/m}^2 \quad (3.a)$$

$$\sigma_t = 20 \text{ tf/m}^2 \quad \text{for } q_u > 133 \text{ tf/m}^2 \quad (3.b)$$

where  $q_u$  is the unconfined compressive strength of cement treated soil.

Accordingly, the method to estimate the maximum pullout load of the pile and the  $\bar{C}_a$  in improved ground had to be newly developed, as it was implausible to consider that the assumed slip surface at pile pullout loading of eq. (1) would occur on the

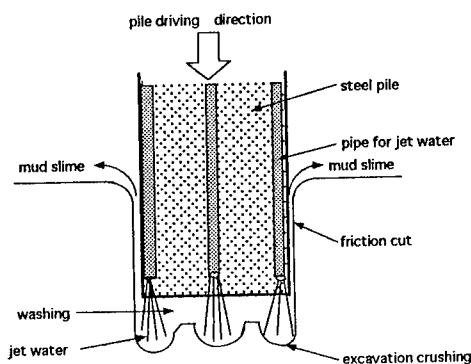


Fig. 1 Hi-jet piling method

Therefore, prior to the construction of the bulkheads, the pullout resistance of steel pipe pile in ground improved by the Deep Mixing method has been investigated by using centrifuge models. In

pile surface in an identical form. Based on results from a series of centrifuge model tests, convenient equations to predict the pullout resistance of a pile are proposed.

## 2 CENTRIFUGE TESTS

### 2.1 Test Procedure

A series of centrifuge model tests were conducted at 50g by changing the combinations of length and diameter of steel pipe piles and the unconfined compressive strength of cement treated ground, as shown in Table 1. The scale in this table is expressed in prototype terms.

Table 1. Test cases

Test code	Pile diameter (m)	Pile length (m)	$q_u$ of ground (tf/m <sup>2</sup> )
A.1.1	1.0	10	33.3
A.2.1	0.5	10	51.3
A.2.2	1.0	10	51.3
A.3.1	0.5	10	100.3
A.3.2	1.0	10	100.3
A.4.1	0.5	10	134.3
A.4.2	1.0	10	134.3
A.5.1	0.5	10	354.8
B.1.1	1.0	5	24.6
B.1.2	1.0	10	24.6
B.2.1	1.0	5.5	75.4
B.2.2	1.0	10	75.4
B.3.1	1.0	10	400.0

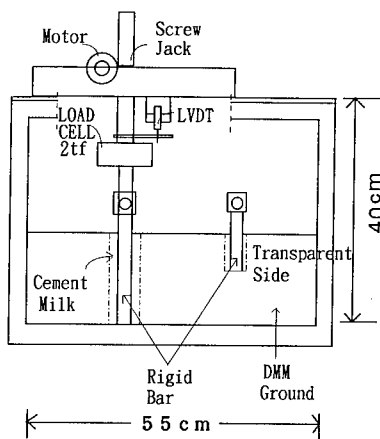
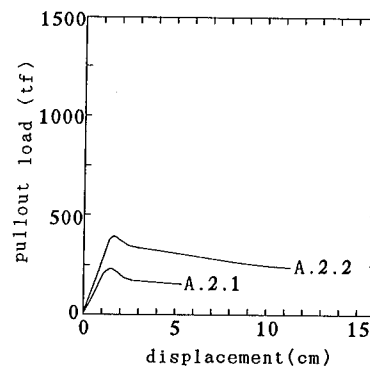


Fig.2 Schematic model system

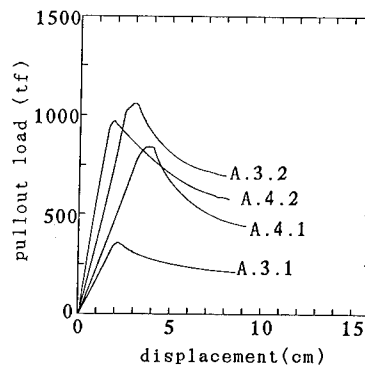
In preparation of the centrifuge models, two brass pipes with predetermined model pile diameters were first spaced on the center line of a rigid box (length=55 cm, width= 15 cm, height= 40 cm) with a transparent plexiglass side; cement treated soil was then poured into the box to a model ground height of 20 cm at 1g, as shown in Fig.2. After the cement treated soil hardened, the brass pipes were withdrawn, and one model pile (a simple rigid bar) was installed in each shaft at 1g. Cement milk was injected into the shaft to fix each pile in place at 1g. The pullout was conducted at 50g by a strain control system with a speed of 0.15 mm/min.

### 2.2 Test Results

Typical relationships between the pullout load and the displacement are shown in Figs.3(a),3(b) and 3(c). The pullout load in every case linearly increases as the displacement and the unconfined compressive strength of the cement treated soil increases.  $\bar{C}_a$  obtained from eq.(1) with these test

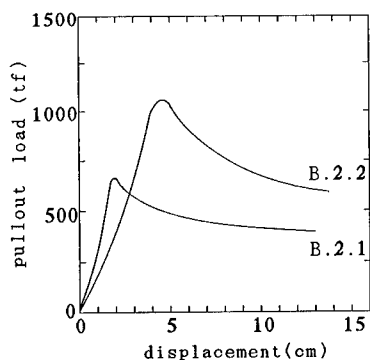


(a)



(b)

Fig.3 Relationships between displacement and pullout load



(c)

Fig.3 Relationships between displacement and pullout load

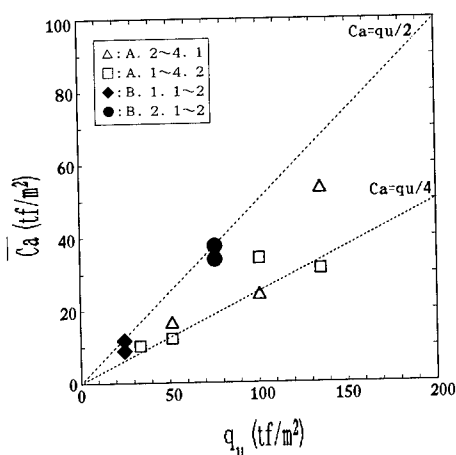


Fig.4  $\bar{C}_a$  based on eq.(1) from test results

results is  $1/4$  to  $1/2$  of the  $q_u$  of cement treated soil as shown in Fig.4. This indicates that the relation  $\bar{C}_a = 10 \text{ tf/m}^2$  for  $C > 10 \text{ tf/m}^2$  in eq.(2.b) can not be used in ground improved by the DMM. The displacement at the maximum pullout load tends to increase as the  $q_u$  of the cement treated soil increases for the case of equivalent pile lengths, regardless in the difference in the pile diameter, as shown in Fig.5. For the case of equivalent  $q_u$ , the displacement increases in proportion to the increase in pile length, as shown in Fig.3(c). From test results of Yamamoto et al.(1982), because the modulus of deformation of the cement treated soil increases as  $q_u$  increases, the displacement should decrease as  $q_u$  increases. The slip surface immediately after reaching the maximum pulling load is shown in Fig.6. The upper cement treated soil is

lifted up in a cone shape with the pullout of the pile. The test results show that the depth of cone head of the cement treated soil adhering to a pile increases as  $q_u$  of the ground increases. It is likely that tensile forces act on this cone surface, and thus, that the sliding failure mode considered in eq.(1) can not occur.

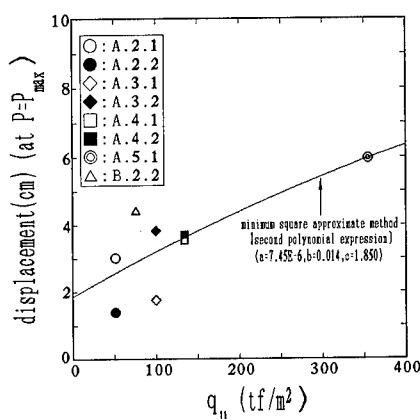


Fig.5 Relationship between  $q_u$  and the displacement at  $p=p_{\max}$

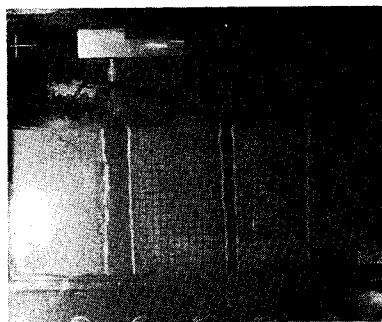


Fig.6 Slip surface at  $p=p_{\max}$

### 3 PROPOSED METHOD IN DMM GROUND

The proposed equations are based on only force equilibrium, with the model in Fig.7 referring to results from this series of centrifuge tests. The depth( $h$ ) of head of the cement treated soil cone adhering to a pile is expressed by eqs.(4.a) and (4.b) based on the equilibrium of the adhesion( $\alpha \cdot q_u \cdot A_1$ ) between the pile and the cone, the cone weight( $W_1$ ) and the tensile force acting on the cone surface (the observed angle of the cone head was  $45^\circ$ );

$$\alpha \cdot q_u \cdot A_1 = \sigma_t \cdot A_3 + W_1 \quad (4.a)$$

$$h = \frac{-a + \sqrt{a^2 + 4\gamma_1' \cdot b}}{2\gamma_1' / 3} \quad (4.b)$$

where  $\alpha$  is a constant (1/2 to 1/4) expressed by  $\bar{C}_a/C$  (Miyake et al., 1992),  $\gamma_1'$  (t/m<sup>3</sup>) the submerged density of cement treated soil,

$$a = \left( \frac{\gamma_1' \cdot R}{3} + \frac{\sigma_t}{\cos 45^\circ} \right)$$

$$b = \left( \frac{2}{3} \cdot \gamma_1' \cdot R^2 - \frac{\sigma_t \cdot R}{\cos 45^\circ} + 2\alpha \cdot q_u \cdot R \right)$$

$\sigma_t$  is the tensile strength (tf/m<sup>2</sup>) obtained from eqs.(3.a) and (3.b),  $R$  is the pile diameter (m), and  $A_1$  and  $A_3$  the outside surface area of a pile within its attached cone and the surface area of the cone, respectively.

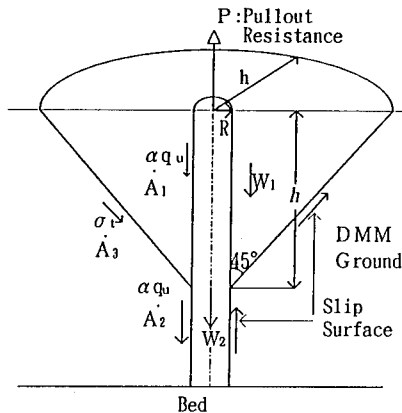


Fig.7 Model for the equilibrium of force at a maximum pullout load

The maximum pullout load can be obtained from eq.(5) by adding the submerged weight ( $W_2$ ) of the pile and the adhesion ( $\alpha \cdot q_u \cdot A_2$ ) between the pile and the cone to the right term of eq.(4.a).

$$\begin{aligned} P &= \sigma_t \cdot A_3 + W_1 + \alpha \cdot q_u \cdot A_2 + W_2 \\ &= \frac{\pi \cdot \gamma_1' \cdot h}{3} (h^2 + h \cdot R - 2R^2) \\ &\quad + \pi \cdot \sigma_t \cdot h (h + R) / \cos 45^\circ \\ &\quad + 2\alpha \cdot q_u \cdot \pi \cdot R (L - h) \\ &\quad + \pi \cdot R^2 \cdot L \cdot \gamma_2' \end{aligned} \quad (5)$$

where  $W_2$  is the submerged weight (tf/m<sup>3</sup>) of the pile,  $L$  the pile length (m), and  $\gamma_2'$  the submerged density (t/m<sup>3</sup>) of the pile.

The relationships between the unconfined compressive strength ( $q_u$ ) of cement treated soil and the depth ( $h$ ) of the cone are shown in Fig.8. The calculated result can quantitatively explain the test

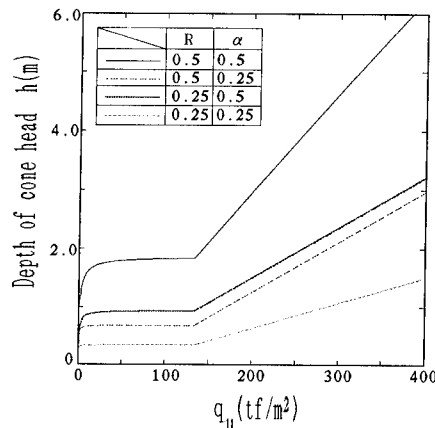


Fig.8 Relationships between  $h$  and  $q_u$

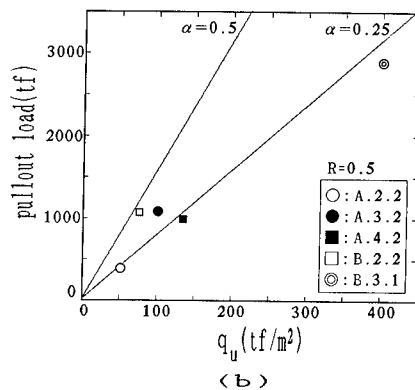
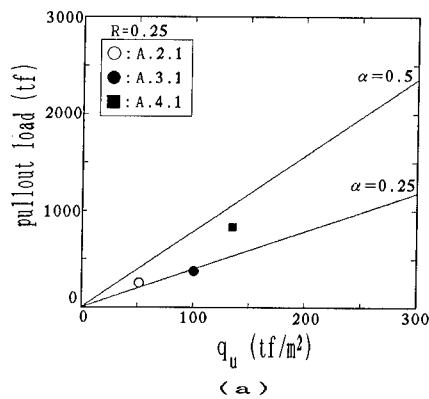


Fig.9 Comparison with calculations and measurements

result of increasing depth( $h$ ) with increasing  $q_u$ . The tendency of the displacement at the maximum pullout load to increase as  $q_u$  increases may be caused by the enlargement of this cone. The values of maximum pullout load obtained from centrifuge model tests are in the range of results from eq.(5) with  $\alpha$  of 1/2 to 1/4, as shown in Figs.9(a) and 9(b). The maximum pullout load for piles in ground improved by DMM from eq.(5) is analogous to the maximum pullout load for piles in clay expressed by eq.(1).

#### 4 FIELD TEST

Based on the preceding result, the raking piles shown in Fig.10 were constructed. Specifications of the raking piles are as follows: the diameter of a steel pipe pile is 0.6 m, the length of the pipe in

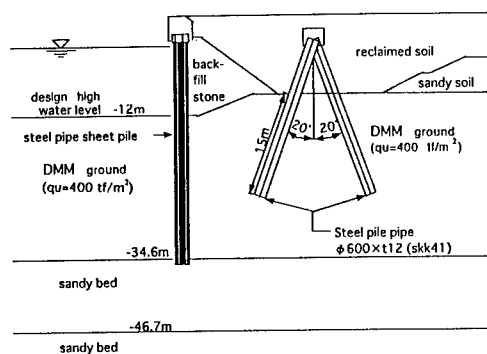


Fig.10 Standard cross section

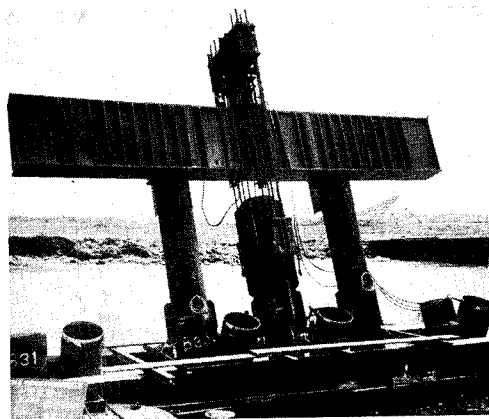


Fig.11 Pullout system in field test

ground is 15 m, the design pullout external force is 23.5 tf, the safety factor for the pullout force is 3, and the allowable pullout force is 706.5 tf. The average unconfined compressive strength of ground improved by the Deep Mixing Method at the pullout test site is 400 tf/m<sup>2</sup> and the average submerged density of the ground is 0.6 t/m<sup>3</sup>. The maximum pullout load which can be achieved is 5662.7 tf for  $\alpha=1/2$ , and 2831.4 tf for  $\alpha=1/4$  from eq.(5). Because the piles used in the pullout test were parts of the bulkhead, as shown in Fig.11, the pullout load was determined from the design pullout external force. The pullout load was applied by a load control system with an electro-hydraulic servo jack. The relationships between the pullout displacement and the pullout load are superimposed on the predicted line using  $\alpha=1/4$ , as shown in Fig.12. The displacement is very small and shows in the elastic range. The predicted displacement at the maximum pullout load is 1.5 times the displacement corresponding to  $q_u=400$  tf/m<sup>2</sup> with a solid line in Fig.5, considering the difference of length between the model pile and the practical pile. From the prediction based on eq.(5), the strength of ground improved by the Deep Mixing Method can be considered to have been too great.

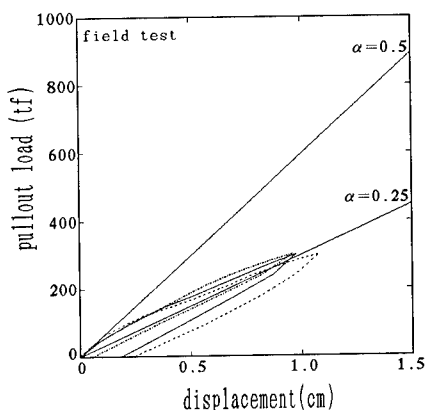


Fig.12 Comparison with predictions and field test results

#### 5 CONCLUSIONS

The authors have used centrifuge model tests with prototype tests in practical issues. As an application to practical construction, we showed that centrifuge model tests offered useful information prior to construction of bulkheads at a site in Tokyo Bay.

1) The sliding mode in the DMM ground has a cone shape and is different from the mode being considered in clay ground. The depth of the cone tends to

increase as the unconfined compressive strength of the ground increases.

2) Based on the equilibrium of force with the sliding mode obtained from this series of centrifuge model tests, equations to estimate depth of the cone and the maximum pullout load have been proposed. The values predicted from these equations agree well with results from the centrifuge model tests.

3) The relationships between displacement and pullout load from field tests plot on the line predicted for  $\alpha=1/4$  in eq.(5). Accordingly, the pile at site can be considered stable.

#### REFERENCES

- Tomlinson, M.J. 1971. Some effects of pile driving on skin friction. Proc. Conf. on Behavior of Piles, Inst. Civil Eng., London, pp.107-114.
- Terashi, M., Tanaka, H., Mitsumoto, T., Niidome, Y. & Honma, S. 1980. Fundamental properties of lime and cement treated soils (2nd Report). Report of the Port and Harbour Research Institute, Vol.19, No.1, pp.33-62.
- Yamamoto, T. & Miyake, M. 1982. Influence of specimen size on unconfined compressive strength of cement treated soil. Journal of the Society of Materials Science Japan, Vol.31, No.341, pp.183-187.
- Miyake, M., Satoh, T. & Matsumoto, M. 1992. Pull-out resistance of a pile in ground improved by the Deep Mixing Method. Proc. 27th Annual Meeting of JSSMFE, pp.29-30.

## Investigation of pile group efficiencies in sand

Tove Feld

*RH & H Consult, Denmark*

D. Bloomquist, F.C. Townsend & M.C. McVay

*University of Florida, Gainesville, Fla., USA*

**ABSTRACT:** Centrifugal model tests, utilizing a unique in-flight pile group driver / loading device, have been performed on model pile groups consisting of 2, 3, and 5 piles having spacings of 2,  $\sqrt{8}$ , or 4 diameters. The model tests reveal group efficiencies ranging from 74% to 97%, with higher efficiencies obtained at larger spacings. Numerical predictions of the load-settlement behavior [using the computer program GROUP] compared quite favorably with the observed model results, thereby demonstrating the viability of centrifugal modeling for computer program verification and vice-versa.

### INTRODUCTION

Design uncertainties often lead geotechnical engineers to perform pile load tests to obtain design parameters, and verify assumptions. However, these load tests are restricted to single piles, as load tests on pile groups are prohibitive due to difficulties in applying such large loads and resulting costs. Consequently, our knowledge concerning pile group behavior is limited, and this deficit suggests using small scale models. Although model tests have been performed at one gravity (Beredugo, 1966; Vesic, 1968), to obtain prototype stresses in a model, one must resort to an increased gravity field to account properly for the self-weight body forces. This high gravity field is easily accomplished using a geotechnical centrifuge.

The objective of this paper is investigate the load-settlement response of axially loaded pile groups in sand and compute the corresponding efficiencies. Accordingly, centrifugal model tests were performed on single piles and pile groups driven in-flight using various pile spacings and subsequently loaded to failure. Observed model response was then compared to numerical predictions using UF's GROUP program. (McVay, et.al, 1989)

### Equipment, and Test Procedure

The University of Florida centrifuge has a radius of 1.6m, and capacity of 7.5 g-tons with a factor of safety of 2.

Electrical power and hydraulic pressures are supplied to the arms via 80 electrical and 2 hydraulic slip-rings. An on-board video camera connected to a VCR and monitor provides visual observation of the experiments.

The centrifugal model tests were conducted in a teflon lined aluminum cylinder 12-in. high by 12-in.-diam (30-cm by 30-cm). The model piles are 12-in. (30cm) long, 3/8-in. (10mm) OD aluminum tubing and driven to an embedment of 9.5-

in. (24cm). Figure 1 illustrates the "X" pattern 5 pile group with a spacing of 2D. The sand used was Reid Bedford sand (SP) with an average grain size of  $d_{50} = 0.23$  mm.

Model preparation consisted of pluviating the sand through a series of stacked sieves to an approximate relative density,  $D_r = 27\%$ . After assembling the in-flight pile driver/loading device on the centrifuge arm and accelerating to 48 g's, the piles were individually driven at the appropriate spacing and subsequently load tested.

### G-Level Installation

To replicate field conditions accurately, for displacement piles it is obvious the piles must be installed in-flight. Accordingly, Bloomquist, et.al., 1991 have developed an in-flight multiple pile driver for installing and testing pile groups. Figure 2 presents a

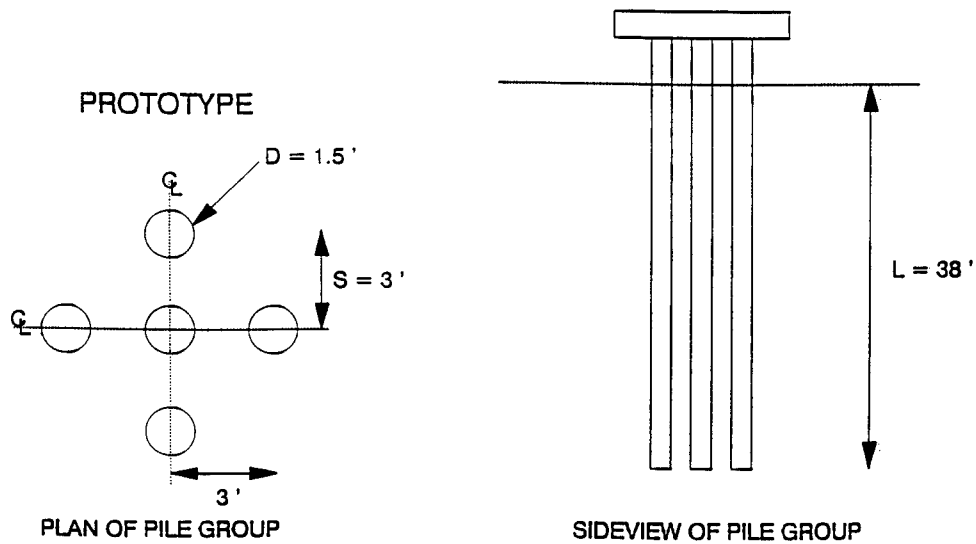


Figure 1 Plan and Sideview of Model Pile Group

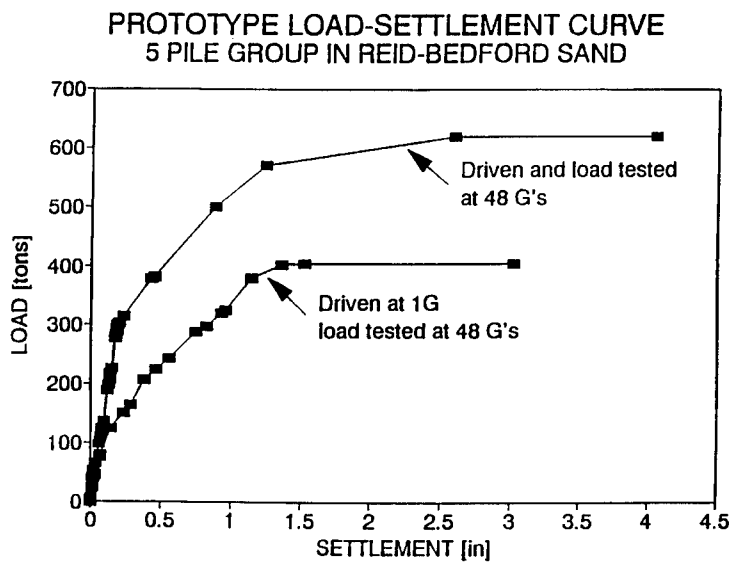


Figure 2 Influence of Installation g-Level



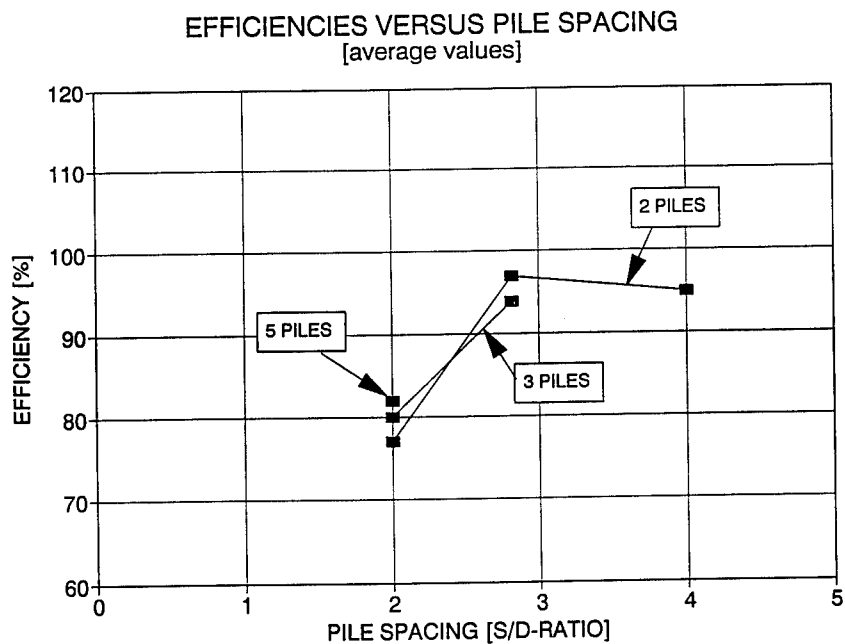


Figure 3 Pile Group Efficiencies vs Pile Spacing

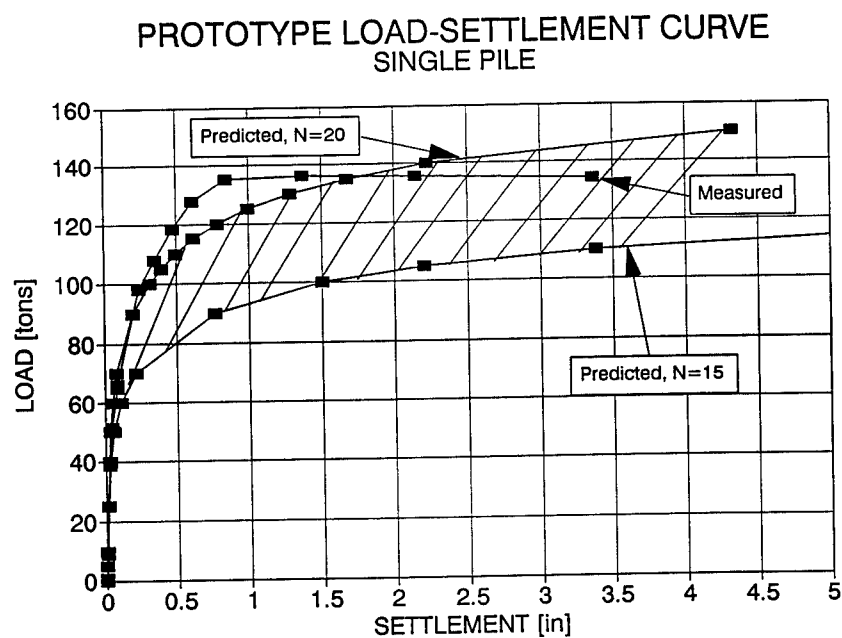


Figure 4 Predicted vs Model Load-Settlement Relationship - Single Pile

comparison between two five pile groups: (a) one installed at 1g and then accelerated and tested at 48 g's, and (b) the other installed and tested at 48 g's. An increase in capacity of 31% occurs due to in-flight installation; thus revealing installation importance.

#### Group Efficiencies

Based upon the pioneering work of Vesic (1968) geotechnical engineers have traditionally assumed group efficiencies equal to or greater than 1.0 for pile groups driven in sand. This conclusion is based upon his tests on 4 and 9 pile groups consisting of 4-in diameter by 60-in long (10-cm by 1.5m) model piles placed by jacking the entire group into sand. Consequently, the stress redistribution and downward movement on adjacent piles created by individually driving the piles may have been masked. Nevertheless, Vesic's (1977) results of 1g pile group model tests show efficiencies greater than one, when "failure" is a  $\delta/B_{\text{group}} \approx 0.1$  to 0.6%.

Beredugo (1966) performed 1g model tests on 3/8-in (10mm) diam by 12-in. long (30cm) model pile groups embedded in a SP sand ( $d_{50} = 0.16\text{mm}$ ). The pile groups were formed by individually pushing model wooden or brass piles to form groups as squares of 2', 3', and 4' piles at spacings of 3 to 9 diameters. He found group efficiencies ranging from 60 to 180 % depending upon sand density, pile roughness, spacing, and group size. Pile groups in loose sand ( $D_r = 62\%$ ) exhibited efficiencies less than unity, for  $\delta/B_{\text{group}} \approx 3.0\%$ .

Monzoori et.al. (1984) performed centrifugal model tests on wooden dowel pile groups at 70 g's. The pile groups at a spacing of approximately 3D were formed by individually pushing each pile by starting and stopping the centrifuge after pushing each pile and repositioning the pushing jack. A pile cap was subsequently placed on the 2 x 4 pile group, which was then accelerated and load tested. Group efficiencies of 1.15 were obtained, using  $\delta/B_{\text{group}} \approx 0.7\%$ .

FHWA's Hunter's Point group load test represents the most recent prototype. (Dimillo, 1989) Hunter's Point was a 5 pile group consisting of closed ended pipe piles 10.75 inches (27.3 cm) OD and 0.365 inch (7.8mm) thick walls 30 ft. (9.2m) long driven at a 3D spacing. The single pile capacity was 110 tons (0.98MN) and group capacity was 520 tons (4.63 MN) for an efficiency of  $\approx 94\%$ , when  $\delta/B_{\text{group}} \approx 3.5\%$ .

#### Model Test Results and Discussion

Tests using pile groups consisting of 2, 3, and 5 piles at spacings at 2,  $\sqrt{8}$ , and 4 diameters were conducted; the results of which are summarized in Figure 3. These efficiencies are based upon ultimate loads occurring at deformations greater than 1 inch (2.5cm). As shown, the results illustrate a dramatic effect of pile spacing on group efficiency. For spacings of 2D, group efficiencies for 2, 3, and 5 pile groups are approximately 80% for  $\delta/B_{\text{group}} \approx 1.4\%$ . As the group spacing increases to 4D, the efficiency approaches 100%. These efficiencies less than one are attributed to inter-pile load shedding, similar to a "downdrag" effect. After the first pile is driven, driving of adjacent piles will cause a load transfer to this earlier driven pile resulting in unequal stresses among the piles. Subsequent loading of the pile cap will cause a redistribution among the group with corresponding settlements. This load sharing among piles means group efficiencies will be less than 100% until the pile spacing exceeds the zone of influence. Although the concept that driving multiple piles causes densification and a corresponding increase in soil stiffness, the inter-pile load shedding has a greater effect. Consequently, efficiencies greater than 100% are not supported by these data.

#### Evaluation of Computer Program GROUP

The load-settlement response for both single piles and pile groups can be predicted using UF's programs TZD or PL-AID (single piles) and GROUP (pile groups), which were written by McVay, et.al (1989). The programs use a hyperbolic representation of the t-z relationship, and in the case of pile groups, far field linear elasticity is used. Although these programs accept either CPT or SPT correlations to estimate initial shear modulus values, we used SPT, and  $G(\text{psi}) = 500N$ . Various assumed SPT values and distributions were tried to obtain a match between observed and centrifuge modeled single pile load settlement response. For the single pile, a uniform  $N = 15$  to 20 blows provided the best match as shown in Figure 4. One difficulty with group predictions based upon a single pile response is that subtle density differences due to multiple pile driving or model preparation are not accounted for. Consequently, a range in N values was used to predict group responses.

Figure 5 presents predicted vs

## PROTOTYPE LOAD-SETTLEMENT CURVE 5 PILES/PILE SPACING 2D

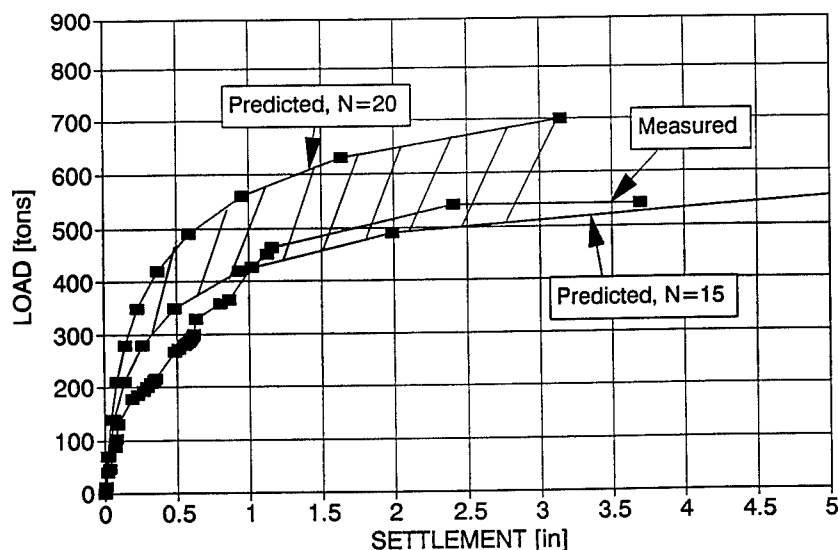


Figure 5 GROUP Predicted vs Model Load-Settlement Relationship  
5 Pile Group at 2D Spacing

measured examples for a 5 pile group spaced at 2D. As shown, the predictions accurately bound the measured centrifuge responses, and demonstrate the viability of centrifugal modeling for computer program verification and vice-versa.

### Conclusions

1. A multiple pile driver for centrifugal model testing has been developed, and is capable of driving a series of piles in any sequence and subsequently load testing the group.

2. Comparisons between in-flight driven and lg statically pushed piles showed a marked difference in capacity. Thus validating the importance of in-flight placement of centrifugal model piles.

3. Pile spacing greatly affects group efficiency, as does  $\delta/B_{\text{group}}$  ratios, with closer spacings and low ratios exhibiting lower efficiencies. For spacings of 2D, group efficiencies for 2,3, and 5 pile groups are approximately 80%. As group spacing increases to 4D, the efficiency approaches 100%. These efficiencies less than one are attributed to inter-pile load shedding, similar to a "downdrag" effect, and means group efficiencies will be less than 100% until the pile spacing exceeds the zone of influence.

4. Comparisons between the computer program GROUP predicted vs centrifugal model measured load settlement responses of 2,3 and 5 pile groups with varying spacings were excellent, and demonstrate the viability of centrifugal modeling for computer program verification and vice-versa.

### References

- Beredugo, Y.O. (1966) "An Experimental Study of the Load Distribution in Pile Groups in Sand" Canadian Geotechnical Jrn. Vol III No. 3, August pp 145-166
- Beredugo, Y.O. (1967) Reply to discussion of "An Experimental Study of the Load Distribution in Pile Groups in Sand" Canadian Geotechnical Jrn. Vol IV No. 3 pp 356-357.
- Bloomquist, D., Feld, T., Townsend, F.C., Gravgaard, J. and Gill, J.J. (1991) "Development of a Multiple Pile Driver/Load Test Device for Pile Groups Studies" Proceedings Centrifuge '91, Boulder, CO

DiMillio, A.F., Ng, E.S., Briaud, J.L.,  
and O'Neill, M.W. (1987) "Pile Group  
Prediction Symposium: Summary Vol. 1:  
Sandy Soil" FHWA Rpt. FHWA-TS-87-221

Lo, M.B. (1967) "An Experimental Study  
of the Load Distribution in Pile  
Groups in Sand" Disc. in Canadian  
Geotechnical Journal, Vol IV, No.3.

McVay, M.C., Townsend, F.C.,  
Bloomquist, D. and Caliendo, J.A.  
(1989) " Numerical Analysis of Verti-  
cally Loaded Pile Groups" ASCE Foun-  
dation Engineering: Current Princi-  
ples & Practices Geotechnical Spec.  
Publ. 22, Northwestern University.

Meyerhof, G.G. (1976) "Bearing Capacity  
and Settlement of Pile Foundations"  
ASCE Jrn of the Geotechnical Engi-  
neering Div., Vol 102, No. GT3.

Monzoori, M., Atkinson, R.H., Ko, H-Y,  
Goble, G.G. (1984) "Centrifugal  
Testing of Model Piles and Pile  
Groups Vol II, Centrifuge Tests in  
Sand" Report No. FHWA/RD-84/003,  
Office of Research & Development,  
FHWA, Washington, D.C.

Poulos, H. and Davis, E.H. (1980) Pile  
Foundation Analysis and Design,  
J.Wiley & Sons, New York.

Vesic, A.S. (1968) "Experiments with  
Instrumented Pile Groups in Sand"  
ASTM Spec. Tech. Publ. 444 pp 177-222

Vesic, A.S. (1977) "Design of Pile  
Foundations" NCHRP Publ. 42, Transpor-  
tation Research Board, National  
Research Council, Washington, D.C.

#### Acknowledgements

This research was sponsored by the  
Florida Department of Transportation as  
a portion of State Project # 99700-  
7500-119, "Evaluation of Settlement of  
Pile Groups in Non-Homogeneous Soil  
Deposits". Dr. J. A. Caliendo, FDOT,  
was the technical coordinator providing  
technical guidance and assistance; we  
greatly appreciate his input to the  
success of this project.

## Pile uplift and pile cap interaction studies in sand

E.A. Dickin & A. Lyndon  
*University of Liverpool, UK*

**ABSTRACT:** Investigations into the behaviour of single piles subjected to uplift forces and the use of circular groups of piles as a means of reducing settlement under structures subjected to intense edge loading are described. Uplift capacity is strongly influenced by pile length/diameter ratio and soil density index. Uplift resistance in dense sand reduces considerably after failure. The pile group study shows that a ground bearing pile cap on dense sand could give significant improvement in stiffness over the same free standing group. However, a critical pile spacing is observed below which the ground bearing component contributes little to stiffness.

### 1. INTRODUCTION

The Liverpool centrifuge, which has been in operation since 1978, has a 13g tonne capacity and an effective radius of 1.15m. The machine is fitted with balanced swinging buckets which are basically 0.57m long, 0.45m wide and 0.23m deep. Its medium size has facilitated several parametric studies, many involving the behaviour of piled foundations. Investigations into the response of piles to lateral load were reported by King et al. (1985), King and Fulthorpe (1986) and by Lyndon and Pearson (1988). Interaction studies between piles in groups subjected to lateral loading were presented by Kulkarni et al. (1985). Subsequent research investigating the uplift capacity of piled foundations with enlarged bases was published by Dickin and Leung (1990, 1992) and Leung and Dickin (1991). Preliminary work on the behaviour of short piled foundations subjected to large moments was reported by Dickin and Wei (1991). Findings from an extended investigation into the side bearing aspects of this problem are presented by Dickin and Nazir (1994). A pilot study on the use of settlement reducing piles below a foundation to a silo was reported by Lyndon et al. (1991). Recent investigations into the performance of

piles experiencing uplift forces and the behaviour of pile groups are described here.

### 2. PILE UPLIFT BEHAVIOUR

The package arrangement in the pile uplift study is shown in Figure 1. Models were tested at a constant rate of displacement of

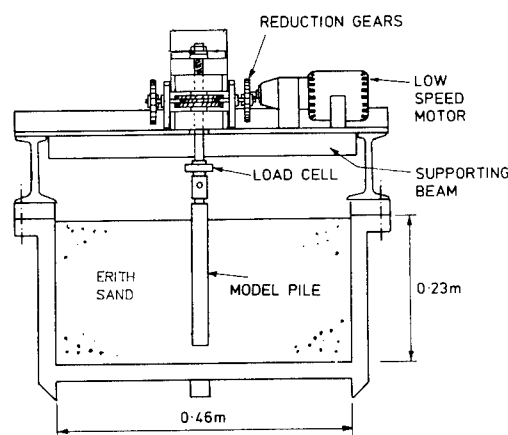


Fig.1. Package arrangement in pile uplift tests

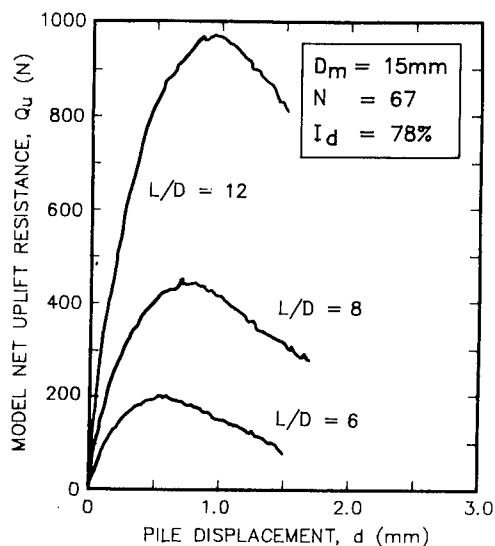


Fig.2 Variation of model net uplift resistance  $Q_u$  with displacement  $d$  for piles in dense sand

0.23mm/minute. The pull was supplied by a small high-torque low speed A.C. motor, manufactured by PARVALUX Ltd., via a custom-built worm and wormwheel arrangement. Uplift resistance was measured by a 8.9kN capacity SENSOTEC load cell and displacement by a 30mm travel SAKAI conductive plastic potentiometer reading to 0.001mm. Output from both transducers was fed to an ORION data logger controlled by a BBC Master series computer. Readings were taken at 10 second intervals until a vertical displacement of 5mm had occurred, which was well beyond the point of maximum resistance in all tests. The centrifugal program included tests on three mild steel model piles with the parent sand stuck to their surfaces using epoxy resin to produce a rough pile/soil interface. Piles with diameters  $D_m=10, 15$  and  $30\text{mm}$  were subjected to the appropriate acceleration factors ranging from  $N=33$  to  $N=67$  gravities in order to simulate stresses around  $0.5\text{m}$  and  $1\text{m}$  diameter prototype piles. All piles were  $200\text{mm}$  long but the testing arrangement limited the maximum embedded length  $L_m$  to  $180\text{mm}$ . Length to diameter ratios examined ranged from 2 to 18. Packages were prepared at unit gravity with the model pile held in position by a temporary cross-piece while sand was rained through a diffuser having  $3\text{mm}$

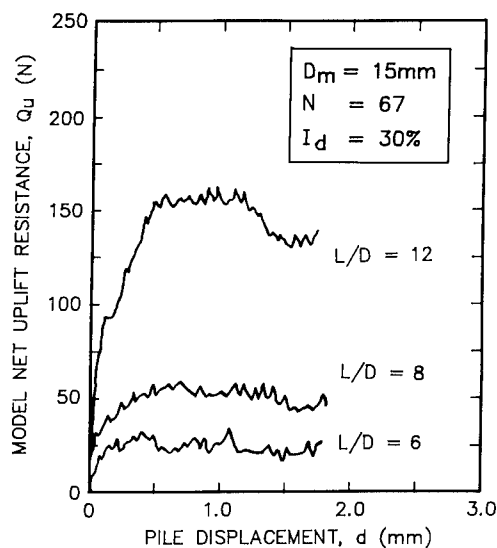


Fig.3 Variation of model net uplift resistance  $Q_u$  with displacement  $d$  for piles in loose sand

diameter holes at  $20\text{mm}$  centres placed directly over the package for tests in loose sand, or mechanically compacted in  $25\text{mm}$  layers using a small vibrator for tests in dense sand. Dickin and Leung (1990) found no significant difference between uplift capacities for piles with enlarged bases in dense sand beds prepared either by this light vibration or by pluviation. Effective unit weights of  $\gamma'=14\text{kN/m}^3$  (density index  $I_d=30\%$ ) and  $\gamma'=16\text{kN/m}^3$  ( $I_d=78\%$ ) were achieved in the research reported here. The laboratory dry Erith sand used is clean, fine and fairly uniform having most of its grains between  $0.125\text{mm}$  and  $0.25\text{mm}$ , a  $D_{50}$  of  $0.20\text{mm}$  and a uniformity coefficient of 1.5.

Typical relationships between the net uplift load  $Q_u$  (i.e. exclusive of pile self weight) and vertical displacement  $d$  are shown in Figures 2 and 3 for tests on  $15\text{mm}$  diameter model piles in dense and loose sand respectively. Piles in dense sand quickly mobilised their maximum uplift capacities after a small movement of between  $0.5\text{mm}$  and  $1\text{mm}$ . In all cases further movement produced a steady reduction in uplift resistance. Similar post-peak behaviour was reported by Nunez et al. (1988) for longer tension piles. In the present research the reduction in the case of the shortest piles was considerable and could be

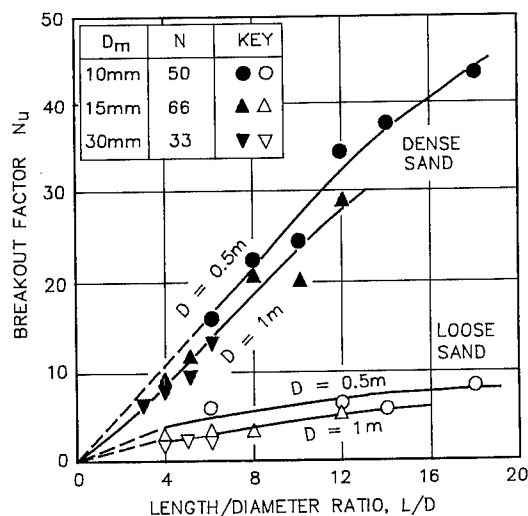


Fig.4 Variation of prototype breakout factor  $N_u$  with length/diameter ratio  $L/D$  for piles in loose and dense sand

attributed to the collapse of sand into the gap formed below the pile as the test proceeded. In contrast, peak resistances for piles in loose sand, defined by the onset of post-peak softening, occurred after slightly larger displacements. Uplift resistances, expressed dimensionlessly as a prototype breakout factor  $N_u = Q_u / \gamma A_b L$  in

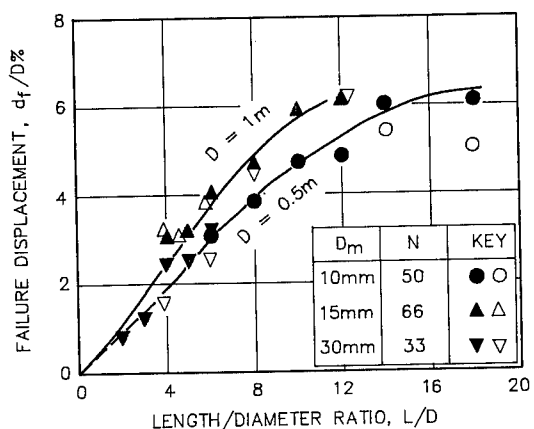


Fig.5 Variation of failure displacement  $d_f$  with length/diameter ratio  $L/D$  for piles in loose and dense sand

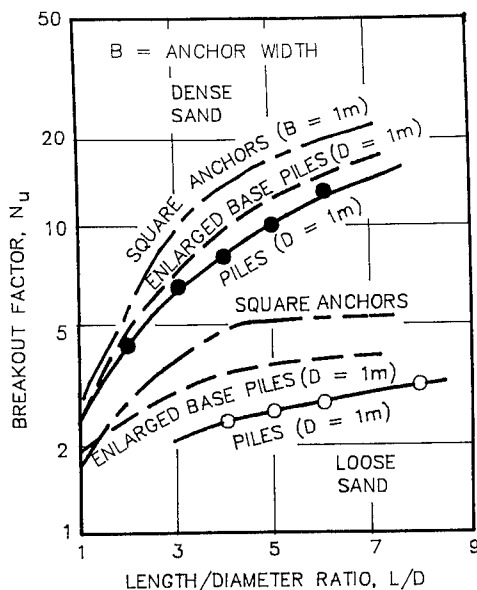


Fig.6 Comparison between prototype breakout factors  $N_u$  for anchor plates and piles with and without enlarged bases in loose and dense sand

which  $A_b$  is the the pile base cross section area, increase markedly with length/diameter ratio and soil unit weight as shown in Figure 4. Breakout factors for 0.5m diameter prototype piles are slightly higher than those for 1m diameter piles apparently indicating a relatively minor influence of size. It may be noted that the ratios between pile circumference and average grain size for the model piles used ranged from approximately 155 to 460, well above the critical value of 40 at which particle size effects were identified by Ovesen(1979) in footing tests. Failure displacements  $d_f$  normalised to pile diameter generally increase with pile embedment ratio and pile diameter as illustrated in Figure 5. Since sand properties and preparation procedures were similar, reasonable comparisons may be drawn between the present results and those from previous uplift studies. Thus it can be seen in Figure 6 that uplift resistances obtained in this research provide a sensible lower bound to uplift capacities for piles with enlarged bases reported by Dickin and Leung(1990) and for square anchor plates by Dickin(1988) as would be anticipated. Considerably smaller pile movements

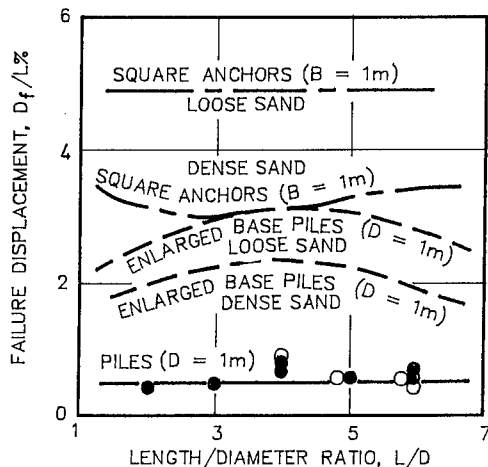


Fig.7 Comparison between failure displacements  $d_f$  for anchor plates and piles with and without enlarged bases in loose and dense sand

were required to mobilise peak resistances than in the previous uplift studies, suggesting that, by comparison, soil mobilisation is essentially localised to the region close to the pile shaft. Figure 7 shows that failure displacements, normalised to pile length (or anchor depth), of approximately 0.6% were observed in the present study for piles in either loose or dense sand, while enlarged base piles required 2% and 3% displacement and anchor plates 3% and 5% displacement in dense and loose sand respectively.

Burland's parameter  $\beta$  for piles in loose sand was found to average 0.3 for the range of pile lengths examined. Much higher  $\beta$  values of the order of unity were obtained for piles in dense sand. However the considerable post-peak reductions in pullout resistance observed in the latter tests were such that these high  $\beta$  values could not be confidently adopted in design.

### 3. SETTLEMENT-REDUCING PILE BEHAVIOUR

The lack of confining pressure at the edge of a shallow foundation on sand, especially when subjected to intense loading, is usually critical to settlement and in the case of a raft the resulting

curvature could be relatively high. Foundations for silo structures may fall into this category and two simple approaches to overcome this problem could be to provide a stiffer raft or additional support at the perimeter. The latter solution is usually more appropriate because resistance is provided at the load position and deals with the cause rather than the effect as in the former case. A satisfactory design may be achieved by including only a sufficient number of piles necessary to reduce the edge settlement to a tolerable amount. This option has been investigated for a particular prototype silo geometry in the research reported.

A typical package arrangement for a load test on a circle of free standing piles is shown in Figure 8. Individual piles in the group consisted of 140mm long, 7.5mm overall diameter sand-coated steel rods. Conditions around a single prototype pile, 600mm in diameter and 11m long, were simulated by testing at 79 gravities. The results of the centrifuge model tests conducted on ring and raft foundations, with and without piles are summarised in Figure 9. The ground bearing rings and plates were structurally separated from the pile heads in order that the cap could react independently with the dry Erith sand subgrade compacted to a density index of 78%. It may be noted that the 24 pile group comprised two rings of piles at pitch circles of 190mm and 150mm.

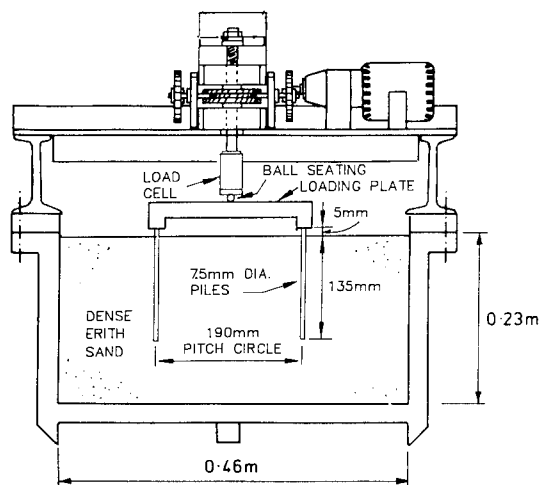


Fig.8 Package arrangement for loading tests on a ring of free standing piles in dense sand



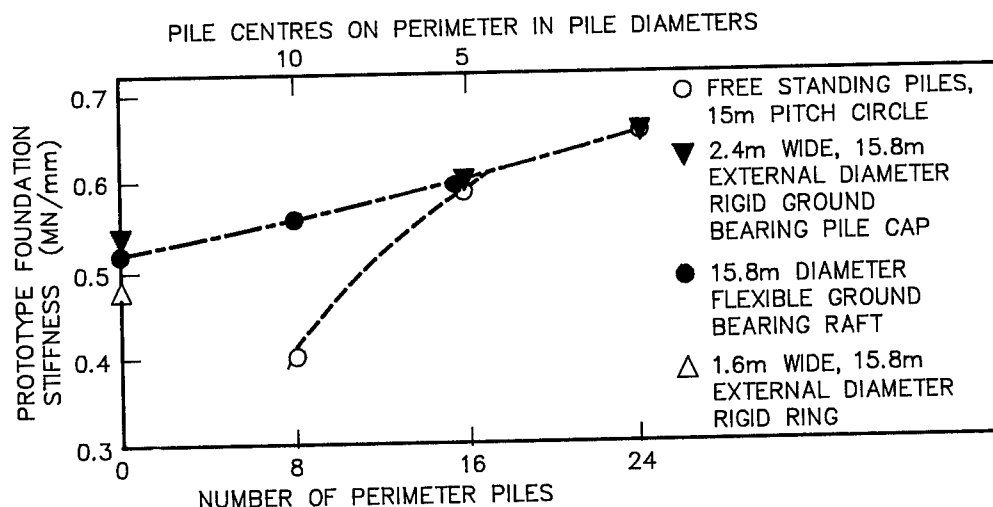


Fig.9 Variation of foundation stiffness with number of perimeter piles

The load/settlement relationships for all the foundation arrangements given in Figure 9 were linear up to a simulated prototype load of at least 40MN. Assuming the prototype structure subjects its foundation to a total edge load of 40MN, the tests show that a flexible surface raft 15.8m in diameter with no piles would experience a 75mm edge settlement. Interpolation from Figure 9 suggests that the same stiffness could be provided by a free standing circle of 12 piles or 8 piles combined with a 1.6m wide ground bearing pile cap. Where 16 or more piles are required to limit settlement a conventional design basis could be adopted, for at closer pile spacings the contribution to stiffness from the ground bearing component of the cap is slight.

#### 4. CONCLUSIONS

The uplift resistance of piles in sand is strongly influenced by pile length/diameter ratio and by the unit weight of the soil. Resistance continues to increase even for deep piles with  $L/D=18$ . Piles in dense sand exhibit considerable post-peak reductions in resistance, the shorter piles producing final values not much higher than those recorded for loose sand.

The group study has shown that the effectiveness of a few perimeter piles, when combined with a ground bearing pile cap, can increase foundation stiffness over that of their free standing equivalent. However, as pile spacing reduces, a critical spacing is reached at which any improvement over that of the equivalent free standing pile group is not significant. This critical spacing is, in this case, of the order of five pile diameters.

The tests reported in this study were not specific to a known field subgrade and the boundary conditions imposed by the container will have influenced the results. Nevertheless it is thought that the tests are meaningful and identify some geometric factors influencing pile behaviour.

#### REFERENCES

- Burland, J. 1973. Shaft friction of piles in clay. *Ground Engineering* 6, No. 3: 30-42.
- Dickin, E.A. 1988. Uplift behaviour of horizontal anchor plates in sand. *Journal of Geotechnical Engineering Division, ASCE* 114, GT11: 1300-1317.
- Dickin, E.A. and Leung, C.F. 1990.

- Performance of piles with enlarged bases subject to uplift forces. *Canadian Geotechnical Journal* 27, No.5:546-556.
- Dickin, E.A. and Leung, C.F. 1992. The influence of foundation geometry on the uplift behaviour of piles with enlarged bases in sand. *Canadian Geotechnical Journal* 29, No.3:498-505.
- Dickin, E.A. and Nazir, R. 1994. Factors influencing the behaviour of side-bearing foundations in sand. *submitted to Centrifuge 94*. Rotterdam: Balkema.
- Dickin, E.A. and Wei, M.J. 1991. Moment carrying capacity of short piles in sand. *Centrifuge 1991*. ed Ko, H.Y. and McLean, F.G. :277-284. Rotterdam: Balkema.
- King, G.J.W., Dickin, E.A. and Lyndon, A. 1985. The development of a medium-size centrifugal testing facility. *Proceedings of Symposium on Application of Centrifuge Modelling to Geotechnical Design*. ed Craig, W.H. :25-26. Rotterdam: Balkema.
- King, G.J.W. and Fulthorpe, J.N. 1986. Centrifugal model tests on laterally loaded single piles. *Proceedings of 3rd Indian Conference on Ocean Engineering*. Bombay: B1-B11
- Kulkarni, K.R., Chandrasekaran, V.S. and King, G.J.W. 1985. Centrifugal model studies on laterally loaded pile groups in sand. *Proceedings of 11th ICSMFE*, San Francisco.
- Leung, C.F. and Dickin, E.A. 1991. Uplift capacity of foundations. *Recent Advances in Geotechnical Engineering III*, Singapore :20-24.
- Lyndon, A. and Pearson, R.A. 1988. Skin friction effects on laterally loaded large diameter piles in sand. *Centrifuge 88*. ed Corte, J.F. :363-369, Rotterdam: Balkema.
- Lyndon, A., Turner, N.G. and Wei, M.J. 1991. Centrifugal modelling of stress-reducing piled foundations on sand. *Proceedings of 4th International Conference on Piling and Deep Foundations*. ed Deep Foundations Institute. :611-616, Rotterdam: Balkema.
- Nunez, I.L., Hoadley, P.J., Randolph, M.F. and Hulett, J.M. 1988. Driving and tension loading of piles in sand in a centrifuge. *Centrifuge 88*. ed Corte, J.F. :353-362, Rotterdam: Balkema.
- Ovesen, N.K. 1979. Discussion 9.3 on the use of physical models in design. *Proceedings of 7th European Conference on Soil Mechanics and Foundation Engineering*, Brighton, Vol.4:319-323.

## Settlement of piled raft foundations on clay

K. Horikoshi & M. F. Randolph

*Department of Civil Engineering, The University of Western Australia, Nedlands, W.A., Australia*

**ABSTRACT:** In the majority of piled raft designs, the capacity of the foundation is estimated by ignoring the contribution of a raft. Consequently, more piles than are necessary are installed beneath the raft and the overall settlement of the foundation automatically becomes negligible. However, from an economical point of view, it is preferable that the foundation is designed in such a way that the settlements are limited to an acceptable level, but where the load-carrying capacity of the raft is taken into account. In this study, the settlement behaviour of a piled raft foundation is examined by means of a series of centrifuge tests, with particular attention paid to differential settlements. Results from a partially piled flexible raft foundation are compared with those from an unpiled raft foundation. In the piled-raft model, capped piles are installed beneath the raft. Independent load tests on single uncapped and capped piles are reported, allowing a full comparison of the performance of each element of the foundation. The test results show that while the raft may carry the major portion of the applied load, a small number of piles situated near the centre of the raft are an effective means of minimizing differential settlement of the foundation.

### 1 INTRODUCTION

In most conventional design methods for piled foundations, the contribution of the pile cap, or raft, to the total capacity is ignored when assessing the required number of piles. As a result, more piles than are necessary are often installed beneath the raft, which leads automatically to much lower levels of overall settlement than could be tolerated by the structure.

Although it is necessary to ensure adequate bearing capacity of the foundation, the primary concern in many cases is the settlement of the foundation. In particular, the differential settlement is a critical consideration in designing a piled raft foundation. However, as discussed by Randolph and Clancy (1993), the conventional approach of a uniform distribution of piles beneath the entire raft is very inefficient at reducing differential settlements.

The aim of a foundation design should be to control total and differential settlements to an acceptable level. As will be shown in this paper, this may be achieved by appropriate location of

piles beneath the central part of the raft, for the express purpose of reducing differential settlements.

A series of centrifuge model tests have been performed at the University of Western Australia. The centrifuge facility comprises an Acutronic Model 661 with a platform radius of 1.8 m and total capacity of 40 g-tonne, as described by Randolph et al (1991).

The piled-raft foundation considered in this study consists of a flexible raft bearing on a thin sand layer overlying medium strength clay. A small number of piles, each with an independent cap, are installed beneath the central region of the raft.

Independent tests have been conducted on single piles, both with and without a small cap, on an unpiled raft and on a piled raft. In order to ensure consistency, tests on all the above elements are included on each soil sample prepared. Three separate samples have been prepared, and excellent consistency has been obtained between the different samples. The paper concentrates on the results from one of these samples, in order to simplify presentation.

## 2 MODEL

Although the piled rafts considered here have application to a wide variety of buildings, it was convenient to use small tanks for the experiments, as shown in Figure 1. Tests were conducted at a centrifuge acceleration of 100 g. Thin-walled cylindrical steel tins (such as used for paint) were used for the model tanks. In addition to their dead weight, and a small amount of water in the bottom of the tanks, load was applied cyclically by adding water to the tins and draining water through solenoid valves which were set on the wall of the strong box.

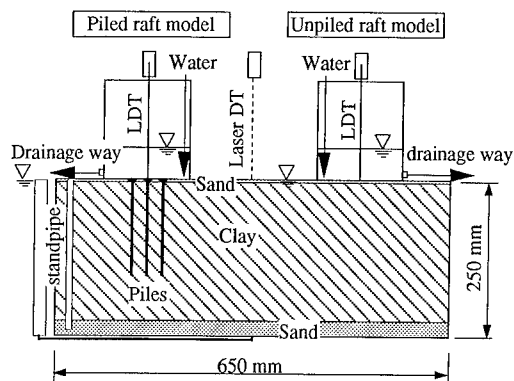


Figure 1 Model used in centrifuge tests

The performance of the piled raft and the unpiled raft were compared at the same time in the same model. The details of the tanks used in the tests are shown in Table 1. The base of the tanks provides an extremely flexible foundation (equivalent to a concrete raft of thickness less than 50 mm).

Table 1 Details of model tanks

Material	Steel	Height	150 mm
Diameter	140 mm	Mass*	0.63 kg
Base and side-wall thickness			0.25 mm

\*including minimal water

The settlement of the raft was measured at three points by using lightweight displacement transducers with a high resolution of 0.003 mm. One transducer was set at the centre of each raft and others were set, diametrically opposed, on the edge. The edge settlement was calculated from the average value of the edge transducers in order to avoid the influence of any tilting.

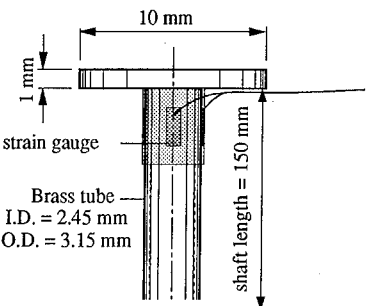


Figure 2 Details of model pile

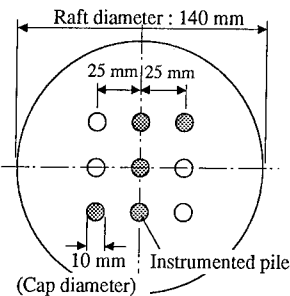


Figure 3 Pile spacing of piled-raft model

Details of the model piles used in this study are shown in Figure 2. The piles are made from tubular brass with an outside diameter of 3.15 mm. At the top of the pile, a 1 mm thick circular cap with a diameter of 10 mm is attached. Strain gauges are located on several piles at the top of the shaft, just below the cap, to measure the axial force transferred to the pile. Piles were installed to a depth of 150 mm in the soil.

A group of 9 piles was installed beneath the model piled raft. Five piles in the group were instrumented with strain gauges. In this study, the pile spacing was set as shown in Figure 3. A thin layer of fine sand (approximately 4 mm thick) was placed between the pile caps and the model raft.

Commercially available kaolin clay was used for the soil, with key properties as shown in Table 2. The soil was consolidated under a vertical surcharge of 300 kPa before the in-flight consolidation due to self-weight. Coarse sand with a thickness of 25 mm was placed as a drainage layer at the bottom of the model. A 5 mm thick layer of fine sand was placed on the surface of the clay to prevent swelling to a slurry at the surface and to offer a drainage layer. The total thickness of the soil was 250 mm.

Table 2 Key properties of kaolin clay

L.L.	61 %	C <sub>c</sub>	0.44
P.L.	27 %	C <sub>s</sub>	0.11
Φ'	23°	γ <sub>sat</sub>	17.5 kN/m <sup>3</sup>

Before the centrifuge tests, three small pore pressure transducers were installed in the soil beneath the edge of each raft. The movement of the soil surface was observed in-flight between the tanks with a laser displacement transducer.

### 3 TESTING PROCEDURES

Model piles were installed in the soil before the centrifuge tests but after the soil had been consolidated under the surcharge of 300 kPa. The model was then consolidated on the centrifuge for about 15 hours without placing the raft models on the soil. At the end of this consolidation period, the centrifuge was halted and the two model rafts were placed on the soil quickly. This procedure was followed in an attempt to simulate an actual construction procedure, where the raft is placed on ground which is fully consolidated. The centrifuge was then restarted to allow (re-)consolidation of the soil with the additional weight of the water and minimal water.

#### 3.1 Cone penetration tests and strength profile

At the end of the above consolidation, cone penetration tests were conducted in-flight to confirm the soil strength. The details of the penetrometer used in this study are described by Stewart et al (1991). The diameter of the cone was 9 mm and the cone was penetrated into the soil at the rate of 3 mm/s.

Profiles of cone resistance were very consistent and the undrained shear strength ( $s_u$ ) of the clay may be deduced from the cone resistance ( $q_c$ ) by:

$$s_u = (q_c - \sigma_v) / N_c \quad (1)$$

where  $\sigma_v$  is the total overburden stress and  $N_c$  is an empirical coefficient. The appropriate value of  $N_c$  is influenced by the overconsolidation ratio of the soil. However, Stewart et al (1991) suggest that a value of 12 is applicable for the kaolin clay used in the tests. The resulting profiles of undrained shear strength are as shown

in Figure 4. This figure indicates that the soil strength increases almost linearly with depth, according to  $s_u = 22 + 1.8z$  kPa, where  $z$  is the equivalent prototype depth in metres.

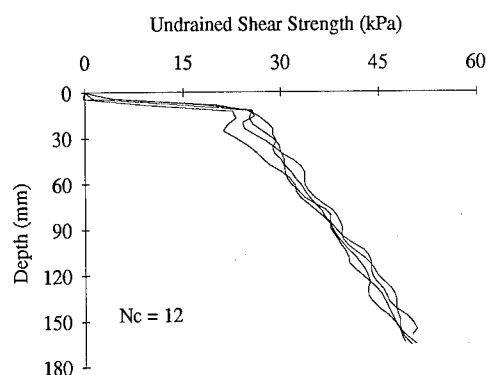


Figure 4 Undrained shear strength profiles

#### 3.2 Single pile loading tests

In addition to the tests on the raft foundations, load tests were also carried out on separate capped and uncapped piles at a constant penetration rate of 0.01 mm/sec. These piles were identical to those under the piled raft, but situated in the centre of the soil sample, between the two tanks. The piles were installed at the same time as the main foundation piles, and were tested just prior to the water loading tests on the tanks.

#### 3.3 Loading of the model tanks

Loading of the model tanks was performed in-flight using water, and in most cases the water level was cycled to allow the unload-reload performance of the foundations to be observed. Water was added to the tanks at an equivalent loading rate of 0.7 kPa/sec and drained at about the same rate. The actual applied load was measured using pore pressure transducers situated inside each tank.

Throughout the tests, the settlements of the tanks, forces in the piles and pore pressures generated in the soil were measured. At the end of any cycling of the load, water was added to the maximum level in the tanks and maintained for several hours to observe the consolidation behaviour of the foundations.

## 4 TEST RESULTS

### 4.1 Single pile performance

#### *Uncapped pile*

The load-settlement curve of the uncapped pile is shown in Figure 5. The ultimate capacity of the pile was about 33 N, although the shaft capacity appears to be mobilised at a load of about 28 N. Allowing for a small zero offset (due to poor contact between the uncapped pile and the loading rod), the full capacity is essentially mobilized at a settlement of 0.3 mm (10 % of the pile diameter). The shaft capacity of 28 N corresponds to an average shaft friction of about 19 kPa, 58 % of the average undrained shear strength.

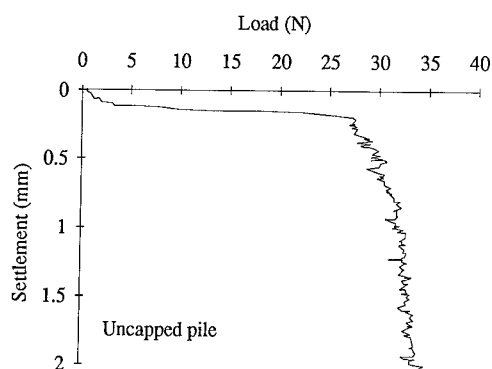


Figure 5 Load-settlement curve of uncapped pile

#### *Capped pile*

The load settlement curve of the capped pile is shown in Figure 6. The total bearing capacity of the capped pile was more than 60 N, of which some 40 N was provided by the pile (as opposed to the cap). At a displacement of 0.3 mm (10 % of the pile diameter), the pile shaft carries a load of 33 N, compared with 28 N for the uncapped pile.

The above results have been confirmed by tests in other soil samples, and it is clear that the small pile cap has a significant beneficial effect on the pile capacity. It is of interest that the shaft capacity of the capped pile is larger than that of the uncapped pile. The main reason for this behaviour is considered to be consolidation of the soil just under the cap during the loading

test, due to the stress transferred from the cap. This will give rise to increased load transfer between the upper part of the pile and the soil.

The approach of Hanna and Meyerhof (1980) was used to estimate the bearing capacity of the pile cap, acting alone. This yielded a value of 16 N. Thus, combining the uncapped pile capacity with the estimated capacity of the pile cap would give a total of 49 N. The main reason for the higher capacity actually measured is probably the different failure mechanism in the case of the capped pile, where the failure surface must make a transition from adjacent to the pile shaft (in the lower part of the pile) to a conical cylinder at the edge of the cap.

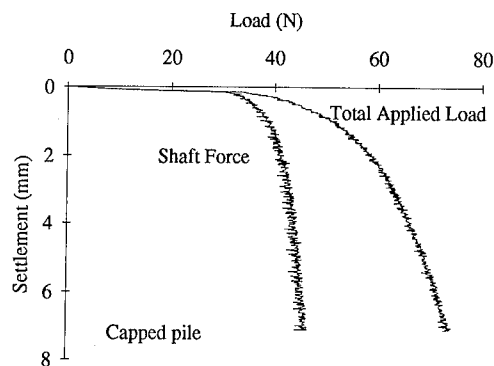


Figure 6 Load-settlement curve of capped pile

### 4.2 Behaviour of raft foundation

#### *Settlement during reconsolidation*

The behaviour of the raft foundations was observed during the in-flight reconsolidation, where each tank with minimal water applied a load of 618 N (average pressure 40 kPa) to the soil. The settlement of each raft centre is shown in Figure 7 with the settlement of the soil. Since the settlements of the rafts were measured from fixed points above the soil box, the raft settlements include the soil settlement.

The differential settlements are shown in Figure 8. In the piled raft profile, negative differential settlement was observed, with the edges of the raft settling more than the centre. This is partly due to concentration of 40 % of the weight of the tank at the edges. The absolute value of the piled raft differential settlement was less than one third of the unpiled raft.

It is also of interest that the majority of the

differential settlement occurred during the initial stages of consolidation.

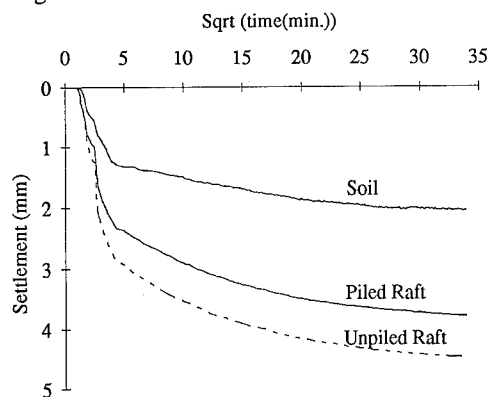


Figure 7 Central settlement during reconsolidation

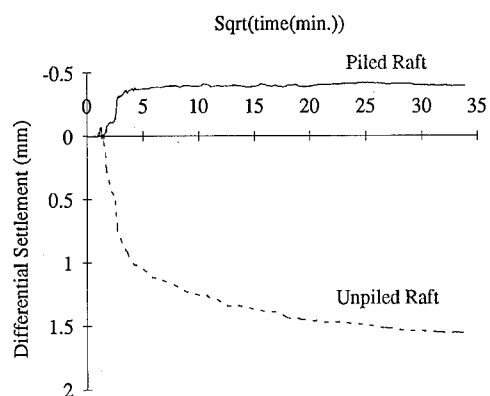


Figure 8 Differential settlement during reconsolidation

#### Settlement during loading test

The load settlement curves for the centre of the rafts are shown for the piled raft and the unpiled raft in Figure 9 and Figure 10 respectively. The results from two separate samples are included in these figures. Both figures indicate the high consistency between samples. The unpiled raft centre settled slightly more than the piled raft centre. By considering the gradient of the re-loading curves, the stiffness of piled raft and unpiled raft in prototype scale was calculated as 960 MN/m and 580 MN/m respectively.

The differential settlements of the rafts during the loading test are shown in Figure 11. The differential settlement of the piled raft was significantly smaller than that of the unpiled raft.

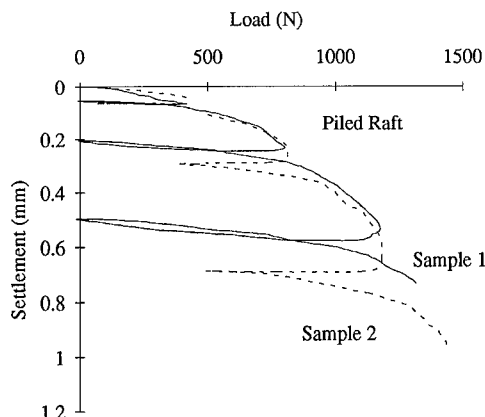


Figure 9 Load settlement curves for centre of piled raft

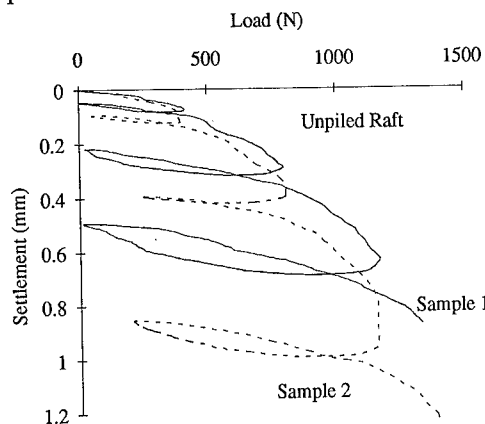


Figure 10 Load settlement curves for centre of unpiled raft

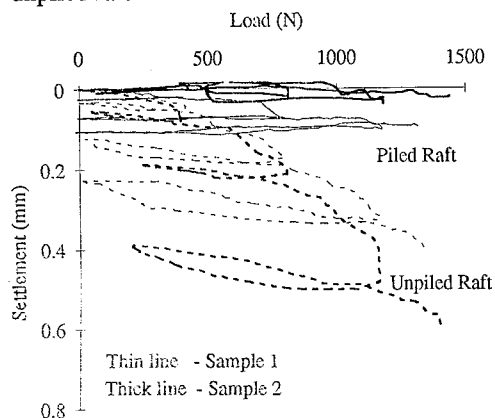


Figure 11 Differential settlement of rafts

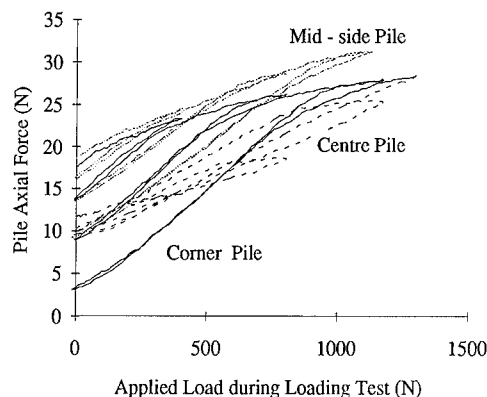


Figure 12 Pile axial force during loading test

#### Load transferred to piles

The pile axial forces were measured throughout the centrifuge test. Results during the cyclic loading test are shown in Figure 12. Since the raft used in the test was extremely flexible, no significant difference was seen in the axial force for each pile.

According to the result of the single pile loading test (Figure 7), it appears that the shaft friction of the piles beneath the raft was not fully mobilized under the applied loading condition. It should be also noted that the capacity of the pile beneath the raft may be larger than that from the single pile loading test. The weight of the tank will have led to some gain in soil strength during reconsolidation, before the main loading test.

The estimated load transferred to all 9 piles during the cyclic loading test is shown as a percentage of the total load in Figure 13. The transferred load was 25 % at the initial stage of the loading test, and this ratio decreased to 14 % as the test progressed. This means that the majority of the applied load was transferred to the soil through the raft and the relative stiffness of the pile group decreased as the applied load increased. It should, however, be noted that the reduction in differential settlement was significant in spite of the low proportion of load transferred to the piles.

## 5 CONCLUSIONS

From the centrifuge tests carried out so far, the following conclusions are drawn:

(1) A small pile cap on the shaft may have a

significant effect on the total bearing capacity. The shaft capacity of the capped pile is also larger than that of the uncapped pile probably due to the different failure mechanism.

(2) Even a small pile group beneath the centre of a flexible raft effectively prevents differential settlement of the foundation.

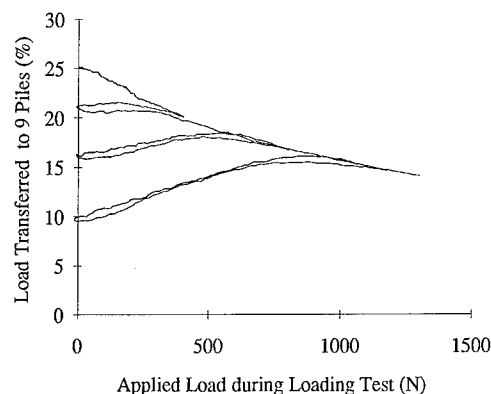


Figure 13 Load transferred to all 9 piles during loading test

## REFERENCES

- Hanna, A.M. & G.G. Meyerhof 1980. Design charts for ultimate bearing capacity of foundations on sand overlying soft clay, *Canadian Geotechnical Journal*, 17, pp 300-303.
- Randolph, M.F., R.J. Jewell, K.J.L. Stone & T.A. Brown 1991. Establishing a new centrifuge facility, *Proc. Centrifuge 91*, University of Colorado, Balkema, pp 3-9.
- Randolph, M.F. & P. Clancy 1993. Efficient design of piled rafts, *Proc. Deep Foundations on Bored and Auger Piles*, pp 119-130.
- Stewart, D.P. & M.F. Randolph 1991. A new site investigation tool for the centrifuge, *Proc. Centrifuge 91*, University of Colorado, pp 531-538.

## ACKNOWLEDGMENT

The authors would like to express sincere appreciation to Taisei Corporation in Japan for the financial assistance to the first author who is employed by that company.



## Modelling the behaviour of piles in sand subjected to axial load

V. Fioravante

ISMES, Bergamo, Italy

M. Jamiolkowski

Politecnico, Torino, Italy

S. Pedroni

ENEL-CRIS, Milano, Italy

**ABSTRACT.** A series of centrifuge tests had been carried out on model driven and bored piles axially loaded. Some of the results obtained are presented mainly to compare the different behaviour of the two types of piles which depends on the installation method. Test interpretation was attempted, based on current knowledge.

### 1. INTRODUCTION

A series of centrifuge tests has been carried out on two types of axially loaded pile model: a displacement pile, pushed in flight into the soil which simulates, to some extent a driven pile (hereafter simply called "driven"), and a non-displacement pile, pre-inserted before the pluvial deposition of the sand, which simulates an ideally bored pile (hereafter called "bored").

To compare the different behaviour of the two types of piles, some of the results obtained are shown.

### 2. TEST SET-UP

#### 2.1. Centrifuge equipment

With the ENEL-CRIS funds, the research was undertaken at the ISMES Geotechnical Centrifuge (IGC), Bergamo, Italy. Complete description and details of the centrifuge is given in Baldi et al. 1988.

#### 2.2. Model Piles

Two model piles were used for the experiments. They are made from a 10 mm diameter, 1.5 mm thick aluminium alloy pipe mounted in sections to include four and five load cells respectively (Fig. 1).

Each load cell is equipped with four active strain gauges glued to the internal pipe surface.

Two of the gauges are aligned in the longitudinal direction of the pile while the other two are aligned in transverse direction of the pile.

The four gauges are connected as a full Wheatstone bridge circuit, to minimise bending and temperature effects. The gauges and wiring are coated with an acrylic moisture barrier. Capillary wires were used to

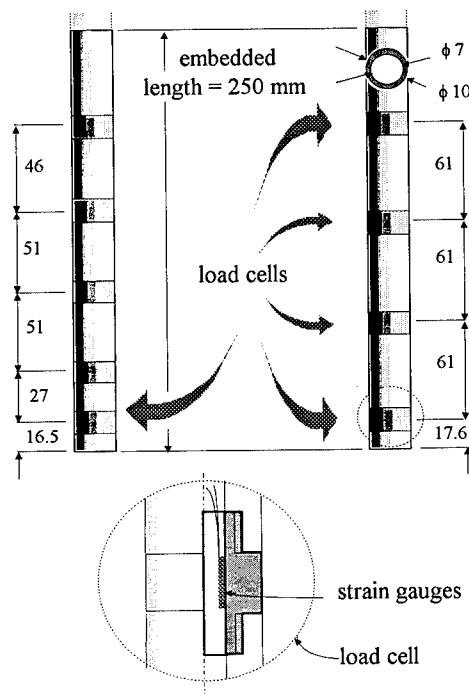


Figure 1 Model piles used in the centrifuge tests

connect the load cells to the multiplexer.

Once mounted to the model piles, the load cells were calibrated to measure axial loads, by loading them axially in a calibration loading frame. The drift of offset and zero load were carefully detected and minimised where possible. The output signals from the load cells were amplified by a factor of 100.

The external surface of the piles used, are smooth because of the minor importance of the shaft friction

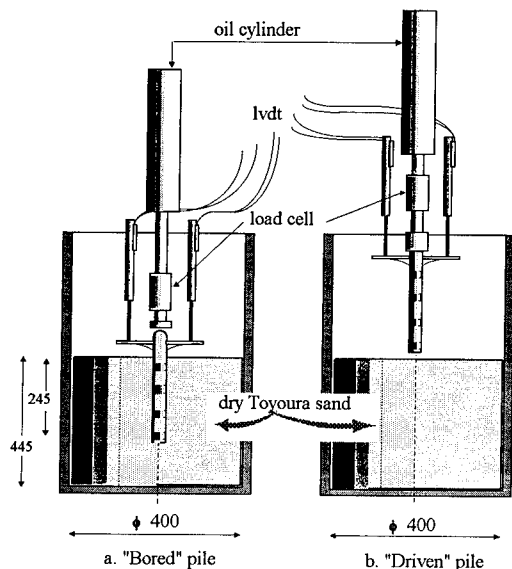


Figure 2. Model Set-up

with respect to the base resistance for the purposes of this research. More attention will be devoted to the shaft resistance in future.

The total length of the piles is variable depending on the loading system used that is different for bored and driven piles. The embedded length is about 250 mm, therefore the slenderness ratio is 25.

The ratio between pile diameter  $D_p$  and the average diameter of the soil particles ( $D_{50}$ ) is equal to  $D_p/D_{50} = 10/0.16 = 62.5$ .

Both model piles used are close-ended and free-headed.

To measure vertical settlements of the pile head, two linear vertical transducers (lvdt) are fixed to the pile top by two brackets as shown in figure 2.

Due to the inherent rigidity of the pile model, the settlement of the pile tip (s) it is assumed to be equal to the one measured at the pile head.

An additional load cell is mounted on the loading piston to measure the total applied load.

### 2.3. Test sand

The pile loading tests were performed on dry Toyoura sand (TOS). It is a well known Japanese test sand whose mechanical properties have been thoroughly documented by numerous researchers [e.g. Tatsuoka et al. 1986, Tatsuoka and Shibuya 1991]; they remark that the difference in its behaviour in both dry and saturated states are negligible.

This soil is a predominantly quartz uniform fine sand with sub-angular grain shape; it has a mean

size,  $D_{50}$ , of 0.16 mm, uniformity coefficient of 1.3 and specific gravity of soil particles of 2.645.

The maximum density  $\gamma_{max}$  (according to ASTM D4254-83) and the minimum density,  $\gamma_{min}$  (by pluviating) are 16.17 kN/m<sup>3</sup> and 13.10 kN/m<sup>3</sup> respectively which correspond to the minimum ( $e_{min}$ ) and maximum ( $e_{max}$ ) void ratio of 0.602 and 0.977 respectively.

### 2.4 Soil model preparation

The soil models were obtained by pluviating sand in air into a cylindrical container at a constant height of fall, by means of a travelling sand spreader; such technique ensures soil uniformity (Passalacqua 1991). The dry models were reconstituted at two reference soil density corresponding to a medium and a high relative density of TOS (i.e.  $D_R=47\sim54\%$  and  $D_R=81\sim91\%$  respectively).

Since the applied acceleration field lightly increases the soil density gathered by pluvial deposition, the density of each sample was measured before and after the centrifuge test; the last one was adopted.

The cylindrical container used has rigid walls to avoid horizontal displacement of the soil; it has an internal diameter of 400 mm, therefore the ratio of soil to pile diameter is equal to 40, enough to minimise boundary effects. The soil sample has about 450 mm of height with the pile at 245~250 mm depth. Therefore the bottom of the container is about 200 mm below the pile tip (i.e. 20 times pile diameter) such to minimise bottom boundary effects.

Bored piles were pre-installed in the soil at 1-g by hanging the pile with thin ties to minimise the disturbance of the deposition and to ensure verticality. Model driven piles were pushed in flight through the soil before the loading tests.

### 2.5. Test program and testing procedures

Nine loading tests on bored piles and six on driven piles have been performed. Two acceleration levels were chosen corresponding to about 30g and 80 g, computed at the free surface of the soil sample. At prototype scale the piles correspond to 0.30 m and 0.80 m in diameter and embedded length of about 8.45 m and 22.35 m, respectively.

The test program is listed in table 1.

Three different procedures were adopted regarding pile installation (before running the loading tests):

a. A pile pre-inserted into the soil (PTT1 to PTT4), was hanged during the centrifuge speed-up. Due to the stress field imposed, the soil settles causing traction forces on the pile because of the negative skin friction.

b. The pre-installed bored pile (PTT5 to PTT9) was

TABLE 1 - Test Program

TEST	MODEL				PROTOTYPE	
	g	$\gamma_d$ kN/m <sup>3</sup>	$D_R$ %	(s/D) <sub>max</sub> %	D m	L m
DRIVEN						
PIT1	80	14.63	48	214	0.8	22.3
PIT1b	80	14.62	48	147	0.8	22.3
PIT2	30	14.71	51	14	0.3	8.4
PIT2b	30	14.61	48	21	0.3	8.4
PIT3	30	15.68	84	142	0.3	8.4
PIT3b	30	15.62	81	172	0.3	8.4
BORED						
PTT1	30	14.53	47	214	0.3	8.4
PTT2	80	14.58	48	147	0.8	22.3
PTT3	30	15.88	91	14	0.3	8.4
PTT4	80	15.83	89	21	0.8	22.3
PTT5	30	14.58	48	142	0.3	8.4
PTT6	30	14.75	54	172	0.3	8.4
PTT7	80	14.73	53	111	0.8	22.3
PTT8	30	15.90	91	194	0.3	8.4
PTT9	80	15.86	90	52	0.8	22.3

free to move during centrifuge speed-up; the stress field imposed caused settlements of both soil and pile; therefore no discontinuity was produced between soil and pile.

c. The model pile was pushed into the soil sample after reaching the selected acceleration (PIT1 to PIT3). The pushing load increased at a constant rate until the pile tip reached 245-250 mm depth; thereafter, the applied load was removed.

A lag of several minutes (15 to 30) separated the subsequent loading test: the piles were axially loaded at a constant rate up to a selected displacement, than unloaded at double speed. For most of the tests a second loading-unloading cycle has been undertaken.

Due to the paper length restrictions, results from the tests PTT1 to 4 involving negative skin friction, are not included.

### 3. TEST RESULTS

#### 3.1. General

The load  $Q$  applied at the head of the pile model is transferred to the soil by shaft capacity ( $Q_s$ ) and base capacity ( $Q_b$ ):

$$Q = Q_s + Q_b \quad [1]$$

where:

$$Q_s = A_s f_s$$

$$A_s = \pi D_p L_p: \text{shaft area of pile}$$

$$D_p = \text{pile diameter}$$

$$L_p = \text{embedded pile length}$$

$$f_s = \text{unit shaft resistance}$$

$$Q_b = A_b q_b$$

$$A_b = \pi D_p^2 / 4: \text{base area of pile}$$

$$q_b = \text{unit base resistance}$$

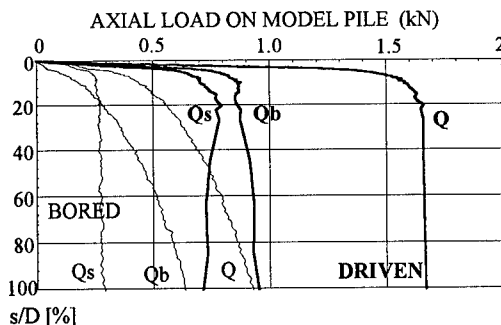


Figure 3. Results of pile load tests PIT1b, PTT7

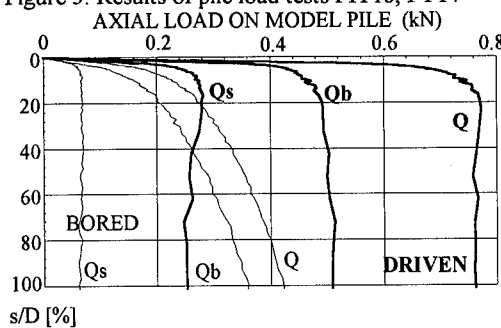


Figure 4. Results of pile load tests PIT2b, PTT6

#### 3.2 Driven and bored pile loading test results

Typical results of the loading tests are shown in figures 3 and 4, where the applied load  $Q$  and corresponding value of  $Q_s$  and  $Q_b$  are plotted versus relative settlement ( $s/D$ ).

Fig. 3 shows a comparison between the resistance mobilised from a driven (PIT1b) and a bored (PTT7) pile in a sand of medium density ( $D_R = 48\sim 53\%$ ) at a field acceleration of 80 g.

In fig. 4 the comparison shown refers to two tests (PIT2b and PTT6) in a sand soil of approximately the same density ( $D_R = 48\sim 54\%$ ) but at a field acceleration of 30 g.

For both bored and driven piles, the ultimate value of shaft capacity  $Q_{s,u}$ , is fully mobilised for a small ( $<0.5$  mm) absolute displacement of the shaft with respect to the surrounding soil.

As expected, the influence of the two different installation procedures is reflected both in  $Q_s$  and  $Q_b$ . The main differences is the magnitude of pile tip displacement required to mobilise the ultimate bearing capacity  $Q_{b,u}$ . In fact, from figures 3 and 4:

$$Q_b \approx Q_{b,u} \text{ per } s/D \leq 10\% \text{ driven}$$

$$Q_b \approx Q_{b,u} \text{ per } s/D > 100\% \text{ bored}$$

Figure 5 shows the ratio  $Q_{bored}/Q_{driven}$  calculated for various relative displacement values, from 3 pairs

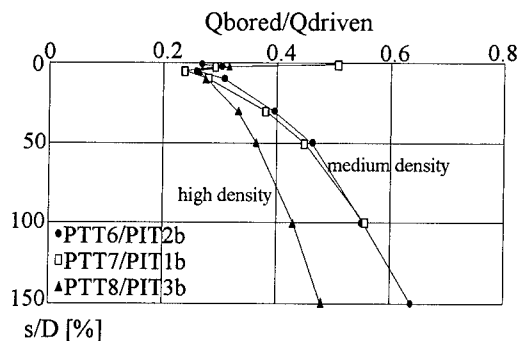


Figure 5 Calculated ratio  $Q_{bored}/Q_{driven}$  vs.  $s/D$

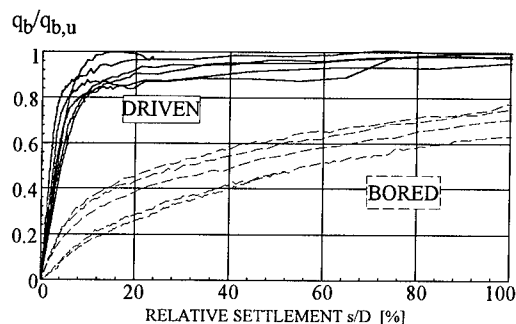


Figure 6 Ratio  $q_b/q_{b,u}$  as function of  $s/D$  for driven and bored pile tests

of bored and driven pile tests; each pair (PTT6/PTT2b, PTT7/PIT1b and PTT8/PIT3b) has about the same density and the same  $g$  level.

The ratio rises as  $s/D$  increases and seems to approach unity for very large settlements; besides at high density this tendency is slower, while it seems to be unaffected by the stress field.

In Figure 6 the ratio between the current unit base resistance and its ultimate value is plotted against  $s/D$  for the driven and bored pile tests.

From the comparison between the bored and driven pile test data a conclusion, according to De Beer (1986), could be that the ultimate bearing capacity of a deep foundation in TOS depends on the relative density of the deposit and on pile length (i.e. state of the effective stresses) but is independent of the installation method that influences only the settlement to mobilise  $Q_{b,u}$ .

#### 4. TEST INTERPRETATION

##### 4.1. Ultimate load $Q_u$

According to Chin (1970, 1972) the method of plotting the pile behaviour as hyperbolic function has

been adopted to evaluate ultimate loads. The method is expressed by Chin as:

$$s/Q = s/Q_u + C \quad [2]$$

where  $C$  is a constant and  $Q$  is the axial load at the particular settlement.

Load test results for driven and bored piles are shown in figures 7 and 8 respectively, where the ratio  $s/Q$  was calculated for various  $s/D$ .

From figure 7 it can be noted that such a relationship seems to be linear, as postulated by Chin, which in his paper refer mainly to driven piles. From this figure it is also evident the repeatability of the tests performed (couples 2/2b and 3/3b) except for PIT1 in which the test conditions were slightly different with respect to PIT1b.

A different behaviour emerges from the analysis of the load tests on bored piles: the  $s/Q$  vs.  $s$  relationship seems to be non linear, so the ultimate load increases as the settlement increases. Therefore, in order to assess a reliable value of  $Q_u$ , it is necessary to refer to a standard settlement for example  $s=10$  mm ( $s/D=100\%$ ). Referring to larger values of  $s$  (e.g.  $s=20$  mm),  $Q_u$  is 20-30 % higher.

The values of  $Q_u$  calculated for the applied load as well as for the shaft ( $Q_{s,u}$ ) and base resistance ( $Q_{b,u}$ ) are reported in Table 2, and transformed to prototype values.

TABLE 2 - Evaluation of ultimate load

TEST	MODEL			PROTOTYPE		
	$Q_u$ [kN]	$Q_{s,u}$ [kN]	$Q_{b,u}$ [kN]	$Q_u$ [MN]	$Q_{s,u}$ [MN]	$Q_{b,u}$ [MN]
DRIVEN						
PIT1	1.4	0.4	1.0	9.0	2.6	6.4
PIT1b	1.67	0.67	1.0	10.7	4.3	6.4
PIT2	0.75	0.3	0.45	0.68	0.27	0.41
PIT2b	0.75	0.25	0.51	0.68	0.23	0.46
PIT3	2.9	1.13	1.77	2.6	1.02	1.59
PIT3b	2.9	1.13	1.77	2.6	1.02	1.59
BORED						
PTT5	0.54	0.1	0.44	0.49	0.09	0.4
PTT6	0.54	0.06	0.48	0.49	0.05	0.43
PTT7	1.3	0.3	1.0	8.32	1.92	6.4
PTT8	1.59	0.21	1.38	1.43	0.19	1.24
PTT9	2.62	0.42	2.2	16.77	2.69	14.08

Since many  $s/Q$  vs.  $s$  plots exhibit a bilinear shape (Fleming, 1991), Chin (1972) suggests that the first part of the relationship represents the mobilisation of shaft capacity while the second part reflects the mobilisation of the base capacity. This seems to be not strictly true for the tests presented.

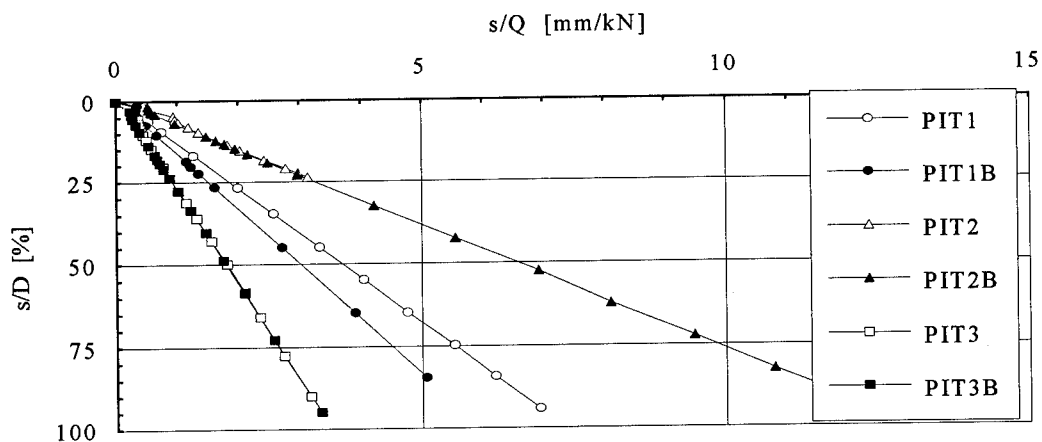


Figure 7. Evaluation of ultimate load for driven piles

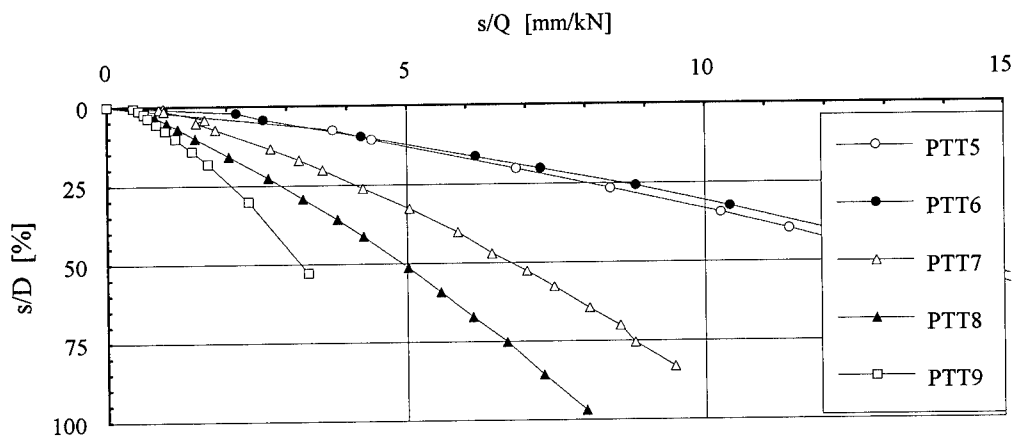


Figure 8. Evaluation of ultimate load for bored piles

#### 4.2. Unit shaft limit resistance, $f_{s,u}$

For piles in sands the ultimate shaft friction  $f_{s,u}$  can be linked to the vertical effective stress ( $\sigma'_v$ ) acting in the vicinity of the pile shaft by means of the following relationship [Poulos (1989)]:

$$f_{s,u} = \sigma'_v \cdot k \cdot \tan \delta = \beta \sigma'_v \quad [3]$$

where:  $\sigma'_v$  is usually taken equal to the effective overburden stress;  $k$ : ratio of horizontal to vertical effective stress acting on pile shaft;  $\tan \delta$  = coefficient of friction at the pile-soil interface.

According to this approach, the test results were analysed making the following simplification:

i. the soil is homogeneous so the density value measured was assumed constant with depth (actually, the non uniform applied acceleration field slightly increases soil density with depth);

ii. since the applied stress field is non linear with depth,  $\sigma'_v$  was correctly calculated in correspondence to the pile tip  $\sigma'_{v,t}$ , than  $\sigma'_{v,t}/2$  was assumed as average value for the following calculations;

iii. the ultimate shaft resistance  $Q_{s,u}$  linearly increases with depth.

Therefore, from eq. 3:  $\beta = f_{s,u} / (\sigma'_{v,t} / 2)$  being the average value of the unit shaft resistance  $f_s$ :

$$f_{s,u} \cong Q_{s,u} / A_s \quad [4]$$

where  $A_s = \pi D_p L_p$ .

Calculated  $\beta$  values are reported in table 3.

TABLE 3 - EFFECTIVE STRESS  $\beta$  APPROACH

TEST	g	D <sub>R</sub>	$\sigma'_{v,t}$	f <sub>s</sub>	$\beta$	q <sub>b,u</sub>	N
	-	%	kPa	kPa	-	MPa	-
DRIVEN							
PIT1	80	48	326	49	0.3	12.7	39
PIT1b	80	48	326	82	0.5	12.7	39
PIT2	30	51	122	37	0.61	5.7	47
PIT2b	30	48	122	31	0.51	6.5	53
PIT3	30	84	132	138	2.1	22.5	170
PIT3b	30	81	132	138	2.1	22.5	170
BORED							
PTT5	30	48	120	12.5	0.21	5.6	47
PTT6	30	54	120	7.5	0.13	6.1	51
PTT7	80	53	322	37.5	0.23	12.7	39
PTT8	30	91	130	26.2	0.40	17.6	135
PTT9	80	90	346	52.4	0.30	28.0	81

#### 4.3. Ultimate base resistance q<sub>b,u</sub>

Following the same assumptions adopted previously q<sub>b,u</sub> is computed as:

$$q_{b,u} = Q_{b,u}/A_b \quad [5]$$

The q<sub>b,u</sub> values are reported in table 3; the same table shows also the values of the experimentally determined bearing capacity factor N:

$$N = q_{b,u}/\sigma'_{v,t} \quad [6]$$

which, for medium density, ranges from 39 to 53 regardless of the installation method and acting stresses. However, at high densities they seem to be influenced by both aspects.

## 5. CONCLUSIONS

The centrifuge pile load tests performed, allow the following conclusions:

1. The tests confirmed that a large difference exists in behaviour of non-displacement and displacement piles embedded in Toyoura quartz sand. This regards both the load transfer mechanism before failure and the behaviour at failure.
2. For comparable relative density and acceleration level the ratio of Q<sub>s,u</sub> (non-displacement) to Q<sub>s,u</sub> (displacement) ranges between 0.19 to 0.45.
3. The ultimate base resistance q<sub>b,u</sub> of displacement piles is mobilised at s/D values ranging between 0.05 to 0.1. In case of non-displacement piles the relative settlement necessary to mobilise the q<sub>b,u</sub> results in one order of magnitude larger values.
4. The values of q<sub>b,u</sub> for both types of piles results of comparable order of magnitude.

5. The obtained results confirm the need to refer the design of bored piles to the critical base capacity Q<sub>b,cr</sub> mobilised at a given value of critical settlement of the pile tip s<sub>cr</sub> corresponding to the achievement of the ultimate limit state [Reese and O'Neill (1988), Ghionna et al (1993)].

## REFERENCES

- Chin, F.K. (1970). Estimation of the ultimate load of piles from tests not carried out to failure. Proc. 2nd SE Asian Conf. Soil Eng. Singapore, 81-92
- Chin, F.K. (1972). The inverse slope as a prediction of ultimate bearing capacity of pile. Proc. 3rd SE Asian Conf. Soil Eng. Hong Kong 83-91.
- Donald, J.B., Chin, H.K. and Sloan, S.W. (1980). Theoretical Analyses of Rock Socketed Piles. Proc. Int. Conf. on Structural Foundation on Rock Sidney Editor Pells. P.J.N. Balkema.
- Fleming, W.G.K. (1992). A new method for single pile settlement prediction and analysis. Geotechnique 42 No. 3 411-425.
- Ghionna, V.N. et al. (1993). Base capacity of Bored Piles in Sands from In-Situ Tests. Proc. 2nd Int. Geotechnical Seminar on Deep Foundation on Bored and Auger Piles. Ghent, Edit. W.F. Van Impe.
- Jamiolkowski M., Lancellotta, R., Lo Presti, D.C.F. and Pallara, O. (1994). Stiffness of Toyoura sand at small and intermediate strain. Proc. XIII ICSMFE New Delhi, India.
- Iwasaki, T., Tatsuoka, F. and Takagi, Y. (1978). Shear Modulus of Sand under Cyclic Torsional Shear Loading. Soils and Foundations n. 1.
- Passalacqua, R., (1991). A sand spreader used for the reconstitution of granular soil models. Soils and Foundations, JSSMFE, Vol.31, n.2, pp. 175,180.
- Poulos, H.G., (1989). Pile behaviour - theory and application Geotechnique 39. No.3 365-415.
- Reese, L.C. and O'Neill, M.W. (1988). Drilled Shafts: Design Procedures and Design Methods. U.S. Dept. of Transportation F-H-A. Publication No. FHWA-HI-88-42
- Tatsuoka, F., Goto, S. and Sakamoto, M. (1986). Effects of some factors and strength and Deformation Characteristics of sand at Low Pressure. Soils and Foundations n. 1.
- Tatsuoka, F. and Shibuya S. (1991). Deformation Properties of soils and Rocks from Field and Laboratory Test. Keynote Lecture - Proc IX ARCSMFE Bangkok.

## Behaviour of axially loaded piles in sand

N.S. Yet, C.F. Leung & F.H. Lee

Department of Civil Engineering, National University of Singapore, Singapore

**ABSTRACT:** This paper presents the findings of an on-going research carried out at the National University of Singapore on the behaviour of axially loaded piles with special attention to pile installation problems in Southeast Asia. A servo-hydraulic system has been developed for installation and load testing of model piles in sand. Effects of sand relative density, stress level, lapsed installation and redrive on the behaviour of pile were studied. In addition, effect of pile creep is also discussed.

### 1 INTRODUCTION

Piles are often used as foundations for high-rise buildings in Southeast Asia. Problems faced in this region include difficulties in pile redriving after unavoidable time lapses such as overnight stoppage on one hand and further penetration despite pile driven to set earlier on the other. Since late 1991, a research program has been embarked upon at the National University of Singapore (NUS) to investigate the performance of piles installed in tropical soils such as soft clay, residuals soils, sand and old alluvium using the centrifuge modelling technique. This paper presents the results of a part of the program on the behaviour of jacked-in piles in sand.

### 2 TESTING EQUIPMENT

All the tests described here were conducted on the NUS geotechnical centrifuge. This 2-m radius centrifuge, which comprises a balanced arm with dual swing platforms has a capacity of 40 g-tonnes. The details of the facility are given in Lee et. al. (1991). Figure 1 shows the experimental set up of the present study. The cylindrical stainless steel container used has an internal diameter of 500 mm and a height of 400 mm. The thickness of the soil sample is 270 mm. The soil used is greyish silica sand with 76% of its particle size ranging from 0.15 mm to 0.30 mm. Its properties are shown in Table 1.

Table 1. The properties of sand

Mean diameter	0.2 mm
Friction angle, $\phi$	30 to 36
Uniformity coefficient	2.4
Specific gravity, $G_s$	2.637
Maximum density, $\rho_{max}$	1660 kg/m <sup>3</sup>
Minimum density, $\rho_{min}$	1332 kg/m <sup>3</sup>

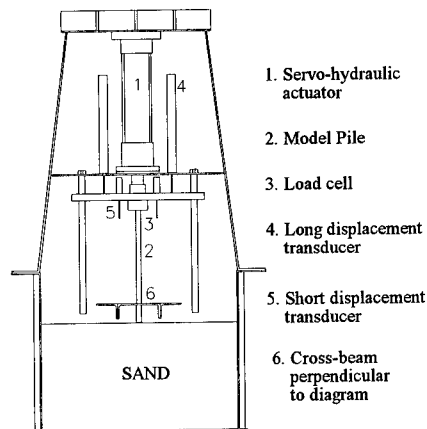


Fig 1 Experimental Setup

Aerial pluviation method is used to prepare sand bed of relative density (RD) less than 70%. Dry sand is rained from a height through small openings at the bottom of a travelling sand spreader. Drop height is maintained constant throughout by gradual upward

adjustment of the spreader. Sand with relative density exceeding 70% was prepared by vibrating the pluviated sand on a vibrating table. When the desired height of sand bed was achieved, the soil surface was levelled by means of a suction pipe.

For saturated sand beds, a steel cover is bolted to the container's top flange with a rubber seal in between to ensure that it is as airtight as possible. Partial vacuum is then applied to the top surface of the soil and deaired water is subsequently allowed to flow into the container through a small hole near to its base. To avoid sand boiling, the rate of water inflow is regulated by a purge meter so that it does not exceed 0.03 litre per second. The volume of water required to saturate the soil is checked against the initial volume of voids.

The model pile is fabricated from aluminium pipe which has a wall thickness of 0.9 mm and an external diameter of 12.6 mm and length of 280 mm. The ratio of pile diameter to soil particle mean diameter is 63. This ratio is considered acceptable as it exceeds the ratio of 30 proposed by Ovesen (1979), and 20 suggested by Bolton et al. (1993).

In all the experiments, the piles are jacked into the soil at a controlled rate using the servo-hydraulic actuator. The same device is used to perform static load testing on the installed pile. The actuator used is a double-acting hydraulic cylinder which has a bore diameter of 50 mm and a stroke length of 190 mm. It is seated on an intermediate holding plate with a 6-mm thick rubber mat in between. The rubber serves to damp the oscillations induced by the dithering of the servo-valve. The servo-valve is mounted very near to the hydraulic actuator to reduce entrapped oil volume and thereby improve system response. It is aligned in such a way that when the platform is swung up, the direction of spool movement is perpendicular to the direction of model gravity.

The pile jacking rig is a 4-legged frame made from stainless steel. It comprises a stiffened top plate to which the top flange of the hydraulic actuator is mounted. Within the rig, there is an intermediate holding plate to which a guide rod is fixed. The guide rod helps to maintain the verticality of pile during installation besides restraining lateral sway. The whole jacking rig is bolted to the cylindrical container by four tension bolts.

### 3 EXPERIMENTAL PROCEDURE

Most of the tests are conducted at 50g. Once the desired gravitational acceleration is achieved, pile installation process commences by activating the

servo-hydraulic control. The model pile will first move down to the soil surface by velocity control. The load control will take over when the pile starts to encounter resistance during penetration. Command load is gradually increased as the pile penetrates until the pre-determined penetration depth of 140 mm is reached. For a pile embedment length of 140 mm, the base of the container would be about 10 pile diameters below the pile tip. This ratio is considered acceptable as it is greater than the recommended value of 5 times suggested by Craig and Sabagh (1994). Throughout the pile installation, the jack load is measured by a load cell which is mounted between the actuator rod and the model pile. Pile penetration is measured by two 200-mm-travel displacement transducers. In addition, the displacement of the soil surface is monitored by 10-mm-travel displacement transducers which are placed at various distances from the pile.

Once the desired pile penetration is reached, the pile is load tested, either by maintained load test procedure or constant rate of loading until failure. In the maintained load test, load is kept constant until no further settlement is observed and the loads are applied over 10 increments up to failure. In the constant rate of loading test, load is increased continuously at a constant speed slow enough to avoid any viscous or inertial effect. Preliminary tests show that the two loading procedures do not show any major differences in the load-displacement response of the pile. Hence majority of the load tests are conducted using the constant rate of loading method to save time. Throughout the load test, the pile load is measured by the same load cell mentioned earlier but the pile displacement is measured by means of two 30-mm-travel displacement transducers. The armature of the transducers was seated onto an independent cross-beam attached to the top flange of the container once the desired pile penetration has been reached.

### 4 BASIC TESTS

The first part of the study consists of tests to verify the pile installation and loading techniques. These include the study of effect of 1g versus 50g pile installation, effect of stress level and effect of soil relative density on the pile performance.

#### 4.1 Effect of 1g versus 50g installation

Figure 2(a) shows the installation load versus pile penetration relationships for piles jacked into sand at



1g and 50g. It is evident that pile installed at 50g requires much higher force than that installed under 1g to the same depth. This is simply due to the prevailing higher overburden stress under 50g. Figure 2(b) shows the load-displacement responses for the two piles which are both load tested at 50g. The pile installed under 1g shows 40% lower capacity than that installed under 50g. Similar reduction in pile capacity has been reported by Federal Highway Administration of Washington (1983) for 1/50 and 1/70 scale models. With the exception of the initial part of the load-displacement curves, the overall stiffness of the pile-soil system is also lower.

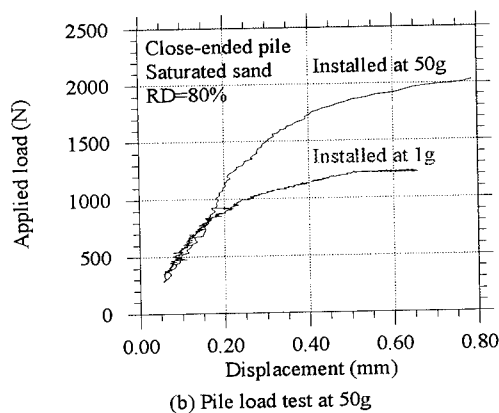
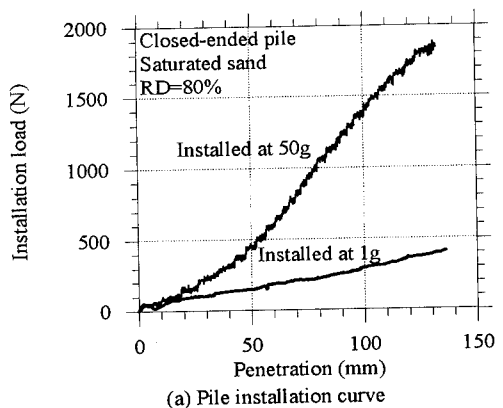


Fig 2 Effect of 1g vs 50g installation

According to Craig (1984), the overall stiffness of pile-soil system is higher when installation is carried out at a higher mean stress level. Pile installation induces soil displacement which increases the lateral stress. If such stress increase occurs under high mean stress, the final stress level will be higher than that

resulting from installation under a low stress regime followed by increase in self-weight due to increased acceleration field.

#### 4.2 Effect of stress level

A series of pile load tests were performed under various acceleration fields on the same pile installed at 50g in sand. In order to compare the test results under different g fields, the normalized load, which is defined as applied load divided by acceleration field  $N$ , are plotted against pile displacement for all the load tests, see Figure 3. The ultimate capacity is correlated with  $N$  as shown in Figure 4. Although the pile has a higher ultimate capacity at higher gravitational field, normalized pile capacity decreases with increasing centrifugal acceleration. Craig and Sabagh (1994) attributed this decreased pile ultimate capacity to the reduction in mobilised angle of friction near pile tip and suppression of dilatancy at high stress level.

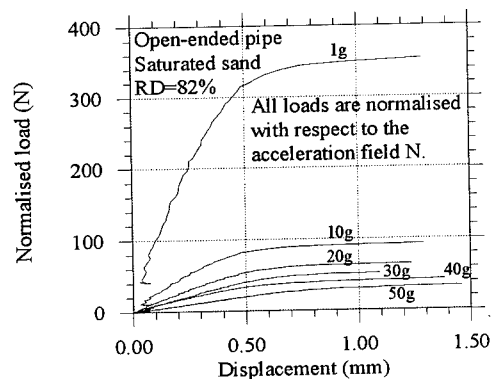


Fig 3 Load-displacement curves for load tests carried out at various  $N_g$

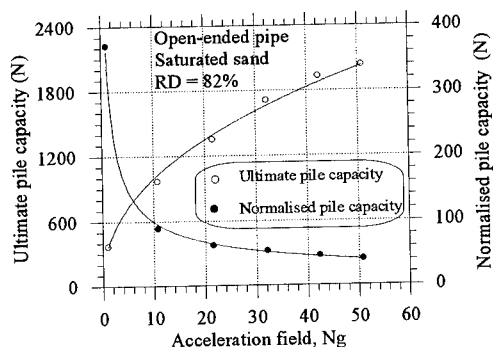


Fig 4 Plot of pile capacity vs  $N_g$

### 4.3 Effect of relative density

Figures 5(a) and 5(b) depict the results of four tests whereby piles are installed and subsequently load tested in sand at relative densities of 47%, 72%, 88% and 95%, respectively. As the relative density increases, bigger force is required to jack in the pile to the same embedment depth. To understand this, it is essential to look into the micro structure of sand, which involves the concept of packing of sand particles. In order to induce inter-granular movement, interlocking between grains must be overcome. For very loosely packed sand, the micro structure is collapsible. Owing to the lack in interlocking, it is rather easy to penetrate pile into loose sand. For dense packed sand, relative motion between grains is difficult because of grain interlocking. This requires a non-proportionately larger force to penetrate the pile. Figure 5(b) shows both the ultimate pile capacity and the overall stiffness of the pile-soil system increase with the relative density of sand.

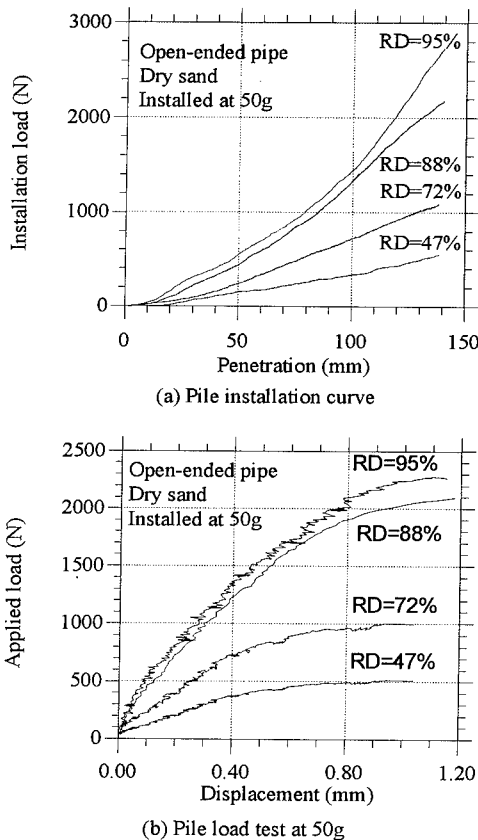


Fig 5 Effect of Relative density

In summary, much of the pile behaviour observed so far is in agreement with the findings of previous researchers. This indicates that the experimental set-up is yielding results that are reasonable and largely consistent.

### 5 EFFECT OF LAPSES IN PILE INSTALLATION

During installation of long piles, stoppages are often unavoidable due to breakdown of pile installation device, joining of pile segments or overnight stoppages. As problems frequently occur when pile installation resumes after stoppages, a special test is conducted to examine the effect of stoppage on pile installation force. In this test, the model pile is first installed to two-third of the desirable pile penetration depth and the command load is reduced to zero and subsequently increased again to continue the pile installation process to full depth after a lapse of 20 minutes. It is observed that the pile penetrates an additional 2 mm (Figure 6) when the previous maximum installation load is reached, indicating that the pile becomes easier to jack in after the time lapse. The exact mechanism is not clearly understood but it could be attributed to stress relaxation of sand. The high temporary stress developed around the pile is believed to have 'relaxed' during the lapse, resulting in lowering of pile carrying capacity with time. The pile capacity is about 85% of the installation load.

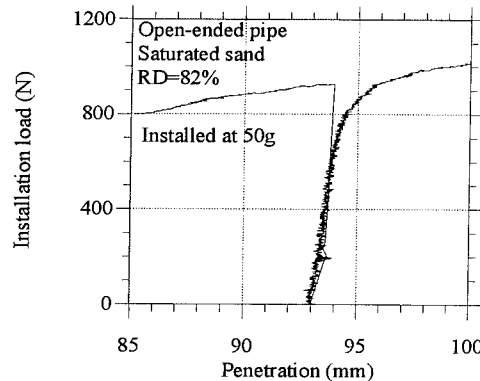


Fig 6 Effect of lapse in installation

### 6 EFFECT OF PILE REDRIVE

A series of tests are performed on the same pile whereby the pile is jacked into the soil with initial relative density of 72% and then completely pulled

out. This procedure is repeated six times. It is observed that the force required to jack the pile into sand increases after each redrive with negligible increase after fifth redrive as shown in Figure 7. This phenomenon may be due to additional soil falling below the pile tip as pile is being pulled-out, resulting in higher sand density. Formation of a conical depression as large as 64 mm in diameter and 14 mm deep on the soil surface is the evidence that soil has been densified. As the soil adjacent to and below the pile becomes denser, larger force is required to jack in the pile.

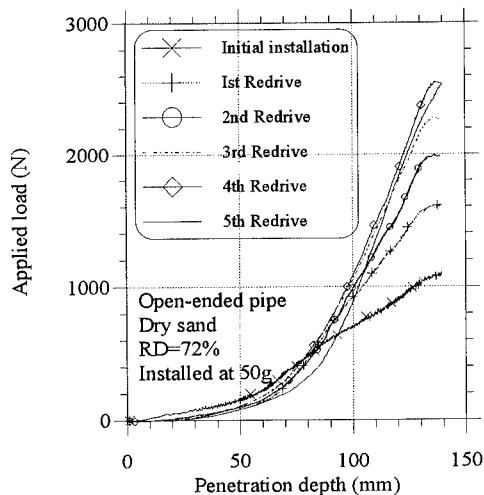


Fig 7 Effect of pile redrive

## 7 SOIL SURFACE MOVEMENT

As shown in Figure 8, during pile installation, the soil surface at a distance of 4.4 diameters from pile axis heaves until the penetration depth exceeds 7 diameters. No additional heaving is observed at greater depth. This appears to suggest that the soil could have displaced radially at depth greater than 7 diameters. At shallower depth, the soil displaced laterally outwards and upwards, causing heave.

During pile loading test, the soil surface subsides with the magnitude of subsidence almost proportional to the applied load. When the pile is unloaded, some of the subsidence was recovered. When the second load cycle is applied, the soil surface subsides again with a smaller magnitude as it has been preloaded.

Figure 9 shows that the magnitude of maximum surface heave during pile installation and magnitude

of subsidence during pile loading decreases with increasing distance from pile axis. Negligible soil surface movement occurs at a distance greater than 10 diameters away from pile axis, both during installation and load tests.

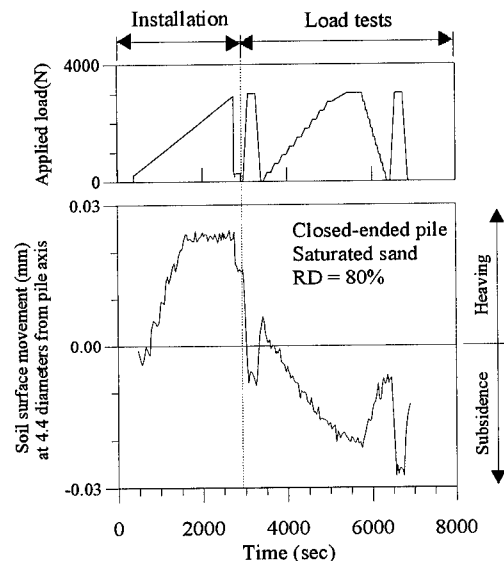


Fig 8 Typical soil surface movement

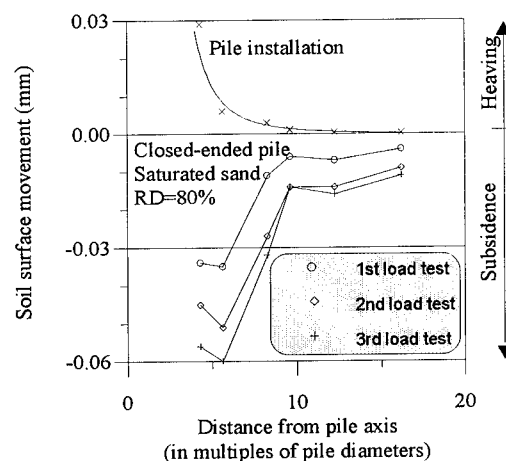


Fig 9 Soil surface movement profile

## 8 PILE CREEP

When the applied load on pile is maintained for a certain period of time, continual settlement of pile

top is noticed. Figure 10 shows the pile settlement-logarithmic time plot under a sustained load of 2.11 kN. The almost linear relationship suggests that the rate of pile creep decreases with time.

This phenomenon could be attributed to crushing and fracturing of soil particles. Crushing at inter particle contacts would allow soil grains to slide relative to one another, resulting in pile creep. It results in finer sand with lower friction angle, so that additional pile movement is required to mobilise the same magnitude of resistance. However, a state is reached whereby further crushing becomes difficult as sand particles become finer, explaining why pile creep diminishes with time at the same load. Bell (1992) suggested that as the confining stress increases, interlocking of sand particles decreases owing to particles becoming more rounded at the points of contact, thereby leading to an increase in the amount of creep. This may result in denser material but it is still easier for shear deformations to occur.

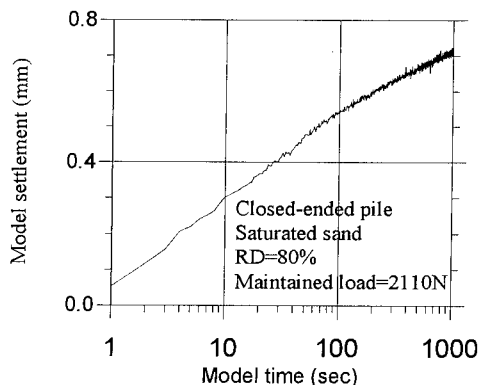


Fig 10 Plot of settlement vs time

#### CONCLUSIONS

A series of centrifuge model tests have been conducted to investigate the behaviour of jacked-in piles in sand. The findings of the basic tests verified that g-level has significant effect on the pile performance and pile installation has to be carried out at the proper g-level.

It is observed that pile capacity decreases after a lapse possibly due to stress relaxation of sand. Increasing difficulty to jack in the pile after every redrive suggests that the soil around the pile has been densified by previous installation. It is also noted that the soil surface heaves during pile installation but

subsides upon loading of pile with the zone of soil surface displacement observed to be within 10 diameters around the pile. In addition, it is found that pile creeps on sustained loading probably because of crushing of soil particles.

#### ACKNOWLEDGMENTS

This project is funded by NUS research grant RP910668. The authors would like to express his gratitude to the university for the funding and also to technical staff at the Geotechnical Centrifuge Laboratory of National University of Singapore.

#### REFERENCES

- Bell, F.G. 1992. *Engineering Properties of Soils and Rock*, Third Edition, Butterworth Heinemann Ltd.
- Bolton, M.D., Gui, M.W., Philips, R. 1993. 'Review of miniature soil probes for model tests'. *Proc. of the Eleventh Southeast Asian geotechnical conference*, Singapore, pp.85-90.
- Craig, W.H. 1984. 'Installation studies for model piles'. *Proc. of Symposium on the Application of Centrifuge Modelling to Geotechnical Design*, Manchester, pp.440-447.
- Craig, W.H., Sabagh, S.K. 1994. 'Stress level effects in model tests on piles'. *Canadian Geotechnical Journal*.
- Federal Highway Administration, Washington 1983. 'Centrifuge tests in sand'. Report No: FHWA/RD-84/003. Vol II
- Lee, F.H., Tan, T.S., Leung, C.F., Yong, K.Y., Karunaratne, G.P., Lee, S.L. 1991. 'Development of geotechnical centrifuge facility at the National University of Singapore'. *Proc. of International conference centrifuge 1991*, pp.11-17.
- Ovesen, N.K. 1979. Discussion on 'The use of physical models in design'. *Proc. of the Seventh European Conference on Soil Mechanics and Foundation Engineering*, Brighton, Vol. 4, pp.319-323.

## Design and limitations of a pile driving robot

A. Zelikson

*LMS, Ecole Polytechnique, Palaiseau, France*

R. D. Raines

*Exxon Production Research Co., Houston, Tex., USA*

P. Malalel

*Group CEA-CESTA, Le Barp, France*

**ABSTRACT:** The paper discusses model tests carried out on the CESTA centrifuge. A model pile at a scale of 1:50 was driven 0.6 m into dense sand and loaded at different depths in penetration, pulling or cycles thereof. The centrifuge was never stopped for the test's duration of 10-20 hours, and all the operations were carried out by a vertical robot. Problems connected with robotics are discussed. Examples of the pile's behaviour are given.

### 1 INTRODUCTION

A robot for pile driving and vertical loading was developed for EXXON Production Research by a team of CEA-CESTA and LMS Ecole Polytechnique. The CESTA centrifuge was used. Several series of tests have been carried out producing numerous results from all aspects of piling foundations. The machine is now proven in every one of its departments and is considered to be a standard tool for research, for parametric studies and for design. It produces large quantities of curves of laboratory quality: free of noise, precise and repetitive. The results look realistic. There are several occasions where a robot is needed for which the experience which was acquired will be useful. Those are simulations of the construction or modification of structures which modify the stresses in the soil. During pile driving and loading high residual stresses are created in the soil which govern the structure's behaviour, and which are mostly obliterated when centrifugation stops.

industrial robots. For driving the most promising similarity was taken to be that of a ram dropped from a given height under control of the sequence and frequency of the blows.

For studies of the pile's safety, cycles of alternating vertical loads were provided for. As testing progressed, those cycles became more and more important. Any meaningful discussion of the results would have to include many of them. This will not be carried out in the present paper. It is important though to show that the data is technically good. A short paragraph and several figures are dedicated for this purpose.

Considerations of scale and size start with the transducers, which fix the dimensions of the model. The pile was an open pipe. The plug of sand in its inside is important and cannot be interfered with. The stress distribution along the pile was to be studied by strain gages, which together with the wires had to be inserted in the pipe's wall, changing only slightly the static and dynamic impedances and restoring the geometry.

Gages 2 mm long and the thinnest Teflon covered wires were used. Shielding was provided by a covering metal strip. The wires were inserted in grooves 0.4 mm by 0.4 mm. The wall thickness could not be made smaller than 1.5 mm. Therefore the scale reduction could not be larger than 50. A model pile's length was fixed preliminarily (at present) to 0.7 m, however future lengths might reach 1.2 m and more (35 - 60 m in situ). The installation is seen in figure 1. The CESTA centrifuge has interchangeable loading

### 2 EQUIPMENT

Many aspects of the piling problem are still unknown and the errors due to relaxations of the similarity requirements could not be estimated. Thus the model had to provide industrial data by direct similarity the precision of which was the central design objective. The machine was built to carry out several types of highly controlled motions of the kind executed by

platforms, and has room up to the wall for experimental cells of 5 m length (and 3 m diameter). At a scale of 1/50, the soil could be instrumented also. It is clear that for the study of groups of piles and of platforms a scale of 1/100 or even less would be needed, making the method of instrumentation unsuitable. In general if a detailed instrumentation of the structure and the soil is to be carried out, then the size of the robot should be estimated by a scale of about 1/50.

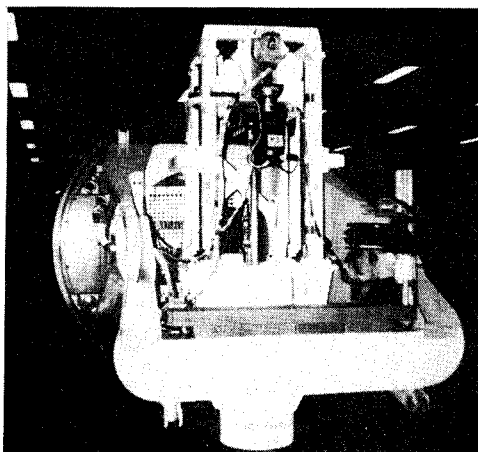


Fig. 1 The Machine

### 3 DRIVING MECHANICS

A robot has two parts: a working head which performs tasks and a carrier which positions the working head. At 1/50th scale, the precision of the driving blow required perfect alignment of the pile's head and the ram. The solution proposed was that of a crossbeam on which guides for both the pile and the ram were installed. The loading programme required displacements in both vertical directions from about one diameter (the present case) up to several diameters. The solution was to load the pile by the cross-beam. The robot consisted of a beam across the cell, which was guided and driven by two big vertical screws, driven by a servo motor.

The driving mechanism had a cylinder inside which a ram, which was guided all the way, was pulled up and dropped by "free" fall on top of the pile's head. Let it be remarked that taking care of the Coriolis acceleration is a constant problem of the construction of simulations. The ram had a rim into which

penetrated two lifting grips. The ram was free to fall when the grips hit two cams. One of the reasons why electro-magnetic drive for the grips was not used was the need to reduce electrical noise. The stroke was changed by moving the cylinder relative to the cams, using a servo motor. Thus the robot had three degrees of vertical motion executed by three motors, which were controlled by one computer.

### 4 TIME CONSIDERATIONS

The power and torque of the motors will depend largely on time scales, as is demonstrated by the piling problem. Dynamic similarity implies conservation of the velocity and the time scale must be equal to the length scale. For centrifuge tests conducted at 50g, the permeability of soil would be 50 times too high. A correction is possible for sands by addition of fines and for silts by changing the pore fluid, but not for clays. If corrections are used, the similarity of both dynamic forces and consolidation pressures is maintained, and studying one of them does not cause perturbations from the other. However there is one more time scale, most pronounced during static tests, to be discussed below.

Tests in the laboratory showed that the maximum frequency of the blows was 3 per second. However, no more than 2 blows per second was possible under 50g unless the motor was changed. Let the nominal mean power needed for 6 blows per second be estimated (12 s interval in situ), at a stroke of 5 cm (2.5 m in situ). Closing and opening of the grips takes half of the time, 1/12 s. The motor turns at a constant speed which is  $10 \times 12 = 120$  cm/s. The ram's mass of 2 kg (250 ton in situ) and the mass of the grips' system are about the same. Together they weight about 2000 N at 50g and the nominal power is  $1.2 \times 2000 = 2.4$  kW. Actually a motor of 2.6 kW was used at a blow frequency of 2 Hz. One way to reduce the power and the torque is to compensate the masses of the parts which do not actually fall (like in a lift). That would half the nominal power. However the fact remains that power losses are very high on the centrifuge. No gear boxes are needed with the servo motors. Reductors, angle converters and belts were used without any trouble, but the larger weights reduced their efficiency. It is seen that by extending the experimental means almost to the maximum the blow frequency in situ could be simulated.

The quasi static loading cycles should be similar to the action of the sea waves, the characteristic

frequency of which is 0.1 Hz. Using the driving and consolidation time scale  $t^* = t(\text{model})/t(\text{prototype}) = 1/50$ , a model frequency of 5 Hz is obtained. However, static load tests are dominated by a pronounced time effect which is apparent during penetration when the load goes above a certain point. That point depends on the loading history. This effect is present in dry sand and seems to be related to grain arrangements. Exponential relaxations of loads with characteristic times of about 2 hours were observed during the static tests. This time effect has been known for a long time. Without a mechanical model the corresponding time scale is unknown. To comply with this phenomenon the time should be conserved. It follows that even in a modified soil-fluid system the consolidation is 50 times too rapid.

The driving system and the loading facilities together with the self weight made the cross beam rather heavy. The maximum speed of the beam had to be sufficient for it to correct the position relative to the pile's head during driving. This was estimated of two penetrations of 1 mm at most per second. The maximum speed was 3.5 mm/s. The reductions were calculated on the base of the cross beam's weight, which was effective during unloading and tension. The motor was no bigger than the one used for driving. The displacements during one way cycling, either in compression or in tension were smaller (at capacity amplitudes) than 2% pile diameter and the corresponding time of travel of one cycle was about 0.3 s. The commutation time of the motors is very short as demonstrated by performing blows at 3 Hz. As a result it can be estimated that one sided cycles of large force amplitudes would be possible at about 3 Hz, i.e.  $\sim 0.06$  Hz in situ, which conforms with the sea waves characteristic frequency, at  $t^* = 1/50$ .

Two way cycling at the same force amplitudes produced displacements which were ten times higher. Therefore it is estimated that the power of the motor which may be used to drive the cross beam puts a limit on the frequency of two way cycle testing. The total time for the driving operations of an open pipe is very small. Even for close ended piles and taking into account delays for dynamic measurements, not more than 3 h should be considered. A day's centrifugation can be extended to 12 h (to 20 in the present tests), which leaves about 9 h for static tests, which is not too much if time effects are considered. The slow loading of the present tests was at 60 mm (i.e. one and a half diameter) per hour.

If consolidation is to be studied during the construction of large soil bodies, then the frequency of the

construction operations should lead to consideration similar to driving. The masses lifted each time would be of an order of magnitude lower than the ram. However the hauling distances would be an order of magnitude higher. Any operations like compaction carried out at high frequencies would create parasitic dynamic effects. Thus even as a day's centrifugation might correctly show the evolution in a clay model 2500 days after the end of the construction, a 250 days construction time could not be properly simulated. Therefore the scale would have to be reduced, say to 1/15. At this scale the present robot might be used to study small diameter piles in light clays.

## 5 CONTROL MOTOR & INSTRUMENTATION

The control of the motors was carried out by modules fixed on the centrifuge's pivot which were commanded by a computer at the command post, using the slip rings to maintain a serial RS232 connection. The motors were each monitored by two electromagnetic encoders supplying  $4 \times 1024$  pulses per turn (5 min precision in the arc). The brushless motors were energized by trains of pulses the signs of which were varied at 10 500 Hz. The present programme used acceleration-deceleration periods of 0.1 s followed by a constant angular velocity. For the stroke's motor and for the pile driving motor the position "0 pulses" was used as a reference for the execution of a programmed number of pulses. The zero position of the stroke was determined by an electromagnetic proximity transducer. During driving the cross beam's motion was started by a similar proximity transducer.

The motor executed a given number of turns then the position of the flag was checked. A similar set-up for loading could be made based on signals from the load cells. In that case a commutation time of 0.2 s would be the minimum. Therefore the maximum frequency of the cross beam was 5 Hz. Up to now commutation was carried out by hitting a key at the command post, thus adding the human time of reaction and the time of communication. As for laboratory testing, machines modules can be bought for the execution of varied loading paths.

For blow precision, the anvil was screwed on the pile. The pile's horizontal motion was restricted at the head by guides on the cross beam and near the surface of the soil. The pile was machined from a solid rod and its lateral motion during the whole course was measured before each test by deflectometers. 0.2 mm total deviation was allowed. That and the base Teflon

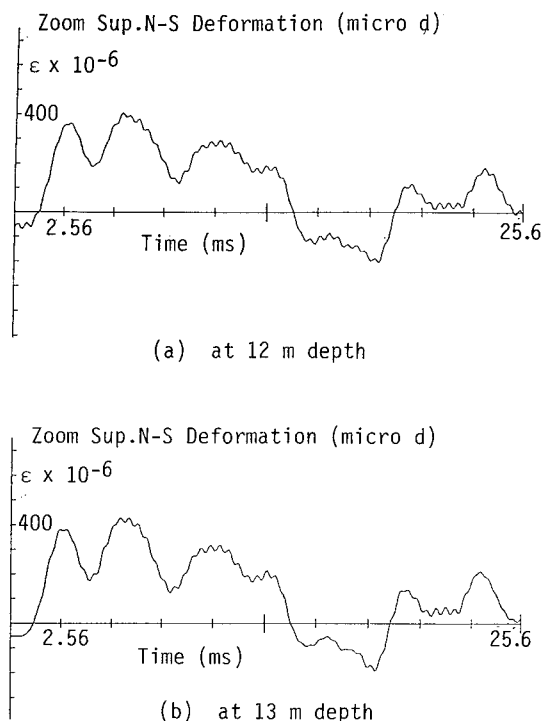


Fig. 2 Graphs of strain ( $\epsilon$ ) versus time

ring of a similar tolerance were a security against friing during static loadings.

The position of the cross beam was monitored by a 600 mm potentiometer of an excellent resolution. Its readings were used to produce control force displacement curves during the static tests and indicated the current depth during driving. The potentiometer's resolution was not enough for the static tests. For that purpose a counter was fixed on the centrifuge's pivot, with input from the encoders. When the times of acceleration-deceleration are not counted the time is as precise as the encoder, as was verified by laboratory tests against LVDT readings. For this procedure the short acceleration/deceleration times of the motors were essential.

The force was measured by four dynamometers fixed on the cross beam. The load was transmitted by contact along the rim of the anvil, which had been locked on the cross beam using two shims pneumatically activated. A miniature accelerometer was fixed on the anvil at its axis.

All the slow static transducer signals were transmitted to the command post. They were monitored for control and also put into a 1/2 Hz sampler which was connected to a data PC for storage.

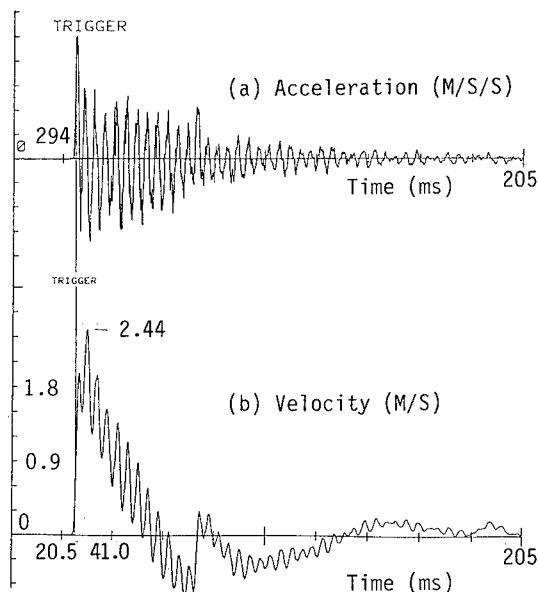


Fig. 3 Integrated Acceleration

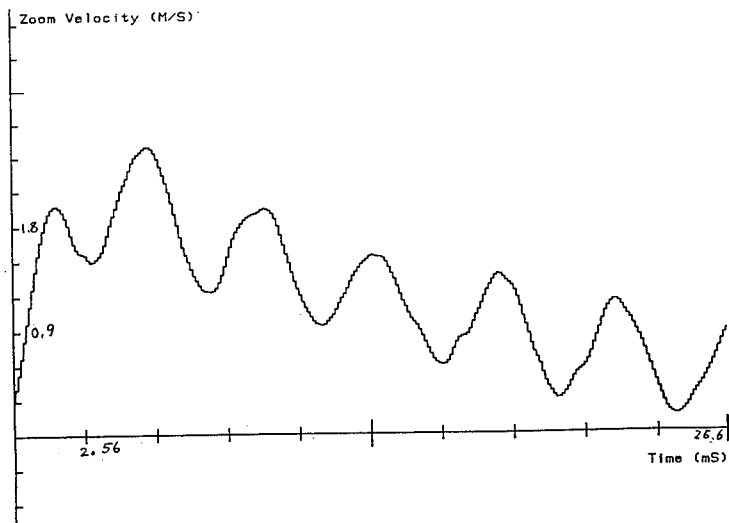
The counter was connected directly. For dynamic and rapid cycling signals a Signal Memory Register of 14 channels was used. By software it was made a "slave" of the data PC. By using a uniform number of integer entries the storage time was made to take 4 s. Therefore blow signals could be acquired, monitored and stored at 20 s intervals.

In fact, during driving the operator has to control the quality of the blows, which he does by monitoring the basic parameters: strain (stress) and velocity at the top. This presents a problem as the velocity is not measured directly. As is known the integrated acceleration requires corrections. An interactive corrected integration software was used which produced rapidly the velocity signals.

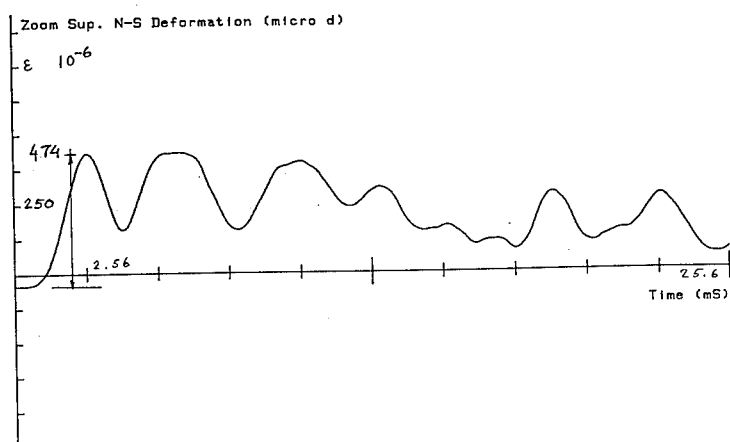
## 6 PILE INSTALLATION & RESULTS

The installation consisted of the robot which was constantly fixed to the swinging platform and of interchangeable cells which were jacked in position from below. Sand raining and careful saturation (aided by  $\text{CO}_2$ ) produced samples of relatives densities above 80%. The Fontainebleau sand used is fine grained and highly silicious. The signature of the blow depends on the cushion which cannot be reduced to scale. Test "cushions" were first tailored in the laboratory. This is based on the fact that prior to the arrival of echoes, the g level is unimportant. Another critical quality is the

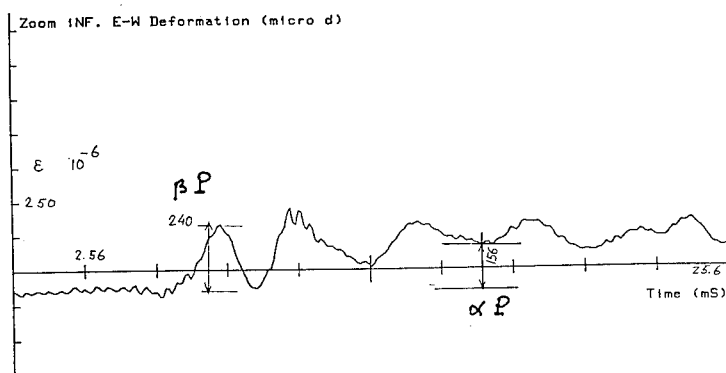




4<sub>a</sub>



4<sub>b</sub>



4<sub>c</sub>

Fig. 4. Blow Signals      b. Head Strain  
a. Head Velocity      c. Toe Strain

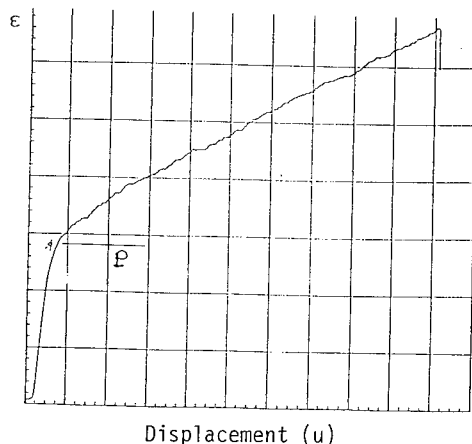


Fig. 5 Toe Strain versus Displacement

mechanical stability during the whole test.

The first thing to consider in the results is the noise. During driving all the motors are turning in close proximity to the transducers and high frequency noise penetrates everything. The power cables were protected by metal tubes. Foil were used everywhere. The nominal maximum frequency was 100 kHz. The sampling step was  $2\mu\text{s}$ . The integration used the trapez rule, the transfer function of which drops rapidly to zero towards the limit of the Nyquist frequency. The result was clean velocity and strain gage signals. This was consistently demonstrated by superimposing curves of different blows. Lack of space precludes a full exposition. An example is given in figure 2, chosen because the signals happened to have a "fine structure". The two graphs are the strains versus time at the pile head. The stroke was 0.5 m in situ. The blows shown in figure 2 were at 12 m depth (penetration of 1.6 cm/blow) and at 13 m (penetration of 1.4 cm/blow).

There were more than 50 blows between them. Both graphs have practically the same "wavelets" superimposed on the main signal. Accordingly those are not noise but part of the signal. The noise must therefore have a smaller amplitude i.e. be less than  $5 \times 10^{-6}$ .

Figures 3 and 4 depict signals from the 6th blow prior to a static loading test at a depth of 20 m. The (corrected) impact velocity is seen to be 2.44 m/s which is 0.78 of the nominal one at a stroke of 0.5 m. According to the stress wave theory, before echoes arrive the beginning of the velocity (v) and the strain (ε) signals at the head are related by  $v = C\epsilon$  ( $C$  = phase velocity = 5.1 km/s). The zoomed curves of figure 4

show that they are effectively so, with a maximum strain of  $474 \times 10^{-2}$  which corresponds to  $2.41 \text{ m s}^{-2}$ .

Many algorithms exist for the determination of the virginal displacement-compression curve and especially of the capacity. Figure 5 depicts the unfiltered strain-displacement curve and figure 4(c) the blow signal at 3/4 diameter (d) from the tip. It is recognised that by a judicious estimation of the displacement-dependent and the velocity-dependent contributions to the capacity of the point might be determined. Figure 5 shows that the static noise at the deepest station was less than 3%.

## 7 CONCLUSIONS

There is reason to claim, as illustrated by the results, that the robot produces blow signals and static loading signals which are clean and consistent, and is a standard tool for piling research. Similarity should be checked by in situ data. The analysis of the piling robot's design showed the strong influence of the scales of time. It also showed that an important parameter of a centrifuge's capacity is the space that could be allocated to the model.

## Development of a miniature pile driving actuator

A.de Nicola & M.F.Randolph

*Department of Civil Engineering, The University of Western Australia, Nedlands, W.A., Australia*

**ABSTRACT:** A miniature pile driving hammer has recently been developed for use on the centrifuge at the University of Western Australia. The paper describes the details of the hammer, which is based on a pneumatically lifted ram that is then allowed to fall freely to provide the impact. The motion of the fast moving piston was monitored in order to verify that the hammer was working correctly, and delivering full energy. The hammer has been used to conduct a number of tests on open and closed-ended piles, driven into uncemented calcareous soil. Results from these tests are presented and the performance of the two pile types compared for loading in both tension and compression.

### 1 INTRODUCTION

The plugging of pipe piles driven into sand is an area of great uncertainty in foundation engineering (Paikowsky, 1990) and the conditions under which piles will plug under both static and dynamic loading need to be explored further. The problem is difficult to analyse analytically or numerically and it is therefore necessary to address the problem experimentally, through tests at full-scale (Brucy et al, 1991) and model scale (Foray et al, 1993).

Centrifuge model tests are an ideal means by which to investigate plugging of piles, since they are considerably less expensive than full-scale tests, and provide the correct stress conditions within the soil plug, which is a major limitation of model tests in calibration chambers.

A miniature pile driving hammer has been developed at the University of Western Australia with the express purpose of studying the plugging of pipe piles driven in sand. The apparatus includes the advantages of a free-falling hammer, rapid blow frequency and the ability to conduct compression and tension static load tests at any stage. Ultimately, tests will be conducted at an acceleration of 100 g, in a fine grained silica flour (minimising scale effects due to the size of the soil particles relative to the pile wall thickness). Model piles of prototype diameter 1.6 m, and wall thickness 55 mm, will be driven to depths of 25 m. Different driving

shoes will be placed at the pile tip in order to assess their effects on the plugging of open-ended pipe piles, and the effect of the displacement ratio on pile capacity in sand.

The present paper describes the development of the pile driving hammer, and tests undertaken to verify its performance. Results from compression and tension tests on open- and closed-ended piles driven into calcareous soil are presented and discussed.

### 2 PILE DRIVING APPARATUS

The centrifuge facility at the University of Western Australia comprises an Acutronic 661 centrifuge with a capacity of 40 g-tonnes and a platform radius of 1.8 m. Details of the facility have been given by Randolph et al (1991).

Standard servo-controlled actuators have been developed to allow in-flight testing such as cone penetration or loading of foundations. Each actuator contains vertical and horizontal degrees of freedom, with actuation speeds of up to 30 mm/s. The pile driving hammer has been designed as a self-contained carriage, which can be fitted to one of the actuators.

Figure 1 shows a schematic diagram of the miniature pile driving hammer attached to an actuator. During driving, the whole carriage is advanced by means of the vertical lead-screw, with a constant drop-height being maintained

through a feed-back loop, using a miniature potentiometer mounted on the carriage. Drop-heights can be varied to a maximum of 20 mm.

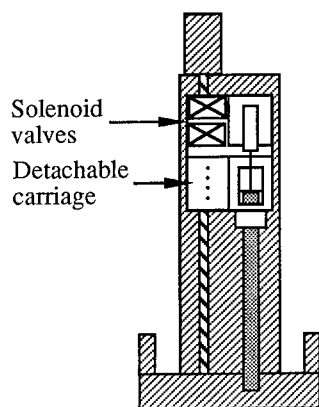


Figure 1 Schematic diagram of pile driving hammer mounted on actuator

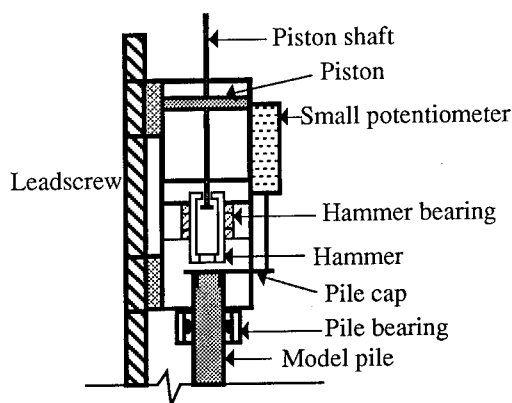


Figure 2 Detailed view of pile driving hammer

A more detailed diagram of the hammer is shown in Figure 2. The main components are a piston, with a shaft that is guided at both ends of the bore in order to minimise friction arising from Coriolis forces, and a hollow ram running between roller bearings. Two double acting pneumatic solenoid valves control the piston movement, driven from a standard compressed air supply at a nominal pressure of 600 kPa.

During operation, the piston is raised and lifts the ram by means of a bolt screwed into the end of the piston shaft. At the end of the stroke, the chamber below the piston is vented, and pressure is diverted to the upper piston, which then

accelerates downwards more rapidly than the ram. In this way, the ram is permitted to fall freely, providing a clean, controllable blow.

The hammer was designed with the two solenoid valves operating in parallel, in order to provide sufficient air flow at high acceleration levels. However, it has been found that the hammer may be operated successfully with only one valve at acceleration levels of up to 50 g.

The hammer may operate either continuously, or with single blows to permit stress-wave measurements. The small potentiometer, fixed to the hammer assembly with its shaft resting on an extension of the pile cap, measures the drop-height and subsequent displacement of the pile for a single blow. During continuous driving, the potentiometer provides the signal for the feedback loop that controls advance of the carriage, maintaining a constant drop-height.

A pile cap is bonded into the top of the pile with a super wick-in loctite. In addition to providing an anvil for the ram and a platform for the potentiometer shaft, the pile cap forms the bearing surface for static loading in compression (upper side of pile cap) and tension (protruding part of the lower side of the pile cap).

For the test results presented here, the pile was guided by teflon supports with three small rounded points of contact separated by 120 degrees. The pile thus has some rotational freedom, which helps to reduce the lateral forces on the bearing during driving. Subsequently, the teflon guides have been replaced by a three point roller bearing based on the same principle, but reducing friction still further.

## 2.1 Operation of Pile Driving Hammer

A key design attribute of the hammer was a requirement to operate at frequencies of up to 30 Hz, in an attempt to maintain the correct ratio between the duration of the transient motions associated with each blow, and the time between blows. Typical prototype blow rates would be 0.5 to 2 Hz. At a given modelling scale, such as 100 g, the hammer should be operated at 100 times the prototype frequency (ie 50 to 200 Hz).

At present, such blow rates are out of reach. However, a blow rate of 30 Hz is sufficient to model events such as consolidation, provided that the coefficient of consolidation of the model soil is reduced. Thus, since consolidation occurs  $N^2$  times faster in the model than the prototype, and the hammer is operated at (approximately)  $N$

times the prototype rate, the rate of consolidation should be reduced by a factor of  $N$  in the model. This may be achieved either by reducing the particle size of the soil (the silica flour for later experiments will have a permeability two orders of magnitude lower than a typical sand) or by using a viscous pore fluid (silicon oil, viscosity 100 times that of water) as in the present case.

The input driving energy into the system can be varied during testing by varying the drop height up to a maximum of 20 mm. In prototype dimensions, this scales to 2 m. An alternative means by which the driving energy can be varied is by changing the ram mass, although this cannot be done during testing. The results presented here have been obtained with a ram mass of 50 grams, although the maximum ram mass is 70 grams (or 70 tonnes in prototype dimensions for tests at 100 g).

## 2.2 Model Pile

The model pile used in the tests has a diameter of 16 mm, wall thickness of 0.55 mm, and may be embedded to a depth of 150 mm. The pile is made from aluminium and has an overall flexibility representative of more slender prototype piles. There are five levels of axial strain gauges located on the outside pile wall. These gauges are referred to as gauges A1 to A5, and are located at distances of 10 mm, 55 mm, 100 mm, 145 mm and 190 mm from the pile tip. Each level comprises a full bridge (including circumferential gauges), so that the effects of bending and temperature drift are minimised. A strip of epoxy resin along the length of the pile protects the axial gauges from damage.

## 2.3 Piston Performance Tests

Initial impact tests performed in clean silica sand revealed that the pile driving hammer was operating inefficiently, with a maximum impact force that was insensitive to drop-height. Consequently, means were devised to monitor the motion of the piston in order to identify the problem. Since the piston velocity is very high, and any contact would effect its operation, a laser displacement transducer was used to follow the piston during a complete blow.

To monitor the piston motion, the actuator unit was placed on the bottom of a strong-box and a laser transducer was mounted on a bridge fixed across the strongbox, placed directly above

the carriage. The actuator was positioned so that the laser beam was focused directly on top of the piston shaft.

The laser output was sampled at a frequency of 4 kHz, using a fast data acquisition card (the same type as used for recording dynamic stress-waves), allowing accurate monitoring of the piston motion. The impact of the hammer was taken by a dummy model pile, resting on a polyurethane block on the floor of the strongbox.

Figure 3 shows a plot of the piston displacement versus time for one of the initial performance tests conducted at 50 g. It also shows the theoretical free-fall response of the ram, which is used as a design guide for the required downward piston velocity. The upward stroke of the piston is characterised by an initial period of acceleration (with a parabolic displacement response), until the bolt connected to the bottom of the shaft makes contact with the ram. At that stage, the velocity is immediately reduced due to the impact. The piston then accelerates again but at a reduced rate.

Under a nominal operating pressure of 500 kPa, the theoretical time for the piston and ram assembly to be raised through the required 20 mm would be about 4 ms (the effective piston area is approximately 400 mm<sup>2</sup> and the piston and ram masses are 20 gram and 50 gram respectively). The additional time evident from Figure 3 is due to frictional effects and back-pressure in the exhaust chamber of the piston.

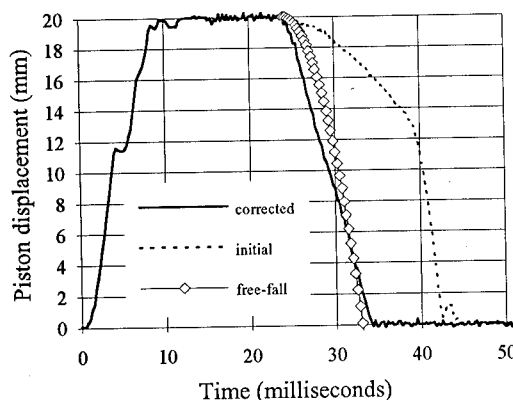


Figure 3 Piston displacement with time

The results from the downward stroke were initially disappointing (see 'initial' curve). In the first part of the stroke, the velocity was very low and comparable velocities with the upward travel

were not achieved until after a time delay of nearly 10 ms. This resulted in the piston 'carrying' the falling ram, and significantly reducing the impact energy.

It was eventually discovered that the behaviour during the downward stroke was due to the mis-firing of one of the solenoid valves at high g-levels, in combination with shock waves generated at the end of the upward stroke by the impact of the ram on the piston housing.

The faulty solenoid valve was removed (to be replaced in due course), resulting in the improved performance shown in Figure 3 (see curve marked 'corrected'). It may be seen that the downward travel of the piston intersects the theoretical free-fall response for the ram at a height of 5 mm. Thus, for strokes of up to 15 mm, the ram will fall completely freely. Even for the maximum drop-height of 20 mm, the interference will be very small, and will probably disappear once the second solenoid valve is replaced.

## 2.4 Dynamic Tests

Figure 4 shows an example of the stress waves recorded for a set of blows at an acceleration level of 50 g. The set-up for the test was similar to that for monitoring the piston motion, but without the laser displacement transducer. The dummy pile in this case had an axial strain-gauge attached to it so that stress wave measurements could be made.

Results are shown from hammer blows conducted at three different drop heights. The shape of the force waves is typical of a full-size drop-hammer, with a rise time which scales to a prototype value of about 2 ms. The efficiency may be estimated from the peak force and the pile impedance of  $Z = EA/c = 0.37 \text{ kNs/m}$  (where  $EA$  is the cross-sectional rigidity of the model pile, and  $c$  is the wave speed). The efficiency of the blow with a 5 mm drop height is about 90 %, while that for the other two blows is about 60 %. The major source of energy loss probably stems from the frictional resistance encountered by the ram as it is forced laterally against its bearing by the Coriolis force.

## 3 TEST RESULTS

The test results presented in this section are from piles driven into calcareous soil obtained from the North West Shelf of Australia. The soil

characteristics are presented in Table 1. The permeability of the soil has been reduced by saturating the soil in silicon oil in order to scale correctly the pore pressure generation and dissipation during installation.

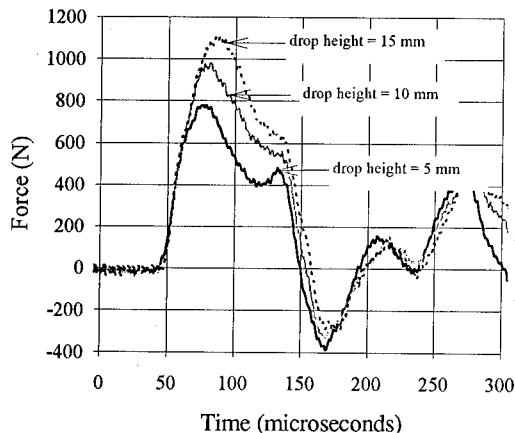


Figure 4 Example stress wave measurements

Results are presented for both open-ended and closed-ended piles. However, it is acknowledged that since the ratio between pile wall thickness and mean particle size is only 4, the results for the open-ended piles will be subject to scaling effects. As discussed earlier, subsequent testing of open-ended piles in silica sand will use a mean particle size of 50  $\mu\text{m}$  in order to reduce further such scaling effects.

Table 1 Summary of calcareous soil properties

Specific gravity	2.77
Calcium carbonate content (%)	95
Mean particle size (mm)	0.13
Minimum dry density ( $\text{kN/m}^3$ )	9.1
Maximum void ratio	2.0
Maximum dry density ( $\text{kN/m}^3$ )	14.0
Minimum void ratio	0.95
Compressibility (@ 400 kPa)	0.15
Critical state friction angle ( $^\circ$ )	38
Coeff. of consolidation ( $\text{mm}^2/\text{s}$ )	16

## 3.1 Installation

In order to model the true driving process correctly, the manner in which prototype piles are installed was followed as closely as possible. The pile was held above the soil surface during spinning up of the centrifuge and consolidation

of the soil. The pile was then allowed to free-fall into the soil with the mass of the ram resting on the pile cap. Driving began once the pile had come to rest. Installation by this method required that the pile is placed at the centre of the box so that initial lateral deflections are not induced from the radial component of the gravity field.

### 3.2 Driving Results

The driving results discussed below have all been conducted with a 50 gram ram, released from a constant drop height of 3 mm (equivalent to 300 mm prototype). The predominate blow frequency used during driving was 10 Hz.

Two closed-ended and two open-ended piles were installed in the calcareous soil sample using the miniature pile driver. Figure 5 shows the driving record for the the second test of each pile type as well as a profile of the cone resistance obtained by averaging a number of cone penetration tests.

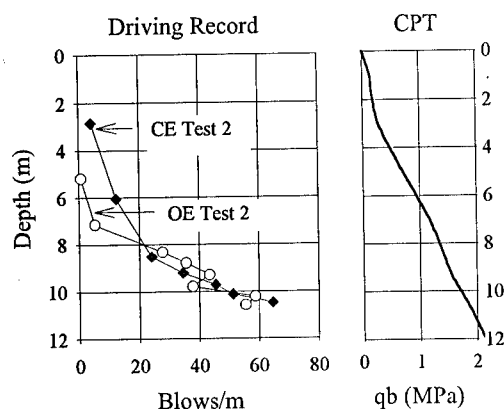


Figure 5 Dynamic driving record

The starting point of each of each of the drives indicates the depth to which the pile has free-fallen under the combined weight of the ram and pile. In the case of the open-ended piles, the pile free-fell up to 6 m whilst for the closed-ended piles, the free-fall was much lower at around 3 m. The initial blows induced very large displacements, especially for the open-ended piles. At full penetration, the blow-counts for the two pile types were similar, although that for the open-ended piles appeared to reach a limit of 55 blows/m, compared with the maximum value of 65 blows/m for the closed-ended piles.

While definitive conclusions cannot be reached from only a small number of tests, it would appear that the open-ended piles penetrated in a partially-plugged manner over the depth range 8 - 11 m. An instrument for monitoring the height of the soil plug during penetration is currently under development, and this will prove most valuable in interpreting the observed performance of open-ended piles.

### 3.3 Static Tests

Static tests were performed for each of the piles driven into the soil sample. Figure 6 shows the response of the top and bottom set of strain gauges for compression and tension load tests on the closed-ended pile. (Since the pile penetration never exceeded 130 mm, the top gauge reading has been calculated from the average of the two uppermost gauges, but has been labelled A4 in the Figure.)

During pile installation, some drift of the strain gauges was observed, and the zero values have been adjusted by amounts of up to 100 N. The basis for this adjustment has been (a) the performance during cyclic tension-compression loops, and (b) the gauge readings after extraction of the piles (but before stopping the centrifuge).

The most striking feature of Figure 6 is the marked effect of the tension-compression loops on the shaft friction and end-bearing. The average shaft friction decreases from 52 kPa during the first compression test, to 27 kPa in the second test. The corresponding results from the tension loops are 25 kPa and 22 kPa respectively. It may be noted that the theoretical ratio of tensile to compressive shaft capacity for this pile is 0.84 (De Nicola and Randolph, 1993), which is consistent with the above data.

Corresponding data for the open-ended pile (single compression and tension loop) are shown in Figure 7. The pile capacity is significantly lower than for the closed-ended pile, with estimated average shaft friction of 42 kPa (compression) and 25 kPa (tension). The strange behaviour of the bottom gauge shown in Figure 7 is due to the effect of high internal stresses from the soil plug, which has led to distortion of the pile, and thus inaccurate gauge readings (note that the strain gauges responded perfectly towards the end of the test when the end-bearing load was removed).

The end-bearing capacity of the closed-ended and open-ended piles continue to increase over

quite large pile movements. At a penetration of 125 mm, the values are 2.0 MPa and 0.5 MPa for the first loops of each load test, and 3.1 MPa for the second loop of the closed-ended pile test. The much higher end-bearing capacity of this pile during the second loop is an interesting phenomenon, and appears to be due to additional soil falling beneath the pile tip during the tension test, and thus adding to the compressed bulb beneath the pile when re-loaded in compression.

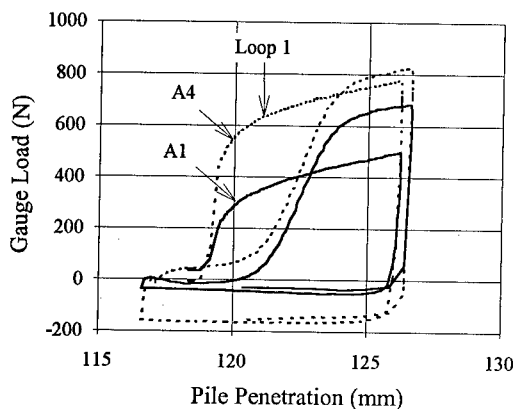


Figure 6 Static load tests on closed-ended pile

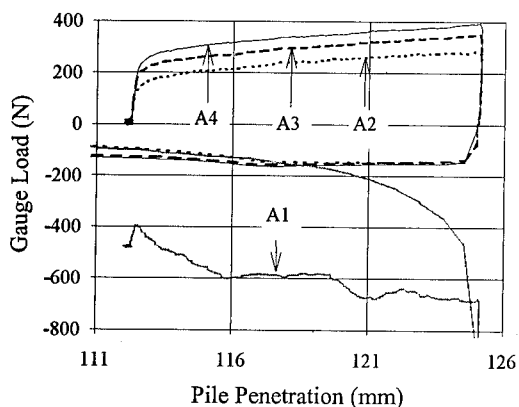


Figure 7 Static load tests on open-ended pile

The relatively low end-bearing capacity of the open-ended pile indicates that it is responding in an unplugged mode. This is partly due to the relatively low aspect ratio of the soil plug (estimated height no more than 6 diameters), and partly due to the rate of loading, which would have led to only partial drainage, and hence to a

reduced plug capacity (Randolph et al, 1991). This will be discussed in further detail in another paper.

Extensive tests conducted by the authors on jacked model piles in the same soil revealed that the skin friction only increased with depth up to prototype depths of approximately 12 m. Thereafter there was a very clear tendency for the skin friction to reach a limiting value. The global average skin friction for jacked piles was around 10 kPa compared with the final value of 22 kPa for the closed-ended driven piles.

#### 4 CONCLUSIONS

A miniature pile driving hammer has been developed successfully for use on a small centrifuge. The hammer can operate at frequencies of up to 30 Hz, or apply single blows for dynamic measurements, and also enables tension and compression static load tests to be conducted without stopping the centrifuge. These advantages make the apparatus suitable to explore a wide variety of driven pile problems.

A set of preliminary tests are reported for open and closed-ended piles driven into calcareous soil. The results confirm the relatively low shaft friction for such piles (particularly for the open-ended pile) and the rapid degradation under cyclic loading. The end-bearing capacity of the open-ended pile was shown to be significantly lower than that for the closed-ended pile, partly due to the relatively short length of soil plug, and partly due to the rate of loading.

#### REFERENCES

- Brucy, F., Meunier, J. and Nauroy, J-F. 1991. Behavior of pile plug in sandy soils during and after driving. Proc. 23rd Annual Offshore Tech. Conf., Houston: 145-154.
- Cyran, T. C., Mehle, J.S. and Goble G.G. 1991. Centrifuge modeling of piles. Proc. of the International Conference Centrifuge 1991: 377-384. Rotterdam: Balkema.
- Foray, P., Colliat, J.L. and Nauroy, J-F. 1993. Bearing capacity of driven model piles in dense sands from calibration chamber tests. Proc. 25th Annual Offshore Tech. Conf., Houston, Paper OTC 7194.
- Randolph, M.F., Leong, E.C. and Houlsby, G.T. 1993. One-dimensional analysis of soil plugs in pipe piles. Geotechnique 61(4): 587-598.



## Studies on laterally loaded pile groups in sand

Michael McVay & David Bloomquist  
*University of Florida, Gainesville, Fla., USA*

Dennis Vanderlinde  
*GeoSyntech, Atlanta, Ga., USA*

Jens Clausen  
*RH & H Consult, Denmark*

**Abstract:** An apparatus for driving individual piles of a group, laterally loading it, and measuring the contribution of each row is described. The device performs these tasks in flight, and can test free head groups of six or nine piles at spacings of three to five pile diameters. Results indicate that the load contributions for the lead, middle, and trail rows were not shared equally. In the loosest case and largest pile spacing ( $D_r = 16\%$ , and 5b spacing), the distribution was found to be 35%, 33%, and 31% (LMT). For the densest and closest spacing ( $D_r = 45\%$ , and 3b spacing), the distribution was 41%, 32%, and 27%. Spacing has an effect on the lateral displacement of the group, and installing them at a lower acceleration results in reduced ultimate load and a different row distribution.

### Background

Several centrifuge researchers have modeled the soil/structure interaction of laterally loaded pile groups. One of the first to simulate a laterally loaded pile was Scott (1981). Piles of two different diameters were tested in uniform, saturated sand. The smaller size was installed at 1 g and then accelerated, while the larger one was suspended in the container and sand placed around it. Results gave an initial pile response similar to the full scale test, however the total response was softer. The author stated that neither method of installation represented the prototype conditions. Barton (1984) conducted a parametric study on groups of two, three and six piles in sand. She found that for the two pile group at 2b spacing, the lead pile carried 60% of the lateral load and the trailing one 40%. However, at 8b spacing, negligible interaction was observed. Oldham (1985), at the University of Manchester, instrumented a single pile with strain gauges and drove it, via a pneumatic jack, into sand. It was then laterally loaded with a hydraulic actuator. The entire driving/loading sequence was performed in flight. Subsequently, Terashi et al., (1990) conducted a series of modeling of models tests on a laterally loaded pile installed at one gravity. They obtained excellent agreement at the various accel-

eration levels. Garnier et al., (1989) were the first to study the lateral influence of pile-soil interaction with two, free headed piles installed at one gravity. Bloomquist et al., (1991) were the first to report on an apparatus to drive, in flight, individual piles (5 piles) and axially load the group. A pertinent finding was that there was a measurable difference between the axial capacity of the group installed at 1 g versus in-flight. Further, the method of driving (e.g., using a drop hammer versus a stepping motor operating at 50 Hz) had no appreciable effect on the group capacity.

This paper presents several improvements on the above device by allowing more piles to be driven (9 total). In addition, it can apply a lateral load to the group and measure the individual row contributions within the group as well as the resulting group displacements.

### Equipment

The pile driving and lateral loading apparatus is shown in Figure 1. The device consists of an aluminum plate bolted to the soil containment bucket (L). This plate has a square opening at its center for the pile cap (O) and two C channels (I) bolted to each side to support the stepping motors (A & K). The stepping motors rotate the ball screws (B) which in turn, raise or lower the top beam (E) through the ball nuts (C). To prevent

twisting of the top beam, pillow block bearings (D) slide through two, 19 mm (0.75 inch) diameter steel shafts (N) which are flange mounted on the aluminum base plate.

Attached to the top beam (E), is the pile driving mechanism or PDM (G) which inserts the piles (M). This is accomplished by using a computer to control the pile driving sequencer (PDS) plate (H). Machined into the sides of the plate are slots for nine miniature air cylinders whose pistons are normally retracted so that the piles are able to slide freely in their respective holes as the PDM moves up and down.

When a particular pile is to be driven, the computer actuates the corresponding air cylinder, which in turn, extends its piston shaft across the hole, effectively blocking it. Since the pile is now unable to slide through its hole, as the PDM is lowered, it forces the pile down through the pile cap and into the soil. The pile driver sequencer plate is connected to the top beam (E) using post-tensioned steel rods thereby creating a rigid system to drive the piles, and to provide a clear distance between the top beam and the PDS plate for the piles to slide through.

The lateral load is provided by a 5.3 kN (1200 lb.) air cylinder (R) shown in Figure 1. Attached to the end of the cylinder is a 4.5 kN (1000 lb.) load cell, and a 6.4 mm (0.25 in.) range LVDT.

A schematic and photograph of the three row, nine pile cap (O) for 3b spacing is shown in Figure 2. The cap is made up of three separate aluminum blocks which transfer the applied lateral load to one another through four load cells mounted between the lead, middle, and trail rows. By measuring the total applied lateral load, the load transmitted to each row can be determined by subtraction. The load cells are connected to the aluminum blocks using screws and adjustable bushings. To prevent each aluminum block (or row) from rotating out of plane, two, 6.4 mm (0.25 in) diameter stainless steel rods are inserted through linear ball bearings in all the blocks.

A bracket containing four O-rings, is mounted on the lead and trail rows. As the exterior piles are inserted through the cap, a groove cut in each pile allows the O-rings to seat themselves when they encounter the groove (Figure 2). Once engaged, the O-rings prevent the bracket and hence the cap from sliding down the piles. To support the pile cap during driv-

ing, an aluminum "trap-door" is connected to the base plate using four air cylinders. The trap-door has a square hole in it to allow the piles to be driven into the soil, but supports the pile cap along its perimeter during driving. Once driving is complete the trap door is lowered, allowing the piles to assume the weight of the cap.

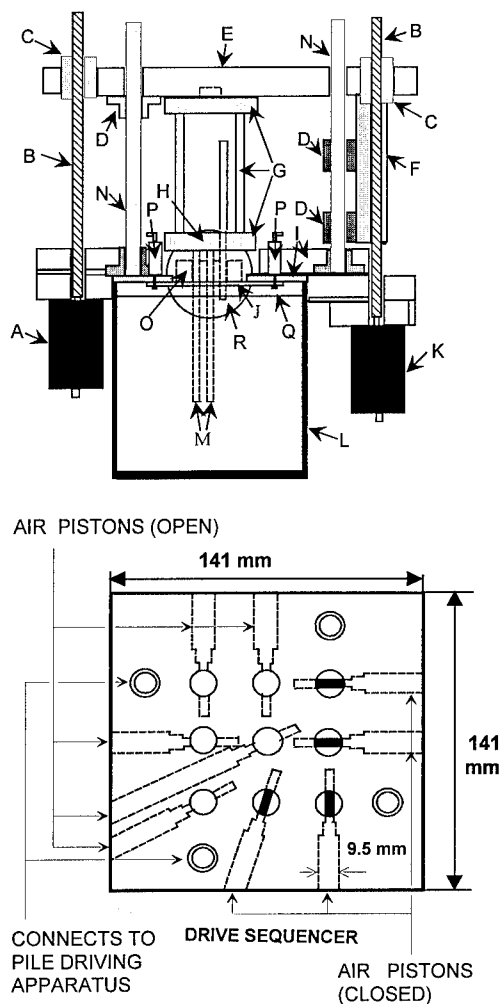
The piles used in this study were constructed of 9.5 mm (0.375 in.) outside diameter and 7.7 mm (0.305 in) inside diameter high strength aluminum tubing. They were 279.4 mm (11 in.) in length from the bottom of the pile cap. At test acceleration (48 gravities), the piles simulated 0.46 m (18 in.) diameter by 13.41 m (44 ft.) long, open ended piles with a flexural stiffness (EI) of  $83.16 \times 10^3 \text{ kN-m}^2$  ( $28.98 \times 10^9 \text{ lbf-in}^2$ ). The model piles had a clear distance of 44.5 mm (1.75 in.) [2.13 m (7 ft.) prototype] between the bottom of the cap and the ground surface.

### Test Setup

Reid-Bedford sand was used because of the abundance of published information on its properties (Saada et al., 1988). It is fine, sub-rounded to subangular, 89% quartz, 9% feldspars, 2% ferromagnesiums, and has a solid density of  $2650 \text{ kg/m}^3$ . Maximum and minimum unit weights have been established as  $16.74 \text{ kN/m}^3$  (106.5 pcf) and  $13.59 \text{ kN/m}^3$  (86.5 pcf), respectively. These values correspond to void ratios of  $e_{\min} = 0.588$  and  $e_{\max} = 0.906$ .

Sample preparation consisted of dry pluviation directly into the sample container. For the low relative density ( $D_r = 17\%$ ) tests, it ranged from  $13.83 \text{ kN/m}^3$  (88 pcf) to  $14.14 \text{ kN/m}^3$  (90 pcf). The 45% relative density samples had average unit weights of  $15.1 \text{ kN/m}^3$  (96 pcf). Triaxial testing of the sand at these unit weights produced friction angles of  $31^\circ$  and  $38^\circ$  respectively.

After reaching test acceleration, the piles were driven individually - for all tests, they were driven row by row. Next, the computer actuated the lateral load air cylinder until contact was made with the cap. At this point, the load cells and the LVDT instrumentation were zeroed. The operator would then key in the prototype load increment and final deformation desired and the control mechanism would apply load increments and record the instrumentation output. The sampling interval used was ten seconds, and continued until two successive lateral



- |                    |                    |
|--------------------|--------------------|
| A. STEPPING MOTOR  | J. TRAP DOOR       |
| B. BALL SCREW      | K. STEPPING MOTOR  |
| C. BALL NUT        | L. SOIL CONTAINER  |
| D. BEARING         | M. PILES           |
| E. TOP BEAM        | N. STEEL GUIDE ROD |
| F. SIDE BEAM       | O. PILE CAP        |
| G. DRIVE APPARATUS | P. AIR PISTON      |
| H. DRIVE SEQUENCER | Q. SOIL SURFACE    |
| I. BASE BEAM       | R. AIR PISTON      |

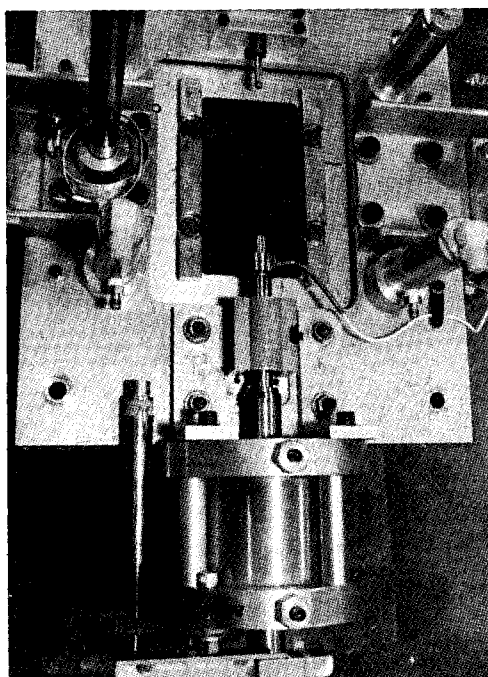


Figure 1. Pile driver & loading mechanism

deformation readings were within 1% of each other. The process was then repeated (loading, reading, etc.) until the final displacement was attained.

#### Test Results

A total of 20 tests were performed. The first results, shown in Figure 3 illustrates the influence of the sand's density on the lateral response (load-displacement). Depicted are the results at 17% and 45% relative density. As expected, the higher density soil provided a stiffer response and higher ultimate loads (25% greater) compared to the 17%  $D_r$  soil. Also shown is the effect of insertion at 1 g versus test acceleration.

It is believed that one possible explanation for the difference between the two curves is the amount of disturbance and heave of the sand that was observed for the 1 g insertion test. The heave (not detected during the 48 g driving), resulted in a loosening of the sand around the piles and hence a reduced lateral capacity.

Figure 4 shows the total load and row distribution for the 3b pile spacing at 45% and 17 % relative density. For the higher density test, the lead row carries more load than the middle and trail rows (41%, 32%, 27%), while the loose sand at  $D_r = 17\%$ , shows row contributions of 37%, 33%, and 30%. From these results, it suggests that the row contributions vary from 41%, 32%,

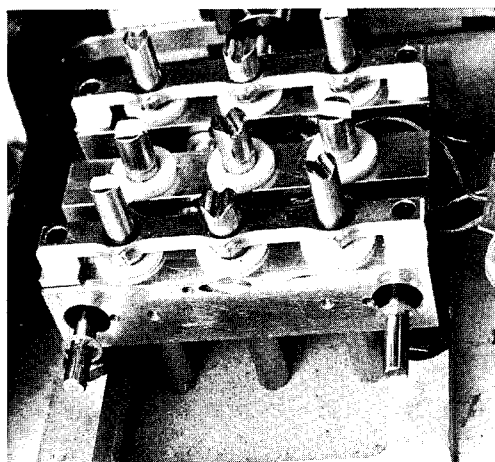
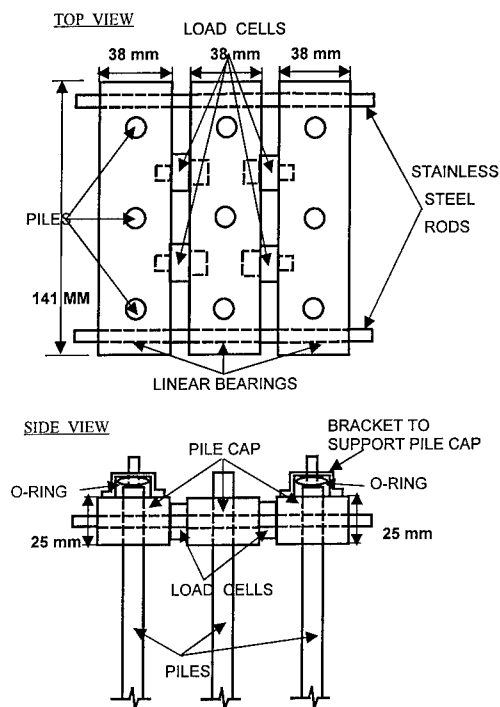


Figure 2. Instrumented pile cap

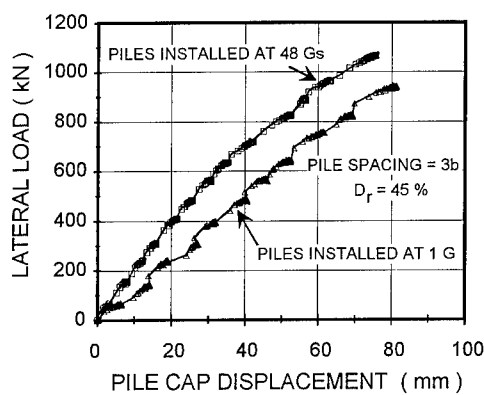
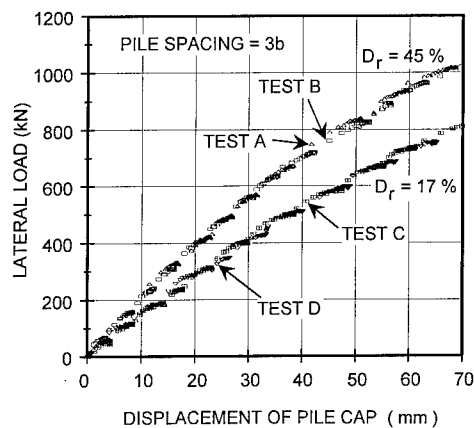


Figure 3. Effect of relative density and installation g level

27% for a medium dense sand to 37%, 33%, 30% for a loose sand. Based on the above trend, it would be reasonable to expect the distribution to approach 33%, 33%, 33% for a very loose sand, since the zone of influence around each pile diminishes as the relative density decreases.

The influence of pile spacing is shown in Figure 5. The figure shows an average 22% de-

crease in lateral resistance as pile spacing decreases from 5b to 3b for similar relative densities. In addition, the influence of 5b pile spacing on the individual row contributions are depicted. This test, at a relative density of 16%, showed individual row contributions of 36%, 33%, 31% respectively. There appears to be a decrease in the shadowing effect between the rows with in-

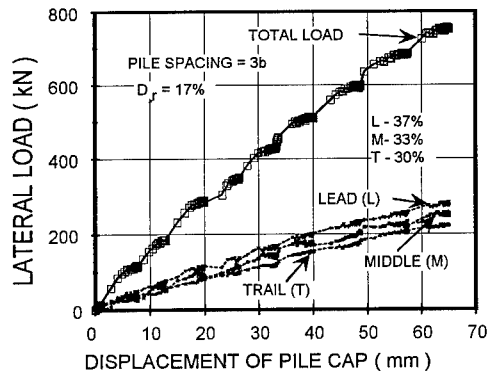
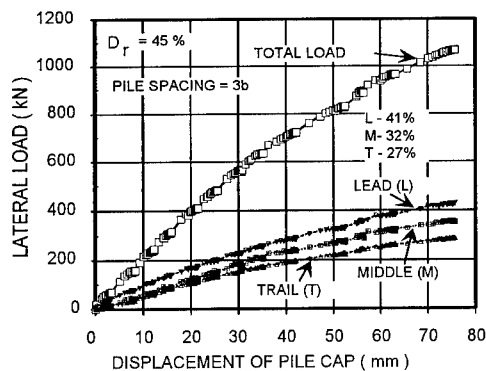


Figure 4. Total and row response at two soil densities

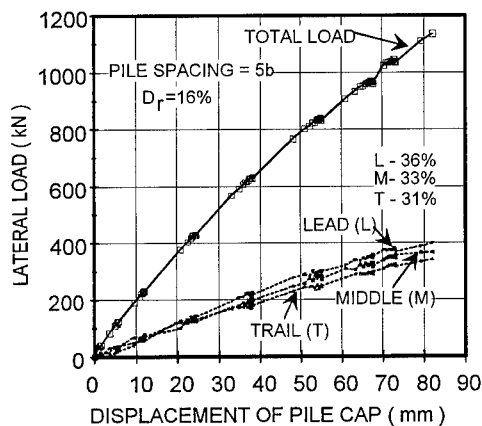
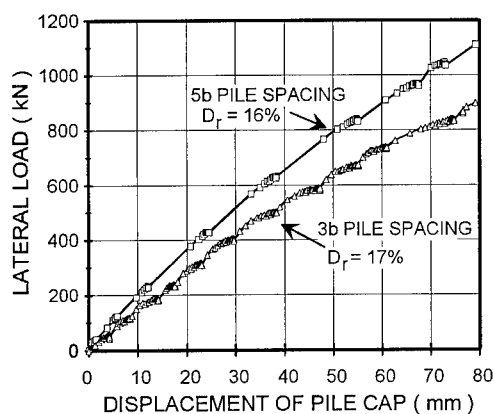


Figure 5. Effect of pile spacing

creased pile spacing. Moreover, it is expected that, with sufficiently wide spacing, load distributions within rows would approach 33%, 33%, and 33% as found by Barton (1984).

### Conclusions

Results of testing in dry sand at various densities and pile spacing suggest the following:

- 1) Driving at 1g results in lower group capacity. This may be a result of the sand loosening to a lower  $D_r$  state during 1 g installation, since high geostatic stresses are absent during the installation process;
- 2) The soil's density affects both the group capacities as well as the individual row contributions. For a nine pile group at 3b pile spacing, the individual row contributions vary from as high as 41%, 32%, 27% for very dense sand to as low as 37%, 33%, 30% for loose sand. The total group

resistance dropped by 22% as the relative density decreased from 45% to 17%;

- 3) The influence of pile spacing on the total lateral capacity of the group was observed. As the pile spacing increased from 3b to 5b, the group capacity also increased; however the distribution among the individual rows within a group became less pronounced. The latter finding supports the shadowing theory proposed by Brown et al., (1988). His theory suggests that the middle row of closely spaced (3b) piles is influenced by the "shadow" of the disturbed soil behind the lead row, and likewise, the trail row by the middle row. As the spacing increases, this effect is reduced.

### References

Barton, Y. O., "Response of Pile Groups to Lateral Loading in the Centrifuge", Proceedings of a

---

Symposium on the Application of Centrifuge Modelling to Geotechnical Design, edited by Craig, W. H., University of Manchester, 1984, pp. 456 - 472.

Bloomquist, D., Feld, T., Townsend, F. C., Gravgaard, J., and Gill, J., 1991, "Development of a Multiple Pile Driver/Load Test Device for Pile Group Studies", Centrifuge 91, edited by Ko, H-Y and McLean, F. G., A. A. Balkema Publishers, Rotterdam, Netherlands, pp. 355 - 359.

Brown, D. A., Morrison, C., and Reese, L. C., 1988, "Lateral Load Behavior of Pile Group in Sand", Journal of Geotechnical Engineering, ASCE, Vol. 114, No., 11, pp. 1261 - 1276.

Garnier, J., Levacher, D., and Cintra, J. C., 1989, "Lateral Loading of a Couple of Piles in Sand in the Centrifuge", Second International Conference on Foundations and Tunnels, pp. 161 - 166.

Oldham, D. C. E., 1985, "Experiments with Lateral Loading of Single Piles in Sand", Application of Centrifuge Modeling to Geotechnical Design, edited by Craig, W. H., A. A. Balkema, Rotterdam, Netherlands, pp. 121 - 141.

Saada, A. and Bianchini, G., editors, 1988, "Constitutive Equations for Granular Non-Cohesive Soils", A. A. Balkema Publishers, Rotterdam, Netherlands.

Scott, R. F. 1981, "Pile testing in a centrifuge", Proc. 10th International Conference on Soil Mechanics and Foundation Engineering, Stockholm, Vol 2, pp. 839 - 842.

Terashi, M., Kitazume, M., Maruyama, A., and Yamamoto, Y., 1991, "Lateral Resistance of a long pile in or near the slope", Centrifuge 91, edited by Ko, H-Y and McLean, F. G., A. A. Balkema Publishers, Rotterdam, Netherlands, pp. 245 - 252.

## Lateral resistance of a long pile in soft clay

M. Kitazume & S. Miyajima

*Port and Harbour Research Institute, Yokosuka, Japan*

**ABSTRACT:** A series of centrifuge model tests was performed on a laterally loaded pile embedded in a normally consolidated clay ground whose undrained shear strength increased with depth. The model ground was initially consolidated on a laboratory floor under vertical pressures which were gradually increased with depth. Then the ground was brought up to 25 g acceleration field to allow to consolidate by enhanced self weight. In the test the relationship between the horizontal load and the displacement was observed as well as the bending moment distribution along the pile. Subgrade reaction and displacement were calculated from observed bending moment along the pile. The coefficient of the subgrade reaction in p-y method was evaluated by the measured moment distribution and compared with the shear strength of the ground. In this paper, the effects of the pile rigidity on the load-displacement relation, bending moment distribution along the pile and the subgrade reaction were discussed in detail.

### 1 INTRODUCTION

In Japan, many construction projects for port facilities have been in progress in coastal areas where very soft clay deposits are often encountered. Pile and pile group foundations are often used for the port facilities such as dolphins, piers and quay walls.

The pile and pile group foundations are subjected to not only vertical loads but also lateral loads due to wave force, earth pressure and/or earthquake motion. The behavior of pile and pile group under the lateral loads is much affected by many factors; the soil properties surrounding the pile and/or the pile group, the flexural rigidity of pile, loading conditions, and so on. To progress these projects safely and economically, it is important to investigate the pile behavior under lateral loads in detail.

Many research engineers have studied on the laterally loaded pile behavior analytically and experimentally. And centrifuge model tests also have been performed for pile foundation, where prototype behavior can be simulated in a scaled model by means of the centrifugal acceleration. Scott (1981), Oldham et al. (1984) and Barton (1984) performed centrifuge model tests on the pile and/or the pile group embedded in dense saturated fine sandy ground. Matlock (1970) and Hamilton et al. (1991) carried out centrifuge tests on piles embedded in clay ground.

However, limited studies were reported which dealt with the behavior of a pile in a normally consolidated clay ground whose shear strength increased with depth, that is often encountered in Japanese coastal area. The behavior of the pile in the normally consolidated clay ground was thought to be much different from that in the clay ground whose shear strength is constant with

depth. Therefore the authors started a series of centrifuge model tests to investigate the behavior of laterally loaded long pile embedded in the normally consolidated clay ground whose shear strength increased with depth. To avoid obtaining misleading conclusions from the model tests, the authors started with a series of tests of a fairly simple situation in which a long pile is embedded in a horizontal clay layer as the first step of the study.

In the field, soil around a pile is thought to be much disturbed due to the pile installation. However, uncontrolled soil disturbance was not simulated in the model test. In this test, the pile in the normally consolidated clay ground was loaded laterally under 25 g acceleration field. The loading tests were carried out for different pile flexural rigidities to investigate its effect on the pile behavior in detail.

### 2 TEST PROCEDURE

#### 2.1 Apparatus

A centrifuge used in this study was the PHRI (Port and Harbour Research Institute) geotechnical centrifuge. The radius of the centrifuge is 3.8 m measured to the surface of the swing platform. The maximum payload is 2.7 tons and the maximum acceleration is 115 g. The details of the PHRI centrifuge and surrounding equipments were reported by Terashi (1985). All the tests were performed in a strong specimen box whose inside dimensions were 70 cm in length, 60 cm in depth and 20 cm in width. In this study, six model piles having various flexural rigidities were used to investigate its effect on the pile behavior. Cylindrical shaped piles are

Table 1 Model pile dimensions

Test No.	Pile Name	Material	Pile Width	Pile Thickness	Pile Rigidity	Embedment $L_p$ (cm)	Loading Height $L_r$ (cm)
			B (cm)	D (cm)	EI (kN·cm <sup>2</sup> )		
TEST1	AC-2	acrylic	2.0	0.2	1.01	40.0	10.0
TEST2	AC-5	acrylic	2.0	0.5	7.99	40.0	10.0
TEST3	AC-6	acrylic	2.0	0.6	10.6	40.0	10.0
TEST4	AL-3	aluminum	2.0	0.3	35.5	40.0	10.0
TEST5	AL-5	aluminum	2.0	0.5	125	40.0	10.0
TEST6	ST-5	steel	2.0	0.5	405	40.0	10.0

often used in the field, but in this model tests a plate shaped pile was used for ease of the model preparation. The properties of the model piles were summarized in Table 1. Width of the pile was 2 cm and constant throughout the test series, but thickness and material of the piles were changed to obtain various flexural rigidities. Strain gauges were installed in pairs at 17 locations along the piles to measure bending moment. Since the strain gauges and wires might affect the flexural rigidity, every pile was loaded as a simple beam for a calibration of the strain gauges and for determining its average flexural rigidity.

## 2.2 Model ground preparation

A typical model setup for the tests was schematically shown in Fig.1. To investigate the effect of pile flexural rigidity experimentally, parametric studies with wide range of flexural rigidities were desired to be carried out. Because it took more than one month for the model preparation and the specimen box used was sufficiently wide in length, two piles were placed in the box at spacing of 23 cm as shown in Fig.1 and were loaded individually to perform parametric tests within the limited period. It was confirmed from preliminary experiments that the pile behavior was negligibly affected by the existence of the other pile if piles were placed at spacing of more than 20 cm.

Two piles were placed at prescribed positions of the specimen box by fixing their bottom ends by means of a clump so that they kept standing vertically during the model ground preparation. After placing the piles, Toyoura sand was poured at the bottom of the box to construct a drainage layer.

It was found from the preliminary tests that the model clay ground having 40 cm and more in thickness was required to satisfy a long pile condition when the model piles listed in Table 1 were used. However, flight time required to complete self weight consolidation of 40 cm thickness clay ground was estimated to be more than two days. To reduce the flight time and to reduce the fatigue damage per test - not only to the centrifuge but also to the research workers involved in the tests, the clay ground was prepared by the following procedure. By this procedure, the flight time required to complete the self weight consolidation was reduced to about eight hours as mentioned later.

Saturated clay slurry having the water content of 120% was poured on the sand layer to prepare the

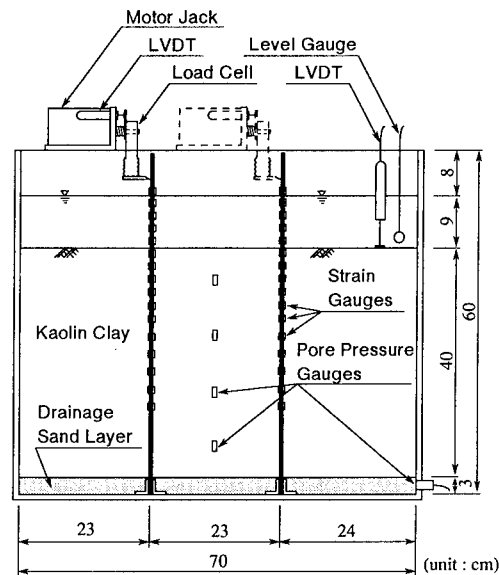


Fig.1 Model setup

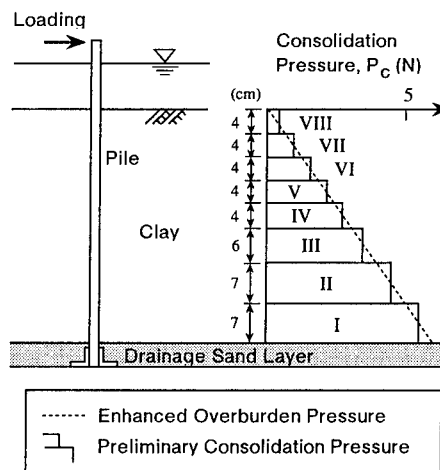


Fig.2 Preliminary consolidation pressure



bottom clay layer I as shown in Fig.2. The clay used in the tests was kaolin clay whose index properties,  $W_L$ ,  $W_P$  and  $I_p$  were 59.0%, 16.8% and 42.2, respectively. The clay was allowed to consolidate on a laboratory floor. The preliminary consolidation pressure of the layer I was  $5.47 \text{ N/cm}^2$  that was equal to the overburden pressure enhanced at the center of this layer in 25 g field. After the completion of the consolidation of the layer I, additional magnitude of clay slurry was poured again for the layer II and consolidated under the prescribed pressure, which was relatively smaller than that of the layer I and also same as the enhanced overburden pressure at the layer II. This procedure was repeated eight times to prepare the soft clay ground of 40 cm in thickness. The clay ground thus prepared had the strength profile that increased with depth by steps.

A linear variable differential transducer (LVDT) was placed at the ground surface and four pore water pressure gauges (PWP gauges) were installed at several depths in the clay ground. A water level gauge was also installed above the clay surface to monitor the decrease of water level due to percolation during the flight. And a loading jack was mounted on the specimen box for horizontal loading to the pile. The model ground thus prepared was brought up to 25 g acceleration field and the excess pore water pressure was allowed to dissipate. Settlement at the ground surface and PWP distributions were measured to monitor the progress of equilibrium of the ground during the flight. The flight time required to complete the equilibrium was reduced to about eight hours.

After the completion of the in-flight equilibrium, one of the two piles was laterally loaded at its top by means of the motor jack. The static cyclic horizontal load was applied by increasing the horizontal displacement at the constant speed of 1.15 mm/min. The relationship between lateral load and lateral displacement at the loading point was measured as well as the bending moment distribution along the pile.

After the loading was completed, the centrifuge was stopped to re-set the position of the motor jack for the other pile. The centrifuge was spun again to 25 g. After the dissipation of PWP developed during this process, the horizontal loading was carried out again for the other pile.

### 3 TEST RESULTS

#### 3.1 The shear strength profile

It was expected that the clay ground that prepared by the above-mentioned procedure had the strength profile that increased with the depth. In order to obtain the shear strength profile of the ground, vane shear tests were carried out under 1 g acceleration field after the loading test and the shear strength profile with depth were shown in Fig.3. The magnitudes agreed with each other and increased linearly with depth. A vane shear test was carried out under 25 g acceleration field to obtain the shear strength under high acceleration field and Fig.3 showed the profile. This profile also increased linearly with depth and agreed with the profile obtained under 1 g field. Therefore the clay ground used in the

loading test had the strength profile increased with depth.

#### 3.2 Load - displacement relations

A total of 6 tests was carried out changing the flexural rigidities of the pile as shown in Table 1. The horizontal load,  $T$  and the horizontal displacement,  $y_{top}$  were measured at the loading point using the cantilever-type load cell and the LVDT, respectively. The load - displacement relations of all cases were obtained and shown in Fig.4. In the figure, the horizontal displacement was normalized with respect to the pile width,  $B$ .

Since the piles were subjected to static cyclic loading, loops of load - displacement relation were obtained as shown in Fig.4. In the first loading stage, the horizontal load rapidly increased with the increase of horizontal displacement. When the horizontal load was gradually removed after reaching to the certain magnitude, some of the horizontal displacement recovered but some magnitude of residual displacement was observed. In the re-loading stage, the horizontal load increased almost linearly till the maximum load experienced in the first loading stage. After that, the horizontal load still increased at a decreasing rate with the increase of

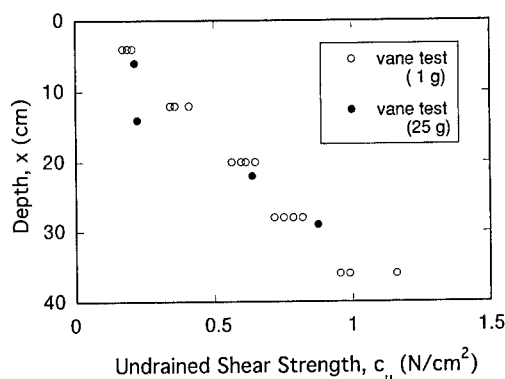


Fig.3 Shear strength distributions

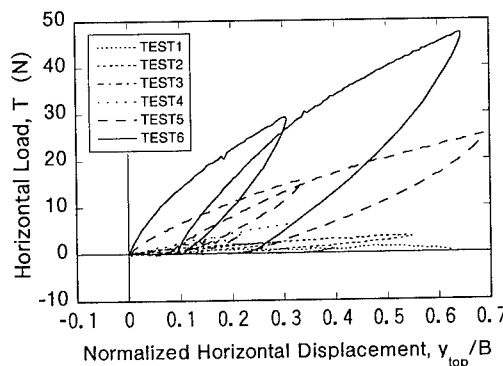


Fig.4  $T - y_{top}/B$  relations

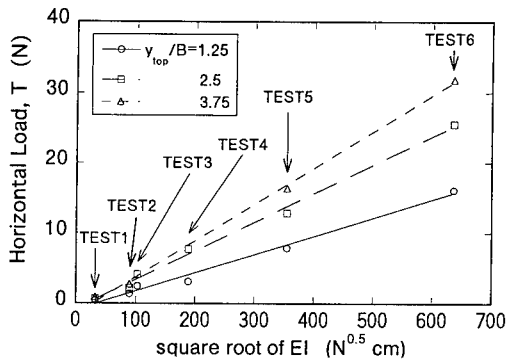


Fig.5 T - square root of EI relations

displacement, but neither peak load nor constant load was observed within the loading test. It was clear that the horizontal load was much affected by the flexural rigidity of the pile. To investigate the effect of pile rigidity on the horizontal load in detail, the horizontal loads at three horizontal displacements were obtained and shown by different symbols in Fig.5. In the figure, the vertical and the horizontal axes showed horizontal load,  $T$  and square root of the pile rigidity,  $EI$ , respectively. It was found that the horizontal load increased almost linearly with the increase of the square root of pile rigidity. This phenomenon was observed regardless of the horizontal displacement,  $y_{top}/B$ .

### 3.3 Bending moment distributions

Bending moment distributions along the pile were measured and some results measured in TEST5 ( $EI=125 \text{ kN}\cdot\text{cm}^2$ ) were shown in Fig.6. It was clear that the magnitude of the bending moment increased with the progress of loading. Relatively large bending moment took place in the region from the surface to the depth of  $x/B=11$ . The maximum bending moment was observed at about  $x/B=3.5$  and this position became slightly deeper with the progress of loading.

Similarly, Fig.7 showed the bending moment distributions obtained in TEST1 ( $EI=1.0 \text{ kN}\cdot\text{cm}^2$ ). The pile rigidity in TEST1 was much smaller than that of TEST5 as shown in Table 1, therefore the magnitude of the moment in TEST1 was about 1/20 of TEST5. And the maximum moment was observed at around the ground surface and the relatively large moment was developed within a small region around the surface.

Figure 8 showed the relation between the maximum bending moments and the pile rigidities. In the figure, the maximum moments at the various loading steps were plotted in all test cases. The moment increased with the horizontal displacement for all cases. It was found that the moment increased almost linearly with the increase of  $EI$ , while the horizontal load increased with the square root of  $EI$ .

The bending moment distributions during the cyclic loading in TEST5 were shown in Fig.9. In the figure, the load - displacement curve was also schematically

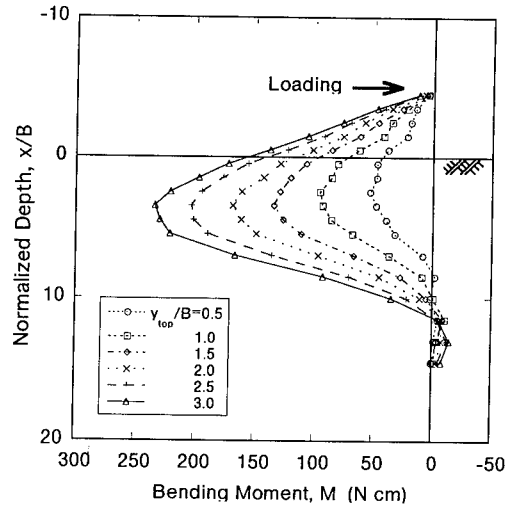


Fig.6 Bending moment distributions (TEST5)

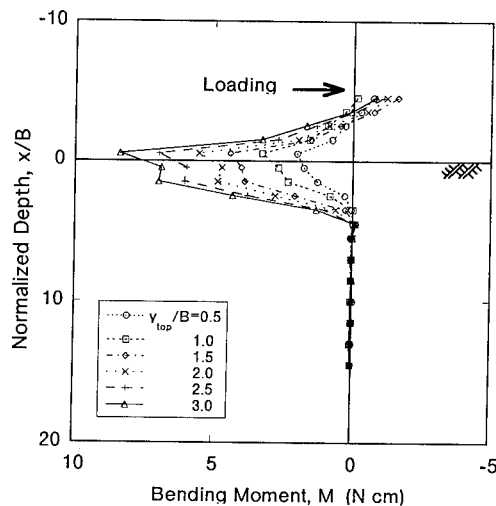


Fig.7 Bending moment distributions (TEST1)

shown together for ease of correspondence. In the figure, three curves indicated by B, D, F were obtained at almost same horizontal load, which was about half of the maximum load in the first stage at C. At D in the unloading stage, the moment was fairly larger than that at the first loading, B. And the moment at F in the re-loading stage was not larger than that at D, but still larger than that at B. These findings showed that the moment distribution was much influenced by the cyclic loading. However, it could be seen that the moment distribution obtained at G was perfectly coincided with that at C. This meant that the effect of the cyclic loading on the bending moment disappeared when the horizontal load in the re-loading stage became equal to or larger than the maximum load experienced before.

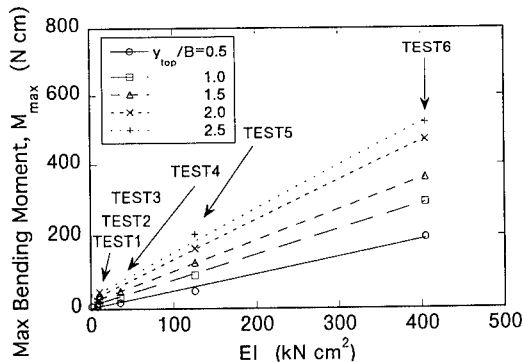


Fig.8 EI - max bending moment relations

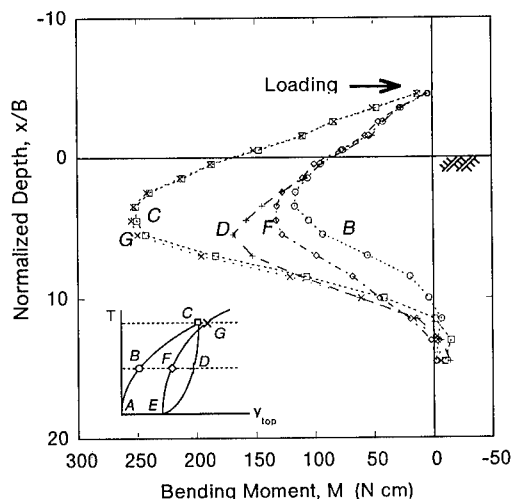


Fig.9 Bending moment distributions within loading cycle

### 3.4 p - y relations

To aid in evaluation of the pile response, a number of the quantities needed to be obtained from the test results. These included the lateral pile displacement and soil pressures on the pile as a function of the depth (the p - y curve). Since the only measurements made were of strains and displacements at discrete locations, some additional data reduction was needed. From simple beam theory, the moment in the pile, M was expressed as follows:

$$M = EI * d^2y / dx^2 \quad (1)$$

where EI, y and x were the flexural rigidity of the pile, horizontal pile displacements and the vertical coordinate along the pile, respectively.

Then the moment may be integrated twice for the displacement, y or differentiated twice for the subgrade

reaction, p. Since the moment at discrete locations were measured along the pile, a numerical scheme was necessary to obtain the pressures and the displacements. Neither p nor y was directly measured in the model test, so that p and y should be calculated from the moment distribution along the pile. As attempts to fit any function on the moment distribution, Finn et al. (1983) recommended cubic splines between successive strain data and Hamilton (1991) recommended 3rd-degree polynomials to fit the strain data. Based on the knowledge and procedure of accumulated studies on the pile deformation in sandy ground (Terashi et al. 1991), the 7th-degree polynomials were used in this study.

Figure 10 showed the calculated p - y relations of TEST5 in logarithmic scale. It could be seen that the logarithmic magnitude of p (described as log-p later) increased linearly with the increase of the logarithmic magnitude of y (described as log-y). The p-y relations at various depths were calculated and plotted in the figure. In the figure log-p increased almost linearly with the increase of log-y and the gradients were 0.2 - 0.5, which meant that the relation between p and y was non-linear. This phenomenon induced the non-linear relationship between the load and the displacement as shown in Fig.4.

As shown in Fig.6, the maximum bending moment was observed at the depth about x/B=3.5 and it was assumed that the behavior of the laterally loaded pile was much affected by the ground where the maximum bending moment was observed. Moreover, Japanese technical standards for construction of the port facilities has adopted for long that the gradient of the p - y relations of 0.5 regardless of the depth. This method was based on the relationship that was found in the early 1960's by the large scale model tests for sand ground and the validity of the method has been confirmed at a number of practices. The relationship (PHRI method) was expressed for the ground whose shear strength increases with depth as follows:

$$p = k_s * x * y^{0.5} \quad (2)$$

where  $k_s$  was defined as the coefficient of subgrade reaction. Therefore the gradient of the p - y relations was assumed to be 0.5 in this paper. Coefficient of subgrade reaction,  $k_s$  was defined from the distribution of the subgrade reaction at the intersection of the fitted p - y line and y-axis. The magnitudes of  $k_s(x/B)$  derived at various depths were shown in Fig.11. Similar procedure was performed for all test cases to evaluate p - y relations, and the magnitudes of  $k_s(x/B)$  were shown together in the figure. The calculated  $k_s(x/B)$  magnitudes well coincided each other and increased linearly with depth. From the distribution of the  $k_s(x/B)$  magnitudes, the  $k_s$  magnitudes were obtained as about  $2 \text{ N/cm}^{3.5}$ . The load - displacement relation was re-calculated using the  $k_s$  obtained above and shown in Fig.12 together with the experiment in TEST5. Although the calculated curve was a little smaller than the experiment in the initial, it could be found these two curves practically coincide each other. This procedure was performed in all test cases and similar coincidence was obtained in all cases. This showed that the PHRI method were also applied in the case of the model test.

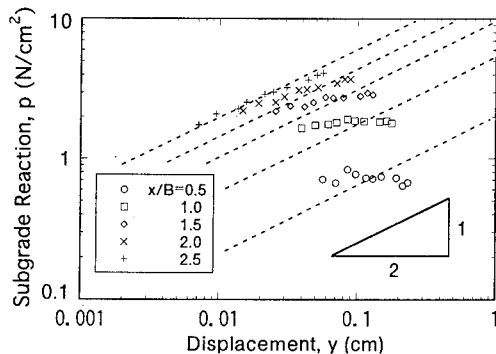


Fig.10 p - y relations (TEST5)

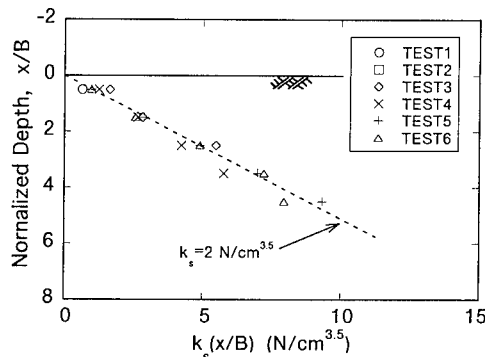


Fig.11  $k_s(x/B)$  distributions

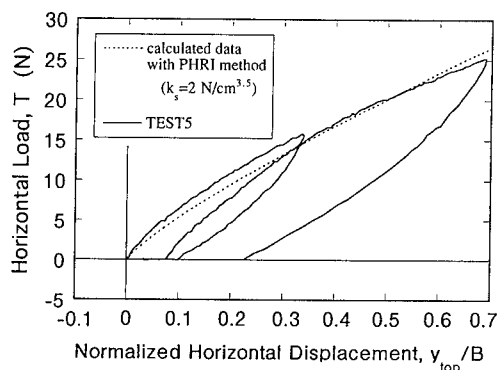


Fig.12 T -  $y_{top}$  relation re-calculated using the obtained  $k_s$

#### 4 CONCLUSIONS

Lateral loading tests of a long pile embedded in a normally consolidated clay ground were carried out in the centrifuge and the following conclusions were obtained.

1) The horizontal load increased almost linearly with the increase of the square root of pile rigidity, EI regardless of the lateral deformation and the bending moment increased almost linearly with the increase of EI.

2) The bending moment distribution was much affected by the cyclic loading, but its effect on the moment disappeared when the horizontal load in the re-loading stage became equal to or larger than the maximum load experienced before.

3) The displacement, y and the subgrade reaction, p were calculated at various depth from the bending moment distributions. The p - y relations showed that the magnitude of log-p increased linearly with the increase of log-y and the gradient of the p - y relations were 0.2 - 0.5.

4) Coefficient of subgrade reaction,  $k_s$  was obtained using the gradient of 0.5 which was based on the Japanese technical standards for construction of the port facilities. The  $k_s$  obtained in the various piles well coincided each other. The load - displacement relation calculated using the  $k_s$  also agree with the measured relation. These phenomena were observed regardless of EI.

#### REFERENCES

- Barton, Y.O. 1984. Response of pile groups to lateral loading in the centrifuge: *Proc. a symposium on the application of centrifuge modeling to geotechnical design*: 456-472.
- Finn, W.D.L., Y.O.Barton and I.Towhata 1983. Seismic response of offshore pile foundations: centrifuge data and analyses: *Proc. 7th Pan-American Conf. on S.M. and F.E.* Vancouver, B.C.
- Hamilton, J.M., T.W.Dunnavant, J.D.Murff and R.Phillips 1991. Centrifuge study of laterally loaded behavior in clay: *Proc. Conf. Centrifuge 91*: 285-292.
- Kitazume, M., T.Endoh and M.Terashi 1988. Bearing capacity of shallow foundations on normally consolidated ground: *Report of Port and Harbour Research Institute* Vol.27, No.3 (in Japanese): 185-203.
- Matlock, H. 1970. Correlation for design of laterally loaded piles in soft clay: *Proc. 2nd Offshore Tech. Conf.*, Houston, Texas: 577-594.
- Oldham, D.C.E., Allott and Lomax. 1984. Experiments with lateral loading of single pile in sand: *Proc. a symposium on the application of centrifuge modeling to geotechnical design*: 122-142.
- Scott, R.F. 1981. Pile Testing in a Centrifuge: *Proc. 10th Int'l Conf. on S.M. and F.E.*, Stockholm, Vol.2: 839-842.
- Terashi, M. 1985. Development of PHRI geotechnical centrifuge and its application: *Report of Port and Harbour Research Institute* Vol. 24, No.3: 73-122.
- Terashi, M., M.Kitazume, A.Maruyama and Y.Yamamoto. 1991. Lateral resistance of a long pile in or near the slope: *Proc. Conf. Centrifuge 91*: 285-292.
- Ting, J.M., C.R.Kauffman and M.Lovicsek. 1987. Centrifuge static and dynamic lateral pile behavior: *Canadian Geotech. J.* 24: 198-207.

## Reducing lateral thrust on piles: The 'buttonhole' method

Sarah Springman & Fraser Bransby  
Cambridge University, UK

Arndt Kremer  
Wuppertal Universität, Germany

**ABSTRACT:** Centrifuge modelling has been used to investigate the advisability of incorporating a low shear strength buffer around the regions of a pile which may be subject to significant lateral passive thrust.

### 1 INTRODUCTION

Embankments constructed near to piled foundations for bridge piers on soft soils cause lateral deformation of the soil, and lateral thrust on the piles. Pile bending moments and displacements, additional to those arising from structural loads, are induced. Designing such piles to German codes may be prohibitively costly since ultimate lateral pressures of  $10c_u$  are assumed to act on the upper regions of the piles, where  $c_u$  is the undrained shear strength of the soil. Techniques which minimise lateral thrust, such as 'buttonhole' piling, in which the pile length in the soft layer is surrounded by an annulus of material with low  $c_u$  (Fig. 1) can be advantageous.

This system was adopted previously at two European sites (Pulsfort et al, 1989), but further trials were required to evaluate the safety, durability and cost-effectiveness by investigating the fundamental soil-structure interactions. Clearly, the integrity of the buttonhole annulus will be important. Gap closure and hence compromise may occur due to excessive lateral soil deformation, eccentric post-construction pile positioning within the buttonhole, collapse due to a fall in bentonite level, loss of bentonite due to leakage at the pile cap boundary, or seepage into the surrounding soil.

Independent of the German approach, design methods for lateral thrusts on piles, proposed by Springman and Bolton (1990) for both ultimate and serviceability limit states, had been based on a series of centrifuge model tests, at 1/100th scale, under an acceleration of 100g, using a 10 m diameter beam. These studies were extended to investigate

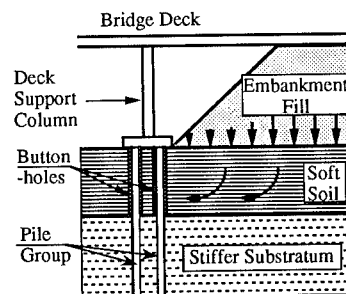


Figure 1 Embankment and buttonhole piles

buttonhole piles. Four additional tests (Table 1) were carried out, in which comparisons were made between two identical sets of geometries and idealisations, but with and without a 'buffer' of bentonite around the upper regions of the piles. New centrifuge modelling techniques were developed, in particular, the use of bentonite under enhanced gravity.

Given more bending moment transducers (BMTs) and a more appropriate modelling of the pile group, only the second pair of tests will be investigated herein. Data are plotted at prototype scale.

### 2 PROTOTYPE IDEALISATIONS

#### 2.1 Geometry and soils

The most critical lateral pile pressures will occur along the centreline of the approach road. Plane strain centrifuge model tests, on a plan area of 20 m x 67.5 m were designed to recreate this 'worst

Table 1. Centrifuge model tests

Date	Test	Buttonhole	Pile length/guide ring/BMT
6/92	EC1	No	160 mm / nil / 4 x 8
8/92	EC2	Yes	160 mm / alloy / 4 x 8
3/93	EC3	No	190 mm / nil / 4 x 12
4/93	EC4	Yes	190 mm / pasta / 4 x 12

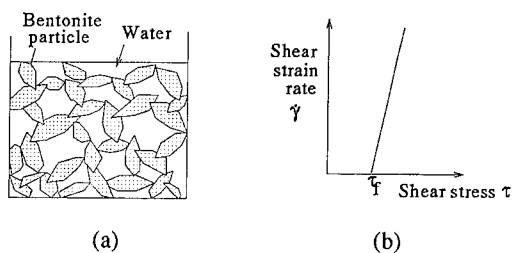


Figure 2 Bentonite

case' two dimensional soil displacement.

The 'embankment' was replaced by a uniform surcharge load applied by an air-pressurised rubber bag, located inside a restraining box. Therefore, no shear forces were applied by the 'embankment' at ground level. Embankment stiffness and any possibility of arching of a sand embankment load were eliminated from the variables.

Laboratory soils with well known properties (Springman, 1993a) were used in the centrifuge experiments. Kaolin represented the upper soft clay layer, and Leighton Buzzard sand 100/170 with a mean particle diameter of (approx) 120 microns was used for the stiffer sand substratum. The stress history of the founding stratum was pre-defined using appropriate loading cycles during a 1g one dimensional consolidation. Relationships between undrained shear strength, overconsolidation ratio and current vertical effective stress (Springman, 1993a) were adopted to calculate the appropriate consolidation stages to create a clay layer with  $c_u$  increasing linearly with depth, so that 25 kPa (top surface) <  $c_u$  < 50 kPa (clay-sand interface).

Site investigation was carried out in the clay to compare predicted and measured  $c_u$ , using a vane shear device whose dimensions had been adapted for the scaling laws applicable under the high gravity conditions in the centrifuge model.

## 2.2 Bentonite

Effective modelling of the low  $c_u$  material in the centrifuge was central to the success of the experiments. In the field, a proportion of cement had been added to the thixotropic high-moisture-content bentonite mixture (Pulsfort et al, 1989), so that long term sedimentation of the bentonite particles was prevented, and a *stable* buffer was created by increasing  $c_u$  slightly through random cementation at particle contacts.

However, the time:strength behaviour of the cement-bentonite slurry may not be replicated correctly in the centrifuge due to experimental lead-time and the disparity between the time scales under high gravity (e.g. 100g) test conditions. The gain of strength of the cement-bentonite material occurs (almost logarithmically following mixing) in real time, whereas model time is accelerated by 100, for sedimentation and filtration (approximately) which implies a constant settling velocity, and by  $100^2$ , for diffusion processes such as consolidation.

A 170 g/l bentonite-water mix was used to give  $c_u = 0.5$  kPa at the time of the centrifuge model test, at a moisture content of between 500 - 1000%. The particles are connected in a 'card house' structure (Fig. 2a). Bentonite behaves like a Bingham fluid in its undisturbed state, with a peak  $c_u$  dependent on strain rate (Fig. 2b). The strength and performance of this material under both 1g and high gravity levels was investigated by Bransby (1992).

The role of the bentonite was to provide a constant volume, low shear strength material, which did not settle by sedimentation or filter into the soil. However, the suctions maintained in the clay following unloading from the 1g pre-consolidation pressures were still in evidence during model making. To prevent water being sucked out of the bentonite, which would then crack, clingfilm was placed on the soil-bentonite interface.

## 2.3 Pile group

A group of 2 rows of 3 piles was made using Dural tubing, to model the bending rigidity of a concrete pile of the same prototype diameter, 1.27 m. The piles were fully fixed into a stiff pile cap (Fig. 3). 8 pairs of full strain gauge bridges (BMT) were fixed on the inside of the tubing with 4 additional pairs glued to the outside of the piles to improve back

analysis of the bending moment data in the upper soft layer. Axial load cells (ALC) measured the degree of uplift on the base of the pile cap during surcharge loading.

The pile lengths were calculated to lead to a flexible response, without any tip displacement and rotation. Analysis would be simpler if these boundary conditions were known.

Guide rings prevented loss of bentonite from the buttonhole (Fig. 3), following settlement of the clay between model making at 1g and reaching equilibrium at 100g. However, these rings were deeper than for a typical prototype, and significant lateral loading was attracted. This overemphasised the shear force acting at pile cap level, and so pasta rings were adopted in the final test. Initially, the pasta was strong (& brittle), restricting any migration of bentonite before it softened in the presence of the groundwater.

### 3 CENTRIFUGE MODEL TEST

#### 3.1 Preparation

Centrifuge model preparation followed usual practice (Springman et al, 1991) for a saturated sand layer (relative density = 70%) of 140 mm depth, with a de-aired kaolin slurry at 120% moisture content placed on the sand (Fig. 4). The clay was consolidated in stages to an overburden pressure of 450 kPa. Pore pressure transducers (PPTs) were inserted into the clay, excess clay was trimmed to a depth of 60 mm and the liner was placed in the strongbox. The pile group was jacked into position.

Displacement transducers were installed for detecting pile group and clay surface movements, lead threads were inserted in the clay parallel to the rows of piles to reveal the mode of internal soil deformation around the piles using radiographic techniques, and black marker pellets were positioned on the front of the clay layer for post-test study of the deformation from in-flight photographs.

The surcharge loading air bag was installed together with the site investigation device, and the instrumentation was connected to the junction boxes for transfer of signals to the control room data acquisition system. The strongbox was mounted on the swing which was then loaded onto the beam.

For the buttonhole tests, the installation of the pile group was a complicated process which demanded

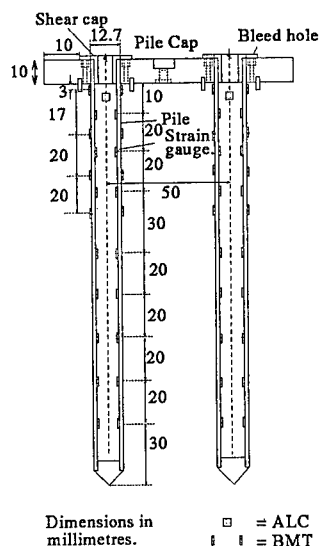


Figure 3 Pile group

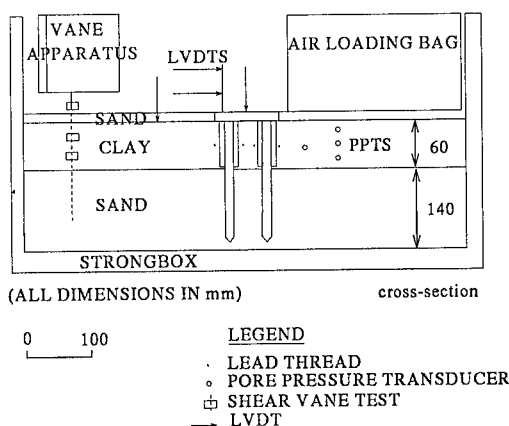


Figure 4 General arrangement

the ability to centre the piles within the 20 mm diameter pre-augered bentonite buttonhole, and to displace bentonite without allowing it to overflow the 3.5 mm thick annulus and leak under the pile cap. The 20 mm internal diameter guide rings were located under the pile cap as a further guarantee of no bentonite loss. Top-up holes had been drilled in the pile cap (Fig. 3) to allow introduction of more bentonite into the buttonhole, and to ensure that there was no air present above the bentonite.

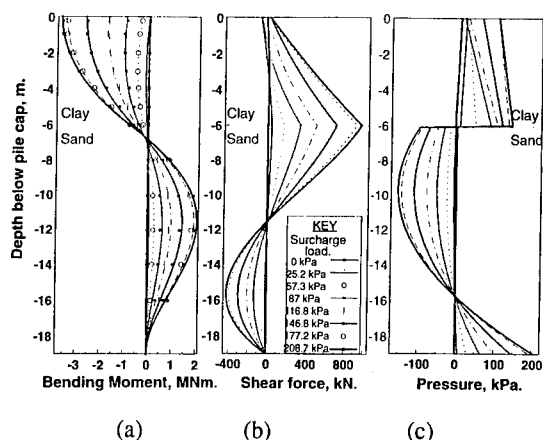


Figure 5 EC3: Front centre pile

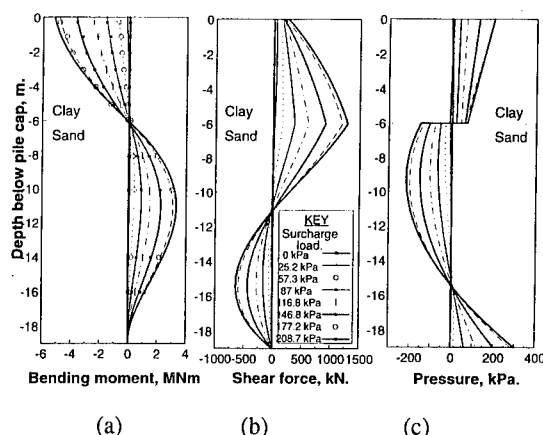


Figure 6 EC3: Rear side pile

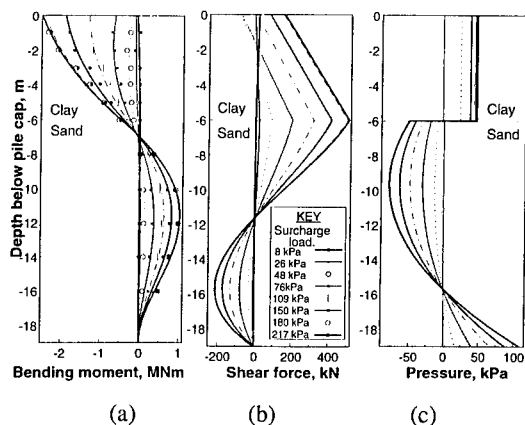


Figure 7 EC3: Front centre pile

### 3.2 Testing regime

Equalisation of the excess pore pressures due to increase from 1g to 100g took about two hours, until the effective stresses in the clay represented that of a 6 m deep layer at prototype scale.

In order to simplify the post-test analysis, the soil was loaded as fast as possible to reproduce undrained behaviour. In the two tests considered here, the load was increased at a steady rate over a period of 2 minutes (14 days prototype scale) to 205 kPa (EC3) and 223 kPa (EC4).

2 hours (2.28 yrs at prototype scale) were allowed for consolidation under the maximum surcharge load. Instrumentation signals were monitored for evaluation of the drained behaviour, and vane shear tests were carried out at two horizons in the clay before the centrifuge was stopped.

The model was X-rayed pre- and post-test to establish the internal deformation pattern around the piles and to reveal the locations of the PPTs. These were checked by careful excavation in the clay layer, and, where relevant, the local positioning of the piles relative to the buttonholes was observed.

### 3.3 Results

Pore pressures, displacements and bending moments are recorded by Bransby (1993) for EC3 and EC4.

Bending moments increased with surcharge load, and, in the buttonhole test (EC4) were 30 - 75% of those in EC3. The maximum moment was at pile cap level (shown negative). The side rear pile moments were the highest (by 10%) relative to the central rear pile, so Figs. 5a, 6a, 7a and 8a show comparative data for the front central pile and the rear side pile for both tests.

Data from up to 12 bending moment transducers (BMTs) on each of these 4 instrumented piles were fitted by a polynomial (2nd or 3rd order in the soft layer and 4th or 5th order from the stiff layer). The first derivative gave an interpretation of the shear force in the pile. The second derivative, an even less accurate estimate, produced a profile of lateral pressure. Double integration, combined with known boundary conditions of pile-head movement, gave the pile displacement profile (Fig. 9).

The shear force diagrams (Figs. 5b, 6b, 7b, 8b) indicated that there was a nett shear force at the pile top, due to adhesion mobilised under the pile cap. The lateral pressures on the pasta guide rings were less than those observed in test EC2 when alloy rings were used, but these were still significant



since the shear forces were greater in EC4 than in EC3.

The predicted lateral pressures on the pile in the clay layer were linear because a 3rd order polynomial had been used to fit moment data in this upper stratum (Figs. 5c, 6c). Average pressures on piles in test EC3 were 140 kPa at full surcharge load, which reduced to constant values between 40-50 kPa (Figs. 7c, 8c) with a buttonhole for a 2nd order bending moment curve.

Lateral pressure on a buttonhole pile was almost non-existent up to a surcharge load  $q = 100$  kPa (Figs. 7c, 8c), approaching a factor  $q / c_u = 3$  as found by Stewart (1991) for serviceability. As expected, the front pile annuli closed up first.

Tolerable movement criteria (USDOT, 1985) of 25 mm lateral displacement, for this pile spacing, cap geometry and shear force at pile cap level, occurred at about  $q = 100$  kPa in EC3, and 180 kPa in EC4 (Figs. 9a, 9b), although the loading was virtually undrained and would over-emphasise the lateral movements. As a counterpoint, rotation of the pile cap was noted, and this would contribute to further significant lateral displacements at deck level.

### 3.4 Internal deformations

Careful post-test excavation of the model EC4 showed that none of the buttonholes were completely closed up, although the gap had reduced from 3.5 mm to less than 1 mm for the front piles. There was some loss in volume of the bentonite. The internal deformation of the soil relative to the pile shown by radiographic exposure of the lead threads (Figs. 10a, 10b), confirmed that the piles reinforced the clay in EC3 by attracting load.

Local deformation occurred around the pile/buttonholes in EC4 suggesting that the buttonhole behaved initially as an almost constant volume inclusion within the clay layer, from which there was neither weakening of the founding stratum, nor contribution to the bearing capacity from the work done in soil shearing past the pile, until the soil deformation had almost caused the gap to close.

### 3.5 Axial behaviour

The ALCs at the top of the pile showed that the cap restrained the vertical soil movement for surcharge loads above 50 kPa in test EC1 (ALCs did not all work subsequently). This behaviour was more

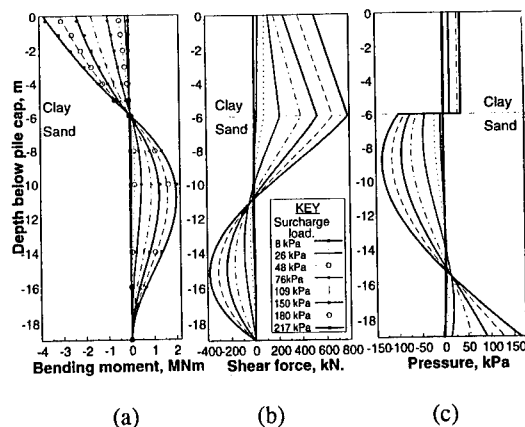


Figure 8 EC4: Rear side pile

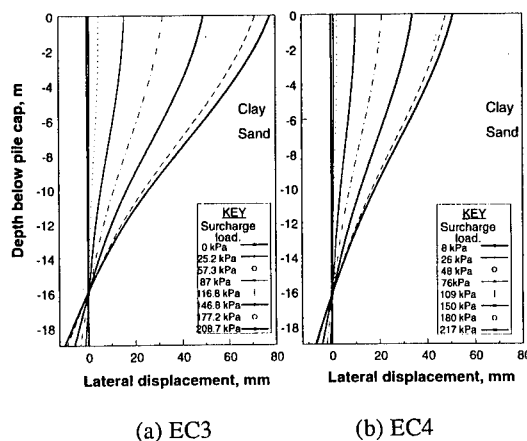


Figure 9 Pile displacement

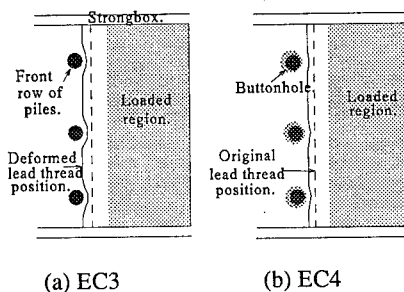


Figure 10 Internal deformations

apparent for the front row of piles. An average uplift pressure of about 70 kPa on the entire pile cap was implied for  $q = 200$  kPa.

The pile group appeared to rotate about 3 m above the pile tips, with similar rotation at pile cap level and this was thought to be caused by the uplift pressure acting under the pile cap. For test EC3, the rigid body rotation of the pier for  $q = 210$  kPa would cause a displacement of about 50 mm away from the surcharge for a cantilever of 10 m in length. In addition to 80 mm (prototype) lateral movement at the pile cap, this would be equivalent to a total of 130 mm at prototype scale at the top of the bridge pier. Clearly the fixity conditions at the bridge deck level, and the construction procedure will need to be considered carefully. For EC4, the equivalent deck movement would be 75 mm.

### 3.6 Long term effects

The pile bending moments reduced by 20 - 40% up to 15 months (prototype) after the application of the surcharge. Clearly, the effects of superstructure load would influence the behaviour of a structure in the field, however, this indicates a trend towards a relaxation of the shear force and lateral thrust on the piles due to consolidation under the surcharge. Axial load cell data also showed that the uplift forces on the pile cap were reduced with time to between 25 - 50% of the peak value observed as the maximum surcharge load was just applied. Displacement did not vary significantly, because the pile had undergone irrecoverable rigid body rotation.

## 4 CONCLUSIONS

Centrifuge model tests have identified mechanisms for deformation at serviceability limit state, and approaching failure towards the ultimate limit state.

A buttonhole pile foundation is appropriate for bridge piers constructed adjacent to a surcharge load, when there is minimal horizontal shear force applied at pile cap level. Adhesion under the pile cap and lateral pressures on the guide rings should be minimised. Lateral thrust, and hence bending moments, lateral displacements and rotations were noticeably smaller when buttonholes were used.

Lateral displacements were manifest immediately following application of the surcharge load. Subsequent movements were very small. Peak bending moments also occurred instantaneously

upon loading, followed by a small reduction towards residual values with time. Uplift on the pile cap affected the rotation of the pile group, and this has important implications for the performance of buttonhole pile foundations in the field.

## 5 ACKNOWLEDGEMENTS

These activities would have been impossible without the assistance of Dr R. Phillips and Messrs N. Baker, S. Chandler, C.H. Collison, P. Ford, J. Chandler, A. Brand, T. Ablett. Advice and comments were gratefully received from Prof. B. Walz, Dr K. Hock-Berghaus, Dr J. Steinhoff (Wuppertal) and Dr M.D. Bolton (Cambridge).

## 6 REFERENCES

- Bransby, M.F. 1992. Piled foundations adjacent to surcharge loads. 1st yr report. Cambridge U.
- Bransby, M.F. 1993. Centrifuge test: Investigation of the buttonhole foundation technique. CUData Report: Tests EC3 & EC4.
- Pulsfort, M., Walz, B., Steinhoff, J. 1989. Slightly stabilised bentonite suspension sheltering piles against lateral passive earth pressure in soft cohesive soils. 2nd Int. Conf. Fndtns & Tunnels.
- Springman, S.M., Bolton, M.D. 1990. The effect of surcharge loading adjacent to piles. TRLCR196.
- Springman, S.M., Randolph, M.F., Bolton, M.D. 1991. Modeling the behavior of piles subjected to surcharge loading. In H. Ko & F. McLean (eds.), Centrifuge '91, p. 253-260, Rotterdam, Balkema.
- Springman, S.M. 1993. Centrifuge modelling in clay: Marine applications. 4th Canadian MGC.
- Stewart, D.P. 1991. The response of piled bridge abutments on soft clay to embankment loading. UWA Research Report: GEO 91100.
- US Department of Transportation. 1985. Tolerable movement criteria for highway bridges. Final Report FHWA/RD-85/107, FHA, USA.

## Single piles and pile rows subjected to static and dynamic lateral load

M. Kotthaus, T. Grundhoff & H. L. Jessberger

*Institute for Soil Mechanics and Foundation Engineering, Ruhr-University Bochum, Germany*

**ABSTRACT:** Single piles and pile rows consisting of three piles are subjected to lateral static and cyclic load with different frequencies and load intensities. Tests on pile rows were restricted to static loads in the direction of their centre line. The pile displacements at the ground line, the load of each pile, the bending moment distribution along the pile and for the dynamic tests the accelerations at different levels were recorded. Using this data the pile-soil interaction is investigated. The development of the bending moment distribution, the subgrade reaction and the pile head displacement are presented for different load frequencies as a function of load intensity and the number of cycles. For the pile rows the pile-soil-pile interaction is determined by means of the measured load distribution within the rows. Finally the experimental results are compared to results of different calculation methods.

### 1 INTRODUCTION

In civil engineering many kinetic phenomena exist, leading to additional cyclic or dynamic loads of building and foundation; for example earthquakes, wind effects on tall buildings, breaking of waves at offshore constructions, effects of traffic on bridges etc.. In these cases, pile group constructions often are used for the foundation. The design of these foundations is a problem, because the soil-structure interaction cannot be described satisfactorily. The existing calculation methods for the static load condition are based on the elastic theory (Poulos 1971, Randolph 1981), p-y or subgrade reaction analyses. Recently experimental results of different types of tests like element-, 1g-model and centrifuge model tests and in-situ tests (Barton 1984, Schmidt 1984, Brown et al. 1987, Brown et al. 1988) have been introduced.

To get more information about the frequency influence on the pile-soil interaction of laterally loaded single piles and pile groups, model tests are carried out in the Bochum Geotechnical Centrifuge ZI. Herein the special points of interest are the frequency dependence of subgrade reaction, changes in the system stiffness and the development of the pile displacement. Static load tests on single piles and

pile rows consisting of three piles were run to get reference values (Kotthaus 1992). Cyclic load tests, restricted to single piles, followed.

### 2 TEST EQUIPMENT

#### 2.1 The model set-up

The used model piles are made of aluminium tubes with an external diameter of  $D = 3.00$  [cm] and an internal diameter of  $d = 2.60$  [cm]. Each of them has an embedded length of  $L = 60$  [cm]. The load input takes place at  $e = 8.50$  [cm] above the ground surface on a special pile head which is fixed without any slack to the tubes. For measuring the applied load, each pile has a pair of strain gauges at the level of the ground surface. The bending moment distribution is observed by two piles, equipped with nine additional strain gauges along the embedded pile length. The choice of this type of model pile is due to the consideration to model long flexible concrete piles. That is to say, at an acceleration of 50g, which is used in the reported tests, concrete piles with an approximate diameter of  $D = 1.50$  [m] and an embedded length of  $L = 30$  [m] are modelled. The comparison of model and prototype parameters is shown in table 1.

Table 1. Characteristic values of model and prototype piles.

Parameter	Model at 50g	Prototype	
		Aluminium annular section	Concrete solid section
External diameter D [m]	0.030	1.50	~1.50
Internal diameter d [m]	0.026	1.30	-
Length L [m]	0.600	30.00	30.00
Young's modulus E [MN/m <sup>2</sup> ]	70000	70000	30000
Resisting moment I [m <sup>4</sup> ]	1.7329 E-8	0.108306	0.252714
Bending resistance EI [kNm <sup>2</sup> ]	1.21303	7581420	7581420

All tests are run in a rectangular rigid container (length/width/height = 0.85/0.42/0.80 [m]). As model soil a fine grained sand with high density of  $D = (\rho - \rho_{\min}) / (\rho_{\max} - \rho_{\min}) = 98 [\%]$  is used (Table 2), placed in the container by pluvial deposition around the already installed piles.

Table 2. Properties of the Bochum Standard Sand.

Parameter	Value
Density of solid particles $\rho_s$ [g/cm <sup>3</sup> ]	2.66
Compactness $\rho_{\min/\max}$ [g/cm <sup>3</sup> ]	1.41 / 1.70
Porosity $n_{\min/\max}$	0.36 / 0.47
50 percent-diameter $d_{50}$ [mm]	0.23
10 percent-diameter $d_{10}$ [mm]	0.12
Uniformity coefficient $C_U = d_{60}/d_{10}$	2.08
Angle of internal friction $\varphi$ [°]	38

A pneumatic loading device which was connected to the loaded structure by a steel cable, was used for the static tests. A load transducer, giving the actual load value to the pneumatic control system, is screwed onto the piston rod. While pile row testing, the pile heads were connected by a rigid bar which was bolted without any slack to the pile heads. Pile row spacings of  $s/D=3$  and  $s/D=4$  were chosen. The piles were stepwise loaded. When a constant value for the displacement was reached the load was increased. Figure 1 shows the typical model set-up of a pile row test.

The dynamic load tests in the centrifuge required special equipment for the loading system. A hydraulic actuator, placed on the containers rim, was used for loading. The pile is coupled with the actuator by a rigid bar, which is hinged connected to the pile head and the piston rod. Similar to the pneumatic system a force transducer within the bar is used for giving the

actual load value to the hydraulic control system. The model set-up of the cyclic single pile tests is shown in Fig. 2.

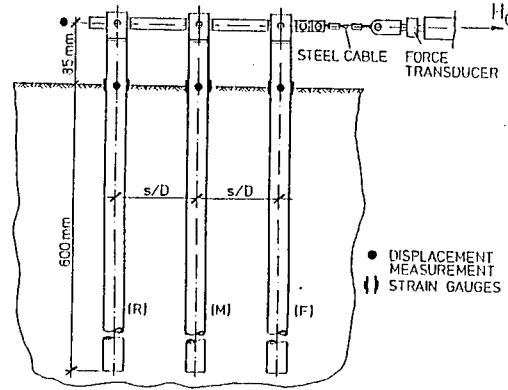


Fig. 1. Schematic model set-up for the static load tests on pile rows.

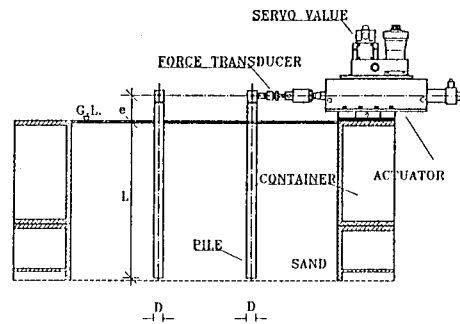


Fig. 2. Cross section of model container for dynamic single pile tests.

The piles were load-controlled tested with a symmetrical, two-way sinusoidal load function. In model scale the load frequencies were chosen to  $f_M=10$  [Hz] and  $f_M=50$  [Hz]. One test corresponds to 1000 load cycles. But only for specified cycles (1, 2, 10, 40, 100, 400, and 1000) the pile displacement at the ground surface and at the pile head as well as the pile load are measured. For a few tests the bending moment distribution is also recorded.

## 2.2 The data acquisition system

For data acquisition a special data acquisition board with an independent processor, maximum 16 single ended, analogue input channels and 2 channels for analogue output, is used. The board is placed in the

slot of a PC. For the operation of 16 channels a maximum scan rate of 14.7 [kHz] is reached. The adjustment of the data acquisition system to the load function, generated by a separate function generator, is done with help of a special software package.

For dynamic testing the first channel of each data acquisition board is used as a trigger channel. When the channel is triggered, the acquisition procedure is starting. In this way the data acquisition can be controlled by sending defined trigger events to the boards. For generating and controlling this trigger a special program is used on a second PC. At defined times an electrical signal is sent to the first channel of the data acquisition board and to the function generator. The first trigger starts the function generator and the data acquisition system. All further trigger signals are used for activating the data acquisition system.

### 3 STATIC LOAD TESTS

#### 3.1 Test results

The interaction of  $n$  laterally loaded piles leads to a reduction in load capacity of the pile group compared to an equivalent number of single piles. To express this reduction the pile group efficiency  $G_w = H_G / (n \cdot H_s)$  is used which is defined by the ratio of the group load  $H_G$  to the single pile load  $H_s$  of  $n$  piles at the same displacement. Herein  $n$  is the number of the piles in the group.

For the design of laterally loaded pile groups the interaction problem is taken into account by means of interaction factors. Different methods with different types of interaction factors are used. On one side there are elastic interaction factors  $\alpha = u_M / u_s$ , they are calculated after methods based on the theory of elasticity (Poulos 1971, Randolph 1981), and on the other side there are experimentally determined interaction factors  $\alpha^* = H_i / H_s$  like the one in the German Standard DIN 4014 (1990) for the design of bored piles (Franke 1988). Herein are  $u_s$  the displacement of a single pile,  $u_M$  the displacement of a unloaded pile due to a loaded single pile,  $H_s$  the load of a single pile under condition of  $u_s = u_i$  and  $H_i$  the load of a group pile under condition of  $u_s = u_i$ .

The definition of the interaction factors differs, so that their use leads to contradictions, above all in regard to the load distribution within the pile groups.

At each of these methods a constant group effect versus the displacement is assumed.

Fig. 3 shows the trend of the pile group efficiency  $G_w$  for the here examined pile rows. It can be seen that the group efficiency depends up to a limiting value of  $(u/D)_{lim} = 0.1$  on the displacement of the system.

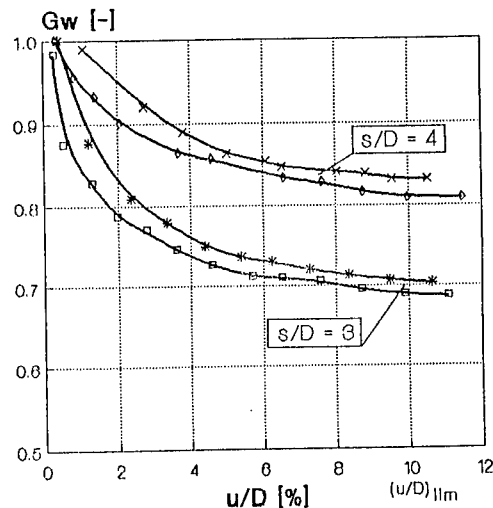


Fig. 3. Pile group efficiency  $G_w$  versus normalised displacement  $u/D$ .

In Fig. 4 the value  $(H_i / H_s)$  of a pile row with a spacing of  $s/D=4$  is plotted against the displacement. This value is identical to the interaction factor  $\alpha^*$  after DIN 4014. It becomes evident that these interaction factors also depend on the displacement up to the limiting value. It is shown that for small displacements the middle pile has a smaller  $\alpha^*$ -value than the rear pile. But the values of both piles decrease and assimilate with increasing displacement. At  $(u/D)_{lim}$  they have the same value.

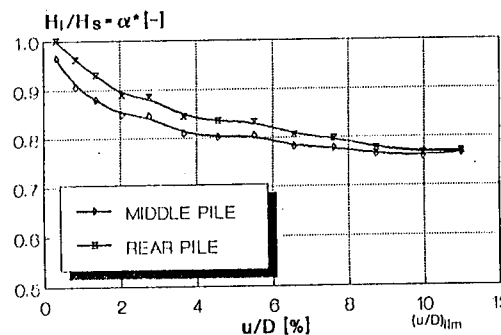


Fig. 4. Development of the interaction factor  $\alpha^*$  ( $s/D=4$ ).

For the experimental determination of the elastic interaction factor  $\alpha$  the pile row has no rigid connection bar. The middle pile of the row was stepwise loaded and the displacement  $u_s$  of the loaded pile as well as the displacement  $u_M$  of the unloaded piles were recorded. The development of the interaction factor  $\alpha$  is plotted in Fig. 5. There it is shown that with increasing displacement the influence to the rear pile decreases down to a small constant value while the influence to the front pile is continuously increasing. It is noteworthy that for very small displacements the front and the rear pile show the same interaction factor. It is also obvious that with increasing pile spacing the influence on the front pile decreases.

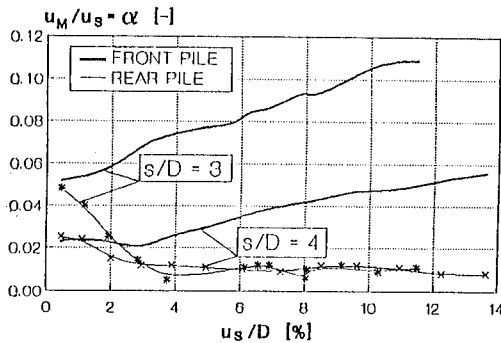


Fig. 5. Development of the interaction factor  $\alpha$  in dependence on the normalised displacement  $u_s/D$  and the pile spacing  $s/D$ .

The displacement depending group effect of the pile rows, shown in Fig. 3, may be explained by analysing the recorded pile forces within the groups. Regarding Fig. 6 three different, characterising ranges of pile row behaviour can be noticed:

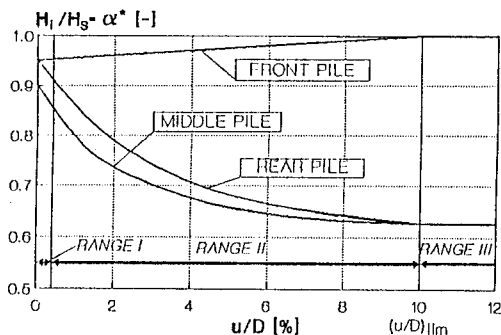


Fig. 6. Qualitative trend of pile forces within a pile row, loaded in the direction of its centre line.

#### - Range I ( $u/D < 0.5$ [%])

According to Novak et al. (1989) this range is characterised by a quasi-elastic soil behaviour. Within the pile row a symmetrical load distribution takes place, where each pile gets less load than an equivalent single pile. In agreement with the elastic theory the front and the rear pile get more load than the one in the middle.

#### - Range II ( $0.5$ [%] $< u/D < (u/D)_{lim}$ )

This is the transition range from quasi-elastic to plastic soil behaviour. The normalised loads of the middle and the rear piles decrease with increasing displacement while the one of the front pile increases up to the value one. Simultaneously the load distribution adjusts according to the load direction.

The soil is unable to transmit tension, but it is able to receive tension as long as the overburden pressure can be reduced. That's the reason for the rapidly decreasing influence of a group pile on to a pile immediately behind it. With increasing displacement a passive zone is activated in front of each pile. The smaller load capacity of the rear piles, in comparison with an equivalent single pile, results from a shielding effect that makes it impossible to activate the full passive zone in front of the rear piles. The extension of this passive zone depends on the level of the regarded soil layer. Since the upper soil layers have a significant influence on the pile behaviour the still existing quasi-elastic conditions in deeper layers lose more and more their influence versus the displacement.

#### - Range III ( $u/D > (u/D)_{lim}$ )

This range is characterised by the plastic soil behaviour. The front pile shows nearly the same behaviour as an isolated single pile. Against this the rear piles get an identical reduced and constant load. This group effect is in agreement to DIN 4014.

### 3.2 Calculation methods compared to the experimental results

Fig. 7 shows the comparison of the experimental pile group efficiency  $G_w$  in comparison to the ones calculated after Randolph and DIN 4014. In the range of  $(u/D)_{lim}$  there is a good agreement between calculated and experimental values. On the other side both calculation methods underestimate the real group efficiency in the range of small displacements. Considering the context above it can be seen that the elastic methods and the method after DIN 4014 view different displacement conditions of a pile group (Kotthaus 1992).

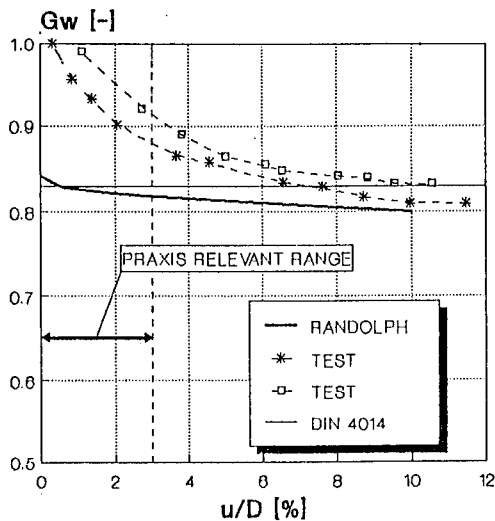


Fig. 7. Experimental and calculated group efficiency ( $s/D=4$ ).

#### 4 DYNAMIC LOAD TESTS

Typical measured load-displacement curves of the pile head are shown in Fig. 8 for a load frequency in model scale of  $f_M=10$  [Hz]. This corresponds to a prototype load frequency of  $f_P=0.20$  [Hz]. It can be seen that on principle the loads increased with the number of cycles while the maximum displacements decreased. Beyond that it is obvious that the gradient of the hysteresis increased degressively with the number of cycles. This is because of the increasing soil stiffness in the course of a test.

The above mentioned change of the soil stiffness can be shown by the development of the bending moment distribution (Fig. 9). With an increasing number of cycles the maximum bending moment is decreasing. The position of the maximum is moving upwards, which indicates the increase of the soil stiffness.

The frequency influence is illustrated by comparing the bending moment distribution of different load frequencies due to identical loads of  $H=0.166$  [kN] (Fig. 10). It is visible that for the static load and the load frequency  $f_P=0.20$  [Hz] nearly the same bending moment distribution is found. That is to say the relative low load frequency causes no change in the pile-soil interaction. For the load frequency of  $f_P=1.00$  [Hz] the bending moment is smaller than the other ones. This may be caused by the inertia forces, which lead to a stiffer system.

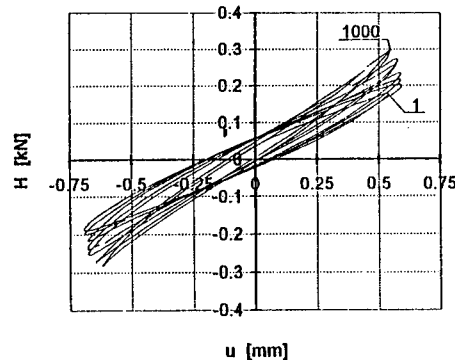


Fig. 8. Load versus pile head displacement in model scale ( $f_M=10$  [Hz]).

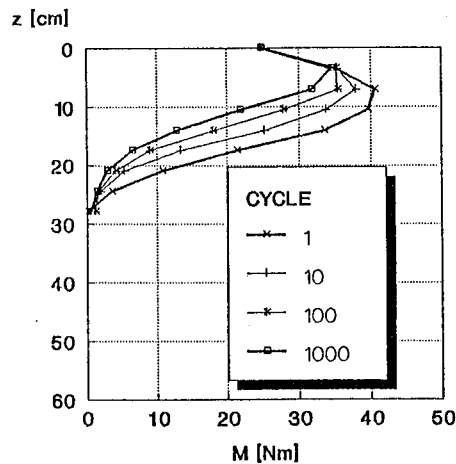


Fig. 9. Bending moment distribution in model scale for a lateral load of  $H=0.290$  [kN] ( $f_M=10$  [Hz]).

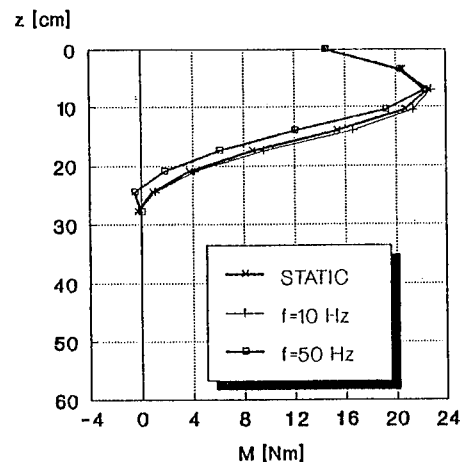


Fig. 10. Bending moment distribution for different load frequencies.

## 5 CONCLUSIONS AND FURTHER WORK

With the static load tests on pile rows of flexible piles in sand it is shown that the group action up to a limiting displacement is a function of the displacement. The principle behaviour of pile rows under static load was analysed and discussed. By comparing known calculation methods with the experimental results the underestimation of these methods could be shown. Further on some principle aspects of the pile-soil interaction during cyclic loading could be shown.

For further work it is aimed to extend the dynamic tests on different and higher load frequencies. In addition to that it is proposed to analyse dynamic loaded pile rows.

## ACKNOWLEDGEMENTS

The investigations reported in this paper are part of the research project SFB 151 "Structural Dynamics" sponsored by the German Research Foundation (DFG) at the Faculty of Civil Engineering at the Ruhr-University Bochum.

## REFERENCES

- Barton, Y. O., Parry, R. H. G. & Finn, W. D. L. (1984). Lateral pile response from model tests in a large centrifuge. Proc. Int. Conf. on Case Histories in Geotechnical Engineering, St. Louis (US), Vol. 3, pp. 1011-1019.
- Brown, D. A., Reese, L. C. & O'Neill, M. W. (1987). Cyclic lateral loading of a large-scale pile group. Journal of Geotechnical Engineering, Vol. 113/2, pp. 1326-1343.
- Brown, D. A. Morrison, C. & Reese, L. C. (1988). Lateral load behaviour of pile groups in sand. Journal of Geotechnical Engineering, Vol. 114/2, pp. 1261-1276.
- DIN 4014 (1990). Borpfähle, Herstellung, Bemessung und Tragverhalten. Beuth Verlag Berlin.
- Franke, E. (1988). Group action between vertical piles under horizontal loads. Proc. 1st International Geotechnical Seminar on Deep Foundations on Bored and Auger Piles. Ghent, Belgium, pp. 83-93.
- Kotthaus, M. (1992). Zum Tragverhalten von horizontal belasteten Pfahlreihen aus langen Pfählen in Sand. Dissertation. Schriftenreihe des Instituts für Grundbau, Ruhr-Universität Bochum, Heft 18.
- Novak, M & Janes, M. (1989). Dynamic and static response of pile groups. Proc. XII ICSMFE Rio de Janeiro, Vol. 2, pp. 1175-1178.
- Poulos, H. G. (1971). Behaviour of laterally loaded piles: II-pile groups. ASCE, Vol. 97, pp. 733-751.
- Randolph, M. F. (1981). The response of flexible piles to lateral loading. Géotechnique 31, No. 2, pp. 247-259.
- Schmidt, H. G. (1984). Großversuche zur Ermittlung des Tragverhaltens von Pfahlreihen unter horizontaler Belastung. Dissertation. Fachbereich konstruktiver Ingenieurbau, TH Darmstadt.



## Effect of slope and soil density on $p$ - $y$ reaction curves for piles in sand

S. Mezazigh, J. Garnier & C. Favraud  
LCPC, Nantes, France

D. Levacher  
LGM, Université Nantes, France

**ABSTRACT:** An extensive program of centrifuge tests was undertaken to study effect of slopes on  $p$ - $y$  curves in sand. The paper at first presents the method developed in a previous series of centrifuge tests to experimentally determine  $p$ - $y$  curves. Bending moment curves are fitted by local quintic spline functions through a crossed validation method and then twice differentiated. These experimental  $p$ - $y$  curves are validated by back analysis. The program of tests on piles near slopes is presented. It includes studies of the effect of distance to the slope, slope angle, soil properties. Sample preparation method, model piles and loading device are described. Deflection-vs- load curves, bending moment curves and derived  $p$ - $y$  curves for piles close to slopes are compared to horizontal ground response.

### 1. Introduction

Subgrade reaction methods have prevailed in the design of laterally loaded piles because they can predict not only the forces in the piles but also their displacements. On the other hand, they require a prior determination of the  $p$ - $y$  reaction curves that relate the horizontal displacement of the pile ( $y$ ), in each layer of soil, to the reaction pressure ( $p$ ) exerted by the soil.

Various methods, based on the results of laboratory, SPT, penetrometer, and/or pressuremeter tests, are used to construct the  $p$ - $y$  curves for a single pile, installed in a soil mass having a horizontal surface, subjected to a static loading.

But problems arise when there is any departure from this ideal situation, which there most often is in practice, and so new research seems necessary.

A study was accordingly undertaken at the LCPC (Laboratoire Central des Ponts et Chaussées) to determine the effect on the  $p$ - $y$  curve of the proximity of a slope, of soil density and of the arrangement of piles in a group. The final objective is to produce coefficients that can apply to the reaction curves determined on single piles in horizontal ground.

The article describes the method used to perform and interpret the tests on centrifuged models, together with the main results obtained in the study of the effect of slopes cut to 2 in 1 and 3 in 2 on pile response.

### 2. Method used

Soil-pile interaction problems are three-dimensional and thus are too complex to be done by theoretical or numerical methods. Given the number of tests necessary, it can not be performed by means of tests on actual piles, either.

Centrifuged small-scale models are another approach that henceforth makes it possible to investigate this type of problem, as has been shown by the work of Bouafia (1990) and Terashi (1991) on the effect of slopes. Earlier tests at the LCPC showed that it was possible, by instrumenting the piles with strain gauges, to measure the bending moments and to determine the  $p$ - $y$  reaction curves experimentally (Bouafia, 1990).

The main difficulty of the method lies in the fitting and double differentiation of the moment curves. Software using spline functions or polynomials was developed at LCPC, and the study showed that quintic spline functions give the best results.

By contrast to what is sometimes done, it is important not to introduce additional conditions or hypotheses (zero pressure at the surface of the soil or at the tip, for example) during these smoothing and differentiation operations. These very restrictive conditions have a decisive influence on the shape of the reaction curves obtained, and so may represent the researcher's a priori idea of the  $p$ - $y$  relation more than the actual physical relationship.

In the software developed at the LCPC (SLIVALICS), the experimental points are fitted

by quintic spline functions based on 6 successive measurement points into which an adjustment parameter  $\rho_0$  is introduced. Depending on the value given to this parameter, the curves may be very precise (they then pass very close to the experimental points but may exhibit slight undulations because of the inaccuracies of the strain gauge measurements) or on the contrary be smoother but then sometimes depart slightly from the experimental values.

For the tests described below, the criterion used to determine the adjustment parameter  $\rho_0$  consists of checking the static equilibrium of the pile. For this, the resultant of the pressures determined by this double differentiation of the moment curves is compared to the force applied at the head of the pile, measured by a force sensor. The adjustment parameter selected is the one that yields a difference less than 5%. No additional hypothesis is therefore imposed in the determination of the pressure curve.

The first study (Bouafia, 1990) performed on piles instrumented with 12 pairs of gauges, also showed that the number of measurement points should be increased to guarantee sufficient precision on the pressure curves obtained, especially at the head and tip of the pile.

### 3. Programme of tests

Since the objective was to study the effect of a slope on the  $p$ - $y$  curves, we decided to test flexible piles placed near slopes of "infinite" height. This choice reduces the number of parameters, in particular by eliminating the height of the slope. Two slopes were investigated (2 in 1 and 3 in 2), and the programme included 59 loading tests distributed over 7 containers (table 1).

#### 3.1. Soil mass

The material used is a fine white Fontainebleau sand, the characteristics of which have been described by Garnier (1994). With the selected type of pile, the ratio between the pile diameter and grain diameter is approximately 900, which is much greater than the minimum value of 40 usually allowed.

The sand is placed in the test containers (1200mm x 800mm) by raining, using an automatic hopper. Two different densities were studied (16.1 kN/m<sup>3</sup> and 15.5 kN/m<sup>3</sup>, giving density indices of 81% and 58%).

This hopper produces a very homogeneous sand mass, with density deviations less than 1% (Garnier, 1994).

Table 1: Programme of pile loading tests

Cont. N°	Slope	Density of the sand (kN/m <sup>3</sup> )	Distance from crest (t/B)
1	2 in 1	16.12	0,1,2,4,10 and 2Ref
2	2 in 1	16.13	0,1,2,3,4 and 3Ref
3	2 in 1	16.19	0,1,2,4,6,10 and 3Ref
4	2 in 1	15.73	0,1,2,4,6,8 and 2Ref
5	2 in 1	15.53	0,1,2,4,6 and 2Ref
6	3 in 2	16.11	0,1,2,4,6,8,10 and 2Ref
7	3 in 2	15.55	0,1,2,4,6,8,10,12, and 2Ref

#### 3.2. Pile and loading procedure

The pile is a tube of AU4G aluminium having an outside diameter of 18 mm, a thickness of 1.5 mm, and a total length of 380 mm, with a penetration length in the soil of 300 mm. The centrifugal acceleration of 40 G therefore simulates a prototype pile 720 mm in diameter with a total embedded length of 12 m ( $EI = 215 \text{ MN.m}^2$ ). It is fitted with 20 pairs of gauges 15mm apart. Three displacement sensors (DP1, DP2, and DP3) located at 65 mm, 20 mm and 0 mm, respectively, from the surface of the soil, and a force sensor FH are used to determine the conditions at the head.

The pile is driven in the sand mass using an hammer (weight 615g). The drop height is 470 mm and number of blows for total penetration varies with the soil density (about 80 when density is 16 kN/m<sup>3</sup> and 50 when density is 15 kN/m<sup>3</sup>). Two or three horizontal loading tests are first performed on piles in the sand mass with a horizontal surface, before the slope is excavated. It is very important to determine accurately the response of the piles in horizontal ground, and in particular the corresponding  $p$ - $y$  curves, since these results are used as a reference.

After these reference tests on level ground, the slope is cut at 1 G and 4 to 6 tests are performed at 40 G on piles located at different relative distances  $t/B$  between the piles centre and the slope (table 1 and fig.1).

Horizontal loading of the pile is performed by a device developed at the LCPC (Garnier, 1994). The tensile force is transmitted to the pile, at the

depth of 40 mm, by a metallic cable (free head condition); the device allows loading by stages.

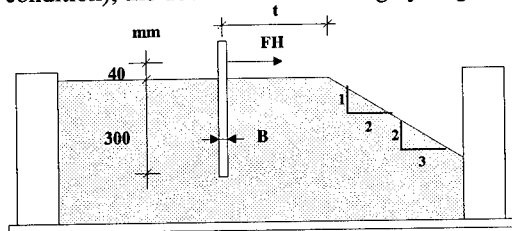


Figure 1: Notation and position of piles in tubs.

#### 4. Results

The programme includes 59 load tests of piles, either in level ground (reference tests) or at distances  $t$  from the slope ranging between 0 and 12 times the diameter of the pile ( $t/B = 0$  to 12).

##### 4.1. Loading curves

These curves give the horizontal displacements of the pile head versus the applied forces. Figure 2, for example, shows the displacements measured on sensor DP1 during loading tests of the three reference piles of tub n° 3; the good repeatability of the results obtained should be noted.

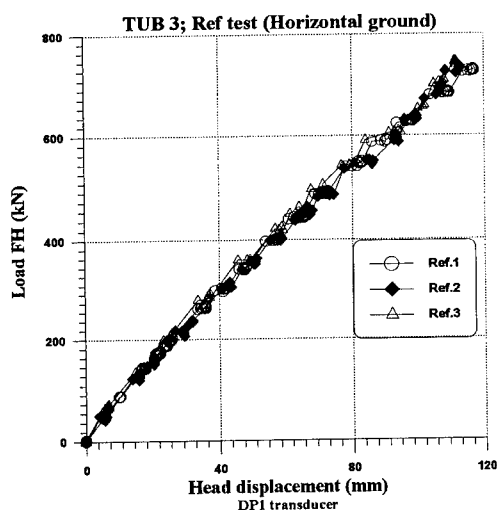


Figure 2: Horizontal displacements of the head.

The effect of the presence of a slope on the displacements at the head is shown in figure 3, which gives the loading curves obtained near a slope cut to 2 in 1 in a dense sand (tub n°3).

For the pile at the slope crest ( $t/B = 0$ ), the displacements for a given load, are multiplied by

a factor of approximately 1.7 with respect to the reference pile in horizontal ground. On the other hand, the test on the pile at  $t/B = 6$  gives displacements very close to those of the reference test (cf. §5).

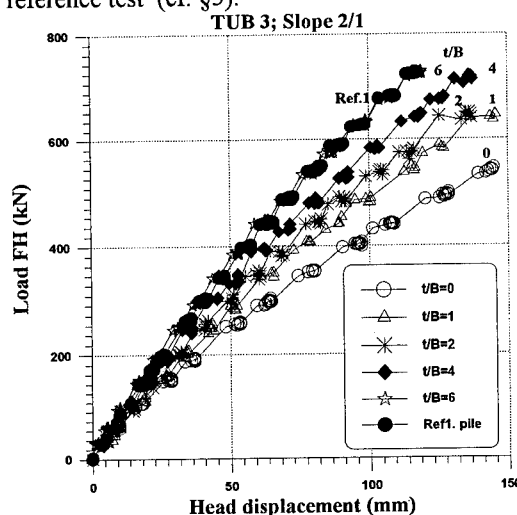


Figure 3: Effect of the slope on loading curves.

##### 4.2. Bending moment curves

As an example, the moment curves recorded during the loading of the reference piles of tub n° 3 are reproduced in figure 4 (lateral load of 540 kN). The evolution of the moment curves as the distance from the crest  $t/B$  varies is also given in figure 4 (tub n° 3, slope cut to 2 in 1).

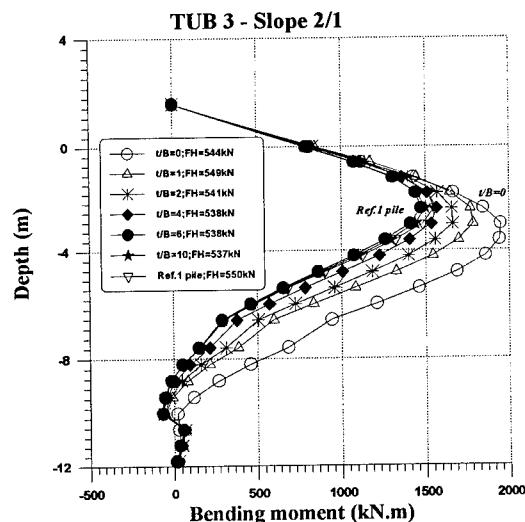


Figure 4: Plot of moment curves as a function of the distance from the crest  $t/B$  (FH=540 kN).

The maximum moment is approximately 25% greater for a pile at the slope crest than for the reference pile.

It is also noted, as already observed previously, that the depth of the point of maximum moment increases regularly as the pile gets closer to the slope. It varies from 0.2L in the horizontal sand mass to 0.28L at the slope crest (L being the embedded length of the pile).

#### 4.3. $p$ - $y$ reaction curves

The horizontal displacement of the piles  $y(z)$  are obtained by double integration of the moments curve. Both constants of integration are given by the displacements measured at the head.

The pressure curves  $p(z)$  are determined by the method described in paragraph 2. An example is given in figure 5, for a pile at a distance  $t/B = 2$  from the crest and a load of 605 kN (tub n° 4).

It is found that the pressures are very low close to the surface, even though the condition  $p=0$  at the surface of the soil was not imposed (cf. §2).

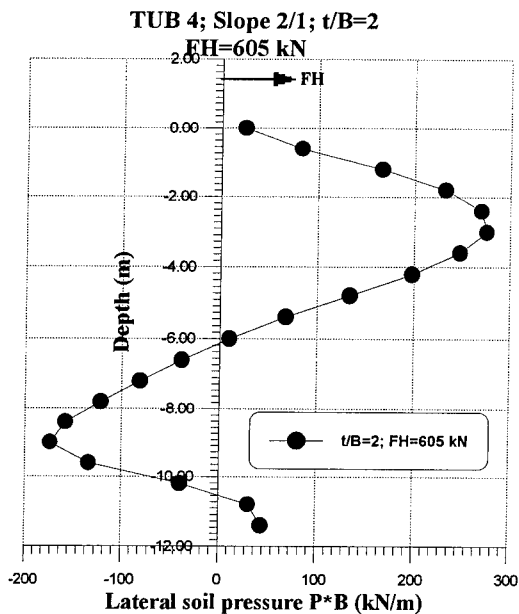


Figure 5: Pressure curves  $pB(z)$ .

For each depth, the  $p$ - $y$  reaction curves are computed from the foregoing data. Figure 6 shows the curves obtained for the pile already mentioned. The lateral strength of the soil increases with depth up to approximately 3.5B to 4B, beyond which the  $p$ - $y$  curves no longer change very much. This value might reflect the

appearance of a critical depth; this point is being investigated in another study.

It is also found that at a depth between 5B and 6B, the pressures and displacements change sign at the same time. But the lateral strength of the soil remains the same, since the slope of the  $p$ - $y$  curves is practically unchanged.

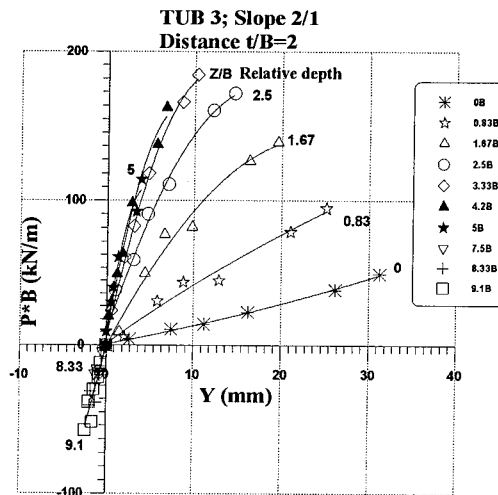


Figure 6:  $p$ - $y$  reaction curves at different depths.

#### 5. Effect of proximity of a slope on pile response

The tests served first to quantify the effect of a slope on displacements at the head. Figure 7 gives, for a slope of 2 in 1, the ratio between the displacement of a pile at distance  $t/B$  and the displacement at the head of the reference pile subjected to the same load.

The following remarks may be made:

- the ratio depends very little on the value of the applied load;
- the ratio reaches 1.6 for a pile located at the crest ( $t/B = 0$ );
- the effect of the slope ceases to be felt at distances greater than 6 or 7B.

The maximum moment in the pile is also affected by the presence of a slope, as indicated by the results in figure 4, for the case of a slope of 2 in 1 and a dense sand.

The maximum moment  $M_{\max}$  is proportional to the load FH applied at the head but the coefficient of proportionality  $m(t/B)$  depends on the distance from the crest:

$$M_{\max} = m(t/B) \times FH$$

All of the results obtained are grouped in figure 8, which shows the evolution of the ratio  $m(t/B)/m_{Ref}$  versus the relative distance  $t/B$  ( $m_{Ref}$  is the value of coefficient  $m$  for the horizontal reference level ground).

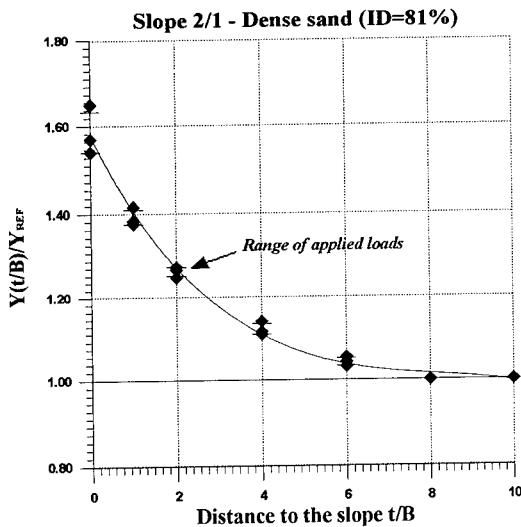


Figure 7: Effect of the presence of a slope on displacements at the head.

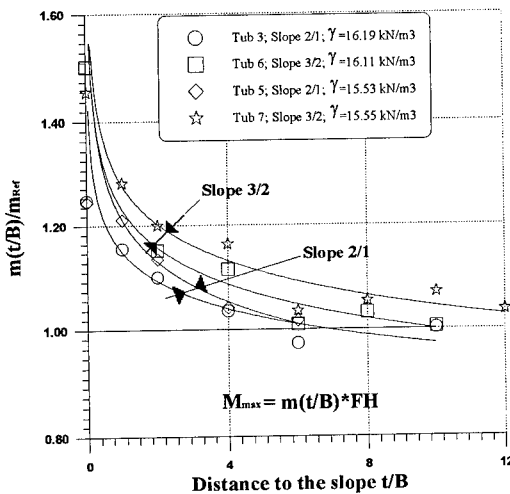


Figure 8: Plot of the ratio  $m(t/B)/m_{Ref}$  with the relative distance  $t/B$

This figure shows that the maximum distance beyond which the slope has no more influence on the maximum moment in the pile is 7 to 8B for the slopes cut to 2 in 1 and 10 to 12B for the slopes of 3 in 2. These limits seem not to depend

much on the density of the sand mass.

It is further noted that, in the worst case of the pile at the slope crest ( $t/B = 0$ ), the maximum moment is increased, with respect to the reference case on horizontal ground, by approximately 50 % for the 3 in 2 slope and 25% for the 2 in 1 slope.

The main objective of this programme concerns the effect of distance from the slope on the  $p-y$  reaction curves. Since these curves depend to a large extent on the depth (figure 6), the analysis was first performed at identical depth. The reaction curves obtained at the depth of 1.67 B, for example, on piles at different distances from the slope, are grouped in figure 9 (slope of 2 in 1, container 3).

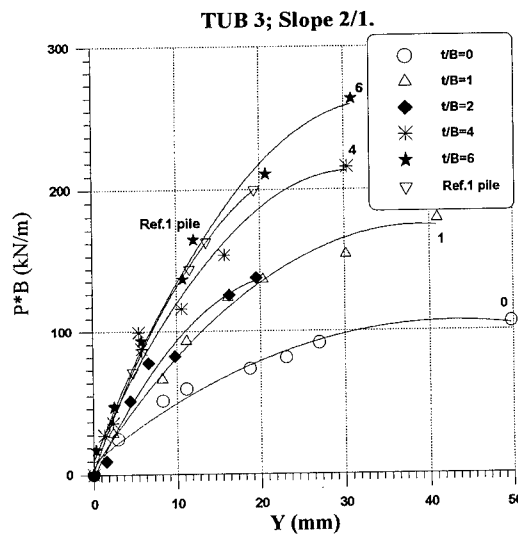


Figure 9: Reaction curves at different distances from the slope ( $z/B = 1.67$ ).

In spite of the difficulty already mentioned of determining the  $p-y$  curves, and their large sensitivity to the inaccuracies that may affect the measurement of the moments, the results seem very logical.

The influence of the slope becomes larger as the pile moves closer to the crest. The presence of the slope is felt both on the reaction modulus (tangent to the origin) and on the ultimate pressure (horizontal plateau). Thus, the initial tangent modulus appears to be divided by a factor of approximately 3 for the pile at the slope crest ( $t/B = 0$ ), with respect to the reference pile.

It may also be noted that the  $p-y$  curves corresponding to the case  $t/B = 6$  and to the reference pile on horizontal ground are practically the same, which confirms the value

already found for the maximum distance beyond which the slope of 2 in 1 no longer affects the response of the pile.

The work in progress consists of determining simple coefficients that could be proposed for common practice. These reduction coefficients  $r(t/B)$  would be applied to the reaction curves of the horizontal reference ground to take into account of the proximity of a slope, according to the following equation:

$$p(t/B) = r(t/B) \cdot p_{Ref}$$

This study has shown that these coefficients  $r$  depend on  $t/B$ , but also on the slope angle. They seem on the other hand to be practically independent of the density of the sand mass and therefore its mechanical characteristics.

Another very interesting result found in the study is illustrated in figure 10. This figure shows the variation of coefficient  $r$  versus  $t/B$  for  $p$ - $y$  curves at different depths (slope of 2 in 1, tub n° 3).

Between the slope crest ( $t/B=0$ ) and the limiting distance beyond which the slope has no more influence, the variation of  $r$  with  $t/B$  appears to be very nearly linear.

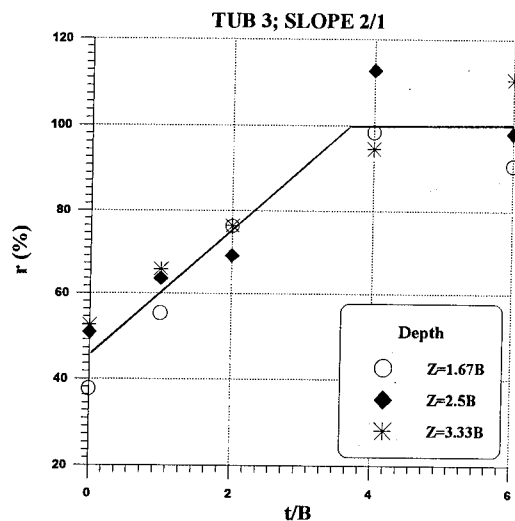


Figure 10: Plot of the coefficient  $r$  versus relative distance  $t/B$  with  $p(t/B) = r(t/B) \times p_{Ref}$ .

On an other hand, it is found that the coefficient  $r$  takes substantially the same values whatever the depth. The findings were the same on all the other cases tested, which could help simplify the expression of these reduction coefficients  $r(t/B)$ .

## 6. Conclusions

The testing programme concerns the experimental investigation of the behaviour of piles laterally loaded at the head. The method allowing determination of the reaction curves was developed in earlier studies. It is applied here to study the effect of a slope on the  $p$ - $y$  curves in a sandy soil.

The results show that the limiting distance beyond which the slope has no more influence is 6 to 8  $B$  for a slope of 2 in 1 and 10 to 12  $B$  for a slope of 3 in 2. These values are practically independent of the shear strength of the sand mass.

At smaller distances, the displacements of the pile and the internal forces increase as the pile is placed closer to the crest. With respect to the case of horizontal ground, for the same load, the displacement at the head of a pile at the crest of a slope cut to 2 in 1 ( $t/B = 0$ ) is multiplied by 1.6 and the maximum moment by 1.25.

The study served in particular to determine directly the effect of the slope on the  $p$ - $y$  curves and define reduction coefficients to be applied to the reaction curves determined on horizontal ground.

These coefficients  $r(t/B)$  seem to depend only on the distance  $t/B$  from the crest and, to a lesser extent, its slope. They are on the other hand practically constant with depth and relatively insensitive to the density of the sand mass.

The tests are being continued for other configurations, and also to study the group effect on the reaction curves.

## REFERENCES

- Bakir N.E, Garnier J., Canepa Y. 1994. Shallow footings loading tests: Effect of testing procedures. Centrifuge 94, Singapore.
- Bouafia A. 1990. Modelisation des pieux chargés latéralement en centrifugeuse. Thèse de doctorat, Université de Nantes : 267 p.
- Bouafia A., Garnier J 1991. Experimental study of  $p$ - $y$  curves for piles in sand. Centrifuge 91. Boulder. Balkema : 261-268.
- Garnier J., Canepa Y., Corté J.F, Bakir N.E 1994. Study of bearing capacity of footings near slopes. XIII ICSMFE. New-delhi. Balkema.
- Terashi M., Kitazume M., Manuyama A, Yamamoto Y. 1991. Lateral resistance of a long pile in or near the slope. Centrifuge 91. Boulder. Balkema : 245- 252.

## Behavior of laterally loaded pile groups in dense sand

Toshihisa Adachi, Makoto Kimura & Hideto Kobayashi  
Kyoto University, Japan

Akira Morimoto  
Ministry of Construction, Japan

**ABSTRACT:** In this study, the interaction between piles group and the ultimate lateral resistance were investigated. First, we conducted a test on two aluminum piles to investigate the interaction between them. It was found that the load distribution ratio of the front pile is larger than that of the rear pile. Second, lateral loading failure tests were conducted on aluminum piles and reinforced mortar piles to investigate the ultimate lateral resistance of single piles. The ultimate load-displacement curves at the pile head, the distribution of the cracks of concrete piles and the deformation pattern of the ground were also investigated experimentally.

### 1. INTRODUCTION

Since the most popularized area in Japan is on an alluvial plain with soft ground, pile foundations are commonly used as the structural foundation. In designing pile foundations, it is important to give consideration to the lateral resistance of piles especially to groups. Various kind of centrifuge model tests have already been done (e.g. Barton, 1984). In this research, two kinds of centrifuge model tests satisfying both the similarity of geometry and mechanics were carried out to investigate the interaction of two piles and the ultimate behavior of a single pile. These piles were assumed to be the bored piles. The centrifuge used in this research is a swinging type with the radius of 2.5 meter, located in Disaster Prevention Research Institute of Kyoto University.

### 2. TEST ON THE INTERACTION BETWEEN 2 PILES (TEST A)

Generally speaking, the research on the lateral resistance of a single pile cannot directly be applied to groups. In group piles, not only the interaction between pile and soil should be considered, but also the interaction between the piles. In this research, centrifuge model test on 2 piles which is equivalent to prototype steel piles is carried out. By changing the position of two piles, we investigated the interaction among pile-soil-pile and the distribution of moment and deformation.

#### 2.1 Outline of the test

Fig.1 shows the outline of apparatus used in the lateral load tests. The soil chamber is 52×24×43 cm

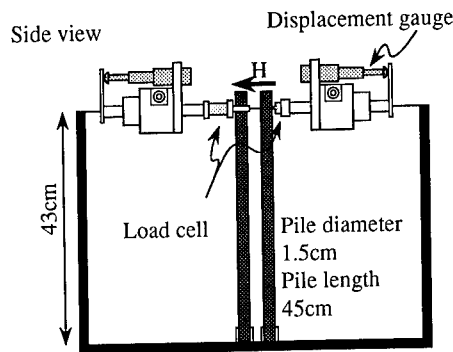


Fig.1 Setup of the experiment (Test A)

Table 1 Pile parameters (Test A)

Test pile (Material)	Diameter	Thickness	Length	Stiffness (EI) N m <sup>2</sup>	Centrifugal acceleration
Equivalent pile (Steel)	60cm	1.2cm	20m	$2.012 \times 10^8$	
Prototype pile (Aluminium)	60cm	4.0cm	16m	$1.996 \times 10^8$	
Test pile (Aluminium)	1.5cm	0.1cm	40cm	77.98	40g

and made of steel. The diameter of the aluminum piles,  $d$ , is 1.5 cm, length  $L$  is 45 cm. In order to measure the moment developed in the pile, 7 pairs of strain gauges were fixed on the pile below the ground surface. The centrifuge acceleration used in the test is 40g. Table 1 lists the parameters of the equivalent piles at 40g.

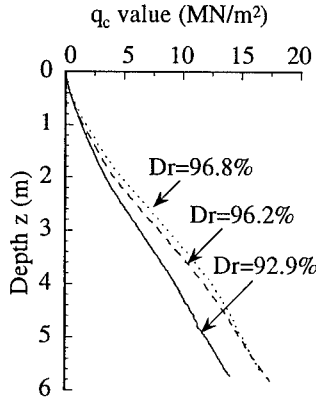


Fig.2 Distribution of  $q_c$  for the soil

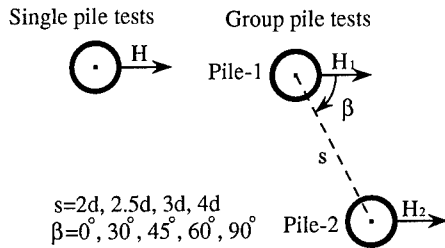


Fig.3 Pile layout

In previous research, pile heads were usually fixed with a cap and the lateral load was applied to the cap. In this research, however, the pile head is free and the displacement is applied independently. Two motors were used to control the displacements of the pile heads with a rate of 1.0 mm/min, of which one is pulling and another is pushing. The test is carried out 10 minutes after the centrifuge reaches 40g. The foot of the pile is fixed. The lateral load is applied 3.5 cm below the pile head.

Using a hopper with an adjustable slit, we can spread dry Toyoura sand to form the model ground. The unit weight of the soil is 1.61 gf/cm<sup>3</sup>,  $D_{50}$  is 1.18 mm, void ratio  $e$  is 0.638, relative density is 90.8 %.

In order to investigate the physical properties of the soil, mini-cone penetration tests were carried out at 40g. Fig.2 shows the prototype distribution of  $q_c$  for the soil. The three curves show the distributions for different densities. In all the cases,  $q_c$  increase linearly with depth. Besides, the cone penetration tests were also carried out after the tests in all cases to investigate the soil disturbance. It is found that the scatter was within 10%.

Fig.3 shows the tests condition on single and 2 piles. For the 2 piles, the distance between their centers,  $s$ , and the angle between a line passing

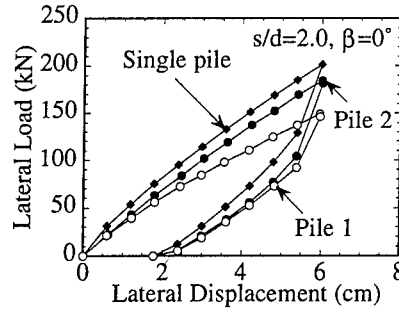


Fig.4 Relation between load and displacement

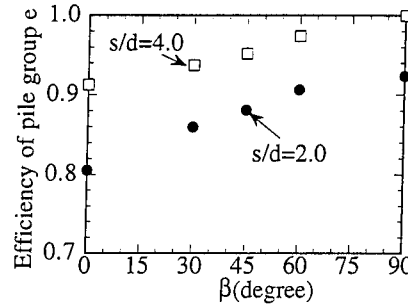


Fig.5 Relation between efficiency of pile group  $e$  and  $\beta$

through their centers and the loading direction,  $\beta$ , were included as a parameter in the test. The rear pile is, hereafter, called pile-1 and the front pile is called pile-2.

## 2.2 Results and analysis

Fig.4 shows the prototype load-displacement curves for single and 2 piles ( $s/d=2.0$ ,  $\beta=0^\circ$ ). If the same displacements are induced on the 2 piles, the sharing of load in the front pile is much larger than the rear pile.

In this present research, we define the efficiency of pile group as

$$\text{Efficiency of pile group, } e = (H_1 + H_2) / (2 \times H_s) \quad (1)$$

Here,  $H_1$ ,  $H_2$ ,  $H_s$  are the lateral loads acting on pile-1, pile-2 and single pile respectively at the same displacement.

Fig.5 shows the relation between  $e$  and  $\beta$ . The larger  $s/d$  is, or the nearer the  $\beta$  be to  $90^\circ$ , the larger the coefficient  $e$  will be and approaches a value near 1.

By differentiating the moment in the pile, we can obtain the subgrade reaction acting on them. Fig.6 shows the distribution of the subgrade reaction with



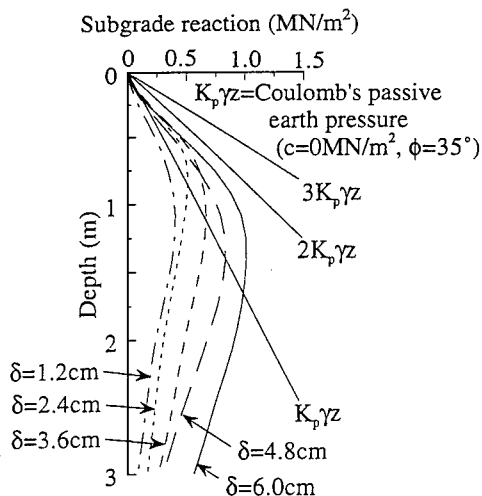


Fig.6 Distribution of the reaction along depth (single pile)

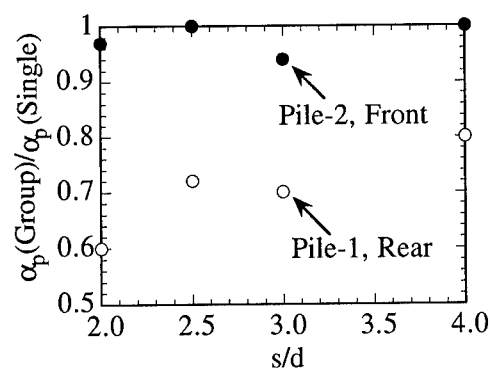


Fig.7 Relation between  $s/d$  and  $\alpha_p$

depth for single pile. The gradient of subgrade reaction to depth is about  $K_p \gamma z$  near the surface. If  $\delta > 2.4$  cm, the gradient will not increase and remain almost constant as  $1.5K_p \gamma z$  which can be thought as the ultimate subgrade force provided by the soil.

Fig.7 shows the relation between  $s/d$  and the reduced ratio of the ultimate force on each pile when  $\delta = 6.0$  cm, and  $\beta = 0^\circ$ . Here  $\alpha_p$  is the ratio of ultimate reactive force to  $K_p \gamma z$ . For pile-1, the closer  $s$  is, the smaller the reduced ratio of reactive force will be, being 0.6 when  $s/d = 2$ . For pile-2, however, the  $\alpha_p$  is not influenced by the  $s$  and is almost equal to 1. Therefore, the evaluation of the subgrade reaction of the front pile can be treated as a single pile.

The displacement of the  $i$ th pile in group piles of  $n$  can be defined as

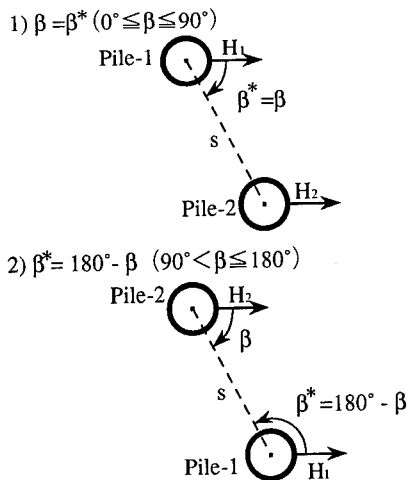


Fig.8 Definition of  $\beta^*$

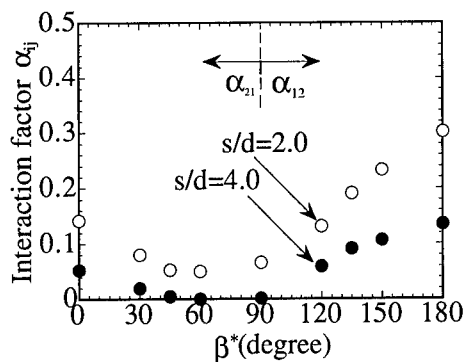


Fig.9 Relation between  $\alpha_{ij}$  and  $\beta^*$

$$\delta_i = \frac{1}{k_s} \sum_{j=1}^n \alpha_{ij} H_j \quad (2)$$

Here,  $k_s$  is the stiffness of a single pile and  $\alpha_{ij}$  is the interaction factor between  $i$ th and  $j$ th pile (Randolph, 1981).  $H_1$  and  $H_2$  are the lateral loads in the test.

We assume that  $\alpha_{ii}$  is equal to 1 and  $\alpha_{12} \neq \alpha_{21}$ . Based on this assumption, we derived the interaction factor,  $\alpha_{ij}$ . We also introduced a parameter  $\beta^*$  (Ochoa and O'Neil, 1989) and investigated the relation between  $\beta^*$  and  $\alpha_{ij}$ . Fig.8 shows the relation between  $\beta$  and  $\beta^*$ . That is, the angle from the loading direction to the direction of influencing pile to influenced pile. By Eq.(2) and  $\beta^*$ , we can obtain the values of  $\alpha_{12}$  and  $\alpha_{21}$ . Fig.9 shows the relation between  $\beta^*$  and  $\alpha_{ij}$ . It is seen that, the larger the  $s/d$ , the smaller the value of  $\alpha_{ij}$  will be. Besides, the value of  $\alpha_{12}$  is larger than  $\alpha_{21}$ . This result is coincident with the result from model test at 1g (Kimura, et al., 1991).

### 3. TEST OF A SINGLE PILE ON ULTIMATE STRENGTH (TEST B)

Generally speaking, the design of piles are based on an elastic analysis in Japan. However in 1986, the method of limit state was first introduced in the Japanese standard manual as the design method for concrete structures. It is important to investigate the ultimate behavior of a pile foundation to establish a rational design method (Kimura, et al., 1993).

In this section, a pile subjected to a large lateral deformation was carried out to investigate its response of pile at ultimate strength. Two types of piles, one aluminum (equivalent to a steel pile), and the another a reinforced mortar pile (equivalent to a cast-in-place pile), were tested. Generally, because of the fact that the cast-in-place pile cannot bear extension, the limitation of elasticity and ultimate behavior will be different for the steel and cast-in-place concrete pile. The difference was investigated in this section.

#### 3.1 Outline of the test

Fig.10 shows the experimental device used in the test. Loading condition is displacement controlled, using a motor and bevel gear as shown in Fig.11. In order to observe the behavior of both the pile and soil, a semi-round pile was used and one of the sides of the box is made of glass.

Two types of model piles were used in the test, an aluminum pipe with a diameter of  $d=20$  mm, wall thickness  $t=1$  mm and length  $L=44$  cm, and another is a reinforced mortar pile with a diameter  $d=24$  mm and length  $L=46$  cm. In order to measure the moment occurred in the pile, 6 pairs of strain gauges were fixed on the pile below the ground surface. The foot of the pile is fixed and the head is free. The lateral load is applied 3.0 cm above ground surface. Besides, in order not to generate any torsion in the semi-round pile, a cap is fixed on the pile head on which the load is applied.

The model reinforced mortar pile was produced based on actual cast-in-place concrete piles used in foundations of highway bridge ( $d=1.2$  m, 24 steel bars (29 mm in diameter) for a cross section, overburden of steel bar = 15 cm, bending stiffness  $EI=3.178 \times 10^9$  Nm<sup>2</sup>).

As to making the model pile, first, 5 steel wires were fixed with instant glue to semi-round brass rings (thickness of 1 mm) to form a steel frame. Next, we prepared the mortar with a ratio of Toyoura sand : cement : distilled water = 2 : 1 : 0.65. Third, we put the steel frame into the specimen mould and pour the mortar into the mould. After one day's curing, the specimen is taken out and put into water for two weeks curing. The one axial strength of the mortar is approximately  $\sigma=30\sim37$  MN. The bending stiffness was then evaluated using a simple cantilever loading test with an average  $EI=4.850 \times 10^2$  Nm<sup>2</sup>. The scattering of the results is less than 7%.

Table 2 gives the value for equivalent steel pile, reinforced concrete pile and prototype of the tested

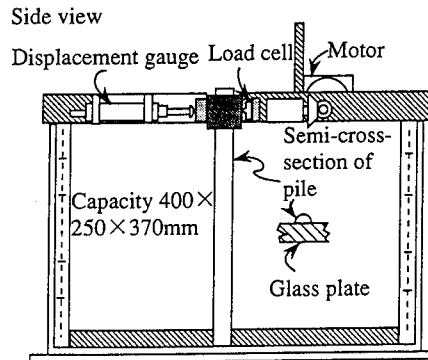


Fig.10 Setup of the experiment (Test B)

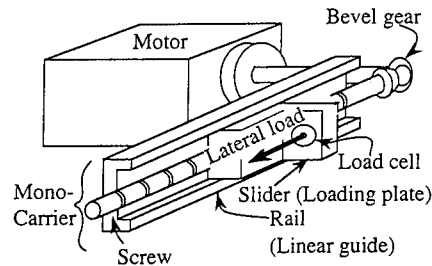


Fig.11 Bevel gear and mono-carrier

Table 2 Pile parameters (Test B)

Test pile (Material)	Diameter	Thickness	Length	Stiffness (EI) Nm <sup>2</sup>	Centrifugal acceleration
Equivalent pile (Steel)	60cm	0.9cm	15m	$1.57 \times 10^8$	
Prototype (Aluminium)	60cm	3.0cm	13.5m	$1.57 \times 10^8$	
Aluminum pipe	2.0cm	0.1cm	45cm	$1.94 \times 10^2$	30g
Equivalent pile (Reinforced concrete)	1.2m		29m	$3.178 \times 10^9$	
Prototype	1.2m		22.5m	$6.061 \times 10^9$	
Model pile (Reinforced mortar)	2.4cm		45cm	$9.699 \times 10^2$	50g

pile. Accelerations are 30g and 50g for the aluminum pile and model reinforced pile respectively.

The model soil is made of Toyoura sand and was prepared in same way as in Test A. The displacement was controlled and used as the loading condition at 2.5 mm/min. The pile was displaced to 100% $d$ , the diameter of the pile.

#### 3.2 Results of tests and analysis

The results of the tests hereafter are all given in

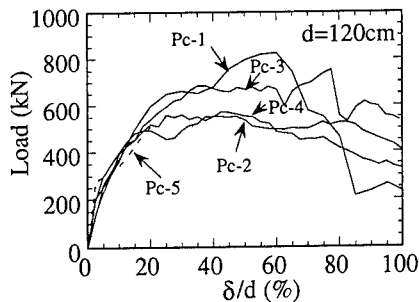


Fig.12 Relation between load and normalized displacement for the reinforced concrete pile

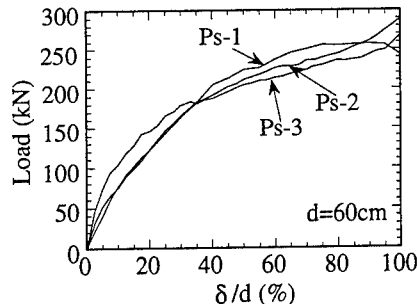


Fig.14 Relation between load and normalized displacement for the steel pile

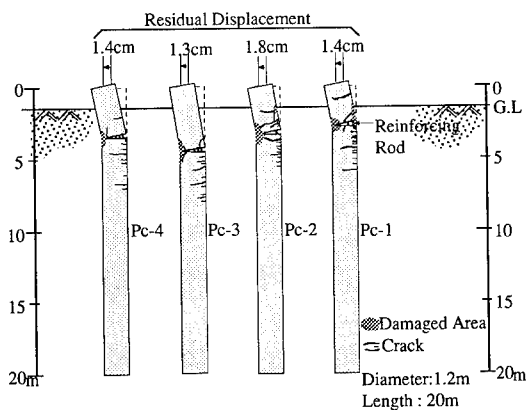


Fig.13 Sketch of crack locations of concrete piles

prototype scale. Five reinforced mortar model piles and three aluminum model piles were tested. Their names are given as Pc-1~Pc-5 and Ps-1~Ps-3 respectively.

#### Relation of load-displacement

Fig.12 shows the relation of load-displacement for Pc-1~Pc-5. The horizontal axle is normalized with respect to the diameter of the pile. The loads increase linearly with displacement when  $\delta/d$  is less than 5% and then the rate decreased between the interval  $5\% < \delta/d < 15\%$ . At the ultimate state, the load decreased and displacements increased rapidly.

Fig.13 shows the sketch of cracks in the piles undergone the deformation of  $100\%d$ . The strain concentration occurred at the cracks 2.5 m~4.5 m below the loading point. Damaged area of mortar occurred at the loading side and the steel wires were exposed. Besides, most of the cracks, were located at the area where the brass rings exist.

Fig.14 shows the load-displacement curves for Ps-1~Ps-3. For the aluminum piles, the load versus displacement rate decreases when  $\delta/d$  is greater than about 30% but no decrease in load was observed.

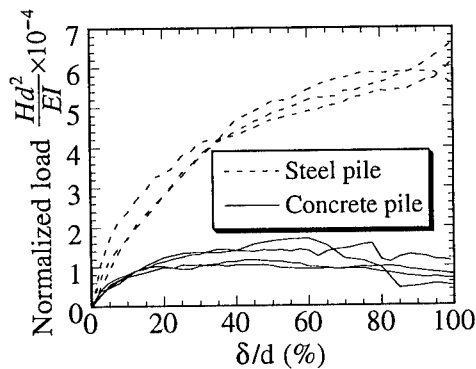


Fig.15 Normalized lateral load and displacement

When the deformation reached  $100\%d$ , torsion occurred 1.8 m from the ground surface.

Fig.15 shows the relation of load-displacement for Pc and Ps in normalized form, that is, the loads were divided by  $EI/d^2$ . From the figure, it is clear that if the  $EI$  and diameter are the same, the aluminum pile can bear more load. The bending stiffness is measured with a stiffness test which is carried out at very small deformations. The application of the test results to large deformation may cause problems. In spite of this shortcoming, the test results can be used to describe the behavior of full scale piles qualitatively because of the fact that the model pile was made very similar to the actual pile.

#### Distribution of deformation

Fig.16 shows the distribution of pile deformation obtained from double integrating the moment of Pc-1 and Ps-1. From the figure, it can be seen that the first steady point of concrete piles became shallower when the deformation of pile head reached to  $10\%d$ . This result is coincident with the conclusion using the full scale tests reported in the reference (Kimura et al., 1993) that the first steady point becomes shallower when the bending stiffness decreases.

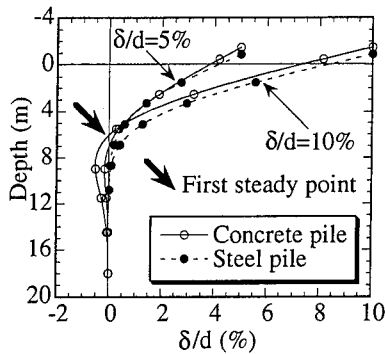


Fig.16 Comparison of the deformation patterns for two kind of piles

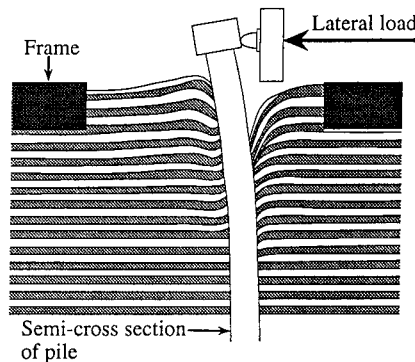


Fig.17 Deformation pattern of both pile and ground ( $\delta/d=100\%$ )

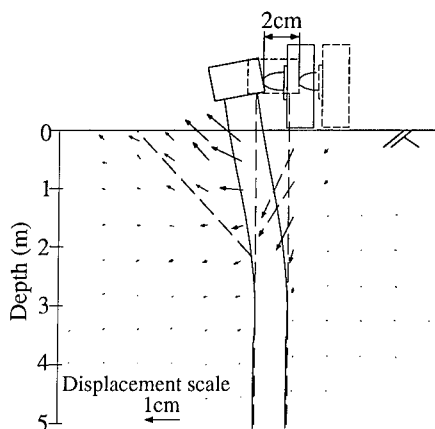


Fig.18 Displacement vector of ground( $\delta/d=100\%$ )

Deformation pattern of the ground around a pile

In order to observe the deformation of the ground, first, the ground is laid with dyed and undyed sand

layers alternatively. Fig.17 shows the deformation pattern scanned from the photo film taken at the time when the test was finished. Though the horizontal deformation of ground cannot be seen clearly, the influence on the ground by the pile subjected to lateral load can be seen clearly. The nearer the ground is to surface, the larger the deformation will be.

Second, Fig.18 shows the displacement vectors which calculated from the targets buried on the surface of the glass. It can be seen that there exist the moving zone/wedge in front of the piles. The influence area in front of the piles are estimated about  $4.0d$  from this figure.

#### 4. CONCLUSION

In this research, the interaction of 2 piles equivalent to steel piles and the ultimate behavior of single pile of different types were investigated. The following conclusions can be given.

1. In two piles, the sharing ratio of the front pile is larger than that of back pile.
2. For the rear piles, the closer the spacing between piles is, the smaller the reduced ratio of reactive force will be. Therefore, the evaluation of the subgrade reaction of the front piles can be treated as a single pile.
3. The influence factor obtained from test results shows that the  $\alpha_{12}$  corresponding to  $\beta^*=180^\circ$  is larger than the  $\alpha_{21}$  corresponding to  $\beta^*=0^\circ$ .
4. For reinforced concrete piles, the ultimate state occurred after the deformation of pile head reached 15% of the diameter.
5. For steel piles, the load will increase even the deformation of pile head reaches to 100% of the diameter.
6. If the diameter and bending stiffness are the same, the ultimate lateral bearing capacity of a steel pile is much larger than that of a reinforced concrete pile.

#### REFERENCE

- Barton, Y.O. 1984. Response of Pile Groups to Lateral Loaded in the Centrifuge, *Application of Centrifuge Modeling to Geotechnical Design..* 457-473. Rotterdam: Balkema.
- Kimura, M. and Shibata, T. 1991: Three Types of Model Tests on Laterally Loaded Pile Groups. *Proc. 9ARC*: 229-232.
- Kimura, M., Nakabayashi, S. and Ito, K. 1993. Field tests and analysis on ultimate behavior of lateral loading bored piles, *Proc. 2nd Deep Foundations on Bored and Auger Piles*: 143-146. Rotterdam: Balkema.
- Ochoa, M. and O'Neil, M.W. 1989. Lateral Pile Interaction Factors in Submerged Sand, *Jour. GE ASCE* 115-3: 31-44.
- Randolph, M.F. 1981. The response of flexible piles to lateral loading: *Geotechnique* 31-2: 247-259.

## The interpretation of data from tests on laterally loaded piles

G.J.W.King

University of Liverpool, UK

**ABSTRACT:** In a model pile test the distribution of bending moment is measured using strain gauges and the deflection and rotation of the pile head are deduced from measured displacements. In order to estimate the deflected shape of the pile and the distribution of soil reaction along the pile, it is necessary to integrate and differentiate the bending moment distribution. This can be achieved by fitting a single polynomial to the data points or by using spline functions between successive data points. The relative merits of these procedures using various orders of polynomial are demonstrated.

### 1 INTRODUCTION

The package arrangement for carrying out lateral load tests on model piles in the Liverpool University centrifuge is shown in Figure 1. The centrifuge and the equipment used to activate the models and record their behaviour have been described in detail by King, Dickin and Lyndon (1984). The results of a study of the effects of independent variation in pile diameter and flexibility, for fairly rigid piles embedded in dense dry sand, have been reported by King and Fulthorpe (1986). Each model pile was fashioned from stainless steel tubing and the angle of interface friction between its machine-finished surface and the dense sand was of the order of  $18^\circ$ . The sand had an effective grain size of 150 microns and a uniformity coefficient of 1.5. It was compacted in layers, 30 to 40mm thick, using a hand vibrator, with a model pile held firmly in position. Its average specific weight was  $16.6\text{kNm}^{-3}$  and its angle of internal friction at average prototype stress level was  $48^\circ$ . The distribution of bending moment down the embedded length of the piles was measured using six pairs of 3mm long foil resistance gauges at 30mm spacings. The gauges were fixed internally and protected using the technique described by King et al (1984) and their behaviour under calibration was linear and perfectly reproducible. The displacement and rotation of the pile at the soil surface were

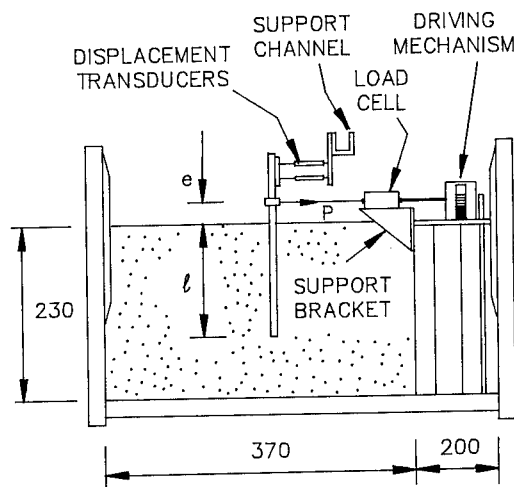


Fig. 1. Package arrangement (dimensions in mm)

calculated from the measured displacements at two positions, on the straight part of the pile, above the pile cap level at which the load was applied. In a particular test the model pile had an internal diameter of 17.93mm, and a wall thickness of 0.57mm, and was embedded in sand to a depth of 210mm. The Young's modulus of the steel was  $2 \times 10^8 \text{ kNm}^{-2}$ . The test was carried out at an average centrifugal acceleration of 40g over the depth of the sand.

Table 1. Measured bending moments together with known end values. (prototype scale)

Depth below ground level 0 1.2 2.4 3.6 4.8 6.0 7.2 8.4  
x(m)

Bending moment 357 1022 1303 1245 923 514 182 0  
 $\bar{M}(\text{kN.m})$

Thus the prototype had an external diameter of 0.76m, an embedded length of 8.4m and a flexural rigidity of 773000 kNm<sup>2</sup>. When a load of 470kN was applied at a height of 0.76m above the sand surface the bending moments recorded were as shown in table 1. These values are plotted in Figure 2 and represent a typical data set which could be joined by hand smooth a smooth curve.

The corresponding values of deflection and rotation at ground level were calculated to be 0.0308m and -0.0098 radians respectively.

In order to estimate the deflected shape of the pile and the distribution of soil reaction along the pile, it is necessary to integrate and differentiate the bending moment distribution. Therefore the distribution has to be expressed mathematically. This can be achieved using the method of least squares to find a single, best-fit, polynomial to the data points or by fitting separate polynomials (spline functions) between successive data points. Single polynomials have been used by King and Fulthorpe (1986) and Terashi et al. (1989) and spline functions by Barton (1982) and Geordiadis et al. (1992). Scott (1981) experienced difficulties with both methods and developed a combined procedure which he found to give satisfactory results for a model pile clamped in a Winkler foundation.

Both methods will be described briefly and then applied to the experimental data, using various orders of polynomial, to illustrate their relative merits and deficiencies.

## 2 CURVE FITTING WITH POLYNOMIALS

This method requires the determination of the coefficients in the polynomial

$$M=c_1+c_2x+c_3x^2+\dots+c_jx^{j-1}+\dots+c_mx^{m-1} \quad (1)$$

of order (m-1), which gives the best fit to the n data values  $x_1\bar{M}_1, x_2\bar{M}_2, \dots, x_i\bar{M}_i, \dots, x_n\bar{M}_n$

Defining the error, E, as the sum of the squares of the differences between the data values,  $\bar{M}_i$ , and the corresponding points on the curve,  $M_i$

$$E = \sum_{i=1}^n (\bar{M}_i - M_i)^2 \quad (2)$$

E is to be minimised by varying the values of c and for a minimum error

$$dE = \frac{\partial E}{\partial c_1} dc_1 + \dots + \frac{\partial E}{\partial c_k} dc_k + \dots + \frac{\partial E}{\partial c_m} dc_m = 0 \quad (3)$$

Since the variable  $dc_k$  are non-zero the derivatives  $\partial E/\partial c_k$  must be zero. Therefore

$$\frac{\partial E}{\partial c_k} = \frac{\partial E}{\partial M_i} \frac{\partial M_i}{\partial c_k} = -2 \sum_{i=1}^n (\bar{M}_i - M_i) x_i^{k-1} = 0 \quad (4)$$

Therefore

$$\begin{aligned} \sum_{i=1}^n \bar{M}_i x_i^{k-1} &= \sum_{i=1}^n (c_1 + c_2 x_i + \dots + c_j x_i^{j-1} + \dots + c_m x_i^{m-1}) x_i^{k-1} \\ &= c_1 \sum_{i=1}^n x_i^{k-1} + c_2 \sum_{i=1}^n x_i x_i^{k-1} + \dots + c_j \sum_{i=1}^n x_i^{j-1} x_i^{k-1} \\ &\quad \dots + c_m \sum_{i=1}^n x_i^{m-1} x_i^{k-1} \end{aligned} \quad (5)$$

There are m such equations which can be expressed as

$$\{T\} = [S] \{c\} \quad (6)$$

in which  $T_k = \sum_{i=1}^n \bar{M}_i x_i^{k-1}$

and  $S_{kj} = \sum_{i=1}^n x_i^{k-1} x_i^{j-1}$

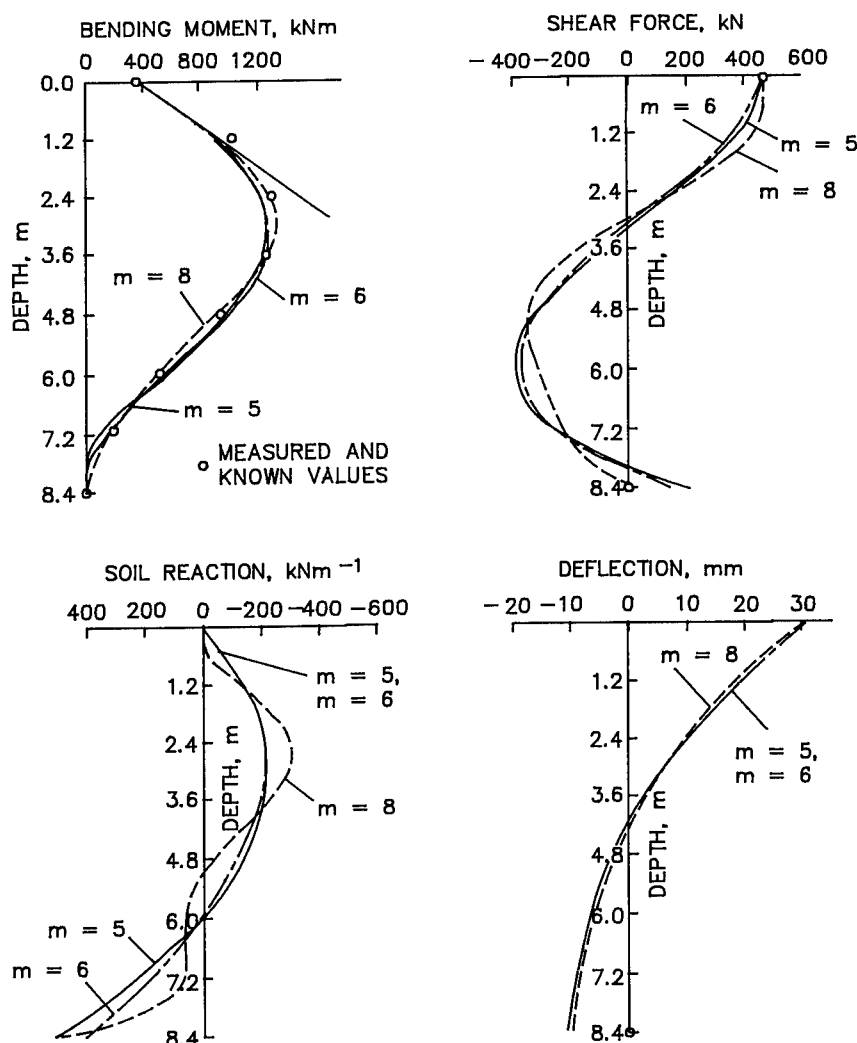


Fig. 2. Calculated distributions using best-fit polynomials

Hence by solution

$$\{c\} = [S]^{-1} \{T\} \quad (7)$$

These equations are modified to suit known boundary values at  $x = 0$ . Here the applied bending moment and shear force are known and, as the soil is cohesionless, the soil reaction at the surface is zero. Therefore

$$c_1 = M_0 = P_e$$

$$c_2 = (dM/dx)_0 = P$$

$$\text{and } c_3 = \frac{1}{2}(d^2M/dx^2)_0 = 0$$

Hence only  $(m-3)$  coefficients remain to be found.

A computer programme, POLYCURVE, is used for determining best-fit polynomials by this method. A computer programme, POLYID, is used for integrating and differentiating polynomial bending moment distributions. For the integration this programme requires the specification of flexural rigidity and the slope and deflection at the starting point.

Distributions of bending moment, shear force, soil reaction and deflection obtained using various orders of polynomial to fit the given data are shown in Figure 2.

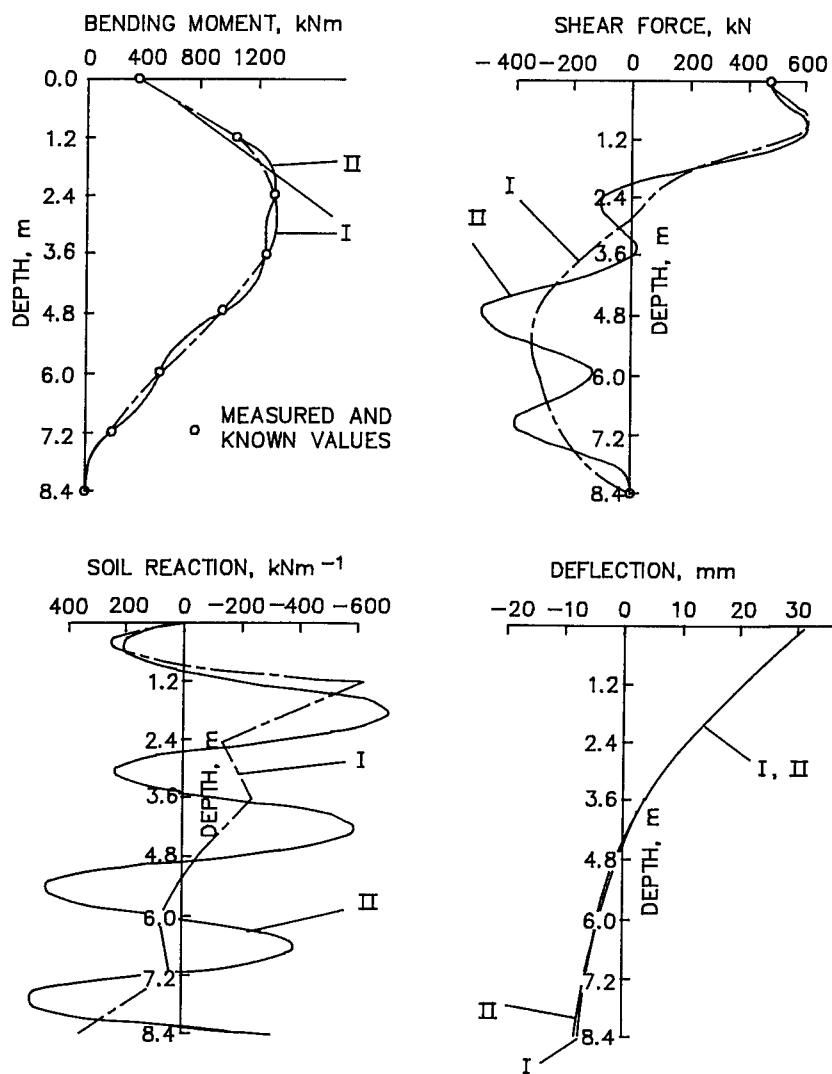


Fig. 3. Calculated distributions using spline functions

### 3 CURVE FITTING WITH SPLINE FUNCTIONS

This method requires the determination of the coefficients of separate polynomials between each data point which provide continuity of values and of a specified number of derivatives at the data points. Third order polynomials (cubic splines), which can preserve continuity up to the second derivative, are often sufficient for engineering purposes. However, when higher order derivatives have to be preserved or additional data values

satisfied, higher order polynomials are required.

In general if

the number of ordinate values =  $v$

the number of specified derivatives =  $d$

the number of separate splines =  $s$

and the number of continuity conditions at each join =  $c$

then  $s$  spline functions will be required with a total number of coefficients.

$$n = v + d + c(s-1) \quad (8)$$



After repeated differentiation of the polynomials, which are each of the form of Eq. (1) of appropriate order, the  $n$  equations at the data points governing their coefficients are derived.

The boundary values at  $x = 0$  dictate that the first three coefficients of the first spline are  $c_1 = P_e$ ,  $c_2 = P$  and  $c_3 = 0$ . After modifying accordingly, the remaining  $(n-3)$  equations are solved using any standard computer programme which can handle large numbers of simultaneous equations.

Once the coefficients in each spline have been determined, programme POLYID is used to integrate and differentiate each spline in turn. The specified values of initial slope and displacement are used for the first and calculated values, at the end of the previous spline, for subsequent ones.

For the given data,  $s=7$ ,  $v=8$ , and, noting that  $dM/dx=0$  when  $x = l$ ,  $d=3$ . If continuity of values and two derivatives is specified  $c = 3$  and therefore, from Eq. (8)  $n = 29$ . This can be accommodated using  $m=5$  for the first spline and  $m=4$  for the other six (Splines I). If continuity of the third derivative is specified  $c=4$  and  $n=35$  and this can be accommodated using  $m=5$  for all seven splines (Splines II).

Distributions of bending moment, shear force, soil reaction and deflection obtained using these two alternatives are shown in Figure 3.

#### 4 DISCUSSION

All of the bending moment distributions shown in Figures 2 and 3 are reasonable. The cubic splines of splines I fit the data points very smoothly but the fourth order splines of splines II oscillate undesirably between the points. The seventh order polynomial gives an excellent fit to this set of data but, with more scattered data, would have produced undesirable oscillations.

When integrated, all these distributions yield very similar deflection diagrams, the polynomials yielding a slightly larger displacement at the bottom of the pile than the spline functions. However, when differentiated, they yield significant differences in the shear force diagrams and very distinct differences in distributions of soil reaction.

The spline functions and the highest order polynomial all show an unacceptable increase in shear force below ground level and the distribution of shear force given by the fourth order splines shows large oscillations. None of the polynomials

show zero shear force at the bottom of the pile although the highest order one is close. Unfortunately the zero moment and shear force boundary conditions at the toe cannot be specified in the polynomial approach.

The distribution of soil reaction given by the fourth order splines oscillates wildly and although that given by the cubic splines shows less oscillation it is of course discontinuous. Only the lower order polynomials show reasonable distributions of soil reaction. Obviously, with a non-zero shear force at the toe, the nett area of the soil reaction diagram will not equal the applied shear force. It should be noted that, for a pile in a continuum, the points of zero soil reaction and zero deflection will not generally coincide.

#### 5 CONCLUSIONS

Integration using any reasonable order of polynomial or spline functions did not present any difficulty and yielded similar results. It should be noted that any inaccuracy in the measurement of pile head rotation will have a more significant affect, than the method of curve fitting, on the calculated displacement at the bottom of the pile and the depth to the point of zero deflection.

Differentiation however, using either polynomials or spline functions, was far from perfect, even though the bending moment data set considered here was quite smooth. The use of spline functions did not produce smooth distributions of shear force and soil reaction. Distributions given by the lower order polynomials were both smooth and realistic except at the very bottom of the pile. Similar results have been found with other sets of experimental data and of course the spline approach is even worse when the data is scattered. The use of fourth or fifth order best-fit polynomials with manual adjustment at the bottom of the pile, as illustrated by King and Fulthorpe (1986) is recommended.

It should be noted that the number of data points and the order of polynomial chosen are independent. A higher order polynomial will not necessarily give a better fit as a lower order one may provide a beneficial smoothing effect.

#### REFERENCES

- Barton, Y.O. 1982. *Laterally loaded model piles in sand. Centrifuge tests and finite-*

- element analysis*. Ph.D. Thesis, University of Cambridge
- Georgiadis, M., Anagnostopoulos, C. and Saflekou, S. 1992. *Centrifugal testing of laterally loaded piles in sand*. Can. Geotech. J., Vol. 29, pp. 208-216.
- King, G.J.W., Dickin, E.A. and Lyndon, A. 1984. *The development of a medium-sized centrifuge testing facility*. Proc. Int. Symp. on the Application of Centrifuge Modelling to Geotechnical Design. Manchester, April, pp. 25-46.
- King, G.J.W. and Fulthorpe, J.N. 1986. *Centrifuge model tests on laterally loaded single piles*. Proc. 3rd Indian Conf. on Ocean Engg., Bombay, December, pp. B1-B11.
- Scott, R.F. 1981. *Pile testing in a centrifuge*. Proc. Xth Int. Conf. on S.M. and Foundn. Engg., Stockholm, Vol. 2, pp. 839-842.
- Terashi, M., Kitazume, M., and Kawabata, K. 1989. *Centrifuge modelling of a laterally loaded pile*. Proc. XIIth Int. Conf. on S.M. and Foundn. Engg., Rio de Janeiro, Vol. 2, pp. 991-994.

## Interaction between foundation of beam-pillar offshore platform and soil

C.G. Bao, M. Li, R.G. Shan & H.H. Wang

*Yangtze River Scientific Research Institute, Wuhan, People's Republic of China*

**ABSTRACT:** This paper deals with a new type of gas platform which consists of a beam-pillar system. The centrifuge model tests were performed to clarify the operational mechanism. Six model tests were carried out under vertical or vertical and horizontal loads. Based on these tests, the share of vertical load carried by the bottoms of pillars and beams and the sides of pillars was given. This provides a scientific basis for platform design.

### 1 INTRODUCTION

The beam-pillar offshore platform is a new type of gas platform with the characteristics of short term construction, low cost and easy movableness. Its operational mechanism, however, is not very clear. It has brought about difficulties to the design, and also to the finite element method to analyze the condition of withstanding loads. In order to discover the mechanism of the platform, centrifugal model tests have been performed. The soil pressure on the bottoms of the platform pillars and beams, and the friction on the sides of pillars have been measured. The soil load transmission way has been revealed. These provide a scientific basis for the platform designing.

It was the first time to carry out the platform model test in the centrifuge in our country. There is only a little introduction and limited achievements could be found from the present references (see Craig, 1983, Craig et al., 1981, Luong et al., 1988). Therefore it was rather difficult for us to do this test. Six model tests were performed respectively and the first one was a trial test. The results were not satisfactory because the measurement equipment was not well prevented from moisture and not well insulated, and the measured data were unstable.

The second test was carried out with only vertical load and the third one with both vertical and horizontal loads. Because of the differences of soil conditions in two models, there was no comparison between these two tests. Having summarised the experiences of the above failed tests, the remaining three tests were successful. The fourth model test and the fifth one were comparative tests with measuring the soil pressure as its main purpose. The sixth model test was to measure friction on the side of pillars.

### 2 MODEL DESIGN AND SOIL PREPARATION

The platform model shown in Fig. 1 was made of steel with an elastic modulus of  $2.1 \times 10^5$  MPa by the scale of 1:150. Thirteen pressure transducers were installed in the fourth or fifth model, three of which were on the pillar bottoms, ten on the beam bottoms. Seven strain gauges were put on the sides of pillars. For the sixth model, as a complementary test to the fourth and fifth one, strain gauges were put on the sides of the pillars. A few LVDT were installed on the top of the platform to measure the settlement during testing.

The soil used in the tests consists of fine sand

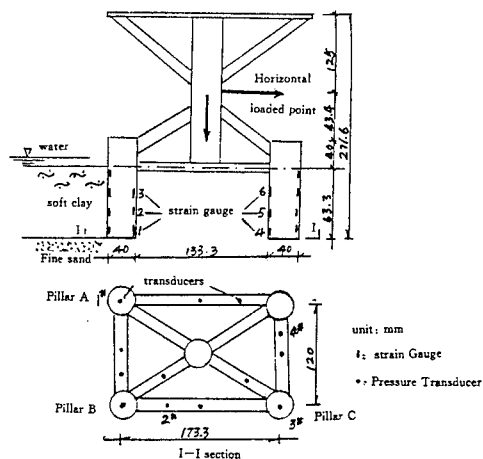


Fig. 1 Model structure and layout of pressure transducer and strain gauges

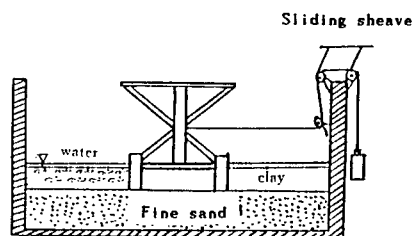


Fig. 2 Sketch of horizontal loading equipment

and soft clay. The liquid limit of the soft clay  $W_L$  is 42.3%, plastic limit  $W_p$  is 23% and its plasticity index  $I_p$  is 19.3%. The platform foundation is located on the fine sand layer.  $e_{max}$  and  $e_{min}$  of the fine sand are 1.147 and 0.516, respectively. The dry unit weight is 16.1  $kN/m^3$ , and the density index  $D_r$  is 0.8.

The test procedure was as follows: (1) filling sand into model box with a thickness of 13.3 cm; (2) putting the model box into the centrifuge and operating it with the acceleration of 150g until the filled sand layer has been consolidated; (3) stopping the centrifuge, and putting the platform model on the sand layer in the model box; (4) filling in the box with the soft clay prepared with water content higher than  $W_L$ . The soft clay layer is 6.33 cm thick and up to the middle axis line of the bottom

beam; (5) covering it with water; (6) installing a LVDT on the top of platform; (6) Putting the model box with the model into the centrifuge and operating it with acceleration of 150g; (8) turning off the centrifuge and applying horizontal load to it after the test has reached a steady state; (9) recording the test procedure.

### 3 TEST EQUIPMENT AND TEST METHOD

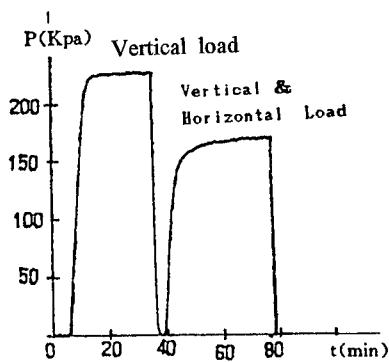
The arm length of the centrifuge is 3m, the radius plus pendent basket is 3.5m, the maximum acceleration is 300g, and its effective capacity is 180 g-ton. The horizontal load was applied as shown in Fig. 2. The mini-transducers with the size of about 5 mm diameter and 1.5 mm thick, made in Japan, were selected to measure the back pressures. The key problem was the insulation of the transducers which need working for a long time under water. It took about half a year to study how to deal with this problem. Finally we found out a way to keep the insulating resistance of the transducers, which had worked in water for 48 hours, over 200  $m\Omega$ . Thus, the reliability of measured results was guaranteed. Data collection was carried out by IMP scattering data collection system.

In the tests, the vertical load and horizontal load were applied, in turn, on the same model instead of on the different models to avoid the effect of inhomogeneity of sample preparation. The vertical load of the platform model was 18.4 N in all, which is equivalent to 62100 kN of the prototype. The horizontal load weighs 3.9 N, which is equivalent to maximum ice pressure of 13160 kN on the prototype.

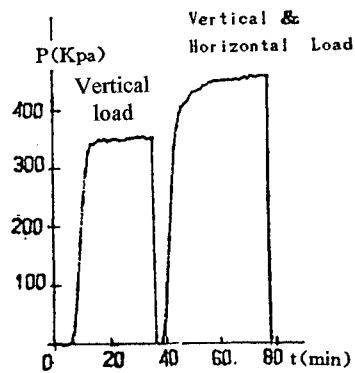
### 4 TEST RESULTS AND ANALYSES

#### 4.1 Reliability analyses

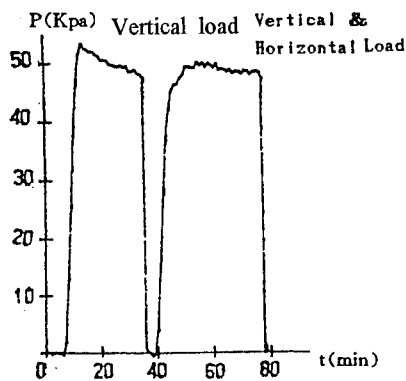
Fig. 3 shows the p-t curves measured by transducers No. 1, 2, 3, and 4. It can be seen that the measured data are rather steady. This indicates the transducers work well and the results are reliable.



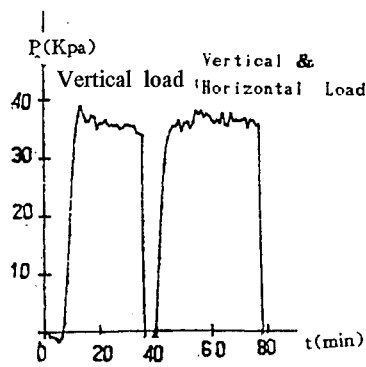
a. p-t curve from No.1  
(at the bottom of pillar A)



c. p-t curve from No.3  
(at the bottom of pillar C)



b. p-t curve from No.2  
(at the beam bottom)



d. p-t curve from No.4  
(at the beam bottom)

Fig.3 p-t curves measured by transducers

#### 4.2 Load transmission and back pressure distribution

From the p-t curves (shown in Fig. 3), it can be seen that when the platform was exerted by a vertical load, the back pressure on pillar bottoms increased gradually up to steady; by contrast, the back pressure on beam bottoms decreased. These indicate that as time lapsed, soft soil beneath the beam bottoms was continuously consolidated and its bearing capacity increased. The soft soil settlement beneath beam bottoms was greater than that of the sand layer beneath pillar bottoms, therefore when the platform was in a stabilized state, most of the loads were bore by pillars.

Comparison with the results measured from the model only under the vertical load, the back pressure measured from the model under both vertical and horizontal loads increased on the bottoms near to extended side of pillars and decreased on the bottoms apart from to the extended side significantly, but that on beam bottoms changed little and was not sensitive to the loading cases. The reason was that the beams were buried shallowly and the back pressure was controlled by the bearing capacity of upper soft soil.

The soil back pressure distributions on pillar and beam bottoms measured by the transducers (see Fig. 1) are shown in Fig. 4 and Fig. 5. Some deviations among the back pressure on

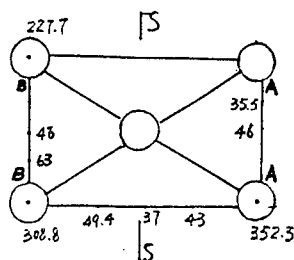


Fig. 4 Back pressure distribution (under vertical load)

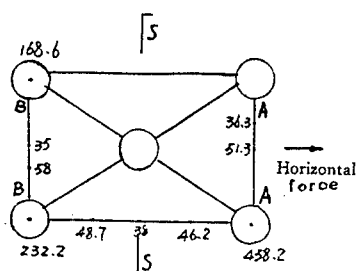


Fig. 5 Back pressure distribution (under vertical and horizontal loads)

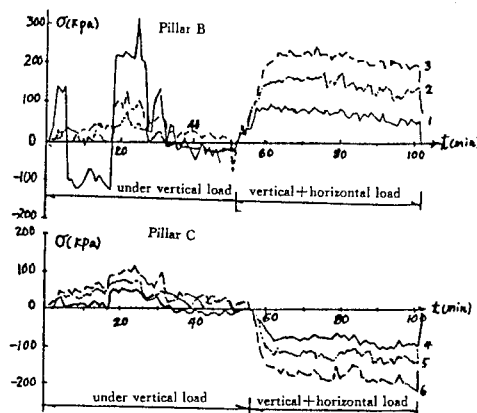


Fig. 6  $\sigma$ - $t$  curves at the points on the side of pillar B and C

the four pillar bottoms can be seen in Fig. 4. This might be due to the inhomogeneity of the prepared sample or the measurement errors. From Fig. 5, it can be seen that the back pressures are changed symmetrically about the

middle section s-s, after the platform was loaded horizontally.

#### 4.3 Stress distribution on the sides of pillars

Fig. 6 shows the curves of stress on the side of pillars versus time,  $\sigma$ - $t$ , for the pillars B and C. It can be seen that when the model was loaded vertically, the stress at each point increased slowly up to a peak, then decreased slowly to a steady value. The occurrence of stress peak was probably due to the fact that the soft soil settled greatly and the friction reached a peak value. After the soft soil consolidation fulfilled the vertical load was unloaded. Then the horizontal load was applied gradually and the vertical load was reloaded. There the measured stress under the both vertical and horizontal loads was steady.

#### 4.4 Share of Load

On the basis of the measured back pressure on bottoms of pillars and beams and the friction on pillar sides at two loading cases, the proportion of the back pressure and the friction to the total load is listed in Table 1.

Table 1 Share of load

Structure	Pillar bottoms	Beam bottoms	Sides of pillars
under vertical load	60%	20%	20%
under vertical & horizontal load	63%	19%	18%

It shows that horizontal load is not of remarkable influence on share proportions of load.

#### 4.5 Characteristics of settlement

Under the exertion of the vertical load, the settlement of the platform was 1.8 mm, and soil around the 4 pillars settled uniformly. But when

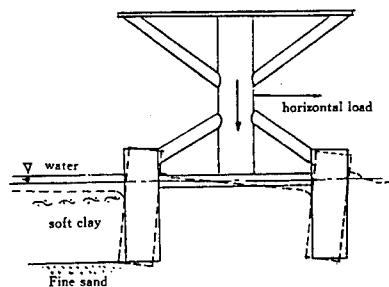


Fig.7 Surface of soft clay after horizontal loading (indicated with dashed line)

the horizontal load was added, the platform settled 0.9 mm more and tilted slightly to the direction of the horizontal load.

Soil surface steps settled totally for 9 mm under both vertical and horizontal loads. It is mainly due to the further consolidation of soft clay layer.

## REFERENCES

- Craig, W.H.1983. Simulation of Foundations for offshore Structures Using Centrifuge Modeling, Developments in Soil Mechanics and Foundation Engineering, Ed. by P.K.Banerjee, Applied Science Publishers, England.
- Craig, W.H.,& Ai.Saoudi, N.K.S. 1981. The Behaviour of some Model offshore Foundations, Proc. 10th Int. Conf. on Soil Mechanics and Foundation Engineering, Stockholm, Vol.2, pp83-86.
- Luong, M.P., Bonaz, R., Pecker, A.&Bourdin, B. 1988. Piles and Pile Groups Under Forced Horizontal Loadings in a Centrifuge(Summary), Centrifuge 88, Proc. of the Int. Conf. on Geotech. Centrifuge Modelling, Balkema. Rotterdam. pp513.

## 5 CONCLUSIONS

(1) It is ideal to perform offshore platform model tests with a centrifuge. Measured results such as back pressure and friction by the use of transducers and strain gauges in the centrifuge are reliable. The results clearly indicate the load share proportion of every structure units.

(2) The pillar bottom pressure accounts for 60% of the load on the platform. Beam bottom pressure shares about 20%. The friction on the sides of pillars is about 20%.

(3) The friction on the sides of pillars and the back pressure on pillar bottoms change as the centrifugal force increasing. When the vertical load  $P$  is low, it is mainly bore by friction on the sides of pillars. When  $P$  increases to a certain value, pillar ends displace and back pressure on pillar bottom is significant. So the maximum of the friction of the sides of pillars and that of the back pressure on pillar bottoms do not occur at the same time. Therefore, this should be paid attention to while designing.

(4) The stability of the beam-pillar platform is good. Its bearing capacity is high, and the settlement is little. The load is shared by pillars and beams.

# Geometric factors influencing the behaviour of side-bearing foundations in sand

E.A. Dickin  
University of Liverpool, UK

R. Nazir  
Universiti Teknologi Malaysia, Johor, Malaysia

**ABSTRACT:** Investigations into the factors influencing the behaviour of side-bearing piled foundations in sand are described. Moment-carrying capacity for short 1m diameter piles increases significantly with pile length/diameter ratio and with the pulling height /pile length ratio. Pile diameter has a significant effect over the range from 0.24m to 1m. The influence of slope proximity and soil packing is also studied. Observed moment limits are compared with predictions from several established design methods.

## 1. INTRODUCTION

Side-bearing pile or pier foundations are widely used, especially when resistance to horizontal loading is the dominant design requirement. Foundations for structures such as electrification gantries, advertisement and information posts primarily experience horizontal shear forces and overturning moments but relatively minor vertical forces which are often insignificant enough to neglect. The lack of adequate information and understanding of soil and pile

interaction makes analytical solutions of the problem complex. Due to this inadequate knowledge, semi-empirical and empirical methods offer the best approach in determining the load capacity for a pile or pier foundation subjected to such lateral loads. A summary of the geometric parameters which influence the behaviour of a side-bearing pile foundation significantly is given in Figure 1.

## 2. TEST EQUIPMENT AND MATERIALS

Tests were performed in the geotechnical centrifuge at the University of Liverpool described in detail by King et al. (1985). The facility has a capacity of 13g tonnes and is fitted with balanced swinging carriages which are essentially 0.56m long, 0.46m wide and 0.23m deep. The fine, dry Erith sand used throughout the testing program has a coefficient of uniformity of 1.5, grain sizes ranging from 0.125mm to 0.25mm and a  $D_{50}$  of 0.2mm. Tests were carried out in dense and loose packings with effective unit weights  $\gamma' = 16.4 \text{ kN/m}^3$  (density index  $I_d = 85\%$ ) and  $\gamma' = 14.4 \text{ kN/m}^3$  ( $I_d = 37\%$ ) respectively. Packages were prepared at unit gravity with the model held in position by means of a temporary cross frame. Dense sand beds were prepared by mechanical compaction in

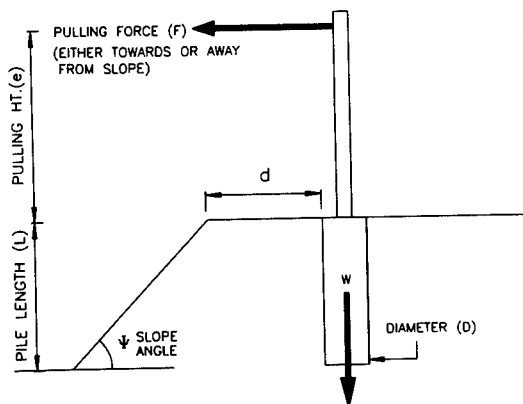


Fig.1. Geometric parameters in side-bearing foundations problems.



25mm layers using a small vibrator, while loose sand beds were prepared by pluviation from a maximum height of 250mm through a baffle containing 4mm diameter holes at 20mm spacings in a rectangular grid. Although Craig(1985) found significant differences in axial capacity between piles installed in flight and at unit gravity, any influence on their subsequent lateral loading response was relatively minor. Hence no significant installation errors are thought to have arisen in the research reported here.

Model foundations were made from stainless steel and ranged from 40mm to 100mm in length. Models 18.5mm and 48.5mm in diameter were fabricated such that, after coating with the parent sand using epoxy resin, their effective diameters were 20mm and 50mm respectively. Mild steel pulling arms, 10mm square in cross section, and ranging from 40mm to 320mm in length, were screwed into the top of the piles. Model piles in the conventional unit gravity tests were formed from 100mm diameter mild steel tube filled with concrete to provide rigidity and were 300mm and 400mm in length.

### 3. ARRANGEMENTS FOR CENTRIFUGAL AND CONVENTIONAL TESTS

A typical package arrangement in the centrifuge is illustrated in Figure 2 which shows details for

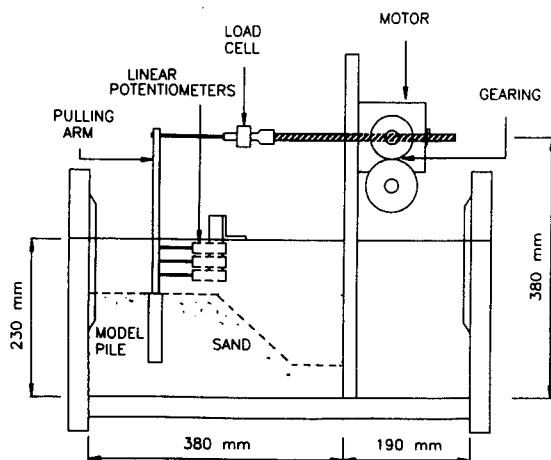


Fig.2. Centrifugal test package arrangement for sloping terrain.

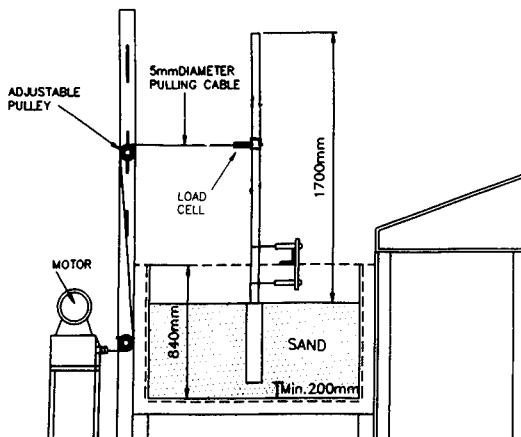


Fig.3. Test arrangement for conventional test.

a test involving sloping terrain. Several major modifications were made to the package from that used by Dickin and Wei(1991) to enable longer piles to be tested at higher pulling levels. These included an extended central partition wall and relocated pulling system. The tests were strain-controlled at a constant rate of horizontal displacement of the pulling cable of 0.4mm/min provided by a PARVALUX model 21SIS geared motor linked to a custom built worm and worm wheel mechanism to increase pulling power. During the test the pulling force and horizontal displacements were monitored by a SENSOTEC 1.14kN capacity load cell and three SAKAI linear potentiometers respectively which were linked to an ORION data logger. The results were processed by a BBC Master computer. Tests were terminated when the pulling force either reached a constant value, decreased in value or after a rotation of between 6° and 8° if the pulling force showed no sign of peaking. Results stored by the BBC computer were then transferred to IBM format and plotted out using UNIRAS subroutines for analysis purposes. A single test usually took an average of 35 minutes to complete.

The general arrangement for the unit gravity tests, which were also carried out in dense Erith sand, is shown in Figure 3. The reinforced bin used was 1.36m long, 1.22m wide and 0.84m deep. Strain-controlled tests were continued until just beyond the peak load value which was observed in all cases.

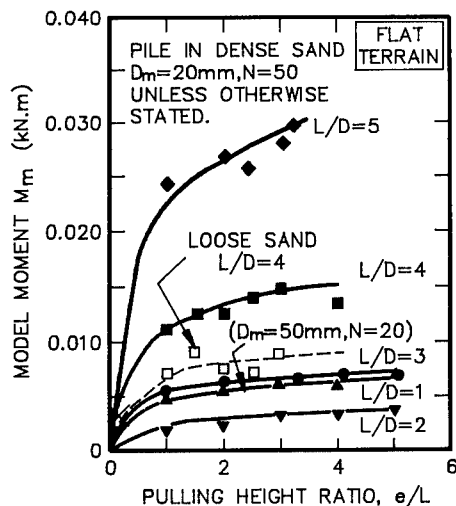


Fig.4. Variation of model moment  $M_m$  with  $e/L$  for piles embedded in dense and loose sand.

#### 4. EXPERIMENTAL PROGRAM AND RESULTS

In series 1, model piles with diameters  $D_m=20\text{mm}$  and  $50\text{mm}$  were tested at acceleration factors  $N=50$  and  $20$  respectively to simulate conditions around  $1\text{m}$  diameter

prototype piles. Test results from this series are summarised in Figure 4 which shows the variation of  $M_m$ , the maximum moment at ground level in model terms, with pulling height ratio  $e/L$  for various embedment ratios  $L/D$ . Values of  $M_m$  increase significantly with both embedment ratio and pulling height. Moments for the shorter piles tend to remain almost constant for pulling height ratios greater than 3 as established by Dickin and Wei(1991). However this is not the case for longer piles. Due to test preparation difficulties, data for a pile with  $L/D=1$  was obtained by testing a  $50\text{mm}$  diameter model at  $20g$ . It may be noted that  $M_m$  from this test exceeded that for a test at  $50g$  on a  $20\text{mm}$  diameter pile with  $L/D=2$ . However, when expressed in dimensionless form as a prototype moment factor  $M'_p = M_p / \gamma' D_p L_p^3$ , where  $M_p = M_m \cdot N^3$ , the results from the  $20g$  tests are consistent with the general decrease in  $M'_p$  with embedment ratio up to  $L/D=4$  as seen in Figure 5. There is some evidence that for larger  $L/D$  ratios no further decrease in  $M'_p$  occurs. This could be confirmed by the testing of longer piles. However, these would be outside the range encountered in the field for side-bearing foundations and would require greater depth than was available in the package described. The longest piles reported by UIC/ORE(1957) and Balfour Beatty(1986) had  $L/D$  ratios of  $4.9$  and  $4.2$  respectively. Moment factors for piles with  $L/D=4$  in loose sand are  $30\%$  lower than those for dense sand, in broad agreement with the findings of Dickin and Wei(1991) for shorter piles. The results for loose sand were rather scattered due to local non-homogeneity during package preparation. Nevertheless, the tests serve to identify the potential variation in moment-carrying capacity due to soil packing. The relationship between pile rotation 'at failure' and pulling height ratio showed considerable scatter. The longer piles loaded at a low level generally required relatively large rotations to mobilise moment resistance. For such piles an appropriate design approach would be based on an allowable rotation rather than one applying a suitable factor of safety to the moment limit.

Results from series 2, in which  $20\text{mm}$  diameter model piles with  $L/D=5$  were tested at different accelerations, are shown in Figure 6 in prototype terms. While limiting moments  $M_p$

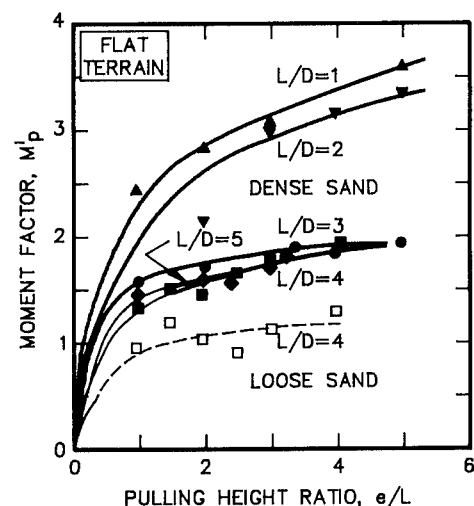


Fig.5. Variation of moment factor  $M'_p$  with  $e/L$  for  $1\text{m}$  diameter piles in dense and loose sand.

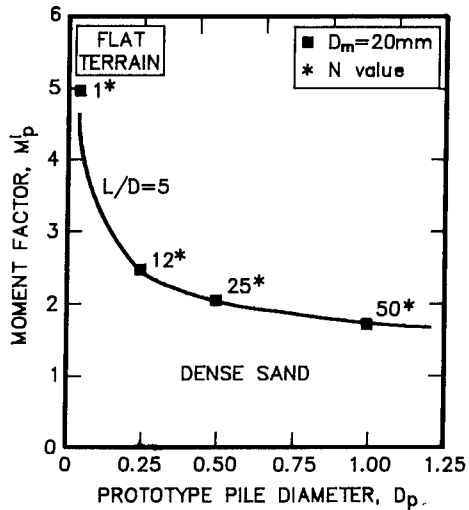


Fig.6. Variation of moment factor  $M'_p$  with pile diameter.

increase considerably with diameter, the moment factor  $M'_p$  reduces significantly with an increase in pile diameter up to  $D_p=1\text{m}$ . Thus the  $M'_p$  value for a 240mm diameter pile is 40% higher than that for its 1m diameter equivalent. The

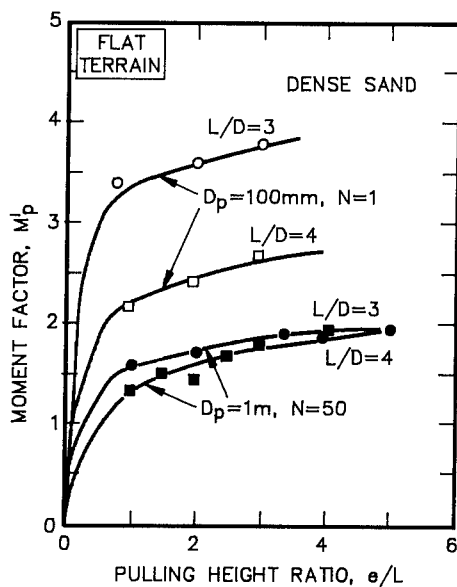


Fig.7. Variation of moment factor  $M'_p$  with  $e/L$  for 100mm and 1m diameter piles in dense sand

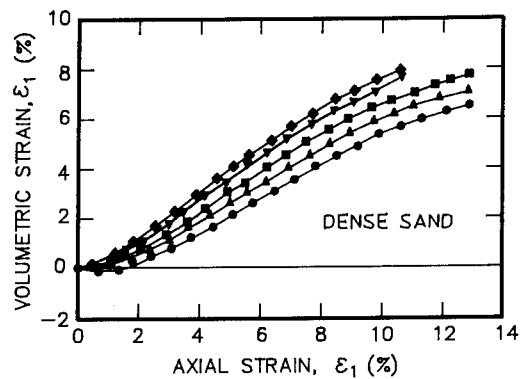
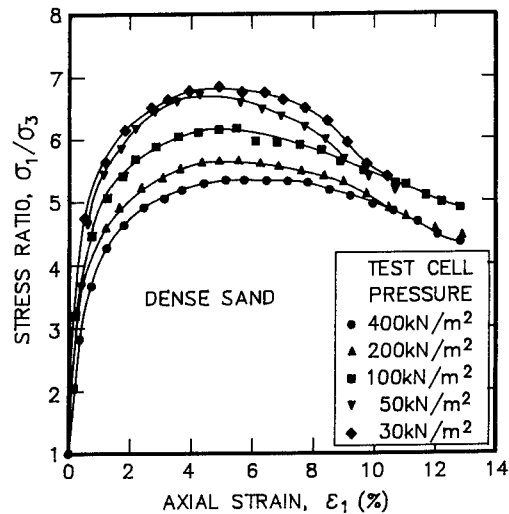


Fig.8. Variation of strength and dilatant characteristics with stress level for Erith sand.

ratio between pile circumference and average sand grain size for the model piles used was in excess of 300, well above the critical value of 40 where grain size effects have been previously identified. Independent evidence of the influence of pile diameter is seen in Figure 7 which shows that moment factors for 100mm diameter piles with  $L/D=3$  and  $L/D=4$  in unit gravity tests exceed those for 1m piles by a factor of at least 50%. This influence of size arises from the stress-dependent behaviour of Erith sand typified by the triaxial test data in Figure 8 obtained by Liem(1988), where both maximum stress ratio and dilation characteristics reduce with increased confining stress level.

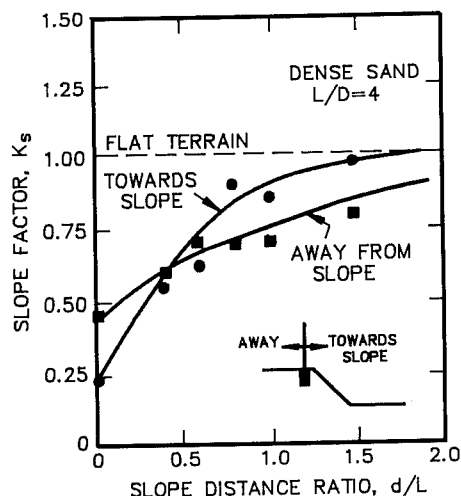


Fig.9. Variation of slope factor  $K_s$  with slope distance  $d/L$  for piles in dense sand.

Side-bearing foundations employed to support gantries carrying overhead power along electrified railway networks are commonly located close to cuttings or embankments. The influence of slope proximity was therefore investigated in series 3 tests, the results from which are summarised in Figure 9. Slope factors  $K_s$ , defined as  $M'_p(\text{sloping terrain})/M'_p(\text{flat terrain})$ , for a pile with  $L/D=4$  close to the top of a 36 degree slope are plotted against slope distance ratio  $d/L$  where  $d$  is defined in Figure 1. On this limited evidence a pile at the top of a slope and pulled towards it has a lower moment value than that of a pile pulled in the opposite direction. However the reverse occurs when  $d > 0.5L$ . The slope effect can be neglected when the pile is at a distance  $d > 1.5L$  and pull is towards the slope. However, at that point, when pulled away from the slope the pile can only develop approximately 75% of its full moment carrying capacity. In contrast, UIC/ORE(1957) tabulate  $K_s$  values of 0.85 and 0.95 for piles with  $d < L$  pulled towards and away from a slope respectively.

Moment factors obtained for  $e/L=3$  from the design formulae of UIC/ORE(1957) and Broms(1964) yield reasonably good agreement with the centrifuge data for dense sand in Figure 10 while, not unexpectedly, methods based on rotational servcibility limits proposed by

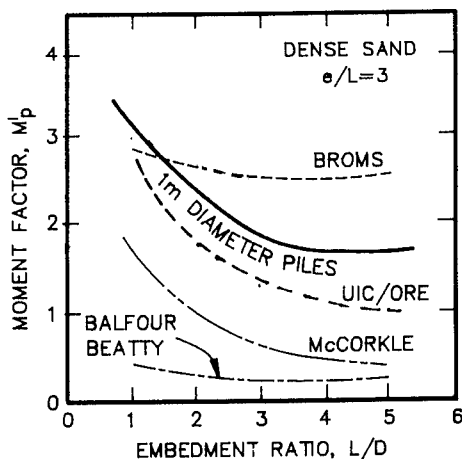


Fig.10. Comparison between moment factor  $M'_p$  obtained from design formulae and centrifugal tests for 1m diameter piles in dense sand.

McCorkle(1969) and Balfour Beatty(1988) significantly underestimate observation by a factor of about 4. Figures 11 and 12 compare predicted values with observation for a pile with  $L/D=4$  for various  $e/L$  values in dense and loose sand respectively. Broms' design method yields best agreement with the centrifuge results for almost all  $e/L$  values for piles in both sand packings. Resistance to rotation is essentially provided by passive soil forces as reflected in Broms' formula which gives the value of  $M = K_p \gamma' DL^3 e / 2(e+L)$ . Whilst, due to the influence of soil effective unit weight, a considerably reduced resistance to overturning would be obtained for piles below the water table, the moment factor  $M'$  would be unaffected since  $M' = K_p e / 2(e+L)$ .

## 5. CONCLUSIONS

The behaviour of side-bearing piled foundations in sand is governed by pile length and diameter and by the level at which lateral loading is applied. The influence of pulling height, although small for piles with  $L/D < 3$  and  $e/L > 3$  is still significant when  $e/L > 3$  for longer piles. Longer piles require the greatest rotations to mobilise their moment limit, especially when subjected to horizontal load at a relatively low level.

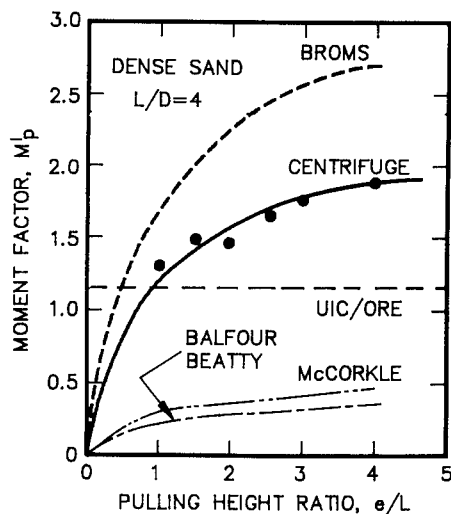


Fig.11. Variation of moment factor  $M'_p$  and pulling height  $e/L$  from design formulae and centrifugal tests for 1m diameter piles in dense sand.

The moment limit also increases with pile diameter. Although the dimensionless moment factor reduces with increased diameter, little further reduction is thought to occur for diameters in excess of 1m.

The moment capacity is also influenced by soil characteristics and ground surface profile. Hence, a considerably reduced moment limit is observed when a pile is located close to a slope. The reduction increases with slope proximity and is dependent upon the direction of pull. For  $d/L > 0.5$ , a pile pulled towards the slope can withstand a higher moment than one experiencing the opposite pull. However if  $d/L < 0.5$  the reverse occurs. The effect of slope can be neglected when  $d/L > 1.5$ . Generally the effect is more critical when pull is away from the slope.

Broms and UIC/ORE formulae predict observation fairly well for piles in both sand packings, while UIC/ORE gives particularly good agreement for piles in loose sand.

## REFERENCES

- Balfour Beatty Construction Ltd. 1986. Design calculation of ORE foundation design method.  
Broms, B.B. 1964. Lateral resistance of piles in cohesionless soils. *Journal of Soil Mechanics*

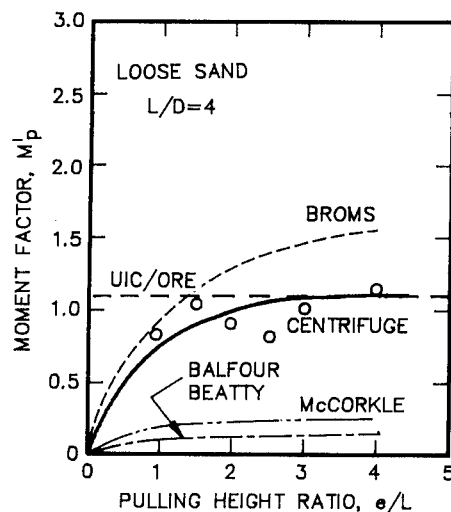


Fig.12. Variation of moment factor  $M'_p$  and pulling height  $e/L$  from design formulae and centrifugal tests for 1m diameter piles in loose sand.

- and Foundation Division, *Proc. of the ASCE*, No.SM3, Vol.90: 79-99.  
Craig, W.H. 1985. Installation studies for model piles. *Proceedings of Symposium on the Applications of Centrifuge Modelling to Geotechnical Design*, ed Craig, W.H.:440-455. Rotterdam:Balkema  
Dickin, E.A. and Wei, M.J. 1991. Moment carrying capacity of short piles in sand. *Centrifuge 1991*, ed Ko, H.Y and McLean, F.G.:277-284. Rotterdam:Balkema.  
King, G.J.W, Dickin, E.A. and Lyndon, A. 1985. The development of a medium size centrifugal testing facility. *Proceedings of Symposium on Applications of Centrifuge Modelling to Geotechnical Design*, ed Craig, W.H.:25-36. Rotterdam:Balkema.  
Liem, D.H.W. 1988. Appraisal of Lade's elastoplastic stress-strain models and their application to vertical anchor behaviour in sand. Ph.D. Thesis, University of Liverpool, UK.  
McCorkle, B.L. 1969. Side-bearing pier foundations, *Civil Engineering - Proc. of the ASCE*: 65-66  
UIC/ORE, (1957). Calculation of catenary masts and foundations, *Interim report No.1*, International Union of Railways/Office for Research and Experiments, Utrecht.

## 8 Shallow foundations

## Bearing response of shallow foundations in uncemented calcareous soil

I. M. S. Finnie & M. F. Randolph

Department of Civil Engineering, The University of Western Australia, Nedlands, W.A., Australia

**ABSTRACT:** Centrifuge model tests have been undertaken to investigate the bearing response of shallow foundations in normally consolidated calcareous sand and silt. The results exhibit a nearly linear increase in bearing pressure with penetration, the gradient of which was virtually independent of diameter. This response is indicative of a punching/local shear type failure mechanism, which was influenced as much by the compressibility of the supporting soil as the frictional strength. The bearing response is interpreted in terms of a bearing 'modulus', the value of which is closely linked to the void ratio of the soil and which is compared with simple analytical approaches involving the one-dimensional compressibility of the soil, and standard bearing capacity theory.

### 1 INTRODUCTION

Shallow foundations provide an alternative to the conventional piled foundations used by the majority of offshore structures in Australian waters, especially for small platforms. Tripod structures on circular foundations of 15 m diameter have been installed in Bass Strait, but have yet to be adopted for the more compressible calcareous soils of the North-West Shelf.

A series of centrifuge tests were performed at the University of Western Australia, to obtain detailed data regarding the performance of shallow foundations, typical in size of those for conventional jack-up rigs and small gravity-base platforms, in calcareous soils characteristic of the North-West Shelf. The paper reviews the observed bearing response in uniform uncemented calcareous sand and silt, and interprets the results in terms of one-dimensional compression of the underlying soil and a traditional bearing capacity approach.

North-West Shelf of Australia. This was mixed with calcium carbonate powder to create a silty-sand, characteristic of prototype sediments that exhibit cone penetration resistances of less than 500 kPa, even at depths greater than 10 m. The two soil types will be referred to as 'sand' and 'silt' hereafter. Key properties of the sand and silt are given in Table 1.

Table 1 Representative soil properties

Property	Sand	Silt
Specific gravity, $G_s$	2.77	2.77
Calcium carbonate content, (%)	95	98
Mean particle size, $d_{50}$ (mm)	0.1	0.03
Coefficient of uniformity, $C_u$	100	45
Min. density, $\gamma_{dmin}$ (kN/m <sup>3</sup> )	9.1	8.0
Max. density, $\gamma_{dmax}$ (kN/m <sup>3</sup> )	14.0	12.3
Compression index, $C_p$	0.15	0.60
Critical state friction angle, $\phi_{cv}$ (°)	39	38
Peak friction angle, $\phi_{peak}$ (°)	43	42

Vertical displacements were applied by an electrical loading actuator, bolted to the top of the strong-box in which the soil was consolidated in flight, as shown on Figure 1. The tests were generally performed at an acceleration level of 100 g. The bearing response is presented in terms of prototype units, assuming a linear scale factor of 1/100. The test

### 2 CENTRIFUGE TESTS

Circular flat foundations, 1 m to 15 m in diameter, were modelled in uniform normally consolidated uncemented calcareous silty-sand and sandy-silt. The sandy-silt was obtained from the sea-bed at the Goodwyn field, on the

results presented here are mainly from samples saturated with water, with foundations loaded at rates sufficiently low to give drained conditions.

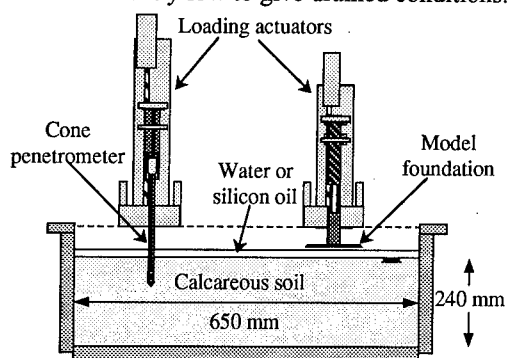


Figure 1 Schematic of test package

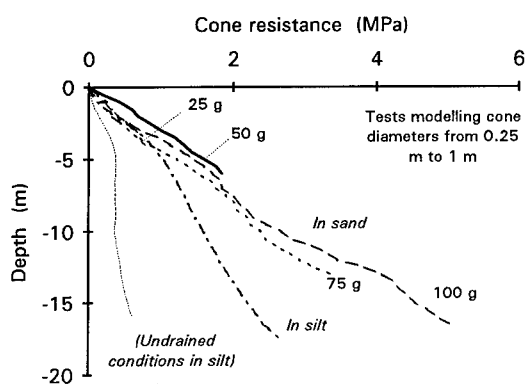


Figure 2 Profiles of cone resistance

Multiple cone penetration tests, with a 10 mm diameter cone, were performed in-flight using a second actuator. Profiles of cone resistance are shown in Figure 2. The profiles are approximately linear with depth (particularly for the calcareous sand), and tests conducted at different  $g$  levels show good agreement when plotted to an equivalent prototype depth.

## 2.1 Results of Foundation Tests

The drained bearing response of circular foundations in normally consolidated sand and silt are shown on Figures 3 and 4. The response was found to be quasi-linear, with a ratio of applied pressure to penetration displacement (referred to here as a bearing modulus) which was relatively independent of diameter. No yield pressure or other indication of 'bearing capacity' was evident.

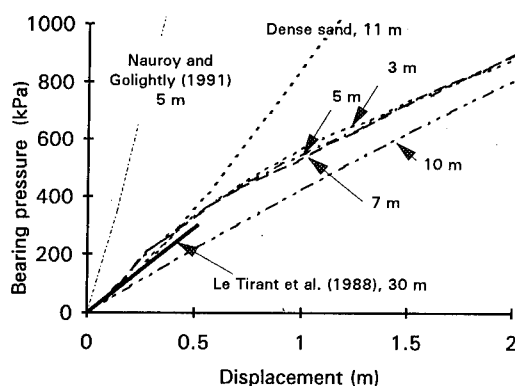


Figure 3 Bearing response in calcareous sand

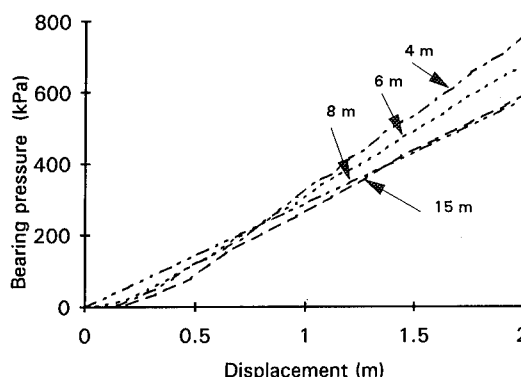


Figure 4 Bearing response in calcareous silt

Also shown on Figure 3 are the results of centrifuge tests reported by Nauroy and Golightly (1991) and Le Tirant et al (1988), and also results from a foundation test in a densified version of the present sand (Finnie 1993). In each case, scaling has been based on the assumption of an effective unit weight for the soil of  $8 \text{ kN/m}^3$ . The test result from Nauroy and Golightly (1991) is significantly stiffer than the other data, the reason for which is not clear.

Where no apparent yield occurs in the bearing response, the 'bearing capacity' is conventionally taken as the bearing pressure to cause a penetration of 10 % of the foundation diameter. An alternative approach, which appears more appropriate for the almost linear foundation response shown here, is to consider the gradient of the bearing response. This may be termed the 'bearing modulus',  $Q = q/w$ , where  $q$  is the average bearing pressure and  $w$  is the displacement (also equal to the current depth of the foundation).



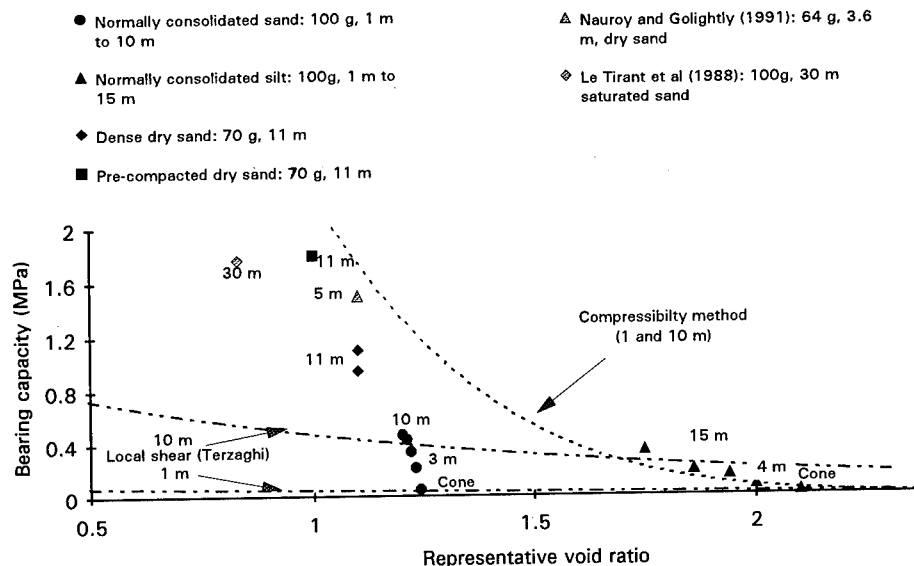


Figure 5 Bearing pressure at penetration of 10 % of foundation diameter

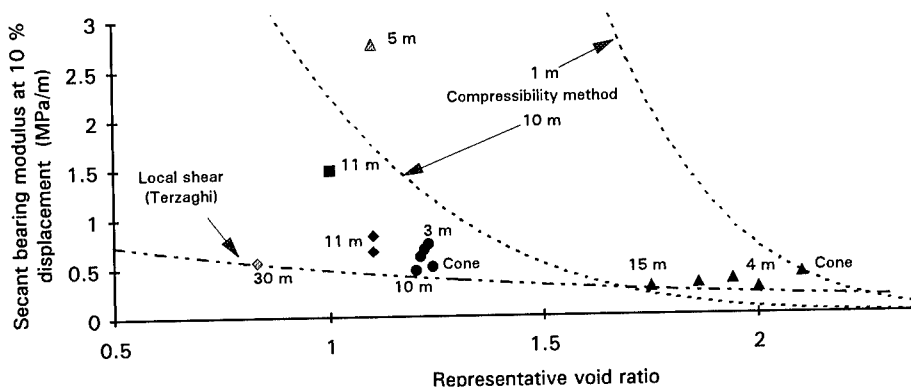


Figure 6 Secant bearing modulus at penetration of 10 % of foundation diameter

The bearing pressure at 10 % displacement, and the secant bearing moduli,  $Q$ , at the same displacement, are shown on Figures 5 and 6 as a function of the average initial void ratio down to a depth of half a diameter. It may be seen that the latter approach provides a more consistent picture (with the exception of the test reported by Nauroy and Golightly (1991)).

It is clear that the void ratio plays a dominant role in determining the foundation response, as proposed by Semple (1988). Other factors also affect the bearing response, in particular the compressibility of the soil. Thus, following Nauroy and Le Tirant (1983), it is interesting to compare the bearing modulus with the limiting compressibility,  $C_{pl}$  (defined at a vertical effective stress of 800 kPa). Table 2 summarises

values of void ratio, limiting compressibility and bearing modulus for the tests.

Table 2 Key properties of centrifuge tests

Property	Sand	Silt	(1)	(2)
Diameter (m)	1→10	1→10	30	5.4
Void ratio, $e_0$	1.2	1.8	0.83	1.1
Compressibility, $C_{pl}$	0.15	0.62	0.20	0.36
Bearing Modulus, $Q$ (kPa/m)	600	300	500	2800

Notes: (1) - Le Tirant et al (1988)  
(2) - Nauroy and Golightly (1991)

Apart from the Nauroy and Golightly result, the bearing modulus varies inversely with the limiting compressibility.

### 3 ANALYSES

The quasi-linear response exhibited by all the tests is indicative of punching shear. The associated mechanism is composed of soil compression immediately beneath the foundation, with localised yield beneath the perimeter, shown schematically on Figure 7.

Vesic (1973) stated that there was a lack of rational methods for adequately assessing the bearing capacity in cases where local or punching shear is expected. The two traditional approaches that have been used are (a) to treat the foundation response as a deformation problem, estimating the penetration of the foundation from the one-dimensional compression response of the material, and (b) to use classical bearing capacity factors, but with a reduced value of friction angle.

These two approaches are explored below. In view of the quasi-linear bearing response, it might seem that the former approach, treating the response as a deformation problem, would be more attractive. However, it will be shown that such an approach does not capture the observed 'diameter-independence' of the bearing modulus. By contrast, treating the response as one of continuous failure, linking the bearing modulus to a classical bearing capacity factor, gives a good correlation with the data.

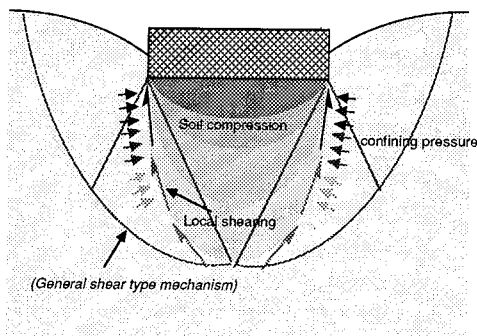


Figure 7 Punching shear mechanism

#### 3.1 Compressibility Approach

Under drained conditions, it appears that the major contribution to penetration of the foundation occurs through compression of the soil immediately below the foundation. Poulos et al (1984) have outlined an approach for calculating this compression, linking the elastic distribution of vertical stress change beneath the

foundation, to the oedometer response of the soil. Numerical integration of the strains then allows estimation of the foundation movement.

It may be shown that the full integration procedure may be simplified, without loss of accuracy, by considering the compression of a layer of soil, of thickness equal to half the foundation diameter, under a uniform vertical stress equal to the applied bearing pressure.

Typical one dimensional compression data are shown on Figure 8, for the sand and silt. The compressibility,  $m_v$ , for the sand and silt may be idealised by the following relationship,

$$m_v = \frac{5}{p_a(1+e_o)(3.3-e_o)^{6.8}} \quad (1)$$

where  $p_a$  is atmospheric pressure (100 kPa) and  $e_o$  is the initial void ratio. The resulting compression response is compared with the data on Figure 8. The fit with the oedometer data for the silt is only moderate at low stress levels. However, void ratios deduced from centrifuge tests, where slight disturbance of the sample led to some densification, support the compression relationship given above (Finnie, 1993).

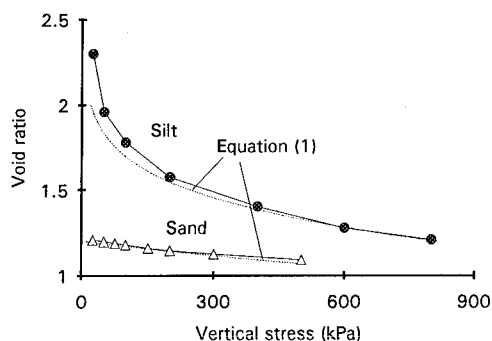


Figure 8 One-dimensional compression response of the calcareous sand and silt

Using the simplified approach of considering the one-dimensional compression of a layer of soil half a diameter ( $D$ ) deep, the bearing modulus,  $Q$ , may be written as

$$Q = \frac{q}{z} = \frac{0.2 p_a}{0.5 D} (1+e_o)(3.3-e_o)^{6.8} \quad (2)$$

where  $z$  is the foundation settlement. Defining the bearing capacity as the pressure reached after a settlement of  $z/D = 0.1$ , the variation of bearing capacity, and the corresponding secant

modulus, with void ratio, are presented on Figure 5 and 6 respectively, for 1 m and 10 m diameter foundations.

The form of the relationship in (2) entails that the bearing 'capacity' is independent of diameter, while the secant bearing modulus is proportional to diameter. Thus, while the approach appears to give reasonable agreement with the measured capacities in silt (Figure 5), the bearing capacity and modulus in the sand is significantly over predicted. Since the sand is less compressible than the silt, foundation settlement will tend to be accommodated by soil yield and displacement, rather than just by compression.

### 3.2 Bearing Capacity Method

The traditional approach for calculating the bearing capacity of a circular foundation of diameter  $D$ , on incompressible frictional soil, with an effective unit weight  $\gamma'$ , is,

$$q_u = 0.3\gamma' DN_\gamma + \gamma' z N_q \quad (3)$$

where  $z$  is the depth of embedment (or penetration from the surface), and the bearing capacity factors are given by (e.g. Hansen, 1968)

$$N_q = e^{\pi \tan \phi} \tan^2(45^\circ + \phi/2) \quad (4)$$

and

$$N_\gamma \approx 2(N_q + 1) \tan \phi \quad (5)$$

The first term in Equation 3 accounts for the component of bearing capacity that is provided by the self weight of the soil, yielding in a general shear type mechanism beneath the foundation, as shown on Figure 7. The second term accounts for the benefit of overburden stress, equal to the self weight of the soil above the level of the foundation.

To account for the reduced bearing capacity, experienced by foundations failing in local shear, compared with general shear, Terzaghi (1943) recommended a reduced friction angle  $\phi_r$  given

$$\phi_r = \tan^{-1}\left(\frac{2}{3} \tan \phi\right) \quad (6)$$

This method has been used successfully in the

field (Dutt and Ingram, 1988), although Poulos and Chua (1985) found that this technique tended to overpredict the bearing capacity of shallow foundations in calcareous soil.

Hull et al. (1988) have presented the following relationship between ultimate friction angle and ultimate void ratio, for a number of calcareous sands:

$$\phi_u = 0.733 - 0.117(e_u - 0.6) \quad (7)$$

This relationship was combined with equation (3) - (5), and the reduction in friction angle given by (6), to give estimates of bearing capacity and secant bearing modulus for a range of void ratios. The results are compared with the experimental data in Figures 5 and 6 (see curves labelled 'Local shear (Terzaghi)').

The agreement is reasonable between with the test results in silt and sand, and the result of Le Tirant et al (1988). The bearing capacity in the dense and precompacted sand is under predicted. In these soils significant dilation may have been mobilised, accounting for the difference.

### 3.3 Alternative Approach

For surface foundations on silica sand, the two terms in equation (3) may be determined independently by taking the gradient of  $dq/dz$  after yield as equal to  $\gamma' N_q$ , and extrapolating back to zero penetration to obtain the first term. However, this approach will not work for the tests reported here on calcareous soil, as the bearing response is virtually linear from the start, with no obvious yield point.

The test results have already been interpreted in terms of a bearing modulus,  $Q$ , and this may be non-dimensionalised as

$$M = \frac{Q}{\gamma'} = \frac{q}{\gamma' z} \quad (8)$$

where  $M$  is a 'bearing modulus factor'.

The procedure used for silica sand, if applied to the current tests, would imply that the first term in equation (3) has a negligible contribution, while the bearing capacity factor,  $N_q$ , may be taken as numerically equal to the non-dimensionalised bearing modulus,  $M$ .

This approach is explored in Table 3, taking the experimental secant bearing modulus at an applied pressure of 200 kPa (given the diameter independent nature of the results, this is more logical than taking the modulus at an arbitrary

normalised penetration). The ultimate friction angle has been used in calculating  $N_q$ .

Table 3 Relative values of  $M$  and  $N_q$

	Sand	Silt	Dense sand
$Q_{exp}$ @ 200kPa: kPa/m	650	300	980
Self-weight, $\gamma'$ : kN/m <sup>3</sup>	8	6	8
Modulus, $M = Q/\gamma'$	81	50	122
Friction angle, $\phi'$ : °	39	38	42
Bearing cap. factor, $N_q$	56	49	85
Ratio, $M/N_q$	1.4	1.0	1.4

The values of  $M$  and  $N_q$  are similar, which implies two alternative approaches for predicting the foundation performance:

(1) The traditional bearing capacity approach of equation (3) may be used, in conjunction with a reduced friction angle (equation (6)), to give the bearing capacity at a penetration of 0.1D.

(2) The bearing modulus may be estimated directly as  $Q = \gamma' N_q$  (equation (4) with no reduction in friction angle).

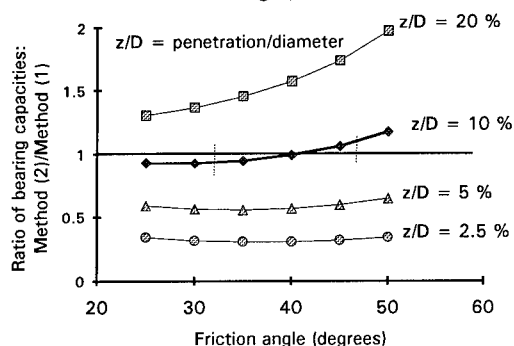


Figure 9 Comparison between proposed and traditional bearing capacity approaches

These two approaches are compared in Figure 9 for a range of penetration values. It may be seen that, for the conventional definition of bearing capacity, at a displacement of 10 % of the diameter, the agreement between the two approaches is within 10 % for friction angles between 20° and 50°.

#### 4 CONCLUSIONS

A series of centrifuge model tests of shallow circular foundations on uncemented calcareous sand and silt have shown that the bearing response is approximately linear, and shows

little variation with the diameter of the foundation. The relationship between bearing capacity and void ratio of the type suggested by Semple (1988), may be explained by the effect of void ratio on compressibility and shear strength. However, the concept of a bearing modulus (gradient of pressure-displacement response) appears more useful than that of bearing capacity.

Estimation of the bearing modulus from the one-dimensional compression response of the material does not match the diameter independent nature of the test data. Instead, an approach based on traditional bearing capacity theory, but ignoring the contribution from the self-weight term ( $N_\gamma$ ), is proposed.

#### REFERENCES

- Dutt R.N. and Ingram W.B. 1988. Bearing capacity of jack-up footings in carbonate granular sediments. *Engineering of Calcareous Sediments*: 291-296. Rotterdam: Balkema.
- Finnie, I.M.S. 1993. *The behaviour of shallow foundations on calcareous soil*. PhD Thesis, The University of Western Australia.
- Hull T.S., Poulos H.G. and Alehossein H. 1988. The static behaviour of various calcareous sediments. *Engineering of Calcareous Sediments*: 1:87-96. Rotterdam: Balkema.
- Le Tirant P. et al. (1988). Centrifuge simulation of the behaviour of a shallow foundation for offshore structure on calcareous sand. *Centrifuge '88*: 345-349. Rotterdam: Balkema.
- Nauroy J-F. and Golightly C (1991). Bearing capacity of a shallow foundation on calcareous sand. *Centrifuge '91*: 387-392. Rotterdam: Balkema
- Poulos H.G. and Chua E.W. (1986). *Bearing capacity of foundations on calcareous sand*. Res. Report No.515, University of Sydney.
- Semple R.M. (1988). The mechanical properties of carbonate soils. *Engineering of Calcareous Sediments*: 2:807-836. Rotterdam: Balkema.
- Terzaghi, K. (1943). *Theoretical soil mechanics*. John Wiley and Sons, New York.
- Vesic, A.S. (1973). Analysis of ultimate loads of shallow foundations. *Journal of the Soil Mechanics and Foundations Division*, A.S.C.E. 99(SM1):45-73.
- Vesic A.S. (1975). Bearing capacity of shallow foundations. *Foundation Engineering Handbook*: Chapter 3:121-147. Van Nostrand Reinford Company.

## Influence of initial conditions on bearing characteristics of sand

Katsutoshi Ueno  
Department of Civil Engineering, Utsunomiya  
University, Japan

Toshihiko Nakatomi  
Asahi Chemical Industrial Co., Ltd, Japan

Kenji Mito  
Nishimatsu Construction Co., Ltd, Japan

Osamu Kusakabe  
Department of Civil Engineering, Hiroshima University,  
Japan

**Abstract:** In centrifuge model test, a model ground prepared under the gravitational field is subjected to a self weight compression due to the accelerating. Therefore it is necessary to know for precise experiments how the initial conditions have changed since the model ground was prepared under 1g, and how the changes affect test results. The authors examined how the effect of initial conditions of sand affected bearing characteristics of a model shallow foundation. First, compression tests on sand imposed by a set of ten cycles of centrifuge operations up to 100g and down to 1g were conducted to examine the change in the void ratio and the initial stress condition represented by the coefficient of earth pressure at rest ( $K_0$ ). Second, loading tests with a circular shallow foundation on sand were performed. A noticeable change in void ratio due to the change in centrifuge acceleration was observed. While about five cycles were required until model conditions stabilized, most of the void ratio changes occurred during the first cycle. The loading test results showed that the ultimate bearing capacity on a dry sand increased with increasing  $K_0$ -value.

### 1 INTRODUCTION

The bearing capacity of shallow foundations on soils has been studied and summarized by many researchers, such as De Beer (1965) and Vesic' (1975). Little attention, however, has been paid to the influence of anisotropic initial stress conditions on bearing characteristics, especially in experimental studies on sand, although the initial stress condition is an important parameter when the behavior of soil is considered.

The anisotropic initial stress condition is usually represented by the coefficient of earth pressure at rest  $K_0 = \alpha_h' / \alpha_v'$ , where  $\alpha_h'$  and  $\alpha_v'$  are effective horizontal and vertical stresses, respectively. D'Appolonia and Lambe (1970), and Iizuka et al. (1987) demonstrated the influence of  $K_0$  on the behavior of shallow foundations on clay by means of finite element analysis. The influence of initial stress condition, however, has not yet been examined experimentally.

In centrifuge model tests, model ground will be subjected to an anisotropic consolidation and/or compression history by the nature of centrifuge operation. It is possible that  $K_0$ -values, i.e., initial stress conditions, will affect test results, even for sands. The authors tackled this problem and conducted two types of centrifuge model tests. First, change in void ratio and in  $K_0$  due to centrifuge operation were measured in order to evaluate

the test procedure. Furthermore, influences of the centrifuge operation on the results of loading tests of shallow footings were examined. The influence of  $K_0$  on bearing capacity of sands is discussed in this paper, based on these centrifuge tests.

### 2 APPARATUS, MATERIAL AND PROCEDURES

The centrifuge used was a balanced beam centrifuge, having an effective radius of 1.18m, driven by a 11kW AC motor, located at Utsunomiya University. Specifications of this centrifuge are tabulated in Table 1. Further detailed descriptions of the centrifuge are presented in Kusakabe et al. (1991).

Table 1. Specification of the centrifuge used

Effective radius	1.18 (m)
Maximum acceleration	120 (g)
Payload	150 (kg)
Capacity	18 (g-t)
Drive power	11 (kW)

The soil container used was a rectangular strong box made of steel plates with 0.009m thickness, with internal dimensions of 0.500m length, 0.152m width and 0.320m depth. The bottom of the container was curved to coincide with the circumference of rotation. The front side was made of a 0.013m thick acrylic plate, reinforced by a steel frame, which permitted visual observation. In order to reduce side friction, the soil container was equipped with two lubrication layers made from silicon grease and 0.2mm thick latex membranes.

The sand used was air dried Toyoura sand which is a uniform fine sand. Indexes of the sand are tabulated in Table 2. The sand was pluviated into the soil container through the air from 0.90 (m) high. After pluviating, the surface of the sand was scraped in order to coincide with the circumferential plane corresponding to the effective radius of the centrifuge. The model sand had average initial thickness ( $H_0$ ) of 0.240 (m) determined by distances from the top of the container to the sand surface measured by a caliper having a scale of  $5 \times 10^{-5}$  (m). In loading tests, initial void ratio ranging from 0.665 to 0.685 and initial dry density ranging from 1.597 to 1.578 ( $\text{g/cm}^3$ ) were determined by the measurements of the total volume and the total weight of the sand. Standard deviations of the initial void ratio and the initial dry density were  $6.26 \times 10^{-3}$  and  $5.94 \times 10^{-3}$  ( $\text{g/cm}^3$ ), respectively. In relative density, these errors were within 81.1 (%)  $\pm$  2.5 (%).

A loading system, shown in Fig. 1, consisted of an electrical jack with a 60W AC motor. This system was used to drive a model footing into sand with a constant loading rate of 1 (mm/min). The steel circular model footing of 0.030 (m) in diameter (B), and 0.040 (m) in thickness was solidly jointed to the jack through a load cell. Settlement of the footing was measured by a LVDT (resolution  $10^{-6}$ (m), capacity  $10^{-2}$ (m), strain gauge type).

Two earth pressure cells were embedded at a depth of around 0.170(m) to measure both vertical stress  $\sigma_v$  and horizontal stress  $\sigma_h$ . Measured vertical stresses were verified by corresponding calculated values according to the following equation:

$$\sigma_v = \int_{r_0}^r \rho_d r \omega^2 dr \quad (1)$$

where  $r$  is the radius at the measuring point in (m);  $r_0$ , radius at ground surface in (m);  $\rho_d$ , dry density of tested sand in ( $\text{kg/m}^3$ );  $\omega$ , rotating rate in (rad/sec). According to preliminary examinations for earth pressure cells, the values measured, of which hysteresis errors were less than 0.5 (%) coincided well with calculated values.

Settlement of the sand surface was measured by another LVDT (DC differential transformer) to obtain void ratio change of the sand under the acceleration at which the loading tests were conducted. All data were acquired by a data logger placed in the laboratory, and sent to a personal computer to be stored and processed. To avoid EMI and to promote precise measuring, the transducers were connected to the data logger by using double shielded and twisted pair cables through a 20 poles slip ring stack.

Parameters addressed in the present study were overcompression ratio (OCR), coefficient of earth pressure at rest ( $K_0$ ) and void ratio change ( $\Delta e$ ), defined as follows:

$$\text{OCR} = \frac{\sigma_{v\max}}{\sigma_v} = \frac{n_{\max}}{n} \quad (2)$$

$$K_0 = \sigma_h / \sigma_v \quad (3)$$

$$\Delta e = -(1 + e_0) \frac{s_e}{H_0} \quad (4)$$

where  $\sigma_v$  is the current vertical stress;  $\sigma_{v\max}$ , the maximum vertical stress;  $n$ , the current centrifuge acceleration;  $n_{\max}$ , the maximum centrifuge acceleration;  $\sigma_h$ , the horizontal stress;  $s_e$ , the surface settlement due to centrifuge acceleration;  $H_0$ , initial thickness of model sand.

Prior to the loading tests, a series of centrifugal self weight compression tests, termed C-tests, tabulated in Table 3, was conducted to examine the void ratio change and the initial stress conditions in sand subjected to a centrifuge acceleration history. In these tests, the sand (initial void ratio ranging from 0.674 to 0.844), was subjected to ten cycles of centrifuge operation up to 100g and down to 1g, at a constant rate of 10 g/min. Surface settlement and both vertical and horizontal stresses were measured in each acceleration of 10g. This operation resulted in a homogeneously distributed overcompression ratio (OCR) along the depth (D).

Table 2. Indexes of Toyoura sand

Specific density, $\rho_s$	2.66 ( $\text{g/cm}^3$ )
Maximum void ratio, $e_{\max}$	0.985
Minimum void ratio, $e_{\min}$	0.602
Coefficient of uniformity, $U_c$	1.34
Internal friction angle, $\phi_d^1$	42 (deg.)
Note: $^1$ CID triaxial compression test, $D_r=70\%$	

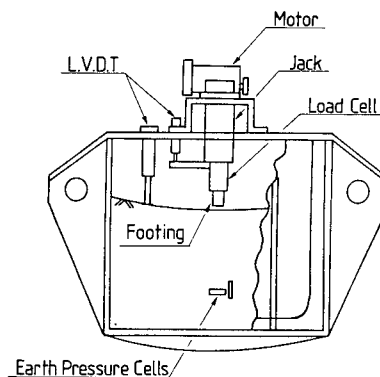


Fig. 1 Setup for experiments

Table 3. Compression test conditions Load

Test name	Void Ratio $e_o$	Relative Density $D_r$ (%)	Cycles Operated $N$ (cycles)	Measuring Depth $D_o$ (m)
C-1	0.674	81.3	10	0.175
C-2	0.709	72.0	10	0.169
C-3	0.716	70.2	10	0.174
C-4	0.753	60.5	10	0.169
C-5	0.774	55.1	10	0.160
C-6	0.844	36.9	10	0.164
C-7	0.676	80.8	7	0.164
C-8	0.705	73.1	1	0.174

In the loading tests, three different types of centrifuge operations were employed. First, in order to obtain datum behavior of the foundation, a series of loading tests (termed LN-tests) was carried out. In this series of tests, after increasing accelerations up to 10g, 25g, 50g and 100g, the accelerations were kept constant. Loading tests on the normally compressed sands were then performed immediately.

Third, in order to examine influences of overcompression history on bearing characteristics of sand, a further series of loading tests (termed LO-tests) was performed. In this series, after obtaining an acceleration of 100g, the accelerations were decreased to 50g, 25g and 10g, corresponding to OCR of 2, 4 and 10. Loading tests on these overcompressed sands were then performed.

Second, in order to investigate the influence of the number of acceleration cycles on bearing characteristics of sand, another series of loading tests (termed LC-tests) was conducted. According to the C-tests, to obtain negligible void ratio change induced by centrifuge operation required at least five cycles of centrifuge operation. Therefore, in this series of loading tests, after imposing a set of 4 acceleration cycles up to 100g and down to 1g, the acceleration was increased up to 100g again and then loading tests on precompressed sands were performed.

Three kinds of test procedures mentioned above, and tabulated in Table 4, provide model ground with homogeneous overcompression ratios, and different initial stress conditions.

Table 4. Loading tests conditions

Test name	OCR	Cycle(s) operated $N$ (cycles)	Acceleration $n$ (g)	The number of tests
LN-1	1	1	100	3
LN-2	1	1	50	3
LN-3	1	1	25	2
LN-4	1	1	10	2
LC-1	1	5	100	2
LO-2	2	1	50	2
LO-3	4	1	25	2
LO-4	10	1	10	3

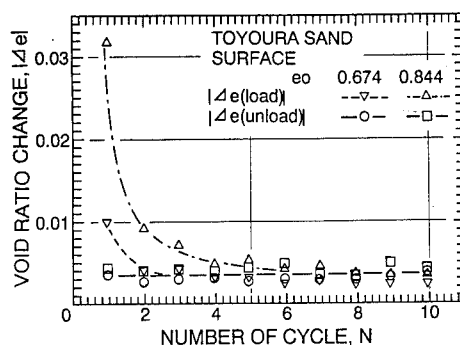


Fig. 2 Void ratio change versus centrifuge operating cycle

gradually decreased with increasing number of operating cycles. Fig. 2 shows the relationship between absolute void ratio change obtained from surface settlement, and the number of acceleration cycles. Fig. 2 indicates that increasing the number of cycles causes decreasing void ratio/load ( $|\Delta e(\text{load})|$ ) ranging from 0.01 to 0.031 in virgin compression to a negligibly small value of around 0.004, which is approximately equal to the void ratio change during the unloading sequence ( $|\Delta e(\text{unload})|$ ) after the fifth loading cycle. In the fifth cycle and later, the absolute values of void ratio change become small enough to neglect the influence on deformation due to the centrifuge operation. Note further, Fig. 2 suggests that precise experiments in dry sand will require either (a) the correction of the initial void ratio estimated under the gravitational field if a measurement of surface settlement under the centrifugal field is available; or (b) at most five cycles of centrifuge operation, even for loose sand, prior to a loading test to safely neglect void ratio change induced by centrifuge operation if the measurement is not available.

Void ratios ( $e$ ) of model sands which have been subjected to both one and five centrifuge cycle(s) up to 100g are plotted against each initial void ratio ( $e_o$ )

### 3 TEST RESULTS AND DISCUSSIONS

#### 3.1 Change in void ratio

Noticeable settlements occurred during centrifuge acceleration up to 100g in the C-tests, while sharp rebounds appeared at the end of operating cycles during the following unloading sequence down to 1g. Although settlements measured increased with increasing number of operating cycles, most settlement was induced in the virgin loading sequence, and the increments of settlement

measured prior to operation in Fig. 3. As shown in Fig. 3, for these particular tests, void ratios under an acceleration of 100g are approximately expressed by a liner equation, that is;

$$e = 0.92e_0 + 0.041 \quad (5)$$

which was obtained by means of least square method. Differences induced by the number of acceleration cycles are rather small, except in the case of  $e_0=0.844$ .

### 3.2 Initial stress condition prior to loading test

$K_0$ -values were obtained from measured vertical and horizontal stresses through a set of ten cycles of centrifuge operation in the C-tests and used to demonstrate initial stress conditions. Typical changes of  $K_0$  during centrifuge operation in dry sand, with initial void ratio ( $e_0$ ) of 0.674, are shown in Figs. 4 (a, b): Fig. 4 (a) shows loading and reloading sequences; Fig. 4 (b), unloading sequences. Since both vertical and horizontal stresses at 1g were so small that they probably contained a large amount of measurement errors, measurements under an acceleration smaller than 10g were eliminated from Figs. 4 (a, b). Figs. 4 (a, b) indicate that: (1) During the virgin loading sequence,  $K_0$ -values slightly change ranging from 0.35 to 0.32. These values are close to the value estimated by Jaky's equation (Jaky (1944)), i.e.:

$$\begin{aligned} K_0 &= 1 - \sin \phi_d \\ &= 0.33 \end{aligned} \quad (6)$$

(2) The number of acceleration cycles does not affect  $K_0$  under an acceleration of 100g in which the overcompression ratio (OCR) is unity; (3)  $K_0$ -values during reloading sequences tend to scatter more than the values during unloading sequences.  $K_0$  under accelerations larger than 50g, where the corresponding OCR is less than two, is a little larger than the value under 100g.  $K_0$  under accelerations less than 50g increases with decreasing acceleration and reaches up to two times larger than the value under 100g. Furthermore,  $K_0$  under 10g (OCR=10)

tended to increase with increasing number of acceleration cycles during both loading and unloading sequences. Finally, it can be concluded that preparing duplicate overcompressed model sand requires conducting a model test during the unloading sequence, and that effective overcompression requires an OCR value at least larger than two.

### 3.3 Influences of centrifuge operation

Fig. 5 shows a comparison of normalized bearing capacity versus settlement behavior of sands for one cycle (LN-tests) and five cycles (LC-tests) of centrifuge operations. Test results obtained from LN-tests are rather scattered, and show slightly higher capacities than ones from LC- tests. No significant influence related to the number of centrifuge cycles appeared among the test results in the range of this study.

### 3.4 Influences of overcompression

Figs. 6 (a-c) show the comparison of overcompressed sand (LO-tests) and normally compressed sand (LN-tests). Because of the effect of stress level on soil properties, LO-tests must be compared with LN-tests, which were conducted under same accelerations. In these figures,

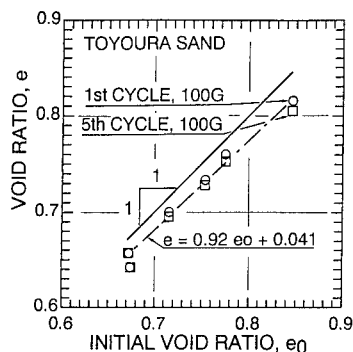
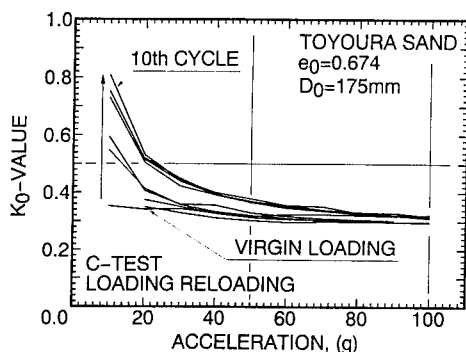
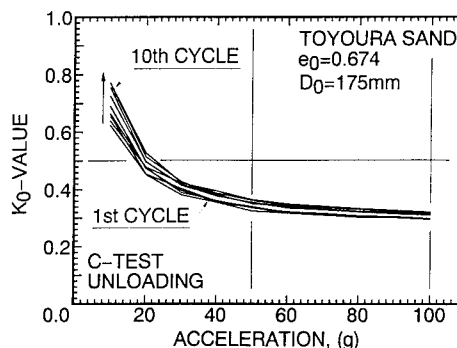


Fig. 3 Void ratio under 100g



(a)



(b)

Figs. 4(a, b)  $K_0$  obtained: (a) loading sequence, (b) unloading sequence



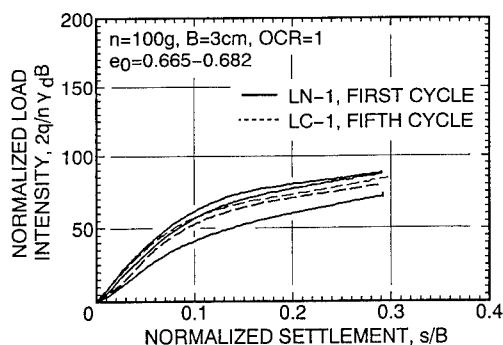


Fig. 5 Comparison of LN-test results and LC-test results

solid lines show LN-tests, while dashed lines show LO-tests. Fig. 6 (a) indicates that curves obtained from LO-tests show slightly higher capacities than curves obtained from LN-tests, and that the OCR only slightly affects bearing characteristics. On the other hand, Fig. 6 (b) and Fig. 6 (c), in which loading tests were conducted under a lower acceleration and higher OCR, show even smaller influence of OCR.

In the test results presented here, failure points were always clear; peaks were emphasized by subtracting the component of embedded depth ( $q_s$ ), which was estimated by fitting onto the linear portion appearing at the end of the curve. Ultimate bearing capacities ( $q_u$ ) were thus detected.

Fig. 7 shows the relationship between OCR and subgrade reaction factor ( $K_s$ ) which were obtained:

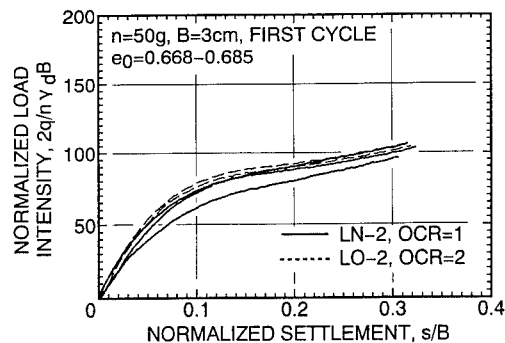
$$K_s = \frac{q_{50}}{s_{50}} \quad (7)$$

where  $q_{50}$  is  $q_u/2$ ,  $s_{50}$  is the settlement when  $q_{50}$  is mobilized. Overcompression leads to higher values of  $K_s$ , and this tendency becomes greater with the stress level.

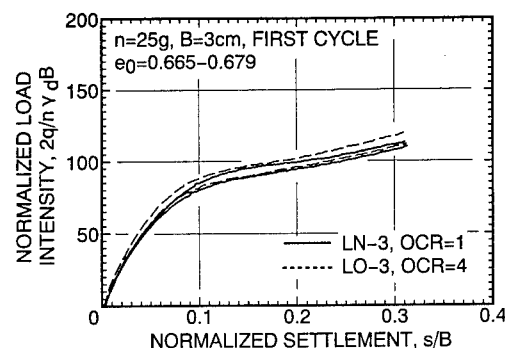
### 3.5 Influences of $K_0$

Although most normalized load intensity-settlement curves duplicated each other, some curves showed extremely low normalized load intensity. This fact implies that there is a parameter lacking which influences bearing characteristics of dry sand.

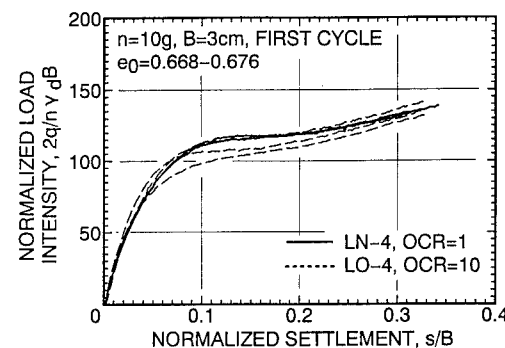
Fig. 8 shows normalized ultimate bearing capacities ( $2q_u/\gamma B$ ) versus  $K_0$  measured in loading tests: hollow marks for LC- and LN-tests (OCR is unity); solid marks for LO-tests (OCR larger than unity). For a set of test results under 10g, values of  $2q_u/\gamma B$  concentrate around 110; even  $K_0$ -values vary from 0.23 to 0.68. On the other hand, for three sets of test results under 25g, 50g and 100g, the values of  $2q_u/\gamma B$  increase with increasing  $K_0$ , and higher stress level leads to a larger influence of  $K_0$ . D'Appolonia and Lambe (1970) concluded that load-settlement behavior predicted by FEM with an anisotropic model was strongly dependent



(a)



(b)



(c)

Figs. 6(a-c) Comparison of LN-test results and LO-test results: (a)50g, (b)25g, (c)10g

upon the initial stress condition. Decreasing  $K_0$  led to decreasing the first yield stress. FEM was applied to anisotropic consolidated clay by Iizuka et al. (1987), who demonstrated the influence of  $K_0$  and concluded that different  $K_0$  caused different failure patterns in the analyzed mesh models. Note that not only on clay but also on sand, increasing  $K_0$  leads to increasing normalized ultimate bearing capacity, and this tendency depends on stress level.

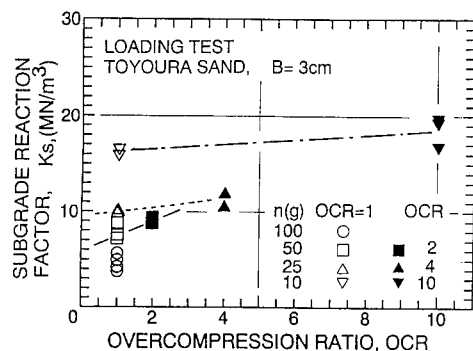


Fig. 7 Effect of overcompression on subgrade reaction factor ( $K_s$ )

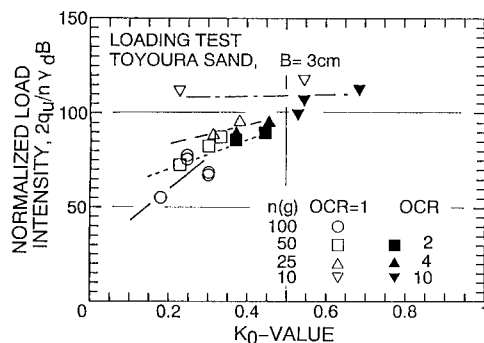


Fig. 8 Influence of  $K_0$  on normalized ultimate bearing Capacity ( $2q_u/mB$ )

The influence of  $K_0$  can be understood as a resultant effect of both strength anisotropy and progressive failure, depending upon stress level.

The limitation of the centrifuge used in this study prohibited applying higher stress levels and higher OCR's. According to Figs. 4 (a, b) and Fig. 8, if a much larger centrifuge had been available, the influence of  $K_0$  and the influence OCR would have appeared more clearly.

#### 4 CONCLUSIONS

In order to investigate the influences of initial conditions affecting bearing characteristics of sand, two types of centrifuge model tests, compression test and loading tests, have been carried out. The following conclusions have been drawn from these test results:

1. Non-negligible settlements due to centrifuge acceleration cycles were observed. Precise experiments in dry sand will require either a measurement of deformation or a correction of void ratio.
2. No significant influences of overcompression and

the number of centrifuge cycles on load-settlement curves were observed over the range of this study.

3. Increasing  $K_0$  leads to increasing normalized ultimate bearing capacity under the acceleration larger than 50g. On the other hand, under the acceleration of 10g, no influence of  $K_0$  exists, even OCR=10. Neglecting the influence of  $K_0$  on overconsolidated soil, as is done in current design methods, would result in a conservative estimation of bearing capacity.

#### ACKNOWLEDGEMENTS

The assistance of the following personnel of Nishimatu Construction, Co. Ltd. is gratefully acknowledged: Chiefs Y. Nomoto and T. Fujii, Messrs. M. Ishibashi and S. Imamura. The authors would like to acknowledge gratefully the help and advice received from Professor Y. Yokoyama and Associate Professor S. Imaizumi at Utsunomiya University, and Research Associate T. Hagiwara, Gunma University.

#### REFERENCES

- D'Appolonia, D. J. and Lambe, T. W. (1970) Method for predicting initial settlement, Proc. ASCE, Vol.96, SM2, pp.523-544
- de Beer, E. E. (1965): Bearing capacity and settlement of shallow foundation on sand, Proc. Sympo. Bearing Capacity and Settlements of Foundations, Duke University, pp.113-122
- Iizuka, A., Yoshimine, T., Ohta, H. and Hata, S. (1987) Bearing capacity and stress distribution in  $K_0$ -consolidated clayey ground, Jour. of Japanese Society of Civil Engineering, Vol. 382, No. III -7, pp.255-263 (in Japanese)
- Jaky, J., (1944) The coefficient of earth pressure at rest, Jour. of Society of Hungarian Architects and Engineers, pp. 355-358.
- Kusakabe, O., Yamaguchi, H. and Morikage, A. (1991) Experiment and analysis on the scale effect of  $M\gamma$  for circular and rectangular footings, Proceedings of the international conference centrifuge 1991, Colorado, Ko (ed.), Balkema, pp. 179-186
- Vesic, A. S. (1975) Bering Capacity of Shallow Foundation, *Foundation Engineering Handbook*, edit by Winterkorn & Fung, van Nostrand Reinhold, pp.121-145.

## Verification of shape factors for shallow foundations on sands

S.A.Aiban

King Fahd University of Petroleum and Minerals, Dhahran, Saudi Arabia

**ABSTRACT:** The centrifuge has been utilized to study the effect of footing shape on the bearing capacity of shallow foundations on sands. A plane strain condition was ensured by testing three adjacent footings of the same width along one line. The load on each footing was measured using a load cell. The failure mechanism was monitored by trimming each sample after failure. Test results have shown that plane strain conditions were modeled properly using this design. Experimental results for the bearing capacity of the rectangular footing (three footings together) were compared with the theoretical solutions and good agreement was obtained. Values for the bearing capacity factors  $N_\gamma$  and  $N_q$  were determined experimentally for the strip (central) footing and these values were used to study the effect of footing shape on the bearing capacity. Description of the work and methods of analysis are given in details.

### 1 INTRODUCTION

The ultimate bearing capacity of shallow foundations is generally determined assuming strip footing and the effect of the foundation shape is usually accounted for using empirical factors. Even though most of the geotechnical engineering problems involving shear strength approximate to a plane strain condition, strength tests are often performed under a conventional triaxial condition for its simplicity and availability. Depending on the initial density of the sand and the confining pressure, the stress-strain and strength characteristics are different under these two strain conditions. Two of the major differences that relate to shallow foundations on sands are the peak strength values and the post-peak response.

The principal stress difference ( $\sigma_1 - \sigma_3$ ) at peak load is higher for the plane strain (PS) tests compared to the conventional triaxial compression (CTC) tests for the same minor principal stress and for all sands prepared under similar conditions. Several investigators, for example, Bishop (1961 and 1966), Cornforth (1964), Lee (1970), Marachi et al. (1981) and Drescher and Vardoulakis (1982) investigated this phenomenon and reported different variations in the values of  $\phi$  from conventional triaxial to plain strain conditions. Results show that  $\phi_{PS} > \phi_{CTC}$ , and according to Marachi et al. (1981)

the difference could be as much as  $7^\circ$  for the high values of  $\phi$  which is the case for dense granular material. Lee (1970) stated that the difference could vary from  $0^\circ$  to  $6^\circ$  or  $8^\circ$  where larger differences are associated with dense sands at low confining pressures, while the smaller differences are associated with either loose sands at all confining pressures or dense sands at sufficiently high confining pressures. The differences in the peak strength values between the PS and the CTC tests are shown in Figure 1. These differences are mainly due to the effect of the intermediate principal stress through its relationship with the external strain condition. A larger restraint against movement of sand particles is encountered in the plane strain case compared to that of the conventional triaxial case (Cornforth 1964).

The post-peak or softening characteristics under these two states are also different. Test results presented by Cornforth (1964), Lee (1970) and Marachi et al. (1981) showed that sands with different initial densities and tested under plane strain conditions, exhibit severe softening, especially dense specimens. In addition, peak and residual states occur abruptly and the axial strain at peak load for plane strain tests is smaller than that for the conventional triaxial tests. This is clearly shown in Figure 1. On the other hand, the amount of

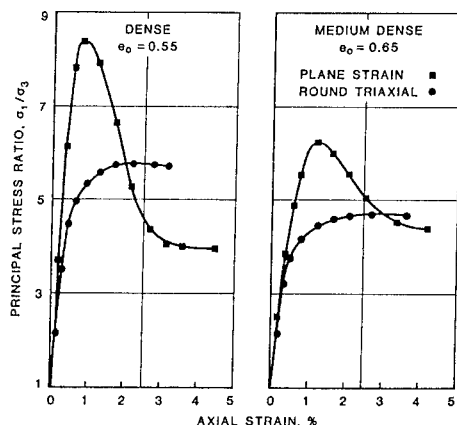


Fig. 1 Comparison of the stress-strain relationship for plane strain and triaxial specimen at the same confining pressure (Marachi et al. 1981).

softening in the CTC tests is less than that in the PS tests and depends on the boundary conditions. Samples tested in the CTC apparatus with lubricated ends show very little softening while the same specimens show larger softening when tested with non-lubricated ends. In addition, the softening occurs in a much smoother manner when compared to that of the PS tests. The softening in the CTC tests with non-lubricated ends is composed of material and geometrical components (Drescher and Vardoulakis 1982). The theoretical and experimental findings of Peters et al. (1988) indicate that shear bands are initiated more easily in PS tests than in the CTC tests. This could explain the severe softening in the case of PS tests. Recent analytical work by Perić (1990) confirmed these findings.

Plane strain conditions under footings are satisfied if the strain in the long direction is zero. This is difficult to satisfy during experimental work and, if this condition is not satisfied, the value of the intermediate stress will decrease and will affect the stress-strain curve, especially its peak value. One of the first attempts to study the effect of the constraint in the intermediate stress direction is the work by Cornforth (1964). He showed that there is no apparent difference in the strength-density relationship for rectangular specimens tested with or without plane strain end clamps if the length-to-width ratio is eight. Similar findings were reported by Lee (1970) where he concluded that rigid plates with lubricated ends are necessary to ensure complete plane strain conditions. Ko and Davidson (1973) focused on those points when performing their

experiments on shallow footings in the laboratory under a 1-g environment. They stated that a rigid container is necessary to ensure plane strain conditions. Marachi et al. (1981) performed tests on rectangular specimens where different values of the intermediate principal strain ( $\epsilon_2$ ) were allowed. They concluded that if the value of  $\epsilon_2$  is less than 40% of the axial strain ( $\epsilon_1$ ) at failure, the value of  $\phi$  will differ by no more than  $1^\circ$  from the value for perfect plane strain conditions. It is worth mentioning that variations of even  $1^\circ$  make large differences in the values of the bearing capacity factors, especially for large values of  $\phi$ .  $N_\gamma$  values could be as much as 22% higher if  $\phi$  is  $46^\circ$  instead of  $45^\circ$ , according to the formula provided by Vesic (1973), for example. It is therefore important to have an experimental setup that will match the assumptions of the theoretical work without deviations.

## 2 TESTING PROCEDURE

The 15 g-ton centrifuge system at the University of Colorado was used in this work. The centrifuge is a Genisco 1230-5 accelerator modified for testing geotechnical models. It has a symmetrical arm that carries a swing-basket at each end. The working radius to the basket floor is 1359 mm (53.5 inches). The centrifuge has 56 electrical slip rings and three fluid ports. The footings have a width of 38 mm (1.5 inches). The central footing is 51 mm (2 inches) long and each external footing is 38 mm (1.5 inches) long. Loading of the footings was performed at a gravity level of approximately 30g at the base of the footings. This resulted in a prototype width of 1.14 meters (45 inches).

Fine U.S. silica sand (F-75) with a uniformity coefficient of 1.7, specific gravity of 2.65 and mean grain size of 0.18 mm was used in all tests. Conventional triaxial tests at different confining pressures were performed and an angle of internal friction of  $42^\circ$  was obtained. The sand was pluviated into an aluminum container that has a square base of 432x432 mm (17x17 inches) and a height of 406 mm (16 inches) with all sides and base measuring 13 mm (0.5 inches) thick. The pluviation height was kept at 762 mm (30 inches) from the surface of the sand and was updated every 25 mm (1 inch). This resulted in a relative density of about 88% which is the maximum achievable density without vibration. The thickness of the sample in the container was at least 152 mm (6 inches) which is four times the footing width.

In order to ensure plane strain conditions, three footings were made adjacent to each other along one line. Each footing has a u-shaped cross-section with longitudinal grooves in the base at different locations from the centerline for different eccentricities. The footings are made of aluminum, and sand was glued at the bottom to simulate rough base conditions while the sides remained smooth. Footings were loaded with a rigid mechanism so that they penetrate the soil uniformly; therefore, the one in the middle was under plane strain conditions. The loading wedges have curved ends to match the grooves in the footings; therefore, upon loading, rotation of the footings around the long axis is possible while translation is prevented. The load on each footing was measured separately using a load cell. The deformation is measured using at least one LVDT on each side of the footings. Measurement of deformation on opposite sides of the footings allows for the calculation of footing rotation throughout the test.

The sample was prepared and tested in a dry state while trimming was done after wetting the sample. One of the objectives of trimming is to study the characteristics of the failure surface. The trimming consists of adding a predetermined amount of water to the sample to make it wet. The front side of the container, normal to the footing axis, was then opened and the specimen is sliced into thin sections using a kitchen spatula. Vertical cuts in the cohesionless material are possible due to the capillary action of the added water. In addition, the presence of the right amount of water changes the color of the sand. The color change depends on the void ratio of the soil in different zones. Upon failure the soil in the failure planes is much looser than that in other regions and therefore the capillary phenomenon is different for these two different areas. The originally white sand becomes gray for all areas other than the slip surface which is looser and retains a white color or much lighter color compared to the other zones.

When the trimming process advances towards the footing edge, the footing is carefully removed. At this point, sections at the exterior as well as the interior footings are smoothed and pictures are taken. The slip lines are traced on transparency sheets for different sections. Plane strain conditions are checked by comparison of failure planes or slip lines at sections in the exterior footings 3 mm from the interior (middle) footing, in the interior footing 3 mm from the exterior and at the center of the middle footing. When the slip lines are identical for these sections the plane strain condition is satisfied. More

details on the testing equipment and sample preparation, testing and trimming are given by Aiban and Znidaršić (1991).

### 3 EXPERIMENTAL VALIDATION

One of the major emphases in this investigation was to ensure plane strain conditions. In the preliminary stage and in all subsequent tests the following measures were taken:

- Uniform deformation of the three footings: This was checked by measuring the deformation on each of the footings at each side. The deformation on the corresponding side of the three footings was found to be the same.
- The shape and size of the failure mechanism: The failure mechanisms at the center and end of the middle footing and at the internal side of the external footings were compared and if they were the same, the test was considered under plane strain conditions. In all tests, this condition was satisfied.
- The characteristics of stress-deformation curves of the middle and end footings: As indicated earlier, the curves for the plane strain case and the general 3-D case are different in terms of the peak load and the softening behavior. Both of these points are observed in the centrifuge tests. Figure 2 shows typical stress-displacement curves for the middle footing, which is under plane strain conditions, and curves for the edge footing where one side of the footing is under plane strain conditions while the other is that of a square footing. The characteristics of the curves in Figure 2 compare very well with those in Figure 1. The higher stress level for the central footing (point A) in Figure 2 compared to that of the edge footing (point C) supports the above arguments. In addition, the severe softening in the case of the central footing (from point A to point B) compared to that (from point C to D) for the edge footing is in agreement with the above findings. This is typical for all loading conditions, except for higher eccentricities, where these differences diminish, as shown in Figure 2.

### 4 EXPERIMENTAL OBSERVATIONS

The ultimate bearing capacity  $q_u$  of shallow horizontal footing under static vertical central loading

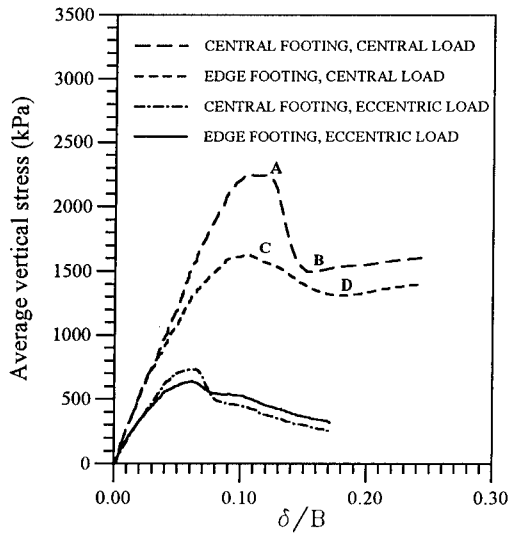


Fig. 2 Comparison of the behavior of the central and edge footings under vertical central and eccentric loading.

on cohesionless soil is generally expressed in the form:

$$q_u = \gamma (D_f + \delta) s_q N_q + \frac{\gamma}{2} B s_\gamma N_\gamma \quad (1)$$

where  $\gamma$  is the unit weight of the soil,  $D_f$  is the depth of the footing below the ground surface,  $B$  is the width of the footing,  $\delta$  is the footing settlement at peak load,  $s_q$  and  $s_\gamma$  are the shape factors and  $N_q$  and  $N_\gamma$  are the bearing capacity factors. The shape factors were introduced in the bearing capacity equation to account for foundation shapes other than strip footing. Several forms of the shape factors were provided by different investigators, two of which will be discussed here: (1) De Beer shape factors given by:

$$s_q = 1 + \frac{B}{L} \tan \phi \quad (2)$$

$$s_\gamma = 1 - 0.4 \frac{B}{L} \quad (3)$$

and (2) Meyerhof shape factors given by:

$$s_\gamma = s_q = 1 + 0.1 \tan^2 (45 - \phi/2) \frac{B}{L} \quad (4)$$

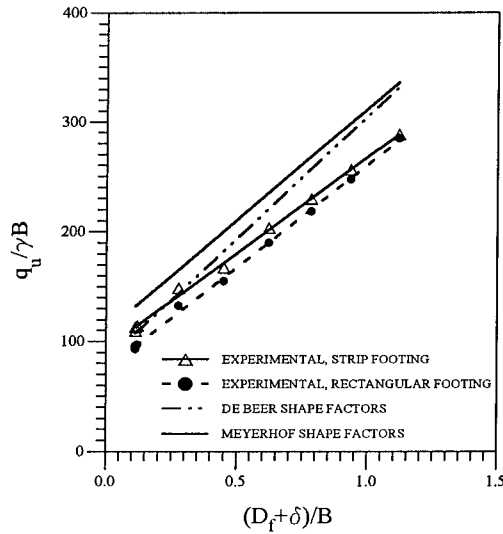


Fig. 3 Normalized bearing capacity for the strip and rectangular footings, the shape factors are based on  $\phi = 44^\circ$ .

The De Beer shape factors were based on extensive small scale laboratory testing and he stated that the  $s_q$  values are dependent on the angle of internal friction, which is dependent on the stress level, while the  $s_\gamma$  values are not.

The above bearing capacity equation can be written in a normalized form as:

$$\frac{q_u}{\gamma B} = \left( \frac{D_f + \delta}{B} \right) s_q N_q + \frac{1}{2} s_\gamma N_\gamma \quad (5)$$

Values of the normalized bearing capacity  $q_u/(\gamma B)$  are plotted against  $(D_f + \delta)/B$  in Figure 3 for different footing embedment values and for central (strip) footing as well as rectangular footing. The rectangular footing consists of the central footing and the two edge footings together and the resulting width-to-length ratio ( $B/L$ ) is 0.3. The strip footing gave higher bearing capacity values compared to the rectangular one. This is expected since  $\phi$  for the strip footing is higher than that of the rectangular one. The resulting relations are linear and the values of  $N_q$  and  $N_\gamma$  can be obtained directly for the strip footing since the shape factors are equal to one. Values of  $N_q$  and  $N_\gamma$  are obtained from the curve as the slope and twice the intercept and were found to be 174 and 186 respectively. When the experimental results for the ultimate bearing capacity of the plane strain case

were compared to the theoretical solutions provided by different authors it was found that the best agreement was observed when using an angle  $\phi$  of  $44^\circ$  in the theoretical solution (Aiban and Znidarčić 1991). This angle was an intermediate value between  $\phi_{CTC}$  and  $\phi_{PS}$  and was adopted in all analysis for the plane strain case when using the analytical solutions.

On the other hand, the values of  $s_q N_q$  and  $s_\gamma N_\gamma$  for the rectangular footing were determined from the figure as the slope and twice the intercept and were found to be 189 and 148 respectively. The experimental values of  $q_u/(\gamma B)$  for the rectangular footing are compared to the theoretical solutions provided by different authors. In the theoretical solutions the values of  $q_u/(\gamma B)$  were evaluated at all experimental values of  $(D_f + \delta)/B$ . This will eliminate the effect of the width of the footing, the unit weight of the soil and the deformation at peak load. Two approaches were followed in computing the theoretical bearing capacity of the rectangular footing:

- a) The  $q_u/(\gamma B)$  values, for  $B/L$  of 0.3, were computed using the experimental values  $N_q$  and  $N_\gamma$ , which were determined for the strip footing, and the shape factors provided by De Beer (1970) and Meyerhof (1963) where  $\phi$  is assumed to be  $44^\circ$ . In this procedure the effect of  $N_q$  and  $N_\gamma$  was eliminated since the experimental values for the same soil and the same loading conditions were used and therefore the accuracy of the shape factors can be predicted. It is clearly shown from the results in Figure 3 that both De Beer's and Meyerhof's shape factors resulted in an overestimation of the normalized bearing capacity of the rectangular footing especially at higher embedment values. Results also showed that predictions using De Beer factors are better than those using Meyerhof factors. The observed overestimation in the  $q_u/(\gamma B)$  values when using the shape factors could be attributed to the shape factors themselves since they were based on small scale experiments. It is known that the values of the angle of internal friction obtained at low stress levels are higher than those obtained at higher stress levels (De Beer 1967). In addition, the stress under the footing is not the same along the failure surface even at peak load since failure occurs in a progressive manner.
- b) The  $q_u/(\gamma B)$  values, for  $B/L$  of 0.3, were computed using the solutions provided by Vesic (1973) and Meyerhof (1963). In Vesic's solution, the  $N_q$  and  $N_\gamma$  values are those provided by

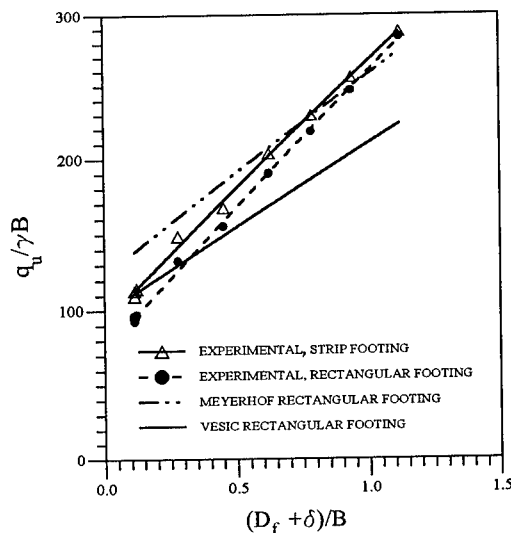


Fig. 4 Normalized bearing capacity for the strip and rectangular footings, the theoretical solutions are based on  $\phi = 44^\circ$ .

Vesic at a  $\phi$  value of  $44^\circ$  and De Beer shape factors were used as suggested by Vesic. In the Meyerhof's solution the  $N_q$ ,  $N_\gamma$ ,  $s_q$  and  $s_\gamma$  values are those provided by Meyerhof at a  $\phi$  value of  $44^\circ$ . Experimental results for both the strip and rectangular footings are compared to the theoretical solutions in Figure 4. It is clearly seen from the figure that the slopes and intercepts of the curves resulting from the theoretical solutions are different from those of the experimental solutions and that indicates different  $s_q N_q$  and  $s_\gamma N_\gamma$ , respectively.

The predictions of the first approach are better than those of the second one, however this requires knowledge of the  $N_q$  and  $N_\gamma$  values for the soil without relying on the theoretical procedures. These findings however should be verified on different soils with different  $\phi$  values for different  $B/L$  ratios.

## 5 CONCLUSIONS

The experimental work undertaken here has produced data for strip and rectangular footings. The bearing capacity for the strip footing was found to be larger than those for the rectangular footing as expected from theoretical solutions. The bearing capacity factors were obtained directly for the strip footing. However, for rectangular footings more tests at different  $B/L$  ratios are needed to enable separation

of the shape factors from the bearing capacity factors. The experimental bearing capacity values were compared to two of the well known theoretical solutions. It was found that good predictions were obtained when the shape factors of these theoretical solutions were used with the experimental bearing capacity factors. When the bearing capacity factors provided by these solutions were used, the bearing capacity values were influenced by  $N_q$  and  $N_\gamma$  values resulting in curves that are not parallel to the experimental ones. Further research is needed using different soils and different B/L ratios before any further conclusions can be made.

#### ACKNOWLEDGMENT

The author wishes to acknowledge the support from King Fahd University of Petroleum and Minerals. The cooperation and support of the Department of Civil, Environmental and Architectural Engineering at the University of Colorado is acknowledged.

#### REFERENCES

- Aiban, S. & D. Znidarčić 1991. Shallow footings on sands under vertical central, eccentric and inclined loads. *Proc. Centrifuge '91 Conf.*: 201-208. Boulder, Colorado
- Bishop, A.W. 1961. Discussion of soil properties and their measurement. *Proc. 5th ICSMFE*, Vol. III: 92-100.
- Bishop, A.W. 1966. The strength of soils as engineering materials. *Géotechnique* 16, No. 2: 91-130.
- Cornforth, D.H. 1964. Some experiments on the influence of strain conditions on the strength of sand. *Géotechnique* 14, No. 2: 143-167.
- De Beer, E.E. 1967. Bearing capacity and settlement of shallow foundations on sand. *Proc. Symp. held at Duke University*: 15-34.
- De Beer, E.E. 1970. Experimental determination of the shape factors and the bearing capacity factors of sand. *Géotechnique* 20, No. 4: 387-411.
- Drescher, A. & I. Vardoulakis 1982. Geometric softening in triaxial tests on granular material. *Géotechnique* 32, No. 4: 291-303.
- Ko, H.Y. & L.W. Davidson 1973. Bearing capacity of footings in plane strain. *J. Soil Mechanics and Foundations Divisions, ASCE* 99, No. SM1: 1-23.
- Lee, K.L. 1970. Comparison of plane strain and triaxial tests on sand. *J. Soil Mechanics and Foundations Divisions, ASCE* 96, No. SM3: 901-923.
- Marachi, N.D., J.M. Duncan, C.K. Chan & H.B. Seed 1981. Plane-strain testing of sand. *Laboratory Shear Strength of Soil, ASTM STP 740*, R.N. Yong & F.C. Townsend, Eds., American Society for Testing and Materials: 294-302.
- Meyerhof, G.C. 1963. Some recent research on the bearing capacity of foundations. *Canadian Geotechnical J.*, Vol. I, No. 1: 16-26.
- Perić, D. 1990. Localized deformation and failure analysis of pressure sensitive granular materials. *Ph.D. Dissertation*, University of Colorado, Boulder, CO.
- Peters, J.G., P.V. Lade & A. Bro 1988. Shear band formation in triaxial and plane strain tests. *Advanced Triaxial Testing of Soil and Rock, ASTM STP 977*, R.T. Donaghe, R.C. Chaney & M.L. Silver, Eds.: 604-627.
- Vesić, A.S., 1973. Analysis of ultimate loads of shallow foundations. *Journal of the Soil Mechanics and Foundation Division, ASCE* 99, No. SM1: 45-73.



## Loading of shallow foundations: Importance of testing procedures

N.E. Bakir & J. Garnier

*Laboratoire Central des Ponts et Chaussées, Nantes, France*

Y. Canepa

*Laboratoire Régional des Ponts et Chaussées, Melun, France*

**ABSTRACT:** This paper describes the experimental conditions and the devices used in loading centrifugal tests of foundations. Different problems are discussed, as the construction and characterization of soil samples, the modelling of strip footings, the criteria of failure for bearing capacity studies. Equipment and methods used for measuring displacements within the soil mass are also presented. In the second part, the importance of the testing conditions is discussed regarding some recent results obtained on the behaviour of foundations near a slope and on the effect of the shape of the footing.

### 1 INTRODUCTION

Some scatter is always observed on the results of tests performed on different centrifuges (Corte et al., 1988) but it can be reduced by a good control of the testing procedures as demonstrated by the VELACS project (Arulanandan and Scott, 1993).

This article reports on the effort done at LCPC in this field, for improving the quality and reproducibility of centrifuge tests on foundations (preparation and characterization of soil samples, choice of footing models, testing equipment, loading procedures).

Most of this work was done in the context of studies of bearing capacity, carried out to improve the French standards or to validate numerical or theoretical models.

In the second part of the paper, to illustrate the importance of these testing conditions, some new results obtained in the latest researches on the behaviour of shallow footings on dry sands are presented.

### 2 EXPERIMENTAL CONDITIONS

#### 2.1 Construction and characterization of the sand samples

The first characteristic to control during preparation of a sand sample is obviously its density even if other parameters may have

significant effects on the results of loading tests, as for example, anisotropy or coefficient of earth pressure  $K_0$  which depends on the rigidity of container (Yamaguchi et al., 1976).

In Fontainebleau sand the relationship between void ratio  $e$  and internal friction angle  $\phi$  is  $e \tan \phi = 0.45$ . It follows that a deviation of 3% on the density ( $\gamma_d = 16.5 \text{ kN/m}^3$  instead of  $16 \text{ kN/m}^3$ ) leads to a difference in bearing capacity higher than 35%.

It is then clear that the mean density measured on the whole sand sample is without interest for shallow foundations tests. Local densities in the upper layer, just below the footing, must be determined.

For this reason, an extensive study of the homogeneity of the pluviated samples and of the distribution of densities was undertaken, by means of calibrated boxes placed at different locations into the rectangular containers (120 cm x 80 cm). The device used for preparing centrifuge sand sample in LCPC is the mobile automatic hopper described by Garnier et al. (1988).

Figure 1 shows the variations of density observed in a vertical half cross-section of one sample (Garnier et al., 1993). It is noted that the variations over the whole container are very small (15.90 to 16.15  $\text{kN/m}^3$ ). Due to wall effects during the raining process, the densities increase very slightly at the edges of the

container but are only 1% higher than in the centre.

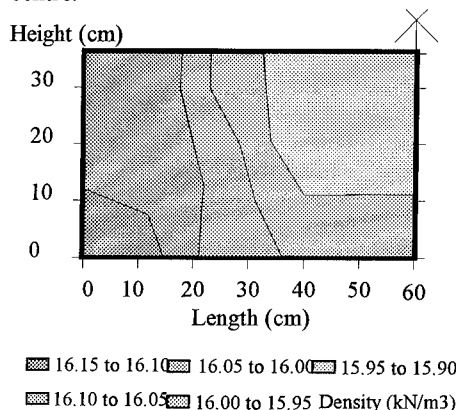


Fig.1 Variation of density over a vertical half cross-section of a sand sample prepared by raining.

For avoiding any wall effect during loading tests, only the central part of the container is used (figure 2). In this volume, variation of density is even smaller ( $\pm 0.6\%$  in dense samples and  $\pm 0.8\%$  in loose samples).

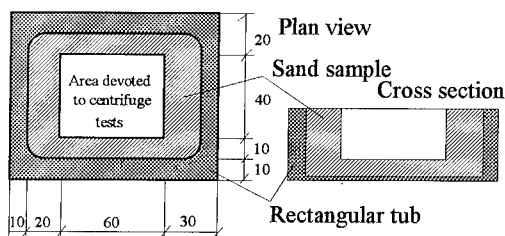


Fig. 2 Extension of the volume of the container used for centrifuge tests.

Homogeneity of density in one pluviated sample is not sufficient and reproducibility has also to be verified.

Figure 3 illustrates that point and gives the distribution of the density measured in the central part of 13 different samples over nearly 3 years. These samples were built in the context of studies of the behaviour of foundations near slopes (Bakir, 1993).

It can be seen that the scatter is very small ( $\sigma = 0.06$ ). The parameters of the hopper remained unchanged (falling height, rate, flow) but a very slight drift of the values with time should be noted. The samples built in 1992 are slightly less dense than those built in 1991.

This difference ( $\sim 0.4\%$ ) may be explained by the evolution of the re-used sand due to handling, and possibly moistening-drying cycles.

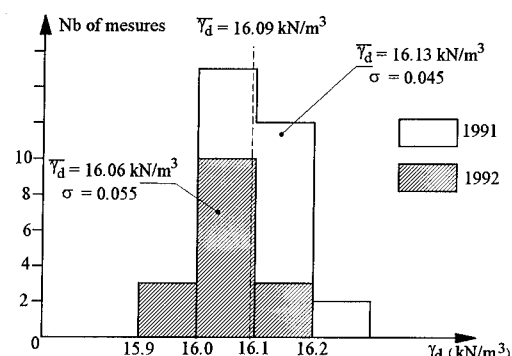


Fig. 3 Distribution of the densities measured on 13 samples built between 1990 and 1992 with the same placement procedure.

The effect of handling seems to be much stronger on shear resistance. Plane shear tests were carried out on the same Fontainebleau sand at a given density ( $15.5 \text{ kN/m}^3$ ) before and after different procedures simulating handling. It was found that the angle of internal friction decreases from  $36^\circ$  (virgin sand) to  $34^\circ$  (old sand).

One must take care of this evolution of test sands and a study is now in progress to specify the conditions and limits of re-use of the same material for preparing several successive samples.

Finally, it is important, once the soil mass has been reconstituted and installed in the basket of the centrifuge, that several cycles of gradual acceleration be performed before the start of the loading tests. This procedure is needed to eliminate the deformations observed in the sand samples during the first few acceleration/deceleration cycles and to stabilize the geostatic stresses inside the sample.

## 2.2 Modelling of strip footing

The theoretical methods of calculating bearing capacity concern only two-dimensional problems (strip footings). To validate these methods experimentally, it is therefore necessary to perform tests under identical conditions and to simulate a plane strain situation. The solution adopted consists of placing the foundation model between two glass plates. This procedure was

selected following tests performed in the context of studies for the validation of numerical models (Rault, 1992).

Figures 4 shows the testing arrangements used. The foundation consists of three parts having the same geometry and equivalent masses, a central measurement cell, and two guard cells.

Two force measurements are made, one on the central footing (giving stress  $q_M$ ) and the other on the whole foundation (giving stress  $q_T$ ).

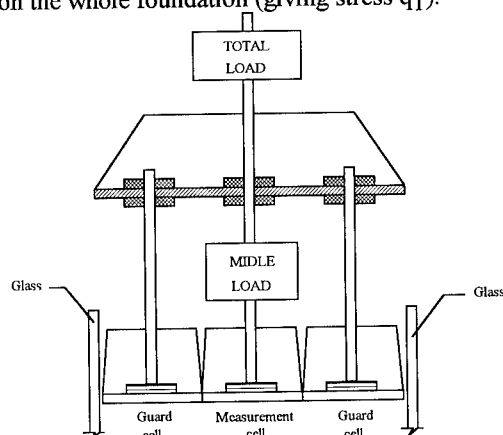


Fig. 4 Model of a strip footing - Force measurement device - Preliminary tests.

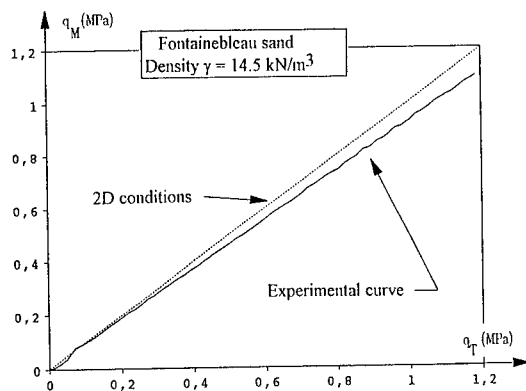


Fig. 5 Model of a strip footing: Variation of the pressure measured in the central cell versus the total pressure.

Figure 5 shows  $q_M$  versus  $q_T$ . It is found that these stresses are practically equal for the whole duration of loading, which indicates that the spurious forces due to friction on the glass are

small (they are on average 7 % of the total pressure).

### 2.3 Criterion of failure, loading devices, loading laws

The choice of criterion of failure can obviously influence the bearing capacity and it must be defined accurately. On dense sand, failure is sudden, with a clearly marked pressure peak (figure 6). This behaviour naturally leads to select the maximum load supported by the soil as criterion of failure.

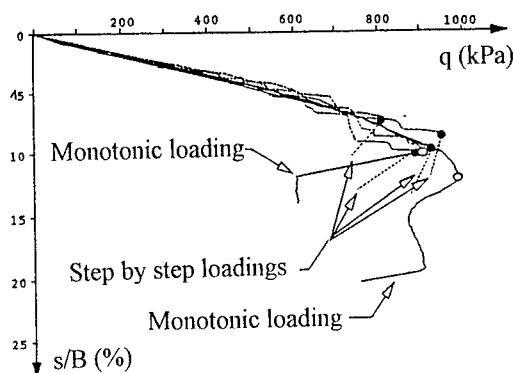


Fig. 6 Settlement curves obtained with different loading modes on the same dense sand.

In this case, it has then been possible to determine experimentally the settlement at failure  $s_r$  and the relative settlement  $s_r/B$ . A relationship is found between this parameter and the failure pressure  $q_r$  or the bearing capacity coefficient  $N_\gamma$ . Figure 7 shows the results obtained on shallow footings near different slopes.

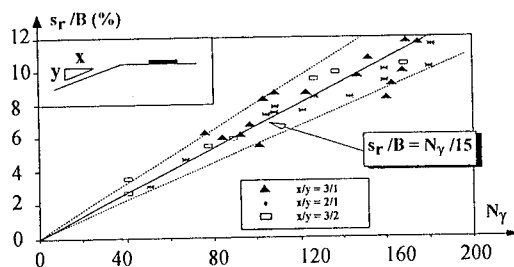


Fig. 7 Relative settlement at failure  $s_r/B$  versus bearing capacity coefficient  $N_\gamma$ .

For all configurations studied (rectangular and strip footings, level ground or slope), the relationship between  $s_r/B$  (%) and  $N_\gamma$  is linear :

$$s_r/B \text{ (%) } = N_\gamma / \alpha$$

The coefficient  $\alpha$  seems to be independent of the conditions of foundation and ground, ranging from 15, for strip footings near slopes, to 19, for rectangular and square foundations resting on level ground.

When no peak load appears (non-embedded foundations on loose sand, for example), another criterion rather than the maximum applied pressure has to be chosen to determine the bearing capacity. The load corresponding to a given settlement ( $s_r/B = 10$  %, for example) is sometimes selected.

This choice may be questionable since the relative settlement at failure is not at all constant but proportional to the bearing capacity as seen on figure 7.

The links between the loading device and the foundation model may also considerably influence the results of loading tests. These conditions must be rigorously controlled, especially when the experimental results are compared to those of numerical calculations.

Most of the tests performed at the LCPC are conducted with the footing allowed to move horizontally and to rotate freely about the point of application of the load so as to avoid any spurious moment and any eccentricity of the force.

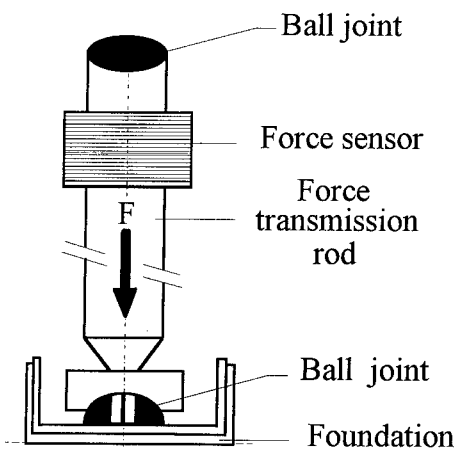


Fig. 8 Ball-joints system used in loading tests of shallow foundations.

For this purpose, two ball joint links are used (fig. 8), one ball joint whose centre corresponds with the centre of the foundations base in contact with soil, a second one at the top of the force transmission rod.

#### 2.4 Movements within a soil mass and failure surfaces.

Most of the theoretical models developed for shallow foundation analysis assume general failure mechanisms. They are based on displacements of rigid blocks, limited by failure surfaces consisting of combinations of logarithmic spirals and straight lines.

To validate these theoretical models it is interesting to carry out special tests where the failure surfaces can be determined.

Two techniques are generally used to study mechanisms of failure.

The first allows after-the-fact determination of the failure surfaces. It traditionally consists of interposing layers of coloured soils when the sand sample is built, then cutting the sand sample after the experiment to locate the shear bands.

The second is suited to the fine study of strains in the soil sample. It allows not only to determine failure surfaces but also to follow the development of the shear bands from the beginning of the loading test. It uses a container with a transparent wall and numerical image processing techniques.

A high-definition CCD I2S camera is carried aboard the centrifuge and aimed at the model.

Direct views of the model are taken during rotation and recorded on a video tape Umatic. They are then processed numerically using a PC/386/20 computer, a digitizing card PIP 1024 and a software developed at the LCPC for centrifuge modelling applications.

The method provides, fully automatically, the displacements of the markers placed in the sample (points or lines).

The accuracy of the method on the measured displacements is 0.1 mm in a 200 mm x 200 mm window.

Figure 9 presents an example of markers placed for measuring displacements in the soil below footings resting on level ground and close to a slope.

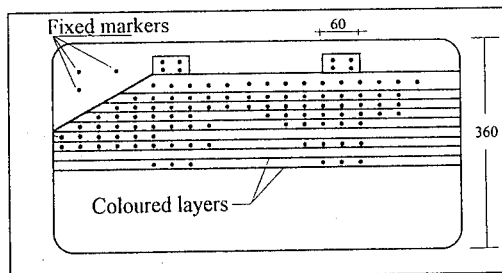


Fig. 9 Example of instrumentation used for determining failure surfaces below footings.

### 3 RECENT EXAMPLES OF APPLICATIONS

#### 3.1 Foundations near slopes

More than 80 centrifuge tests were carried out at LCPC but this problem has also been studied by Lebegue, Dembicki and Zadroga, Giroud, Shields and Bauer, Gemperline, Terashi and Kitasume, Kimura. The results have been presented and compared by Bakir (1993) and Garnier et al. (1994).

From this experimental data base, a general analytical expression is derived for bearing capacity of rectangular and strip footings near slopes. These proposed coefficients are now included into the new French code of practice (CCTG, Fascicule 62, Titre V).

Table 1 presents a generalized bearing capacity reduction coefficient  $i_\beta$ , where  $d$  is the distance to the crest. This reduction coefficient due to the slope has to be applied to the bearing capacity of the same footing, resting on level ground. Such reference bearing capacity can quite easily be calculated by usual methods based either on laboratory or in situ tests results.

Table 1. Analytical expression of bearing capacity reduction coefficient  $i_\beta$ .

$$i_\beta = q_r (d/B)/q_r (\text{horizontal soil})$$

- For  $d/B \leq 6 C_f$

$$i_\beta = 1 - C_f [1.8 \tan \beta - 0.9 (\tan \beta)^2] [1 - d/C_f 6B]^2$$

- For  $d/B > 6 C_f$

$$i_\beta = 1$$

with  $C_f = 1 - 0.4B/L$  (shape factor)

The shape factor  $C_f$  depends on the ratio  $B/L$  (where  $L$  is the length of the rectangular foundation), and its value has been derived from another series of centrifuge tests (§3.2).

The failure surfaces below strip footings have also been investigated using the methods described previously in paragraph 2.4.

As shown in figure 10, it is observed that the strains are concentrated in very narrow shear bands, about 10 grain's diameters thick, and that these surfaces bound three distinct zones, in movement on an immobile mass.

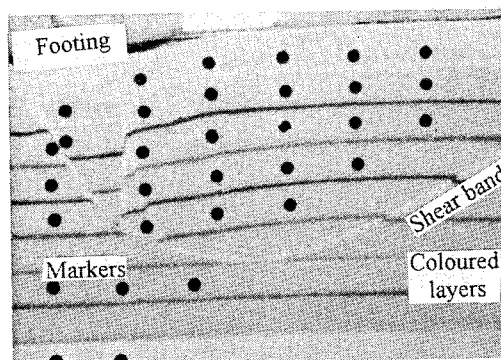


Fig. 10 Failure surfaces observed below a shallow strip footing on level ground.

In these three zones, the strains are practically zero and the volumes of soil can be regarded as rigid blocks.

Figure 11 illustrates the global movements observed in the case of a strip footing at the top of a 2/1 slope.

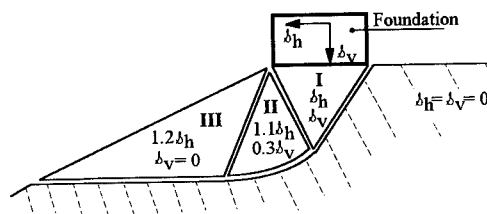


Fig. 11 Diagram of the failure surfaces observed in experiments on shallow foundations near slopes.

No significant discrepancy is found between theoretical and experimental failure surfaces, neither near slopes, nor on level ground.

### 3.2 Shape effect

Seventeen loading tests have been performed on rectangular footings ( $1 \leq L/B \leq 7$ ) placed on dry sand masses having horizontal ground.

Figure 12 shows the evolution of coefficient  $i_F$  (ratio between the pressure of failure of a rectangular foundation and that of a strip foundation having the same width) with the ratio  $L/B$ .

This figure includes the proposals of various experimenters (Weiß, Gemperline, De Beer). In light of these tests, it turns out that De Beer's proposal comes closest to the experimental range of values we found.

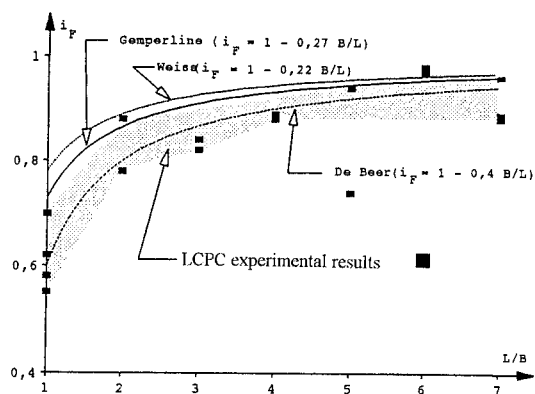


Fig. 12 Comparison of the experimental results on bearing capacity reduction coefficients related to the shape of the foundation.

### 4 CONCLUSIONS

Studies on centrifuge small-scale models have significant advantages over tests at actual sites. They make it possible to repeat the experiments on "identical" soil masses, and so to perform extremely valuable parametric studies.

However, it is important to conduct these programmes with the greatest possible rigor. With suitable automatic raining hoppers, it is now possible to guarantee a very large repetitiveness and very good homogeneity of the test samples (variations of density less than 1 %). Densities must be determined locally, below the foundation and not on the whole sample.

The same precautions must be taken in the modelling of the foundations, in the choice of loading devices and procedures, and in the

choice of criteria of failure, in the case of investigation of the bearing capacity.

In the longer term, it is probable that standardization of some phases of tests on centrifuge models (preparation and characterisation of soil samples, loading procedures) will be necessary so that the test results obtained on different installations will be directly comparable.

### REFERENCES

- Arulanandan, K. and Scott, F. 1993. Project VELACS - Control test results, J. Geot. Eng. ASCE, Vol. 119, no.8, August 1993, pp. 1276-1291.
- Bakir, N.E. 1993. Etude sur modèles centrifugés de la capacité portante de fondations superficielles. Thèse de Doctorat, Ecole Centrale de Nantes, 193 p.
- Corte, J.F., Fargeix, D., Garnier, J., Bagge, G., Fuglsang, L., James, R.G., Shi, Q. and Tan, F. 1988. Centrifugal modelling of behaviour of shallow foundation - cooperative test programme, Proc. Centrifuge 88, Paris, pp. 325-336.
- Garnier, J. and Cottineau, L. M. 1988. La centrifugeuse du LCPC: moyens de préparation des modèles et instrumentation, Proc. Centrifuge 88, Paris, pp. 83-90.
- Garnier, J., Kus, B. and Levacher, D. 1993. Cartographie des densités de massifs de sable reconstitués par pluviation, 6<sup>ème</sup> colloque Franco-Polonais, Douai, pp. 105-112.
- Garnier, J., Canepa, Y., Corte, J.F. and Bakir, N.E. 1994. Etude de la portance de fondations en bord de talus, Proc. XIII ICSMFE, New Delhi.
- Rault, G. 1992. Essais en centrifugeuse de chargement de fondations sur un sol bicouche, Rapport d'essais pour le Groupe Validation de Modèles Numériques du Greco Géomatériaux, 39 p.
- Yamaguchi, H. - Kimura, T. and Nariaki, F. 1976. On the influence of progressive failure on the bearing capacity of shallow foundations in dense sand, Soils and Foundations, Vol. 16, no.4, pp. 11-21.

## 9 Embankments and slopes

## Simulation of a sand column trial embankment

Bujang B. K. Huat

*Faculty of Engineering, University Malaysia Sarawak, Malaysia*

William H. Craig

*Department of Engineering, University of Manchester, UK*

**ABSTRACT:** The Malaysian Highway Authority (LLM) has run a major field exercise involving a number of trial constructions using different techniques of ground improvement for an embankment crossing an extensive, deep deposit of soft clay. Attempts have been made using centrifuge model techniques to simulate a trial embankment section built on sand columns. Whilst precise simulation of the field situation has not been practical, for a number of reasons, the essential features of the prototype have been retained. The model results have been found to be consistent with those of the field studies.

### 1 INTRODUCTION

A sand column improvement scheme has been incorporated in Section 6/5 of the Malaysian Highway Authority (LLM) trial embankment project on the Seremban to Ayer Hitam expressway. A general description of this site and objectives of the field trials have been outlined by Huat et al. (1991) in a paper on piled embankment, and are reported more fully by LLM (1989).

Sand or stone columns offer one solution to the problems of stability and settlement posed by construction of road embankments on soft ground. For reasons of economy under a widespread loading, granular support columns need to be widely spaced. The ultimate load capacity of the columns is insufficient to support the whole applied loading hence a significant proportion of the applied load will be carried by the ground between (Greenwood & Kirsch, 1984). This load sharing process between the columns and original ground will invariably influence the settlement behaviour of the treated foundation complex with simultaneous and interdependent changes of soil-column stress ratios, pore pressure and resul-

ting stiffness in both soil and column, depending on several parameters including area ratio and loading rate. This paper describes an attempt made to model the essential features of the prototype and to investigate the effect of the above mentioned parameters on the composite ground performance.

### 2 FIELD STRUCTURE

Figure 1 shows a cross section and instrumentation of the prototype sand column scheme as built. 462 compacted sand columns 0.7 m diameter for the upper 10 m above sand drains (uncompacted columns) 0.5 m diameter for the lower 10 m, were installed vertically in a square grid at 2.2 m centres in the 20 m deep clay foundation. The area ratio,  $A_c/A$  was 0.08 at the top of the column, where  $A$  is the total plan area attributed to a column of cross section  $A_c$ . Instrumentation installed included settlement gauges, piezometers, an inclinometer and landslip meters.

A total fill thickness of 9.9 m inclusive of a 1 m sand blanket was to be placed. Some 90 % of the primary consolidation settlement was expected by the end of the 15



month construction period, leaving 1.1 m of surcharge to be removed to give the desired embankment level of 6 m. A minimum factor of safety against slope instability of 1.2 was computed, assuming a gain in strength using the method proposed by Aboshi and Suematsu (1985). The actual performance of the field structure in terms of settlement, stability, generation and dissipation of excess pore water pressure is described below.

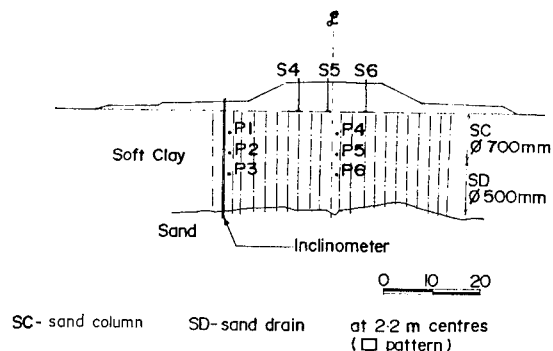


Figure 1: Prototype embankment (scheme 6/5)

### 3 MODEL TEST - CONSTRUCTION & INSTRUMENTATION

A series of centrifuge model tests has been performed, each nominally at 1 : 100 scale using essentially the same equipment and general techniques as in the earlier simulation of an adjacent piled structure described by Huat et al (1991). Troll clay was used to model the foundation and was consolidated from slurry to the required undrained strength profile, while mixed fill was used to simulate the embankment section. The sand columns were formed of fine Mersey River sand with  $D_{50}$  of 0.2 mm. Arguably this represents a 20 mm gravel at 1 : 100 scale, hence a stone rather than a sand column, but the intrinsic strength of the material would still be that of a sand.

Figure 2 shows a cross section and instrumentation of the model embankment. Ninety sand columns, 9 mm diameter, were installed to full depth of the clay foundation 200 mm, in a square grid spacing

of 35 mm, giving  $A_c/A = 0.05$ , slightly smaller than that of the prototype.

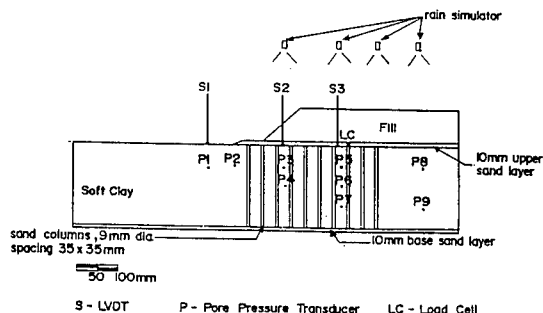


Figure 2: Model embankment

Ideally the EI of the column should be scaled down by  $100^4$  relative to the prototype, but since the in-situ values are not exactly known, the sand columns were only modelled to approximately scaled dimensions and installed in the densest possible state to a similar area ratio as in the prototype. Modelling of the sand columns involved utilisation of a freezing technique, similar to that described by Shinsha et al. (1991). Lengths of flexible plastic tubing, 9 mm internal diameter, 220 mm length (open at both ends) and with a slot cut down one side were used as reusable formers. These were held straight on a wooden template. The slot of each tube was first sealed with a tape, and a cloth plug was fitted to the lower end. Dry sand was then poured into each tube with a thin wire inserted at the centre to provide rigidity to the column whilst being handled. By tapping the board the sand was densified to an estimated relative density of 90 %. The assembly was slowly submerged in water until saturated, and placed inside a freezer for two hours. Once frozen, the tubes were recovered one at a time. The frozen columns were then withdrawn from the tube and inserted inside prebored vertical holes in the clay foundation layer. Once the ice had melted the wire insert was slowly withdrawn, tamping the sand column in the process.

Pore pressures within the model were measured with miniature Druck transducers, and the surface settlements were measured with LVDTs. Spaghettti displacement indicators were used to reveal subsoil deformations. Continuous undrained strength profiles were obtained during centrifuge runs using a cone penetrometer, in addition to vane and penetrometer data and water content profiles obtained before and after each test. General methods of soil bed preparation, of test and instrumentation have been described by Huat et al. (1991). The model foundation was subjected to a bedding run at 100 g for approximately 1 hour, the purpose being to ensure initial equilibrium between compressible columns and their surrounding clays. The centrifuge was brought to a halt and the full embankment section was formed by lifting into place a precompacted block of fill above a 10 mm upper sand layer which acted as a drainage blanket. The staged construction of the prototype was simulated by spinning the model at 62g for 37 mins (99 days), at 76g for 17 mins (68 days), and at 88g for 22 mins (118 days) before the simulation of full embankment at 100g for several hours.

#### 4 PROTOTYPE & MODEL PERFORMANCE

The prototype at Section 6/5 was instrumented as shown in Figure 1. Installation of the columns took place in March and April 1987, after placement of a 1 m working platform and drainage blanket of sand, and construction of the embankment began in April 1988 and continued until June 1989, with intermittent rest periods, Figure 3. However in November 1988 (Days 223 - 225) the fill thickness was reduced from 8 m to 6.9 m after significant lateral movements and tension cracks were observed on Day 213 at both slope and crest of the embankment. Stabilising berms shown in Figure 1 were constructed, before the fill was brought to final thickness, 9.2 m.

Figure 3 also shows the field settlement and pore pressure records. Both rate of settlement

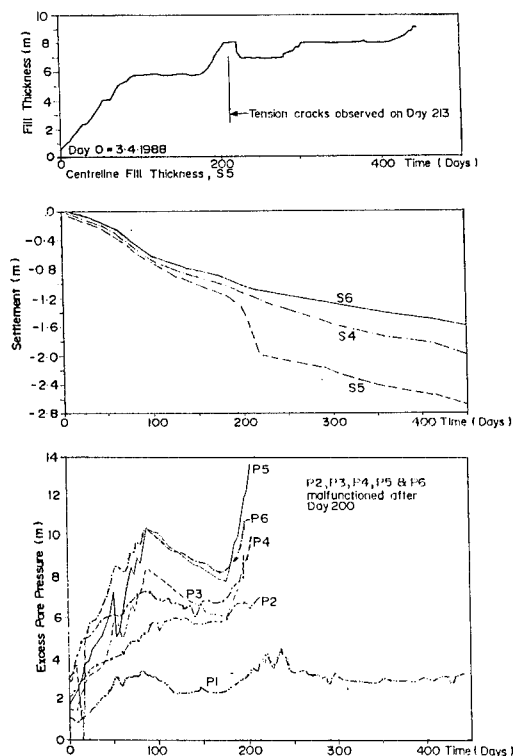


Figure 3: Field results

and reduction in excess pore water pressure were significantly larger than those at a nearby control section without any foundation treatment (LLM 1989). Unfortunately, all piezometers except P1 malfunctioned from Day 200 onwards, but during the construction pause periods (Days 100 - 170), some 43% of excess pore water pressure had dissipated with larger dissipation shown at the shallowest piezometers, P1 and P4. Ignoring dissipation due to vertical drainage, coefficient of consolidation back calculated from Barron's equation was around 1 m<sup>2</sup>/yr, half the value assumed in the original design based on laboratory oedometer testing. This seems to suggest that installation of the column, in particular driving of the casing, caused the formation of a smear zone and reduced soil permeability in the vicinity of the column. The importance of this effect has been recognised (Hansbo, 1987),

but, owing to the close spacing of the columns rapid dissipation of excess pore pressure had still been achieved.

A final settlement of 3.1 m was expected beneath the centre of the embankment. This gives only a modest settlement improvement  $n = 1.32$  (defined as the ratio of untreated to treated ground settlement) for 4.1 m final untreated ground settlement calculated using conventional 1D method, because the improvement area ratio was fairly small. The end-of-construction (Day 450) settlement of the treated ground was 2.6 m.

Figure 4 shows the plot of maximum lateral deformation ( $y$ ) versus centreline settlement ( $s$ ) plot. The initial ground deformation up to Day 180 under 6 m of fill was similar to that at the control section with  $\Delta y / \Delta s = 0.27$ . However from Day 180 to 200, when the fill thickness was raised to 8 m,  $\Delta y / \Delta s$  increased sharply to 0.75. Unfortunately the inclinometer became inaccessible from Day 201 onwards but measurements from the landslip meter installed beneath the embankment toe indicated a substantial increase in movement between Day 200 - 220. This resulted in formation of tension cracks described above, attributable to the instability of the adjacent piled scheme (Section 6/4) as well as to a period of heavy rainfall on the site. The calculated factor of safety against undrained failure was still greater than unity (Mizuno et al., 1989). Subsequent removal of 1.1 m of surcharge and construction of berms on both sides of the embankment appear to have been successful in containing an overall collapse. The width of the crack did not increase beyond Day 225, and filling to 9.2 m was resumed on Day 285.

Figures 5, 6 and 7 show results of the model test. Rapid dissipation of excess pore water pressure was in evidence beneath the embankment centre (Figure 5), and at locations closest to the drainage boundaries (transducers P5 & P7), when compared with the section without the sand columns (transducers P8 & P9). Average

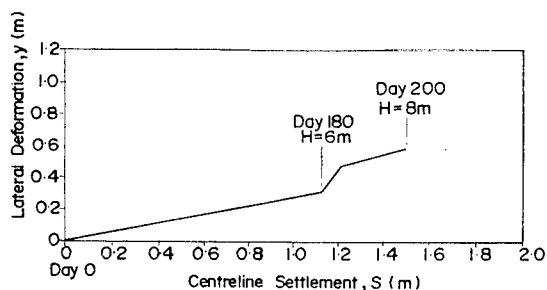


Figure 4: Field lateral deformation - settlement

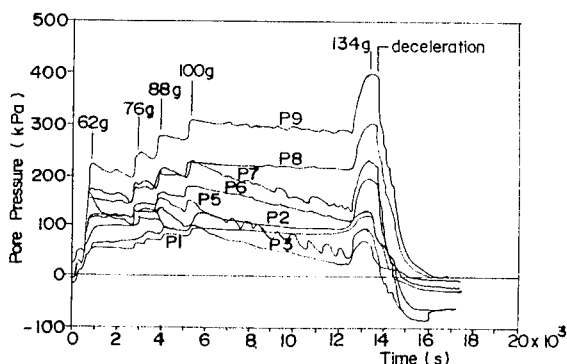


Figure 5: Pore water pressure of model

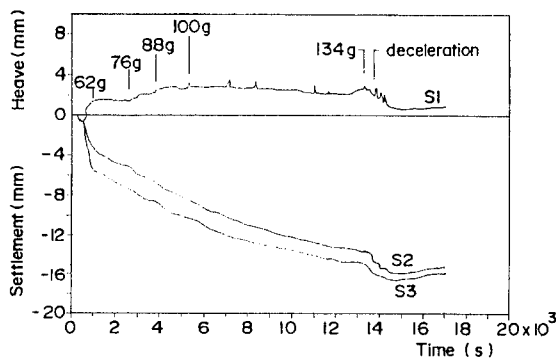


Figure 6: Settlements of model

degree of consolidation ( $U$ ) at the centre of the column section was 48 % at the end of the simulated construction, and after 2.08 hours (2.37 yrs) was 93 % compared with 30 % at the untreated section. No delayed pore pressure response or continued rise in pore pressure

after end of construction was observed beneath the toe and slope of the model embankment, although pore pressure stagnation did initially occur (transducers P2 & P3). Transducer P1 located 60 mm (6 m) forward of the toe indicated no apparent pore pressure development beyond the extent of the loaded area, with pore pressure ratio ( $\Delta u/\Delta \sigma_v$ ) remaining close to 0.8 at 100g and at 134g. The rapid dissipation of excess pore water pressure resulted in rapid consolidation settlement (LVDT S2 & S3, Figure 6). During simulation of the embankment construction only a small heave was observed at the toe, and this recompressed once further consolidation was allowed after end of construction. At the end of 2.08 hours acceleration at 100 g (2.37 yrs) a total settlement of 15.3 mm (1.53 m) was measured beneath the embankment centre. A final settlement of 16.5 mm (1.65 m) was expected for the treated foundation giving a settlement improvement,  $n$ , of 1.36. This was close to that of the prototype. End of test observation of the model, consistent with the above, indicated no apparent failure even after the acceleration was brought to maximum, 134g (12.3 m fill). The spaghetti indicators deformed uniformly with depth without any sharp changes or break (Figure 7), and no crack was observed at the embankment slope. It can also be seen from Figure 7 that the columns deformed with the surrounding soil, both columns and clay appeared to have settled together with equal strain. Figure 8 shows the initial and final clay shear strength measurements from the

model foundation together with calculated strength gains obtained using a method described by Barksdale (1987). Significant strength increase through consolidation was observed beneath the embankment centre but not under the untreated section or at a location 200 mm (20 m) forward of the toe where there had been minimal consolidation.

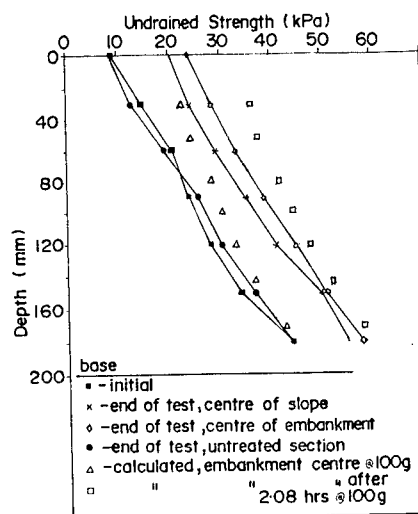


Figure 8: Shear strength of model

## 5 CONCLUSIONS

An attempt has been made using centrifuge model techniques to be simulate a trial embankment section built on sand columns. Whilst precise simulation of the field situation has not been practical, the essential features of the prototype have been retained. The model results have been found to be consistent with those of the field studies.

The centrifuge modelling permits monitoring of consolidation effects within a few hours. Inclusion of the columns reduces soil drainage path lengths, and naturally increases the rate of excess pore pressure dissipation. Installation of the columns by displacement techniques such as use of the casing driver for sand may reduce soil permeability due to formation of smear zones along the column boundary but since the

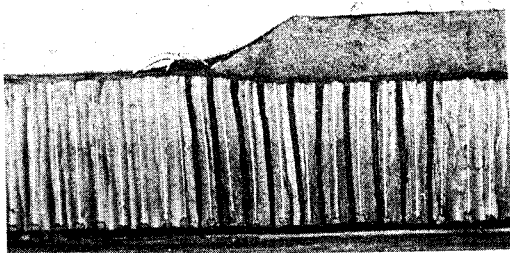


Figure 7: Section of model, photographed after end of test

columns are closely spaced, rapid dissipation of excess pore water pressure can still be achieved.

The behaviour of the composite soil/sand column foundation is complex but, in general as the soil consolidates, strength gain increases the degree of confinement afforded by the soil to the column, improving embankment stability.

#### 6 ACKNOWLEDGEMENT

The field data is made available by the Malaysian Highway Authority.

#### 7 REFERENCES

- Aboshi, H. & N. Suematsu (1985): The State of the Art on Sand Compaction Pile Method. Proceedings 3rd. NTI International Geotechnical Seminar, Singapore, pp. 1 - 12.
- Barksdale, R.D. (1987): State of the Art for the Design and Construction of Sand Compaction Piles. US Army Corp of Engineers, Report No. REMR-GT-4, Washington DC, 55 p.
- Huat, B.K.K., W.H. Craig & C.M. Merrifield (1991): Simulation of a Trial Embankment Structure in Malaysia; Proceedings Conf. Centrifuge 91, (editors) Ko and McLean, Balkema, Rotterdam, pp. 51 - 57.
- Greenwood, D.A. & K. Kirsch (1984): Specialist Ground Treatment by Vibratory and Dynamic Method. Piling and Ground Treatment, Thomas Telford Limited, London, pp. 17 - 45.
- Hansbo, S. (1987): Design Aspects of Vertical Drains and Lime Column Installation. Proceedings 9th South East Asian Geotechnical Conference, Bangkok, pp. 8.1 - 8.12.
- LLM (1989): Prediction and Performance. Proceedings of International Symposium on Trial Embankments on Malaysian Marine Clay, Malaysian Highway Authority, Kuala Lumpur, November 6 - 8.
- Mizuno, Y., W. Shibata & Y. Kanda (1989): Trial Embankment with Sand Compaction Pile Method at Muar Flats. Proceedings International Symposium on Trial Embankments on Malaysian Marine Clays, Kuala Lumpur, Vol. 2, pp. 2.53 - 2.66.
- Shinsha, H., K. Takata, Y. Kurumada & N. Fujii (1991): Centrifuge Model Tests on Clay Partly Improved by Sand Compaction Piles. Proceedings Conf. Centrifuge 91, (editors) Ko and McLean, Balkema, Rotterdam, pp. 311 - 318.

## The behaviour of soft subsoil during construction of an embankment and its widening

A.G.I. Hjortnæs-Pedersen & H. Broers  
*Delft Geotechnics, Netherlands*

**ABSTRACT:** To study the behaviour of soft subsoil during construction of an embankment and its widening centrifuge tests were performed in the large centrifuge of Delft Geotechnics. The aim of the study was to determine the relation between the stability during staged construction of the embankment and its widening and the developed vertical and horizontal deformations. A part of the study was also to validate calculation programs based on Mohr-Coulomb and Cam-Clay soil models. A Dutch clay, remoulded however, was used as soil foundation material.

### 1 INTRODUCTION

In order to increase the capacity of the infrastructure, it is often necessary to widen the existing railroad and motorway embankments. The widening of an embankment build on soft subsoil results in considerable horizontal and vertical deformations of the subsoil. The horizontal deformations caused by a widening are difficult to predict with actual calculation methods. Therefore it was decided to investigate experimentally in the centrifuge of Delft Geotechnics the behaviour of the subsoil during staged construction of an embankment and its widening. The subsoil was prepared from a remoulded natural Dutch soft clay (Oostvaarderplassen) and selfweight consolidated in the centrifuge to obtain stress conditions corresponding to the real site. To determine the soil properties of the remoulded natural clay used to prepare the soil foundation and to study the influence of the preparation method, an extensive laboratory programme was carried out involving both standard and not standard tests on undisturbed and remoulded natural clay samples.

A number of in-flight stage constructed embankment tests have been carried out in the past, Almeida (1985), Basset (1981) to study the behaviour of the soil foundation below the embankment. In this study, both the existing embankment and its widening have been stage constructed in flight in a fully controlled way with respect to profile making and loading sequence using the hopper facility of Delft Geotechnics, Allard (1994) capable of constructing a great variety of embankment combinations in a controlled way.

The staged construction of the embankment and its widening happened according to a predicted scheme based on effective stress analysis (Bishop, FEM-

programme PLAXIS), where the time period between the construction stages depended on the calculated degree of consolidation related to a certain prescribed stability.

Two tests were carried out. In both tests, the first embankment was constructed in a similar way following a scheme related to a calculated safety factor of 1.2. The widening in one test was constructed in accordance with 1.2 and in another with 1.05. During construction of the embankments excess pore pressures, dissipation and surface settlement were measured. Vertical and horizontal deformations in the subsoil were measured using image processing. Cone penetration tests were carried out in flight to measure the tip resistance along the depth.

The paper focus on the preparation and the performance of the tests including the parameter study of the model soil. Measured pore pressures, settlements and local deformations during staged construction of the widening are presented. At this stage, the measurements are compared with the results of the FEM-program PLAXIS based on the Mohr Coulomb soil model. Furthermore it is evaluated, whether the actual obtained stability factors of the widenings are in agreement with the predicted ones.

### 2 MODEL SET-UP

The prototype embankment, its widening and the clay foundation, as shown in Fig. 1, is scaled at 1:120. The height of the clay foundation is 8.5m, the total heights of embankments I and II (widening) are respectively 8.65m and 10.65m. Embankment I is constructed in 7 stages and embankment II in 9. The actual height of each stage follows from predictions performed with effective stress analyses. The angle

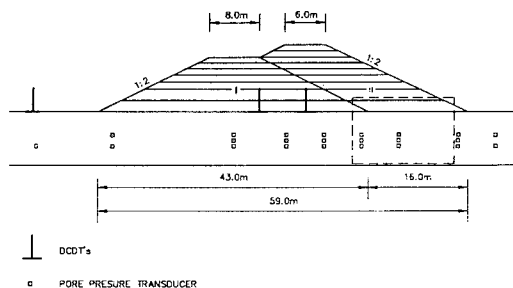


Fig. 1 Prototype dimensions.

of slope of the embankments was 1:2. The model set-up consist of two phases. The first phase is related to creation of the initial stress condition of the soil foundation and the second phase is related to the construction of the embankments. The length profile of the model set-up belonging to phase 2 of the test is seen in Fig. 2.

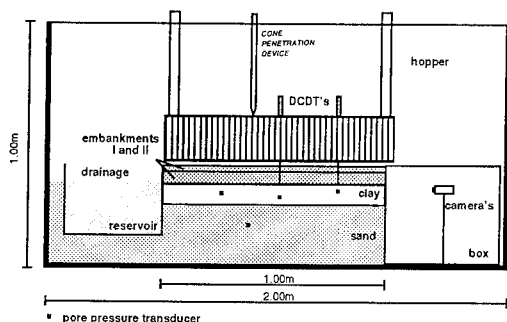


Fig. 2 Model set-up, length profile belonging to phase 2 of the tests.

A sand layer was placed below the model clay. The sand layer was connected to a reservoir built into the model container to assure proper drainage during the whole test. Drainage holes were made in the walls of the reservoir to control the mean water level. Two pore pressure transducers were placed in the sand layer to control that no excess pore pressure was build up in the drainage layer. During phase 1 a light weight foam foreseen with a filter was placed on top of the clay slurry. The load creating the in-situ stress condition of the soil foundation is applied using the sand hopper. The foam prevents the rained sand grains to penetrate into the soft slurry.

Through the hopper the vertical surface settlement is measured at 6 positions using DCDT's. To measure the excess pore pressure during the staged construction and to follow the dissipation in between the stages, 23 pore pressure transducers (DRUCK PCDR81) were placed at 3 levels in the clay foundation. A cone penetrometer with a diameter of 7mm was mounted on a frame connected to the large

centrifuge container in order to perform cone penetration tests in-flight through the hopper.

In front of the model, a box is placed in which high resolution camera's, etc. are mounted to follow and measure by means of image processing the deformation of the clay foundation during testing. In Fig. 3 the cross section of the model including the embankments is seen together with the position of instrumentation and equipment.

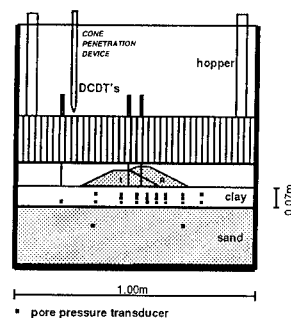


Fig. 3 The cross section of the model set-up.

### 3 PREPARATION OF MODELS

#### 3.1 Soil material

A remoulded natural dutch clay (Oostvaarder-plassen clay) was used to prepare the clay foundation. Many other centrifuge model tests involves Speswhite kaolin, see e.g. Almeida (1985) due to the relatively high permeability. In the present test dissipation of excess pore pressure would happen too fast to fulfil the requirement of the construction scheme of the embankments. Further, it was required to use a soft clay with compressibility and strength parameters in the neighbourhood of a typical dutch clay. Dependant of the characteristics of the clay, the strength and consolidation properties will be different between natural and remoulded clay, (Skempton, (1943). When mixing natural clay with deaired water the properties are influenced by the initial stage below a certain isotropic stress level.

To determine the soil properties of the remoulded model clay and to study the influence of the preparation method, an extensive laboratory programme was carried out involving both standard and not standard tests on undisturbed and remoulded natural clay samples, Hjortnaes (1993). The remoulded material used in the laboratory tests was prepared as the slurry for the centrifuge test, see section 3.2.

Three types of soil parameters were derived:

- mechanical parameters,
- strength parameters and
- consolidation/compression parameters

The results of the laboratory tests are seen in Table 1. The strength parameters were derived from

a number of high quality triaxial tests carried out on natural samples and remoulded clay sample. The remoulded clay samples were prepared from a clay bread preconsolidated with a surcharge of 15 kPa, corresponding to the surcharge of the natural samples. Comparing the undrained shear strength of the remoulded and undisturbed clay samples at similar water content, the clay can be characterized as medium sensitive.

To validate a numerical program FSCONBAG developed at Delft Geotechnics, Greeuw (1992) based on the theory of finite strain proposed by Gibson (1967), and to predict the duration and settlement of slurry consolidation of the centrifuge tests, the relations between the effective vertical stress and void ratio,  $\sigma'_v(e) - e$ , and the permeability and void ratio,  $k(e) - e$ , were determined using the results of hydraulic consolidation tests performed in a special developed test set-up and selfweight consolidation tests performed in a small centrifuge.

Table 1 Properties of OVP-clay, (1) oedometer test, (2) table centrifuge tests, (3) hydraulic consolidation tests, (4) triaxial test (CU).

Mechanical properties			
specific gravity	(d <sub>s</sub> )		2.53
liquid limit (LL)			112.8 (%)
plasticity index (PI)			84.1 (%)
plastic limit (PL)			28.7 (%)
unit weight ( $\gamma$ )			15.2 (kPa/m)
liquidity index (LI)			0.74
ignition loss			9.51 (%)
Consolidation/strength properties			
<i>Remoulded OVP clay</i>			
cons. coef. (1)	( $c_v$ )		5.0E-09 (m <sup>2</sup> /s)
cons. coef. (2)	( $c_v$ )		2.0E-08 (m <sup>2</sup> /s)
comp. coef. (1)	( $C_p$ )		8.0
comp. coef. (2)	( $C_p$ )		7.3
$\sigma'_v(e)-e$ (2)			$\exp(8.37-2.3e)$
$\sigma'_v(e)-e$ (3)			$\exp(9.37-2.59e)$
$k(e)-e$ (3)			$\exp(-22.6+2.6e)$
friction angle(4)	( $\phi$ )		28.4 (°)
cohesion (4)	( $c$ )		3.9 (kPa)
$c_u/\sigma'_v$ (-)			0.37
<i>Natural OVP clay</i>			
cons. coef. (1)	( $c_v$ )		3.0E-09 (m <sup>2</sup> /s)
comp. coef. (1)	( $C_p$ )		6.3
friction angle(4)	( $\phi$ )		32.0 (°)
cohesion (4)	( $c$ )		6.8 (kPa)
$c_u/\sigma'_v$ (-)			0.40

In both tests the maximum effective stress was 45 kPa at the bottom of the sample at the end of the consolidation corresponding to the in-situ stress profile of Fig. 4(a) without surcharge. The selfweight slurry consolidation can not be described by the conventional theory of Terzaghi, but with the finite strain theory (Gibson, 1981), which takes into

account, that the void ratio  $e$  differs with the effective vertical stress  $\sigma'_v$  along the height of the sample and that the permeability depends on the void ratio. The relations derived from the two type of tests were in good agreement with each other, see Table 1.

The average consolidation coefficient and the compression coefficient were determined from standard oedometer tests carried out on samples preconsolidated at 15 kPa. The same parameters were determined from selfweight consolidation tests carried out on samples preconsolidated with a maximum effective stress of 45 kPa at the bottom of the sample. In both tests the maximum load was 150 kPa. The derived compression coefficient from the different tests were comparable, while the average consolidation coefficients derived from the oedometer test were underestimated, see Table 1.

### 3.2 Centrifuge models

The slurry used for the centrifuge tests was prepared by mixing deaired water with the natural soft clay until an initial water content of 140% was reached being well above liquid limit of the clay. The slurry was mixed for several hours under vacuum in order to get rid of entrapped air and to obtain a homogeneous slurry. The slurry was poured down into the model container, where the deaired, saturated pore pressure transducers were placed already. Phase 1 of the tests involved preparation of

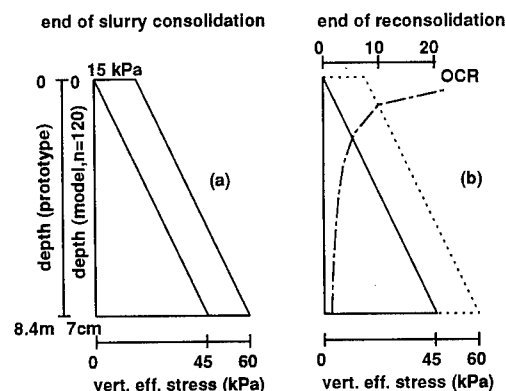


Fig. 4 The stress profile at the end of slurry consolidation and reconsolidation.

the clay foundation. The slurry was selfweight consolidated for 10 hours at a rotational velocity of 137.8 RPM corresponding to 120g. On a light weight foam resting on top of the clay surface, a surcharge of 15 kPa was uniformly dumped in flight using the hopper. The consolidation continued until the stress profile of Fig. 4(a) was obtained. At the end of the slurry consolidation a cone penetration test was carried out in flight with a velocity of 2cm/s. The centrifuge was stopped to place a grid of



contrast colour on the clay and to remove the foam with the surcharge.

The hopper was filled with Eastern Scheldt sand ( $n_{\min}=0.35, n_{\max}=0.46$ ) according to the scenario made for the aimed stage constructed embankment (Allard, 1994). The average porosity of the embankment at 120g, was 0.40 corresponding to an internal friction angle of  $\phi=35^\circ$ .

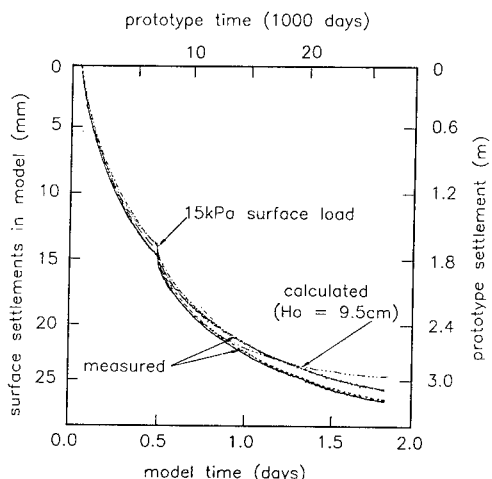


Fig. 5 Calculated and measured settlement during slurry consolidation

The settlement measured during slurry consolidation has been compared with the results of FSCONBAG, Greeuw (1992), see Fig. 5. The parameters related to selfweight consolidation as given in table 1 have been used as input for the program. The deviation in the measured settlement is due to a difference in initial height caused by the circular shape of the clay surface undergoing the centrifugal force. The total settlement at the two measuring positions vary between 0.026m and 0.027m (model scale) while the calculated becomes 0.025m being somewhat underestimated. However, still a good agreement is found between the measurements and the calculation.

#### 4 TEST PROCEDURE

The test procedure followed during phase 2 of the tests, involving the construction of the embankments, was:

- The clay foundation was reconsolidated until the stress profile in Fig. 4 (b) was reached. The final stress profile over the height corresponds to the conditions of the site where the natural clay was deducted.
- At the end of the reconsolidation of the clay foundation a cone penetration test was carried out with a velocity of 2cm/s, (only in the second test).
- Embankment I was constructed in 7 stages, see Fig. 6. In between each stage the developed excess

pore pressures were allowed to dissipate according to a scheme predicted with Bishop and PLAXIS. A safety factor of 1.2 has been used in the predictions.

- After construction of the whole embankment I the generated excess pore pressures were allowed to dissipate until 95% consolidation was reached.
- Embankment II was constructed in 9 stages according to Fig. 6. In between each stage the developed excess pore pressures were allowed to dissipate according to a scheme predicted with Bishop and PLAXIS. A safety factor of 1.05 has been used in the predictions in one of the tests and 1.2 in the other.
- After construction of the whole embankment II the generated excess pore pressures were allowed to dissipate until 80% consolidation was reached. This phase was included to follow the residual deformations after total placement of the widening.

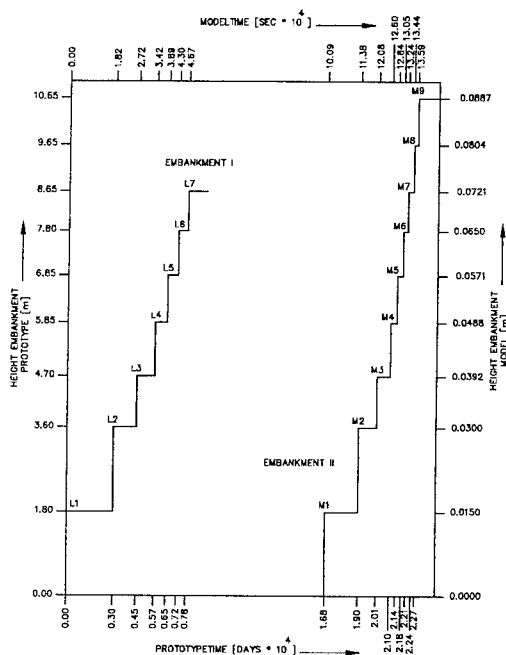


Fig. 6 Loading history of the embankments I and II.

#### 5 RESULTS OF MEASUREMENTS

##### 5.1 The undrained shear strength.

The resistance forces measured at the end of the slurry consolidation and before construction of the embankment were converted into the undrained shear strength using eq. (1), where  $f_c$  is the tip resistance,  $N_c$  the tip bearing capacity factor and  $q$  the initial in situ total stress.

The results of the measurement are seen in Fig. 7.

$$c_u = \frac{(f_c - q)}{N_c} \quad (1)$$

It is seen, that there is a very good agreement between the undrained shear strength measured at the end of the slurry consolidation in the two test, thus the obtained stress profile was identically. The influence of the surface load is seen close to the surface. In one of the tests the cone touched the foam just before entering the clay.

The influence of the sand layer below the clay foundation is measured in the clay at a distance 3 times the diameter of the cone, which is in accordance with expectations.

Using  $N_c=14$ , which is the typical empirical value of Dutch normal consolidated (NC) clay, the relation  $c_u/\sigma'_v=0.37$  is determined from the regression line describing the strength of the NC clay (Fig. 4(a)), not influenced by the underlying sand layer. This is in agreement with the average results of the triaxial tests.

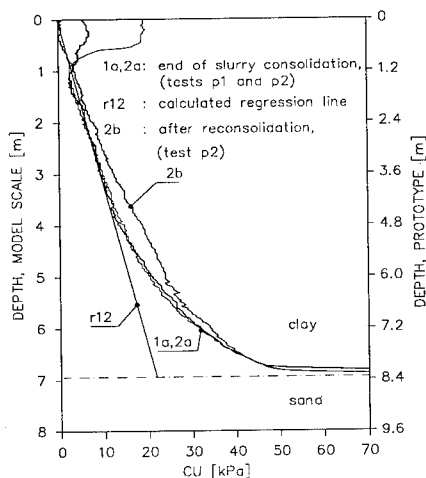


Fig. 7 Measured undrained shear strength as function of depth.

From the cone penetration performed just before placement of the embankment a similar average relationship of  $c_u/\sigma'_v = 0.41$  in the over consolidated layer is obtained using an average value of  $N_c=15$ . The reported empirical  $N_c$  values belonging to OC-clay are higher ( $N_c=15-20$ ), than for NC-clay which vary between ( $N_c=10-15$ ), see e.g. Lunne (1986).

## 5.2 Pore pressures and deformations.

Test results related to the test, where the widening is constructed in accordance to a predicted safety factor of 1.05, are mainly presented. To follow the excess pore pressures developed as a consequence of the loading history and the dissipation in between the stages a representative set of measurements in one

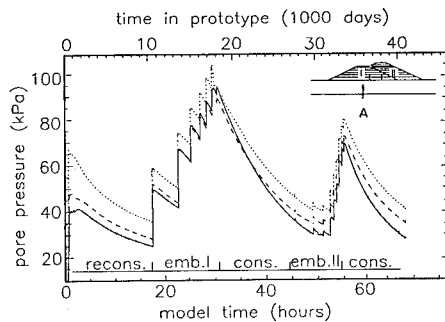


Fig. 8 Measured pore pressures during the whole test p2, in vertical A.

vertical is shown in Fig. 8

In Fig. 9, 3-dim. profile plots show, how the excess pore pressures are developed during the construction of the stages M3 and M9 of embankment II (widening). The pore pressures present just before placement of the embankment have been used as references. The excess pore pressures present just before construction of the M3 stage represents the residual excess pore pressures following from the construction of the stages M1 and M2.

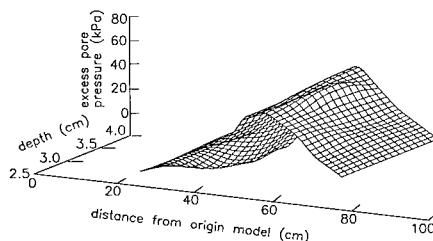
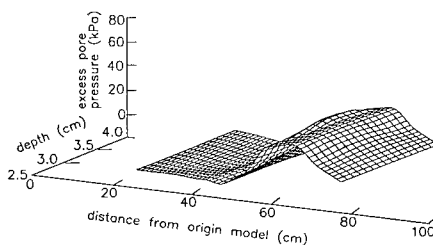


Fig. 9 Excess pore pressures just after construction of stages M3 and M9.

Immediately after construction of a stage the influence of the additional load is seen. Due to stress redistribution the measured excess pore pressure does not represents the actual load as applied, especially

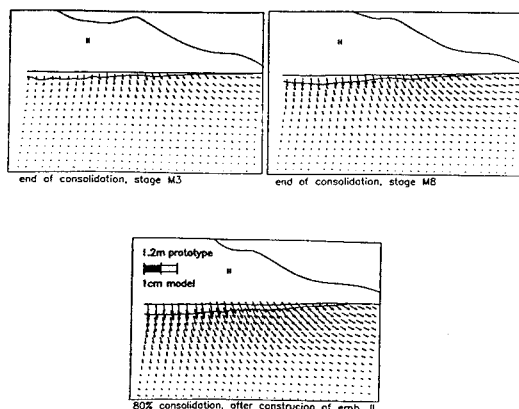


Fig. 10 Displacement vectors below embankment II.

not close to the toe and at higher stages. After each construction stage the excess pore pressure continue to rise up to 15 % of the instant increase of excess pore pressure due to loading. This can be due to redistribution of pore pressures and due to the development of plasticity especially close to the toe of the slope, where most rise is measured.

The isochrones of the pore pressure along the depth would have been more obviously in the plots, if additional measurements had been performed closer to the boundaries. However, still an indication of the building up of excess pore pressures following the loading sequence is seen.

Below the slope of the widening horizontal and vertical deformations have been measured using image processing on a grid with 4mm distance between the lines. In Fig. 10 the displacement vectors belonging to the end of the dissipation of stages M3 and M8 are shown together with the stage at 720min. (80% consolidation) after construction of embankment II. The measurements at the moment just before construction of the widening have been used as reference. The mean water level, the clay layer, and the surface of the embankment are seen, for the area of image processing, see Fig. 1.

In Fig. 11 the horizontal deformation at location 64.8 cm and 71.7 cm are presented in inclinometer plots. In Fig. 12 the local vertical deformation measured at 1 cm below the clay surface are presented in inclinometer plots. Each set of measurements represent the situation at the end of a each stage just before applying a new one. Also the deformations 720 min (in reality 7200 days) after the end of the construction are shown.

During construction of embankment II, the largest vertical deformation was measured to be 0.45 cm (0.54m in prototype) below the centre of the slope of the widening, just outside the toe of embankment I. Below the toe of the embankment II the largest deformation was found to be 0.3cm (0.36m in prototype). The total maximum/minimum

deformations after 80 % consolidation were respectively 0.72cm/0.5cm, (0.86m/0.6m in prototype). The differential settlement occurs mainly during construction, while during final consolidation hardly no difference is found.

The largest horizontal deformation was measured close to the toe of the widening 0.31 cm (0.37 m in prototype). After 80 % consolidation the total

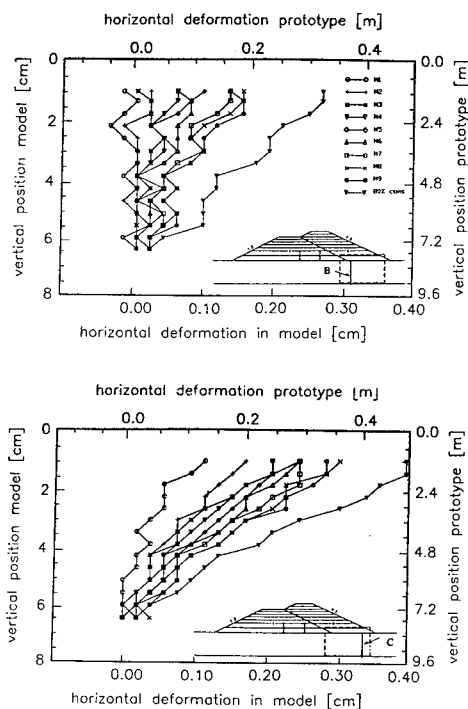


Fig. 11 Horizontal inclinometer plots during staged construction of emb. II, verticals B and C.

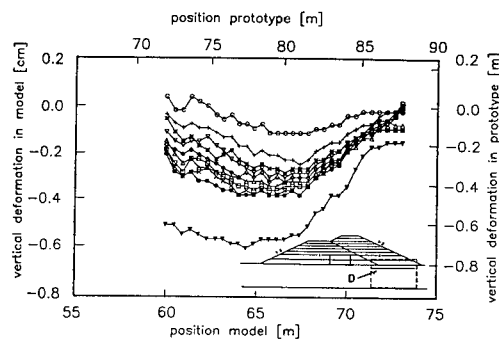


Fig. 12 Vertical inclinometer plots during staged construction of emb. II, (level D).

maximum horizontal deformation became 0.40 cm (0.48 m in proto-type). From profile measurements performed after the test it was found that the measured angle of slope of the widening corresponded to the prescribed of 1:2. This is due to the accuracy by which an embankment can be made with the hopper. This is of great importance, when performing stage constructions in accordance with safety factors.

## 6 MEASUREMENTS COMPARED WITH PLAXIS

### 6.1 Parameter choice

In table 2 a summary is given of the soil properties used in the finite element calculations, see also section 3.1.

Table 2 Soil properties used in the FEM calculations.

Soil properties for FEM calculation		
OVP remoulded clay		
unit weight $\gamma$	[kPa/m]	15.2
cohesion $c$	[kPa]	3
friction angle $\phi$	[°]	24
Shear mod. $G$	[kPa]	140
poison ratio $\nu$	[-]	0.35
consol. coeff. $c_v$	[m <sup>2</sup> /s]	2E-8
permeability $k$	[m/day]	2.84E-5
Eastern Scheldt sand		
unit weight $\gamma$	[kPa/m]	15.2
cohesion $c$	[kPa]	1
friction angle $\phi$	[°]	35
Shear mod. $G$	[kPa]	5000
poison ratio $\nu$	[-]	0.33

The shear modulus  $G$  and the permeability  $k$  depend on the effective isotropic stress level in the soil. The parameters used in the FEM calculations correspond to the average effective stress level in the subsoil before loading and the maximum surcharge of the widening.

### 6.2 FEM calculations.

The construction of the embankment and the widening has been simulated with the finite element program PLAXIS. The calculations are based on an elastic-plastic Mohr-Coulomb soil model and on elastic consolidation. In the comparison between results of centrifuge test and calculation the prototype dimension is used.

In Fig. 13 the calculated development of excess pore pressure due to building of both embankments is shown at two locations, one situated under the right slope of embankment I and one situated under the toe of the embankment II (widening).

Furthermore the measured excess pore pressure under the slope of the widening is given.

Comparison between the calculated and the measured excess pore pressures shows that the measured excess pore pressures generated during the construction of embankment II (widening) are about 15 percent higher than the calculated excess pore pressures. One explanation is the instant compressibility of the modelled subsoil in the calculations, which results in an increase of the effective stresses directly after loading.

An other possible explanations is the development of excess pore pressures in the centrifuge model test due to plastic deformations.

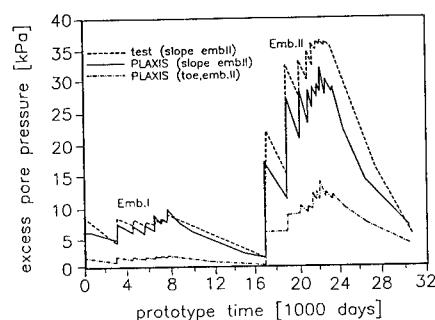


Fig. 13 Excess pore pressure under slope and toe of embankment II

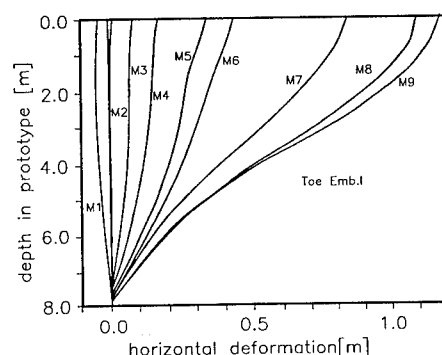


Fig. 14 Horizontal deformations below the toe of emb. I, vertical B in Fig. 11.

In Fig. 14 and Fig. 15 the horizontal deformations, below, at the right side of the toe of embankment I and under the toe of embankment II (widening) are presented. Only the deformations caused by the construction of embankment II (layer M1-M9) are shown. The calculated horizontal deformations for the last three layers (M7-M9) show a sudden increase caused by a relative low slope stability.

For the first 6 layers (M1-M6) the calculated safety factor is  $SF > 1.08$ . For the last three layers (M7-M9) the  $SF < 1.05$ . Due to this low slope stability large plastic zones occur resulting in large deformations.

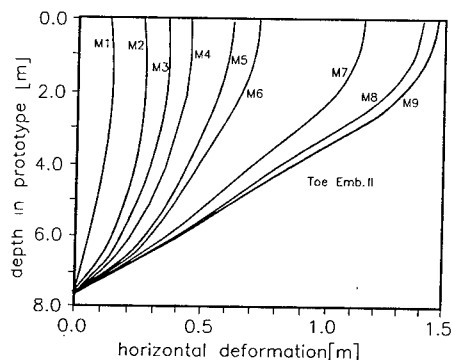


Fig. 15 Horizontal deformation below toe of emb. II, vertical C in Fig. 11.

Comparison between the calculated and measured horizontal deformations, see also Fig. 11, shows an overestimation of the horizontal deformation with a factor ranging from 2 to 3, for safety factors  $SF > 1.08$ . When the safety factor becomes  $SF < 1.05$  the calculated horizontal deformations largely overpredict the measured deformations.

In Table 3 a summary is given of the measured and calculated maximum vertical deformation below the toe of emb. I and between emb. I and II after construction of layer M6 ( $SF > 1.08$ ) of embankment II, at the end, and after 80% consolidation.

Table 3. Measured/calculated vertical deformations after construction of emb. II.

	centrifuge test /PLAXIS		
location	after M6	after M9	80% cons.
toe emb. I	0.40m/1.13m	0.54m/1.31m	0.86m/1.02m
between emb. I/II		0.30m/0.58m	0.60m/0.72m

## 7 CONCLUSION

The behaviour of the subsoil during and after the construction of combined embankments can be studied very well by means of centrifuge testing. It has been possible to compare experimental and calculated results in an optimum way, due to the fully controlled construction of the embankments using the hopper. At this stage a number of

conclusions can be drawn:

The settlement during selfweight consolidation in the centrifuge test (preparation of the model soil) agrees with the theory of finite strain.

The cone penetration tests show reproducible vertical effective stress profile of the subsoil. A good agreement is obtained between the strength parameters of laboratory and cone penetration test.

The measured excess pore pressures during staged construction of the widening is about 15% higher, than obtained from the calculation.

Just after construction of embankment II (widening), the vertical deformations calculated below the toe of embankment I and between embankments I and II are 2 to 2.5 times larger than the measured. However, after 80% consolidation good agreement is obtained.

The calculated horizontal deformations (Mohr-Coulomb model) are 2 to 3 times larger than the measured deformations for a safety factor above 1.08. A better agreement would be obtained by the Cam-Clay model.

Slope instability did not occur in the test opposite to the calculations.

## 8 ACKNOWLEDGEMENTS

The authors would like to thank all the colleagues of Delft Geotechnics, who contributed to the project.

## 9 REFERENCES

- Allard M.A., Hjortnæs-Pedersen A.G.I., Out J. (1994), "Performances of a sand hopper." , Centrifuge 1994, Singapore.
- Almeida, M.S.S, Davies, M.C.R, Parry, R.H.G, (1986), "Numerical Modelling of a centrifuged embankment of Soft Clay." Can. Geotech. J. 23, 103-114 (1986)
- Basset, R.H., Davies, M., Gunn, M, Parry, R. (1981), "Centrifugal Models to evaluate Numerical Methods.", ICSMFE, Stockholm.
- Greeuw, G., van Ommen, A., (1992) "FSCONBAG, a computer program for simulation of large strain consolidation."
- Gibson, (1981), "The theory of 1-dim. consolidation of saturated clays. Can. Geo. J. 18, pp. 280-293.
- Hjortnæs-Pedersen, A.G.I, Broers, H., (1993) "Behaviour of the subsoil due to construction of combined embankments". Delft Geotechnics, report SE-51053/3.
- Hjortnæs-Pedersen, A.G.I, Broers, H., (1993), "Material properties of Oostvaarderplassen clay" Delft Geotechnics Report SE-704441/1.
- Lunne, T., et. al (1986), " Laboratory and field evaluation of cone penetrometers." ASCE, In Situ '86, Virginia, Proceedings, pp. 714-729.
- Nelissen, H.A.M. (1991), "The Delft geotechnical centrifuge," Centrifuge 1991, Ko and Mclean Editors, pp. 35-42, Balkema Rotterdam Publishers.

## Failure of embankments due to seepage flows and its countermeasure

J. Takemura, T. Kimura & A. Hiro-oka

*Tokyo Institute of Technology, Japan*

H. Muraishi

*Railway Technical Research Institute, Tokyo, Japan*

**ABSTRACT:** Two series of centrifuge model tests were carried out to investigate the stability of loose embankments subjected to a seepage flow. One is a modelling of prototype for an unreinforced embankment with the prototype height of 3.5m under 25g and the other is tests for embankments reinforced with piles under different conditions of pile density and profile of water surface. Observed behaviour in the model embankment was very similar to that in the large scale 1g model. It was found that the deformation at the initial stage cannot be prevented by reinforcement with pile, however the catastrophic failure followed by the deformations can be prevented by the reinforcement.

### 1 INTRODUCTION

In Japan many railway and road embankments fail due to prolonged or heavy rainfalls during the rainy or typhoon season. These failures often cause main traffic lines to close, resulting in much inconvenience to the public and considerable economic loss. Many of the existing railway embankments were constructed quite long time ago without proper compaction and thus easy to fail by ground water flow in it. In the case where failure is detected, emergency reinforcement is usually done by driving piles in the slope of the embankment. This kind of countermeasure is purely empirical and the urgency of the situation makes it very difficult to observe the performance of reinforced embankment. Hence the effectiveness of the reinforcement has been hardly understood quantitatively.

The failure of embankments by rainfall or ground water flow is considered to be caused by many factors, i.e. increase of self weight and reduction of strength due to increase in the degree of saturation, and the decrease of effective stress due to a rise of ground water level. Scaling law of various types of ground flow in a centrifuge model were examined by Goodings (1984). Kimura et al. (1991) conducted a series of centrifuge model tests to investigate the failure mechanism of fills subjected to a heavy rain.

Two series of centrifuge model tests are carried out in this study. One is a modelling of prototype for an unreinforced embankment and the other is

for a reinforced embankment. In the former, centrifuge model tests were conducted, simulating a 1g scale a 3.5m high embankment which was failed by raising the ground water level in the embankment. In the latter, a series of failure tests for the model embankments reinforced with vertical piles were also conducted in a similar manner as in the former test to investigate the effects of the pile density and the rising rate of ground water.

### 2 TEST PROCEDURES AND CONDITIONS

#### 2.1 Modelling of prototype – Test Series I

##### 2.1.1 Large scale 1 g test

Large scale 1g model tests were conducted at Railway Technical Research Institute (Sugiyama et al. ;1993) to investigate the performance of an embankment subjected to a seepage of ground water. Model embankment was built from loosely compacted Inagi sand with dry density of  $1.21\text{g/cm}^3$  and water content of 21% in a large container with 1.2m in width, 5m in depth and 6m in breadth. Considering the geometric symmetry, half cross section of embankments with height of 3.5m and upper width of 5m was modeled as shown in Fig.1. Inclination of the slope was 1:1.5 and a gravel drainage was provided at the toe of the slope. Originally, rainfall with intensity of 30mm/h was rained on to the

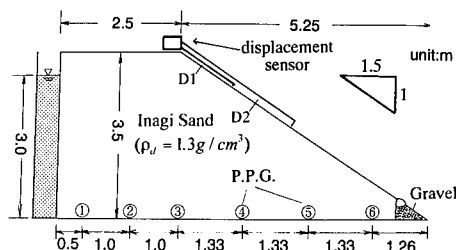


Fig.1 Large scale 1g model

Table 1 Properties of Inagi Sand

Specific gravity (Gs)	: 2.66
Average grain size (D <sub>50</sub> )	: 0.2mm
Uniformity coefficient (U <sub>c</sub> )	: 3.2
	ρ <sub>d</sub> = 1.3g/cm <sup>3</sup> ρ <sub>d</sub> = 1.5g/cm <sup>3</sup>
Permeability (k <sup>*</sup> )	: 1.1x10 <sup>-4</sup> m/sec    6.1x10 <sup>-6</sup> m/sec
Cohesion (c <sup>1</sup> **)	: 4.4kPa    7.5kPa
Friction angle (φ <sup>1</sup> **)	: 33.0°    34.0°

\* : in full saturation

\*\* : in w=27%

model in order to create an unstable condition. After 10 hours, however, erosion took place at the shoulder of embankment without of any failure and then this test was abandoned. At this point, no substantial increase of pore water pressures at the base of the embankment was observed. Seepage test was then conducted by supplying a constant water pressure with a head of 3m from the side of model as shown in Fig.1. From the measurement after the test, dry density and water content of embankment were found to changed to 1.3g/cm<sup>3</sup> and 27% respectively due to the rainfall.

### 2.1.2 Centrifuge model simulating the 1 g test

Modelling of prototype was done by simulating the above mentioned 1g test in a centrifuge model. In this test, only seepage test was carried out for the model made by Inagi sand which had identical dry density and water content as that in the 1g model embankment after the rainfall. Properties of the Inagi sand are given in Table 1.

Model for the centrifuge test is contained in a steel strong box with 440mm in width, 150mm in breadth and 350mm in depth. The box has two tanks at both sides and an impermeable rigid base at the bottom that is concave with a curvature equal to the centrifugal radius; 1300mm. Side walls between tanks and box were accommodated with filter papers as drainage bound-

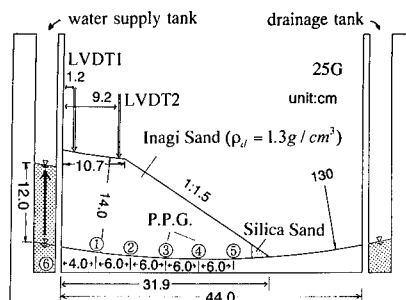


Fig.2 Setup for centrifuge model : Test Series I

aries. The sand with water content of 27% was placed in the box and compacted by a bellofram cylinder into a layer with 2cm in thickness. This was continued until the total thickness reached 16cm at the centre of the box and a 14cm tall model embankment was formed using a template. A slight curvature corresponding to the radial variation of the centrifugal acceleration was given to the surface of the embankments and coarse silica sand was put at the toe of the slope as a drainage. Before the compaction of the sand, pore water pressure transducers were placed on the surface of the base as shown in Fig.2. Japanese noodles were inserted between the front face and the embankment as deformation tracers and two LVDTs were set on the top surface of the embankment. The completed model shown in Fig.2 was mounted on to Mark II TIT centrifuge and centrifugal acceleration was increased to 25g. Under this acceleration, the height of the prototype modelled was identical to the large scale 1g model; 3.5m. The seepage test was carried by feeding water to supply tank behind the model from the laboratory floor through a slip ring until the head of water pressure of 12cm ( 3m in prototype ) and this head was then maintained. The head was increased very quickly in less than 10sec to simulate the sudden supply of water pressure in 1g model.

### 2.2 Embankment with piles – Test Series II

In Test Series II, seepage tests were carried out for the model embankment reinforced with vertical piles. Inagi sand with water content of 27% was also made used of in this test series. The setup for Test Series II in which a loosely compacted model embankment with height of 12cm rests on a well compacted lower 8cm thick layer is shown in Fig.3. The procedure for building the embankment is very similar to that for Test Series I. The lower layer was prepared by

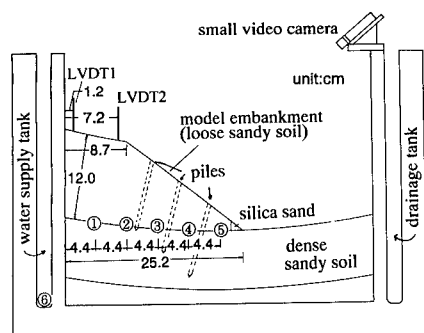


Fig.3 Setup for Test Series II

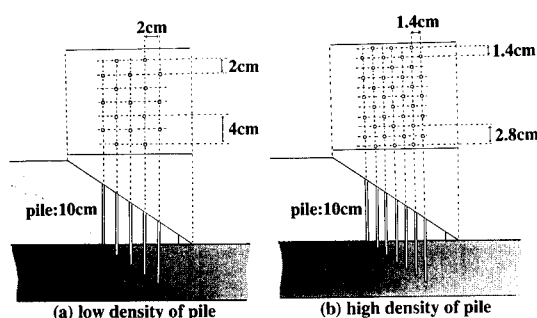


Fig.4 Arrangements of piles

compacting using high pressure of about 250kPa to obtain dry density of  $1.5\text{g/cm}^3$ . After completing the lower layer, pore water pressure transducers were placed at the surface of the layer as shown in Fig.3. The upper embankment portion with dry density of  $1.3\text{g/cm}^3$  was then compacted and the embankment with a slope of 1:1.5 inclination was cut by using a template. After preparing the embankment model, at the sloping part of the embankment piles were inserted radially with the centre of the centrifuge. Tests were carried out for three different reinforcement conditions, i.e., without reinforcement, reinforcement with normal density and finally with high density of piles. The arrangements of piles are illustrated in Fig.4. Seepage tests in 50g field were performed in a similar manner as in Test Series I and changing the rising rate of water table in the water supply tank.

The level of water table was maintained after it reached the height of 9cm from the bottom of the embankment. The time from bottom to this level were 22 to 29sec for the quick tests and 90 to 170sec for the slow tests. Test conditions for Test Series II were summarized in Table 2. During the seepage test, deformation of the embankments was recorded by a photo-camera

Table 2 Conditions for Test Series II

Test No.	Dry Density of embankment $\rho_d$	Pile density	Rising rate of water table in supply tank *
SS1	$1.3\text{g/cm}^3$	without	quick:22s
SS2	$1.3\text{g/cm}^3$	$0.125\text{pile/cm}^2$	quick:28s
SS3	$1.3\text{g/cm}^3$	$0.25\text{pile/cm}^2$	quick:29s
SL1	$1.3\text{g/cm}^3$	without	slow:170s
SL2	$1.3\text{g/cm}^3$	$0.125\text{pile/cm}^2$	slow:90s
SL3	$1.3\text{g/cm}^3$	$0.25\text{pile/cm}^2$	slow:110s

\*: time from bottom to 9cm height of embankment

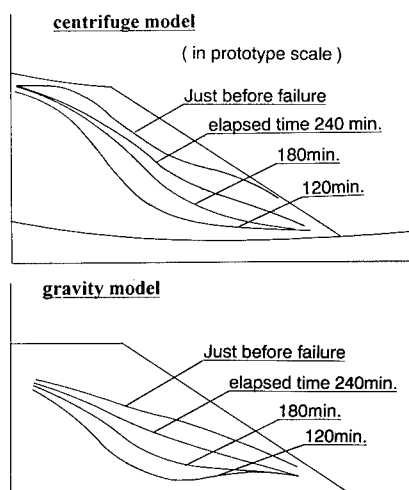


Fig.5 Variations of ground water surfaces in embankment: Test Series I

and the observation of slope was made by a small video camera mounted at the top of the strong box.

### 3 TEST RESULTS AND DISCUSSIONS

#### 3.1 Modelling of prototype - Tests Series I

Variations of ground water surfaces in embankments obtained from measured pore water pressures are illustrated in Fig.5 for both centrifuge and 1g models. Time in the figures is given in prototype scale. Although relatively high pressure existed near the toe of slope at the initial stage (120min.) in 1g test due to the storage of water from the previous rain, movements of the ground water surface during seepage tests are similar for both models.

Settlements at the top of embankment meas-



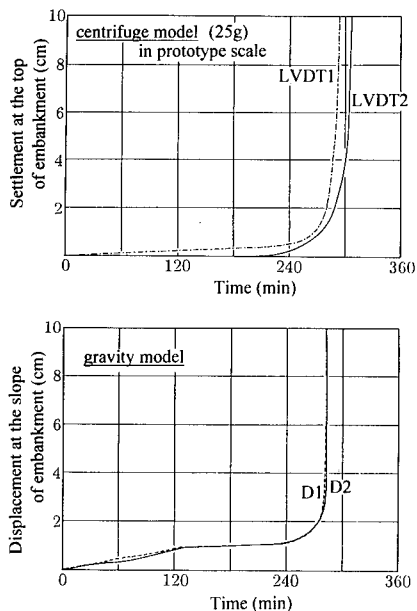


Fig.6 Comparison of deformation of embankment 1g and centrifuge model:Test Series I

ured by LVDTs in the centrifuge test and displacements at the slope measured by positioning sensors in the 1g test are given in Fig.8. Because of the difference of measuring points it is difficult to compare the absolute value of displacements for both tests, but it is possible to investigate the progress of the deformations of embankments during seepage tests. Small settlements and displacements are detected from the initial stages in both tests. This is not due to the shear deformation of the embankment followed by a failure but the compression of the embankment. After 240min in prototype, scale both settlements and displacements suddenly increased showing the onsets of failure. Observed deformations and failure surfaces for both tests are shown in Fig.7. As the large container for 1g test has no side window, the failure surface of the 1g model was detected by inclinometers inserted in the embankments. Catastrophic failure, that is, very deep and large slip surfaces can be seen in both models.

From the comparison of the various test results between the 1g and centrifuge models it can be said that observed behaviour of the ground water in the model embankment and failure pattern were very similar, implying the validity of centrifuge model for the problems treated in this study.

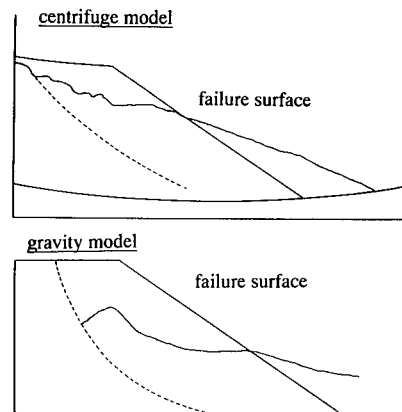


Fig.7 Observed failure surfaces in embankments :Test Series I

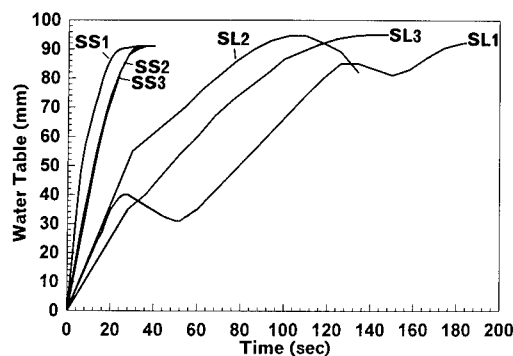


Fig.8 Variations of water tables in supply tank

### 3.2 Embankment with piles – Test Series II

Variations of water tables in water supply tank during seepage tests for Test Series II is shown in Fig.8. The value of water table is given as the height from the bottom of the loosely compacted embankment. Some differences can be seen in the slow tests (SL1–3), however, the rates of the slow tests were 4 to 6 times slower than those of quick tests.

Fig.9 shows the failures of embankment of test SS1, SL1,SL2 and SL3. Very clear slip surfaces were observed for embankments without piles in both the quick and slow tests. The slip surface and deformation area in the former embankment are, however, wider and deeper than those in the latter. Slip failure was restricted in slope in the embankment with piles and only a very small toe failure took place in the embankment with high density of piles (SL3). From the observation of the slope by the video camera, it was found that all failures of embankments were initiated by a toe failure and this triggered a catastrophic fail-

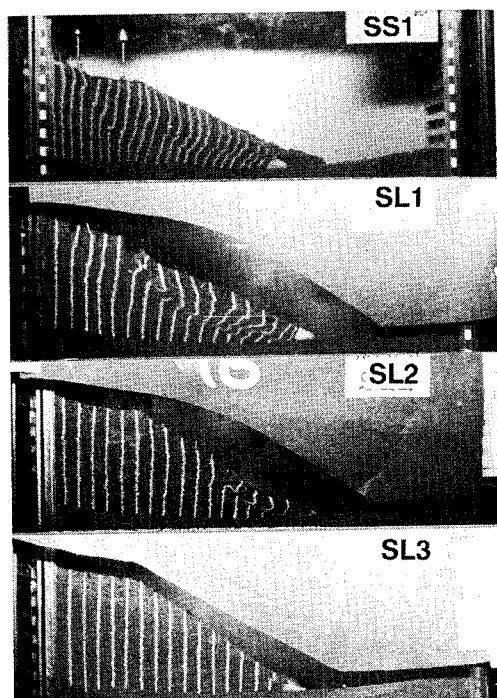


Fig.9 Failures of embankments (SS1,SL1,SL2 & SL3)

ure for the unreinforced embankments. But for the reinforced embankments failure progressed up along the surface of the slope and finally was prevented by the piles.

Settlement-time curves during seepage tests are given in Fig.10. For the quick tests, similar increases of settlements followed by steeper increases can be seen at the initial stage of seepage irrespective of reinforcement conditions. Following this increase, the effectiveness of the reinforcement with piles appears resulting in lesser final settlements for the higher density of piles. This trend is very clear for tests SS2 and SS3 in which the variations of water table in the supply tank with time are almost identical. Similar trend can be seen for the slow tests, however final settlements of the embankments with piles are smaller than that of the same embankments for the quick tests.

Relationships between the head near the toe (P4) and settlement measured by LVDT2 for all tests except SL3 are shown in Fig.11. In test SL3, pore pressure transducer at P4 did not work properly. An interesting feature is that all tests form a single unique curve until the head of 4cm and settlements of 4mm. The heads became greater than the height of the slope above the P4,

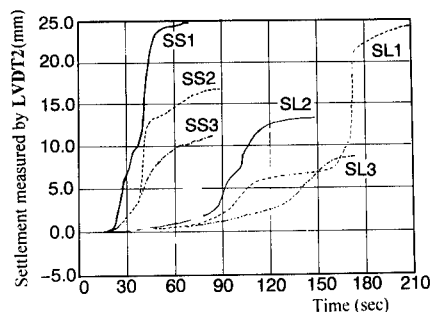


Fig.10 Settlement-Time curves during seepage tests

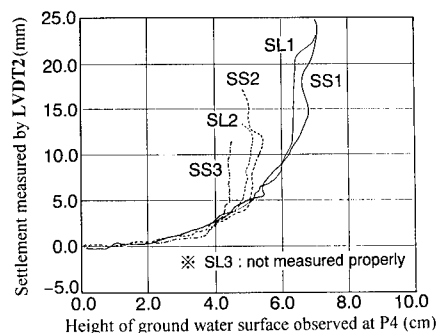


Fig.11 Relationship between the head near the toe(P4) & settlement measured by LVDT2

5cm, in tests without piles;SS1 and SL1. Failed soil covering the slope is considered to be responsible for this. From Figs.10 and 11, it can be seen that even for the reinforced embankments with piles, settlements or deformation still occurred to some extent due to the rise of ground water flow. A catastrophic slip failure took place in the embankment without piles just after the deformation of embankment. However, in the reinforced embankments, this type of failure was prevented by the piles. Some relative displacement between soil and piles are required so that an effective resisting force acts from the piles to the moving part of the embankment, especially for the very loose embankments as used in this tests.

Stability analyses were attempted by using the modified Fellenius method for the embankments without piles at various conditions of ground water flow as shown in Fig.12. Angle of shearing resistance and apparent cohesion listed in Table.1 were used for the portion above the water surface and for the saturated portion below the surface, zero apparent cohesion and same angle of friction as in Table.1 were used. Calculated variation of safety factor with time is shown in

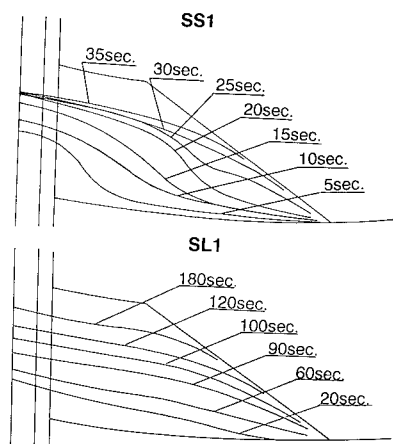


Fig.12 Variations of ground water flow

Fig. 13. Sudden decrease in safety factor was given in the quick test;SS1 rather than the slow test;SL1. Quick rise of water table in the supply tank made the ground water surface concave and at the time when the water surface is close to the slope, the level of the water beneath the edge of the slope rose up to a very high level. On the other hand in the embankment for slow test, the ground water surface is always convex and when the ground water surface is close to the slope as before, the water level beneath the slope edge did not rise up to a high level. This is a reason for the difference of the variation of safety factor.

Fig 14 shows failure surfaces obtained from the stability analyses. Slip surface for the quick test;SS1 reaches wider area than the case of the slow test;SL1, which compares well with the observed failure surfaces shown in Fig.9. The level of the water near the toe is very important in the sense that an initial failure takes place at the toe and becomes a trigger for the following large failure. This failure was determined by the profile of ground water surface at the time of initial failure as shown in Fig.12.

#### 4 CONCLUSIONS

Two series of centrifuge model tests were conducted to investigate the stability of embankments subjected to a seepage flow. One is a modelling of a prototype unreinforced embankment and the other for the reinforced embankments. Following conclusions were obtained.

(1) Observed behaviour of the ground water in the model embankment and failure pattern were

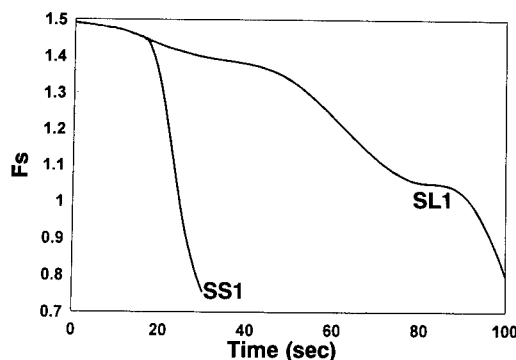


Fig.13 Calculated variation of safety factor for embankments without reinforcement

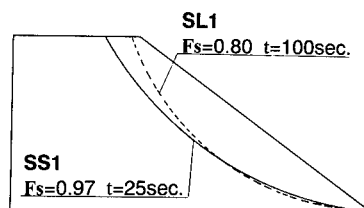


Fig.14 Calculated slip surfaces

very similar to these in the large scale 1g model, implying the validity of centrifuge model.

(2) Even for the reinforced embankments with piles, settlements or deformation occurred to some extent due to the rise of ground water flow. A catastrophic slip failure after this deformation is prevented by the reinforcement.

(3) The failure pattern of the embankments is influenced by the profile of ground water surface when the surface closes near the toe of the slope and toe failure occurs.

#### REFERENCES

- Goodings,D.J. 1984. Relationships for modelling water effects in geotechnical centrifuge models. Proc. Symp. on Application of Centrifuge Modelling to Geotechnical Design, 1-24, Manchester, Balkema.
- Kimura,T.,J.Takemura,N.Suemasa. and A.Hirooka 1991. Failure of fill due to rain fall. Proc. Centrifuge 91, 509-516, Colorado, Balkema.
- Sugiyama,T., H.Muraishi, K.Kagawa, K.Kusano and K.Mizushima 1993. Estimating the timings collapse of embankment slope based on experiment of large scale model. Procs. Annual Meeting JSSMFE, 2, 2167-2168.

## Study of settlement of embankment

Z.R. Yue, X.M. Zhang & S.T. Jing

Shijiazhuang Railway Institute, Hebei, People's Republic of China

**ABSTRACT** Four centrifuge model tests have been conducted and the distribution of vertical stress and displacement in railway embankment filled with compacted fine-grained soil was obtained. The relationship between settlement and compaction factor (the ratio of dry unit weight to maximum dry unit weight), and the height of embankment are analyzed in this paper. The increment of settlement and stress resulted from loading is studied. The method of predicting settlement and reducing settlement is discussed as well.

### 1 INTRODUCTION

In consideration of economy, the fine-grained soil, the liquid limit of which is less than 42%, is allowed to be used to fill the railroad embankment (The Railroad Bed Design Code). Without enough compaction, considerable settlement may develop in the embankment. It is difficult for trains to reach the design velocity in a short term, and many kinds of railroad bed damages, such as sink holes, are often caused by the settlement. The expenses spent in overcoming the damages take a considerable proportion in the total cost of railroad maintenance every year (Tang 1983). Furthermore, since the highspeed railroad and the heavy hauling railroad are to be developed in the coming years in our country, there must be more strict limits to settlement. Therefore, predicting and controlling the settlement of embankment become important tasks.

Chang and Yang (1988) established the GEOTRACK model and LJXY model to calculate the stress and displacement of the railroad bed by the finite element method. The reliability of the models depends on the verification of large amounts of engineering practice.

The technique of geotechnical centrifuge modelling meets the similarity relationship between small scale model and prototype, so the behaviour of small scale model could extrapolate to the performance of the projected prototype. At the same time, the shortcomings such as the high cost of the prototype test and the difficulty in controlling the prototype test could be avoided. It is an effective means to study embankment performance by centrifuge model test.

### 2 FACILITIES OF CENTRIFUGE

#### 2.1 Centrifuge and monitoring facilities

All the experiments described in this article were conducted at the Yangtze River Scientific Research Institute in a large centrifuge with an effective radius of 3m (Wang, 1988). The machine driven by a d.c. motor of 410 kw is able to take a 1000 kg model package to 300 gravities and its Max. pay-load is over 500 kg. It has 57 poles of slip rings and 4 channels of hydraulic joints and 2 channels of pneumatic joints. The internal dimensions of the model container, which is used in this test, is 560mm long, 230mm wide, and 390mm high.

The machine was equipped with an advanced data collecting and processing device, the isolated measurement pods (IMP), which was fixed on the arm near the axis of the centrifuge, moving together with the arm. Only 2 poles of slip rings were used for the IMP to communicate with the external computer, so that it has a lot of advantages such as being strong in anti-interference and having a large number of measuring points.

#### 2.2 Loading way

It is proved by tests that common pneumatic controlling system is able to work stably. Therefore it is chosen for the purpose of loading.

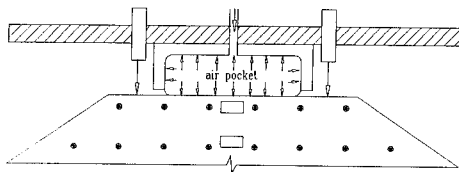


Fig.1 The arrangement of the instruments on the model inside the model container

### 2.3 The error of nonuniformity of centrifuge force field

With the height of the model being 0.25m and the ratio of the effective radius to the height of the model being 12.0, this error may be insignificant (Schofield, 1980).

## 3 TEST PROCEDURE

### 3.1 Soil and model

A fine-grained soil (PL = 16.1%, LL = 26.3%) was used throughout this investigation. The maximum dry unit weight and the optimum water content, determined by the standard Proctor compaction test, is 18.02 kN/m<sup>3</sup> and 15.0%, respectively. According to the position of the soil in the plasticity chart, it should be a silty clay, which is allowed to be used to fill railroad embankment (The Railroad Bed Design Code).

Compaction factors of the four models are 0.8, 0.85, 0.9, 0.95, respectively. But the top width, height and ratio of side slope of them are the same. (W = 110 mm, H<sub>m</sub> = 250 mm, 1:1.5, vertical to horizontal).

### 3.2 Model making and test steps

First, remolded sample with optimum water content is prepared. Before compacting, the wall of the model container is painted with vaseline, then a sheet of polyethylene film is pasted on the wall, which can largely eliminate the side wall effect on the stress and settlement measurement (Yue, 1992). The soil is compacted layer by layer evenly. During the period of compaction, transducers are set at the middle of the embankment model at different depths. There is a vertical distance of 40 mm between the transducers. Some small markers are embedded in soil for observing the displacement, which can be seen through the perspex window of the model container. When compaction is finished, the redundant soil is excised and the design model is formed (Figure 1). Two LVDT are fixed on top of the model container, which is vertical to the top of the model and is used to measure the settlement. A rectangular box of Aluminium alloy without bottom, with a emulsion air pocket inside, is fixed on

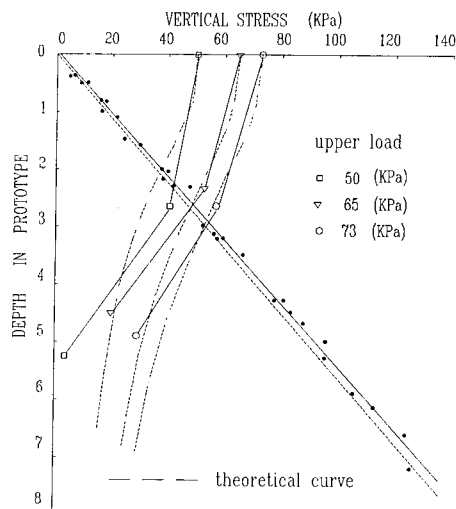


Fig.2 Distribution of vertical stress along the axis of symmetry of the cross section of the embankment

middle top of the model container. Its aperture is close to the top of the model. The air pocket is connected with the pressure hose from external air bottle, through which the high-pressure air is applied to model loading.

The test steps were as follows:

Accelerating the machine to the desired magnitude of  $G$ , maintaining the rotating velocity, monitoring the pressure and settlement, applying static loading by the pneumatic loading system when the settlement becomes constant in general and ending test when the settlement becomes constant once more. Throughout the whole procedure the computer collects data at a velocity of 2~6 times a minute.

## 4 TEST RESULTS AND DISCUSSION

### 4.1 Distribution of the vertical stress

Typical measurements of the soil pressure transducer as a function of the depth of prototype are shown in figure 2. The depth of prototype is the result of the transducer depth in model multiplied by  $G$ . The distribution of pressure before loading represents the distribution of the overburden stress along the axis of symmetry of the cross section of the embankment. All of the dots nearly form a straight line. By means of linear regression this line can be expressed as  $\sigma = 1.06\gamma Z$ , and its correlation coefficient equals 0.993. It is in agreement with the distribution of overburden stress in semi-infinite body  $\sigma = \gamma Z$  (1).

The superimposed stress caused by loading (Fig. 2) conforms approximately to Boussinesq distribution in the upper portion of the embankment. When the depth exceeds 3m, the magni-

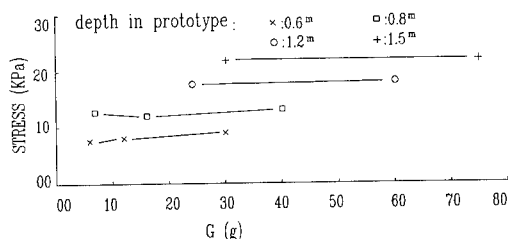


Fig.3 Verification of similarity relation

tude of test fades down more quickly than the theoretical one does. The higher the compacting-factor is, the quicker the fading is.

Test results in figure 2 show that the slope shape of the embankment has little effect on the vertical stress along the axis of symmetry of the cross section of the embankment. Therefore, the vertical stress can be calculated by equations used in a semi-infinite body.

The upper load of railroad consists of the weight of ballast, crosstie, track, and train. Its magnitude is about 57KPa (The Railroad Bed Design Code) and the depth of its influence less than 5m from figure 2.

Because the influence of the slope shape is so small as mentioned above, the concept of modelling of model could be used to test roughly the similarity relation. It is indicated in figure 3 that though the magnitude of G and the depth in the model are different, the overburden stress, which represents the stress in the same depth of prototype, are approximately equal to each other.

#### 4.2 Determination of the final settlement

For convenience,  $\Delta$  is defined as the settlement of model divided by the height of model or the settlement of prototype divided by the height of prototype, and is referred to as 'relative settlement' hereafter.

The development of the settlement is infinite, but the time of test is finite, it is necessary to determine the final settlement of test by finite test data obtained. If the data of time and settlement under constant G is coincident with the hyperbola:

$$\Delta = \frac{t}{at+b} \quad (2)$$

and the a and b are constants, the final settlement can be gained:

$$\lim_{t \rightarrow \infty} \Delta = 1/a$$

The equation (2) can be changed into a straight line:

$$\frac{t}{\Delta} = at + b$$

The results by linear regression are shown in figure 4 and table 1. the correlation is satisfactory.

Table 1 final relative settlement

Model	a	b	1/a (%)	r
1	90.9	516.3	1.10	0.99
1+	309.0	5800.0	0.32	0.94
3	754.3	5700.0	0.13	0.99
3+	1035.0	10100.0	0.09	0.98
4	754.7	13500.0	0.13	0.99
4+	897.6	31453.0	0.11	0.98

+ : after loading

#### 4.3 Influence of compacting factor on settlement

A significant fact is shown in figure 5 that the compacting factor, K, when equaling 0.9, is the turning point. When it is greater than 0.9, the magnitude of relative settlement is low, and so is the rate at which the relative settlement increases as the compaction factor decreases. When it is less than 0.9, the relative settlement increases sharply as the compaction factor decreases, especially for the high embankment. The fact proves that the regulation is unreasonable that the compaction factor of underlying of railroad embankment is allowed to be not less than 0.85 (The Railroad Bed Design Code). Because even if we raise the magnitude of compacting factor from 0.85 to 0.9, there would be a little increase of work, but the settlement would be reduced largely. As a result, there will be a considerable increase in economic benefit.

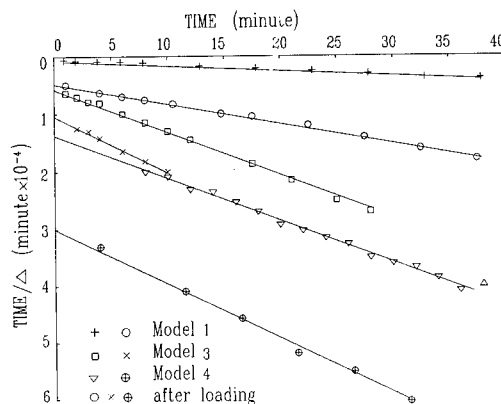


Fig.4 Time divided by relative settlement versus time

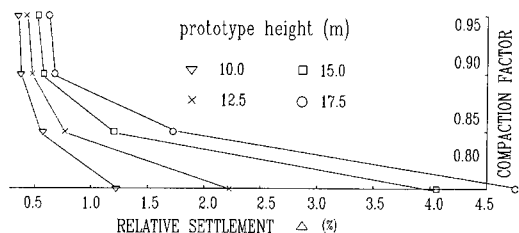


Fig.5 Compaction factors versus relative settlement curve

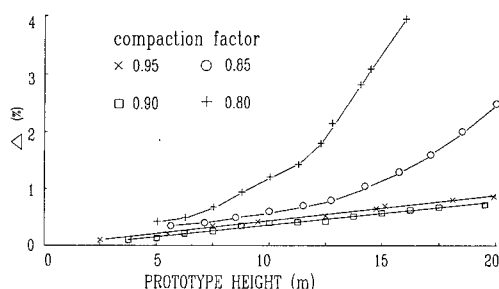


Fig.6 Relative settlement versus prototype height for different compaction factor

#### 4.4 Influence of the height of the embankment on settlement

Figure 6 plots the relative settlement as a function of the height of the embankment without loading. There is no doubt that the increasing of the embankment height leads to the increasing of relative settlement. The lower the compaction factor is, the greater the increasing rate of the relative settlement is. When the compaction factor is greater than 0.9 the rate seems to be constant. This is analyzed as follows: In fact, the compacted fine-grained soil is in the state of overconsolidation. There must be a preconsolidation pressure,  $P_c$ , and  $P_c$  is the increasing function of compaction factor. When the maximum overburden stress in embankment,  $\gamma H$ , is less than  $P_c$ , the deformation is mainly of an elastic one. The relation between the relative settlement and the embankment height forms a straight line. When the embankment height increases and  $\gamma H$  comes over  $P_c$ , a plastic deformation will be caused, and the relative settlement increases abruptly, so that the relation between the relative settlement and the embankment height is non-linear. Therefore, the ideal method should be based on the vertical stress mentioned above, and  $P_c$  as well as  $e \sim \log p$  curve gained from compression test, using the layer-wise summation method used in semi-infinite body, to calculate the settlement of embankment. The details are omitted here.

By means of linear regression, equations to predict settlement can be obtained:

$$\Delta = aH + b \quad (3)$$

$$S = aH^2 + bH \quad (4)$$

The constants  $a$  and  $b$  have relation to compaction factor and soil classification. The magnitude of  $a$ ,  $b$  and  $P_c$  of silty clay used in these tests are shown in table 2. It is necessary to note that the condition of equation (3) and (4) is  $H < P_c/\gamma$ .

Table 2 constants of settlement prediction

Model	a	b	$P_c$ (KPa)	r
1	0.062	0.107	83	0.95
2	0.053	0.029	128	0.97
3	0.043	-0.043	270	0.99
4	0.040	-0.041	490	0.99

Table 3 The influence results of loading

Model	height of prototype (m)	before loading $\Delta$ (%)	after loading $\Delta$ (%)
1	14.36	4.16	5.34
2	11.99	1.62	2.32
3	20.28	0.96	1.21
4	19.75	0.84	1.17

#### 4.5 Influence of loading on settlement.

It is indicated in table 3 that after upper load of railroad is applied the final relative settlement, in which case the compaction factor is greater than 0.9, is about 1%. The increment of relative settlement after loading decreases as the compacting factor increases.

## 5 CONCLUSIONS

The distribution of vertical stresses along the axis of symmetry of the cross section of the embankment can be determined approximately by equations used in the elastic semi-infinite body.

There must be a preconsolidation pressure,  $P_c$ , in compacted soil. The top settlement of the embankment has a close relation with the compaction factor and the embankment height. When  $H < P_c/\gamma$ , the relation between the relative settlement and the embankment height is a straight line, and the settlement of fine-grained soil can be predicted by equation (3) and (4).

In order to reduce the settlement of the railroad embankment, the compaction factor should be greater than 0.9, to be more exact, the preconsolidation pressure should be greater than the

maximum vertical stress of the embankment.

The work to gain the scaling relation of time of the settlement by means of modelling of model has not been conducted yet.

#### REFERENCES

- Chang C S, Adegoke C W, Selig Z F, GEOTRACK model for railroad track performance, ASCE. Vol. 106. No. GT11.
- Schofield A N, 1980, Cambridge geotechnical-centrifuge operation, *Geotechnique*, Vol. 30, 3: 227—268.
- Tang G Y, 1983, The trial research of railroad bed work in southwest area, *road bed engineering*, 1: 8—16.
- Wang X D, 1988, Studies on the design of large scale centrifuge for geotechnical and structural tests, *Centrifuge in soil mechanics*, 81—90. Rotterdam: Balkema.
- Yue Z R, 1992, Centrifuge model tests on lateral pressure on walls retaining compacted clayey backfill, *Chinese journal of geotechnique engineering*, 72: 90—95.
- Yang C W, Chai J C, 1988, Computing method of stress and strain in railroad bed, *road bed engineering*, 18: 48—51.
- Zuo Z S, 1988, The magnitude of compression of earth—fill, *road bed engineering*, 21: 15—19.



## Embankments with base reinforcement on soft clay

M.D. Bolton & J.S. Sharma  
*Cambridge University, UK*

**ABSTRACT:** The behaviour of reinforced embankments on soft clay has been investigated by centrifuge model testing. A parametric study was conducted in which the type of the reinforcement and the depth of the clay foundation were varied. The effect of wick drains in the clay foundation on the behaviour of reinforced embankments was also studied. Direct measurement of tensions induced in the reinforcement was carried out using load cells constructed on the reinforcement. The displacement of the clay foundation is strongly influenced by its depth. The smaller the depth, the smaller the displacements. The reinforcement placed directly on top of the clay seems to attract less tension than that buried in the middle of a sand layer. Presence of wick drains in the clay hastens its consolidation considerably. It also appears to reduce the lateral displacement of the clay foundation.

### 1 INTRODUCTION

The design of embankments founded on soft clay is primarily influenced by the potential instability during or immediately after the construction of the embankment. One of the solutions to this short-term instability problem is to provide a geosynthetic reinforcement at the interface between the embankment and the soft clay foundation. Although this technique is widely used now-a-days and data is available from detailed finite element analyses and instrumented field trials, the behaviour of reinforced embankments on soft clay is far from clear. This paper describes an investigation into the behaviour of such embankments using centrifuge model testing.

### 2 CENTRIFUGE TESTS

Centrifuge model testing, because of its ability to reproduce the same stress levels in a small-scale model as in a full-scale prototype, is a powerful tool in exploring soil-structure interaction problems. In the present study, six

1:40 scale centrifuge model tests were performed using the Cambridge University 10m balanced beam centrifuge. Figure 1 shows the details of a typical centrifuge model. Table 1 gives a brief description of each of the six centrifuge tests. Due to the inherent symmetry about the centre line, only one half of the structure was modelled. Such an arrangement helped in constructing a reasonable sized model within a relatively small strongbox. A special clamp was built to anchor the model reinforcement to the right side of the liner. This clamp, while preventing the horizontal movement of the reinforcement, allowed for its vertical movement following the settlement of the clay foundation. A smooth nylon sheet was glued to the inside vertical surfaces of the liner in order to reduce the friction between the liner and the soil. The speswhite kaolin clay was consolidated to a maximum vertical pressure of 100kPa in a consolidometer. Two days before the day of centrifuge test, it was unloaded and removed from the consolidometer and trimmed to the dimensions of the model. The clay block and the liner were then placed in a strongbox. A matrix of small black plastic markers was

installed on the front surface of the clay block. These markers were used for the measurement of clay displacements from the photographs taken in-flight through the front perspex window.

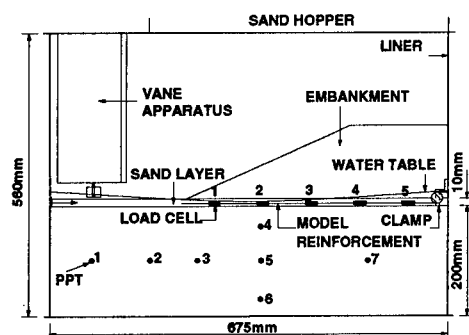


Figure 1 A typical centrifuge model

Table 1 Description of the centrifuge tests

Test code	Depth of clay	Type of reinforcement
JSS7	200mm	Geotextile
JSS8	200mm	Unreinforced
JSS9	200mm	Geogrid
JSS11	100mm	Geogrid
JSS12	100mm	Geotextile
JSS14	200mm	Geotextile*

\* Wick drains installed in the clay.

Two types of model reinforcements, geotextile and geogrid, were used in the present study. The model geotextile was supplied by Akzo Industrial Corporation b.v., Netherlands and the model geogrid was supplied by Netlon Corporation, U.K.. The process of scaling down the prototype reinforcement to obtain the model reinforcement was discussed in detail by Springman et al. (1992). Figure 2 shows the load-extension curves (supplied by the manufacturers) for the two model reinforcements. Table 2 gives the properties of the prototypes represented by these model reinforcements at 40g. Figure 3 shows the position of load cells constructed on the model reinforcement for measuring tension induced in it. A typical load cell consists of approximately 12.5mm wide and 0.7-1.5mm thick strip of

epoxy resin cast across the entire width of the reinforcement. The epoxy strip is reinforced with a combination of insulated copper wires and carbon fibre strips.

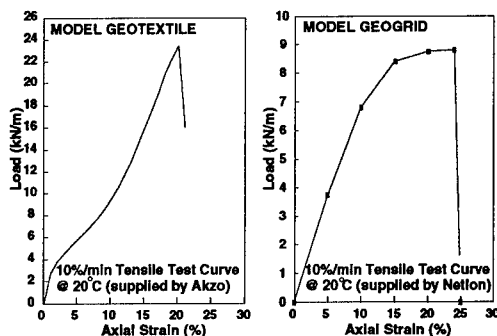


Figure 2 Load-extension curves for model reinforcements

Table 2 Tensile strengths of the reinforcements @ 10% axial strain.

Type	Model	Prototype
Geotextile	9.5 kN/m	380 kN/m
Geogrid	6.8 kN/m	272 kN/m

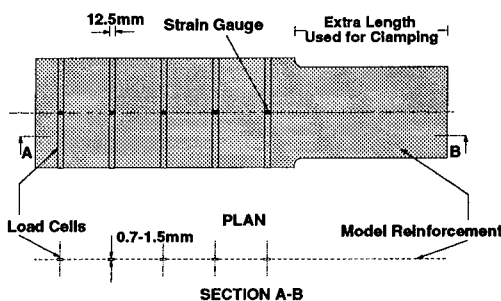


Figure 3 Position of load cells on model reinforcement.

The method of construction of load cells was different for each of the two model reinforcements. Figure 4 shows the details of the load cells. The procedure for the calibration of these load cells was described in detail by Springman et al. (1992) and hence is not reported here. Figure 5 shows the response of the load cells during the calibration. The load cells constructed on model geogrid were an

order of magnitude stiffer than those constructed on model geotextile which meant that their outputs were noisier than those from the geotextile load cells.

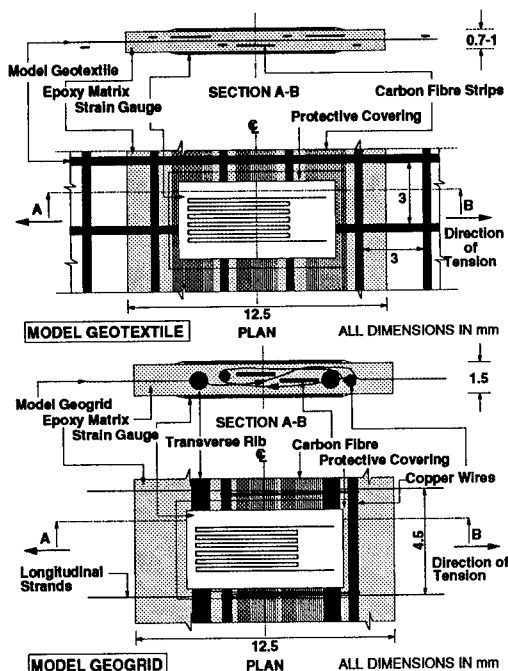


Figure 4 Details of reinforcement load cells

The calibration curves for both types of load cell are presented in Figure 6. They were fairly linear for the geotextile load cells but were non-linear for the geogrid load cells. The calibration procedure was repeated several times before and after centrifuge model testing and the calibration curves were found to be repeatable. The sheet of reinforcement with the calibrated load cells was attached to the clamp and placed directly on top of the clay for all the tests except test JSS11 for which the model reinforcement was buried at the centre of a 10mm thick sand layer.

After the clay foundation reached pore pressure equilibrium in the centrifuge, vane shear tests were carried out at different depths in order to measure the consistency of the model. Figure 7 shows the undrained shear strength profile of the clay measured by the in-flight vane shear tests. An embankment was then placed in-flight in 20 stages (15 sec time interval between successive stages) by pouring sand from a hopper mounted on the top of the strongbox.

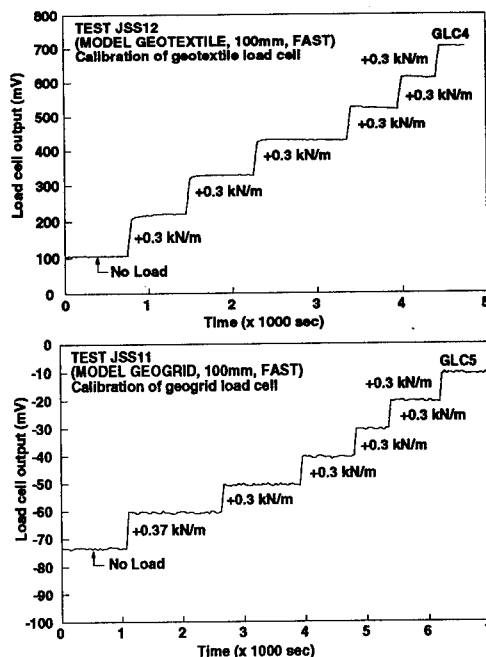


Figure 5 Response of a typical load cell during calibration.

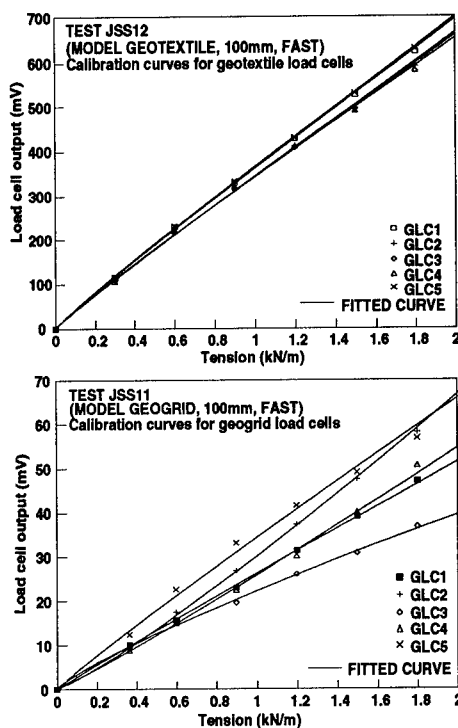


Figure 6 Calibration curves for the load cells

The rapid construction of the embankment caused significant deformation of the clay foundation. The clay foundation for test JSS8 (unreinforced) failed when about 85% of the embankment was constructed (Figure 8). The undrained shear strength obtained from back analysing the centrifuge test was 13.8 kN/m<sup>2</sup>. In the analysis, the friction between the sides of the liner and the soil was neglected.

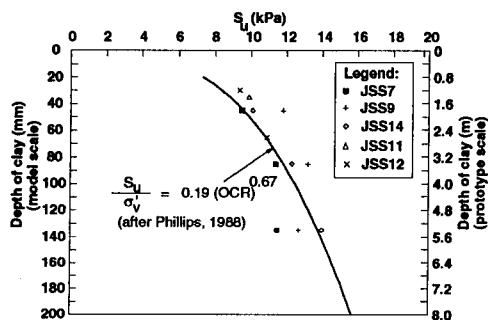


Figure 7 Undrained shear strength profile of clay

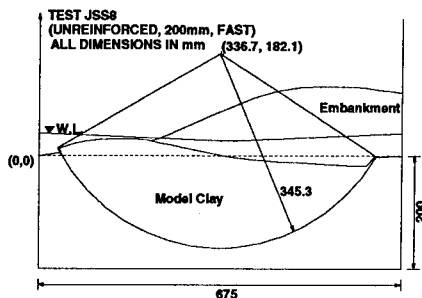


Figure 8 Failure of unreinforced clay foundation

Pore pressures in the clay and the tension in the reinforcement both increased as a result of the embankment construction. Figure 9 shows the pore pressures in the clay during embankment construction for tests JSS7 and JSS11. Faster dissipation of excess pore pressures between the successive stages occurred in the case of test JSS11 because of the shallower depth of clay. Figures 10 and 11 show the tension induced in the model reinforcement during the embankment construction for tests JSS7 and JSS11. The tension profile for both the tests reached a plateau beyond the crest of the embankment towards its centre line but for test JSS11, the tension was much less beneath the slope of the embankment as compared to that for test JSS7.

The consolidation of the clay foundation was nearly complete after 6 hours for test JSS7 and 1.5 hours for test JSS11. There was a small reduction in the reinforcement tension during consolidation for both the tests. Hence, the critical phase for the structure is the undrained loading due to rapid construction of the embankment. Figure 12 shows the displacement of the clay foundation just after the embankment construction for tests JSS7 and JSS11. The displacement increases towards the surface unless the clay foundation fails.

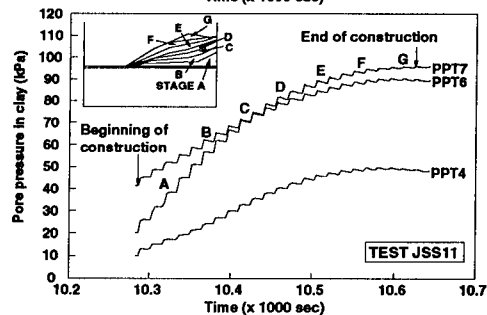
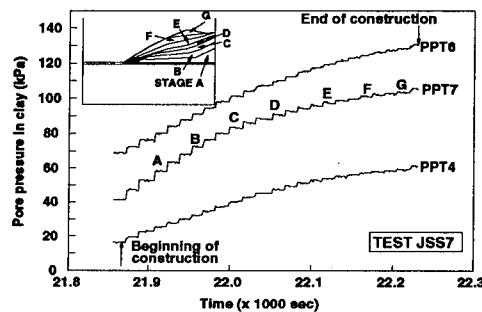


Figure 9 Pore pressure in clay foundation during embankment construction

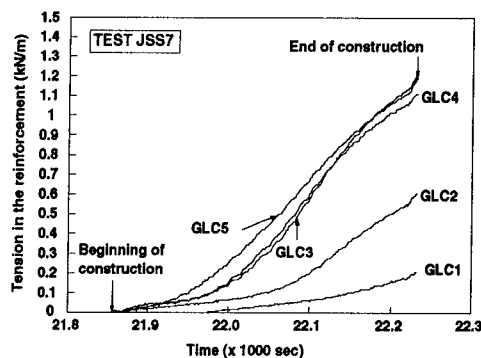


Figure 10 Tension induced in the reinforcement during embankment construction (Test JSS7)

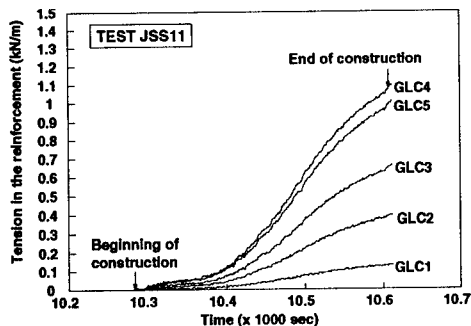


Figure 11 Tension induced in the reinforcement during embankment construction (Test JSS11)

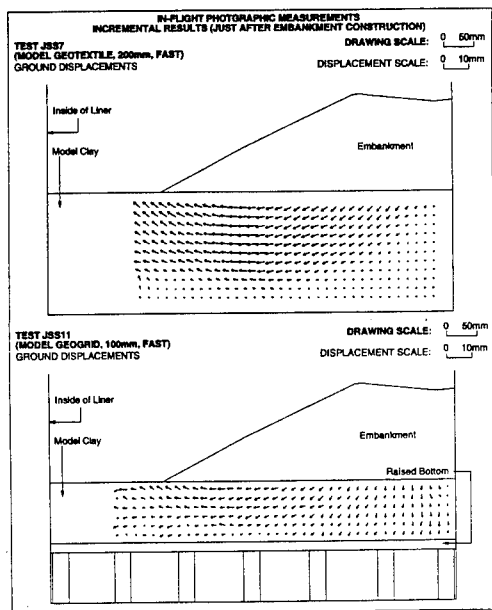


Figure 12 Displacement of clay foundation just after the embankment construction

### 3 WICK DRAINS IN MODEL CLAY

For natural clay deposits, the horizontal permeability is generally much greater than the vertical permeability. Also, in most situations, the horizontal extent of such deposits is much greater than their depth. Therefore, the consolidation of such deposits can be hastened by installing vertical drains: wicks, made up of geocomposites, are typically used. It has become a common practice to use base

reinforcement of the embankment in conjunction with the installation of wick drains as a possible solution to the problem of short-term instability. Test JSS14 was carried out in order to investigate the influence of wick drains on the consolidation of clay and on the soil-reinforcement interaction. A twisted multifilament polyester string, approximately 1.5mm in diameter, was used as model wick drain. The wick drains were installed @ 32mm c/c in a square layout and they extended through the entire depth of the whole clay foundation (200mm). The installation was carried out after the clay block was trimmed to the required depth. It was done with the help of a stainless steel hypodermic needle (2.94mm outer diameter and 2.2mm inner diameter) which acted as a plunger. The installation process has been described in detail by Sharma (1994). The water table achieved in-flight was about 35mm higher than the desired water table (about 5mm above the top of clay foundation) due to an unavoidable technical snag. Otherwise, the test arrangement was similar to that for test JSS7.

As expected, the clay reached pore pressure equilibrium much more quickly in test JSS14 (less than two hours as compared to about six hours for test JSS7). The dissipation of excess pore water pressures during embankment construction was also faster as seen from figure 13. The tension induced in the reinforcement during embankment construction (figure 14) was significantly higher than that recorded for test JSS7. Figure 15 shows the displacement of the clay foundation just after the construction of the embankment. The displacements were much smaller than those recorded for test JSS7 (figure 12).

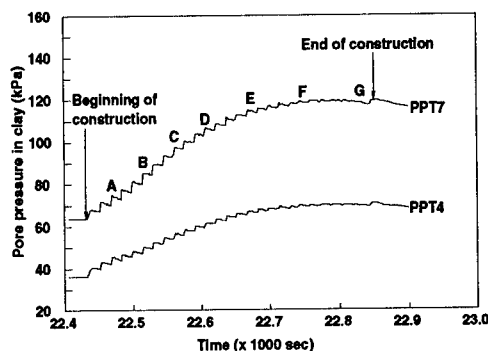


Figure 13 Pore pressure in model clay during embankment construction (test JSS14)

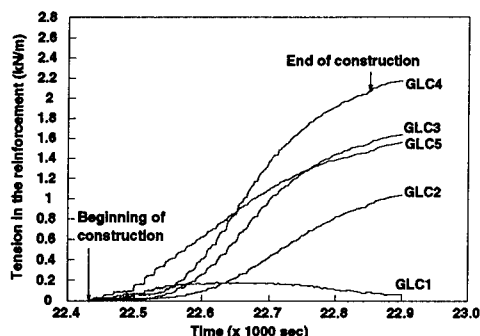


Figure 14 Tension induced in the reinforcement during embankment construction (test JSS14)

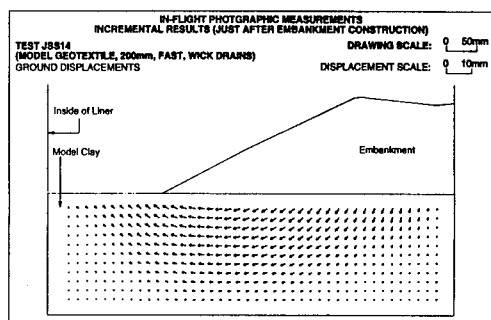


Figure 15 Displacement of clay foundation just after the embankment construction (test JSS14)

#### 4 CONCLUSIONS

The behaviour of commonly used prototype reinforcements (geotextiles and geogrids) has been replicated reasonably well by the model reinforcements. Load cells on these model reinforcements have worked quite satisfactorily as evident from their calibration results. The undrained displacement of a clay foundation seems to be strongly influenced by its depth: the smaller the depth, the smaller the displacements. Reinforcement placed directly on top of the clay seems to attract less tension than that buried in a layer of sand. This may be due to the increase in the adherence at the bottom soil-reinforcement interface. The presence of wick drains in a clay foundation reduces its consolidation time considerably. It also seems to reduce the displacement of clay foundation. However, the presence of a higher water table may also have been influential in reducing the displacement. The tensions in the reinforcement

were significantly higher for test JSS14 as compared to test JSS7. Increase in the adherence at the clay-reinforcement interface due to the presence of the ends of the wick drains, protruding out of the clay foundation, may be the reason.

#### ACKNOWLEDGEMENT

The tests reported here were carried out by the second author under a research contract placed with A.N. Schofield and Associates by the Transport Research Laboratory (TRL), UK. The views expressed here are solely those of the authors.

#### REFERENCES

- Phillips, R. 1988. Centrifuge lateral pile tests in clay: Task 2 & 3. A report to Exxon Production Research Corp. by Lynxvale Ltd., Cambridge, U.K..
- Sharma, J. 1994. Behaviour of reinforced embankments on soft clay. Ph.D. thesis, Cambridge University (in process).
- Springman, S.M., Bolton, M.D., Sharma, J. and Balachandran, S. 1992. Modelling and instrumentation of a geotextile in the geotechnical centrifuge. *Proc. Int. Symp. on Earth Reinforcement Practice, Kyushu*: 167-172. Rotterdam: Balkema.

## Evaluation of the cut-off structures of a rockfill dam

Limin Zhang & Ting Hu

Chengdu University of Science and Technology, People's Republic of China

Jun Zhang

Fumin Real Estate Company, Zhuhai, People's Republic of China

**ABSTRACT:** To evaluate the performance of proposed connection structures between underground concrete cut-off walls and the dam core, five centrifuge model tests were carried out. The stresses in the walls and the settlement of the dam were recorded during these tests. A data analysis method was introduced to extrapolate the data to the prototype from the models which were tested at 200g but were scaled down by 800 times.

### 1 INTRODUCTION

In most parts of the Mingjiang river and the Daduhe river in Sichuan province, river beds are covered with alluvial layers as deep as 20m to 100m. Anti-seepage measures of dam foundation are key problems in designing rockfill dams on such sites. In the 1940's, this was done by excavating a cut-off trench, placing an upstream blanket, or constructing steel sheet pile walls. In the 1950's and 1960's, slurry trench and grouting curtain methods were developed. The 110m deep gravel pervious foundation of Aswan dam, Egypt, was successfully treated by cement slurry grouting. On the other hand, the idea of concrete cut-off walls has been developed since 1954. Compared with other anti-seepage measures, concrete cut-off walls are reliable, economic, and fast to construct. At present the largest concrete cut-off wall is 131m deep, built for Manicouagan 3 dam, Canada (Dascal 1979a).

In the whole anti-seepage system of a rockfill dam, the connection joints between the dam core and the foundation cut-off walls are the weakest places. As a result of stress concentration and marked differential settlement in this area, plastic flow and tensile crack may occur in the soil around the joint. The ability of seepage resistance in turn decreases. Take Manicouagan 3 dam as an example, high pore pressure was observed at the top of the gallery during operation (Dascal 1979b).

A breakthrough in understanding the mechanism of concrete cut-off walls is that the walls are basically compressive elements subjected to soil pressure at the top and downdrag force on the shafts, rather than the traditional bending elements described by beams on elastic medium. The

pressure on the walls would be large enough to break the walls unless a properly designed connection joint meets the following requirements:

1. Ensure the reliability of seepage resistance during construction and operation.
2. Alleviate the wall load transferred from the gallery to a minimum.
3. Try not to damage the strength of the concrete.
4. Easy to construct and economic.

In response to the above requirements, many types of connection joints are developed. Among them the most important types are directly inserted joint, soft joint, and vacant joint. In soft joints, some gaps exist between the cut-off walls and the grouting galleries, and such soft material as IGAS is poured into the gaps. In the prototype hydroelectric power project, the rockfill dam is 188m high above the ground and the cut-off walls go down 75m into the alluvial layers. Five design layouts are suggested: two direct connection schemes in which the walls come into the core material directly, and three indirect schemes in which the walls are connected to a grouting gallery with different kinds of interfaces, as shown in Fig.1. This paper, together with other physical model tests and numerical analyses, aims to evaluate the performance of these schemes.

### 2 MODELLING TECHNIQUES

#### 2.1 The centrifuge

The CUST geotechnical centrifuge was put into operation in 1991. Fig.2 is a sketch of this centrifuge. The main characteristics of this machine are:

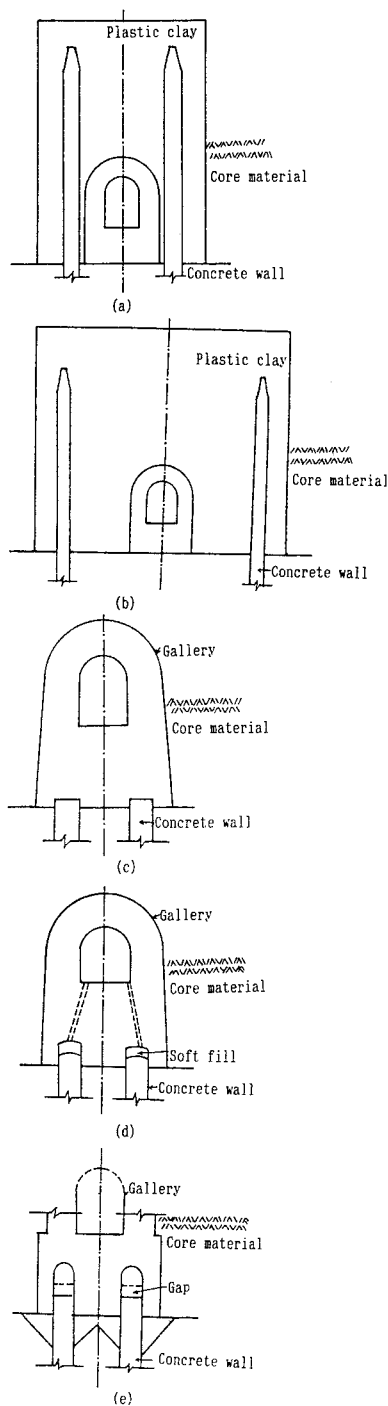


Fig.1 Schemes of connection joints proposed (a) direct connection I, (b) direct connection II, (c) Stiff connection, (d) soft connection, (e) vacant connection

Capacity: 25GT;  
Effective radius: 1.54m;  
Maximum acceleration: 250G;  
Model container size: 0.6m × 0.4m × 0.4m;  
Signal sliprings: 32 rings;  
Driving power: 30kW;  
Rotary joints: 20MPa for oil, 0.6MPa for water.

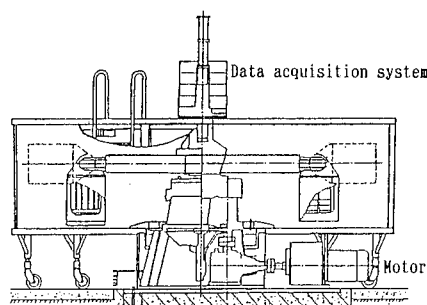


Fig.2 Sketch of the CUST geotechnical centrifuge

## 2.2 Method of data extrapolation

The geometric size of the prototype profile is as large as 940m by 253m. It is impossible for the centrifuge to accommodate such a structure by the 'equal gravitational stress concept'. In the earlier works, this problem was avoided by partial structure modelling(Mikasa et al. 1980), or by extrapolation from the recorded acceleration – displacement and acceleration – stress curves(Liu 1990, Zhu 1990) . On the other hand, the method

Table 1. Useful similitude scales in centrifuge model test (prototype / model)

Property	Scale for equal stress model	Scale for unequal stress model
Displacement	$n$	$n_1^2 / n$
Stress, strain	1	$n_1 / n$
Area	$n^2$	$n_1^2$
Volume, mass	$n^3$	$n_1^3$
Force	$n^2$	$n_1^3 / n$
Elastic modulus	1	1
Friction angle	1	1
Cohesion	1	1
Poisson's ratio	1	1
Time:		
consolidation	$n^2$	$n_1^2$
dynamics	$n$	$\sqrt{n_1 n}$
creep	1	$\sqrt{n_1 / n}$



of unequal stress centrifuge modelling was put forward (Zhang & Hu 1990, 1991). First, models were built according to a geometric scale  $n_1$  which could accommodate the whole profile. Then, these models were tested in the centrifuge at  $n$  gravities. Generally,  $n_1$  is far larger than  $n$ . The tested results were interpreted by means of the similitudes for unequal stress centrifuge models (Zhang & Hu 1990). The useful similitude scales are listed in Table 1. In this test series,  $n_1=800$ ,  $n=200$ .

### 2.3 Soil gradation

Fig.3 shows the results of mechanical analysis of the soils to be modelled. The maximum particle diameter of the dam core is 80mm, whereas those of dam foundation and rockfill materials go up to 400mm and 800mm respectively. Therefore, particle size should be reduced to get the soils accommodated in the model container. According to the results of comparison studies regarding to granular soil (Zhu, 1990), performance of dams can be properly represented when the maximum model material diameter is in the range of  $1/40 - 1/160$  that of prototype. In this test series, the maximum diameters are 10mm, 5mm, 2mm for rockfill, alluvial and transitional materials, and core material respectively. For the alluvial and rockfill materials, the gradation below 2mm diameter is the same as that of the prototype so that their original properties can be guaranteed. The physical indices of these materials are listed in Table 2.

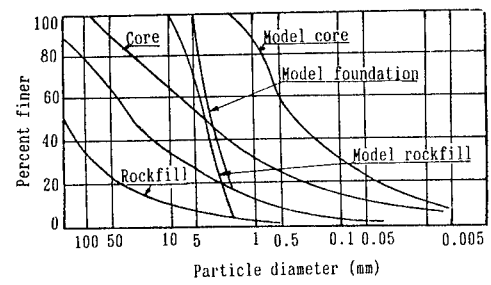


Fig.3 Particle size distribution of materials

Table 2 Physical indices of materials

Material	Unit weight ( $\text{kN/m}^3$ )	Friction angle (degree)	Cohesion (kPa)
Alluvial layer	23.0	42.0	0.0
Core	24.0	35.5	54.0
Shell rock	23.0	43.0	0.0
Transitional material	22.0	42.0	0.0
Wall soil interface	—	11.0	20.0

### 2.4 Concrete works

The grouting galleries are modelled by microconcrete galleries with approximately the same strength and elastic modulus as those of in-situ values, which are 38.2MPa and 32000MPa for the prototype after 28 days curing, and 36.4MPa and 29300MPa for the models respectively. The prototype concrete cut-off walls are 1.4m thick. If they are reduced 800 times to 1.7mm, it will be very difficult to mold the concrete slabs. To facilitate the process, aluminium sheets are used to simulate the concrete walls. To ensure the similarity requirements, the thickness of the aluminium sheets are such that the bending stiffness of model concrete wall is similar to that of in-situ walls,

$$E_m^{al} I_m^{al} = E_m^c I_m^c \quad (1)$$

$$t_m^{al} = \sqrt[3]{\frac{E_m^c}{E_m^{al}}} \frac{t_c}{n_1} \quad (2)$$

where,  $E_m^{al}$ —elastic modulus of aluminium;

$E_m^c$ —elastic modulus of concrete;

$I_m$ —moment of inertia;

$t_m^{al}$ —thickness of aluminium sheet;

$t_p^c$ —thickness of prototype concrete wall;

$n_1$ —geometric scale.

Substitute  $E_m^a=75000\text{MPa}$ ,  $E_m^c=32000\text{MPa}$ ,  $t_p^c=1400\text{mm}$ ,  $n_1=800$  into Eq. 2, we have  $t_m^{al}=1.3\text{mm}$ . The real vertical stress in the concrete walls is accordingly,

$$\sigma_m^c = \frac{t_m^{al}}{t_p^c} n \sigma_m^{al} \quad (3)$$

Where,  $\sigma_m^{al}$  is the measured model stress in aluminium sheets.

## 3 PERFORMANCE OF CONNECTION STRUCTURES

### 3.1 Directly inserted scheme I (walls 8m apart)

Model No.1 is illustrated in Fig.4. The double walls stretch 75m into the ground layer and are 8m apart. The model is 32.6cm high when scaled down by 800 times. During the tests, the model is centrifuged to 50G, 100G, 150G, and 200G in stages and remains at 200G for a half hour. After the displacement field is recorded, water is poured into the model reservoir to the design normal water level, then the model is tested on 200g for

another half hour, and then the displacement field is recorded again. In the whole test process, the stresses of the model walls are monitored by the data acquisition system using strain gauges. The stress distributions along the walls are shown in Fig.5. The maximum compressive stresses in the upstream and downstream walls are 39.43MPa and 41.41MPa respectively after construction, and 47.86MPa, 33.13MPa respectively after reservoir impounding. The maximum values occur at about 0.45H from the bottom.

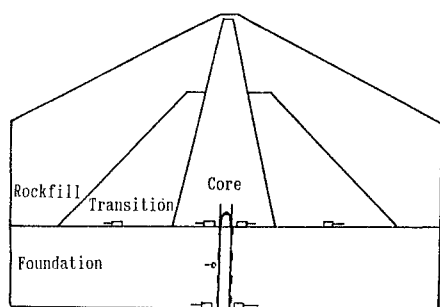


Fig.4 Setup of model No.1

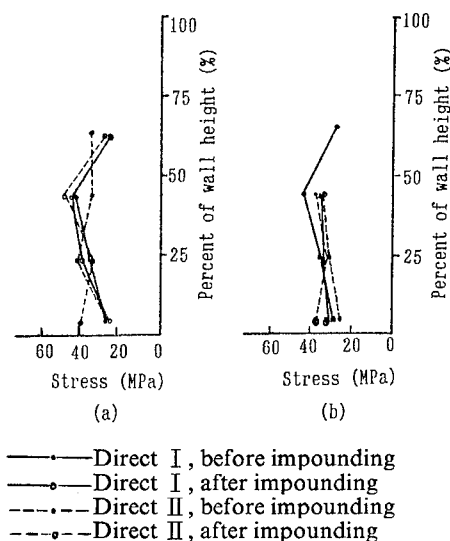


Fig.5 Stress distributions along the walls  
(a) upstream wall, (b) downstream wall

### 3.2 Directly inserted scheme II (walls 20m apart)

In model No.2, the walls are 20m apart, i.e., they are not in contact with the grouting gallery. Other construction characteristics and test procedure of this model are the same as those of model No.1. The maximum compressive stresses in the upstream wall and the downstream wall are

39.68MPa, 33.1MPa after construction, and 47.55MPa, 37.05MPa after reservoir filling, as shown in Fig.5. The positions where the maximum values occur descend down to about 0.25H from the bottom. The small decrease in the top load causes the decrease of the neutral points of negative friction of the walls.

### 3.3 Stiff joint, soft joint, and vacant joint

The dam profile in which the cut-off walls are connected to the gravel soil core through a gallery is shown in Fig.6. The walls go down 75m into the alluvial layer in the lower part. In the stiff joint scheme (model No.3), the top part is linked to the gallery by reinforced concrete; in the soft joint scheme (model No.4), the wall is linked to the gallery through some soft fill such as IGAS. In the vacant joint scheme (model No.5), there is a gap about 2.0m high between the wall and the gallery. Test procedures similar to that of model No.1 were carried out. Fig.7 and Fig.8 compares the stress distributions of the aforementioned three schemes along the walls. Before reservoir impounding, the maximum stresses in the upstream walls are 66.1MPa, 38.05MPa, 31.38MPa for the stiff, soft, and vacant joints respectively, and 51.34MPa, 33.13MPa, 33.13MPa respectively in the downstream walls. After reservoir impounding, the maximum stresses in the upstream walls and downstream walls are 62.78MPa, 35.97MPa, 32.67MPa and 53.0MPa, 39.75MPa, 33.13MPa respectively.

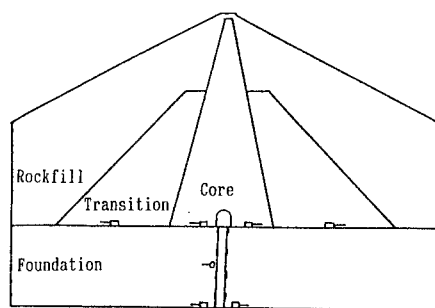
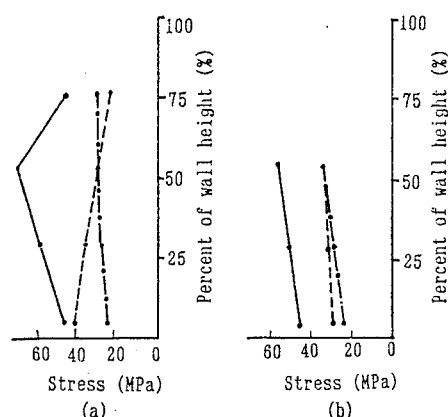


Fig.6 Setups of model No.3, No.4, and No.5

From the above analyses, it can be seen that the maximum compressive stresses in the cut-off walls are below 47.8MPa, 41.4MPa, 66.1MPa, 39.75MPa, and 33.13MPa respectively for the five connection schemes in the discussed sequence. In view of the recent technical standards of bulk concrete production for dams, it is a common practice to produce concrete with 28 days compressive strength around 40MPa. However, it is still difficult to get concrete stronger than 50MPa without adding much expensive fibre. Therefore, the soft and vacant joints are the best choices for this project. The directly inserted

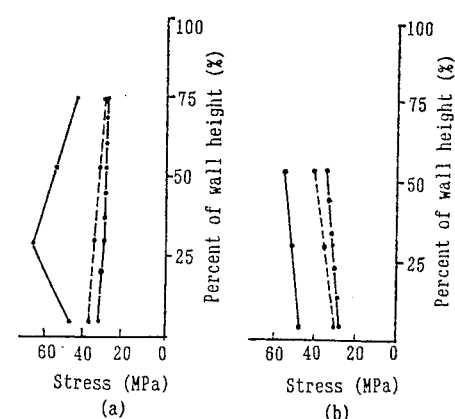
Table 3. Measured crest settlement and horizontal displacement (in cm)

		Direct I	Direct II	Stiff	Soft	Vacant
Crest settlements	After construction	387.6	222.4	220.5	295.1	216.7
	After impounding	346.7	261.1	255.5	406.7	264.0
Maximum horizontal displacement	After construction	88.0	56.0	40.0	64.0	32.0
	After impounding	128.0	120.0	72.0	96.0	64.0



— Stiff joint  
 - - - Soft joint  
 - · - Vacant joint

Fig.7 Stress distributions of the cut-off walls before impounding (a) upstream wall, (b) downstream wall



— Stiff joint  
 - - - Soft joint  
 - · - Vacant joint

Fig.8 Stress distributions of the cut-off wall after impounding (a) upstream wall, (b) downstream wall

scheme with the walls 20m apart is also recommendable.

### 3.4 Settlement and horizontal displacement

Table 3 summarizes the maximum settlement and horizontal displacement of the above five models. Taking test errors into account, it is regarded that the joint types do not affect the displacement markedly. The maximum displacements after construction and after impounding are 2.2m and 2.6m in the vertical direction, and are 0.6m and 1.0m in the horizontal direction. As these model tests are not carried out by staged construction method, the actual settlement is likely to be smaller than 2.6m.

## 4 CONCLUSIONS

Through a series of centrifuge model tests, the applicability of the five suggested cut-off wall joint structures have been evaluated. The vacant joint scheme alleviates the compressive stress in the walls most effectively. The directly inserted joints also have considerable load relief function and are easy to construct. The stiff connection scheme is not feasible because the stress in the walls will be as high as 66.1MPa under which the wall concrete will rupture.

## ACKNOWLEDGEMENTS

Financial support from Chengdu Hydroelectric Power Investigation and Design Institute, and research grant from National Committee of Education are acknowledged.

## REFERENCES

- Dascal O. 1979. Structural behaviour of Manicouagan 3 cut-off. Canadian Geotechnical Journal, 16(1):200-221.
- Dascal O. 1979. Hydraulic efficiency of the Manicouagan 3 cut-off. Canadian Geotechnical Journal, 16(2):351-367.
- Liu Linde and Jianhong Tang 1990. Centrifuge model testing and numerical modelling of a rockfill dam constructed on deep alluvial layers. Research report, Chengdu Hydroelectric

- Investigation and Design Institute.
- Mikasa M. 1980. Modelling geotechnical structures by the use of centrifuge forces. *Soils and Foundations* (in Japanese), 28(5):15-33.
- Zhang Limin and Ting Hu 1991. Centrifuge modelling of the Pubugou high-rise rockfill dam. *Centrifuge'91*, Ko(Ed.) 1991, p.45-50. Rotterdam, Balkema.
- Zhang Limin and Ting Hu 1990. Yielding and failure properties of unequal stress centrifuge models. *Journal of Chengdu University of Science and Technology*, (2) 7-12.
- Zhu Weixing et al. 1990. Centrifuge model testing of the Xibeikou concrete faced rockfill dam. Research report, Nanjing Water Conservancy and Hydroelectric Power Institute.

# Stability of decomposed granite soil slopes

S. Yoshitake & K. Onitsuka  
Saga University, Japan

**SYNOPSIS** Centrifuge model tests are performed on slope models made from compacted unsaturated decomposed granite soil to clarify its characteristics of slope failure patterns. The results show that the failure occur in shallow surfacial slope. The values of shear strength under low confining pressure are important and necessary for the analysis of such shallow slope stability. In addition, shear resistance varies with strain during the shearing process. The failure characteristics of decomposed granite soil slope were simulated by finite element method considering the mobilizing process of shear resistance with the increase in strain, especially under low confining pressure.

## 1. INTRODUCTION

Decomposed granite soil is widely distributed in the western part of Japan. Decomposed granite soil slopes, for example, natural slopes and artificial slopes of compacted materials, are stable under normal dry condition but become unstable when wet during rainy season. Most failures are shallow sliding failures of 1.0 to 2.0m depth. Such shallow failure is one of the characteristics of decomposed granite soil slopes. The values of shear strength, including the effect of soaking, under low confining pressure are important and necessary for slope stability analysis. In particular, the strength parameters  $c$  and  $\phi$  are vital in the slope stability analysis, and generally, peak strength values have been used regardless of the magnitude of strain. However, for the soil to mobilize a certain strength, it is necessary that corresponding strain is produced to its shear stress state. Shear resistance varies with strain during the shearing process (Lambe, 1960; Schmertmann and Osterberg, 1960; Hayashi, 1982). The mobilized cohesive component( $c_m$ ) and frictional component( $\tan \phi_m$ ) responsible for a

Table-1 Soil properties

Sampling site		Saga city Kawakubo
Density of soil particles $\rho_s(\text{g/cm}^3)$		2.64
Optimum water content $w_{opt}(\%)$		11.0
Maximum dry density $\rho_{dmax}(\text{g/cm}^3)$		1.94
Grain size Distribution (%)	Gravel	36
	Sand	52
	Silt	7
	Clay	5
Plasticity index $I_p$		NP
Classification		SM

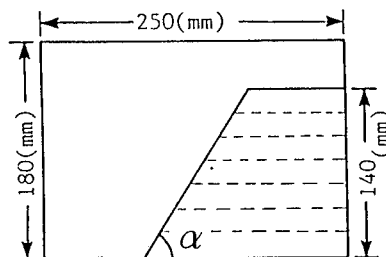


Fig.1 Shape of slope for centrifugal model test

certain strain are called coefficients of shear resistance in this study. Stability analysis is done on decomposed granite slope considering the variation of these coefficients during shearing process and its results are compared with those derived from centrifuge model slope tests.

## 2. SAMPLES AND TEST APPARATUS

### 2.1 Triaxial compression tests

The samples used here are decomposed granite soils. The soil properties are shown in Table-1. Sample from air-dried soil with particles finer than 2mm were prepared as to correspond to the optimum water content. These were statically compacted in a mould( $\phi 5 \times 10$ cm) by a compression apparatus. Consolidated drained triaxial compression tests were carried out under low and moderate confining pressures. The range of lateral pressure is from 1.96 ( $\text{kN/m}^2$ ) to 15.7 ( $\text{kN/m}^2$ ) considered as low pressure and from 19.6 ( $\text{kN/m}^2$ ) to 157 ( $\text{kN/m}^2$ ) for moderate pressure.

### 2.2 Centrifuge model tests

Fig.1 shows the shape of slope for centrifuge model test. The height of model slope is 14cm. Decomposed granite soil was compacted to seven equal layers of 2cm at the optimum water content and 80% of maximum dry density. In order to observe the sliding surface at failure, a layer of Kaolin was placed between every layer. The model slopes were then formed by cutting with various inclinations, .

## 3. VARIATION OF SHEAR RESISTANCE COEFFICIENTS ( $c_m$ , $\tan \phi_m$ ) WITH SHEAR STRAIN

Fig.2 shows Mohr's stress circles under low and moderate confining pressures. The gradient of the Mohr's envelope in the region of low confining pressure is greater than that for moderate confining pressure. The angle of shearing resistance  $\phi_a$  is greater, and the apparent cohesion  $c_a$  is less, when the confining pressure is low. It is considered that the difference in shear strength for low and moderate confining pressure is based

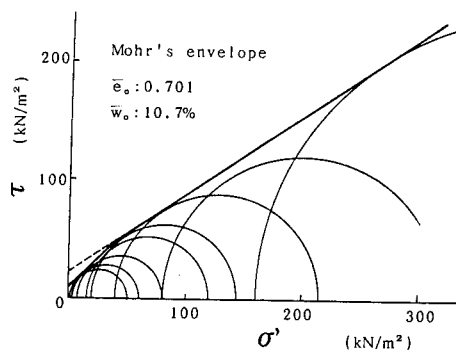


Fig.2 Mohr's stress circles

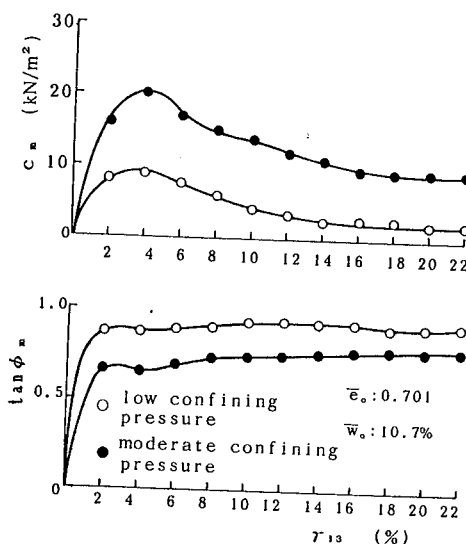


Fig.3 The variation of shear resistance coefficients with shear strain

on the degree of particle crushing at both pressures (Onitsuka and Yoshitake, 1988). Fig.3 shows the variations of shear resistance coefficients with the increase in strain under low and moderate confining pressure. The coefficients of shear resistance are plotted against shear strain  $\gamma_{13}$  (see Hayashi, 1982), where  $\gamma_{13} = \epsilon_1 - \epsilon_3$ ,  $\epsilon_1$ : axial strain,  $\epsilon_3$ : lateral strain. The cohesive component ( $c_m$ ) reaches peak at the primary state during shear and somewhat decreasing after that, regardless of the magnitude of confining pressures. On the

other hand, the frictional component ( $\tan \phi_m$ ) gradually increases with increase in shear strain and then gradually approaches a constant value under both low and moderate confining pressures. Cohesive component-shear strain relations are in close correspondence with the deviator stress-shear strain relationships (figure not shown). It suggests, therefore, deviator stress-shear strain relationships depend mainly on cohesive component-shear strain relations and is virtually unaffected by the frictional component-shear strain relations.

#### 4. CENTRIFUGE MODEL TESTS OF DECOMPOSED GRANITE SOIL SLOPE

Centrifuge model tests were conducted to investigate the failure characteristics of decomposed granite soil slope. The shapes of the decomposed granite soil slopes at failure are shown in Figs.4 and 5. In Fig.4, the inclination of slope was eighty degrees ( $80^\circ$ ) and the centrifuge acceleration at slope failure was ninety times the gravitational acceleration ( $90g$ ). In this case, the mode of slope failure was a slide on top of the slope rather than slip failure, and hence the slip surface is not clear. Because the inclination of slope was steep for this case, tension cracks were found near the top of slope. In Fig.5, the inclination of slope is sixty degrees ( $60^\circ$ ) and the centrifuge acceleration at slope failure is one hundred and seventy times the gravitational acceleration ( $170g$ ). In this case, a sliding surface is clearly observed and the shape of sliding surface shows a nearly circular sliding surface. Shallow sliding failure patterns for decomposed granite soil slope were observed in the centrifuge model tests. Fig.6 shows the position of sliding surfaces obtained from centrifuge model tests and circular arc method using peak strength parameter ( $C_d, \phi_d$ ) under low and moderate confining pressures. It was also found that under low confining pressure the position obtained from circular arc method is close to that with the model test. The calculated safety factors are 0.86 and 0.90 for low and mod-

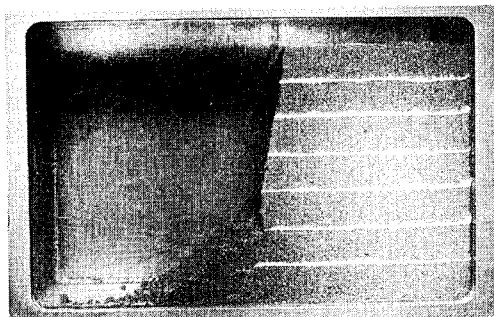


Fig.4 Slope failure  
(slope angle  $80^\circ$ )

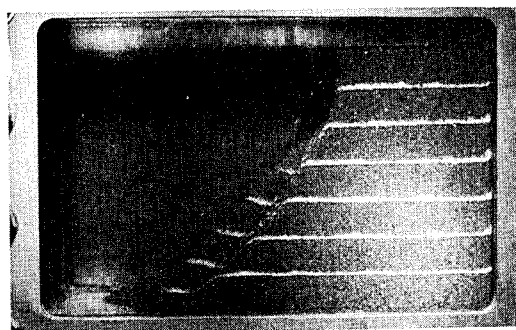


Fig.5 Slope failure  
(slope angle  $60^\circ$ )

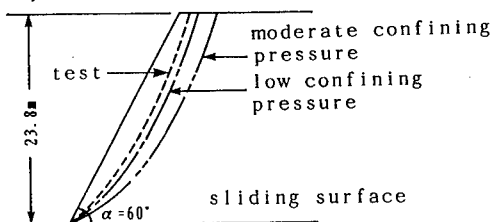


Fig.6 Sliding surface

erate confining pressure, respectively, which appear to be less, especially for low confining pressure, as compared to the value of 0.96 for the sliding surface obtained from centrifuge model test. In addition, using the strength parameters obtained from direct shear tests, the calculated safety factors are 0.98, 1.01 and 1.08 for the above determined sliding surfaces corresponding to confining pressure and from model test, respectively. Apparently, the use of parameters from direct shear tests

resulted in somewhat larger factors of safety than those obtained using the strength parameters from triaxial compression tests. The location of sliding surfaces, however, are identical for both test methods. In calculating the safety factors for the case of centrifuge model tests, the sliding surface used in calculation was considered as a circular arc, in the light of the failure mode observed in the model test. The above results exhibit that it is essential to consider and study the shear characteristics, especially strength characteristics under low confining pressure, in the stability analysis of decomposed granite soil slope. The location of sliding surface and the corresponding safety factor values obtained from centrifuge model test are somewhat different from those obtained through calculation. This may be due to the increase of the strength of decomposed granite soil caused by the dead weight consolidation in the stage of increasing centrifuge acceleration.

## 5. SLOPE STABILITY ANALYSIS

In the case of slope for which the depth of sliding surface is shallow, stability analysis using peak strength parameters under low pressures is more reasonable. Also, the coefficient of shear resistances ( $c_m$ ,  $\tan\phi_m$ ) can be expressed as a function of strain. Considering the variation of the coefficients of shear resistances ( $c_m$ ,  $\tan\phi_m$ ) with the increase in strain, the failure characteristics of decomposed granite soil slope were simulated by the finite element method. Non-linear secant modulus method is adopted in the stability analysis of decomposed granite soil slope. Fig.7 shows the given homogeneous decomposed granite soil slope which is in plain strain state. It is represented with 169 finite elements with 107 nodes. The analysis is done in following sequence:

1. The maximum shear stress and shear strain in every finite element are calculated in the light of the element dead weight, using initial deformation modulus,  $E_0$  and Poisson's ratio,

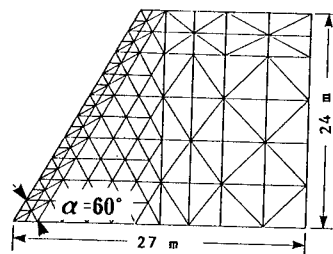


Fig.7 Finite element mesh

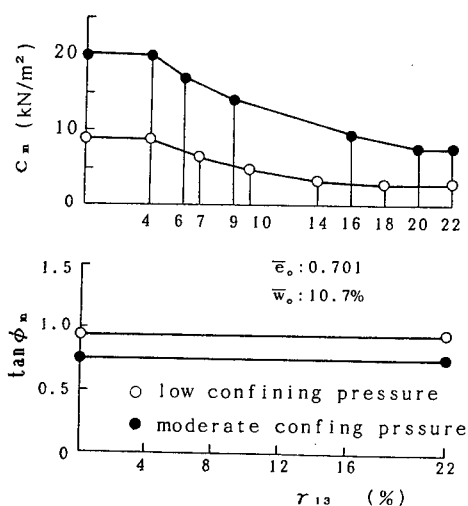


Fig.8 Simplified coefficients of shear resistance-maximum shear strain relationship

$\nu_0$  obtained from triaxial test.

2. The coefficients of shear resistance of every element corresponding to the known shear strain obtained in step 1 are evaluated on the basis of the relationships of the coefficients of shear resistance versus shear strain shown in Fig.8, which are approximately expressed in straight lines instead of the curved relationships shown in Fig.3.
3. The following equation is used to judge whether the local failure occurs in terms of the known coefficients of shear resistance:

local safety factor,  $F_L$



$$F_L = \frac{\sin \phi_m \times (\sigma_1 + \sigma_3) / 2 + c_m \times \cos \phi_m}{(\sigma_1 - \sigma_3) / 2}$$

4. If  $F_L$  is less than unity,  $E_0$  is replaced by  $E_i$  determined in following equation:  $E_i = E_0 \times F_L$ .
5. Return to step 2, iterative calculation and judgment are done. If the mean value of  $F_L$  for all elements is less than unity, the calculation is terminated.

The results of slope stability analysis considering the variation of the coefficients of shear resistance with the increase in shear strain under low and moderate confining pressure, are shown in Fig.9, in which  $n$  represents the iterative calculation steps and the parts with  $F_L \leq 1.0$  show the distribution of the local failure elements. In the initial stage of calculation, local failure occurs at the toe of slope. In the progress of the iterative calculation, a local failure region develops through the surface layer of the slope and finally reaches the top of the slope, resulting in slope failure. The mean value of  $F_L$  is equal to 0.97. Therefore, the slope failure mechanism can be considered to consist of the following process: (a) local failure which occurs at the elements in the toe of slope, (b) gradual development of failure elements and (c) finally, slope failure occurs. From the investigation of failure tests on the decomposed granite soil slope in the centrifuge model tests, it was also found that the initial failure occurs at the toe of the slope with large strain and failure region gradually develops, thus, finally resulting in slope failure. It is impossible to show this phenomenon with the circular arc method in limit equilibrium method. At the stage of slope failure ( $N=7$ ), the sliding surface obtained from centrifuge model test is located in a narrow and long element region with  $F_L \leq 0.8$ , showing the position of sliding surface obtained from centrifuge model test is almost identical with the analysis results. Fig.10 shows the results of slope stability analysis considering only the variation of shear resistance coefficients with the increase of

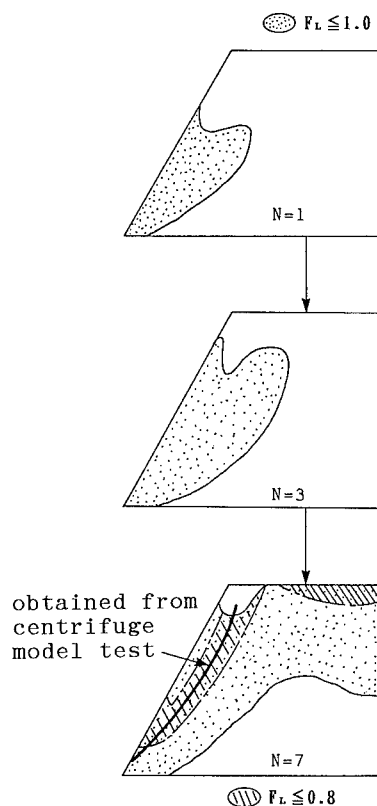


Fig.9 Results of slope stability analysis(considering the variation of shear resistance coefficients under low and moderate pressure)

shear strain under moderate confining pressure. As shown in Fig.10, the progressive case of local failure elements is a little different from that in low confining pressure which considers the variation of shear resistance coefficients. However, the progression of local failure elements which is determined in iterative calculation, can not reach the top of the slope when considering only the variation of shear resistance coefficients in moderate confining pressure. This indicates no slip failure. So it is not suitable to simulate the slope failure in doing stability analysis with only considering variation of shear resistance coefficients in moderate confining pressure because slip failure occurs in centrifuge model tests. Therefore, a stability

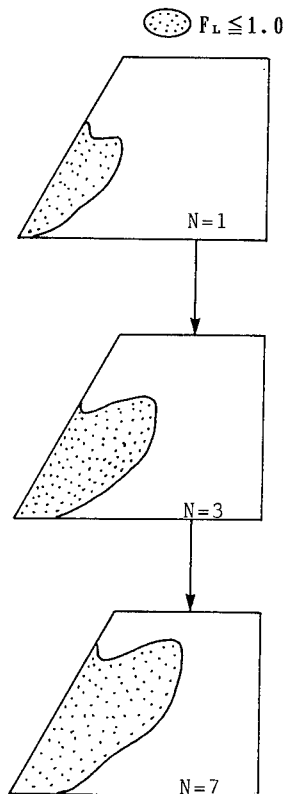


Fig.10 Results of slope stability analysis(only considering the variation of shear resistance coefficients under moderate pressure)

analysis which considers the variation of the coefficients of shear resistance, especially under low confining pressure, can explain the failure pattern or failure occurrence phenomenon of decomposed granite soil slope very well.

## 6. CONCLUSIONS

Centrifuge model tests were conducted on decomposed granite soil slope. The slope failure characteristics were clarified. The safety factors of decomposed granite soil slope were calculated by the circular arc method using peak strength parameters under low and moderate confining pressures. In addition, the failure characteristics of decomposed granite soil slope are simulated by the finite element

method considering the variation of coefficients of shear resistance with the increase in strain.

- 1)The cohesive component reaches peak at the primary state during shear and somewhat decreasing after that, regardless of the magnitude of confining pressures.
- 2)Frictional component increases gradually with increase in shear strain and gradually approaches a constant value for both low and moderate confining pressures.
- 3)Shallow sliding type of failure of the decomposed granite soil slope is observed in the centrifuge model tests. Using peak strength parameter under low pressure, the position of sliding surface obtained from circular arc method is close to that from the model tests.
- 4)Slope stability analysis which considers the variation of the coefficients of shear resistance, especially under low confining pressure, can explain the failure pattern or failure occurrence phenomenon of decomposed granite soil slope very well.

## REFERENCES

- Hayashi, S.(1982): A study of three-dimensional friction rule of soils, Dr. Eng. Thesis, Kyushu University. (In Japanese)
- Lambe, T.W. (1960) : A mechanistic picture of shear strength in clay, Research Conference on Shear Strength of Cohesive Soils, Soil Mechanics and Foundation Division, ASCE, pp.555-586.
- Onitsuka,K. and Yoshitake,S.(1988): Shear characteristics of decomposed granite soil compressible under low pressure, Proc. J.S.C.E., Vol.400, III-10, pp.141-150(In Japanese).
- Schmertmann, J.H. and Osterberg, J.O. (1960): An experimental study of development of cohesion and friction with axial strain in saturated cohesive soils, Research Conference on Shear Strength Cohesive Soil, Soil Mechanics and Foundation Division, ASCE, pp.643-694.

## Stability of cut slopes in Ariake clay

K. Onitsuka & K. Yamamoto

Department of Civil Engineering, Saga University, Japan

**ABSTRACT:** An extremely soft clay, Ariake clay, is widely deposited around Ariake Bay, located at the western part of Japan. Many cases of failure have been reported on the cut slopes formed by excavation in such clay deposit for watercourse and building constructions. In this study, centrifugal model tests are performed on simulated cut slope of undisturbed and artificially consolidated Ariake clays to obtain the critical heights. Such experimental critical heights are compared with the calculated critical heights using Taylor's chart with unconfined compressive strength and triaxial compressive strength. The comparison shows that the calculated critical height using triaxial compressive strength is much closer to that with the centrifugal test than that using unconfined compressive strength. This indicates that the compressive strength from triaxial test of Ariake clay is valid for the slope stability analysis. The slope stability analysis is also carried out to investigate the failure process and deformation pattern of the cut slope.

### 1 INTRODUCTION

Extremely soft Ariake clay layer, generally with a thickness of 10-30 m, is widely deposited around Ariake Bay located at the western part of Japan. Many cases of cut slope failure have been reported in this area. In this study, centrifugal model tests are performed on simulated cut slopes of undisturbed and artificially consolidated Ariake clay to obtain the critical heights and to investigate the failure patterns (Onitsuka et al., 1992).

The critical heights obtained by centrifugal tests are compared with the calculated values by Taylor's chart using unconfined compressive strength and triaxial compressive strength. The slope stability analysis is also done to investigate the failure process and deformation pattern of the slope. In addition, the experimental and calculated critical heights are also compared with actual critical heights reported for the cut slopes in practical engineering.

Although Matsuo et al. (1982) have indicated some problems in Taylor's chart and proposed a modified chart, this modified chart is the same as Taylor's chart for the slopes greater than 53°. Since the slopes of slope models used in this study are generally greater than 53°, Taylor's chart is adopted for simplicity.

### 2 SAMPLES

Two kinds of Ariake clays (called Sample 1 and Sample 2) are taken at Ashikari, Ogi-gun in Saga prefecture of Japan. Their physical properties are shown in Table 1. The sampling method of undisturbed samples and the forming method of artificially consolidated samples are stated as follows:

**Undisturbed samples:** Undisturbed samples are taken at about 1.5m below the ground surface with polyvinyl chloride pipes (diameter: 30cm, thickness: 1cm, height: 20cm). They are covered with two polyvinyl chloride boards (length: 40cm, width: 40cm, thickness: 1cm), and kept in a water tank.

**Artificially consolidated samples:** The same clays as the undisturbed samples are remolded and packed into a rectangular container (length: 25cm, width: 15cm,

Table 1. Basic Properties of Ariake Clay

Sample	①	②
Density (g/cm <sup>3</sup> )	2.659	2.661
Natural Water Content w <sub>n</sub> (%)	143	154
Liquid Limit w <sub>L</sub> (%)	115	123
Plasticity index I <sub>p</sub>	74	71
Fine Sand (%)	2.4	0.9
Silt (%)	33.6	38.6
Clay (%)	64.0	60.5

height: 20cm), and de-aired. Then consolidation loads are incrementally increased to make artificially consolidated samples. The final load is chosen as 20 kPa, which is close to the overburden pressure in situ, with total loading time of about 12 days.

### 3 EXPERIMENT METHOD

#### 3.1 Unconfined compression test and triaxial compression test

Isotropically consolidated undrained shear triaxial tests are carried out under the consolidation stresses of 25, 50, 75 and 100 kPa. Both unconfined compression and triaxial compression tests are performed at a strain rate of 1%/min with the size of specimen of  $D=3.5\text{cm}$  &  $H=8.8\text{cm}$ . Triaxial compression test is not carried out for Sample 1.

#### 3.2 Centrifugal model test

A simulation method for cut slope was reported on centrifugal model test (Kimura et al., 1988), in which a cut model slope was first made, then a part of it was filled with a liquid with the same unit weight as the sample. The liquid was gradually drained in a centrifugal acceleration test to simulate the continuous excavation process. However, in this study, a simple method is used in which the slope is formed at a fixed slope angle. Then centrifugal acceleration is increased till the model slope fails.

In order to obtain reasonable experimental results in centrifugal model tests, the following measures are proposed in this study.

1. In order to reduce friction between specimen and container, "Kanten" is used instead of generally used silicone grease as a friction coating agent. "Kanten" is a kind of Japanese food, showing a state between solid and liquid.

2. Since drain occurs in the centrifugal tests for undisturbed specimen, the ground model of undisturbed specimen is consolidated first by centrifugal load of 120g. This test is called self-weight consolidation in this paper. Then, the slope model is cut for doing slope model failure test.

##### 1) Reducing friction on the model test

In order to study the effect of "Kanten" on reducing friction, centrifugal slope model failure tests are performed on the same slope model made of the same artificially consolidated samples with slope

90°, but with two different agents as the friction coat in the inner wall of container: silicone grease and "Kanten". The reason of using artificially consolidated samples is that their strength and unit weight are more homogeneous than those of the undisturbed samples.

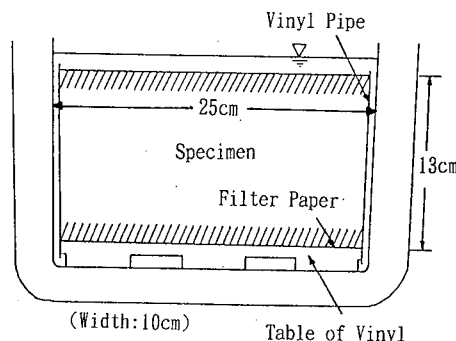


Fig.1 Self-Weight Consolidation Model

##### 2) Self-weight consolidation test

In order to make the slope model of undisturbed clays no drain occur during the centrifugal slope model failure test, the undisturbed samples are consolidated first under a centrifugal acceleration of 120g for the maximum limit time of 2 hours. The height of all the undisturbed samples for self-weight consolidation are arbitrarily chosen as 13cm, because different heights result in different degree of consolidation. Double drainage is employed for self-weight consolidation to hasten the consolidation process. "Kanten" is used to reduce the friction. Water content and unconfined compressive strength of the model ground are measured when the self-weight consolidation test is finished. The self-weight consolidation test model is schematically shown in Fig.1, similar to that reported by Takada et al. (1988).

##### 3) Slope failure test

In order to investigate the location of sliding surface in a slope, centrifugal model tests are performed on the slope models made of both undisturbed and artificially consolidated samples. The slope angles of the slope models are 45°, 60°, 75° and 90°. For undisturbed specimen, the self-weight consolidation test is first performed under 120g for two hours, then the slope model is cut for slope model failure test. The failure for all slope models occurs at centrifugal acceleration less than 120g.

## 4 EXPERIMENT RESULT AND STUDY

### 4.1 Results of unconfined compression test and triaxial compression test

Figs.2 through 4 show the results of unconfined compression test and triaxial compression test. Since the stress-strain relationship of undisturbed specimen shows strain-softening, while for artificially consolidated specimen it shows strain-hardening, the undrained strength is taken as the peak value for the undisturbed specimen, while the value at the strain of 15% is taken for the case of artificially consolidated specimen. From Fig.2, it can be seen that the compressive strength of undisturbed specimen is larger than that of artificially consolidated one, and the strength of vertical specimen is stronger than that of horizontal one. From Fig.4, it can be seen that the unconfined compressive strength is close to the triaxial compressive strength for the undisturbed specimen, but much less than the triaxial strength for the artificially consolidated specimen.

### 4.2 Result of centrifugal model test

#### 1) Reducing friction on the model test

Fig. 5 and Table 2 show the experimental results for reducing friction on the model test. The equivalent critical height of the actual slope at failure obtained in the centrifugal model test with "Kanten" as friction coating agent in the inner wall of container is closer to the critical height calculated by Taylor's chart than that using silicone grease. And the slip surface using "Kanten" is deeper than that with using silicone grease. The above results indicate that friction between inner wall of container and specimen is reduced by using "Kanten" instead of silicone grease.

#### 2) Self-weight consolidation by centrifugal load

After loading centrifugal acceleration of 120g for 2 hours, about 2 mm settlement occurs in undisturbed specimen, but no settlement occurs in artificially consolidated specimen. The results of vertical distribution of water contents and unconfined compressive strengths measured from the self-weight consolidated specimen are discussed below.

#### a) Vertical distribution of water content

Fig. 6 shows the distribution of water

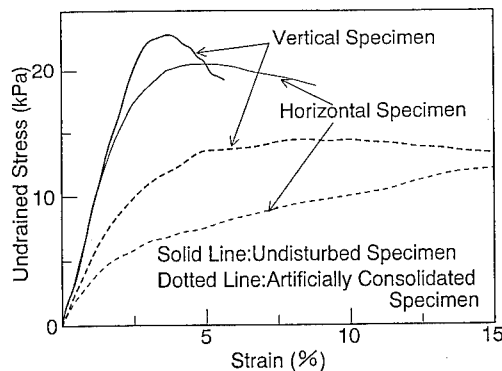


Fig. 2 Stress-Strain Curve (Sample ①)

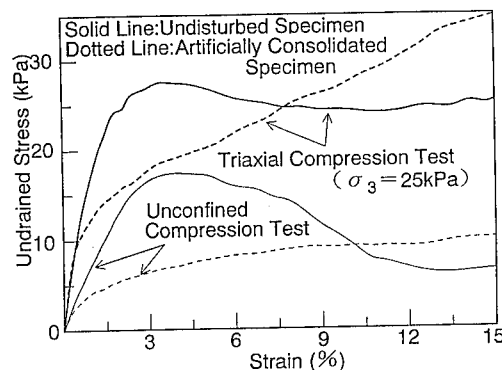


Fig. 3 Stress-Strain Curve (Sample ②)

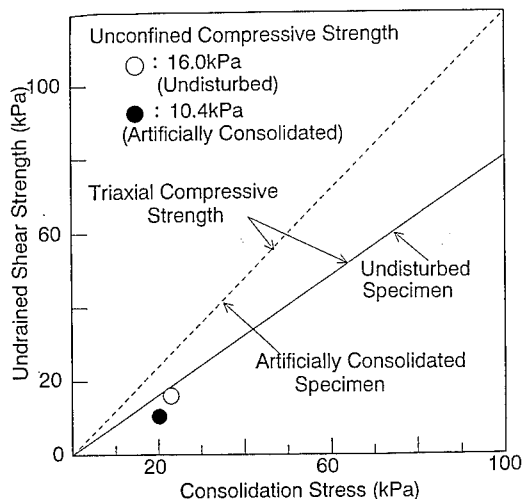


Fig. 4 Relation between Consolidation Stress and Undrained Shear Strength (Sample ②)

Table 2. Results for reducing friction on the model test (Sample ①)

	Critical Height by Experiment①	Critical Height by Calculation②	$\frac{②}{①}$	Style of Failure
Silicone Grease	3.25m	1.93m	0.594	Toe Failure
Kanten	2.93m	1.93m	0.658	"

Table 3. Unconfined Compression Test Before and After Self-Weight Consolidation (Sample ①)

		Undisturbed		Artificially Consolidated	
		V.	H.	V.	H.
Before	$q_u$ (kPa)	22.2	19.5	14.4	12.0
	$E_{50}/(q_u/2)$	76	115	71	35
After	$q_u$ (kPa)	22.9	20.1	15.5	13.3
	$E_{50}/(q_u/2)$	101	103	40	31

※V. = Vertical Specimen, H. = Horizontal Specimen.

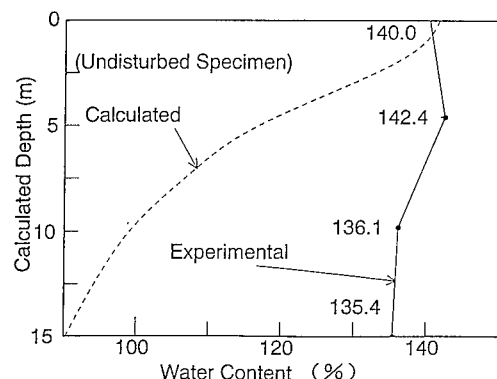


Fig.6 Vertical Distribution of Water Contents (Sample ①)

contents in the vertical direction for the self-weight consolidated specimen. The measured water content is low in the lower part of the specimen because of self-weight consolidation. And comparing this distribution with that calculated in the  $e$ -log  $p$  curve, it can be seen that in the upper part of the specimen, experimental value is close to the calculated one. In the lower part the former is much higher than the latter. This is attributed to which the time of the self-weight consolidation is too short to make the specimen to be completely consolidated.

#### b) Unconfined compressive strength

Unconfined compressive strength and degree of disturbance of self-weight consolidated specimen are compared with those of sample without consolidation. Table 3 shows the average results for each case. In many

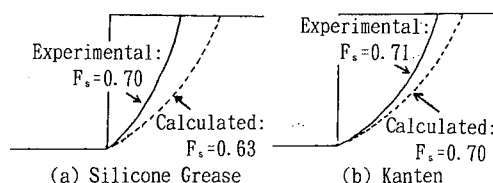


Fig.5 Results for Reducing Friction (Sample ①)

cases, undrained strength increases under loading centrifugal force, but the extent of sample disturbance also increases. The increase of disturbance due to consolidation is caused by the failure of soil structure under quick consolidation.

### 3) Slope failure test

Tabs. 4&5 show the centrifugal test results and the calculated values by Taylor's chart. Figs. 7 through 10 are the results of slope failure tests. Circular slip surfaces are observed in the undisturbed specimen of Sample 1 (shown in Fig.7) and the artificially consolidated specimen of Sample 2 (shown in Fig.10). From Table 5, it can be seen that the safety factor calculated by unconfined compressive strength is much less than unity, while the safety factor by triaxial compressive strength is close to unity.

It was reported that failure of timbering of a cut in the field condition occurred at the depth of about 3m, which is close to the result of centrifugal model test on undisturbed sample with slope 90°.

## 5 FEM ANALYSIS

### 5.1 Analysis method

FEM analysis is carried out on the slope model with slope 45° of artificially consolidated specimen of Sample 2. The analysis process are summarized as follows: 1)calculate the maximum shear stress  $\tau_{max}$  and the maximum shear strain  $\gamma_{max}$  for each element with the initial deformation modulus  $E_0$  and the initial Poisson's ratio  $\nu_0$ . 2)obtain the cohesion stress  $c$

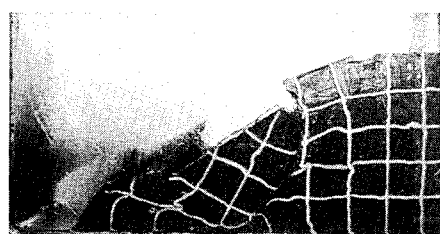
Table 4. Results of Slope Failure Test (Sample ①)

	Slope	Critical Height by Experiment①	Critical Height by Calculation②	② ①	Style of Failure
Undisturbed Slopes	45°	6.32m	4.54m	0.718	Base failure
	60°	4.68m	4.17m	0.891	Toe failure
	75°	4.24m	3.66m	0.863	"
	90°	2.94m	3.09m	1.051	" (by Tension crack)
Artificially Consolidated Slopes	45°	—	2.79m	—	No slip surface
	60°	—	2.61m	—	"
	75°	—	2.29m	—	"
	90°	2.93m	1.93m	0.659	Toe failure

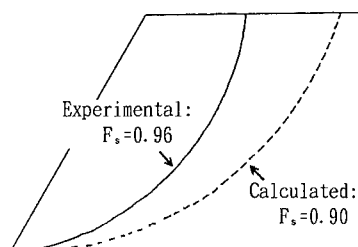
Table 5. Results of Slope Failure Test (Sample ②)

	Slope	Critical Height by Experiment①	Critical Height by Calculation②	Critical Height by Calculation③	② ①	③ ①	Style of Failure
Undisturbed Slopes	45°	—	3.41m	3.87m	—	—	Many Cracks
	60°	—	3.18m	3.61m	—	—	"
Artificially Consolidated Slopes	45°	5.0m	2.13m	4.84m	0.426	0.968	Base Failure
	60°	4.5m	1.99m	4.51m	0.442	1.002	"
	90°	3.3m	1.46m	3.33m	0.442	1.009	"

※Critical height ② are calculated with unconfined compressive stress, while critical height ③ are calculated with triaxial compressive stress.

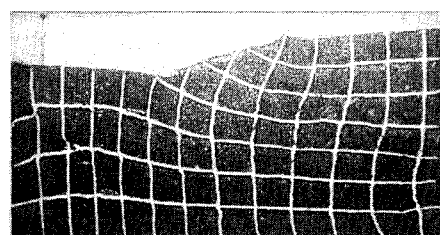


(a)



(b)

Fig. 7 Result of Undisturbed Slope 60° (Sample ①)

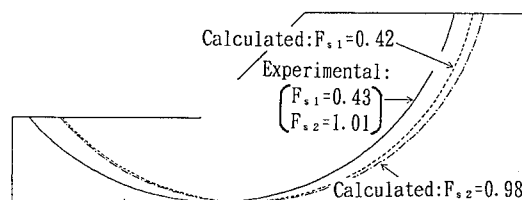


(a)



Fig. 9 Result of Undisturbed Slope 60° (Sample ②)

Fig. 8 Result of Artificially Consolidated Slope 45° (Sample ②)



(b)

※ $F_{s,1}$  is calculated with unconfined compressive strength, and  $F_{s,2}$  is calculated with triaxial compressive strength.

Fig. 10 Result of Artificially Consolidated Slope 45° (Sample ②)

of each element responsible for the maximum strain with consideration of the variation of cohesion stress during the shear process (shown in Fig.11). 3) calculate the local safety factor  $S_F = c / \{ (\sigma_1 - \sigma_3) / 2 \}$  for each element using the obtained  $c$  value in step 2). New deformation modulus  $E_i (= E_o \cdot S_F)$  is obtained instead of  $E_o$  for the elements with  $S_F < 1$ . 4) iteration calculation is carried out in step 1) through 3) till  $S_F \geq 1$  for all elements. It should be noted that total stress method is adopted in this analysis. The abscissa of the stress-strain curve from triaxial compression test shown in Fig.11 is represented in terms of  $\gamma_{13} = \epsilon_1 - \epsilon_3$ . In addition, the curve is approximately idealized by several segments of straight line.

## 5.2 Analysis result

Fig.12 shows the distribution of the maximum shear strain at the end of FEM analysis. Fig.13 shows the deformation state of the slope at the end of FEM analysis. The deformation pattern shown in Fig.13 is similar to that of the slope of Sample 1 without exhibiting slip surface.

## 6 SUMMARY

1) In the centrifugal model test, slip surface occurs in the undisturbed specimen of Sample 1 and the artificially consolidated specimen of Sample 2. The cause of the difference in the pattern of failure for the two specimens, however, is not well understood.

2) The triaxial compressive strength is larger than the unconfined compressive strength for both undisturbed and artificially consolidated specimens. The unconfined compressive strength is close to the triaxial compressive strength for the undisturbed specimen, but much less than the triaxial strength for the artificially consolidated specimen. In addition, the safety factor of the slope calculated using unconfined compressive strength is much less than unity, while the safety factor using triaxial compressive strength is close to unity, indicating that the compressive strength from triaxial test is valid for the slope stability analysis.

3) The deformation pattern obtained by FEM analysis is very similar to that observed in the centrifugal slope model test without exhibiting slip surface. In addition, in the centrifugal slope model test, the failure occurs first at the toe of the slope and then develops gradually toward the top of the slope. This observation is the same as that in FEM analysis.

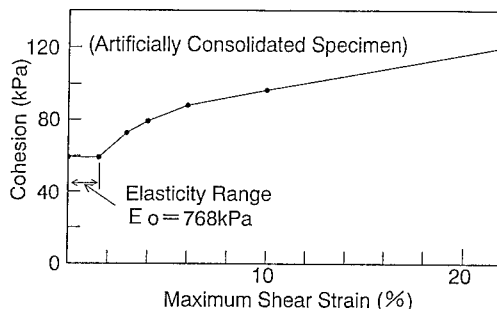


Fig.11 Change of Cohesion

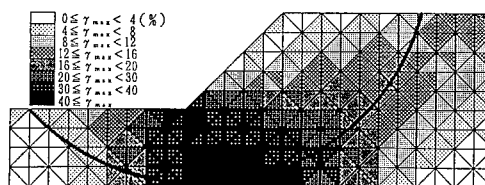


Fig.12 Distribution of Maximum Shear Strain  
※Bold solid line is slip surface by centrifugal model test.

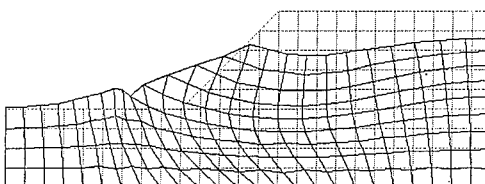


Fig.13 Deformation of Slope

## REFERENCES

- Kimura, T. and Kusakabe, O. and Takada, N. 1988. Application ( Excavation, Tunnel, Underground pipes ). Tsuchi-to-Kiso, The Japanese Society of Soil Mechanics and Foundation Engineering 36-6:79-85.
- Matsuo, M. and Suzuki, H. 1982. Stability charts of pure cohesive simple slopes. Tsuchi-to-Kiso, The Japanese Society of Soil Mechanics and Foundation Engineering 30-9:51-57.
- Onitsuka, K. and Yoshitake, S. 1992. Centrifugal model test on slope of Ariake clay. 47th National Conf. of JSCE:820-821.
- Takada, N. and Fujii, N. 1988. Centrifugal model test 5 Application ( Problems about consolidation and stability problem ). Tsuchi-to-Kiso, The Japanese Society of Soil Mechanics and Foundation Engineering 36-4:79-84.



## Effect of soil stress-strain characteristics on slope failure

M. Kitazume

*Port and Harbour Research Institute, Yokosuka, Japan*

M. Terashi

*Nikken Sekkei Nakase Geotechnical Institute, Kawasaki, Japan*

**ABSTRACT:** It is well known that a natural clay which has experienced a long term secondary compression and/or cementation exhibits a brittle nature in its stress – strain relation, while a remolded or reconsolidated clay shows a ductile nature. A series of centrifuge model tests was performed to investigate the effect of the stress – strain characteristics on behavior during slope instability. In the tests, two clay samples were prepared where one was consolidated at a room temperature and the other was consolidated at a high temperature of 75 degrees Celsius to duplicate the aging effects. The slopes made of two clays were brought to a high acceleration field until an entire failure took place. It was found that the deformation and the failure mode of the slope was much affected by the stress – strain characteristics.

### 1. INTRODUCTION

Centrifuge model tests have been frequently performed to study slope stability, bearing capacity, interaction of soil and structure, and so on. In these tests, clay samples remolded and reconsolidated at a room temperature have been often used as a model material. This procedure has an advantage to provide a possibility of simulating in-situ stress history in a centrifuged scaled model ground to a certain extent. The use of the reconsolidated soil increases the reproducibility of the model test in comparison with use of a natural soil block.

However, it is well known that a natural clay which has experienced a long term secondary compression and/or cementation exhibits a brittle nature in its stress – strain relation, while a reconsolidated clay shows a ductile behavior. Because of the difference in the stress – strain characteristics of these two clays, modes of deformation and/or failure in the model tests may be quite different from those of the real life behavior. Therefore it is necessary to duplicate a clay having the aging effect in order to investigate the real life behavior in the scaled model test. Tsuchida et al. (1991) successfully duplicated an aged clay specimen which is remolded and reconsolidated at a high temperature of 75 degree Celsius. It is found from unconfined and triaxial tests that the clay thus manufactured has a brittle nature similar to a natural clay. The high temperature might accelerate chemical actions in clay particles and cementation.

A series of centrifuge model tests was performed in order to investigate the effect of the stress – strain characteristics on the behavior during slope instability. In the tests, two kinds of clay samples were pre-

pared where one was consolidated at a room temperature ( R-clay ) and the other was consolidated at a high temperature of 75 degree Celsius ( H-clay ). The clay slopes were brought to a high acceleration field until a slope failure took place. Failure mode and deformation of the clay slope were investigated in detail.

### 2. TEST PROCEDURE

#### 2.1 Equipment

The centrifuge apparatus used in the tests is PHRI Geotechnical Centrifuge as shown in Fig.1, which

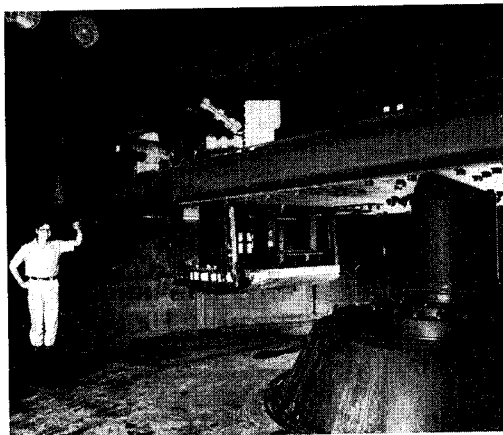


Fig. 1. PHRI Geotechnical Centrifuge

has an effective radius of 3.8m, maximum pay load of 2.7ton and maximum acceleration of 115g. Details of the machine and the surrounding equipments were reported by Terashi (1985).

The specimen box used in the test series has inner dimensions of 50cm long, 10cm wide and 35cm high. One side of the box is made of a perspex window, 50mm thick, allowing visual and photographic observations from a stationary position at the side wall of the centrifuge pit by means of stroboscopic light during the test.

Clay samples used in the tests are a natural marine clay, Yokohama Daikoku Clay, whose index properties were obtained by Tsuchida et al.( 1991 ) and shown in Table.1.

Table.1 Index Properties

density of soil particles( $\text{g}/\text{cm}^3$ )	2.698
consistency limit	
liquid limit (WL)	78 (%)
plastic limit (Wp)	32 (%)
plasticity index (Ip)	46
grain size distributions	
sand fraction	4 (%)
silt fraction	51 (%)
clay fraction	45 (%)

## 2.2 Model Preparation

Toyoura sand was poured at first in the bottom of specimen box to create a drainage layer. Then the clay slurry well remolded at a water content of 120% was poured in the box.

For the R-clay sample, the clay slurry was compressed one dimensionally on laboratory floor and allowed to consolidate at the prescribed pressure. For the H-clay sample, on the other hand, the specimen box filled with clay slurry was placed in a hot tub ( Fig.2 ) at a temperature of 75 degree Celcius. Several thermometers were installed in the clay slurry to monitor the temperature increase. The clay temperature increased to 75 degree after about ten hours in the hot tub. Then vertical pressure on the clay was gradually increased to the

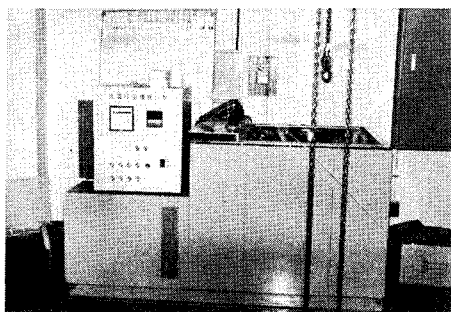


Fig.2. Hot tub

prescribed pressure and was kept constant at 75 degree during the consolidation. After the completion of the consolidation, the H-clay sample was cooled down to room temperature. Then the front window of the box was removed and the clay cake was carefully cut to the slope shape whose height and gradient were 15cm and 1:1 respectively. Visual target markers were placed on the front surface of the clay cake to observe the deformation and slip line of the ground as shown in Fig. 3 and 4. One of the markers was Japanese soumen noodles for qualitative observation and the other was glass grain markers for quantitative observation. In the figure 3, a set of white straight lines and white spots represent the noodles and target markers respectively.

The box was re-assembled and several displacement transducers ( LVDTs ) were placed to monitor the ground deformation at the crest and the toe of the slope. To avoid water level change during the test, water was poured into the box so that the clay ground in the box was fully submerged during the flight. The clay slopes thus prepared were brought to a high acceleration field until a slope failure took place. During the flight, the displacements at the crest and the toe of the slope were measured to detect the slope failure. Photographs were also taken during the flight to obtain the ground deformation in detail.

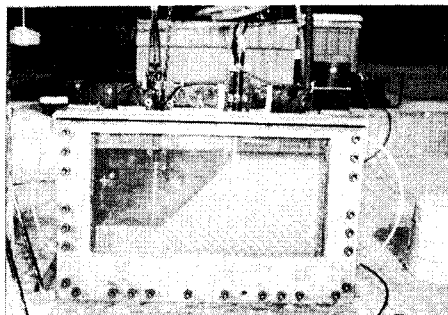


Fig. 3. Model Ground

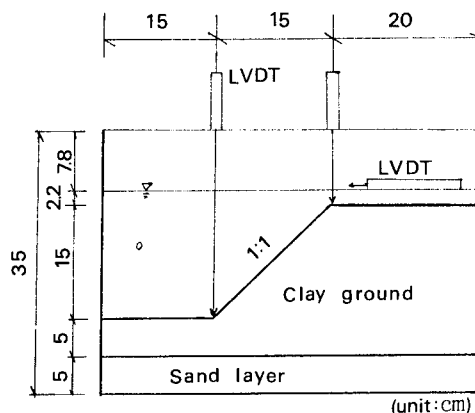


Fig. 4. Setup of the model slope

### 3. THE STRESS-STRAIN CHARACTERISTICS OF THE CLAY

Unconfined compression tests were conducted on the clay cakes removed from the slope. The stress-strain curves for the R-clay and the H-clay are plotted together in Fig. 5. Because the consolidation pressure were different in each test case, the axial stress in the vertical axis is normalized with respect to the consolidation pressure,  $p_c$ .

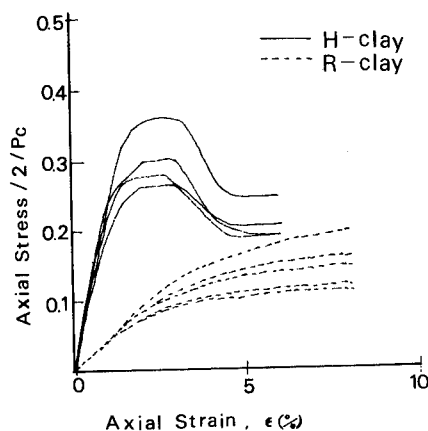


Fig. 5. The stress-strain curves

The axial stress for the R-clay gradually increases with the increase of the axial strain and no clear peak is observed. For the H-clay, on the other hand, the axial stress rapidly increases with the axial strain and shows a clear peak at around the axial strain of 2 - 3%. After reaching the peak strength, the stress decreases rapidly and keeps almost a constant value for the further axial strain.

In the H-clay specimens after the unconfined compression test, the clear slip line is observed but not in the R-clay. It is found from the compression tests that the R-clay shows ductile stress - strain characteristics while the H-clay manufactured by the consolidation at a high temperature shows brittle characteristics.

Figure 6 shows the relationship between the consolidation pressure,  $p_c$  and the undrained shear strength,  $C_u$ . The shear strength of both clays increases linearly with the increase of the consolidation pressure. That shows the strength of the H-clay is  $0.09 \text{ kgf/cm}^2$  larger than that of the R-clay regardless the consolidation pressure,  $p_c$ . This increment of the shear strength might be caused by the cementation effect between the clay particles accelerated at a high temperature.

It is also found in Fig. 5 that the post peak strength of the H-clay is nearly equal to or slightly higher than that of the R-clay samples, which shows the cementation effect disappears after large deformation.

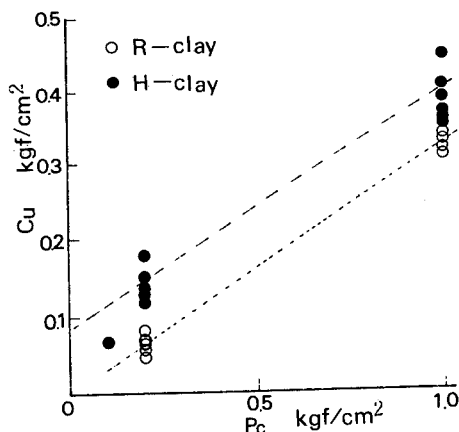


Fig. 6.  $C_u$  and  $P_c$  relation

### 4. TEST RESULTS

Total of 5 tests were carried out changing the shear strength of the clay slope and the surcharge pressure on the top of the slope, as shown in Table 2. In the table, undrained shear strength,  $C_u$  indicates a peak value obtained by the unconfined compression tests. And terms R and H represents the R-clay and the H-clay respectively. In this present paper, two tests without surcharge ( Case 2 and 7 ) will be discussed.

Table 2. Test Cases

Case		slope Height (cm)	$C_u$ (kgf/cm <sup>2</sup> )	surcharge (g/cm <sup>2</sup> )	g at failure
2	R	15	0.057	0	62.6
3	R	15	0.072	0	75.1
5	H	15	0.132	.0038	70.0
6	R	15	0.046	.0038	41.0
7	H	15	0.068	0	70.0

R: remolded clay

H: aged clay

#### 4.1 Acceleration at failure

The displacements at the various points of the slope were measured during the increase of the centrifugal acceleration. The relationships between the displacements and the centrifugal acceleration are plotted in Fig. 7. In the figure, the vertical axis shows the normalized displacement,  $\delta/h$  where  $\delta$  and  $h$  are displacement and the slope height respectively. Because the shear strength of the clay slopes are different in each test, the horizontal axis also shows the normalized value,  $\alpha = \gamma'nh/C_u$  in which  $\gamma'$ ,  $n$ , and  $C_u$  are submerged unit weight of the clay,

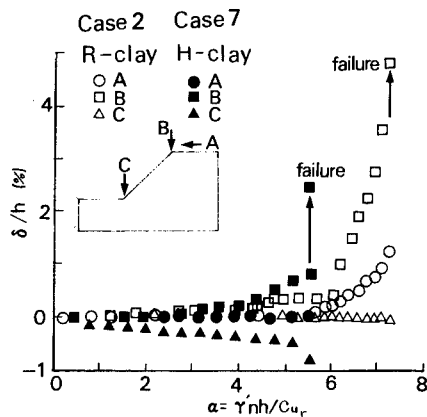


Fig. 7. Displacements - Acceleration

centrifugal gravity and residual undrained strength of the clay, respectively. In case 2 of the R-clay slope, the settlement at the crest of the slope (B) gradually increases with the increase of  $\alpha$ . When  $\alpha$  becomes larger than 6, relatively large settlement takes place very rapidly. An entire failure of the slope takes place when the normalized acceleration,  $\alpha$  exceeded 7. For the H-clay slope, on the other hand, the settlement at the crest of the slope gradually increases with the increase of  $\alpha$ . An entire slope failure suddenly takes place at  $\alpha = 5.5$  and the settlement of the crest at failure is 1% of  $\delta/h$ , which is much smaller than that of the R-clay slope.

#### 4.2 Vertical Settlement at Failure

Figure 8 shows the relationship between the vertical displacement at the crest of the slope,  $\delta/h$  and horizontal distance of the slip line at the top of slope,  $B/h$  at failure. All test results listed in Table 2 are plotted in the figure. The figure shows that failures of the H-clay slope takes place at  $\delta/h$  of 1 – 2%. But in the R-clay slope values of  $\delta/h$  at failure is 5 – 7%, which means a relatively large deformation is necessary to mobilize the shear strength along the slip surface in the R-clay slope. This phenomenon is caused by the difference in the stress – strain characteristics already shown in Fig. 5.

It is also found that the horizontal distance,  $B/h$  for the H-clay is larger than that of the R-clay. It can be concluded from this figure that both the failure mode and the magnitude of deformation are dependent upon the stress – strain characteristics.

#### 4.3 Deformation of the Slope

The failure patterns obtained from the displacements of soumen noodles after the test are shown in Fig. 9. The noodles originally placed in parallel as straight lines were bent and cut at the slip circle. It

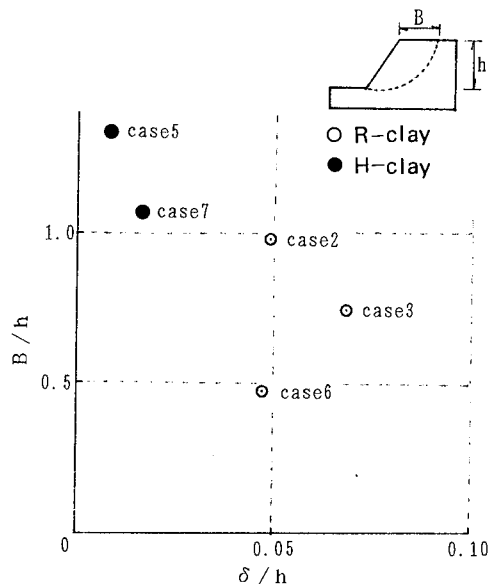


Fig. 8.  $\delta/h$  -  $B/h$  at failure

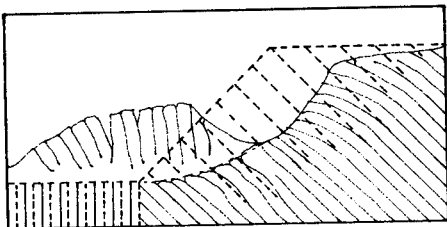
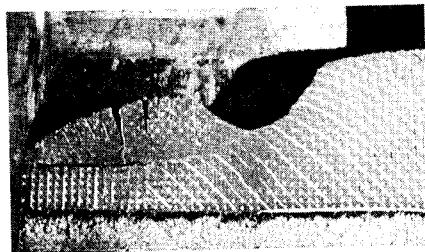
can be seen that the clear slip failure takes place in the both cases. But in the R-clay slope, the soumen markers were bent at around the slip line as shown in Fig. 9 (a). This means the shear zone in the R-clay was wide. This phenomenon may be caused due to the ductile characteristics where the larger strength can be mobilized at the larger strain.

However in the H-clay slope as shown in Fig. 9 (b), the soumen markers were clearly cut at the slip line and negligible bending of the markers could be observed at around the slip line. The H-clay has a brittle characteristics, which characterized the clear peak strength and the following rapid decrease in strength. Therefore the large deformation concentrates within the narrow zone and causes the sharp slip line.

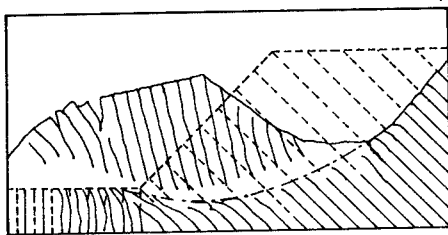
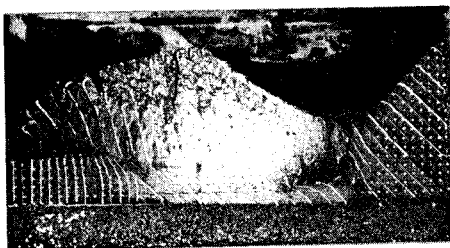
On the front face of the ground, visual target markers were also placed at the grid pattern with about 1 cm spacing. Shear strains developed in the ground were calculated from the displacement of the markers considering one square grid of markers as an isoparametric element. The maximum shear strain developed in the ground was calculated and its progresses are shown in Fig. 10 and 11. In the figure,  $F_s$  corresponds to the safety factor against failure which is defined as a ratio of acceleration at failure to current acceleration.

In case 7 of the R-clay, it can be seen in Fig. 10 that with decrease of the  $F_s$ , the region of the large strain extends around the toe of the slope and its magnitude also increases. At the stage close to the failure (Fig. 10 (d)), large shear strain develops widely in the slope.

In the H-clay slope shown in Fig. 11, shear strain developed is smaller than that of the R-clay. The magnitude and extent of the shear strain slightly



(a) R-clay slope  
Fig. 9. Deformation of slope



(b) H-clay slope  
Fig. 9. Deformation of slope

increases with the decrease of the  $F_s$ , but the magnitude remains small even just before the failure as shown in Fig. 11 (d). It can be seen that the failure pattern of the slope is much affected by the stress - strain characteristics.

## 5. CONCLUSIONS

A description of centrifuge model testing on slope failure has been presented, and the effects of stress

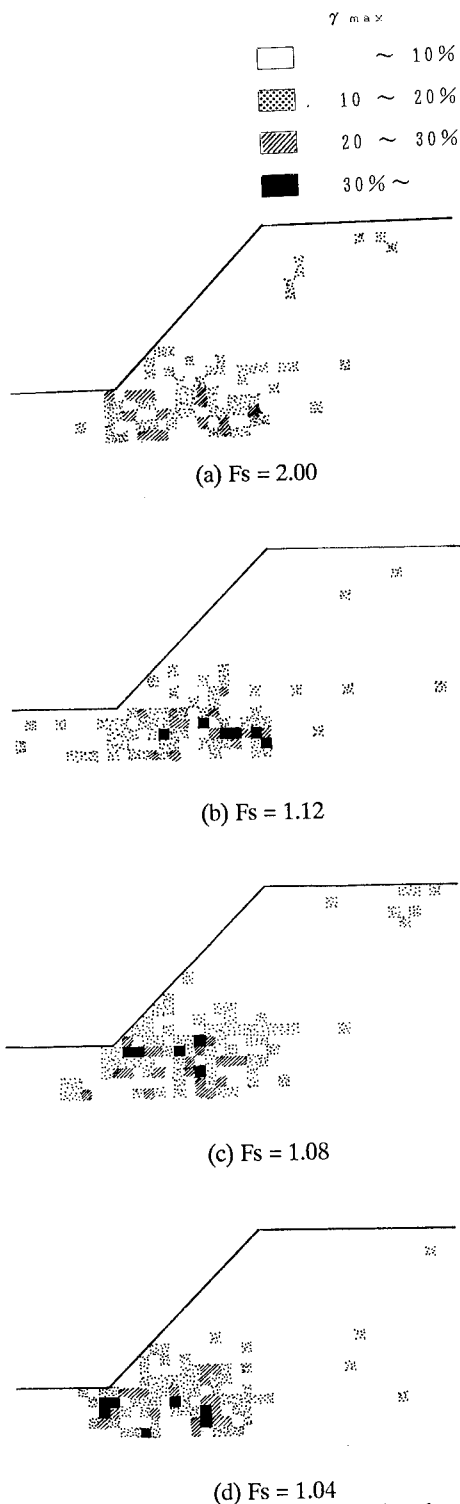
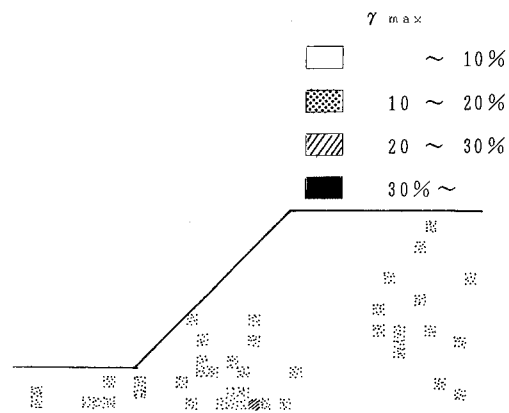


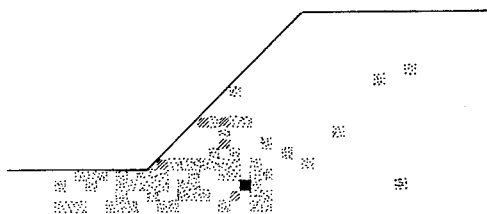
Fig. 10. Shear strain in the R-clay slope



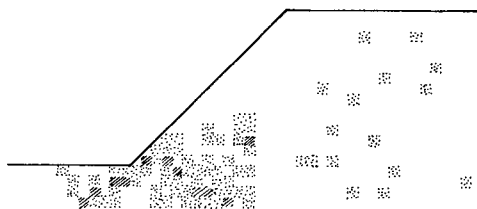
(a)  $F_s = 2.28$



(b)  $F_s = 1.16$



(c)  $F_s = 1.07$



(d)  $F_s = 1.02$

Fig. 11. Shear strain in the H-clay slope

– strain characteristics of the clay on slope failure has been discussed. The conclusions obtained in this study are summarized as follows;

1. The reconsolidated clay, prepared at a room temperature showed ductile stress–strain characteristics. The clay consolidated at a high temperature showed brittle behavior which was characterized by a clear peak strength and the following rapid decrease of shearing resistance.

2. The R-clay slope showed a slope failure after relatively large deformation, while the H-clay slope showed a sudden failure at small deformations.

3. The failure mode and deformation of the slope were much affected by the stress – strain characteristics of the clay.

#### REFERENCE

Terashi, M.: "Development of PHRI Geotechnical Centrifuge and its Application", Report of the Port and Harbour Research Institute, Vol.24, No.3, pp. 73–122, 1985

Tsuchida, T., Kobayashi, M. and Mizukami, J. : "Effect of Aging of Marine Clay and its Duplication by High Temperature Consolidation", Soils and Foundations, Vol.31, No.4, pp. 133–147, Dec. 1991.

## Bearing capacity of a foundation on protected slopes

M. Terashi, K. Saitoh & N. Katakami

*Nikken Sekkei Nakase Geotechnical Institute, Kawasaki, Japan*

Y. Yamamoto

*Central Japan Railway Company, Tokyo, Japan*

Y. Taniguchi

*Railway Technical Institute, Tokyo, Japan*

**ABSTRACT:** Slope instabilities are occasionally found along the railway embankments in Japan. A new slope protection measure called COLUMN PROTECTION is proposed by the Central Japan Railway Corporation. In the paper the effect of the new slope protection measure was compared with the current technique by a series of centrifuge model tests.

### 1 INTRODUCTION

Slope instabilities are occasionally found along the railway embankments in Japan. The detailed investigation of the recorded instabilities of unprotected embankment slopes has revealed that most of the failures took place in the embankments with sandy materials, that the slip surfaces appeared at the relatively shallow depths, and that the failures were associated with heavy rains.

The extent of a slope failure has been limited in scale and no substantial problem has been reported. However, to minimize the maintenance works, slope protection measures have been undertaken. Because these embankments are under operation, the protection should be constructed without interrupting the railway operation.

The most common protection has been the placement of thin concrete plates on the slope with the aim of reducing the water permeation into the slopes. To keep the concrete plates in position, concrete grid with shallow steel piles was adopted. Hereafter in this paper, this system is called PGP system. No failure records have been reported on PGP-protected slopes. The mechanism of this improved stability is considered firstly to be the time delay of the water table rise due to heavy rain. Less important but also probable is the reinforcement effect by the concrete grid, plates and piles. The latter effect, however, has not been quantified and ignored in the stability analysis.

Recently an alternative slope protection measure called COLUMN PROTECTION is proposed which is a combination of the

flexible surface cover and treated soil columns. The surface cover is intended to reduce the water permeation into the slopes. The treated soil columns are aimed to keep the surface cover in place and to reinforce the slope as well. Hereafter in this paper, this system is called CLM system. The CLM system is said to reduce the cost of PGP system by 20 to 35 %.

In the present study, the emphasis is placed on the investigation and comparison of the reinforcement effects of both systems; PGP and CLM. A series of centrifuge model tests was conducted to determine the bearing capacity of a foundation on top of the slope which creates a shallow failure plane in the slope. The influence of water infiltration and change of the ground water level are studied separately by Railway Technical Research Institute and will be reported elsewhere.

### 2 DETAILS OF SLOE PROTECTION SYSTEMS

In the construction of PGP system, the H-shaped steel piles are driven and the reinforced concrete grid is placed and connected to the driven piles. Then the concrete plates are placed in the openings of the grid. The typical layout and dimension of the PGP system in the cross section is shown schematically in Fig. 1. Towards the longitudinal direction, these piles are installed in each 4 m distance. The flexural rigidity of a pile in the slope direction,  $EI$  is  $2.1 \text{ MN m}^2$ . The contact pressures of the concrete plates and concrete grid are 2.45 kPa and 9.8 kPa respectively.

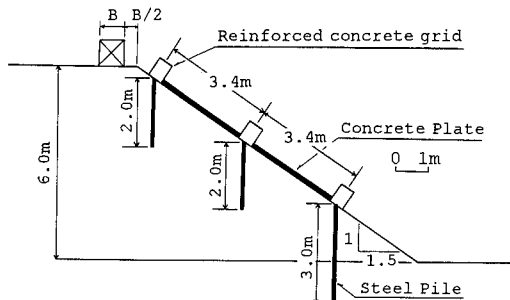


Fig. 1 PGP system of slope protection

As the land cost is extraordinarily high in the urban area of Japan, there are strong needs to create a space by reducing the width of existing railway embankment. This would be realized by cutting and steepening the existing slope to vertical. CLM system was originally developed to reinforce the vertical cut wall. In the case of ordinary earth anchor, anchor length should be long enough to get the sufficient skin friction along the anchor length. The COLUMN is a combination of core and surrounding treated soil. As the apparent surface of anchor is increased by increasing the diameter of treated soil column and thus the merit of the system is said that the sufficient skin friction could be obtained with shorter anchor length.

Fig. 2 shows the procedure to manufacture the COLUMN. A core material of the COLUMN is either a deformed steel bar or a FRP (fiber reinforced plastic) rod. Before the execution, the core is installed in a hollow space of mixing shaft. The shaft has cutting blades and mixing blades at its tip as shown in the figure. The blades are rotated and the machine is inserted to a prescribed depth. While withdrawing the machine, the core is left in place and the

cement milk is injected. Thus the space in the immediate vicinity of the core material is filled with cement milk and the surrounding soil is mixed and treated with cement. In the end, the core is tightened to the facing block which will be shown schematically in Fig. 3.

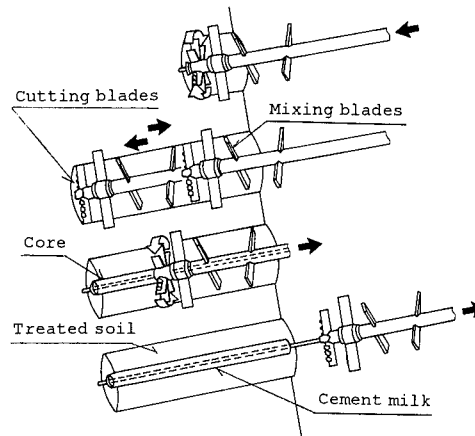


Fig. 2 Execution procedure of the COLUMN

The proposed layout for the slope protection of the CLM system in the cross section and that in the longitudinal direction are shown in Fig. 3. The expected tensile rigidity, EA of the core material is from 0.17 MN to 5.8 MN. The expected diameter of the COLUMN is 40 cm and the expected unconfined compressive strength of the treated soil is in the order of 1 MPa. Fig. 4 shows the experimental set-up of the proposed slope protection by the COLUMN and the surface cover.

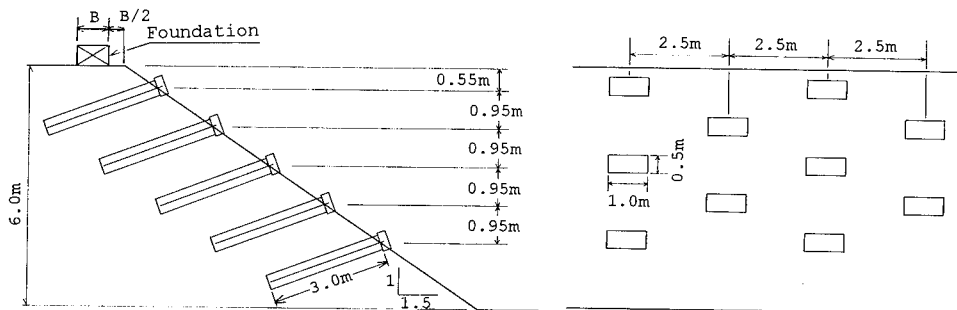


Fig. 3 CLM system for slope protection





Fig. 4 CLM system in full-scale set up

### 3 MODEL TEST CONDITIONS

The typical size of the existing railway embankment is six meters high and the slope is 1 vertical to 1.5 horizontal as shown in Fig. 1 and 3. This prototype earth structure was reduced in scale by 1/40, prepared in the strong specimen box which has inside dimensions of 60 cm deep, 20 cm wide and 75 cm long as shown in Fig. 5. All the model tests were conducted in the plane strain condition under the high acceleration of 40 g. One side of the strong box is made of glass to allow the photographic measurement by 35 mm data camera and real time observation by television system.

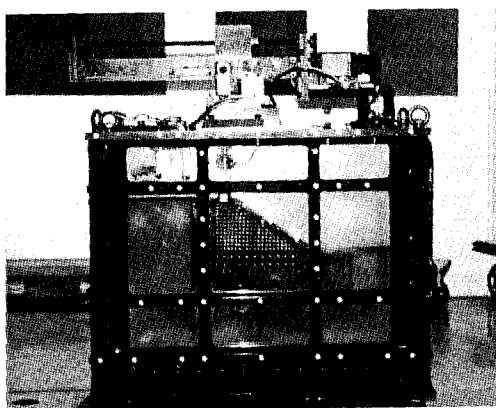


Fig. 5 Strong Box and a model slope

The material used for the embankment was Toyoura Standard Sand which is a fine uniform sand having uniformity coefficient,  $C_u$  of 1.38, the effective grain size,  $D_{10}$  of 0.13 mm and the density of soil particles,  $\rho_s = 2.66 \text{ g/cm}^3$ . The sand was used because of its well known characteristics and relative ease in preparing model embankment of desired density.

The model ground was prepared at the laboratory floor by means of multiple sieve method of sand raining. To reduce the friction, both the front and the rear walls of the specimen box were treated by silicone oil film and rubber membrane. As shown in Fig. 5, target markers were printed on the rubber membrane for the photographic instrumentation. The dry density,  $\rho_d$  of the ground was controlled to  $1.63 \text{ g/cm}^3$  where  $\rho_{d, \text{max}} = 1.64$  and  $\rho_{d, \text{min}} = 1.33 \text{ g/cm}^3$ . The average density of the model ground and its uniformity was determined in advance by a series of preliminary experiments and confirmed for each test by weighing the total weight.

Slope protections by PGP system and CLM system were modeled by the following manner. The model grid was manufactured by plastic resin and the model concrete plates were represented by the lead shot. By this, the contact pressures of the reinforced concrete grid and concrete plates were modeled correctly. Less importance was placed in the simulation of the flexural rigidity of these materials which was in the safe side in modelling the prototype. Model pile was made of steel and the flexural rigidity was simulated correctly but the cross section was not H-shaped but rectangle. In the case of the CLM system, the prototype tensile rigidity of the core material has a certain range as described before. The selected core material was FRP rod with nominal diameter of 3 mm and its tensile rigidity is 208 kN. The treated soil column with an outer diameter of 1 cm is simulated by cement mortar with the same unconfined compressive strength. Fig. 6 shows the model grid and concrete plates. Fig. 7 shows the model FRP rod and one of the prototype scale FRP rod. Fig. 8 shows the modelled COLUMN with 1 cm diameter and its core.

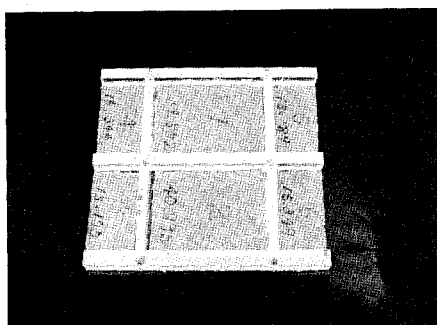


Fig. 6 Model grid and concrete plate

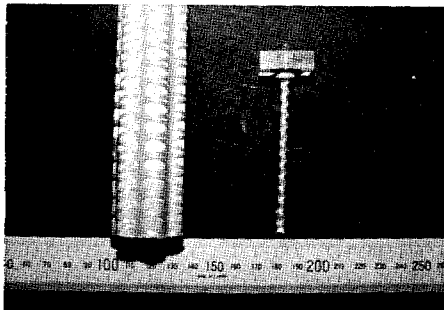


Fig. 7 Model and Prototype FRP rod

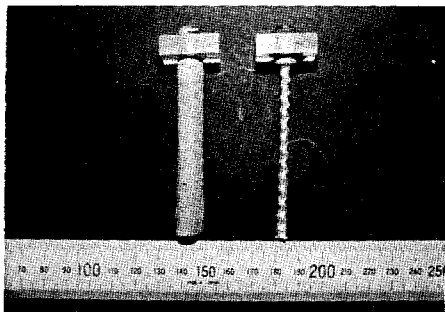


Fig. 8 Modelled COLUMN and its core

In the preparation of unprotected slope, the sand was rainfall to the sufficient thickness. Then the slope was created by sucking sand particles by vacuum pump. In the case of PGP protected slope, model piles are pushed into the completed model slope statically and then model concrete grid and plates are placed on the slope. In the case of CLM protected slope, sand raining was conducted in stages and in each stage sand particles were sucked and model COLUMN was placed.

A foundation made of aluminum with high rigidity was used for the bearing capacity tests. The width,  $B$  of the foundation was 2 cm wide and 20 cm long. The bottom of the foundation was glued with the same sand to represent the rough base condition. The foundation was placed on top of the slope at a distance  $W = 0.5 B$  from the crest at 1 g laboratory floor. The vertical and horizontal loads were applied to the foundation after the model was brought into 40 g field, depending on the test conditions which will be described later.

The bearing capacity tests were conducted under the vertical load and under the combination of vertical and horizontal loads. The vertical load component was applied to the foundation through a set of

bearings which enabled the free rotation and free horizontal movement of the foundation. The horizontal load component was applied by a straight edge to one side of the foundation close to the foundation bottom. The vertical load was given by stress-control and the horizontal load component was given by strain-control. Both loading systems can be seen in Fig. 5.

To execute a series of model test, NNGI geotechnical centrifuge which is Acutronic Model 665 (Fig. 9) was used. The radius of the centrifuge is 2.7 m measured to the surface of swing platform. The maximum payload is 1 ton at 100 g and 0.5 ton at 200 g, thus the maximum capacity of the centrifuge is 100 g-tons.

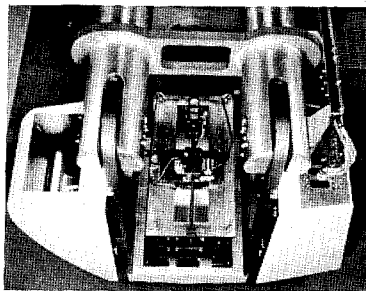


Fig. 9 NNGI geotechnical centrifuge

#### 4 BEARING CAPACITY TEST RESULTS

Bearing capacity tests were conducted in five series. Series I was for the unprotected slopes. Series II to IV were for the PGP-protected slopes in which the slopes of Series II were reinforced by piles only, slopes of Series III were reinforced by the grid and concrete plates only, and slopes of Series IV were reinforced by a full PGP system. Series V was for the slopes protected by the CLM system. In the tests for the CLM system, the influence of the surface cover was ignored.

When a foundation is subjected to an arbitrary combination of vertical load,  $V$ , horizontal load,  $H$  and moment,  $M$ , components, the failure envelope is created in the  $V$ - $H$ - $M$  space by a cigar shape as shown in Fig. 10 (Terashi, and Kitazume, 1987). It is convenient to create this sort of envelope in  $V$ - $H$  plane to understand the difference of the reinforcement effect of different protection measures. In each test series, therefore, the bearing capacity under vertical load and that under the inclined load were investigated. The vertical bearing capacity of the slopes was investigated in advance and the inclined loading test was conducted by increasing

the horizontal load component under the constant vertical pressures which were varied from two thirds to one half of the vertical bearing capacity.

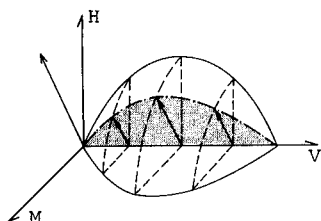


Fig. 10 Failure envelope in V-H-M space

All the test conditions and the test results are summarized in Table 1 where  $V/A$  and  $H/A$  represent the vertical load component and horizontal load component per unit area at the failure of slopes.  $N_r$  is the bearing capacity factor for the vertical load component.  $k_v$  and  $k_h$  are the initial tangent of the load-displacement curve for vertical loading and horizontal loading respectively.

#### 4.1 Vertical bearing capacity

Vertical load and vertical displacement relations for all the vertical bearing capacity test results are shown in Fig. 11. The solid curve in the figure shows the test results of unprotected slope. The reinforcement with the grid and concrete plate leads to the increase of bearing capacity by around 20 % in comparison with unprotected slope. As is expected, the vertical piles installed in the slope give

no substantial influence on the ultimate bearing capacity. CLM system further increases the bearing capacity by 30 %. The scatter of the test results for the same condition is considered to be caused by the disturbance of sand due to the installation of protections.

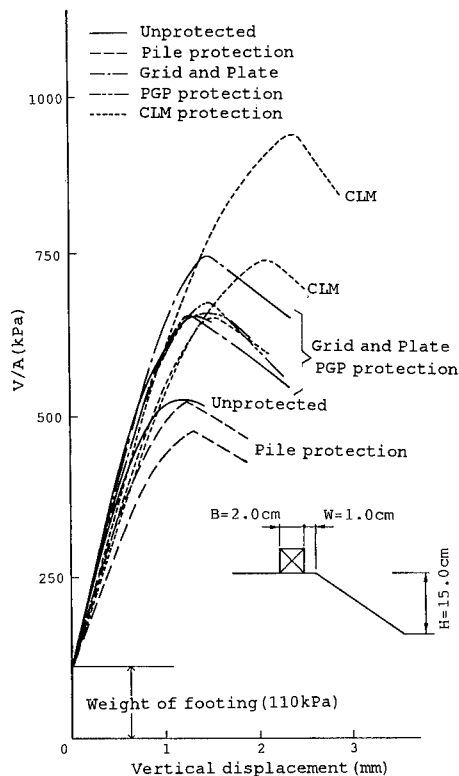


Fig. 11 Vertical bearing capacity test

Table 1 Test cases and test results.

		$N_r$	$V/A$ (kPa)	$H/A$ (kPa)	$k_v$ (MPa)	$k_h$ (MPa)
Series I	Unprotected	87.17	554.2	0.0	19.9	-
		107.71	684.8	0.0	21.0	-
		51.79	329.3	74.2	21.2	3.2
		68.25	433.9	35.0	18.9	2.8
		59.69	379.5	48.0	14.6	2.9
Series II	Pile protection	79.15	503.2	0.0	13.9	-
		86.01	546.8	0.0	15.4	-
		51.83	329.5	32.1	24.6	1.9
		51.75	329.0	69.3	22.5	1.7
		52.64	334.7	51.0	18.0	2.1
Series III	Grid and Plate	107.32	682.3	0.0	20.3	-
		122.04	775.9	0.0	20.3	-
		72.1	458.4	104.9	22.4	2.6
		64.78	411.8	88.2	22.3	2.7
		59.38	377.5	73.0	20.8	3.3
Series IV	PGP protection	108.4	689.2	0.0	21.2	-
		110.48	702.4	0.0	21.6	-
		55.99	356.0	55.9	19.0	3.9
		54.68	347.7	80.4	19.6	4.2
		54.45	346.2	77.2	18.1	2.5
Series V	CLM protection	147.79	939.6	0.0	18.2	-
		107.28	682.1	0.0	17.3	-
		97.54	620.1	120.5	22.4	34.7
		120.97	769.1	0.0	16.8	-
		67.48	429.0	78.6	24.2	3.0

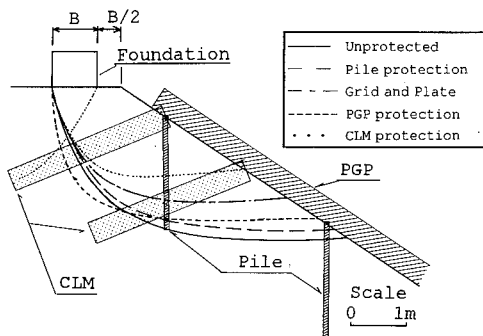


Fig. 12 Slip surface obtained from vertical loading.

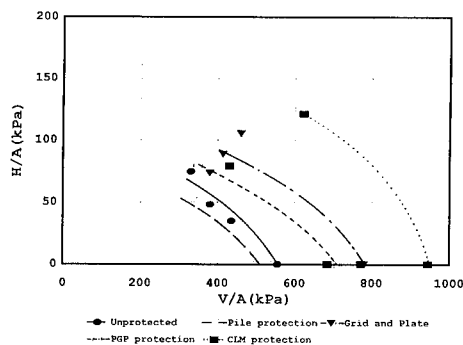


Fig. 13 Comparison of reinforcement effect in V-H plane

Fig. 12 shows the slip surface detected by the displacement of the target markers. The effective reinforcement resulted in the change in the shape and the position of slip surface. This tendency in the change of slip surface is similar to those obtained for the geotextile reinforcement (Tatsuoka, 1992).

#### 4.2 Inclined load test

The vertical load component is plotted against the horizontal load component for each bearing capacity test in Fig. 13. This is a part of the failure envelope in V-H space as explained earlier.

There is no appreciable difference between the bearing capacities of the unprotected slopes (Series I) and the slope with vertical piles only (Series II). The reinforcement by concrete plate and grid (Series III) expands the failure envelope in V-H plane. In addition to the slope protection of Series III, vertical piles

are added in Series IV. There is again no appreciable difference between Series III and Series IV. The reinforcement by CLM system further expands the failure envelope as shown in Fig. 13.

#### 5 CONCLUDING REMARKS

The slope protection system currently applied and a newly proposed system are explained in some detail. A new system is said to be cost saving and easier to construct. The reinforcement effects of both systems are compared by a series of centrifuge model test.

Although the estimated cost of the CLM system is 65 to 80 % of the PGP system, the reinforcement effect is much higher in CLM system.

Investigations of the failure records of unprotected slopes and a series of large scale model tests are conducted in parallel with the present study by the Central Japan Railway Corporation and Railway Technical Research Institute. The details of these parallel studies will be reported elsewhere by Kojima et al.(1994), Taniguchi et al.(1994), and Yamamoto et al.(1994).

#### REFERENCES

- Kojima, K. et al: Model tests for embankment slope protections, Proc. 29th Japan National Conf. on SMFE, June 1994
- Taniguchi, Y. et al: Model tests of reinforced slopes in bar in a centrifuge, Proc. 29th Japan National Conf on SMFE, June 1994
- Terashi, M. and Kitazume, M.: Bearing capacity of a foundation on top of high mound subjected to eccentric and inclined load, Report of Port and Harbour Research Institute, Vol. 26-2, 1987
- Tatsuoka, F.: Permanent cut of an embankment slope by soil nailing allowing very small deformation, Earth Reinforcement Practice, Proc. of IS Kyushuu, 1992
- Yamamoto, Y. et al: A consideration on estimation of slope-protects, Proc. 29th Japan National Conf. on SMFE, June 1994

## Geotextile reinforced cohesive slopes on weak foundations

Ali Porbaha & Deborah J. Goodings  
*University of Maryland, College Park, Md., USA*

**ABSTRACT:** Centrifuge model tests were performed to study the behavior of geotextile reinforced cohesive backfill retaining structures on weak foundations using 152 mm high models. Lengths and configurations of the reinforcements were changed to examine the failure mechanisms of the models. Excessive deformations amounting to failure were accompanied by geotextile rupture or strain, but never by pullout. Longer reinforcement improved model performance but slope angle was the more influential parameter in these models. The beneficial effects of variable length reinforcement were greater in the flattest slopes,  $\beta=45$  degrees.

### 1 INTRODUCTION

Substantial cost savings can be achieved if reinforced soil retaining walls are constructed with on-site marginal soils as backfill, rather than requiring import of granular soils. Research in centrifuge models of geotextile reinforced vertical retaining walls with cohesive backfill, performed by Alvarez (1988) and Suah (1989), and summarized by Goodings (1989), showed that such walls can be stable to heights of up to 26 m, depending on reinforcement geometry, type, and soil properties, when founded on rigid bases. Those researchers determined that deformations occurring in the bottom-most reinforced layers of soil were very important to the behavior of the upper layers of the walls. Their observations led the authors to study the effects on stability, first, when walls are inclined, and second, when they are founded on a thin weak foundation layer.

### 2 EXPERIMENTAL METHOD

The development of this work springs from.

and is parallel to, that of various other researchers using the centrifuge to model reinforced soil structures. (see, for example, Bolton et. al., 1978, 1982; Taniguchi et. al., 1988; and Mitchell et. al., 1988). In this study, the University of Maryland centrifuge used is a 2.7 m diameter Genisco model 1230-1 G-accelerator with a capacity of 15 g-ton.

For similarity between centrifuge models at  $N$  times earth's gravity, and the full-scale prototypes, the model geotextile simulant must have strength  $1/N$  times that in the prototype, when measured in units of force per unit length. In these models Pellon tru-grid, was used as the geotextile simulant. This fabric is manufactured by Pellon Co. as an interfacing material with a thickness of 0.0006 mm. It is non-woven and made of 40% rayon and 60% polyester. The peak tensile strength of this material is 0.18 kN/m at 20% strain, measured following the ASTM D4595 standard. This is almost one quarter of the strength of the fabric described by Goodings (1989).

The soil used as the backfill, the retained fill, and the foundation, in all models was Hydrite Kaolin type "R" processed by Dry Branch

Kaolin Company in New Jersey, USA. The liquid limit is 50% and the plastic limit 33%. The maximum dry unit weight in a standard Proctor test is  $14.2 \text{ kN/m}^3$  at an optimum moisture content of 29%. To produce a weak soil for these models the kaolin was mixed at a water content of 35% and then compressed slowly over a period of 5 minutes to a maximum vertical stress of  $175 \text{ kN/m}^2$ . When that stress was reached the load was immediately removed. This produced a layer of soil 19mm in thickness with dry unit weight of  $12.3 \text{ kN/m}^3$ . The inside vertical side boundaries of the rigid aluminum containers (400mm by 300mm by 300mm deep) were sprayed with silicon, and overlain with a thin plastic film to reduce boundary friction, following Santamarina(1984). This reduces, but does not eliminate, side boundary friction.

After foundation preparation, a block was laid on the foundation to provide a lateral support during model wall construction. The first layer of reinforcement was then placed on the remaining exposed portion of the foundation, a layer of soil placed, in turn, on it, and the geotextile folded back into the soil to provide a flexible facing for the slope. The length of the geotextile overlap, stretching back into the wall was 32 mm in all models. The compression stress was then applied. This process was repeated for eight successive layers until the model wall was 152 mm high on a 19mm thick foundation. For steep slopes, lateral supports were of increasing area as the wall became higher, giving the models a stepped profile (Figure 1). The lateral support blocks were then removed. The top and exposed side of the model were sprayed with paint to highlight the development of tension cracks in the white clay. The model was then mounted on the centrifuge.

Each test involved loading a model by increasing gradually the centrifugal acceleration until either model failure occurred or the maximum permissible load on the centrifuge arm was reached. After a test, the model was disassembled to examine the deformations of the reinforcements at different elevations. The coordinates of the failure surface were recorded

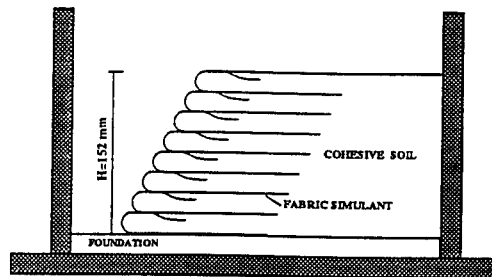


Figure 1: Profile of a typical geotextile reinforced model.

using a profilometer, measuring the vertical profile at 10 mm horizontal intervals through various model cross-sections. Direct shear tests were performed on specimens retrieved at various depths in the unfailed rear portion of the model after failure. The straight line Mohr-Coulomb total stress strength parameters were  $\phi=21$  degrees, and  $c=19.4 \text{ kN/m}^2$ . Other samples were taken to measure moisture content.

This paper describes seven models built on weak foundations, although it is but a small part of a larger study. All models had eight layers of the same reinforcement material, but slope angle and reinforcement length were varied. The geometric configurations and other testing data of those seven models are provided in Table 1. Descriptions of the behaviors of individual models are outlined in Porbaha (1994).

### 3 RESULTS OF MODEL TESTS

All seven models with weak foundations, with the exception of model M-9 with variable reinforcement length, failed due to a combined mechanism of sliding and base failure which once begun, progressed steadily and gradually as acceleration was increased. In each wall or slope, the bottom layer of reinforced soil directly above the foundation layer underwent differential compression, meaning that the portion of the soil layer closest to the face of the slope or the wall compressed most, and compression decreased with

Table 1. Geometrical configuration of tested models.

Model No.	Slope Angle (degree)	L (mm)	L/H Ratio	H <sub>p1</sub> (m)
M-8	90	178	1.17	7.3
M-5	90	102	0.66	5.8
M-10	80.5 (1H:6V)	VARIABLE	0.66-1.27	4.8
M-7	80.5 (1H:6V)	102	0.66	4.4
M-4	71.6 (1H:3V)	76	0.50	9.9
M-9	45 (1H:1V)	VARIABLE	0.66-1.27	10.0
M-6	45 (1H:1V)	102	0.66	11.4

L= Length of model reinforcement (mm)

L/H= Length of model reinforcement as a multiple of model height

H<sub>p1</sub>= Prototype equivalent height at tension crack (m)

increasing distance from the face of the wall. The consequence of this differential compression was that the upper reinforced layers then had an uneven base, thereby causing the walls and steep slopes to tilt forward significantly, well before failure occurred. This differential compression and tilting forward was observed also by Alvarez (1988) and Suah (1989) in their models of vertical reinforced cohesive soil walls on rigid foundations. In the models of this study, the presence of a thin, weak, equally soft, and unreinforced clay foundation aggravated the differential compression of the base of the walls and the slopes. Other cracks also developed, sometimes well before failure and to an owner these cracks may be unacceptable. Certainly cracks can lead to local straining in the geotextile which may creep to failure even at a fixed stress level. Creep behavior was not examined in these tests. There was, finally, a bearing capacity failure by squeezing of the thin foundation layer beneath the reinforced zone of soil.

In spite of these similarities there were pronounced differences in performance of models with different lengths of reinforcement. When reinforcement was long, as it was in the vertical model wall of M-8 with length: height ratio (L/H) of 1.17, failure activity was contained entirely within the reinforced zone. The continuous vertical line in Figure 2 shows

the extent of the reinforcement. The first tension crack of the model started when the stress equivalent height was 7.3 m, and in this model alone failure occurred clearly and catastrophically at a stress equivalent height of 11.5 m. Clear-cut rupture occurred in the top five layers and severe strain in the bottom three layers of reinforcement. There was some squeezing in the thin foundation, but the contribution of reinforcement to improvement in wall stability was clear and substantial. There was no evidence of pullout failure.

When reinforcement length was shorter, in these models with L/H less than or equal to 0.66, the model failure began behind the reinforced zone (external failure), or, in some cases, was a combination of external and internal failure, depending on slope angle. But the stress equivalent point at which "failure" occurred was often unclear, since "failure" involved either a marked but steady flattening of the original slope angle as acceleration was increased (the case for most of the slopes), or a steady and progressive slumping in the case of steep profiles. Geotextiles were often strained locally but did not rupture. Certainly there was still no pullout failure. This behavior had two implications: first, it was not possible to pinpoint failure, even though the owner of such a slope would identify the after-test configuration as a failure, which is also the case in the field; and second, at full scale the flattening or slumping is likely to occur during the construction process.

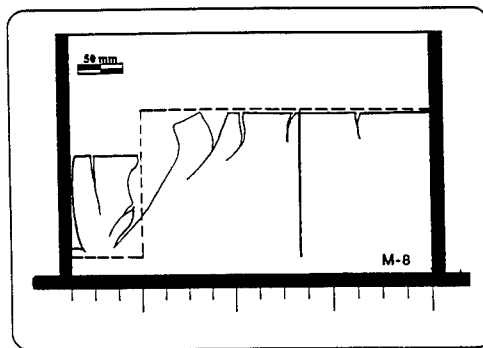


Figure 2: Profile of model M-8 after the centrifuge test. (Maximum acceleration = 76 g)

For vertical wall model M-5, with  $L/H=0.66$ , the first tension crack developed when the stress equivalent height was 5.8 m or 20% less than for M-8, the vertical model with  $L/H=1.17$ . The positions of the cracks were similar, but greater reinforcement length had added to resistance to the opening of cracks in M-8. Wall slumping continued with increased acceleration to a stress equivalent height of 16.6 m. The after-test profile is shown in Figure 3, and it is similar in shape to model M-8. The shorter reinforcement had led to development of additional external retrogressive failure surfaces.

For model M-7, with a steep slope of 80.5 degrees and  $L/H=0.66$ , the first tension crack developed when the stress equivalent height was 4.4 m, less than for the 90 degree model M-5, also with  $L/H=0.66$ . The experiment was continued to a maximum stress equivalent height of 21.3 m, and the final shape of the gradually deforming model is shown in Fig. 4.

Model M-4, with a somewhat flatter slope angle of 71.6 degrees and  $L/H=0.50$ , underwent slow external failure with a single and clear-cut rotational slip failure well behind the reinforcement at a stress equivalent height of 9.9 m. This model with shorter reinforcement and a flatter slope was more stable, and would have a lower construction cost than a steeper model with longer reinforcement. There was no rupture of the reinforcement. The first tension crack opened at failure. The post failure profile is shown in Figure 5.

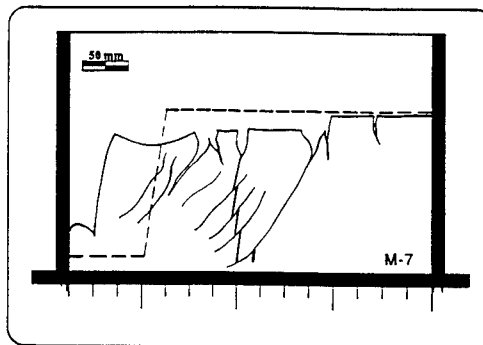


Figure 4: Profile of model M-7 after the centrifuge test. (Maximum acceleration = 140g)

Model M-6, with a slope angle of 45 degrees and  $L/H=0.66$ , began to show cracks behind the reinforcement at a stress equivalent height of 11.4 m, the largest value for any slope or wall in the study. At the end of the test (stress equivalent to a slope height of 22.8m), the crest of the slope was lower by 16.7% compared to the original slope height and the slope had become more stable at its final inclination of 35 degrees. The slip surface was entirely behind the reinforced section and there was no rupture of reinforcement. The final profile is shown in Figure 6.

The effect of variable length reinforcement with depth was investigated for one steep and one flat slope, and the results compared with models having constant length reinforcement at

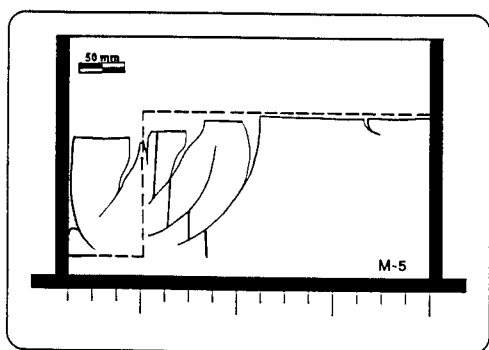


Figure 3: Profile of model M-5 after the centrifuge test. (Maximum acceleration = 109g)

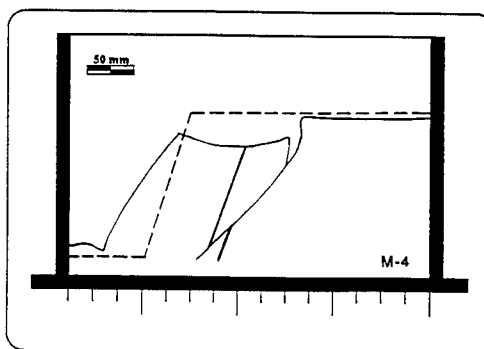


Figure 5: Profile of model M-4 after the centrifuge test. (Maximum acceleration = 146g)



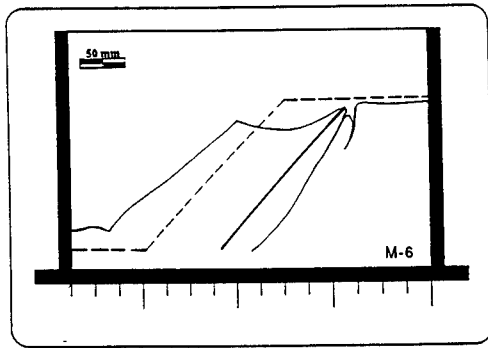


Figure 6: Profile of model M-6 after the centrifuge test. (Maximum acceleration = 150g)

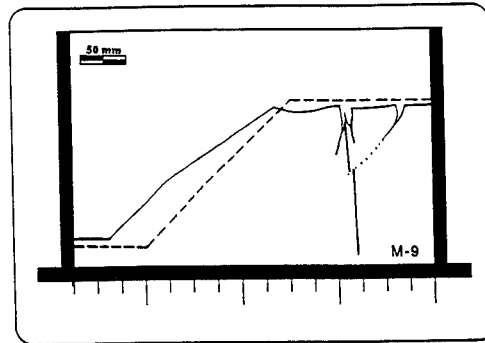


Figure 8: Profile of model M-9 after the centrifuge test. (Maximum acceleration = 158g)

similar slope angles. The steep models M-7 and M-10 were identical in geometry (80.5 degree slope), but different in reinforcement configuration. Model M-7 had a constant length of reinforcement of 102 mm ( $L/H=0.66$ ), and model M-10 had variable length reinforcement, varying from 102 mm ( $L/H=0.66$ ) at the top, to 193 mm ( $L/H=1.27$ ) at the bottom, so that a line joining the ends of reinforcements was vertical, rather than parallel to the slope face. The first tension crack developed at a stress equivalent height of 4.6 m, which was about the same as for M-7, thereby emphasizing the role of the uppermost reinforcement in crack development or prevention. The shapes of the deformed slopes are shown in Figures 7 and 4. In such a

steep slope, there was little effect of varying reinforcement length.

The two flatter models M-6 and M-9 were also identical in slope geometry (45 degree slopes), but different in reinforcement configuration. Model M-6, had a constant length of reinforcement ( $L/H=0.66$ ), and model M-9, with identical slope geometry, had reinforcement length varying from 102 mm ( $L/H=0.66$ ) at the top, to 235 mm ( $L/H=1.54$ ) at the bottom, again making a vertical line joining the ends of reinforcements. Comparison of after test profiles in Figures 6 and 8 shows that overall stability was superior in M-9, where the reinforcement intersected a developing failure surface much sooner than in M-6. In such a flat slope, these results confirm that bearing capacity problems can be reduced by increasing the length of reinforcement for the bottom layers, but not eliminated.

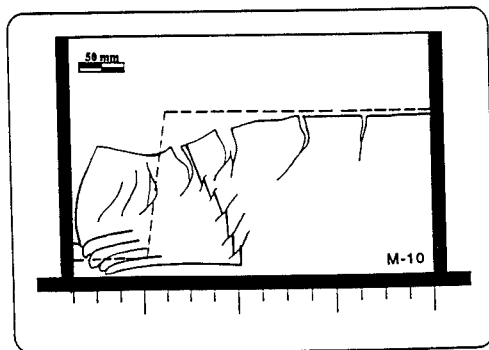


Figure 7: Profile of model M-10 after the centrifuge test. (Maximum acceleration = 98g)

#### 4 DISCUSSION AND CONCLUSIONS

Six of the seven walls and slopes in this study underwent either clearcut failure or excessive deformation amounting to failure. Deformation and failure were accompanied by geotextile rupture or strain, but there was no evidence of pullout, consistent with results of steeper model walls on rigid foundations with stronger reinforcement, described by Goodings (1989). This is a function of the relative values of

rupture load, and soil-geotextile friction which exceeds the strength of the soil alone.

In general, longer reinforcement improved wall or slope performance. Reinforcement which was larger at greater depths improved overall wall performance most effectively when slope angle was flatter, but it did not improve appreciably the point at which first cracking was observed. Slope angle still has a greater effect on behavior of walls and slopes on weak foundations, than reinforcement length, even when reinforcement length was sufficient to contain the failure zone. Certainly deformations of the walls and slopes themselves, and of the foundations were large depending on stress level, and must be taken into account in design even at stress levels significantly less than those indicated to cause failure.

#### ACKNOWLEDGEMENT

The authors gratefully acknowledge the support of the US National Science Foundation and the contributions of Polyfelt, Inc. Atlanta, Georgia, USA, in particular from Dr. Barry Christopher, through additional funding, advice, and testing of geotextile simulants.

#### REFERENCES

- Alvarez, T.A. 1988. Centrifuge model testing of geotextile reinforced cohesive soil walls, M.S. Thesis, University of Maryland: 1-184.
- Bolton, M.D., Choudhury, S.P., and Pang, R.P.L. 1978. Reinforced earth walls: a centrifuge model study, Symposium on earth reinforcement, ASCE Annual Convention, Pittsburgh: 252-281.
- Bolton, M.D., and Pang, R.P.L. 1982. Collapse limit states of reinforced retaining walls, *Geotechnique*, Vol. 32, p:349-368.
- Fugulsang, L.D., and Ovesen, N.K. 1988. The application of the theory of modeling to centrifuge studies, *Centrifuge in Soil Mechanics*, Rotterdam. Balkema: 119-129.
- Goodings, D.J. 1989. Effects of poorly draining backfill on geotextiles for earth reinforcement on vertical soil slopes, Bureau of Research, Maryland State Highway Administration, Report No. FHWA/MD-89/6, 1- 51.
- Mitchell, J.K., Jaber, M., Shen, C.K., and Hua, Z.K. 1988. Behavior of reinforced soil walls in centrifuge model tests, *Centrifuge 88*, Rotterdam, Balkema: 259-271.
- Porbaha, A. 1994. Centrifuge modeling of geotextile reinforced cohesive soil retaining systems, PhD dissertation, Dept. of Civil Eng., University of Maryland, College Park: 1-178.
- Santamarina, J.C. 1984. Effect of adjacent soils on reinforced soil structures- centrifuge model testing, M.S. thesis, University of Maryland, College Park: 1-157.
- Schofield, A.,N., 1980. Cambridge geotechnical centrifuge operations, *Geotechnique*, Vol. 20, p: 227-268.
- Suah, P.G. 1989. Further centrifuge model testing of geotextile reinforced cohesive soil walls, M.S. thesis, University of Maryland, College Park: 1-154.
- Taniguchi, E., Koga, Y., Yasuda, S., Morimoto, I. 1988. A study on stability analysis of reinforced embankments based on centrifugal model tests. *Proc. Int'l Symposium on Theory and Practice of Earth Reinforcement*, Japan. Rotterdam, Balkema: 485-490.

## Studies on the stability of model rock slopes

D.P.Stewart, D.P.Adhikary & R.J.Jewell

Department of Civil Engineering, The University of Western Australia, Nedlands, W.A., Australia

**ABSTRACT :** Physical models of rock slopes have been tested in the centrifuge to study certain aspects of slope instability. The particular problems examined here are (i) flexural toppling failure in closely foliated rock masses, and (ii) the influence of underground workings on slope stability. This paper describes the modelling techniques used and presents the results of some of these experiments. The experimental results are compared with analytical methods and conclusions are drawn regarding the usefulness of the centrifuge in rock mechanics research.

### 1 INTRODUCTION

Effective assessment of the stability of rock slopes is essential in open pit mining, particularly given the recent trend towards the adoption of steeper open pit slopes. Increased risks of pit wall failure have accompanied the trend towards steeper pit walls, leading to the need for a clear understanding of the mechanics of rock slope instability to assist in the verification of design techniques. Analytical techniques in current use can be limited by poor or inappropriate input data and incomplete understanding of some important modes of instability. Small scale models can be useful to examine behavioural mechanisms and assess the suitability of various methods of analysis. Clark (1984) reviewed the state of rock mechanics modelling on the centrifuge, and identified the potential benefit from combined mathematical and physical modelling of rock mechanics problems.

Research is in progress at the University of Western Australia in collaboration with the Department of Minerals and Energy of Western Australia and the CSIRO, to verify currently applied analytical methods for slope stability by comparison with physically observed events in centrifuge models and in the field. The initial focus of this study is the development of flexural toppling failures in closely foliated rock masses, and the influence of underground workings on slope stability.

#### *1.1 Previous rock mechanics centrifuge studies*

Bucky (1931) published one of the earliest references to the use of a centrifuge in geotechnical engineering, describing some simple experiments on the behaviour of beams under self-weight loading, relevant to the design of underground openings in rock. Most subsequent centrifuge modelling in rock mechanics has also centred on underground mine studies (eg Hoek, 1965 and Stephansson, 1971).

Although several studies of soil slope stability have been conducted on the centrifuge (Schofield, 1978), very little work on rock slope stability has been reported. Sugawara et al (1983) and Goldstein et al (1966) describe some studies involving slopes comprised of homogeneous materials, with some tests including a single discontinuity. Other work involving photoelastic studies on the centrifuge has been reported, although the majority of rock slope model testing has been with base friction equipment or tilting tables.

A potential problem with small scale rock mechanics modelling is the lack of similitude due to scale effects, such as in joint stiffness (Iglesia et al, 1991). While this problem may be a major shortcoming in some situations, physical modelling can still be of benefit if the shortcomings are recognised and either (i) are not considered to have a major influence on the

aspect being studied; or (ii) can be accounted for adequately in a numerical analysis.

## 2 MODELLING TECHNIQUES

Experimental modelling in rock mechanics is usually performed using artificial rock materials compatible with the experimental technique being used. Stimpson (1970) provides a comprehensive review of possible modelling materials that could be used to represent rocks. More recently, Johnston and Choi (1986) have described a model material that reproduces the engineering behaviour of Melbourne mudstone, and Indraratna (1990) describes the development of a material to model soft sedimentary rocks.

For the experimental studies described here, it was desired to examine some problems of general applicability to rock slope design, and hence the model materials were required to behave like "rock" in general, without attempting to model any specific rock type or weathering grade. Thus it was desired to produce an artificial rock of high stiffness that would fail in a brittle fashion, have internal frictional strength, and relatively low tensile strength.

A number of alternative materials were experimented with as part of this study. The experiments described here were generally conducted on samples made from mixing either Portland cement or gypsum with fine sand (silica, ilmenite or garnet,  $G_s = 2.65, 4.5$  and  $4.1$  respectively). The latter two minerals were used to obtain higher bulk densities (around  $2500 \text{ kg/m}^3$ ). The sand provides internal frictional strength as well as acting as a filler.

The sand and cementing agent were mixed together with water, and then either vibrated into a mould or mixed at a consistency suitable for pouring into a mould without segregation before setting. The latter technique has been most successful in producing laminated models where the layers of "rock" are separated by thin sheets of greased paper to simulate a foliated rock mass. Where Portland cement was used, the samples were cured for 28 days under saturated conditions. The samples must be dried to remove all free water before centrifuge testing, otherwise transient water flow will occur under the increased gravitational forces. Drying was carried out at temperatures of less than  $50^\circ\text{C}$ .

The centrifuge testing procedure followed in this work involved gradually increasing the speed of the centrifuge until failure of the

models developed through increased self-weight. Displacement at various points was monitored with transducers and also with video imaging techniques through a window in the strongbox. The experiments were performed on the geotechnical centrifuge at the University of Western Australia (Randolph et al, 1991) in a "plane-strain" strongbox of 200 by 650 mm in plan dimensions and 470 mm internal height. In the tests conducted to date, no significant difference in model behaviour at the sides and centre of the strongbox has been observed.

## 3 FLEXURAL TOPPLING IN FOLIATED ROCK

Flexural toppling is a mode of slope failure generated in a closely foliated rock mass, where the foliation dips steeply into the slope face and there is no persistent cross jointing. Failure occurs due to bending of the columns of rock formed by the discontinuities as shown in Figure 1, resulting in tensile failure of the rock. This form of slope instability is relatively common in Western Australian gold mines, where the mineralised bodies currently being mined are hosted by closely foliated rock masses. However, slope design and back analysis in these situations is normally performed on the basis of a block toppling mechanism, where failure is postulated to be the result of sliding or toppling of blocks of material on a second set of flatly dipping discontinuities (Goodman and Bray, 1976). While block toppling has received a considerable amount of attention in research, flexural toppling has not been widely studied.

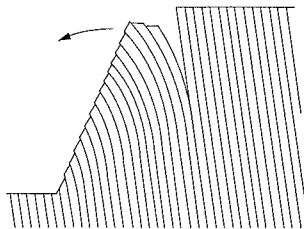


Figure 1. Flexural toppling failure in a foliated rock mass.

### 3.1 Centrifuge models

The range of centrifuge models tested to date is summarised in Table 1, illustrating the range of foliation spacings and rock strengths examined

so far. Further tests are in progress to extend the range of parameters studied. Some of the models listed in Table 1 were prepared by assembling pre-cast sheets together to form a slope, while others were produced by casting a large laminated block of material as described earlier, and then cutting into a slope shape. The latter method has been found to produce the best samples, with perfectly fitting discontinuities.

Table 1. Details of flexural toppling models

Test No.	H/t	Slope angle (deg)	Discon. angle (deg)	$\sigma_t$ (MPa)	$\phi_d$ (deg)
1	30	80	70	0.17	40
2	80	60	63	11.0	17
3	81	90	70	11.0	17
4	33	61	80	1.10	22
5	83	90	80	11.0	17

where : H = slope height, t = discontinuity spacing,  $\sigma_t$  = tensile strength from beam testing,  $\phi_d$  = friction along discontinuities from direct shear testing.

A photograph of a typical test after failure on the centrifuge is shown in Figure 2. It should be noted that motion of the rock mass after failure was halted by an instrumentation mounting, and hence the post-failure geometry is probably only indicative of the general direction of motion during failure, and not the final slope profile. However, the collapse mechanism evident in the model compares well with flexural toppling



Figure 2. Post-failure geometry of flexural toppling model test no. 1.

failures observed in the field, being characterised by bending of slabs of rock into the open pit and leading to the development of deep tension cracks.

### 3.2 Limit equilibrium analysis

Aydan and Kawamoto (1992) proposed a new limit equilibrium method based on the flexure of a series of columns. The approach is illustrated in Figure 3, where a basal failure plane is assumed to originate at the toe of the slope. The forces acting on the columns are determined, and the height that the normal intercolumn forces act above the basal plane ( $\eta$  in Figure 3) is assumed. The tensile stress at the basal plane is calculated for each column, and failure occurs when the tensile strength is exceeded.

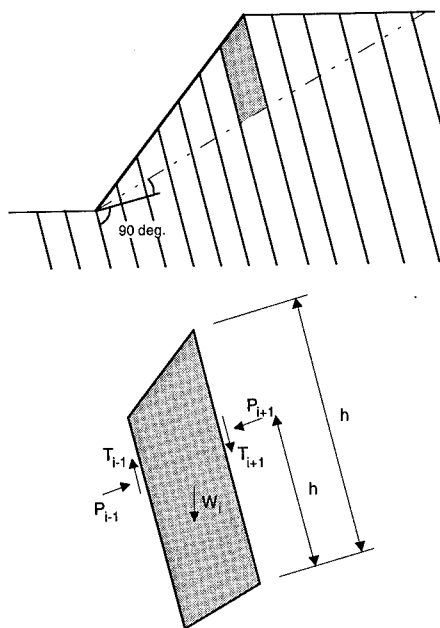


Figure 3. Limit equilibrium analysis of flexural toppling, modified from Aydan and Kawamoto (1992).

In the original derivation, the basal plane was assumed to be normal to the discontinuity set and  $\eta$  between 0.75 and 1.0 assumed. This analysis was found to reproduce the general trends evident in field data on flexural toppling, and to adequately predict the behaviour of base friction models with H/t = 5 to 14. However, this approach was found to be grossly conservative

for the centrifuge models described here ( $H/t = 30$  to  $80$ ), and it was not possible to find a single value of  $\eta$  that matched all tests.

Observation of experimental results indicated that the angle of the basal failure plane was generally about  $10$  to  $15^\circ$  above the normal to the foliation (Figure 2). Accordingly, the orientation of the basal plane ( $\theta$  in Figure 3) was varied and the value of the side force height coefficient,  $\eta$ , that matched the point of collapse of the centrifuge model determined. The results of these calculations are shown in Figure 4 as the relationship between  $\theta$  and  $\eta$  for each of the five model tests. The curves for all tests meet at about  $\theta = 10$  to  $11^\circ$  and  $\eta = 0.5$ , indicating that this combination of parameters should enable the limit equilibrium analysis to predict flexural toppling failures relatively accurately.

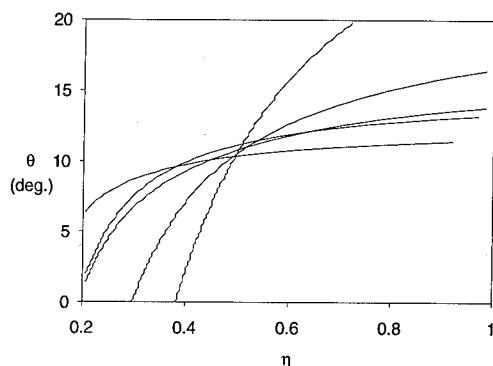


Figure 4. Correlation of limit equilibrium analysis with centrifuge test results.

### 3.3 Numerical modelling

Numerical modelling of block and flexural toppling instability has been performed by a number of research workers using finite difference, finite element and distinct element codes. However, flexural toppling has generally been analysed where  $H/t$  ratios are quite low ( $5$  to  $10$ ). When attempting to model the centrifuge tests described here, considerable problems were experienced such as (i) the requirement to include cross-jointing with intact rock strength and the very long solution time with a distinct element code; and (ii) the generally poor representation of flexural toppling with a ubiquitous joint model.

To circumvent these problems, a new numerical approach is being developed where the closely foliated rock mass is represented by a

continuum approximation for an assemblage of flexible plates. This special continuum incorporates the joint properties and the stress-strain relationship of a thin plate. This approximation saves a vast amount of computing time compared to the other methods, and has yielded some promising initial results.

## 4 INTERACTION OF UNDERGROUND WORKINGS WITH OPEN PIT SLOPES

The influence of underground workings on open pit slope stability is a major issue at an increasing number of mine sites throughout the world. The issue arises both where abandoned workings are present in the pit walls, or where new underground mines are developed below the base of an existing pit. The interaction of a slope with underground voids is relatively complex and not always well modelled with limit equilibrium methods.

### 4.1 Centrifuge models

The layout of a preliminary centrifuge model to examine the collapse mechanism of a slope where open pit mining is progressing through old underground workings is shown in Figure 5. The model was formed by vibrating a mixture of ilmenite and Portland cement into a mould containing formers to produce three rectangular voids. Test cylinders cast at the time of model preparation were tested in triaxial compression, and indicated the following strength parameters:

peak strength :  $c' = 180$  kPa,  $\phi' = 43^\circ$   
residual strength :  $c' = 40$  kPa,  $\phi' = 36^\circ$

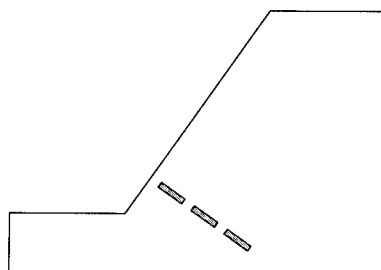


Figure 5. Layout of a centrifuge model with abandoned underground workings.

The model was tested by increasing the rotational speed of the centrifuge until failure occurred at  $170$  g, as illustrated in Figure 6. The model was monitored by several video cameras,

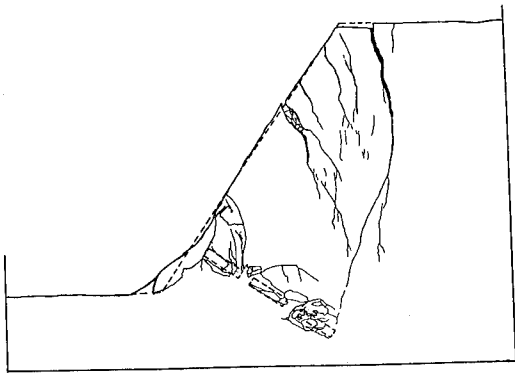


Figure 6. Failure mechanism of centrifuge model with abandoned underground workings.

and surface displacements were measured at a number of points. During the test, surface spalling was observed on the slope face directly above the uppermost open stope, long before failure of the slope itself occurred. Overall collapse appeared to have been initiated by simultaneous caving of the open stopes together with a shallow slip extending from the area of surface spalling down to the toe of the slope. A large and relatively intact block of material then rapidly slumped downwards into the voids along a failure path intersecting the lower stope.

#### 4.2 Analysis

Analysis of the collapse of the centrifuge model shown above is relatively difficult since limit equilibrium analyses do not model the correct failure mechanism for this particular situation. However, with a relatively large number of stopes distributed throughout the rock mass, limit equilibrium methods are more applicable, as found by Rehwoldt (1989).

To more accurately represent the collapse mechanism of the model, numerical modelling was performed using the finite difference program FLAC (Itasca, 1991). The model rock material was represented with a strain-softening Mohr-Coulomb constitutive model, where friction angle and cohesion are reduced as plastic strain occurs. Strength parameters were selected on the basis of triaxial test data quoted earlier.

Failure of the numerical model occurred in a similar way to the centrifuge model, with collapse of the open stopes leading to downward sliding of the overlying block of material. The failure mechanism that developed in the numerical model extended up from the

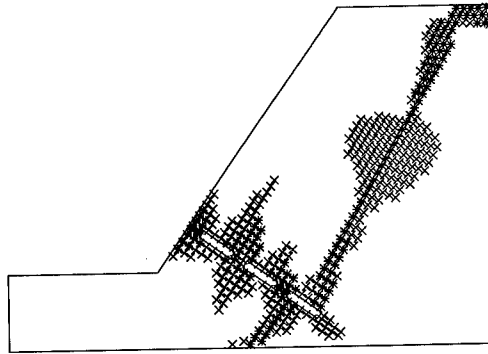


Figure 7. Extent of plastic zones at failure in the numerical model; \* at yield; X elastic, at yield in past.

lowermost stope to the surface of the model, in a similar fashion to the physical model, Figure 7. However, the deep tension crack evident in the physical model was not reproduced. It is possible that with further refinement of the fineness and orientation of the mesh that a slightly better match might be obtained.

The gravity level at failure was reproduced almost exactly by the numerical model described. However, further analyses based on the peak strength of the material using a standard Mohr-Coulomb constitutive model indicated a failure level near to 300 g, well above the actual point of failure. This suggests that strain-softening may be a significant factor in some slope stability situations, and that the strength used in design may need to be chosen carefully if a strain-softening approach is not used.

Regions of tensile stress developed in the numerical model before failure are indicated in Figure 8 and appear to correlate reasonably well

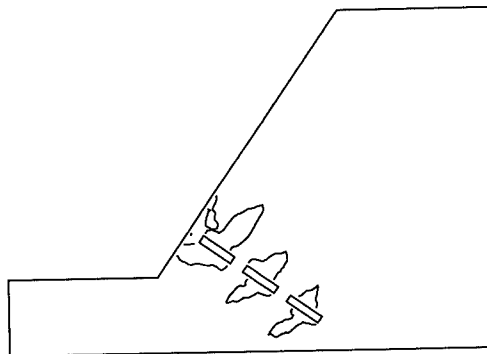


Figure 8. Regions of tensile stress before failure in the numerical model.

with the zones of collapse above the voids and the region of surface spalling observed in the physical model.

#### 4.3 Future work

The preliminary centrifuge model test described here has enabled some qualitative assessment of the mechanism of collapse of a slope containing voids. Future tests of this nature will be more heavily instrumented to more accurately capture the collapse of the open stopes and will be conducted on models containing various distributions and sizes of voids.

## 5 CONCLUSIONS

The experimental work described here shows great promise for the validation of analytical methods for some complex modes of rock slope instability. The research on flexural toppling is leading to a better fundamental understanding of this problem, and to the development and validation of both simple and complex methods of analysis. Data from field failures will be incorporated into the study to provide a strong basis for validation of these techniques.

The influence of underground workings on open pit slope stability is a more site specific problem in that each site will have a different distribution of voids and different geological conditions. However, idealised models can be useful in conducting a critical assessment of various analytical approaches.

The work described here was performed on a medium size centrifuge and illustrates that general rock mechanics studies can be performed on such a machine. Modelling of hard rock will necessarily require a large capacity centrifuge capable of relatively high g levels.

## ACKNOWLEDGMENTS

These studies were largely funded by the Western Australia-China Economic and Technical Research Fund. The guidance of Dr Chris Swindells from the Geological Survey of Western Australia is greatly appreciated. Initial development of modelling materials was performed by Chris Windsor from the CSIRO Division of Exploration and Mining.

## REFERENCES

- Aydan O. and T. Kawamoto 1992. The stability of slopes and underground openings against flexural toppling and their stabilisation, *Rock Mech. Rock Engng.*, **25** (3), 143-165.
- Bucky P.B. 1931. Use of models for the study of mining problems, AIMME Tech. Publication No. 425.
- Clark G.B. 1984. Modelling in rock mechanics and geology, Proc. Symp. Application of Centrifuge Modelling to Geotechnical Design, Manchester, 171-191.
- Goldstein M., M. Berman, B. Goosev, T. Timofeyeva and A. Turovskaya 1966. Stability investigation of fissured rock slopes, Proc. 1st Congress ISRM, **2**, Lisbon, 175-178.
- Goodman R.E. and J.W. Bray 1976. Toppling of rock slopes, ASCE Spec. Conf. Rock Engineering for Foundations and Slopes, Boulder, **2**, 201-234.
- Hoek E. 1965. The design of a centrifuge for the simulation of gravitational force fields in mine models, *J. SAIME*, **65**, No. 9, 455-487.
- Iglesia G.R., H.H. Einstein, R.V. Whitman, H.L. Jessberger and U. Guttler 1991. Trapdoor experiments with simulated jointed rock, Proc. Centrifuge '91, Balkema, 561-567.
- Indraratna B. 1990. Development and applications of a synthetic material to simulate soft sedimentary rocks, *Geotechnique*, **40** (2), 189-200.
- Itasca Consulting Group 1991. Program FLAC, Fast Lagrangian Analysis of Continua, v. 3.2.
- Johnston I.W. and S.K. Choi 1986. A synthetic soft rock for laboratory model studies, *Geotechnique*, **36** (2), 251-263.
- Randolph M.F., R.J. Jewell, K.J.L. Stone and T.A. Brown 1991. Establishing a new centrifuge facility, Proc. Centrifuge '91, Balkema, 3-9.
- Rehwoldt E.B. 1989. Effects of abandoned underground workings on open pit slope stability, Master of Science thesis, University of Nevada, Reno.
- Schofield A.N. 1978. Use of centrifugal model testing to assess slope stability, *Canadian Geotechnical Journal*, **15**, 14-31.
- Stephansson O. 1971. Stability of single openings in horizontally bedded rock, *Engineering Geology*, **5**, 5-71.
- Stimpson B. 1970. Modelling materials for engineering rock mechanics, *Int. J. Rock Mech. Min. Sci.*, **7**, 77-121.
- Sugawara K., M. Akimoto, K. Kaneko and H. Okamura 1983. Experimental study on rock slope stability by the use of a centrifuge, Proc. 5th Congress ISRM, Melbourne, C1-C4.



## Studies of rock slopes for the Three Gorges Project

S. H. Han & H. H. Wang

*Yangtze River Scientific Research Institute, Wuhan, People's Republic of China*

**ABSTRACT:** In this paper, some considerations with regard to the applications of the centrifugal model tests (CMT) to the study of rock slopes including the use of equivalent model materials and test techniques are discussed. Experimental results with reference to the deeply excavated rock slope of the ship lock of the Three Gorges Project and those to the stability problem on the Lianziyan rock cliff are presented. Some topics on rock mechanics and rock slope stability which may be studied by CMT in the near future are put forward.

### 1. INTRODUCTION

The Three Gorges hydraulic engineering complex is the key construction for harnessing the Yangtze River (Changjinag) in China. The project is located in the middle of Xiling Gorge on the Yangtze River with its dam site at Sandouping about 40 km west of the city of Ichang, Hubei Province. The maximum height of the concrete gravity dam is 175 m, the total axis length is 2,335 m. The reservoir has a total storage of 39.3 billion cu. m. The total installed capacity of the power plant amounts to 18,200 MW. The navigation structures consist of a double-line of five-step continuous ship locks. Rock slope problems in the design on the Three Gorges Project are of two classes: (1) the natural slopes at the bank of the reservoir such as Lianziyan cliff and Huanglashi cliff which are liable to slide; (2) the artificial slopes of the deep excavation of the ship locks, the ship lift, the power house and the diversion channel. Total excavation volume amounts to 60,000,000 cu. m. The stability of these slopes should be carefully investigated.

Factors influencing the stability of excavated rock slopes are numerous e.g. fissures, faults and other discontinuities in the rock mass, the virgin state of geostress in the rock, the condition of ground water, the process of excavation and the consequences of earthquake force and explosion, etc. The statics of deeply excavated rock slope comprises engineering

geology, rock mechanics, structural engineering, construction technology. It is a subject related to various fields of engineering sciences.

Centrifugal model tests (CMT) can be applied to investigate rock slope problems (Clark, 1985) with peculiar advantages. The prototype stresses can be simulated accurately because the gravitational force field experienced by a centrifugal model can be amplified by several hundred times. Time relation between prototype and model may be simulated on centrifugal models also, and this makes the centrifugal modelling technique attractive in the studies of time-dependent problems in rock mechanics and opens up even broader prospect for the centrifugal test.

In this paper several test techniques used in the centrifugal model study for the rock slope problems on the Three Gorges Project such as the preparation of equivalent model materials, the application of moire technique and the simulation of excavating the rock mass are briefly described. Examples representing three kinds of the rock slope problems met in the design of the Three Gorges Project are presented. The test results obtained by CMT are compared with those obtained by geomechanical model test and finite element (FE) analysis. It is believed that the CMT method may be effectively used to study rock slope problems and yield reliable results.

Table 1 Model materials

Prototype	Granite rock	diabase rock
filler	barite powder	barite powder, limestone powder
binding agent	secondary plaster, water	plaster, water
additives	—	oil
Remark	cast to form, properly dried	pressed to form

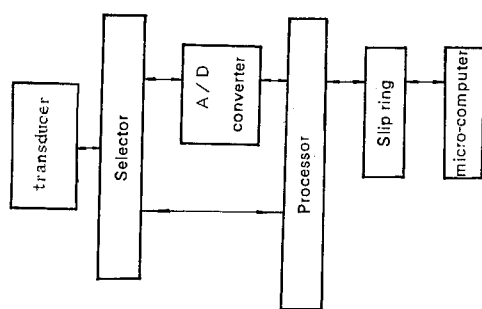


Fig. 1. The measuring, data acquisition and processing system.

## 2. STUDIES ON MODEL MATERIALS

In CMT for rock mechanics problems, if prototype materials, such as rock and concrete, are chosen as model materials, it often requires very large model to reproduce structures of the rock mass. Therefore, equivalent model materials are commonly used in centrifugal models to study problems on rock mechanics at present. Equivalent model material refers to some artificial material specially prepared such that the material must satisfy the similarity requirements of some principal mechanical characteristics. In the model study of high rock slope problem for the Three Gorges Project, the following model materials have been chosen and given in Table 1. These model materials satisfy the similarity laws by and large, furthermore, they meet the general requirements for model materials, i.e. stable properties, economical, easily available, not poisonous and of good workability etc. The surface of the models are coated with electric resistance strain gages and moire grids.

## 3. TESTING TECHNIQUES

### 3.1 Hydraulic slip rings

The loads: water pressure, sediment pressure and geostress on the model are applied by means of a special loading system. Generally slip rings for liquid or pneumatic pressure are used. Liquid or pneumatic pressures can be transmitted stably into the package and applied to the model through divisors and pneumatic bags or jack system. In the slip ring system, there are 7 channels among which 3 are for oil pressure, 2 for pneumatic pressure, 1 for liquid pressure and 1 spare unit. These are used to apply the boundary geostress and to simulate the excavation of rock slopes. The maximum oil pressure amounts to 20 MPa, that of the pneumatic pressure amounts to 3 MPa.

### 3.2 Electrical measuring system.

By means of the data-acquisition and process system (Fig. 1), the signals are recorded through the multiple channel selector, digital-module converter and microprocessor, and converted to digital signals and put into the micro-computers via the electrical slip rings. This system is good at anti-interference and can be used for the measurement of multiple points. The data measured are to be processed by microcomputer. The system has been used to measure the response of the rock slope models with satisfactory results.

### 3.3 Application of moire technique.

In CMT, displacement measurement in deep excavations in rock mass and on rock slopes are always necessary. Common types of displacement transducers are hardly workable when subjected to a high gravitational field. Therefore, recourse to optical methods has been made. Moire method generally results in good accuracy under conventional circumstances in laboratory, yet the technique of photography for the centrifugal model at flight must be established first. In practice the high speed photography and the stroboscopic photograph did not work well due to many technical difficulties. Through repeated tests, photography in the package (Fig. 2) is adopted to satisfaction in CMT for the rock slope problem in the Three Gorges project. Furthermore,

continuous photograph can be achieved at a centrifugal acceleration of less than 50g.

Superimposition of the reference grating and the specimen grating is done by direct contact. The specimen grating is attached to the measured plane of the model, and the reference grating to a rigid glass plate set close to the model. The horizontal component of the in-plane displacements are obtained by analysis of the moiré fringes, see Fig. 3. Further details on the technique of measurement and the accuracy of the measured data have been described by Han and Wang (1991).

#### 4. CENTRIFUGAL TESTS OF ROCK SLOPES

##### 4.1 Simulation of excavation of rock slopes

The geological section 12-12' of the ship lock in the Three Gorges Project is studied. The schematic section of the plane model in which the major geological structures are carefully reproduced with the minor and unimportant details simplified or omitted as shown in Fig. 4. The dimension of the lock chamber is 35 m wide by 50 m high. The maximum depth along the highest slope is about 140 m. The range of simulation is: (a) width 480 m; (b) depth of 161 m below the lock. The geometric scale of the model to the prototype is 1:100.

In order that stress and displacement measurements can be performed simultaneously, the modulus of elasticity of model material is set at about 1,000 MPa. Model materials have been selected on the basis of similarity requirements and tested systematically for their deformability characteristics. Polyester membrane is used in the model to simulate the fault. It is carefully finished so that the desired value of frictional coefficient ( $f=0.3$ ) is obtained. The tests were conducted at 58g.

Geostress field is created by applying proper, equivalent surface loads on two sides of the model (Fig. 5). In fact only pneumatic pressure is applied by inflatable rubber bags. Determination of the boundary condition and the magnitude of the distributed load have been discussed by Han and Wang (1991).

Excavation of the rock slopes is simulated as follows. A weak surface is artificially made along the line of excavation in the section of the lock chamber. The weak surface should be capable of transmitting the pressure and the shear except tension. After the initial stress field in the model had been established with the application of the centrifugal load and geostress boundary conditions, the excavated parts of

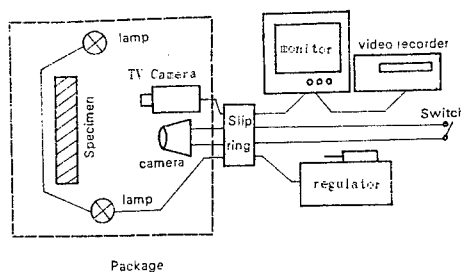


Fig. 2 Photography system in the centrifuge, a schematic representation.

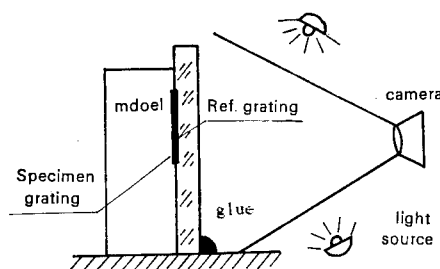


Fig. 3 Arrangement of the in-plane moiré method

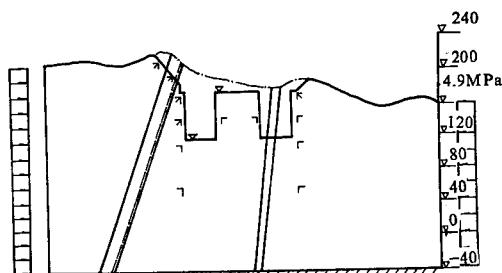


Fig. 4 Schematic illustration of the lock slope model

the rock mass were relieved by the pneumatic and the mechanical devices specially designed and installed in the package. Changes of stresses and displacements in the rock mass before and after excavation were monitored by means of electrical resistance measurement and moiré patterns. As a matter of fact, excavation of the model is accomplished in two steps: (1) part of the excavated rock mass above the top of the lock chamber is relieved by means of pneumatic bags; (2) the remaining part is relieved by the mechanical device. Introduction to the weak surface would have an influence on the initial stress field in the model. This has been examined by FE analysis.

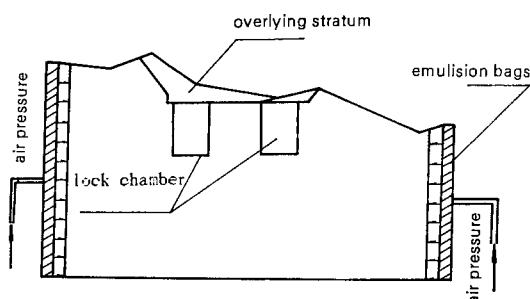


Fig. 5 Equivalent boundary load on the model

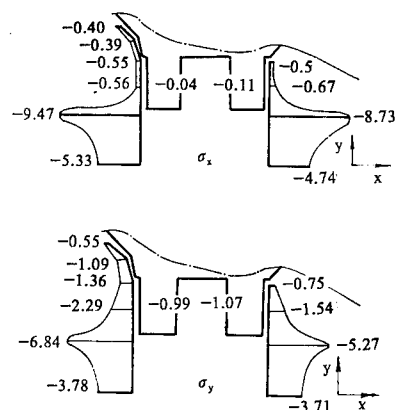


Fig. 6 Stress distribution in the rock mass after excavation of the lock chamber. (unit: MPa)

The differences between the displacements on the side walls and on the base plate of the lock chamber obtained by two methods are only 5%.

The horizontal and vertical stress components after excavation of the lock chamber is shown in Fig. 6. All stress components are monitored by the strain gauges. Fig. 7 shows the horizontal displacements due to excavation, which are obtained by in-plane moiré method. These results have been compared with those obtained by FE analysis and by geomechanical model tests. The stresses observed from CMT are reasonably close to those predicted by FE analysis, while the displacement values noted from CMT lie between those obtained by 2-dimensional and 3-dimensional geomechanical model tests.

#### 4.2 Failure mechanism of rock slopes

The total length along the axis line of the ship lock in

the Three Gorges Project is about 1,600 m. A major discontinuity passes through the lock chambers and it is likely to endanger the stability of the high steep rock slope of the lock chamber. The cross section at lock chamber 1 (see Fig. 8) is chosen as the typical section of potential failure and studied by CMT. The programs of model tests including the conceptional design of geological structures, model laws of statics, model materials and testing techniques are the same as those of the above mentioned model tests.

In order to study a weak surface (labelled as F215 hereafter), strain gauges are placed at its top surface and various elevations across the fissures of the model fault. Displacement meters are installed in the upper and lower plate of F215 respectively. Video display and recording of the model have been taken during the test.

Some important findings are as follows:

- (1) During excavation, the deformation state of the top surface of F215 changes from compression to tension and eventually yields. This is an evil omen of the instability of the lock slope.
- (2) Shear and compression failures occur in certain area near the lower corner at the side wall of the lock chamber. This shows that the lower corner is the most dangerous position in the section of the lock chamber.
- (3) As the lock chamber is excavated, the geostresses are relieved, the bottom plane of the excavated rock heaves (resilient deformation). The underlying stratum (diabase rock) that bears the overburden of the total weight of the triangle shaped rock mass is of relatively low strength, so that the contact surface between the granite rock and the diabase rock cracks in tension. This reveals the hidden dangerous area in the rock mass around the lock, see Fig. 8.

#### 4.3 Stability of dangerous rock cliffs

Section CK<sub>2</sub>N10°W of the dangerous rock cliff Lianziyan is studied and the conceptual model is shown in Fig. 9. Studies are devoted to the stability of the rock cliff under the action of gravity force, interstitial water pressure and earthquake force, and the effectiveness of the reinforcement measures. In CMT, the seismic load is replaced by an equivalent static load. The inertial force due to earthquake is substituted by the static force proportional to the mass of the rock body. Liquid pressure slip rings and loading system are used for applying loads to the model. In order that the gravity force and seismic

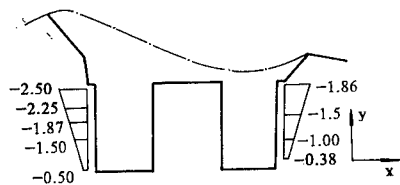


Fig. 7 Horizontal displacements in the rock mass due to excavation of the lock chamber (unit: cm)

force can be simulated simultaneously, the model has been revolved through an angle inclined to the base such that the resultant of gravity and inertial force due to earthquake is in the same direction with that of the centrifugal force.

During stormy weather, storm run-off poured into the fissures, joints in the rock creates a high pressure head in a short time since the rock is relatively impervious. Such phenomenon is studied in CMT by an interstitial water pressure which is applied to the model after the establishment of the centrifugal force field. This is succeeded by the following technique. Thin emulsion bags are applied to the joint surfaces in the model rock. The lower end of the bags are connected to the boxes which are fully filled with liquid and pneumatic bags. By pressing the plate of the box pneumatically, the liquid in the joints are forced to raise to the desired water head.

As for modelling the prestressed anchorage cable used for reinforcing the dangerous rock, it is difficult to satisfy both the geometric scale and the ratio of similitude for deformation modulus. Fig. 10 shows the arrangement of anchorage cables on the model.

The model test gives a glimpse of possible failure mode of the dangerous rock cliff under the action of earthquake force and interstitial water pressure, finds out the dangerous area that is most liable to slide. It further shows that a concrete plug against slide constructed at the exploited area in coal deposit is of significant effectiveness and that anchorage cable used to reinforce the fractured rocks may improve the integrity of rock mass as a whole and enhance the safety factor of the rock cliff.

## 5. CONCLUSIONS

A series of centrifugal model tests have been conducted to study the stability of rock slopes for the important Three Gorges Project in China. Through the accomplished work, it is established that the range of applications of CMT for rock mechanics and rock

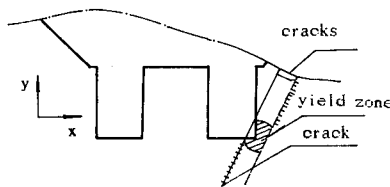


Fig. 8 Failure state of rock mass around the lock with the most disadvantageous geological structure

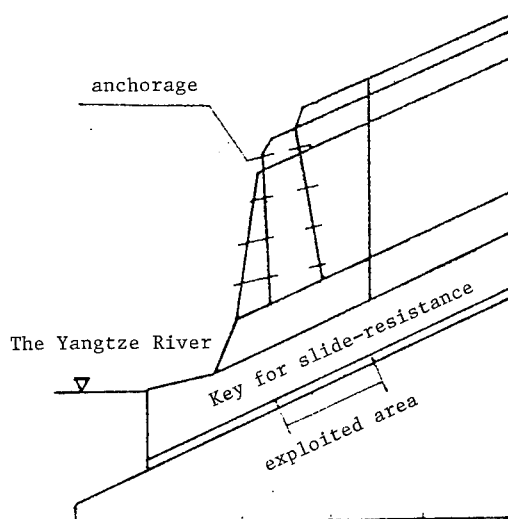


Fig. 9. Scheme of the reinforcement measures for the Lianziyan cliff

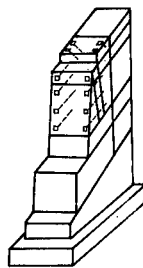


Fig. 10 Layout of anchorages

slope problems can be widened at least to the following aspects:

- (1) Engineering measures for improving unstable slopes such as anchorages;
- (2) Effects of explosion, earthquake forces and interstitial water pressure on the stability of slopes;

- 
- (3) Studies on the stress, deformation and stability of underground cavities;
  - (4) Study of complex structures such as rock-fill dam with concrete facing;
  - (5) Examination of safety factor of the structure and rock foundations.

#### REFERENCES

- Clark, G.B. 1985. Modelling in rock mechanics and geology, In Application of Centrifuge Modelling to Geotechnical Design. ed. W.H. Craig, A.A.Balkema, Rotterdam, pp.381-402.
- Han, S.H. & Wang, H.H. 1991. Applications of centrifuge model technique to the rock slope problems with reference to Three Gorges Project, Proc. 2nd Symposium on Centrifuge Modelling Techniques, Shanghai, China. June 1991, pp171-191 (in Chinese).

## 10 Deep excavations and tunnels

## Stability of deep excavations in soft clay

S.D.Zhang

*Shanghai Institute of Railway Technology, People's Republic of China*

H.D.Zhang

*Shanghai Baosteel the 20th Metallurgy Construction Co., People's Republic of China*

**ABSTRACT:** This paper presents the research work on excavation stability of a large metro station built on muddy clay foundation by both geotechnical centrifugal model which shows the process and quantity of deformations, and FEM which describes the deformation in mechanical behavior. The results of research are in concord with the monitoring in field, so that it is possible by this way to predict excavation stability and influence on the environment.

### 1. INTRODUCTION

As development of the city construction more attentions are paid on the excavation stability of deep foundation and the safety of surrounding buildings and pipelines. Based on field monitoring, model tests and theoretical analyses, some calculation methods in theory or in experience were summed up. One of them applied popularly was put forward by R. B. Peck in experience for evaluating environmental settlements in 1969 (Peck, 1969). Nowadays for theoretical analyses both critical equilibrium and circle sliding methods are usually accepted, which can't offer materials of deformations in quantity. Depending on computation technique the FEM is getting more popular applied in research but the centrifugal model has been playing a practical part on deep excavations specially in Shanghai, China.

The main three problems in excavations are the heave of pit bottom, surrounding settlements and deformations of the lateral supporting, which depend on not only the soil characteristics, depth and area of the excavation, buried length of the lateral supports, level of the ground water and arrangement of the supporting struts, but also the process of construction, ground loading and prestress of the struts, etc. The problem of the deep excavation are so complicated that it is difficult to predict what will take place, and easy to see different kinds of failures in excavation projects.

Since the geotechnical centrifuge of Shanghai Institute of Railway Technology was founded in

1986 the Authous have been doing a series of centrifugal tests on practical engineerings such as shaft No. 1 of Yanan Road (E) tunnel (Zhang and Chen, 1987), the excavation of Xujiahui metro station that now is presented.

### 2. CENTRIFUGAL MODEL TESTS

#### 2.1 Purpose of Tests

Located in the centre of downtown area Xujiahui metro station is one of the three largest stations of the No. 1 Shanghai metro which is to run from the Shanghai Railway Station to Xin Longhua in southwestern Shanghai along the 14.57 km-long line. The soil layers in this project area belong to saturated muddy clay and silty clay mainly.

Having the dimensions of 600m in length, 20m in width and 17m in depth, the excavation of station was supported by both diaphragm walls with dimensions of 30m in length and 0.8m in thickness, and struts which arranged in five levels of 1.95m, 4.95m, 7.95m, 10.95m and 13.95m to the ground level individually and spacing 3m in every level horizontally, were made of steel pipes with dimensions of 609mm in diameter and 15mm in thickness. Numerous crisscrossed underground pipes and cables surrounding the station in addition to buildings near by demanded the reliable environmental protection.

Because of no such experience to depend on the centrifugal models tests were carried on for predicting



environmental settlements, stability of the excavation, deformation of the diaphragm wall, struts stress etc., based on which suitable measures could be applied in different construction stages.

## 2.2 The Centrifuge

The centrifuge located in Shanghai Institute of Railway Technology in the first one in China produced for the special geotechnical purpose. The major specifications are 155cm in effective radius of action, 200g in max. acceleration, 20g-t in nominal capacity and 15kw in power of an electrical motor. The inner dimension of the model box is 48×32×24cm. This centrifuge is equipped with closed circuit T. V, high speed photographing which is 2-3 μs in half pulse width with the power of 40J, and a slipring stack with 24 signal channels for transducers, 6 electrical current sliprings for power supplying and 2 hydraulic slips to allow flow of compressed air or liquid to the model. All outputs are transferred into the operation desk in the control and observation room.

## 2.3 Preparation

The characteristics of soil layers at the excavation area are shown in Fig. 1. The ground water level is 0.5m below the surface in average of a year.

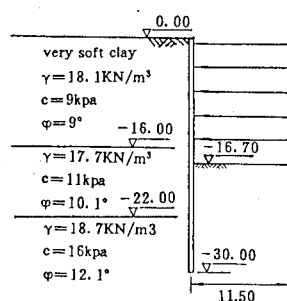


Fig. 1 section and characteristics of soil layers

### (1). Making Soil Samples of the Centrifugal Model

The original samplings of natural soils which were normally consolidated, were applied to make centrifugal models. Having saturated to 80~120 percent of water content the soil sample was moved in a centrifugal model box with two layers of drainages laid on surface and under base individually, then consolidated in the centrifugal acceleration for every soil layers until the consolidation degree was beyond

90 percent with the exception of top layer to 96 percent. The model time scale is expressed as following:

$$t_m = t_p / n^2$$

In the state of centrifugal acceleration  $ng$  the consolidating time  $t_m$  in the model is to be decreased to  $1/n^2$  times of consolidating time  $t_p$  in the corresponding prototype.

Besides controlling consolidation degree in simulation of soil layers it is important to make the strength of model soils almost the same as the strength of soil layers in the corresponding prototype, therefore two the same boxes of model soils were put on each end of the centrifuge, one of which was specially for usage of the geotechnical and micro-vane shear tests. The comparison of the shear strength between model and prototype soil layers are shown in Fig. 2.

### (2). Simulation of the Diaphragm Walls and Struts

A piece of perspex in thickness of 8mm was chosen as the simulated diaphragm. Because the stiffness of perspex is less than that of concrete of the diaphragm wall, the simulated thickness was 1.2m at 150g in order to have almost the same deformation as that of the 0.8m thick prototype. Limited to the dimension of the model box, the height of model diaphragm wall was 20 cm in model scale  $N=1/150$  simulating prototype of 30m. Both semi-section for observing environmental deformations in process of the construction, and whole section for recording the deformation of the excavated pit were made selecting pipes of red copper with dimensions of 5 mm in external diameter, 1mm in thickness as simulated struts according to simulation theory in strength. There were screws arranged at both ends of the strut for regulating the prestress.

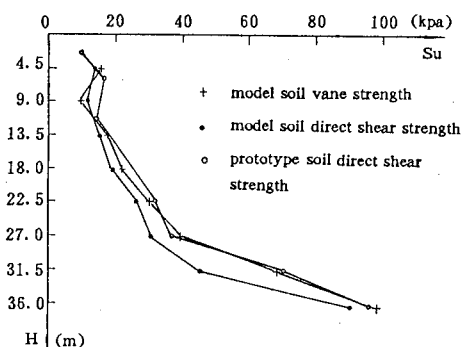


Fig. 2 comparison of the shear strength

### (3). Instrumentation

For measuring deformations of soil layers and diaphragm walls a set of photo-marks arranged in

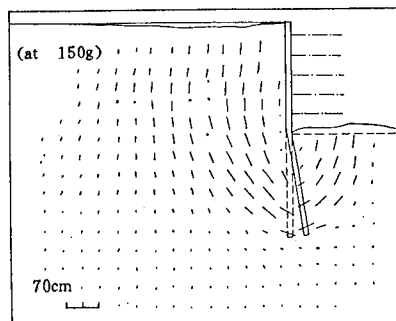


Fig. 3 soils deformations and wall foot kicking

square was installed in the inner side of the thick transparent perspex plate for photographing by a high-speed camera. The micro-earth pressure cells and piezometers were buried in back of the wall. Closed circuit T. V and video device were also applied to record the whole process of tests.

#### (4). Excavation

Because of the struts, it is difficult to carry out excavation in the centrifuge model which is in-flight. At each stage the centrifuge was stopped and the model was excavated to a certain depth, then was re-started and accelerated to the model scale condition. Within excavation depth of about 10m, the bottom heave was just in elastic deformation. In case of the plastic deformation which would pay significant influence to the result tests, there was only one stage allowed when the excavation depth went beyond 10m under this kind of excavating process.

### 3. CONTENTS AND RESULTS OF THE TESTS

#### 3.1 Contents of Tests

(1). Measuring the heave of pit bottom, the settlements in environmental area and the deformation of walls.

(2). Observing deformations of the soil layers under bottom in each stage of the excavation.

(3). Slope stability testing in longitudinal direction of the excavating pit with slope rate 1/3 and 1/4 in model scale  $N=1/150$  and  $N=1/180$  individually according to the designer's demands.

#### 3.2 Results of Tests

(1). Fig. 3 shows the deformations of soil layers and walls when the excavated depth was 17m (11.3cm in model with 150g of acceleration), indicating the 40m of influenced extent behind the wall with 21cm of the maximum settlement in location of 15m about to the wall. The displacement at the wall foot took place accompanied with

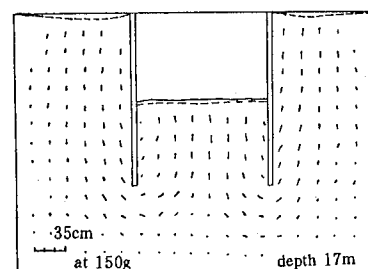
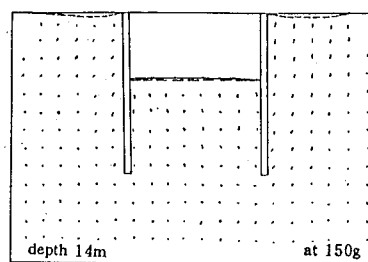
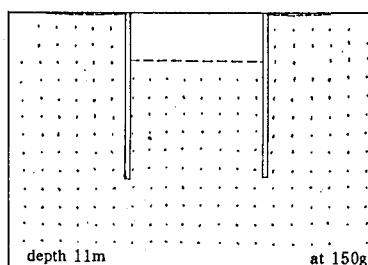
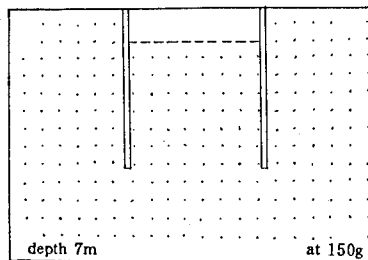


Fig. 4 soil deformations and bottom heave in several excavation depth

horizontal movement of soils shown obviously by the photo-marks, the phenomena of which indicated some soil sliding and wall foot kicking.

(2). The deformations in some excavation stages, which were getting deepen as the centrifugal acceleration was increased, were shown in Fig. 4. The plastic area in outside the wall was formed at beginning of 13m in excavated depth, through the wall foot then developed to the inner side of the wall,

caused the heave of the pit bottom. The relationship between the bottom heave and the environmental settlement collected in tests, was developed in proportion about 2.5 : 1 and shown in Fig. 5, so that the foundation improvement in both sides of the wall should be considerable when the depth of excavation exceeding 11m.

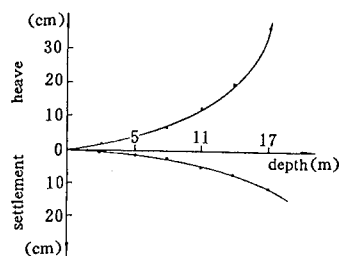


Fig. 5 relationship between bottom heave and environmental settlement

(3). The excavation of the prototype was carried on in longitudinal direction of the station. Fig. 6 and table 1 shows a failure state in one of the slope stability tests with slope rate 1/4, model scale  $N=1/180$ , indicating the cracks on the top of slope, 1.4m ( in prototype) the maximum horizontal displacement and 0.63m the maximum vertical heave both located at the toe of the slope, almost 50cm of the settlement at the top of the slope and 50cm of the horizontal displacement at the toe of the slope, so that the slope rate in prototype should be decreased to keep up the slope stability.

methord	radiue (m)	coordinate	
		x (m)	y (m)
O centrifuge test	43	28	-30
O' circular arc analysis	44	30	-24
O''	46	30	-32

#### 4. NONLINEAR FEM OF THE EXCAVATION STABILITY

Based on the Mohr-Coulomb criteria, the yield of soils is determined in this program of the FEM. The program also counts the residual stress in cross-points, which caused in the unloading process beneath the excavating surface has obvious influence on the distribution of the plastic area.

The results of the computations are in accord with the results of centrifugal tests, indicating the development of plastic area from out side to inside of

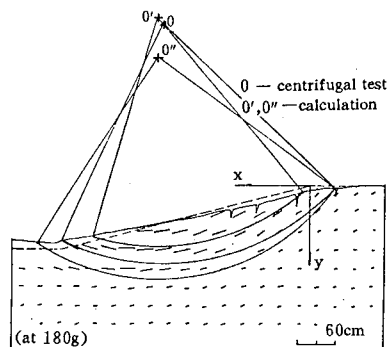


Fig. 6 slope deformation

Table 2 comparison between FEM and centrifugal test

	centrifugal test	FEM
pit bottom heave (cm)	33	30.7
maximum settlement distance from wall (m)	10~15	13~30
maximum settlement (cm)	13~21	12.5
ground settlement range (m)	35~40	50

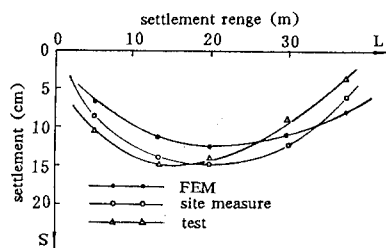


Fig. 7 surrounding settlement and range

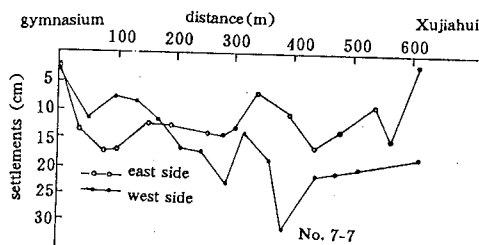


Fig. 8 settlements along both sides of Xujiashui metro station

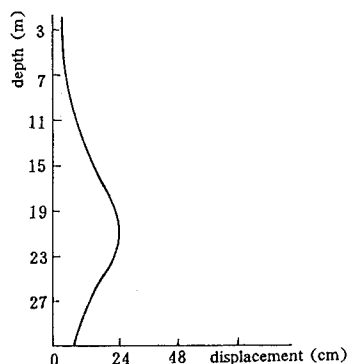


Fig. 9 deformation of the diaphragm wall with 17m excavated depth

the pit, the maximum displacement of the wall 4.14cm at top and 8.05cm at the level of excavated bottom. The comparison between the numerical model and the centrifugal test is shown in Fig. 7. Table 2.

## 5. FIELD MONITORING

Having lasted for eight months, the main structure of Xujiahui metro station was fulfilled on September 22, 1991. The settlements along both sides of the station monitored during the construction period, shown in Fig. 8 were 15cm in average, 30.8cm in max. on September 3 at the location No. 7-7, on which point the displacement of the diaphragm wall towards the pit was 80cm in max. and extended for 40m in the longitudinal direction. Fig. 9 shows one of the measured displacements of normal walls with 20~24cm in max. at 2m below bottom of the pit. In 1991 several times of slope sliding took place and caused struts broken on the raining season because no attention payed on results of the centrifugal tests.

The monitored data from the field were in accord with results of the centrifugal tests and calculations of the FEM.

## 6. CONCLUSION

(1). Having formed a series of geotechnical centrifuges in China, nowadays we are dealing with the geotechnical problems in both design and construction stage using the centrifugal model with advanced technique. Because of no experiences in construction of huge underground projects such as Xiajiahui metro station, the centrifugal model provides a useful method to research excavation in large scale to predict the influence on the environment and to compare with the numerical model, although there are still some troubles

remaining in making centrifugal models, measuring methods in accuracy, and simulating the procedure of the excavating process, etc..

(2). The results of the centrifugal tests are in accord with the monitored data in the field and became a valuable experience for such kind of excavating projects.

## REFERENCE

- Peck, R. B (1969). Deep excavations and tunneling in soft ground. 7<sup>th</sup> ICSMFE state-of-the-art volume (225—290).  
 Zhang, S. D and Chen, X. L (1987) Centrifuge tests of a large shaft. proceeding of the annual underground engineering conference in Shanghai (121—130).

## Excavation in soft clay using an in-flight excavator

T. Kimura, J. Takemura, A. Hiro-oka, M. Okamura & J. Park  
*Tokyo Institute of Technology, Japan*

**ABSTRACT :** A centrifuge excavator with which the process of excavation can be simulated in-flight was developed. With this excavator three different model tests were conducted; namely on unsupported excavation, and excavation with a supporting sheet pile wall with or without ties. Two different clay layers with increasing strength, one normally consolidated and the other overconsolidated, were dealt with. Deformations of clay and sheet pile walls, earth pressures on the walls and pore pressures in clay were measured during excavation. It has been found that undrained conditions can be assumed for excavation in soft clay. The importance of considering the strength anisotropy in the stability analysis has been pointed out. The results of centrifuge model tests are compared with field observations.

### 1. INTRODUCTION

Only a limited number of small scale model tests have been carried out to study the stability of excavated ground, although the problem is of overriding importance in countries like Japan and Singapore where major industrial development takes place in the coastal areas. This is simply because it is not possible to simulate prototype behavior correctly with small scale models due to the lack of stress similarity. The development of centrifuge modeling technique enabled us to reproduce prototype behavior using the small scale models.

Two types of centrifuge model tests have been previously conducted with respect to excavation. In the first type, a model for excavation prepared in the laboratory in advance is mounted on a centrifuge and then subjected to increasing centrifugal acceleration to cause failure (Lyndon and Schofield; 1972, Kimura et al.; 1993). The second type is to simulate the progress of excavation by replacing the part of soil to be excavated with a liquid with a unit weight identical to that of excavated soil and draining the liquid out of the areas to be excavated (Kusakabe; 1982, Bolton and Powrie; 1987). Either type, however, fails to provide accurate information with respect to the progress of deformations of a supporting wall and development of earth pressures or pore pressures during excavation, because actual excavation is not carried out in the tests. Discrepancy is more serious for extremely soft soil, in which soil-structure interaction plays a very important role.

The authors have developed an in-flight centrifuge excavator and published the results of first series of the tests (Kimura et al.; 1993). In this paper, an attempt was made to strike out the difference in behavior

between normally consolidated and overconsolidated clay strata using data obtained in the first series of the tests. Comparison of the results of centrifuge tests with field observations was also attempted.

### 2. CENTRIFUGE MODEL TESTS

#### 2.1 Centrifuge excavator

The in-flight excavator which the authors developed is illustrated in Fig.1. It consists of a movable table, a cutting blade and a soil retaining gate. The movable table can move back and forth on a pair of linear-way rails. The thrust is provided by a stepping motor through a timing belt and a pair of screw rods to the table. The vertical movement of the cutting blade and the soil retaining gate is conducted by worm gears built in to stepping motors. The details of the excavator

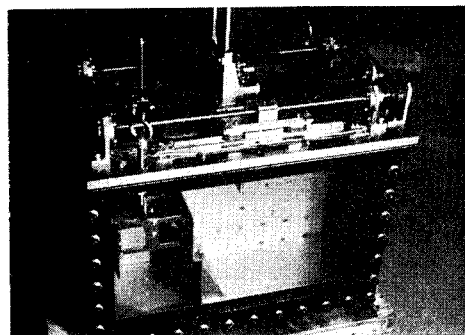


Fig.1 Centrifuge excavator

Table 1 Physical properties of kaolin clay

Specific gravity	(G <sub>s</sub> )	: 2.61
Liquid limit	(w <sub>L</sub> )	: 77.5%
Plastic limit	(w <sub>p</sub> )	: 30.3%
Compression index	(C <sub>c</sub> )	: 0.65
Swelling index	(C <sub>s</sub> )	: 0.10
Void ratio at 98kPa on N.C.line		: 3.05
K <sub>0</sub> for N.C.		: 0.6
Permeability at 98kPa on NC		: 2.0x10 <sup>-9</sup> m/sec

Table 2 Test conditions

Test No.	Model Ground	Acceleration	P <sub>c0</sub>	P <sub>0</sub>	Sheet Pile
SP00	uniform	50g	50kPa	10kPa	unsupported
SP01	NC	50g	10kPa	10kPa	without
SP02	OC	50g	30kPa	10kPa	without
SP03	NC	50g	10kPa	10kPa	unsupported
SP04	OC	50g	30kPa	10kPa	unsupported
SP05	NC	50g	10kPa	10kPa	tie backed
SP06	OC	50g	30kPa	10kPa	tie backed

P<sub>c0</sub>: pre-consolidation pressure at the surface

P<sub>0</sub>: surcharge pressure during test

tor can be found elsewhere(Kimura et al.;1993). The excavator is mounted on a steel-made strong box with 500mm in length, 360mm in depth and 150mm in width. The box has a diaphragm wall with 110mm in height at the position of 160mm away from the side wall as shown in Fig.1. Model ground is made in the space behind this wall and the space in front is left open to accommodate excavated soil.

Excavation proceeds while the centrifuge is in flight. First of all the cutting blade is pushed down into clay, the movable table is then pushed forward skimming off clay and finally excavated clay is pushed to be dumped in the open space. This cycle is repeated until excavation reaches a predetermined depth. The soil retaining gate supported by a screw rod moves up and down along the side wall of the soil box and diaphragm wall. When the cutting blade is lowered into clay to carry out excavation, the gate is also lowered so that the top of the gate comes just a little lower down than the level of the blade edge.

## 2.2 Soil

Kaolin clay with physical properties shown in Table 1 was used in the model tests. The results of undrained triaxial compression and extension tests conducted on K<sub>0</sub> consolidated specimens with OCR equal to 1.0 and 2.5 are illustrated in Fig.2. Compression strength is greater both for normally and overconsolidated specimens as in usual soft marine clays, exhibiting strength anisotropy. It is interesting to notice that positive pore pressures are registered even for the specimens with OCR equal to 2.5 both in compression and extension. The relationship between the rate of undrained strength to consolidation pressure,  $c_u/\sigma'_{vc}$ , and OCR for the clay is shown in Fig.3. The ratio of the rate in extension and compression, which is usually referred to as strength anisotropy factor  $m$ , is constant, 0.6, up to OCR equal to 3. The

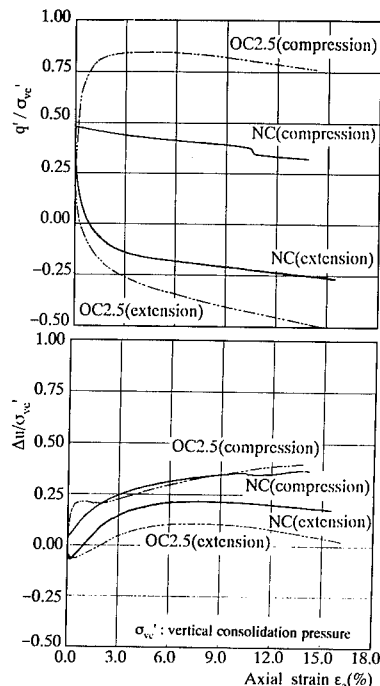


Fig.2 Results of triaxial tests for K<sub>0</sub> consolidated kaolin clay

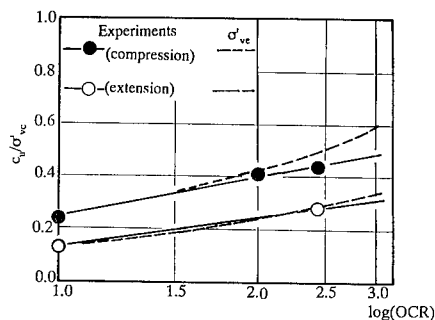


Fig.3 Undrained strength of kaolin clay

broken lines show the rate theoretically calculated assuming that the strength is in proportion to equivalent consolidation pressure  $\sigma'_{vc}$ . The theory compares reasonably well with observation, although the theory tends to give slight overestimation with the increase in OCR.

## 2.3 Test procedures and conditions

The stability of vertical cuts in soft normally consolidated(NC) and overconsolidated(OC) clay with undrained strength increasing with the depth was investigated with the newly developed centrifuge excavator described in 2.1. The strength profiles and OCR of models used in the tests are illustrated in Fig.4. For

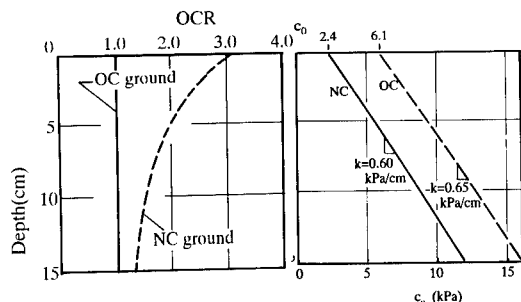


Fig.4 Undrained strength and OCR profile in model grounds

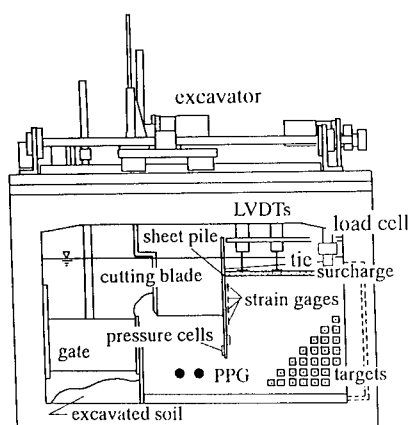


Fig.5 Test setup

these two types of model ground, excavation tests with three different supporting conditions were carried out; unsupported, supported by a sheet pile wall without ties and supported with a tie backed sheet pile wall. The test conditions are summarized in Table 2.

The procedures for preparing the models are as follows. First of all, an acrylic block was placed in the space for accommodating excavated soil, a 20mm thick layer of silica sand was laid on at the bottom of the strong box as a drainage layer. Slurry remolded at a water content 1.5 times the liquid limit was carefully deaired and poured into the strong box. Laboratory floor consolidation was conducted stepwise under a pressure of 10kPa for NC model ground and 30kPa for OC model ground. On the half way of consolidation process, consolidation was once stopped to allow pore pressure transducers (Druck;PDCR81) to be inserted into clay. Subsequently brass rods giving rise to a surcharge pressure equal to consolidation pressure on the lab floor in 50G field were placed at the surface and centrifugal consolidation was carried out in 50G to form clay layers with strength increasing with the depth. The OC model ground prepared in this way is equivalent to the NC model ground with preload of 20kPa.

On completion of centrifugal consolidation, the cen-

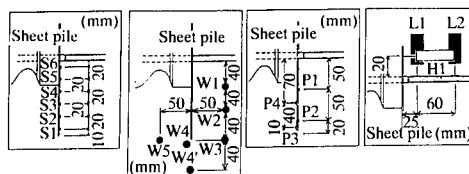


Fig.6 Position of various sensors

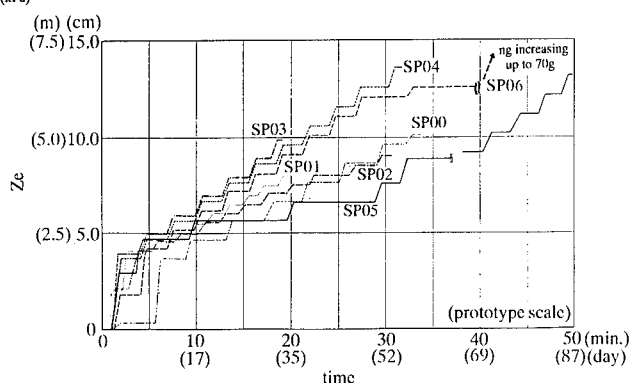


Fig.7 Progress of excavation

trifuge was stopped and the brass rods were removed. For supported excavation, a model sheet pile wall was inserted into clay. Finally surface markers were placed on the side face of clay. The model sheet pile wall used in the tests was made of aluminum with 2mm in thickness and 180mm in length. It was instrumented with six strain gauges and two earth pressure cells (Kyowa;PS-2KA) at each side of the wall as shown in Fig.5 and 6. The thickness of clay was 180mm and the total depth of the model ground, clay plus the drainage layer, was 200mm. The model sheet pile wall was pushed down to 120mm in clay at a distance of 140mm from the diaphragm wall. After all these preparation works, a layer of zircon sand giving a surcharge pressure of 10kPa in 50G was laid on at the surface of clay and LVDTs were placed at several locations. For the model sheet pile wall with ties, the wall was bound with the tie to a load cell to measure load in the tie. The excavator was then mounted on the strong box. A completed model is illustrated in Fig.5. The model was taken to the centrifuge and centrifugal consolidation was conducted once again.

Having confirmed dissipation of excess pore pressures, excavation was started following the procedures described in 2.1. Since it was extremely important to maintain the overall balance of the centrifuge, excavation was conducted under water without lowering the water table in the model. Hydrostatic pressures were identical in the front and back side of the sheet pile wall. Seepage or migration of pore water is caused only by excess pore pressures generated during excavation. Considering this, the authors take

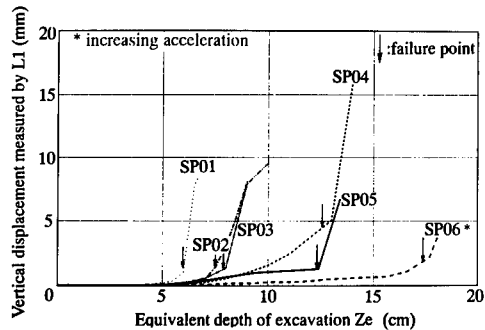


Fig.8 Progress of settlements measured by LVDT:L1

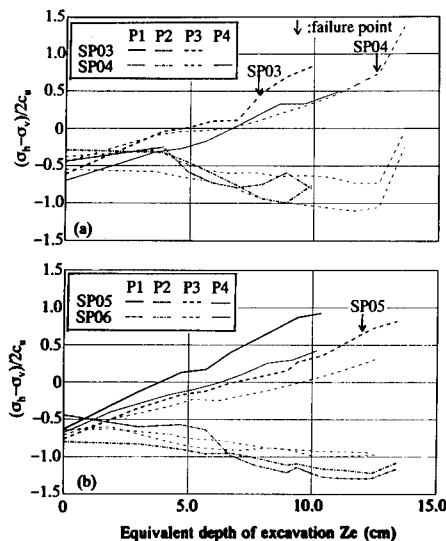


Fig.9 Variation of  $(\sigma_h - \sigma_v)/2c_u$  during excavation

a view that the existence of water does not change the essential features of excavation in soft clays and that the submerged unit weight  $\gamma'$  plays a substantial role in determining mechanical behaviour of soft clay in this test series.

The progress of excavation is shown in Fig.7. The horizontal axis  $z_e$  is an equivalent excavation depth defined by considering the effect of removing the surcharge as

$$z_e = p_0 / \gamma' + h \quad (1)$$

where  $p_0$  is the surcharge pressure equal to 10kPa and  $h$  the actual height of excavation. The height of excavation in one step was 5mm for the unsupported case and 10mm for supported excavation. In SP06 for supported excavation with ties in OC ground, the model ground was brought to failure by increasing centrifugal acceleration after having been left for 1 hour, equivalent to about 100 days in prototype scale, after excavation, since failure did not take place at the

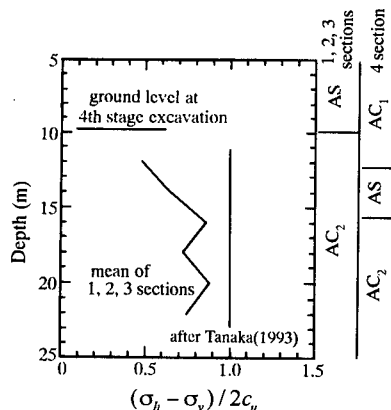


Fig.10 Observed horizontal earth pressure in passive side at construction site of Haneda airport

maximum height of excavation.

Measurements of horizontal earth pressures, pore pressures in clay, strains of the wall, settlements of unexcavated parts and horizontal movements of the model sheet pile wall were taken by using various probes shown in Fig.6. Measurements of deformations in clay were also conducted by photographing and water contents were measured after the tests.

### 3. TEST RESULTS AND DISCUSSIONS

#### 3.1 Deformations in clay and earth pressures

The progress of settlements measured with the LVDT located at 25mm away from the sheet pile wall is illustrated in Fig.8. The arrows in the figure indicate failure. For models with identical strength profile the depth of excavation causing failure becomes greater in the sequence of unsupported excavation, supported excavation without ties and with ties, indicating the effect of retaining soil. The magnitude of  $z_e$  corresponding to failure for OC ground is 1.3 to 1.6 times greater than that of NC ground, which shows the effect of preloading. In NC ground, a sudden increase in settlements takes place with the progress of excavation, while in OC ground, the increase is somewhat gradual. This difference in settlements can be explained by the results of triaxial tests shown in Fig.2 that the strain for failure in NC clay is much smaller than that for OC clay in the compression condition. Since the compression condition corresponds to the active condition, it is expected that an active zone is formed behind the sheet pile wall at small strains or early stages of excavation for NC model ground.

The variation of the ratio  $(\sigma_h - \sigma_v)/2c_u$ , that is the difference between the horizontal and vertical earth pressure divided by twice the undrained strength, is plotted against  $z_e$  in Fig.9. The ratio represents the extent of mobilization of shearing strength in clay in undrained conditions. The ratio assumes the value of 1.0 and -1.0 at full mobilization for the passive and



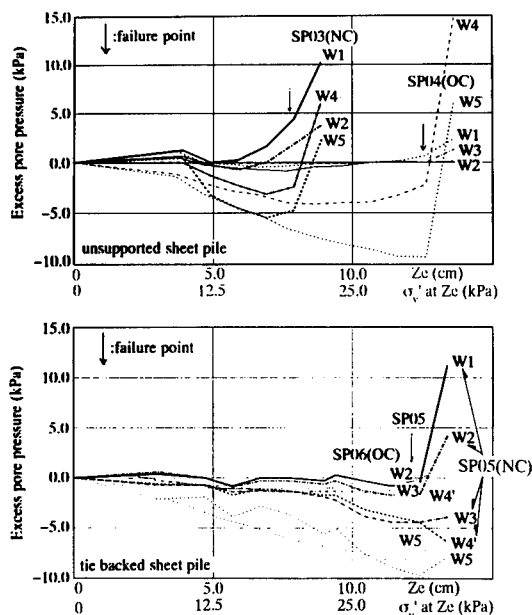


Fig.11 Variation of excess pore water pressures during excavation

active zone respectively. The compressive strength obtained from Fig.3 was taken as  $c_u$ . In all the cases the ratio at the back decreases towards the active state and the ratio at the front increases towards the passive state as excavation proceeds. At failure the ratio is approximately -1.0 in the active side and it is considerably smaller than 1.0 in the passive side. The ratio in the passive side continuously increases even at the stages when the ratio in the active side becomes constant. This confirms that the active state is achieved at smaller strains than the passive state.

In excavation works at the site of Haneda project, excessively large displacements of sheet pile walls took place. Tanaka(1993) examined the case and found out that the horizontal earth pressure in the passive side was much smaller than Rankine pressure as shown in Fig.10, although in the active side the pressure reached that of Rankine. He concluded that the strength anisotropy is responsible for this. A similar result was obtained also in this centrifuge model tests. As discussed in 2.2, the strength anisotropy factor for Kaolin clay used in the tests is 0.6. At failure in the passive side observed in the model tests, indicated by arrows in Fig.8, the ratio  $(\sigma_h - \sigma_v)/2c_u$  is approximately 0.6, reflecting the results of triaxial tests.

### 3.2 Pore pressures in clay

The measured variation of pore pressures with the progress of excavation is illustrated for the four supported cases(SP03 – SP06) in Fig.11. At stages before failure, the pore pressures measured with W5 located in the area beneath the bottom of excavation are negative and similar in magnitude. Negative pore

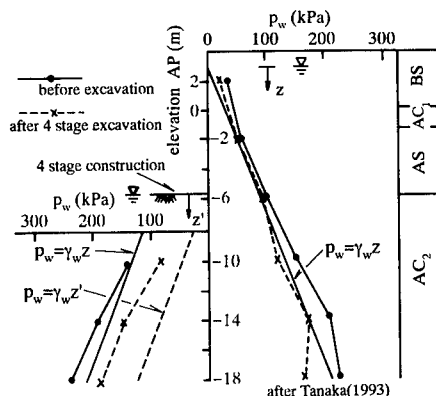


Fig.12 Observed pore pressure distributions at construction site of Haneda airport

pressures are generated because total mean stresses decrease due to excavation in this area. The magnitude of negative pore pressures is much smaller than the effective overburden pressure  $\sigma'_v$  lost in excavation as shown in the figure. The pore pressures measured with W1 and W2 located in the area behind the sheet pile wall are small. In this area the horizontal earth pressures decrease due to tilting of the sheet pile wall, leading again to the reduction in total mean stresses. The reason why large negative pore pressures were not built up in the areas of W5 and W1 and W2 may be that negative pore pressures were canceled out by positive pore pressures generated by shear deformations of clay in these areas. In fact, high positive pore pressures are generated even in the condition of extension for this Kaolin clay as can be seen from Fig.2.

Although failure was observed both in SP03 and SP05 for NC ground, there is a distinct difference in pore pressures in the active side. The pore pressures in SP03 start increasing before failure but in SP05 they show a sudden increase only at the point of failure. Suppression of shear deformations by the tie backed sheet pile wall is considered to be responsible.

Since the permeability of the Kaolin clay is not very small as shown in Table 1, it may not be possible to assume that the undrained condition can be maintained in this model tests, if large negative pore pressures are registered. This can certainly happen for heavily overconsolidated clay. Fortunately this is not the case with soft clays commonly found in coastal areas in Asian regions as shown above. This justifies the assumption of undrained condition for soft clay during excavation and validates the stability analysis based on total stresses. Pore pressures measured at the Haneda site are illustrated in Fig.12, which indicates that negative pore pressures are not generated. Tanaka(1993) drew a conclusion from this that the decrease in the undrained strength due to swelling can be neglected for soft clays.

Failure did not take place even at the maximum height of excavation in SP06, the case of excavation

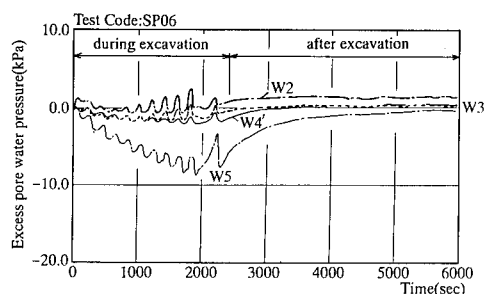


Fig.13 Variation of excess pore water pressure during and after excavation

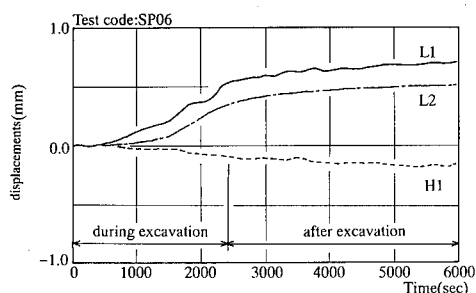


Fig.14 Observed displacements during and after excavation

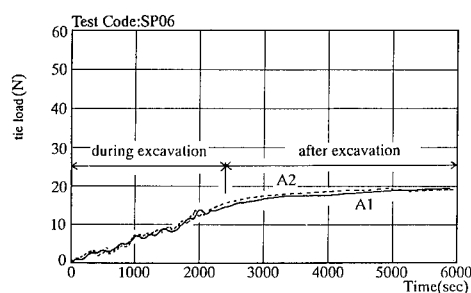


Fig.15 Variation of tie loads during and after excavation

in OC ground with tie backed sheet pile wall. As mentioned earlier, the model was brought to failure by increasing centrifugal acceleration after having been left for 1 hour in 50G after excavation. As a matter of fact, considerable consolidation or swelling can take place during this period, because 1 hour in 50G is equivalent to 100 days in prototype scale. The measured variation of pore pressures during this period is shown in Fig.13. Although the negative pore pressure registered with W5 has dissipated, pore pressures in other locations show no change, indicating that the change in effective stresses in clay during this period is negligible. The deformations of

unexcavated parts and the wall and measured tie loads are given in Fig.14 and 15 respectively. Slight increase in the deformations and loads seem to be also related to the dissipation of negative pore pressures. At 6000 seconds, all the quantities tend nearly to constants, indicating that the excavated model ground is stable in the sense of long term. The model failed at 68G in the subsequent test, implying that the safety factor of the excavated model ground at 50G was at least 1.36. This leads to an important conclusion that, for excavation in soft clay which generates positive pore pressures in shearing, the safety factor of 1.4 for short term stability guarantees the stability for long term.

#### 4. CONCLUSIONS

The stability of vertical cuts in soft clay under different conditions was investigated using an newly developed in-flight centrifuge excavator. Conclusions drawn from this study are as follows.

- (1) Mechanical behavior observed in this centrifuge model tests using the in-flight excavator agrees well with field observations, justifying the tests of this type.
- (2) The advantages of preloading, supported excavation and use of tie backed sheet pile wall have been confirmed.
- (3) It has been confirmed that the importance of considering the strength anisotropy in analyzing the stability in excavation. This is particularly important for normally consolidated clay, because it has a small value of  $K_0$ .
- (4) For normally consolidated or moderately over-consolidated soft clay which generates positive pore pressures in shearing, negative pore pressures develop only in the area beneath the bottom of excavation. However, since the magnitude is small, no substantial decrease in the effective stresses of clay takes place after excavation. The safety factor of 1.4 for short term stability seems to guarantee the stability for long term.

#### REFERENCES

- Bolton, M.D. and Powrie, W. (1987). The collapse of diaphragm walls retaining clay. *Geotechnique*, Vol.37, No.3, pp.335-353
- Kimura, T., Takemura, J., Hiro-oka, A., Suemasa, N. and Kohda, M. (1993). Stability of unsupported and supported vertical cuts in soft clay. *Procs. 11th Southeast Asian Geotech. Conf.*, pp.61-70
- Kusakabe, O. (1982). Stability of excavation in soft clay. Ph.D thesis, Cambridge University
- Lyndon, A. and Schofield, A.N. (1970). Centrifuge model test of short term failure in London clay. *Geotechnique*, Vol.20, No.4, 440-442
- Tanaka, H. (1993). Passive earth pressure and shear strength in braced excavation. *Procs. of Geotech. Sympo., Tyubusibu, JSMFE*, pp.37-42 (in Japanese)

## Modelling diaphragm wall installation and excavation processes

W. Powrie, D.J. Richards & C. Kantartzi

Queen Mary and Westfield College, University of London, UK

**ABSTRACT:** Techniques and apparatus for centrifuge modelling of diaphragm wall installation processes and sequences of excavation and propping are described, and their success is discussed with reference to centrifuge test data.

### 1 INTRODUCTION

Designers of diaphragm-type retaining walls in clay soils are becoming increasingly aware of the effects of construction activities on the performance of the structure. Ground movements during wall installation may be important in their own right, while the changes in lateral stress which occur during slurry trenching and concreting can have a significant effect on post-excavation wall movements, bending moments and prop loads. For multi-propped walls or walls propped at formation level, ground movements are also influenced by the detailed sequence of excavation and propping in front of the wall, and whether or not temporary props are used.

In order to investigate these issues, two series of centrifuge model tests have been carried out at Queen Mary and Westfield College. Techniques have been developed to simulate the excavation under bentonite slurry and subsequent concreting of a diaphragm wall panel in clay; and the installation and/or removal of props at various levels during excavation in front of an in situ wall which is already in place. In this paper, the centrifuge modelling procedures are described and discussed, with reference to typical data from each series of model tests.

### 2. DIAPHRAGM WALL INSTALLATION

#### 2.1 Model preparation and geometry

The centrifuge model for the diaphragm wall tests (Figure 1) was formed from a block of speswhite kaolin clay, of plan dimensions 200mm x 550mm and depth 285mm, contained within an aluminium strongbox with a perspex viewing window in the front face.

The sample was prepared by one-dimensional

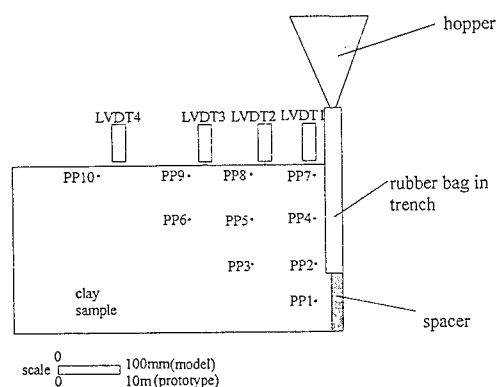


Figure 1. Centrifuge model for diaphragm wall tests.

compression from a slurry of water content 100% to a vertical effective stress of 1250kPa. The sample was then allowed to swell back to a vertical effective stress of 250kPa before being trimmed to the required depth of 285mm. The unit weight of the clay at this stage was approximately  $17.5\text{kN/m}^3$  (unit weights are quoted at normal gravity). A 185mm-deep slot, simulating the excavation for the diaphragm wall, was cut at the right-hand edge of the clay sample, and the clay removed was replaced by a rubber bag filled to a level of approximately 90mm above the soil surface with sodium chloride solution of unit weight  $11.4\text{kN/m}^3$ . A rigid spacer below the slot was used to reduce the effective half-width of the trench to 5mm at model scale. At a scale of 1:100, the slot represented one half of a 1m-wide diaphragm wall trench, 18.5m deep. The model was instrumented with Druck miniature pore water pressure transducers, and displacement transducers (lvdt's) to monitor the movement of the soil surface. Black plastic marker beads were embedded into the visible face of the model, so that soil movement patterns could be deduced from a videotape recording of the model made during the centrifuge test.

The stress history of the clay sample was intended to simulate that of an overconsolidated clay deposit in the field. The sample was removed from the consolidation press at a vertical effective stress (250kPa) greater than that at the base of the sample under equilibrium conditions in the centrifuge at 100g, so that the strain path experienced by the entire sample immediately prior to the simulation of excavation would have been one-dimensional vertical swelling. The sample was allowed to swell in the centrifuge at 100g for a period of 2-3 hours, until steady hydrostatic pore water pressures had been established and the rate of settlement of the soil surface was negligible. Water was supplied to both the soil surface and a sand drain at the base of the sample. The lateral stresses imposed on the soil adjacent to the trench at the end of the initial period of swelling are similar to those typically observed in overconsolidated clay deposits in the field.

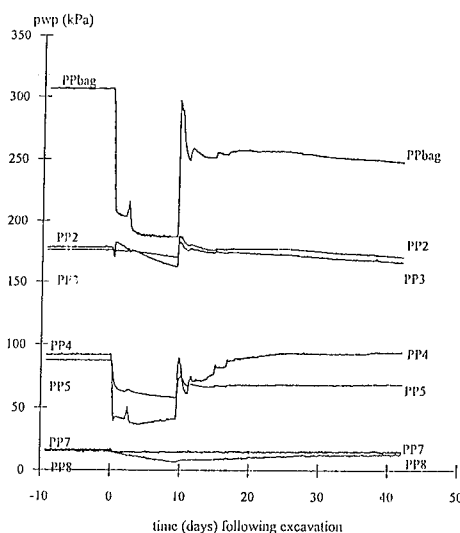


Figure 2. Changes in pore water pressure during excavation under bentonite and concreting.

## 2.2 Simulation of slurry trench excavation and concreting

When equilibrium conditions in the clay sample had been established, the reduction in horizontal total stress which occurs during excavation of a diaphragm wall trench under bentonite slurry was simulated by draining the sodium chloride solution down to the level of the soil surface through a valve-controlled overflow pipe. The fluid remaining in the rubber bag was then diluted with fresh water to a unit weight of 10.6 to  $10.8\text{kN/m}^3$ , which is typical of bentonite support slurries used in practice. A shutter at the base of a hopper mounted above the trench was then opened using a pneumatic piston, allowing a mixture of iron powder, plaster of Paris, cement and fine sand to fall into the rubber bag. The mixture was designed to have a unit weight when deposited under water of approximately  $24\text{kN/m}^3$ , and to set in about 10 minutes, modelling the concreting phase of diaphragm wall installation. Pore water pressures and soil movements were monitored during excavation and concreting, and for a period of approximately 30 minutes thereafter.

### 2.3 Typical results

Typical results are shown in Figure 2 (changes in pore water pressure during excavation under bentonite slurry and concreting) and Figure 3 (settlement profiles).

During excavation, the pore water pressures closest to the trench fall as a result of the reduction in lateral stress, and the soil surface settles considerably. During concreting, the pore water pressures tend to return towards their initial values, and a small recovery of the soil surface is apparent. These results are comparable with field observations (Symons & Carder, 1992) and indicate that appropriate changes in lateral stress are being transmitted to the soil.

### 2.4 Discussion

The verisimilitude of the model depends largely on the suitability of the stresses and drainage boundary conditions imposed at the interface between the soil and the trench at various stages. Generally, the extent to which moisture transfer from the trench to the soil occurs during the installation of a diaphragm wall panel is very limited, and the soil further than 50mm (at field scale) or so from the trench remains unaffected. It was therefore considered appropriate to model the interface between the soil and the trench as effectively impermeable.

The shear strength of a 4% bentonite suspension in water (which is typically used as a slurry support in practice) is very low, and there seems little doubt that the lateral stresses exerted on the soil during the slurry trench phase of diaphragm wall construction correspond to the

fluid pressure of the bentonite suspension. The lateral stresses exerted during concreting, however, are rather less certain, and may be smaller than the fluid pressure of wet concrete due to the strength of the mix, or because the concrete at the base of the panel begins to set before the pour is completed (Clayton & Milititsky, 1983). In the centrifuge, concreting was simulated using a particulate material rather than a fluid. The lateral stress distribution imposed on the soil adjacent to the trench in the model at this stage would therefore be expected to be similar to that imposed in the field, except perhaps for a transient effect because the simulated concrete was placed initially as a hydraulic fill rather than using a tremie pipe.

The time taken to lower the level of the salt solution in the rubber bag and dilute it with fresh water was between 50 and 60 seconds, which corresponds to between 6 and 7 days at full scale. The simulated concrete took approximately 7-10 minutes to set, corresponding to 50-70 days at field scale. These times are rather longer than would be usual in reality: 1 day for the excavation of the trench under bentonite (ie 10 seconds at model scale), and 30 days or so for the concrete to set (ie 5 minutes at model scale), are probably more typical. This means that the degree of excess pore water pressure dissipation which occurred during excavation and concreting in the model is greater than that which would occur in the field. The more significant discrepancy is in the time taken to excavate the trench. In a problem such as this, settlements due to shear as the clay softens are usually more significant than swelling as negative excess pore pressures dissipate. Ground movements will therefore tend to be larger than if the simulated excavation of the trench had been carried out more quickly.

Centrifuge model tests using the apparatus shown in Figure 1 have been carried out with different initial groundwater levels, different diaphragm wall panel widths (to investigate three-dimensional effects), and different initial earth pressure profiles. The initial earth pressure profile is altered by changing the excess height and the density of the fluid in the rubber bag: this is discussed more fully in Section 3.4.

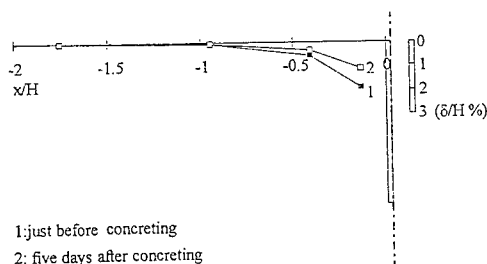


Figure 3. Surface settlements

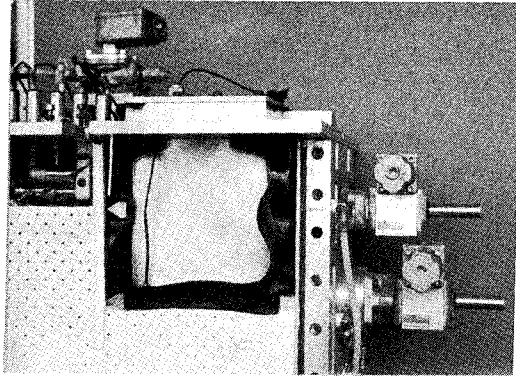


Figure 4. Cross section through model

Further tests are currently in progress, in which lateral total stresses are measured using Kyowa miniature pressure cells.

### 3. EFFECTS OF PROPPING SEQUENCE

#### 3.1 Model preparation and geometry

The centrifuge models used to investigate the effects of propping sequences during excavation in front of an in situ wall were made from blocks of speswhite kaolin of dimensions 200mm x 550mm on plan x 300mm deep. The clay was consolidated to a maximum vertical effective stress of 1250kPa and allowed to swell back to a vertical effective stress of 80kPa. This was so that during reconsolidation in the centrifuge, the soil would generally move downward relative to the wall, preventing the possible premature mobilization of passive side soil/wall friction on excavation in front of the wall which might occur if the most recent relative movement had been in the opposite sense. On removal from the consolidation press, a slot was cut in the clay into which the model wall was inserted. The excavation in front of the wall was also made at this stage, the soil removed being replaced by two interconnected rubber bags filled with zinc chloride solution mixed to the same unit weight as the kaolin sample ( $17.5\text{kN/m}^3$ ). Props were installed in front of the wall, both at the level of the retained soil surface and just above dredge level. A cross sectional view of the model is

shown in Figure 4, in which the rubber bags are cut away to reveal the stainless steel displacers used to reduce the volume of zinc chloride solution required.

Each prop was supported in linear bearings at two locations, and passed through a Bosch pneumatic locking device on the outside of the strongbox (Figure 6). During reconsolidation in the centrifuge, the locking devices were held in the open position, so that the props were free to slide and would not support the wall. Water was supplied to the retained soil surface, the excavation cavity and a sand drain at the base of the sample, all at the piezometric level of the retained soil surface.

The model was instrumented with Ivd't's, Druck miniature pore water pressure transducers and black plastic marker beads. The model retaining wall was strain gauged to measure bending moments at six places along its depth, and two load cells were incorporated into each prop.

The geometry of the 1:100 scale model is based on a full-size retained height of 10m (after construction of the carriageway slab). The strong-box end plate represents the plane of symmetry between two diaphragm walls on either side of a road cutting. The half width of the carriageway is 21.5m at field scale, which perhaps represents a practical upper limit.

#### 3.2 Simulation of excavation and propping

At the end of the reconsolidation phase, the water supplies to the excavation and to the sand drain at the base of the sample were switched off, and the locking device on the top prop was activated to hold the prop in position, representing the installation of a structural roof slab. The water level in front of the wall was then lowered to the excavated soil surface, and the zinc chloride solution was drained simultaneously from the rubber bags into catch tanks located outside the strongbox, to simulate excavation in front of the wall. Once the zinc chloride solution had drained away (as indicated

by a pressure transducer in one of the rubber bags), the bottom prop was locked in place, representing the installation of a carriageway prop and the construction sequence was complete.

The rate of excavation was controlled by a pre-set needle valve connected in line between the outlet from the rubber bags and the solenoid-operated drain valve. After excavation, the test was continued for a number of hours, to observe changes in prop loads, wall bending moments, pore water pressures and soil movements as long-term equilibrium conditions were approached.

### 3.3 Typical results

Figure 5 shows the development of prop loads during and after excavation in front of the wall.

These results demonstrate that the prop bearings and locking devices function as required, preventing the development of prop loads until after each prop would have been installed in a field situation. The magnitudes of the prop loads are broadly comparable with those from finite element analyses of a similar construction sequence and excavation geometry (Powrie & Li, 1991).

### 3.4 Discussion

Perhaps the main criticism of this modelling technique is that it was necessary to install the wall prior to reconsolidation of the clay sample in the centrifuge. This means that the changes in stress and pore pressure which would in reality result from wall installation must be either ignored or simulated.

There is a growing body of data which suggests that after the excavation under bentonite and concreting of a diaphragm wall panel, the pore water pressures return approximately to their initial values (Figure 2 of this paper and Symons & Carder, 1992). The changes in lateral effective stress during wall installation are rather less certain, and it would perhaps in any case be

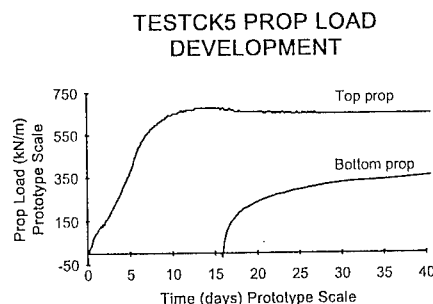


Figure 5. Prop load development

unwise to generalize too broadly. In the present tests, it has been assumed that the post-installation lateral stresses can reasonably be represented by an earth pressure coefficient of unity. This is not a necessary assumption, however, and some tests have been carried out to simulate the high pre-excavation earth pressure coefficients which may still be present following the installation of, for example, a wall formed from cased bored piles. The increased pre-excavation lateral stresses were achieved by extending the rubber bags to 115mm above the top of the retained soil surface. By filling the rubber bags to some level above the retained soil surface, the horizontal stresses imposed on the wall during reconsolidation will be increased. The density of the fluid must be reduced to give  $K=1$  at the bottom of the rubber bag, so that the vertical stresses inside and outside the bag are equal. The criticism remains that any reduction in lateral stress supposedly due to wall installation is imposed across the entire model, whereas in reality it would be confined to the zone of soil near the wall. This will not militate against the validity of the results, however, because the behaviour of the wall is influenced primarily by the soil closest to it.

The time taken to drain the bags varied for each test despite the needle control valve having been calibrated under a 10m head of zinc chloride solution to give an intended excavation time corresponding to 30 days at field scale. The longest time taken for excavation corresponded to 41 days at field scale, and the shortest time to 2.5 days, which was due to the drainage pipe fracturing when the control valve was switched

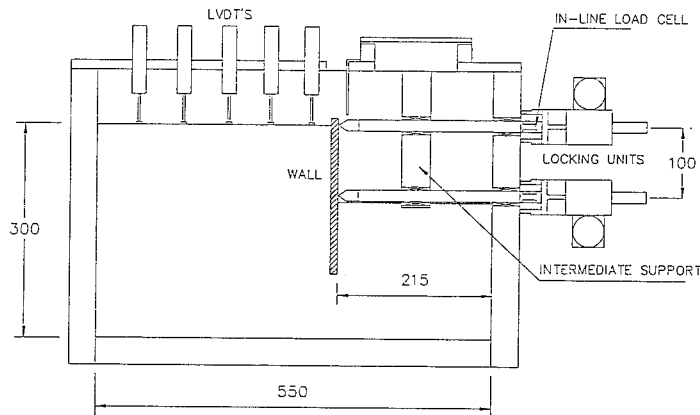


Figure 6. Cross section through multi-propped retaining wall centrifuge model.

on. In situations such as this, where the sequence of operations on site involves a delay between the start of excavation and the provision of support, ground movements may be influenced to some extent by the timescale of events. The fact that the centrifuge tests were carried out with the retained soil surface flooded (ie acting as a drainage boundary) will tend to result in a higher sensitivity to variations in excavation time in the centrifuge model than in reality. .

#### 4. CONCLUSIONS

Techniques have been developed to simulate the excavation under slurry and concreting of a diaphragm wall trench, and the installation of props in a realistic construction sequence during excavation in front of a wall which is already in place. The well-known method of simulating excavation during a centrifuge test by draining a fluid from a rubber bag has been used extensively in the model tests discussed in this paper. By choosing appropriate fluid densities and excess fluid levels above the soil surface, a variety of pre-excavation lateral stress profiles has been simulated. Experimental results from tests indicate that the techniques are satisfactory. However, the control of the timing of construction events can be difficult. Differences in timing can lead to variations in the ground

movements which occur while the excavation is only partly supported, particularly when there is a close drainage boundary in the model. This is a factor which must be taken into consideration in the interpretation of centrifuge test results and their comparison with field data.

#### ACKNOWLEDGEMENTS

The work on diaphragm wall installation effects was carried out with the financial support of the Science and Engineering Research Council. The work on excavation and propping sequences was carried out under contract to the Transport Research Laboratory. The views expressed in this Paper are not necessarily those of the Department of Transport. The authors are grateful to Drs S A Jefferis, I F Symons and R N Taylor, and Messrs R Nelson, B Nicholson and H Skinner for technical advice and assistance.

#### REFERENCES

- Clayton, C R I & Milititsky I (1983). Installation effects and the performance of bored pile in stiff clay. *Ground Engineering*, pp17-22.
- Powrie, W & Li, E S F (1991). Finite element analyses of an in situ wall propped at formation level. *Geotechnique* 41 No. 4, pp499-514.



Symons, I F & Carder, D R (1992). Stress changes in stiff clay caused by the installation of embedded retaining walls. Proc Int Conf on Retaining Structures, Cambridge.

## Deformation and failure characteristics of vertical cuts and excavations in clay

Y. Toyosawa, N. Horii, S. Tamate & S. Hanayasu

*Research Institute of Industrial Safety (RIIS), Ministry of Labour, Tokyo, Japan*

S. K. Ampadu

*University of Science and Technology, Kumasi, Ghana (Presently: RIIS, Japan)*

**ABSTRACT:** To study the un-supported trench deformation characteristics and failure mechanisms due to excavation, centrifuge model tests on remoulded kaolin were undertaken. Two types of tests were carried out in the centrifuge. In the first series, trench excavation was simulated by the in-flight draining away of a heavy liquid from a trench at a predetermined acceleration. In the second series, the acceleration was increased until failure occurred in the model vertical cut. The progress of deformation during excavation was obtained from the displacement of targets on the model measured from a sequence of photographs taken at intervals of about 0.3 seconds. From the calculated strains the development of  $\gamma_{max}$  up to collapse was evaluated. Good agreement was obtained between the observed circular failure mode and the results of analysis using the circular arc method and strength parameters obtained from  $K_0$  consolidated triaxial compression tests on the same material.

### 1. INTRODUCTION

Accidents due to trench failure frequently occur on construction sites. The available statistics show that of all fatal accidents during trench excavation in Japan, over 90% occurred as a result of collapse of unsupported or insufficiently supported trench walls, (Toyosawa et al., 1993). The need to decrease these accidents is currently a major concern not only in Japan, but in several other countries as well. For the purpose of establishing effective countermeasures, it is necessary, therefore, to first of all understand the failure mechanisms involved. This paper focuses on the pre-collapse deformation behavior and failure mechanism of unsupported trench as observed in centrifuge tests.

In general, in order to simulate the excavation process in centrifuge model tests, one of four methods may be used: (1) simulating the progress of excavation by draining a heavy fluid, (2) simulating excavation by increasing centrifugal acceleration, (3) simulating the excavation by removal of a bag of the material from the excavation area, Azevedo (1983), and (4) using an in-flight excavator with a moveable

blade, Kimura et al. (1993). In this investigation, two series of model tests using methods (1) and (2) were carried out on samples of remoulded kaolin clay. In method (1), the rate of excavation in the prototype can be fairly well simulated and the effective stress equilibrium conditions can also be sustained.

Based on the results of these centrifuge model tests, the deformation characteristics and the progress of failure in these slopes were studied. Slope stability analyses using the circular arc method was performed on the prototype. The undrained shear strength used in the stability analysis was obtained from triaxial compression tests.

### 2 DESCRIPTION OF TEST EQUIPMENT

The specifications and dimensions of the RIIS centrifuge used in this investigation are shown in Fig. 1. The centrifuge has a maximum acceleration of 200G and a maximum payload of 500 kgf.

Fig. 2 is a schematic diagram of the layout of the recording system of the centrifuge. A 35

aluminium targets were set at all cross lines of the mesh. Figs. 4 and 5 show the layout of the model excavations and the mesh. For the trenches, i.e., Fig. 4, each trench was supported by a 0.2 mm thick rubber bag filled with a heavy fluid (zinc chloride) which has been prepared to have the same unit weight as that of the kaolin clay. The model was then set in the strong box which is 500 mm long, 450 mm deep and 200 mm wide.

### 3.2 Centrifuge model tests

Two types of centrifuge model tests were performed. The first type of centrifuge model test was performed on trenches of the type shown in Fig.4 and are referred to as the TRE series in this paper. In this type of test, after mounting the strong box in the centrifuge the accel-

Table 1. Index properties of the kaolin clay

Liquid limit	86.9%
Plastic limit	34.7%
Plastic index	52.2
Specific gravity	2.69
Grain size distribution	Silt 12% Clay 88%

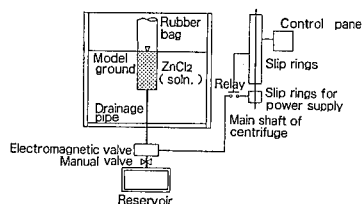


Fig.3 System for simulation of excavation

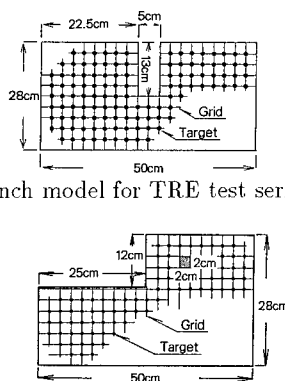


Fig.4 Trench model for TRE test series

664

ation was gradually increased until the designated acceleration,  $G$ , was attained. This designated acceleration was then maintained constant and trench excavation was simulated in-flight by draining away the heavy fluid from the bag at the predetermined rate. The set up for the simulation of in-flight excavation is shown schematically in Fig. 3. The specimen characteristics as well as the centrifuge test conditions and a summary of the test results are shown in Table 2. It may be seen from the table that the rate of excavation in the model, i.e., the rate of draining away the fluid ranged from as slow as 1.1 mm/sec in test TRE3 to as fast as 11.1 mm/sec in test TRE4. Using centrifuge scaling laws, these correspond to rates of excavation in the prototype of 0.5 m and 4 m per 8 hour work day respectively.

In the second type of tests performed in the centrifuge called the SLV test series, slopes of the type shown in Fig. 5 were used. The acceleration was continuously increased until complete collapse of the slope occurred. The approximate values of the acceleration at which collapse was observed and the corresponding

depth of the prototype excavation are also tabulated in Table 2.

In both series of tests, photographs of the mesh on the model face were taken at every rotation of the centrifuge. These photographs were later used for the analysis of the failure mode as explained later. At the end of the test, the water content at various heights of the model was measured. The average values are shown in Table 2 and the distribution was found to be uniform implying fairly uniform strength.

### 3.3 Triaxial Compression Tests

A series of triaxial compression tests were performed on samples of the same clay reconsolidated along both isotropic and approximate  $K_0 = 0.70$  reconsolidation stress paths to mean effective pressures of 1.6 kgf/cm<sup>2</sup> for the  $K_0$  specimens and 2.0 kgf/cm<sup>2</sup> for the isotropic specimens. These consolidation pressures correspond to the same effective vertical stress of 2.0 kgf/cm<sup>2</sup>. The test conditions and a summary of the results are given in Table 3.

Table 2. Summary of test conditions and results

Test Name	$\sigma'_{vp}$ <sup>a</sup> kgf/cm <sup>2</sup>	$w$ <sup>b</sup> %	$G$ <sup>c</sup> g	Rate of excavation		Depth of excavation		Progress of failure kgf/cm <sup>2</sup>	$c_u$ <sup>d</sup>	$(F_s)_{min}$ <sup>e</sup>
				Model mm/sec	Prototype cm/hr	Model cm	Prototype m			
TRE1 <sup>f</sup>	1.5	63.3	50	3.4	24	—	—	Sequential collapse of both sides	—	—
TRE2	1.5	57.7	50	5.6	40	12	6.0	Wedge type collapse, one side only, shear band observed at opposite toe	0.29	1.12
TRE3	2.0	54.6	70	1.1	6	14	9.1	Wedge type collapse of both sides	0.36	0.94
TRE4	2.0	55.1	80	11.1	50	12	9.6	Wedge type collapse, one side only, shear band observed on opposite toe	0.38	0.92
TRE5	2.2	53.2	80	8.0	36	12	9.6	Circular arc type collapse, shear band at both toes, propagated gradually, collapse on both sides	0.42	0.99
SLV1	1.5	59.6	55	NA <sup>g</sup>	NA	12	6.6	Circular arc type collapse, shear band propagated gradually.	0.27	0.97
SLV2 <sup>h</sup>	1.5	57.6	55	NA	NA	12	6.6		0.27	0.96
SLV3	2.0	56.6	80	NA	NA	12	9.6		0.36	0.86

<sup>a</sup>Preconsolidation pressure

<sup>b</sup>Average water content at the end of test

<sup>c</sup>Acceleration during test, constant for TRE test series. For SLV tests tabulated values are approximate values at which collapse

was observed

<sup>d</sup>Obtained from  $c_u/\sigma'_{vp} = 0.18$  for TRE3 and SLV tests and 0.19 for other tests

<sup>e</sup>Safety factor for critical circle

<sup>f</sup>Collapse occurred as soon as drainage of fluid started

<sup>g</sup>Not applicable

<sup>h</sup>This model ground was reconsolidated in the centrifuge at 100g for 40 hours before trimming.

## 4 ANALYSIS AND DISCUSSION OF TEST RESULTS

### 4.1 Sequence of failure

Typical photographs of the slope at various stages of the test are shown in Figs. 6 and 7 for TRE and SLV test series respectively. Figs. 6(a) and (b), respectively, are photographs showing the deformation of the model in test TRE4 just before and just after the appearance of the shear band. For all TRE tests except TRE1, it was observed that the trenches collapsed when drainage of the fluid was nearly completed. For TRE1 collapse occurred soon after the start of drainage. Failure was initiated when the face of the trench bulged into the excavation. For tests TRE2 and TRE4, while one side of the trench wall collapsed the other side remained stable, (Fig. 6(b)). Shear bands, however, were observed at the toe of the stable side. The observed failure surfaces in the TRE series can be classified as either wedge type in which the resulting surfaces were nearly linear as was observed in tests TRE2 and TRE4 or circular arc as was observed in TRE5.

Fig. 7 are photographs showing the displacement at different accelerations of the model slope during test SLV1 near failure. In this test series, it was observed that at the initial stage of failure, the toe of the vertical cut moved inwards as shown in the photograph of Fig. 7(b). The failure line then propagated upwards until collapse. The same failure pattern was observed for all the SLV test series irrespective of differences in the strength of ground. The failure surfaces were all circular arc in the SLV test series.

### 4.2 Behavior of strain development

From the negative film of the photograph taken by the 35 mm camera the coordinates of positions of the targets were measured using a film motion analyzer with an accuracy of 0.02mm. Using these coordinates, the displacements of the targets were calculated and the strains in the model ground were computed from triangular elements of the mesh. The average strain from four targets of the original square was used as the representative strain of that square.

Figs 8 to 10 show the contours of maximum shear strain, in percent, during trench excavation for tests TRE2 and TRE4 respectively. These figures illustrate the development of strain prior to failure. Two stages in the development can be observed. The first stage, as shown Figs. 8(a) and 9(a) involves the development of a fairly uniform strain over a relatively large area behind the trench wall as excavation progressed. The second stage involves the concentration of strains near the toe of the slope as

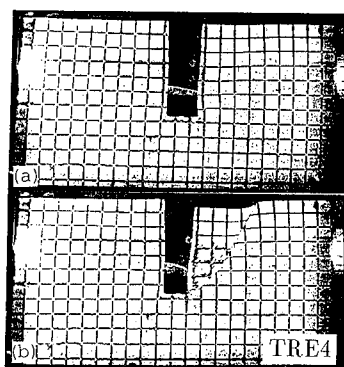


Fig.6 Model just before and just after collapse.

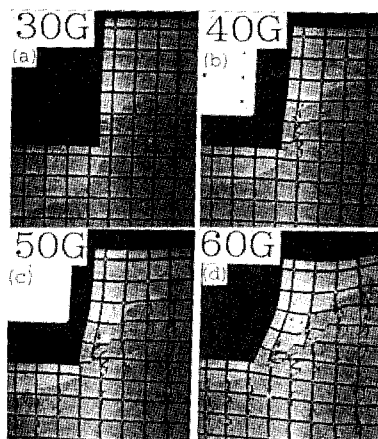


Fig.7 Sequence of failure in vertical cut.(SLV1)

Table 3. Summary of conditions and results of triaxial compression tests

Test Name	K <sup>a</sup>	w <sup>b</sup> %	$\sigma'_{vc}$ <sup>c</sup> kgf/cm <sup>2</sup>	$\dot{\epsilon}_a$ <sup>d</sup> %/min	$c_u$ <sup>e</sup> kgf/cm <sup>2</sup>	$c_u/p'_c$	$c_u/\sigma'_{vc}$
IS20S2	1.00	49.2	2.0	0.02	0.43	0.22	0.22
AS20S2	0.70	52.8	1.6	0.02	0.37	0.23	0.19
AS20S5	0.70	52.9	1.6	2.00	0.41	0.26	0.21

<sup>a</sup>K= $\sigma'_h/\sigma'_v$  during re-consolidation

<sup>b</sup>Water content at end of test

<sup>c</sup>Preconsolidation pressure

<sup>d</sup>Strain rate during triaxial compression

<sup>e</sup>Undrained shear strength,  $c_u = q_{max}/2$

shown in Fig. 8(b) and the appearance of slip lines first at the toe and finally its propagation to the surface of the ground. Depending on the strength of the model ground, different magnitudes of maximum strain were recorded as shown in Figure 8(a) and 9(a) for models TRE4 and TRE2 respectively.

For the vertical cuts, it was observed that the strain concentrated around the toe as the acceleration was increased as shown in Fig. 10. The development of strain in TRE tests is therefore, different from that in SLV tests.

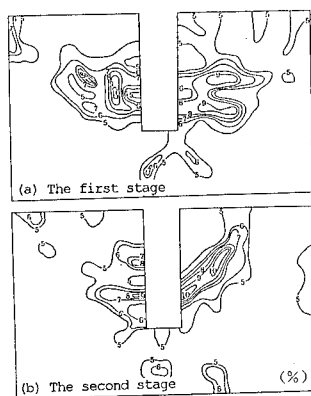


Fig.8 Contours of maximum shear strain during trench excavation (TRE2)

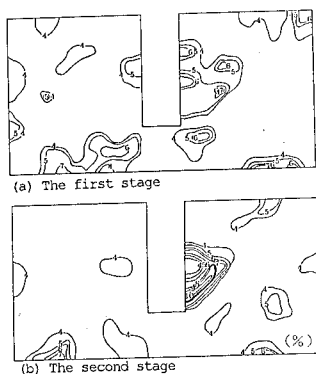


Fig.9 Contours of maximum shear strain during trench excavation (TRE4)

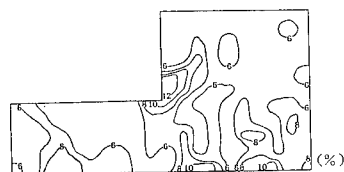


Fig.10 Contours of maximum shear strain during increasing acceleration (SLV3)

#### 4.3 Slope stability analysis

Figs. 11 (a) and (b) show the stress paths and the stress-strain curves respectively during triaxial compression. The deviator stress and the mean effective pressure are normalised by the consolidation pressures,  $p'_c$ . Fig. 12 shows the dependency of the normalised undrained shear strength,  $c_u/\sigma'_{vc}$ , on the strain rate. Shown in the same figure are the results of an investigation into the effect of strain rate on the same type of kaolin reported by Mukabi et al. (1991). The results of that study confirms the trend of increasing undrained strength with increasing strain rate as observed in this study. The figure also shows some anisotropy in strength in terms of  $c_u/\sigma'_{vc}$ .

The selection of the most appropriate strain rate for field loading has been the subject of much debate. The results of the analysis of the rate of maximum shear strain development at the toe of the model in tests TRE3 and TRE4 showed that the strain rate may be considered uniform only during the initial stages of the test. As failure approaches the strain rate increases. The average maximum shear strain rate in the model was about 0.0024%/min for test TRE3 and 0.024%/min for TRE4, the ex-

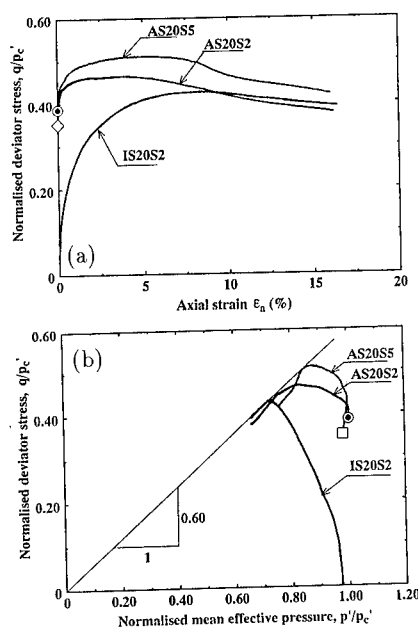


Fig.11 Stress paths (a) and Stress-strain curves (b) during triaxial compression

cavation rate of about 0.5 m and 4 m respectively per 8 hour work day. The value of  $c_u$  used in the slope stability analysis was obtained from  $c_u/\sigma'_{vp}=0.18$  for the slow tests i.e. TRE3 and the SLV series and 0.19 for the other tests.

The minimum factor of safety obtained using the undrained strength thus calculated and the height of the prototype are tabulated in Table 2 and it can be seen that the factor of safety is close to 1. Fig. 13 shows excellent agreement between the critical failure circle and the observed failure arc in the centrifuge model test.

## 5.CONCLUSION

Based on the results of centrifuge tests simulating excavation, the following conclusions may be made from the discussions above:

1. The same circular arc failure surface was observed in all vertical cuts (SLV test series), irrespective of the strength of the model ground. On the other hand, for trench excavation (TRE test series), both wedge type failure and circular arc failure were observed.
2. Photographic measurements show that prior to failure, the strains concentrated around the toe in vertical cuts (SLV tests). However, in trench excavation (TRE tests), the strains were observed over a large area behind the trench wall.
3. For both trench and vertical cuts, at the onset of failure, the strains concentrated around the toe of the slopes and the shear band appeared in this area first.
4. Using the strength parameters from tri-

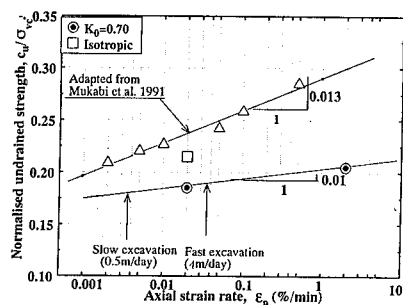


Fig.12 Undrained shear strength on strain rate

axial compression tests on  $K_0$  specimens taking into account the effect of strain rate, the simplified Bishop's method based on a circular failure surface, gave excellent agreement with the observed failure mode in the centrifuge.

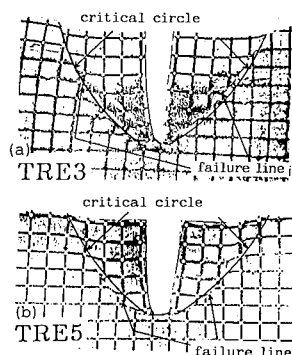


Fig.13 Calculated and observed failure arcs

## REFERENCES

- Azevedo, R.F., 1983. Centrifugal and analytical Modeling of Excavation in Sand. Ph.D. Thesis, University of Colorado at Boulder.
- Bolton, M.D. 1993. Mechanisms of ground deformation due to excavation in clay. Excavation in urban areas. Proc. 2nd KIG Forum. Kobe, Japan.
- Kimura, T., Takemura, J., Hiro-Oka, A., Sue-masa, N., Kouda, N.(1993). Stability of unsupported and supported vertical cuts, 11th Southeast Asian Geotechnical Conference, Singapore, p.61-70.
- Kusakabe, o. 1982. Stability of excavations in soft clays. Ph.D. thesis, Cambridge University.
- Mukabi, J.N., Tatsuoka, F. and Hirose, K., 1991. Effect of strain rate on small strain stiffness of kaolin in CU triaxial compression. 26th Annual Conf. of JSSMFE, Nagano, Japan.
- Toyosawa, Y., Horii, N and Tamate, S., 1993. Analysis of Fatal Accidents Caused by Trench Failure, Third International Conference on Case Histories in Geotechnical Engineering, June, St. Louis, U.S.A., p.751-758
- Ryan Phillips, 1986. Ground deformation in the vicinity of trench headings. Ph.D. thesis, Cambridge University.

## Modelling the soil nailing – Excavation process

S. Frydman & R. Baker

*Technion, Israel Institute of Technology, Haifa, Israel*

A. Levy

*Terre-Arme'e Ltd Natanya, Israel (Formerly: Technion, Haifa, Israel)*

**ABSTRACT:** The paper describes a study of nailing of a vertical excavation in a clayey-sand soil. The testing procedure consisted of running the model in stages. In each stage, an increment of excavation, nail installation and facing attachment was carried out at centrifuge static conditions, and the model was then accelerated to the design  $g$  level to establish a steady state condition. The study indicated that the facing has a structural influence on excavation behaviour, but that nail rigidity is insignificant, at least for horizontal nails. Cracks occur prior to development of large deformations in the soil, and control the location of the failure surface and stability of the system. The axial loads in the nails, particularly as the cut approaches failure, may be greater than are commonly assumed.

### 1 INTRODUCTION

Experimental study of the soil nailing process in excavation stabilization presents considerable difficulties. Full scale studies are expensive, and consequently few such tests, with only little replication checking and variation of design features, can be performed. On the other hand, the use of small scale models is faced with other problems.  $1g$  models are unsuitable for scaling reasons. The use of centrifuge models is difficult due to the complexity involved in excavating and installing nails and facing during centrifuge operation. Previous centrifuge studies of soil nailing (e.g. Shen et al., 1982) have been carried out using the gravity switch on procedure, wherein the model is first built to final excavation dimensions, with nails and facing included, and increasing centrifuge acceleration is applied until collapse occurs. It is not clear that the behaviour of a model tested in this way is generally representative of that of a prototype situation. The stepped nature of the excavation process, and its possible effects, are not observed in gravity switch on tests. In the prototype, each row of nails becomes active in

turn, and the displacement pattern develops accordingly, while in the model all nails become active concurrently.

The present paper presents an investigation in which an attempt was made to reproduce the incremental nature of the soil excavation nailing process.

### 2 THE TEST METHOD

The ideal method for modelling the field construction procedure would obviously be through the use of a robotics system, capable of excavating, installing nails and fixing them to a facing during centrifuge operation. As robotics were not available, a compromise was adopted, and the procedure consisted of running the model in stages. The model was initially built with a horizontal soil surface, without any nails. Initial equilibrium conditions of the soil profile were established by running the model at design  $g$ -level. The centrifuge was then stopped, and the test continued in stages. In each stage, an increment of excavation, nail installation and facing attachment was carried out at centrifuge



static conditions, and the model was then accelerated to the design g-level (the same for all stages) to establish a steady state condition. Progressive stages were performed until collapse occurred. This procedure clearly does not reproduce the influence of in situ stresses during nail installation, and may introduce some disturbances due to starting and stopping the centrifuge. However, it is felt that the major effects of the incremental nature of the excavation and nail installation stages would be reasonably represented.

### 3 THE TEST PROGRAM

#### 3.1 General

The underlying purpose of the investigation was to check the feasibility of satisfactorily modelling the main features of the nailing process in the centrifuge, using stage testing. Within this framework, the testing program was designed to study the development of the failure mechanism in nailed excavations, while considering the effects of the facing, and nail stiffness. Juran and Elias (1991) suggested that the facing of the soil-nailed structure is not a major structural load-carrying element, but rather ensures local stability of the soil between reinforcement layers, and protects the ground from surface erosion and weathering effects. They also suggested that nail stiffness is of significance, while Jewel and Pedley (1990) considered the effect to be generally insignificant.

#### 3.2 The soil tested

The soil used for the models was a red, silty sand (SM), containing 16% fines. The models were prepared at a dry unit weight of  $16 \text{ kN/m}^3$ , (85% of Proctor maximum), and optimum moisture content; simple shear tests carried out on samples compacted to these conditions indicated a small cohesion (of the order of 10 kPa) and a friction angle of  $26^\circ$ . It is difficult accurately define the value of cohesion in materials of this type (with small cohesion values) from laboratory strength tests. A value was estimated on the basis of centrifuge modelling of slope failure of

an unsupported cut, and this is described below.

#### 3.3 The centrifuge system

The centrifuge system has been described previously (e.g. Leshchinsky et al, 1981, Frydman and Keissar, 1987, Frydman and Weisberg, 1991). It is a Shaevitz, model B-12-C with an arm radius is 1.5 m., and it can carry up to 50 kN-g at a maximum acceleration of 70g.

#### 3.4 The models

Two model sizes were tested during the investigation. Initially, the model boxes which had been used in previous centrifuge studies, with internal dimensions 330 X 200 X 100 mm. were used. In order to allow testing of larger models and to perform modelling of models, additional tests were carried out in larger boxes, with internal dimensions 476 X 476 X 150 mm. All model dimensions in the larger models were exactly twice those of the smaller models. The small models were tested at 50g, and the large ones at 25g, the speed of the centrifuge being adjusted so that these acceleration values were effective at the mid height of the excavation in each stage. Excavation stages were 25 mm. and 50 mm. for small and large models respectively. One row of nails was installed at midheight of each excavation stage. Horizontal nail spacing, nail diameter and length were: 25 mm., 1 mm., 75 mm. (small models), and 50 mm., 2 mm., 150 mm. (large models).

Nails were generally tubular, stainless steel. The effect of nail flexibility was examined by additional tests on small models with 1 mm. dia. soldering wire nails of very low flexural rigidity. Different installation procedures were used for the two nail types. The steel nails were pushed into the excavated face following each excavation stage and then connected to the facing. The flexible solder nails could not be pushed into the excavated face, and so they were preplaced in the soil at their exact locations during compaction of the models. During excavation, the ends of the nails in the relevant row were exposed, and connected to the facing.

All nails were placed within  $10^\circ$  of horizontal.

The facing was modelled by aluminium plates, 2 mm. (small) or 4 mm. (large) thick, and height and depth equal to the dimensions of one excavation stage. The nails penetrated through holes in the plates, and were connected to them with clamps, and fast acting glue. The rows of plates were connected to each other using fast acting glue (small models), and screws (large models). Fig. 1 shows the cross section of an excavated model, to prototype dimensions.

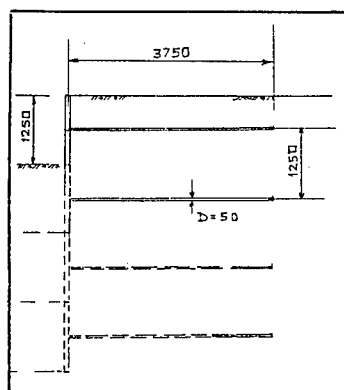


Fig. 1. Model Cross-Section to Prototype Dimensions (mm.)

In one of the large models, two of the nails were instrumented with strain gauges for load and moment measurement.

## 4 MODEL TESTS

### 4.1 Unsupported excavation

Three tests were performed on small models prepared without nails or facing. These tests served as a reference base for evaluating the stabilizing effect of nailing, and also allowed an improved estimation of the cohesion effective in the models. The first test was performed using gravity switch on - the model was prepared and excavated to 100 mm. in the laboratory, and then subjected to increasing acceleration in the centrifuge. Collapse, in the form of an extremely shallow slide, occurred at 25g. Using Taylor's

stability chart for a vertical slope with a friction angle of  $26^\circ$ , a stability number of 0.16 is obtained, yielding a cohesion value of 8 kPa.

The two additional tests were performed in stages, similar to those used in the rest of the research - centrifuge run at 50g and excavation stages of 25 mm. In both tests, shallow slips occurred when the cut face was 75 mm. high (3 excavation stages). In this case, Taylor's stability chart yields a cohesion value of 12 kPa.

The difference in estimated cohesion is probably due to the different modelling techniques. In the stage tests, the unexcavated profile is first brought to equilibrium under 50g, resulting in consolidation, and strengthening of the material. In the gravity switch on case, the unsupported cut is subjected to an increasing acceleration field without having benefitted from the stabilizing effect of prior consolidation. The higher value of 12 kPa would, therefore, appear to be more relevant to the present investigation.

### 4.2 Nailed excavation without facing

In order to check whether the facing has a structural function, three models were tested without facing - 2 small models, one with steel nails and one with solder nails, and one large model with steel nails. The two smaller models showed almost identical behaviour; shallow slips occurred following excavation and nailing to 75 mm. (3 excavation stages) in a mechanism very similar to that observed in the unsupported cuts. The large model behaved essentially similar to the smaller ones, allowing for natural variability between models.

### 4.3 Nailed excavation with facings

The behaviour of four models is described here - two small models, one (6B) with steel nails and one (6A) with solder nails, and two large models with steel nails, one of them (model 7A) at a lower dry unit weight ( $16.6 \text{ kN/m}^3$ ) and higher moisture content. These tests served to demonstrate the effects of nail rigidity and soil density, and to perform modelling of models.

Figs. 2a and 2b show displacement contours

following excavation to 100 mm. and 125 mm in model 6B, while fig. 3 is for 100 mm. excavation in model 6A. The magnitudes of the displacements in model 6A at 100 mm. excavation were in between those at 100 mm. and 125 mm. excavation in model 6B. The displacement field seen in model 6B at 125 mm. excavation appears to be a development of that seen in model 6A at 100 mm. excavation. Fig. 4 shows maximum shear strain contours in model 6B at 100 and 125 mm. excavation; shear strain patterns in model 6A were similar. At 100 mm. excavation, a peak shear strain of about 6% developed in both models. This does not appear to be a failure condition. At 125 mm. excavation large displacements (fig. 2b) and shear strains (fig. 4b) developed indicating a collapse condition. In both models, two sets of tension cracks developed, after excavation to 100 mm. in model 6B and after 75 mm. in model 6A. The first crack developed about 40 mm. back from the excavation face, and the second in the region above the end of the nails. Zones of high shear strain and slip surfaces appeared to develop from the excavation base towards the tip of the closer of these cracks.

The above observations indicate that there was no basic difference in behaviour between the solder and steel nailed excavations, small differences being due to natural variability between models. This collaborates prior claims that nail rigidity has no significant effect on behaviour of nailed excavations. It should be pointed out that Juran and Elias (1991), who suggested that nail rigidity may be significant, also found that for horizontal nails, this is not the case. Additional tests with nails at other inclinations would therefore be required in order to check this effect.

Large model 7B, prepared to similar conditions as model 6B, behaved similarly, developing similar patterns of shear strain and cracks.

The similarity of these two models, and the similarity of the unfaced small and large models, indicate that modelling similitude was upheld in the study.

Comparison of the faced and unfaced models shows that facing significantly increases stability of the excavation, and results in deepening of the slip surface at collapse.

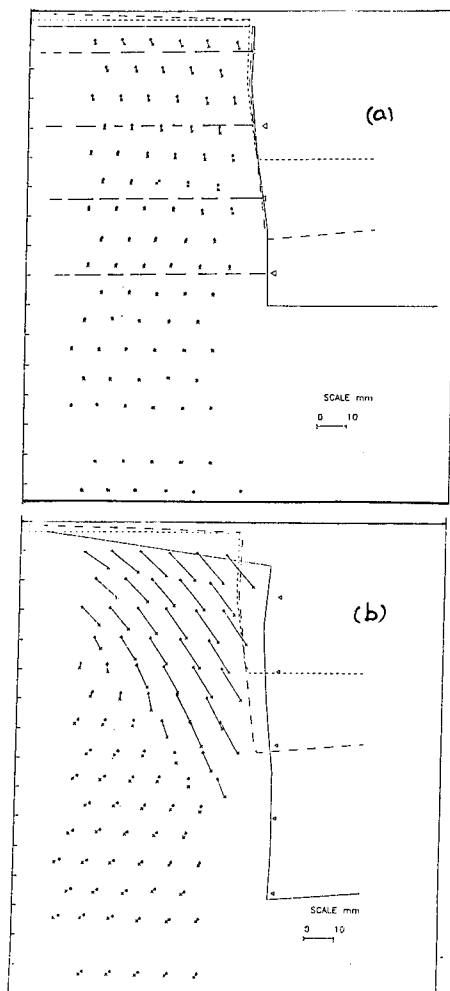


Fig. 2. Displacement Contours, Model 6B

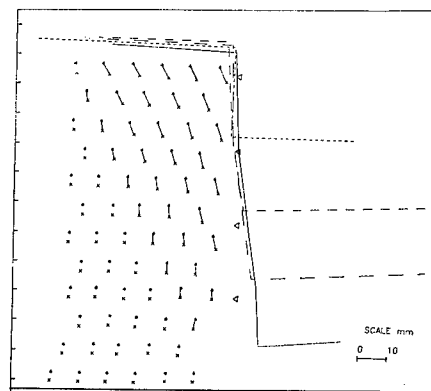


Fig. 3. Displacement Contours, Model 6A

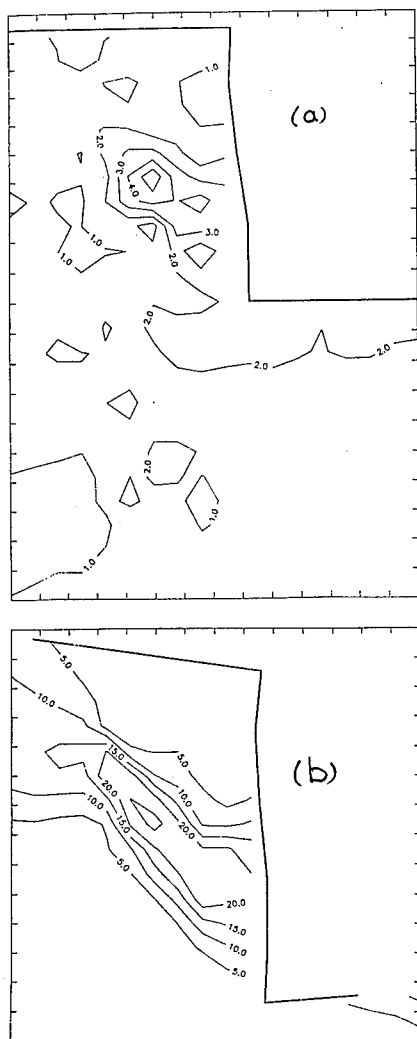


Fig. 4. Shear Strain Contours, Model 6B

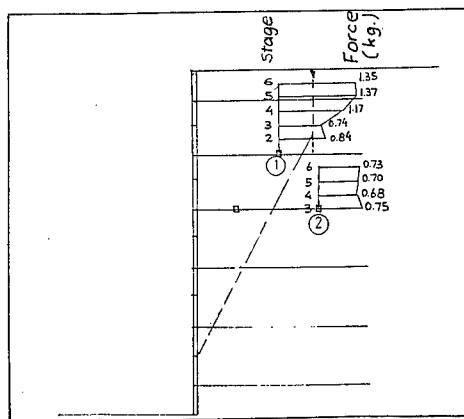


Fig. 5. Axial Force in Nails, Model 7B

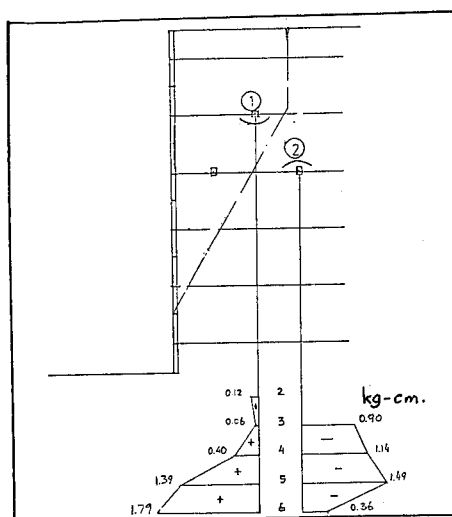


Fig. 6. Moment in Nails, Model 7B

In large model 7A, prepared at lower dry unit weight and higher moisture content, significant displacements and cracks began to develop after 100 mm. excavation. Failure developed at 150 mm. excavation. The importance of soil conditions is evident from comparison of the behaviour of this model and model 7B.

#### 4.4 Forces and moments in nails

Figs. 5 and 6 show axial force and moment at two points on two nails in model 7B, together with the estimated slip surface location.

Maximum possible axial forces in the nails were estimated from the expression  $T = \pi d l \mu z n \gamma$  where  $d$  = nail diameter,  $l$  = effective bond length of nail,  $\mu$  = friction coefficient between nail and soil, and  $z n \gamma$  = vertical normal stress at depth  $z$  in a model in flight at acceleration  $n g$ . The effective length,  $l$ , was taken, in the first 3 excavation stages, as the distance from the free end of the nail to the measurement point. In the following stages,  $l$  was taken as the shorter of this distance and that from the nail end to its intersection with the slip surface.  $\mu$ , was taken as 0.28, from laboratory pull-out tests. Table 1

shows calculated and observed values of  $T$ .

The measured and calculated  $T$  values at point 2 were of the same order of magnitude, remaining constant throughout the test. At point 1, similar orders of magnitude were, again, observed in stages 2 and 3, but then measured values increased significantly, and were much greater than those calculated. This may be explained by reference to the moment measurements shown in fig. 6. The signs of the moments indicate flexural shapes as shown in the figure. The downward flexure in the region of point 1 could lead to an arching effect, with stress transferred to the free end of the nail. The vertical stress acting on the bond length,  $l$ , would then be greater than  $\sigma_{zy}$ , resulting in a larger possible value of  $T$ .

#### 4.5 Effect of facing element connection

In some small models, glueing of the facing elements was not effective, and a plastic hinge developed at the connection during flight, resulting in failure of the excavation. In these cases, failure occurred at smaller excavations than when the connections were stable.

### 5 CONCLUSIONS

Modelling of soil nailing in the centrifuge using a stage procedure was found to be feasible, and appears preferable to the gravity switch on approach.

Facing has a structural effect. Nail rigidity does not influence behaviour of the excavation, at least for horizontal nails.

Moderate variations in in-situ conditions of the soil may dramatically influence stability.

Tension cracks develop before development of large strains in the soil. Prior researches have noted crack development at 0.3-0.4 times the failure excavation height from the cut face. As the cracks develop prior to failure, it appears more correct to state that failure occurs when the excavation reaches a depth of 2.5-3 times the distance of the crack from the cut face. The failure mechanism and system stability are controlled by the existence of the crack.

Table 1. Calculated and observed forces in nails.

Stage	Nail 1		Nail 2	
	T calc	T meas	T calc	T meas
2	5.8 N	8.4 N	-	-
3	5.8 N	7.4 N	4.9 N	7.5 N
4	3.8 N	11.7 N	4.9 N	6.8 N
5	3.8 N	13.7 N	4.9 N	7.0 N
6	3.8 N	13.5 N	4.9 N	7.3 N

The axial forces which develop in the nails near failure may be significantly greater than those calculated using simple pullout theory.

### 6 REFERENCES

- Frydman, S. and Keissar, I. 1987. Earth pressure on retaining walls near rock faces. *J. Geotech. Eng., ASCE*, 113: (6), 586-599.
- Frydman, S. and Weisberg, E. 1991. A study of centrifuge modelling of swelling clays. *Centrifuge 1991*, (Ed. N-Y Ko and F.G. McLean). 113-120. Balkema, Rotterdam.
- Jewell, R.A. and Pedley, M.J. 1990. Soil nailing design: the role of bending stiffness. *Ground Engineering* 23:(2), 30-36.
- Juran, I. and Elias, V. 1991. Ground anchors and soil nails in retaining structures. In: *Foundation Engineering Handbook* (Ed. H-Y Fang) Van Nostrand Reinhold, N.Y.
- Leshchinsky, D., Frydman, S. and Baker, R. 1981. Study of soil structure interaction using finite elements and centrifugal models. *Canadian Geotech. J.* 3: 345-359.
- Shen, C.K., Kim, Y.S., Bang, S., and Mitchel, J.F. 1982. Centrifuge modeling of lateral earth support. *J. Geotech. Eng., ASCE* 108:(9), 1150-1164.

## Modelling of a large underground excavation in China

W.Liu

*Department of Civil Engineering, Northern Jiaotong University, Beijing, People's Republic of China*

K.M.Lee

*Department of Civil and Structural Engineering, The Hong Kong University of Science and Technology, Hong Kong*

S.D.Zhang

*Department of Civil Engineering, Shanghai Institute of Railway Technology, People's Republic of China*

**ABSTRACT:** Centrifuge model test of a major underground excavation is described. The excavation is planned for the construction of a major underground parking structure and shopping plaza in Shanghai, China. The overall area of excavation is about 22,000 m<sup>2</sup>, and the maximum depth of excavation is 11.15 m. The excavation is constructed by the "bottom-up excavation" technique. A four-stage centrifuge model test was adopted to simulate the overall construction sequences. Results of the centrifuge model test were then used to assist the engineers in the design and field instrumentation of the project.

### 1. INTRODUCTION

In 1990, a major underground parking structure and shopping plaza, named People's Square, was started to construct in a busy downtown location at the City of Shanghai, China. The overall area of excavation is about 22,000 m<sup>2</sup>, and the maximum depth of excavation is 11.15 m. The project site comprises a total length of 176m and a width of 145m, which, up to present, is the largest urban underground structure in soft ground in China. Because of the adverse soft clay conditions in Shanghai, the large volume of excavation, the proximity of tall buildings, and the existing underground pipelines and utilities to the project site, the design and construction stages of the project must be extremely carefully engineered.

Because of the difficulty and significance of the project, centrifuge model testing is required to verify the feasibility of the design concept. The results from the model test could provide useful information in regards to the construction sequences and precautionary measures. Therefore, centrifuge model testing constituted a major component of the project design and planning.

The excavation of the People Square was constructed by the so-called "bottom-up excavation" technique (see Fig. 1). It basically has two important construction components: firstly, the construction of diaphragm wall to surround the

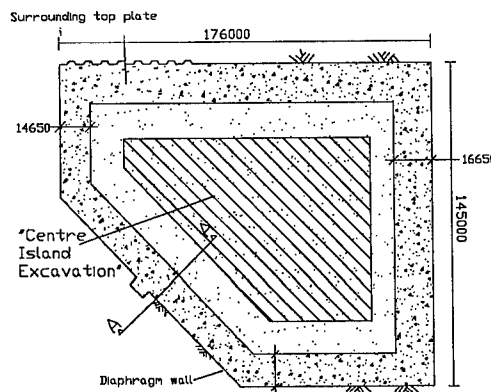


Fig. 1 Excavation layout

perimeter of the site and the construction of supporting piles and structural truss; secondly, the excavation of the ground and the construction of the main structure. The diaphragm wall is 18.85m deep with a 600mm thick  $\pi$  shaped wing wall. This together with the supporting piles and structural truss becomes the major support of the subsequent underground excavation. The excavation is first carried out at the centre location of the site. This is followed by subsequent construction and excavation steps as of the "bottom-up excavation" procedure.

The centrifuge modelling of these construction sequences can be considered in four stages. Each stage was trying to simulate the most critical

condition associated with each construction sequence. All the tests were conducted at a 1.55m radius centrifuge of maximum acceleration of 200g. The maximum payload is 200kg at 200g. The facility is installed at the Department of Civil Engineering, Shanghai Institute of Railway Technology.

## 2. CONSTRUCTION MODELLING CONDITIONS

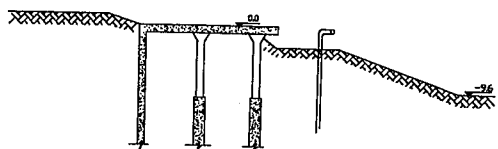
### 2.1 Critical cross-section

According to the excavation layout as indicated in Fig. 1, section A-A is considered as the most critical section. This assumption is based on the facts that section A-A has the longest unsupported span length, the close proximity of tall building and underground pipelines adjacent to the excavation section, and the weakest structural support at this section (a total thickness of surrounding top plate of 14.6 m along section A-A as compared with that of 16.65 m on the other section). This section was therefore selected as the test section in the centrifuge modelling test.

### 2.2 Construction sequence

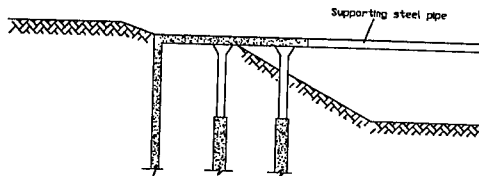
In accordance with the design engineers, the overall construction scheme can be divided into 13 stages. After a careful consideration of these construction stages, four critical construction sequences can be identified and modelled by centrifuge test.

**Critical Stage 1:** the construction process of this stage is illustrated in Fig. 2. The  $\pi$  shaped diaphragm wall, two rows of supporting piles, and the supporting top plate were installed. Excavation was proceeded at the centre portion of the site to a depth of 9.6 m. The un-excavated area extended to the right of the diaphragm wall by a width of about 29 m and then tapered off to the bottom of excavation by a 1:1.5 side-slope. A surcharge pressure of 20 KPa on the un-excavated side (i.e., to the left side of the diaphragm wall) was assumed.



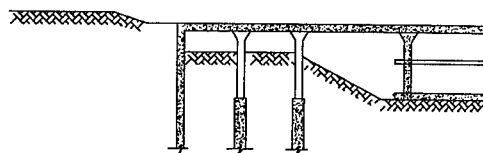
**Fig. 2** Construction sequence for the "Critical Stage 1"

**Critical Stage 2:** temporary supporting steel pipes were erected to provide lateral support to the top plate. The maximum span of this temporary steel pipes was 46 m. Excavation at the centre portion was extended towards the diaphragm wall and leaving an un-excavated width of 17 m (see Fig. 3).



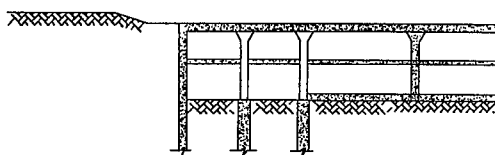
**Fig. 3** Construction sequence for the "Critical Stage 2"

**Critical Stage 3:** temporary supporting steel pipes were removed and the parking structure on the right side of the top plate was constructed. Excavation at the centre portion was almost completed excepting a small portion of un-excavated soil next to the diaphragm wall as illustrated in Fig. 4.



**Fig. 4** Construction sequence for the "Critical Stage 3"

**Critical Stage 4:** this represents the final stage of construction, where the excavation and the mid-level parking structure were completed (see Fig. 5). The bottom floor slab was partially completed and it leave a small section adjacent to the diaphragm wall to be constructed.



**Fig. 5** Construction sequence for the "Critical Stage 3"

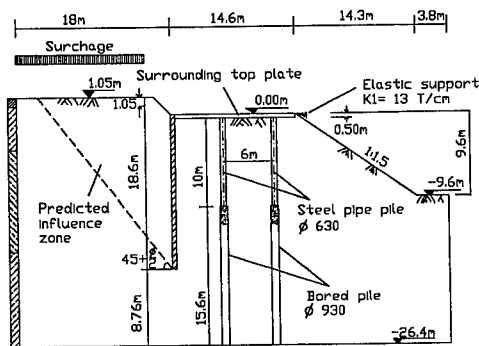
### 2.3 Centrifuge modelling criteria

During the centrifuge model testing, a plane strain section along A-A was considered. A number of important factors have to be considered, which are

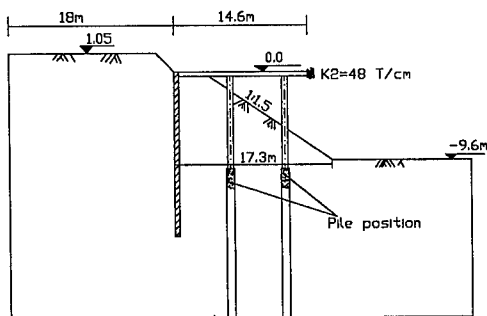
summarized as the following:

- i) An active Rankine pressure zone behind the diaphragm wall has to be considered. Based on the classical theory, a distance of at least the influence zone of  $45^\circ + \phi/2$  projected from the bottom of the wall has to be considered. In the model, a distance of 18 m was adopted (see Fig. 6).
- ii) The possibility of ground movement has to be considered, and appropriate dimension allowance has to be made for the possible ground movement.
- iii) The dimension of the "strong" box and the optimum level of acceleration must be considered.

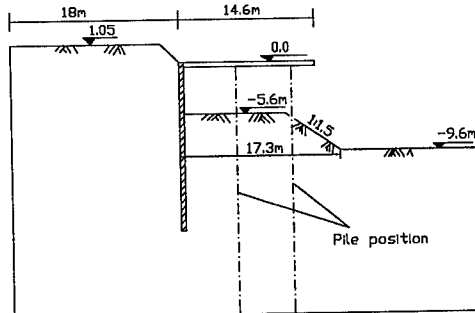
Based on the above mentioned factors, a modelling scale of 1:120 was adopted. Four centrifuge models were constructed to simulate the construction sequence of the Critical Stage 1, 2, 3, and 4. The schematic figures of these four models are shown in Figs. 6, 7, 8, and 9, respectively.



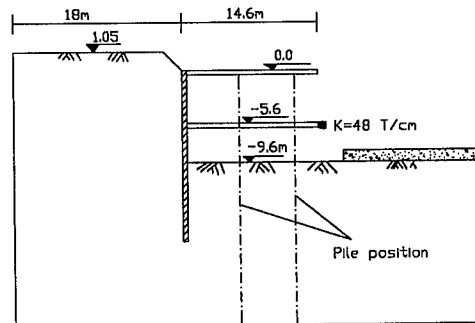
**Fig. 6** Centrifuge model of the Critical Stage 1 (to be scaled down by a factor of 120)



**Fig. 7** Centrifuge model of the Critical Stage 2 (to be scaled down by a factor of 120)

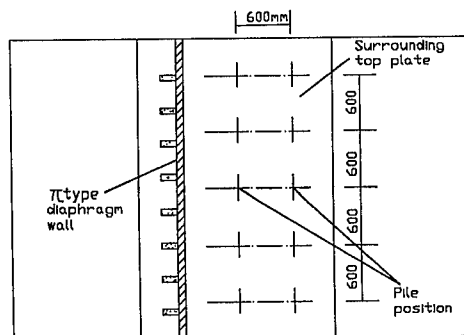


**Fig. 8** Centrifuge model of the Critical Stage 3 (to be scaled down by a factor of 120)



**Fig. 9** Centrifuge model of the Critical Stage 4 (to be scaled down by a factor of 120)

The plan view of the model adopted in the analysis is shown in Fig. 10. The dimensions indicated in the figure are the prototype model size value (i.e. scaled down by a factor of 120), and it is applicable for all four stages of construction simulation.



**Fig. 10** Plan view of the centrifuge model

## 2.4 Consideration of boundary conditions

One of the major concern in the proposed model test is in the consideration of the modelling technique of the lateral support provided by the top



plate and the temporary supporting steel pipes. The lateral support of the top plate is resulted from the 3-dimensional lateral restrain effects of the structure surrounding the excavation. During the construction stage where the temporary steel pipes were required, the 3-dimensional space frame effects surrounding the excavation further increase the lateral support to the top plate. To model these 3-dimensional effects in a 2-dimensional plane strain simulation, elastic beam deflection analysis was carried out to determine the corresponding equivalent lateral supports. It is considered that two elastic supports can be provided on the front and rear ends of the model as indicated in Fig. 11. Based on the elastic analysis, the elastic supports with a stiffness constant (K) of 0.3 Tonne/cm is required for the case of top plate alone, while a stiffness constant of 48 Tonne/cm is required for the case of top plate with temporary support steel pipes.

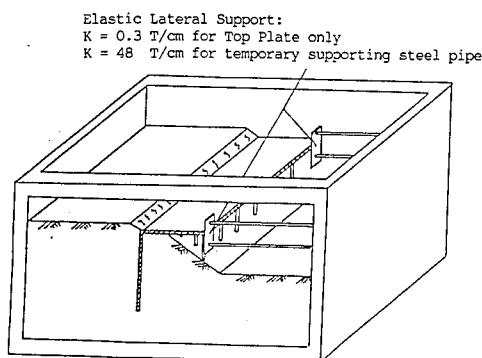


Fig. 11 Isometric view of the test model showing the arrangement of lateral support

### 3. MODELLING MATERIALS

#### 3.1 Soil materials

The excavation was mainly constructed in a layer of soft Shanghai clay. This soil can be classified as a soft silty clay with natural water content of 50% to 60%, liquid limit in the range of 36% to 45%, and plasticity limit of 20% to 24%. The Liquidity Index is between 1.3 to 1.6 while the Plasticity Index is between 17% to 24%. The undrained shear strength of the soil is generally in the range of 20KPa to 40KPa.

It is generally recognized that it would be extremely difficult to obtain "undisturbed" soil sample from the field for centrifuge model test. Therefore, soil sample obtained from the field has to be reconstituted and consolidated to the shear strength and water content similar to those in the field.

In this study, large block of soil sample was obtained in the site by mechanical excavator from a depth of 4m. The soil was a greyish soft silty clay with a natural water content of about 33%.

The soil sample was then remoulded and mixed with additional amount of water to a water content around 46%. The soil slurry was then placed in the strong box and consolidated under centrifuge acceleration. The consolidation and compression process was allowed to continue until at least 95% of consolidation was achieved. Soil layer of different strength was consolidated in the centrifuge at different acceleration g-values. A typical reconstituted soil profile adopted in the modelling analysis is shown in Fig. 12. Shear strength parameters determined by laboratory vane tests and water contents obtained from the reconstituted sample were compared with the values obtained from the "undisturbed" samples. The difference in the  $\phi$  angle obtained from the two type of samples is generally within  $3^\circ$ .

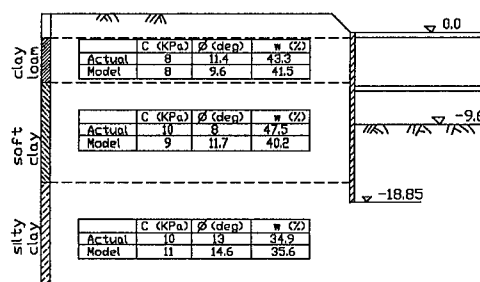


Fig. 12 Reconstituted soil profile

#### 3.2 Wall and surrounding top plate

It is impossible to construct a scale down model of the reinforced concrete diaphragm wall in 1:120 scale. To correctly simulate the soil-structure interaction behaviour under the modelling scale, one should consider the corresponding elastic deflection of the wall in response to the earth pressure. In the model study, 3 mm thick aluminum plate was employed. The bending stiffness of the aluminum

plate is calculated to be similar to that of the reinforced concrete diaphragm wall with a scale ratio of 1:120. The surrounding top plate is also modelled by the use of aluminum plate following the same concept as the diaphragm wall.

In modelling the two rows of supporting piles, the following two factors have to be considered: i) the lateral support provided by the row piles to the surrounding top plate and the diaphragm wall; ii) the result of increased lateral stability against slippage of the soil mass behind the diaphragm wall. In the model, the upper portion of the supporting piles was constructed by using a steel bar of equivalent stiffness to the steel pipes (the diameter of the steel pipe is scaled down by a factor of 120). The lower portion of the supporting piles was constructed by aluminum bar with equivalent scaled stiffness to the bored piles in the field. The upper and lower portion of the piles were connected by steel screw and contact cement.

#### 4. TESTING PROCEDURE

The overall study took 3 months to complete. Majority of the time was used to consolidate the reconstituted soil slurry. During the consolidation process, lab vane test was used to determine the strength of the reconstituted clay to see if the design shear strength and water content were achieved. In this study, two model boxes were constructed. The first box was used to simulate the Critical Stage 1, 2, 3, and 4 as indicated in Figs 6, 7, 8, and 9. The model is first built in accordance with Fig. 6 to model the Critical Stage 1. Since the soil deformation was relatively limited after the first test. The box was then unloaded from the centrifuge and further excavation was proceeded to model the next stage of construction. The box was then re-mounted to the centrifuge and continue for next test. This process was repeated for all four stages of construction. Since the last construction stage was considered to be the most critical, an additional model box was built to model the Critical Stage 4 separately. In each of the model test, it took about 1.5 hours to achieve the design acceleration of 120g in the centrifuge. The test model was then accelerated at a constant 120g for 3 minutes. This is equivalent to about one month in real time scale. All the tests were recorded by in-flight video camera and high speed pictures.

#### 5. ANALYSIS OF RESULTS

Based on the high speed photos taken during the test, ground displacement vectors and deformed shape of the supporting structure can be obtained. These results are shown in Figs 13, 14, 15, and 15 for Critical Stage 1, 2, 3, and 4, respectively. It should be noted that the displacement vectors shown in each figure are the absolute displacements resulted from each construction stage.

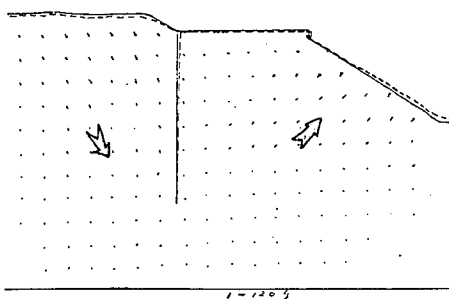


Fig. 13 Displacement vectors of the ground after "Critical Stage 1" construction

After the construction of Critical Stage 1, the top of the diaphragm wall deflected towards the excavation by about 5 cm (in prototype scale), the soil mass behind the wall remained stable with a maximum surface settlement of about 4 cm.

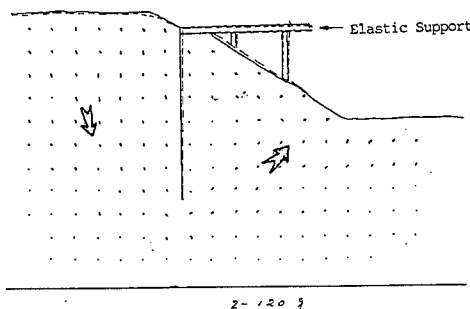
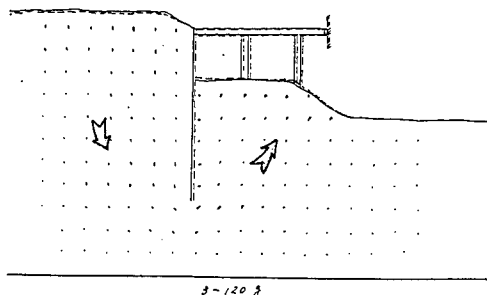


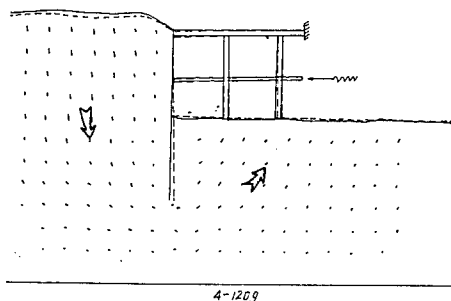
Fig. 14 Displacement vectors of the ground after "Critical Stage 2" construction

After the stage 2 construction, because of the installation of the temporary lateral supporting pipes at this stage, further excavation only resulted in very small additional ground movements.



**Fig. 15** Displacement vectors of the ground after "Critical Stage 3" construction

Because of the additional ground excavation adjacent to the diaphragm wall during the stage 3 construction, lateral movement of the wall towards the excavation was observed. This lateral movement was then resisted by the two rows of supporting pipes, the overall lateral movement of the wall is limited to about 5 cm. The maximum surface settlement behind the wall is found to be around 6 cm.



**Fig. 16** Displacement vectors of the ground after "Critical Stage 4" construction

After the stage 4 construction, excavation inside the diaphragm wall was completed to a design depth of 9.6 m. It can be seen that the diaphragm wall was rotated slightly in counter-clockwise direction. As a result of this rotation, the bottom portion of the wall deflected about 10 cm towards the excavation. The counter-clockwise rotation also resulted the upper portion of the wall to move back almost to its original position. As a result of this rotation, the ground subsidence behind the wall is observed to be in the range of 6 to 10 cm. A slight rebound of the soil at the bottom of excavation is observed. It should be noted that the design of the supporting

row pipes and top plate performed very well as a space truss unit in resisting the lateral movement of the diaphragm wall and ensuring the stability of the excavation.

## 6. CONCLUSION

Results of the centrifuge model tests indicated that:

- 1) The basic design concept and proposed construction sequence is technically feasible.
- 2) The diaphragm wall and supporting top plate and piles can have a significant contribution to the stability of the underground excavation.
- 3) The results indicated that the maximum deflection of the diaphragm wall is about 10cm and the maximum ground settlement behind the wall is amount to about 10cm.

The construction of the People's Square is now near completion. The behaviour of the ground during actual construction is monitored by field instrumentation. The general observed ground pressure and deformation behaviour are general consistent with that predicted by the centrifuge model tests.

## 7. ACKNOWLEDGEMENT

The authors would like to thank the Department of Civil Engineering, Shanghai Institute of Railway Technology for their support and permission to publish the information as described in this paper. In addition, the authors would like to thanks Mr. Kenny Ma of HKUST for his accurate drafting of the figures given in the paper.

## The influence of a bored tunnel on pile foundations

Adam Bezuijen & Joost van der Schrier  
*Delft Geotechnics, Netherlands*

**Abstract:** The influence of a bored tunnel on an existing pile foundation has been investigated by means of model tests in a geotechnical centrifuge. Three tests were performed: one preliminary test with limited instrumentation for a tunnel in saturated sand and two tests with a soil model of sand with clay (layers) on top. The tunnelling was simulated by a model tunnel; a specially designed cylinder of which the diameter could be reduced. 6 piles were placed at different distances from the model tunnel and the load-settlement behaviour during reduction of the model tunnel diameter was monitored. The test results show that load-settlement behaviour was influenced by the horizontal distance from the pile to the model tunnel and the soil material that surrounded the model tunnel. Pile settlement was measured at larger distances from the tunnel when it was surrounded by sand. The settlement trough is measured as a function of the decrease in diameter of the model tunnel. The results from the settlement trough are compared with existing formulae of Peck and Verruijt.

### 1 Introduction

In regions with soft soil layers, most buildings are founded on piles to use the strength of stiffer layers at greater depth. In such a region it is likely that a bored tunnel, constructed for a metro or an underground part of a railway, will be founded in the same stiff soil layer as the pile tips of a pile foundation. During the boring process somewhat more soil is removed than the volume of the tunnel, leading to changes in the stress state of the soil. The influence of these changes on the bearing capacity of an adjacent pile foundation is of importance when a bored tunnel is planned in an urban area with many pile foundations. The interaction between loaded foundation piles and a tunnel under construction is difficult to model with (numerical) calculation programs, since it is a 3-dimensional problem and modelling the influence of the tunnel is only possible if the stress distribution around the driven piles is modelled properly. Therefore, this influence has been investigated in a model test in the geotechnical centrifuge of Delft Geotechnics (Nelissen, 1991). The tunnelling process was simulated by a model tunnel; a cylinder with the possibility to change the diameter in a controlled way. A decrease in

the diameter of the model tunnel simulates the tunnelling process in which some more soil is removed than corresponds with the diameter of the tunnel. Six piles at different distances from the tunnel, loaded to 75% of their ultimate bearing capacity, were used to investigate the pile-tunnel interaction. In the tests, the diameter of the model tunnel was reduced and the settlement of the piles was monitored, as well as the depth and form of the settlement trough at the soil surface. This paper describes the test set-up and the results of the tests. The consequences for practice are discussed.

### 2 Test set-up

The prototype situation is a tunnel with a diameter of 7 m. This 7 m is in-between the diameter for a metro (6 m) and a single track railway tunnel (8-9 m). The prototype pile had a diameter of 0.4 m. A model scale of 1:40 was chosen.

A cross-section of the model is shown in figure 1. It shows the soil model, the piles and the model tunnel. The soil model consisted of two layers of clay of 0.19 m, with a sand layer of 0.02 m in-between. The clay layers were preconsoli-

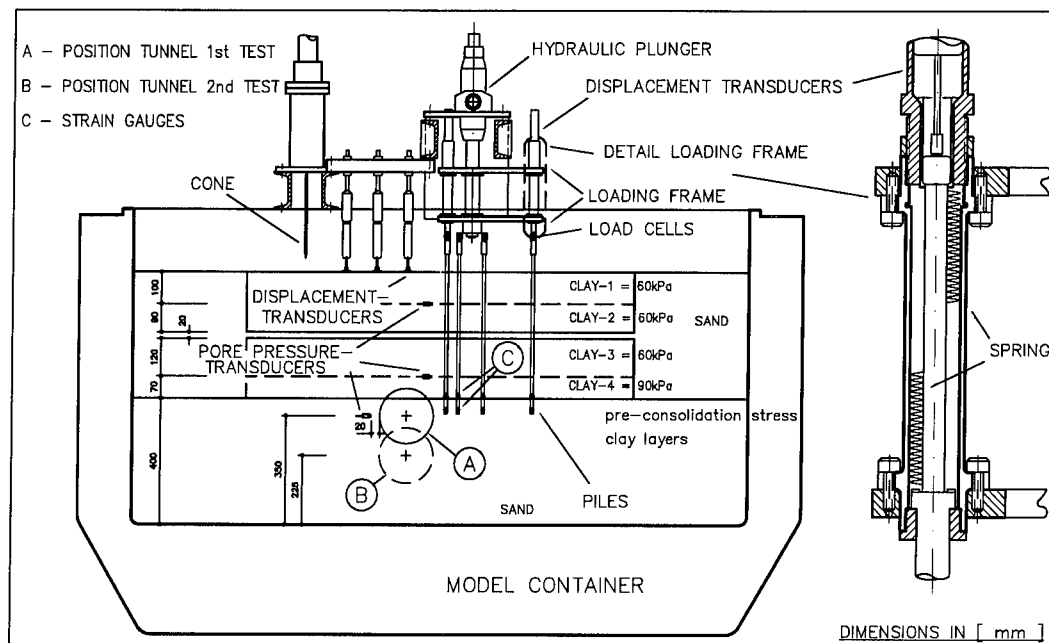


Figure 1: Cross-section through the centrifuge model.

dated. For handling the clay layers it was necessary to over-consolidate the top layers (1 and 2). The bottom layers (3 and 4) were normally-consolidated. The clay used in the tests was Speswhite kaolin clay. The sand layer between the clay layers functioned as a drainage layer during the reconsolidation in the centrifuge. Three tests have been performed:

1. a preliminary test with a soil model of only densified sand with the same configuration of model tunnel and pile as shown in figure 1, but with the centre of the tunnel and the pile tips 35 cm below the sand surface.
2. the 1st final test with the configuration of figure 1 and the tunnel at the high position (position A in figure 1).
3. the 2nd final test with the tunnel at the low position (position B in figure 1).

In all models the phreatic line was equal to the soil surface. The sand used is Eastern Scheldt sand, some properties of the clay and sand used are listed in table 1. After the tunnel was placed, the sand was densified by a vibration needle. Two piles were located at both 0.04 and at 0.08

Table 1: Properties of Speswhite kaolin clay and Eastern Scheldt sand.

properties clay	
unit weight constituent	26.1 kN/m <sup>3</sup>
liquid limit (LL)	69.0%
plasticity index (PI)	31.0%
plastic limit (PL)	38.0%
$\gamma$ at W = 50%	17.0 kN/m <sup>3</sup>
$c_u/\sigma'_v$	0.21
$I_r (=G/c_u)$	200
Friction angle $\phi$	23°
Cohesion	0 kPa
Properties sand	
unit weight constituent	26.5 kN/m <sup>3</sup>
D <sub>50</sub>	180 $\mu$ m
Friction angle at D <sub>r</sub> =70%	45°

m from the tunnel, one at 0.16 m and one at 0.32 m, resulting in a total of 6 piles. The positions of the piles were determined in a way to minimize group effects.

The piles were closed aluminium tubes with a diameter of 0.01 m. Forces on the piles have been monitored by a load cell on top of the piles and strain-gauges at 0.05 m and 0.01 m from the pile tip. The load cell on top of the pile measured

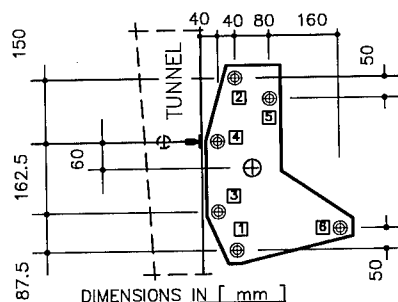


Figure 2: Top view on piles and loading frame.

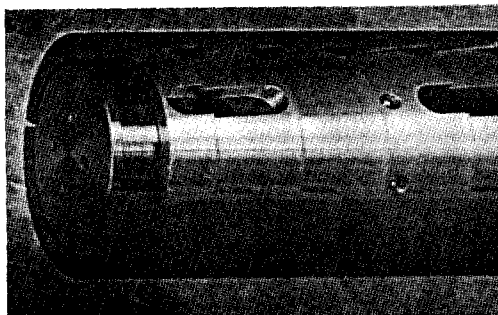


Figure 3: Detail of the model tunnel.

the total load. The strain-gauge at 0.05 m was situated at the transition between sand and clay in the model and enables, knowing the load on top of the pile, to determine the friction of the clay along the pile shaft. The strain gauge close to the pile tip was used to monitor the tip force.

The piles were connected by springs to a loading frame. The positions of the piles in the loading frame can be seen in figure 2. The load on the piles could be controlled by a plunger on the loading frame. The springs had a stiffness of 0.1 kN/mm. The loading on the piles was calculated to be between 1.2 and 2 kN. With the springs chosen, a pile settlement of 1 mm implied a load reduction less than 10%. With the loading frame designed in this way it was possible to penetrate 6 piles with one plunger and to have a more or less force-controlled situation during the decrease in diameter of the model tunnel. The model tunnel consisted of 4 synthetic tunnel elements, placed on an aluminium core. By moving the core relative to the tunnel elements, the outer diameter could be varied (see figure 3). The entire model tunnel was covered by a rubber sack, which ensures watertightness and prevents intrusion of soil particles. The actual diameter of the tunnel was monitored by two displacement transducers mounted between the tunnel elements.

### 3 Test Procedure

The tests started with the model pile tips 15 mm above the actual testing position. The test procedure was as follows:

1. Reconsolidation of the clay model under its self weight at 40 g load. After 6 hours 95% consolidation was obtained.
2. When 95% consolidation was reached, a cone

was penetrated in flight with a penetration speed of 0.15 m/s, comparable to the penetration speed in prototype.

3. The piles were penetrated to the actual testing position. This penetration was performed to acquire a stress state around the piles comparable to the stress state of a driven pile. The maximum penetration force was measured. Then the pile loading was reduced to 75% of the maximum penetration force to achieve a working load comparable with a heavily loaded pile in prototype. The reduction of load was not performed in the preliminary test.
4. The diameter of the tunnel was reduced continuously with the loading frame at a fixed position. The load-settlement curve of the piles was measured under the changed boundary conditions.
5. The frame was pushed further to determine the ultimate loading capacity, after large pile settlement. This step was not performed in the preliminary test.

## 4 Results

### 4.1 Overview

Results of the preliminary test are shown qualitatively in figure 4. In this figure the piles and tunnel are represented to scale. The number in the tunnel represents the relative decrease of the cross-sectional area of the tunnel. The measured settlement of the piles and the settlement trough are shown. This test showed large settlements of the piles close to the tunnel (much more than 1 mm) and, therefore, also a significant reduction in the pile resistance, as represented by the arrows below the pile. All piles had the same

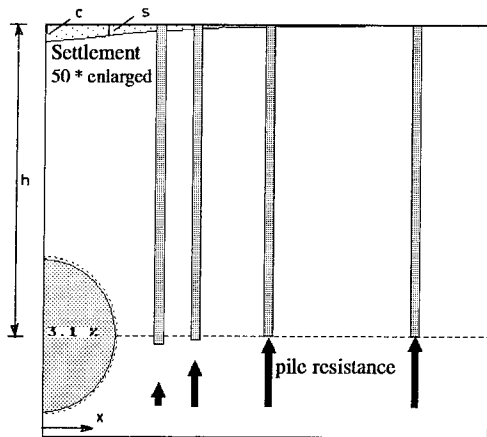


Figure 4: Results the preliminary test. The piles were all on the dashed line before the reduction of the tunnel diameter (all dimensions to scale).

resistance before the reduction of the diameter of the model tunnel. The tests with clay layers above the tunnel show comparable results. The analysis of the results presented below focuses on the settlement trough measured above the tunnel and the pile settlement.

#### 4.2 Settlement trough

The settlement trough at ground level was measured at two positions during the preliminary test and at three positions during the final tests (see figure 1). The results have been fitted with formulae presented by Peck and Verruijt. The formula of Peck (presented in Attewell et al. (1986)) is empirically based and written as:

$$s = ce^{-0.5(x/\sigma_s)^2} \quad (1)$$

where  $s$  is the settlement,  $x$  the horizontal distance from the centre of the tunnel and  $c$  and  $\sigma_s$  are parameters defining the depth and the width of the trough. Attewell et al. also present relations for  $\sigma_s$  depending on the type of soil. Sagaseta (1987) has presented a calculation method to derive an analytical solution of the equations describing the deformation caused by a diameter decrease in an incompressible elastic half space. Based on this method Verruijt (1993) derived for a compressible elastic half space:

$$s = 2(1 - \nu) \frac{\Delta V}{\pi h} \frac{1}{1 + (x/h)^2} \quad (2)$$

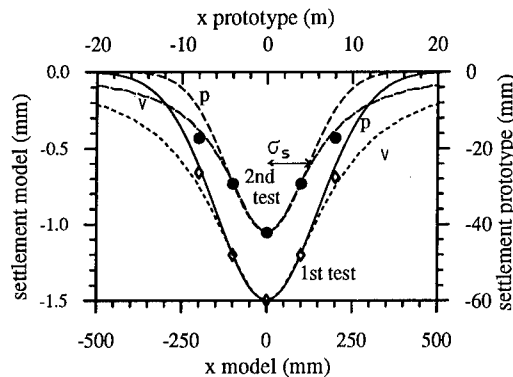


Figure 5: Settlement trough at 3 % volume decrease of the model tunnel in the 1st and 2nd test. Measurement points (with the same values on the negative X-axis to impose a symmetric curve) and fits with the formulae of Peck (p) and Verruijt (v).

where  $h$  is the depth of the center of the tunnel,  $\Delta V$  the volume loss,  $V$  the total volume of the tunnel and  $\nu$  the poisson ratio of the soil.

The equations can be fitted well with the measurement points (see figure 5). The mean values found for the parameters of equation 1 and 2 during the volume decrease are listed in table 2. From these results it appeared that the preliminary test and the second test — the tests where the tunnel was surrounded with sand — have comparable results for the settlement trough. The test with  $\frac{1}{5}$  of the model tunnel in clay has a wider settlement trough and a lower value of  $\nu$ . The value of  $h$ , found when fitting the settlement trough to equation 2, is much less than the actual depth of the tunnel. This means, that although the equation for the settlement trough as derived by Verruijt can be reasonable, the soil is not behaving as an elastic material, as is assumed in the derivation of the formula, and plastic deformation occurs. This can also be concluded from the values of the poisson ratio. A value larger than 0.5 indicates, that there

Table 2: Mean values of the parameters in equations 1 and 2 for the settlement trough

parameter	prel. test	1st test	2nd test
$\sigma_s$ (mm)	115	151	117
$h$ (mm)	98	202	150
$\nu$ (-)	0.57	0.33	0.65

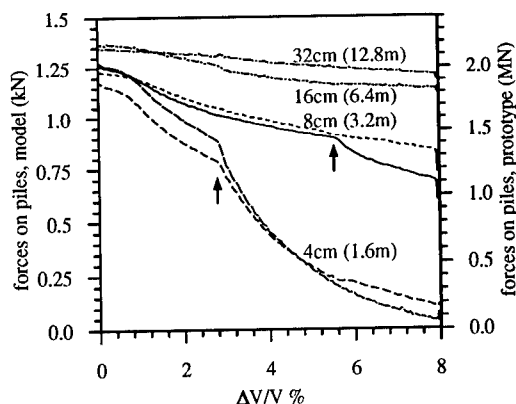


Figure 6: 2nd test: forces on piles during decrease in volume, the arrows indicates the point at which the settlement of the piles stops because the spring was pushed out completely (prototype distances between brackets).

is an increase in volume of the material during deformation. This is not possible for an elastic material. However, it is possible during plastic deformation and is well known for dense sand as dilatancy. Indeed it is found that the value of  $\nu$  is only higher than 0.5 when the model tunnel is completely surrounded with sand.

This dilatancy of the sand around the tunnel can be measured in this model test because there is complete control of the tunnel volume. This is not the case when tunnelling is performed in the field. In field measurements, the volume decrease is measured from the settlement trough under the assumption that the volume taken at depth is equal to the volume of the settlement trough at ground level. Such a procedure is not always justified as appears from figure 5, which shows the settlement troughs for the 1st and 2nd test, both at 3% decrease of tunnel volume. Due to dilatancy of the sand in the 2nd test, the volume of the settlement trough is smaller than in case of the 1st test.

### 4.3 Pile settlement

Figure 4 shows that the volume decrease of the model tunnel has a distinct influence on the pile foundation leading to a reduction of the bearing capacity and consequently to pile settlement. As an example of the reduction in bearing capacity, the results of the 2nd test are presented in figure 6 as a function of the relative decrease

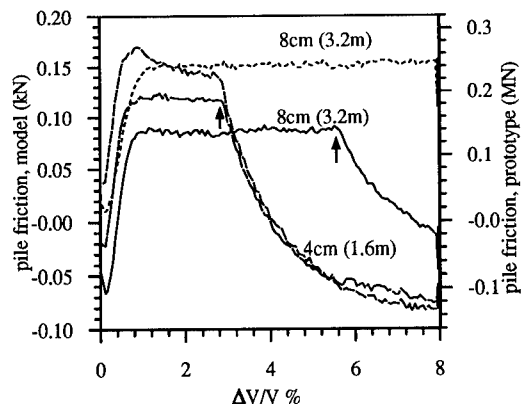


Figure 7: 2nd test: friction measured on piles.

in volume of the tunnel. For the piles at 0.04 and one at 0.08 m from the tunnel the reduction in bearing capacity is such, that the springs mounted on the loading frame reached their maximum stroke. This happened when the bearing capacity of the pile became less than appr. 0.9 kN, and no further settlement was possible. For these piles, ongoing soil deformation around the tunnel, by further decrease of volume, led to a rapid decrease in the bearing capacity. This result was also clearly demonstrated by the friction measured on the piles (see figure 7). The magnitude of the pile settlement is larger than the settlement of the clay, therefore positive friction developed on the piles. However, when the settlement of some of the piles stopped, negative friction developed, because the settlement of the soil continues. The pile settlement at 1% volume decrease of the model tunnel as measured in the 3 tests is shown in figure 8. In this figure, a mean value with deviation is presented for the locations with two piles at the same distance. A low value of volume decrease was chosen because at a larger value the settlement is limited by the stroke of the springs in the loading frame.

From this figure, it is clear that the pile settlement was largest in the preparatory test. In this case the pile loading was larger relative to the bearing capacity of the pile. For the 1st test the distance, in which piles were influenced by the tunnel, is smaller than for the 2nd test. This appeared to be true for different values of volume decrease. In the preliminary test as well as in the 2nd test, the model tunnel was completely surrounded with sand. Deformations in this sand influenced the pile foundations at a larger distance.



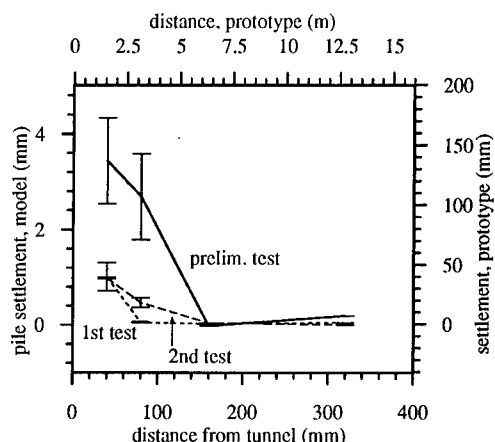


Figure 8: Pile settlement in the various tests at 1% decrease of tunnel volume. The settlement measured for the pile at 0.32 m distance is not realistic, but the result of a small deformation of the loading frame

The following mechanism is proposed: the tunnel deformations cause a reduction of the horizontal stresses in the soil. This reduction reduces the bearing capacity of the piles. This is due to the fact that in case of driven piles an important part of the bearing capacity is realized from the high horizontal stresses that develop during pile driving. In a stiff soil such as sand, a prescribed deformation leads to changes in stresses over larger distances and therefore to a reduction of horizontal stress over a larger distance.

## 5 Conclusions

The results of the tests as presented in this paper lead to the following conclusions:

1. A geotechnical centrifuge appears to be a valuable tool for studying the interaction between a bored tunnel and an existing loaded pile foundation.
2. The volume loss prescribed, by changing the tunnel diameter, can be more than the volume loss measured at ground level due to dilatation of the sand.
3. The width of the settlement trough is smaller in the tests where the tunnel is completely surrounded with sand (the preliminary and 2nd test). On the other hand the distance on which pile settlement can be measured is larger in these tests.

4. Pile settlement can be quite significant, if the volume loss is 1% or more and the distance between the pile and the tunnel is less than 1 tunnel diameter (0.175 m or 7 m in prototype). However, extrapolation of the results from the test makes it reasonable to assume that shorter distances, or larger volume loss are acceptable, in the case where the tunnel is placed for a less substantial part in the foundation layer.

## 6 Acknowledgements

The authors gratefully acknowledge the participants in this project, who provided the necessary funds:

- Municipal Management Amsterdam
- Public Works Rotterdam
- Nederlandse spoorwegen
- Bored tunnel combination:
  - Ballast Nedam Beton en Waterbouw BV, Hollandsche Beton-en Waterbouw BV, Structon Betonbouw BV, Ways und Freytag GA
- Dirk Verstoep BV
- van Hattum en Blankevoort
- Koninklijke van Drunen BV
- Delft Geotechnics
- Ministry of transport and public works
- de Weger Architects and Consulting engineers
- Ministry of Economic Affairs

The authors further acknowledge J. Out for the design of the equipment (model tunnel and pile loading frame), T. van Dijk, F. Kop and W. Lönning for their assistance during preparation and testing.

## 7 References

- Attewell P.B., Yeates J., Selby, A.R. (1986). *Soil Movements Induced by Tunnelling and their Effects on Pipelines and Structures*. Blackie, London. ISBN 0-216-91876-6.
- Nelissen H.A.M. (1991) *The Delft geotechnical centrifuge*, Proc. Int. Conf. Centrifuge '91, Boulder Colorado.
- Sagaseta C. (1987). *Analysis of undrained soil deformation due to ground loss*, Geotechnique 37, No. 3, 301-320.
- Verruijt A. (1993). *Elastostatics of a half space*. Lecture notes "Soil Dynamics", University of Technology, Delft.

## Behavior of stacked-drift-type tunnels

A. Onoue, H. Kazama & H. Hotta  
*Shimizu Corporation, Tokyo, Japan*

T. Kimura & J. Takemura  
*Tokyo Institute of Technology, Japan*

**ABSTRACT:** A series of centrifuge model tests was performed in order to investigate the behavior of stacked-drift-type tunnels. Model tunnel composed of 20 aluminum rods was placed in either dry silica sand or saturated kaolin clay ground. Ground surface settlements, tunnel deformations, earth pressures acting on drifts and contact pressures between drifts were measured under centrifugal acceleration of up to 100 g. Differences between data obtained from sand ground cases and those from clay ground cases are discussed. Test results are next compared with existing test results on varied pipes and furthermore with in situ data obtained from Mt. Baker Ridge Tunnel.

### 1 INTRODUCTION

Since it has become increasingly more difficult in recent years to secure space for public roads in urban areas in Japan, most of the projected highways are being planned for construction underground. In an effort to facilitate these projects, relevant organizations have been investigating construction methods for large-diameter tunnels capable of accommodating six lanes of traffic.

A good example of a large-diameter tunnel is Mt. Baker Ridge Tunnel in Seattle, Washington, featuring an internal diameter of 19.4 m. This tunnel was constructed by using the "stacked-drift" method, in which the structural lining was composed of 24 interlocking small-diameter concrete-filled tunnels (drifts) constructed prior to interior soil excavation. This method has advantages not only in its low construction cost but also in its small influence on ground surface settlement (Robinson et al., 1987). The stability mechanism, and the relationship between the earth pressures acting on drifts and the contact pressures between drifts are, however, still unclear for this type of structure.

This paper presents the outline of a stacked-drift-type tunnel construction method being planned for the saturated soil deposits in Japan, and then on the centrifuge test results concerning the behavior of the structural lining.

### 2 OUTLINE OF TUNNEL CONSTRUCTION METHOD

Figure 1 presents a schematic of the construction process. Shield machines enable of placing thick backfill concrete are to be used for the drift construction. Considering the saturated soil condition, these shield machines are of the closed type. After the primary drifts having a spacing of less than the drift diameters are individually constructed, the secondary drifts are constructed between the primary ones by scraping the backfill concrete on both sides. The primary and secondary drifts are then unified to form the structural lining. The internal soil core

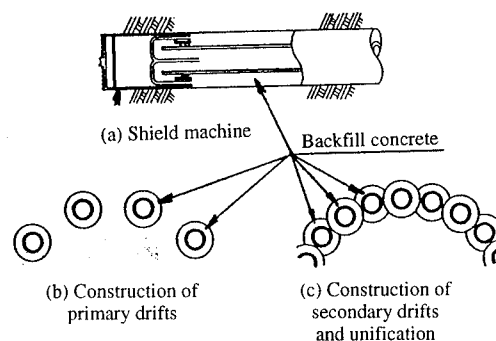


Fig. 1 Construction process of stacked-drift-type tunnels

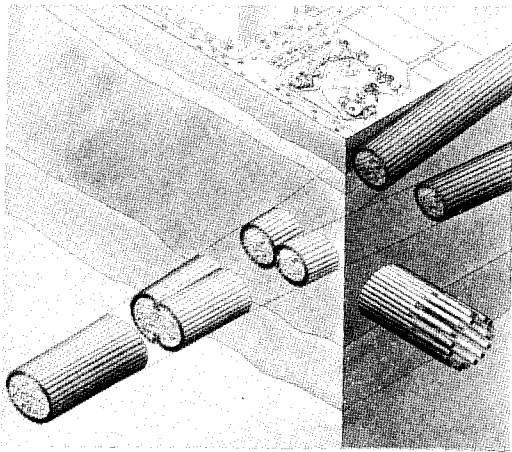


Fig. 2 Perspective of stacked-drift-type tunnels

is next removed, and the large-diameter tunnel is completed. Figure 2 illustrates the case in which two double-decked tunnels - one with three lanes of traffic and the other with two lanes each way - are joined into one tunnel offering five lanes each way.

### 3 TEST METHOD

#### 3.1 Tunnel model

Figure 3 depicts the model of the tunnel and ground prepared for testing. Each tunnel model is composed of 20 aluminum rods slightly less than 15 cm long. In cross section, 10 of these rods are round shaped and have a diameter of 2 cm (secondary drifts) and the others are grooved

( $r = 1$  cm) on two sides (primary drifts). These two types of rods are arranged alternately to compose a circular liner having an internal diameter of 10 cm, and form a stacked-drift-type tunnel model.

#### 3.2 Ground model

The dimension of the container prepared for the centrifugal test was 50 cm  $\times$  15 cm  $\times$  40 cm in the clear. Latex membranes were adhered to the fore- and backside walls of the container in order to reduce friction. Either dry silica sand (Toyoura standard sand) or saturated kaolin clay was used as the ground material. Each type of ground was made as follows.

1. The dry silica sand was poured uniformly around the tunnel model. Dry unit weight,  $\gamma_d = 1.6 \times 10^{-2}$  N/cm<sup>3</sup>; void ratio,  $e = 1.7$ ; and relative density,  $D_r = 0.87$ . The ground surface was leveled so that the cover height at the crown of the tunnel was 8 cm (whole ground height: 30 cm). On the surface, a lead shot layer 5 cm thick, which is equivalent to a sand layer 22 cm thick in weight, was placed as surcharge.

2. Clay ground: The deaired slurry of kaolin clay was consolidated with a pressure of 0.2 MPa in the container. Saturated unit weight,  $\gamma_{sat} = 1.6 \times 10^{-2}$  N/cm<sup>3</sup>; void ratio,  $e = 1.6$ ; and water content,  $w = 60\%$  after the consolidation. The cover height was 8 cm at the crown of the tunnel (whole ground height: 30 cm). A lead shot layer 3 to 5 cm high, which is equivalent to a clay layer 12 to 21 cm thick in weight, was placed as surcharge.

#### 3.3 Measurements and centrifugal loading

Measurements were conducted on the following items as shown in Fig. 3:

1. Ground surface settlements at the center and at the edge by using LVDTs;
2. Tunnel deformation in either the vertical (shown in Fig. 3) or horizontal direction by using a laser displacement meter;
3. Earth pressures acting on drifts by using two types of aluminum rods as detailed in Fig. 4 or rods fitted with small pressure meters (6 mm in diameter, in clay ground cases); and
4. Contact pressures between drifts by using aluminum rods shown in Fig. 4 (b).

Centrifugal loadings were applied up to an acceleration of 100 g. Loadings and unloadings

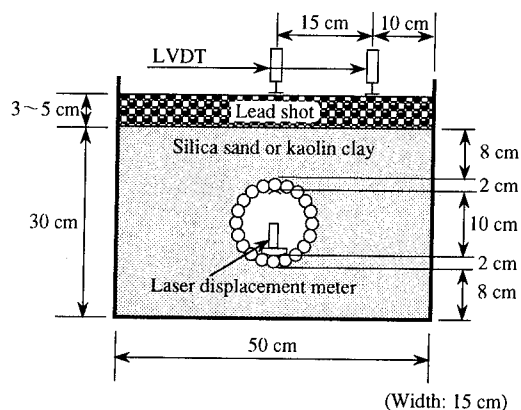


Fig. 3 Model of tunnel and ground

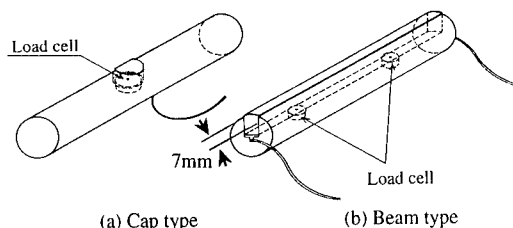


Fig. 4 Aluminum rods with pressure meter

were repeated two to four times in each case.

#### 4 TEST RESULTS AND DISCUSSION

##### 4.1 Features of measured values during the loading and unloading process

Figure 5 shows the variation in measured values corresponding to the centrifugal acceleration in one of the sand ground cases. After the first unloading, about one half of the value at 100 g remains in both the ground surface settlement and the tunnel deformation, mainly due to the plastic deformations caused by the self-weight compression of the ground. Moreover, the increments developed during and after the second loading are almost constant and seem to be elastic. Some similar residual amounts exist in earth pressures and contact pressures between the drifts. Each measured value is therefore indicated in two ways: one is the measured value itself at 100 g in the first loading, and the other is the mean increment during and after the second loading.

In the clay ground cases, the residual values are much smaller and the behavior seems to be more elastic as seen in Fig. 6.

##### 4.2 Ground surface settlement and tunnel deformation

The averaged ground surface settlements at both the center and the edge, and the tunnel deformations in both the vertical and horizontal

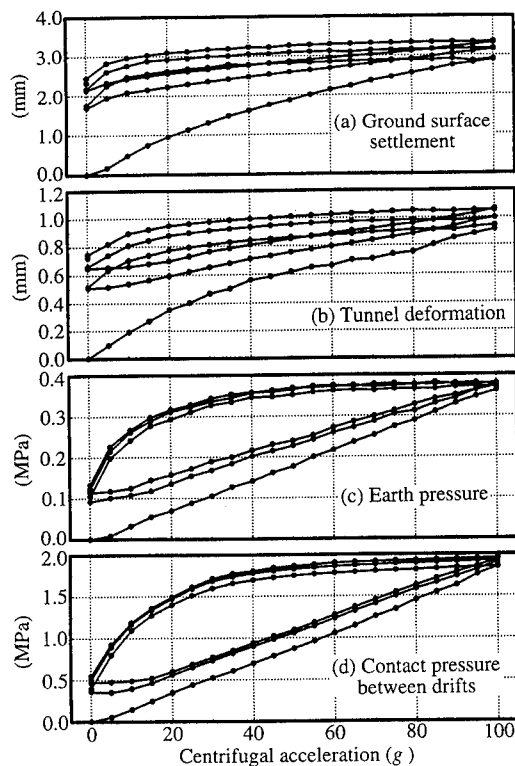


Fig. 5 Measured values corresponding to centrifugal acceleration in sand ground case

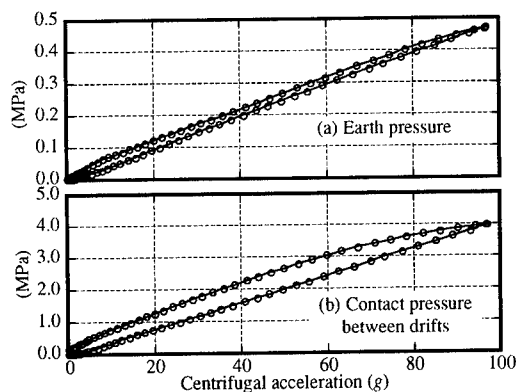


Fig. 6 Measured values corresponding to centrifugal acceleration in clay ground case

Table 1 Ground surface settlements and tunnel deformations

Ground type	Loading	Ground surface settlement		Tunnel deformation	
		Center	Edge	Vertical compression	Horizontal extension
Dry silica sand	1st	4.1	3.8	1.5	0.4
	During and after 2nd	2.2	2.1	0.7	0.2
Saturated kaolin clay	1st	14.8	10.0	0.6	2.3

directions are tabulated in Table 1. Since the present test procedure does not simulate the actual construction process, there is no point in evaluating these values quantitatively. In both cases, ground surface settlements at the center are greater than those at the edge. The vertical diameter of the tunnel decreases whereas the horizontal one increases with increasing acceleration. Thus, the tunnel deforms into a depressed ellipse.

#### 4.3 Earth pressure

Figure 7 shows the distribution of earth pressure in the sand ground cases. In the figure, each earth pressure is normalized by the overburden pressure at the measuring depth. The normalized earth pressure is slightly less than 0.3 at the crown and the invert and about 0.8 near the springline. These values are considerably different from the existing centrifugal test results obtained for buried pipes in dry sand.

Let us here compare the present test results with those obtained by Tohda et al. (1991) on rigid and flexible pipes in dry silica sand as shown in Fig. 8. On rigid pipes, the earth pressure is about the same as the overburden pressure at the crown and the invert, and normalized earth pressure at the springline is about 0.2, which is very close to the  $K_0$  (coefficient of earth pressure at rest) value calculated by using Jaky's formula. Similar test results were also derived by Hagiwara et al. (1989) and Mito et al. (1990). When the pipe is flexible, the distribution of normalized earth

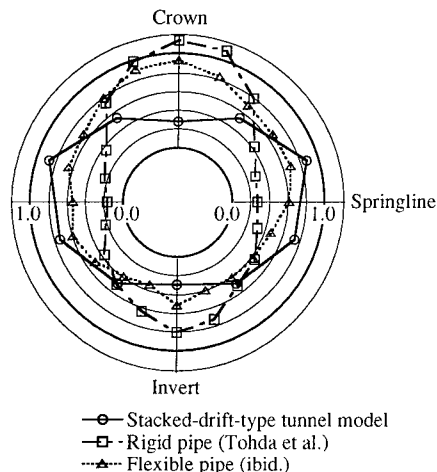


Fig. 8 Difference in normalized earth pressure distribution between stacked-drift-type tunnel model, rigid pipe and flexible pipe

pressure is more uniform because of the redistribution of earth pressure due to the deformation of the pipe. For the stacked-drift-type tunnel, this trend becomes extreme. The earth pressures at the crown and the invert are "active," whereas those near the springline are "passive," which agrees with the deformation form. Such a trend probably results from the flexibility of deformation and the lack of the tensile stress transmitted between the drifts because they are not rigidly connected but rather simply contact each other.

The mean normalized earth pressures in the clay ground cases shown in Fig. 9 are almost 1

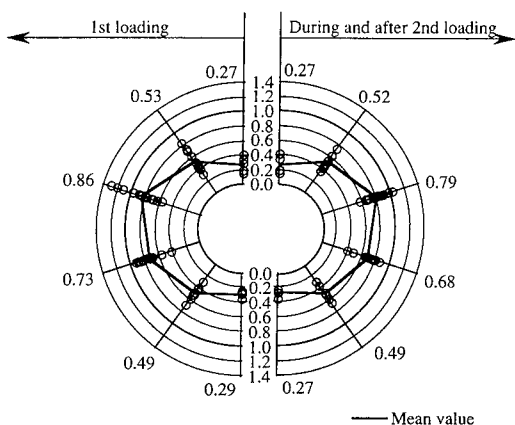


Fig. 7 Normalized earth pressures in sand ground cases

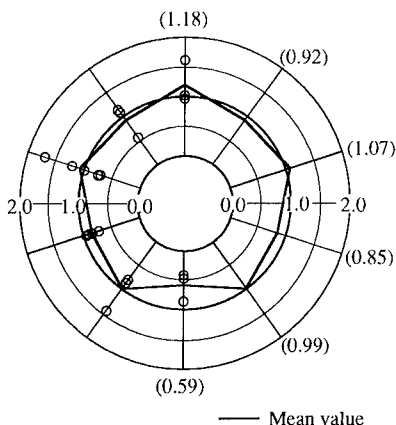


Fig. 9 Normalized earth pressures in clay ground cases

along the circumference except at the invert. This demonstrates that the tunnel is subjected to pressure acting hydrostatically with a  $K_0$  value of almost 1, and that Poisson's ratio ( $\nu$ ) of saturated clay is close to 0.5 as calculated from the theoretical relationship;  $K_0 = \nu/(1-\nu)$ . Hence, the ground is considered to be in the undrained condition in the vicinity of the tunnel.

#### 4.4 Contact pressure between drifts

Figure 10 shows the distributions of contact pressures between the drifts in the sand ground cases. The shapes of the mean contact pressure distribution are similar to those of the earth pressures. The ratio of the mean contact pressure near the springline to that at the crown

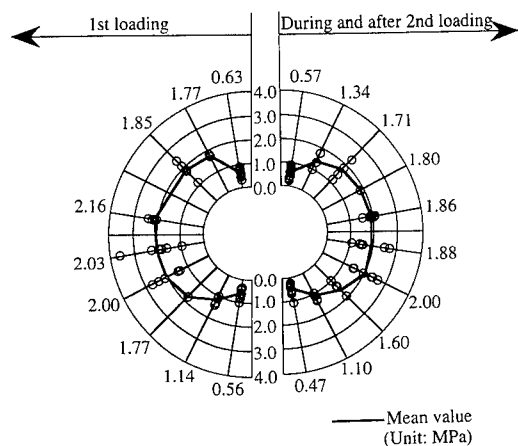


Fig. 10 Contact pressures between drifts in sand ground cases

is about 3.3. According to the test results derived for the three types of pipes having external diameters of 8 cm and thicknesses of 2 mm in dry silica sand as presented by Nakamatsu et al. (1990), this ratio (thrust ratio) is proportional to the flexural rigidity in the angle direction. Applying this relationship to the present test results, the stacked-drift-type tunnel model exhibits a flexural rigidity of about 47  $\text{N}\cdot\text{m}^2/\text{m}$  as indicated in Fig. 11. Although this seems to contradict the fact that the stacked-drift-type tunnel model does not transmit tensile stress, it behaves as if it exhibited some flexural rigidity under the restricted condition.

Figure 12 shows the distribution of contact pressures between the drifts in the clay ground cases. Compared to the sand ground cases, contact pressures in the clay ground cases are more uniform and about 1.5 times larger at the springline and six times larger at the invert.

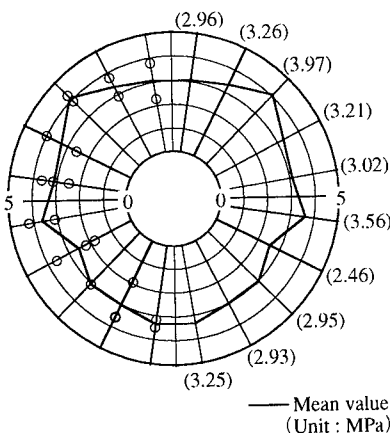


Fig. 12 Contact pressures between drifts in clay ground cases

#### 4.5 Tunnel stability mechanism

Deducting from the test results, the stability mechanisms of the stacked-drift-type tunnel are different in sandy and clayey grounds. In the sand ground cases, the tunnel deforms into a depressed ellipse and is stabilized by the combination of passive earth pressure near the springline and the arch action generated by the upper half of the tunnel and cover sand.

Conversely, in the clay ground cases, both earth and contact pressures are larger than those in the sand ground cases. Compared to the sand

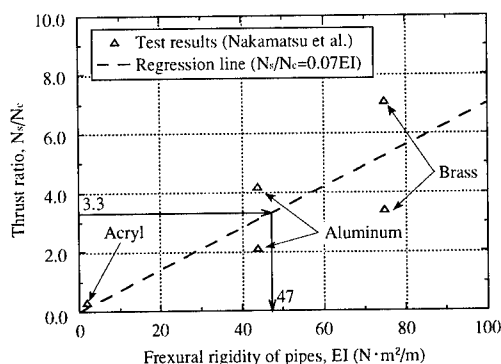


Fig. 11 Relationship between flexural rigidity of pipes and thrust ratio

ground cases, rigidity of the ground is smaller, and hence, considerable stress concentration on the tunnel model seems to occur, resulting in the tunnel being stabilized by deformation permitting the contact pressures between drifts to become uniform.

## 5 COMPARISON WITH THE IN SITU DATA AT MT. BAKER RIDGE TUNNEL

Figure 13 shows the in situ data measured at the Mt. Baker Ridge Tunnel construction site.

Contact pressures between drifts measured at Mt. Baker Ridge Tunnel and the present test results in both the sand and the clay ground cases are compared in Table 2, in which the in situ data are calculated from the total thrusts and the test data are the mean values measured during the first loadings. Relative contact pressures normalized by the respective value at the springline are also indicated in parentheses. The ground through which Mt. Baker Ridge Tunnel was constructed consists of primarily hard silt or clay, having SPT blow counts of over 30, as well as a minor amount of dense sand. Normalized contact pressure measured on site is close to the sand ground test results at the crown and close to clay ground ones at the invert. Hence, the ground condition at Mt. Baker Ridge Tunnel is considered to be a mixture of clayey and sandy ground.

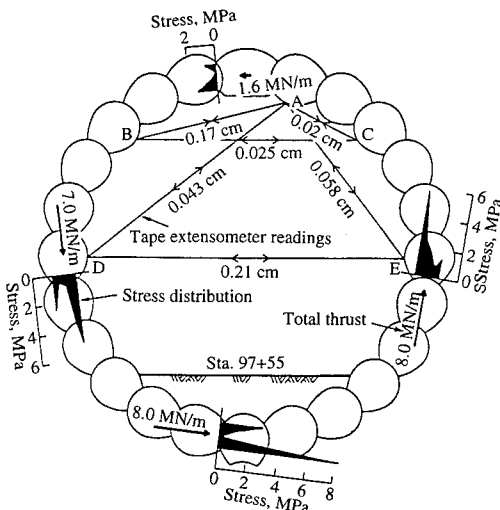


Fig. 13 In situ data at Mt. Baker Ridge Tunnel

Table 2 Comparisons of contact pressures between drifts between in situ data at Mt. Baker Ridge Tunnel and test results (Unit: MPa)

	Crown	Springline	Invert
In situ data at Mt. Baker Ridge Tunnel	0.94 (0.21)	4.41 (1.00)	4.71 (1.06)
Test results (sand ground cases)	0.63 (0.31)	2.03 (1.00)	0.56 (0.28)
Test results (clay ground cases)	2.96 (0.83)	3.56 (1.00)	3.25 (0.91)

## 6 CONCLUSION

The behaviors of stacked-drift-type tunnels both in sand ground and in clay ground were investigated through a series of centrifuge model tests. The test results confirmed that the behavior of stacked-drift-type tunnels is quite different from that of ordinary tunnels. The findings also revealed that the stability mechanism of the tunnels is different in sandy and in clayey grounds.

## REFERENCES

- Hagiwara, T., O. Kusakabe, T. Nomoto & K. Mito 1989. Experiments to measure earth pressures on rigid buried pipes in dry sand. *Proc. 44th JSCE*, 3, Nagoya, Japan: 936-937. (in Japanese)
- Mito, K., T. Nomoto, T. Hagiwara & O. Kusakabe 1990. Measurements of earth pressures on rigid tunnel in dry sands using centrifuge. *Proc. 25th JSSMFE*, Okayama, Japan: 1739-1742. (in Japanese)
- Nakamatsu, U., T. Nomoto, T. Hagiwara & O. Kusakabe 1990. Measurements of bending moments and thrusts in flexible tunnels in dry sand by centrifuge. *Proc. 25th JSSMFE*, Okayama, Japan: 1735-1738 (in Japanese)
- Robinson, R. A., M. S. Kucker, A. I. Feldman & H. W. Parker 1987. Ground and liner behavior during construction of the Mt. Baker Ridge Tunnel. *Proc. 1987 Rapid Excavation and Tunneling Conf.*, New Orleans, Louisiana, Vol. 1: 309-328
- Tohda, J., H. Yoshimura, K. Oki & H. Seki 1991. Centrifuge model tests on several problems of buried pipes. *Centrifuge 91*: 83-90. Rotterdam: Balkema.

## Response of a tunnel lining due to an adjacent twin shield tunneling

H. Yoshimura & K. Miyabe

*Konoike Construction Co., Ltd, Osaka, Japan*

J. Tohda

*Osaka City University, Japan*

**ABSTRACT:** 3-D centrifuge model tests on the adjacent construction of parallel twin shield tunnels with external diameters of 9.75 m were conducted to investigate the response of an initially constructed tunnel lining due to driving a shield machine in the vicinity of the tunnel lining. A model of the shield machine and a pipe that simulated the existing tunnel lining were buried in dry sand, considering different distances and tunnel formations. Circumferential distributions of bending strains in the tunnel lining wall were measured at six sections during a 150 G flight, when the shield machine was pushed or pulled so as to either increase or release ground stresses in front of the machine face. Measured bending strains fully quantified the effects of the investigated factors on the response of the existing tunnel lining due to the adjacent twin shield tunneling. The effect of the presence of the shield machine was also discussed.

### 1 INTRODUCTION

Due to not only its advantage to avoid the surface traffic congestion during construction, but also to the fact that its construction technique has been improved both to cope with difficult ground conditions and to minimize ground deformation, the shield tunneling method has been widely employed in Japan to construct roads, railways, and large pipelines in the ground. Recently, this method is also being applied to construct the new large-scale urban infrastructures, such as underground regulating reservoirs, flood ways and parking spaces.

When constructing large underground spaces by the shield tunneling method, multiple shield tunneling is increasingly being employed, due to its economy. However, the multiple shield tunneling generates a new problem; each tunnel must be constructed very close within the widths of public roads, and in such a case, the behavior of the initially constructed tunnel lining, induced by an adjacent construction of another tunnel, has not been made clear yet. The current Japanese design standards (19-83, 1988) state that influence of adjacent shield tunnelings should be considered when an advancing tunnel approaches the other within a transverse clearance equivalent to the external diameter of the advancing tunnel. Nevertheless, there is poor or no re-

commendation as to the procedure to evaluate the magnitude of such an influence. On the other hand, it is difficult to obtain site data to estimate the net influence, because grouting was employed as counter-measures in almost all the adjacent shield tunnels constructed hitherto.

Thus, 1/150-scaled 3-D centrifuge model tests on parallel twin shield tunnelings were conducted to quantify the influence, on an initially constructed tunnel lining, of driving an adjacent shield machine. The prototype twin shield tunnels tested have same external diameters of 9.75 m, the minimum cover height being 20 m; the prototype of the existing tunnel lining is an assembly of precast reinforced concrete segments. An aluminum-alloy pipe, having an external diameter  $D$  of 6.5 cm, was used in the tests to simulate the existing tunnel lining. The pipe and a model of the shield machine were buried in dry sand ground within different distances and in different tunnel formations (vertical and horizontal). The models were put into a centrifugal acceleration field of 150 G (G: gravitational acceleration), and the shield machine was pushed or pulled in the ground so as to either increase or release the ground stresses in front of the machine face. In the course of the tests, circumferential distributions of bending strains produced in the wall of the pipe were measured at six sections.



This paper details the test procedure and discusses the effect, on an existing tunnel lining, of an adjacent twin shield tunneling, based on the test results.

## 2 MODELING OF TWIN SHIELD TUNNELS

The prototype twin shield tunnels tested have external diameters of 9.75 m, serving as a pair of two-lane road tunnels. They are constructed in parallel below 20 m depths in non-cohesive ground, by using a mechanical shield machine having a length of 7.5 m. The prototype of the existing tunnel lining is an assembly of reinforced concrete segments having thicknesses of 50 cm, which is ordinarily used in 10 m class lining shield tunnelings.

Figs. 1 (a) and 1 (b) show 1/150-scaled models for the existing tunnel lining and the shield machine. These figures are for the case where the two tunnels are installed horizontally within the smallest tunnel clearance of 0.3 cm. Both models, made of aluminum-alloy, have external diameters  $D$  of 6.5 cm, whose surfaces are smoothly finished.

The model of the existing tunnel lining is a pipe having a wall thickness  $T$  of 0.25 cm and a length of 33.4 cm. This thickness was determined so as to satisfy the following relationship between the flexural stiffness of the linings:  $EI/(R)^3$  in models  $=EI/(R)^3$  in prototypes, where  $E$ : Young's modulus of the lining material,  $I$ : inertia moment of the lining, and  $R$ : neutral radius of the lining. Although the  $EI/(R)^3$  values used in the design are usually reduced to be around 80 % of the net values to account for the stress relief at the joints, this reduction is neglected in the above equation. The weight of the pipe per unit longitudinal length,  $W$ , was adjusted as 2.3 kgf/cm under 150 G, so as to have almost the same  $W/D$  value of that of the prototype, where  $D$  is the external diameter of the pipe. As shown in Fig. 1 (b), strain gauges were stuck onto the outer and inner surfaces of the pipe at 8 or 4 measuring points in the six sections, (a) to (f), to measure the circumferential distributions of the bending strains produced in the wall of the pipe. The section (b) was coincident with the section occupied by the shield machine face. A thin sheet of polyvinyl chloride was pasted on the outer surface of the pipe to avoid damages on the strain gauges and connecting wires.

Fig. 2 shows the details of the model shield machine system and the hydraulic cylinder. The shield machine system consists of three parts, A to C. The model machine (A-part) has a length of 5 cm,

whose face and shell are respectively formed by a plain 0.5 cm thick plate and a cylindrical vessel. They are connected by means of a load cell to measure the earth pressures acting on the machine face,  $p_a$ . Another load cell in the B-part is used to measure the value of  $p_b$ , the sum of  $p_a$  and

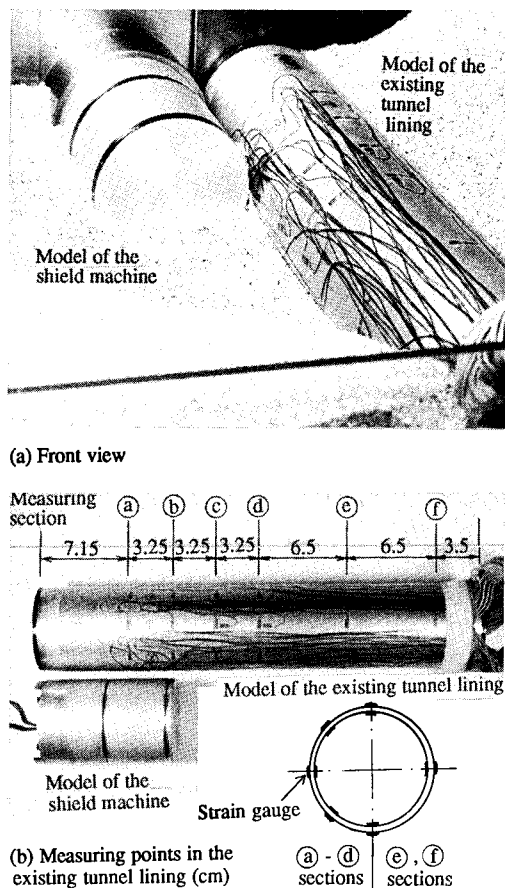


Fig. 1. Model of the twin shield tunnels.

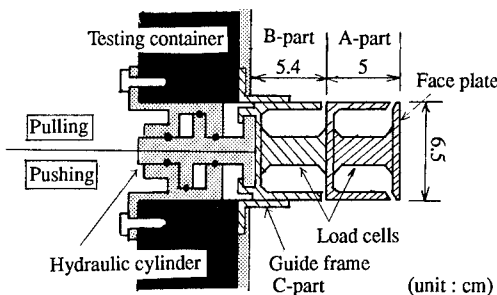


Fig. 2. Details of the model shield machine system.

the friction force acting along the outer surface of the shield machine per unit face area. A vessel in the B-part covers this load cell, and it is inserted into a guide frame (C-part). The guide frame is designed to allow vertical sliding along the wall of the testing container, so that the model machine system can follow the ground settlement, produced in the centrifugal acceleration field. The weight of the shield machine system per unit longitudinal length,  $W$ , is 13.3 kgf/cm under 150 G, and its  $W/D$  value is 1.65 times that of the prototype shield machine. Clearances of 0.1 cm, both between the face and the vessel in the A-part, and between the two vessels, are covered by two sheets of thin vinyl tape to avoid sand jamming.

The hydraulic cylinder is fixed to the back wall of the testing container. One edge of its piston is in contact with the bottom of the vessel in the B-part, allowing slidable movement. The other edge of the piston is connected to a displacement gauge to measure displacement of the model machine system. The cylinder is used for pushing or pulling the model machine, so as to either increase or release the ground stresses in front of the machine face; this machine driving simulates actual construction conditions, in which the mucking ratio is either smaller or greater than 100 %.

### 3 MODEL, EQUIPMENT AND TEST PROCEDURE

Fig. 3 shows the model setup. The testing container, made of aluminum-alloy, was a strong box, whose internal dimensions were 44.3 cm  $\times$  43.8 cm  $\times$  33.5 cm. The cover height of the model shield machine was constant to be 13.3 cm, which corresponds to 20 m in the prototype scale. The model of the existing tunnel lining was installed within clearances,  $C$ , of 0.3 cm ( $=0.05 D$ : 0.45 m in the prototype scale), 3.25 cm ( $=$

0.5  $D$ : 4.9 m) and 6.5 cm ( $=D$ : 9.75 m) against the model machine, either at the lateral-side or at the lower-side of the model machine (horizontal and vertical tunnel formations). In the vertical tunnel formation, the cover height of the existing tunnel lining,  $H$ , differed in each case.

Air-dried silica sand, whose properties are shown in Table 1, was used as a model ground material. The uniform dense model ground was prepared by pouring the sand into the testing container from a small hopper, through a circular nozzle of 1 cm in diameter, in the direction of the longitudinal axes of the model tunnels; the pouring height was maintained as 50 cm. The density of the ground was  $1.55 \pm 0.02$  g/cm<sup>3</sup>.

The models were put into a centrifugal acceleration field of 150 G ( $G$ : gravitational acceleration), by using the Mark-5 centrifuge of Osaka City University, which is of a swing bucket type, having a nominal radius of 2.56 m. The distributions of the bending strains produced in the wall of the existing tunnel lining were measured and simultaneously memorized on a personal computer, while the shield machine was either pulled until the value of  $p_a$  reached 0 kgf/cm<sup>2</sup>, or pushed until  $p_b$  reached 13 kgf/cm<sup>2</sup>. The  $p_b$  value of 13 kgf/cm<sup>2</sup> corresponds to the maximum pressure that is usually caused by a 10 m class mechanical shield machine.

Table 2 shows the test contents and conditions. Four tests, in which only the model of the existing tunnel lining was installed in the ground at different depths, were carried out to obtain the bending strains, without effects of both the presence and the driving of an adjacent shield machine. The total number of the tests was 12.

Table 1. Properties of sand.

$G_s$	Grain size	$U_c$	$\rho_{dmax}$	$\rho_{dmin}$	$\rho_d$
2.65	0.24-1.4 mm	1.75	1.58 g/cm <sup>3</sup>	1.32 g/cm <sup>3</sup>	1.55 g/cm <sup>3</sup>

Table 2. Contents and conditions of the tests.

Kind of tunneling	Tunnel formation	Clearance $C$ (cm)	Cover height* $H$ (cm)	Machine driving
Twin	Horizontal	0.3	13.3	Push, Pull
		3.25	13.3	Push, Pull
	Vertical	0.3	20.1	Push, Pull
		3.25	23.1	Push
Single	—	—	13.3, 20.1	—
			23.1, 26.3	

\* Cover height of the tunnel lining

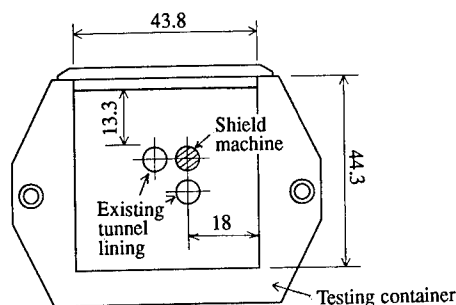


Fig. 3. Scheme of the model setup (unit : cm).

#### 4 TEST RESULTS

In the following, bending moments,  $M$ , produced in the wall of the existing tunnel lining, are presented as measured results, calculated through  $M = \epsilon ET^2/6$ , where  $\epsilon$  are the measured bending strains.  $M$  are taken as positive when inducing tensile stresses in the internal surface of the model. In addition,  $\Delta M$  denote increments of  $M$ , whose initial values are taken as the values measured just before driving the adjacent shield machine;  $\Delta M$  are used to indicate the effect of the machine driving.

Fig. 4 illustrates the circumferential distributions of the bending moment  $M_0$  in the wall of the existing tunnel lining in polar coordinates, obtained in the single tunneling cases with different cover heights  $H$ ; the data plotted in the figure are the average values among the data measured at the six measuring sections under 150 G. With an increase in  $H$ ,  $M_0$  at the top, bottom and sides of the lining increase and converge to constant values.

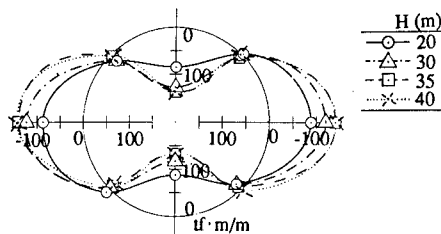


Fig. 4. Distributions of  $M_0$  for different  $H$  in single tunneling tests.

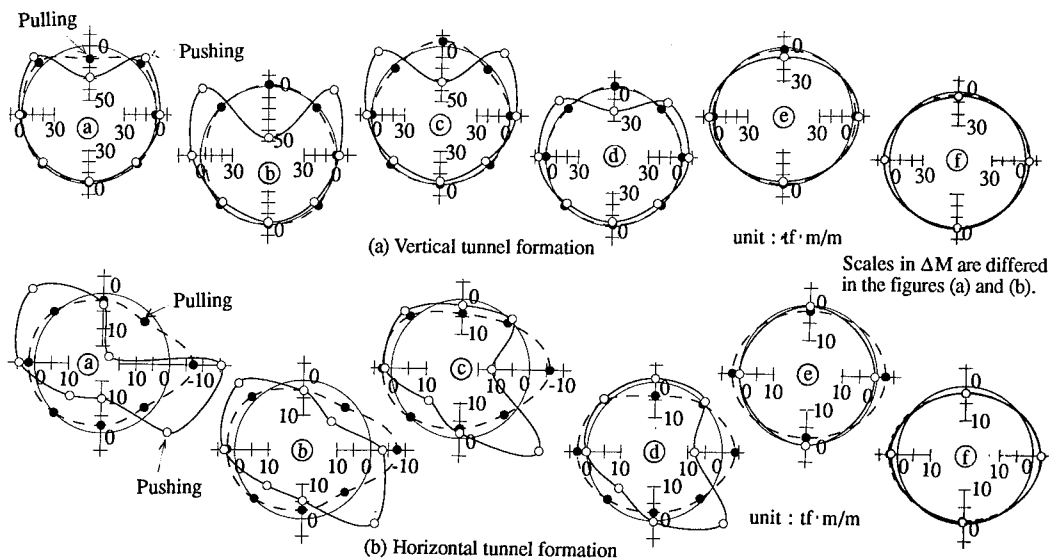


Fig. 6. Distributions of  $\Delta M$  measured in the six sections for different tunnel formations ( $C = 0.3$  cm).

Fig. 5 shows the relationship between  $\Delta M$  at the lining crown and  $p_b$  for the six sections, measured in the course of pushing the adjacent shield machine; this is for the case of the vertical tunnel formation with a clearance of  $C = 0.3$  cm between the two tunnels. Before pushing the machine (at  $\Delta M = 0$ ),  $p_b$  was recorded as  $0.39$  kgf/cm<sup>2</sup>. With an increase of  $p_b$ ,  $\Delta M$  increase in all the sections, except when  $p_b > 10$  kgf/cm<sup>2</sup> in the section (a), located behind the machine face section (b). The values of  $p_a$  were recorded as  $0.72$  kgf/cm<sup>2</sup> before pushing the machine, and as  $10$  kgf/cm<sup>2</sup> when  $p_b = 13$  kgf/cm<sup>2</sup>.

Fig. 6 illustrates the circumferential distributions of  $\Delta M$  in polar coordinates for the six sections, measured both at

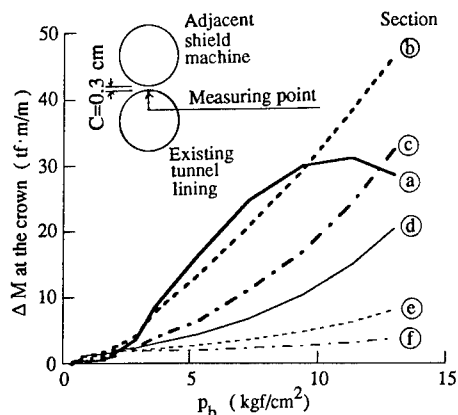


Fig. 5.  $\Delta M$  vs.  $p_b$  during pushing the shield machine (vertical tunnel formation,  $C = 0.3$  cm).

$p_b=13 \text{ kgf/cm}^2$  when pushing the adjacent machine and at  $p_a=0 \text{ kgf/cm}^2$  when pulling it. The figures, (a) and (b), show respectively the data obtained for the cases of the vertical and horizontal tunnel formations; the clearance between the two tunnels was  $C=0.3 \text{ cm}$  ( $=0.05 D$ ) in both cases. Note that the scales in  $\Delta M$  are differed in both figures. Fig. 6 indicates that:

1. In the vertical tunnel formation shown in the figure (a), the pushing of the adjacent shield machine changes  $\Delta M$  at the lining crown in any sections to great extent, being the most remarkable in the section (b), while the pulling of the shield machine only changes  $\Delta M$  at the lining crown in the section (a). These changes in  $\Delta M$  leads to unsafe region for the lining.

2. In the horizontal tunnel formation shown in the figure (b), the values of  $\Delta M$  are considerably smaller than those in the vertical tunnel formation. Nevertheless, the pushing of the shield machine changes  $\Delta M$  at the machine-side (right-hand side) springline toward the positive-side in the sections (c) and (d), and toward the negative-side in the sections (a) and (b); the change in  $\Delta M$  in the latter two sections leads to the unsafe region for the lining. On the other hand, the pulling of the machine changes  $\Delta M$  toward the negative-side at the machine-side springline in any sections; this change in  $\Delta M$  also leads to the unsafe region for the lining.

Fig. 7 indicates distributions of  $\Delta M$  along the longitudinal axis of the existing tunnel lining for all the twin tunneling cases, measured at  $p_b=13 \text{ kgf/cm}^2$  when pushing the adjacent shield machine and at  $p_a=0 \text{ kgf/cm}^2$  when pulling it. In the figures (a) and (b), the vertical axes denote changes respectively the  $\Delta M$  measured at the lining crown in the vertical tunnel formation, and at the machine-side springline in the horizontal tunnel formation; the horizontal axes in the figures denote  $L/D$ , where  $L$  is the distance from the section (b) corresponding to the machine-face position, and  $D$  is the external diameter of the lining. The figures (a) and (b) show that:

1. When pushing the machine, the smaller the clearance between the tunnels, the greater  $\Delta M$  it generates; it also brings the peak position of  $\Delta M$  closer to the section (b).

2. When pulling the machine, appreciable change in  $\Delta M$  is seen only in the area of  $-0.5 < L/D < 0.5$ , adjacent to the section (b).

Fig. 8 indicates the relationship between the moment increase index  $\alpha$  and the clear-

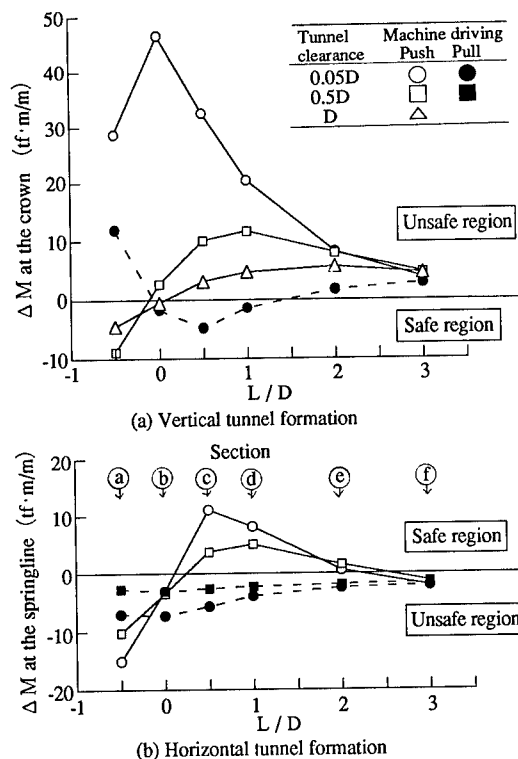


Fig. 7.  $\Delta M$  vs.  $L/D$  for different tunnel formations.

ance  $C$  between the two tunnels. The index  $\alpha$  is defined to represent the isolated effect of the machine driving on the existing lining, as follows:

$$\alpha = |M_0 + \Delta M_{\max}| / |M_0|$$

where,  $\Delta M_{\max}$  are the maximum values of the unsafe region of  $\Delta M$  shown in Fig. 7, and  $M_0$  are the bending moments at the respective points (at the crown in the vertical tunnel formation and at the springline in the hor-

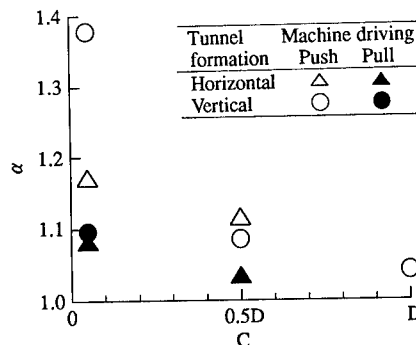


Fig. 8. Moment increase index  $\alpha$  vs. tunnel clearance  $C$ .

horizontal tunnel formation), measured in the single tunneling tests (cf. Fig. 4). In the above equation,  $M_0$  are used as the standard bending moments, due to the following reason. Actual twin shield tunnels are constructed separately, whereas in the tests the model twin shield tunnels were installed in the model ground simultaneously. Thus, the bending moments  $M_1$ , measured before driving the model machine and used as the initial values of  $\Delta M$ , include the effect of the presence of the shield machine, and therefore,  $M_1$  are inadequate to represent the isolated effect of the machine driving on the existing tunnel lining.

Fig. 8 shows that: 1) the smaller the clearance between the tunnels, the greater  $\alpha$  it generates, 2) the pushing of the adjacent shield machine increases the value of  $\alpha$  more markedly than the pulling of it, and as a result, 3) the combination of the smallest clearance and the pushing of the machine generates remarkably great value of  $\alpha$ , in particular, in the vertical tunnel formation. These results are consistent with the field data reported in the literature (Hashimoto, 1984).

Finally, the effect of the presence of the adjacent shield machine on the existing tunnel lining shall be represented here. Fig. 9 shows the test results, measured in the test of the vertical tunnel formation with the smallest tunnel clearance of 0.3 cm; the two tests with identical conditions (the pushing and pulling tests) generated almost the same results. Circumferential distributions of  $M_1$ , measured before the machine driving in the two sections (a) and (b), together with that of  $M_0$ , are illustrated in polar coordinates in the figure. The solid-line in Fig. 9, furthermore, denotes the distribution of  $M_1/M_0$  at the lining crown along the lining axis. This distribution of  $M_1/M_0$  is modified into that illustrated in broken-line in the figure, by

considering the difference in the weights between the model and prototype machines, as described in the chapter 2.

Even the modified distribution of  $M_1/M_0$  indicates that the presence of the adjacent shield machine increases drastically the bending moment at the lining crown in the sections (a) and (b). Fortunately, this drastic increase in the bending moment was only measured under the present test conditions, the vertical tunnel formation and  $C=0.3$  cm.

## 5 CONCLUSIONS

A series of 1/150-scaled 3-D centrifuge model tests on adjacent parallel twin shield tunneling fully quantified the effects of the following factors on the bending moments of an existing tunnel lining: condition of driving an adjacent shield machine, and distance between the two tunnels as well as their formations. The main conclusions obtained by this study are as follows:

- (1) The driving of the adjacent shield machine to increase the ground stresses in front of the machine face affects the bending moment more remarkably than the driving of the machine to release the ground stresses.
- (2) The smaller the clearance between the tunnels, the greater the increase in bending moment of the existing tunnel lining it generates.
- (3) The combination of machine driving to increase the ground stresses and small clearance between the tunnels is critical for the twin shield tunneling, in particular, in the vertical tunnel formation.
- (4) The weight of the adjacent shield machine drastically increases the bending moment of the existing tunnel lining, when the shield machine passes very close above the existing tunnel.

## REFERENCES

- Japan Railway Civil Engineering Association. 1983. Guideline for design and application of shield tunnels.
- Japan Society of Civil Engineers. 1988. The standard specifications for tunnels.
- Hashimoto S. 1984. Results of shield tunneling in vertical close to existing shield tunnels. Proc. of JSCE. No.352/3-2:1-22.
- Nakazawa J. Miyabe K. Yoshimura H. Takada N. & Tohda J. 1992. Centrifuge model tests on laterally adjacent construction of shield tunnels. Proc. of the 47th Annual Conference of JSCE. 3:92-93.

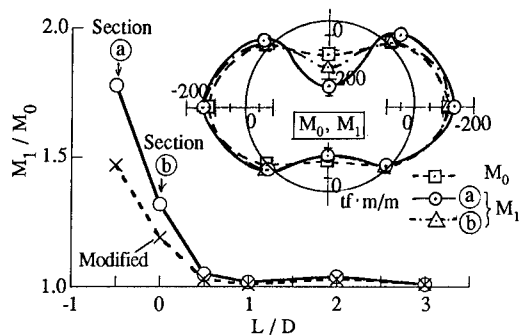


Fig. 9.  $M_1/M_0$  vs.  $L/D$ , and distributions of  $M_0$  and  $M_1$  (vertical tunnel formation,  $C=0.3$  cm).

## A miniature shield tunneling machine for a centrifuge

T.Nomoto, K.Mito & S.Imamura

*Nishimatsu Construction Co., Ltd, Tokyo, Japan*

K.Ueno

*Department of Civil Engineering, Utsunomiya University, Tochigi, Japan*

O.Kusakabe

*Department of Civil Engineering, Hiroshima University, Japan*

**ABSTRACT:** This paper presents a few years' experience of developing a miniature shield tunneling machine for centrifuge tests. The process of shield tunneling is rather complex and the need for the shield machine representing the prototype construction process is discussed. Details of the shield machine are given and the performance of the machine is shown. Some initial data are also presented and the repeatability of the test is confirmed. The paper also describes the difficulties and limitations of the machine at the present stage.

### 1 INTRODUCTION

Centrifugal modeling has provided valuable information on lining stresses of buried structures (James and Larsen, 1977), and the importance of modeling of construction process of a buried rigid pipe was demonstrated by Tohda et al. (1988). Stability of clay ground during shield tunneling has also been investigated by centrifuge studies by Mair (1979). Actual behavior of ground deformation due to shield tunneling and lining stresses, however, is greatly affected by many factors: ground conditions, the type of shield machine, construction procedure, magnitude of tail void, and furthermore workmanship. The problem is truly three-dimensional and numerical modeling still remains difficult, although some promising developments were reported by Rowe and Lee (1992). The authors have tackled the problem of lining stresses of shield machines by conducting centrifuge tests. Measurements of earth pressure on a rigid model tunnel and of lining stresses were attempted (Kusakabe et al, 1990). The authors have become strongly aware that the modeling of construction sequence is of vital importance to evaluate the realistic lining stresses after construction. This paper reports on a few years' development of a

miniature shield machine for a small centrifuge, and some initial data are presented.

### 2 DEVELOPMENT OF A SHIELD MACHINE

Meaningful results may be obtained from centrifuge tests, which must satisfy the followings: (1) Reproduction of the stress history and initial stress condition of the ground, (2) Simulation of tail void during shield excavation, (3) Realistic reproduction of stress level, and (4) Reproduction of shield tunneling process. To meet these requirements, a miniature shield machine was developed for centrifuge tests, as will be described below. A beam-type centrifuge of Utsunomiya University was used, specifications of which are shown in Table 1.

Table 1 Specifications of Centrifuge

Effective radius	1.18 (m)
Maximum acceleration	120 (G)
Load capacity	0.15 (t)
Drive motor	11 (kW)
Specimen loading method	Swing-up type

## 2.1 System

The test system was developed in three stages from Mark 1 to Mark 3. Knowledge obtained from Mark 1 and Mark 2 was utilized to develop Mark 3. The improvements introduced into Mark 3 are as follows: (1) An excavation unit was put on two rails to reduce frictional resistance considerably. (2) A motor capable of producing its rated torque throughout its rotational speed range was used for propulsion. (3) The configurations of the cutter, the muck inlets in the cutter, and the screw conveyor for muck removal were modified for smooth flow of excavated material. (4) A duralumin frame was used to reduce the weight of the model. The length of the system was increased to make internal mechanical detailing easier.

Fig. 1 is a general view of the miniature shield machine. The shield machine is divided into two parts: a soil container and a shield section. The shield section can further be subdivided into a triple pipe section, which models the shield tunneling machine and the tunnel lining, and a drive section. The inside dimensions of the container are 200 x 200 x 290mm. Because of the dimensional restrictions of the centrifuge used, the container is not large enough to be free from the influence of the side walls of the container.

Fig. 2 shows the structure of the triple pipe section. The outermost pipe represents the shield machine and is made of a  $\phi 50$ mm aluminum pipe. The intermediate pipe, made of a  $\phi 40$ mm aluminum pipe, models the tunnel lining. Strain gauges to measure earth pressures are installed on the inside and outside of the intermediate pipe. The innermost pipe is a mucking pipe designed for preventing the load of muck from acting on the intermediate pipe. The innermost pipe houses a screw conveyor to move the muck backward. The cutter is located at the front end of the screw conveyor.

The drive section includes a drilling motor and a propulsive motor, whose specifications are summarized in Table 2. The drilling motor drives the cutter and the screw conveyor. The propulsive motor moves the three pipes forward and the outermost pipe backward.

Fig. 3 shows the measuring system diagrammatically. The items measured in the experiment are strain in the intermediate pipe, ground surface displacement, and earth pressure. Like the operations of the centrifuge

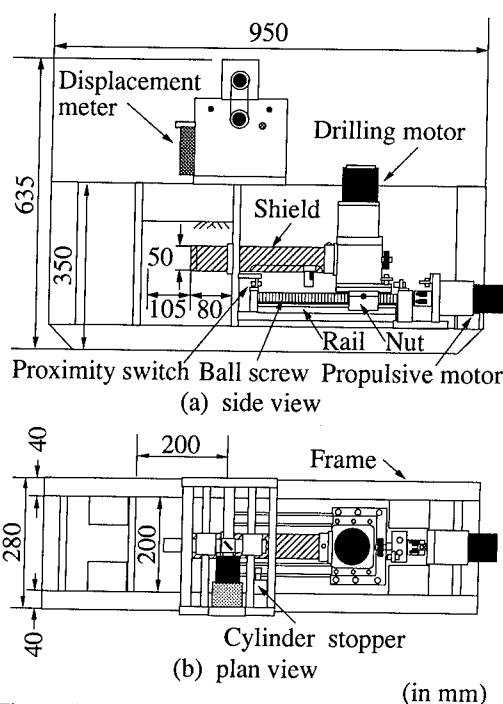


Fig. 1 General view of the shield machine

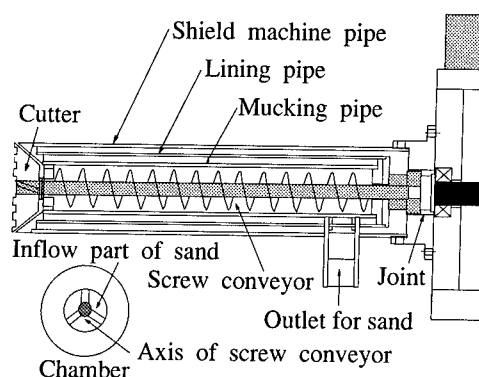


Fig. 2 Triple pipe structure

Table 2 Specifications of drive motors

	Drilling Motor	Propulsive Motor
Output (W)	40	50
Voltage (V)	100	100
Speed reduction ratio	1/50	1/200
Speed range ( $\text{min}^{-1}$ )	1.8 ~ 28	1.5 ~ 15
Torque (N·m)	2.0 ~ 10	20

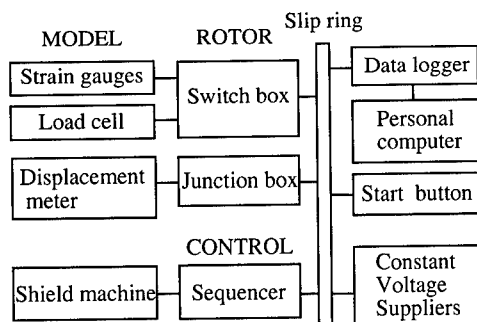


Fig. 3 Measuring systems

test, the measurement is controlled by a sequencer, and measurement data are stored in a data logger.

Fig. 4 shows the arrangement of the strain gauges. Table 3 shows the specifications of the intermediate pipe. Strain measurement was continued, at intervals of about 2 seconds, from the beginning of propulsion until the miniature shield machine is pulled out completely. Earth pressure acting on the intermediate pipe is estimated from stress resultants, which are calculated from strains after the shield machine is pulled out.

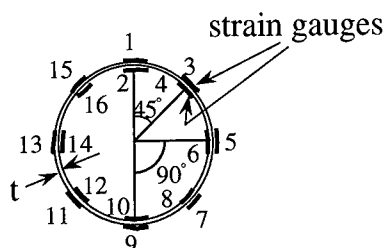


Fig. 4 Location of the strain gauges

Table 3 Properties of model tunnel

Material		aluminum
Outer diameter	D (mm)	40.05
Thickness	t (mm)	1.05
Length	L (mm)	261.5
Specific gravity	Gs	2.69
Young's modulus	E (kPa)	$7.1 \times 10^7$
Poisson's ratio	$\nu$	0.33

Fig. 5 illustrates the configuration of the ground surface displacement measurement system. The system uses a laser displacement meter that travels on a motor drive. In the experiment, displacement in the direction perpendicular to the direction in which the shield machine is driven was measured above the points of measurement of strain in the intermediate pipe. Measurements were taken at 9 points spaced 2cm apart transversely; measurement was continued throughout the process of excavation, one cross section every 30 seconds.

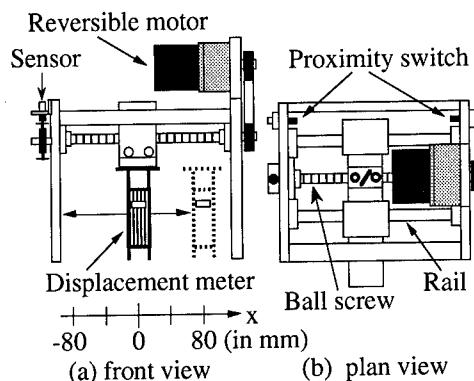


Fig. 5. Ground surface displacement measurement system

Fig. 6 shows the points at which earth pressures were measured. Two load cells having a measuring range of 0–49 ( $10^4$  N/m<sup>2</sup>) were installed, one vertically and the other horizontally. As in the case of the strain measurement, measurements were taken at 2 second intervals.

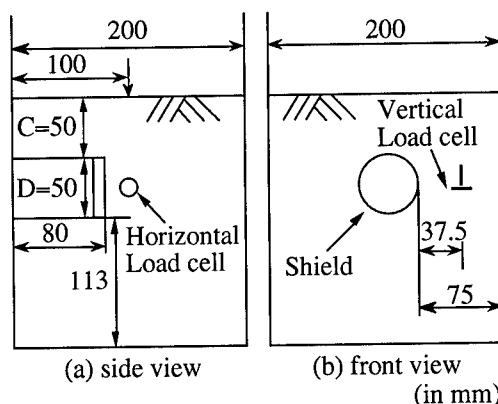


Fig. 6 Locations of load cells in the ground



## 2.2 How it works

The miniature shield machine is activated by remote control via a slip ring after a field of a predetermined level of centrifugal acceleration is achieved. The subsequent operations of the shield machine from excavation to extraction until the tail void occurs are controlled automatically by the sequencer installed on the beam. The advancing rate and the rotational speed of the cutter are determined on the basis of their values used in a stable excavating condition in the gravitational field and are preset in the sequencer.

Excavation starts when centrifugal force acting on the model ground has reached a predetermined level. In the excavation process, the ground in its initial state of stress is excavated by the cutter mounted at the front end of the triple pipe structure, and muck is carried backward by the screw conveyor. During this process, the face is stabilized by balancing the rotational speed of the cutter and the advancing rate. The driving distance is up to 105mm because of the dimensional restrictions of the container. When the driving distance reaches 105mm, a proximity switch is activated and the excavating operation is terminated. On completion of excavation, a pneumatic cylinder stopper is activated so as to prevent the intermediate pipe and the innermost pipe from moving backward together with the outermost pipe. Then, a signal is sent to reverse the rotation of the drilling motor, and the outermost, or shield machine, pipe begins to move backward. During the extraction of the outermost pipe, earth pressure begins to act on the intermediate, or lining pipe. When the outermost pipe returns to its initial position, the strain gauges installed on the intermediate pipe are completely exposed in the ground, ready for measurement. Fig. 7 illustrates this arrangement.

## 2.3 Performance of the machine

In view of the results of the preliminary excavation tests, an improvement was made. The inlet of the screw conveyor was enlarged and the speed reduction ratio of the propulsion motor was doubled so that thrust was increased.

Fig. 8 compares the cutter rotation speeds and advancing rates before and after improvement. Combinations of the cutter rotation speed and

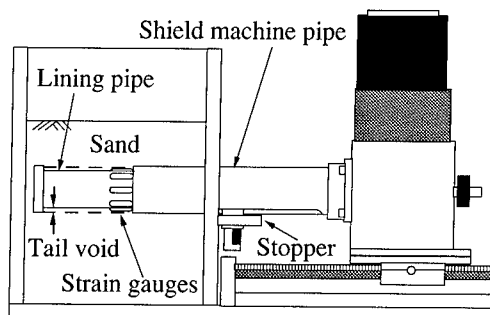


Fig. 7 Reproduction of tail void

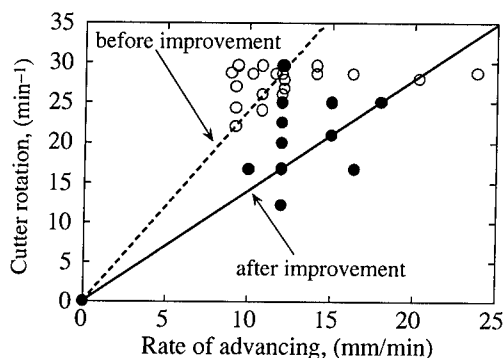


Fig. 8. Relationship between advancing rate and cutter rotation speed

the advancing rate that minimize influence on the ground surface before and after improvement are approximated by a broken line and a solid line, respectively. As shown, the optimum advancing rate at the same cutter rotation speed after improvement is nearly twice as high as that before improvement, indicating an improvement in excavation performance. As a result of trial excavation after improvement, the optimum combination of a cutter rotation rate of  $16.7 \text{ min}^{-1}$ , and an advancing rate of  $v=12 \text{ mm/min}$  was chosen.

The shield tunneling process was examined using X-ray radiography in order to confirm the efficiency of muck removal and the behavior of the ground around the shield. Fig. 9 is a radiograph showing the shield machine in operation. Round spots in the figure are lead shots. As the figure shows clearly, muck (dry sand in this particular case) near the face is efficiently taken in as the shield machine advances.

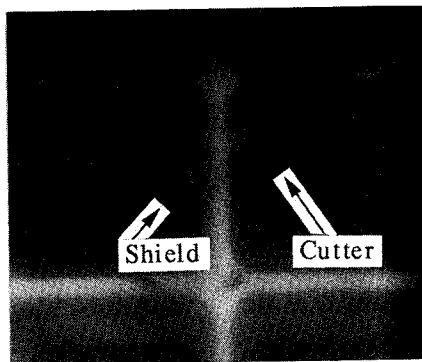


Fig. 9 X-ray radiograph taken during shield excavation

### 3 RESULTS OF CENTRIFUGE TESTS

The objective of the experiment was to examine if the miniature shield machine operates as expected in a centrifugal force field. In the centrifuge test, 3 cases at 25G and 1 case at 50G were conducted. The model ground was prepared by means of air pluviation using dry Toyoura sand ( $G_s=2.66$ ,  $e_{max}=0.985$ ,  $e_{min}=0.602$ ,  $Dr=70\%$ ,  $\phi(\text{triaxial})=42.0$  degrees). Because of the dimensional restrictions, the model ground was prepared with the triple pipe section projecting into the container by 80mm.

The results of these cases are given and discussed below.

#### 3.1 Surface settlement

Figs. 10 and 11 show ground surface displacement during shield excavation and after the occurrence of tail void, respectively.

Small ground surface displacements after shield excavation indicate that the stable excavation was carried out in all the cases. Ground surface settlements after the occurrence of tail void form a trough-like depression, although settlement in IU-1 is greater than in the other cases. For the purpose of comparison, Fig. 11 also shows R. B. Peck's (1969) settlement error curve (solid line) based on the maximum settlement  $y_0$  right above the tunnel drawn from IU-2 data. As shown, the settlement error curve agrees well with the trough-shaped patterns of other curves drawn from measurement data. Absolute values of settlement are not discussed

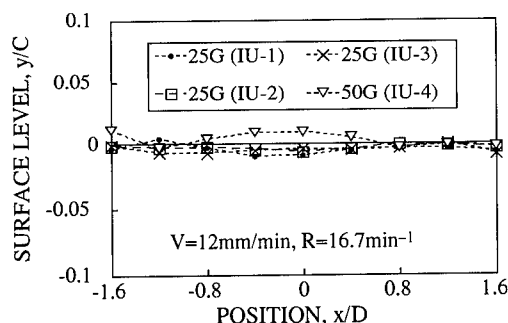


Fig. 10 Ground surface displacement during excavation

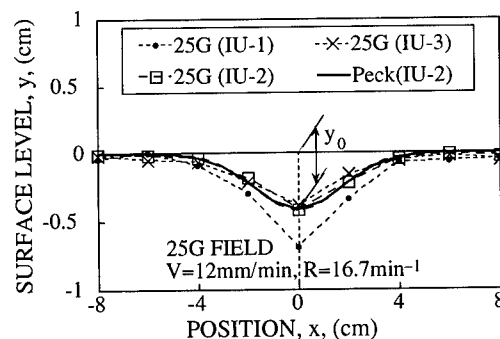


Fig. 11 Ground surface displacement during extraction

here because the tail void is as large as 10% of the outside diameter of the tunnel, as compared with 1–2% in the case of the prototype situations.

#### 3.2 Lining stresses

Fig. 12 shows changes in measured strains at the crown of the tunnel (see Fig. 4) obtained from the 3 cases of experiment at 25G. The tendencies of the measured strains correspond well to the progress of shield excavation and the extraction of the outermost pipe (occurrence of tail void), indicating a good repeatability of the tests. The reason why strains occurred in the intermediate pipe during excavation may be that the O-rings located between the outermost pipe and the intermediate pipe, which were installed because of the need to create a space for leads connecting to the strain gauges, transmitted some load.

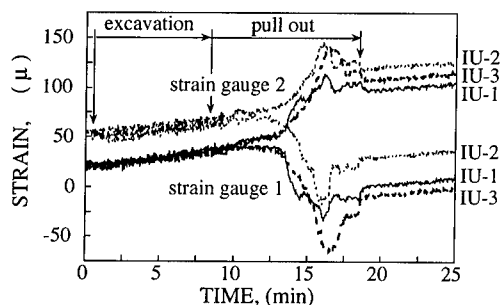


Fig. 12 Changes in strain at the crown with time

### 3.3 Change in earth pressure

Fig. 13 shows two sets of measured ground stresses obtained from the two tests (IU-2, IU-3). The figure reflects the tendency of vertical earth pressure to increase sharply and of horizontal earth pressure to decrease on completion of excavation. Interpretation of the results needs further studies.

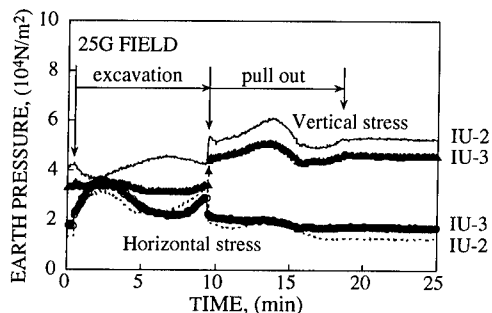


Fig. 13. Changes over time in earth pressure

## 4 CONCLUDING REMARKS

This paper tried to demonstrate the potential use of centrifuge test for the study of shield tunneling process. A miniature shield tunnel model was developed, and the process of shield tunneling was successfully reproduced in a centrifugal force field. The smallness of the centrifuge used, however, imposed severe restrictions in terms of dimensions and weight on the model, and an attempt to evaluate earth pressure acting on the tunnel lining

quantitatively was not yet fulfilled. The main difficulties are (1) the tail void was as large as 10% of the outside diameter of the shield, as compared with 1–2% for the prototype machine, (2) the part (80mm) of the tunnel model that was projecting into the container from the early stages of tunnel model preparation may have affected initial stress before excavation, and (3) the possible influence of boundary conditions due to the smallness of the container on the tunnel lining cannot be ignored.

The authors therefore plan further tests using a larger centrifuge. The next stage of the test will involve the use of a  $\phi 100$ mm shield machine in a field of centrifugal force in the order of 100G.

## ACKNOWLEDGMENTS

The authors are deeply indebted to Mr. T. Hagiwara of Gunma University, and Mr. T. Fujii of Nishimatsu Construction Co., Ltd. for their help.

## REFERENCES

- James R. G. and Larsen H. 1977. Centrifugal model tests of buried rigid pipes, *Proc. of 9th ICSMFE* (1): 567-570
- Rowe R. K. and Lee K. M. 1992. Subsidence due to tunneling. Evaluation of a prediction technique. *Canadian Geotechnical Journal*. 29 : 941-954
- Mair R. J. 1979. *Centrifugal modeling of tunnel construction in soft clay*, Ph. D thesis, Cambridge University
- Tohda J., Mikasa M. and Hachiya M. 1988. Earth pressure on underground rigid pipes: Centrifuge model tests and FEM analysis, *CENTRIFUGE* 88': 395-402
- Kusakabe O., Hagiwara T., Nomoto T., Mito K. and Nakamatsu U. 1990. Experimental evaluation of earth pressures and lining stresses of tunnels in sand. Proceeding of International Congress on Tunnel and Underground Words, *Today and Future*: 529-536
- Peck R. B. 1969. Deep excavations tunneling in soft ground Proceedings. *7th ICSMFE*, Mexico City: 225-290

## Behaviour of a tunnel lining embedded in a Bentonite quartz flour water mixture in granular soil

D.König & H.L.Jessberger  
*Ruhr-Universität Bochum, Germany*

P.Chambon  
*Ecole Centrale Nantes, France*

P.Dangla  
*Laboratoire Central des Ponts et Chaussées, Paris, France*

**ABSTRACT:** One method to allow displacements between soil and tunnel lining and to activate the bearing capacity of the soil without breaking up is to embed the tunnel lining in a layer of a Bentonite quartz flour water mixture. The behaviour of such an interactive system - tunnel lining, surrounding mixture and soil - under the self weight of the overburden was studied by centrifuge model tests and numerical analyses.

### 1 INTRODUCTION

To master difficult situations in tunnelling - e.g. high overburden pressure in the case of deep tunnels or changing earth pressure in connection with tension and compression in the soil due to mining activities - with economic restrictions new design and construction methods are required. One method to allow displacements between soil and tunnel lining and to activate the bearing capacity of the soil without breaking up is to embed the lining in a layer of a Bentonite quartz flour water mixture.

In this case the stress and strain of the tunnel lining is highly influenced by the time dependent deformations of the Bentonite quartz flour water mixture (BQFWM). Displacements of the soil and of the tunnel lining tend to be disconnected by placing the BQFWM between both elements. Usual theories are based on the assumption that soil and lining displacements are identical at the contact surface. Due to this, these theories are not applicable without reservation to the prediction of the behaviour of the system tunnel lining, surrounding mixture and soil.

The interaction behaviour of this system under the self weight of the overburden was studied by centrifuge model tests and numerical analyses. The centrifuge model tests were carried out in the Bochum geotechnical centrifuge Z1 (Jessberger & Güttler 1988). A tunnel with a diameter  $D = 6$  m placed in dry sand in a depth of  $C/D = 4$  ( $C$ : overburden) was simulated. The thickness of the BQFWM layer  $f$  was varied. The stress and strain of the tunnel lining was measured as well as displacements within the soil.

Numerical simulations based on the experimental test conditions were performed at the Ecole Central Nantes using the finite element code CESAR-LCPC. Special attention was paid to the coupling between elastoplastic behaviour and consolidation phenomenon.

The design of the centrifuge model test is described in section 2.1. The results of the experimental studies are presented and discussed in section 2.2. Section 3.1 includes the description of the numerical analyses. The results of the numerical analyses are presented and discussed in section 3.2.

### 2 CENTRIFUGE MODEL TEST

#### 2.1 Design of the model

Figure 1 shows the cross section of the centrifuge model. A section of an infinite tunnel was simulated. The tunnel model is a brass tube with an outer diameter of 60.5 mm and a thickness of 0.5 mm. 32 strain gauges were installed inside and outside in a section in the middle of the tunnel to measure the surface strains tangential to the circular lining.

The tunnel model has been surrounded by a BQFWM of a certain thickness  $f$ . The properties of the BQFWM are summarized in Table 1. More information is shown by König & Jessberger (1993). The tunnel with the BQFWM has been placed in the centre of a strong box, which was filled with Bochum standard sand (Table 2).

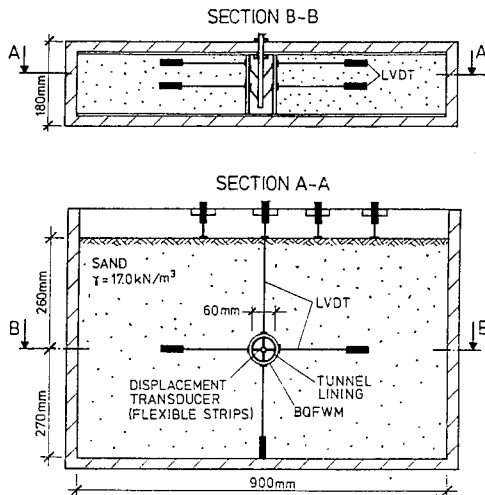


Figure 1: Strong box with tunnel model

Table 1: Properties of the BQFWM

Bentonite	22 % by weight
Quartz flour	31 % by weight
Water	47 % by weight
Water content	88%
Liquid limit	150.8 %
Plastic limit	38.6 %
Plasticity	112.2 %
Permeability	1.5 10 EXP -11 m/s
density of solid particles	2650 kg/m³
Density (porosity: 0.70)	1494 kg/m³
Angle of internal friction	< 4°
Cohesion	22.5 kPa

Table 2: Properties of Bochum Standard Sand

Density of solid particles	2660 kg/m³
Minimum index density	1410 kg/m³
Maximum index density	1700 kg/m³
Average grain size diameter d 50	0.23 mm
Uniformity coefficient	2.08
Angle of internal friction	38°

To measure deformations of the tunnel lining, flexible strips provided with strain gauges were fixed on a rigid beam inside the tunnel. The surface settlements as well as the deformations at the outer surface of the BQFWM at the crown, the springings and the invert were measured by LVDT's.

During preparation the strong box was placed in a horizontal position and the front plate was removed. The rigid beam with the flexible stripes was fastened

to the back plate. The tunnel embedded in the BQFWM was fixed by an installation support on the beam. Then the strong box was filled with sand by pluvial deposition.

The complete model fixed in the centrifuge bucket was accelerated to the selected g-level of 100 g. So the increasing self weight of the overburden loaded progressively the tunnel lining and the BQFWM. The dimensions of the model and of the simulated prototype are shown in Table 3.

Table 3: Dimensions of the model (M) and of the simulated prototype (P)

TEST		2TU12	2TU13	2TU14	2TU10	2TU11
D	M [ cm ]	6.05	6.05	6.05	6.05	6.05
	P [ m ]	6.05	6.05	6.05	6.05	6.05
f	M [ cm ]	0	0.225	0.225	0.475	0.975
	P [ m ]	0	0.225	0.225	0.475	0.975
Da	M [ cm ]	6.05	6.5	6.5	7	8
	P [ m ]	6.05	6.5	6.5	7	8
C	M [ cm ]	22.975	22.75	22.75	22.5	22
	P [ m ]	22.975	22.75	22.75	22.5	22

$D_a = D + 2 f$ , outer diameter of the tunnel with BQFWM

## 2.2 Test results

The results of the centrifuge model tests are presented in model scale.

The deformations of the tunnel lining and of the outer surface of the BQFWM layer with a thickness of  $f = 4.75$  mm are shown in Figure 2. The left part of the Figure represents the deformations observed just after accelerating the model to the selected g-level, the right part the deformations after 600 minutes centrifuging. The settlement of the soil below the tunnel invert was eliminated. Following effects are observed just after accelerating the model:

- On accelerating the model to the selected g-level the tunnel deforms to an ellipse.
- The outer surface of the BQFWM follows the deformation of the lining due to undrained conditions (loading was fast compared to the consolidation rate).

After 600 minutes the situation changes as follows:

- Consolidation of the BQFWM leads to inward displacements of the soil at the crown as well as at the springing.
- A translatory displacement of the tunnel lining is caused by consolidation of the BQFWM under the invert of the lining.
- A slight relaxation of the deformed tunnel lining appear.
- No significant invert uplift takes place.

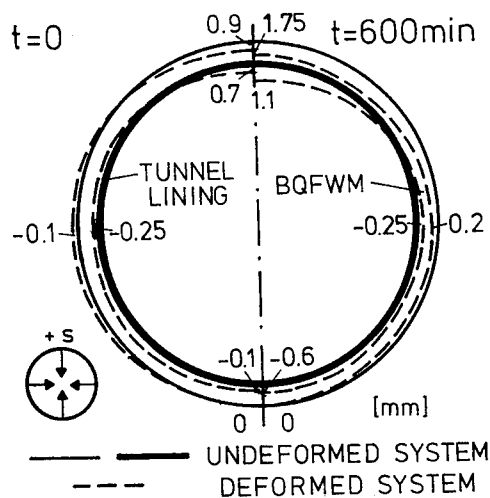


Figure 2: Deformations of the tunnel lining and of the outer surface of the BQFWM

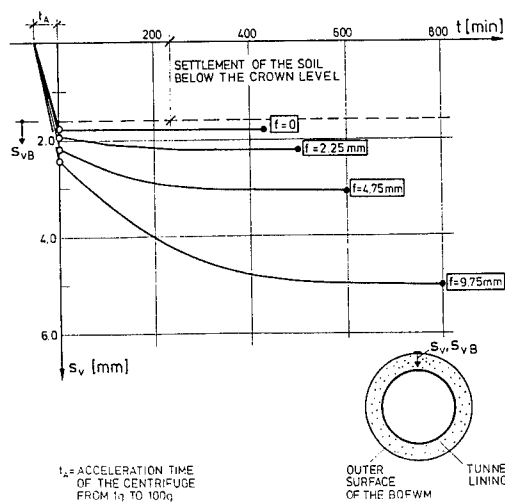


Figure 3: Vertical displacements of the outer surface of the BQFWM at the crown

The total vertical displacement of the outer surface of the BQFWM at the crown is plotted in Figure 3 versus time. The four curves represent the results of four tests with different thickness  $f$  of the BQFWM layer.

On increasing the self weight of the soil during accelerating the model in the centrifuge initial vertical displacements are noticed. These displacements are caused by the settlement of the soil below the tunnel,

by initial settlements of the BQFWM and by deformation of the tunnel lining. The settlement of the soil below the tunnel invert was found to be 1.3 mm, below the crown level to be 1.6 mm by centrifuging the strong box sand filled without tunnel model.

Consolidation of the BQFWM at the invert and at the crown leads to an increase of the vertical displacements. The greater the thickness of the BQFWM layer the greater are the observed displacements. After several hours the displacements stabilized.

The crown settlement  $s_{vB}$  is defined as the difference of the total vertical displacement of the outer surface of the BQFWM to the settlements of the soil below the crown level as shown in Figure 3. The further analysis is concentrated on the influence of the crown settlement  $s_{vB}$  on the vertical load on the tunnel lining. The vertical load  $\sigma_{vT}$  on the tunnel lining was found in three steps:

- From the data of the strain gauges installed at the springings of the lining the normal forces  $N$  in the springings of the lining were calculated.
- Equilibrium between the normal forces  $N$  and the vertical load on the lining was assumed (Figure 4).
- The vertical tunnel load was calculated to:

$$\sigma_{vT} = 2 N / D$$

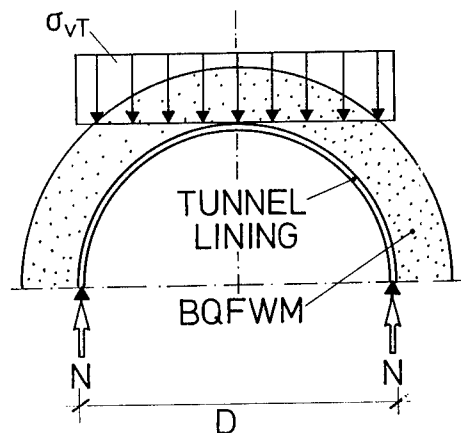


Figure 4: Calculation of the vertical load on the tunnel lining  $\sigma_{vT}$

The influence of the crown settlement  $s_{vB}$  on the vertical tunnel load  $\sigma_{vT}$  is shown in Figure 5. The vertical tunnel load  $\sigma_{vT}$  in relation to the factor  $\gamma n D$  is plotted versus the dimensionless crown settlement  $s_{vB} / D_a$ . The Figure includes the results of four centrifuge model tests simulating a tunnel with

BQFWM of different thickness and of one test simulating a tunnel without BQFWM. The results of the tests simulating a tunnel with BQFWM are represented by curves. The start point of each curve (unfilled circle, compare with Figure 3) corresponds to the initial crown settlement measured just after spin up the model to the selected  $g$  level. The end of each curve (filled circle) corresponds to the stabilized crown settlement measured after consolidation of the BQFWM. For the test without BQFWM the curve is reduced to one point.

The theoretic vertical tunnel load on an undeformed tunnel ( $s_{vB}/D_a = 0$ ) is calculated to  $\sigma_{vT}/\gamma n D = \gamma n C/\gamma n D = C/D = 23/6 = 3.8$ . This value is marked on the ordinate.

The developments of the vertical tunnel load  $\sigma_{vT}$  as function of the crown settlement  $s_{vB}$  observed for the tests simulating a tunnel with BQFWM show similar principles:

- The initial crown settlement leads to a strong reduction of the vertical tunnel load in comparison to the theoretic vertical tunnel load on an undeformed tunnel.
- The increase of the crown settlement due to consolidation of the BQFWM introduce a further reduction of the vertical tunnel load.
- Finally the crown settlement and the vertical tunnel load stabilized when equilibrium between vertical stress in the soil, drained stress conditions in

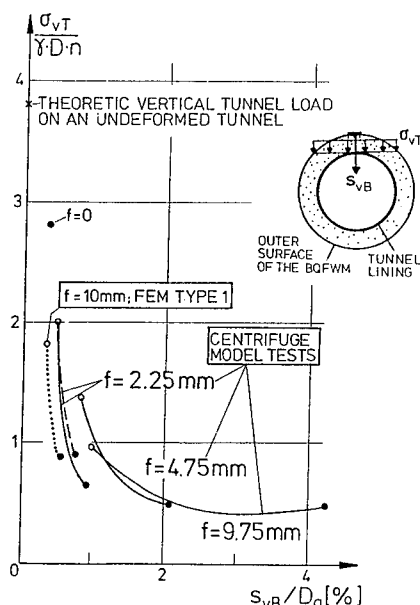


Figure 5: Vertical tunnel load  $\sigma_{vT}$  as function of the crown settlement  $s_{vB}$

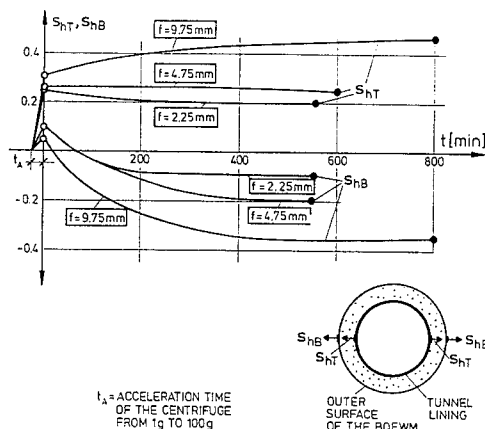


Figure 6: Horizontal lining displacement  $s_{hT}$  and horizontal displacement of the outer surface of the BQFWM  $s_{hB}$  at the springings as function of time

the BQFWM and resistance of the tunnel lining is reached.

The general connection between crown settlement and vertical tunnel load is shown by the all test results together:

- Smallest crown settlements cause a strong reduction of the vertical tunnel load in comparison to the theoretic vertical tunnel load on an undeformed tunnel.
- A crown settlement  $s_{vB}/D_a = 2\%$  leads to a reduction of the vertical tunnel load of 90%.
- For crown settlements larger  $s_{vB}/D_a$  than 2% the vertical tunnel load stabilized.

Similar results are published by Potts (1976). The reduction of the vertical tunnel load might be explained by activation of shear forces in the overburden due to deformations and by arching effects.

The behaviour of the tunnel lining embedded in the BQFWM at the springing is shown in Figure 6. The horizontal displacements of the tunnel  $s_{hT}$  and of the outer surface of the BQFWM  $s_{hB}$  are plotted versus time. The following effects are demonstrated by the results:

- On accelerating the model to the selected  $g$ -level, outward displacements of the lining  $s_{hT}$  and of the undrained BQFWM  $s_{hB}$  are observed.
- Consolidation of the BQFWM leads immediately to a reversal of the displacement direction of the outer surface of the BQFWM  $s_{hB}$ .
- Inward displacements of the outer surface of the BQFWM  $s_{hB}$  occur due to further consolidation of the BQFWM.
- The development of the horizontal displacements of the tunnel  $s_{hT}$  depends on the thickness of the

BQFWM. In case of a small layer of the BQFWM ( $f = 2.25$  mm) the deformed lining relaxes slightly. In case of a thick layer ( $f = 9.75$  mm) the outward deformation increases.

The observed deformation behaviour indicates that the horizontal load on the tunnel lining  $\sigma_{hT}$  is reduced by the consolidation of the BQFWM as well as the vertical tunnel load  $\Delta\sigma_{vT} = f(s_{vT})$ . The principle of the soil structure interaction for the system tunnel lining with and without BQFWM deduced from the presented test results is shown in Figure 7. The soil structure interaction of a tunnel without BQFWM is characterized as follows:

- Small crown settlements  $s_{vT}$  lead to a small reduction of the vertical tunnel load  $\Delta\sigma_{vT} = f(s_{vT})$  in relation to primary stress conditions  $\sigma_{vT}^0 = \gamma \cdot C$ .
- The horizontal tunnel load  $\sigma_{hT}$  is reduced by the consolidation of the BQFWM as well as the vertical tunnel load  $\Delta\sigma_{vT} = f(s_{vT})$  in relation to primary stress conditions  $\sigma_{hT}^0 = \gamma \cdot C \cdot K_0$  (passive stress path).

The behaviour of the tunnel with BQFWM after consolidation is different:

- The consolidation of the BQFWM causes an increase of the crown settlements  $s_{vB}$  and a further reduction of the vertical tunnel load  $\Delta\sigma_{vT} = f(s_{vB})$  without additional deformations of the tunnel lining.
- The inward displacement of the outer surface of

the BQFWM  $s_{hB}$  at the springings leads to a decrease of the horizontal tunnel load  $\sigma_{hT}$  (active stress path).

- The reduction of the vertical and horizontal tunnel load ( $\Delta\sigma_{vT} = f(s_{vB})$  and  $\Delta\sigma_{hT} = f(s_{hB})$ ) cause a reduction of the normal forces in the lining in relation to the normal forces caused by primary stress conditions ( $\sigma_{vT}^0$  and  $\sigma_{hT}^0$ ).

- The influence of the BQFWM on the bending moments in the lining might depend on the relation of the vertical tunnel load to the horizontal tunnel load.

### 3 FINITE ELEMENT CALCULATION

#### 3.1 Finite element mesh, boundary conditions and material properties

The interaction behaviour of a tunnel lining embedded in a 10 mm thick layer of the BQFWM was simulated by a two dimensional finite element calculation assuming plane strain conditions. The dimensions of the finite element mesh are based on the geometry of the strong box used for the model tests (Figure 8). Horizontal displacements are set to zero on the side corresponding to the edges of the box and on the symmetry axis, while vertical displacements are zero along the base.

The finite element mesh is shared between three groups of isoparametric displacement elements, corresponding to the three considered materials. The sand is simulated by six nodes triangles (T6) filling the outer part of the mesh, and by a ring of eight nodes quadrilaterals elements (Q8) in contact with the BQFWM. The layer of the BQFWM and the brass tunnel lining are simulated by two rings of the Q8 elements.

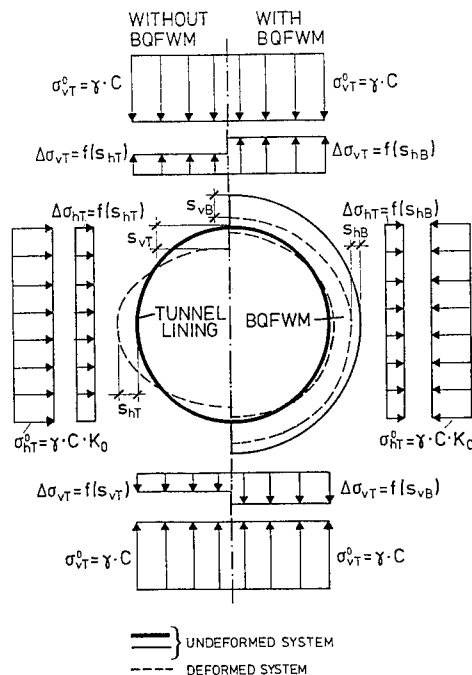


Figure 7: Principle of the soil structure interaction for a tunnel lining with and without BQFWM

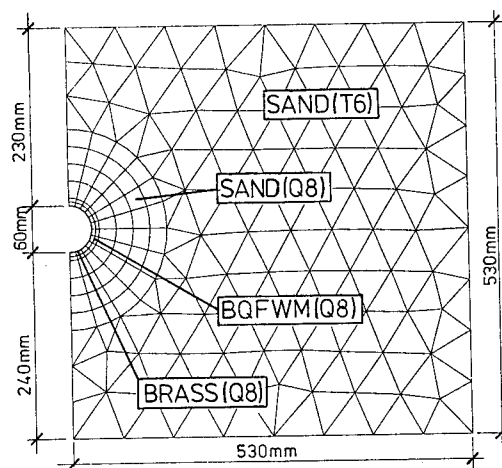


Figure 8: Finite element mesh



For the presented calculation the behaviour of the sand is supposed to be elastoplastic. The Young's modulus is assumed to be  $E = 50 \text{ N/mm}^2$  in respect to compression tests. An associated Mohr Coulomb failure criterion is used. The friction angle  $\phi$  has been determined from stress path triaxial tests at confining pressures close to the theoretic earth pressure at the tunnel level.

The BQFWM is described as a thermoporoelastoplastic medium. Elastoplastic equations are coupled with diffusion equations (Dangla 1992). This allows to take into account the time effect due to the consolidation of the BQFWM and the re-distribution of stresses within the soil. In addition to elastoplastic parameters specific data related to the porosity have been entered. All geotechnical parameters either come from our laboratory tests or from literature on Bentonite (Table 4). The displacement boundary conditions are completed by setting zero the pressure at surface level and the fluid flow through the edges of the strong box.

The calculation is performed using an implicit integration scheme, which is unconditionally stable, so that loading can be done in one step. Different time steps are calculated, the first one corresponds to the initial state, at which the selected  $g$  level is reached. The last time step corresponds to the characteristic time of the problem (Dangla 1992), from which no significant evolution occurs.

Two calculations have been performed. In the first one the accelerating time of the centrifuge from  $1g$  to a  $g$ -level of  $100g$  of  $240 \text{ s}$  has been simulated by increasing the volumetric weight of the materials from their real value to a hundred times this value in 10 steps. A second calculation simulated an immediate increase of the volume weight realising ideal undrained conditions of the BQFWM at  $100g$ .

Table 4: Geotechnical parameters used in the finite element calculation

Material	Sand	BQFWM	Brass
Behaviour	Elastoplastic	Elastoplastic	Elastolinear
$E \text{ [N/mm}^2\text{]}$	50	1	$8 \cdot 10^4$
$\nu$	0.33	0.2	0.33
$\gamma \text{ [N/mm}^3\text{]}$	$0.17 \cdot 10^{-4}$	$0.15 \cdot 10^{-4}$	$0.83 \cdot 10^{-4}$
$\gamma_r \text{ [N/mm}^3\text{]}$	$1 \cdot 10^{-8}$	$1 \cdot 10^{-5}$	$1 \cdot 10^{-8}$
$n$	0.36	0.71	0.1
$l/M$	0	0	0
$k/\gamma \text{ [mm}^4/\text{sN}]$	5880	$1 \cdot 10^{-3}$	$1 \cdot 10^6$
$b$	1	1	0
$c \text{ [N/mm}^2\text{]}$	$1 \cdot 10^{-3}$	$2.25 \cdot 10^{-2}$	-
$\phi \text{ [}^\circ\text{]}$	38	1	-
$\beta \text{ [}^\circ\text{]}$	1	1	0

### 3.2 Results of the calculation and comparison with the test results

The results of the finite element calculation are presented in Figures 5, 9 and 10. The calculation results show a similar soil structure interaction as the results of the centrifuge model tests. But it is obvious that the calculated vertical deformations are much smaller than the measured one. This can be explained by the constitutive model and the parameters describing the behaviour of sand and BQFWM. Improvement in the constitutive model and the parameters is the topic of further work.

The results of the numerical analysis and of the experimental studies are compared in Figure 5. The dimensionless vertical tunnel load  $\sigma_{vT} / \gamma n D$  is plotted versus the dimensionless crown settlement  $s_{vB}/D_a$  as mentioned above. The calculation results correspond to the measured ones, if the difference in thickness of the BQFWM is neglected.

Calculated and measured horizontal displacements of the tunnel lining  $s_{hT}$  and of the outer surface of the BQFWM  $s_{hB}$  at the springings are plotted versus time in Figure 9. The general development of the displacement is calculated analogues to the measured one. Outward displacements of the springings of the tunnel lining were noticed in both cases. The behaviour of the outer surface of the BQFWM in the springing is characterized by initial outward displacements just after loading, and inward displacements when further consolidation occurs.

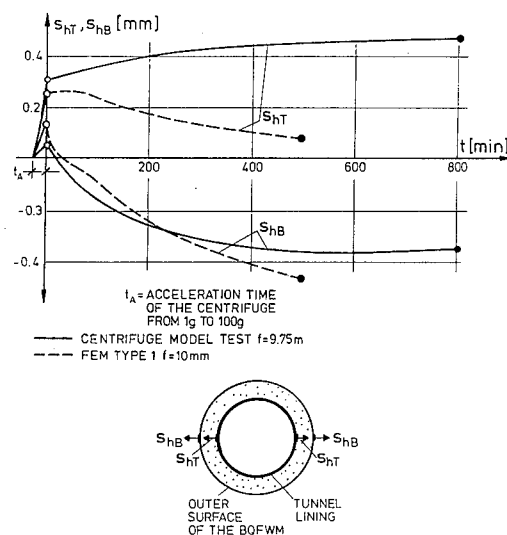


Figure 9: Development of the horizontal displacements of the tunnel lining and the outer surface of the BQFWM at the springings

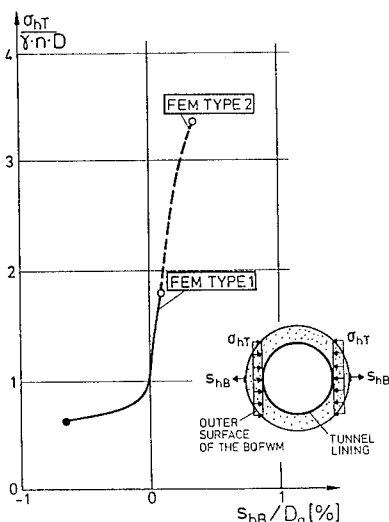


Figure 10: Horizontal earth pressure as function of horizontal displacement of the outer surface of the BQFWM at the springing

The influence of the horizontal displacement of the outer surface of the BQFWM  $s_{HB}$  on the horizontal tunnel load  $\sigma_{HT}$  is shown in Figure 10 by the results of the finite element calculation. The dimensionless horizontal tunnel load  $\sigma_{HT} / \gamma \cdot n \cdot D$  is plotted versus the dimensionless horizontal displacement of the outer surface of the BQFWM  $s_{HB} / D_a$ .

The initial displacements of the undrained BQFWM due to a high horizontal tunnel load are outwards and indicate the activation of passive earth pressure conditions in the sand close to the springings of the tunnel. The reverse of the displacement direction of the outer surface of the BQFWM due to consolidation of the BQFWM leads to a reduction of the horizontal tunnel load. Further reduction of the horizontal tunnel load caused by inward horizontal displacements of the outer surface of the BQFWM indicate active earth pressure conditions in the sand close to the springings of the tunnel.

## SUMMARY AND CONCLUSION

One method to allow displacements between soil and tunnel lining and to activate the bearing capacity of the soil without breaking up is to embed the tunnel lining in a layer of a Bentonite quartz flour water mixture (BQFWM). The behaviour of such an interactive system - tunnel lining, surrounding BQFWM and soil - under the self weight of the

overburden was studied by centrifuge model tests and numerical analyses.

The presented results show a time dependent reduction of the vertical and horizontal tunnel load due to the consolidation of the BQFWM. At each state of consolidation the relation between earth pressure, stress conditions in the BQFWM and lining resistance changed. In a further state of consolidation, stable equilibrium conditions were reached.

The reduction of vertical and horizontal tunnel load cause a decrease of the normal forces in the lining. The influence of the BQFWM on the bending moments in the lining might depend on the relation of the vertical tunnel load to the horizontal tunnel load.

The combination of experimental studies and numerical analyses allow an almost complete understanding of the interaction behaviour of the system. The precondition for performing the numerical analyses is the inclusion of the consolidation behaviour of the BQFWM, which is realized by describing the BQFWM as thermoporoelastoplastic medium.

Further investigations have to be focused on the following aspects:

- Improvement in the constitutive model and the parameters of the FE-calculation
- Influence of the stiffness of the tunnel lining on the interaction behaviour
- Specification of a minimum thickness of the BQFWM to achieve a maximum reduction of the load on the lining without breaking up the soil.

## ACKNOWLEDGEMENTS

This investigations were supported by the German Federal Ministry of Research and Technology. The fruitful cooperation with the Dyckerhoff & Widmann AG, Germany, is gratefully acknowledged. We appreciate that Ole Syllwasschy performed the FEM calculations at the LCPC in Nantes.

## REFERENCES

- Jessberger, H.L. & U. Güttler. 1988. Bochum Geotechnical Centrifuge. *Proc. Inter. Conf. Centrifuge 88*: 33-44. Paris: Balkema.
- König, D. & H.L. Jessberger 1993. Applicability of a Bentonite Quartz Flour Water Mixture to Underground Structures. *Proc. 13th ICSMFE*. New Delhi: Balkema.
- Potts, D.M. 1976. Behaviour of Lined and Unlined Tunnels in Sand. *Ph.D. Thesis. University of Cambridge*
- Dangla, P. 1992. Methodes de resolution numérique en thermo-poro-anélasticité. *Etudes et recherches des LCPC*. pp 45. Paris: LCPC ed.

## Face stability of tunnels constructed using the mechanical precutting tunneling method

A. Skiker & P. Chambon  
*Ecole Centrale de Nantes, France*

E. Leca  
*Laboratoire Central des Ponts et Chaussées, Paris, France*

J. Garnier  
*Laboratoire Central des Ponts et Chaussées, Nantes, France*

**ABSTRACT:** Centrifuge tests have been performed on the LCPC geotechnical centrifuge in Nantes, in order to observe some aspects of the behavior of the tunnel and of the soil surrounding a model tunnel equipped with a vault ahead of the tunnel face as in the mechanical precutting method. The tests were performed in sands. This paper deals with the first results gained from these centrifuge tests. Some tests have been undertaken in dry sand. In some other tests, attention has been paid to the influence of the hydrostatic water table. The results obtained permit to determine the failure process, its geometry and its extension with respect to the face. The ground response before failure and face pressures at failure were recorded and analyzed.

### 1) INTRODUCTION

During recent years, several projects have been undertaken to improve infrastructure especially in cities. The congestion of construction at the surface in urban area and interest to protect the environment have often brought the engineer to opting for underground construction (pipes, tunnel, subway etc...). Many of these projects have to be constructed in difficult soil conditions and with strong constraints. Among problems, engineers are often faced to, during the construction of tunnels, face stability is one of primary concern, particularly when the excavation is performed in a soft soil and in urban area at shallow depth. Indeed, movements of soil may reach the surface and create subsequent damage to adjacent structures (Peck 1969).

Different excavation methods, taking advantage of technological advances like the New Austrian Tunneling Method or the pressurized shield, are available. They partially overcome some of these problems.

In soft ground tunnelling, a temporary support of the face is necessary, such as shotcrete when using the NATM. In case of shield tunneling the

support of the face is provided by a fluid pressure (air or bentonite) or earth pressure balance in accordance with the characteristics of the soil.

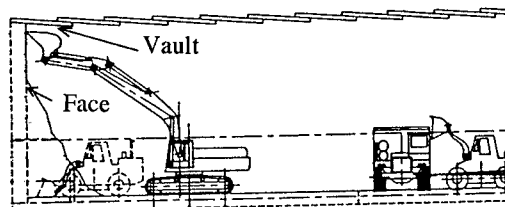


Figure 1. Sketch of the vault (Bougard & al.).

More recently, in France, another tunnel excavation has been introduced: the mechanical precutting method. It has been firstly applied in rock soils since 1970 (Bougard & al. 1977) and extended to soft soils, with primary use for small lengths of tunnels, small diameter tunnels or for partitioned face profiles. The method has recently been successfully used currently on full and large sections (Galaure's tunnel, France). The specificity of this method in comparison with other techniques consists in excavating a groove ahead of the tunnel face (Figure 1). The groove is filled immediately with concrete. This

allows to build an arch into the soil ahead of the tunnel face, which supports the surrounding soil mass during excavation.

It is believed that this technique should minimize the disturbance imposed to the soil.

The problem of tunnel face stability in soft ground tunneling is not recent. Several methods have been already developed to assess the supporting pressure required to ensure stability (Leca 1989). Some tests have been carried out using 1g model (Atkinson & al. 1975) or *ng* models using centrifuge (Mair 1979; Chambon 1991) and have been compared with field data or theory calculations based on the limit analysis.

Those studies underline the usefulness of models for the engineer as well as for the researcher.

An investigation program started recently in Europe ( France, Spain and UK ) to adjust the mechanical precutting technique to difficult soil conditions. It consists of experimental and theoretical studies. Within this project, an experimental program has been planned where centrifugal modelling is the experimental technique used for the investigation. This paper concerns the face stability of shallow tunnels during excavation with the mechanical precutting method. Despite the vault effect, self stability of the face can't be obtained in non-cohesive material without any support. For this reason air pressure on the face had to be applied. The experimental results should allow to validate theoretical results obtained on the basis of limit analysis. The tests were carried out on the LCPC centrifuge. The first series of tests were performed in dry sand. In another series the effect of water in sand was introduced. The purpose of these tests is to determine :

- the limit pressure ( the lowest pressure on the face to ensure its stability),
- the geometry of failure, its volume and extension from the face,
- surface displacements versus pressure on the face.

## 2 DESCRIPTION

A three-dimensional physical model was designed to carry out the tests. The model is shown on the figure 2. It mainly consists of :

- a 5 mm thick aluminium AU4G pipe; the cylinder is 300 mm in length ( sufficient to avoid boundary effects on the face) and 100 mm in

outer diameter; it is considered as infinitely stiff;

- a second 5 mm thick aluminium pipe, 300 mm in length, with an exterior diameter of 90 mm;

- a half cylindrical Inox shell, 1.6 mm thick, designed to model the vault installed between the two pipes; it can be displaced longitudinally in the soil to vary the length of the vault;

- a flexible 3/10 mm thick rubber membrane placed inside the smaller pipe; its function is, on the one hand, to ensure the air tightness inside the device which represents the tunnel once the air pressure is applied, and, on the other hand, to follow accurately the soil movements;

- two HBM transducers, fixed inside the smaller diameter pipe near the face and equipped with long rods, the extremities of which are stuck to the membrane; they make it possible to measure horizontal displacements of the face during the test;

- a stop disc placed inside the inner tube. During the preparation of the soil mass and before any air pressure is applied inside the tunnel, the disc coincides with the face; once an air pressure is applied inside the rubber membrane, this disc is moved back into the tunnel a few millimeters from the face; it is useful to stop the face collapse so that accurate observation of the failure mechanism will be possible. The other opening of the tunnel is sealed by an aluminium disc with access provided for the pressure device, electric wires of transducers and other components.

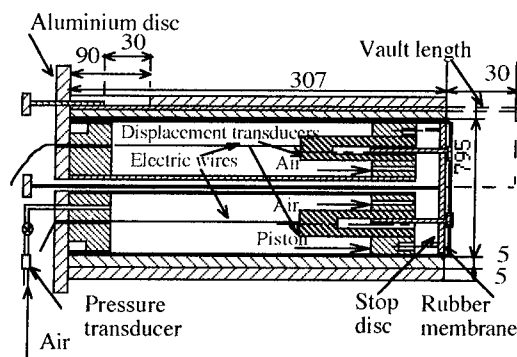


Figure 2. View of the tunnel model

### 2.1 Mechanical and geometrical characteristics of the model

The basic dimensions of the model are chosen to

simulate a tunnel prototype which is 5 m in diameter excavated in a Fontainebleau sand (Garnier et al. 1994), which is a fine sand frequently found in France. The tunnel is placed at shallow depth, the distance between the soil surface and the crown is being 10 m. Table 1 shows the prototype and model dimensions.

Table 1. Prototype and model dimensions.

	Prototype	Model
Diameter D	5 m	10 cm
Depth to tunnel crown C	10 m	20 cm
Vault length	1.5 m	3 cm

The scale of the model is 1/50; thus all tests were carried out at 50 g.

In this study, the purpose is not to simulate the whole excavation process, but only to get a simplified representation of the problem and study the effect of relevant parameters. The physical model used assumes that the vault is already constructed in the soil mass. An unfavourable case has been chosen in this study which corresponds to the maximum of soil excavated at the face before another vault is constructed; the length of the vault considered on this model corresponds to the recovery between two successive vaults.

## 2.2 Preparation of the model

The LCPC hopper is used to fill up the container, to obtain a unit weight of  $16 \text{ kN/m}^3 \pm 0.5\%$ .

The tunnel model equipped with the two face displacement transducers (HBM) and the pressure transducer is installed in the container on a 6 cm sand layer which is supposed thick enough not to have any boundary effect on the tunnel.

Calibrated boxes are placed into the container, so it is possible to check the homogeneity of the unit weight of the soil. The container is then filled by pluviated sand. Horizontal coloured layers of sand are sprinkled at different levels in the vicinity of the tunnel face while preparing the container.

When the model is on the centrifuge basket, an air pressure is applied inside the tunnel to compensate for earth pressures at the tunnel axis level, it is adjusted from the control room

using a manometer. The stop disc is removed as mentioned above. The half cylindrical shell representing the vault is next thrust into the soil 3 cm ahead of the face (Figure 3). This procedure was checked at 1 g and proved to produce no disturbance effects. The responses of transducers are stored at each step to supervise the disturbance that may affect the mass of soil.

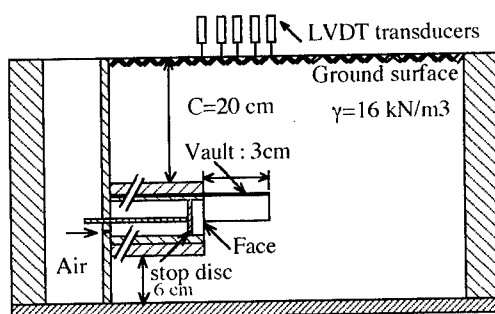


Figure 3. View of the container.

## 3 CENTRIFUGAL TESTS AND RESULTS

### 3.1 Centrifugal test in dry sand

The tests are performed in 3 steps :

1st step: The strong box placed inside the centrifuge basket is accelerated to the selected g-level: 50 g step by step. For each acceleration step, the internal pressure is increased to balance the increase in total earth pressure estimated at axis level.

2nd step: After the 50 g acceleration level has been reached, all pressure parameters are maintained a few minutes to stabilize self-weight stresses and strains.

With the LVDT transducers, face stability is controlled continuously by means of automatic data acquisition.

3rd step: At 50 g, slow and progressive decrease of internal pressure is executed, to simulate the tunnel excavation process.

In dry sand, 3 different steps can be observed during the test (figure 4) :

step1 : The first decrease in pressure does not induce any measurable displacement at the face: this phase is represented in Figure 4 by the almost vertical part of the curve. It corresponds to a state of stability of the soil mass.

step2: below a certain pressure value, small movements of the face are noticed at each decrease in face pressure. This phase is represented by the intermediate curved part in the figure 4.

step3: The rubber membrane moves suddenly into the tunnel, as failure occurs. This phase corresponds to the horizontal part in the figure 4.

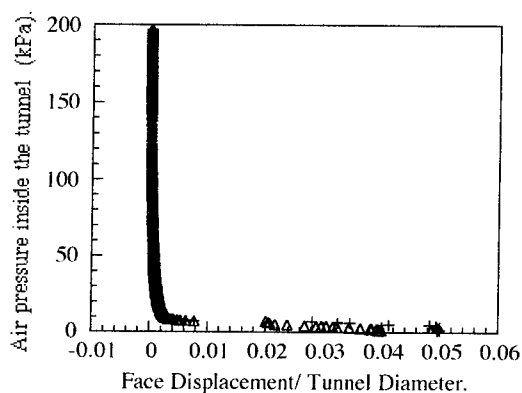


Figure 4. Pressure decrease versus face displacement in dry sand.

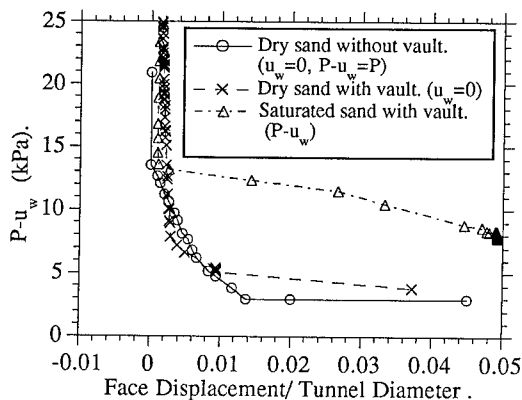


Figure 5. Decrease of pressure versus displacement face in the vicinity of the failure.

### 3.2 Centrifugal tests in sand with hydrostatic water table

A second set of tests has been carried out to study the effect of water on face stability. The preparation of the container is similar to that for a dry sand, with a few changes when preparing the mass of soil. The pressure level can be

controlled by pore pressure transducers within the soil as well as a direct measurement of the water table by a LVDT transducer. Saturation of the mass of soil is done in the centrifugal room.

Figure 5 shows the results of tests performed in dry sand with or without a vault, and in saturated sand with a vault.

For tests performed in saturated sand, the hydrostatic water pressure at tunnel axis level is subtracted from the internal air pressure  $P$  acting onto the tunnel face.

### 3.3 Failure pressure in dry sand and in presence of a hydrostatic water table

It is assumed that failure corresponds to the sudden and fast face displacement of 1mm (50mm in prototype unit) or more. Table 2 indicates values of internal pressures at failure which were obtained for different centrifuge tests under constant boundary conditions.

Table 2. Failure pressure  $P_d$  in dry sand.

Test	$P_d$ (kPa)	$P_d/\sigma_v$ (%)	$\gamma_d$ (kN/m <sup>3</sup> )
Tu1	6.9	3.4	16
Tu3	3.4	1.7	15.8
Tu5	4.6	2.3	16.0
Tu6.1	3.8	1.9	16.1
Tu6.2	7.0	3.5	16.1
Tu7	5.1	2.6	16.2

As it has been shown for tunnels without vault (Chambon 1991), the face failure is reached for lower internal pressures, in comparison with the earth pressure at rest at the tunnel axis,  $\sigma_v = n \gamma_d (C + D/2) = 200$  kPa, as indicated in table 2. The experimental results show that the face can't be self stable without any support pressure, even with the presence of the vault ahead the face. However a low internal pressure ensures local counterbalance of the face and therefore the overall stability of the tunnel.

Table 3. Failure pressure  $P_w$  in saturated sand.

Test	$\gamma_d$ kN/m <sup>3</sup>	$P_w$ (kPa)	$u_w$ (kPa)	$P_d+u_w$ (kPa)
Tu4	16.0	121.3	107.5	112.6
Tu8	16.2	120.6	108.3	113.4

The tests carried out with a water table above the tunnel have shown that the failure occurs

very suddenly, before any measurable displacement of the face. Table 3 indicates the pressure obtained at failure.

Comparison can be made in Table 3 between  $P_W$  and  $P_d + u_W$  where  $P_W$  is the failure pressure measured in saturated sand,  $P_d$  is the mean failure pressure in dry sand obtained from table 2 and  $u_W$  is the hydrostatic water pressure at tunnel axis level.

It is apparent that the water pressure,  $P_W$ , at failure is slightly greater than  $P_d + u_W$ .

In saturated sand, failure is reached for an internal pressure in the tunnel comprised between the hydrostatic pressure at tunnel invert and tunnel crown levels.

### 3.4 Failure mechanism in dry sand and in saturated sand

Particular attention was paid to the failure mechanism. From the different observed traces, it can be concluded that the failure is initiated at the face as indicated in Figure 6 and then propagates to the crown of the vault. The observed traces show that collapse doesn't reach the ground surface.

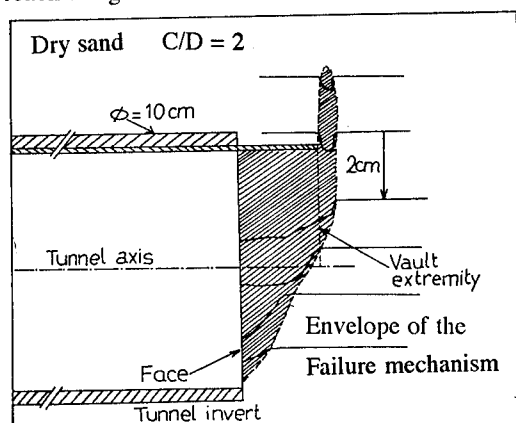


Figure 6. Failure mechanism in dry sand along tunnel axis.

Two zones of failure can be identified:

within the vault area: strains originate at the face, involving its whole area, and vanish near the extremity of the vault; a picture of the failure area observed along the center plane is shown in Figure 6: failure is limited to an area comprised between the face and the extremity of the vault.

Above the vault: soil displacements are limited to the centerplane and extend less than one tunnel radius over the vault.

Few tests performed in saturated sand show that failure develops within two areas, as for dry sands:

within the vault area: the failure area is similar to that obtained for dry sands,

above the vault: the geometry of the failure area has a bulb shape which extends upwards from the vault area; failure extends a few more than one tunnel radius above the vault, but doesn't reach the soil surface.

### 3.5 Ground surface displacements

Figure 7 shows the soil settlement observed when reducing the internal pressure, until failure is reached. Small soil movements occur at the beginning of the test; the displacements increase rapidly at the moment of failure, but maximum values remain small (in the order of 0.1% of tunnel diameter).

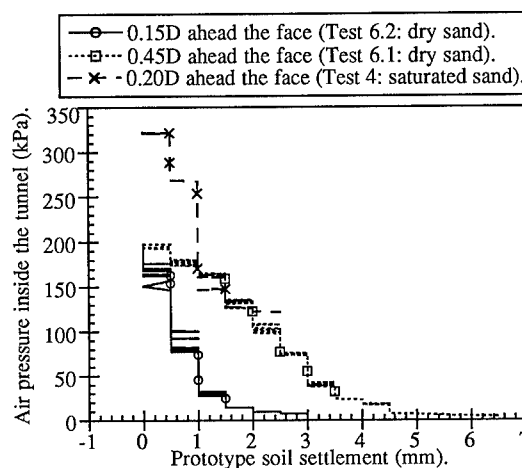


Figure 7. Soil settlement for different tests.

In presence of water, the tests carried have shown that the surface displacements are in the order of 0.05% of the tunnel diameter.

The subsidence trough recorded ahead of the face, just before failure, is shown in Figure 8. Trough settlement are of low magnitude, experimental trough profile is similar to the shape usually observed over tunnels (Peck 1969).

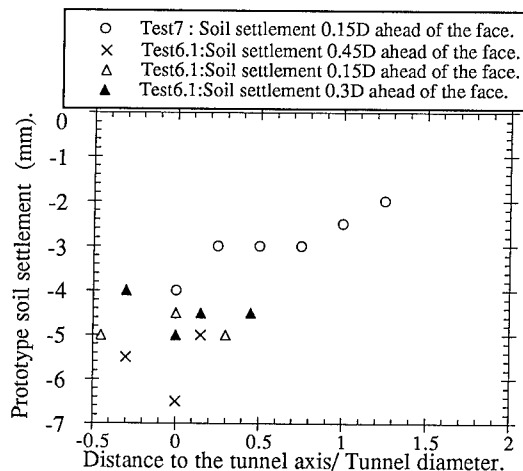


Figure 8. Profile of surface displacement .

#### 4 CONCLUSION

The tests described in this paper, using a threedimensional physical model, allowed to study the effect of a vault in front of the face on tunnel face stability. Two cases were considered, with a dry sand and with the presence of a hydrostatic groundwater table.

In dry sand, failure is sudden and is preceded by little face movement. The failure pressure obtained is low, with no significant difference with test results already carried out without a vault.

With a groundwater table, the tests have also shown that failure is instantaneous and soil movements are negligible before failure.

Failure is initiated at the face and covers the whole face area; it extends to the extremity of the vault, with little propagation over the vault.

**ACKNOWLEDGEMENTS:** The authors wish to acknowledge PERFOREX for their help and participation to this research.

#### REFERENCES

Atkinson J.H., Brown E.T., Potts M. 1975. Collapse of unlined tunnels in dense sand. *Tunnels and tunneling*, May 1975. pp. 81-87.

Bougard J.F. , François R. , Longelin R. 1977. Le prédécoupage mécanique, un procédé

nouveau pour le creusement des tunnels. *Revue Tunnels et Ouvrages souterrains*, n°22, 23 & 24.

Chambon P., Corté J.F. 1991. Etude sur modèles réduits centrifugés. Application aux tunnels à faible profondeur en terrain meuble pulvérulent. Etude et recherche des laboratoires des Ponts et Chaussées. 163p.

Garnier J., Canepa Y., Corte J.F., Bakir N.E., 1994 Study of bearing capacity of footings near slopes XIII ICSMFE, New Delhi.

Leca E. 1989. Analysis of NATM and shield tunneling in soft ground, Ph.D. Virginia Polytechnic Inst. and St. Univ. Virginia. USA. 450p.

Mair. R.J. 1979. Centrifugal modelling of tunnel construction in soft clay, PhD Thesis Cambridge University. 142p.

Peck, R.B. 1969. Deep excavation and tunneling in soft ground. State of the art Report, Int. Conf. on SMFE, Mexico, pp. 225-290.



## Compensation grouting

M.D. Bolton, C.Y. Chin & Y.C. Lu  
Cambridge University, UK

**ABSTRACT** Two grouting devices have been commissioned which are capable of making injections in centrifuged models. One is capable of pumping sand from a hopper above the surface of a package accelerating on a beam centrifuge. The other can create hydro-fractures through the injection of fluid from a syringe mounted on a central turn-table in a small drum centrifuge. They are to be used to explore the prevention of ground subsidence due to tunnelling. The means of simulating a subsidence trough is also explained.

### 1 INTRODUCTION

Interest in the UK is being shown in the use of displacement grouting to compensate for subsidence caused by tunnelling, shown exaggerated in Figure 1. Grout is injected at an intermediate level between the tunnel crown and the ground surface, as the heading advances: see Figure 2. The grout is intended to support the overburden without de-stabilizing the tunnel face. Since the support must not be lost when the grouting pressure is relaxed, displacement grouting is generally done with granular material.

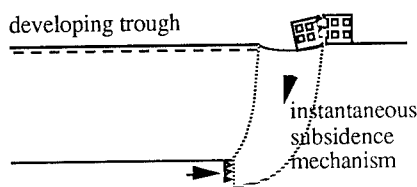


Fig 1 Subsidence due to tunnelling

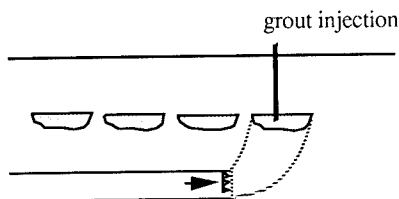


Fig 2 Compensation grouting

Two extremes may be recognised in the nature of these granular injections. They may be drained injections of a granular mortar (sand, cement etc) which behaves as a frictional material, or they may be undrained injections of a slurry of suspended particles (silica flour, PFA, cement, bentonite etc) which behaves as a viscous fluid during injection. These extremes are exemplified in the contrasting techniques of compaction grouting and hydro-fracture grouting.

### 2 MODELLING A SUBSIDENCE TROUGH

The objective is to simulate the typical subsidence trough which might be experienced above a 3.75 m diameter tunnel heading, with 7m of cover. Figure 3 shows a simple method of generating a given amount of ground loss, at a predictable rate. Working at 1:50 scale, a 75 mm diameter motorised tunnel facing-shore is initially held flush with the back face of a container (long, into the paper) which holds a block of clay 150 mm wide along the line of movement. Subsidence can be initiated by retracting the shore, permitting soil to flow plastically into the volume thereby created.

It must be recognised that the local pattern of subsidence will be different in the case of a retracting shore, compared with that of soil squeezing into an advancing heading. Nevertheless, the settlements for soft kaolin clay recorded in plan in Figure 4a, and sketched in section in Figure 4b at exaggerated scale, are roughly consistent with the empirical Gaussian

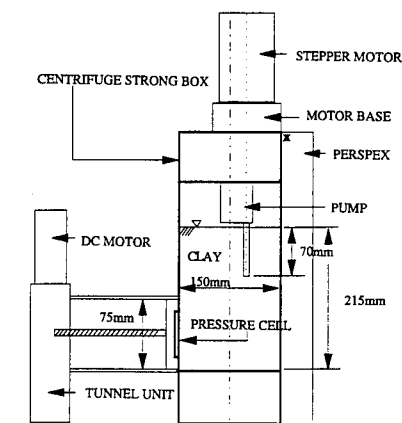


Fig.3 Tunnel and pump assembly.

profile usually assumed, and those observed previously in centrifuge models of tunnels: Mair et al (1993). The maximum settlement above the tunnel was about 1.8 mm (90 mm prototype scale) for an 8 mm retraction. Figure 5 shows an approximately linear relationship between tunnel displacement and surface settlement one diameter ahead of the face, with a ratio between the two of about 5.

The volume of the 150 mm length of trough was found to be roughly equal to the 37 ml of retraction. The full 8 mm of retraction per 150 mm of model section may be expressed as a proportional volumetric change of  $8 / 150$ , but "ground loss" is more properly defined as the ratio to the cross-sectional area of the tunnel of the cross-sectional area of the fully developed trough, rather than the attenuated trough ahead of the face. Taking the appropriate areas at the plane of the tunnel shore, the maximum equivalent ground loss would be approximately 7.5%. This would be two to four times greater than should be obtained with appropriate tunnelling techniques, and offers a useful range within which compensation grouting can be assessed.

The scatter in Figure 5 is quite small, confirming the controllability of subsidence using this technique. The retraction of the shore at a constant rate provides a constant rate of ground loss for trial compensation, at least in the case of soft clay ( $c_u \approx 20$  kPa), as used here. A total pressure cell is incorporated into the model shore, as shown in Figure 3, so that the equilibrium of the whole plastic mechanism can be assessed. Pore pressure transducers buried at various locations in the clay are used as sensitive indicators of change, and to assist in back-analysis.

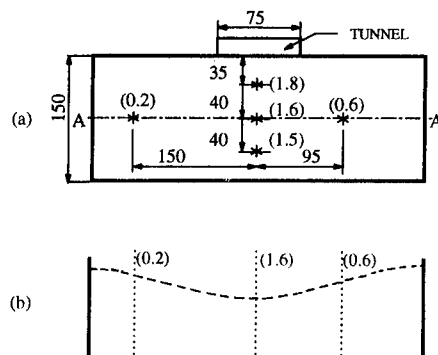


Fig.4 Surface settlements for 8mm tunnel retraction  
(a) Plan with spot levels (in mm, shown in brackets)  
(b) Settlement profile for section AA.

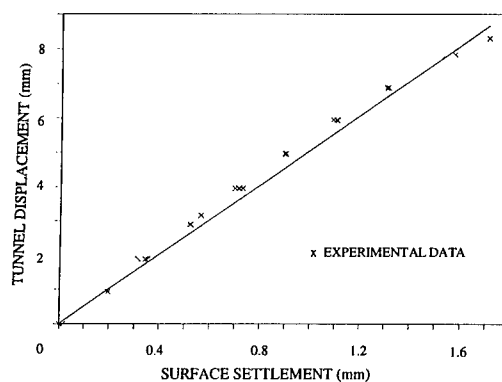


Fig.5 Tunnel displacement vs. surface settlement.

### 3 COMPACTION GROUTING

Figure 3 showed a sand pump located above the soil surface, capable of injecting dry granular material above and in front of the tunnel unit. Figure 6 shows a schematic section of the sand injector which has been used to simulate compaction grouting in clay at 50g on the Cambridge beam centrifuge. A stepper motor drives a screw feed which collects dry sand from a surrounding hopper. The inner hopper is located on PTFE guides, and the weight of sand inside is monitored by a load cell.

The pump is installed just before the package is mounted on the centrifuge. The outer tube is first inserted to the correct depth from the clay surface, the material inside being augured away. The unit is then lowered into place.

The pump was used to force uniform 0.8 mm Leighton Buzzard sand into kaolin clay,

precompressed to 125 kPa, with  $c_u \approx 20$  kPa at a depth of 70 mm at 50g. An injection of 125 g of sand occupying roughly 75 ml was carried out in a period of 2 minutes. Such a fast injection must leave the clay undrained; some allowance for strain-rate effects may be necessary in analysis.

As with the tunnel simulator, local pore pressures and surface displacements were monitored. There is some uncertainty over the quantity of sand trapped in the threads of the screw at any stage, but the final situation can be determined by direct physical examination, and intermediate states can be interpolated from the number of revolutions of the motor. Figure 7 indicates the ball of sand eventually exposed within the clay after the commissioning test. In this case, no subsidence was occurring during the injection, but the crown of the ball nevertheless remained at the opening in the delivery tube. The ball was pushed down as it expanded, causing regional

rather than local heaving, which was monitored by LVDTs. Pore pressure in the clay below the injector, at C in Figure 7, rose by 150 kPa during pumping.

The sand pump will be used to create simple one-shot compensations for tunnelling subsidence. The intention is to study the mechanisms of plastic flow from around the injector towards the tunnel unit, and to vary conditions in order to assess the sensitivity of residual surface displacements to the location, magnitude, and timing of injections.

#### 4 HYDRO-FRACTURE GROUTING

The injection of cement grout to fracture clay and induce permanent heave is well established as a remedial technique. The Tube à Manchette (TàM) system is usually used in which a grouted annulus around a perforated tube, sealed externally with rubber sleeves, is selectively burst by high pressure grout retained in sections by a packer system. The system has also been used ahead of an advancing tunnel face to compensate for subsidence as it occurs, through the monitoring of structures and the extensive use of ground instrumentation. Many injection tubes are used, usually fanning out from drilled shafts, to guarantee control of surface displacements.

The proper range of application of the technique, and the most efficient means of effecting it, are not yet clear. The mechanisms of hydro-fracture initiation and propagation in different soils, using grouts of different composition, are not well understood.

Preliminary hydro-fracture grouting tests have been carried out in a small drum centrifuge. Adhesives rather than particulate suspensions have been used in the first instance to investigate fracture mechanisms in kaolin, at different over-consolidation ratios.

The ANS&A mini-drum centrifuge, Figure 8, is an 800 mm diameter drum driven by a DC brushless servo motor capable of 1000 rpm. A ring channel holds containers of soil. The injection equipment sits centrally on a turn-table which can rotate in synchronisation with the ring channel. For these experiments two containers were used, one to accept grout and one to act as a counter-weight.

The injection equipment consisted of a 24 volt DC motor driving two pulleys via a belt. This provides linear motion to a screw feed, pushing against a plunger in a medical hypodermic syringe filled with the adhesive Loctite 241, which has a viscosity of 100 cP at 20°C. A 5 mm OD nylon tube connects the syringe to an aluminium nozzle embedded 50 mm in

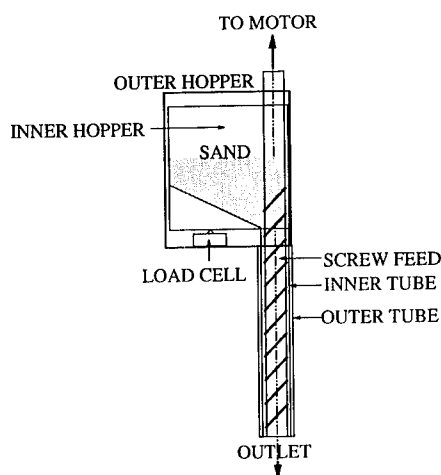


Fig.6 Pump for compaction grouting.

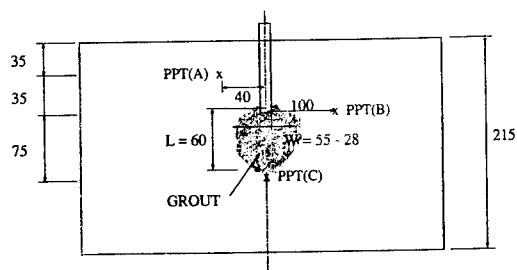


Fig.7 Section through sand injection, showing pore pressure transducer locations (all dimensions in mm).

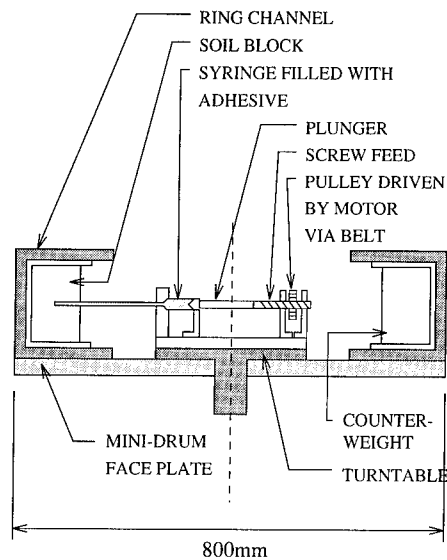


Fig.8 Cross-section of ANS&A mini-drum centrifuge with fluid injection equipment.

range 250 - 750 kPa, simulating the puncture of a grout annulus.

The instrumentation consisted of LVDTs to measure the rate of injection and heave of the soil surface, pore pressure transducers in the soil at the level of the injection, and strain gauges on the plunger to monitor the pressure in the syringe.

## 5 MINI-DRUM HYDRO-FRACTURE TESTS

Dry Speswhite kaolin was mixed to 120% water content with de-ionised water, under vacuum. The soil containers were positioned in a consolidometer, and the clay slurry was poured over to cover them. The clay was consolidated in stages to 60 kPa. The containers were then extracted and placed in the mini-drum centrifuge. Varying over-consolidation ratios could be achieved by varying the rotational speed of the mini-drum. The sample was brought into a known water pressure condition prior to the injection being carried out.

Figure 9 shows the data of an injection conducted at 25g in test CYC 10 on clay at an OCR of 7.2. Prior to injection the clay at the point of injection had been permitted to swell back into equilibrium at  $\sigma_v' = 8$  kPa.

At  $t = 36$  seconds the motor was started. This caused an increase of pressure in the syringe, as an air bubble trapped below the piston was compressed.

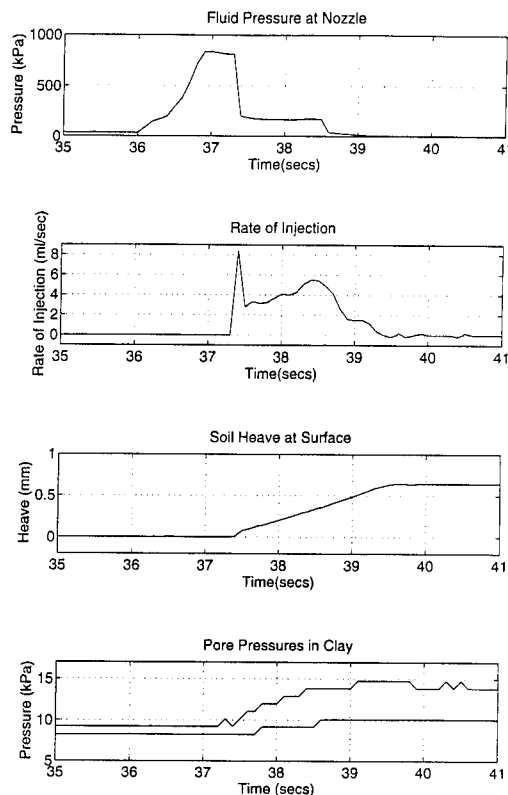


Fig 9 Data of hydro-fracture from test CYC 10.

At 37.4 seconds the ball was ejected at a pressure of about 800 kPa, and the soil was fractured. From 37.4 to 39 seconds the grout was injected at a rate of about 4 ml/sec at a nozzle pressure of about 175 kPa, more than sufficient to lift the soil block above against its self-weight and boundary shear strength. During the injection, the ground close to the injector heaved at a roughly constant rate, reaching 0.6 mm, while pore pressures in the clay on either side of the injector were seen to increase. The plunger hit the bottom of the syringe at 38.5 seconds, but the trapped bubble of compressed air was able to sustain the injection for another second. Thereafter injection stopped but the heave remained.

Following each test, the clay sample was removed and baked for 1 hour at 150°C to allow the adhesive to set. The adhesive being blue, it was possible to trace its extent in the clay. Figure 10 shows the sub-horizontal fracture surface from test CYC 10: it consists of three zones. The central circular mark is the impression of the nozzle. The larger circular patch

enclosing it, dark due to its being full of blue adhesive, was inflated to a thickness of about 5 mm, presumably in the pumping phase which followed initial hydro-fracture. The larger fracture zone to the right of this, with lighter colour due to its being only about 2 mm thick, was held to be the maximum extent of hydro-fracture created when the ball was first ejected from the tube. This hypothesis must be explored in further tests.

The injection in CYC 10 was conducted on heavily over-consolidated clay,  $OCR \approx 7.2$ , at which the effective stress ratio  $K_0$  should have been about 1.5. It was found that injections at  $OCR > 3$ , on the dilatant side of critical states, always resulted in sub-horizontal fractures, whereas for  $OCR < 3$  the adhesive was found to have created a ball around the nozzle, rather reminiscent of the compaction grouting described earlier. This is consistent with the view that fracture requires the soil state to be strain softening, and that the fracture surface runs normal to the direction of minimum compressive total stress.

## 6 SIMILARITY CONDITIONS FOR FRACTURE

Before centrifuge tests can properly be described as models, the similarity conditions must be known. Before dimensionless groups can be formed, the physics of the phenomenon must be imagined. Then the essential dimensionless groups can be derived, and the whole modelling hypothesis validated in centrifuge tests.

Two phenomena need attention – fast fracture when the pumping rate is high enough to create a dynamic event, and inflation at a steady pressure just sufficient to lift the overburden above a pre-existing fracture. No criterion for fast hydro-fracture propagation currently exists which treats soil as a two-phase material subject to effective stress analysis, though recent work by Murdoch (1993) draws attention to the role of fluid pressures and fluid migration into the tip of a slowly propagating fracture. However, especially if T&M grouting is to be used, it seems necessary to consider the possible lateral extent of fast fractures caused during the period in which injection pressure exceeds that necessary for slow propagation.

Consider the following hypothesis, therefore. Since the soil aggregate is “cracked” at the outset, with complete freedom of particles to separate on any surface, fracture must relate not to the solid phase but to the fluid phase. A consistent physical description of fast hydro-fracture, sketched in Figure 11, would therefore be the prying open of a crack which begins to propagate like a pair of shear waves, back to back,

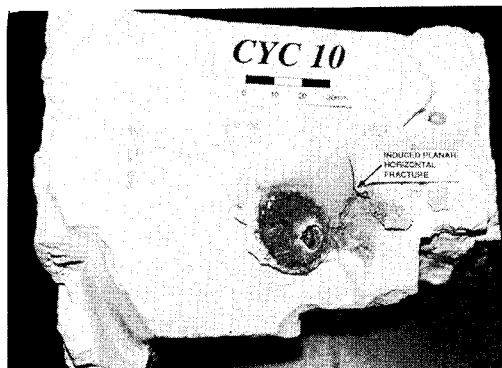


Fig.10 Fracture surface observed in test CYC 10.

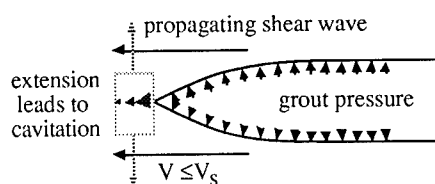


Fig.11 Fast hydro-fracture hypothesis.

at the shear wave velocity  $V_s$ . A zone of soil in front of the crack tip begins to extend in a direction normal to the propagation direction. Transverse tension, together with fast shearing on inclined planes if the soil is dilatant, leads to the creation of strong negative pore pressures ahead of the tip. If the ambient pore pressure was small enough, this can lead to cavitation or de-gassing, followed by the invasion of grout from the crack tip into the vapour-filled cavities, and therefore to the continued propagation of the fracture.

The propagation rate  $V$  will depend on the velocity of shear waves. Any such surge of grout of density  $\rho$  and viscosity  $\mu$  will induce a shear stress  $\tau$  on the sides of the crack which will tend to reduce grout pressures at the tip. If the crack is of mean thickness  $h$ ,  $\tau$  for a turbulent boundary layer may be written

$$\tau = \frac{\rho V^2}{R^m}$$

where  $m$  is some exponent less than unity to be applied to Reynold's number, defined as

$$R = \frac{\rho V h}{\mu}$$

From the foregoing discussion, it will be necessary to achieve a correct stress history, and correct effective stresses and pore water pressures prior to modelling fast fracture. Then the speed of stress waves will be replicated and, in the scenario traced above, grout velocities in the model should equal those in the prototype.

The criteria governing the thickness  $h$  of a fast hydro-fracture are not clear, and require examination. Ideally, however, the full-scale thickness would be reduced by factor  $n$ , together with the radius  $r$ . Since grout volumes should be scaled down by  $n^3$ , and cross-sectional areas by  $n^2$ , the duration of fast pumping must ideally be reduced by factor  $n$  in the model to achieve full-scale grout velocities. If the grout in the model has similar density  $\rho$  and viscosity  $\mu$  to the grout in the field, the Reynold number will be reduced by factor  $n$ , which will tend to increase fluid friction. This will tend to cause a more significant pressure drop in the model, so injection pressures would be higher than those needed at full scale to extend a scaled-up fast fracture.

Conditions for slow inflation of a pre-existing fracture will be similar to those for compaction grouting. Grout viscosity will be negligible but the transient flow of pore fluid in the soil, or bleed from the grout, may be significant. The usual reduction factor of  $n^2$  for the duration of an event subject to a diffusion process should theoretically be applied in this phase if the precise degree of transient flow were required in prototype materials are placed in a model. However, as with other dynamic centrifuge models, it will usually be possible to conduct meaningful tests with a time reduction of  $n$ . Bleed in cement grouts can be reduced by using micro-fine cement, or additives such as bentonite. Seepage in clay soils will be negligible even at time factor  $n$ , and the degree of transient flow in sands can be replicated using a  $d_{10}$  particle size scaled down by factor  $\sqrt{n}$ . Strain rates in the model will then be  $n$  times higher than the prototype, so element tests for model analysis should ideally be conducted at equivalent fast rates. It will be an objective to demonstrate the validity of this modelling of the slow inflation process, which should be capable of careful pressure control, and to determine whether it offers the required pattern of compensation.

## 7 CONCLUSIONS

The proper scaling of grout injections will require further study. A working hypothesis is that the duration of pumping should be reduced by the scaling ratio  $n$  in models centrifuged at  $n$  gravities. Fast fracture propagation would be correctly modelled only if the viscosity of the grout were similarly reduced by  $n$  in models, which is practically impossible, but it remains to be determined whether viscosity is a strong or weak parameter.

Devices have been commissioned to make single-phase injections. A screw device has been used successfully to perform compaction grouting of sand injections in soft clay. A syringe has been used to perform injections of a fluid.

Compaction grouting has been seen to lead to the expansion of a ball of sand which is pushed outwards and downwards beneath the delivery pipe. Fluid injection has been seen to lead to simple cavity expansion in lightly over-consolidated clay on the "wet" contractile side of critical states, and to fracture propagation in heavily over-consolidated clay on the "dry" dilatant side of critical states.

A small and convenient drum centrifuge has proved effective in permitting a rapid development of the concepts concerning hydro-fracture, which required ad-hoc adaptations of technology and a fast turn-around time. A large balanced beam centrifuge has proved effective in the development of models at larger scale which will permit a complex simulation of compensation grouting for the elimination of subsidence due to tunnelling.

## 8 ACKNOWLEDGEMENTS

The assistance of Mr Arthur Timbs in the design of the sand pump and tunnel shore, of Mr Steve Chandler in the execution of the beam centrifuge tests, of Mr Chris Collison in the design and commissioning of the mini-drum injection equipment, and Mr Neil Baker in the arrangements for data acquisition, are gratefully acknowledged. The authors are grateful to Professor Andrew Schofield for his permission to use the ANS&A mini-drum. This work is funded by a grant awarded by the UK SERC.

## 9 REFERENCES

- Mair R.J., Taylor R.N. and Bracegirdle A. 1993. Subsurface settlement profiles above tunnels in clays, *Geotechnique* 43, No.2, 315-320.
- Murdoch L.C. 1993. Hydraulic fracturing of soil during laboratory experiments, Parts 1, 2 and 3. *Geotechnique* 43, No.2, 255-287.

## 11 Pipes and anchors

## FE elastic analysis of earth pressure on buried flexible pipes

J. Tohda & L. Li

Osaka City University, Japan

H. Yoshimura

Konoike Construction Co., Ltd, Osaka, Japan

**ABSTRACT:** Circumferential distributions of normal and tangential earth pressures acting on two model flexible pipes, accurately measured in 12 centrifuge model tests, were compared with those calculated by FEM based on linear elastic theory. The analysis yielded pressure distributions that conformed well to the measured ones, when considering the effect of measured friction forces acting on the testing container wall on the measured earth pressures. This agreement revealed that the earth pressure problem of buried flexible pipes, which has been considered as one of ultimate-equilibrium problems, should be treated by the elastic theory, as well as in the case of buried rigid pipes.

### 1 INTRODUCTION

Earth pressure acting on buried pipes is a typical soil-structure interaction problem involving various complicated factors. However, current design methods for buried pipes, based on traditional ultimate-equilibrium methods such as Marston-Spangler theory, can not treat reasonably effects of these factors on the earth pressure, resulting in many serious accidents in Japan. Since 1979, one of the authors has studied earth pressure on buried rigid pipes through a full-scale field test, centrifuge model tests, and an elastic analysis (Tohda 1991). These studies fully clarified the effects of almost all factors on earth pressure acting on rigid pipes, and provided a new design concept based on the elastic theory for rigid pipes (Tohda et al. 1990a).

Following these studies, the authors began a study on earth pressure on buried flexible pipes. The first target in this study was to develop a technique to measure accurately the earth pressure on flexible pipes, because reliable data had not been obtained for this case and many analyses had not been verified by experiment. This target has been accomplished through a series of centrifuge model tests using specially designed model pipes with different flexibilities (Tohda et al. 1990b).

This paper reports FE elastic analysis for typical 12 cases among these centrifuge model tests to investigate whether

the elastic theory can be applied to the earth pressure problem of flexible pipes, as well as to that of rigid pipes.

### 2 OUTLINE OF CENTRIFUGE MODEL TESTS

Fig. 1 shows two aluminum model pipes with an external diameter  $D$  of 9 cm and wall thickness of 0.95 mm and 3.5 mm, named as Flexible-pipe and Rigid-pipe according to their flexibilities. Their surfaces were finished to be smooth. Two rings of each pipe were connected by means of 20 and 40 supporting beams, respectively, on which 20 load cells were mounted to measure both

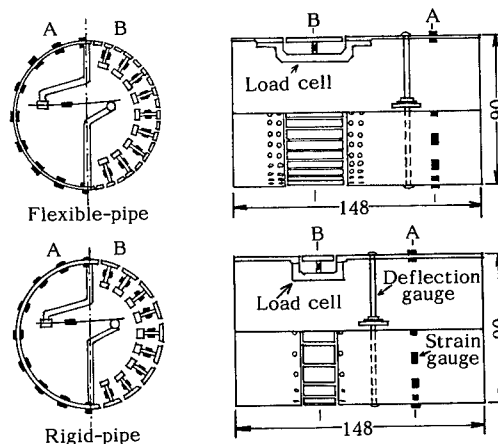


Fig. 1. Model pipes (unit: mm).



normal and tangential earth pressures. Bending strains along the pipe circumference and vertical pipe deflection were also measured by strain gauges and a deflection gauge.

Fig. 2 shows 2-D models for three types of pipe installations: ditch-type with sheet-piling (Ditch-S), embankment-type (Embk.), and ditch-type without sheet-piling (Ditch-0). The models, having a cover height  $H=9$  cm, ditch width  $B_d=13$  cm, and thickness of sand bedding  $H_b=4$  cm, were constructed in a scale of 1/30 of the prototype shown in the table of Fig. 2. A pair of model sheet-piles used in the Ditch-S model was 5 mm thick aluminum plates and was extracted simultaneously during centrifuge flight. In the Embk. and Ditch-S models, a pair of rigid steel walls with a smooth surface was placed at both ends of the ground as boundaries. The ditch in the Ditch-0 model was formed by a pair of rigid steel walls with a rough surface. These models were put into a centrifugal acceleration field of 30 G (G: gravitational acceleration) by using Mark-5 centrifuge of Osaka City University.

An air-dried silica sand, whose properties are shown in Table 1, was used as ground material. Two model grounds, dense and loose, were prepared by pouring the sand into the testing container from different heights, parallel to the longitudinal axes of the pipes. Table 2 shows densities and mechanical properties of the grounds. Their strength parameters, together with friction angles both against the pipe surface and against the rough ditch wall, were measured by means of a direct shear apparatus.

Typical results, measured in the Ditch-S models, are represented in Figs. 3 and 4. The marks plotted in Fig. 3 denote the

Table 1. Properties of silica sand.

$G_s$	Grain size	$U_c$	$\rho_{dmax}$	$\rho_{dmin}$
2.65	0.24-1.4mm	1.75	1.58 g/cm <sup>3</sup>	1.32 g/cm <sup>3</sup>

Table 2. Densities and mechanical properties of sand grounds.

Ground	$\rho_d$ (g/cm <sup>3</sup> )	$c_d$	$\phi_d$	$\phi_p$	$\phi_w$
Dense	1.55	0	47°	17°	45.5°
Loose	1.43	0	36°	16°	44.5°

$c_d$  and  $\phi_d$ : strength parameters under CD condition.  $\phi_p$ : friction angle against the pipe surface.  $\phi_w$ : friction angle against the rough ditch wall.

bending strains of the two model pipes, measured in the three test stages, ③, ④ and ⑤ (cf. Fig. 4), for the dense ground; the angle  $\theta$  is measured from the pipe top. Fig. 4 shows earth pressure distributions on the two pipes, measured at 6 test stages during the sheet-pile extraction process for the dense and loose grounds. In the figures, the normal and tangential earth pressures,  $\sigma$  and  $\tau$ , are illustrated in polar coordinates; the compressive  $\sigma$  and downward  $\tau$  are taken as positive. The maximum pipe deflection was recorded at the test stage ⑤ as 3.7 mm (dense ground) and 5 mm (loose ground) for the Flexible-pipe, and 0.13 mm and 0.12 mm for the Rigid-pipe.

High accuracy in the earth pressure measurement was confirmed in all the tests by an excellent agreement between the measured bending strains and bending strains calculated through the principle of minimum work under the measured earth

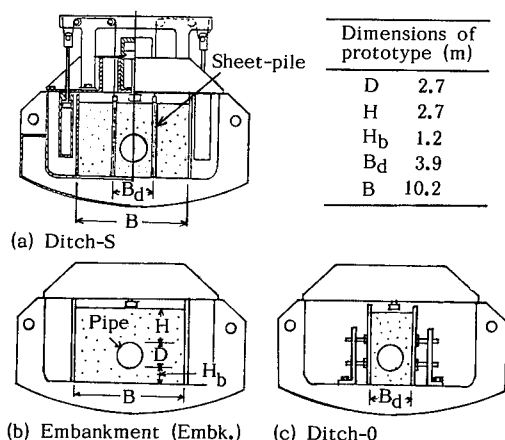


Fig. 2. Models for three types of pipe installations.

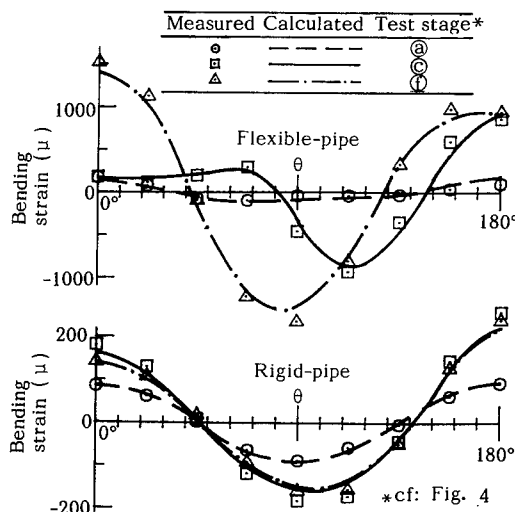


Fig. 3. Measured and calculated bending strains for the dense ground in the Ditch-S models.

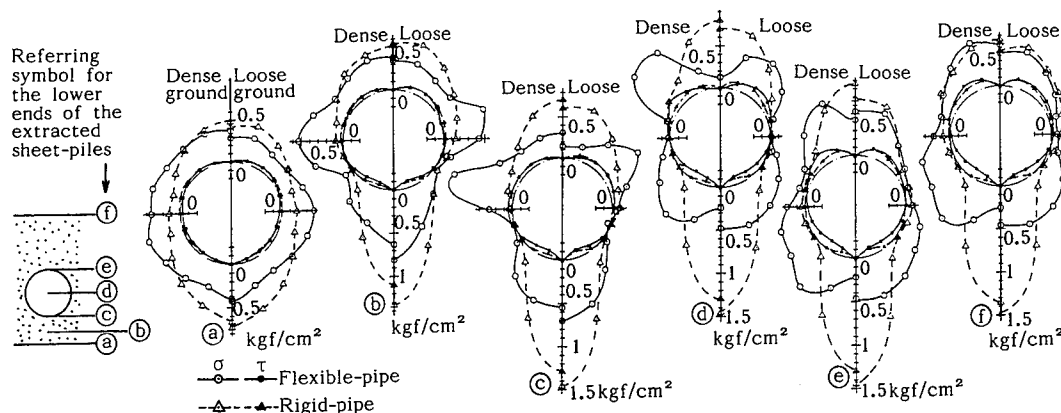


Fig. 4. Change in measured earth pressures,  $\sigma$  and  $\tau$ , due to the sheet-pile extraction in Ditch-S models.

pressure conditions, together with by the satisfaction of the external force equilibrium. The "curves" in Fig. 3 are examples of such calculated bending strains in the Ditch-S models.

### 3 FE ELASTIC ANALYSIS

#### 3.1 FE mesh, material properties and boundary conditions

The analysis was carried out by using a program with an isoparametric element under plane strain condition. Fig. 5 shows the FE mesh, in which the areas corresponding to those of the tested models were employed. Soil and pipe are assumed to be isotropic and elastic bodies. Table 3 shows the material properties used in the analysis.

Elastic moduli of the soil,  $E$  (deformation modulus) and  $\nu$  (Poisson's ratio) were obtained through  $K_0$ -compression test using a rectangular box (12 cm  $\times$  12 cm  $\times$  H=10 cm), in which axial strain  $\epsilon_1$  and lateral stress  $\sigma_3$  ( $=\sigma_2$ ) at each level of axial stress  $\sigma_1$  were measured under the condition of  $\epsilon_2=\epsilon_3=0$  ( $=K_0$ -condition).  $E$  and  $\nu$  of the soil were calculated through the following equations:

$$\nu = \frac{\sigma_3 / \sigma_1}{1 + \sigma_3 / \sigma_1}, \quad E = \frac{1 - \nu - 2\nu^2}{1 - \nu} \cdot \frac{\sigma_1}{\epsilon_1}$$

Fig. 6 illustrates the measured values of  $E$  against  $\sigma_1$ , showing that  $E$  depends on the axial stress level. The  $E$  values of the soil in Table 3 are those corresponding to the ground stress level under 30 G at the mid-height of the model ground. On the other hand, it was found that  $\nu$  does not depend on the axial stress level, because the measured  $\sigma_3 / \sigma_1$  values

were almost constant.

Special attentions were paid to three boundary conditions, in the lateral and bottom boundaries of the ground and at the

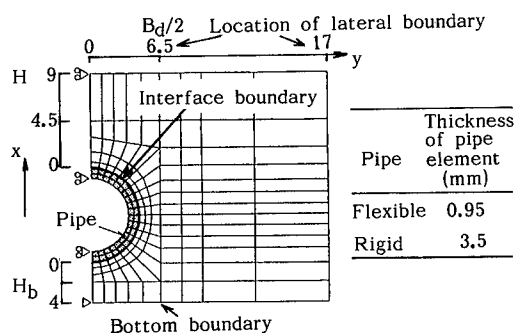


Fig. 5. Finite element mesh (unit: cm).

Table 3. Material properties used in the analysis.

Property	Soil		Pipe	
	Dense	Loose	Flexible	Rigid
$E$ (kgf/cm <sup>2</sup> )	30	16	740000	740000
$\nu$	0.35	0.38	0.33	0.33
$\gamma$ (gf/cm <sup>3</sup> )*	1.55 $\times$ 30	1.43 $\times$ 30	8.77 $\times$ 30	3.72 $\times$ 30

\* $\gamma$ : unit weight under 30G.

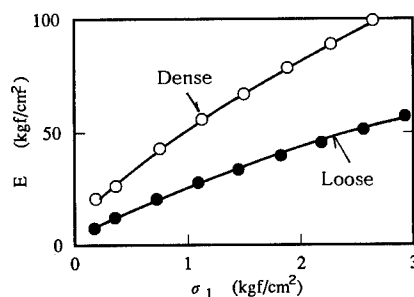


Fig. 6. Deformation modulus  $E$  of soil vs.  $\sigma_1$ .

pipe surface (cf. Fig. 5).

#### (1) Lateral boundary conditions

The following conditions were employed in the lateral boundaries of the ground for the three types of pipe installations, as shown in Fig. 7. In the figure,  $u$  and  $F$  denote respectively displacement and external force at the nodal points in the boundaries; subscripts,  $x$  and  $y$ , denote vertical and horizontal directions.

- a) Embk. model: at  $y=B/2$  (Fig. 7-①)  
 $K_0$ -condition ( $u_y=F_y=0$ ).
- b) Ditch-0 model: at  $y=B_d/2$  (Fig. 7-②)  
 Rough ditch-wall condition with separation, failure, and frictional slip.
- c) Ditch-S model: at  $y=B_d/2$  (Fig. 7-③)  
 \*Before the sheet-pile extraction (Ⓐ):  
 Smooth sheet-pile wall condition (=  $K_0$ -condition).  
 \*At the test stages Ⓑ through Ⓔ during the sheet-pile extraction:  
 Vacant hole condition within the region from the ground bottom to 0.5 D above the lower ends of the extracted sheet-piles, and  $K_0$ -condition in the upper part, as shown in Fig. 7-③. The depth delimiting these two conditions was determined by considering the sand movement towards the spaces left by the extracted sheet-piles.  
 \*After the sheet-pile extraction (Ⓕ):  
 Vacant hole condition from the ground bottom to the ground surface.

#### (2) Bottom boundary conditions

Smooth bottom condition ( $u_x=0$ ;  $u_y \neq 0$ ,  $F_y=0$ ) was employed at the bottom of the ground.

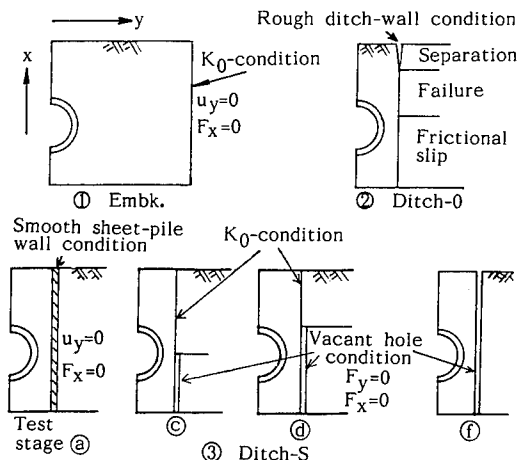


Fig. 7. Lateral boundary conditions in the ground for the three types of pipe installations.

The other condition, rough bottom condition ( $u_x=u_y=0$ ), generated almost the same results in any of the present cases when  $H_b=4$  cm.

#### (3) Interface boundary conditions

Semi-smooth condition with separation, failure, and frictional slip was employed at the pipe surface by using a curved parabolic joint element. The calculating procedure is as follows:

First, the tangent shear and normal stiffnesses of the joint element,  $K_s$  and  $K_n$ , were assumed as  $K_s=3$  kgf/cm<sup>2</sup>/cm and  $K_n=1000$  kgf/cm<sup>2</sup>/cm. The  $K_s$  value was determined by trials for calculated tangential stresses in the joint elements, so as to obtain good agreement with the measured ones in the Embk. model, the most simple one. The  $K_n$  value was also determined by trials to avoid both the fluctuation of the calculated stresses and excessive intrusion of the joint elements into the pipe elements. The calculation was repeated until the stresses in the joint elements converged through the followings: Where  $\tau \geq \tau_f$  (failure area),  $K_s$  was decreased by multiplying  $\tau_f/\tau$  to satisfy  $\tau < \tau_f$ , in which  $\tau_f$  is the shear resistance calculated through  $\tau_f = \sigma \tan \phi_p$  ( $\sigma$ : calculated normal stress and  $\phi_p$ : frictional angle at the pipe surface). Where  $\sigma$  is tensile (separation area),  $K_s=K_n=0$ . Where  $\tau < \tau_f$  (frictional slip area), the values of  $K_s$  and  $K_n$  were maintained as initial values.

Examples of the trial calculations to determine the initial values of  $K_n$  and  $K_s$  are shown in Figs. 8(a) and 8(b). The greater  $K_n$  generates the greater  $\sigma$ , while the greater  $K_s$  generates the smaller  $\sigma$  at the pipe top and bottom. Nevertheless, their changing ranges are not great.

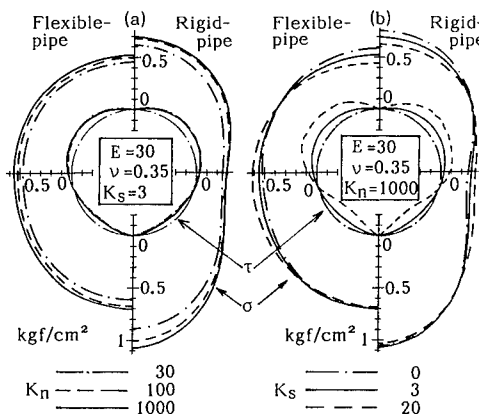


Fig. 8. Change in earth pressure due to  $K_n$  and  $K_s$  for Embk. model (unit of  $K_n$  and  $K_s$ : kgf/cm<sup>2</sup>/cm).

## 4 COMPARISON BETWEEN TEST AND ANALYSIS

### 4.1 Primary comparison

Fig. 9 shows a typical comparison between the calculated earth pressures (the right-half of the figure) and measured ones (the left-half of the figure); this is for the case of the Embk. model with loose ground. The solid-line and broken-line curves denote the data for the Flexible-pipe and Rigid-pipe, respectively. The figure shows that the distribution shapes of the calculated pressures agree well with those of the measured ones, while their pressure intensities are appreciably greater than those of the measured ones. Similar results were obtained for the other tests, except for the data at the test stages ① through ③ during the sheet-pile extraction process in the Ditch-S models. In the latter cases, both shapes and intensities of the calculated earth pressures agreed with the measured ones.

As described before, the accuracy in the earth pressure measurement was confirmed in all the tests. Furthermore, the changing ranges of the calculated earth pressures due to joint element stiffnesses were not so great, at least in the Embk. models, and soil elastic moduli were reasonably determined through the  $K_0$ -compression tests. Therefore, some other factors should exist to cause the quantitative difference. Frictional force acting on the walls of the testing container was expected to be the main cause. In order to confirm this, an Embk. model test using the Flexible-pipe under the loose ground condition was carried out by using the

testing container, whose inside walls were lubricated by means of both two sheets of rubber membrane 0.2 mm thick and silicon grease. The thick-line and thin-line curves in the left-half of Fig. 10 show, respectively, the measured earth pressure distributions with and without lubrication. The intensities of the data with lubrication are greater than those of the data without lubrication. Also, the data with lubrication show good agreement with the calculated ones illustrated in the right-half of Fig. 10, as expected.

This result suggests that the intensities of the measured earth pressures, except for the exceptional data in the Ditch-S models, should be modified by considering the reduction due to the frictional force acting on the testing container. Furthermore, the reason why the exceptional data in the Ditch-S model conformed to the calculated ones without the modification was explained to be caused by the reduction of the frictional force due to the sand movement towards the vacant spaces left by the extracted sheet-piles.

Thus, the total soil weight, both in the Embk. models and inside of the ditch delimited by the sheet-piles in the Ditch-S models, were measured for different ground thicknesses under 30 G, by means of a load cell mounted on the bottom of the testing container. According to the test results, the ratio of the net total soil weight to the measured one (named as friction ratio) was 123 % for the dense and loose grounds in the Embk. model, and 130 % for both grounds in the Ditch-S model, when the thickness of the ground tested was equivalent to a half of that of the model ground. In the Ditch-O model, the ratio was calculated as 114 % by distributing the friction force, measured in the Embk. models, to the front and back areas of the testing container walls within the ditch.

### 4.2 Secondary comparison

The left-half of each figure in Fig. 11 shows the measured earth pressures for the dense ground, which are modified by multiplying the friction ratios described in 4.1, except for those at the test stages ③ and ④ in the Ditch-S models. The calculated earth pressures corresponding to these cases are shown in the right-halves of the respective figures. These calculated earth pressures conformed well to the measured ones. It was confirmed, furthermore, that the calculated pipe deflections showed excellent agreement with the measured pipe deflections with the above modification. Fig. 12 is an example of such comparison

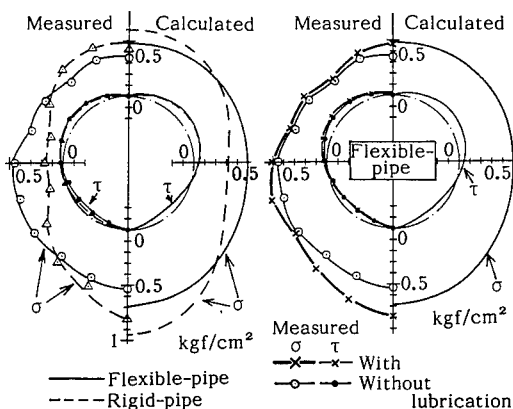


Fig. 9. Comparison between the tests and analyses in the Embk. models (loose ground).

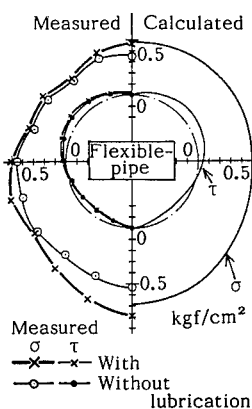


Fig. 10. Effect of the lubrication on the measured earth pressures in the Embk. model.

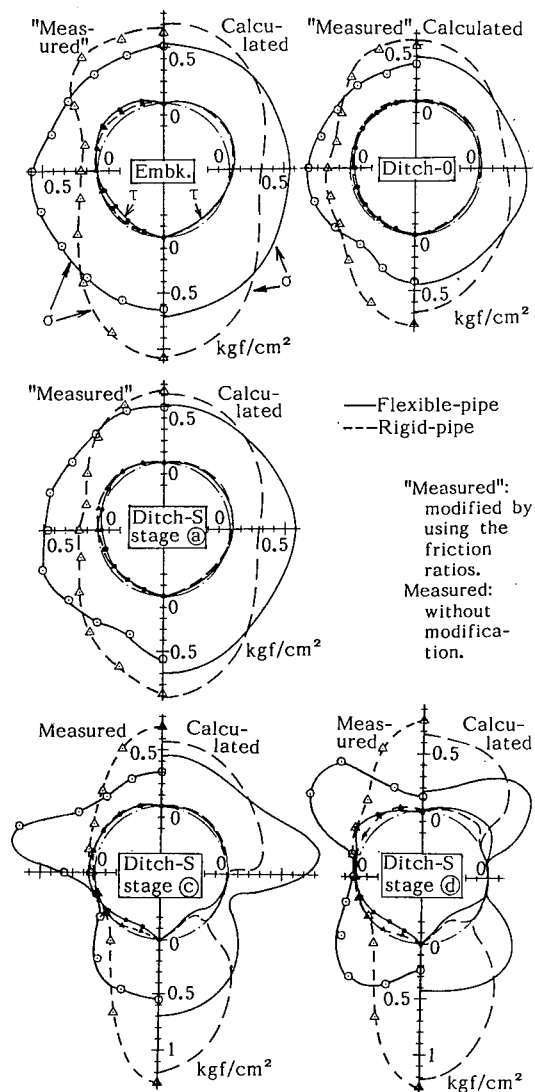


Fig. 11. Measured and calculated earth pressures for three types of pipe installations (dense ground).

between the calculated and measured pipe deflections in the Ditch-S model.

The loose ground yielded similar agreements described above. Thus, the tests and analysis fully backed up each other, showing the followings:

1. The assumptions employed in the analysis simulated well the actual conditions in the tests.
2. The difference in the lateral boundary conditions in the ground yielded the difference in the earth pressures between the three types of pipe installations.
3. This also caused the drastic change in the earth pressures due to the sheet-

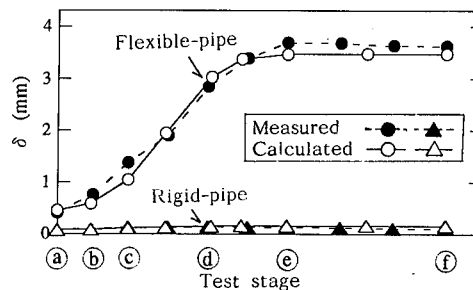


Fig. 12. Measured and calculated pipe deflections  $\delta$  during sheet-pile extraction process in Ditch-S model (dense ground).

pile extraction in the Ditch-S models.

4. The mechanism of the earth pressure on buried flexible pipes can be explained through the linear elastic theory, because the boundary conditions, together with deformation properties of the soil and pipe, are critical factors in this problem.

## 5 CONCLUSIONS

FE elastic analysis yielded results that conformed well to earth pressures on two model flexible pipes measured in 12 centrifuge model tests, when considering the effect of the frictional forces acting on the testing container wall on the measured earth pressures. This agreement confirmed the applicability of the elastic theory to explain the mechanism of earth pressure on buried flexible pipes, as well as in the case of buried rigid pipes. Thus, this study offers a rational method to reconsider systematically earth pressure problem of buried pipes having any flexibilities as a soil-structure interaction.

## REFERENCES

- Tohda, J. et al. (1990a). FE elastic analysis of measured earth pressures on buried rigid pipes in centrifuged models. Proc. of ASCE Inter. Conf. on Pipeline Design and Installation, Las Vegas, U.S.A., pp.557-571.
- Tohda, J. et al. (1990b). Earth pressure acting on buried flexible pipes in centrifuged models. Proc. of ASCE Inter. Conf. on Pipeline Design and Installation, Las Vegas, U.S.A., pp.17-31.
- Tohda, J. (1991). Earth pressure acting on buried pipes. Developments in Geotechnical Aspects of Embankments, Excavations and Buried Structures, Balkema, Rotterdam, pp.331-346.

## Soil structure interaction of partially buried flexible pipes

M. Javenmard & A. J. Valsangkar

Department of Civil Engineering, University of New Brunswick, Fredericton, N.B., Canada

**ABSTRACT:** Centrifuge model tests have been performed on fully and partially buried flexible pipes. The stiffness of the model flexible pipe and the soil cover were varied in the test program. The primary objective was to investigate the deformations of partially buried pipes by physical modelling.

### 1 INTRODUCTION

The behaviour of fully and partially buried flexible pipes is one of the complex soil structure interaction problems. Previous studies have shown that the problem is difficult to solve analytically, but can be studied by physical modelling. This approach of physical modelling using geotechnical centrifuge has been used to study the behaviour of fully buried flexible pipes and culverts by Valsangkar and Britto (1979), McVay et. al (1986 and 1993), Craig and Mokrani (1988), Stone et al (1991), and Tohda et al (1991).

At present, 2m to 4m diameter fibreglass reinforced plastic pipes with effective stiffness of 1-2 kPa/m are being installed in Eastern Canada and United States to replace old wood stave pipes for transmission of water to drive turbines of small hydroelectric plants. In this type of application, the flexible pipe is only partially buried (Fig. 1), and the pipe is provided with internal cruciform supports during backfilling. The critical conditions for the performance of such pipe are immediately after the cruciforms are removed, and during the maintenance stage, when the pipe is empty and soil pressures act on the thin walls of the pipe. During normal operations, the pipe transmits fluid under pressure and counteracts the lateral earth pressures. Application of classical methods of earth pressure acting on a cylindrical

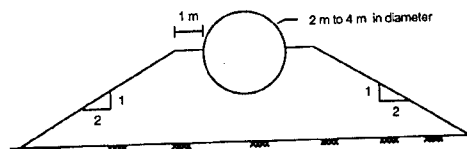


Fig. 1. Partially Buried Pipe

shell leads to prediction of deformation of the pipe, of the order of 33 percent of the diameter of the pipe (ABCO, 1988). However, these predictions are inconsistent with the field data on few prototype structures which show the pipe does not deform excessively after removal of cruciforms. The present centrifuge tests were therefore undertaken to study the deformations of very flexible partially buried pipes.

Model tests with shallow soil cover were also undertaken to compare the performance of partially buried pipes with that of fully buried pipes with shallow cover and to add to the limited data base on the behaviour of very flexible pipes with shallow soil cover.

### 2 SCALING LAWS AND CENTRIFUGE

#### 2.1 Scaling laws for pipe deflection:

The effective stiffness of a pipe affects its deformation which in turn affects the resulting

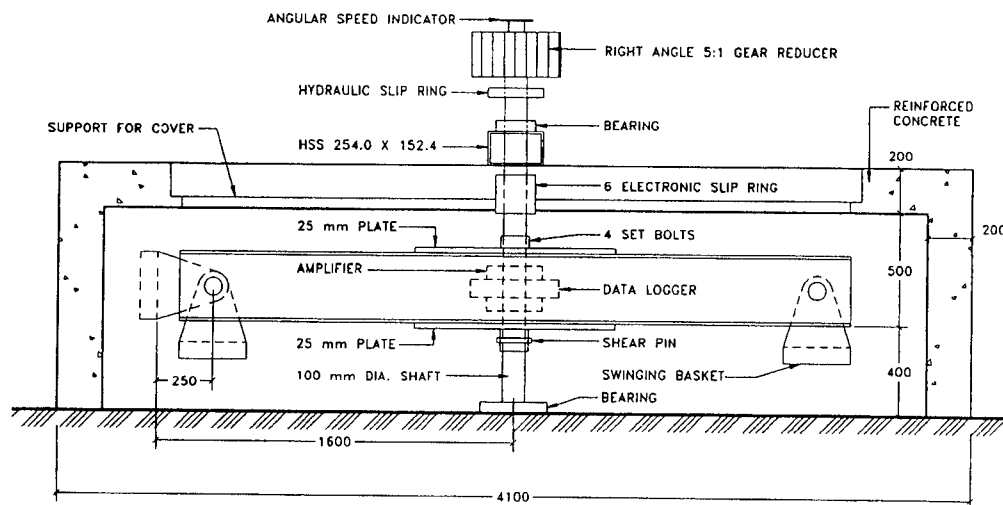


Fig. 2. Centrifuge Facility

earth pressure. The effective stiffness, also defined as the ring stiffness factor, is a measure of pipe flexibility and is defined as:

$$\text{effective stiffness} = \frac{EI}{R^3} \quad \dots\dots 1$$

where  $E$  = Young's modulus of the pipe material,  $I$  = second moment of area per unit length of the pipe,  $= t^3/12$  where  $t$  = pipe wall thickness, and  $R$  = radius of the pipe.

A rigid pipe has an effective stiffness in the order of  $10^3$  kPa/m whereas flexible pipes have effective stiffness of 10 kPa/m or less.

The flexible pipes used in the construction industry are made from fibreglass reinforced plastic or steel. In the present study, only model steel pipes were used. It was shown by Valsangkar and Britto (1979) that the correct modelling of deflections of very flexible pipes can be achieved by satisfying the following scaling law:

$$\frac{E_m I_m}{R_m^3} = \frac{E_p I_p}{R_p^3} \quad \dots\dots 2$$

where subscripts 'm' and 'p' refer to the model and prototype respectively.

Therefore, if the same pipe material is used to

construct the model pipe as the prototype, similarity conditions are satisfied.

If different pipe materials are used in the model testing, the results can still be used for a prototype structure using general law proposed by Bolton and Powrie (1987) which leads to the following relationships (Stone, et. al 1991):

$$E_m = X E_p \quad \dots\dots 3$$

$$t_m = t_p / NX^{1/3} \quad \dots\dots 4$$

where  $N$  = scaling factor.

## 2.2 Centrifuge

All the tests were performed on a newly commissioned centrifuge designed and built at the University of New Brunswick (Fig. 2). The centrifuge is designed for a maximum payload of 100 kg at 200g, at an effective radius of 1.6m. The centrifuge is equipped with swinging platforms, data acquisition system mounted on the arm, electric slip-rings and one hydraulic slip-ring. Details of the centrifuge facility are reported by Bryden (1993).

### 3 EXPERIMENTAL PROGRAM

#### 3.1 Model pipes

The model pipes were 152 mm in length and 50mm in diameter. The pipes were fabricated from flat sheets of steel shim of 0.076mm and 0.050 mm thickness. The effective stiffnesses of the model pipes were 0.488 and 0.3 kPa/m respectively. These stiffnesses correspond to very flexible pipes and are comparable to the effective stiffness of model pipes tested by Valsangkar and Britto, (1979). All tests were done at 60g to represent a prototype flexible pipe of 3m diameter. Model pipes were instrumented with ten miniature strain gauges as shown in Fig. 3.

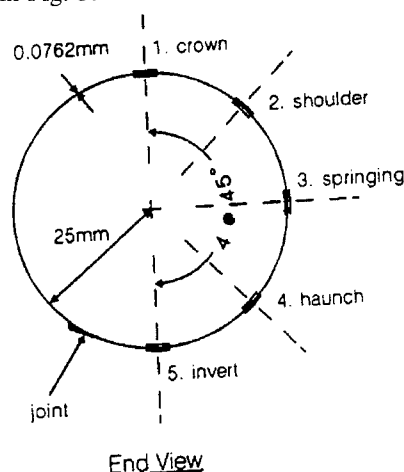


Fig. 3. Strain Gauge Locations

The pipe was seated between plexiglass end caps of 50mm diameter in order to prevent the backfill from filling the inside of the pipe. The pipe was attached to the end caps with soft rubber sheaths. This type of end connection has been proven not to impose any end restraints on the behaviour of pipe (Valsangkar and Britto, 1979).

#### 3.2 Soil and model preparation

Fine grained silica sand which was air dried was used as backfill around the pipe. The properties of the silica sand are presented in Table 1.

Table 1. Properties of silica sand

$G_s$	Grain size mm	$C_u$	$C_c^*$	$\rho_s(g/cm^3)$ (average)
2.66	0.150-0.425	1.7	0.9	1.63

+  $C_u$  = uniformity coefficient

\*  $C_c^*$  = coefficient of curvature

The strong box used for the model tests had internal dimensions of 255mm long, 195mm wide and 150mm high, which allowed testing of one model pipe at any given time (Fig. 4). For the fully buried flexible pipes, the sample was prepared in the strong box by pouring the sand parallel to the longitudinal axis of the pipe to achieve uniform density around the pipe. The sand was placed using air pluviation method. For partially buried pipe, the sand was placed perpendicular to the longitudinal axis as placement parallel to the longitudinal axis was not practical. This change in the sand placement technique was assumed not to affect the test results, as Tohda et al. 1991 report that pouring of sand in a direction parallel or normal to the longitudinal axis of the pipe did not affect behaviour of model flexible pipes in centrifuge testing.

### 4 MODEL TEST RESULTS

The geometries of the model tests reported in this paper are presented in Table 2. Parameter C, D and S are defined in Fig. 4.

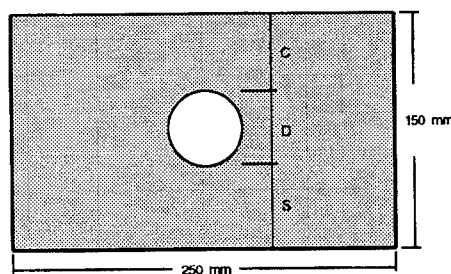


Fig. 4. Cross-section of Strong Box



Table 2. Model Geometries

Test No.	C/D	t <sub>m</sub> (mm)	S/D
1	0.5	0.050	1
2	0	0.050	1
3	-0.5	0.050	1
4	-0.5, -0.25	0.050	1
5	0.5	0.076	1
6	0	0.076	1
7*	0	0.076	1

\* In test 7 a line load was placed at 0.75R from the centerline.

The response of the model pipes is presented in terms of hoop thrust and bending moments induced in the pipe wall which were determined using the following equations:

$$M = \frac{(\epsilon_o - \epsilon_i)Et^2}{12(1 - \mu^2)} \quad \dots\dots 5$$

and

$$T = \frac{(\epsilon_o + \epsilon_i)Et}{2(1 - \mu^2)} \quad \dots\dots 6$$

where

$\epsilon_o$  = circumferential strain on the external face of the pipe

$\epsilon_i$  = circumferential strain on the internal face of the pipe

E = Young's modulus of the pipe material

$\mu$  = Poisson's ratio of the pipe material, and

t = thickness of the pipe wall

The results for tests 1, 3, 5 and 6 are presented in Figs. 5 to 8. The hoop stress induced in the pipe wall is non-uniform and decreases as the soil cover is decreased from 0.5D to -0.5D, for the pipe with 0.05mm wall thickness (Fig. 5). In contrast, the measured hoop stresses for pipe with wall thickness of

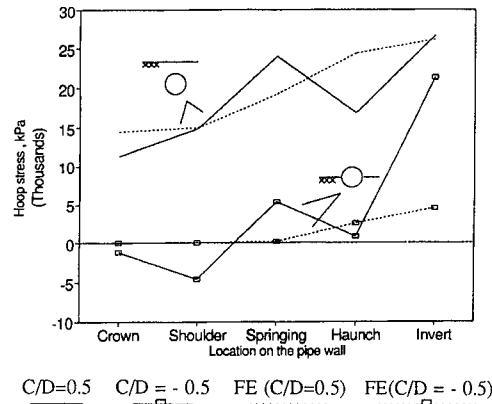


Fig 5. Hoop Stresses for Pipe: t = 0.05mm

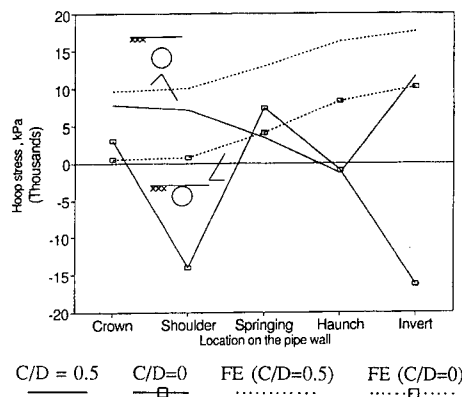


Fig. 6. Hoop Stresses for Pipe: t = 0.076mm

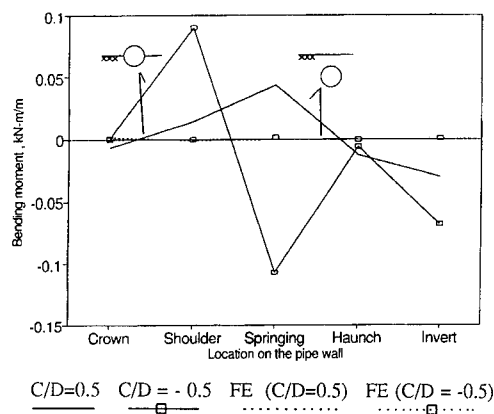


Fig. 7. Bending Moments for Pipe: t = 0.05mm

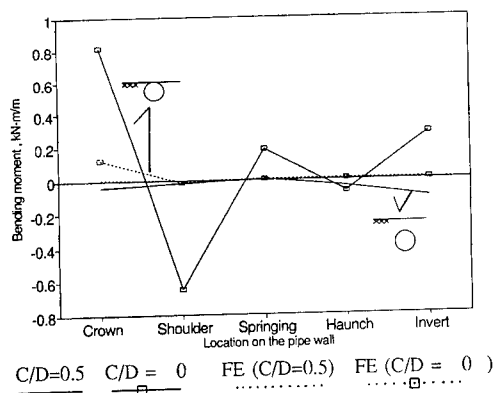


Fig. 8. Bending Moments for Pipe:  $t = 0.076\text{mm}$

0.076mm, show no similar trend and the hoop stresses appear to be considerably non-uniform for the condition of zero soil cover. (Fig. 6).

The bending moments for fully buried pipes with positive soil cover indicate that the eccentricity of the thrust will be in general within the middle third of the pipe wall. In contrast, significant bending moments were measured for 0.076mm thick pipe with zero soil cover when compared to fully buried pipe with a soil cover equal to 0.5D (Fig. 8). Similar trend was also noted for pipe with a wall thickness of 0.050mm.

In tests 2, 4 and 7, the model pipes failed by local buckling. In tests 2 and 7, the backfill around the pipe was symmetrical and up to the crown level. The thinner pipe failed with this configuration, whereas for the thicker pipe a line load of 48kN/m at the soil surface lead to buckling failure. In test 4, the backfill around the partially buried thinner pipe was unsymmetrical, which led to local buckling failure.

## 5 FINITE ELEMENT ANALYSIS

The finite element analysis was performed using the commercially available software ANSYS. The pipe was modelled with 24 beam elements, and isoparametric quadrilateral elements were used for modelling of soil in plane strain conditions. The Young's modulus of soil was

assumed to be stress level dependent and the soil around the pipe was assumed to consist of 20, 15 and 10 layers for C/D ratios of 0.50, 0, and -0.5. The stress level dependent Young's modulus of soil was calculated using the following dimensionless parameter experimentally determined by Duncan et. al (1980) for a silica sand similar to the one used in the present testing program.

$K$  = modulus number = 1400;  
 $n$  = modulus exponent = 0.74;  
 $K_b$  = bulk modulus number = 1080;  
 $m$  = bulk modulus exponent = 0.15;  
 $R_f$  = failure ratio = 0.90  
 Poisson's ratio = 0.46

The numerical analysis was performed without any interface elements. Furthermore, the numerical computations were made assuming that the soil around the pipe was placed in layers. In comparison, the centrifuge tests were performed which can be classified as "gravity switch-on". This aspect has been investigated by Britto (1980), who concluded that in the linear finite element analysis, the results obtained are not influenced by whether the backfill around flexible pipes is simulated in thin layers or as a single thick layer.

The comparison of linear finite element analysis with the stress dependent Young's modulus and the centrifuge data is presented in Figs 5 through 8. For pipe with wall thickness of 0.05mm, the variation of hoop stress for C/D ratio of 0.5 is reasonably well predicted by the finite element analysis (Fig. 5). In contrast, the predicted hoop stresses are lower for the partially buried pipe with C/D ratio of -0.5. The predicted hoop stresses for pipe with wall thickness of 0.076mm were not even exhibiting qualitative trends observed in the experimental program.

The bending moments predicted by the finite element analysis were considerably lower than those measured in the centrifuge tests. Similar observations have been made by Britto (1980), who also used the linear finite element analysis to study the behaviour of flexible pipes.

## 6 CONCLUSIONS

Following conclusions are drawn from the present study:

(i) Partially buried pipe with effective stiffness of 0.3 kPa/m and backfill up to springing level did not experience excessive deformation. As the relative stiffness of the model pipes was  $1/5^{\text{th}}$  of the flexible pipes used in practice, it is concluded that the current practice of placing soil backfill up to springing level will not lead to excessive deformations. This conclusion is also confirmed by satisfactory performance of prototype structures.

(ii) Buckling failure is likely to occur for very flexible pipes with effective stiffness less than 1 kPa/m, when the soil cover is zero or the backfill around the partially buried pipe is unsymmetrical.

(iii) The commercially available linear finite element analysis used in this study does not predict the behaviour of partially buried flexible pipes.

## ACKNOWLEDGEMENTS

The funding for this research was provided by NSERC Operating grant awarded to the second author. The financial assistance to the first author was provided by the Government of Iran.

## REFERENCES

- ABCO (1980). Design brief: NYSEG - Cadyville Penstock. ABCO Plastics Ltd. Nova Scotia, Canada.
- Bolton, M.D. & W. Powrie 1987. the collapse of diaphragm walls retaining clay. *Geotechnical* 37:
- Britto, A.M. 1979. Thin walled buried pipes. Ph.D Thesis, Cambridge University, England.
- Bryden, P.J. 1993. Centrifuge modelling of flexible buried pipes. M.Sc.E. Thesis, University of New Brunswick, Fredericton, Canada.
- Craig, W.H. & A. Mokrani 1988. Effect of static line and rolling axle loads on flexible culverts buried in granular soil. *Centrifuge '88*, Corte (ed): 385-394 Balkema, Rotterdam.
- Duncan, J.M., P. Byrne, K.S. Wong & P. Mabry 1980. Strength and bulk modulus parameters for finite element analyses of stresses and movements in soil masses. Report No. UCB/GT180-01, College of Engineering, Office of Research Services, University of California, Berkeley, CA.
- McVay, M.S. & Papadopoulos 1986. Long-term behaviour of buried large-span culverts. *Journal of the Geot. Eng. Div., ASCE*, Vol. 112: 424-442.
- McVay, M.S., P. Papadopoulos, D., Bloomquist and F.C. Townsend 1993. Long-term behaviour of large-span culverts in cohesive soils. Transportation Research Board Meeting, Washington, D.C., USA.
- Stone, K.J.L, P.J. Hensley & R.N. Taylor, 1991. A centrifuge study of rectangular box culverts. *Centrifuge '91*, 107-112, Boulder, Colorado, Balkema.
- Tohda, J., H. Yoshimura, K. Ohi, and H. Seki 1991. Centrifuge model tests on several problems of buried pipes. *Centrifuge '91*, 83-90, Boulder, Colorado, Balkema.
- Valsangkar, A.J. and A.M. Britto, 1979. Centrifuge tests of flexible circular pipes subjected to surface loading. Supp. Report 530, Transport and Road Research Laboratory, Crowthorn, UK.

## Study of pipelines subjected to landslide conditions

M.J. Paulin & J.I. Clark

*C-CORE, Centre for Cold Ocean Resources Engineering, Memorial University of Newfoundland, St. John's, Nfld, Canada*

F. Poorooshasb

*Formerly: C-CORE, Centre for Cold Ocean Resources Engineering*

M. Rizkalla

*NOVA Corporation of Alberta, Calgary, Alb., Canada*

**ABSTRACT:** The state-of-practice (SOP) for pipeline design in areas where pipelines may move relative to the soil involves discretising the pipeline into segments and coupling the segments to the soil via a set of spring/sliders. Much of the theory behind this SOP is derived from other geotechnical applications such as pile/soil interaction. There is little or no physical verification of the mechanisms or the magnitude of forces assumed during pipeline displacement. This paper presents an experimental model examination of displaced pipelines, using the centrifuge modelling technique to create similitude between model and full scale.

In this paper, the SOP is presented. The experimental program and the results of eight pipeline model tests are then presented. These results are discussed, with particular reference to the magnitude of loads transmitted to the pipes and the development of the pipeline/soil interaction. The test results are compared with the loads which would be predicted by the SOP design calculations. The main conclusion is that the SOP formulation appears to be unconservative, predicting loads acting on the pipeline about 50% lower than those measured experimentally.

## INTRODUCTION

When a buried pipeline is subjected to ground movement such as a landslide or by downslope creep of soil, the pipe's integrity and operating safety are both matters of concern. In finite element modelling (FEM) techniques used in pipeline analyses, the interaction between the pipe and soil is commonly described by spring elements. The parameters describing these spring elements have generally been assumed from other soil/structure interaction studies (e.g. anchors and piles) and much of the experimental and analytical work cited in pipeline analysis has been undertaken from a foundation design perspective.

Review of the literature has indicated that there is little realistic pipeline-specific experimental information available. Studies carried out by the NOVA Corporation of Alberta have shown that typical rates of ground movements for creeping type landslides experienced by the industry range from less than 1 cm/yr to 6 cm/yr. Lateral

pipeline/soil experiments reported are generally small in scale, ignore construction considerations such as the presence of a distinct backfill material, and generally use idealized soils. Experimental work in this field needs to be extended.

A simple engineering analysis of the pipeline/soil interaction problem can be expressed as (Rizkalla et al., 1992):

$$P_{ult} = DC_u N \quad (1)$$

where  $P_{ult}$  is the ultimate load transferred to the pipe,  $D$  is the pipeline diameter,  $C_u$  is the undrained shear strength of the soil, and  $N$  is the interaction factor.

The objectives of this experimental program were to examine the phenomenon of pipeline/soil interaction, and, specifically, to determine the value of  $N$ , the shape of the load-displacement curve, and the effect of trench width and depth upon the interaction.

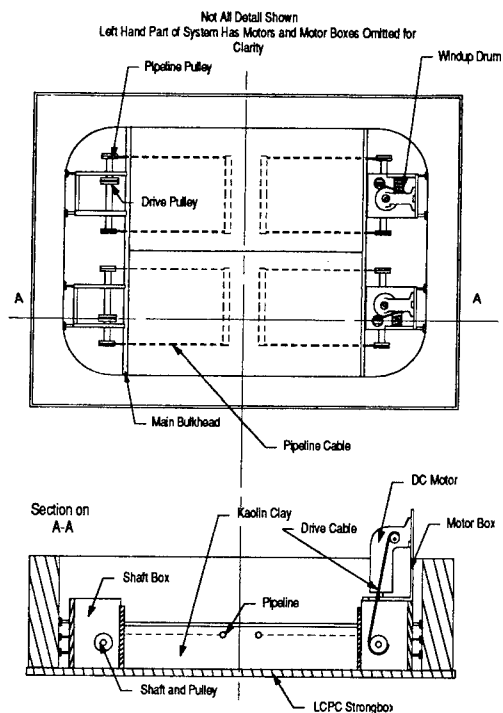


Figure 1. The package used in the present test series. For clarity, the DC motors are omitted from the left hand side of the package.

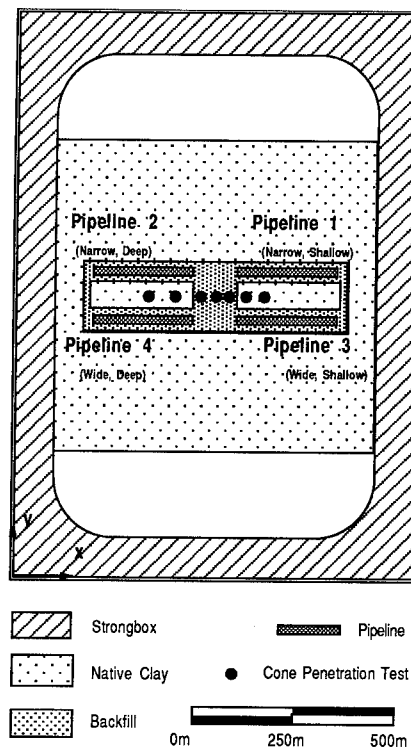


Figure 2. Test Set A geometry showing pipeline and CPT locations.

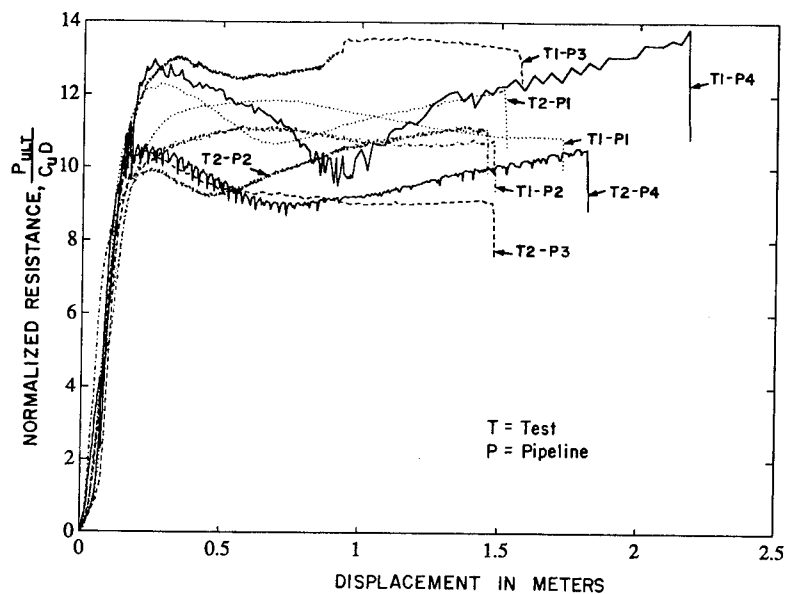


Figure 3. Normalized prototype force displacement data.

TABLE 1: Trench geometry undrained shear strength measurements

Test Set	Test	Trench Width	Trench Cover Depth	C <sub>u</sub> In Situ (kPa)	C <sub>u</sub> Backfill (kPa)	Evidence of Desiccation
A	Pipeline 1	2.00m	0.92m	22.0	17.34	Strong
A	Pipeline 2	2.00m	1.52m	13.80	12.54	Strong
A	Pipeline 3	2.75m	0.92m	17.61	14.64	Strong
A	Pipeline 4	2.75m	1.52m	10.24	9.73	Weak
B	Pipeline 1	2.00m	0.92m	8.50	7.29	Weak
B	Pipeline 2	2.00m	1.52m	8.50	7.29	None
B	Pipeline 3	2.75m	0.92m	8.29	7.29	None
B	Pipeline 4	2.75m	1.52m	8.29	7.29	None

TABLE 2: Summary of pipeline test results.

Test Set	Pipeline	Peak Resistance per Unit Length (kN/M)	Normalised Peak Resistance Normalised to		Distance to Peak Resistance (m)
			Backfill Strength	In-Situ Strength	
A	1	196	11.9	9.4	0.61
A	2	131	11.0	10.0	0.63
A	3	182	13.1	10.9	0.34
A	4	118	12.8	12.1	0.26
B	1	85	12.3	10.5	0.27
B	2	69	10.0	9.3	0.23
B	3	73	10.5	9.3	0.21
B	4	74	10.7	9.4	0.22

TABLE 3: Comparison of experimentally derived interaction factors and SOP factors

Test Set	Pipeline	Experimental Interaction Factor (N) Normalised to			CGL Recommended Interaction Factor (N) Based on Hansen (1961)	Rowe and Davis (1982) Interaction Factors (N)	
		Backfill Strength	In Situ Strength	Average Strength		Assuming Immediate Breakaway	Assuming No Breakaway
A	1	11.9	9.4	10.5	5.5	4.3	9.5
A	2	11.0	10.0	10.5	6.0	4.7	11.1
A	3	13.1	10.9	11.9	5.5	4.3	9.5
A	4	12.8	12.1	12.4	6.0	4.7	11.1*
B	1	12.3	10.5	11.3	5.5	4.3	9.5*
B	2	10.0	8.5	9.2	6.0	4.7	11.1*
B	3	10.5	9.3	9.9	5.5	4.3	9.5*
B	4	10.7	9.4	10.0	6.0	4.7	11.1*

## LATERAL PIPELINE/SOIL INTERACTION

Much of the work related to the formulation of spring-slider pipeline-soil interaction models has been adapted from other branches of geotechnical engineering. Most attention has focused on predicting the ultimate resistance to pipeline movement. The experimental work that does exist is largely laboratory-based, uses idealized soils and does not adequately address the influence of construction-related factors on pipeline-soil interaction.

Rowe and Davis (1982) simulated the behaviour of vertically oriented smooth anchors in saturated clay using elasto-plastic finite element analyses. For such anchors, the limiting loading cases are those in which the back of the anchor either remains in contact with the surrounding soil (no breakaway condition) or else breaks away immediately (immediate breakaway condition).

The monograph by the Committee on Gas and Liquid Fuel Lifelines (CGL, 1984), entitled "Guidelines for the Seismic Design of Oil and Gas Pipelines Systems", concluded that pertinent data on laterally displaced pipelines in clay indicate a trend toward increased levels of ultimate load until  $H/D$  ratio (depth to pipe's spring line divided by diameter) reaches a value of 6. Furthermore, the CGL suggests that the bearing capacity model of Hansen (1961) can be used to estimate the maximum horizontal pipeline force per unit length in clay.

The SOP formulations routinely used in design are based on the work of Rowe and Davis (1982) and the CGL (1984) guidelines. In a later section, the results of the centrifuge program will be compared to these formulations.

## EXPERIMENTAL PROGRAM

### *Experimental description*

The experimental program was conducted at the Laboratoire Central des Ponts et Chaussées (LCPC), Centre de Nantes. The facility houses an Acutronic 680-1 centrifuge which has an effective radius of 5.5m and has a payload capability of over two tonnes at 100 gravities.

The experimental program consisted of two centrifuge test sets; Test Set A and Test Set B. Four tests were conducted within each of the test sets. During the experiments, conducted at an

acceleration level of 50 gravities, the rigid model pipelines were moved laterally through normally consolidated and overconsolidated kaolin clay. The pipelines had been placed in model trenches at 1 gravity; these trenches were then backfilled to simulate construction procedures. The trench depths and widths were varied during the experimental program to determine the effect of the variation. As the pipelines were displaced, force displacement curves were obtained. Particular attention was paid to the peak load and the displacement required to develop loads.

A schematic of the centrifuge test package is shown in Figure 1. The strongbox containing the equipment was a standard LCPC strongbox, 800 by 1200mm in internal plan and 360mm deep. The central section of the box contained kaolin clay which was retained by two bulkheads. Trenches were carved in the clay to the required width and depth to contain the model pipelines. Clay slurry was then used to backfill the trenches after the pipelines had been positioned. Each of 4 pipelines was pulled through the clay by a pair of tension cables which were connected to a prime mover, a DC variable speed gear drive, by means of pulleys mounted on a shaft. The pipelines were displaced at a nominal speed of  $1\text{mm s}^{-1}$ . Data were collected prior to, during, and after the displacement of each pipeline.

During the progress of the test, the water level was kept constant by using a weir. The soil sample was probed with a miniature cone penetrometer to obtain the shear strength value required in Equation 1. After the tests, the sample was extruded from the strongbox and sectioned on the lab floor. Internal inspection was undertaken to determine displacement patterns within the soil.

### *The prototype*

The prototype of the model described above is a system of four pipeline segments buried in overconsolidated kaolin clay. Prior to consolidation in the centrifuge, the clay was one-dimensionally preconsolidated to a vertical effective stress of 160 kPa. The backfill clay was normally consolidated in the centrifuge.

The stainless steel pipelines were 0.95m in diameter and 12.5m long. They were pulled by a pair of stainless steel cables 0.158m in

diameter. At one end of each pipeline, an electrical cable approximately 0.25m in diameter was pulled through a lubricated plastic channel.

The pipelines were pulled horizontally but were free to move vertically. The movements at either end of each pipeline were constrained to be the same.

The base of the pipeline trenches were located approximately 5m above a hard impermeable surface. There was 0.92m of clay cover above each shallow pipeline and 1.52m cover above each deep pipeline. The water table was 3.1m above the hard impermeable surface and about 1.9m below the base of the pipeline trenches. The trench geometry for each test is presented in Table 1.

## TEST RESULTS

### *Review of the experimental procedures*

The measured shear strength of the *in situ* material was lower than expected from empirical correlations for 100% saturated kaolin clay. As a result, a distinct difference in strength between the *in situ* and backfill materials was not achieved. This obscured the effects of the ditch width. The shear strengths of the soil interpreted at the springline of the pipelines are presented in Table 1. The cone penetrometer test locations from Test Set A are presented in Figure 2.

Above the water table some desiccation had occurred so the magnitudes of the effective stresses within this region could not be determined exactly. To reduce desiccation during the second test, a layer of thin plastic film was used to cover the surface of the soil. The film reduced desiccation to some extent, but did not eliminate it completely.

### *Pipeline force-displacement records*

During Test Set A, of the 4 pipelines, Pipelines 1, 2, and 3 were displaced at nominally constant rates. Pipeline 3 was accelerated at the end of its displacement, but this appeared to have very little effect on the results. Pipeline 4 was displaced initially at a very low rate and then stopped. After a period of 30 minutes, excitation was reapplied. Figure 3 shows a plot of nondimensionalized force versus displacement. These results indicate that the effect of the

loading being stopped and then reapplied was negligible.

The initial pipeline response is one of increasing force with displacement. For Pipeline 3 and Pipeline 4, the peak load is followed by a decrease in load and then a subsequent slow increase. The peak is observed between a pipeline movement of 0.25 to 0.5 diameters, and the subsequent decrease in response is at the minimum at approximately the point where the pipeline first contacts the native material. The subsequent rise is observed as the pipeline begins to penetrate the native material. This peaked behaviour is more marked than it was in the other two tests. Table 2 summarises the test results.

The results obtained during Test Set B were similar to those obtained in Test Set A. These results are presented in Table 2 and Figure 3. A peak in resistive load was observed in each test; a post peak minimum and subsequent rise occurred in all tests except Pipeline 3.

## DISCUSSION

### *Force-displacement curves*

Several points may be made as a result of examining Table 2. There is some scatter in the displacement required to normalized peak resistance, with extremes of 0.26m and 0.63m. This is a function of different shapes of the peak. Pipeline 3 and Pipeline 4 display much sharper peak behaviour than Pipeline 1 and Pipeline 2. This was possibly because the effect of the softer backfill was more pronounced in the wider trenches.

Contrary to intuition, it is not obvious that trench cover depth has any significant effect. Deeper pipelines would be expected to display a greater resistance to displacement but this is not apparent from this test series.

The initial portions of the force/displacement curves all coincide (see Figure 3). At a normalised resistance of about 9 the displacement curves begin to diverge, but before this point they coincide. A theoretical means of predicting the stresses on a pipeline due to relative motion is suggested by this linear portion and this would give an indication of the correct point for remedial action.



### *Comparison of centrifuge modelling and SOP*

Table 3 compares the back-calculated interaction factor  $N$  of Equation (1) from the centrifuge tests with the recommended factors of Hansen (1961) and Rowe and Davis (1982). For the conditions modelled, the Hansen interaction factors tend to underestimate the magnitude of loads transferred to the pipeline by nearly 50%. Similarly, the Rowe and Davis factors assuming "immediate breakaway" conditions significantly underestimate the loads transferred to the pipe.

There is agreement between the experimentally derived interaction factors and the Rowe and Davis factors for the "no breakaway" conditions for the five tests marked with an asterisk in Table 3. Reasonable agreement (within  $\pm 20\%$ ) was achieved in these cases. However, the possible development of a "no breakaway" condition was unlikely because the experimental set-up precluded the development of suction behind the displaced pipeline by introducing air through the conduit around the pulley cables and in turn through the partially shallow pipe section.

The practical implications of the SOP formulations underestimating the magnitude of ground movement induced loads being transferred to a buried pipeline are significant. This study has indicated that the lateral pipe/soil interaction inputs to pipeline stress analysis based on the presently accepted formulations may lead to errantly favourable assessments of the integrity and operating safety of pipelines in unstable ground conditions. Such errant assessments may contribute to decisions delaying necessary remedial strain relieving operations.

### SUMMARY AND CONCLUSIONS

Eight model pipelines were tested to investigate the soil response to laterally displaced buried pipelines. The experimental program is relevant to studies being carried out by pipeline engineers to determine the effects of slowly creeping slopes on buried pipelines. The two primary objectives of this experimental investigation were to obtain force-displacement curves for the buried pipelines and to ascertain the effects of trench width and cover depth.

As a result of the experimental program and comparison with SOP, the following conclusions were reached:

1) Centrifuge modelling appeared to be a suitable technique for determining the soil response to laterally loaded pipelines.

2) The loads predicted by the SOP were approximately half of those measured in this test program. The current SOP may be unconservative.

3) The effects of trench geometry were negligible compared to effects due to variations in soil properties.

4) A further test program is required to elucidate the effects of trench geometry when there is a significant difference between backfill and native material properties and to investigate the effect which rate (and hence drainage) has on the lateral load transfer to a pipeline.

### ACKNOWLEDGEMENTS

The authors gratefully acknowledge the support of NOVA Gas Transmission Division management and the Natural Sciences and Engineering Research Council for their support of this study. Special thanks are extended to Dr. Jacques Garnier and the capable staff at LCPC.

### REFERENCES

- CGL (Committee on Gas and Liquid Fuel Lifelines) (1984). "Guidelines for the Seismic Design of Oil and Gas Pipeline Systems". American Society of Civil Engineers.
- Hansen, J.B. (1961). "The Ultimate Resistance of Rigid Piles Against Transversal Forces". Bulletin 12, Danish Geotechnical Institute, Copenhagen, Denmark.
- Rizkalla, M., Poorooshasb, F., and Clark, J.I. (1992). "Centrifuge Modelling of Lateral Pipeline/Soil Interaction". In Proceedings of the 11th Offshore Mechanics & Arctic Engineering Conference, June 7-11, Calgary, Alberta, Canada, 13p. Insert.
- Rowe, R.K. and Davis, E.H. (1982). "The Behaviour of Anchor Plates in Clay". *Geotechnique*, Volume 32, No. 1, pp. 25-41.

## Performance of buried corrugated HDPE pipe

S.M. Sargand, T. Masada, B. Mao & V.S.R. Yalamanchili  
*Ohio University, Ohio, USA*

J.O. Hurd  
*Ohio Department of Transportation, Ohio, USA*

**ABSTRACT:** A scaled-down corrugated high density polyethylene (HDPE) pipe, installed in granular backfill under a shallow cover, was tested in a centrifuge environment. The centrifuge test results on the model pipe were compared with the response of a prototype 0.94 m (37 inch) diameter corrugated HDPE pipe and the prediction of the modified Iowa formula. The deflection of the model pipe showed good agreement with that of the prototype. The modified Iowa formula overpredicted the deflections of the prototype and model pipes under lower loads and underpredicted them under higher loads. Under constant-load tests performed with the centrifuge model, the deflection of the model pipe reached an equilibrium after approximately 80 minutes of constant loading, and the deflection lag factor was observed to be about 1.2. Overall, the study demonstrated that the centrifuge modeling is a promising technique for predicting deflection response of buried HDPE pipes.

### 1 INTRODUCTION

In the past few decades, plastics have been applied to many commercial products. One example is the corrugated circular pipes used for drainage under highways. Traditionally, pipes made of galvanized steel, aluminum, and concrete were utilized in such applications. The increased use of plastic pipes is due to the fact that plastic materials are more cost-effective, lighter-weight, and chemically stable. However, in-situ performance of the plastic pipes is difficult to predict, since they possess very low stiffness and derive strength through interactions with the surrounding backfill soils. The Center for Geotechnical and Environmental Research (CGER) at Ohio University has been conducting a series of in-situ load tests to study structural performance of various types and sizes of flexible plastic pipe products buried in granular backfill.

Researchers in the geotechnical and other related engineering fields are increasingly seeking a laboratory simulation method to predict the performance of prototype structures. Field tests with the prototype is generally prohibitive, and realistic modeling is often limited even by sophisticated mathematical tools due to

complexities involved in the problem, which are represented by nonuniform nature and nonlinear behavior of soils, soil-structure interaction phenomena, and time-dependent nature of the soil/structure responses. A promising technique that has emerged in attempting to overcome these shortcomings is the centrifuge modeling method. This technique has been applied to a wide variety of problems related to earthquakes, foundation engineering, hydraulic engineering, and environmental sciences.

There have been a limited number of centrifuge modeling studies conducted on flexible pipe. Trott et al. (1984) tested a 1 m (39.4 inch) diameter smooth-walled steel pipe buried in dry sand and compared its performance to that of a 108 mm (4.25 inch) diameter centrifuge model pipe buried in the same sand. Both of the pipes were instrumented with strain gages and displacement transducers. The test data were presented in terms of measured circumferential strain, hoop stress, bending moment, and vertical deflection. Except for the deflections, the test results agreed reasonable between the prototype and model pipes. The vertical deflection of the centrifuge model pipe was at least two times larger under each corresponding load condition. Tohda et al. (1991) performed a series of

centrifuge model tests to 1) measure earth pressure on flexible pipes, 2) develop suitable construction techniques to reduce damages to flexible pipe during sheet-pile extraction, and 3) develop a design chart for high density polyethylene (HDPE) pipes. To achieve the third objective, they conducted load tests on a 707 mm (27.8 inch) diameter prototype, corrugated HDPE pipe and two centrifuge model HDPE pipes at scaling factors of 1/6.2 and 1/15. These scaling factors were based on the outside diameter ratios. The pipes were each buried in a silica sand. In both loose and dense backfilling conditions, the vertical deflection of the centrifuge model pipes was about 25 to 40 % higher than that of the prototype under any given load intensity. No constant load test was performed to observe time-dependent behavior of the HDPE pipes.

In this study, a miniature corrugated flexible HDPE pipe was tested under load in a centrifuge environment. Deflection response of the model pipe was measured and compared to field performance of a prototype 0.94 m (37 inch) diameter corrugated HDPE pipe and prediction by the modified Iowa formula. Also, constant-load tests were performed under a centrifuge acceleration field to gain insights into time-dependent deflection response of the plastic pipe and the deflection lag factor associated with the modified Iowa formula.

## 2 IN-SITU TESTING OF PROTOTYPE HDPE PIPE

A 0.94 m (37 inch) diameter, corrugated, HDPE

pipe of 6.1 m (20 ft.) length was instrumented and tested in the field by the CGER.

Dimensional characteristics of this pipe are summarized in Table 1. Eight biaxial strain gages were installed both on the inside and the outside surfaces of the pipe at the mid-length cross-section. The pipe was placed in a trench and backfilled in 0.2 to 0.25 m (8 to 10 inch) thick lifts of crushed limestone material. The gradation of this soil satisfied specifications for the Ohio Department of Transportation (ODOT) #310 base coarse, having the following characteristics:

$D_{100} = 25$  mm,  $D_{80} = 16$  mm,  $D_{60} = 10$  mm,  $D_{50} = 9$  mm,  $D_{30} = 6$  mm,  $D_{10} = 0.84$  mm, and about 3% finer than 0.075 mm.

Each lift was compacted with a vibrating plate tamper to minimum 95% of the standard Proctor maximum dry density value  $20.1 \text{ kN/m}^3$  (128 pcf) near the optimum moisture content (5.5%). The final height of cover was 0.3 m (12 inches) above the pipe crown.

Once the backfilling was completed, a 1.83 m (6 ft.) square loading platform was positioned above the instrumented section of the pipe, under two hydraulic cylinders. Load was applied to the pipe/soil system incrementally by pressurizing the hydraulic cylinders. Figure 1 illustrates the schematic of the prototype pipe installed at the CGER pipe test site. Under each load increment, strain readings were obtained by computerized data acquisition units, and deflected cross-sectional shape of the pipe was recorded near the instrumented section by a rotating linear

Table 1 Dimensional Correlations Between Prototype and Centrifuge Model Pipes

Parameter	Prototype Pipe	Centrifuge Model Pipe	Scaling Factor
Diameters (mm) :			
Outside	1,004.1	40.1	25.02
Inside	872.0	32.5	26.82
Mean	938.0	36.3	25.83
Corrugation (mm) :			
Pitch	171.5	6.4	—
Depth	68.6	2.8	—
Moment of Inertia ( $\text{cm}^4/\text{cm}$ )	7.767	$2.87 \times 10^{-5}$	22.80
Height of Soil Cover (mm)	304.8	13.4	22.80

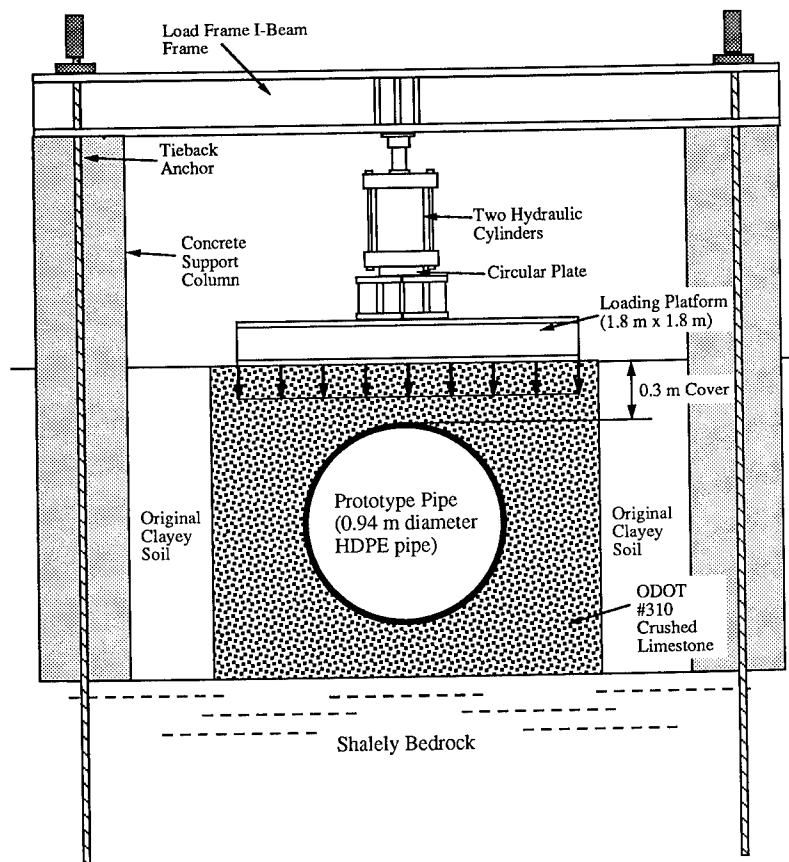


Fig. 1 A Schematic of Prototype Pipe In-Situ Test Set-Up

variable differential transformer (LVDT) unit mounted on a specially designed light-weight I-beam, suspended horizontally into the pipe. The duration of each load increment was about 15 minutes, and three sets of data were obtained from the sensors per load increment. The LVDT data indicated that a duration of 10 minutes was more than sufficient for the deflection response to stabilize. The vertical diameter change reached 8.8% under the maximum load of 1,640 kN applied to the loading platform, which corresponds to surface pressure of 491 kPa (71.2 psi) at the top of the backfill soil.

### 3 CENTRIFUGE MODEL TESTS

Concepts behind the centrifuge modeling technique are described in numerous sources (Craig et al. 1988; Monzoori et al. 1984). The centrifuge test device utilized in this study can hold up to 45.4 kg (100 lbs.) at an arm length of

1.36 m (4.46 ft.) and produce a maximum acceleration of 200g. A miniature corrugated HDPE pipe specimen, manufactured by the same company which produced the prototype pipe, was available for this study. As presented in Table 1, the scaling factor based on the mean diameter ratio between the prototype and model pipes was 25.83. An alternate scaling factor (22.8) was computed by taking 4th root of the ratio based on the moment of inertia values between the prototype pipe wall section and the model pipe wall section. Since it was not possible to satisfy both of these scaling relations, the scaling factor based on the moment of inertia ratio (22.8) was used. The moment of inertia ( $I$ ) of the wall section has a direct influence over performance of flexible pipes. This is reflected in the general expression of  $(EI/R^3)$  for the ring stiffness of a pipe having Young's modulus  $E$  and radius  $R$ .

The experimental set-up for the centrifuge test is shown in Figures 2a and 2b. A representative sample of the crushed limestone

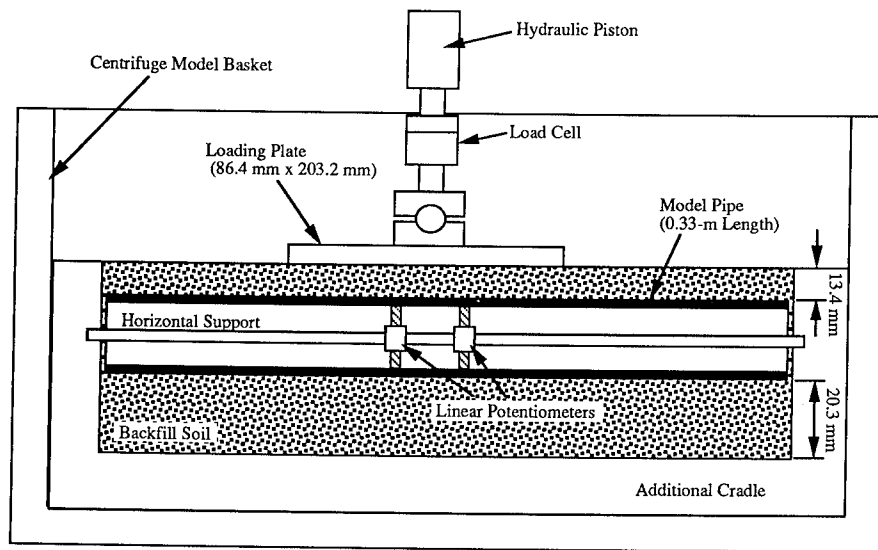


Fig. 2a A Schematic of Typical Centrifuge Model Pipe Test Set-Up (Side View)

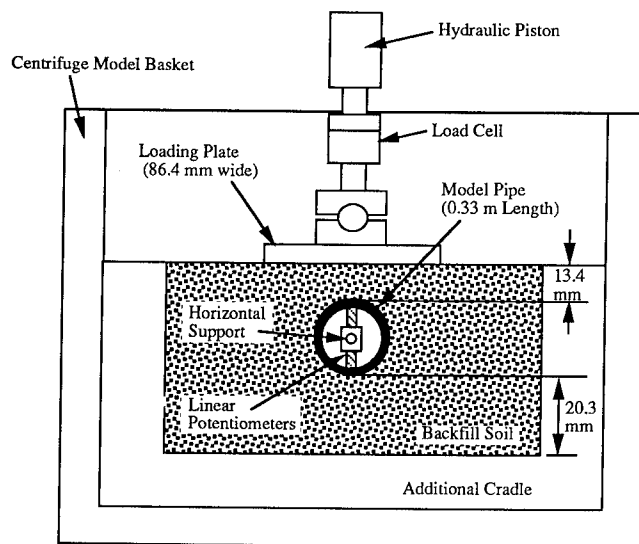


Fig 2b A Schematic of Typical Centrifuge Model Pipe Test Set-Up (Cross-Sectional View)

material, used in the prototype pipe test, was obtained and sifted through a U.S. No. 4 sieve (4.75 mm opening). This modified backfill soil was compacted at the base of the centrifuge box to form a bedding layer. Then the model pipe was positioned with a special vertical deflection measuring system attached to a horizontal

support inserted through the pipe. Two small linear potentiometers were fixed to the support. The typical calibration factor for the potentiometers was 0.076 mm/ohm (0.003 inch/ohm). Backfilling was done by placing the soil in three lifts. Final height of cover above the crown was 13.4 mm (0.526 inch) to match

the 305 mm (12 inch) cover the prototype pipe had in the field. Moisture content and dry density of the modified backfill were determined by the correction procedures outlined in the literature by Hausmann (1990). When the original soil was at its optimum moisture content, the coarse fraction, retained on No. 4 sieve, had moisture content 1.5 to 2.0% lower and maximum dry density about the same as that of the original soil. Based on this information, the optimum moisture content for the modified soil was determined to be 9%. The moisture content and the maximum dry density of the modified soil were controlled carefully so that they would remain after conversion nearly identical to the average values recorded at the in-situ test site. At the end of backfilling, a rigid loading plate was positioned over the buried model pipe, and a hydraulic loading piston was attached to the center of the plate. The width of this plate was about 10% larger than the scaled down width of the platform used in the prototype pipe test. The length of this plate was longer than that of the actual platform after scaling. These conditions should not matter as long as the width of the plate was significantly larger than 3 times the pipe diameter and the intensity of stress underneath the loading plate remains the same. Once the entire centrifuge model was set up, it was subjected to a 22.8g gravitational field. Resistance readings from the two potentiometers

were monitored as the hydraulic load was applied incrementally to the pipe/soil system, maintaining the same load intensity (or surface pressure) as in the prototype test in the field in each increment.

#### 4 TEST RESULTS

Figure 3 compares the vertical deflection response that resulted from four centrifuge model tests with the response of the prototype pipe and deflection prediction calculated from the modified Iowa formula. The deflections plotted in this figure are all considered short-term deflection. Information on the modified Iowa formula can be found in several publications such as the one by Moser (1990). It has the following standard form:

$$\frac{\Delta x}{d} (\%) = \frac{100D_L KP}{0.149(PS) + 0.061E'}$$

where  $\Delta x$  = horizontal pipe deflection;  $d$  = pipe mean diameter;  $D_L$  = deflection lag factor;  $K$  = bedding constant;  $P$  = pressure on the pipe;  $PS$  = pipe stiffness; and  $E'$  = modulus of soil reaction. The modified Iowa formula prediction was made with assumptions that the pipe would deform into a nearly perfect ellipse and that the vertical and horizontal deflections would be about the same.

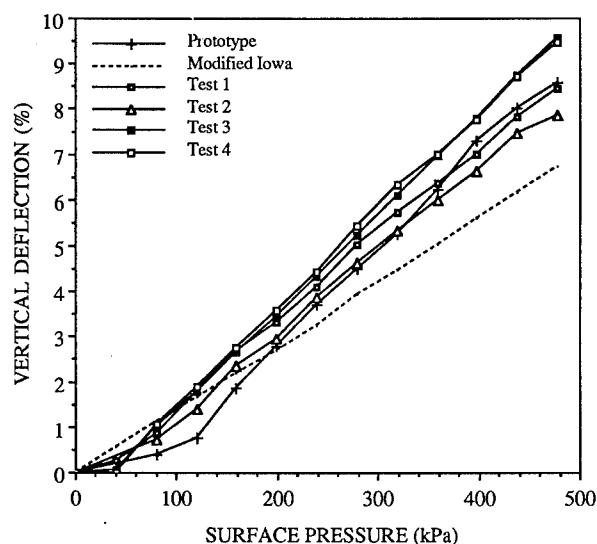


Fig. 3 Comparison of Centrifuge Test Results with Prototype Pipe Response and Modified Iowa Formula Prediction

The vertical deflection was computed with:  $d = 36.3 \text{ mm} = 1.43 \text{ inches}$ ;  $D_L = 1.0$ ;  $K = 0.13$ ;  $PS = 383.1 \text{ kPa} = 55.56 \text{ psi}$ ; and  $E' = 13.8 \text{ MPa} = 2,000 \text{ psi}$ . The modified Iowa formula resulted in a linear load-deflection response, since the pipe stiffness and the modulus of soil reactions were assumed constant throughout the loading. Nonlinear deflection responses were observed during the field prototype and centrifuge model tests. Results from the four centrifuge tests under almost identical conditions were consistent and remained within  $\pm 1.0\%$  of the prototype pipe response. The small variations among the centrifuge test results were due to slight differences in the backfill density and moisture content. In the lower pressure range, the prototype pipe exhibited the least deflection. This may be due to the difficulty in simulating the field backfilling process during the set-up for the centrifuge models. Deflection of the centrifuge models approached very close that of the prototype above pressure of  $193.1 \text{ kPa}$  ( $28 \text{ psi}$ ). The prediction by the modified Iowa formula overestimated the responses of the prototype and centrifuge model pipes at lower pressure and underestimated them at higher pressure.

Often, a concern with the buried flexible pipe is its continuing deformation with time under a constant load condition. This is called

creep behavior. Most plastics, including HDPE, exhibit creeping. Figure 4 presents the results of four constant-load tests performed on the centrifuge model pipe under  $22.8g$  gravity field. In these tests, resistance readings from the potentiometers were monitored while the model pipe was subjected to a constant surface pressure of  $318.5 \text{ kPa}$  ( $46.19 \text{ psi}$ ). It was observed that the deflection rate of the pipe decreased exponentially as the time elapsed. In all the tests, the pipe deflection stabilized after about 80 minutes. On the average, about 50% of the overall creep deflection took place within the first 5 minutes; 75% within the first 15-20 minutes; and, 90% within the first 40-45 minutes. Table 2 summarizes the key results from the constant-load tests. According to the scaling relations, the scaling factor for time is 1 between the prototype and the model for creep. Based on the results from the centrifuge model and prototype pipe tests, the duration of time over which creep behavior exists is relatively short for HDPE pipes buried in a dense, stiff backfill material. The average value of the deflection lag factor yielded from the study was 1.21. In general, published literature (Unibell PVC Pipe Association 1983; Moser 1990) recommends a conservative value of 1.5 for the deflection lag factor for plastic pipes.

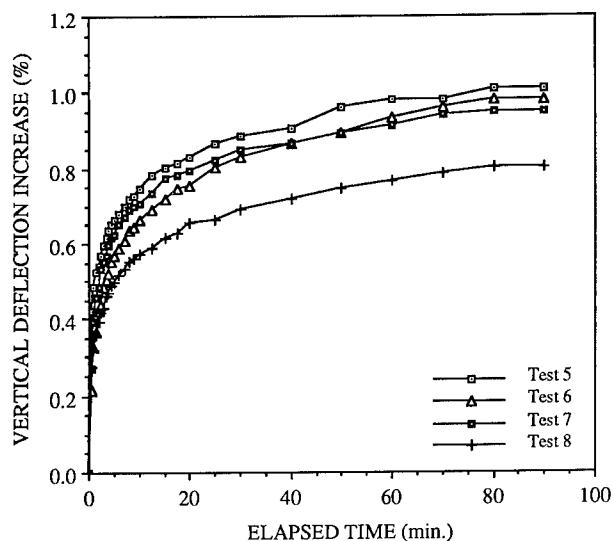


Fig. 4 Deflection Performance of Centrifuge Model Pipe Under Constant-Load Test

Table 2 A Summary of Constant-Load Test Results

Test No.	Surface Pressure (kPa)	Vertical Deflection (%)		Increase in Deflection (%)	Deflection Lag Factor
		Short-Term	Long-Term		
5	318.5	4.95	5.96	1.01	1.204
6	318.5	4.12	5.10	0.98	1.238
7	318.5	5.03	5.98	0.95	1.189
8	318.5	4.00	4.80	0.80	1.200
Average		4.525	5.460	0.935	1.207

Notes: Short-Term = After 2 seconds ; Long-Term = After 90 minutes

## 5 CONCLUSIONS

The following conclusions were drawn based on the results and findings of the current study: (1) The centrifuge modeling technique can be applied successfully to simulate deflection responses of larger diameter corrugated HDPE pipe buried in granular backfill under shallow cover.

(2) The scaling factor based on the moment of inertia ratio proved to be more effective than that based on the diameter ratio for centrifuge model testing of flexible plastic pipes.

(3) The modified Iowa formula has a tendency to overestimate the actual deflection of plastic pipe under relatively low intensity loads and underestimate it under higher intensity loads.

(4) The deflection response of the HDPE pipe installed in granular backfill stabilized within 80 minutes.

(5) The deflection lag factor for the HDPE pipe installed in granular backfill remained around 1.2.

## 6 ACKNOWLEDGEMENTS

The authors are grateful to the Ohio Department of Transportation (ODOT) and the Federal Highway Administration (FHWA) for funding the prototype plastic pipe testing program conducted at Ohio University. Supply of the prototype and centrifuge model pipes by Advanced Drainage System (ADS), Inc. (Columbus, Ohio) is also appreciated.

## 7 REFERENCES

- Trott, J.J., Taylor, R.N., and Symons, I.F. 1984. "Tests to Validate Centrifuge Modeling of Flexible Pipes." Proceedings of a Symposium on the Application of Centrifuge Modeling to Geotechnical Design, Engineering Department, University of Manchester.
- Tohda, J., Yoshimura, H., and Seki, H. 1991. "Centrifuge Model Tests on Several Problems of Buried Pipes." Proceedings of the International Conference Centrifuge 1991. A.A. Balkema, Rotterdam.
- Craig, W.H., James, R.G., and Schofield, A.N., Eds. 1988. "Centrifuge in Soil Mechanics." Proceedings of the International Conference Centrifuge 1988. A.A. Balkema, Rotterdam.
- Monzoori, M., Atkinson, R.H., Ko, H-Y., and Goble, G.G. 1984. "Centrifuge Testing of Model Piles and Pile Groups." Final Report for the Federal Highway Administration, FHWA/RD/83/003, Volume 2, November 1984.
- Hausmann, M.R. 1990. "Engineering Principles of Ground Modification." McGraw-Hill, Inc., New York, New York.
- Moser, A.P. 1990. "Buried Pipe Design." McGraw-Hill, Inc., New York, New York.
- The Unibell PVC Pipe Association. 1983. Handbook of PVC Pipe Design and Construction.



## Uplift resistance of buried pipelines in granular materials

C.W.W. Ng & S.M. Springman

Engineering Department, Cambridge University, UK

**ABSTRACT:** Uplift resistance of sand backfill and sand overlain by rockfill to the vertical movement of a buried pipeline has been measured in a mini-drum centrifuge. The reliability of the centrifuge test results has been verified by the technique of modelling of models, and also compared with some published full-scale test results and a theoretical plastic solution.

### 1 INTRODUCTION

Buried pipelines are used extensively in the transportation of oil and gas in both offshore and onshore conditions. When a pipeline is operated at higher than ambient temperatures it will try to expand. If it is axially restrained, for example by the friction of the surrounding soil, a compressive axial force is produced. The pipeline will then tend to buckle in the direction of least resistance, usually vertically upwards. This phenomenon is called upheaval buckling (offshore) or overbend instability (onshore). The resulting pipeline response to such buckling or overbend might be unacceptable in terms of vertical movement (protrusion through the cover or out of the trench), or excessive yielding of the pipe material (leading to fracture and spillage). Upheaval buckling must therefore be taken into account when designing buried pipelines.

A number of full scale and reduced scale tests at one gravity were conducted by various researchers to measure the uplift resistance to the vertical movement of a buried pipeline (Schaminée *et al* 1990; Morgan *et al* 1993). Moreover, Dickin & Leung (1992) investigated the influence of foundation geometry on the uplift behaviour of belled piles in sand using centrifuge techniques. For buried pipelines, the uplift resistance is of practical importance since it stabilises them against upheaval buckling induced by the axial compression generated by internal temperature and pressure.

In the present investigation, a newly developed mini-drum centrifuge at the Cambridge University Geotechnical Centrifuge Centre provided the enhanced gravity environment, in which pipelines

could be pulled by an actuator through sand backfill and sand overlain by rockfill. The objectives of the centrifuge tests were: firstly to validate the test results of modelling of models using the mini-drum centrifuge and secondly, to determine the effect of rockfill on top of the sand backfill on the uplift resistance of a buried pipeline.

### 2 THE MINI-DRUM CENTRIFUGE

The 0.8m diameter drum centrifuge at Cambridge University was invented by Prof. A.N. Schofield (ANS&A patent pending, 1993) and it consists of an outer shaft with a 0.8m diameter face plate and a central shaft with a 0.28m diameter central plate. Using a clutch system, the outer plate can be spun at a maximum speed of 1000 r.p.m., which is equivalent to 447g at the base of the drum channel, whereas the central plate can rotate at  $\pm 100$  r.p.m with respect to the outer shaft speed. Either soil containment boxes or a ring channel can be chosen for model making with drainage to various points in the drum. Currently the mini-drum is equipped with a dedicated PC based data acquisition system, including 16 channel multiplexer encoders with channel display.

A pull-out actuator was designed to lift the pipeline in flight. A low speed motor was powered by a direct current at a variable voltage (up to 30 V), and the motor rotated a lead screw mounted inside a brass nut to retract a linking rod, instrumented to measure axial force, which was connected to a buried model pipeline. At 30 V, the actuator can pull out a model pipeline at 0.2mm/sec. The maximum allowable retraction was about 30mm. It is more

economical and efficient to carry out the pull-out tests in the mini-drum than the existing 10m beam centrifuge at Cambridge University.

### 3 TESTING PROGRAMME

Two series of tests were carried out to determine the uplift resistance provided by various fills to a buried pipeline. Initially three tests were conducted either at nominal 25g or 40g (i.e., 22.2g & 35.9g at the centre of model pile respectively). It should be noted that the local centrifugal acceleration is not constant with soil depth, but varies linearly with radial distance from the axis of rotation for a given constant angular velocity. This resulted in less than 6% error in the measured peak uplift resistance (Ng & Springman 1993).

Tests and results are described at prototype scale. Sand was used as the backfill material. This series of tests was intended to validate the experimental results using the mini-drum by comparing them with some published full-scale test data. Subsequently, another three tests were performed at nominal 40g, to investigate the effect on the uplift resistance of using a rockfill berm. A summary of the tests is given in Table 1.

Table 1. Details of each test.

Ref. no.	Nominal g-level	Backfill material
MT1	40	sand only
MT2	40	sand only
MT3	25	sand only
MT4	40	sand, gravel, sand
MT5	40	sand, gravel, sand
MT6	40	sand, gravel with wallpaper paste & polystyrene

### 4. EXPERIMENTAL PROCEDURE

#### 4.1 Sand backfill tests: MT1-3

For tests MT1-2, an approximate 0.45m diameter D pipeline, buried at 1.5m below ground, was modelled in a soil containment box which was 165x165x110mm high. Leighton Buzzard 100/170 sand was mixed with water at a moisture content of about 3%. A summary of some properties of the 100/170 sand is given in Table 2.

After locating an aluminium model pipe of length  $L=164\text{mm}$  in the box, the moist sand was tamped around the pipe and up to the required depth. The void ratio  $e$ , of the backfill was found to be about 0.84, i.e. relative density is equal to 43%. This was calibrated in an identical spare soil containment box, which was filled up with moist sand using the same tamping technique.

Table 2. Leighton Buzzard 100/170 sand (Tan 1990).

Item	Quantity
Diameter of finest 10 percentile	0.095mm
Specific gravity	2.65
Minimum void ratio $e_{\min}$	0.613
Maximum void ratio $e_{\max}$	1.014
Critical state angle (estimated)	$32^\circ$

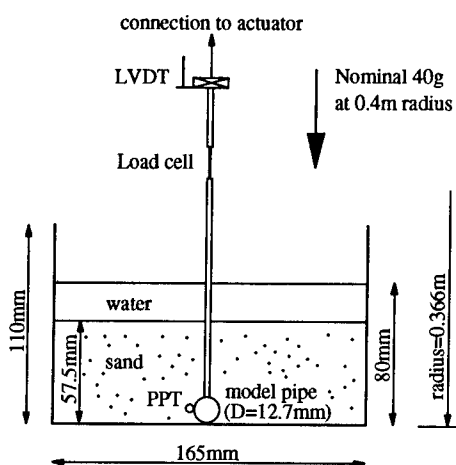


Fig.1 Horizontal section of models MT1 & 2

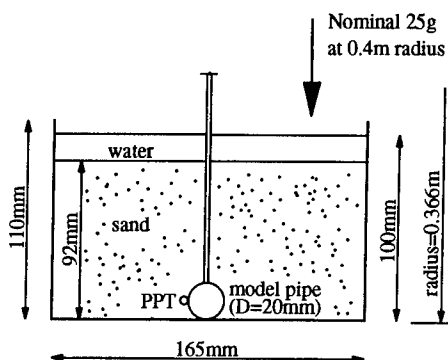


Fig.2 Horizontal section of model MT3

Schematic diagrams of the centrifuge model used in MT1-2 and in MT3 are shown in Figs.1 & 2 respectively. The models were prepared when the drum centrifuge axis was horizontal (i.e. the sand surface was horizontal) and this axis was turned 90° to vertical before testing. In this position, the sand surface was able to maintain a vertical face in the containment box as a result of suction induced.

A linear variable differential transducer (LVDT) and a load cell with a maximum capacity of 220N were used to measure the movement of the model pipe and the pull-out force respectively. In addition, a pore pressure transducer (PPT) was fixed adjacent to the model pipe to record pore pressure changes as the model pipe was being pulled out by the actuator in flight.

At the start of a test, the outer and central shafts of the mini-drum were set to rotate at about 47 r.p.m (i.e. 1g at the base of drum channel). The purpose of this operation was to check the safety of all fittings and fixings. Subsequently, the speed of rotation was increased in stages to the desired value for each particular test. At the required angular rotation, water was supplied to the ring channel to saturate the model and the water level was maintained at the same position in the soil containment box throughout the test. Once the soil sample was saturated, the model pipe was pulled out by the actuator at a speed of 0.09 mm/sec (motor run at 15 V). This is practically the slowest pulling speed that can be achieved in the current mini-drum set up. Displacement of the model pipe, pulling force and pore pressure measurement at the pipe location were plotted versus time on a computer screen and the model was monitored throughout the test using a stroboscope.

#### 4.2 Sand and rock backfill tests: MT4-6

Particles of crushed gravel, between 5-10mm nominal diameter, were used in tests MT4-6 to model the effect of rockfill on top of the sand backfill.

Similar techniques to those used in the first test series were adopted for preparing the sand backfill in these tests. However, these methods could not be applied to retaining a vertical gravel face until a sufficient centrifugal force was reached to ensure stability, because the size of voids between particles was too large to maintain suction.

Initially, some of the moist sand was used to hold the gravel in place before testing, as shown in Fig.3. This method was adopted for tests MT4-5.

Secondly, a solution of wallpaper paste was used to provide a temporary "cementation" effect at the points of contact of the gravel. Once the test centrifugal force was reached, water was flushed through the sand and gravel backfill, dissolving the wallpaper paste and removing any bonding developed in the gravel. Various ratios of dry wallpaper powder to water were experimented with to see if the bonding was sufficient, and whether it would be removed by flushing. This proved to be extremely difficult and so an alternative solution was sought.

The gravel was held temporarily in place by using 164.5x164.5x10mm of polystyrene placed on top of the gravel backfill as shown in Fig.4. The polystyrene will float when the model is saturated with water, once an appropriate gravity has been reached. It was found, by trial and error, that a combination of these methods was effective, using a wallpaper powder-water mix of 1:15 by weight. The bonding created by the paste was destroyed in the presence of water.

Apart from model preparation, the testing procedures, data acquisition and model monitoring during the test were the same as the first test series.

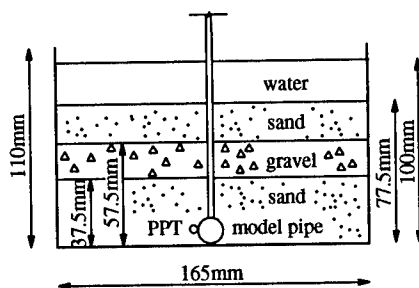


Fig.3 Horizontal section of models MT4 & 5

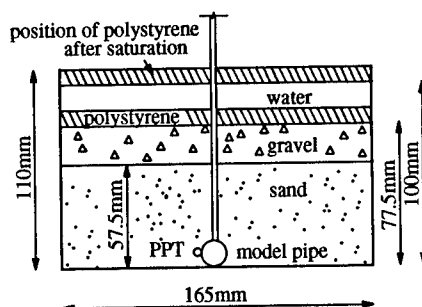


Fig.4 Horizontal section of model MT6

## 5. ANALYSIS OF TEST RESULTS

### 5.1 Modelling of models: MT1-3

Modelling of models (Schofield 1980) is a technique commonly used to check the reliability of centrifuge test data. The same physical event is modelled at two different scales to see whether the same phenomenon can be observed in both tests. It was found by Malushitsky (1981) that a ratio of 1.5 in "g" levels between two tests at different scales gave satisfactory results. Accordingly, a ratio of 1.6 (nominal 40/25) was selected for the present investigation.

Before carrying out tests for modelling of models, two tests were conducted at the same "g" level in order to ensure repeatability was achieved in the mini-drum centrifuge. The results of these two tests MT1-2 are shown in Fig. 5 together with a summary in Table 3. It can be seen that both the shape of the uplift force and the excess pore pressure (p.p.) versus displacement are consistent with each other, and the difference between the two measured values of  $F^*$  (uplift force  $F$  minus weight of lifting mechanism and model pipe  $W$ ) is less than 7%. This gives confidence in the model preparation techniques and the mini-drum facilities.

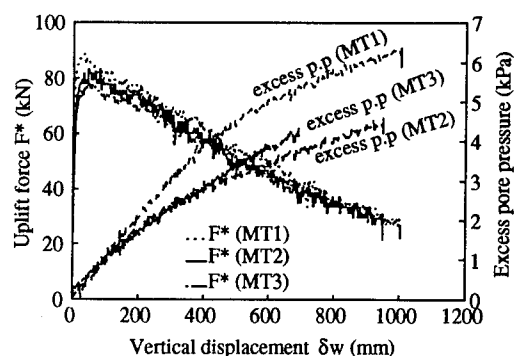


Fig.5 Test results of MT1-3 (prototype)

An equivalent test (MT3) to those modelling the same prototype event at 40g was conducted at 25g and the results are also shown in Fig.5 and Table 3. The difference in the measured peak  $Q^*$  (uplift resistance normalised with respect to the pipe diameter and the effective overburden of soil above the pipe), in the MT3 test is less than 8% of the mean of the previous two tests MT1-2. Fig. 6 shows the normalised plots of all three tests. It can be seen that

Table 3. A summary of test results (prototype).

Ref. no.	Peak $F^*$ (kN)	Peak $Q^*$	$\delta w/D$	Excess pore pressure at peak $F^*$ (kPa)
MT1	88.7	2.7	0.08	0.35
MT2	83.2	2.5	0.11	0.50
MT3	77.7	2.8	0.12	0.60
MT4	140.5	3.2	0.18	-0.13
MT5	148.0	3.4	0.12	0.45
MT6	135.3	3.1	0.13	0.59

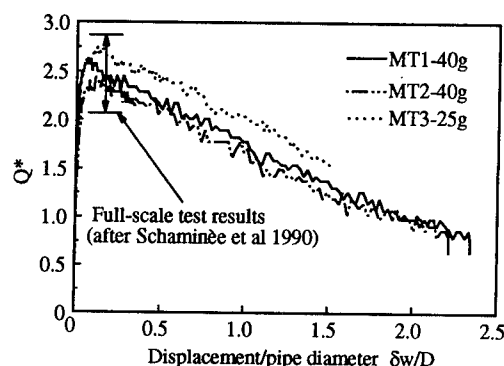


Fig.6 Normalised plots of tests MT1-3

the measured peak values of  $Q^*$  all lie within the full-scale test results reported by Schaminée *et al* (1990).

The excess pore pressures generated at the peak pulling force are very small in all three tests. These measurements confirm that the tests were conducted sufficiently slowly for the purpose of determining the peak uplift resistance and the measured values represent the resistance of sand in a drained condition. A detailed discussion of the pore pressure measurement and sources of error during the tests is given in the report by Ng & Springman (1993).

### 5.2 Observed failure mechanisms & plastic solution

At the end of each test, the observed failure mode was recorded. A typical failure profile is shown in Fig.7. The angle between the slip plane and the vertical  $\psi$  ranged from 21-27° at the end of tests MT1-3. These observed failure modes suggest that the vertical slip model for cohesionless backfill, proposed by Schaminée *et al* (1990), may need to be

modified to allow for soil dilation, in the case of medium to dense sands. Fig.8 shows an idealised failure mechanism of plastic slip. By considering the work done by the external forces and by the internal stresses for an increment of plastic slip, and applying the condition of normality, an upper bound plastic solution for a drained test can be found and expressed as follows:

$$Q = \gamma'(DH^* + H^{*2} \tan \phi) \quad (1)$$

where  $H^*$  is model pipe burial depth from soil surface to the centre of the pipe,  $H$  is the model pipe burial depth from soil surface to the top of the pipe,  $Q$  is the uplift resistance per unit length on the model pipe during the tests ( $=F^*/L$ ),  $\gamma'$  is submerged unit weight of soil,  $\phi$  is the angle of dilation and  $\delta w$  is increment of displacement. Since  $\delta w$  was small, as compared with  $H^*$ , when the peak uplift resistance was observed (Table 3), it was therefore ignored during the derivation of equation (1).

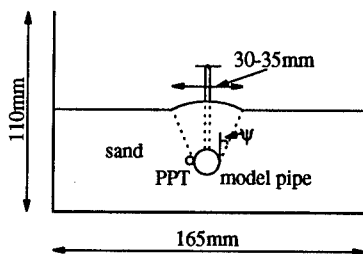


Fig.7 Observed failure mechanism for MT1-3

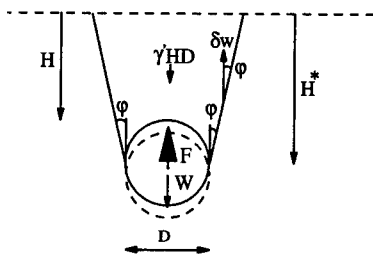


Fig.8 Plastic slip mechanism

As the condition of normality is assumed, this will imply that  $\phi = \phi'$ , which is the angle of friction. For comparison with the measured peak  $Q^*$ , equation (1) can be re-arranged as follows

$$Q^* = \left( \frac{H^*}{H} \right) \left( 1 + \frac{H^*}{D} \tan \phi \right) \quad (2)$$

where  $Q^*$  is equal to  $Q/(D\gamma'H)$ .

By substituting the dimensions of the tests and assuming  $\phi = 24^\circ$ , which is the mean value of the observed angles  $\psi$  in the three tests, into equation (2), peak  $Q^*$  is equal to  $1.1 + 2.0 = 3.1$ . This is the upper bound solution to the problem and it corresponds well with the test results (Fig. 6).

### 5.3 Modelling of rockfill: MT4-6

The results of the three tests are summarised in Table 3, and Fig.9 shows the plot of uplift force  $F^*$  versus vertical displacement  $\delta w$ . The observed behaviour of each test was consistent despite different model preparation techniques. Moreover, the difference in the measured peak  $F^*$  between the mean of MT4-5 and MT6 is less than 7%. These results seem to suggest that the peak resistance of the soil is not affected by whether sand backfill is on the top of gravel or vice versa and also that the initial bonding developed in the gravel by using wallpaper paste seems to be effectively destroyed following water saturation and flushing. As in MT1-3, the measured excess pore pressures at the peak  $F^*$  were insignificant and hence the measured resistance can be regarded as drained.

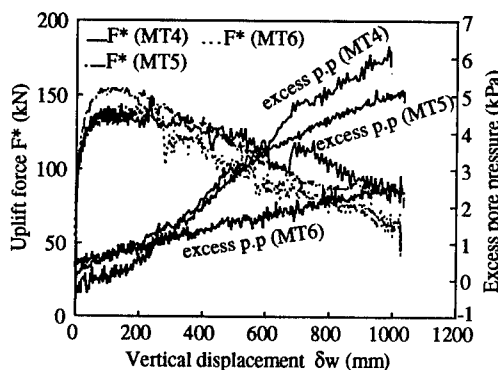


Fig.9 Test results of MT4-6 (prototype)

It is also clear from Table 3 and Fig.9 that the uplift resistance provided by soil is increased by placing an additional 600mm rockfill on top of the 1.5m layer of sand. The average increase in the

measured peak  $F^*$  is 70%, i.e.,  $(141.3-83.2)/83.2 \times 100\%$ .

Fig. 10 shows the normalised plots of  $Q^*$  versus  $\delta w/D$ . By placing the additional layer of rockfill, the measured increase in  $Q^*$  is 21%, i.e.,  $(3.23-2.67)/2.67 \times 100\%$ . The enhanced peak uplift resistance is mainly due to the increase of the  $(H^*/D)$  ratio rather than the mobilised  $\phi'$ . The rockfill merely provides the overburden effect and the peak uplift resistance is still governed by the strength of the sand. It is possible to illustrate this idea by substituting model dimensions and the average measured peak  $Q^*$  values from the two test series into equation (2), which will give the mobilised  $\phi'$  value of  $18.4^\circ$  and  $19.0^\circ$  for the first (MT1-3) and second (MT4-6) group of three tests respectively.

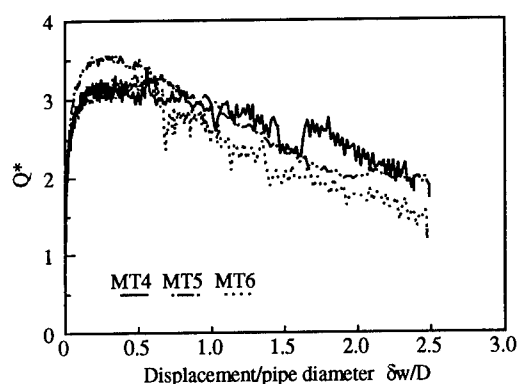


Fig.10 Normalised plots of tests MT4-6

## 6 CONCLUSIONS

Uplift resistance of buried pipelines in sand, with and without a rockfill berm, has been measured using a mini-drum centrifuge. The reliability of the centrifuge data is verified by the technique of modelling of models, and also compared with some published full-scale test results and a theoretical plastic solution. These show good agreement. The use of the mini-drum centrifuge to model important effects arising from buckling of buried pipelines is proved to be accurate, reliable and economical.

For modelling the effect of rockfill, wallpaper paste and polystyrene have been used to hold the gravel temporarily in place during rotation of the drum through  $90^\circ$ , and subsequent increase in speed to impose 40g on the model. The test results suggest that the peak resistance of the soil is not affected by whether sand backfill is on the top of gravel or vice versa and also the initial bonding developed in the

gravel by using wallpaper paste seems to be completely destroyed following water saturation and flushing. Placing a layer of rockfill on top of the sand backfill was found to increase the uplift resistance of the soil to the vertical movement of a buried pipeline. The increase in uplift resistance is mainly due to the additional overburden of rockfill rather than any increase in the mobilised angle of friction.

## 7 ACKNOWLEDGEMENTS

These laboratory tests were carried out with the assistance of Messrs C. Collison, S. Chandler, A. Brand, T. Curtis, Dr. S.P.G. Madabhushi and Ms K. Batereau. Their help is gratefully acknowledged. Finally, the authors would like to thank Professor A.N. Schofield and Dr. M.D. Bolton for useful discussions and to Andrew Palmer & Associates for their permission to publish the test results of modelling of models.

## REFERENCES

- A.N. Schofield & Associates (ANS&A). 1993. Type R mini-drum system. Geotechnical Centrifuge Technology, Cambridge, U.K.
- Dickin, E.A. & Leung, C.F. 1992. The influence of foundation geometry on the uplift behaviour of piles with enlarged bases. *Can. Geo. J.*, 29, No.3, 498-505.
- Malushitsky, Y.N. 1981. *The centrifuge model testing of waste-heap embankments*. Cambridge University Press, Cambridge, England.
- Morgan, V.R., Ng, C.W.W. & Springman, S.M. 1993. *Uplift resistance of buried pipelines in a sand/clay matrix at one gravity*. A.N. Schofield & Associates' data report to Andrew Palmer & Associates, UK.
- Ng, C.W.W. & Springman, S.M. 1993. *Uplift resistance of buried pipelines in a mini-drum centrifuge*. A.N. Schofield & Associates' data report to Andrew Palmer & Associates, UK.
- Schaminée, P.E.L., Zorn, N.F. & Schotman, G.J.M. 1990. *Proc. Offshore Technology Conf. Houston, Texas*. 563-572.
- Schofield, A.M. 1980. Cambridge Geotechnical Centrifuge Operations. *Géotechnique*, 25: No.4: 743-761.
- Tan, F.S.C. 1990. *Centrifuge and theoretical modelling of conical footings on sand*. Ph.D thesis, Cambridge University, UK.

## Performance of ground anchor models under repeated loading

J.M.Carey

*Sage Engineering Limited, UK (Formerly: Department of Engineering, University of Manchester, UK)*

W.H.Craig & C.M.Merrifield

*Department of Engineering, University of Manchester, UK*

**ABSTRACT:** Monotonic and repeated loading tests are reported on model low pressure grouted ground anchors in the centrifuge. The effects of repeated loading on the ultimate pull-out capacity, side friction distribution and generation of end bearing resistance are investigated at various embedment depths. Conclusions are drawn on matters associated with the magnitudes of the load amplitudes and the consequent behaviour of the anchors.

### 1 INTRODUCTION

There has been a substantial increase in use of ground anchors in the construction industry in recent years in both temporary and permanent works. This has extended to the application of ground anchors as elements to resist uplift, in particular in buoyant structures such as deep basements and road underpasses founded below high and fluctuating ground water tables. Other possible causes of fluctuating external loads on an anchor include daily temperature changes, wind loading and wave loading in shallow water.

Research to date on the behaviour of anchors subjected to repeated loading has mainly been carried out using model plate or fluke anchors (Al-Mosawe, 1979; Andreadis *et al.*, 1981). Such research has shown that under repeated loading anchors can fail at load levels much smaller than their static ultimate pull-out capacity. Despite these findings, ground anchors in the field subjected to repeated loading have performed satisfactorily. This has prompted the British Standards Institution, (1989), through its code of practice for ground anchorages, to call for further research to clarify the issue.

Centrifuge work on models of plate anchors under monotonic loading has been summarised by Dickin (1988).

This paper presents results of an investigation of the behaviour of models of low pressure grouted anchors under repeated loading, carried out in a geotechnical centrifuge in order to reproduce prototype stress levels.

### 2 MODEL AND EQUIPMENT

The experimental work described in this paper is an extension of that described by Merrifield and Williams (1988) and Merrifield and Carey (1991). The centrifuge facilities are described in detail by Craig and Rowe (1981) and Carey (1993).

A specially designed instrumented model ground anchor was used in order to determine the mobilisation and distribution of shear stresses along the fixed anchor length during loading. The arrangement with principal dimensions is shown in Figure 1. The model anchor had a free anchor length consisting of a 10mm diameter smooth hollow rod and a fixed anchor length of 25mm diameter (D) and 150mm overall length (L). The embedment depth (h) could be varied between 150-300mm with corresponding variations in embedment ratios (h/D) of between 6 and 12. The fixed zone consisted of five tubular sections each supported on an independent cruciform-shaped load cell. The load cells formed part of the internal spine of the anchor with each of the four arms behaving as a cantilever. Strain-gauges on the cantilevers measured the bending caused by the shear stresses acting on the outside of the tubular section. The outside surface of each tubular section was knurled to give a roughness or asperity height of approximately 0.5mm. With a sand  $D_{50}$  of 0.22mm the shearing may be assumed to have occurred within the sand adjacent to the anchor body.

The ratio of nearest rigid boundary distance from the anchor centreline to the radius of the

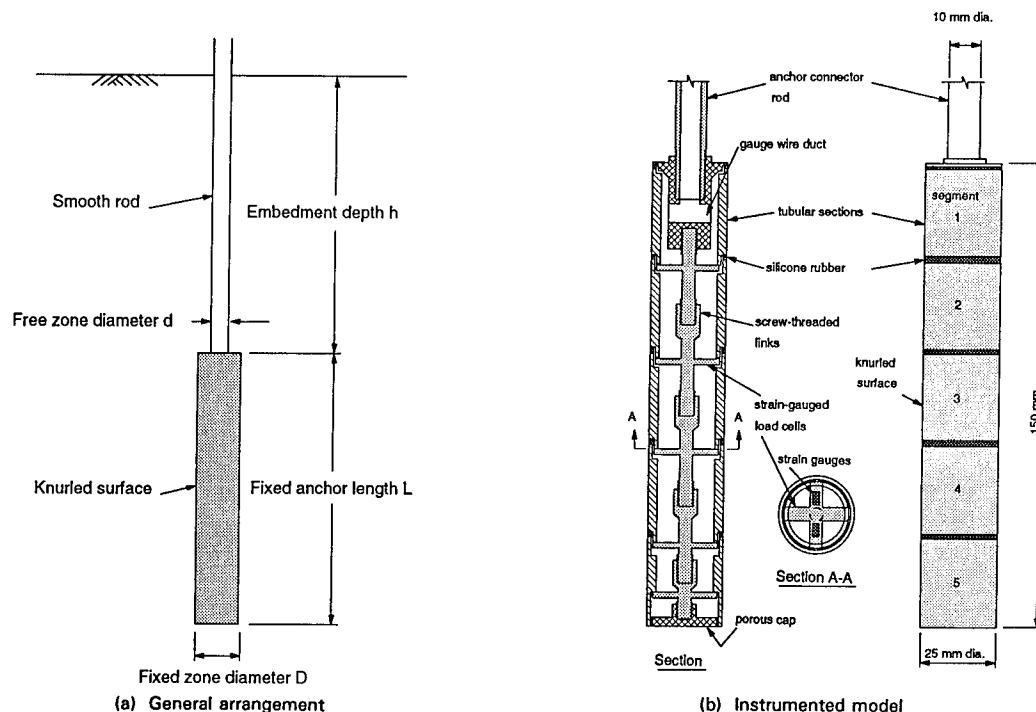


Fig.1 Model ground anchorage

fixed zone was 22.4:1, sufficiently large to prevent the influence of boundary effects. At the deepest anchor location the base of the fixed anchor zone was a minimum of 10mm from the base of the rigid model container. As all tests were carried out in dense dry sand the proximity of the boundary is considered to have presented no problem.

The anchor was tensioned in flight by a remote servo-controlled actuator of 10kN capacity. The load applied to, and resultant displacement of, the anchor head were monitored continuously. Changes in horizontal earth pressure were monitored by earth pressure cells embedded in the soil adjacent to the anchorage as reported by Lee (1991) and Carey (1993).

### 3 TEST PROCEDURE

The object of the research was to investigate the load-displacement characteristics of a vertically tensioned anchor embedded at various depths in dry sand. All tests were undertaken at 31.5g. The

effect of a change in the g level and thus the stress level at which comparable tests were undertaken was reported by Merrifield and Williams (1988).

The anchors were installed in a uniformly dense dry sand bed of relative density 87-92% ( $\rho \approx 1.7 \text{ t/m}^3$ ) at unit gravity by clamping in position and pluviating the sand through a roller sand spreader. Mersey river sand with a  $D_{50}$  of 0.22mm and Uniformity Coefficient of 1.5 was used throughout the investigation. The angle of friction between the knurled surface of the fixed anchor zone and the sand, measured in direct shear at test stress level, was found to be  $39^\circ$ .

After allowing the anchor to bed in at 31.5g the tension load to the anchor, applied through the vertical actuator, was varied sinusoidally at 0.5Hz. In any one test the anchor was subjected to 'parcels' of loading containing around 1000 cycles at each load level and as many as 15,000 cycles in all.

The instrumentation was logged over two consecutive cycles in every ten. The sample rate



ensured an adequate definition of anchor behaviour with time for at least one full cycle.

## 4 RESULTS

### 4.1 Effect of repeated loading on ultimate pull-out capacity

The envelope of the load cycles that were applied to the instrumented anchor in Test 3-6 with  $h/D=12$  and  $h/L=2$  is shown in Figure 2(a). The envelope is produced by the plots against time of the maximum and minimum values of load logged over two consecutive load cycles every ten cycles. In this test the peak-to-peak (p-p) amplitude of the cyclic loading was kept constant at approximately 0.5kN, which was 12.5% of the static ultimate pull-out load ( $T_f$ ) of the same anchor subjected to monotonic loading when embedded at the same depth in Test 3-2. The mean load level was progressively increased after each parcel of loading until failure was reached in the form of anchor pull-out.

The envelope of the anchor response, produced by comparable plots of the maximum and minimum displacements, is given in Figure 2(b).

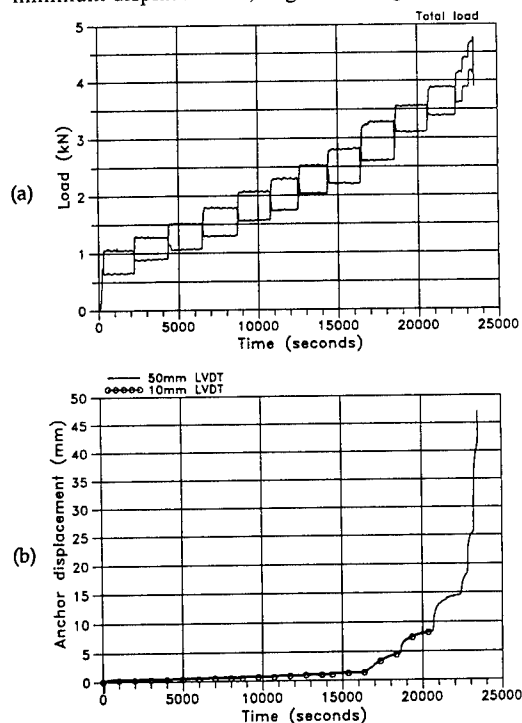


Fig.2 Time history of load and displacement, Test 3-6

The maximum and minimum load-displacement envelopes for two cyclic Tests 3-5 and 3-6 are plotted in Figure 3 along with the load-displacement response of the same anchor under monotonic loading (Test 3-2). The peak-to-peak amplitude of the cyclic loading in Test 3-5 was 12.5% and in Test 3-6 varying between 23-60% of  $T_f$  (Test 3-2). This shows that the ultimate pull-out load of the anchor under small amplitude cyclic loading (i.e. 12.5%  $T_f$ ) was 13% greater than  $T_f$  whilst the anchor, subjected to large amplitude cyclic loading (varying between 23-60%  $T_f$ ) the ultimate pull-out load was found to be 24% lower than that attained under monotonic loading.

These results indicate that, while large amplitude repeated loading can cause a significant degradation in anchor performance, loading cycles of amplitude 10-15%  $T_f$  can improve the performance, in terms of the ultimate monotonic pull-out capacity, of a ground anchor with  $h/D=12$  and  $L/D=6$ .

### 4.2 Effect of repeated loading on side friction distribution

The maximum and minimum load-displacement envelopes for each segment of the fixed anchor length for Test 3-6 are plotted in Figure 4, along with the segmental load-displacement relationships of the anchor under monotonic loading in Test 3-2. This shows that:

- 1) maximum side friction is mobilised at the same anchor displacement of 1.5mm under both

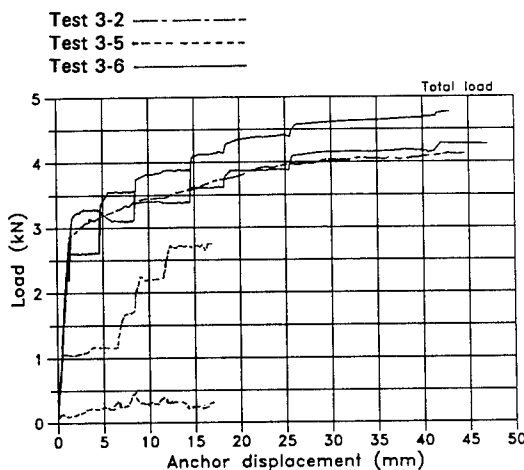


Fig.3 Total load-displacement response Tests 3-2, 3-5 and 3-6

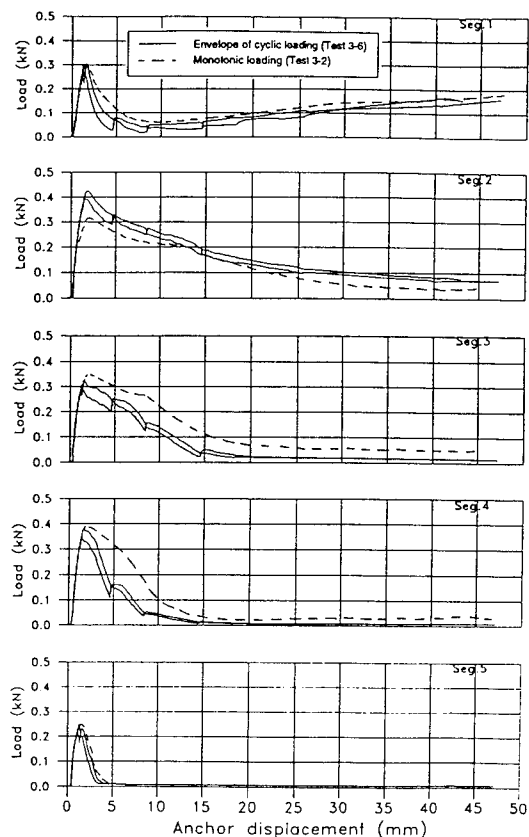


Fig.4 Comparisons of the distribution of side friction under monotonic and cyclic loading. ( $h/D = 12$ )

monotonic and low amplitude cyclic loading; and

2) at small displacements ( $< 1.5\text{mm}$ ) there is no measurable difference in the distribution of side friction along the fixed anchor length between monotonic and cyclic loading. At greater displacements the fall in side friction is more rapid under cyclic loading.

#### 4.3 Effect of repeated loading on side friction and end bearing

The resistance due to end bearing can be deduced by subtracting the sum of the self-weight of the anchor and the integration of the segmental loads from the total load recorded, assuming negligible frictional resistance due to the smooth anchor rod.

The maximum and minimum values of side friction and end bearing are plotted against the associated anchor displacements in Figure 5, along with the comparable responses of the

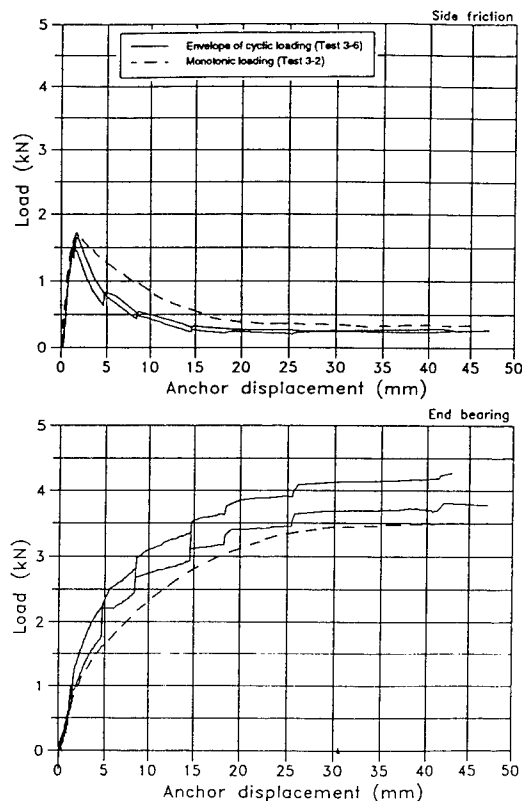


Fig.5 Comparisons of the mobilisation of side friction and end bearing under monotonic and cyclic loading ( $h/D = 12$ )

anchor under monotonic loading. This shows that the magnitudes of ultimate side friction and ultimate end bearing under small amplitude cyclic loading were 102% and 123% respectively of those obtained under monotonic loading.

In contrast, the magnitudes of ultimate side friction and end bearing at an anchor displacement of 15mm under large amplitude cycling loading (Test 3-5) were found to be 26% and 82% respectively of those obtained under monotonic loading.

It is apparent that the two components of resistance were affected differently during cyclic loading. For example, during small amplitude cyclic loading, the magnitude of side friction resistance was unchanged whereas end bearing resistance was enhanced by the soil densification associated with stress and strain repetitions.

It is believed that the degradation in side friction during large amplitude cyclic loading was due to

soil densification beside the fixed anchor zone associated with repetitions of large amplitudes of shear strain. Although soil densification is associated with an increase in angle of friction,  $\phi'$ , it can also result in a reduction in horizontal earth pressure. Whilst the fixed anchor body is able to move upwards to maintain or increase the end bearing pressure in the contracting soil above, the reduction in void ratio beside the fixed anchor body leads to a reduction in horizontal pressure and, therefore, a loss of side friction capacity.

These results are consistent with those of Boulon and Foray (1986) who found that the cyclic loading of tension piles induces a contraction (or densification) of the sand and a progressive decrease in normal stress. The results of the present tests suggest that such behaviour only occurs above a cyclic load peak-to-peak amplitude of 10-15%  $T_r$ . The determination of the critical amplitude of cyclic load is an area where further effort might be concentrated.

#### 4.4 Influence of embedment depth

In Test 3-7, the instrumented anchor was again subjected to small amplitude cyclic loading (12%  $T_r$ ), but this time with an embedment ratio ( $h/D$ ) of 6. The maximum and minimum values of side friction and end bearing are plotted against the associated anchor displacements in Figure 6 at the same scale as Figure 3 and 5. This shows that the magnitudes of end bearing and side friction at the displacement required to mobilise the ultimate pull-out load were 100% and 112%, respectively, of the values obtained in a comparable monotonic pull-out test at the same depth, suggesting that small amplitude cyclic loading can also improve the performance, in terms of its ultimate pull-out capacity, of a shallow ground anchor ( $h/D=6$ ), as well as of a relatively deep anchor ( $h/D=12$ ).

## 5 CONCLUSIONS

- 1) A cyclic load of large amplitude applied to the fixed anchor length has the effect of reducing the side friction capacity relative to the static ultimate side friction capacity. It is believed that large amplitudes of load densify the soil local to the fixed anchor body resulting in an increase in  $\phi'$ . However, the densification results in a local reduction in lateral earth pressure and this tends to reduce the shear strength in the vertical plane. The overall effect is that of a reduction in anchor

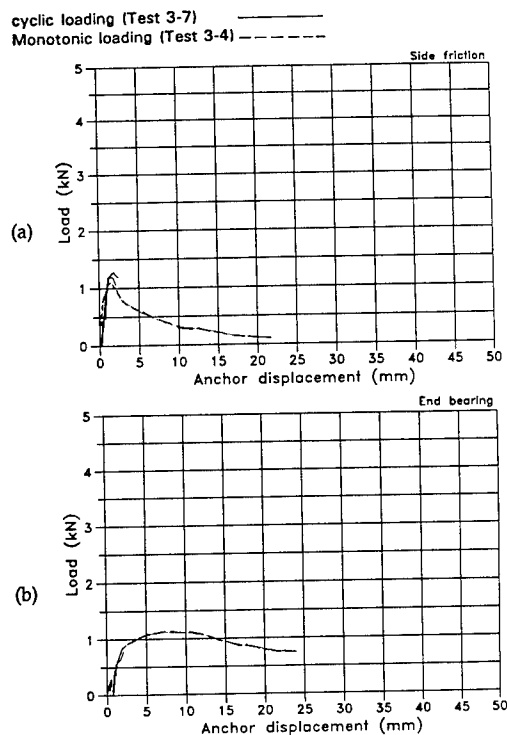


Fig.6 Comparisons of the mobilisation of side friction and end bearing under monotonic and cyclic loading ( $h/D = 6$ )

side friction capacity. Present tests show, however, that a cyclic variation in load on the fixed anchor length with peak-to-peak amplitude of less than 10-15% of static ultimate pull-out load is too small to reduce side friction capacity. 2) Except with very large amplitudes, cyclic loading enhances the end bearing capacity of a ground anchorage for two reasons: (i) there is soil densification and the associated increase in  $\phi'$ , and (ii) the fixed anchor body is able to move forwards and compensate for the reduction in volume of the soil mass.

## 6 ACKNOWLEDGEMENTS

This work was funded by the United Kingdom Science and Engineering Research Council as part of a larger project to investigate anchorage behaviour in a tidal environment (Carey, 1993).

## 7 REFERENCES

- Al-Mosawe, M.J. 1979. The effect of repeated and alternating loads on the behaviour of dead and prestressed anchors in sand. M.Sc. thesis, University of Sheffield.
- Andreadis, A., Harvey, R.C. & Burley, E. 1981. Embedded anchor response to uplift loading. *Jnl. Geotech. Engng. Am. Soc. Civ. Engrs* 107: GT 1, 59-78.
- Boulon, M. & Foray, P. 1986. Physical and numerical simulation of lateral shaft friction along offshore piles in sand. *Proc. 3rd Int. Conf. Numerical Methods in Offshore Piling*, Nantes, France, p.127-147.
- British Standards Institution 1989. British standard code of practice for ground anchorages. BS 8081: 1989. H.M.S.O.
- Carey, J.M. 1993. The behaviour of ground anchorages in a tidal environment. Ph.D. thesis, University of Manchester.
- Craig, W.H. & Rowe, P.W. 1981. Operation of a geotechnical centrifuge from 1970-1979. *Geotech. Test. J., Am. Soc. Test. Mat.* 4: 19-25.
- Dickin, E.A. (1988). Stress-displacement of buried plates and pipes. *Proc. Int. Conf. on Geotech Centrifuge Modelling, Centrifuge 88*, Paris p. 205-214.
- Lee, C-J. 1991. Pull-out capacity of high pressure grouted anchorages modelled in the centrifuge. *Proc. Int. Conf. on Geotech. Centrifuge Modelling, Centrifuge 91, Boulder*, p.145-151.
- Merrifield, C.M. & Carey, J.M. 1991. Ground anchorages - Mobilisation of shear and prediction of pull-out loads. *Proc. Int. Conf. on Geotech. Centrifuge Modelling, Centrifuge 91, Boulder*, p.161-167.
- Merrifield, C.M. & Williams, A.R. 1988. Pull-out capacity and load-displacement characteristics of vertical anchorages modelled in the centrifuge. *Proc. Int. Conf. on Geotech. Centrifuge Modelling, Centrifuge 88, Paris*, p.215-221.

## Model testing and theoretical analysis of drag anchors in sand

S. R. Neubecker & M. F. Randolph

*Geomechanics Group, The University of Western Australia, Nedlands, W.A., Australia*

**ABSTRACT:** The results of a theoretical approach for determining the ultimate holding capacity of drag anchors in sand is discussed. Drag anchors penetrate and rotate in the soil as they are dragged along until they reach an ultimate configuration. Therefore to calculate the ultimate holding capacity of an anchor in sand it is necessary to consider the forces acting on the anchor at a pre-ultimate embedment stage. The results of this theoretical work have been calibrated against a series of centrifugal model anchor tests.

### 1 INTRODUCTION

The past decade has seen the emergence of Floating Production Storage and Offloading (FPSO) facilities for offshore oil extraction as an increasingly popular alternative to traditional fixed platforms, particularly in the South-East Asian region. This trend has highlighted the lack of engineering knowledge about the behaviour of the high capacity drag anchors which are used to secure these facilities.

The current design methods for drag anchors both in sand and clay rely solely on empirical data with very little consideration given to soil properties. This raises uncertainties about the performance of drag anchors in sand and clay and magnifies these uncertainties in more complex soil stratigraphies such as calcareous sediments and calcarenite layering, which are prevalent off the North-West coast of Australia.

There has been little work done on the theory of drag anchor behaviour. LeLievre and Tabatabaee (1979,1981) proposed an upper bound limit equilibrium method for determining the forces on an anchor based on a wedge type failure of the soil. Carchedi (1984) developed this idea further to include sloping sea floors. This method is suitable only if the anchor is at ultimate holding capacity

and the anchor penetration and orientation is known.

A new theory has been developed to consider force equilibrium of an anchor at a pre-ultimate stage. This theory will eventually be used to predict the penetration and rotation of an anchor during the embedment phase and therefore provide a complete analysis of drag anchor behaviour including evaluation of drag distance to ultimate holding power, effect of drag speed on load development, and the formation of soil heave in front of the anchor.

A plane-strain model anchor was built so that the sides of the anchor flukes scraped along walls of a plane strain box causing the failure mode of the soil to be essentially two-dimensional (2-D). This failure mode was observable through a perspex window in the box and showed that the wedge failure mechanism was an appropriate choice of soil failure for the theoretical analysis. These 2-D tests were used to validate the 2-D theory and then to calibrate the theory for a three-dimensional situation.

### 2 THEORY

The theory developed by LeLievre and Tabatabaee (1979, 1981) is a two dimensional limit equilibrium approach that considers the

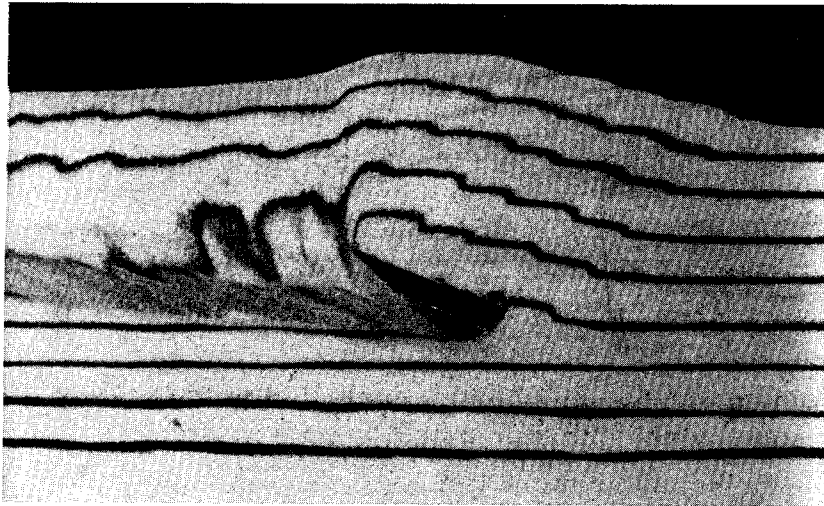


Figure 1. Photograph of soil failure in plane strain test.

failure mode of the soil as a rigid block type. The plane strain centrifuge tests that were conducted allowed this block type failure to be observed through a perspex window as shown in Figure 1. In this picture the anchor is being dragged to the right, with the band of mixed soil indicating the path of the anchor. The edge of the fluke may be seen together with clearly defined failure surfaces extending upwards from both the leading and trailing edges of the fluke.

The theory that was developed considers the following forces acting on the anchor :

- T - Chain tension
- $W_a$  - Anchor weight
- $W_s$  - Soil weight
- S - Side friction on soil mass
- R - Internal soil reaction
- $F_f$  - Fluke force
- $F_s$  - Shank force

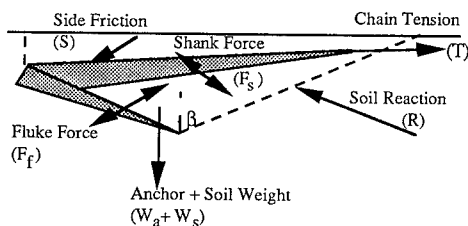


Figure 2. Forces considered in soil/anchor system

If a free body diagram of the anchor plus the soil wedge is considered the forces that are to be in equilibrium include  $W_a$ ,  $W_s$ , S, R and T.  $F_f$  and  $F_s$  are omitted because they are internal to the free body. Of these forces  $W_a$  is known and both the soil mass ( $W_s$ ) and the side friction (S) can be calculated for a given soil wedge angle  $\beta$ . The soil mass is calculated simply by the product of the soil density and the volume of the mobilised soil wedge. The side friction is calculated by integrating the stress to cause shearing over the area of sliding soil.

$$S = \int_A \gamma' \cdot d \cdot K \cdot \tan \delta \, dA \quad (1)$$

- $\gamma'$  = soil density
- d = depth to element of area
- K = earth pressure coefficient
- $\delta$  = soil/wall interface friction angle

This leaves only two unknown variables, T and R, which can then be solved using the two force equilibrium equations. The failure angle  $\beta$  is then varied until a minimum value of T is found, hence it is an upper bound solution to the problem.

The other forces acting on the anchor,  $F_f$  and  $F_s$ , can be deduced by considering a free body diagram of the anchor where the forces acting are  $F_f$ ,  $F_s$ ,  $W_a$  and T.  $F_f$  and  $F_s$  are the only two unknown forces and are therefore easily solved by force equilibrium.

One of the weaknesses of this theory is that the force on the shank,  $F_s$ , is calculated based on force equilibrium considerations of the anchor only. Hence if two similar anchors with different shank widths were analysed, this theory would produce the same result for the force on the shank.

Another limitation of the theory is that the position of the anchor in the soil must be known precisely in order to apply the limit equilibrium calculation. This is difficult to estimate accurately since the anchor rotates and penetrates to an unknown extent during embedment.

## 2.1 Revised limit equilibrium

The existing theory of LeLievre and Tabatabaee (1979,1981) was adapted for a pre-ultimate condition by the addition of a force on the back of the fluke -  $F_{fb}$ . It has been observed experimentally that the back of the anchor is in contact with the soil during the initial stages of embedment so the presence of a force there seems appropriate.

The new limit equilibrium calculation is now performed in two parts. The first is to consider a free body diagram of the soil only (Figure 3). The force delivered from the shank to the soil ( $F_s$ ) has been assumed to be equal to the ultimate bearing capacity of the shank in the sand. This is justified because the relative motion of the failed soil with respect to the anchor must be parallel to the front of the fluke, implying that the shank is cutting through this failure wedge.

This leaves only two unknowns - the soil reaction ( $R$ ) and the fluke force ( $F_f$ ) - which can be solved using force equilibrium equations.

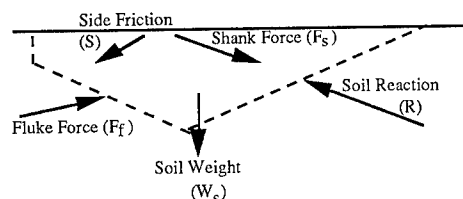


Figure 3. Free body diagram of soil only

Once again the soil wedge angle  $\beta$  is varied until a minimum value of  $F_f$  is found (note that  $F_f$  is proportional to  $T$  so this corresponds to a minimum value for  $T$  also). The second stage is to consider a free body of the anchor only (Figure 4), where once again there are two unknowns - the force on the back of the fluke ( $F_{fb}$ ) and the chain load ( $T$ ). These forces are then solved using force equilibrium.

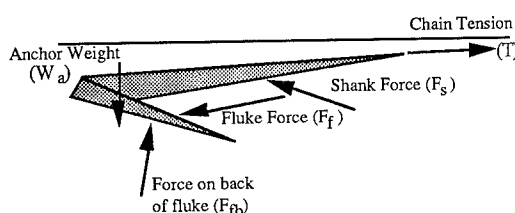


Figure 4. Free body diagram of anchor only

Using this approach it is now possible to evaluate all the forces present in the soil anchor system in a way that is applicable to a pre-ultimate condition. Note that when the anchor approaches the ultimate configuration, the force on the back of the fluke tends to zero so that the anchor is free to move away from the soil behind the fluke and form a void.

A major advantage that this new approach has over the existing theory is that the force on the shank ( $F_s$ ) is evaluated based on its geometric properties. Previously this force was found by considering force equilibrium of the anchor only and took no account of the size or shape of the shank.

## 2.2 Anchor motion analysis

Having developed an analysis method for defining the force system of an anchor at a pre-ultimate stage, work is currently under way to predict the motion of the anchor during embedment. An approach is being developed that considers the anchor at successive positions as it penetrates the soil. At each position a minimum work principle is used to estimate the incremental rotation and penetration hence allowing the complete embedment history to be followed. This in turn leads to an estimate of the ultimate

configuration of the anchor, and hence ultimate holding capacity (UHC).

The energy method is applied by considering the energy that is dissipated by friction, gravity and bearing when the anchor is moved some nominal displacement. This energy is the sum of the dot products of the force and displacement vectors for each force and must balance the energy that is applied to the system by pulling on the chain. Components of penetration and rotation that occur as the anchor moves along are then varied until a minimum value of dissipated energy is found. The movement associated with this minimum value is then considered to be the path of least resistance that the anchor will take.

Preliminary results of this analysis are very encouraging as they exhibit trends that are typically displayed in drag anchor behaviour. However the application of this analysis is still in a developmental stage although comparisons with experimental data (see later) show moderate agreement.

### 3 EXPERIMENTAL RESULTS

#### 3.1 Two-dimensional tests

A series of anchor drags was performed in dense and loose silica sands in the geotechnical centrifuge at the University of Western Australia. The anchor that was used in these tests was a simplified plane strain anchor with principal dimensions shown in Figure 5. These anchor dimensions were based on the overall dimensions of a complex commercial 38 tonne anchor at a 1:80 scale.

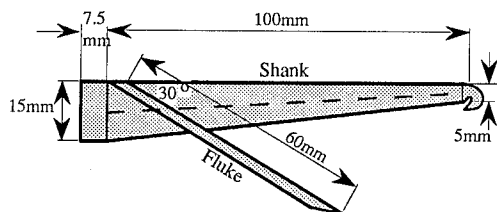


Figure 5. Plane strain anchor dimensions

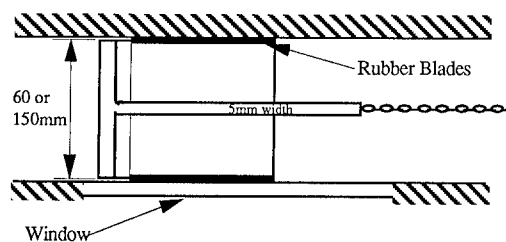
Two different fluke widths were tested with this anchor, one being 60 mm and the other 150 mm. The fluke width to length ratio of 1

with the 60 mm wide fluke is in realistic proportions, whereas the 150 mm fluke was used to compare results rather than to model a real anchor. Both anchors were tested in the centrifuge at a g-level of 40 and the anchor weight was designed to be in proportion to the fluke width ie.

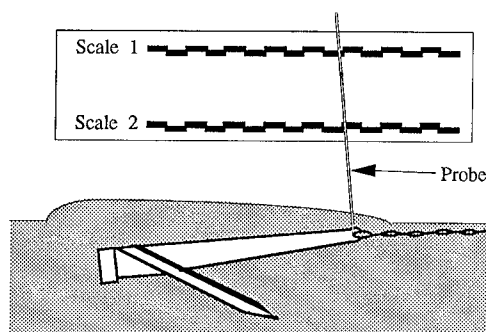
60 mm fluke width > 80 gram anchor

150 mm fluke width > 200 gram anchor

A tracking device was designed so that the position of the anchor (penetration, displacement & rotation) could be calculated at any point in the embedment phase of the anchor. This device consisted of a probe that was connected at the shackle of the anchor at right angles to the shank, as shown in Figure 6. The movement of this probe past a system of scales allowed the three position coordinates to be determined by simple geometry.



a) Plan View



b) Side Elevation

Figure 6. Plane strain anchor

The edges of the fluke were lined with a rubber blade that prevented sand jamming between the anchor and the wall and hence allowed the failure wedge of the soil to be 2-dimensional. A window in the side of the strongbox allowed the failure wedge of soil to



be observed directly. The sand was prepared with coloured layering which gave a clear indication of the location of the failure surface and the formation of a soil heave in front of the anchor (see Figure 1). The discrete nature of consecutive slip surfaces indicates the 'slip-stick' behaviour of the drag anchor, which was also observed by oscillations in the load-displacement curves.

The parameters for loose soil used in the centrifuge tests are presented in Table 1. The value of  $K=0.6$  was proposed by LeLievre et al (1981). Note that variations in  $K$  have little effect on the final results.

Table 1. Soil data (loose) for centrifuge tests.

Soil Type	Silica, $d_{50}=0.3\text{mm}$
Friction Angle	$\phi'=37^\circ$
Density (effective)	$\gamma'=8.9\text{ kN/m}^3$
Dilation Angle	$\psi=10^\circ$
Sidewall Friction	$\delta=10^\circ$
Earth Pressure Coeff	$K=0.6$

The anchor was fitted with strain gauges down the shank that enabled the measurement of both moment and tension in the shank. It is possible, by examining the moment variation down the shank, to evaluate the size of the distributed load that is acting on it. This force on the shank  $F_s$  is equal to the bearing resistance of the shank in the soil and is used in the limit equilibrium solution as described previously.

After having calculated the geometry of the anchor at a series of points in the early

embedment stage, the revised limit equilibrium calculation was applied at these points and a value for chain tension was found. This theoretically based chain tension was then compared with the experimental value that was measured during the test.

Note that to evaluate the mobilised soil mass for use in the calculation, the volume of soil heaved above the anchor needs to be determined. In the two dimensional case this volume can be predicted quite accurately.

Figure 7 shows how the experimental load development curves for the plane strain anchor compare with theoretically derived values for load at a series of points in the embedment stage. It can be seen from these figures that the theory is well verified by the experimental results.

These results are very encouraging as they indicate that the model for calculating the static resistance of the anchor is accurate and therefore the problem is reduced down to one of predicting only the movement of the anchor during embedment.

Figure 7 also shows the results of a motion analysis of the anchor, exhibiting reasonable agreement but the need for further refinement.

### 3.2 Three-dimensional tests

A series of centrifuge tests is under way in which the plane strain anchor is tested in an unconstrained manner, ie. the soil is free to fail in a three dimensional mode. The aim of these tests is to see how the two dimensional theory compares when it is applied to a more

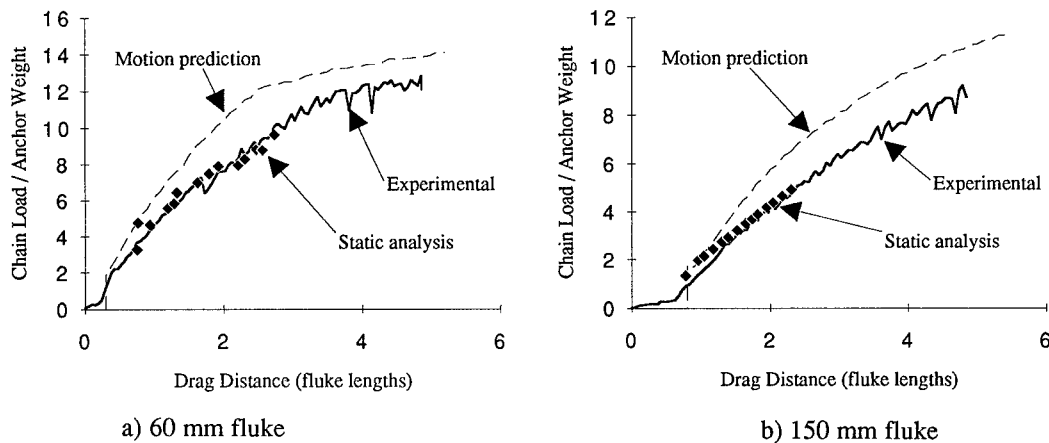


Figure 7. Plane strain test results compared to static analysis and motion prediction

realistic three-dimensional situation.

The testing procedure was much the same as in the two dimensional case and included the use of the tracking probe once again to pinpoint the anchor for equilibrium calculations. The force on the shank was also evaluated during the test for use in the limit equilibrium calculation. It was found that the force on the shank  $F_s$  was significantly smaller in the three dimensional tests compared with the two dimensional ones. This is not surprising since in the two dimensional case the soil is constrained so that the lateral stresses are greater and hence the bearing capacity should be greater.

Another difference between the two and three dimensional cases is the extra weight of soil that is present in the three dimensional condition. The failure surface is no longer constrained by a plane strain wall and so a failure plane will occur outwards from the anchor at the dilation angle to the soil displacement. This means that more soil is mobilised by the anchor and hence the soil weight will be greater. This extra soil weight has been incorporated into the theory.

Figure 8 shows test results and for a 3-D test in the same silica sand, but in a dense state ( $\gamma=10.5 \text{ kN/m}^3$ ,  $\phi'=45^\circ$ ). The results from the theoretical analysis are generally lower than the experimental results, however the slopes of the theoretical and experimental load curves are quite similar. An explanation for this could be that at present the size of the soil heave that adds to the mobilised volume of soil is an estimation only. The three dimensional soil heave is much more complex than the two dimensional case and further refinement may be needed in the estimation of heave volume to improve results.

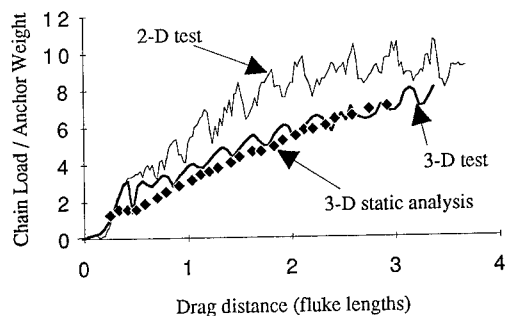


Figure 8. 3-D test results vs. theory and 2-D test results (60 mm fluke)

It is interesting to note that the force developed in the 2-D test in loose soil was more than that developed in dense soil. This is because in loose soil the anchor is able to penetrate deeper into the soil and mobilise a greater soil volume. This trend is consistent with the findings of Carchedi (1984).

#### 4 CONCLUSIONS

A method has been demonstrated that allows an accurate evaluation of the capacity of a plane strain drag anchor in sand. Comparison of the theoretical analysis results with a series of anchor tests in the centrifuge is very good.

This two dimensional method can also be applied to a three dimensional case provided that account is taken of the extra mobilised soil volume due to three dimensional failure planes and extra soil heave. Differences in shank resistance between the two cases also need to be considered.

The application of this theory relies on accurate information about the position of the drag anchor in the soil. Work is currently under way to predict the motion of the anchor so that the geometry of the anchor at any point during penetration can be evaluated. Early results of a motion analysis using a minimum work approach are very encouraging.

#### REFERENCES

- Carchedi, D. R. (1984), Model study of plate and drag anchors in dry sand, PhD Thesis, University of Rhode Island.
- LeLievre, B. and Tabatabaee, J. (1979), Holding capacity of marine anchors in sand. Proceedings, First Canadian Conference on Marine Geotechnical Engineering, Calgary, Alberta, 301-310.
- LeLievre, B. and Tabatabaee, J. (1981), The performance of marine anchors with planar flukes in sand, Canadian Geotechnical Journal, Vol. 18, 520-534.
- Tabatabaee, J. (1980), Theoretical and experimental investigations on marine anchors, PhD Thesis, Department of Civil Engineering, University of Waterloo, Waterloo, Ontario, Canada.

## 12 Miscellaneous topics

## An examination of the integrity of stone columns in soft clay

D.P. Stewart & M. Fahey

Department of Civil Engineering, The University of Western Australia, Nedlands, W.A., Australia

**ABSTRACT :** A proposed major extension to an iron ore handling yard was located in an area underlain by soft alluvial clay. Stone columns were proposed to limit differential movement of rails supporting the stacking/reclaiming machines. As part of the investigation for the project, a series of centrifuge model tests were undertaken to examine various aspects of the project including whether the integrity of the stone columns would be maintained under the high imposed stresses. The results of these model tests are presented and discussed in the light of current design methods for stone columns.

### 1 INTRODUCTION

Port Hedland on the north-west coast of Western Australia is one of the world's major iron ore exporting ports. As illustrated in Figure 1, ore handling yards at Port Hedland typically comprise large stacking/reclaiming machines which run on rails on top of 3 m high embankments adjacent to the ore stockpiles. With stockpiles of up to 20 m in height having a bulk unit weight of around  $26 \text{ kN/m}^3$ , the stockpiles exert a vertical stress of up to 500 kPa on the subgrade.

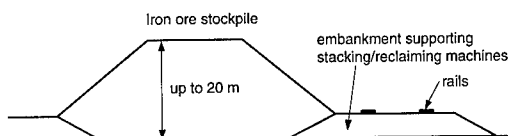


Figure 1. Cross-section through a typical iron ore stockpile.

A major new ore handling yard was proposed in an area underlain by about 3 m of hydraulic fill over soft alluvial clay of up to 3 m thickness. It was proposed to install stone columns beneath the stacker/reclaimer embankments to limit differential vertical and horizontal movements of the rails for the stacking/reclaiming machines and to increase the stability of the stockpiles against gross failure.

As part of the investigation for the project, a series of centrifuge model tests were carried out at The University of Western Australia to examine various aspects of the project, and to test some of the design assumptions. The work was aimed at assessing the expected magnitude of vertical and horizontal movements of the stacker/reclaimer embankment, and what reductions could be expected due to installation of stone columns. There was also some concern expressed about maintaining the integrity of the stone columns under the very high imposed stresses from the ore stockpile. It was postulated that stone columns beneath the stockpile could actually shear, and thus lose much of their effectiveness.

### 2 TESTING PROGRAM

Centrifuge model testing was performed on the 40 g-tonne Acutronic model 661 geotechnical centrifuge at The University of Western Australia (Randolph et al, 1991). Internal dimensions of the strongboxes used for the testing were 650 x 390 mm in plan view and 325 mm in height. The models were tested at a gravity level of 100, and therefore the field dimensions were scaled down by a factor of 100.

In total, four centrifuge models were tested as shown in Table 1. The layout of each test was similar to that illustrated in Figure 2, although the positions of instrumentation and the precise

Table 1. Centrifuge model configurations

Test no.	Stack/reclaim embankment	Stone columns
1	yes	none
2	yes	beneath stack/reclaim embankment only
3	no	none
4	no	beneath and beyond toe of ore stockpile

layout varied slightly between tests. The clay and upper sand layers were 30 mm thick in the model, and the stacker/reclaimer embankment was 30 mm high.

A disturbed bulk sample of clay from the field site was obtained to conduct the centrifuge testing. All other soils were chosen to be approximately representative of the field materials. Fine graded silica sand was used for the embankment and the sand layers indicated on Figure 2. Fine cast iron shot was used to represent the iron ore in the stockpile. This material has a mean particle size of about 0.35 mm, and a bulk density of 4 Mg/m<sup>3</sup>. This high density meant that the loading from a 20 m high ore stockpile (density = 2.6 Mg/m<sup>3</sup>) could be represented by a 120 mm high stockpile of iron shot at 100 gravities.

The centrifuge samples were prepared by mixing the clay at a water content of twice the liquid limit ( $w_l = 106$ ). Salt was added to the water to approximate the salinity of sea water since the clay was originally deposited alluvially in a coastal environment. The slurry was then consolidated in a centrifuge strongbox under a uniform vertical pressure approximately

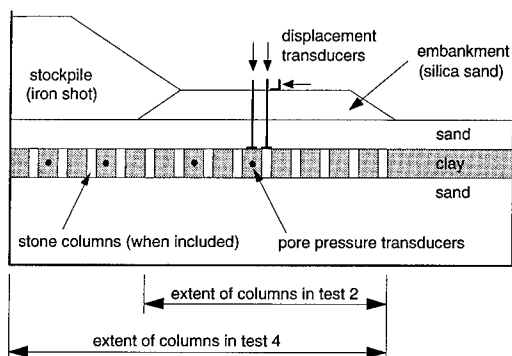


Figure 2. General layout of centrifuge models (precise layout varied between tests).

equivalent to the expected overburden stress at the mid-depth of the model clay layer. After full consolidation, "stone" columns, if required, were installed by inserting a 12 mm (1.2 m) diameter thin-walled tube into the clay through a guiding template. The tube was then extracted to remove a cylinder of clay, and the hole backfilled with fine sand, lightly tamped into place. The columns were placed on a 35 mm (3.5 m) square grid, resulting in a replacement ratio of 9 %. After placing the upper sand layer and mounting various transducers and equipment, the model was placed on the centrifuge and allowed to consolidate under 100 g. Under these conditions, the undrained shear strength of the soft clay stratum was estimated to be 23 kPa.

In tests 1 and 2, the stacker/reclaimer embankment was then formed in-flight by pouring sand in one increment from a sand hopper (Randolph et al, 1991). Full consolidation of the clay under the embankment was allowed before the centrifuge was stopped and the hopper moved, filled with iron shot and the centrifuge restarted. After allowing for reconsolidation of the clay, the ore stockpile was constructed in six equal increments with 30 second (3½ day) delays between each stage. In tests 3 and 4, the stacker/reclaimer embankment was not included, and so the ore stockpile was constructed as above without stopping to move the sand hopper. After construction of the ore stockpile, full consolidation was allowed to occur before ending the test. In test 1, a period of only about one month prototype scale was allowed before the speed of the centrifuge was increased in attempt to cause failure of the stockpile. Failure did not occur, although vertical and lateral deformations increased substantially.

Instrumentation of the model included miniature pore pressure transducers installed in the soft clay, and displacement transducers to measure vertical and horizontal movement of the soil surface.

### 3 TEST RESULTS

The results of the centrifuge model testing are presented in terms of prototype units only. Model lengths and displacements have been scaled up by a factor of 100 (N), while model time has been scaled by a factor of 10 000 (N<sup>2</sup>).

### 3.1 Surface displacements

The surface deformations measured during the stockpile construction phase of each centrifuge test are summarised in Table 2. Examining these data, it is apparent that the inclusion of stone columns beneath the stacker/reclaimer embankment has a number of benefits. Apart from the initial reduction in settlement of the stacker/reclaimer embankment, the stone columns reduced the magnitude of surface heave and lateral movement by approximately half (comparing tests 1 and 2).

Table 2 : Summary of surface deformations measured during the stockpile construction phase in each centrifuge test.

Test No.	Heave at toe (mm)	Lateral displacement at toe (mm)	
		After one month	Long term
1	15	70	-
2	8	30	85
3	65	115	160
4	7	90	130 to 140

By comparing tests 1 and 3, the stacker/reclaimer embankment itself had a very significant effect on the magnitude of heave generated by the ore stockpile. This is partly due to the physical weight of the embankment, and partly due to strength gain in the soft clay under the embankment's load. By contrast to the reduction in heave, lateral deformations at the surface were reduced by a much smaller proportion. Similar observations can be made comparing tests 3 and 4, where stone columns beneath the stockpile reduced heave markedly, but had relatively little effect on reducing lateral movement beyond the toe. In this test series, stone columns were only effective in markedly reducing lateral deformations when overlain by the stacker/reclaimer embankment. It is believed that this is because the columns were stiffer when carrying greater axial load, and therefore provided more restraint to movement when the embankment was present.

Surface heave measured in tests 1 and 2 during the first two months after commencing stockpile construction is shown in Figure 3. The vertical

deformations occurred relatively quickly, reaching a plateau soon after completion of construction. In test 2, settlement was observed in the long term as excess pore pressures dissipated. The cyclic nature of the curve for test 1 is a function of the displacement transducer's resolution. A transducer with finer resolution was used in test 2.

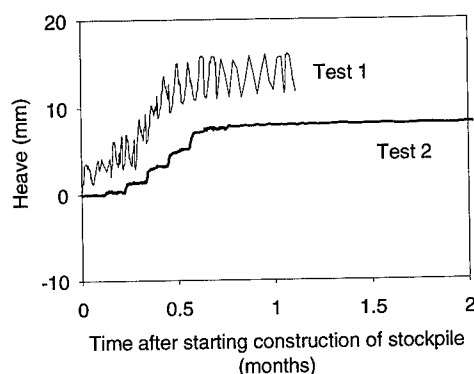


Figure 3 : Heave at toe of stockpile measured in tests 1 and 2.

Lateral surface movement measured in tests 1 and 2 during the first two months after commencing stockpile construction is shown in Figure 4. The lateral displacement data clearly show the stockpile construction increments, since the laser displacement transducer was temporarily blinded by dust from the iron shot used to construct the stockpile. The lateral movements may be observed to be more strongly time dependent than the heave recorded at the same point. A consistent feature of the data is that a small lateral movement towards the stockpile was recorded initially, with movement away from the stockpile in later stages. This response is probably due to slight overconsolidation of the clay, and is consistent with the "drained" and "undrained" responses described by Tavenas et al (1979) from field data on lateral displacements adjacent to embankments on soft clay.

The long term development of surface lateral displacement is shown in Figure 5. The data indicate that significant lateral deformations were still occurring some 12 months after construction of the ore stockpile, particularly where stone columns were installed. The break in the curve for test 4 is due to the centrifuge

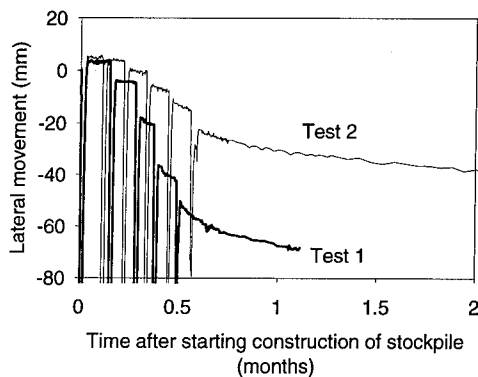


Figure 4 : Surface lateral movement at toe of stockpile measured in tests 1 and 2. Negative movement is away from stockpile.

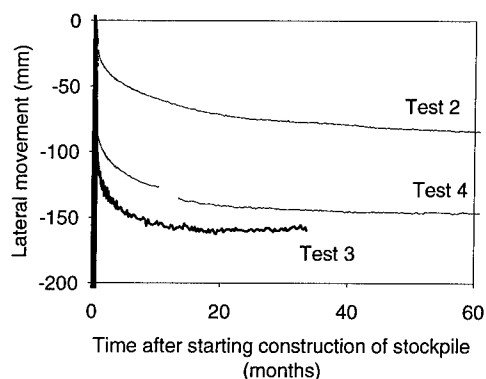


Figure 5 : Surface lateral movement at toe of stockpile measured in tests 2, 3 and 4.

slowing down to 20 g before ramping back up to 100 g because of a power surge during a storm. The data after the break should be treated with caution, but appear to match up reasonably well with the initial part of the curve.

### 3.2 Sub-surface displacements

In addition to measurement of surface displacements during the centrifuge tests, video imaging techniques were used to monitor the deformation of various points within the model by viewing through a window in the side of the strongbox. Two horizontal lines of point markers were placed on the side of the soft clay stratum at 1/4 and 3/4 depth of the layer. The results from video image measurement of the top row of markers at the end of test 4 are shown in Figure 6. The resolution of the current video system is

0.4 mm true scale, equivalent to 40 mm prototype scale. The window in the side of the strongbox does not extend over the full length of the box, and so movements could only be monitored in the central portion of the model. After completion of the test, the sample was dissected, and the position of the top of the stone columns measured. The average positions of the columns in several rows are also shown in Figure 6. The two measurements are in good agreement, although as expected it would appear that slightly higher lateral movements occurred at some depth within the soft clay layer than at its surface.

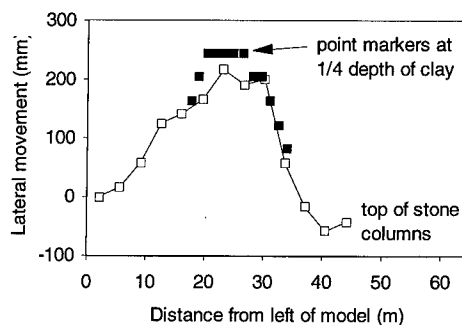


Figure 6 : Lateral movement of top of stone columns and of clay markers measured in test 4.

### 3.3 Stone column integrity

One of the purposes of the centrifuge testing program described here was to assess the proportion of vertical load attracted by the stone columns. The details of this work are described by Stewart and Fahey (1994), however in the two tests where stone columns were included, stress concentration factors ( $n$ ) of 4.2 and 4.6 were derived from the experimental data, where  $n = \text{stress on the stone column} / \text{average stress on the clay}$ . These values are consistent with stress concentration factors derived from field measurements (Mitchell, 1981). Using these values of  $n$ , a surface load of 500 kPa from the ore stockpile would generate an axial stress of about 1600 to 1700 kPa on the stone columns.

Hughes and Withers (1974) describe a simple approach for estimating the capacity of an axially loaded stone column based on an estimate of the limit pressure in a pressuremeter test. Ignoring any increase in limit pressure due to the higher overburden stress from the ore stockpile, this approach gives an axial capacity

of the stone columns in the region of 450 kPa. However, if a higher limit pressure is used to account for the increased overburden stress, an axial capacity of around 2000 kPa may be calculated. Therefore, some concern was expressed that the stone columns might fail by shearing or suffer a large amount of distress.

During dissection of test 4, the clay layer was sectioned along the centreline of several rows of stone columns to examine their integrity. It was clearly evident from this work that some of the columns underwent vertical deformation by "barrelling", while others both barrelled and leaned over to one side, and others showed little visible deformation. The extent of these deformations is illustrated in Figure 7 in relation to the ore stockpile location, and can be compared with the lateral movements illustrated in Figure 6. It is obvious that none of the columns had failed by shearing, and that the barrelling that occurred was likely to have generated additional confining stress around the columns, and thus inhibited this type of failure. It is believed that shear failure of stone columns under an extensive load is unlikely to occur unless a gross bearing capacity type failure is generated. Greenwood and Kirsch (1984) arrived at similar conclusions.

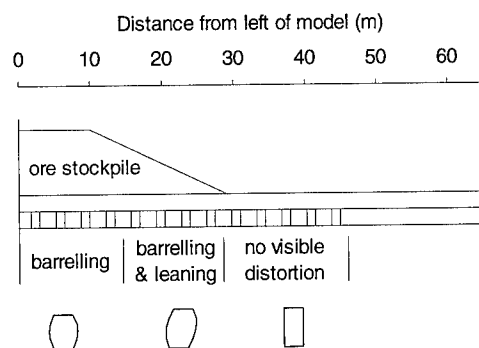


Figure 7 : Regions of stone column distortion in centrifuge test 4

#### 4. IMPROVED SHEAR RESISTANCE

Stone columns are usually installed to limit the magnitude of settlement due to a surface load. While the columns may provide a significant benefit in terms of increased shear resistance of the soft layer, this is not always accounted for in design. In the present application beneath a high iron ore stockpile, increased shearing resistance

by inclusion of stone columns was a requirement of the ground improvement works.

An assessment of the increased shear resistance of a clay-column system can be made with conventional slip circle techniques. Generally this is performed by neglecting the stress concentration on the columns (Greenwood and Kirsch, 1984), leading to an underestimate of their frictional strength. The application of this approach leads to the conclusions that very considerable replacement ratios (area of stone columns/total area) are required, together with substantial overburden pressure to obtain a significant increase in stability.

To enable an accurate assessment of the gain in shearing resistance, the stress concentration on the columns must be taken into account so that their frictional strength is properly calculated. There are two alternative approaches for the inclusion of columns in this way into a slip circle analysis:

- (i) derivation of equivalent cohesion and friction angles for the improved soil layers as proposed by Priebe (1978), without direct inclusion of the columns as soil layers; or
- (ii) direct inclusion of the columns in the analysis by way of equivalent trenches to maintain the same replacement ratio.

If the columns are included directly in the analysis, stress concentration can be allowed for by (a) factoring up the soil densities directly above each equivalent column and factoring down the densities above the surrounding clay (Waterton and Foulsham, 1984); or (b) factoring up  $\tan\phi$  of the columns. The second of these approaches probably requires less input data to be generated.

To provide a simple quantification of the increased shearing resistance available from the stone columns, calculations similar to those performed by Priebe (1978) were carried out. Strength parameters relevant to the centrifuge models were used, with  $s_u = 23$  kPa for the soft clay, and  $\phi = 40^\circ$  for the columns. The results are shown on Figure 8 as the ratio of the average shear strength of the clay-column combination to the original shear strength of the soft clay. Curves for stress concentration factors of 1 and 4 are shown, indicating the potential benefit of allowing for stress concentration. The reinforcing effect of the stone columns is obviously substantial, and increases as the magnitude of the surface load increases.



Therefore, in the centrifuge models described here, the region of improved clay beneath the ore stockpile would have been strengthened substantially, while the improved region adjacent to the stockpile would not. Figure 8 also suggests that high replacement ratios are not necessarily required to give a marked increase in stability.

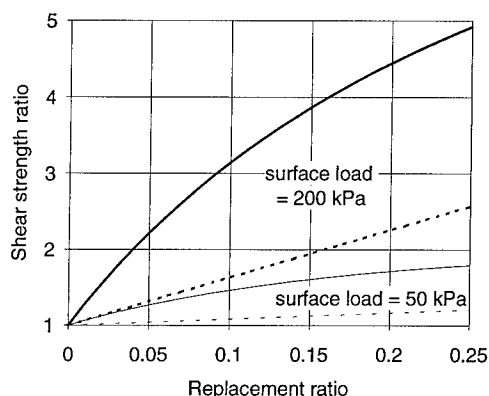


Figure 8 : Estimated increase in shearing resistance for the centrifuge models. Dashed lines :  $n = 1$ , solid lines :  $n = 4$ .

A research project is in progress to further examine the shear strength of a clay-column system, with a view to formulating guidelines for stability analysis of stone column reinforced clays. The work involves testing of an equivalent stone column in soft clay in a direct shear apparatus, with independent measurement of stresses on the column and the clay.

## 5. CONCLUSIONS

A number of centrifuge tests were conducted to examine the influence of stone columns on reducing surface deformations due to construction of an iron ore stockpile imposing a surface load of up to 500 kPa. A major concern prior to this work was the integrity of the stone columns under such a high load.

It was found that the stone columns were quite effective in reducing vertical deformations beneath and adjacent to the loaded area, although had a relatively small influence on reducing lateral deformations. Post-test dissection indicated that the columns did not undergo shear failure, but purely deformed by bulging and leaning. It is believed that shear failure of stone columns under an extensive load

is unlikely to occur unless a gross bearing capacity type failure is generated. The increase in shearing resistance of a soft clay layer due to the presence of stone columns can be substantial, although depends on the magnitude of the surface loading and the stress concentration on the stone columns.

## ACKNOWLEDGMENTS

The centrifuge testing program described here was performed for BHP Engineering, as part of the geotechnical investigation for expansion of the Nelson Point ore handling facility at Port Hedland, which is operated by BHP Iron Ore Pty Ltd. The assistance of Trevor Osborne of Osborne Geotechnical, is gratefully acknowledged.

## REFERENCES

- Greenwood D.A. and K. Kirsch 1984. State-of-the-art - Specialist ground treatment by vibratory and dynamic means, Proc. Int. Conf. Advances in Piling and Ground Treatment, Thomas Telford, London.
- Hughes J.M.O. and N.J. Withers 1974. Reinforcing of soft cohesive soils with stone columns, *Ground Engineering*, May, 42-49.
- Mitchell J.K. 1981. Soil improvement - state-of-the-art, Proc. 10th ICSMFE, 4, Stockholm, 509-565.
- Priebe H. 1978. Abschätzung des Scherwiderstandes eines durch Stopfverdichtung verbesserten Baugrundes, *Die Bautechnik*, 8.
- Randolph M.F., R.J. Jewell, K.J.L. Stone and T.A. Brown 1991. Establishing a new centrifuge facility, Proc. Centrifuge 91, Balkema, 3-9.
- Stewart D.P. and M. Fahey 1994. An investigation of the reinforcing effect of stone columns in soft clay, Proc. ASCE Spec. Conf. Settlement 94, Texas A&M Univ., June.
- Tavenas F., C. Mieuassens and F. Bourges 1979. Lateral displacements in clay foundations under embankments, *Canadian Geotechnical Journal*, 16, 532-550.
- Waterton C.A. and D.A. Foulsham 1984. The design, construction and performance of a road embankment founded on stone columns, Proc. 4th ANZ Conf. Geomech., Perth, 1, 351-356.

## Earth pressure change during rotational failure of retaining wall

Koji Kawasaki

Taisei Corporation, Yokohama, Japan

R.Neil Taylor

The City University, London, UK

**ABSTRACT:** Finite element analyses and centrifuge tests have been carried out to investigate the earth pressure change against a retaining wall when it is about to undergo a rotational failure beneath the base prop level. From the finite element analyses, it was found that the earth pressure against the rotating part of the wall decreased rapidly while the earth pressure against the stationary part of the wall increased. A model wall with a hinge mechanism was used to simulate the rotational failure in centrifuge tests conducted at 80g. The results suggest that the sliding mass which should be considered to predict earth pressures against the rotating part of the wall can be approximated by the zone enclosed by: the ground surface, the retaining wall, the logarithmic spiral from the toe of the retaining wall and a vertical straight line connecting the spiral to the surface.

### 1. INTRODUCTION

Most retaining walls are used as temporary structures during excavation. From this point of view they are required to be economical as long as they are stable and satisfy the condition relevant to serviceability, i.e. acceptable displacements.

In practice, this affects the determination of factors of safety, what surcharge pressure are considered, the design earth pressure distribution, the required depth of penetration and so on.

Also it may be that different clients have their own standards or codes.

Even if a retaining wall has been designed and constructed perfectly under some standard or code, it may be that some natural or man made activity would cause a rapid reduction of factor of safety.

For instance Simpson (1992) considered the following example:

Two walls, A and B, are assumed to be placed in sandy ground ( $\phi' = 40^\circ$ ). They have the same length 10m, but the excavation at wall B is 0.5m deeper. Wall A, penetrating 2m, would be acceptable by current British standards, but wall B is on the point of failure. Such extra excavation or some passive soil softening might occur easily. But in practice, redistribution of active earth pressure onto the prop might make any wall slightly safer than simple calculations suggest.

This paper examines the earth pressure change and redistribution of active

pressure below the lowest prop level when that part of the wall is about to fail by the rotation about the lowest prop.

For this purpose, finite element analyses and centrifuge tests have been carried out.

### 2. THE MODEL RETAINING WALL

The model retaining wall for both analyses and experiments is shown schematically in Fig.1.

A stiff retaining wall, 15m in length, is placed in the dry sand layer. Then, excavation proceeds to the planned

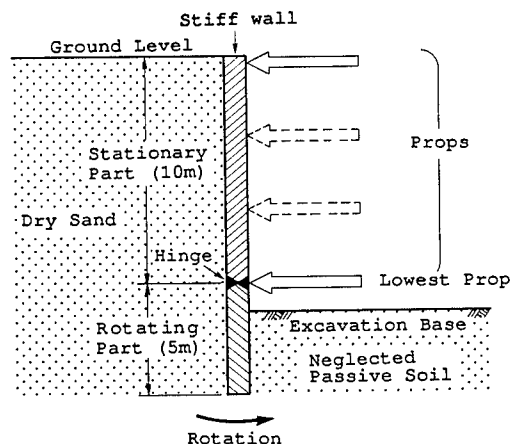


Fig.1 Model retaining wall and ground

formation level while simultaneously placing props, the lowest of which is installed 10m below the ground level.

After the excavation is carried out up to the planned base, a structural hinge of the wall is assumed to develop at the point 5m above the bottom of the wall, i.e. 10m below the ground level, because of perhaps some extra excavation or softening of passive soil.

The hinge level of the wall coincides with the level of the lowest prop. Consequently rotational failure about the hinge is likely to occur, which means the lower part of the wall, 5m between the hinge and the wall base, starts to rotate about the hinge. On the other hand, the upper part of the wall, 10m between the ground level and the hinge, is still stationary.

For the sake of simplicity and safety, the influence of the passive soil is neglected.

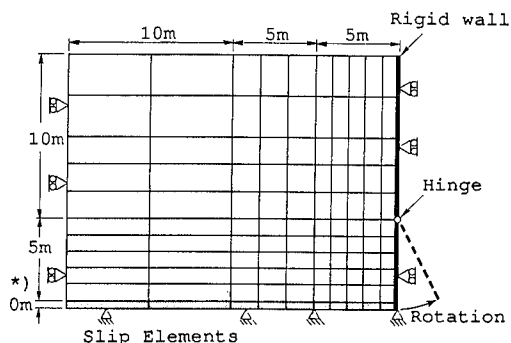
### 3. FINITE ELEMENT ANALYSES

To investigate the earth pressure change due to wall rotation, finite element analyses were carried out. The program used was CRISP 90.

The idealized geometry and finite element mesh are illustrated in Fig.2.

As shown in Fig.2, vertical boundaries are restrained horizontally and free to slide vertically. The upper horizontal boundary is free and the lower one is restrained only in the vertical direction. The interface between the lower horizontal boundary and the soil is modelled using slip elements. The properties of the slip elements and the main body of the soil are listed in Table 1.

Initial in situ horizontal stresses were calculated using:  $\sigma_h = (1 - \sin \phi) \cdot \sigma_v$ . Rotational displacements around the



\*) As shown in Table 1, 0.05m is replaced in the slip elements

Fig.2 Finite element mesh

Table 1 Input data and soil properties

Soil model	elastic perfectly plastic	Slip element	
Yield criterion	Mohr-Coulomb	Angle of friction	11.3°
Bulk unit weight	15kN/m <sup>3</sup>	Modulus in the normal direction	12,000kN/m <sup>2</sup>
Young's modulus	10,000kN/m <sup>2</sup>	Shear modulus	4,000kN/m <sup>2</sup>
Poisson's ratio	0.25	Residual shear modulus	4kN/m <sup>2</sup>
Angle of friction	30°	Thickness	0.05m

hinge are given as follows. The total rotational displacement of up to 1m in the horizontal direction at the toe was achieved with four increment blocks. In the first increment block, the final horizontal displacement at the toe was up to 0.05m, in the second one up to 0.2m, in the third one up to 0.5m and in the last one up to 1m. In each increment block the displacement to be achieved was uniformly divided into fifty increments.

Fig.3 shows the lateral stress distribution against the retaining wall at the end of each increment block.

As the rotation advances, lateral stresses at and above the hinge level increase whereas lateral stresses below the hinge level decrease.

From studies of the effects of wall deformation on earth pressures, for example by Potts & Fourie (1986), it can be shown that the earth pressure change

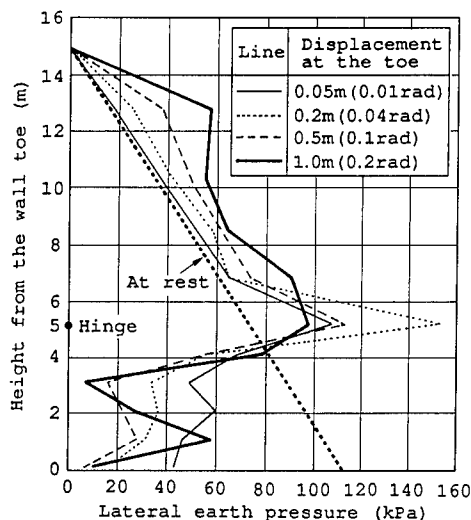


Fig.3 Earth pressure change due to wall rotation

due to wall deformation during a small degree of rotation is greater than that after large deformation.

The results show the lateral earth pressure on the rotating part of the wall is sharply reduced, while the lateral pressures on the stationary part increase rapidly in the vicinity of the hinge; however away from the hinge, the pressure changes are more gradual.

Although the results indicate that the earth pressure redistribution along the rotating part of the wall makes the wall slightly safer, the props would need to be stronger than calculated for the initial state.

#### 4. TEST PROCEDURES

##### 4.1 Apparatus for the model wall and loading system

The model wall and loading system are illustrated in Fig.4.

The model wall was fabricated using 12.7mm thick Aluminium alloy plate. It was made in two parts, with a 12.5cm long stationary part having a concave lower edge and a 6.25cm long rotating part with a convex upper edge. The lower, rotating section was connected to the upper section by wires which passed through the full height of the stationary section and were terminated at tensioning screws.

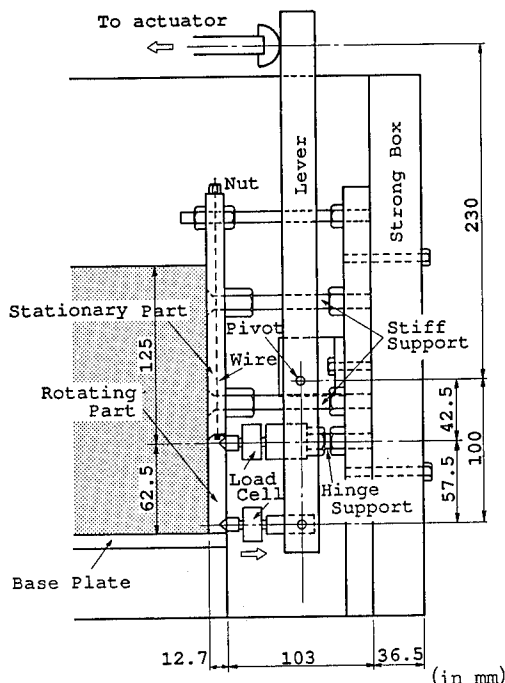


Fig.4 Side view of the apparatus

This gave a low friction hinge and also prevented the toe of the rotating part of the wall from rubbing on the aluminium base plate.

The stationary part of the wall was fixed in place by four  $\phi 10$ mm bolts; the rotating part of the wall was propped by two upper pinned supports at hinge axis level and one lower pinned support.

The distance between the upper and lower supports was 5.75cm, i.e. 4.6m in the prototype.

The backward rotation of the lower part of the wall was controlled by a lever system. At the initial state this lower support was supported by the pivot bolted to the strong box and the actuator at the force applied point, which was at the upper end of the lever.

By moving the actuator in the direction away from the lever, the lower support was able to move backwards away from the soil.

According to the difference between the two arms, from the pivot to the applied force point or the lower support point, the moving speed of 0.06~0.09 mm/sec at the actuator was equivalent to 0.026~0.039 mm/sec at the lower support point. This corresponded to a rotational rate of 0.027~0.041 rad/min.

Three load cells were used to measure the forces on the rotating part of the wall: two in the upper props at hinge level and one in the lower prop.

The movement of the actuator was also measured by a displacement transducer during the test.

A solid state video camera provided continuous pictures of the vertical plane during the centrifuge test.

##### 4.2 Calibration of the wall

The apparatus, especially the rotating part of the wall, was calibrated using a rubber bag containing water. A pore pressure transducer was set at the bottom of the bag to measure the maximum pore pressure and hence to estimate the total pressure on the rotating part of the wall. The acting prop forces were also measured by load cells installed in each support.

The measurement of pore pressure, prop forces and rotational displacement was carried out at the test centrifuge acceleration of 80g.

By comparing the measured forces with the theoretical values, a "correction line" was determined, which was applied to all the raw experimental data. The difference between the measured data and theoretical prop forces was considered to come from mainly friction at the hinge and tension of wires which supported the rotating part of the wall from the stationary part.

#### 4.3 Centrifuge tests with sand

After installation of the apparatus in the strong box, fine Leighton Buzzard sand was placed behind the wall.

For loose packing, sand was placed by a scoop; for medium dense packing, sand raining from 1m height was adopted.

During sand placing, horizontal straight lines of coloured sand were laid adjacent to the perspex window every 2cm to assist with making the ground deformation or slip planes clear.

Table 2 shows the test loading paths; in tests K-2 and K-4, the centrifuge acceleration was raised to 160g before the rotation at 80g; this was to induce a larger coefficient of earth pressure K than in tests K-1 and K-3.

The model displacement at the wall toe was a maximum of 13mm.

Table 2 Test cases

Case	Density (t/m <sup>3</sup> )	Void ratio	Loading path
K-1	1.427	0.86	1g→80g→Rotation
K-2	1.427	0.86	1g→160g→80g→Rotation
K-3	1.594	0.66	1g→80g→Rotation
K-4	1.594	0.66	1g→160g→80g→Rotation

### 5. TEST RESULTS AND DISCUSSION

#### 5.1 Calibration of the wall

As the system for supporting the rotating part of the wall was sensitive, some tests were carried out with different adjustments to the tension of wires and hinge supports.

In each case, both upper and lower prop forces were compared with theoretical values.

Fig.5 shows simplified typical correction lines which were derived from:

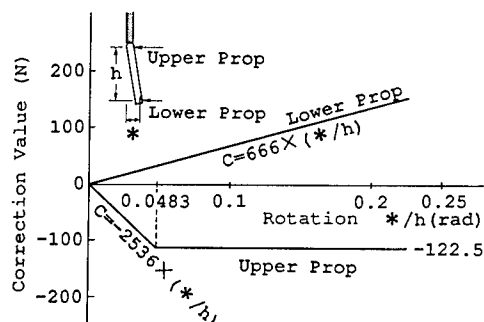


Fig.5 Correction line

[Theoretical prop force] minus [Experimental prop force].

All the data were corrected by the lines in Fig.5.

#### 5.2 Centrifuge tests with sand

##### 5.2.1 Test results

In addition to the centrifuge tests, some direct shear tests were performed using a steel box 25.3cm long, 15.2cm wide and 20.4cm high to measure the angle of friction for loose and medium dense sand and the coefficient of frictional resistance between sand and an aluminium alloy plate.

For loose sand the angle of friction was about 30°; for medium dense sand peak angle of friction of 38° was measured. The coefficient of frictional resistance between sand and an aluminium alloy plate was about 0.2, which was independent of the sand density (and hence void ratio), which in this test series from ranged 1.487 to 1.646 t/m<sup>3</sup>.

A typical prop force history (test K-4) is shown in Fig.6.

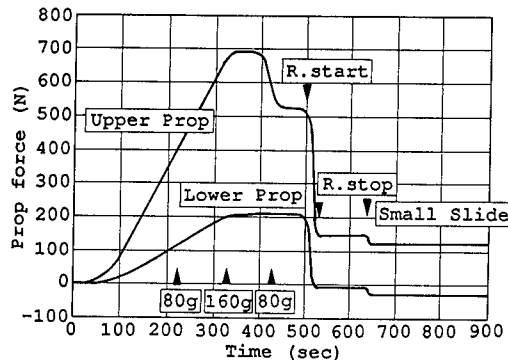


Fig.6 Prop force history (test K-4)

As soon as the rotation started, prop forces reduced rapidly and often the rotation ceased even though the lower prop was still going backwards. Thus a very small prop force was needed to prevent failure developing. In test K-3, clear rupture lines were observed as shown in Fig.7.

For all tests, actual values of coefficient of earth pressure at the rotating part are shown in Table 3. All the coefficients of earth pressure are smaller than those at rest might be.

This was probably because each prop stiffness, especially the lower one, was not high enough to maintain the at rest condition and the active state had already formed.

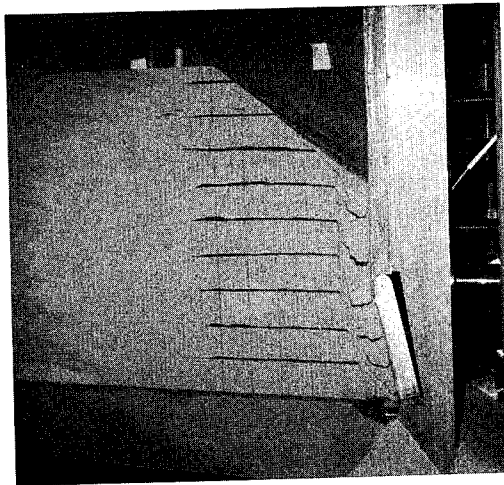


Fig.7 Rupture lines (test K-3)

Table 3 Coefficient of earth pressure

Case	80g	160g	80g			
			Rotation start	Rotation stop	Small Slide	Failure
K-1	0.26	—	0.26	0.07	0.07	—
K-2	0.25	0.23	0.39	0.14	0.12	—
K-3	0.19	—	0.19	0.03	0	0
K-4	0.2	0.18	0.31	0.06	0.06	0.04

### 5.2.2 Analysis of sliding mass and Prop force

As an example, simulation of the sliding mass in test K-1 is attempted as follows.

The observations in test K-1 are used to identify a sliding mechanism of collapse.

First, a sliding surface is assumed as SAB Shown in Fig.8.

1. Line SA is vertical and straight; point A is 2cm from the wall in the model

2. Line AB is a logarithmic spiral, and intersects horizontal lines: at an angle  $90^\circ$  at A, and at an angle  $(90^\circ + \frac{\pi}{2})$  at B.

The centre of the logarithmic spiral is O in Fig.8.

Then, the vertical stress distribution on AR is treated as a surcharge, S, which can be considered in the three different ways.

Way-① full vertical stress just above AR (corresponding to the self weight of block SARQ)

Way-② reduced by the frictional resistance on both sides, SA and QR (Arching effect)

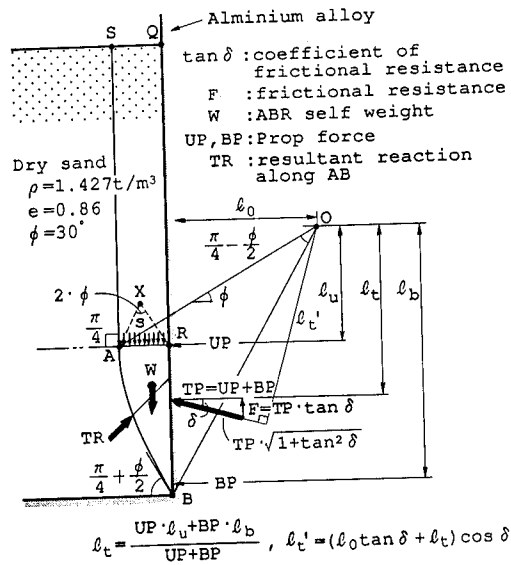


Fig.8 Assumed sliding mass (test K-1) (based on experimental observation)

Way-③ Self weight of triangle ARX; the vertical angle at X is  $2 \cdot \phi$  and this triangular mechanism is based on a suggestion by Atkinson and Potts (1977). (Arching effect)

In considering the clockwise and counterclockwise moments about the logarithmic spiral centre O, the moment by TR is zero because the vector TR is directed toward the centre O. The clockwise moment deduced using the load cell measurement in test K-1 is compared with counterclockwise moments calculated from the possible surcharge on AR in Table 4.

Although, there might be some errors, Table 4 implies that before rotation, at the active state, prop forces might be predicted by considering the full self weight of sliding mass SABQ; the prop

Table 4 Moments about the logarithmic spiral centre O (test K-1) (N·cm/cm in the model)

Clockwise (using measured prop force and calculated from: $TP/\sqrt{1+\tan^2\delta}\cdot l_c'$ )		Counterclockwise		
		Self weight W	Assumed surcharge	Total
Before rotation	221	59	Way-① 202	261
At Sliding	56		Way-② 75	134
			Way-③ 14	73

forces just before or at sliding is smaller than those obtained by taking arching effects into account; clearly substantial arching must be taking place.

## 6. CONCLUSIONS

This paper investigated the earth pressure change due to rotational displacement below the lowest prop level of a retaining wall. The earth pressure change was assumed to be caused by the lack of resistance in passive soil because of excess excavation, soil softening and so on.

Finite element analyses and centrifuge tests indicate the following.

1. The reduction of earth pressure due to wall rotation about the lowest prop occurs at and below the centre of rotation. The reduction is large and sudden and occurs immediately after the rotation starts.

In contrast, above the lowest prop level earth pressure tends to increase. This should be taken into account when considering safety against rotational failure; a greater prop capacity may be required.

2. The rotational displacement increases, the point at which the resultant earth pressure acts tends to rise in the vicinity of the hinge.

3. In the zone obtained by rotational failure, below the lowest prop level, arching effects can be considerable and should be taken into account.

In practice, the sliding mass is considered to predict the earth pressure against the rotating part of the wall; based on experimental observations, it was approximated by the zone enclosed by: the ground surface, the retaining wall, the logarithmic spiral from the wall toe and the vertical straight line connecting the spiral to the surface.

To better define this zone, it still remains how to determine the point at which the logarithmic spiral and the vertical straight line meet.

## ACKNOWLEDGMENT

This study was carried out at Geotechnical Engineering Research Centre, City University.

The authors would like to express their appreciation to Prof. J.H. Atkinson and Dr. B. Simpson for their advice and suggestions.

The support and technical assistance of members of the G.E.R.C. is gratefully acknowledged.

## REFERENCES

- Atkinson, J.H. & Potts, D.M. (1977); Stability of a shallow circular tunnel in cohesionless soil, *Geotechnique* 27, No.2, 203~215.
- Potts, D.M. & Fourie, A.B. (1986); A numerical study of the effects of wall deformation on earth pressures, *International Journal for Numerical and Analytical Methods in Geomechanics*, Vol.10, 383~405.
- Simpson, B. (1992); Retaining structures: displacement and design, *Geotechnique* 42, No.4, 541~576.
- Terzaghi, K. (1943); *Theoretical soil mechanics*. New York: Wiley, 66~76

## Modeling the stress history of Pisa clay

Mariacristina Pepe  
Technical University, Torino, Italy

Raffaele Renzi  
ISMES, Bergamo, Italy

**ABSTRACT:** The centrifuge potentiality in the reproduction of a natural deposit stress history is presented. A procedure is proposed to evaluate the maximum pressure, actually experienced by specimens, by interpreting load test results. The obtained yield stresses are in good agreement with the maximum past pressures induced by the consolidation process. As far as the reproduction of Pisa site conditions is concerned, the reliability of the soil model is checked by comparing model stress history with that of the natural deposit and by performing a cone penetration test. Measured tip resistances are very similar to the values recorded in the real deposit.

### 1 INTRODUCTION

This note presents results of a research undertaken to develop a procedure to model the Leaning Tower of Pisa site conditions. The study was conducted using the ISMES Geotechnical Centrifuge, which is described by Baldi et al. (1988).

The preparation of specimens, the application of the stress history and the response of models during vertical loading by means of a shallow circular foundation are described. Load test results are used to evaluate the stress history actually experienced by specimens, which is compared with the stress history of the natural deposit.

### 2 SOIL FOUNDATION CHARACTERISTICS

Figure 1 shows the profile of soil formations underlying the Leaning Tower of Pisa. The layer thickness remains more or less constant beneath the Tower foundation and the boundaries are essentially horizontal.

For modeling purposes, a scaling factor of 125 was adopted, allowing to model 40 m of soil thickness. The soil profile was subdivided in 4 formations:

formation 1 representing the superficial part of horizon A, consisting of slightly clayey and sandy yellow silt with interbedded lenses of sand and clay;

formation 2 representing the medium uniform grey sand layer located at the

bottom of horizon A;  
formation 3 representing the clayey layers B1 and B2;  
formation 4 representing layers extending below elevation -22.5 m, msl.

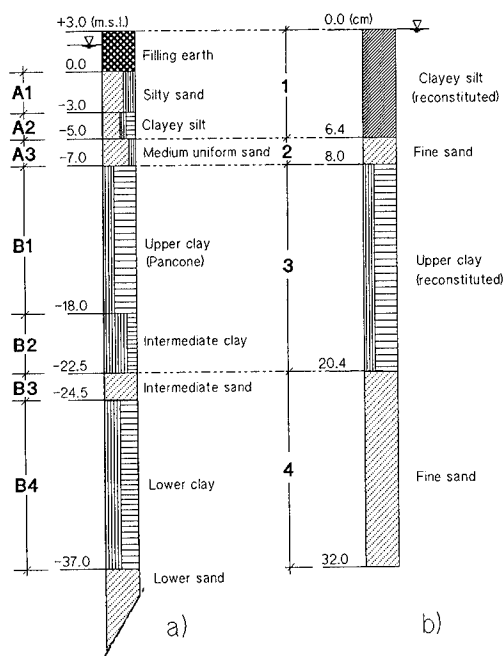


Fig.1 Soil profile: a) Field conditions  
b) Centrifuge model



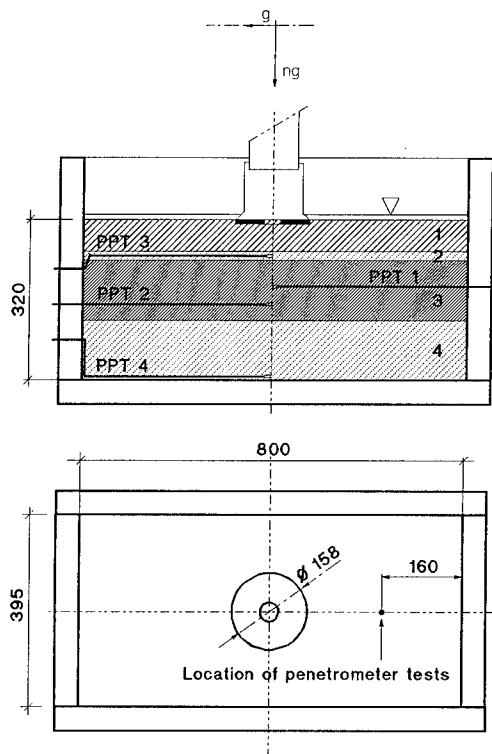


Fig.2 Model geometry

To prepare the afore-mentioned formations were used:

- a low plasticity clayey silt for formation 1
- the natural "Pancone" clay for formation 3
- a medium fine sand for formation 2 and 4.

The scaling factor of 125 was also used to model the 19.58 m diameter of Tower foundation by a 158 mm diameter rigid plate. The plate was located centrally on the soil model surface, at a depth of 12 mm. This aimed to reproduce the original position of Tower foundation, assumed to be 1.5 m below ground surface.

The soil model was retained within a rectangular container, having internal length and width equal to 800 and 395 mm, respectively (see figure 2). Its wall has holes to allow the installation of miniature pore pressure transducers. Holes also exist in the base to allow drainage of the specimen. The walls were coated with teflon to minimize the sidewall friction.

The soil model preparation includes the following procedures:

1. A 130 mm dry uniform sand layer is

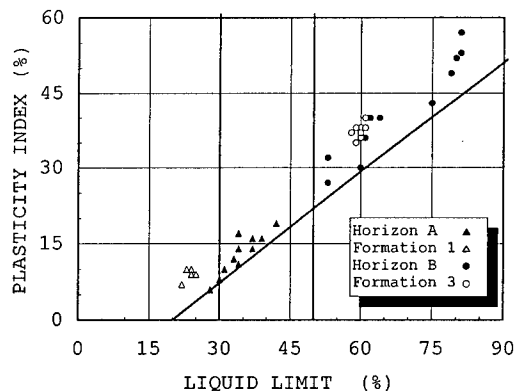


Fig.3 Casagrande's plasticity chart

pluviated into the test container and filled with deaired water. It is then covered with a filter paper. A pore pressure transducer (PPT4 in figure 2) is buried beneath the layer.

2. Clay layers are reconstituted from slurries, by adding dry powder to tap-water, step by step, in order to avoid the formation of clots. Once the appropriate amount of powder has been poured, slurries are mixed for about 2 hours under a vacuum of an atmosphere. The resulting slurries have a final water content that is about twice the liquid limit, in the case of clayey silt, and 1.5 times the liquid limit in the case of clay. Just after mixing, the clay slurry is placed into the test container through a tube. An unconsolidated specimen height of 210 mm is necessary to achieve a 124 mm thick clay layer. The clayey silt slurry is placed into a consolidometer having the same dimensions of the test container. Figure 3 shows the Casagrande's plasticity chart for formation 1 and 3.

3. Clay and clayey silt slurries are consolidated step by step until a uniform vertical effective stress of 50 and 300 kPa, respectively, are reached. Top and bottom drainages are allowed during consolidation. Figure 4 shows typical records of clay slurry settlement under the 50 kPa effective stress. The initial heights ( $H_0$ ) of the three specimens considered are also quoted.

4. Free water is removed from the top of the clay specimen. Base drains are closed and the vertical stress reduced to 0 kPa. The sand layer simulating layer A2 is pluviated into the test container and then filled with deaired water. A pore pressure transducer (PPT3 in figure 2) is buried into the layer.

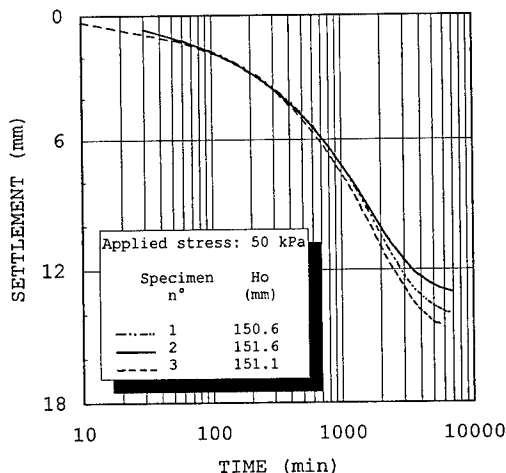


Fig.4 Records during the 50 kPa step of 1g consolidation

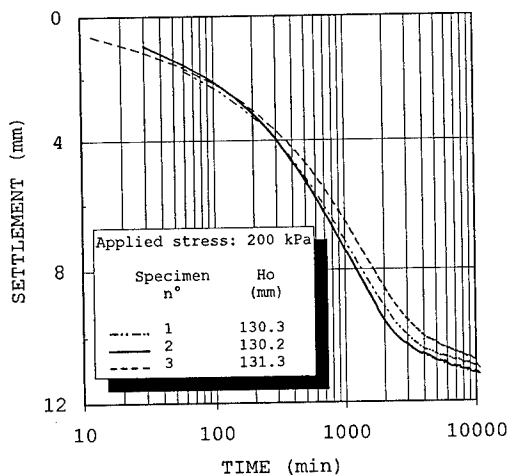


Fig.5 Records during the last step of 1g consolidation

5. At the end of the 300 kPa loading increment, the clayey silt specimen is allowed to swell under 100 kPa for 1 day. Free surface water is then removed, base drains closed and the vertical stress reduced to 0 kPa. Lateral walls of the consolidometer are removed. The upper part of the specimen is trimmed to have the appropriate height and the layer is transferred into the test container via a steel plate and a vacuum pump.

6. Two pore pressure transducers are inserted into the clay layer (PPT1 and PPT2 in figure 2).

7. The vertical load on the specimen is increased until a uniform vertical stress

of 200 kPa is reached. The loading schedule is given in Table 1.

Table 1: Preconsolidation phase  
- Loading schedule -

Step	Applied stress kPa	duration days
1	25	1
2	50	1
3	100	3
4	200	7

Figure 5 shows typical records of settlement under the last step of 200 kPa. Again the initial heights (H<sub>0</sub>) of the three specimens considered are quoted.

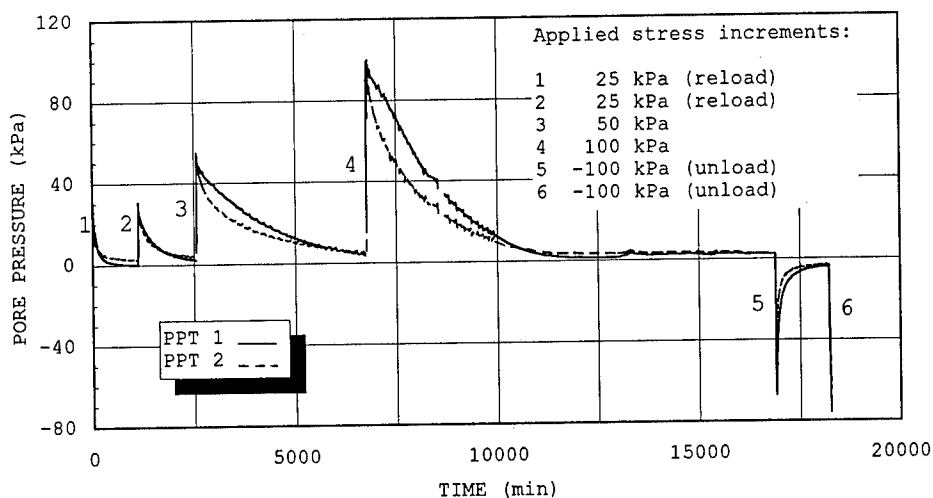


Fig.6 Pore pressure records during 1g consolidation

8. The specimen is unloaded in 2 steps: the vertical stress is reduced from 200 kPa to 100 kPa, letting the specimen swelling under the vertical stress of 100 kPa for 1 day. Free surface water is then removed, base drains are closed and the vertical stress is reduced to 0 kPa. Typical records of pore pressure measurements from PPT 1 and PPT 2 during loading and unloading steps are shown in figure 6.

9. The rigid plate is founded 12 mm below the specimen surface. Tap-water is added until 20 mm of standing water are reached. The test package is arranged and the centrifuge started within 6 hours from the specimen unloading to 0 kPa, to minimize the clay layer swelling.

### 3 CENTRIFUGE TESTING

Tests were performed at a rotational velocity equal to 242 rpm. The magnitude of the imposed gravitational field was 125 g at the radial distance of 1906 mm from the axis of rotation, i.e. 6 cm below the model surface.

A reaction frame, supporting an actuator to apply load and a miniaturized piezocone, was mounted on the test container. During in-flight reconsolidation the piezocone tip was maintained above the soil specimen. Piezocone location is provided in figure 2.

The sequence of the adopted operations is summarized as follow:

1. Full reconsolidation of the specimen under its own weight.

2. Execution of a cone penetration test and subsequent wait for the dissipation of penetration pore pressure with the piezocone withdrawn to its initial position. Penetration rate equal to 2 cm/s was adopted.

3. Application of a vertical load equal to about 6 kN in 168 minutes.

4. Wait for a period of time equal to about 15 hours. Complete dissipation of loading induced pore pressures takes place during this period.

At the end of tests, just after stopping the centrifuge, free water is removed from the top of the specimen and samples are taken at different heights in order to determine the final water content.

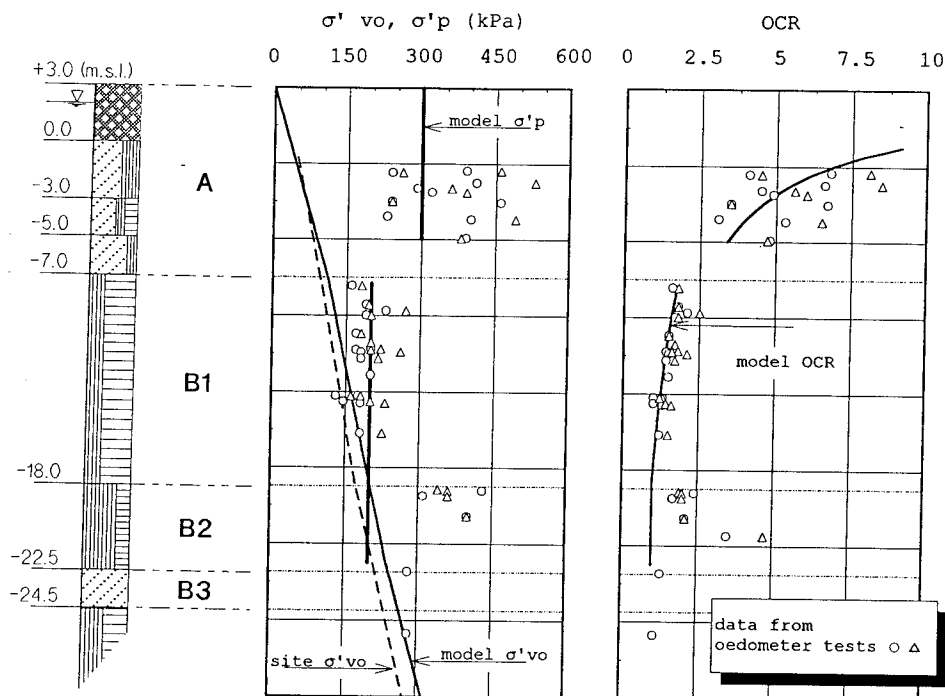


Fig.7 Stress history of cohesive layers

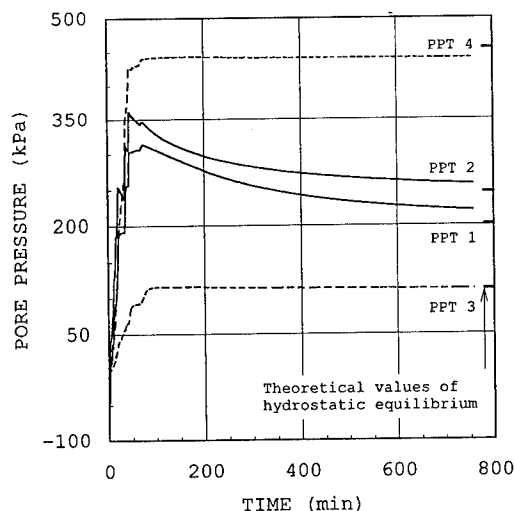


Fig.8 Pore pressure decay during centrifuge reconsolidation

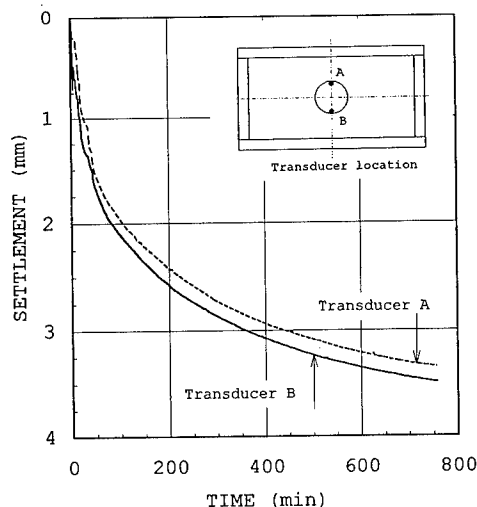


Fig.9 Specimen settlement during centrifuge reconsolidation

#### 4 REMARKS

As far as the reliability of the model is concerned, in figure 7 the model maximum pressures and the values of preconsolidation pressure  $\sigma'_p$  obtained from oedometer tests on piston samples from horizon A and B (open points) are compared. The values of overconsolidation ratio  $OCR = \sigma'_p / \sigma'_{vo}$  have been computed referring to the values of the effective overburden stress, whose trend versus depth is shown in the same figure.

Figure 8 shows the pore pressure transducer measurements. The centrifuge speed was increased in 25 g steps to the test acceleration of 125 g. The degree of consolidation achieved at any point where the pore pressures were measured was about 95%. Theoretical values of pore pressure at the end of consolidation are indicated in figure.

Figure 9 shows the specimen settlement during this phase.

Typical records of tip resistance and pore pressure profiles are provided in figure 10.

Figure 11 shows a typical record of pore pressure variation during the loading phase and the subsequent dissipation. Pore pressure measurements have been interpreted in order to obtain the preconsolidation pressure, by using the following procedure (see also Leroueil et al. (1990)):

1. If the excess pore pressure is plotted versus the pressure applied at the surface, the expected trend should be

linear until a first yield is obtained.

2. According to this statement, a break point is so defined in figure 12.

3. By evaluating through the theory of elasticity the induced total vertical stress, corresponding to the break point, the vertical effective stress increment at yield can be computed:

$$\Delta\sigma'_v (\text{yield}) = \Delta\sigma_v - \Delta u$$

4. Finally, the yield stress should be:

$$\sigma'_y = \sigma'_{vo} + \Delta\sigma'_v (\text{yield})$$

The obtained results are reported in Table 2, where a comparison with the maximum past pressure  $\sigma'_p$  induced by the consolidation process is also shown.

Table 2: Maximum past pressures induced by consolidation process

Test	PPT	$\sigma'_{vo}$ kPa	$\Delta q$ kPa	$\Delta\sigma_v$ kPa	$\Delta u$ kPa	$\Delta\sigma'_v$ kPa	$\sigma'_y$ kPa	$\sigma'_p$ kPa
1	1	169	182	64	57	7	176	200
	2	206	180	45	43	2	208	200
2	1	174	150	51	45	6	180	200
	2	212	140	33	24	9	221	200
3	1	178	145	47	37	12	190	200
	2	215	144	33	27	6	221	200

The difference between the computed and the expected values is within 10%. This result emphasizes the potentiality of the above procedure, and, at the same time, the reliability of the soil model preparation technique.

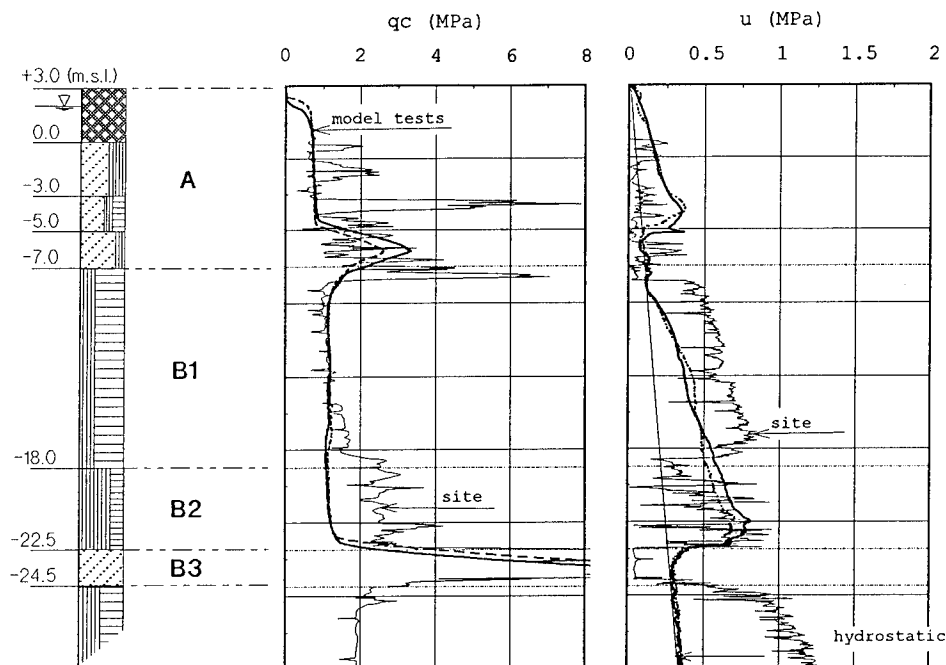


Fig.10 Tip resistance and penetration pore pressure profiles

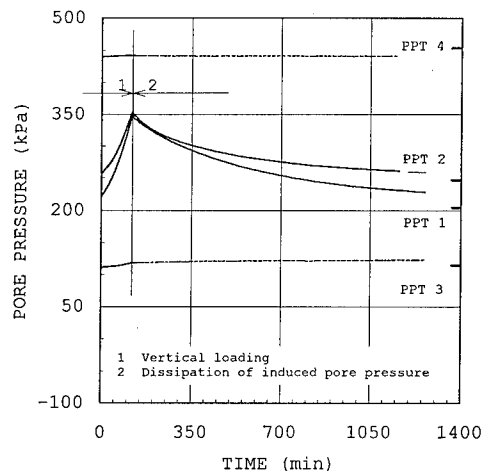


Fig.11 Pore pressure records during loading phase and subsequent dissipation

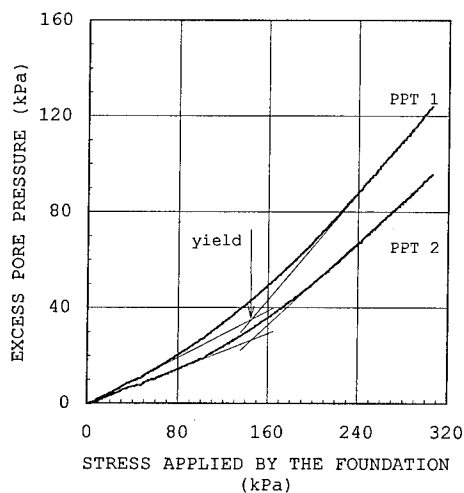


Fig. 12 Definition of yield stress  $\sigma'_y$

#### REFERENCES

- Baldi G., Belloni G., Maggioni W. 1988. The ISMES geotechnical centrifuge. Centrifuge 1988. Cortè (ed). Rotterdam, Balkema.
- Jamiolkowski M., Lancellotta R., Pepe M.C. 1993. Leaning Tower of Pisa - Updated information. Proceedings of 3rd Conference on Case Histories in Geotechnical Engineering. St. Louis.
- Leroueil S., Magnan J.P., Tavenas F. Embankments on soft clays. 1990. Ellis Horwood.
- Ministero dei Lavori Pubblici. 1971. Ricerche e studi su la Torre pendente di Pisa e i fenomeni connessi alle condizioni di ambiente. 3 vol. I.G.M.

## Experiment and analysis of earth pressure on an axisymmetric shaft in sand

T. Fujii

*Nishimatsu Construction Co., Ltd, Tokyo, Japan*

T. Hagiwara

*Department of Civil Engineering, Gunma University,  
Japan*

K. Ueno

*Department of Civil Engineering, Utsunomiya University,  
Tochigi, Japan*

A. Taguchi

*Fukushima Prefectural Office, Japan*

**ABSTRACT :** A series of centrifuge model tests was carried out at 100 G in an attempt to evaluate earth pressures acting on the lining of an axisymmetric shaft in a dry sand. Earth pressures were measured at rest and during the process of shaft wall movement of up to a 2 mm horizontal displacement. An axisymmetric elasto-plastic FEM was performed to compare with the experimental observations. It was found that present design codes overestimate the earth pressures at deeper positions and the calculated earth pressure distribution coincides well with the measured one for the prototype depth of up to 20 m.

### 1 INTRODUCTION

As demand increases for underground space, circular shafts have been adopted because of its structural advantages against external force. The earth pressures given by two-dimensional Coulomb and Rankine theories are generally used in present design codes because of their simplicity. Up to now, several theories have been proposed to calculate the earth pressures on vertical shafts and an excellent review was made by Prater(1977). However, these theories are based on idealized, rigid plastic soil behaviour and more realistic stress-strain behaviour of the material has not been considered. Beresantsev(1958) applied the Sokolovski 'step-by-step' method for the limit equilibrium plane strain problem with axial symmetry. The results of Beresantsev give smaller earth pressures compared with those based on Rankine's two-dimensional theory at deeper points.

On the other hand, a series of centrifuge tests was performed to study the behaviour of deep, vertical shafts in a dry sand by Lade et al.(1981). It was clear that the horizontal earth pressures measured in the model tests were smaller than Rankine's active earth pressures and larger than those obtained by Beresantsev's formula. Centrifuge model tests by Konig(1991) showed that an arching effect affects the three dimensional stress redistributions around unsupported excavations during shaft construction.

It was indicated that the classical theories

based on two-dimensional models overestimate the earth pressures acting on an axisymmetric deep shaft. However, field data, and experimental and analytical studies on an axisymmetric deep shaft are very limited and the design procedures for the earth pressures of deep shafts have not been well established to date.

This paper describes the results of centrifuge model tests to clarify earth pressures acting on an axisymmetric deep shaft lining in a dry sand. Interpretation of the results is presented and compared with an axisymmetric elasto-plastic FE analysis and Beresantsev's formula.

### 2 CENTRIFUGE TESTS

The centrifuge used in this series of tests is a balanced beam centrifuge at Utsunomiya University. The centrifuge has an effective radius of 1.18 m and specifications of the centrifuge are summarized in Table 1.

The soil container used was a strong rectangular box made of steel plates, of which internal dimensions are 262 mm wide, 498 mm long and 299 mm deep. All data returning via the centrifuge slip rings (20 poles) were recorded at constant intervals in a personal computer through a data logger. The prototype displacement mode induced around the axisymmetric shafts during execution is considered to be perfectly axisymmetric as shown in Fig. 1(a). However, this mode is very difficult to model experimentally.

Table 1 The specifications of the centrifuge

Effective radius	1.18 (m)
Max. acceleration	120 (G)
Max. pay load	150 (kg)
Variable speed motor	11 (kW)

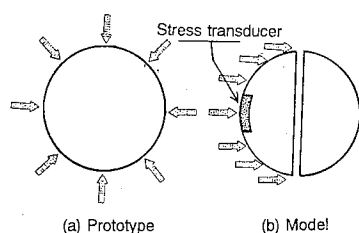


Fig. 1 Displacement mode of an axisymmetric shaft

As a first approximation, the authors attempted to simulate the displacement mode shown in Fig.1(b) during this study.

The model vertical shaft was made in the form of a cylinder and was constructed by aluminum, as shown in Fig.2. The model shaft consisted of two semi-cylinders to allow one of the semi-cylinders to move horizontally. The shaft was 360 mm high and had a diameter of 60 mm. The thickness of the shaft was 25 mm and the stiffness of the shaft was considered to be rigid. Five small size stress transducers (24 mm width  $\times$  10 mm height) capable of measuring horizontal earth pressure were embedded in the shaft at 50 mm intervals. The earth pressures were measured near points perpendicular to the direction of the shaft lining movement to simulate the earth pressures of prototype. The surface shape of the transducers has the same curvature as the surface of the shaft (see Plate 1). From the results of the surface measurements by a roughnessmeter, the maximum height of the surface profile was  $3 \mu\text{m}$ . The surface of the shaft is considered to be a smooth condition. The maximum capacity of the transducers was 147 N. The sand used was air-dried Toyoura sand ( $D_{50}=0.18 \text{ mm}$ ) and physical properties are summarized in Table 2.

Fig.3 shows a schematic illustration of the test system in which the model shaft is set up in the model sand layer. Centrifuge test procedures were generally as follows:

The model shaft was placed vertically on the base plate of the container. The soil was placed by means of air pluviation. The pouring height

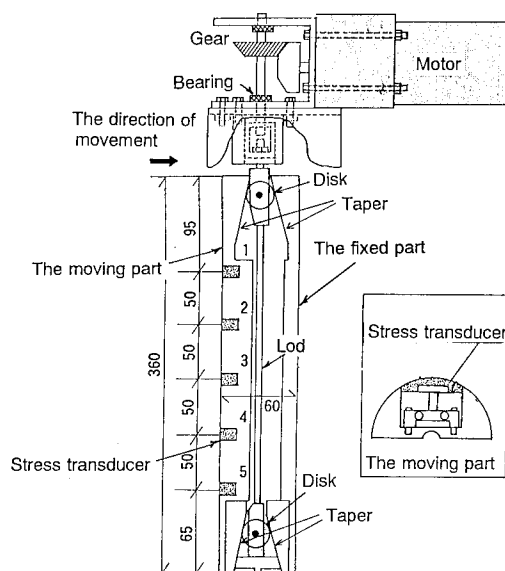


Fig. 2 Model shaft

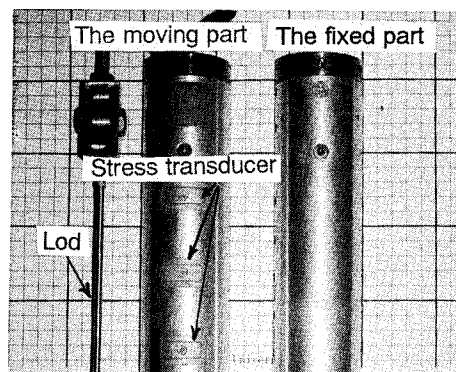


Plate 1 Model shaft

was maintained at 750 mm for the dense sample ( $Dr=70\%$ ) and 50 mm for the loose sample ( $Dr=10\%$ ). The height of sand layer was chosen to be 200 mm due to restrictions on the maximum capacity of the package. The centrifuge was accelerated to 100 G in about ten minutes while measuring the change in the earth pressures at 10 G intervals. A prototype shaft with a diameter of 6 m and a length of 20 m was modeled.

The horizontal displacement of the shaft lining was imposed by a geared motor. As the rod moved downward by operating the motor, one side of the shaft lining moved inward through contact between the disks and the tapers shown in Fig.2.

Table 2 Physical properties of Toyoura sand

Specific gravity	G <sub>s</sub>	2.66
Maximum void ratio	e <sub>max</sub>	0.98
Minimum void ratio	e <sub>min</sub>	0.60
D <sub>50</sub> (mm)		0.18
Uniformity coefficient	U <sub>c</sub>	1.52

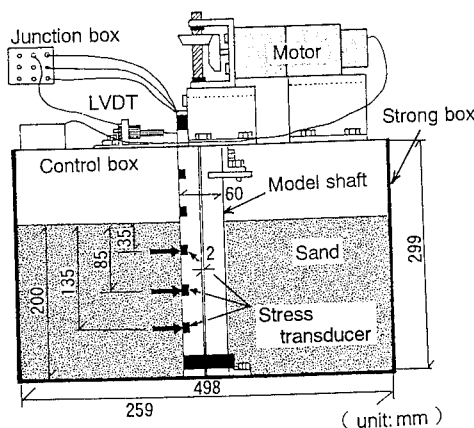


Fig. 3 Test system

A uniform movement was achieved from top to bottom of the shaft. The displacement of the moving part of the shaft lining was conducted with a constant rate of 1.30 mm per minute to produce the change of earth pressure from  $K_0$  state to the active state. The earth pressures at rest and during wall movement of up to 2 mm horizontal displacement of the shaft were measured at three locations on the shaft lining. Horizontal movement of the top of the shaft lining was measured by an LVDT. Four centrifuge tests were conducted in dense ground and 2 tests in loose ground to examine the effect of soil density. In addition, the centrifuge model tests were performed to investigate the influence of the wall friction of the shaft. The model shaft was roughened with sand paper and a condition of  $15.5^\circ$  as the value of the angle of wall friction ( $\delta$ ) was modeled.

### 3 ANALYSIS

An analysis was carried out to verify the test results using an FE program with an elasto-plastic model. Fig.4 shows the FE mesh ( $H/r = 6.66$ ,  $H$ : the depth of sand layer,  $r$ : the radius of the shaft, the element number:64, the nodal number:531). In the present analysis, the

movement mode of the shaft lining was modeled as an axisymmetric problem. Finite elements used are iso-parametric rectangular elements consisting of 20 nodal points. Eight Gauss points were used for numerical integration. The geometrical size and boundary conditions are identical to the model tests, namely the side wall of the strong box (B-B' surface) and the base(A'-B' surface) are smooth, as shown in Fig. 4.

The Mohr-Coulomb failure criterion was applied to the soil and the Drucker-Prager failure criterion was used as the plastic potential for the soil. The calculation was carried out under the associated flow rule that the dilatancy angle ( $\psi$ ) for the plane strain condition coincides with the internal friction angle( $\phi$ ). The displacement mode from  $K_0$  state to the active state was simulated by the horizontal displacement of nodes of the AA'C'C section of up to 2 mm in 2000 steps. The earth pressures were evaluated by the Gauss points of elements (①-⑧ shown in Fig. 4). The material properties and input parameters for the analysis are listed in Table 3. The internal friction angles of the model

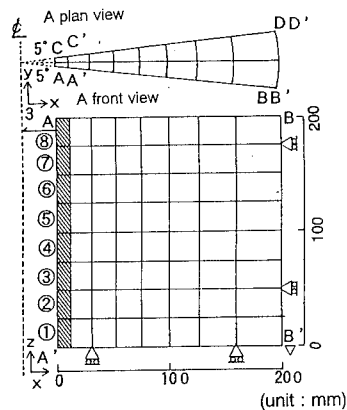


Fig. 4 Finite element mesh

Table 3 The material properties and input parameters for the analysis

Soil density	Dr(%)	70	10
Modulus of elasticity	E (kN/m <sup>2</sup> )	19600	4900
Poisson ratio	$\nu$	0.375	0.375
Unit weight	$\gamma_s$ (kN/m <sup>3</sup> )	14.90	13.43
Internal friction angle (triaxial test)	$\phi$ (°)	42.0	34.0
Coefficient of earth pressure at rest	$K_0$	0.33	0.44



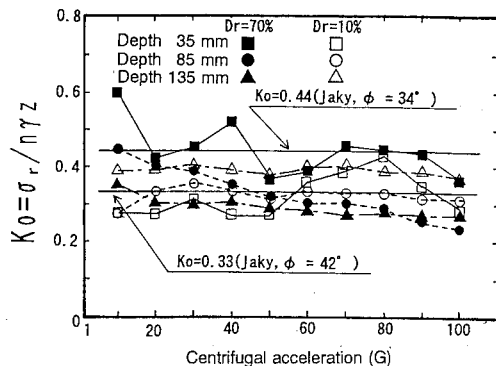
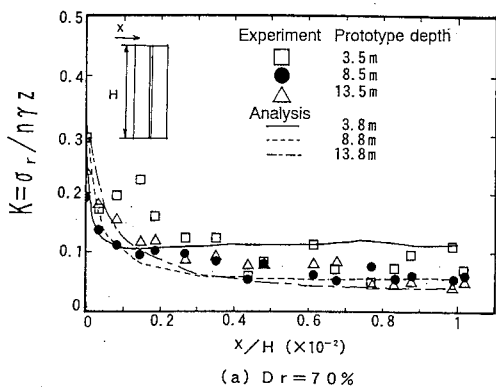
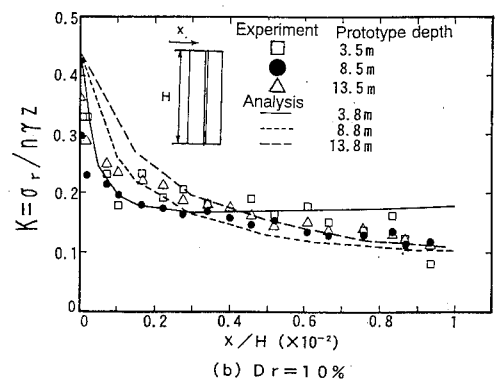


Fig. 5 Change in  $K_o$  with increasing centrifugal acceleration



(a)  $Dr = 70\%$



(b)  $Dr = 10\%$

Fig. 6 Change in  $K$  with movement of shaft lining

ground were taken from the test data of triaxial compression tests of the Toyoura sands. The coefficient of earth pressure at rest ( $K_o$ ) was determined according to Jaky's equation.

## 4 TEST RESULTS AND DISCUSSION

### 4.1 Coefficient of earth pressure at rest ( $K_o$ )

According to the results of the centrifuge tests, which give the centrifugal history for the homogeneous model sand layer, the centrifugal history has been found to be strongly affected by the stress state of the model ground. The centrifugal history means the change of the stress in the model ground due to the acceleration and deceleration of centrifuge. It was reported that the values of  $K_o$  in the model ground decrease with depth in centrifuge tests.

Fig. 5 shows the change of the coefficient of earth pressure at rest ( $K_o$ ) with centrifugal acceleration. In the case of dense ground ( $Dr=70\%$ ),  $K_o$  decreases with the centrifugal acceleration and at the 100 G stage  $K_o$  approaches 0.33, which is similar to the value given by Jaky's equation. The values of  $K_o$  at deeper positions such as at depths of 85 mm and 135 mm equal Jaky's results at a lower G-level, which is at about 20 G.

On the other hand, the results of loose ground ( $Dr=10\%$ ) are smaller than that of Jaky's equation, independent of the depth and the centrifugal acceleration. This is because the loose ground has more complicated centrifugal history than the dense ground.

### 4.2 The change of $K$ with the movement of shaft lining

Figs.6(a),(b) show the change of  $K (= \sigma_r / n \gamma z, \sigma_r$ : the measured horizontal earth pressure,  $n \gamma z$ : the overburden stress) with the displacement of the shaft lining. The general trend of the experimental values appears to agree well with the analytical results. The values of  $K$  are constant at strain level in the vicinity of  $x/H = 1 \times 10^{-2}$ . Earth pressures at this strain level are considered to be almost at the active state as determined from these figures.

### 4.3 The distribution of active earth pressure ( $K_a$ )

The comparison between the observed and the computed active earth pressures is shown in Fig. 7 where normalized earth pressures  $\sigma_r / n \gamma z$  are plotted versus normalized depth  $z/r$  together with Beresantsev's results. Beresantsev(1958) derived the simplified formula for evaluating stresses acting on a vertical cylindrical surface:

$$\sigma_r = r \gamma \frac{\sqrt{K_a}}{\lambda - 1} \left[ 1 - \left( \frac{r}{r_b} \right)^{\lambda - 1} \right] + q \left( \frac{r}{r_b} \right) + c \cot \phi \left[ \left( \frac{r}{r_b} \right)^{\lambda} K_a - 1 \right]$$

where

$\sigma_r$ : earth pressure

$r$ : radius of the shaft

$\gamma$ : unit weight

$c$ : cohesion

$q$ : surcharge pressure

$$K_a = \tan^2 (45^\circ - \phi/2)$$

$$r_b = r + z \sqrt{K_a}$$

$$\lambda = 2 \tan \phi \tan (45^\circ + \phi/2)$$

The straight solid line  $K_0$  in each figure indicates the initial distribution of horizontal earth pressure at rest calculated as  $K_0=0.33$ ,  $K_0=0.44$  and the straight dash-dotted line  $K_a$  is the distribution of Rankine's active earth pressure by using  $\phi=42^\circ$  and  $\phi=34^\circ$ .

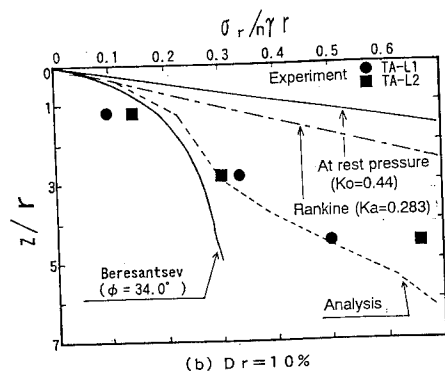
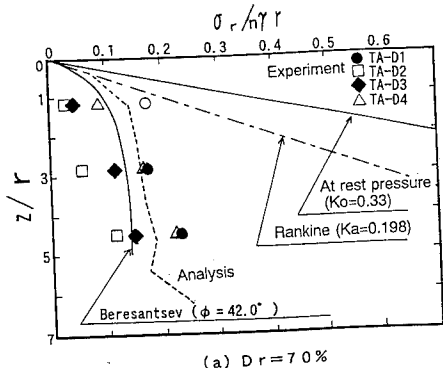


Fig. 7 Comparison of normalized horizontal earth pressure distributions

It appears from this comparison that the earth pressures measured are smaller than Rankine's active earth pressures and the difference between experimental and Rankine's two-dimensional results comes to be greater at the deeper points. The reason may be that the redistribution of stress at the deeper points is made by means of the arching effects which develop with the movement of the shaft lining. The results of the loose ground are somewhat different from those of the dense ground. In the case of the loose ground, both the numerical and experimental active earth pressures increase with depth at deeper positions and they are larger than those of Beresantsev. In all the cases of the experimental and analytical results, the earth pressures substantially increase near the bottom of the shaft. It appears from Fig.7 that these results are higher than those calculated from Beresantsev's formula. Lade et al.(1981) also showed similar data from centrifuge model tests on deep shaft models.

It should be noted that it was very difficult to model the bottom condition of prototype shafts because of the complexity of the boundary conditions and execution process in the field. Further research concerning this problem should be undertaken. It was seen from Figs. 7(a),(b) that both the measured and calculated earth pressure distributions coincide well with those calculated from Beresantsev's formula for axisymmetric shafts to a certain depth.

#### 4.4 Influence of wall friction of the shaft

Fig.8 shows the observed pressure distributions for the cases of friction angle  $\delta = \phi$ ,  $\delta = 2/3 \phi$  and  $\delta = 0^\circ$ . The results of experimental earth

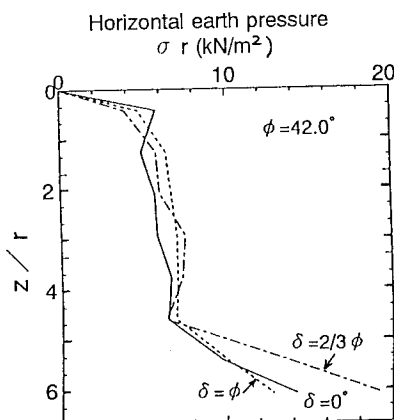


Fig. 8 Influence of wall friction of the shaft in Analytical results

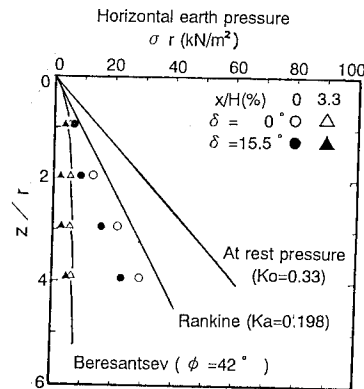


Fig. 9 Influence of wall friction of the shaft in Experimental results

pressure distributions are roughly constant regardless of the wall friction of the shaft lining.

An FE analysis considering the influence of wall friction of the shaft was performed. The FE mesh in Fig.4 was used. Thin elements were placed on the front of the elements (①~⑧ in Fig.4) to consider the influence of the wall friction. Wall friction of the shaft was modeled by the change of material parameter at these elements. The values of wall friction angle on the shaft were changed so that  $\delta = 42^\circ$ ,  $28^\circ$  or  $0^\circ$ .

It was assumed that the results in Fig. 7 are suited to the case of  $\delta = 0^\circ$ . Fig.9 shows the computed pressures distributions for the cases of  $\delta = 42^\circ$ ,  $28^\circ$  and  $0^\circ$ . While the results have some scatter at the bottom, the results describe well the tendency that the earth pressure distribution is little affected by the wall friction. In the case of two-dimensional active earth pressure, it has been indicated that the effects of the wall friction angle can be practically neglected. Sokolovski(1960) also showed similar solutions on the basis of the theory of plasticity.

Consequently, it can be concluded from Fig. 8 and Fig.9 that the shape of horizontal earth pressure distributions on an axisymmetric shaft is not much affected by the wall friction of the shaft as in the two-dimensional problems.

## 5 CONCLUSIONS

A series of centrifuge model tests was conducted and elasto-plastic FEM analyses were also performed. Because of the limitations of modeling techniques which may be used realistically in centrifuge models, it is not possible to apply the results directly to practical problems. However, the results can be used in the calibration of

numerical models and Beresantsev's formula can be compared against the results of the centrifuge tests. Then the test data can be used with greater confidence. Further, the followings can be concluded.

1. Centrifuge modeling techniques were successfully used for a study of earth pressure on the axisymmetric deep shaft. The earth pressure at rest and the active earth pressures on the axisymmetric shaft in sand were measured by the developed model shaft with small stress transducers.
2. The distributions of  $K_0$  change with increasing centrifugal acceleration due to the effect of the centrifugal history. The values of  $K_0$  under 100 G are consistent with the values based on the Jaky's equation in the case of dense ground.
3. Measured horizontal earth pressures from the  $K_0$  state to the active state agreed well with the analytical values from the elasto-plastic FEM and the Beresantsev's formula. It is assumed that a strain level of  $10^{-2}$  was sufficient to reach the active state in the case of the axisymmetric shaft.
4. The distribution of  $K_0$  with increasing centrifugal acceleration and the active earth pressure distributions under 100 G are affected by the relative density of the soil.
5. Two-dimensional Rankine active earth pressures overestimate the active earth pressures at the deeper positions on the axisymmetric shaft.
6. The active earth pressure distributions are only minorly affected by the wall friction of the shaft.

## ACKNOWLEDGEMENTS

The authors would like to express their appreciations to Professor O. Kusakabe, Hiroshima University, Professor K. Ugai, Gunma University, Mr. Y. Nomoto, Mr. K. Mito and Mr. M. Ishibashi, Nishimatsu Construction Co.,LTD. for their support and helpful discussion for improving the paper.

## REFERENCES

- Beresantsev, V.G. 1958. Earth pressure on the cylindrical retaining walls, Conference on earth pressure problems, Vol. II, Brussels : 21-27.
- Konig, D., Guttler, U. and Jessberger, H.L. 1991. Stress redistributions during tunnel and shaft constructions, Proc. of Centrifuge 91': 129-135.
- Lade, P.V., Jessberger, H.L., Makowski, E and Jordan, P. 1981. Modeling of deep shafts in centrifuge tests, Proc. 10th ICSMFE, Vol.1: 683-691.
- Prater, E.G. 1977. An examination of some theories of earth pressure on shaft linings, Canadian Geotechnical Journal 14: 91-106.
- Sokolovski, V. V. 1960. Statics of soil media, London: Butterworth.

## Study of sinkholes in weakly cemented sand

W.A. Abdulla & D.J. Goodings

University of Maryland, College Park, Md., USA

**ABSTRACT:** Sinkhole development in a profile with a weakly cemented sand overlain by an uncemented sand and underlain by a karst limestone is studied. The thirteen models tested have examined the interaction between the thickness of the cemented sand layer, the thickness of the uncemented sand overburden, and the size of the opening in the karst formation. The cemented sand failed as a plug, with soil strength calculated in a limit equilibrium analysis. The overburden pressure over the cavity at collapse was less than the geostatic overburden pressure, becoming less with increasing depth relative to size of the cavity opening and approaching some asymptotic value. The results compare favorably to predictions from work of other researchers.

### 1 INTRODUCTION

Sinkhole development causes enormous damage around the world, so much so that it is now the subject of an international United Nations cooperative study program. There are various geotechnical configurations which can lead to sinkhole development, and some of these have been the subject of analytical studies (see, for example, Ketelle et al., (1987)), 1g laboratory model studies (see, for example, Hodek, et al., (1984), and Chen and Beck (1989)), and centrifuge model studies (see, for example, Howell and Jenkins (1984), and Craig (1990)).

The mechanics of the sinkhole problem are related to undesired conditions of surface subsidence when an engineered underground cavity, such as a tunnel, collapses, and to desired granular flow, such as occurs in operation of silos. They exist in a variety of geotechnical configurations. In arid environments, one profile prone to sinkhole development involves sand overlain karst limestone bedrock. Evaporation pumping of a brackish ground water table in the sand can lead to development of a layer within the sand which is weakly cemented, overlain, in turn, by dry uncemented sand. If an entrance to a cavity develops on the surface of the bedrock, the weakly cemented sand may not be able to

bridge the opening, so that collapse into the cavity may occur, followed by subsidence in the uncemented sand. Such a condition has led, on occasion, to extensive damage in Kuwait, and this configuration is the subject of this research.

### 2 MODEL PREPARATION

Thirteen centrifuge models of sinkholes developing in a weakly cemented sand layer have been tested to date. Each model was constructed in an aluminum box which is 387.5 mm by 362 mm in area, and 324 mm in depth. The box was built with a false bottom, in which a circular opening was fabricated in the center to simulate the opening to a cavity at the top of the limestone bedrock. Below this opening is a space into which soil may flow. During model preparation, the circular opening in the false bottom of the model container was plugged to form a continuous horizontal base. This plug was removed after model preparation to allow soil to fall into the space below the opening during centrifuge testing.

The method of preparing the weakly cemented sand layer involved using type III Portland cement, following the techniques of Sitar et al. (1980) and Clough et al. (1981). This method

was used in preference to cementation by wax, natural salts, or lime, which Sitar et. al. (1980), Akili and Torrance (1981) and Poulus (1982) showed to be difficult to produce uniform and reproducible samples. Layers of dry Ottawa sand (ASTM C-109 : see Table 1), mixed with 2% (by weight of dry sand), type III Portland cement, and 8% moisture (by dry weight of sand) were compressed to build up the desired thickness of weakly cemented sand with a dry unit weight of the cemented sand of 16.2 kN/m<sup>3</sup>. The ratios of sand : water : cement were based on the experience of Clough et al. (1981). The box was then wrapped in plastic to prevent evaporation while the cement cured for five days, which is equivalent to 28 days curing of type I Portland cement. Finally, the model was dried at 70° C and the plug in the false bottom of the box was removed.

Table 1. Physical properties of Ottawa sand ( ASTM standard C-109)

Cu	2.6
D <sub>50</sub>	0.38 mm
$\gamma^1_{\max}$	17.75 kN/m <sup>3</sup>
$\gamma^2_{\min}$	15.63 kN/m <sup>3</sup>

(1) ASTM method (D-4253)

(2) ASTM method (D-4254)

In eight of the thirteen models a layer of the same Ottawa sand, but without cement, was pluviated onto the finished cemented layer using the double diffuser raining technique adopted by various researchers, such as Rad and Tumay (1986), and Eid (1987). The unit weight was 16.3 kN/m<sup>3</sup> (Dr=36%). A cross was then spray painted on the top finished surface of all models, with its center over the center of the opening to highlight the onset of surface subsidence.

The peak angles of friction measured in the direct shear apparatus for the sand at normal stresses between 25 kN/m<sup>2</sup> and 632 kN/m<sup>2</sup> were 32° for uncemented and 29° for cemented sand at dry unit weights of 16.3 kN/m<sup>3</sup> and 16.2 kN/m<sup>3</sup> respectively; the post peak angles of friction was 30° for both uncemented and cemented sand. The sand cemented with 2% Portland cement had a peak cohesion of 43 kN/m<sup>2</sup>. These values are similar to those

reported by Clough, et al. (1981), Rad and Tumay, (1986), and Acar and Al-Tahir, (1986) for their weakly cemented sands.

The indirect Brazilian test for tensile strength was conducted according to ASTM (D-4123), and showed tensile strength of 19 kN/m<sup>2</sup>. At 44% of peak cohesion, the tensile strength is well within the ranges expected according to Mitchell (1976) and Sitar et al. (1980).

After preparation, each model was loaded onto the University of Maryland geotechnical centrifuge (30,000 g-lb, 2.7 m diameter). The model was accelerated in increments holding each increment for one minute, and watching for sinkhole development before proceeding to the next level. Sinkhole development was sudden and easily identified on the overhead continuous video picture of the model surface in the ten models that collapsed. When surface subsidence was complete, the centrifuge was gradually stopped, and the geometry of the sinkhole was measured. Because it became useful to examine the plug of cemented soil after it had broken away from the original continuous layer of cemented sand, a sponge was placed, in models 7 through 13, 16 mm below the bottom of the cemented layer to catch the falling cemented plug before it hit and shattered on the base of the model box. One result of this was that in those models the surface subsidence of the uncemented sand overburden was often incomplete, however, it did not prevent sinkhole development.

The model geometries of the thirteen centrifuge models tested to date are summarized in Table 2. Collapse was sudden and clear in ten models at accelerations,  $N_g$ , shown in Table 2. Failure did not occur in three models, numbered 1,3 and 5. All the sinkholes formed were smaller in diameter than the box width so that side boundary effects were considered to be negligible.

### 3 RESULTS

Inspection of the collapsed portion of the cemented layer after testing in the ten models that failed revealed that the center part of the cavity roof, marked with a cross, failed as a single otherwise uncracked plug. The remaining uncollapsed portion of the cemented layer, encircling the circular cavity, did not, in general, have vertical sides but had, rather, an overhang,

Table 2. Geometries of centrifuge models

Model #	D <sup>1</sup> (mm)	Hc <sup>2</sup> (mm)	Hs <sup>3</sup> (mm)	$\gamma_s^4$ (kN/m <sup>3</sup> )	N <sub>f</sub> <sup>5</sup> (g)
5	38.1	9.5	57.2	16.45	>180 <sup>6</sup>
6	38.1	9.5	76.2	16.02	172
1	50.8	13.0	0.00	0.00	>141 <sup>6</sup>
2	50.8	13.0	82.1	16.51	98
3	50.8	12.7	160.3	16.30	>104 <sup>6</sup>
4	50.8	12.7	76.2	16.30	102
7	101.6	12.7	0.00	0.00	56
13	101.6	12.7	0.00	0.00	99
11	101.6	12.7	38.1	16.34	41
9	101.6	12.7	76.2	16.33	43
8	101.6	25.4	0.00	0.00	111
12	101.6	25.4	76.2	16.34	65
10	101.6	31.8	0.00	0.00	115

(1) D = cavity diameter.

(2) Hc = thickness of cemented sand layer.

(3) Hs = thickness of uncemented overburden cemented layer.

(4)  $\gamma_s$  = dry unit weight of uncemented overburden sand.

(5) N<sub>f</sub> = acceleration at failure.

(6) no failure occurred.

curving upward from the edge of the support at the bottom of the cemented layer into the cemented layer. Since the thickness of the cemented layers in the models were small, having a maximum thickness of 31.8 mm, a straight line approximation to the curved failure surface was made, as shown in Figure 1. The cemented sand overhang angles,  $\beta$ , in models without uncemented sand overburden varied between a maximum of 84° to a minimum of 24°, with an average of 54.7°. Models with uncemented overburden had steeper overhang angles, likely a result of the flow of the uncemented overburden past the weakly cemented sand overhang. The sinkholes in the uncemented overburdens were circular with an inclination,  $\alpha$ , ranging from 41° to 32°, close to post peak friction angle.

#### 4 ANALYSIS

There were two mechanisms in the development of these sinkholes. The first was the fallout of the plug of the cemented sand layer, and the second was the influence of the uncemented sand on loading that plug.

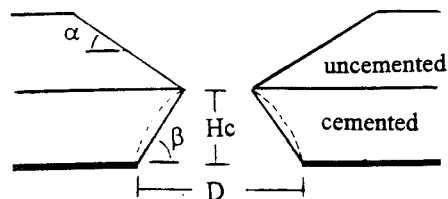


Figure 1. Sinkhole configuration in both cemented and uncemented sand layers.

#### 4.1 Failure in cemented sand

In considering the fallout of the plug of the cemented sand by itself, the mechanics of weak rocks over cavities is relevant. Stimpson and Ahmed (1991) examined two-dimensional collapse of rock strata over cavities with two center points of surface loading, and they identified collapse to be progressive and tensile in nature. Cracks developed at a point within the stratum, close to but not at the upper surface, which then propagated upward to the top surface at the points of the load application and downward toward the edge of the cavity. As the ratio of the width of the cavity became larger, relative to the thickness of the stratum, the cracks become more arched in shape (see Figure 2). Collapse occurred either when the cracks become continuous from the bottom to the top of the stratum, which was the case for thin cross-sections, or when the thin uncracked portion of the stratum above the arched crack pattern failed in compression, which occurred in initially thick cross-sections. A central vertical crack developed but did not reach the top surface. The collapses and failure surfaces

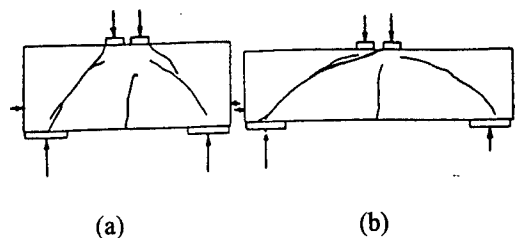


Figure 2. failure surface (a) thick section, (b) thin section.(after Stimpson and Ahmed, (1991))

observed in the three-dimensional failure surfaces in the weakly cemented sand in this work are similar to Stimpson and Ahmed's two dimensional observations. The variation of the slope angle of the failure surface reported could be attributed, then, to model geometry. Vertical cracks at the bottom center of the plug, observed by Stimpson and Ahmed, were not seen here.

A limit equilibrium analysis may be applied to the fallout of the plug. The self-weight of the plug at the point of failure,  $F_{dc}$ , is :

$$F_{dc} = \frac{\pi \left( D - \frac{Hc}{\tan \beta} \right)^2}{4} HcN\gamma \quad (1)$$

This will be equal at failure to the vertical component of the resisting force,  $F_{rc}$ , around the perimeter of the plug which is due to a function of the tensile strength,  $t$ , of the cemented sand layer, and some value of mobilized cohesion,  $c_m$ , that will be less than 43 kN/m<sup>2</sup>:

$$F_{rc} = \pi \left( D - \frac{Hc}{\tan \beta} \right) \frac{Hc}{\sin \beta} (t \cos \beta + c_m \sin \beta) \quad (2)$$

Here,  $D$  is cavity diameter,  $Hc$  is thickness of cemented sand layer,  $N$  is the collapse acceleration,  $\gamma$  is dry unit weight of the cemented sand,  $\beta$  is angle of cemented sand overhang taken to be the average value of 54.7°.

Models 7, 8, 10 and 13 failed with no uncemented overburden. Since the centrifuge permits observation and/or control of all aspects of failure, and if the tensile strength,  $t$ , of the cemented layer is taken equal to 19 kN/m<sup>2</sup>, then the mobilized cohesion becomes the only unknown in equations 1 and 2. In models 8, 10 and 13, corresponding values of  $c_m$  are 24.2 kN/m<sup>2</sup>, 23.4 kN/m<sup>2</sup> and 23.7 kN/m<sup>2</sup>, which are less than the peak cohesion as expected. With these values of  $t$  and  $c_m$ , model 1, with no uncemented overburden, and no failure for a maximum acceleration of 141g, is predicted to fail at 222g, which exceeds the capacity of the centrifuge. Model 7, however, identical in geometry to model 13 failed at just over half the acceleration at failure for model 13. In the absence of other test data thusfar, the result of this model is considered to be an outlier.

#### 4.2 Effect of overburden pressure over a cavity

In model tests where an overburden sand existed, the accelerations at collapse were less than those for otherwise identical geometries but without overburden, although, the calculated overburden pressure was less than a full calculated geostatic overburden. That observation is consistent with the findings of Atkinson and Potts, (1977), and of Ono and Yamada, (1993), although those studies involved collapse of tunnels along their full longitudinal axes brought on in models by reducing the model tunnel pressure at a constant self weight.

Having observed failure in models with no overburden, the limit equilibrium analysis can be used to calculate the loading from the uncemented overburden at failure. Averaging that loading over the area of the top of the plug, the vertical stress from that overburden,  $\sigma_z$ , is :

$$\sigma_z = \frac{4(F_{rc} - F_{dc})}{\pi \left( D - \frac{2Hc}{\tan \beta} \right)^2} \quad (3)$$

where  $F_{rc}$  and  $F_{dc}$  are calculated from equations 1 and 2 at the actual collapse accelerations for the tests with overburden, assuming  $\beta = 54.7^\circ$ ,  $t = 19$  kN/m<sup>2</sup>, and  $c_m = 23.8$  kN/m<sup>2</sup> ( the average for models 8, 10 and 13). The overburden stress ratio,  $R_{\sigma_z}$  of  $\sigma_z$  calculated in equation 3 compared to the full geostatic stress due to overburden ( $=N\gamma H_s$ ), are given in Table 3 for the six models failing with an uncemented overburden. Those ratios are plotted in Figure 3

Table 3. Model tests with overburden

Model #	Hs/D'	$R_{\sigma_z}$	D/Hc
5	2.3	<.17 <sup>1</sup>	4.0
6	3.1	0.14	4.0
2	2.5	0.32	3.9
3	4.9	<0.14 <sup>1</sup>	4.0
4	2.3	0.31	4.0
11	0.5	0.58	8.0
9	0.9	0.27	8.0
12	1.2	0.37	4.0

(1) no failure occurred.

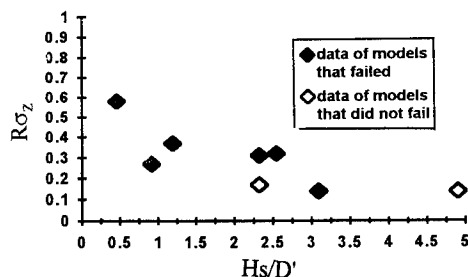


Figure 3. Effect of overburden over cavity at collapse.

as a function of a measure of the model geometry,  $Hs/D'$ , where  $D'$  = the predicted diameter of the opening at the top of cemented layer, or  $(D - (Hc/\tan\beta))$  where  $\beta = 54.7^\circ$ . Results from models 3 and 5, which did not fail, are also plotted on Figure 3 using different symbols from that used for other data. The position of those points indicate the upper most values of  $R_{\sigma_z}$  models 3 and 5 could have based on the assumptions stated for calculation of  $R_{\sigma_z}$ . As  $Hs/D'$  increases, indicating greater relative depth of overburden, the ratio  $R_{\sigma_z}$  decreases, likely approaching some asymptotic value.

Model 3 with  $Hs/D' = 4.9$  did not show collapse over the course of testing. Calculations of  $R_{\sigma_z}$  for that model showed a value of less than 0.14. Model 5, geometrically similar to model 4, but with all absolute dimensions (except particle size) equal to 75% of those in model 4, did not fail, so that  $R_{\sigma_z}$  calculated is less than 0.17. This may indicate the onset of grain size effects with the diameter of the cavity,  $D$ , equal to 100 grain diameters, although model 6, with identical grain size,  $Hc$ , and  $D$  did fail.

Such low values of  $R_{\sigma_z}$  indicate substantial arching is occurring in the overburden. Janssen's equation, reported by Kutter et al. (1988) as an upper limit for the overburden pressure for predicting collapse of soil into cavities formed by underground explosions, is in close agreement with these experimental results when adapted for these configurations and the soil properties of the uncemented overburden. So also is Ono and Yamada's (1993) solution for collapse into shallow tunnels, adapted to this axisymmetric condition. Their predictions are shown in Figure 4 for comparison to these experimental data.

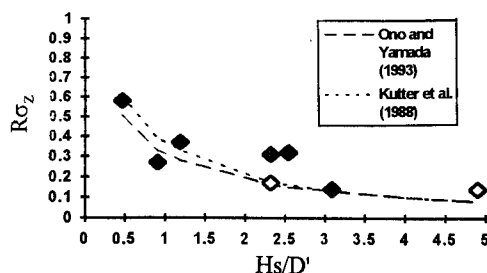


Figure 4. Comparison of arching predictions to data of this study. ( $\blacklozenge$  and  $\diamond$  are data from Figure 3)

## 5 CONCLUSION

In model in which the collapse of a weakly cemented layer of sand bridging a circular opening over a cavity, the weakly cemented soil dropped out as a plug with an inclined overhang failure surface. This behavior is similar to collapses of weak rock strata into unsupported cavities. A limit equilibrium analysis was applied to the plug in models with no overburden. When the effect of the uncemented sand overburden was then considered, a substantial reduction from the total geostatic stress was observed. These reductions observed in the experiments are in good agreement with predictions based on Janssen's equation used by Kutter et al. (1988) for centrifuge models of soil collapse, and Ono and Yamada's (1993) equations for collapse into shallow tunnels.

## REFERENCES

- Acar, B.Y. and A.E. El-Tahir 1986. Low Strain dynamic properties of artificially cemented sand. *Journal of Geotechnical Engineering, ASCE*, Vol. 112, No. 3:1001-1015.
- Akili, V. and J.E. Torrance 1981. The development and geotechnical problems of sabkha, with preliminary experiments on the static penetration resistance of cemented sands. *Quarterly Journal of Engineering Geology*, London, Vol. 14:59-73.
- Atkinson, J.H. and D.M. Potts 1977. Stability of a shallow circular tunnel in cohesionless soil. *Geotechnique* 27, No. 2:204-215.
- Chen, J. and B. Beck 1989. Qualitative modeling of the cover-collapse process. *Proc. 3rd*.



- multidisciplinary conference on sinkholes and the engineering and environmental impact of karst*. ST. Petersburg Beach, Florida, Oct. 2-4:89-95.
- Clough, G.W., N. Sitar, R. Bachus & N. Rad 1981. Cemented sand under static loading. *Journal of Geotechnical Engineering, ASCE*, Vol. 107, No. GT6: 799-817.
- Craig, W.H. 1990. Collapse of cohesive overburden following removal of support. *Canadian Geotechnique*. Vol. 27:355-364.
- Eid, W.K. 1987. *Scaling effect in cone penetration testing*. Ph.D. thesis, Virginia Polytechnic Institute and State University.
- Hodek, R.J., A.M. Johnson & D.B. Sandri 1984. Soil cavities formed by piping. *Proc. 1st. multidisciplinary conference on sinkholes*. Orlando, Florida, Oct. 15-17:249-253.
- Howell, F.T. and P.L. Jenkins 1984. Centrifuge modeling of salt subsidence features. *Proc. of Symposium on the Application of centrifuge to geotechnical modeling*, Manchester, U.k., April 16-18:193-202.
- Ketelle, R.H., W.E. Manrod, E.C. Drumm & J. Ben-Hassine 1987. Soil mechanics analysis of plastic soil deformation over a bedrock cavity. *Proc. 2nd. multidisciplinary conference on sinkholes and the environmental impact of karst*. Orlando, Florida, Feb. 9-11:383-387.
- Kutter, B.L., J.D. Chang & B.C. Davis 1988. *Centrifugal modeling of the collapse of cavities in dry sand*. Report to Lawrence Livermore National Laboratory from Center for Geotechnical Modeling, University of California, Davis.
- Mitchell, J.K. 1976. The properties of cement-stabilized soils. *Proceedings, workshop on materials and methods for low cost road, rail, and reclamation work*, Leura, Australia, Sept. 6-10, pp. 365-404.
- Ono, K. and M. Yamada 1993. Analysis of the arching action in granular mass. *Geotechnique* 43, No. 1:105-120.
- Poulos, H.G., M. Uesugi & G.S. Young 1982. Strength and deformation properties of bass strain carbonate sand. *Geotechnical Engineering*, Vol. 13:189-211.
- Rad, N.S. and M.T. Tumay 1986. Effect of cementation on the cone penetration resistance of sand: a model study. *Geotechnical Testing Journal*, Vol. 9:117-125.
- Sitar, N., G.W. Clough & R.C. Bachus 1980. *Behavior of weakly cemented soil slopes under static and Seismic loading conditions*. The John A. Blume Earthquake Engineering Center, Stanford University, Report No. 44.
- Stimpson, B. and M. Ahmed 1991. Failure of a linear voussoir arch: a laboratory and numerical study. *Canadian Geotechnical Journal*, Vol. 29:188-194.

## Ice scouring of the seabed

P.R. Lach & J.I. Clark

*Centre for Cold Ocean Resources Engineering, Memorial University of Newfoundland, St. John's, Nfld, Canada*

**ABSTRACT :** Ice scouring represents a potential impediment to the safe and economical design of marine pipelines and other seabed structures in cold ocean waters. This paper describes a centrifuge test programme undertaken to investigate the interaction of an ice feature and the seabed soil. Model scours were created in instrumented samples of saturated clay to provide information on the effects of scour, including pore water pressure changes within the soil, surface and sub - scour soil deformations, and the model iceberg loading. Test variables included the prescribed soil stress history and the model iceberg attack angle, width, and buoyant weight. The physical model idealization of the problem is discussed, and experimental procedures and some representative test results are presented.

### 1 INTRODUCTION

Curvilinear sea bottom features which are commonly one half to two metres in depth, tens of metres wide, and hundreds of metres or several kilometres long are characteristically found covering extensive portions of the polar continental margins. These features are attributable to gouging or scouring by drifting ice masses in the form of icebergs or sea ice pressure ridges which come into contact with the seabed. This phenomenon poses a threat to prospective subsea installations and, in particular, offshore oil and gas pipelines.

In North America, comprehensive field surveys of ice scouring have been carried out in the potential production areas for offshore hydrocarbon reserves, which include the Grand Banks of Newfoundland and the Beaufort Sea. These studies have yielded a considerable database of information on the distributions of scour characteristics including scour depth, width, orientation, and spatial and temporal frequencies (Canadian Oil and Gas Lands Administration, 1990). These data may be used in probabilistic analyses to provide a quantitative assessment of the risk of ice contact associated with a proposed pipeline burial depth.

A buried pipeline may also be damaged in a circumstance where the ice itself did not contact it directly. Physical model tests conducted at one

gravity in a laboratory scour tank facility (Poerooshasb et al., 1989; Poerooshasb, 1989; Paulin, 1992) supported evidence from investigations of relic features and small scale field observations (Woodworth - Lynas, 1992) of large sub - scour soil movements. As illustrated in Figure 1, a pipeline situated within a zone of large plastic soil deformation below a scouring body of ice will be displaced unless the soil is very soft and able to flow around the pipeline. A deterministic model of the interaction between the ice and soil is required to evaluate the soil deformation induced in the vicinity of the pipeline during a scouring event.

Very little information exists on ice scour processes and effects to allow for verification of the predictions of physical behaviour furnished by theoretical studies. Direct measurements of scour effects beneath the modern seabed are generally not feasible and high resolution geophysical data are not sufficiently well - defined to permit confident evaluation of soil deformation. Physical simulations of ice scouring have thus far involved small or medium - sized model tests in which the stress scale has not been altered. To address the deficiencies inherent in conventional small scale modelling of geotechnical phenomena, a research programme was recently conducted which applied the method of centrifuge modelling to the study of ice scouring. This paper describes the idealization of the problem

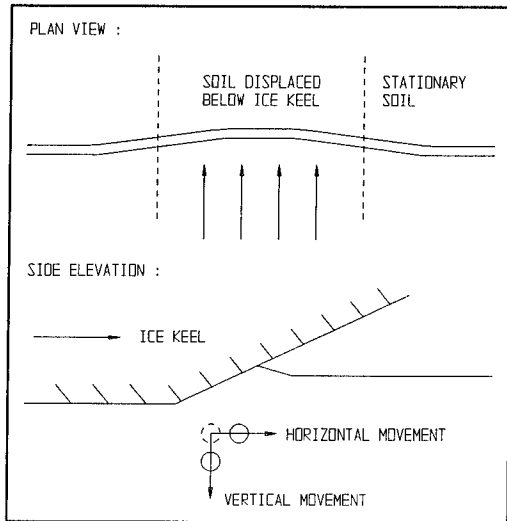


Fig. 1 Pipeline in zone of large soil deformation and implementation of the centrifuge model tests.

## 2 IDEALIZATION OF FIELD CONDITIONS

Ice scouring is a complex event which involves the interaction of an ice feature (subject to environmental driving forces which may include wind, wave, current, and pack ice forces) and the seabed soil. The ice feature may be independent or it may reside within a relatively continuous ice sheet. It may experience uplift or rotational movements and these movements may be resisted by its buoyant weight or through forces generated between the feature and a surrounding ice sheet. The ice keel may also be irregular in shape and its geometry may be altered through abrasion and fracture. In addition, the seabed may exhibit a significant slope or unusual surface morphology. Finally, the insitu soil conditions may be variable and these conditions may be modified as a result of pipeline trenching.

A variety of ice scour event scenarios can be envisaged depending on the environmental driving forces which are acting, the characteristics of the ice feature, and the seabed conditions. Nonetheless, field evidence indicates that most scour features are uniform in cross-section over long distances and that, in surveyed regions of ice-scoured terrain, the seabed is often almost horizontal. A simple steady state scouring condition may, therefore, represent the most relevant condition in practice and also forms a rational starting point for quantitative

analysis (Palmer et al., 1989).

Accordingly, scouring in the present study involved the horizontal movement of a model ice feature through a homogeneous, level seabed. It was assumed that driving forces were large enough to sustain motion of the ice at a constant velocity. The model ice feature was free to lift or rotate during the event to attain a steady state level. These movements were determined by its buoyant weight and the forces developed between the soil and ice, as would be the case for an iceberg or any independent body of ice. The ice keel was idealized as a rigid body, with the implication that its shape was representative of the equilibrium geometry achieved during steady state scouring. The model iceberg configuration, shown in Figure 2, was defined by the attack angle of a planar leading face, and the length, width, and depth of the portion of the model in contact with the soil. These parameters may be varied over ranges considered relevant to the field situation, to investigate their influence on the effects of scour.

The soil type in which the tests were conducted was reconstituted saturated Speswhite kaolin clay. The stress history of the soil was prescribed to establish desired stress states in the sample without detailed reference to a specific prototype. General reference was made to soil conditions in Beaufort Sea regions vulnerable to ice scouring (eg. O' Connor, 1982; Crooks et al., 1986) to ensure that results were obtained which were relevant in practice. The model scouring events were regarded as an approximation to the case of a dynamic event

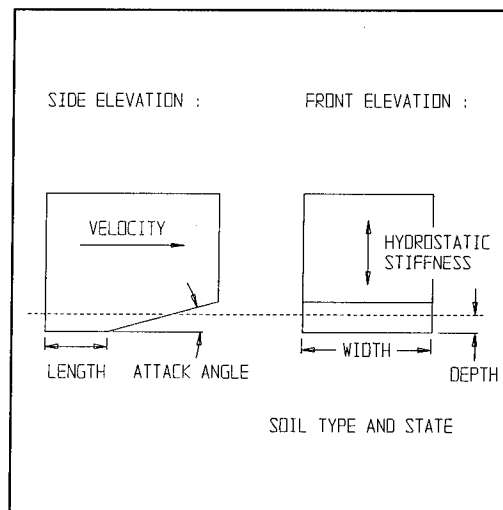


Fig. 2 Model iceberg geometry and parameters of the scour problem

in an impermeable soil. The inertial time scale factor was applied such that the specified rate of scouring for the model was equal to the prototype velocity. A velocity of approximately 0.1 m/s, representative of a typical iceberg drift speed, was selected for the notional full scale event to be replicated in each test. The tests were sufficiently rapid for essentially undrained conditions to prevail, corresponding with expected field conditions for scouring in clay.

### 3 TEST DESCRIPTION AND PROCEDURE

The model ice scour tests were performed on the beam centrifuge at the University of Cambridge Geotechnical Centrifuge Centre in Cambridge, England. The tests were carried out using 1 / 100 scale models at a nominal acceleration level of 100 g. Each clay sample was one - dimensionally uniformly consolidated in the laboratory from a slurry. The maximum vertical effective stress imposed in the laboratory ranged from 110 to 200 KPa, and was selected to obtain the desired profile of overconsolidation ratio at equilibrium in the centrifuge. The near surface clay of each sample was in an overconsolidated state and exhibited undrained shear strengths of between 10 and 20 KPa.

A cylindrical tub, 850 mm in diameter and 400 mm deep served to contain the clay both during laboratory preparations and in - flight on the centrifuge. The final thickness of the clay within the tub was about 180 mm. Eight miniature pore water pressure transducers were installed at particular locations within each sample to provide a means of defining the soil response during consolidation and the scouring event.

Surface soil displacements were evaluated based on photographic evidence of lead shot markers placed at prescribed locations. To measure sub - surface soil displacements, grids constructed of easily deformable materials were positioned at sections both parallel - and perpendicular - to the scour axis. Each grid comprised horizontal and vertical members set at ten millimetre intervals. Horizontal members consisted of segments of very fine solder attached to strands of coloured, dry spaghetti. After placement within the sample, the spaghetti became pliable due to the presence of water but retained its initial configuration. Lead powder trails were injected into the sample to form the vertical members of a grid. The post - test deformed patterns of each grid were determined using radiography.

Model pipeline segments were used to provide qualitative information on the plastic deformation which may be experienced by typical full scale pipelines situated at different depths below a scouring ice keel. The model pipeline segments were 800 mm lengths of stainless steel tubing with an outside diameter of 6.35 mm and a wall thickness of 0.25 mm. The maximum yield strength of the tubes was about 380 MPa. Prior to a test, the model pipeline segments were set into trenches excavated within the sample and the trenches were then backfilled with the clay that had been removed. The segments were buried at different depths, at sections perpendicular to the scour axis.

Each model iceberg was constructed of aluminum, to simulate a rigid keel of specified geometry, and balsa wood, to provide buoyancy and ensure a particular hydrostatic stiffness in free surface water. Three inductive pressure transducers were used to measure pressures on the inclined and bottom faces of the model iceberg. Four pore water pressure transducers were also used to measure water pressures at the corners of the model. These measurements permitted evaluation of the vertical position and orientation of the model, as well as the total vertical force acting between the model and the soil. Redundant measurements of the vertical movements of the model could be obtained using two linearly variable differential transformers. The transducers were oriented such that the spindle of each device protruded upward from the top surface of the model. The top of each spindle was fitted with a low friction pad which rested on a guide rail spanning the tub. The enhanced self weight of the spindle at the test acceleration level ensured that contact with the rail was maintained during the event.

Figure 3 shows a drawing of a vertical section through the test package along the scour axis. The drive system consisted of an electric motor which pulled a flexible cable attached to the front of the model iceberg. A tension load cell was connected in - line with the cable to measure the horizontal force developed when the model iceberg was advanced. A small aluminum cone fixed to the cable in front of the load cell was used to activate two micro - switches which then stopped the motor when the model iceberg had travelled a predetermined distance. The horizontal position of the model was monitored using a rotary potentiometer coupled to one end of the motor shaft, and also using a position transducer linked by cable to the model iceberg.

To initiate the scouring event, the electric motor was triggered remotely and the model iceberg was

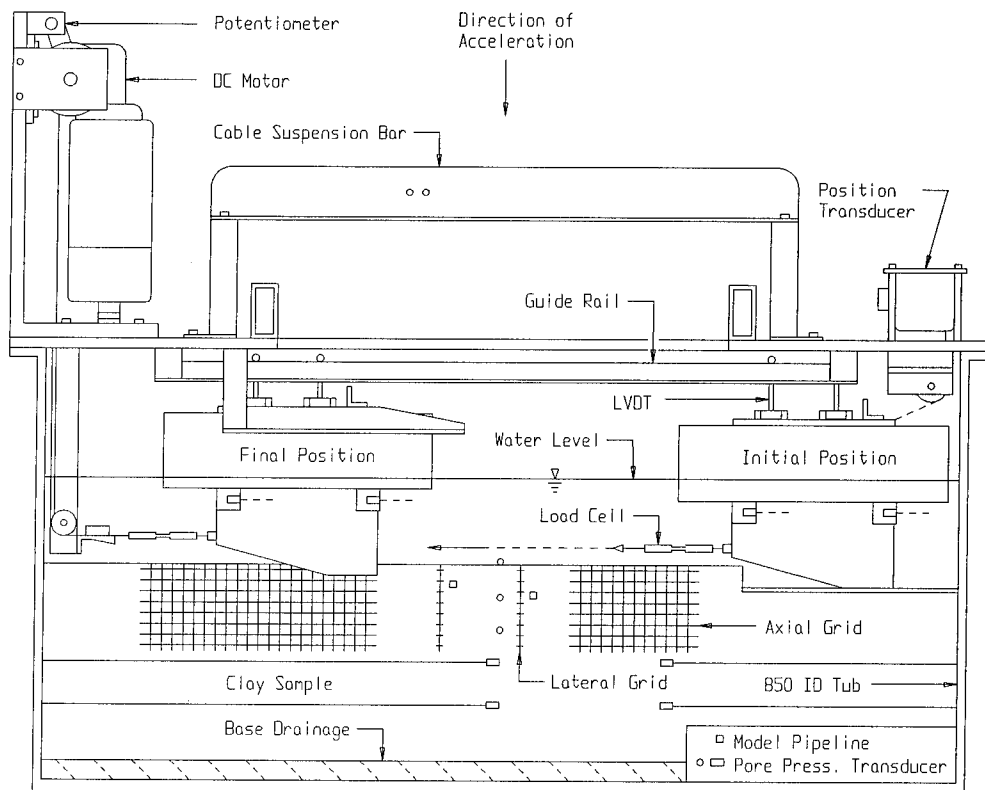


Fig. 3 Test package - vertical section at scour axis (some transducers out of plane)

pulled across the sample at a constant velocity to create the scour. The direction of travel was specified parallel to the axis of rotation of the centrifuge in order to minimize errors due to the radial gravity field and Coriolis accelerations. The total distance travelled was about 460 mm and the time elapsed during the event was less than seven seconds. The test velocity was achieved almost immediately, and prior to the establishment of steady - state scouring conditions. After the completion of a test, a detailed site investigation and radiographic examination were carried out, primarily to determine the soil deformation associated with the model scour.

A series of nine tests were performed. Test variables included the clay laboratory pre - consolidation stress, and the model iceberg width, attack angle, and buoyant weight. A modelling of models test was also conducted at 125 g to check the internal consistency of the method.

#### 4 INITIAL TEST RESULTS

Data acquired in the first test of the series are described briefly in the following. In this test, the clay was consolidated in the laboratory under a uniform vertical effective stress of 140 KPa. The model iceberg width was 100 mm and the attack angle was set at 15 degrees to the horizontal. The vertical stiffness of the model in free surface water was about 26 N / mm. The buoyant weight varied with the vertical position of the model in proportion to this value.

Figure 4 shows a plan view drawing of the Test 1 model scour. This was the shallowest scour created during the test series. A steady - state scour depth of 3.8 mm was established following a period of uprise from the initial position. Berm elevations averaged 2.3 mm above the original surface level, including heave of the soil immediately adjacent to the scour and a limited amount of loose or spoil material. A semi - circular shaped (in plan view)

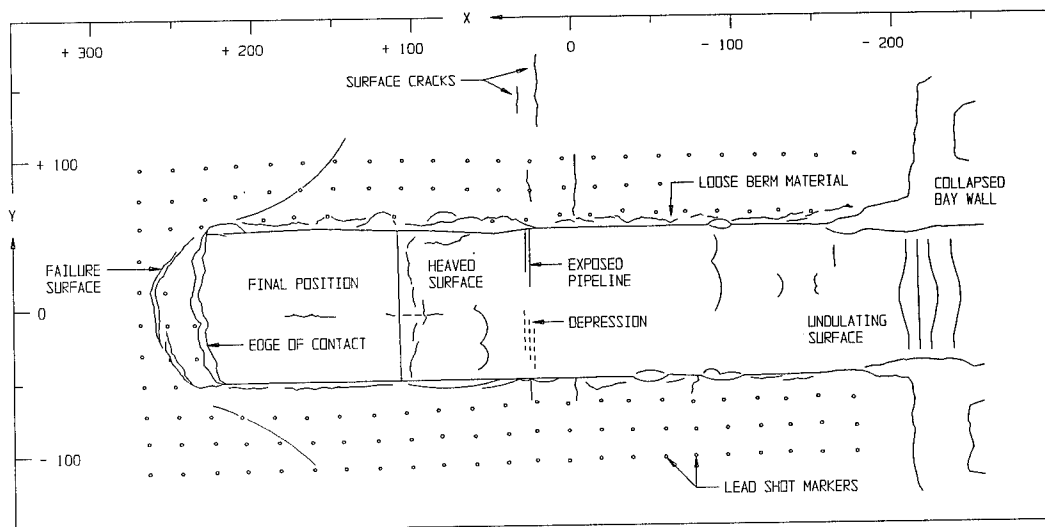


Fig. 4 Plan view of Test 1 scour (scales in mm)

rupture surface was evident in front of the final position of the model iceberg. The model pipeline segment situated nearest to the surface was partially exposed within the scour incision. A depression and soil surface fractures formed in the vicinity of this pipeline indicating movement had occurred over a substantial portion of its length.

Pore pressure changes were measured by eight transducers within a zone which extended a distance of 150 mm both laterally outward from the scour axis and vertically with depth. The maximum recorded increase in pore pressure was 61 KPa for a transducer located at a depth of 55 mm and near to the edge of the scour.

Figure 5 shows a plot of the force developed at the model - soil interface during the scouring event versus the horizontal position of the model. In this test, the vertical component of force was nearly three times as large as the horizontal component. The average magnitudes of the vertical and horizontal components were 0.60 and 0.22 KN respectively at model scale. The inclination of the resultant force vector increased during the event and in the steady - state region the vector angle was almost perpendicular to the scouring face of the model.

Figure 6 shows the initial and displaced configuration of one of the lateral grids used to evaluate soil deformation. The grid shown comprised lead powder trails originally injected at 45 degrees to the sample surface. Vertical soil displacements occurred in a pattern similar to the

morphology of the scoured surface and gradually attenuated with depth below the scour. Horizontal displacements in the direction of travel of the model iceberg were larger and decreased more abruptly with depth. In this test, soil movements were negligible (within the limits of error of the measurement technique) at a depth of approximately 25 mm below the base of the scour. The post - test deformed grid patterns also allowed for the interpretation of failure mechanisms which occurred during the scour process.

## 5 CONCLUSION

The large forces exerted directly on the seabed by scouring ice must be transmitted into the soil below the scour, thereby inducing high stresses and large deformations. To facilitate rational pipeline designs, a theoretical model which provides acceptable predictions of these sub - scour effects must be developed. This paper described a centrifuge model test series carried out to obtain insights into soil behaviour during a scouring event and to yield data with which suitable analytical methods can be developed and verified.

The centrifuge test programme demonstrated the utility of a particular apparatus and procedures. Physical features observed in field investigations of both modern and relic scours were replicated in the model tests. A better understanding of the mechanics of scouring was obtained through the

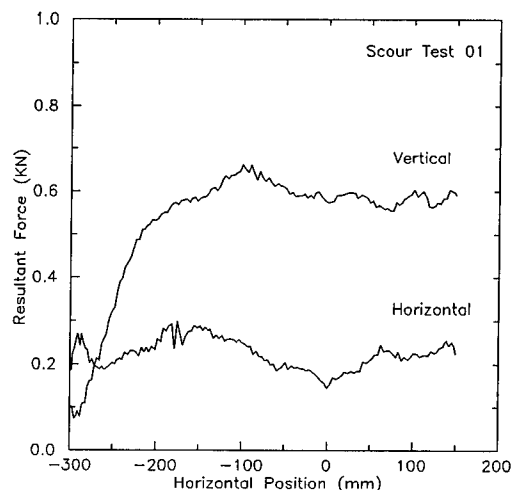


Fig. 5 Horizontal and vertical components of the model scour force

measurement of scour forces and corresponding stress and displacement fields within the soil. Each test may be examined as a unique event which represented a possible full scale scouring situation and for which accurate data on the effects of scour were collected. As a result, tests of this type may be expected to play an important role in the creation of design standards for pipelines situated in ice scoured terrain.

#### ACKNOWLEDGEMENTS

The authors wish to thank Professor Andrew Schofield and the Soil Mechanics Group at Cambridge University for the provision excellent facilities and invaluable technical assistance. In addition, we wish to express our appreciation to Dr. Farrokh Poorooshasb and Dr. Colin Smith for their involvement in the study. Partial sponsorship for this project was provided by the Government of Canada through the Program on Energy Research and Development.

#### REFERENCES

- Canadian Oil and Gas Lands Administration, 1990. Proc. Workshop on Ice Scouring and the design of Offshore Pipelines, Calgary, Alberta.
- Crooks, J.H.A., Jefferies, M.G., Becker, D.E., Been, K., 1986. Geotechnical properties of Beaufort Sea clays. Proc. 3rd Canadian Conf. on Marine Geotechnical Engineering, St. John's, Newfoundland : 329 - 343.
- Lach, P.R., Clark, J.I., and Poorooshasb, F., 1993. Centrifuge modelling of ice scour. 4th Canadian Conference on Marine Geotechnical Engineering, St. John's, Newfoundland, Vol. 1 : 356 - 374.
- O' Connor, M.J. and Associates, 1982. An evaluation of the regional surficial geology of the southern Beaufort Sea. Report to the Geological Survey of Canada.
- Palmer, A.C., Konuk, I., Love, J., Been, K., and Comfort, G., 1989. Ice scour mechanisms. Proc. 10th International Conference on Port and Ocean Engineering under Arctic Conditions, Lulea, Sweden, Vol. 1 : 123 - 132.
- Paulin, M.J., 1992. Physical model analysis of iceberg scour in dry and submerged sand. M.Eng. Thesis, Memorial University of Newfoundland, St. John's, Newfoundland.
- Poorooshasb, F., 1989. Large scale laboratory tests of seabed scour. Contract Report for Fleet Technology Limited, C - CORE Contract No. 89 - C15.
- Poorooshasb, F., Clark, J.I., and Woodworth - Lynas, C.M.T., 1989. Small scale modelling of iceberg scouring of the seabed. Proc. 10th International Conference on Port and Ocean Engineering under Arctic Conditions, Lulea, Sweden, Vol. 1 : 133 - 145.
- Woodworth - Lynas, C.M.T., 1992. The geology of ice scour. Ph.D. Thesis, University of Wales. 269 p.

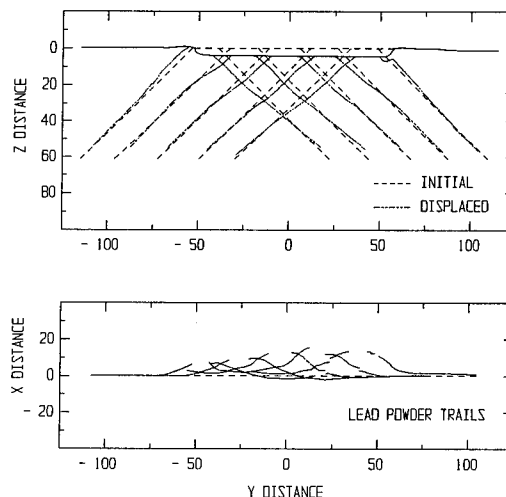


Fig. 6 Trace of lead powder grid in cross - section and plan view (scales in mm)

## Collapse of cavities in sand and particle size effects

Bruce L. Kutter

*University of California, Davis, Calif., USA*

Jiang-Dong Chang

*Shin Hwa Cheong Development Company, Singapore*

Barbara C. Davis

*Lawrence Livermore National Laboratory, Calif., USA*

**ABSTRACT:** The collapse of uniform sands into spherical cavities buried at a depth of three diameters is studied. In modeling of models experiments at 11, 33 and 66 g, the volume of the surface crater varied between about 0 and 80% of the cavity volume depending on the ratio of cavity diameter to mean grain size, indicating that particle size must be scaled for similarity in this problem.

### 1 INTRODUCTION

The collapse of soil into underground openings is of general interest for a number of different problems. In mining engineering sublevel caving, collapse of an ore body is used as a means of removal of ore at a mine heading. The withdrawal of oil or gas or coal seams can result in subsidence of a large area of overlying soil. Stone and Brown (1993) conducted a centrifuge model study of the collapse of soil due to "ground loss" caused by mining or faulting. In materials handling, bins and hoppers involve similar situations with granular material flowing out of an opening of fixed size at the base of the container.

The work reported here is part of a study to investigate the collapse of soil into explosion produced cavities.

Underground nuclear tests produce large cavities due to vaporization and cavity expansion. After some time, the pressures within the cavity drop and the overlying soil may collapse into the cavity. The zone of collapsing soil is sometimes called a "chimney". If the chimney reaches the surface, a surface crater begins to form, which is not desirable. The more serious concern is the possibility that radioactive gasses trapped in the cavity could escape to the atmosphere.

The current study has been conducted in order to develop an understanding of the

mechanisms of collapse into underground cavities so that the conditions leading to surface crater formation and the possibility of the escape of radioactive gasses can be better understood. This centrifuge model test series has been carried out on an idealized problem of spherical cavities buried in uniform clean sands. The dimensions of the model could not be made large enough to model actual prototypes. Dynamic cavity formation is not studied; the collapse is modelled by slowly draining fluid from a buried cavity lined with latex rubber.

One of the important goals of this work is to carry out "modeling of models" tests in order to verify the validity of the scaling laws used in centrifuge modeling.

In centrifuge model tests, it is conventional to use the same material in model and full scale prototype. This is done as a convenient means for keeping the same material properties (e.g. strength and moduli) in model and prototype. In cases where the particles are large compared to the dimension of the model, it may be necessary for obvious reasons to scale the particle size. Another problem arises when strain softening materials (such as dense sand) deform on rupture planes or shear bands. If the thickness of the shear bands does not scale as the other model dimensions do, a scale effect may be found.



## 2 MODELING TECHNIQUES

Four uniformly graded sands were chosen as testing materials, Monterey 0/30, Fontainebleau, Crystal Amber, and Nevada sand. The grain size distributions for these four soils are shown in Fig. 1. The maximum and minimum densities (for calculation of relative density,  $D_r$ ), the mean-grain sizes and the coefficients of uniformity are summarized in Table 1.

Most of the tests were conducted using the 1.1 m radius Schaevitz centrifuge at UC Davis. This centrifuge can carry 90 kg models to 100 g acceleration (10 g-ton) or 27 kg models to 175 g (5 g-ton). The tests on this small centrifuge included 25 mm diameter and 50 mm diameter model cavities tested at either 33 g or 66 g.

Four tests (only two of these are reported here) were conducted using the 9.2 m radius centrifuge at Davis. This centrifuge is now capable of carrying 4500 kg models to 50 g. The tests on the large centrifuge used 150 mm

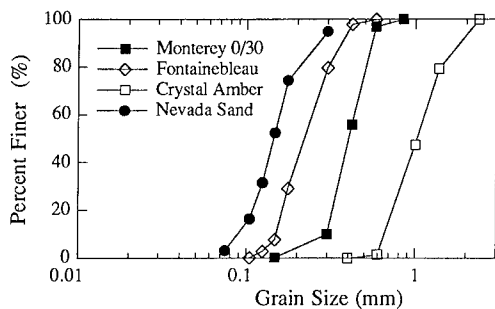


Fig. 1 Grain size distributions for four sands

Table 1. Material properties of tested sands

Sand Type	$G_s$	$\rho_{dmax}$ Mg/m <sup>3</sup>	$\rho_{dmin}$ Mg/m <sup>3</sup>	$D_{50}$ (mm)	$\frac{D_{60}}{D_{10}}$
Monterey sand	2.670	1.75	1.41	0.404	1.50
Fontainebleau sand	2.610	1.69	1.40	0.217	1.44
Nevada sand	2.618	1.69	1.41	0.146	1.70
Crystal Amber sand	2.622	1.73	1.41	1.01	1.28

diameter model cavities buried at depths of 450 mm and 750 mm and tested at 11 g. The 150 mm diameter cavity was a model of the 25 mm and 50 mm diameter cavities tested at 66 g and 33 g on the Schaevitz centrifuge.

The aluminum sample container for tests on the small centrifuge had 33 x 25 x 25 cm inside dimensions (length x width x height). Model cavities were held open by pressurized rubber bags which were prepared by dipping a spherical mold into latex liquid to make an 0.5 mm thick membrane with two outlets, one outlet for flow into or out of the bag, and another for a pressure transducer, as shown in the general test setup in Fig. 2. Bags with either spherical or hemispherical shape and either 25.4 mm or 50.8 mm diameter were made for different experiments.

The tests on the large centrifuge were conducted in a 0.6 x 0.6 x 1.5 m tall box. A 150 mm diameter cavity was made by attaching the appropriate fittings to a standard commercially available toy rubber ball.

Sand was pluviated into the containers to the level of the base of the cavity, the cavity and pressure transducer were installed and then sand was pluviated to cover the cavity. In the small centrifuge, horizontal lines of lead shot were placed at 25 mm elevation intervals along a centerline of the cavity.

In the tests on the large centrifuge, layers of colored sand were substituted for the lead shot; x-rays could not be used due to the large thickness of the samples.

As the sample container was filled, the water level in supply reservoir was raised to supply the cavity with enough pressure to balance the overburden pressure (see Fig. 2). In some tests, the cratering process was sensed by an

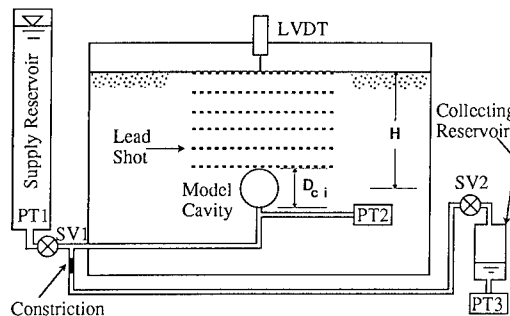


Fig. 2 Schematic of model

LVDT resting directly above the cavity on the sand surface.

The centrifuge was spun up to the test accelerations summarized in Table 2. After letting the centrifuge spin a while to check the correctness of the instrument outputs, the valve SV1 (see Fig. 2) was first shut off. This prevented water in the supply reservoir from draining into the collecting reservoir. Valve SV2 was then opened and solution drained from the cavity to the collecting reservoir. The volume of water gathered in the collecting reservoir, monitored by pressure transducer (PT3), permitted calculation of the volume change of the cavity. As the water drained from the cavity, the chimney collapse process started. The cavity internal pressure was sensed by the pressure transducer (PT2) located beside the cavity (see Fig. 2). Cavity pressure during collapse ranged between 3%

and 15% of the overburden pressure, indicating that very low stress levels exist during the collapse.

For tests with hemispherical cavities located against the observation window, the propagation of the collapse was monitored through a mirror by a video camera mounted on the centrifuge. In addition to the video camera, pictures were taken by stroboscopic photography using a 35 mm camera mounted on the top of the centrifuge. The final mechanism of deformation for spherical cavities on the small centrifuge was revealed by the X-ray radiographs taken after each test.

For the test with a spherical cavity on the large centrifuge the crater was filled with plaster and the sample was laid on its side after the test. The window was then removed and the sand was moistened. This provided enough apparent cohesion that the soil could be

Table 2. Initial conditions and results for centrifuge tests

Test	Sand Type <sup>1</sup>	Cavity Shape <sup>2</sup>	Cavity Diameter (mm)	Centrifuge Accel. (g) <sup>3</sup>	Initial Soil Density (Mg/m <sup>3</sup> )	Normalized Cavity Depth <sup>4</sup>	Normalized Cavity Diameter D <sub>ci</sub> /D <sub>50</sub>	Normalized Crater Volume	Initial Dr (%)	Final Dr (%)
3	M	H	25.4	68	1.70	3	63	0.0	88	--
4	M	S	50.8	34	1.70	3	126	0.36	86	21
5	M	H	50.8	34	1.70	3	126	0.19	88	--
6	F	S	50.8	34	1.63	3	234	0.50	89	22
7	M	S	25.4	69	1.71	3.5	23	0.0	92	--
8	F	S	25.4	70	1.67	3	117	0.33	98	5
9	M	S	25.4	70	1.75	3	63	0.13	100	7
10	M	S	50.8	33	1.55	3	126	0.34	47	-12
11	M	S	50.8	33	1.71	5	126	0.16	91	46
12	M	S	25.4	66	1.70	3	63	0.19	99	-22
13	M	S	25.4	66	1.49	3	63	0.17	29	-16
14	N	S	50.8	33	1.62	3	348	0.64	76	14
15	CA	S	24.	66	1.71	3	24	0.0	96	-19
16	M	H	152.	11	--	3	376	--	--	--
17	M	H	152.	11	~1.63	5	376	0.36	~79	--
19	N	S	152.	11	1.63	3	1041	0.767	79	18

<sup>1</sup>M = Monterey 0/30 sand, F = Fontainebleau sand, N = Nevada sand, CA = Crystal Amber sand

<sup>2</sup>H = Hemispherical, S = Spherical

<sup>3</sup>g<sub>ave</sub> = (g<sub>sand surface</sub> + g<sub>cavity center</sub>)/2

<sup>4</sup>Normalized Cavity Depth = H/D<sub>ci</sub> (see Fig. 2)

carefully excavated to reveal the deformed shape of the layers of colored sand.

Density measurements at various points in and around the chimney were taken by a new method. Approximately 3 cm<sup>3</sup> samples of moist sand were removed with a small spoon to make a neat, approximately hemispherical, hole. The removed sand was dried and weighed. The volume of the hole was measured by pouring melted paraffin wax into the hole and squeezing out the excess wax by covering the hole with a small flat sheet of plastic. After cooling, the hardened wax was weighed in the lab. To compute the volume of the sample, account was taken of the fact that paraffin has a significant increase in density as it solidifies.

### 3 RESULTS-SURFACE CRATER VOLUME

Table 2 summarizes the test conditions and some results. All cavities had prototype diameters of approximately 1.74 m. In all but tests 11 and 17, the cavities were buried at a depth of 3 diameters;  $H/D_{ci} = 3$  (see Fig. 2). In tests 11 and 17,  $H/D_{ci} = 5$ . All of the tests were conducted with initially dense sand (relative density,  $D_r > 80\%$ ) except tests 10 ( $D_r = 47\%$ ) and 13 ( $D_r = 29\%$ ).

For each test on spherical cavities, the initial and final relative densities of the sand in the chimney are given in Table 2. Note the very low relative densities that are found in the chimney after the collapse. In some tests negative relative densities were calculated. This unusual result will be discussed later.

Figure 3 shows the gradual development of the collapse of a cavity traced from stroboscopic photographs of test 5. This model consisted of a hemispherical cavity placed against the Plexiglas window. The collapse begins just above the cavity and the chimney then gradually progresses upward as the cavity fluid is allowed to drain out of a rubber bag. When the zone of collapsing soil reaches the surface, a crater begins to form.

Perusal of Table 2 reveals that there is a large scatter in values of normalized crater volume (crater volume is normalized by the initial cavity volume). In all tests, however, irrespective of the sand type and initial density, the volume of the surface crater is less than the initial volume of the cavity. In two tests (tests

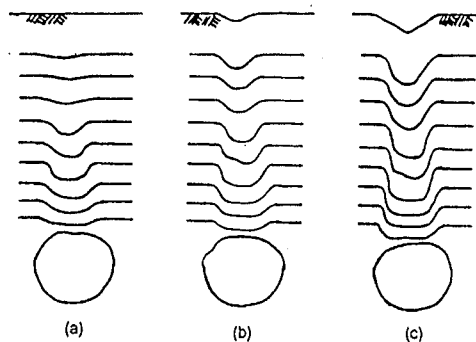


Fig. 3 Observed progress of collapse from hemispherical cavity against window

3 and 15) no surface crater was observed. Of course, the difference between the crater volume and cavity volume is explained by dilation of the collapsing sand.

#### 3.1 Edge effect

Tests 3, 4, and 5 supposedly represented the same prototype cavity buried in the same soil (Monterey sand). By comparing the crater volumes from tests 4 and 5, an edge effect is apparent--the hemispherical cavity (test 5) produced a normalized crater volume about half as large as the spherical cavity (test 4). The small hemispherical cavity (test 3) produced no crater at all.

#### 3.2 Density effect

Since the difference between crater volume and cavity volume is caused by dilation, it might be expected that denser soils, being more dilatant, would produce smaller surface craters. This is not necessarily the case. As seen by comparing tests 9, 12, and 13 or test 4 with test 10, density seems to have no consistent effect on crater volume.

#### 3.3 Size effects

By comparing test 4 (Monterey sand,  $D_{50} = 0.404$  mm) with 6 (Fontainebleau sand,  $D_{50} = 0.217$  mm) in Table 2 it is seen that grain size

appears to be important--the collapse in fine sand produced a larger crater. By comparing tests 6 with 8 or 4 with 12 it is also apparent that the initial cavity size has an effect on the normalized crater volume. The combined influence of these factors is illustrated in Fig. 4 which plots normalized crater volume against the normalized cavity diameter  $D_{ci}/D_{50}$ . Except at the extremes, all of the data points representing spherical cavities buried at a normalized depth of 3.0 (square symbols) plot along one line. Data points representing hemispherical cavities (+ symbols) plot below the heavy line. This is expected since the edge

effects for hemispherical cavities restrict the cavity collapse process. Deeper cavities, at normalized depths of 3.5 and 5, (x symbols) also produce smaller surface craters as expected.

For  $D_{ci}/D_{50}$  between about 30 and 350 there appears to be a linear relationship between  $V_{cr}/V_{ci}$  and  $D_{ci}/D_{50}$  on the semi-logarithmic plot. The significant size effect illustrated in Fig. 5 is at first discouraging to a centrifuge modeler. One of the common assumptions of a centrifuge modeler is that the soil particles are small enough that the soil can be assumed to be a continuum.

A centrifuge modeler might, however, be encouraged by the indication that if grain size is scaled, that is, if the ratio of  $D_{ci}/D_{50}$  is held constant, similitude appears to hold. For example, the Fontainebleau sand used in this study has a grain size which is approximately half of that for the Monterey sand. A 25 mm cavity in Fontainebleau sand should closely simulate a 50 mm cavity in Monterey sand. This is indeed supported in Fig. 4 for the cluster of points at  $D_{ci}/D_{50} \approx 120$ ,  $V_{cr}/V_{ci} \approx 0.35$ .

If the cavities were buried in an incompressible soil, the normalized crater volume would be 1. Since the sands all tended to be dilatant, the normalized crater volume should be less than 1. It would therefore be expected that the linear relationship for  $30 < D_{ci}/D_{50} < 350$  is not expected to continue

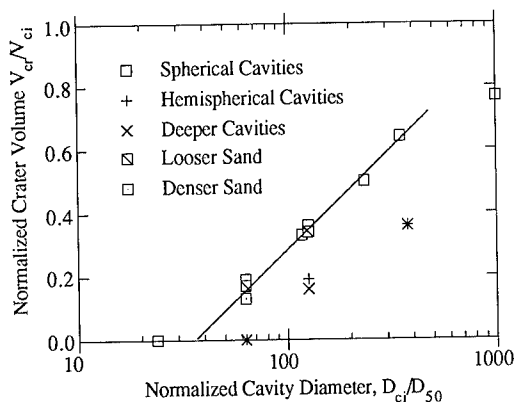


Fig. 4 Relation between crater volume and mean grain size

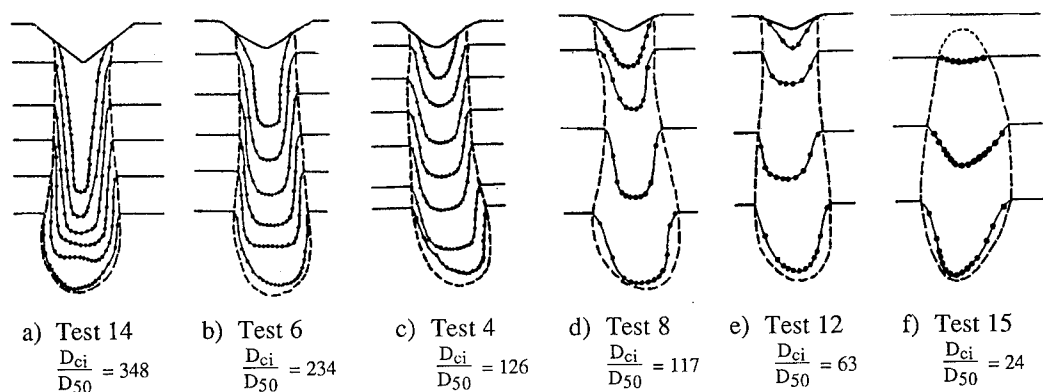


Fig. 5 Collapse patterns observed in post-test x-rays or excavation.

$\frac{D_{ci}}{D_{50}}$  decreases from left to right

forever; it should be asymptotic to  $V_{cr}/V_{ci} = 1$ .

In order to obtain data at higher  $D_{ci}/D_{50}$  values, the finest sand was used and a large box on the large centrifuge was needed to carry a 150 mm diameter cavity. In fact, it does appear that the grain size effect (i.e. the slope of the curve in Fig. 4) reduces as  $D_{ci}/D_{50}$  increases above about 350. The value of  $D_{ci}/D_{50}$  necessary to avoid size effects is very large compared to analogous numbers used by other centrifuge modelers studying different problems. For example, Bagge and Christensen (1977) suggested that for footings on sand, grain size effects become negligible when the foundation dimensions are greater than about 15 grain diameters.

#### 4 RESULTS-DEFORMATION MECHANISMS

Cross-sections showing the collapse pattern of seven tests on dense sands are given in Fig. 5. They are given in order of decreasing  $D_{ci}/D_{50}$  ratios. Note that crater size tends to decrease as  $D_{ci}/D_{50}$  decreases.

The first cross-section shown in Fig. 5 was obtained by excavation of sand in the large centrifuge. The crater was filled with plaster and the box was laid on its side and the window was removed. The soil was moistened to provide some apparent cohesion and then excavated to provide the photograph shown in Fig. 6. Note the interbedded core of the chimney. This core is formed by slumping of sand into the surface crater. The colored sand from the top surface of the sample produced the dark core. This photograph also shows some evidence that the collapse was not exactly symmetrical near the cavity. The asymmetry may be due to a preferred folding mechanism of the rubber lined cavity or may be a result of a natural instability.

There was at one time some concern about the radiograph data in that it is possible that the heavy lead shot particles were not falling into the chimney at the same rate as the sand particles. This concern appears to be unwarranted as the results from the large centrifuge with colored sand and no lead shot (Fig. 6) gave results which correspond quite closely to the radiograph results for test 14 (Fig. 5).

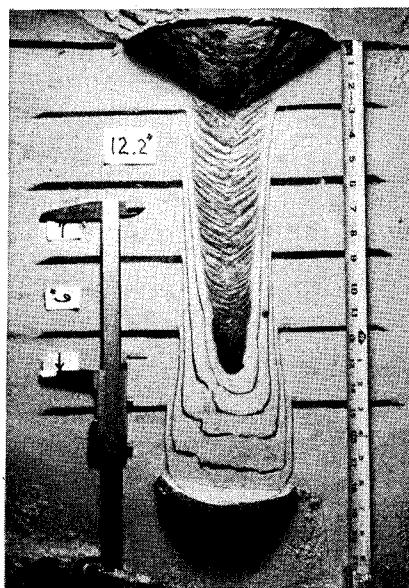


Fig. 6 Photograph of excavated sample from large centrifuge

The data in Fig. 5 was used to estimate the dilation of the collapsed soil. The chimney was assumed to be axisymmetric and the volume of soil within the dotted lines in Fig. 5 was calculated. The difference between cavity volume and crater volume was then assumed to be caused by dilation of the sand. Since the initial density was known, the final density and relative density were calculated as summarized in Table 2. Note the very low densities that were observed in the collapsing soil. Calculated final relative densities for cavities with a depth of three diameters are all between +22 and -22%. A relative density less than 0 is unlikely, so some errors must be suspected in the calculation procedure. Probable causes of the error are that the lead shot was not placed exactly on the center line of the collapsing chimney, or that the chimney was not axisymmetric. Also note that a 20% error in relative density can be caused by about a 4% error in actual density.

It is apparent, however, that the sand in the collapsing chimneys does indeed become very loose. This phenomena was independently verified in test 19 by direct density measurements on the large centrifuge sample. The density of 5 small soil samples at different

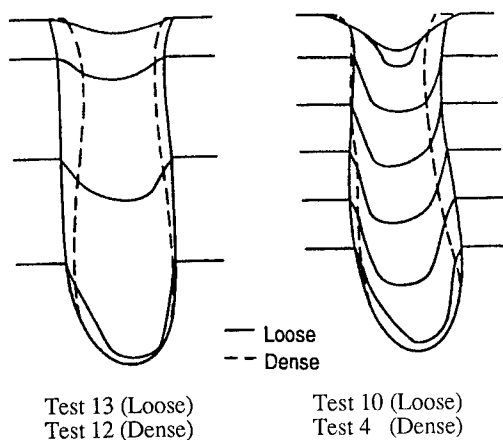


Fig. 7 Difference in shape of collapsing soil for loose and dense sand

points within the chimney varied between 1.41 and 1.52 Mg/m<sup>3</sup> with a mean of 1.46 Mg/m<sup>3</sup> ( $D_r = 18\%$ ) while the density of the surrounding soil from six samples averaged 1.63 Mg/m<sup>3</sup> ( $D_r = 79\%$ ).

Two tests (tests 10 and 13) were conducted using loose Monterey sand to determine the influence of density on the collapse process. Table 2 summarizes the densities of the soil in the chimney before and after collapse. As seen in Fig. 7, the chimney is larger in diameter for the loose sample. But, as seen in Table 2 and Fig. 4, the net crater volume for a given sand type and cavity diameter is very similar for tests in loose and dense sand. Compare test 5 with test 10 or tests 9 and 12 with test 13 in Table 3.

The dense sand dilated more per unit volume, but more sand was involved in the collapse mechanism in loose sand. The net effect was that the total crater volume was not affected noticeably. The shape of the craters was affected by density. As seen in Fig. 7a, the surface crater in loose sand is wider and shallower so that the slope of the crater never reached the angle of repose as it did for the dense samples.

## 5 CONCLUSIONS

1) Due to dilatancy, the volume of the surface crater formed by collapse of a cavity in dry

sand is less than initial cavity volume.

2) The collapse/crater formation process appears to be a strong function of the normalized cavity size (cavity diameter/particle diameter =  $D_{ci}/D_{50}$ ). As particle size increases or cavity size reduces, the normalized size of the resulting surface crater reduces.

3) The size effect spans the range  $30 < D_{ci}/D_{50} < 1000$ . In order to achieve reasonable comparisons in "modeling of models" tests for this problem the grain size must be scaled.

Reducing the particle size in a model reduces the interparticle contact forces, and hence grain crushing may not be modeled. Collapse into relatively shallow cavities involves unloading and low stress levels, a condition for which grain crushing is unlikely to be important. In other problems such as bearing capacity, scaling of grain size may not be feasible, and may be less important.

## 6 REFERENCES

- Bagge, G. and S.N. Christensen 1977. Centrifugal testing on the bearing capacity of circular foundations on the surface of sand. *DIALOG 1-77*, Danmarks Ingeniorakademi, Bygningsafdelingen, Lyngby.
- Chang, J.D. 1989. Centrifugal modeling of collapse of underground cavities in sands. *M.Sc. Thesis, U.C. Davis*.
- Kutter, B.L., J.D. Chang, and B.C. Davis. 1988. Centrifugal modeling of the collapse of cavities in dry sand. *Final Report to Lawrence Livermore National Laboratories, PO# 1761303*, December.
- Stone, K.J.L. and T.A. Brown 1993. Simulation of ground loss in centrifuge model tests. *Geotechnical Testing Journal, ASTM*, Vol. 16, No. 2, pp. 253-258, June.

## Effect of particle size on localisation development in model tests on sand

R.J.White, K.J.L.Stone & R.J.Jewell

*The University of Western Australia, Nedlands, W.A., Australia*

**ABSTRACT:** A series of centrifuge model tests have been performed to investigate the effect of particle size on model test kinematics. By scaling all model dimensions relative to the average particle size, and inducing a vertical boundary discontinuity in flight, the pattern of localisation development can be studied. The results of numerical analyses conducted on the model tests have also been reported.

### 1. INTRODUCTION

The use of small scale modelling has long been employed to assess and predict the performance of prototype structures. With the advent of centrifuge modelling techniques, the problems associated with reproducing prototype stress levels in small scale models has been overcome. However, the effect of scaling particle size has not been well addressed. Previous work, (Stone, 1988 and Stone and Wood, 1992) suggests that the formation and propagation of localisations is dependent on the value of mobilised dilation within the deforming zone of soil. For a particular soil the relative displacement across a localisation required to achieve the critical state (or zero dilation) within the localisation will be a function of the grain size and stress level. The attainment of critical state conditions within a localisation will induce a kinematic instability and results in the formation of successive localisations. Consequently, a scale effect in terms of particle size will be observed where granular soil is undergoing localised deformation.

A series of centrifuge tests have been

performed on the Acutronic 661 geotechnical centrifuge at the University of Western Australia in order to obtain a better understanding of the effect of particle size on the kinematics associated with the development and propagation of localisations through a soil body.

The centrifuge tests were performed on two sands of differing particle size. A vertical boundary discontinuity was induced at the base of the soil model using a trap-door system, (Stone and Brown, 1993) and the soil response observed. The results from the tests illustrate the effect of particle size on the model test kinematics.

Numerical analyses of the model tests were conducted using FLAC, (Fast Lagrangian Analysis of Continua) and are briefly reported.

### 2. MATERIAL PROPERTIES

The tests reported in this paper were performed on models using two grades of silica sand with similar grading curves (Figure 1) and particle angularity. The basic material properties are presented in Table 1.

Table 1. Basic material properties.

Sand Type (B.S. sieve)	50/100	20/30
	Sand 1	Sand 2
Average Particle Size ( $D_{50}$ )	0.25	0.5
$e_{max}$	0.75	0.67
$e_{min}$	0.53	0.52
$\phi_{cv}$	35	35

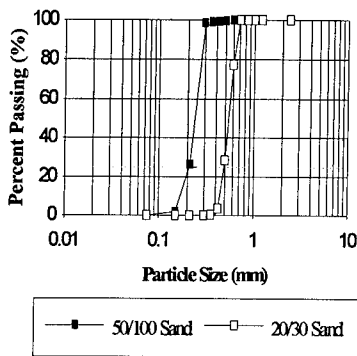


Figure 1. Grading curves for sands used in model tests

### 3. CENTRIFUGE MODELS

#### 3.1 Scaling Considerations

The principal scaling argument for these series of tests is based on the assumption that the relative displacement across a localisation is directly proportional to the induced boundary displacement at the base of the model. Hence, geometrically similar displacements across a localisation will be maintained if

$$(\Delta_B/D_{50})_{\text{sand 1}} = (\Delta_B/D_{50})_{\text{sand 2}} \dots\dots 1$$

where,  $\Delta_B$  = introduced boundary displacement (mm)

$D_{50}$  = average particle size of the material (mm)

To maintain geometric similarity between models of differing grain size, the physical dimensions of the models are scaled to equal multiples of the average particle size. Furthermore, since the value of mobilised dilation will also be influenced by the stress level the models are tested at acceleration levels

providing identical stress gradients, refer to Table 2 for test details.

Three model tests are reported. Two tests (RJW01 and RJW02) which maintain geometric similarity relative to the average particle size, and one test (RJW03) where geometric similarity is not maintained, see Table 2.

Table 2: Sand Model Details

Test Code	Ht. mm	Max Disp ( $\Delta_B$ )	G-Level	$D_{50}$ (mm)
RJW01	75	10	150	0.25
RJW02	150	20	75	0.5
RJW03	75	10	150	0.5

### 4. MODEL PREPARATION

#### 4.1 General Model Details

All physical model testing was conducted under plane strain conditions. The plane strain boxes used in the tests had internal dimensions, 650 mm long, 200 mm wide and 450 mm high.

#### 4.2 Sand Models

The models were prepared by pluviation through air to produce a dense uniform sample. Thin horizontal coloured sand layers and discrete plastic markers were placed at regular intervals in the model to provide a better visual picture of the localisation patterns both during and after testing. All models were prepared to a relative density ( $I_D$ ) = 0.9.

During the centrifuge test the model face and the induced vertical boundary displacement were recorded using miniature video cameras, (Randolph et al., 1991). The boundary displacement ( $\Delta\delta$ ) induced by the trap door at the base of the model was monitored via a laser and target system (shown in Figure 2). The displacement was shown on a LCD (Liquid Crystal Display) placed in the field of view of the video camera monitoring the front face of the model. Consequently, the development of localisations could be associated with a degree of trap door displacement.



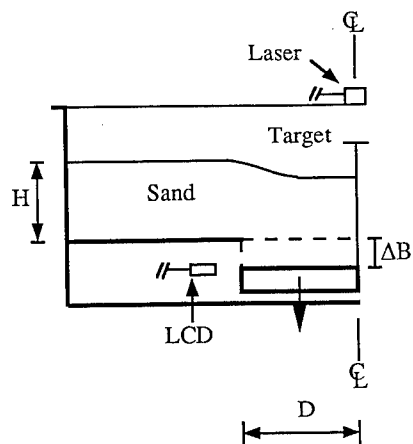
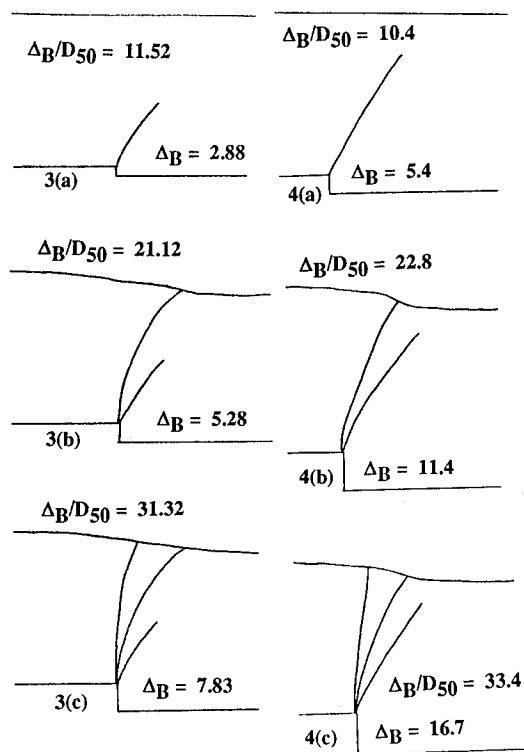


Figure 2. Centrifuge test arrangement



Figures 3a to 3c; Trace of rupture patterns for 50/100 sand, and 4a to 4c for 20/30 sand.

## 5. CENTRIFUGE MODEL TEST RESULTS

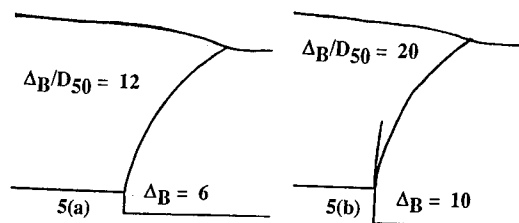
The centrifuge model test results are presented in terms of traces of the localisation development at various boundary (trap door) displacements. The localisation patterns were symmetric about the centreline of the model and hence only half the model response is shown here.

### 5.1 Test Results

For all the tests the introduction of a boundary displacement resulted in the formation and propagation of regions of localised deformation from the edges of the induced base discontinuity. For all the tests an initial localisation formed at an angle of approximately 30 degrees to the vertical, (Figures 3(a), 4(a) and 5(a)). For tests RJW01 and RJW02 a second localisation developed with continued displacement of the base. This localisation extended initially vertically from the base discontinuity, but curving out over the dropping part of the base as it continued to propagate (Figures 3(b) and 4(b)) eventually extending through to the soil surface. With continued displacement at the base a third localisation developed in tests RJW01 and RJW02 extending vertically from the base discontinuity through to the soil surface; see Figures 3(c) and 4(c) showing the final model response for these tests. During the development of multiple shear bands it was observed that the formation of secondary and tertiary localisations coincided with movement of the preceding localisation ceasing. The transition between shear band formation was quite abrupt and the soil between the localisations remained relatively undisturbed. In test RJW03, where geometric similarity was not maintained, only one localisation developed and continued to propagate through to the model surface, (Figure 5(a) and 5(b)).

## 6. NUMERICAL ANALYSIS

Numerical simulations of the model tests were performed using the finite difference package FLAC (Cundall, 1992).



Figures 5(a) and 5(b), Trace of rupture patterns for test RJW03.

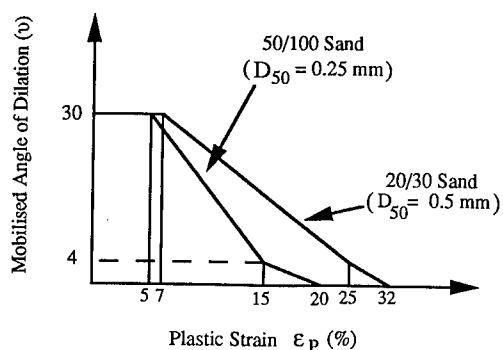


Figure 6. Variation of mobilised angle of dilation with plastic strain

## 6.1 Soil Model

The soil model used for the numerical analyses was a strain hardening post peak softening model. The advantage of this model is that it allows the user to represent arbitrary hardening and softening behaviour based on linear relationships between angles of friction and dilation with plastic strain. From a laboratory study involving direct shear testing of the two sands, approximate relationships between plastic strain and mobilised dilation were derived. These relationships were used as the basis for the linear piece wise functions of mobilised angle of dilation with plastic strain for the two sands shown in Figure 6.

## 6.2 Model Results

The numerical model results are reported here in terms of shear strain increment (ssi) at three stages of incremental base displacement.

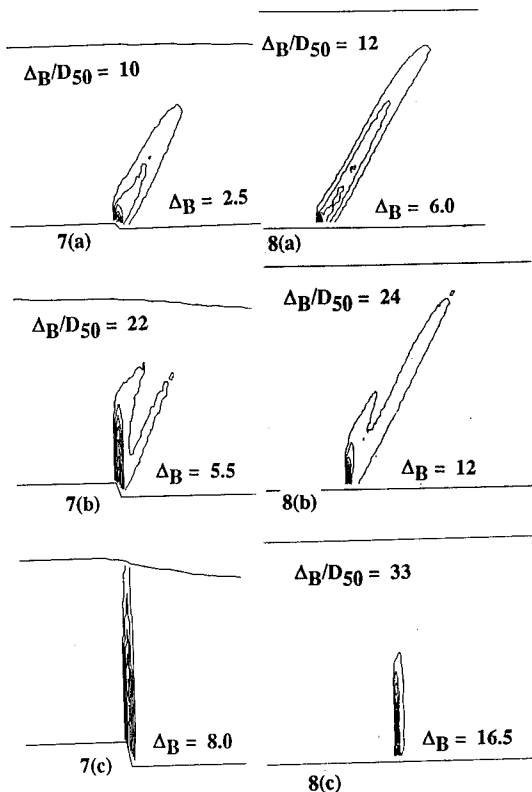
For all simulations the introduction of a

boundary discontinuity (trap door) resulted in the formation and propagation of regions of localised deformation into the overlying soil. As with the physical model tests an initial localisation developed at an inclination of about 30 degrees to the vertical, see Figures 7(a), 8(a) and 9(a). Further base translation on the numerical simulations where geometric similarity is maintained (simulating RJW01 and RJW02), shows the formation of a second rupture surface propagating vertically from the base then curving in towards the model centreline, Figures 7(b) and 8(b). The transition was quite sudden and the mesh between the two localisations remained undisturbed consistent with the physical model tests. Figures 7(c) and 8(c) shows that final orientation of the localisation is vertically above the base discontinuity with development of the previous ruptures ceasing. For the simulation where geometric similarity was not maintained (RJW03) the initial localisation shown in Figure 9(a) jumped directly to the final vertical orientation, Figure 9(b) without developing the intermediate (secondary) rupture surface.

## 7. DISCUSSION

### 7.1 Dilation and Stress Level

The direction in which a localisation develops is dependent on the applied displacement and the associated values of dilation mobilised within the localisation. It has been shown, (Bolton, 1986) that increasing the stress level results in decreasing values of measured dilation in shear tests. It has also been shown that increasing stress levels results in increased relative displacements required to reach critical state conditions associated with zero dilation, (Stone, 1988). The attainment of critical state conditions along an initial localisation results in kinematic instability with the associated boundary movements, and a new zone of localised deformation forms. The curvature of the localisations towards the model centre is a result of increasing angles of dilation with decreasing vertical stress levels. The final vertical localisation extending from the base to



Figures 7a to 7c contours of shear strain increment from FLAC simulation of RJW01; and 8a to 8c of RJW02.

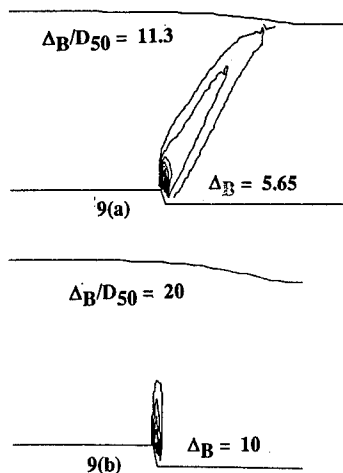
the free surface is consistent with the only permissible solution for zero angle of dilation.

## 7.2 Particle Size Effects

The generation of secondary and tertiary localisations occurs when kinematic instability occurs in an active localisation due to a reduction in the value of mobilised dilation towards the critical state. Since increasing the particle size results in increased relative vertical and horizontal displacements required to reach critical state conditions (White, 1993) then greater boundary displacements will be required to achieve critical state conditions for coarser sands.

## 8. CONCLUSIONS

The small scale model tests reported here have



Figures 9(a) and 9(b) contours of shear strain increment on FLAC analyses of RJW03.

indicated that a scale effect (in terms of particle size) is evident where localised deformation occurs. However, it is possible to maintain geometric similarity with localisation development and propagation in different sands if all the dimensions and displacements are scaled in accordance to the ratio of particle sizes; ie. the particle size can be considered an absolute scale.

The numerical analysis has shown that it is possible to implicitly include the particle size effect observed in the model tests by relating the hardening and softening response of the material to degrees of plastic strain.

## 9. References

- Bolton, M. D. (1986). The strength and dilatancy of sands, *Geotechnique* 36, No. 1 pp 65-78.
- Cundall, P.A., (1992) *FLAC User's Manual*, ITASCA Consulting Group, Inc., Minneapolis, Minnesota, U.S.A.
- Cundall, P. A. and Board, M. (1988). A microcomputer program for modelling large strain plasticity problems, *Numerical Methods in Geomechanics (Proceedings of the 6th international conference, Innsbruck, April, 1988)*, vol 3, pp. 2101-2108. Rotterdam: A. A. Balkema

- Randolph, M. F., R. J. Jewell, K. J.L. Stone and T. A. Brown (1991) Establishing a new centrifuge facility, Proc. Centrifuge 91, University of Colorado, Ed. Hon-Yim Ko, Balkema.
- Stone, K. J. L., (1988). Modelling of rupture development in soils, Ph.D Thesis, University of Cambridge.
- Stone, K. J. L. and D. M. Wood, (1992). Effects of dilatancy and particle size observed in model tests on sand, Soils and Foundations, Vol. 32, No. 4, pp. 43-57.
- Stone, K. J. L. and T. A. Brown, (1993), Simulation of ground loss in centrifuge model tests, Geotechnical testing journal, vol. 16, No. 2, June 1993, pp. 253-258
- White, R. J. (1993) Particle size effects in discontinuous soil mechanics, M.Phil Thesis, University of Western Australia.

## Behavior of suction caissons under static uplift loading

M.J. Morrison & E.C. Clukey

*Exxon Production Research Co., Houston, Tex., USA*

J. Garnier

*LCPC, Nantes, France*

**Abstract:** Results are presented from part of a comprehensive centrifuge program performed to determine the response of suction caissons when used as foundation elements for Tension Leg Platforms (TLPs). Specifically, a comparison of centrifuge and 1-g tests performed in soils having similar strength profiles is presented.

The verification program involved simulation of some earlier 1-g model tests that were performed in a natural clay deposit. The centrifuge program was performed in reconsolidated samples of the natural clay and also in Speswhite clay.

Once the 1/10th scale model suction caissons were installed, they were subjected to either static inclined uplift or, in other tests, to cyclic loading. The agreement observed between the force versus displacement relationships for the four static centrifuge tests and the results from the 1-g test validated the use of centrifuge modelling for this application. Furthermore, the tests also indicated relatively small differences in behavior between the two types of clay tested.

### 1 INTRODUCTION

One possible solution for Tension Leg Platform (TLP) foundations is a relatively new concept referred to as suction caissons.

Suction caissons, like piles, are generally cylindrical in shape but have larger diameters and much shallower penetration depths. The term "suction" refers to two different factors affecting the foundation, i.e. 1) the controlled reduction of pressure at the caisson head during the installation process and 2) the passive reduction of pressure mobilized during uplift.

Suction caisson foundation systems offer several advantages, the first of which is ease of installation. Installation involves the reduction of pressure in the caisson head, thereby creating a differential pressure. The installation can therefore rely on pumps rather than underwater pile drivers required for deepwater pile installation. This results in reduced installation time, and significant

cost savings. Also, since the final penetration depth is much shallower, the suction caisson does not have to penetrate into the deeper soil layers, making installation easier and quicker.

Once installed, the pull-out resistance comes largely from (1) a combination of self weight and ballast which may be placed on the top of the caisson, 2) a significant amount of reverse end bearing which is mobilized during uplift.

### 2 INDUSTRY EXPERIENCE

In the late 1970s to early 1980, Shell Offshore Research and Single Buoy Moorings Inc. began investigating relatively small (4 to 5m diameter by 5 to 7 m long) suction caissons for use in the North Sea (Cuckson, 1981). Several of these suction caissons were installed in the North Sea for testing or as anchorages for small mooring docks.

In the late 1980s Exxon Production Research Company (EPRCo) became involved with

these foundations when they were first proposed for the Snorre TLP in the North Sea. The Snorre foundation consists of four Concrete Foundation Templates (CFT). Each CFT consists of a tri-cluster of cells, each cell being about 17m in diameter, with skirts designed to penetrate about 12m into the seabed.

For Snorre, the static pretension forces from the hull buoyancy are resisted by the submerged weight of the CFT and the solid ballast which is placed in compartments on top of the CFT in order to avoid any long term creep effects in the form of uplift. In calm weather conditions, the soil resistance is therefore not mobilized. When the TLP is exposed to environmental forces resulting in increased tether forces, the soil bearing resistance is mobilized through skirt friction and suction under the domes (Fines et al, 1991).

EPRCo subsequently performed a study to determine the feasibility and approximate configuration of a steel caisson for use with a TLP in Gulf of Mexico (GOM) conditions. Due to differences in soil conditions, water depths, environmental loading and construction material, a significantly different foundation evolved compared to the Snorre CFTs. These differences, the conservatism used in the previous design cases, and the limited amount of experimental test data available to develop reasonable design parameters, suggested that additional testing was required before suction caissons could be adequately considered for GOM applications.

A centrifuge testing program was therefore initiated in 1989 with LCPC in France to study the behavior of a suction caisson foundation system with the approximate geometry determined from the previous feasibility study. The key technical objective of the program was to establish the efficiency and reliability of the suction mechanism in resisting applied loads, and hence provide an opportunity to reduce design conservatism and reduce both the caisson size and the amount of ballast required. The program involved both static and cyclic pull-out tests performed on single-cell and multi-cell caissons installed in

soils representative of deepwater GOM conditions (Clukey and Morrison, 1993). As part of this program, the validity of the centrifuge modelling technique needed to be verified for this particular application, and a special set of tests was therefore performed for this purpose.

### 3 CENTRIFUGE VERIFICATION TESTS

The verification program involved simulating some 1-g model tests that had been performed at an earlier time to validate the design procedures being developed for Snorre's foundation system. These field model tests (Dyvik et al, 1993) used steel caissons having a model geometry of approximately 1:13 of the prototype envisaged at that time (Figure 1), and were performed by the Norwegian Geotechnical Institute (NGI) at Lysaker, Oslo in a clay deposit considered to have properties similar to the clay at the Snorre location.

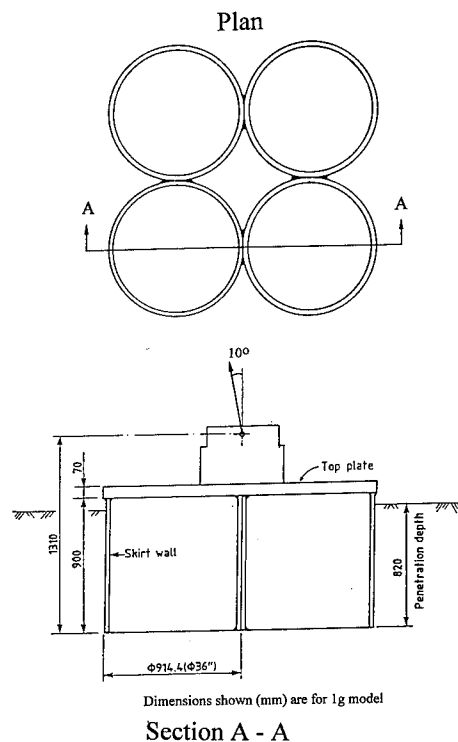


Figure 1: Model Geometry

As part of the overall centrifuge program, EPRCo contracted with LCPC to perform a series of tests simulating these earlier 1-g field model tests. These tests were performed at accelerations of 10g on a caisson having dimensions 1/10th of those of the NGI field test model. In order to evaluate the effect of soil type, these tests were performed in reconsolidated samples of both Lysaker clay (used by NGI) and Speswhite clay as routinely used in centrifuge testing and as adopted for the main centrifuge program.

As discussed in more detail in the following subsections, these tests involved installing the model caisson into the soil deposit, and then establishing its resistance to a pull out load applied at 10 degrees from vertical. Although both static and cyclic tests were performed, this paper will focus on the results from the static tests.

### 3.1 Soil conditions

Soil conditions at the Lysaker site consisted of about 1.2 m of peat and organics overlying very soft clay. For the 1-g model test performed by NGI approximately 1.8 m of overburden soil was removed from the site. In situ strengths at the Lysaker site were established from field vane tests and are shown on Figure 2. Also shown on Figure 2 are a strength profile as established by NGI from Direct Simple Shear (DSS) tests performed on recovered soil samples.

Review of these data leads to the following observations:

1. In situ field vane strengths are significantly higher than the DSS strength profile established by NGI.
2. In situ strengths at a depth of about 2m were significantly lower than those measured at 1.5 and 2.5 m. These lower strengths complicate selection of the shear strength profile to be used for evaluation of the skin friction acting on the caisson.

The strength profile selected for modelling in the centrifuge program is shown in Figure 2 as a shaded area. This profile was weighted towards the in situ vane strengths rather than

the DSS tests and corresponds to a linear increase in strength of 2 kPa/m.

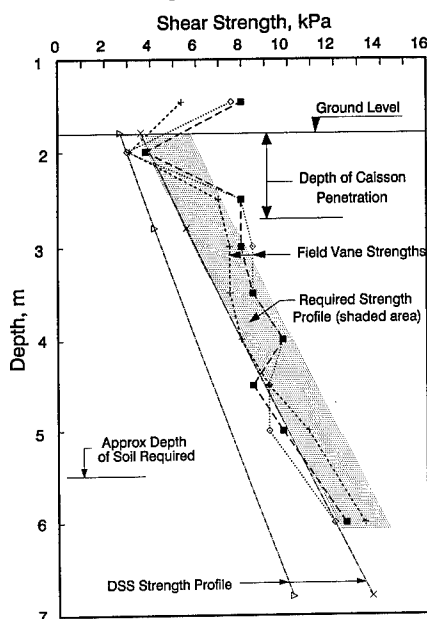


Figure 2: In Situ Strengths

LCPC prepared the centrifuge soil samples by placing layers of slurry into a 90-cm diameter drum and imposing vertical pressures (applied by an air pressure controlled ram) having magnitudes as established from preliminary trials. Following initial consolidation, the drum was then moved to the centrifuge for final self-weight consolidation. During preliminary preparation of the Lysaker clay specimens, it was found that the coefficient of consolidation of the Lysaker clay was only about one-third that of Speswhite clay, such that longer sample preparation times were required.

Sample strengths were established from cone penetrometer tests performed in flight at 10 g both immediately before and after each pull-out test. Specifically, strengths were evaluated from the penetrometer results and correlations were established between vane tests and penetrometer values. From the main centrifuge program on Speswhite clay, it was found that the ratio of the cone resistance,  $q_c$ , to the undrained shear strength,  $S_u$ , was about

18.5 whereas this ratio was subsequently shown to be 14.5 for Lysaker clay.

A compilation of the strength profiles achieved for the four static centrifuge tests is presented in Figure 3.

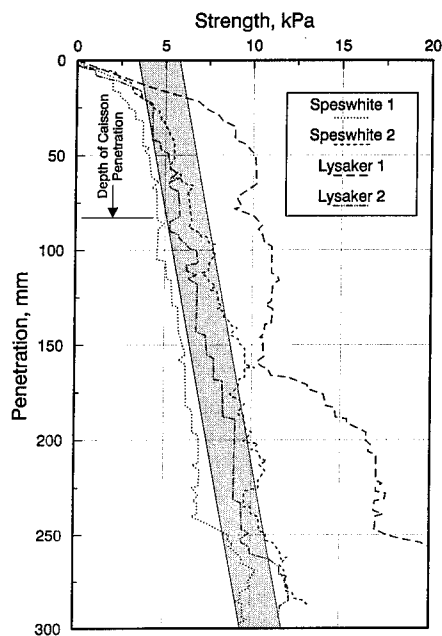


Figure 3: Shear Strength Profiles

The profile from the first test performed on Speswhite clay lies close to the lower side of the desired profile, while the profile for the test on Lysaker clay was significantly on the high side of the desired profile. In order to provide a better comparison on the effect of the soil type, it was decided to perform two additional tests having profiles on the opposite side of the band from those achieved during the first tests. As shown in Figure 3, the strength profile in the second test on Speswhite fell within the desired profile over the depth of penetration of the caisson, and was close to the upper bound of the desired profile below the bottom of the caisson. The profile in the second test on Lysaker fell within the desired profile, and it was therefore concluded that the influence of soil strength and soil type had been adequately bounded by these tests.

### 3.2 Test procedures

The caisson model, having overall dimensions of 18.8 cm by 9 cm depth, was made from stainless steel. The surface area to be embedded in the soil was roughened with abrasive paper in order to provide caisson roughness similar to that from the 1-g model program.

The test set-up (Figure 4) allowed the caisson to be installed and subsequently loaded without stopping the centrifuge to change out any of the equipment.

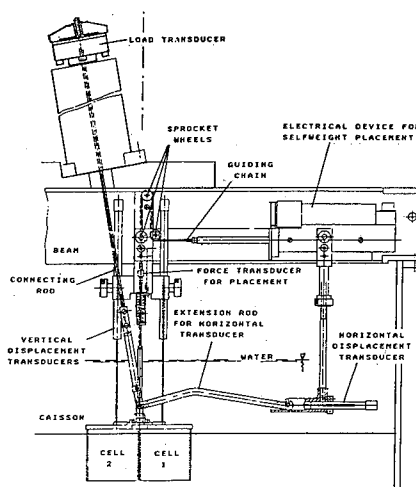


Figure 4: Equipment used in Centrifuge Tests

The sequence of operations was as follows:

1. After preliminary consolidation in the laboratory, the clay was reconsolidated at 10 g for a period of 24 hours giving a degree of consolidation in excess of 90%. In fact, due to the consolidation pressures employed in the laboratory (at 1-g), the top part of the sample would be swelling in the centrifuge (under self-weight consolidation at 10-g), whereas the lower part was consolidating.
2. Installation of the caisson at 10 g under self weight followed by application of suction.
3. Rotation in the centrifuge for a further 2.25 hours in order to balance external and internal pore pressures in the caisson, and to allow dissipation of pore pressures due to installation of the caisson.
4. Perform cone penetrometer test in flight to establish the strength profile.



5. Loading of the caisson using a servo-activated hydraulic jack.

In order to provide comprehensive information on caisson and soil behavior during the different phases of the test, instrumentation was included allowing monitoring of:

1. Load, displacement (horizontal and vertical) and rotation of the caisson.
2. Position of the soil plug inside the caisson.
3. Water pressure in the cells comprising the caisson.
4. Pore pressure in the soil at three points.

In all, a total of seventeen different measurements were made during the course of these tests.

The caisson was initially allowed to penetrate the soil under its own self-weight, reaching from 79% to 97% of the required penetration of about 82 mm in this manner. During this phase, the caisson head valves were kept open to prevent build-up of pressure in the head. The valves were then closed and the pressure in the cells was then reduced until the pressure differential between the outside and the inside caused the caisson to reach the final penetration. No problems were encountered with verticality during installation.

Prior to starting the loading phase, a period of 2.25 hours was allowed for dissipation of pore pressures created by installation. This simulated NGI's 1-g tests in which a nine-day period was allowed to elapse between installation and loading. Loading then commenced by application of tension via a cable connected to the servo-controlled hydraulic jack, which was aligned to apply the load at an inclination angle of 10 degrees (from vertical). Since the tests were intended to simulate undrained conditions, the loading was applied relatively quickly, with the time to reach peak load typically being of the order of about two minutes. Load was applied until fairly large displacements (corresponding to 15% to 30% of the caisson height) were achieved. Displacement of the caisson and pore pressures in the caisson cells and soil were monitored throughout this process. Soil

displacements could not be monitored but attempts were made to identify and map the main failure surface by using a colored spaghetti which had been inserted into the soil.

### 3.3 Test results

The combined results from all four static tests are presented in Figure 5 as curves of force versus displacement.

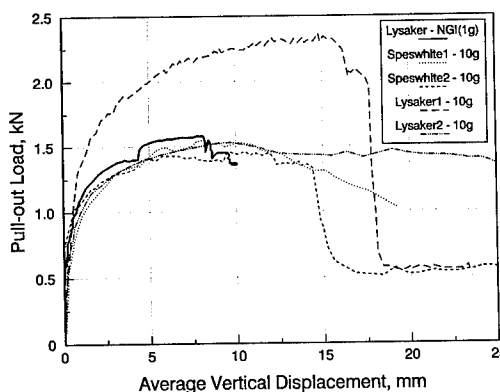


Figure 5: Results of Static Pull-out Tests

With the exception of the centrifuge test performed on the Lysaker clay having the higher strength profile, the results display very good similarity. Also included in Figure 5 are the results from the static model test performed by NGI at 1 g (scaled to the centrifuge units). It will be noted that, for the soil strengths within or close to the desired range which was considered representative of the field conditions, there is very good agreement between the results of the tests performed at 1 g and 10 g.

Pore pressures were measured in the cells comprising the caisson and in the soil at and below the tip of the caisson. Measurements of changes of pore pressure in the cells during pull-out have been categorized according to the cell location (cell one experiences the greatest uplift displacement), and are presented in Figure 6 as curves of changes of pore pressure versus average vertical displacement. Due to failure of a

solenoid value, no suction was mobilized in cell two during the second Speswhite test.

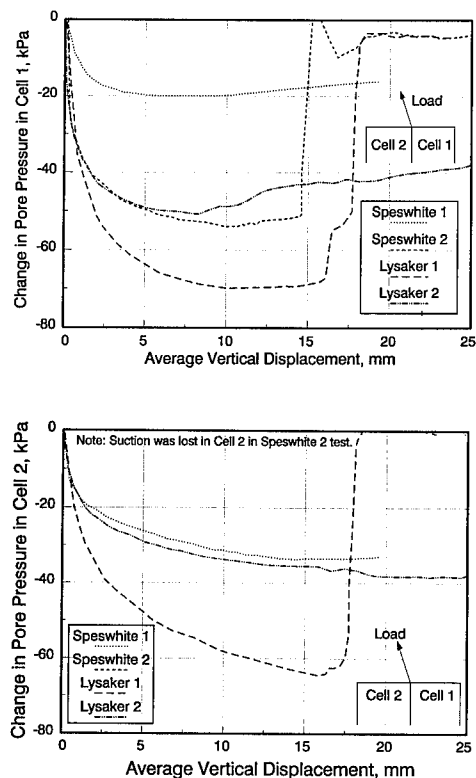


Figure 6: Pore Pressure Changes

The following observations can be made:

1. Changes in pore pressure were higher in cell one than in cell two in two of the three cases for which full results were obtained. This would be expected because, due to the direction of loading, the upward vertical displacements were higher in cell one than in cell two, and results are plotted here in terms of average (or overall) vertical displacement. The apparently opposite trend observed in the first test performed on Speswhite clay seems most likely attributable to a problem with the transducer.
2. Suction pressures in the first test with Lysaker clay were higher than those observed in the other tests. This is consistent with the significantly higher strength and higher pull-out load that was observed in this test.

3. With the exception of the higher suction pressure observed in the first test on Lysaker (and the questionable value observed on one transducer in the first test on Speswhite clay), the results show consistent trends and similar values.

## CONCLUSIONS

The agreement observed between the force versus displacement relationships for the three centrifuge tests having similar strength profiles and the results from the 1-g model test performed by NGI strengthen the credibility of using centrifuge modelling for this application. In addition, initial evaluations also indicate that differences in behavior observed between the two types of clay tested were small. This is important because it improves confidence in generalizing the results derived from centrifuge tests performed on Speswhite clay to other natural clay deposits. Finally, the efficiency of centrifuge testing should be emphasized. Once the set-up is developed, additional tests can be conducted relatively rapidly and inexpensively.

## ACKNOWLEDGEMENTS

The permission of the partners in the Snorre project to allow publication of their data in this paper is gratefully acknowledged.

## REFERENCES

- Clukey, E.C. and Morrison, M.J. 1993. A Centrifuge and Analytical Study to Evaluate Suction Caissons for TLP Applications in the Gulf of Mexico. *Proc. ASCE Conference on Foundations*, Dallas, TX.
- Cuckson, J. 1981. The Suction Pile Finds its Place. *Offshore Engineer*, April, p80-81.
- Dyvik, R., Andersen, K. H., Hansen, B.H., and Christophersen, H.P. 1993. Field Tests of Anchors in Clay. I: Description, *ASCE Geotechnical Journal*, October, p 1515.
- Fines, S. & Stove, O.J. 1991. Snorre TLP Tethers and Foundations. Paper 6623, *Proc. 23rd Annual OTC*, Houston, TX.

## Displacement of gravity caisson resting on sand key

C.F. Leung

*Department of Civil Engineering, National University of Singapore, Singapore*

E. Khoo & A.C. Toh

*Engineering Division, Port of Singapore Authority, Singapore*

**ABSTRACT:** Model tests were conducted to investigate the vertical and horizontal displacements of gravity caissons under anticipated prototype loading conditions in the field. Test data on immediate and service-loading caisson displacements were obtained for caissons resting on sand keys of various densities and thickness. The results showed that there would be significant reduction in caisson displacements if the sand relative density increased from 40% to 70% or if the required sand key thickness decreased from 15 m to 4 m.

### 1 INTRODUCTION

Gravity caissons are used as wharf structures in many parts of the world. Such a caisson is a box-like structure which is sunk through water to the prescribed founding depth and subsequently becomes an integral part of the permanent infrastructure. Fig. 1 shows a typical sequence of construction for wharf structures made up of gravity caissons. There are several stages which impose loadings onto the caisson foundation system. The first stage consists of floating, towing, aligning and infilling the caisson to form a row of caissons. The caisson's self weight is initially resisted by buoyancy and then subsequently sunk by infilling with water to the prescribed level, see Fig. 1 (c). The caisson cells are then filled with sand. The second stage is the sand backfilling behind the caisson for reclamation, see Fig. 1(d). The third stage includes the service loadings on the caisson which comprise live loads acting on top of the caisson and live loads as well as soil improvement surcharge loads on the backfill behind the caisson.

In the past few years, the Port of Singapore Authority had considered using gravity caissons as wharf structures for its proposed Third Container Terminal. Since the operation of heavy port machinery requires ground movement on and behind the caisson to be kept within strict limits, an important aspect which needs to be addressed is the settlement and ground displacement on and behind the caisson. In view of

this concern, a joint Port of Singapore Authority-National University of Singapore research study has been in force since early 1992 to investigate the vertical and horizontal displacements of gravity caissons supported on sand keys of various densities and thickness. The results of the joint study are presented in this paper.

### 2 EXPERIMENTAL SETUP

Terashi et al. (1990) conducted centrifuge model tests on caissons resting on sand compaction piles. Load actuators were employed to simulate the imposition of vertical and horizontal loads on the caisson. However, this setup was not able to simulate correctly the backfilling process which simultaneously imposes vertical and horizontal pressures on the foundation soil and caisson, respectively. Khoo et al. (1993) conducted tests on a gravity caisson resting on a sand key. Some improvements in simulating the backfilling process were made by adopting the use of a latex bag containing ballast liquid to exert these two pressures in the test model. However, the model setup was still not perfect as the coefficient of lateral pressure is 1 for liquid and this does not simulate the actual field situation. In addition, it was not possible to simulate the frictional interface contact between the sand backfill and the caisson wall. In the present work, the simulation of backfill process is further

improved by means of an in-flight sand hopper.

The tests were conducted at 100g on the National University of Singapore geotechnical centrifuge whose features have been described in detail by Lee et al. (1991). To simulate a plane-strain condition, the model container has internal dimensions of 570 mm length, 540 mm high and a narrow width of 200 mm. The container is made of stainless steel with one perspex face. In the preliminary study, it was found that the test results were greatly affected by the friction between the steel-sand and perspex-sand interfaces. A systematic and careful study was hence conducted to reduce this side friction, reported by Khoo et al. (1994). It was established that such side friction can be greatly reduced by lining the internal surfaces of the container with greased polyethylene sheets.

Fig. 2 shows a typical experimental setup. The sand employed is fine sand with a minimum void ratio = 0.64, maximum void ratio = 0.99,  $D_{10}$  = 0.23 mm and coefficient of uniformity = 1.83. The sandbed was prepared by pluviating sand through water and then flushing with a strong jet of water to bring the sand particles into suspension in the water thereby eliminating all the shear bond stresses between the particles. Time was allowed for the suspended sand particles to settle gradually back to the bottom. The sand was then compacted in layers to the desirable relative density (RD) to the final prescribed height of 150 mm on a vibrating table. The simulated sand key thickness at 100g is hence 15 m which is the worst case expected at the project site.

The model caisson with external dimensions of 180 mm width, 200 mm length and 210 mm height is made out of composite steel and concrete. A steel box with a wall thickness of 3 mm and a base thickness of 4 mm is encased externally by 10 mm of concrete. The external surface of concrete serves to maintain the necessary interface properties of sand and concrete contact. The internal steel box serves to provide the rigidity and strength as well as holding the ballast liquid. The model caisson was then carefully placed at the desirable location on the sandbed. A polyethylene gasket was then placed behind the caisson to prevent the sand backfill from falling into the gap between the caisson and the container boundaries. De-aired water was then siphoned into the model container until the water level reached 160 mm above the top of the sandbed.

The model container was then carefully transported and placed on the centrifuge test platform. The assembly of displacement transducers and their respective gantries were secured in appropriate positions as shown in Fig. 2. Two drained tubes, which

are connected to storage containers placed on the centrifuge arm, were also installed. During the tests, ballast liquid in the form of Zinc Chloride (ZnCl) solution, would be drained into the model caisson through the drain tubes to simulate the various vertical loadings imposed on the caisson. ZnCl is commonly used as the ballast liquid (see for example Bolton et al., 1988) as the unit weight of the solution of different concentration ranges from 14 kN/m<sup>3</sup> to 20 kN/m<sup>3</sup> which is similar to those of soils. Miniature pressure transducers were placed inside the caisson to monitor the height and hence the weight of the ballast liquid.

The sand hopper assembly consisting of hopper and deflector plates was then attached onto the top of the model container just behind the caisson. This assembly enabled the in-flight formation of backfill behind the caisson. A systematic study has also been conducted by varying the size of trap holes and position and arrangement of deflector plates to ensure that the final backfill surface is even and of uniform unit weight. Sand hoppers are also commonly used in centrifuge tests, see for example, Bolton and Sun (1991). The final preparation stage involves the fixing of a micro-camera to a supporting frame directly in front of the perspex window to enable the entire experiment to be videoed.

### 3 EXPERIMENTAL PROCEDURE

The three main activities in the simulation of construction and loading sequence are: (a) infilling of the caisson, (b) backfill behind caisson and (c) live loads acting directly on the caisson. One good way to explain the simulation procedure is to follow the sequence of events observed from a typical test. Fig. 3 shows the variations of caisson pressure, vertical and horizontal displacements versus time for a test whose sandbed has a RD of 50%. The average caisson pressure is derived from the self weight of caisson plus weight of ballast liquid divided by the caisson cross-sectional area.

From time A to B [stage AB in Fig. 3], the model was subjected to centrifuge acceleration from rest to 100g field. The changes in the vertical displacement were due to the changes in the self weight of the empty caisson and the movement of the transducer gantries during centrifuge spin-up. The change in horizontal displacement was entirely due to the movement of the transducer gantry as no lateral movement was expected at this stage. Once the model is subjected to 100g field at time B, the solenoid

valve of one of the storage containers was electronically opened to release ballast liquid into the model caisson to simulate the sand infill within the caisson. Thus there is a rapid increase in caisson pressure and vertical caisson displacement from time B to C [stage BC in Fig. 3]. The video pictures revealed that sand infill has been completed by time C. However, further vertical caisson movement was noted after time C indicating possible creep in the sand key. Creep or aging of sand was noted by Mitchell (1984) in a field blast densification test on sand. Schmertmann (1991) suggested that a possible mechanism of ageing or creep could be due to small slippage of sand particles that produce a significant net increase in particle-to-particle interlock. This results in rearrangement of soil particles into slightly denser particulate structures. Schmertmann also observed that sand with lower density would cause more aging particle movements in a given time. There is practically no horizontal displacement from time B to D as the caisson was only subjected to vertical loading.

At time D, the hydraulic piston was electronically powered on to release sand contained within the hopper into the model container directly behind the caisson to simulate the backfill process. The video pictures revealed that the height of backfill rose slowly but non-uniformly with more sand adjacent to the caisson. After numerous trials, the angle of the deflector plates and the amount of sand in each compartment of the hopper were predetermined to achieve a final uniform height of 250 mm of backfill. This is equivalent to a prototype backfill height of 21 m plus a surcharge load of 60 kPa. The effect of the backfill was clearly reflected in the significant horizontal displacements of the caisson, as shown in stage DE of Fig. 3. In addition, the transducers situated at the seaward side of the caisson registered greater settlement than those situated at the leeward side. This implied that the caisson had settled and tilted forward under the action of the backfill. This tilting movement is also confirmed by the higher magnitude of horizontal displacement registered by transducer H2 as compared to that of H1 which was placed at a lower elevation. By assuming that the caisson tilts about its toe, the horizontal movements can be separated into tilting and sliding movements respectively.

At time F, additional ballast liquid was released into the caisson through the second drain tube to simulate live loading on the caisson. As illustrated in stage FG in Fig. 3, this additional load caused a prescribed increase in the caisson pressure from 410 kPa to 480 kPa. At this stage, the vertical displacement transducers registered further settlement with the

highest settlement again observed at the caisson toe. Concurrently, H1 and H2 also showed significant horizontal movement as shown in Fig 3(c). This implies that the caisson tilted forward again under the influence of this 'live' load. Although the primary effect of vertical load was to induce settlement, it had also a secondary effect of inducing the caisson to tilt forward slightly. Such phenomenon was probably attributed to the localised soil plasticity around the caisson toe which had been subjected to considerably higher loading pressure due to the backfill and to the lack of overburden on the sand key directly in front of the caisson toe. Deceleration of the centrifuge from 100g to 1g took place at time H which was confirmed by the rapid decrease in caisson pressure at stage HI shown in Fig. 3(a).

To conduct a detailed analysis on the load-displacement behaviour of the caisson, the results are re-plotted in Fig 4 to depict the infill, backfill and live load responses of the caisson. Fig 4(a) shows that the caisson settled uniformly during the infilling and the load-settlement response was linear. It should be noted that the initial zero datum of the vertical displacement is not strictly correct because there is already a slight effective bearing stress acting on the sand at 100g due to the increase in self weight of the empty caisson during centrifuge spin-up. This stress would have caused the foundation to settle somewhat. The magnitude of this settlement may be estimated by extrapolation of the linear load-settlement curve. Fig 4(b) shows the plot of caisson horizontal displacement with respect to time. The time variable was chosen because it was not possible to determine the horizontal earth pressure exerted on the caisson back-wall due to the non-uniform sand height during the sand filling process. Both Fig 4(b) and 4(c) show that the settlement at the caisson toe was significantly larger than that at the caisson heel. This behaviour suggested that the caisson toe is experiencing the maximum stress at the last two stages.

#### 4 EFFECT OF DENSITY OF SAND KEY

Hydraulic sandfilling usually results in a rather loose sandbed at a RD of 35% to 40%. Underwater densification of sandbed is economically feasible up to a limiting RD of 65% after which the incremental densification cost becomes prohibitive. In view of this, tests were carried out to examine the displacement of caisson supported on sand keys with RD ranging from 40% to 70%.

Fig. 5 summarises the maximum vertical and

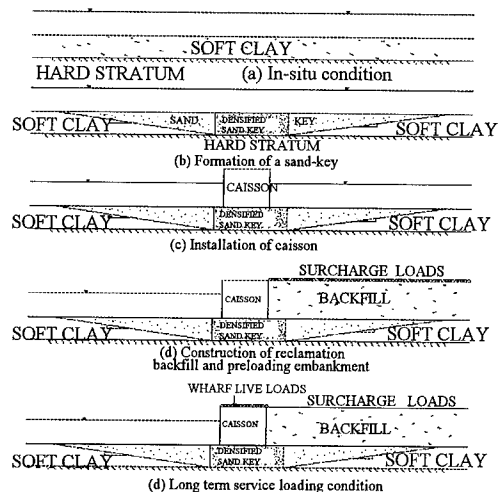


Fig 1 : Schematic of changes to soil conditions during the construction of caisson

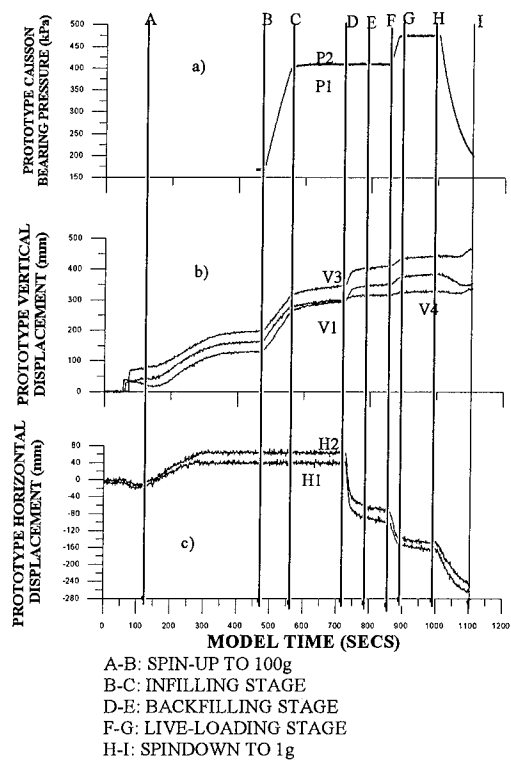
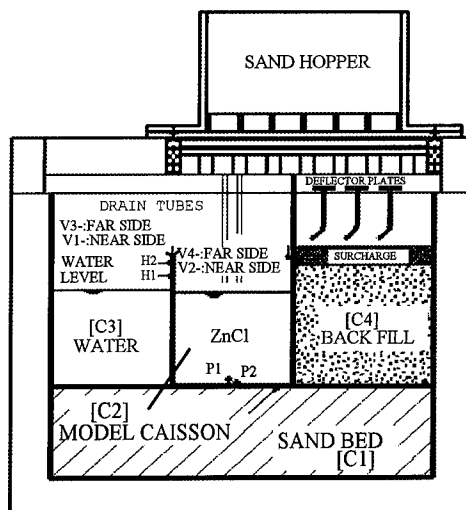


Fig 3 : Time Records of Prototype Response (Relative Density = 50%)



P : PRESSURE TRANSDUCER  
V : VERTICAL DISPLACEMENT TRANSDUCER  
H : HORIZONTAL DISPLACEMENT TRANSDUCER

Fig 2 : Typical Setup of Centrifuge Test

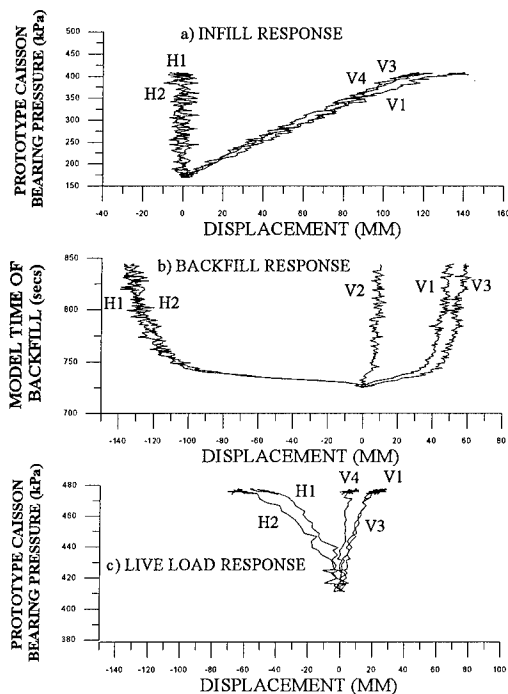


Fig 4 : Prototype Response at various construction stages (Relative Density = 50%)

horizontal displacements of the caisson at various construction stages for caissons supported on sand of various RD. It was evident that a significant amount of vertical caisson settlement would occur during the infilling and backfilling stages. The magnitude of vertical settlement at the end of the infilling stage ranging from 78 mm to 148 mm for RD ranged from 70% to 40%, respectively. At the end of the sand backfilling stage, the caisson further settled by 21 mm to 68 mm and moved in the seaward direction by 60 mm to 98 mm for the range of RD under study. At the end of the live loading stage, the caisson further settled by 17 mm to 29 mm and moved in the seaward direction by 104 mm to 118 mm. The magnitudes of caisson displacements are comparable to the field displacements reported by Sehested et al. (1989) on caissons resting on 3-m and 6-m rock sill underlain by stiff clay. They noted that the settlement ranged from about 100 mm to 350 mm after sand infilling of caisson. After sand backfilling, the additional caisson settlements ranged from 60 mm to 100 mm and the horizontal caisson displacements were recorded to range from 31 mm to 307 mm.

The caisson movements experienced during the infilling and backfilling stages were relatively large. However, as long as the displacements are immediate in nature, adjustments to the final level of the caisson wharf structure can easily be made in the construction of the decking beams and pavements to account for these movements. Thus the primary concern is centred on the caisson movements upon live loading as it would now be more difficult to implement adjustments to maintain the strict limit required by the operation of heavy port machinery. The additional caisson movements during the live loading stage were relatively small as the maximum incremental caisson settlement was less than 30 mm.

The trend observed in Fig 5(a) shows that the settlement of the caisson toe at various stages of construction decreases inversely with increasing RD of the sand. A significant decrease in settlement seemed to occur between RD of 60% and 70%. A similar trend was observed for the horizontal displacement of the caisson with a minor discrepancy for RD=40% for the last construction stage as shown in Fig 5(b). As suggested by the results given in Fig 5, the sandbed foundation stiffness increased as the relative density increased leading to lower incremental caisson settlement during the crucial live loading stage. Hence, it is advisable to compact the sandbed to keep the caisson displacements within acceptable limits.

## 5 EFFECT OF SAND KEY THICKNESS

In actual field conditions, the range of sand key thickness is expected to vary from 0 m to 15 m. Hence, two additional tests were conducted to investigate the effect of thickness of sand key,  $H_s$ . The tests were conducted on sand key of RD=50% and  $H_s$  of 40 mm and 90 mm, respectively. Fig. 6 summarises the maximum vertical and horizontal displacements of the caisson for different  $H_s$  at various construction stages. At the end of the live loading stage, the magnitude of final vertical settlement increased from 139 mm to 217 mm for the range of  $H_s$  from 4 m to 15 m, respectively. The corresponding range of final horizontal caisson movement ranged from 129 mm to 197 mm. These results suggested that the difference in sandbed thickness along the length of the wharves could result in differential displacements between adjacent caissons. The actual prototype condition will warrant a three-dimensional analysis as the plane strain condition is no longer valid.

## 6 CONCLUSION

A series of centrifuge model tests was performed to study the behaviour of gravity caissons resting on sand keys of various RD. The test results indicated that an increase in the RD of sandbed from 40% to 70% would result in a significant reduction in the caisson displacement. The magnitudes of immediate caisson displacements under construction loading and long term caisson displacements under service loading were observed and provided useful information for the design of gravity caissons. The second part of the study involving caisson resting on sand keys of different thickness revealed a potential problem of differential displacement between adjacent caissons.

## ACKNOWLEDGEMENT

The experiments were conducted under a joint Port of Singapore Authority - National University of Singapore (PSA-NUS) Research Collaboration Study on Caisson Foundation. The authors wish to express their appreciation to PSA for financially supporting the project and for permission to publish the paper. The valuable contribution by Dr F H Lee in the joint study is gratefully acknowledged.

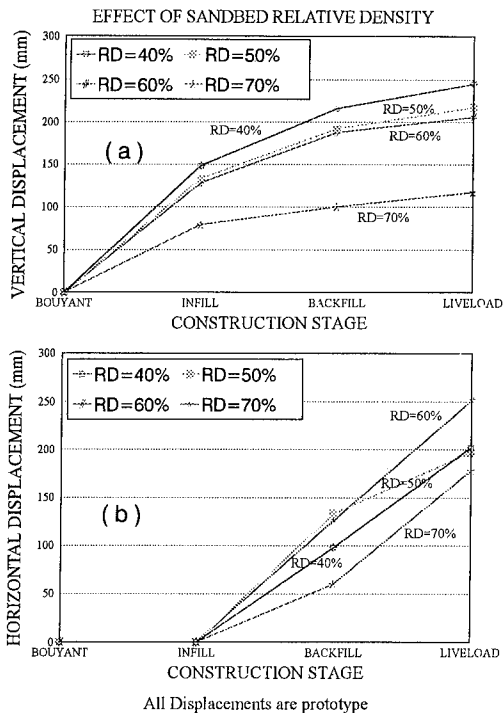


Fig 5 : Effect of Sandbed Relative density

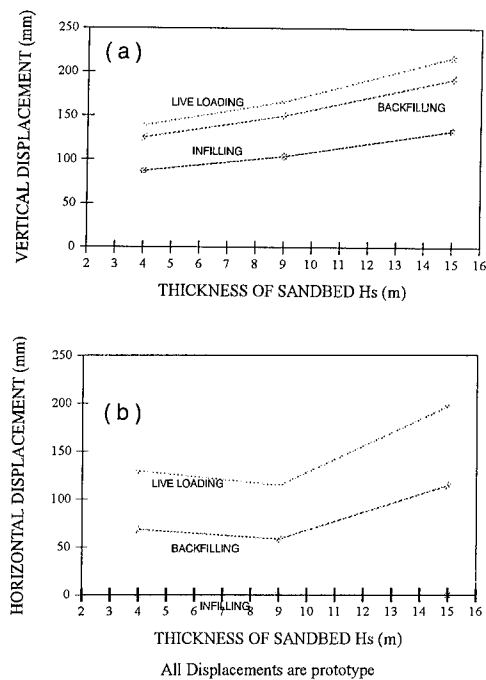


Fig 6 : Effect of varying sandbed thickness ( $H_s$ )  
(Relative Density=50%)

## REFERENCES

- Bolton, M.D., Powrie, W. & Stewart, D.I. 1988. The design of deep in-situ walls. Proc. Int. Conf. Centrifuge 88, Paris, p.405-414. Rotterdam, Balkema.
- Bolton, M.D. & Sun, H.W. 1991. The displacement of bridge abutments on clay. Proc. Int. Conf. Centrifuge 1991, Boulder, p.91-98. Rotterdam, Balkema.
- Khoo, E, Leung, C.F., Lee, F.H. & Toh, A.C. 1993. Centrifuge model study of caisson foundation. Proc. 11th Southeast Asian Geot. Conf., Singapore, p.559-564.
- Khoo, E, Okumura, T & Lee, F.H. 1994. Side friction effects in plane strain models. Proc. Int. Conf. Centrifuge 94, Singapore. Rotterdam, Balkema.
- Lee, F.H., Tan, T.S., Leung, C.F., Yong, K.Y., Karunaratne, G.P. & Lee, S.L. 1991. Development of geotechnical centrifuge facility at National University of Singapore. Proc. Int. Conf. Centrifuge 91, Boulder, p.11-17. Rotterdam, Balkema.
- Mitchell, J.K. 1986. Practical problems from surprising soil behaviour. J. of Geot. Engr, ASCE, 112:259-289.
- Schmertmann, J.H 1991. The mechanical aging of soils, J. of Geot. Engr, ASCE, 117:1288-1239.
- Sehested, K.G., Wong, N.E. & Thaw, Y.J. 1989. The design and construction of R.C. caisson deep water quay walls at Tanjong Berhala harbour - Malaysia. (Private communication)
- Terashi, M., Kitazume, M. & Minagawa, S. 1990. Bearing capacity of improved ground by sand compaction piles. Deep Foundation Improvements, Design, Construction, and Testing, ASTM STP 1089, ASTM, Philadelphia.



## Author index

- Abdulla, W.A. 797  
 Adachi, T. 509  
 Adhikary, D.P. 629  
 Aiban, S.A. 547  
 Akamoto, H. 251  
 Allard, M.A. 83, 133  
 Allersma, H.G.B. 47, 289, 325  
 Ampadu, S.K. 663  
 Arulanandan, K. 25  
 Arulmoli, K. 203  
 Astaneh, S.M.F. 221  
 Atkinson, J.H. 417
- Babasaki, R. 41  
 Bagge, G. 77, 101  
 Baker, R. 669  
 Bakir, N.E. 553  
 Bao, C.G. 521  
 Bezuijen, A. 681  
 Bloomquist, D. 437, 479  
 Bolton, M.D. 101, 587, 719  
 Bransby, F. 491  
 Broers, H. 567  
 Brownell, K.C. 177, 313, 331
- Campbell, R.G. 405  
 Canepa, Y. 553  
 Carey, J.M. 759  
 Chambon, P. 705, 713  
 Chan, E.S. 183  
 Charlie, W.A. 331  
 Chin, C.Y. 719  
 Clark, J.I. 57, 739, 803  
 Clausen, J. 479  
 Clukey, E.C. 823  
 Collison, C.H. 121  
 Cooke, B. 387, 411  
 Corté, J.F. 63, 77  
 Craig, W.H. 363, 561, 759
- Dangla, P. 705  
 Davies, M.C.R. 319  
 Davis, B.C. 809  
 de Nicola, A. 473  
 De, A. 301, 375  
 Dean, E.T.R. 121
- Dickin, E.A. 443, 527  
 Dobry, R. 139, 227  
 Dou, Y. 69  
 Du, Y. 35
- Elgamal, A.-W. 139  
 Esquivel, E.R. 89  
 Evans, D.C. 381
- Fagan, M. 25  
 Fahey, M. 773  
 Favraud, C. 503  
 Feld, T. 437  
 Fiegel, G.L. 145  
 Finnie, I.M.S. 535  
 Fioravante, V. 455  
 Foxworthy, J.E. 203  
 Fragaszy, R.J. 177, 313  
 Frydman, S. 669  
 Fujii, T. 791
- Garnier, J. 101, 503, 553, 713, 823  
 Gobert, A.T. 277  
 Goh, K.L. 109  
 Goodings, D.J. 393, 623, 797  
 Gopal Madabhushi, S.P. 127  
 Goto, Y. 169  
 Grundhoff, T. 497  
 Gui, M. 77  
 Guzina, B.B. 271
- Hagiwara, T. 791  
 Han, L. 35  
 Han, S.H. 635  
 Hanayasu, S. 663  
 Hayashi, H. 257  
 Hellawell, E.E. 357  
 Higuchi, Y. 151  
 Hiro-oka, A. 13, 575, 649  
 Hjortnæs-Pedersen, A.G.I. 83, 567  
 Hollopeter, C.A. 177  
 Honda, M. 257  
 Horii, N. 663  
 Horikoshi, K. 449  
 Hotta, H. 687  
 Hsu, Y.S. 121
- Huat, B.B.K. 561  
 Hudson, M. 145  
 Hurd, J.O. 745
- Idriss, I.M. 145, 169  
 Iizuka, E. 197  
 Imamura, S. 699  
 Inatomi, T. 197
- Jagannath, S.V. 203  
 James, R.G. 121  
 Jamiolkowski, M. 455  
 Javenmard, M. 733  
 Jessberger, H.L. 95, 101, 265, 307, 497, 705  
 Jewell, R.J. 629, 817  
 Jia, P. 35  
 Jiang-Dong Chang 809  
 Jin, P.F. 53  
 Jing, P. 69  
 Jing, S.T. 581  
 Jun Zhang 593
- Kantartzi, C. 655  
 Katakami, N. 617  
 Katoh, Y. 431  
 Kawasaki, K. 151, 779  
 Kazama, H. 687  
 Kazama, M. 197  
 Khonke, T. 169  
 Khoo, E. 115, 829  
 Kimura, M. 509  
 Kimura, T. 13, 425, 575, 649, 687  
 King, G.J.W. 515  
 Kita, K. 295  
 Kitazume, M. 485, 611  
 Ko, H.-Y. 3, 89, 221, 239, 245  
 Kobayashi, H. 509  
 Koehorst, B.A.N. 289  
 Koga, Y. 215  
 König, D. 101, 705  
 Kooijman, A.P. 325  
 Koseki, J. 215  
 Kotthaus, M. 497  
 Kremer, A. 491  
 Kubodera, I. 169

- Kusakabe, O. 541, 699  
Kutter, B.L. 145, 169, 809
- Lach, P.R. 803  
Lakeland, J. 169  
Laue, J. 77, 265  
Law, H.K. 239, 245  
Leca, E. 713  
Ledbetter, R.H. 63  
Lee, F.H. 115, 183, 461  
Lee, K.M. 675  
Leung, C.F. 461, 829  
Levacher, D. 503  
Levy, A. 669  
Li, J.K. 53  
Li, L. 727  
Li, M. 521  
Li, S.Q. 53  
Li, X.S. 169  
Liaw, C.Y. 183  
Ligtenberg, I.A.G. 289  
Limin Zhang 593  
Liu, F.D. 53  
Liu, L. 227  
Liu, W. 675  
Lu, Y.C. 719  
Luong, M.P. 283  
Lyndon, A. 443
- Mahmud, M.B. 301, 375  
Malalel, P. 467  
Manzari, M. 25  
Mao, B. 745  
Maruyama, A. 251  
Masada, T. 745  
McVay, M.C. 437, 479  
Meaney, R. 57  
Merrifield, C.M. 363, 369, 759  
Mezazigh, S. 503  
Millan, D.E.L. 57  
Mitchell, R.J. 345, 351  
Mito, K. 541, 699  
Miyabe, K. 693  
Miyajima, S. 485  
Miyake, M. 251, 431  
Mokutani, S. 425  
Morimoto, A. 509  
Morrison, M.J. 823  
Muraishi, H. 575  
Muraleetharan, K.K. 203
- Nagase, H. 239  
Nagura, K. 151  
Nai-Hsin Ting 209  
Nakatomi, T. 541  
Nazir, R. 527  
Neubecker, S.R. 765  
Ng, C.W.W. 753  
Ng, T.G. 183
- Nicolas-Font, J. 63  
Nomoto, T. 699  
Norrish, A. 163
- Ohbo, N. 257  
Okamoto, O. 295  
Okamura, M. 13, 425, 649  
Okumura, F. 425  
Okumura, T. 115  
Olen, K.L. 177, 313  
Onitsuka, K. 599, 605  
Onoue, A. 687  
Oshima, A. 337  
Out, J.G. 83
- Pak, R.Y.S. 239, 271, 277  
Park, J. 649  
Paulin, M.J. 57, 739  
Pedroni, S. 455  
Pepe, M. 785  
Perdriat, J. 63  
Petersen, S.E. 387  
Phillips, R. 57, 101  
Pilgrim, N.K. 233  
Poorooshab, F. 739  
Porbaha, A. 623  
Powrie, W. 655  
Pu, J.L. 53  
Purcell, M. 177, 313
- Raines, R.D. 467  
Randolph, M.F. 405, 449, 473, 535, 765  
Rault, G. 77  
Renzi, R. 77, 101, 785  
Richards, D.J. 655  
Rizkalla, M. 739  
Ru, L. 35
- Saitoh, K. 617  
Sargand, S.M. 745  
Sato, M. 157  
Satoh, T. 431  
Savvidou, C. 357, 381  
Scavuzzo, R. 245  
Schenkeveld, F.M. 133  
Schofield, A.N. 63, 381  
Schürmann, A. 95  
Scott, R.F. 25, 257  
Sekiguchi, H. 295  
Shan, R.G. 521  
Sharma, J.S. 587  
Siemer, Th. 307  
Skiker, A. 713  
Sluis, W. 169  
Springman, S.M. 163, 491, 753  
Steedman, R.S. 63  
Stewart, D.P. 629, 773  
Stone, K.J.L. 817  
Stratton, B.C. 345  
Sture, S. 221
- Sun, Y.S. 53  
Suzuki, K. 41  
Suzuki, Y. 41
- Taguchi, A. 791  
Takada, N. 337  
Takahashi, A. 215  
Takemura, J. 13, 425, 575, 649, 687  
Tamate, S. 663  
Tan, T.S. 25  
Tanaka, M. 151  
Taniguchi, Y. 617  
Tauscher, R.C. 169  
Taylor, R.N. 417, 779  
Taylor, T. 177, 331  
Terashi, M. 611, 617  
Ting Hu 593  
Toh, A.C. 829  
Tohda, J. 693, 727  
Townsend, F.C. 437  
Toyosawa, Y. 663  
Tuff, K. 57
- Ueno, K. 541, 699, 791
- Valsangkar, A.J. 733  
van der Schrier, J. 681  
Van Laak, P.A. 139  
van Niekerk, W.J. 325  
Vanderlinde, D. 479  
Villar, H.P. 363, 369  
Voss, H.M. 63
- Wada, M. 251, 431  
Wang, H.H. 521, 635  
Wang, W. 35  
White, R.J. 817  
Whitman, R.V. 209  
Wilkinson, K. 163  
Wittkop, R.C. 203
- Yalamanchili, V.S.R. 745  
Yamamoto, K. 605  
Yamamoto, Y. 617  
Yet, N.S. 461  
Yin, K.T. 53  
Yoshimura, H. 693, 727  
Yoshitake, S. 599  
Yue, Z.R. 581
- Zelikson, A. 467  
Zeng, X. 25, 145, 169, 191, 233  
Zhang, H.D. 643  
Zhang, S.D. 643, 675  
Zhang, X.M. 581  
Zheng, J. 257  
Zhixian You 399  
Zhu, S. 35  
Zimmie, T.F. 301, 375  
Znidarčić, D. 399

This volume contains a collection of more than hundred papers which have been contributed by centrifuge researchers all over the world. It provides a useful source of reference for the state of art and information on the applications of centrifuge modelling in various geotechnical fields.

Topics: Keynote lectures and VELACS report; Centrifuge facilities; Equipment and instrumentation for centrifuge tests; Earthquake effects; Dynamic problems; Contaminant transport and flow problems; Deep foundations; Shallow foundations; Embankments and slopes; Deep excavations and tunnels; Pipes and anchors.